IGARSS'96

1996 International Geoscience and Remote Sensing Symposium

IEEE

University of
Nebraska
Lincoln

NASA

NOAA

OFFICE OF
NAVAL RESEARCH

U.R.S.I.

Remote Sensing
for a Sustainable Future

Volume III

Burnham Yates Conference Center
Lincoln, Nebraska USA
27-31 May 1996

IGARSS'96

1996 International Geoscience and Remote Sensing Symposium

Remote Sensing
for a Sustainable Future

Volume III

19970520 019

Editor:	Tammy I. Stein
Editorial Assistant:	Jennetta Brunk
Production:	IEEE Publications

Additional copies of the IGARSS'96 Digest are available from the following source:

Institute of Electrical and Electronics Engineers, Inc.
Single Copy Sales
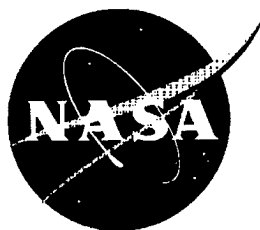445 Hoes Lane
PO Box 1331
Picataway NJ 08855-1331

IEEE

IEEE Geoscience and Remote Sensing Society

University of
Nebraska
Lincoln

University of Nebraska, Lincoln

National Aeronautics and Space Administration (NASA)
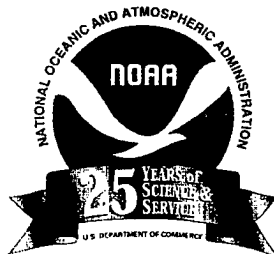
National Oceanic & Atmospheric Administration (NOAA)

Office of Naval Research (ONR)

IGARSS'96 TECHNICAL SPONSOR

U.S. National Committee
Union Radioscientifique Internationale

IGARSS'96 COOPERATIVE SPONSORS

Canon/Modern Methods Inc.

Center for Advanced Land Management Information Technologies, UNL

Center for Communication and Information Science, UNL

Center for Electro-Optics, UNL

Center for Laser Analytical Studies of Trace Gas Dynamics, UNL

Centurion International, Inc.

College of Engineering and Technology, UNL

Department of Electrical Engineering, UNL

ERDAS, Inc.

High Plains Climate Center, UNL

Li-Cor, Inc.

U.S. Geological Survey EROS Data Center
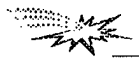
Ram Narayanan
General Chairman

Robert McIntosh
Technical Program Co-Chairman

Calvin Swift
Technical Program Co-Chairman

Barbara Emil
Finance Chairman

James Merchant
Publications Chairman

Steve Reichenbach
CD ROM Chairman

Jim Lacy
WWW Chairman

Tammy Stein
Director of Conferences and Information Services, GRSS

LOCAL HOST COMMITTEE

Dennis Alexander
Mark Anderson
Ezekiel Bahar
Blaine Blad
John Boye
Mark Cockson
Natale Ianno
Robert Maher
Robert Palmer
Donald Rundquist
Karen St. Germain
Khalid Sayood
Tracy Soukup
Elizabeth Walter-Shea
Jon Welles

Dennis Alexander, University of Nebraska-Lincoln
Werner Alpers, University of Hamburg
Mark Anderson, University of Nebraska-Lincoln
Ghassem Asrar, NASA Headquarters
Kultegin Aydin, Penn State University
Ezekiel Bahar, University of Nebraska-Lincoln
Ronald Birk, Sverdup Technology Inc.
Andrew Blanchard, University of Missouri-Columbia
Dan Cress, Sandia National Laboratories
John Curlander, Vexcel Corporation
John Curtis, US Army WES
Don Deering, NASA Goddar Space Flight Center
Craig Dobson, University of Michigan
Fernando Echavarria, University of Nebraska-Lincoln
Edwin Engman, NASA Goddard Space Flight Center
Stephen Frasier, University of Massachusetts
Prasad Gogineni, University of Kansas
Richard Gomez, US Army TEC
Bill Grant, NASA Langley
Martti Hallikainen, Helsinki University of Technology
Jim Irons, NASA Goddard Space Flight Center
Akira Ishimaru, University of Washington
Thomas Jackson, USDA Hydrology Lab
James Kalshoven, NASA Goddard Space Flight Center
Timothy Kane, Pennsylvania State University
Roger Kassebaum, Millard North High School-Omaha
Wolfgang Keydel, Institut fur Hochfrequenztechnik
Nahid Khazenie, NASA Goddard Space Flight Center
Roger Lang, George Washington University
Ellsworth LeDrew, University of Waterloo
Fuk Li, Jet Propulsion Laboratory
Charles Luther, Office of Naval Research
Harlan McKim, US Army CRREL

David McLaughlin, Northeastern University
James Mead, University of Massachusetts
Nasir Memon, Northern Illinois University
James Merchant, University of Nebraska-Lincoln
David Meyer, EROS Data Center
Wooil Moon, University of Manitoba
Richard Moore, University of Kansas
Ram Narayanan, University of Lincoln-Nebraska
Eni Njoku, Jet Propulsion Laboratory
Robert Palmer, University of Nebraska-Lincoln
William Plant, University of Washington
Jeff Plaut, Jet Propulsion Laboratory
Paul Racette, NASA Goddard Space Flight Center
John Reagan, University of Arizona
Steven Reichenbach, University of Nebraska-Lincoln
Jack Rinker, US Army TEC
Christopher Ruf, Pennsylvania State University
Donald Rundquist, University of Nebraska-Lincoln
Khalid Sayood, University of Nebraska-Lincoln
Thomas Schmugge, USDA/ARS Hydrology Laboratory
Khalid Siddiqui, SUNY College at Fredonia
Alois Sieber, Joint Research Centre-Ispra
Karen St. Germain, University of Nebraska-Lincoln
Mikio Takagi, University of Tokyo
Jim Tilton, NASA Goddard Space Flight Center
Dennis Trizna, Naval Research Labs
Leung Tsang, University of Washington
Fawwaz Ulaby, University of Michigan
Bruce Wallace, Army Research Laboratory
Elizabeth Walter-Shea, University of Nebraska-Lincoln
JoBea Way, Jet Propulsion Laboratory
Edward Westwater, NOAA/ERL/WPL
Simon Yueh, Jet Propulsion Laboratory

IGARSS'96

1996 International Geoscience and Remote Sensing Symposium

Table of Contents

NA -- Not available at time of printing.

INTERACTIVE AREA 2 -- Marine/Ocean

⚡ INTERACTIVE AREA 4 -- Geophysical Modelling
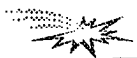
INTERACTIVE AREA 5 -- Missions and Programs

INTERACTIVE AREA 5 -- Electromagnetic Problems

INTERACTIVE AREA 6 -- Educational Initiatives

INTERACTIVE AREA 7 -- SAR Interferometry

INTERACTIVE AREA 8 -- Techniques and Instrumentation

TPES -- Youth Enhancing Space: KidSat

TPT -- Daytime Operation of Lidar Systems

TPV -- Image Segmentation

TPZ -- Microwave Remote Sensing of Vegetation

TET -- Educational Initiatives

WAAM -- Land Cover: Tropical Forests and Vegetation

WAED -- Remote Sensing of Littoral Submesoscale Processes I

WAF -- Sea Ice Remote Sensing (Models, Techniques and Applications) I

WAP -- SAR Interferometry and Geoscience Applications

WAZ -- Soil Moisture I

WPAA -- Weather Information Systems

WPCP -- Polarimetric Radiometry

WPED -- SAR Applications for Oceanography

WPES -- Educational Initiatives II

WPF -- Research Progress Under the ONR Sea Ice Electromagnetics ARI

WPP -- SAR Processor Systems and Algorithms

THAES -- Educational Initiatives III

THAH -- Emerging Technologies and Techniques

THPAA -- Passive Remote Sensing of the Environment

FAAM -- Land Cover Characterization Using BRDF Models and Data

FAAA -- Active Remote Sensing of the Lower Atmosphere

FACP -- Subsubsurface Electromagnetic Sensing at Deeper Depths

FAED -- Remote Sensing of Littoral Submesoscale Processes III

FAES -- Land Cover: Agricultural

FAP -- SAR Interferometry Processing Algorithms

FAV -- Method of Data Analysis

FAZ -- Surface Temperatures: Observations and Applications

FPCP -- Surface Scattering

FPP -- Land Cover: Inventory and Monitoring

IGARSS'96

1996 International Geoscience and Remote Sensing Symposium

Technical Papers

Kilometer-Scale Global Albedo from MODIS

Wolfgang Wanner (1), Alan H. Strahler (1), Baojin Zhang (1), and Philip Lewis (2)

(1) Center for Remote Sensing, Boston University, 725 Commonwealth Avenue, Boston, MA 02215, USA,
Tel. +1-617-353-2088, Fax +1-617-353-3200, e-mail wanner@crsa.bu.edu, alan@crsa.bu.edu, bjzhang@crsa.bu.edu
(2) Remote Sensing Unit, University College London, 26 Bedford Way, London, WC1H 0AP, UK,
Tel. +44-171-387-7050-5557, Fax +44-171-380-7565, e-mail plewis@geog.ucl.ac.uk

Abstract – Directional-hemispherical and bihemispherical spectral and broadband 1-km land albedos will be available from the MODIS BRDF/albedo product routinely starting in 1998.

Introduction

In climate and weather modeling, three key parameters related to the land surface that need to be taken into consideration are the aerodynamic roughness length, surface resistance, and albedo. Of these, we will provide bimonthly global albedo to the user community at a spatial resolution of one kilometer derived from Earth Observing System (EOS) MODIS and MISR sensor data in form of the MODIS BRDF/Albedo Product [1].

The MODIS BRDF/Albedo Product

In 1998, the cross-track scanning MODIS sensor and the along-track imaging MISR sensor will be launched on board NASA's EOS-AM-1 platform. Data from both of these sensors will be combined to rountinely produce global databases of bidirectional reflectance and albedo. Albedos and BRDF will be given in seven MODIS spectral bands centered at 460, 555, 659, 865, 1240, 1640, and 2130nm, of which the first four have corresponding MISR spectral bands. Additionally, albedos will be produced in two broadband ranges, divided by 700nm, and for the total spectral range.

The product will provide both black-sky (directional-hemispherical) and white-sky (bihemispherical) albedo, defined below. Black-sky albedo will be given parametrized for its solar-zenith angle dependence, allowing recovery of values for any solar zenith angle using a small look-up table that will be delivered with the product. Black-sky albedo will also be given explicitly for the median sun-angle of the observations, which is a function of geographic latitude and the time of year. Additionally, white-sky albedo will be provided.

The temporal resolution of the product will be 16 days (the MISR two-look repeat time). The spatial resolution will be one kilometer, allowing reliable deduction of subresolution variability of albedo for use in coarse-resolution grids (for example in GCMs) in regions of small-scale landscape heterogeneity.

The MODIS BRDF/albedo product will provide the BRDF of each pixel by giving the parameters of one of six semiempirical kernel-driven BRDF models [1,2], where each model is suited for a structurally different type of land cover and is chosen after consideration of the RMSEs found for each model in inverting the observed multiangle reflectances. The land cover class of the pixel is used for choosing a model if the angular

sampling available is deemed insufficient. Both albedo and BRDF will be delivered with a full range of quality controls providing information about the extent of angular sampling that went into the retrieval and expected error margins.

Black-Sky and Whitye-Sky Albedo

Land surface albedo provides a first-order feedback of radiation into the atmosphere. It characterizes the average or integral reflective properties of a land surface under prevailing illumination conditions as the integral ratios of upwelling and downwelling radiances, where illumination is assumed not only from the direction of the sun but the hemispherical distribution of diffuse skylight due to atmospheric aerosols is fully taken into account.

It is in this form that land surface albedo enters into theories of radiation transport in the atmosphere, such as are used in climate models and in atmospheric correction. However, due to the dependence of the downwelling irradiance and hence of the albedo on atmospheric state, this expression of albedo is of use only in applications that require knowledge of albedo at the exact time of satellite overpass.

If albedo is to be used in climate and biosphere models, it needs to be decoupled from the atmospheric state found during the satellite observations and expressed as an intrinsic surface property that may later be coupled to a different atmospheric state. The MODIS BRDF/albedo product takes this requirement into account by providing two measures of albedo that are intrinsic surface properties. Each describes one of two limiting cases: the case of absence of diffuse skylight, i.e., directional illumination from the sun alone, and the case of perfectly diffuse illumination. The former, termed "black-sky albedo" (α_{bs}), is a function of solar zenith angle. The latter, termed "white-sky albedo" (α_{ws}), is a constant. These albedos are derived as the directional-hemispherical and the bihemispherical integrals of the surface bidirectional reflectance distribution function (BRDF):

$$\alpha_{bs}(\theta_s; d\lambda) = \frac{2}{\pi} \int_0^{2\pi} \int_0^{\pi/2} \rho(\theta_s, \theta_v, \phi; d\lambda) \cos\theta_v \sin\theta_v d\theta_v d\phi,$$

$$\alpha_{ws}(d\lambda) = 2 \int_0^{\pi/2} \alpha_{bs}(\theta_s; d\lambda) \sin\theta_s \cos\theta_s d\theta_s,$$

where θ_s and θ_v are solar and view zenith angles, respectively, ϕ the relative azimuth between viewing and solar direction, $d\lambda$ is the wave band, and ρ is $\pi \cdot$BRDF.

Albedos will be derived through integration of the BRDFs obtained from inverting atmospherically corrected multiangular reflectances against BRDF models. The combined MODIS and MISR observation geometry makes such inversions feasible. The models used are semiempirical kernel-driven BRDF models employing kernel functions derived from physical considerations of theories of volume and surface scattering of light. They are the RossThin-LiSparse, the RossThick-LiSparse, the RossThin-LiDense, the RossThick, and the LiDense models, described by Wanner et al. [2]. Additional provisions are made for snow and water reflectances. These models have been shown to provide adequate fits to field-observed BRDF data [3].

NOISE SENSITIVITY ANALYSIS

The sensitivity of the albedos derived to random noise is dependent on the angular distribution of the reflectance samples obtained. This distribution is specific to the orbital and instrumental characteristics of the MODIS and MISR sensors, and varies with latitude and time of year. Using the xsatview software developed by Barnsley and Morris, we have simulated the viewing geometries encountered in each 16-day period by MODIS and MISR, and have investigated the sensitivity of various parameters to random noise. Due to the mathematical form of the BRDF models used, this analysis could be carried out analytically using a theory of deriving so-called weights of determination by Gauss (see [4], and [5] at this conference). This analysis is independent of the form of the BRDF observed.

Fig. 1 shows on the top left the dependence of expected black-sky albedo error on latitude for four different days of the year (left), where black-sky albedo has been derived at the mean sun angle during the observations and assuming the RossThick-LiSparse model as an example. A random noise RMSE in fitting of 10 percent was assumed in producing these plots, but note that the linear nature of kernel-driven models implies that the error scales linearly with the RMSE. As can be seen, the error in albedo is smaller than the observation error, signifying a stable retrieval of albedo at the prevailing sun zenith angle. There is a slight dependence on sampling latitude. On the top right, Fig. 1 shows, for different latitudes, the error expected when predicting black-sky albedo at different solar zenith angles, where the observations were made at the respective solar zenith angle giving by sampling and at different latitudes. The plot shown is for sampling on the first day of the year. All curves show best retrievals in the zenith angle range where the sun is actually to be found in the sky during the observations. Extrapolation of black-sky albedo to sun zeniths of more than about 60 degrees is problematic.

On the lower left, Fig. 1 shows the white-sky albedo error, again using the example of the RossThick-LiSparse model and assuming a 10 percent noise RMSE. Deriving white-sky albedo requires extrapolation of the BRDF to angles where no observations were made, hence the error is larger than for the black-sky albedo at mean sun angle. But still it is less than the noise level; it depends strongly on the latitude. Observe the shift of error as the zenith of the sun shifts with season.

A numerical 3D discrete ordinate radiative transfer code provided by Myneni [6] was used to generate different types of forward BRDFs. These were BRDFs of 6 land cover types (biome types), such as grassland/cereal crops, brushland, or forest. The MODIS BRDF/albedo models were then inverted for 16-day MODIS/MISR sampling as a function of latitude and time of year. The purpose of this study was to investigate success and failure of model interpolation and extrapolation under realistic sampling conditions.

Fig. 1 shows, in the middle panels, results for black-sky albedo using the example of a grassland/cereal crop BRDF and sampling on day of the year 192. The red band results are shown on the left, the NIR results on the right. Black-sky albedo was retrieved at the mean sun zenith angle of the observations and at 10 degrees solar zenith, requiring extrapolation of the observed BRDF. In the red, the absolute error is less than about 0.002 in most cases, with albedo values of typically 0.036. This gives an error of about 5 percent. The extrapolated albedos are better if the zenith extrapolated to is close to the actual mean zenith of observations. In the NIR, albedo at the mean sun zenith is mostly accurate to about 0.02, with albedos of about 0.42. This again is an accuray of about 5 percent. The accuracy of albedos extrapolated to 10 degrees solar zenith is about 10 percent.

The lower right panel shows that the accuracy of white-sky albedo retrieval varies with latitude. At favorable latitudes, it may be retrieved to within a few percent, or 0.01 in the red and 0.05 in the NIR, given true values of 0.037 and 0.44, respectively. At less favorable latitudes the errors are up to 0.02 in the red and 0.07 in the NIR, or 45 and 16 percent. There is, however, a clear bias to overestimating the white-sky albedo. Improvements of this aspect of the models used are necessary and will possibly allow improved retrievals in the future.

One should also keep in mind that these results completely depend on the assumption that the numerical forward model produces BRDFs that resemble those found in nature at all zenith angles. Accuracies of the actual product may therefore differ.

REFERENCES

[1] Strahler, A. H. et al., "MODIS BRDF/Albedo product: Algorithm Technical Basis Document", version 3.2 and update, NASA EOS MODIS Doc., 65 pp., 1995.

[2] Wanner, W., X. Li, and A. H. Strahler, "On the derivation of kernels for kernel-driven models of bidir. reflectance," J. Geophys. Res., 100, pp. 21,077–21,090, 1995.

[3] Hu, B., W. Wanner, X. Li, and A. H. Strahler, "Validation of kernel-driven semiempirical BRDF models for application to MODIS/MISR data," this conference.

[4] Whittaker, E., G. Robinson, "The Calculus of Observations," Blachie and Son, Glasgow, 397 pp., 1960.

[5] Wanner, W., P. Lewis, and J.-L. Roujean, "The influence of directional sampling on bidirectional reflectance and albedo retrieval using kernel-driven models", this conf.

[6] Myneni, R. B., Asrar, G., and F. G. Hall, "A 3D radiative transfer method for optical remote sensing of vegetated land surfaces," Rem. Sens. Env., 41, pp. 105–121, 1992.
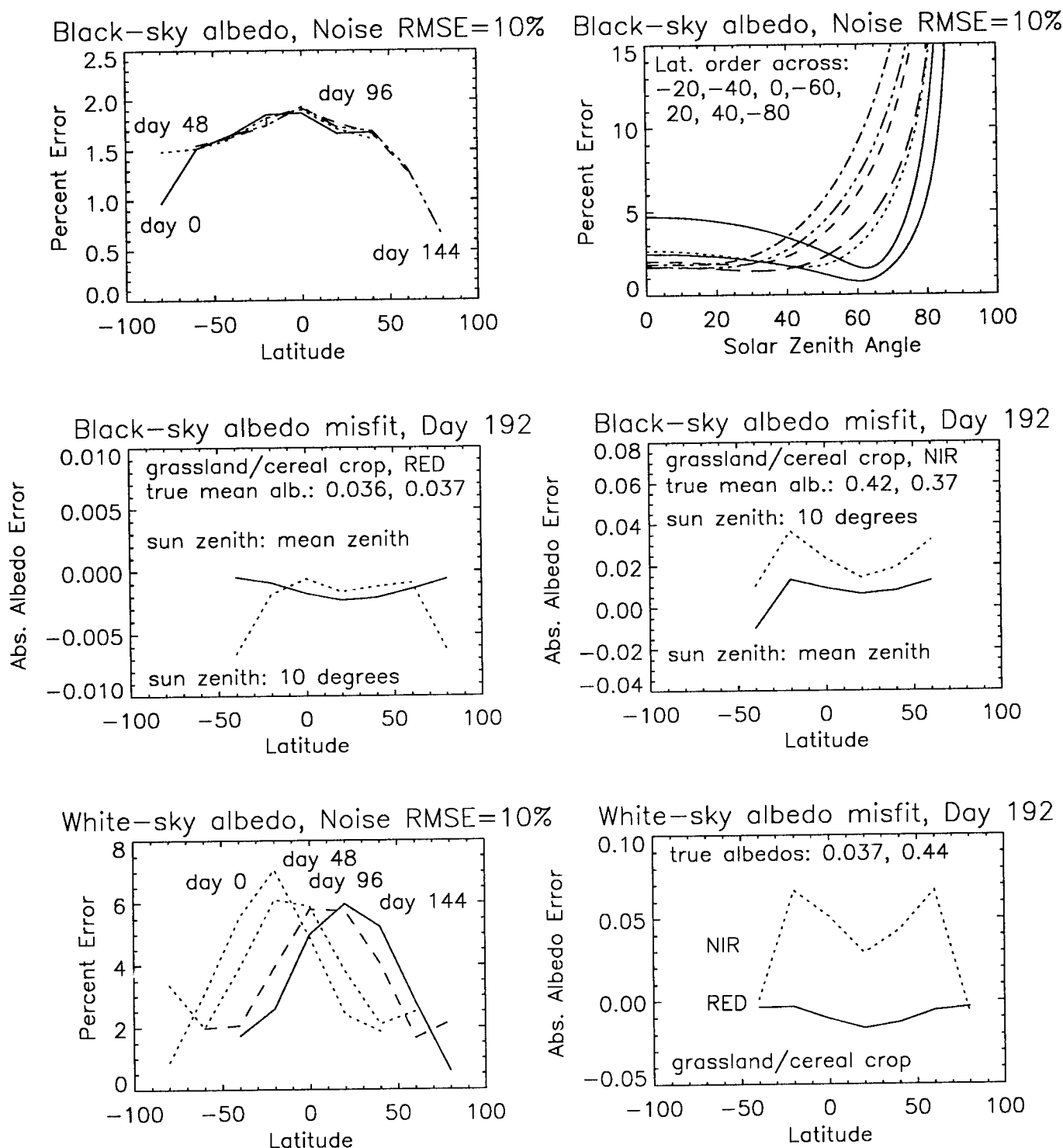
Figure 1: Expected noise and misfit errors for 16-day MODIS/MISR sampling. The noise cases assume the RossThick-LiSparse model is used, the misfit analysis uses the least-RMSE model found in inversion. In order: black-sky albedo noise error at mean sun angle of observations; black-sky albedo noise error for day of year 0; absolute black-sky albedo misfit error for day of year 192, red band, nadir and mean-sun zenith values; same for the near-infrared band; white-sky albedo noise error, white-sky albedo misfit absolute error for day 192.

The Influence of Directional Sampling on Bidirectional Reflectance and Albedo Retrieval Using Kernel-Driven Models

Wolfgang Wanner (1), Philip Lewis (2) and Jean-Louis Roujean (3)

(1) Center for Remote Sensing, Boston University, 725 Commonwealth Avenue, Boston, MA 02215, USA,
Tel. +1-617-353-2088, Fax +1-617-353-3200, e-mail wanner@crsa.bu.edu, alan@crsa.bu.edu, bjzhang@crsa.bu.edu
(2) Remote Sensing Unit, University College London, 26 Bedford Way, London, WC1H 0AP, UK,
Tel. +44-171-387-7050-5557, Fax +44-171-380-7565, e-mail plewis@geog.ucl.ac.uk
(3) Meteo France, 42 avenue Gustave Coriolis, 31057 Toulouse Cedex, France,
Tel. +33-61079343, Fax +33-61079626, e-mail roujean@meteo.fr

Abstract – The error in bidirectional reflectance and albedo retrievals due to random noise in the observed reflectances is found to be less than the noise RMSE using 16-day MODIS-MISR angular sampling.

INTRODUCTION

Global space-based retrievals of the bidirectional reflectance distribution function (BRDF) and albedo over land will be possible in the near future using the Earth Observing System's (EOS) MODIS and MISR sensors or the POLDER instrument. BRDF information is useful for normalizing satellite-acquired data sets and for deriving key surface parameters, mainly atmospherically corrected albedo for use in climate studies.

Little work, however, has been done on the sensitivity of BRDF and albedo retrievals to angular sampling patterns even though the impact of these on product accuracy is possibly substantial. With any instrument, the angular distribution of samples obtainable in a given time period will vary with geographic latitude and time of year, and be also determined by instrument and orbit characteristics. Cloud masking will further reduce the set of available angular reflectances. In this paper we evaluate in a practical case the impact of angular sampling effects on BRDF and albedo derivation.

Two effects mainly have an influence on retrieval accuracy as a function of angular sampling:
(1) Sensitivity to random noise. Analysis is carried out under the assumption that the RMSE found in inverting a model against observations is due to random "noise-like" errors in the observed reflectances, due for example to fluctuations in surface properties, misregistration, atmospheric correction errors etc.
(2) Misfit sensitivity. Analysis is carried out under the assumption that the RMSE found in inversion is due to an inherent partial inability of the model used to fit the observations even in the absence of "noise". Investigating this effect is important in view of the many assumptions that are commonly made in operationally feasible BRDF models.

In this paper, we focus on the noise sensitivity analysis alone, although the misfit analysis is of equal importance (selected results are presented in the paper Wanner et al. [1] at this conference). We study the behavior of semiempirical BRDF models under conditions of sampling by MODIS and MISR, and how the semiempirical Rahman model [2] behaves under the same circumstances.

THE EXPERIMENT

We here investigate sampling effects with respect to the MODIS BRDF/albedo product, using the sampling patterns and BRDF models characterizing it. The product is slated for production at a spatial resolution of one kilometer once every 16 days and in seven spectral bands from combined MODIS-AM and MISR data starting in 1998. The MODIS-AM sensor is an across-track imager with a swath width of 2330km, and a repeat rate shorter than 2 days (mostly shorter than 1 day). MISR is an along-track imager with a swath width of 364km using four fore-, four aft- and one nadir-pointing camera. The two-look repeat rate is 16 days. In this time, each sensor produces a string of observations across the viewing hemisphere with rather constant relative azimuth and solar zenith angles. The two strings from the two instruments are nearly orthogonal; their respective azimuthal distance from the principal plane varies with latitude and time of year, as does the mean solar zenith of the observations and the number of observations from MODIS.

The analysis was carried out for the BRDF models that are scheduled for use in the MODIS BRDF/albedo product: the RossThick-LiSparse, RossThin-LiSparse, RossThin-LiDense, RossThick and LiDense semiempirical kernel-driven BRDF models [3]. These are capable of modelling a wide variety of volume and surface scattering behavior and which will be employed depending on the scattering behavior observed.

NOISE SENSITIVITY OF KERNEL-DRIVEN MODELS

The behavior of kernel-driven linear models under the conditions of limited and varying angular sampling can be studied analytically due to the mathematical form of these models. It is given by the the so-called "weights of determination", calculated using theory that originates with Gauss [4]. Kernel-driven models give the reflectance R in form of a sum, $R = \sum f_i k_i$, where f_i are the model parameters and k_i are mathematical functions ("kernels") giving basic BRDF shapes depending only on sampling geometry. The expected error in a term u given by a linear combination of model parameters, $u = \sum f_i U_i$ (e.g., R itself at a given combination of angles, or integrals of the BRDF such as directional and diffuse albedo), is given by $\epsilon_u = e/\sqrt{w_u}$, where e is the estimate of standard error in the observed data (approximated by the RMSE in model fitting), and $1/w_u$ is the weight of determination of term u under the sampling considered. This weight is given through

$1/w_u = [U]^T[M^{-1}][U]$, where U is a vector composed of the terms U_i and M^{-1} is the inverse matrix providing the analytical solution to the problem of inverting a set of reflectances R_i for model parameters f_i minimizing a given error function. Note that this analysis is independent of any specific BRDF function.

In an extensive investigation, we have studied the sensitivity to random noise of the several BRDF models listed above using sampling for a variety of combinations of the MODIS and MISR sensors, and for different periods of data accumulation. From these, we here report selected findings on 16-day sampling only for 3 different sensor combinations. Both interpolating and extrapolating the BRDF were tested in that nadir reflectance and directional-hemispherical ("black-sky") albedo were derived both at the mean sun angle of the observation and for nadir sun. Additionally, bihemispherical ("white-sky") albedo and the model parameters themselves were investigated.

Table 1 summarizes findings. The base case studied was 16-day sampling for combined MODIS and MISR data, as for the MODIS BRDF/albedo product. We further investigate whether using MODIS data alone is an option, and whether a second MODIS sensor to be launched on the EOS-PM-1 platform is a potential substitute for MISR in view of the three additional bands that MODIS has over MISR. Table 1 lists first the median weights of determination found for sampling throughout the year and at all latitudes. Given are the values found for the BRDF model with the smallest and with the largest median weight. Second, it gives the worst-case range of values. Range here is defined as the central two thirds of values occurring.

Results show that the MODIS-AM/MISR sensor combination will allow retrieval of the BRDF with an accuracy that is smaller than the RMSE of the inversions (weights if determination smaller than one). Retrieval of nadir reflectance and black-sky albedo at the mean prevailing sun zenith angle is very stable and more reliable than deriving these quantities for a nadir sun. But even the latter, requiring extrapolation of the BRDF to angles where typically no observations were made, is possible with an accuracy of less than the value of the RMSE. The same is true for the white-sky albedo. The expected error of the model parameters themselves is larger than that of derived quantities. Naturally, cloud cover will increase these error estimates. Assuming that the angular distribution of samples is not affected by loss of observations due to clouds, the weights of determination can be shown to increase as $1/\sqrt{N}$, where N is the number of observations.

Using the MODIS-AM sensor alone yields a worse product quality, notably for nadir-view nadir-sun totally angle corrected reflectance, and nadir-sun albedos. This emphasizes the importance of combining MISR data with MODIS data for a sound retrieval. The MODIS-AM/MODIS-PM sensor combination will allow a better retrieval than when using MODIS-AM alone, but is not as good as using MODIS-AM/MISR. This suggests that MISR should also be used in retrievals after the launch of MODIS-PM in the four bands concerned.

Fig. 1, in the top two panels, visualizes the dependence of noise-induced error in BRDF-interpolating and BRDF-extrapolating reflectances and albedos on latitude and time of the year for MODIS-AM/MISR sampling and for the RossThick-LiSparse model. An RMSE of 10 percent was assumed in converting weights of determination to percentage error (note that errors scale linearly with the RMSE). The plots illustrate nicely that interpolation of the BRDF can be conducted with confidence, but that the error of extrapolation also is less than the assumed noise RMSE.

NOISE SENSITIVITY OF THE RAHMAN MODEL

The RPV BRDF model [2] is slated for use in the MISR BRDF/albedo product. It is here investigated for MODIS-AM/MISR 16-day sampling for comparison. Since it is a nonlinear model, noise sensitivity is a function of spectral band and BRDF observed, and studying it required tedious numerical evaluation. Using four field-observed BRDF types and five levels of noise in 250 individual random realizations, equivalent weights of determination were derived. The finding is that with respect to reflectances and albedo the RPV model behaves rather similar to the kernel-driven models; the retrievals are of comparable reliability. However, at least two of the model parameters themselves are instable (weights of determination $\gg 10$) due to redundancy of the respective BRDF component functions in the angle domains sampled.

Fig. 1 shows, in the bottom panels, results for the red and the near-infrared band for one day of the year using a field-measured hardwood BRDF dataset by Kimes et al. [5]. Note similarities and differences with the RossThick-LiSparse model shown in the top left panel for the same day.

CONCLUSIONS

BRDF and albedo c, n be retrieved from noisy reflectance data both at the prevailing mean sun angle of observations and at other angles to within a fraction of the noise RMSE under conditions of angular sampling as obtained from the combined MODIS and MISR sensors, and using kernel-driven BRDF models or the RPV model.

In judging the results it is important that the random noise error investigated here implies little about a second type of error, the misfit error, which is essential in determining how well a given model extrapolates. Only after judging noise sensitivity and misfit error together, and considering actual sampling patterns, can general conclusions about BRDF/albedo retrieval accuracies be drawn.

REFERENCES

[1] Wanner, W., A. Strahler, B. Zhang, and P. Lewis, "Kilometer-scale albedo from MODIS," this conference.
[2] Rahman, H., B. Pinty, and M. M. Verstraete, "Coupled surface-atmosphere reflectance (CSAR) model, part 2," J. Geophys. Res., 98, pp. 20,791–20,801, 1993.
[3] Wanner, W., X. Li, and A. H. Strahler, "On the derivation of kernels for kernel-driven models of bidir. reflectance," J. Geophys. Res., 100, pp. 21,077–21,090, 1995.
[4] Whittaker, E., G. Robinson, "The Calculus of Observations," Blachie and Son, Glasgow, 397 pp., 1960.
[5] Kimes, D. S., et al., "Directional reflectance distributions of a hardwood and a pine forest canopy," IEEE Trans. Geosci. Remote Sens., 24, pp. 281–293, 1986.

Table 1: Median Weights of Determination (left) and Worst-Case Ranges of Weights of Determination (right).
Left: smallest and largest median error of models; Right: smallest and largest worst case model error.

16–day sampling		Median Error Weights			Worst-Case Ranges of Error Weights		
		MODIS–AM + MISR	MODIS–AM	MODIS–AM+PM	MODIS–AM	MODIS–AM	MODIS–AM+PM
Interpolation	Rnad	0.18–0.23	0.30–0.40	0.17–0.23	0.18–0.28	0.29–0.44	0.17–0.25
$\theta_s = \langle \theta_s \rangle$	bsa	0.16–0.18	0.25–0.55	0.15–0.29	0.15–0.20	0.40–0.72	0.23–0.41
Extrapolation	Rnad	0.17–0.93	0.28–3.45	0.16–1.94	0.73–1.08	1.47–5.72	0.86–3.18
$\theta_s = 0$	bsa	0.18–0.28	0.29–0.82	0.17–0.45	0.19–0.49	0.30–2.54	0.17–1.47
Global, $\int \theta_s d\theta_s$	wsa	0.17–0.42	0.31–1.60	0.18–0.95	0.21–0.82	0.66–2.42	0.40–1.41
Parameters	f_{vol}	0.15–0.89	0.39–2.01	0.23–1.19	0.33–1.76	1.21–3.52	0.72–1.97
	f_{geo}	0.27–0.60	0.68–2.32	0.39–1.28	0.45–0.69	0.99–3.73	0.58–1.99

Rnad = reflectance at nadir view angle; bsa = black-sky albedo; wsa = white-sky albedo; f_{vol} = volume scattering kernel coefficient; f_{geo} = surface scattering kernel coefficient.
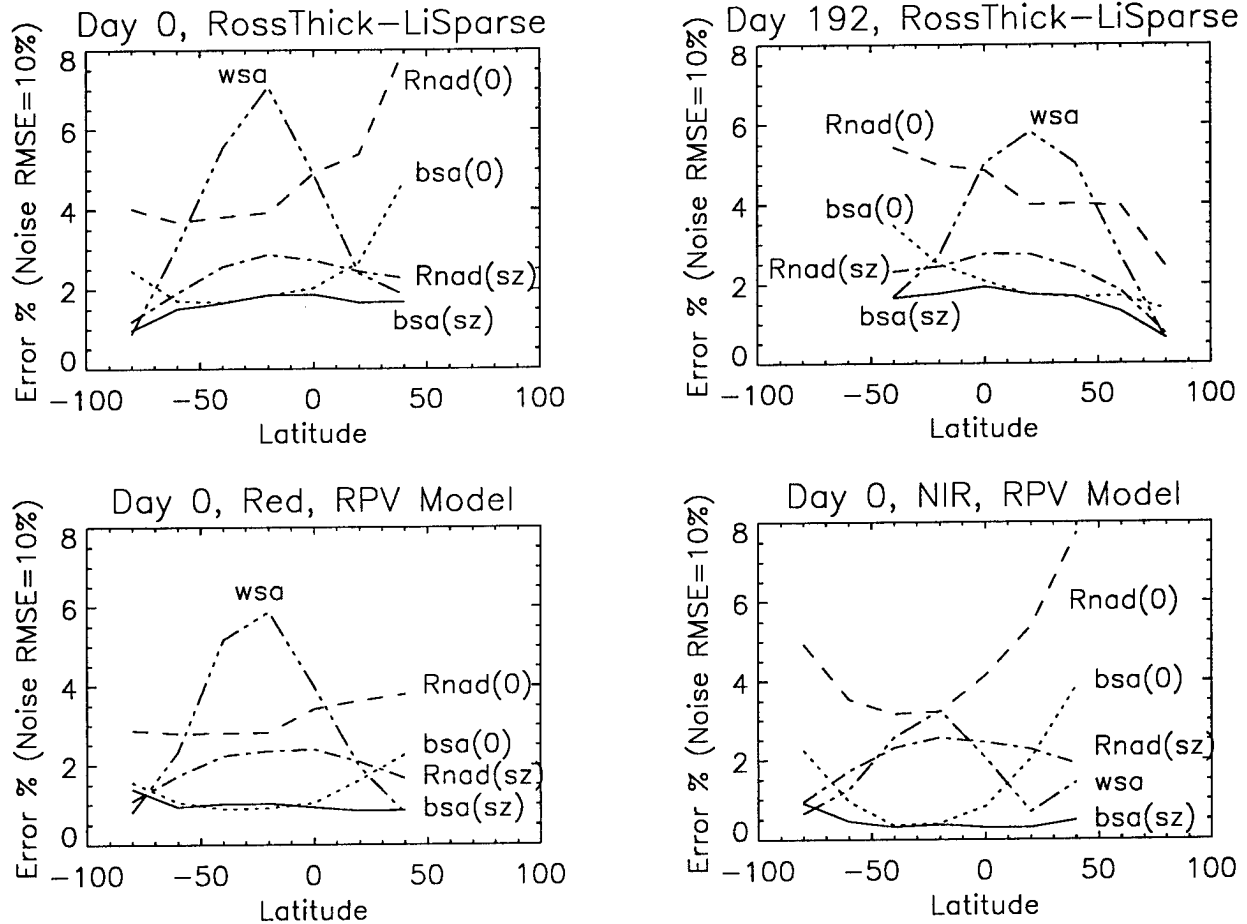
Figure 1: Noise error sensitivity of the RossThick-LiSparse semiempirical BRDF model for 16-day MODIS/MISR sampling on two different days of the year (top) and for the Rahman model (bottom) for the red (left) and NIR (right) band on Kimes hardwood data; Rnad(sz), bsa(sz) = nadir-view reflectance and black-sky albedo at mean sun zenith; Rnad(0), bsa(0) = nadir-view reflectance and black-sky albedo at nadir sun; wsa = white-sky albedo.

Semiempirical Modelling of Bidirectional Reflectance Utilizing the MODIS BRDF/Albedo Algorithm Models

H. Peter White, John R. Miller
Department of Physics and Astronomy, & Institute for Space and Terrestrial Science, York University
4700 Keele St., North York, Ontario, M3J 1P3, Canada
Phone: 416-736-2100 ext. 33854 / Fax: 416-736-5626 / email: white@eol.ists.ca / URL: http://eol.ists.ca

Raymond Soffer
Instrument Services Laboratory, Institute for Space and Terrestrial Science
4850 Keele St., North York, Ontario, M3J 3K1, Canada

Wolfgang Wanner
Center for Remote Sensing, Boston University
725 Commonwealth Avenue, Boston, MA 02215, USA

Abstract -- BRF's of an artificial conifer canopy were observed and modelled using the MODIS BRDF/Albedo algorithm. Derived BRDF functions show a reasonable agreement with the BRF observed in the illumination plane. The algorithm shows the ability to provide a reasonable BRDF for illumination conditions not used in the function derivation, which are based entirely on in-plane BRF data.

INTRODUCTION

Multiband, multiangular measurements of the reflectance of artificial conifer stands have been acquired with the Compact Airborne Spectrographic Imager (CASI) using a laboratory canopy modelling facility (CMF) This includes a collimated illumination source enabling the extraction of reflectance spectra in the visible/NIR wavelength regions, and 13 cm models of conifer crowns sprayed with a cellulose material that mimics the spectral response of needles [1]. The conifer models were designed to be similar to typical trees found at the BOREAS Old Jack Pine SSA Tower Flux Site. Reflectance was measured in the principal illumination plane at view zenith angles (VZA) between -60 to 60 degrees with illumination zenith angles (IZA) set to 16.5, 45 and 69.5 degrees, covering an area that would scale up to 33m x 33m. Canopy coverage was varied from 17 to 52% and understorey (background) reflectance was either a black or a white (salt) covered surface.

These datasets were investigated using an early version of the MODIS BRDF/Albedo algorithm developed at Boston Univ. [2] utilizing and testing its ability to accurately model the measured BRF of an artificial canopy and to produce a BRDF function that captures the observed variations of BRF with IZA. This algorithm is designed to test several

combinations of kernels, and provide the best fit linear combination of these kernels to observed BRF [3]. Kernels include two volume scattering derivations based on the formulas of Ross [4], one thick and one thin approximation, as well as three geometric derivations, two derived from the modelling approach of Li and Strahler [6] for sparse and dense canopies, and one based on the random placement model of Roujean [5].

METHODOLOGY

A preliminary version (version 2.4) of the MODIS BRDF/Albedo algorithm was used to parameterize the measured BRF in two ways. First, each set of BRF with a specific IZA were used to produce the corresponding BRDF algorithm function. Second, all angular measurements were combined to derive a single BRDF function. These were then compared to the original data to evaluate their ability to reproduce the observed BRF for various IZAs. The derived cross-plane BRF and complete BRDF surface were visually inspected. The two extreme cases of black and white background and canopy cover ranging from 17 to 52% allowed a test of the flexibility of the algorithm to handle a wide variety of canopy types.

Black velveteen cloth was used as a black understorey, providing a near-isotropic visible/NIR reflectance (between 1-2%). Common table salt was used as a white understorey providing a near-isotropic reflectance between 80-100%, mimicking the high contrast situation of a snow covered understorey [1]. CMF models are thus referred to as, B (black understorey) and S (salt/snow understorey). Tree placements were derived from random placements with the caveat that no two trees could be within 1 canopy radius of each other (the edge of one canopy could not enclose the trunk of a neighboring tree) [1]. A limited set of CASI
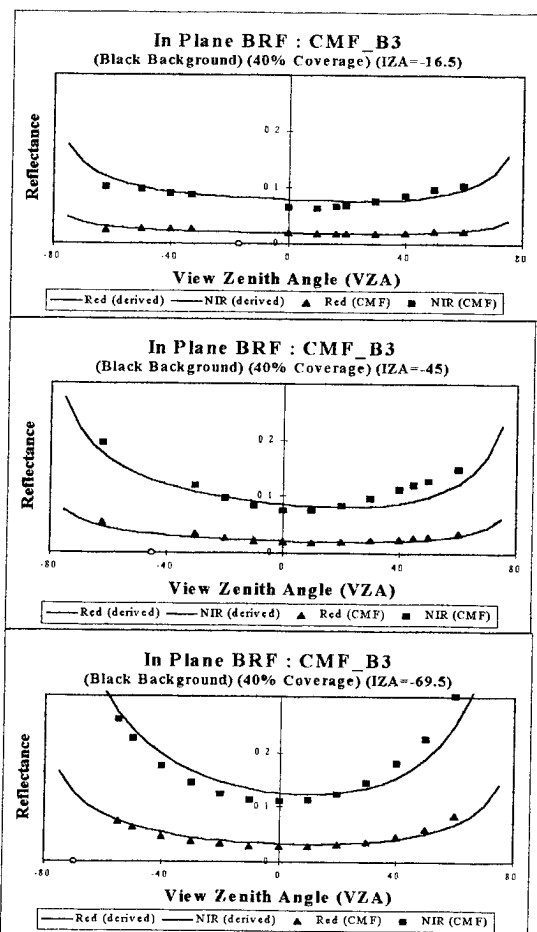
Figure 1: Measured and multi-IZA Derived BRF

observations from the BOREAS SSA Old Jack Pine site taken during the February campaign were also investigated.

CMF_B MODEL RESULTS

One common feature with CMF_B models was the similarity of the sunlit to shaded ground area reflectance. Here, the shadow created contrasts used by geometric scattering kernels becomes a very minor - if not insignificant - part of the BRF. This is seen in the results provided by the
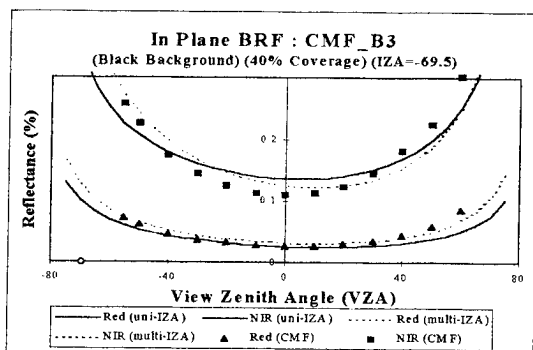
Figure 2: multi-IZA and uni-IZA (IZA=-16.5°) Derived BRF for IZA=-69.5°

algorithm. As shown for the CMF_B3 example (Fig.1), the BRDF function derived from the multi-IZA data set matches the measurements in both magnitude and shape for all IZA's. The model to best reproduce the observed data was based on the Ross Thin kernel with isotropic scattering and no geometric scattering. The geometric scattering kernels do begin to appear if the BRDF function derivation is performed on a unique IZA data set, for cases of small IZA. But even here it remains a minor influence. This can be expected as more of the understorey surface is viewed at smaller IZA, providing the low contrast shadows a higher significance in the observed BRF. The small IZA (IZA=-16.5°) based derivations still reproduce the large IZA data with a good degree of accuracy, (Fig.2). In all cases, the derived off-plane BRF's are symmetric on either side of the illumination plane, and keep the basic "bowl" shape seen with the in-plane derivations.

CMF_S MODEL RESULTS

In contrast to the CMF_B models, the white understorey CMF models provide high contrast shadowing effects on the observed reflectance, which become more significant for
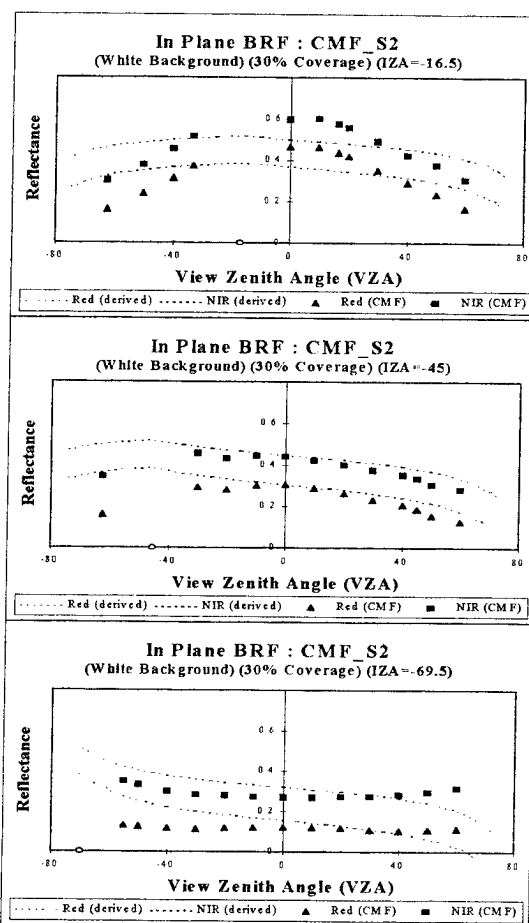
Figure 3: Measured and multi-IZA Derived BRF

1412

smaller tree densities and smaller illumination zenith angles. This is seen in the derived BRDF function for all models ranging in canopy coverage of 17 to 52%. Shown in Fig.3 are the derived BRDF function and the measured CMF BRFs for the 30% canopy coverage model, where the BRDF derivation is based on the multi-IZA dataset. The derived BDRF function provides a reasonable fit to the magnitude and shape of the BRF observed for all three IZAs. A departure between the derived and measured BRF exists in the algorithm's ability to reproduce the shape of the BRDF at smaller IZA. When individual IZA datasets are used, the derived function also suffer the same difficulty. Comparisons to other canopy BRF observations indicate that the slope observed in the measured BRF is steeper than might be normally expected for a natural canopy, and thus may not be well suited for the MODIS BRDF/Albedo algorithm. The shape of the curves do match much better for larger IZA, where volume scattering becomes more significant.

The hot-spot region is not observable with the CMF. Yet the derived uni- and multi-IZA BRDF functions are able to place the hot-spot in the proper location for all three IZA datasets, an important feature of any general BRDF function.

SOUTH OLD JACK PINE RESULTS

A preliminary subset of CASI data from the SSA old jack pine site has been calibrated to reflectance, and provides an excellent opportunity to test the ability of the algorithm to reproduce field observations of a canopy with a snow covered understorey. The dataset tested is small - only 6 BRF's. All points have approximately the same IZA, and thus Fig.4 could be considered as a first order in-plane BRF curve. A BRDF function was derived and from this function, BRF's were determined for the same illumination/view orientation as the observations. As seen, the function reproduces the observed data well, especially in the visible bands, even with a limited number of data points. Further work is planned as more data becomes available.

CONCLUSIONS

All measured BRF's of the various artificial canopies were reproduced by the algorithm, with small RMSE. The models are capable of finding the right magnitude and general shape of the BRDF, but in some cases the CMF observed values fall off much steeper in the backscattering direction than predicted by the algorithm. When the derived functions were used to produce a full BRDF surface, each surface showed expected shapes, even though only illumination plane BRF data was used in the derivation. These functions were also able to match the changes in the curvature of the observed reflectance as a function of IZA, including IZA's not used in the function derivation.
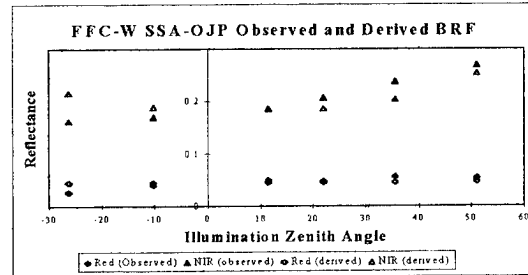
Figure 4: Measured and multi-IZA Derived BRF for FFC-W at SSA-Old Jack Pine Site

Comparisons of black to white understorey canopy datasets show a change in kernel weighting, with the shadow driven geometric kernels becoming less relevant with a black background (when the cast shadows do not become easily visible) or with increasing IZA. The hot-spot feature (significant in the geometric kernels) is well positioned in the derived BRDF, **even when** no observations of the hot-spot region are provided in the derivation.

Derived BRDF functions with relatively large geometric kernel parameters do appear to have some difficulty reproducing the measured CMF BRF. This difficulty has not been observed in other canopy derived BRDF investigations [2], however, none of these datasets included a white (snow) understorey. BRF measurements of a natural canopy with a snow covered understorey are well modelled in the small CASI SSA-OJP dataset, but does not include the hot-spot region. Additional analysis of larger datasets from natural canopies are planned to investigate this further.

REFERENCES

[1] Raymond Soffer, "Bidirectional Reflection Factors of an Open Tree Canopy by Laboratory Simulation", Thesis Document, Graduate Programme in Earth and Space Science, York University, December 1995

[2] Alan H. Strahler, and J. Muller, "MODIS BRDF/Albedo Product: Algorithm Theoretical Basis Document", version 3.2 and update, NASA EOS MODIS Doc., , in press.

[3] Wolfgang Wanner, X. Li, and A. H. Strahler, "On the Derivation of Kernels for Kernel-Driven Models of Bidirectional Reflectance", J. Geo. Res., September 1995

[4] K. Ross, The Radiation Regime and Achitecture of Plant Stands, Dr. W. Junk Publishers, The Hague, 1981.

[5] L. Roujean, M. LeRoy, and P. Y. Deschamps, "A Bidirectional Reflectance Model of the Earth's Surface for the Coorection of Remote Sensing Data", J. Geophys. Res., v.97, 1992.

[6] Li and A. H. Strahler, "Geometric-optical Bidirectional Reflectance Modelling of a Conifer Forest Canopy", IEEE Trans. GeoSci. Remote Sens.,v24, 1986.

ANALYTIC FORMS OF BIDIRECTIONAL REFLECTANCE FUNCTIONS FOR EARTH RADIATION BUDGET STUDIES

Natividad Manalo-Smith [1] and G. Louis Smith [2]

1. Analytical Services and Materials, Hampton, VA 23666; tel. 804-827-4630; FAX 804-825-8659; e-mail: n.m.smith@larc.nasa.gov
2. Atmospheric Sciences Division, NASA Langley Research Center, Hampton, VA 23681; tel 804-864-5678; e-mail: g.l.smith@larc.nasa.gov

INTRODUCTION

Earth radiation budget studies have been instrumental in enhancing our understanding of climate processes. The radiation field emerging from a point at the top of the Earth's atmosphere (TOA) is the quantity of primary interest and can be derived from satellite-measured radiances by applying appropriate bidirectional reflectance functions (BDRFs). BDRFs, which account for the anisotropy of the reflected radiation field [1] are dependent upon the viewing geometry (i.e. directions of the incoming and outgoing rays), the underlying geographical type (ocean, land, snow, desert, land-ocean mix), the overhead cloud cover (clear, partly cloudy, mostly cloudy, overcast), and conditions of the intervening atmosphere.

A set of BDRFs was developed by Suttles et al. [2] from radiance measurements collected from NIMBUS 7 Earth Radiation Budget (ERB) [3] and the Geostationary Operational Environmental Satellite (GOES) instruments and was used to process Earth Radiation Budget Experiment (ERBE) data. These mean models for the ERBE scene types were tabulated for discrete bins of solar zenith angle, viewing zenith angle, and relative azimuth angle. Due to the constraints of the sun-synchronous orbit of the NIMBUS 7, angular bin coverage was limited. Future radiation budget-monitoring missions, such as the Clouds and Earth's Radiant Energy System (CERES) instrument [4] will require BDRFs that satisfy reciprocity (i.e. interchanging the incident and reflected angles yield the same flux contribution) and are continuous over angular grid boxes. Moreover, correctly modelled BDRFs must convert radiances measured from different viewing angles for the same area to the same flux. Unfortunately, the set of BDRFs used by ERBE resulted in shortwave fluxes which increased from nadir to limb.

The present paper uses an analytic expression for the BDRF formed by applying a fit to the tabulations of Suttles et al. [2]. The form of this expression, based on theoretical considerations, consists of model parameters that correspond to physical processes in the surface and atmosphere [5,6]. The effectiveness of these models in accounting for anisotropy at any given viewing direction is examined with data obtained when the scanning radiometer was operated in alongtrack mode. Operation in this mode allows for an area along the groundtrack to be viewed over the full range of view zenith angles. The clear ocean BDRF is tuned with Dlhopolsky's BDRF [7] which generally produces less albedo growth than does the Suttles et al. clear ocean model. BDRFs are presented for the following ERBE scene types: clear ocean, clear land, clear desert, partly cloudy (PC) over land and mostly cloudy (MC) over ocean scenes.

METHODOLOGY

The reflected flux M at the TOA is given by
$$M = Sa(\varsigma)\cos\varsigma \quad (1)$$
where S is the solar flux at TOA, $a(\varsigma)$ is the TOA albedo, and ς is the angle of incidence. The reflected radiance L is a function of viewing geometry (Fig. 1). The anisotropy of the radiation field is accounted for by the BDRF R which relates M and L by
$$R(\theta, \phi, \varsigma) = \pi L(\theta, \phi, \varsigma)/M \quad (2)$$
The quantity $r(\theta,\phi,\varsigma) = R(\theta,\phi,\varsigma)\,a(\varsigma)$ is defined as the bidirectional reflectance. The analytic expressions are formulated in terms of reflectance. The form of these models comply with reciprocity.

The bidirectional reflectance for clear and partly cloudy over ocean scenes is expressed in the following empirical form

$$r(\theta, \phi, \varsigma) = C_1 + \frac{C_2(1 + \cos^2\gamma)}{(uu_0)^{C_3}} + \frac{C_4\left(C_5 - 1\right)}{(uu_0)^{1.5}\left(C_5 - \cos\alpha\right)^2} \quad (3)$$

where $u = \cos\theta$, $u_0 = \cos\varsigma$, γ is the scattering angle, i.e. the angle through which the ray is turned as it is reflected, and α is the angle from the line of specular reflection. These angles are defined by $\cos\gamma = vv_0\cos\phi - uu_0$ and $\cos\alpha = vv_0\cos\phi + uu_0$, where $v = \sin\theta$ and $v_0 = \sin\varsigma$. The second and last terms on the right hand-side account for the Rayleigh scattering from the atmosphere and the specular reflection from the ocean surface, respectively. The first term accounts for other diffuse scattering processes. Integrating (3) over the upwelling hemisphere yields the albedo [5]. The model coefficients are tabulated on Table 1.

Following Staylor's parameterization of clear desert BDRF [8], an azimuthal model for land, snow,

desert, mostly cloudy over ocean and overcast scenes is developed in the following form.

$$\frac{\Delta r}{\Psi}(model) = \frac{1 + K(G + \cos\gamma)^2}{1 + K\left[G^2 - 2Guu_o + (uu_o)^2 + \frac{1}{2}(vv_o)^2\right]} \quad (4)$$

where G and K are determined by matching Suttles et al. tabulations. The model reflectance is computed as

$$r(model) = \omega r_{Ray} + \Psi\left[\frac{\Delta r}{\Psi}(model)\right] \quad (5)$$

where $\Psi = A + Bx^2$, ω accounts for the change in the amount of Rayleigh scattering over a cloudy scene, and r_{ray} is the second term in (3). A and B are regression coefficients and $x = (uu_o)/(u+u_o)$. The corresponding model albedo is given in [6]. The model coefficients are listed on Table 2. Dividing the model reflectance by the model albedo yields the scene BDRF.

Table 1: Model Coefficients for Clear and PC Ocean

Scene Type	C_1	C_2	C_3	C_4	C_5	D
Clear Ocean [1]	0.010	0.023	0.800	0.006	1.060	0.011
Clear Ocean [2]	0.005	0.027	0.900	0.008	1.100	0.016
PC / Ocean	0.030	0.047	0.577	0.008	1.157	0.016

[1] ERBE-tuned   [2] Alongtrack-tuned (Dlhopolsky)

Table 2: Model Coefficients for Land, Snow, Desert, MC / Ocean and Overcast Scenes

Scene Type	A	B	G	K	ω
Clear Land	0.002	0.384	0.138	0.650	1.000
Clear Snow	0.011	2.517	0.675	0.188	1.000
Clear Desert	-0.003	0.784	0.025	0.412	1.000
PC / Land	0.009	0.643	0.350	0.875	0.917
MC/ Ocean	0.024	0.812	0.525	0.988	0.758
MC / Land	0.030	1.019	0.643	0.988	0.758
Overcast	0.018	1.537	0.550	0.625	0.668

RESULTS

To validate the models, fluxes are computed with alongtrack data radiances by applying the scene BDRF (2). Fluxes at various viewing angles are normalized to near nadir values to get flux ratios. Fig. 2 shows the flux ratios as a function of view zenith for clear ocean for $26°<\varsigma<37°$ determined by applying the ERBE, analytic and Dlhopolsky models. Albedo growth is observed for all three models. At $\theta=30°$, the errors are in the order of

2% for all cases while at $\theta=70°$, the errors are in the order of 34% for ERBE, 21% for the analytic model, and 17% for Dlhopolsky in the backscatter region while in the forward scatter direction, these errors are in the order of 35% for both the ERBE and analytic models and 31% for Dlhopolsky.

Comparisons of the analytic and ERBE operational BDRFs are illustrated for selected scene types for a particular solar zenith angle range. The radial coordinate corresponds to view zenith angle, θ, and ϕ varies from $0°$ (forward scatter) to $180°$ (backscatter) in the angular coordinate. Clear land BDRFs in the $60°<\varsigma<66°$ range, depicted on Fig. 3, are similar for both models and show that land is primarily a backward reflector. Both show near-isotropic characteristics for $\theta<30°$ and ϕ near $90°$ which may be attributed to less intervening atmosphere where scattering is not significant. BDRFs for clear desert (Fig. 4) for $46° < \varsigma < 53°$ are nearly isotropic in the forward scatter region for both models and like land, are more back-reflecting in this angular range. ERBE BDRF is slightly more limb-brightened than the analytic BDRF. Fig. 5 shows that the BDRF for partly cloudy over land $(53° < \varsigma < 60°)$ is limb-brightened in both the forward and backward scatter directions. The BDRF for mostly cloudy over ocean in the same zenith angle range is significantly limb-brightened in the forward direction(Fig.6).

CONCLUSION

A simple analytic formulation of BDRF to model the anisotropy of reflected radiation for ERBE scene types was presented. The model coefficients were derived by applying a fit to the Suttles et al. BDRF tabulations which were used to process ERBE data. For each scene type, a single set of model parameters is required for application to any combination of viewing geometries. This analytic form satisfies reciprocity and is continuous from one angular bin to another. The analytic BDRF is validated with ERBE observations and have shown good agreement. Results of this study will be used for mission-planning and data interpretation of next-generation earth radiation budget missions.

REFERENCES

[1] Smith, G. L., R. N. Green, E. Raschke, L. M. Avis, J. T. Suttles, B. A. Wielicki, and R. Davies, Inversion methods for satellite studies of the earth's radiation budget: Development of algorithms for the ERBE mission, Rev. Geophys., 24, No. 2, 407 - 421, 1986.

[2] Suttles, J. T., R. N. Green, P. Minnis, G. L. Smith, W. F. Staylor, B. A. Wielicki, I. J. Walker, D. F. Young, V. R. Taylor and L. L. Stowe, Angular Radiation Models

for Earth-atmosphere System, Vol. 1, NASA Reference Publication 1184, 1988.

[3] Smith, W. L., J. Hickey, H. B. Howell, H. Jacobowitz, D. T. Hilleary, and A. J. Drummond, Nimbus-6 Earth Radiation Budget Experiment, **App. Opt.**, 16, No. 2, 306 - 318, 1977.

[4] Barkstrom, B. R., Earth radiation budget measurements: pre-ERBE, ERBE, and CERES. "Long-Term Monitoring of the Earth's Radiation Budget, Bruce Barkstrom, Editor, **Proc. SPIE 1299**, 52-60, 1990.

[5] Manalo, N., G. L. Smith, W. F. Staylor and R. N. Green, Statistical Properties of Bidirectional Reflectance Functions, **Proc. of the 12th Conference on Probability and Statistics in the Atmospheric Sciences**, 122-127, 1992.

[6] Manalo-Smith, N., W. F. Staylor and G. L. Smith, Analytic Forms of Bidirectional Reflectance Functions, **Proc. 7th Conf. on Satellite Meteorology and Oceanography**, 542-545, 1994.

[7] Dlhopolsky, R. and R. Cess, Improved Angular Directional Models for Clear Sky Ocean Derived from the Earth Radiation Budget Satellite Shortwave Radiances, **J. Geophys. Res.**, Vol. 98, No. D9, 16713 - 16721, 1993.

[8] Staylor, W. F. and J. T. Suttles, Reflection and Emission Models for Deserts Derived from Nimbus 7 ERB Scanner Measurements, **J. Climate and Appl. Met.**, Vol. 25, 1986.

Fig. 1 Viewing Geometry

ζ: solar zenith angle
θ: viewing zenith angle
φ: relative azimuth angle
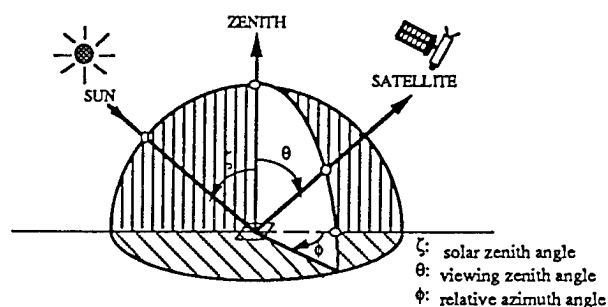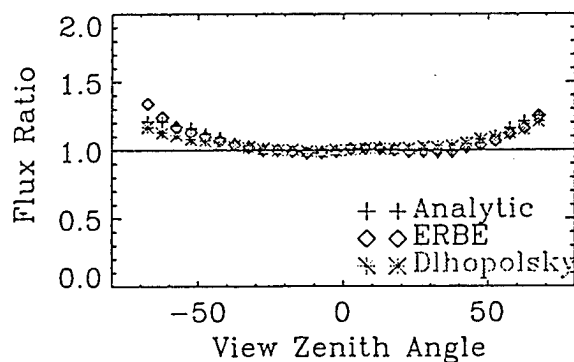
Fig. 2 Ratio of Alongtrack SW Flux for Clear Ocean (26°<ζ<37°)
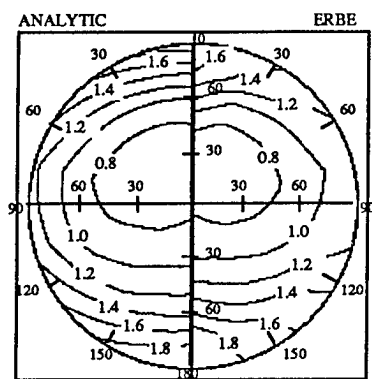
Fig. 3 Bidirectional Reflectance Function for Clear Land (60°<ζ<66°)
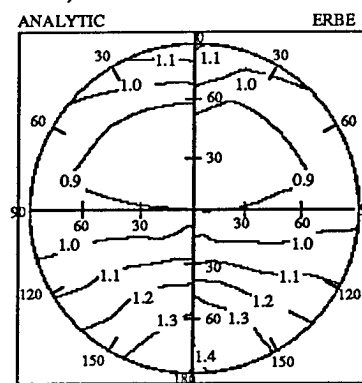
Fig. 4 Bidirectional Reflectance Function for Clear Desert (46°<ζ<53°)
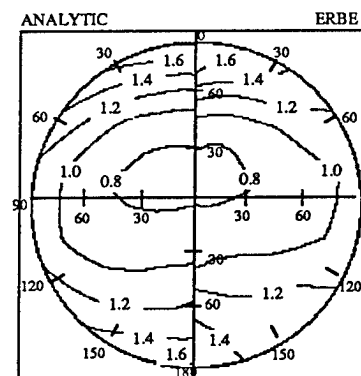
Fig. 5 Bidirectional Reflectance Function for Partly Cloudy / Land (53°<ζ<60°)
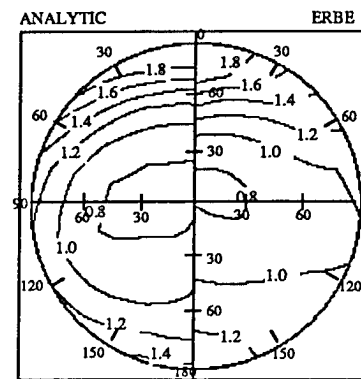
Fig. 6 Bidirectional Reflectance Function for Mostly Cloudy / Ocean (53°<ζ<60°)

1416

Estimating Hemispherical Reflectance and Selected Biophysical Parameters for Boreal Forest Canopies Using Spectral Bidirectional Reflectance Data Acquired by ASAS

Carol A. Russell, Laboratory for Global Remote Sensing Studies, Department of Geography/UMCP
Code 923, NASA/GSFC, Greenbelt, MD 20771, 301-286-9416, 301-286-0239 (fax), car@quartz.gsfc.nasa.gov

James R. Irons, Biospheric Sciences Branch, Code 923, NASA/GSFC, Greenbelt, MD 20771
301-286-8978, 301-286-0239 (fax), jim_irons@gsfc.nasa.gov

Philip W. Dabney, Sensor Development and Characterization Branch, Code 925, NASA/GSFC, Greenbelt, MD 20771
301-286-9153, 301-286-1757 (fax), pdabney@asas.gsfc.nasa.gov

Abstract - Advanced Solidstate Array Spectroradiometer (ASAS) hyperspectral, multiangle data were obtained over BOREAS sites in Saskatchewan and Manitoba, Canada during four field campaigns in 1994. Flown aboard the NASA C-130B at an altitude of approximately 5000 m above ground level, ASAS acquired off-nadir data from 70 degrees forward to 55 degrees aft along-track, in 62 contiguous spectral bands ranging from 400-1025 nm. These measurements were collected to develop linkages between optical remote sensing data and biophysical parameters at the canopy level, and to provide an intermediate level in the process of scaling local ground conditions to satellite observations. ASAS at-sensor radiances over various canopies were atmospherically corrected using the Second Simulation of the Satellite Signal in the Solar Spectrum (6S) and at-surface reflectance factors were derived. Using the multiangle spectral reflectance factors, spectral hemispherical reflectance (PAR, red, and nir) was estimated, and spectral vegetation indices, including hemispherical measures, were calculated. The values of the SVIs varied widely depending on the particular angular inputs to the calculation.

INTRODUCTION

As part of the Boreal Ecosystem Atmosphere Study (BOREAS) international field experiment, the Advanced Solidstate Array Spectroradiometer (ASAS) obtained hyperspectral, multiangle digital image data over boreal forest canopies in Saskatchewan and Manitoba, Canada during four field campaigns in 1994. BOREAS is a large-scale international investigation focused on understanding the exchanges of radiative energy, sensible heat, water, carbon dioxide, and trace gases between the boreal forest and the lower atmosphere [1]. One of the BOREAS objectives is to develop methods for applying process models over large spatial areas using remote sensing and other integrative modeling techniques. The ASAS measurements can be used to establish linkages between optical remote sensing data and biophysical parameters at the canopy level, and to provide an intermediate level in the process of scaling local ground conditions to satellite observations.

SENSOR DESCRIPTION

ASAS is an airborne imaging spectroradiometer modified to point off-nadir by NASA/GSFC for the purpose of remotely observing directional anisotropy of solar radiance reflected from terrestrial surfaces. The sensor is capable of along-track off-nadir tilting, and acquired data at 70°, 60°, 45°, 26° forward of nadir, nadir, and 26°, 45°, and 55° aft of nadir over the BOREAS sites. For these data, the effective dimensions of the ASAS CCD silicon detector array are 512 spatial elements by 62 spectral elements. Spectral band centers range from 404-1025 nm and are spaced approximately 10 nm apart, with a full-width-half-maximum of about 11 nm. The array generates digital image lines in a pushbroom mode as the aircraft flies forward. For the datasets included in this study which were acquired at an altitude between 5000-6000 m above ground level and at an aircraft speed of 230 knots, the across-track ground pixel size is about 3 m at nadir and 7 m at 60 degrees off-nadir. The along-track pixel size (consistent for all view angles) is roughly 3 m.

SITES

BOREAS study areas are located in Saskatchewan north of Prince Albert (Southern Study Area or SSA) and west of Thompson, Manitoba (Northern Study Area or NSA). Reference [1] gives some detailed location maps. The data presented in this paper were collected on July 21, 1994 over three different SSA Tower Flux sites. Flux measurement towers and scaffold towers at these sites are located near the center of a 1 km² area of relatively homogeneous vegetation cover. The three canopy covers examined here are Old Black Spruce, Old Jack Pine and Old Aspen. Separate ASAS datasets over these targets were collected in, perpendicular to, and oblique to, the solar principal plane (spp) at solar zenith angles (sza) ranging from 34-37°.

METHODS

An interactive display system was used to subset image pixels for analysis. Areas of homogeneous canopy adjacent to the scaffold tower and/or under the PARABOLA tramway were selected. Since the datasets included in this study were not geo-rectified, care was taken to encompass the same subareas from each of the multiple view angles. Ground size of the subset areas ranged from hundreds of square meters up to several thousand square meters. The mean and standard deviation of radiances in W m⁻² sr⁻¹ μm⁻¹ for 62 spectral channels were calculated from the subsets in each view angle. To derive at-surface spectral reflectance factors, 6S (Second

Simulation of the Satellite Signal in the Solar Spectrum) [2] was applied to the spectral at-sensor radiances. The US62 standard atmospheric model and a continental aerosol model were selected to characterize the atmosphere above the BOREAS sites. In addition, a total aerosol optical depth for the atmospheric column (at 550 nm) was supplied for each dataset. Optical depth measurements were obtained from BORIS (BOReas Information System).

From this point, multiangle spectral bidirectional reflectance factors (BRFs) can be input directly into models for estimating hemispherical reflectance, or into calculations of Spectral Vegetation Indices (SVIs). However, an additional step is necessary if BRF values for bandwidths other than (for example, broader than) the ASAS channels are desired for analysis. For this, a numerical trapezoidal integration method is used, which essentially computes an average of the reflectance factors from the included ASAS bands (determined by specifying a min and max wavelength), weighted by each band's downwelling solar flux (generated by 6S). For these analyses, reflectance factors for photosynthetically active radiation, or PAR (400-700nm), red (630-690nm) and near-infrared (760-900nm) were simulated.

To estimate hemispherical reflectance (R_h) from a set of discrete BRFs, this analysis used the equation developed by Walthall et al. [3] which describes reflectance as a function of view zenith, view azimuth, and solar azimuth angles:

$$R (\theta, \phi) = a\theta^2 - b\theta\cos\phi + c \quad (1)$$

where $R (\theta, \phi)$ is the percent reflectance factor, θ is the view zenith angle, and ϕ is the view azimuth angle relative to the solar principal plane. The coefficients a, b, and c are empirically derived by fitting (1) to the distribution of ASAS BRFs using multiple linear regression. Integrating (1) over the 2π sr solid angle provides an analytical expression for hemispherical reflectance: $R_h = (2.305 \ a/\pi) + c \quad (2)$
Using equation (2), R_h for PAR, red and nir spectral regions was estimated using view angles from various combinations of flightlines (data collected in planes parallel, perpendicular, and oblique to the spp).

Spectral vegetation indices (Simple Ratio and NDVI) were calculated using backscatter, nadir, and R_h estimations of red and nir. The Simple Ratio (SR) is the nir value divided by the red value, while the Normalized Difference Vegetation Index (NDVI) is the (nir value - red value)/(nir value + red value). All methods described above are given in greater detail in [4].

RESULTS AND DISCUSSION

At-surface reflectance factors observed in the solar principal plane for the Old Black Spruce, Old Aspen, and Old Jack Pine canopies are shown in Figures 1, 2, and 3 respectively. Note for all 3 canopies the extremely low reflectance in the visible, especially in the forward scatter direction, and the much greater nir reflectance which is highest for the Old Aspen site. The low visible ASAS values are not surprising given a decreasing signal response below 490 nm and such dark targets in the visible. Additionally, at the low end of the

Figure 1. RFs (z-axis) for Old Black Spruce as a function of wavelength (x-axis) and view zenith angle (y-axis)

Figure 2. RFs (z-axis) for Old Aspen as a function of wavelength (x-axis) and view zenith angle (y-axis)

Figure 3. RFs (z-axis) for Old Jack Pine as a function of wavelength (x-axis) and view zenith angle (y-axis)

visible 6S calculates path radiances greater than the radiances received at the sensor, and consequently the at-surface radiances in the visible become negative. When this occurs, the RFs are set to zero for plotting purposes. For all canopies, RFs increase in the backscatter direction, with the greatest RFs usually marking the anti-solar (hotspot) position. For the OBS and OA data (sza of 34° and 35° respectively) the hotspot was captured at 45° backscatter, about 11° off the sza, while the OJP data recorded the hotspot at 26° backscatter, about 9° off the sza.

Hemispherical reflectances (R_h) estimated using [3] are shown in Table 1 for OBS and OA. For PAR estimations, the extremely low values for ASAS channels below 529 nm were arbitrarily set to the response at 529 nm, based on cursory examination of some ground based observations. PAR and red R_h are greater for the Old Black Spruce canopy, while the Old Aspen canopy has a nir R_h roughly double that of the spruce. Time-coincident PAR measurements on the ground at OA yielded a value for Rh(par) of 2.8-2.9%.

Figure 4. LAI for OA and OBS stands vs. NDVI.

Table 1. Rh estimations (in %) using view zenith angles from different combinations of flightlines oriented parallel, perpendicular, and/or oblique to the solar principal plane.

Flightline Orientation	Rh(par) .4-.7μm	Rh(red) .63-.69μm	Rh(nir) .76-.9μm
OBS:			
Parallel	3.2	2.8	16.9
Pa + Obl	2.7	2.3	15.7
Oblique	2.1	1.8	14.5
Pa+Perp+Obl	2.4	2.0	14.8
Pa+Perp	2.5	2.1	14.9
Perp+Obl	1.9	1.6	13.8
Perpendicular	1.7	1.4	13.1
OA:			
Parallel	2.3	1.8	36.3
Pa + Obl	2.2	1.7	33.2
Oblique	2.1	1.7	31.6
Pa+Perp+Obl	2.0	1.6	32.3
Pa+Perp	1.9	1.5	33.1
Perp+Obl	1.9	1.5	31.0
Perpendicular	1.7	1.3	30.1

Values of NDVI for the OA and OBS canopies are plotted against Leaf Area Index (LAI) and the daily green fraction of absorbed PAR (fPAR) in Fig. 4 and 5 respectively. NDVI values derived from the various directional reflectances plot closely together for the OA stand but show a wide variability for the OBS stand. In Fig. 5, though the fPAR of the two stands is virtually the same, NDVI values range from about 0.65-0.92. Within clusters, backscatter relectances produce lower NDVIs than nadir and hemispherical reflectances.

Figure 5. Green fPAR for OA and OBS stands vs. NDVI.

ACKNOWLEDGMENTS

REFERENCES

[1] P. Sellers, F. Hall, H. Margolis, R. Kelly, D. Baldocchi, G. denHartog, J. Cihlar, M.G. Ryan, B. Goodison, P. Crill, K.J. Ranson, D. Lettenmaier, and D.E. Wickland, "The Boreal Ecosytem-Atmosphere Study (BOREAS): an overview and early results from the 1994 field year," Am. Meteor. Soc. Bull., vol. 76, pp. 1549-1577, Sept. 1995.

[2] D. Tanre, J.L. Deuze, M. Herman, R. Santer, and E. Vermote, " Second simulation of the satellite signal in the solar spectrum - 6S code," [abs], IEEE Proc. of the 10th Annual International Geoscience and Remote Sensing Symposium, vol. I, p. 187, 1990.

[3] C. Walthall, J.M. Norman, J.M. Welles, G. Campbell, and B.L. Blad,"Simple equation to approximate the bidirectional reflectance from vegetative canopies and bare soil surfaces," Appl. Opt., vol. 24, pp. 383-387, 1985.

[4] C.A. Russell, C.L. Walthall, J.R. Irons, and E.C. B. de Colstoun, "Comparison of airborne and surface spectral bidirectional reflectance factors, spectral hemispherical reflectance and spectral vegetation indices,"Jour.Geophys. Res., vol. 100, pp. 25509-25522, Dec. 1995.

An Integrated Approach to Estimating LAI Using Multitemporal and Multidirectional Remote Sensing Measurements

J. Qi and M. S. Moran

USDA-ARS Water Conservation Laboratory, 4331 E. Broadway Rd. Phoenix, AZ 85040

Tel. (520) 670-6380 ext. 151 Fax (520) 670-5550 Email:qi@tucson.ars.ag.gov

ABSTRACT

Leaf area index (LAI) is one of the most important physical parameters in controlling hydrological processes across the geosphere-biosphere-atmosphere boundaries. Estimation of this parameter using remote sensing techniques has been associated with computation of vegetation indices (VIs). The inversion of bidirectional reflectance distribution function modeling approaches appear to be promising, but require simultaneous bidirectional observations. Attempts have been made to substitute multitemporal observations for simultaneous multidirectional measurements. This approach works well if the surface of interest consists of slow-growing vegetation. When applied to fast-growing vegetative surfaces, multitemporal observations cannot be used in BRDF model inversion because of changes in vegetation amount. In this study, a growth compensation model is proposed with the use of VIs, which is applied to multitemporal observations over a fast-growing alfalfa canopy. The compensated data are then used in the inversion of BRDF models to estimate LAI. The results showed that this approach is promising and there exists a potential for operational applications.

INTRODUCTION

Remote sensing has been used as a tool to infer properties of surface vegetation. In the past, the amount of vegetation, its spatial distribution, and its optical properties, have been associated with indices computed from remotely sensed data. This approach is simple, but case-sensitive. Relationships developed for one type of vegetation, or at different geographic location, are difficult to extrapolate to another type of vegetation or geographic locations.

With advances in space technology, more remote sensing platforms are to be launched with remote sensors capable of sensing the surface at multiple angles. These off-nadir measurements provide a more objective view of the ground surfaces and can, therefore, be used to infer vegetation properties in a more quantitative manner. Recent advances in bidirectional reflectance distribution function (BRDF) modeling have lead to quantitative assessment of such vegetation properties as percentage cover and leaf area index via model inversion procedures[1,2].

A major requirement in BRDF inversion is simultaneous multidirectional measurements. Current space-borne sensing systems do not have such capability, although the scheduled launch of advanced sensing systems such as the earth observing system (EOS) will have these capabilities. An alternative is to use multitemporal observations of different view angles, such as the daily observations acquired by the advanced very high resolution radiometer (AVHRR).

Applications of such data for model inversion are limited to the surfaces, such as desert areas, where vegetation may change little within a month period. Remote sensing measurements within this time frame can be regarded as multidirectional measurements, meeting the inversion requirement. In regions such as agricultural areas where vegetation changes rapidly, multitemporal measurements may not be suitable for BRDF modeling inversion, because these observations are actually made over different targets. To be able to use multitemporal observations from remote sensing platforms in model inversions it is necessary to take into account the effects due to changes in surface targets. The objective of this study is to develop strategies of incorporating the vegetation growth into the BRDF model approaches for estimations of vegetation physical properties.

AN INTEGRATED APPROACH

To interchangeably use multitemporal and multidirectional remote sensing measurements, a strategy of using sliding window and vegetation growth compensation model is described in Fig.1.
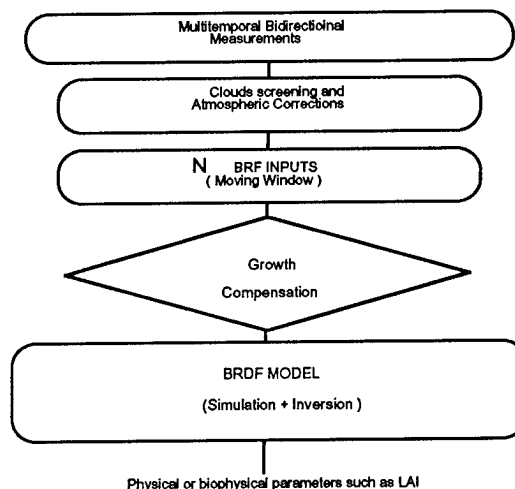
Fig. 1. Graphic presentation of an integrated approach to estimates of physical properties with BRDF models.

The multitemporal measurements are first subject to cloud screening and atmospheric corrections using compositing techniques. Variations in the remaining data will be due either to the bidirectional properties of the ground surfaces and /or to the growth of the vegetation canopy.

In the next, a sliding window will be selected, for example, from day 1 to day N, where N should be large enough such that the moving window will encompass statistically enough quality pixels (data points) to be used in the subsequent BRDF model inversion procedure. Note that the remaining N pixels should represent N independent observations of the same target, because each data point (each day's measurement) will be collected with different sensor geometric configurations due to the mechanics of the satellite sensing system and orbiting characteristics of the satellite. Experience from analysis of data obtained with the AVHRR data indicates that N is usually between 10 and 30 days. Vegetation during this N day period may have increased (growth) or decreased (harvesting, deforestation, fire, natural senescence etc.). Growth compensation will be checked by evaluating the spectral vegetation indices. If the vegetation increase is large enough to result in significant differences in observed radiometric signals, a growth compensation will be performed. If not, the data will be passed on to the next step for model inversion.

VEGETATION GROWTH COMPENSATIONS

We propose two techniques to overcome the inversion problems due to vegetation growth. The first technique is to develop a compensation model to offset the increases or decreases in radiometric measurements. During a growing window period (N days), vegetation may change (Fig.2).
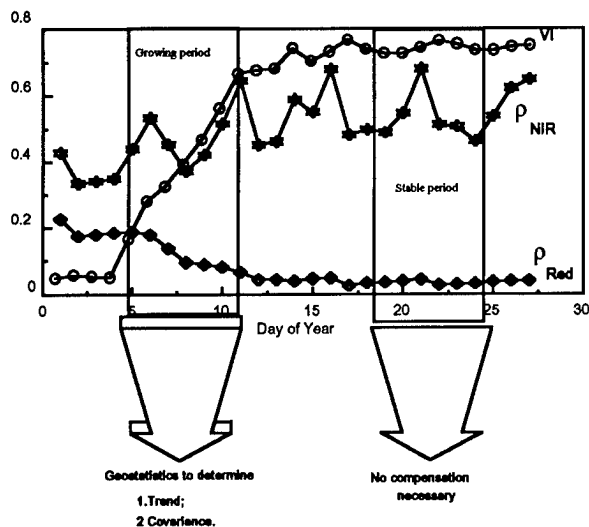
Fig.2 An illustration of vegetation growth compensation techniques.

If no changes in vegetation architecture is assumed, the cause of increased /decreased radiometric reflectances will be most likely due to changes in vegetation density. In this case, the data points within that window period apparently can not be used for BRDF inversion and a compensation model is needed. The compensation can be determined by examining the corresponding spectral vegetation index (normalized for external effects such as soil and atmosphere) by computing the statistical trend and variations for each spectral band. Then, an offset will be made based on the value of the computed trends, and the variation is assumed to be due to bidirectional effects. Once compensated for vegetation growth, the data will be passed to the next step for a model inversion.

The second technique is to locate a window period (Fig. 2) where vegetation is in stable stage. Data within this window period are used in model inversion, from which model parameters are obtained. Some of these parameters, such as leaf optical properties, can be assumed to change little with seasons and, therefore, can be used as known input parameters to the model itself for subsequent inversion procedures. Example parameters in the SAIL model [3] are the soil reflectances and leaf optical properties. The remaining variable parameter is leaf area index (LAI).

RESULTS

A total of two data sets was used to demonstrate the application of the proposed approach. In the first case, ground-based data were used while in the second case, satellite observations were used in inverting the SAIL model to estimate LAI values.

Case Study 1
The first data set was collected over a growing alfalfa canopy at the University of Arizona Campus Agricultural Center, Tucson, Arizona, from September 1 to 18 , 1995. The multitemporal bidirectional measurements were made each day at the time when the scheduled VEGETATION sensor on SPOT 4 satellite will pass over. The geometric configuration of the radiometer used was set to be the same as the VEGETATION sensor daily viewing angles at the target, and the spectral bands are identical to the SPOT high resolution visible (HRV) sensors. This data allowed us to investigate whether the multitemporal observations can be used a model inversion.

Fig.3a is the temporal bidirectional reflectances in red and near-infrared regions, with their corresponding reflectances compensated for vegetation growth within a growing period (from day of year 268 to 279). The data within this period were used in an inversion procedure of the SAIL model with and without vegetation growth compensations.
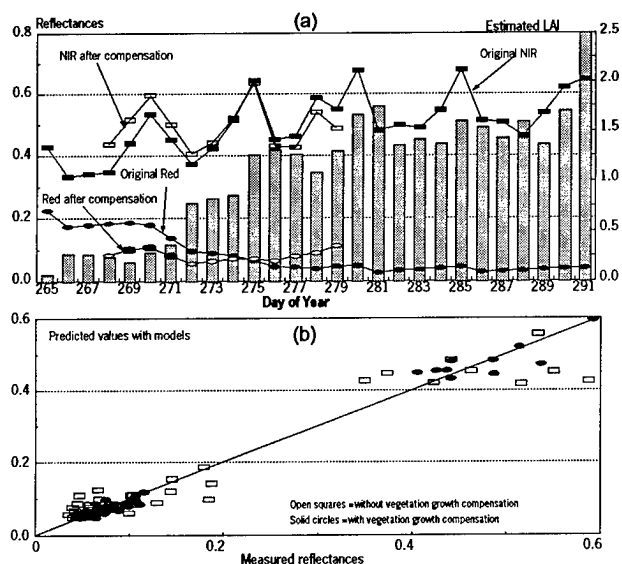
Fig.3 Temporal profiles of reflectances and estimated LAI values (upper) and comparison of measured vs. predicted reflectances using BRDF models (lower).

Fig.4 Temporal AVHRR data (upper) and estimated LAI values (lower) using the integrated approach.

Fig. 3b compares the predicted values with measurements when the data were used in inversion and simulation procedures with and without vegetation growth compensations. The model did not properly predict the measured reflectance values when parameters were used from inversion using data without compensation. Using data within this period of time would consequently affect the estimation of physical properties of vegetation when model inversion is used.

Using the second technique, we applied the data within a window period (Fig. 3a) where vegetation reached stable stage (full coverage) to invert SAIL model to obtain leaf optical properties and soil reflectances. These parameters were used as known parameters in the subsequent inversion of all data to estimated LAI values. The estimated LAI values are depicted in Fig.3a as vertical bars. The estimated LAI values reasonably represent the seasonal changes of the alfalfa canopy.

Case Study 2

A second data set contained AVHRR observations over a semi-arid region near Niamey, Niger from May to October 1992. Fig.4a shows the temporal variations of the NIR reflectances. When the second technique was applied to this data set for LAI estimation, the results (Fig. 4b) seemed to reasonably represent vegetation growth. The predicted LAI values in the early season did not match composited normalized difference vegetation index (NDVI). This may result from various sources of noise due to atmosphere and soil effects on the observed AVHRR data.

DISCUSSION

This approach uses multitemporal measurements for BRDF model inversion procedures with compensation for vegetation growth. This approach was validated with two data sets and appeared promising. It should be validated with more remote sensing data, especially with multitemporal observations.

A sensitivity analysis is needed to study the effect noise in the remote sensing measurements. The vegetation growth compensation was made with a simple regression technique at this time to find the trend. Other means such geostatistics should be explored. Since this approach requires model inversion and simulation, it may be difficult to apply this approach to large data sets in an operational manner. In conclusion, further study is needed to explore this approach with more multitemporal remote sensing data and ground measurements of those parameters of interests.

REFERENCES

[1]S. Jacquemoud, "Inversion of the PROSPECT+SAIL canopy reflectance models from AVIRIS equivalent spectra:theoretical study," Remote Sens. Environ. 44:281-292, 1993

[2] J. Qi , F. Cabot, M. S. Moran, and G. Dedieu, "Biophysical Parameter retrievals using multidirectional measurements", Remote Sens Environ.,54:71-83, 1995

[3]W.Verhoef, "Light scattering by leaf layers with application to canopy reflectance modeling, the SAIL model", Remote Sens. Environ. 16:125-141, 1984.

Comparison of Vegetation Index Compositing Scenarios:
BRDF Versus Maximum VI Approaches

W.J.D. van Leeuwen[1*], A.R. Huete[1], S. Jia[1], and C.L. Walthall[2]

[1]Department of Soil, Water and Environmental Science, University of Arizona, 429 Shantz Building #38, Tucson, AZ 85721, USA, tel 520-621-8514, fax 520-621-1647, e-mail *: leeuw@ag.arizona.edu

[2]USDA-ARS, Remote Sensing Research Laboratory 116 Bldg. 007, BARC-West, Beltsville, MD 20705, USA

Abstract -- Satellite sensors, such as the AVHRR, SPOT and soon to be launched MODIS, MISR, VEGETATION and GLI acquire bidirectional reflectance data under different solar illumination angles. These systems will capture the strong anisotropic properties that vary with relative amounts and types of vegetation and soil within each pixel. Therefore, some knowledge of the bidirectional reflectance distribution function (BRDF) is a requirement for successful interpretation of directional reflectance data and vegetation indices, and derivation of land-cover-specific biophysical parameters. The objectives of this research were: a) to parameterize empirical and semi-empirical BRDF models for different land cover types and MODIS spectral bands, b) utilize the BRDF models to correct off-nadir measurements to nadir-equivalent values for vegetation index (VI) compositing and biophysical interpretation and c) compare different vegetation index compositing scenarios.

High spectral (10-12 nm), and spatial (3 m at nadir), resolution bidirectional reflectance factor (BRF) measurements from the Advanced Solid State Array Spectroradiometer (ASAS) flown on the NASA C-130B aircraft were used for the analysis. Leaf area index (LAI) measurements were made concurrently at most of the study sites which included deciduous and coniferous forest, grassland and shrub savanna land covers. The normalized difference vegetation index (NDVI) and modified VI (MVI) were selected as classifiers in five different vegetation index composite scenarios:
- a maximum VI based on apparent reflectance data,
- a maximum VI based on at-surface reflectance data,
- a BRDF standardized VI, based on at-surface reflectances at nadir view angle (using a representative sun angle),
- a BRDF normalized VI, based on at-surface reflectances at nadir view and nadir sun angles,
- a normalized bidirectional VI distribution function (BVIF).

Nadir-equivalent VI accuracy and predictability were evaluated for all compositing scenarios using the measured nadir observations as a reference. Extrapolation of the BRDF models to nadir sun angles was found to be inaccurate. VI composite scenarios based on the standardization of reflectances to nadir view angles was more accurate than the maximum VI approach. The results of the analysis emphasize the importance of standardizing BRF for vegetation index compositing schemes and retrieval of biophysical parameters.

INTRODUCTION

The interpretation and utilization of vegetation index data on a global scale is affected by a combination of factors such as the surface soil and vegetation properties, atmospheric conditions and the solar illumination and sensor characteristics. There is a wide range of variability among these factors, affecting each vegetation index and therefore their biophysical interpretation in a specific way. This will be a major issue when dealing with forthcoming data from the Moderate Resolution Imaging Spectroradiometer (MODIS) [1].

The Advanced Very High Resolution Radiometer (AVHRR) normalized difference vegetation index (NDVI) compositing scenario is based on a maximum NDVI approach and includes additional cloud screening and data quality checks [2]. Although the maximum NDVI approach was designed to select pixels without clouds and closest to nadir within a 10-day period, research has shown that these assumptions cannot be sustained. Selected pixels often have large view angles and are not always cloud-free [3,4]. Since residual clouds and the view angle alter the surface reflectances and thus the VIs, comparisons of global vegetation types will not be consistent throughout the year.

The objective of this research was to compare different vegetation index compositing scenarios utilizing bidirectional reflectance data for a range of vegetation types.

DATA AND METHODS

Major land cover types included in this study are deciduous and coniferous forest (Oregon Transect Ecosystem Research Project - OTTER, Boreal Ecosystem Atmosphere study-BOREAS), grassland (First ISLSCP Field Experiment - FIFE) and shrub savanna sites (Hydrologic, Atmospheric pilot Experiment in the Sahel - HAPEX-Sahel). High spectral resolution bidirectional reflectance factor (BRF) measurements were made with the Advanced Solid State Array Spectroradiometer (ASAS) instrument flown at ~5000m altitude. The ASAS reflectance data were convolved into the first three MODIS bands (ρ_{red}, ρ_{nir}, ρ_{blue}; 620-670 nm, 841-876 nm, 459-479 nm) and corrected for atmosphere effects with "6S". Aerosol optical depth data from the airplane and field sunphotometers and variable aerosol distributions and atmosphere profiles were used to correct for atmospheric effects and calculate reflectance factors. For each target all scenes were co-registered after which average apparent and surface reflectances were extracted for each MODIS band for an area of about 1-2 km^2. The view zenith angles ranged between 0° and 60° in both the forward scatter and backscatter direction. The NDVI and modified vegetation index (MVI) were used as classifiers in the five composite scenarios:

$$NDVI = (\rho_{nir} - \rho_{red})/(\rho_{nir} + \rho_{red}),\tag{1}$$

$$MVI = 2.5\ (\rho_{nir} - \rho_{red})/(1 + \rho_{nir} + 6\rho_{red} - 7.5\rho_{blue}).\tag{2}$$

In this study two BRDF models were used to model the BRF and VI data. The empirical Walthall BRDF model [5]:

$$\rho(\theta_v,\ \phi_s,\ \phi_v) = a\theta_v^2 + b\theta_v \cos(\phi_v - \phi_s) + c,\tag{3}$$

where the reflectance ρ is a function of the view zenith angle θ_v, and the sun and view azimuth angles ϕ_s, ϕ_v ; a, b and c are coefficients obtained using a least square fitting procedure. c is equal to the nadir reflectance. The semi-empirical Roujean model:

$$\rho(\theta_s,\ \phi_s,\ \theta_v,\ \phi_v) = k_{iso} + k_{geo}\ f_{geo} + k_{vol}\ f_{vol},\tag{4}$$

where f_{geo} and f_{vol} are functions related to geometric and volume scattering components; k_{iso} represents the isotropic bidirectional reflectance (for $\theta_s = \theta_v = 0$), k_{geo} and k_{vol} are parameters related to several canopy geometric and optical properties [6]. Roujean's BRDF model was inverted to compute the reflectances at the mean and nadir solar zenith angles and nadir view zenith angle. Both models were parameterized for both MODIS band reflectance data and vegetation index data.

RESULTS AND DISCUSSION

An example of ASAS BRF (apparent and at-surface reflectances for three MODIS bands) are given in Fig. 1 for "tigerbush", collected during HAPEX (1992). Graphical presentations of the different vegetation types will appear in a future communication. The difference between TOA and at-surface reflectance factors are minimal for all data sets because they were collected under fairly clear sky conditions (all aerosol optical depths @ 550 nm were below 0.27). For most vegetation types, the backscatter direction had the highest reflectance response. Although the hot spot effect (increase in reflectance when view and solar zenith and azimuth angles are the same) was barely noticeable (around -45° in Fig. 1), hot spot effects can be seen in some of the peak MVI responses in Fig. 2.

The vegetation index response about nadir showed significant variability and was different for each vegetation type (Fig. 2). Both the NDVI and MVI were affected by the view angle, but the MVI showed larger deviations about nadir.

The results of the five composite scenarios are presented for the MVI and partly for the NDVI (Table 1). Percentages of absolute difference, between the measured nadir VIs and the VIs resulting from the different composite scenarios, were computed for each vegetation type. The mean difference and standard deviation for all vegetation types were computed per composite scenario to show the differences in performance (Table 1). The larger the mean difference, the larger the "error" with respect to nadir-equivalent estimation of the VI. The maximum VI scenarios generally showed a preference for off-nadir view
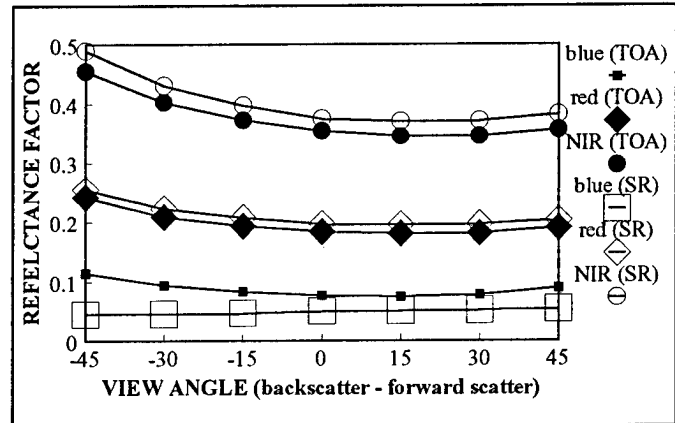
Fig. 1: BRF for HAPEX Tigerbush site (Sept 3, 1992, solar zenith angle 45°; data in solar principal plane) MODIS bands blue, red and near infrared, (TOA - top of atmosphere reflectance; SR - surface reflectance).
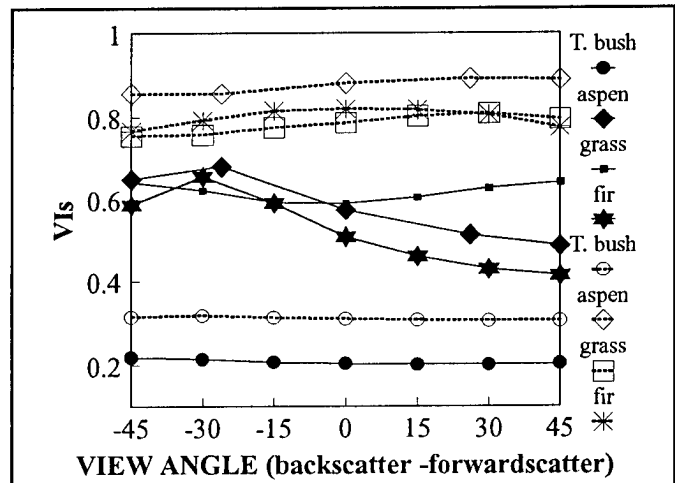
Fig. 2: Effect of surface anisotropy on MVI and NDVI for Tigerbush (HAPEX), Aspen (BOREAS), Douglas fir (OTTER), and Grassland (FIFE) (— MVI, ----- NDVI).

angles for both the NDVI and MVI and both the principal solar plane and the plane orthogonal to this. The hot spot affected the NDVI, but forward scatter view angles were preferentially selected for the maximum NDVI composite scenario. The maximum MVI scenario preferentially selected the backscatter direction. Maximum VI composite scenarios for at-surface reflectances and apparent reflectances had larger errors than the BRDF based scenarios, except for the BRDF scenarios with extrapolation to nadir sun and nadir view zenith angles. The latter scenario (scenario 4, Table 1) resulted in unrealistic estimates of reflectances and VIs. This was likely due to lack of variable solar zenith angles in the data sets. The bidirectional vegetation index function (BVIF) composite scenario was successful with only slightly higher errors than the BRDF composite scenario. The main disadvantage of the BVIF will be the loss of the actual surface reflectances needed to compute other VIs for instance.

The BRDF models (Walthall and Roujean) performed equally

1424

well for most vegetation types. A simple BRDF model seemed adequate to model the BRDF for a range of global vegetation types and produced nadir-equivalent VIs with a mean absolute error of about 0.62% for the MVI and 0.18 % for the NDVI, (respective standard deviations were 0.7% and 0.46 %).

CONCLUSIONS

Although limited measurements were available to model the BRDF for all combinations of view/sun azimuth and zenith angles, the parameterization of the BRDF models and the response of NDVI and MVI were different for most land cover types. A BRF correction of off-nadir reflectance factors to nadir equivalent values seems very much needed for both vegetation indices (NDVI and MVI), especially for higher vegetation covers. Maximum VI compositing scenarios introduced larger errors than the BRF composite scenarios (extrapolation to nadir view angle, at a representative sun angle), except when a BRDF model was used to extrapolate to surface reflectances with both nadir view and nadir sun angles. The results emphasize the importance of standardizing BRFs for vegetation index compositing schemes and retrieval of biophysical parameters.

ACKNOWLEDGMENTS

REFERENCES

[1] Running, S.W., Justice, C., Salomonson, V., Hall, D., Barker, J., Kaufmann, Y., Strahler, A., Huete, A., Muller, J.P., VanderBilt, V.,Wan, Z.M., Teillet, P. and Carneggie, D., "Terrestrial Remote Sensing Science and Algorithms planned for EOS/MODIS," Int. J. Remote Sensing, 1994, Vol. 15(17), pp 3587-3620.

[2] Eidenshink, J.C. and Faundeen, J.L., "The 1km AVHRR global land data set: first stages in implementation," Int. J. Remote Sensing, 1994, 15(17), pp. 3443-3462.

[3] Cihlar, J., Manak, D., and Voisin, N., "AVHRR Bidirectional Reflectance Effects and Compositing," Remote Sens. Environ., 1994, Vol 48, pp. 77-88.

[4] Moody, A. and Strahler, A.H., "Characteristics of composited AVHRR data and problems in their classification," Int. J. Remote Sensing, 1994, 15(17), pp. 3473-3491.

[5] Walthall, C.L., Norman, J.M., Welles, J.M., Campbell, G., and Blad, B.L., "Simple equation to approximate the bidirectional reflectance from vegetative canopies and bare soil surfaces," Applied Optics, 1985, 24(3), pp. 383-387.

[6] Roujean, J-L., Leroy, M., and Deschamps, P-Y, "A Bidirectional Reflectance Model of the Earth's Surface for the Correction of Remote Sensing Data," J. Geophys. Res., 1992, Vol. 97, No. D18, pp.20455-20468.

Table 1: Overview of the at-nadir NDVI and MVI from ASAS data for a range of vegetation types with estimates of measured leaf area index (LAI). Five composite scenarios were compared with reference to the nadir NDVI and MVI; 1) the maximum VI for apparent reflectances (TOA-top of atmosphere), 2) maximum VI for at-surface reflectances (SR), 3) VIs based on nadir-view-equivalent reflectances obtained with the Walthall BRDF model and the Roujean BRDF model, 4) VIs based on nadir view/sun equivalent reflectances obtained with the Walthall BRDF model and the Roujean BRDF model, and 5) nadir equivalent VIs based on substitution of the reflectances by VI values in Walthall's and Roujean's model. Future communications will include the presentation of all BRDF results for the NDVI. (where: (B) = BOREAS, (O)=OTTER, (F)=FIFE, (H)=HAPEX, pp - principal plane; op - orthogonal plane).

Vegetation type	LAI	sun zenith (°)	reference SR nadir MVI	reference SR nadir NDVI	TOA[1] max MVI	view angle (°)	TOA[1] max NDVI	view angle (°)	SR[2] max MVI	view angle (°)	SR[2] max NDVI	view angle (°)	MVI[3] Walt. BRDF	MVI[3] Rouj. BRDF	MVI[4] nadir Rouj.	MVI[5] Walt. BVIF	MVI[5] Rouj. BVIF	MVI[4,5] nadir BVIF
Old Black Spruce (B) pp	3.5	33.7	0.280	0.744	-14.31	-45	5.81	30	-7.05	-45	0.00	45	-0.55	-0.30	12.00	-0.80	-0.60	20.25
Old Black Spruce (B) op	3.5	33.5	0.285	0.730	-3.42	0	5.31	0	0.00	0	-0.19	26	1.09	0.97	16.77	1.06	0.97	22.93
Old Aspen (B) pp	2.4	34.7	0.574	0.882	-21.01	-60	3.09	26	-10.5	-26	-1.67	55	-2.18	-1.44	4.39	-2.70	-1.96	5.64
Old Aspen (B) op	2.4	36.1	0.540	0.890	-7.07	-26	4.08	0	-0.38	-26	0.00	0	0.17	-0.16	22.69	0.15	-0.17	38.15
Alder tree forest (O) pp	4.3	34.6	0.461	0.913	-26.76	-45	7.00	30	-14.4	-45	-2.21	45	-1.13	-1.15	32.42	-1.34	-1.42	96.74
Old Forest (O) pp	6.4	32.3	0.422	0.920	-26.41	-45	7.24	30	-15.7	-45	-1.96	45	-1.17	-1.18	45.41	-1.49	-1.56	143.29
Waring Woods (O) pp	5.3	30.7	0.354	0.623	-14.85	-30	2.46	30	-8.15	-30	-1.79	-15	-1.17	-1.16	20.61	-1.35	-1.36	36.70
Douglas Fir (O) pp	8.6	31.5	0.509	0.820	-21.23	-30	4.54	15	-14.6	-30	0.00	0	-2.11	-2.09	29.16	-2.55	-2.51	88.52
green grass (F) pp	1.3	48.3	0.589	0.785	-23.03	-45	4.14	15	-5.30	45	-2.34	30	-0.53	-0.75	21.20	-0.40	-0.68	221.86
green grass (F) op	1.3	42.4	0.598	0.784	-15.28	-45	3.98	30	-5.01	-45	-2.02	30	-0.62	-0.55	-28.33	-0.61	-0.54	138.45
senescent grass (F) pp	0.2	54.3	0.296	0.482	-10.78	45	-1.30	30	-5.64	45	-2.48	30	-0.66	-0.64	13.92	-0.71	-0.67	19.99
senescent grass (F) op	0.2	60.8	0.304	0.482	-11.52	45	-0.16	-30	-3.72	45	-0.96	-45	-0.02	-0.11	22.55	0.00	-0.10	30.19
Fallow savanna (H) pp	0.5	36.0	0.219	0.302	-7.35	-45	-2.57	-45	-3.26	-45	-2.74	-45	-0.20	-0.17	2.98	-0.20	-0.18	3.84
Tigerbush (H) pp	0.5	43.0	0.203	0.309	-5.66	-45	-0.62	0	-1.50	-45	-0.79	-30	0.01	-0.02	3.55	0.02	0.00	10.00
mean absolute difference for all vegetation types					-14.91		3.07		-6.81		-1.37		-0.65	-0.62	15.66	-0.78	-0.77	63.00
Standard deviation					7.22		2.90		4.90		0.94		0.82	0.70	16.10	0.97	0.85	61.33

Retrieval of Canopy Structural Parameters From Multiangle Observations Using an Artificial Neural Network

Abdelgadir A. Abuelgasim, Sucharita Gopal and Alan H. Strahler
Center For Remote Sensing and Department of Geography, Boston University,
725 Commonwealth Avenue, MA 02215. (617) 353-5233 Fax (617) 353-3200

ABSTRACT

This paper describes a procedure for the retrieval of canopy structural parameters (e.g. height, shape, density) from multiangle reflectance measurements using an artificial neural network (ANN). The objective is to train a neural network to learn the association of canopy structural parameters with its corresponding directional reflectance pattern. The Li-Strahler [1] geometric-optical mutual shadowing model is used to simulate the bidirectional reflectance of a canopy based on the geometry of the trees. The reflectance generated from the model is used as an input to a multilayer feed-forward neural network, with the canopy structural parameters as outputs. ANNs have great potentials to learn the relation (or any continuous function) between input patterns and desired outputs without any prior knowledge of the mapping function. Using the neural network retrieval approach, the R^2 between the model predicted canopy parameters and the actual parameters of density is 0.85 and 0.75 for the tree crown diameter and canopy height.

INTRODUCTION

The main objectives of this article are to assess and explore the use of artificial neural networks in inverse modeling of the bidirectional reflectance of a forest. The problem of inverse modeling in remote sensing is treated here as a mathematical relationship between a set of input parameters and a set of output parameters, that is canopy parameters and corresponding bidirectional reflectances. Multilayer feed-forward neural networks learn adaptively by examples to approximate an input-output relation or a mapping function between a canopy's bidirectional reflectance distribution function (BRDF) and its structural parameters. The assumption here is that the bidirectional reflectance of a canopy is a function of the geometry of its constituent elements (tree height, shape), the spatial distribution of the elements, and the illumination and viewing geometry. This implies that the bidirectional reflectance of the canopy is particular to the canopy's structural parameters, and that canopies with different parameters will exhibit different bidirectional reflectance.

This study uses a data set that is simulated using the Li-Strahler geometric-optical mutual shadowing model [1]. The model predicts the bidirectional reflectance of tree canopies based on the geometry of the trees, their spatial distribution, the component signatures of the canopy elements, and the viewing and illumination geometry. This model is used to generate a large data set for training and testing the neural network. A typical input to the network in this case consists of the bidirectional reflectance, a set of parameters that describe the typical spectral signatures of the elements present in the scene, and the set of parameters that describe the illumination and viewing geometry (Fig 1). The output from the network will be the canopy structural parameters in reference to density, crown shape and height.

Figure 1
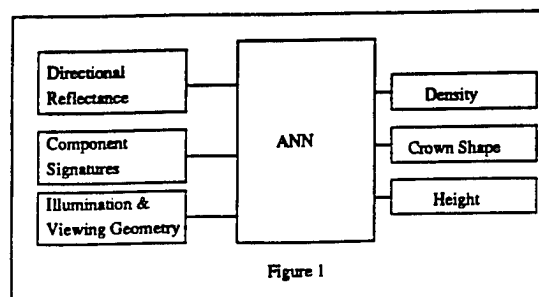
METHODOLOGY

The Li-Strahler geometric-optical mutual sha-

dowing model is used to simulate the bidirectional reflectance of different canopy types with varying parameters of tree geometry and spatial distribution. For the tree geometry three vegetation covers were simulated: (a) conifer, (b) savanna, and (c) shrubland. For this, 2200 canopy sites are simulated where each site has its unique tree geometry and density. In calculating the model's BRDFs, the solar illumination angle is varied from 15° at increments of 5° to a maximum of 60°. The component signatures are chosen to be similar to reflectance signatures typical at the red spectral band. This data set was divided to a training set of 2000 observations and a testing data set with 200 observations.

The input data set used in this study consist of reflectance values and component signatures, where most of these values cluster in a range between 0.03 and 0.25. It was necessary to preprocess these values to enhance the variability. Hence, a logarithmic transformation is applied to the input values.

NEURAL NETWORK MODELING

This study uses a multilayer feed-forward neural network to perform the canopy inverse modeling. Such networks approximate the mathematical relation between a set of input parameters and a set of output parameters through a supervised learning approach. Previous studies [2] and [3], have shown that a multilayer feed-forward neural network can approximate any continuous input-output relation provided it contains the sufficient number of hidden units. An extensive description and review of the multilayer feed-forward networks and the algorithm used for training called "backpropagation" is given in [4].

A neural network with three fully connected layers is developed to estimate the three canopy parameters, density, crown shape, and canopy height. The input vector consists of 22 variables, where 18 represent the bidirectional reflectance of a canopy in the principal plane and across the principal plane (from +60° in the backward scattering direction to -60° in the forward scattering direction at increments of 15°.) The other 4 parameters represent the 3 component signatures and the solar illumination angle. The output vector consists of three units representing, the density, crown shape and canopy height. The hidden layer consists of 30 processing units.

For training the network, a hyperbolic function is used as the network's activation function. The transformed logarithmic values are scaled between −1.0 and 1.0 for the inputs and −0.8 and 0.8 for the outputs. A learning rate of 0.3 and a momentum of 0.4 are used during training. Training was stopped when the root mean square error was less than 0.01.

RESULTS AND DISCUSSIONS

Table 1 reports the results of testing the prediction and generalization ability of the network. It shows the R^2 values between the network-predicted canopy parameters and actual canopy parameters. The R^2 for the density parameter is approximately 0.85 and 0.75 for both the crown shape and height parameters.

Table 1

Canopy Parameter	R^2
Density	0.858
Crown Shape	0.759
Height	0.758

An interesting issue in the analysis of the retrieval of canopy parameters is to study the effect of the modification of the input vector on the performance of the network estimation. This is investigated by two approaches. The objective of the first is to analyze the contribution of the across principal plane information in the estimation procedure. This is tested by performing the inversion using the principal plane reflectance only and assessing the network performance. The second approach involves reducing the principal plane reflectance measurements and observing the network performance.

New networks are developed for both cases. In the first approach, the neural network consists of a reduced input vector with 13 units. The hidden layer and the output layer remain unchanged. The network is again tested for the estimation of the three canopy parameters. Table

2 shows the R^2 of the testing data set of the three parameters. For the second case, the input vector is modified by deleting the the input units representing the bidirectional reflectance at -60° and +60°. A network with 11 input units, 30 hidden units and 3 output units is trained and tested. Table 3 shows the R^2 of the testing data set for the three parameters.

Table 2

Canopy Parameter	R^2
Density	0.843
Crown Shape	0.554
Height	0.526

Table 3

Canopy Parameter	R^2
Density	0.788
Crown Shape	0.524
Height	0.552

The results in Table 1 shows that accurate estimation of different canopy parameters from multiangle measurements can be achieved through the use of multilayer neural networks. The inversion of the canopy parameters worked fairly well, capturing between 75% to 85% of the total variance in the data. The density parameter is best estimated with an R^2 of 0.85 and 0.75 for both the crown shape and canopy height.

A decrease in the accuracy of the estimation for the crown shape and canopy height is noted when across principal plane reflectance's are excluded. Similarly, a decline is noted upon reducing the extreme measurements on the principal plane. Note that the BRDF information generated by the Li-Strahler model is not uniformly distributed. Both the principal plane and across principal plane contain important information about the surface's BRDF.

CONCLUSIONS

The study demonstrates that neural networks can be effective in the estimation of canopy parameters from multiangle reflectance measurements. Such networks provide an alternative viable approach for inverse canopy modeling, and offer many advantages over the conventional statistical methods. Multilayer neural networks learn adaptively to approximate the mathematical relation between a set of input parameters and a set of output parameters, without a priori knowledge of the mapping function. Future research in this area can be directed towards estimating other canopy biophysical parameters such as leaf area index (LAI) from reflectance measurements.

ACKNOWLEDGEMENTS

REFERENCES

[1] Li, X. and Strahler, A. H. (1992), Geometric optical bidirectional reflectance modeling of the discrete crown vegetation canopy: Effect of crown shape and mutual shadowing, IEEE Trans. Geosci. Remote Sens., 30:276-292.

[2] Hornik, K., Stinchcombe, M., and White, H., (1989), Multilayer feed-forward networks are universal approximators, Neural Nets., 2:359-366.

[3] Cybenko, G. (1989), Approximation by superpositions of sigmoidal function, Mathematics of Control, Signals, and Systems, 2:303-314.

[4] Rumelhart, D.E., Hinton, G.E., and Williams, R.J. (1986a), Learning representations by back-propagating errors, Nature., 323:533-536.

OBSERVATIONS AND MODELLING OF RADIOMETRIC SIGNATURES OF STORMS IN THE FREQUENCY RANGE OF 90-220 GHz

J. R. Wang, C. Kummerow, and P. Racette
NASA/Goddard Space Flight Center, Greenbelt, MD 20771
Tel: (301) 286-8949
FAX: (301) 286-1762
Email: wang@sensor.gsfc.nasa.gov

W. Olson and J. Zhan
Caelum Research Corporation, Silver Spring, MD

ABSTRACT

During the past three years, a number of observations have been made with an airborne Millimeter-wave Imaging Radiometer (MIR) over the storms in the western Pacific Ocean and in the coastal region of the eastern United States. MIR measured radiometric signatures of these storms at six frequencies of 89, 150, 183.3±1, 183.3±3, 183.3±7, and 220 GHz. Analyses of these measurements show that brightness temperatures (T_b) at all frequencies are strongly depressed. In some cases the T_b depression displays a strong frequency dependence of scattering by hydrometeors. In other cases there is a leveling off of scattering at high frequencies, i.e., T_b values at 150 and 220 GHz are quite comparable. A few high-towering scattering cells are found to display unique signatures at the three water vapor channels near 183.3 GHz which in turn could be used to identify these cells. A series of calculations with a backward Monte Carlo technique, using profiles of hydrometeors generated by a cloud model, are performed to simulate some of these observed features. Results from these calculations are compared with observations and their implications on the storm structures will be discussed.

INTRODUCTION

Microwave radiometric measurements of precipitating systems have been conducted from both aircraft and satellite altitudes for nearly two decades [1-2]. Most of these measurements were limited to frequencies < 90 GHz. Only a few studies with frequencies > 90 Ghz have been reported in the literature [3-4]. These studies have contributed much towards our understanding of some unique features associated with the scattering of radiation near 90 and 183 GHz by atmospheric hydrometeors. However, the rich information contained in these high frequency observations over rain storms remains to be explored fully. In this paper we report the observations of rain storms during the TOGA/COARE (Tropical Ocean Global Atmosphere/Coupled Ocean Atmosphere Response Experiment) mission

by a Millimeter-wave Imaging Radiometer (MIR) aboard a NASA ER-2 aircraft. The differences in T_b values observed over storms at different frequencies are described. The implications from the features displayed by the three water vapor channels near 183.3 GHz are discussed.

THE MEASUREMENT RESULTS

A series of flights were made for TOGA/COARE in the western Pacific during January-February of 1993. MIR is one of several key instruments aboard the ER-2 aircraft for this mission. A typical flight normally lasted about 6 hours and covered a variety of atmopsheric conditions. The MIR signatures over a typical storm region observed between 0446 and 0457 UTC on January 19 are displayed in Fig. 1. Here the variations of the T_b values at nadir for 89, 150 and 183.3±3 GHz channels are shown in the middle portion of the figure; those for 220 GHz channel and 13 μm channel from MAS (MODIS Airborne Simulator) at the top of the figure, and the variations for the differences of T_b's between pairs of water vapor channels are shown in the bottom of the figure. There is a strong correlation among all the MIR channels as expected, especially in the regions of scattering characterized by low T_b values. The T_b values in the three window channels of 89, 150 and 220 GHz suggest a strong frequency dependence of scattering, i.e., T_b's are generally lower the higher the frequency of observations. The 13 μm channel from the MAS stay within ±5 K of the median value of about 215 K with a single exception at about 0454 UTC where its T_b values drop to below 190 K. This occurs at the place where T_b's from all the MIR channels are at their lowest values and corresponds to a convective cell with a significant updraft of hydrometeors that cause a strong scattering of radiation at the MIR frequencies. The presence of such a towering cell is confirmed by a strong radar reflectivity at 15 km altitude near the location of the ER-2 aircraft at 0454 UTC [5]. It can also be inferred from the signatures of the three 183.3 GHz channels.

It is stipulated that the dispersion of the water vapor channels, i.e., the positive values of the T_b differences at the
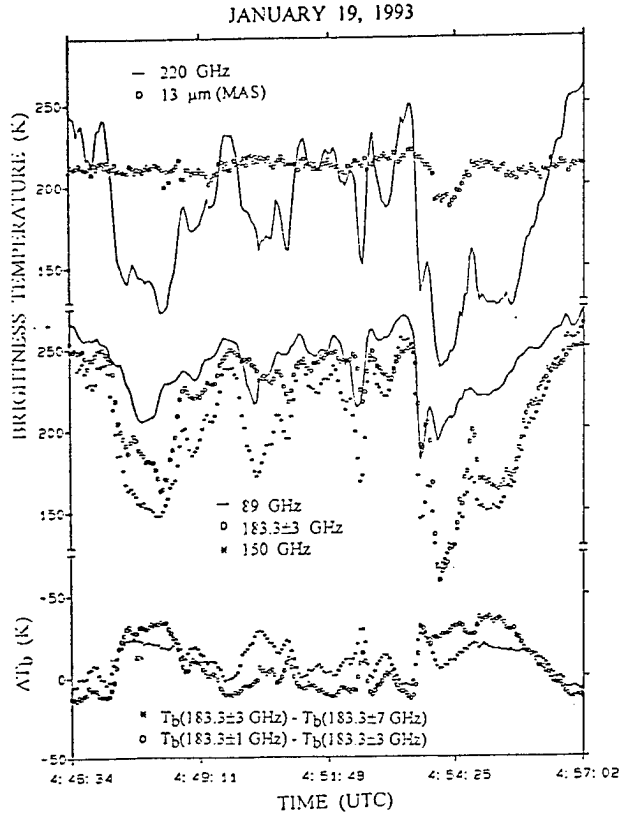
Fig 1. Time variations of brightness temperatures observed by MIR and MAS over a storm in western Pacific.

Fig. 2. The variations against total precipitable water of the brightness temperatures and their differences calculated for the three channels near 183.3 GHz

bottom of Fig. 1, is caused by a small amount of water vapor above the scattering media. The situation is qualitatively analogous to that reported previously by Wang et al. [6] for a dry atmosphere over the cold ocean background. Much could be learned from those reported results. Fig. 2 shows the variations of T_b and their differences against the total precipitable water ρ (g/cm^2) for these water vapor channels. The calculations are made for a dry atmosphere with different ρ values over an ocean background. The curves for the differences in T_b's between two frequencies ν_1 and ν_2 are denoted by $\Delta T_b(\nu_1, \nu_2)$ in the bottom of the figure. Notice that, at $\rho > 0.7$ g/cm^2, the atmosphere becomes opaque to all three water vapor channels and T_b values monotonously decrease with ρ; T_b at 183.3±1 GHz assumes the lowest value because its weighting function peaks at the highest altitude among the three channels. The interesting features occur in those region with $\rho < 0.7$ g/cm^2 where $T_b(\nu)$'s and $\Delta T_b(\nu_1, \nu_2)$'s show more rapid changes. As ρ decreases, the 183.3±7 GHz channel begins to see the cold surface background and $T_b(183.3\pm7)$ is the first to show a decrease. This is followed in sequence by the 183.3±3 GHz and the 183.3±1 GHz channels as ρ decreases further. The 183.3±7 GHz curve intersects the 183.3±3 GHz curve at $\rho \cong 0.63$ g/cm^2, and then the 183.3 GHz curve at $\rho \cong 0.58$ g/cm^2. The 183.3±3 GHz curve intersects the 183.3±1 GHz curve at $\rho \cong$

0.31 g/cm^2. This sequence of occurrences is observed by the MIR from data collected over all scattering cells without a single exception. Two examples are shown in Fig. 3 where the observed variations of $\Delta T_b(\nu_1, \nu_2)$'s from portion of Fig. 1 and from another event observed over southern Florida on October 5, 1993 are plotted.

The dotted horizontal lines in Fig. 3, like the horizontal dashed line in Fig. 2, provide a reference where $\Delta T_b(\nu_1, \nu)_2$'s change sign. A close examination of the figure reveals that, going from the quiescent to the scattering media in the time axis, the $\Delta T_b(183.3\pm3, 183.3\pm7)$ curve changes from negative to positive values first. This cross-over from negative to positive regions is followed in sequence by $\Delta T_b(183.3\pm1, 183.3\pm7)$ and $\Delta T_b(183.3\pm1, 183.3\pm3)$ curves. This sequence of cross-overs is reversed leaving from the scattering to the quiescent media. Even the $\Delta T_b(\nu_1, \nu_2)$'s over the small and weak scattering cell at 0453 UTC in Fig. 3a follow this general trend. Once crossing these thresholds to the region of scattering with decreasing ρ (Fig. 2), $\Delta T_b(\nu_1, \nu_2)$'s first increase and then decrease with the decrease in $T_b(\nu)$'s. The minima in $\Delta T_b(\nu_1, \nu_2)$ indicated by the arrows in Fig. 3 correspond to the locations of the lowest ρ for these scattering cells. For the event on January 19, this occurs at ~ 0454 UTC (Fig. 1) where minima in both $\Delta T_b(\nu_1, \nu_2)$'s and $T_b(\nu)$'s are observed. Since it is unlikely to have a hole

1430
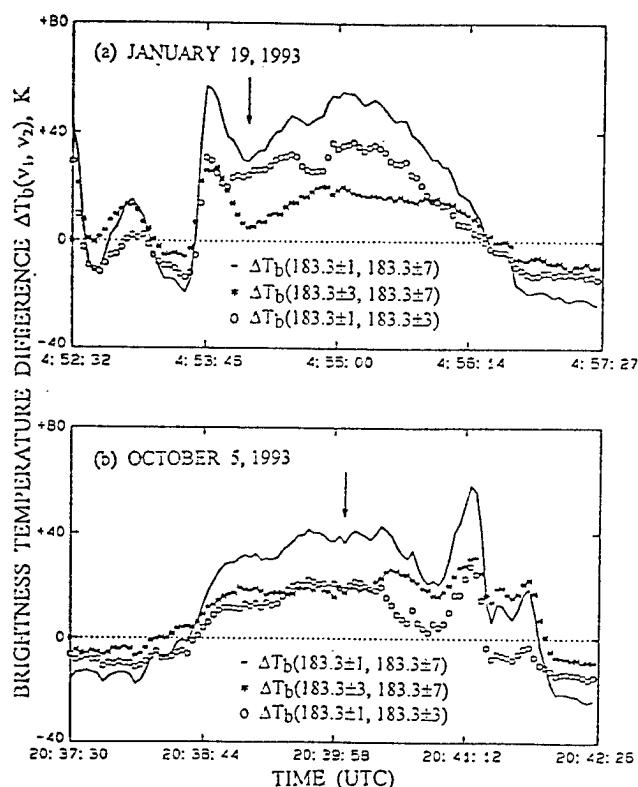
Fig. 3. Time variations of the brightness temperature differences observed from the MIR water vapor channels on (a) January 19, 1993 and (b) October 5, 1993.

of a few km in size deficient of water vapor in the atmosphere, a plausible picture would be a towering scattering cell.

RADIATIVE TRANSFER CALCULATIONS

Calculations of upwelling T_b's have been made with a backward Monte Carlo technique [7], based on profiles of hydrometeors generated by a cloud model [8]. The cloud model was used to simulate a squall line in a tropical oceanic environment. In general, computed T_b values were sensitive to assumptions regarding the size distributions and material densities of the ice hydrometeor species (cloud ice, graupel, snow, and frozen drops). In regions of the simulated squall line where significant ice hydrometeors were present, computed T_b's at 220 GHz were ~5-20 K below those at 150 GHz. These 150 T_b's in turn were ~10-40 K below those at 89 GHz. The negative to positive cross-overs in the $\Delta T_b(183.3\pm3, 183.3\pm7)$, $\Delta T_b(183.3\pm1, 183.3\pm7)$, and $\Delta T_b(183.3\pm1, 183.3\pm3)$ curves were also simulated using the model squall line.

CONCLUSIONS

Radiometric measurements over a few storms in the western Pacific were made with an airborne MIR in the frequency range of 89-220 GHz during January-February 1993. Results showed a variety of frequency dependence of the scattered millimeter-wave radiation, reflecting a complex structure and distribution of the atmospheric hydrometeors. The signatures at the three 183.3 GHz channels were shown to be useful in identifying towering cells and other scattering characteristics. Calculations of upwelling T_b's using a backward Monte Carlo technique provided results that showed features of frequency dependence roughly consistent with the MIR measurements. The cloud model is currently being fine-tuned to match calculations with measurements so as to infer the structure of hydrometeors

REFERENCES

1. T. T. Wilheit, A. T. C. Chang, M. S. V. Rao, E. B. Rodgers, and J. S. Theon, "A satellite technique for quantitatively mapping rainfall rates over the oceans," J. Appl. Meteor., 16, 551-560, 1977.

2. R. W. Spencer, H. M. Goodman, and R. E. Hood, "Precipitation retrieval over land and ocean with the SSM/I: Part I: Identification and characteristics of the scattering signal," J. Atmos. Ocean. Tech., 6, 254-273, 1989.

3. R. F. Adler, R. A. Mack, N. Prasad, H.-Y. M. Yeh, and I. M. Hakkarinen, "Aircraft microwave observations and simulations of deep convection from 18 to 183 GHz. Part I: Observations," J. Atmos. Ocean. Tech., 7(3), 377-391, 1990.

4. I. M. Hakkarinen and R. F. Adler, "Observations of convective precipitation at 92 and 183 GHz: Aircraft results," Meteor. Atmos. Phys., 38, 164-182, 1988.

5. J. R. Wang, J. Zhan, and P. Racette, "Storm-associated microwave radiometric signatures in the frequency range of 90-220 GHz," J. Atmos. Ocean. Tech., submitted, 1995.

6. J. R. Wang, T. T. Wilheit, and L. A. Chang, "Retrieval of total precipitable water using radiometric measurements near 92 and 183 GHz frequencies," J. Appl. Meteor., 28(2), 146-154, 1989.

7. L. Roberti, J. Haferman, and C. Kummerow, "Microwave radiative transfer through horizontally inhomogeneous precipitating clouds," J. Geophys. Res., 99(D8), 16707-16718, 1994.

8. W. K. Tao and J. Simpson, "Goddard cumulus ensemble model, part I: Model description," Terrest. Atmos. Ocean. Sci., 4(1), 35-72, 1993.

Observed and Theoretical Millimeter Wave Emission in the Tropics

J. B. Snider
Cooperative Institute for Research in Environmental Sciences (CIRES)
University of Colorado/NOAA
R/E/ET6
325 Broadway
Boulder, CO 80303-3328 USA
TEL: 303-497-6735/FAX: 303-497-6978/email: jsnider@etl.noaa.gov

D. A. Hazen
NOAA/ERL/Environmental Technology Laboratory
R/E/ET6
325 Broadway
Boulder, CO 80303-3328 USA
TEL: 303-497-6366/FAX: 303-497-6978/email: dhazen@etl.noaa.gov

Abstract -- Surface measurements of atmospheric emission at 20, 31, and 90 GHz have been compared to theoretical values calculated from simultaneous radiosonde measurements and well-known absorption models. Measurements were made at continental locations in the United States, and islands and ships in the Atlantic and tropical western Pacific Oceans. Observations of clear sky emission in the tropics during 1993 showed much poorer agreement with theoretical emission than observed at continental locations. The reason for the larger discrepancy in the tropics may be due to errors in the radiosonde humidity element element when operated in the extremely humid environment. In order to obtain additional insight into the cause of the discrepancy, a second set of simultaneous emission and radiosonde measurements in the tropical Pacific region was obtained during a cruise of the NOAA research vessel Discoverer from 15 March to 13 April 1996. Measurements and theoretical emission are compared for both the 1993 and 1996 data sets.

INTRODUCTION

As part of the nation's research program in climate and global change, the Environmental Technology Laboratory (ETL) operated microwave radiometers at several domestic and international locations during the period 1987-1994. In addition to climatic data, the radiometers provided new information for the evaluation of absorption models which predict the total absorption of millimeter waves, hence emission, from a profile of temperature and humidity measured by a radiosonde.

Previous papers presented comparisons of measurements and theory for five locations in the United States and abroad [1], [2]. These papers also pointed out that comparisons in the tropics show a much larger variance than was found in the temperate zones. This paper presents the initial observations in the tropical western Pacific region. A second experiment to be conducted in the tropics in March-April 1996 is described; its objective is to obtain greater insight into the poor agreement between measurements and theory found in the tropics.

METHODOLOGY

Microwave Radiometers

ETL employed dual-channel radiometers operating at (1) 20.6 and 31.65 GHz, and (2) 23.87 and 31.65 GHz. In addition, a three-channel system operating at 20.6, 31.65, and 90.0 GHz, was used. All three systems employ triple-switching and offset parabolic antennas with beamwidths ranging from 4.0 deg for the two-channel systems to 2.5 deg for the three-channel radiometer. The measurement accuracy of the radiometer systems is monitored by continuously recording critical engineering data, i. e., component temperatures and system gain; the uncertainty in each emission (brightness temperature) measurement caused by fluctuations in radiometer components can be readily calculated since the variance of each term in the radiometer equation can be calculated from the engineering data [2].

Radiometers are calibrated by means of tipping curves [3] which yield a calibration factor, C_F, that relates input brightness to output voltage. The uncertainty in C_F is found by calculating its variance observed over a large number of tipping curves.

Due to the variability in radiometer temperatures and gain, and the uncertainty in the calibration factor, radiometer measurement accuracy varies with time. In the comparisons of measurements and model predictions discussed below, the measurement accuracy has been calculated over 30-min intervals beginning with the start of each radiosonde flight.

Measurement Locations

Measurements were made at the following locations in the temperate zone: Wallops Island, VA (WAL), Coffeyville, KS (COF), Porto Santo Island, Portugal (PSO), and the research vessel (R/V) *Malcolm Baldrige* (BAL) steaming in the region between the Azores and the Madeiras in the northern Atlantic Ocean. In the tropical Pacific region, measurements were made at Kavieng, Papua New Guinea (KAV), located on the island of New Ireland.

Radiosondes

Eighty percent of the radiosonde data was obtained with the Vaisala model RS80 sounder with HUMICAP humidity sensors; remaining data were recorded using the VIZ (U.S.) sounder with hygristor humidity sensors. Although the accuracy of the radiosonde humidity sensor is stated to be ±5 percent, comparison of measurements with theoretical values of atmospheric emission, discussed below, suggest that this value may not always be achieved in the tropical atmosphere.

Absorption Models

Theoretical emission was calculated from radiosonde profiles of temperature, pressure, and humidity using two absorption models of Liebe: the 1987 version [4] which we refer to as RTE87, and Liebe's 1993 updated model [5] which we refer to as RTE93. The essential differences in the two models was discussed in [2] and will not be repeated here.

DISCUSSION

Table 1 contains a summary of the comparisons of observed and theoretical millimeter wave emission for the five measurement locations described above. The comparisons are limited to clear sky conditions to avoid possible complications caused by liquid water. Considering the coefficients of determination[1] for the total data set, it is clear that the agreement between measurements and theory is more highly variable in the tropics than in the temperate zone. Some improvement in coefficient of determination is obtained by limiting the comparison to those differences that fall within the 99 percent uncertainty level of the radiometric measurement although the tropical data are still more variable than the temperate zone data.

---

[1]The percentage of the observations that is "explained by" a linear least squares fit to the data.

Table 1. Agreement Betweeen Measured and Theoretical Brightness Temperature for (1) Data Within 99 Percent Confidence Limits of the Radiometer Measurement, and for (2) Total Amount of Data At All Measurement Locations Combined.

Location	Frequency (GHz)	Absorption Model	Data Within 99% Limits			Total Data Set		
			Sample Size	rms ΔT (K)	Coefficient of Determination (Percent)	Sample Size	rms ΔT (K)	Coefficient of Determination (Percent)
WAL, COF, PSO, BAL	20.6	RTE87	158	0.917	98.5	302	1.641	97.1
		RTE93	166	0.859	99.2		1.497	97.1
WAL, COF, PSO, BAL	31.65	RTE87	23	0.548	97.2	302	2.005	96.9
		RTE93	217	0.519	98.9		0.822	98.9
WAL, COF, PSO	90.0	RTE87	170	2.223	98.5	235	2.873	97.9
		RTE93	147	2.533	99.0		4.411	97.9
KAV	23.87	RTE87	47	1.081	96.5	110	3.533	75.2
		RTE93	12	1.462	92.1		6.238	75.1
KAV	31.65	RTE87	90	1.111	79.7	110	1.751	59.3
		RTE93	17	1.916	79.4		4.742	57.1

The most obvious reason for poor disagreement between observed and theoretical emission is that the zenith-pointing radiometer and the radiosonde, whose sampling volume is dependent upon the upper level winds, observe different regions of the atmosphere. However, for the Kavieng data, a study of radiosonde balloon tracks show that soundings sampled a volume on average within 23 km (maximum distance 43.3 km) from the launch site where the radiometer and radiosonde are collocated. Since the atmosphere is generally uniform over such distances, it is unlikely that very much of the poor agreement is caused by sampling different regions of the atmosphere.

Another problem, sometimes encountered at Kavieng, was solar heating of the humidity element after initial system calibration but prior to balloon launch. However, solar heating would only affect radiosondes launched during the daylight hours. Unfortunately, no diurnal variation could be detected in the comparisons of measurement and theory. As a result, solar heating of the humididy element cannot be the general cause of the large discrepancies.

Wetting of the humidity element by liquid water as the radiosonde encountered clouds could also cause errors in the humidity measurement. Unfortunately, there is no way to confirm whether the radiosonde encountered cloud liquid if the balloon is outside the view of the microwave radiometer.

By process of elimination, we conclude that unknown factors influence the performance of the HUMICAP humidity sensor when operated in the tropical atmosphere. These factors may include use of a "bad" batch of humidity elements in the 1993 measurements, undetected operational errors, wetting by cloud liquid, or nonlinear response of the humidity sensor in the extremely moist tropical atmosphere.

TROPICAL WESTERN PACIFIC CRUISE

In an attempt to shed more light upon these questions, a second set of observations are planned for the period 15 March to 13 April 1996. During this experiment, ETL will operate a two-channel microwave radiometer on the NOAA R/V *Discoverer* on a cruise extending from American Samoa to Manus Island, Papua New Guinea, to Honolulu, Hawaii. Radiosonde data will be obtained by ETL personnel throughout the cruise. In addition, independent measurements will be made by a RAMAN lidar operated by the Department of Energy. Preliminary data from the cruise will be discussed during presentation of the oral version of this paper at IGARSS '96.

REFERENCES

[1] J.B. Snider, "Observed and theoretical atmospheric emission at 20, 30, and 90 GHz: Recent results from land- and ocean-based locations," in Microwave Radiometry and Remote Sensing of the Environment, D. Solimini, Ed., VSP, Zeist, The Netherlands, 1995.

[2] J.B. Snider, D.A. Hazen, A.J. Francavilla, W.B. Madsen, and M.D. Jacobson, "Comparison of observed and theoretical millimeter wave emission: Implications for remote sensing of atmospheric water," Proc. 1995 International Geoscience and Remote Sensing Symposium (IGARSS'95), Firenze, Italy, July 10-14, Vol. II, pp. 1129-1132, 1995.

[3] D.C. Hogg., F.O. Guiraud, J.B. Snider, M.T. Decker and E.R. Westwater: "A steerable dual-channel microwave radiometer for measurement of water vapor and liquid in the troposphere," J. Climate Appl. Meteorol., Vol. 22, 1983, pp. 789-806.

[4] H.J. Liebe and D.H. Layton, "Millimeter-wave properties of the atmosphere: Laboratory studies and propagation modeling," Nat. Telecom. and Inform. Admin., Boulder, CO, Rep. 87-24, 1987.

[5] H.J. Liebe, G.A. Hufford, and M.G. Cotton, "Propagation modeling of moist air and suspended water/ice particles below 1000 GHz," AGARD 52nd Spec. Meet. of the Electromagnetic Wave Propagation Panel, Palma de Mallorca, Spain, 17-21 May 1993.

Atmospheric Microwave Absorption Parameter Estimation Near 22 GHz

Sandra L. Cruz Pol, Christopher S. Ruf
Communications and Space Science Laboratory
Pennsylvania State University, University Park, PA 16802
(814) 863-5940/(814) 865-2363/ fax (814) 863-8457
sandra@rufece.psu.edu/ ruf@rufece.psu.edu

Stephen J. Keihm
Jet Propulsion Laboratory
M/S T-1182
California Institute of Technology, 4800 Oak Grove Drive
Pasadena, CA 91109-8099
(818) 354-3656/ fax (818) 354-4341/ Stephen.J.Keihm@jpl.nasa.gov

Abstract--Atmospheric absorption parameters at microwave frequencies are estimated using synthesizer radiometer data from experiments at San Diego Miramar, CA and at West Palm Beach, FL. Measurements of well-calibrated downwelling brightness temperatures, T_B, at up to nine frequencies spanning the 22.235 GHz water vapor line are compared to model predictions using radiosonde measurements at each site. Model parameters are adjusted by non-linear regression to fit the radiometer data.

INTRODUCTION

Water vapor emission model uncertainty is often the dominant error source for microwave remote sensing of the troposphere [1]-[3]. Absorption line shape models have been developed by Gross [4], Van Vleck-Weisskopf (V-W)[5], and Lorentz [5] based on the rotational-vibrational resonances of water vapor molecules. The V-W line-shape function agrees better [6] with the laboratory-controlled data measured by Becker and Autler [7]. This line shape has been used in Liebe [8] and, with some modifications, Rosenkranz [9] models to describe water and oxygen emission spectra. An empirical continuum term has been added to account for excess attenuation between absorption spectra data and theoretical models. The physical phenomena behind the excess absorption in the continuum might be due to inaccuracies in the far wing line shape of vapor resonances [10], the exclusion of the effects of water clusters [11] and/or forbidden transition between energy levels on these line functions [12]. Although this excess has still to be understood, empirical modifications are needed to obtain more accurate agreement between measurements and theory.

In this work, the Liebe and Rosenkranz models are modified to optimally adjust the line strength, line width,

oxygen strength and continuum terms in the 20 to 30 GHz range. The water vapor absorption coefficient is given by,

$$\alpha_{water} = 0.0419 f^2 [T_L + T_S + T_C] \tag{1}$$

where, T_L, T_S and T_C, refer to the line strength, line shape and continuum terms and are given by,

$$T_L = 0.0109\, C_L\, e\, \theta^{3.5} \exp(2.143(1-\theta)) \tag{2}$$

$$T_S = \frac{w}{f_z}[1/X + 1/Y]$$

with,
$$X = (f_z - f)^2 + w^2) \tag{3}$$
$$Y = (f_z + f)^2 + w^2)$$

$$T_C = C_C\left(1.13 \times 10^{-8}\, e p\, \theta^3 + 3.57 \times 10^{-7}\, e^2 \theta^{10.5}\right). \tag{4}$$

The width parameter, w, is given by,

$$w = 0.002784\, C_W\left(p\, \theta^{0.6} + 4.8\, e\, \theta^{1.1}\right). \tag{5}$$

In the above equations, θ denotes the temperature ratio, 300/T, where T is in Kelvin, p denotes the dry air partial pressure, and e the water vapor partial pressure, both in millibars. The oxygen absorption coefficient is a copy of the Rosenkranz 1992 model with a scalar factor C_X, defined as,

$$\alpha_{oxygen} = C_X\, \alpha_{R'92}\,. \tag{6}$$

Equations (1)-(6) introduce the following parameters; water vapor line strength C_L, line width C_W, continuum C_C and oxygen strength C_X. This modified model is used to

compare the radiosonde-derived brightness temperatures with measured water vapor radiometer (WVR) data.

EXPERIMENT DESCRIPTION

The experiment consisted of the collection of data at two National Weather Service radiosonde launch sites. These were chosen for their contrasting (winter-San Diego (dry) and spring-West Palm Beach (humid)) natural conditions to provide constraints on both the 22.235 GHz vapor emission line and the level of oxygen emission in the 20-32 GHz interval.

The experiment included two independently calibrated WVR's which provided measurements at 20.0, 20.3, 20.7, 21.5, 22.2, 22.8, 23.5, 24.0 and 31.4 GHz. Inter-comparison of T_B data at frequencies common to both instruments indicate absolute calibration accuracies of about 0.5 K [13].

At both sites, radiosonde data were obtained from the National Climatic Data Center (NCDC). These provided height profiles of pressure, air temperature and dew point temperature. The relative humidity was derived from the temperature, dew point and air pressure information using the Goff-Gratch formulation [14] for saturation water vapor density.

DATA ANALYSIS AND RESULTS

The radiometer data was averaged over one half hour for the times corresponding to the radiosonde balloon data launch. This was then used as the ground truth for comparison purposes with the radiosonde derived T_B.

Fig. 2 Brightness temperature spectra comparison between radiometer data (WVR) and radiosonde-derived data with new and nominal parameters for a vapor burden of 2.3 g/cm².
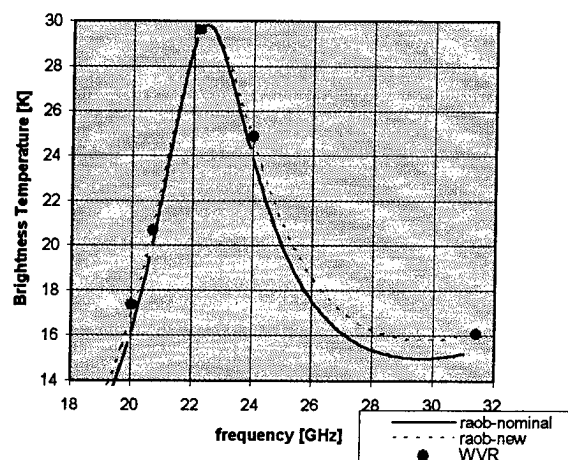
Fig. 3 Brightness temperature spectra comparison between radiometer data (WVR) and radiosonde-derived data with new and nominal parameters for a vapor burden of 1.3 g/cm².

The T_B was calculated using the radiative transfer integral applied to the balloon profiles. The parameters C_L, C_W, C_C and C_X were estimated using the Newton-Raphson iteration method. A selection of C_L =1.0, C_W =1.0, C_C =1.2 and C_X =1.0 yields absorption values within 0.5% of Liebe's (1987) [8] model and the exact Rosenkranz's(1992) [9] model. These are referred to as the nominal values of the parameters.

The NCDC data suffered from the radiosondes inability to properly measure dew point temperature for levels of relative humidity outside a range of 22% to 95%. To reduce this effect, a 50% probability factor was applied to relative

Fig. 1 Brightness temperature spectra comparison between radiometer data (WVR) and radiosonde-derived data with new and nominal parameters for a vapor burden of 2.9 g/cm².

humidity values outside this range, i.e., the relative humidity is set to 11% whenever it is less than 22% and to 50% whenever it is higher than 100%.

Only those profiles with small differences between T_B calculated this way and with the uncorrected relative humidity values were used. The retrieved parameters were found to be C_L=1.058, C_W=1.073, C_C=1.281 and C_X=1.036, indicating that the current parameters underestimate the emission spectra by 3 to 7 percent.

Figs. 1-3 depict plots of the brightness temperature for three climatological conditions. Each graph has a plot corresponding to the model with the nominal values of the four parameters and the new parameters. Also shown are the radiometer measured brightnesses. The plots show that the new estimated parameters agree closer to the WVR data.

The rms difference between modeled and measured T_B was reduced by 32%, from 1.56 K to 1.06 K, with the new parameters. Sensitivity analysis shows that the standard deviations on the C_L, C_W, C_X parameters are 5% or less, and 8% for C_C assuming 0.5K noise in the TB data. Correlation analysis between coefficients shows a high correlation between the errors in oxygen and the continuum terms.

REFERENCES

[1] J.W. Water, "Absorption and Emission by Atmospheric Gases," Methods of Experimental Physics, M.L. Meeks, Vol. 12C, Chapter 2.3 , pp. 142-176, Academic Press, New York, 1976.

[2] G. M. Resch, "Water Vapor--The Wet Blanket of Microwave Interferometry," Atmospheric Water Vapor, A. Deepak et al editors, pp. 265-281, Academic Press, 1980.

[3] C. Prabhakara and G. Dalu, "Passive Remote Sensing of the Water Vapor in the troposphere and its Meteorological Significance," Atmospheric Water Vapor, A. Deepak et al editors, pp. 355-373, Academic Press, 1980.

[4] E.P. Gross, "Shape of Collision-Broadened Spectral Lines," Phys. Rev., Vol. 97, pp. 395-403, January 15, 1955.

[5] J.H. Van Vleck, V.F. Weisskopf, "On the Shape of Collisionally Broadened Lines," Reviews of Modern Physics, Vol. 17, pp. 227-236, April-July 1945.

[6] R.J. Hill, "Water vapor-absorption line shape comparison using the 22-GHz line : The Van Vleck-Weisskopf shape affirmed," Radio Science, Vol. 21, pp. 447-451, May-June 1986.

[7] G.E. Becker, and S.H. Autler, "Water Vapor Absorption of Electromagnetic Radiation in the Centimeter Wave-length Range," Phys. Rev. , Vol. 70, pp. 300-307, 1946.

[8] H.J. Liege and D.H. Clayton, "Millimeter-wave properties of the atmosphere: Laboratory studies and propagation modeling," Nat. Telecom. and Inform. Admin., Boulder, CO, NIT Rep. 87-24, 1987.

[9] H.J. Liebe, P.W. Rosenkranz, and G.A. Hufford, " Atmospheric 60-GHz oxygen spectrum: New laboratory measurements and line parameters," J. Quant. Spectrosc. Rad. Transfer, Vol. 48, pp. 629-643, 1992.

[10] H.A. Gebbie, "Observations of Anomalous Absorption in the Atmosphere," Atmospheric Water Vapor, pp. 133-141, A. Deepak et al editors, Academic Press, 1980.

[11] R. A. Bohlander, "Spectroscopy of Water Vapor," Ph.D. Thesis, Dept. of Physics, Imperial College, London , 1979.

[12] P.W. Rosenkranz, "Absorption of Microwaves by Atmospheric Gases," Chapter 2, Jansenn ed.,1990.

[13] S.J. Keihm, "Preliminary Processing Results of J1 Sweeper, J3 and D2 WVR Data from the San Diego Miramar and the West Palm Beach Radiosonde Station," Jan. 1995, Jet Propulsion Laboratory, California, unpublished.

[14] J.A. Goff, "Final Report of the Working Subcommittee of the International Joint Committee on Psychrometric Data," Trans. on Amer. Society of Mechanical Engineers, vol. 71, pp. 903-913, Dec. 1948.

Recent advances in satellite sounding at the U.K. Meteorological Office.

B. R. Barwell

NWP Division

UK Meteorological Office

London Road, Bracknell, Berkshire RG12 2SZ, U.K.

Tel:+44-01344-854507 Fax:+44-01344-854026 Email: brbarwell@meto.govt.uk

Abstract— Several improvements have recently been made at the U.K. Meteorological Office to the system for deriving temperature and water vapour soundings from global satellite sounding data and for assimilating them into a numerical weather prediction model. The most significant changes include the assimilation of retrieved water profiles and the introduction of a new scheme for extending the model temperature profile to the upper stratosphere. The latter involves the use of stratospheric sounding channels to infer upper level temperatures and is capable of producing realistic retrievals even when the stratospheric circulation is disturbed and the model analyses poor. This is illustrated by the stratospheric warming in January 1995. Care is required to ensure that the extrapolation scheme does not allow any positive feedback within the overall retrieval system. New developments in satellite instrumentation and data processing promise further benefits from satellite sounding data in the near future and ensure that the data will continue to play an important role in numerical weather prediction.

I. INTRODUCTION

Vertical temperature and water vapour profiles derived from satellite sounding data have been produced operationally at the U.K. Meteorological Office for many years. Two systems are in use; the Local Area Sounding System (LASS) which processes data received locally at the satellite receiving station at Lasham in southern U.K., and the Global Sounding System (GLOSS) which processes global 120km resolution data received from the National Environmental Satellite, Data, and Information Service (NESDIS) in the U.S.A. [1]. This paper describes recent improvements to the GLOSS system.

II. THE GLOSS RETRIEVAL SYSTEM

The data received from NESDIS consists of brightness temperatures from the three sounding instruments on the NOAA polar orbiting satellites; the High-resolution Infrared Radiation Sounder (HIRS), the Microwave Sounding Unit (MSU) and the Stratospheric Sounding Unit (SSU). (See [2] for a description of the spacecraft and instrumentation.) NESDIS adjust the data to nadir view and also adjust the MSU data to unit surface emissivity. Where possible, the effect of clouds is removed from the HIRS data so they can be regarded as clear sky observations [3]. Locally computed bias corrections using the method described in [4] are applied to the data to improve the mean fit to background brightness temperatures computed from a numerical model forecast.

The GLOSS system uses an iterative non-linear inversion scheme [5] to generate vertical temperature and humidity profiles from the satellite measurements. This one-dimensional scheme is the first of two steps used to assimilate the data into the Unified Model, the Office's operational global numerical weather prediction model [6]. The background atmospheric profile used for this step is taken from the model's six-hour forecast. The second step consists of the assimilation of the vertical profiles into the Unified Model and is performed using the 'Analysis Correction' scheme developed in the Meteorological Office [7], temperatures at all levels being assimilated over the sea and sea ice but only at 100hPa and above over land.

III. RECENT CHANGES TO THE GLOSS SYSTEM

Since information about the vertical profile of water vapour is derived mainly from three HIRS channels, the vertical resolution is very limited. In addition, these channels provide useful data only in cloud-free (and therefore relatively dry) areas because they are affected by clouds in the field of view. In spite of these limitations, experiments in which water vapour profiles were assimilated as well as temperature profiles over the sea indicated a small improvement in forecast quality. In particular, better verification against radiosonde observations was achieved in many cases through alleviation of a moist bias in the model. Similar results have been reported from other centres [8].

A second improvement to the GLOSS system described in the next section concerns the vertical extrapolation of the background temperature profile. Forecast temperatures from the operational model are used up to 15hPa, but in order to use the SSU data and highest HIRS channels, the temperature profile must be extrapolated to

0.1hPa. Until late 1994 the extrapolation method used a regression scheme in which temperatures at selected pressure levels from 1000hPa to 15hPa were used as predictors. The regression coefficients were derived using a library of combined radiosonde/rocketsonde profiles from NESDIS and were applied directly to model forecast profiles. However, large systematic differences between observed and background temperatures for the SSU channels were observed in monthly mean fields in the extratropical regions. Differences with a similar geographical pattern though smaller in magnitude were also seen in channels whose weighting functions included the upper troposphere.

The cause of the differences was traced to poor extrapolated temperatures in the upper stratosphere: on one day studied in detail the regression produced an extrapolated profile in the range 1-10hPa which was 5-15K colder than the mean of the rocket profiles from which the regression coefficients had been derived. Clearly, the climatology of the rocket profiles at some or all of the predictor levels was different from the climatology of model forecast profiles.

IV. NEW EXTRAPOLATION

To overcome the problem, a new extrapolation scheme was devised in which no model-derived quantities are used as predictors. The best alternative information on the stratospheric temperature profile is then provided by the satellite data itself as no other source of data with sufficiently good coverage is available. Therefore, although independent data would have been preferable, we use the observations from the SSU channels and a few high-level channels from the other instruments as predictors in a linear regression scheme.

Using the NESDIS rocket data as typical of the range of atmospheric states, a radiative transfer model [9] was used to compute simulated observations of the predictor channels for each profile. Least squares regression was then used to produce coefficients which gave the best prediction of the rocket temperatures at stratospheric levels from these simulated observations. The regression coefficients are used in GLOSS to produce a stratospheric temperature profile using actual observations as predictors. This is added to the top of the forecast profile from the model.

Unlike the old scheme which was a true extrapolation in the sense that data within the range of model levels was used to infer data outside that range, the new scheme is more of a profile 'estimation' since it uses as predictors quantities directly influenced by the temperatures to be inferred. Thus the error magnification often associated with the process of extending data beyond its range of validity is reduced.

With the new scheme, biases between mean rocket and mean extrapolated profiles are due to mean differences between observed and computed brightness temperatures. These are much smaller than the differences between rocket and forecast temperatures responsible for the poor extrapolation found previously.

It is tempting to refine the procedure further by applying the bias correction to the observations before using them in the extrapolation so as to overcome biases in the radiative transfer model. This does indeed help to reduce systematic differences between observed and calculated brightness temperatures but it has other undesirable effects. Since the extrapolation forms part of the background profile, and the background profile is used in the derivation of the bias correction coefficients, using these coefficients in the extrapolation procedure completes a feedback loop. Then, as the bias correction coefficients are updated each month, they can drift to a state where they ensure good agreement between observations and background with neither being very representative of reality. Using observations in the extrapolation without bias correction breaks the circuit and prevents the problem from developing.

V. STRATOSPHERIC WARMINGS

One advantage of using satellite observations as predictors for extrapolating the model temperature profile becomes apparent during the warmings which often occur in the winter stratosphere. The Unified Model has its top level at about 5hPa and uses an upper boundary condition of no vertical motion at this level. It therefore has great difficulty in representing warmings in the stratosphere since they are symptomatic of large-scale descent and consequent adiabatic heating. Of course, the satellite observations have no such difficulty so that their use as predictors enables the background profile to follow stratospheric temperature disturbances regardless of how well they are represented in the model forecast.

An example of a stratospheric disturbance occurred in January 1995 when an extensive area of warm air developed over northern Siberia. (GLOSS profiles were not being assimilated operationally at that time but the NESDIS retrievals were.) The numerical analyses showed very little rise in temperature but preserved an area of very cold air north of the U.K. Subsequently, the warm air drifted closer to the area of the model's cold air and very large differences between analysis and retrievals occurred. The few radiosonde data in the area supported the satellite retrievals rather than the model analyses. The differences were so large that many of the satellite-derived profiles in the area were flagged by standard quality control procedures and therefore not assimilated. Thus they were unable to correct the model where its errors were greatest and the unrealistic analyses persisted until the

stratospheric circulation returned to a more settled state. As well as poor analyses and forecasts, excessively strong stratospheric jets have sometimes been observed at such times in a limited area version of the operational model sufficient to threaten its numerical stability. Although stability can be restored by halving the model timestep, the forecast then uses more computer resources and production of forecasts is delayed.

VI. FUTURE DEVELOPMENTS

A significant step forward in satellite sounding capability will come with NOAA-K, the first of a new generation of polar orbiting satellites scheduled for launch in the near future. This will include a HIRS instrument similar to the current operational ones and two new microwave instruments making up the Advanced Microwave Sounding Unit (AMSU). Of these, AMSU-A is a development of the MSU having higher horizontal resolution and more channels which will enable more vertical detail of the temperature profile to be retrieved in cloudy conditions. AMSU-B is a new 5-channel instrument designed to provide more detailed information on the atmospheric water vapour profile which will enable usable water vapour profiles to be derived in cloudy areas for the first time. Data from this instrument should also enable some physical properties of clouds to be inferred.

In the longer term, radiances measured by sounding instruments will be assimilated directly into numerical models using fully three-dimensional variational methods without the need to produce atmospheric profiles first. Such techniques are currently under development in the Meteorological Office and elsewhere and are an essential step to the ultimate goal of a practical four-dimensional assimilation scheme. Together with the long-term plans for the provision of polar orbiting satellites by the U.S. and European space agencies, it is clear that satellite sounding data will continue to be a major component of the global observing system in the foreseeable future.

REFERENCES

[1] A.J. Gadd, B.R. Barwell, S.J. Cox and R.J. Renshaw, "Global processing of satellite sounding radiances in a numerical weather prediction system", Q. J. R. Meteorol. Soc., vol. 121, pp. 615–630, April 1995.

[2] W.L. Smith, H.M. Woolf, C.M. Hayden, D.Q. Wark and L.M. McMillin, "The TIROS-N operational vertical sounder", Bull. Am. Meteorol. Soc., vol. 60, pp.1177–1187, October 1979.

[3] L.M. McMillin and C. Dean, "Evaluation of a new operational technique for producing clear radiances", J. Appl. Met., vol. 21, pp.1005–1014, July 1982.

[4] J.R. Eyre, "A bias correction scheme for simulated TOVS brightness temperatures", ECMWF Res. Dep. Tech. Memo. No. 186, October 1992.

[5] J.R. Eyre, "Inversion of cloudy satellite sounding radiances by non-linear optimal estimation. Part I: Theory and simulation for TOVS", Q. J. R. Meteorol. Soc., vol. 115, pp. 1001–1026, July 1989.

[6] M.J.P. Cullen, "The unified forecast/climate model", Meteorol. Mag., vol. 122, pp. 81–94, April 1993.

[7] A.C. Lorenc, R.S. Bell and B. Macpherson, "The Meteorological Office analysis correction data assimilation scheme", Q. J. R. Meteorol. Soc., vol. 117, pp. 59–89, January 1991.

[8] A.P. McNally and M. Vesperini, "Variational analysis of humidity information from TOVS radiances", Eumetsat/ECMWF Fellowship Programme Res. Rpt. No. 1, November 1995.

[9] J.R. Eyre, "A fast radiative transfer model for satellite sounding systems", ECMWF Res. Dep. Tech. Memo. No. 176, March 1991.

Influence of Scattering in the Absorbing Line Structure in Two-Phase Media

M.L.German, V.P.Nekrasov and E.F.Nogotov

Heat & Mass Transfer Institute, Belarus Academy of Sciences,

15, P.Brovka St., Minsk, BELARUS, 220728

Phone: 007-0172-685132/ Fax: 007-0172-322513/ E-mail: mgm@avtlab.itmo.minsk.by

INTRODUCTION

Study of the mechanism of radiation propagation in two-phase media (gas and solid particles) has a significant number of engineering. These include radiative and combined heat transfer, direct and inverse problems in spectroscopy of scattering medium, heat transfer enhancement in thermal and nuclear engineering and metallurgy, etc. The development of modern technology and enhancement, some ecology problems have aroused a growing interest to radiative transfer in technical and natural media.

Of special interest is the correct registration of two-phase medium gas component radiation selectivity. As is obvious from the experimental and theoretical investigations [1-4], the scattering of radiation tends to the changing of contour outgoing from radiation medium and thus to the changing of the line contour averaged absorption coefficient of medium.

Because of this on attempted registration of radiation selectivity in finite spectral ranges the errors result up to 50 %. Clearly the correct registration of gas component radiation selectivity can be carried out with direct integration by contour of absorption lines. However this approach has the following limitations: a) it takes a lot of computer time and leads to the loosing of result efficiency; b) when diagnosing the two-phase medium the spectral range averaged characteristics of radiation are measured and the correct determination of medium characteristics is impossible without an account of influence of scattering processes.

In this connection the authors give some results of investigation on influence of radiation scattering on its transfer in two-phase media in present paper.

MODELS AND RESULTS

The investigation is based on the numerical solution of equation of radiation transfer in homogeneous plane layer of absorbing, emitting and scattering media with transparent boundaries. The registration of scattering anisotropy is carried out in transport approximation. Then the transfer equation may be written for the oriented emissivity of medium thus:

$$m\frac{dI(m,l)}{dl} + (x+ay)\,I(m,l) = \frac{ay}{2}\int_{-1}^{1} I(m',l)dm' + x. \qquad (1)$$

Here $I(m,l)$ is the oriented emissivity of medium in point l in the direction of $m = \cos(O)$ (O is angle between radiation propagation direction and axis Ol); x, y - the respective coefficients of medium absorption and medium scattering; a - a doubled part of downward radiation scattering on its interaction with elementary volume of medium. We also consider the Shuster's number $w = ay/(x+ay)$ and optical thickness of layer by absorption $t = xL$, L - geometric thickness of layer.

At present a lot of reliable methods [5-7] for solution of the equation (1) are known. That is why we do not describe the transfer equation solution.

We consider the dependence of the oriented emissivity of layer for $m = 1$ on its optical thickness t by absorption and part of scattering w (Fig. 1). The results show there are three ranges for t, which differ in their nature of influence of scattering part w on emissivity of medium: 1) $t < 0.5$ - the function $I(w)$ is increasing; 2) $0.5 < t < 2$ - function $I(w)$ has an extremal character; 3) $t > 2$ - function $I(w)$ is decreasing. The same situation is along the contour of absorption line. The values t and w are varying and correspondingly the emissivity of medium along the line contour and the average emissivity in absorption line range are varying.
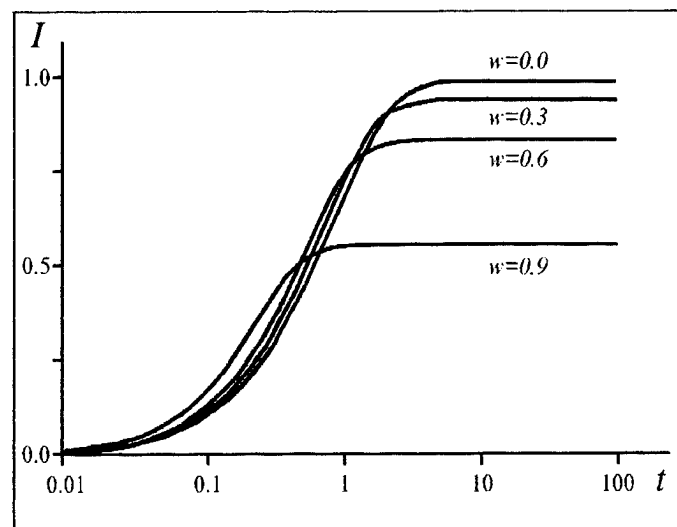
Fig. 1. Influence of scattering on the emissivity of homogeneous layer: $I = I(t,w)$.
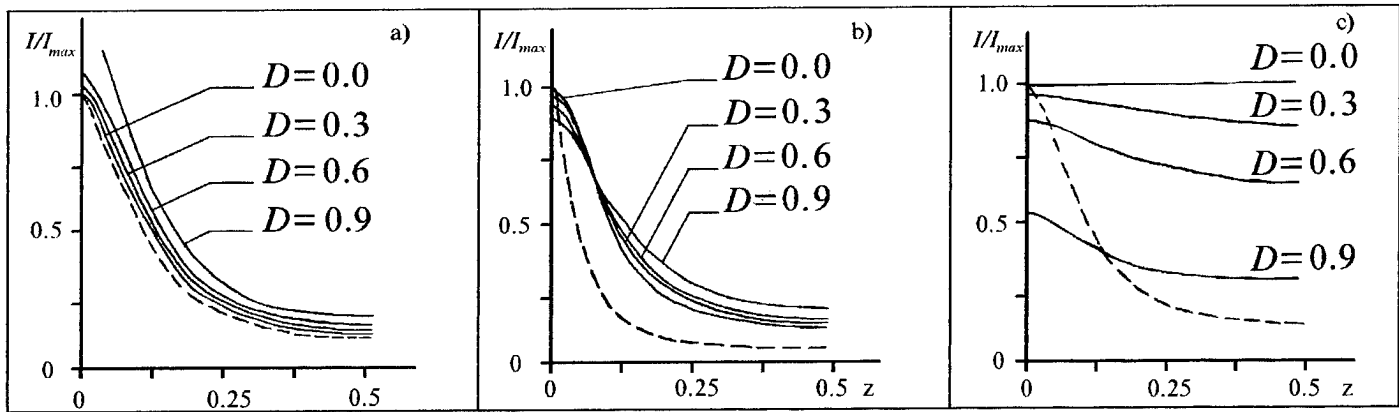
Fig. 2. Distribution of medium emissivity along absorption line contour: a) $[g/d] = 0{,}1$; $t_a = 0{,}1$;

b)$[g/d] = 0{,}05$; $t_a = 0{,}5$; c) $[g/d] = 0{,}1$; $t_a = 50$.

For example we consider the medium emissivity for the model of Elsasser absorption band with Lorentzian line contour [6]. In this case the optical thickness of medium takes the form:

$$t(z,[g/d],[sL/d]) = \frac{sL}{d}\frac{sh(2pg/d)}{ch(2pg/d)-\cos(2pz)},\qquad (2)$$

s, g - strength and half-width of absorption line; d - distance between lines; $z = [(f-f_0)/d]$ - frequency parameter characterizing the distance from line center f_0 by frequency f; $p = 3{,}1415...$

We enter next parameters into the consideration:

a) $t_a = [sL/d]$- gray optical thickness of layer by absorption; b) $D = [ay/(ay+[s/d])]$- gray Shuster's number.

When solving the equation (1) along the absorption line contour $(-0.5 < z < 0.5)$ we obtain some values of medium emissivity $I(z,[g/d],t_a,D)$. The average of selective component optical thickness by absorption line contour is the value $t_0 = t(z_0,[g/d],t_a)$ such that

$$I(z_0,[g/d],t_a,D) = \int_{-0,5}^{0,5} I(z,[g/d],t_a,D)dz.\qquad (3)$$

One can see from the equation (3) that $t_0 = t_0([g/d],t_a,D)$.

It is seen from equation (2) that the medium optical thickness varies along absorption line contour, during with the variation can reach some exponents depending on g/d. In accordance with this the value of local Shuster's number

varies along the absorption line contour too, that is it decreases toward the line center. With the regularities of t and w parameters' influence on the medium emissivity the possible influence of scattering on outgoing radiation contour can be predicted beforehand:

1) with the increasing of gray Shuster's number D the emissivity of medium can increase along the absorption line contour. (Fig.2(a));

2) with the increasing of D the emissivity of medium can decrease in the center and increase at the "wings" of absorption line. (Fig.2(b));

3) with the increasing of D the emissivity of medium can decrease along the absorption line contour. (Fig.2(c));

The line contour averaged optical thickness of selective component $t_0(D)$ varies in accordance with the influence of scattering on outgoing radiation contour. The indicated functions can be: a) decreasing (Fig.3(a)); b) increasing (Fig.3(b)); c) having an extremal character (Fig.3(c)). With this the varying of $t_0(D)$ can be quite essential and reach up to 50 % and more. Consequently, if on computing the characteristics of radiation transfer in finite spectral range the function $t_0(D)$ is not accounted then the essential errors can be obtained.

Let us enter into the consideration the errors which appear on ignoring the influence of part D of the scattering processes on the absorption line contour averaged optical thickness of selective component:

$t_1 = t_0([g/d],t_a,[D = 0])$; $t_2 = t_0([g/d],t_a,D)$;

$e = [I(t_2,D)/I(t_1,D)]$. Here t_1 - an average optical thickness of selective component for nonscattering medium; t_2 - an average optical thickness of selective component for

1442
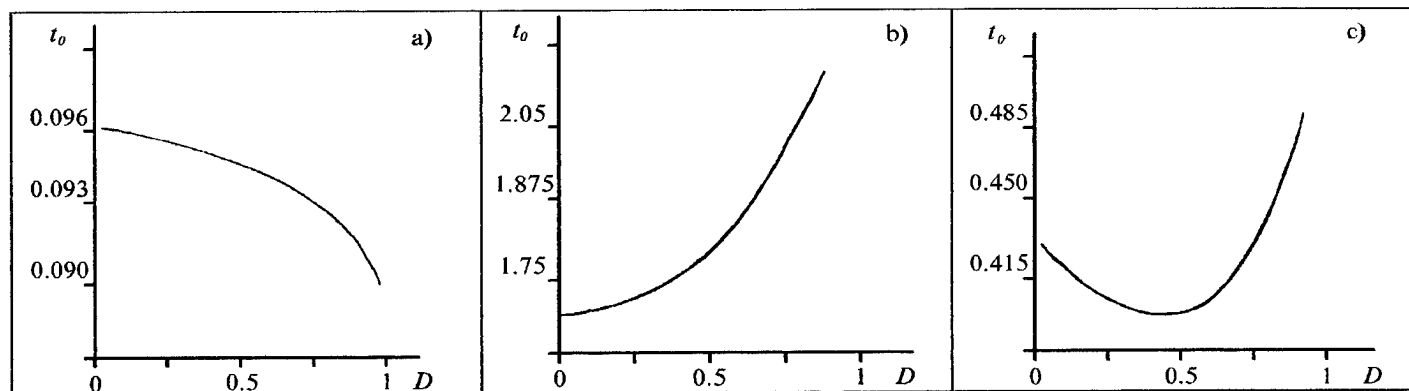
Fig. 3. Influence of gray Shuster's number on the line contour averaged optical density of medium:

a)$[g/d] = 0{,}1$; $t_a = 0{,}1$; b) $[g/d] = 0{,}1$ $t_a = 3$; c)$[g/d] = 0{,}01$; $t_a = 3$.

scattersing medium; e - ratio of medium emissivity computed in final spectral interval with the calculation of influence of scattering on the contour of outgoing radiation and the same characteristic obtained without the calculation of influence of scattering part on the line contour averaged optical thickness of selective component. The investigation shows the ignoring of influence of scattering on the average optical thickness of selective component can lead to errors up to 50 % depending on "fine" line structure parameters ($[g/d],[s/d]$), geometric thickness of layer and part of scattering processes (Fig.4).

Fig.4. The errors which appear when ignoring the influence of scattering on the absorption line contour averaged optical thickness of selective component.

·············· $[g/d] = 0{,}1$; $t_a = 3$.

———— $[g/d] = 0{,}01$; $t_a = 3$.

CONCLUSION

The results show the influence of scattering on the line contour averaged coefficient of medium absorption needs to be accounted. The approximating formulas which connect the average coefficient of medium absorption with parameters of "fine" line structure ($[g/d],[s/d]$), the geometric thickness of medium (L) and the part of scattering processes (D) can be developed for various models of absorption bands.

REFERENCES

[1] G.A. Damoto and W.C. Wang, "Radiative transfer in homogeneous nongray gases with nonisotropic particle scattering", J. Heat Transfer, vol. 8, N 2,1974, pp.385-390.

[2] I.A. Vasilieva, "Shape of spectral lines emitted from a gas in the presence of a condensed phase", JQRST, vol. 33, N 3, 1986, pp. 171-178.

[3] D.G. Goodwin and J.L. Ebert, "Rigorous bound on the radiative interaction between real gases and scattering particles", JQRST, vol. 37, N 5, 1987, pp. 501-508.

[4] W. Malkmus, "Some comments on the extension of band models to include scattering", JQRST, vol. 40, N 3, 1988, pp.201-204.

[5] W.A. Fiveland, "Discrete-ordinate solutions of the radiative transport equation for rectangular enclosures", J. Heat Transfer, vol. 106, 1084, pp. 699-706.

[6] K.S. Adzerikho, E.F. Nogotov and V.P. Trofimov, "Radiative heat transfer in two-phase ", CRC Press, Boca - Raton - Ann Arbor - London - Tokyo, 1993.

[7] M.L. German, "The influence of the optical properties of two-phase medium and its boundary surfaces on the radiative heat transfer in the furnaces", Thesis (in Russian), Minsk, 1993, p. 131.

ATMOSPHERIC EFFECTS DUE TO DIFFERENT PARTICLE SHAPES ON PROPAGATION

Dr Osman YILDIRIM
Hava Harp Okulu
Department of Electronics
Turkish Airforce Academy,34807 Istanbul,Turkey
Phone:90(212)6632490 Fax:90(212)5741819

Abstract It is known that the attenuation of electromagnetic waves by hydrometeors in the atmosphere may result from both absorption and scattering, depending on the size and shapes. When the particles are small with respect to wavelength, attenuation is considerably simplified for small particles. In this study, the attenuation of electromagnetic waves in millimeter wavelengths has been calculated for isotropic dielectric geometric shapes such as disc, rod, and sphere. Modified Rayleigh-Gans approach is applied for calculation of attenuation due to geometric shapes whose physical size are small compared to wavelength.

INTRODUCTION

The exact solution of the scattering of a plane wave by isotropic, homogeneous sphere was obtained by Mie in 1908, and is usually called the Mie Theory. Mie separated the field equations into groups, one is transverse magnetic and the other is transverse electric. By matching boundary conditions at the surface of the sphere, he obtained the cross-sections of spherical particles.

Rayleigh developed the theory of scattering of electromagnetic waves by small particles and also presented an approximate theory for particles of any shapes and size having a small relative index of refraction. Further contributions were made by Debye in 1915. Then years later, Gans rederived the scattering formulas for a homogeneous sphere.

FORMULATION OF THE PROBLEM

A plane electromagnetic wave incident on an arbitrarily oriented dielectric object. The plane wave is assumed to have polarization $\vec{q}$ and to be propagated in the $\vec{i}$ direction,shown in Fig.1, then

$$\vec{E}_{inc}(\vec{r}) = \vec{q} E_o e^{j k_o \vec{i} \cdot \vec{r}} \quad (1)$$

Where E_o is the magnitude of incident wave, k_o is propagation constant. $\vec{i}$ is the unit vector in the direction of wave propagation whereas $\vec{q}$ is the vector for the direction of its polarization.
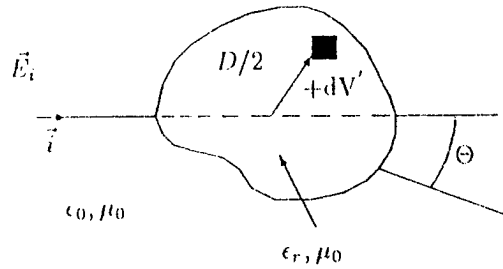
Fig.1 Geometry for approximation

When the particle is illuminated by a plane wave propagation in the direction $\vec{i}$, scattering direction $\vec{o}$ can be described by angles θ_s, ϕ_s measured with respect to cartesian coordinates z and x respectively. It is necessary to express variables in the coordinates of reference frame. Let us assume x^1, y^1, and z^1 are unit vectors in the primed system, they can be expressed in terms of the reference system by using Euler angle rotation. By using $\vec{x}^1 = A(\phi,\theta,\chi)\vec{x}^o$ one can easily obtain

$$z^1 = \cos\phi\sin\theta\vec{x}^o \sin\theta\sin\phi\vec{y}^o \cos\theta\vec{z}^o \quad (2)$$

Here matrix A can be thought of as an operator. The matrix, A, is acting on unprimed system and transforming it into the primed system. The spherical angles of incident wave θ, ϕ are measured with respect to a polar axis z and x respectively. For incident direction [1,2]

$$\vec{i} = -\sin\theta_i \vec{x}^0 - \cos\theta_i \vec{z}^0 \qquad (3)$$

The scattering amplitude for homogeneous and isotropic scatterer,

$$F(\vec{o},\vec{i}) = \frac{k^2(\epsilon_r - 1)}{4\pi} \int\limits_V -\vec{o} \wedge [\vec{o} \wedge \vec{E}(\vec{r})]dV \qquad (4)$$

where $F(\vec{o},\vec{i})$ indicates the amplitude, phase and polarization of the scattered field. In order to calculate scattering amplitude, we have to know the value of field inside the scatterer. Taking the axes of three dimentional scatterer as $\vec{r}^0$, $\vec{\theta}^0$, and $\vec{\phi}^0$ we can obtain the field inside the scatterer as [3]

$$\vec{E} = E_h \vec{h}^o + E_v \vec{v}^o = \vec{E}_h + \vec{E}_v \qquad (5)$$

where

$$\vec{E}_h = E_{hr}\vec{r}^o + E_{h\theta}\vec{\theta}^o + E_{h\phi}\vec{\phi}^o \qquad (6)$$

$$\vec{E}_v = E_{vr}\vec{r}^o + E_{v\theta}\vec{\theta}^o + E_{v\phi}\vec{\phi}^o \qquad (7)$$

$\vec{E}_h$ shows the field inside the scatterer for horizontal polarization whereas $\vec{E}_v$ indicates the field inside the scatterer for vertical polarization. Appliying matrix transformation, spherical polar unit vectors can be obtained in terms of cartesian coordinates.

$$\vec{r}^o = \sin\theta\cos\phi\vec{x}^o + \sin\theta\sin\phi\vec{y}^o + \cos\theta\vec{z}^o \qquad (8)$$

$$vec\theta^o = \cos\theta\cos\phi\vec{x}^o + \cos\theta\sin\phi\vec{y}^o + \sin\theta\vec{z}^o \qquad (9)$$

$$\vec{\phi}^o = -\sin\phi\vec{x}^o + \cos\phi\vec{y}^o \qquad (10)$$

By considering the geometry which is shown in Fig.1, $\vec{r}^o$ can be chosen in coincidence with scattering direction $\vec{o}^o$, therefore, we can write

$$\vec{o}^o = \sin\theta_s\cos\phi\vec{x}^o + \sin\theta_s\sin\phi\vec{y}^o + \cos\theta_s\vec{z}^o \qquad (11)$$

For horizontal components of field,

$$E_{hr} = E_{ih}\sin\theta\sin\phi \qquad (12)$$

$$E_{h\theta} = E_{ih}\cos\theta\sin\phi \qquad (13)$$

$$E_{h\phi} = E_{ih}\cos\phi \qquad (14)$$

For vertical components of field,

$$E_{vr} = E_{iv}(\sin\theta_i\cos\theta - \cos\theta_i\sin\theta\cos\phi) \qquad (15)$$

$$E_{v\theta} = E_{iv}(-\cos\theta_i\cos\theta\cos\phi - \sin\theta_i\sin\theta) \qquad (16)$$

$$E_{v\phi} = E_{iv}(\cos\theta_i\sin\phi) \qquad (17)$$

By using polar components instead of cartesian components, horizontal and vertical field polarization for rotated dielectric ellipsoid will be

$$E_{hr} = \frac{E_{ihr}}{[1 + \frac{abc}{2}(\epsilon_r - 1)A_r]} \qquad (18)$$

$$E_{h\theta} = \frac{E_{ih\theta}}{[1 + \frac{abc}{2}(\epsilon_r - 1)(19)A_\theta]} \qquad (20)$$

$$E_{h\phi} = \frac{E_{ih\phi}}{[1 + \frac{abc}{2}(\epsilon_r - 1)A_\phi]} \qquad (21)$$

where a, b,and c are the axes of ellipsoid. By changing the values of L[2], we can find internal field for any shape.

In this study we examine geometric shapes such as disc, rod, and sphere. Scattering amplitude can be found easily since internal field is known. Horizontal amplitude functions, K_h can be obtained as [4,5]

$$K_h = \frac{k^2(\epsilon_r - 1)E_{ih}}{4\pi}$$
$$(\sin^2\theta\sin^2\phi\frac{1}{1+L_1(\epsilon_r-1)}$$
$$+\sin^2\phi\cos^2\theta\frac{1}{1+L_2(\epsilon_r-1)}$$
$$+\cos^2\phi\frac{1}{1+L_3(\epsilon_r-1)})$$
$$\int_{V_p} e^{jk_o\vec{V}.\vec{x}}dx \qquad (22)$$

Vertical amplitude function, K_v,

$$K_v = \frac{k^2(\epsilon_r - 1)E_{iv}}{4\pi}$$
$$[(-\cos\theta_i\sin\theta\cos\phi + \sin\theta_i\cos\theta)^2$$
$$\frac{1}{1+L_1(\epsilon_r-1)}$$
$$+(\cos\theta_i\cos\theta\cos\phi + \sin\theta_i\sin\theta)^2$$
$$\frac{1}{1+L_2(\epsilon_r-1)}$$
$$+(\cos\theta_i\sin\phi)^2$$
$$\frac{1}{1+L_3(\epsilon_r-1)}]$$
$$\int_{V_p} e^{jk_o\vec{V}.\vec{x}}dx \qquad (23)$$

When K_h and K_v are known the attenuation may be calculated by changing L's value. Attenuation, $A_{v,h}$ is evaluated by

$$A_{v,h} = 8.686 Im(K_{v,h}10^5 dB/km \qquad (24)$$

REFERENCES

[1] A.Ishimaru, Wave propagation and scattering in random media, Academic Press, New York,1978

[2] H.C.Van de Hulst, Light scattering by small particles, Dover, New York, 1957

[3] O.Yildirim, Atmospheric effects due to different particle shapes on propagation, M.Sc.Thesis,Bosphorus University,1986 on Antennas and Propagation, Vol.AP-32,1984

[4] D.M.LeVine, The radar cross-section of dielectric discs, IEEE Trans. on Antennas and Propagation, Vol.AP-32,1984

[5] K.Shimizu, Modification of the Rayleigh-Debye Approximation, J. Opt.Sci.Ame., V.73(4),1983

JPL Wind Radiometer Measurements

William J. Wilson and Simon H. Yueh
Jet Propulsion Laboratory, California Institute of Technology
Bldg.. 168-327, 4800 Oak Grove Drive
Pasadena, California 91109
Phone: (818) 354-5699 / FAX: (818) 393-4683
Email: wilson@merlin.jpl.nasa.gov

Abstract - The purpose of the JPL Wind Radiometer program is to develop and demonstrate low cost instruments for remotely measuring ocean wind vectors from space. The microwave emission from the ocean surface is elliptically polarized and the degree of polarization and angle is a function of the surface wind speed and direction. JPL has developed a set of microwave polarimetric radiometers at 19 and 37 GHz (WINDRAD), which have been used on the NASA DC-8 aircraft for remote measurements of ocean surface wind vectors. A summary of all the ocean polarimetric data vs. wind speed and incidence angle from three flights in 1994 and eight flights in 1995 is presented. These data show clear wind direction signals at wind speeds from 3 to 24 m/s and incidence angles of 45° to 65°.

INTRODUCTION

Global mapping of near surface ocean winds is crucial for many meteorological, oceanographic and atmospheric studies. In the past from Seasat, ERS-1, to the present development of NASA's Scatterometer (NSCAT, to be launched in 1996), spaceborne wind radars have been the only instruments to provide a global monitoring of ocean surface wind vectors with frequent and adequate temporal-spatial coverage. The principle of wind scatterometry is based on the fact that electromagnetic backscatter varies periodically as a function of the azimuthal angle between the wind direction and the radar look direction. This is because the water ripples (capillaries) induced by ocean wind are smoother in the crosswind direction and rougher in the up- or downwind direction. Recently however, experimental observations and analysis [Etkin et al., 1991; Wentz, 1992; Yueh et al., 1995] have shown that the directional features of water ripples also cause the emitted thermal radiation, or the radiometric brightness temperatures, to be elliptically polarized. The degree of polarization and angle is a function of the surface wind speed and direction and will cause the brightness temperature to vary over azimuth angles by a few degrees Kelvin. This azimuthal dependence of brightness temperatures thus make it possible for passive microwave radiometers to provide both wind speed and wind direction measurements over the ocean surface.

JPL has had a strong interest in measuring wind vectors from space and has been responsible for developing the NASA scatterometer instruments NSCAT and SEAWINDS. When it was discovered that a passive radiometer instrument could be 2-5 time less expensive than a scatterometer instrument, JPL began a program to study this technique. This program included the development of 19 GHz and 37 GHz polarimetric radiometers (WINDRAD) which have been used on the NASA DC-8 aircraft to study this technique. Fifteen (15) successful Wind radiometer aircraft flights have been made since November 1993 -- four in 1993, three in 1994 and eight in 1995. These data show that there is a clear wind direction signal at wind speeds from 3 to 24 m/s and incidence angles from 45° - 65° .

A set of measured 19- and 37-GHz polarimetric data taken on April 17, 1995 at moderate wind speed is shown in Figure 1 for 45° incidence angle. Data are plotted continuously in azimuth angle with increments of 360° added for each additional circle flight around the NDBC buoy 46005 located off the Oregon coast. (These data are typical of the aircraft data with wind speeds from 3 to 14 m/s.) The top curve is the vertical polarization (T_v), the second is the horizontal polarization (T_h), the third is the second Stokes parameter, Q (= T_v - T_h), and the fourth curve is the third Stokes parameter, U (= T_{45} - T_{-45}), The instrument noise is <0.05 K. Thus, all the "noise" on the data is from the atmosphere or ocean surface. Note that in clear weather the 19- and 37-GHz signals have similar amplitudes, which shows that the wind signals have a broad frequency range.

At 45° incidence angle, the T_h , Q and U azimuth signals have a strong second harmonic component -- peaks in the upwind and downwind directions. The Q azimuth signal has even symmetry [cos (AZ)] about the wind direction, with the upwind direction having the largest value. The U azimuth signal has odd symmetry [sin (AZ)] and has a 90° azimuth phase difference relative to the Q signal. This suggests that there will be excellent ambiguity selection skill in estimating wind direction. Also notice that the U data has significantly less "atmospheric noise" than the T_v , T_h , and Q data, especially near -630° azimuth. The fact that the U
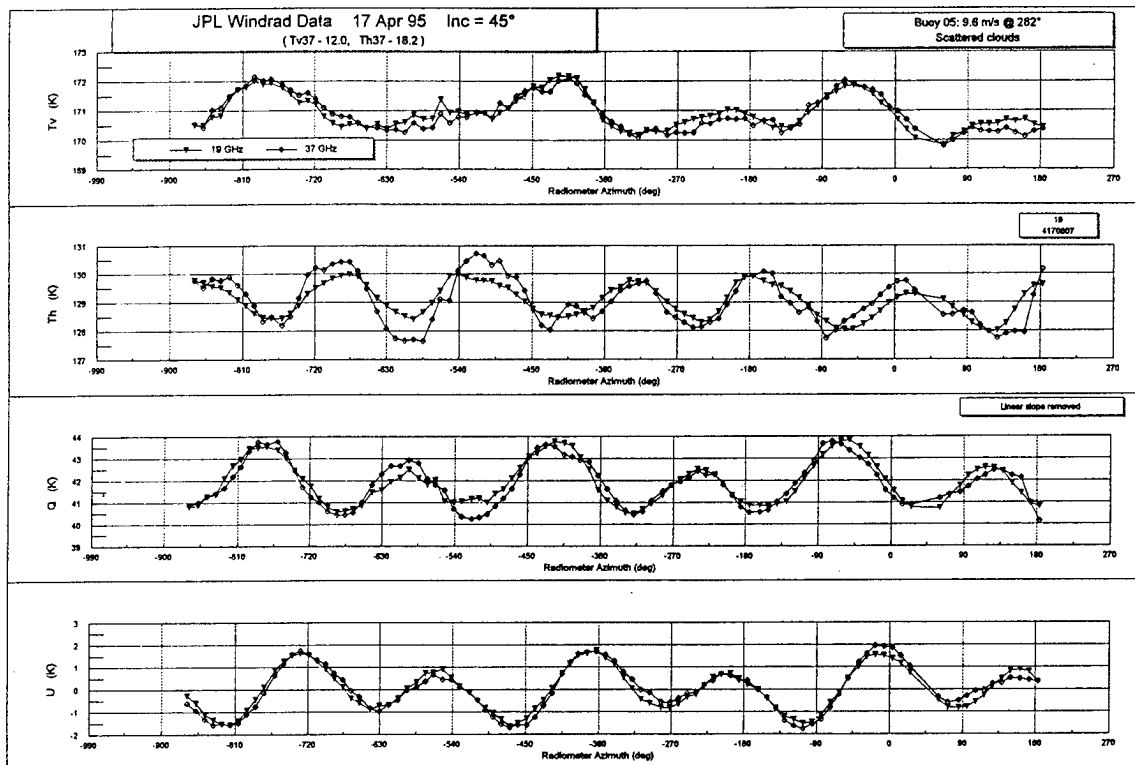
Figure 1. Measured 19 and 37 GHz polarimetric data on April 17, 1995, as a function of azimuth angle for an incidence angle of 45°. The wind speed was 9.6 m/s at 5 m height, the direction was 282°, and the weather was scattered clouds. T_v is the vertical polarization, T_h is the horizontal, Q is their difference ($T_v - T_h$), and U is the difference between T_{+45} and T_{-45}. Notice the 90° phase difference in azimuth between Q and U. Data are plotted continuously in azimuth angle with increments of 360° added for each additional circle flight around the NDBC buoy 46005. The 37 GHz T_v and T_h have been plotted using an offset of -12.0 and -18.2 K respectively, for ease of comparison.

azimuth signal is more insensitive to clouds, suggests that it will be possible to use this signal for wind direction measurements even with moderate cloud cover. Aircraft polarimetric measurements have also been made at incidence angles of 55° and 65°.

A summary of the 1994 and 1995 polarimetric U azimuth data, with low atmospheric attenuation, is shown in Figure 2. This plot shows the peak-to-peak azimuth signal for the U Stokes parameter vs. wind speed for the 45°, 55° and 65° incidence angles. It is likely that the scatter in the data is mainly due to errors in the reported buoy wind speed due to time and location differences.

These summaries show that the 45° incidence angle azimuth data has the largest peak-to-peak signal and has detectable signals for wind speeds above 3 m/s. The 55° incidence angle data has a lower signal amplitude and would be detectable only for winds above 4-5 m/s. At wind speeds > 5 m/s, the 65° incidence angle data only has a first harmonic,

and its peak-to-peak amplitude is lower by a factor of ~2 from the 45° incidence angle The amplitude of this data goes through zero near 5 m/s and shows a strong second harmonic component for winds < 5 m/s. The 65° incidence angle data is also more sensitive to the atmospheric attenuation because of the longer path through the atmosphere.

These aircraft results show that passive polarimetric radiometers have a strong potential for global ocean wind measurements. The aircraft measurements and the analysis of the data have also narrowed the instrument parameters for a spaceborne radiometric sensor for measuring wind vectors.

The next step will be to demonstrate this instrument in space, to show how well it will measure wind vectors under a wide variety of wind and weather conditions.

1448

Administration and the National Polar-orbiting Operational Environmental Satellite System Integrated Program Office.

REFERENCES

Etkin, V.S., M.D. Raev, M.G. Bulatov, Yu.A. Militsky, A.V. Smirnov, V.Yu. Raizer, Yu.A. Trokhimovsky, V.G. Irisov, A.V. Kuzmin, K.Ts. Litovchenko, E.A. Bespalova, E.I. Skvortsov, M.N. Pospelov, and A.I. Smirnov, *Radiohydrophysical Aerospace Research of Ocean*, Report II, p-1749, Academy of Sciences, USSR, Space Research Institute, 1991.

Wentz, F.J., "Measurement of oceanic wind vector using satellite microwave radiometer," *IEEE Trans. Geosci. Remote Sensing*, vol. 30, pp. 960-972, Sept. 1992.

Yueh, S. H., W. J. Wilson, F. K. Li, W. B. Ricketts, and S. V. Nghiem, "Polarimetric measurements of sea surface brightness temperatures using an aircraft K-band radiometer," IEEE Trans. Geosci. Remote Sensing, Vol. 33, No. 1, 85 - 92, 1995.
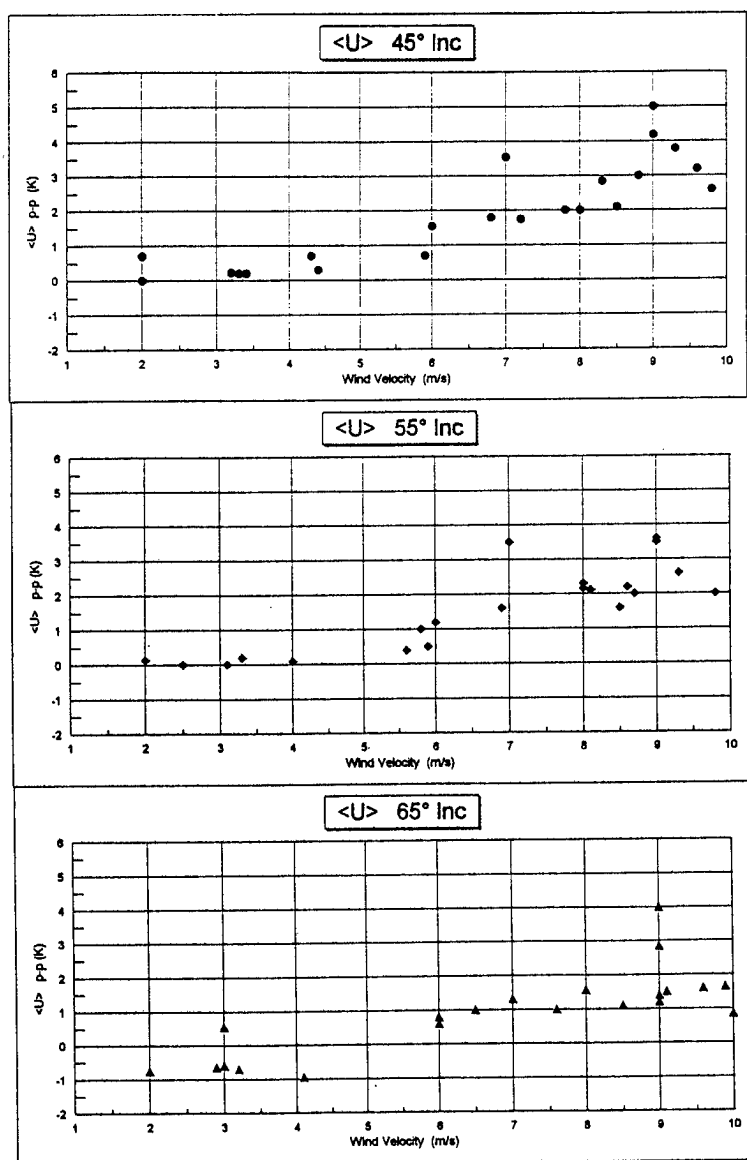
Figure 2. Summary of the peak-to-peak U azimuth signal data vs. wind velocity for the 1994 and 1995 WINDRAD data. The negative values in the 65° incidence angle data <5 m/s, represent a 180 phase shift from the >5 m/s data.

SURFACE AND AIRBORNE RADIOMETRIC OBSERVATIONS DURING THE COASTAL OCEAN PROBING EXPERIMENT: AN OVERVIEW

E.R. Westwater, V.G. Irisov, and L.S. Fedor
Cooperative Institute for Research
 in Environmental Sciences (CIRES)
University of Colorado/NOAA
Boulder, Colorado 80309
tel: (303) 497-6527; fax: (303) 497-3577
email:ewestwater@etl.noaa.gov

Yu. G. Trokhimovski
Environmental Technology Laboratory
NOAA/ERL, R/E/ET1
325 Broadway
Boulder, Colorado 80303-3328

Abstract--Radiometric observations obtained during the September 1995 Coastal Oceans Probing Experiment are presented. The radiometric goals of the experiment included the determination of the accuracy of polarimeters in measuring ocean wind speed and direction, the study of the frequency and angular response of microwave radiometers to wind and internal waves, and the comparison of radiometric, polarimetric, and scatterometric response to the ocean surface. Observations include those from a scanning 5-mm-wavelength radiometer deployed on the R/V *FLIP*, a blimp-borne dual-channel radiometer at 23.87 and 31.65 GHz, and a blimp-borne 37-GHz polarimeter. Ground truth, to which these observations can be compared, was obtained from *FLIP* data and includes wind speed and direction and atmospheric stability.

INTRODUCTION

During September–October 1995, the Environmental Technology Laboratory (ETL) organized the Coastal Oceans Probing Experiment (COPE) off the Oregon coast. The principal objectives of the study were to observe the signatures of the ocean surface with radars, lidars, and radiometers, and to correlate these signatures with *in situ* measurements. The *in situ* observations were primarily taken from the Floating Instrument Platform (*FLIP*), a research vessel operated by the Scripps Institute of Oceanography. Microwave radiometric and polarimetric observations were taken from a blimp, while two microwave radiometers were operated on *FLIP*. Other blimp-mounted instruments included an X-band scatterometer, an altimeter, a Global Positioning System (GPS) receiver, and an infrared thermal imager, all operated by the University of Washington.

ETL blimp instruments included a 37-GHz polarimeter that measured the first three Stokes parameters, a dual-frequency radiometer at 23.87 and 31.65 GHz, orthogonally polarized infrared radiometers at 10.6 μm, and a video camera. All of the ETL instruments could be scanned in both elevation and azimuth, and viewed approximately the same area on the ocean surface with coordinated scans. The goals of the radiometric study were to determine the accuracy to which wind direction could be measured by polarimeters, to determine the frequency and angular response of microwave radiometers to wind and internal waves, to study the effects of cloud and rain on the

observations, and to compare radiometric and scatterometric observations.

Both a rapidly scanning 5-mm radiometer and a dual-channel Water Vapor Radiometer (WVR) were operated from *FLIP*. The 5-mm radiometer was used to measure air-sea temperature difference, as well as low-altitude temperature profiles, and the WVR measured integrated amounts of water vapor and cloud liquid. Observations with the 5-mm radiometer and the WVR radiometers are used to compare with blimp and *in situ* measurements taken under a variety of atmospheric and oceanic conditions.

The blimp that was operated during COPE was rented from a commercial firm, LTA USA, based in Eugene, Oregon, and was an ideal platform for this experiment. During a typical flight, a pilot and three scientific personnel were on board. The payload of 1600 lbs. was sufficient to carry the crew and the scientific equipment. Typically, a transit time of about an hour was needed to fly from the runway in Tillamook, Oregon, to the *FLIP* site, although winds were not always favorable. Over the ocean, our observation altitudes ranged from 150 to 500 m, and were known to at least 10 m. The range of surface speeds varied from 0 to about 10 m s^{-1}; the lower speeds allowed one to hover over a feature of interest.

INSTRUMENTATION AND TYPICAL RESULTS

Scanning 5-mm-Wavelength Radiometer

A rapidly scanning 5-mm-wavelength radiometer (scanning rate = 1.3 Hz) was deployed on R/V *FLIP*. The primary purpose of the radiometer was to measure air-sea temperature difference and to provide temperature profiles to an altitude of about 300 m. In particular, this instrument provides the continuous measurements of atmospheric stability that are necessary for the interpretation of both radar and radiometric/polarimetric observations of the ocean surface [1,2]. As examples of raw radiometer data, in Figs. 1 and 2 we show angular scans during unstable and stable conditions. Here, we measure angles from the nadir, i.e., 90° is the horizontal direction. Note the completely different angular profiles between the unstable (Fig. 1) and the stable (Fig. 2) profiles. Independent *in situ* measurements verified the stability characteristics of the profiles; in particular, the air-sea
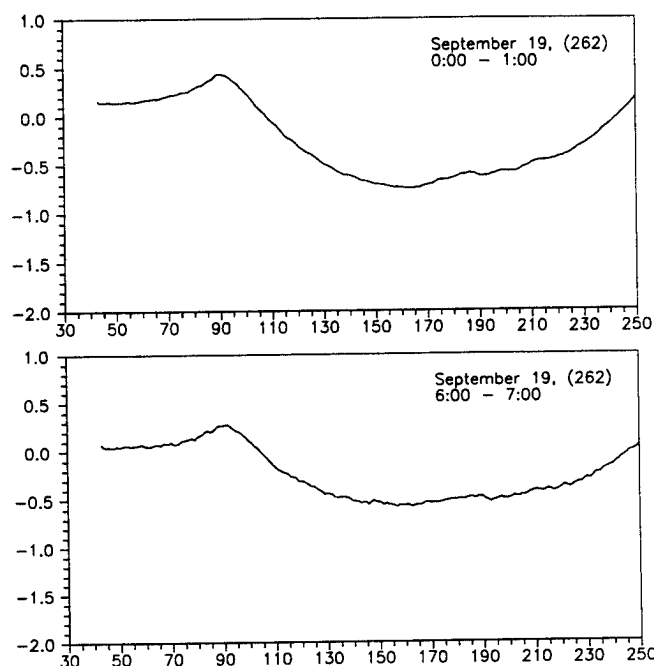
Fig. 1. One-hour averages of scanning 5-mm-wavelength radiometer data (K) as a function of angle from the nadir. Data taken during unstable conditions on R/V *FLIP* of the Oregon coast, September 19, 1995. Times are given in UTC. A constant offset has been subtracted from the data.
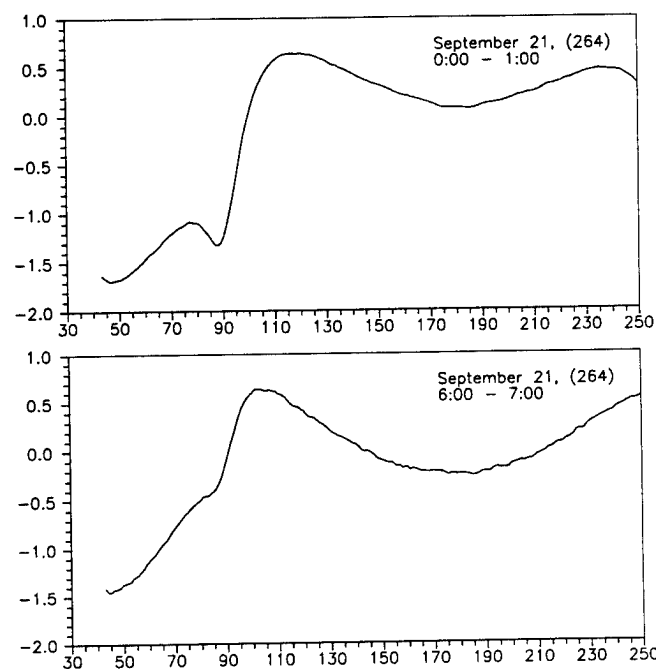
Fig. 2. One-hour averages of scanning 5-mm-wavelength radiometer data (K) as a function of angle from the nadir. Data taken during stable conditions on R/V *FLIP* of the Oregon coast, September 21, 1995. Times are given in UTC. A constant offset has been subtracted from the data.

temperature difference reached 6°C on day 264. Initial quantitative results obtained by this radiometer during COPE are given by Trokhimovski et al. [3,4].

Blimp-Borne Dual-Frequency Radiometer

ETL developed and deployed a dual-channel radiometer at 23.87 and 31.65 GHz in the San Clemente Ocean Probing Experiment [5] and the Verification of the Origins of Rotation in Tornadoes Experiment [6] from aircraft platforms. The two frequencies share a common antenna (offset parabola), have equal beamwidths (3.6° half-power beamwidth), and are orthogonally polarized. Each channel has a double-sideband receiver with a total bandwidth of 1 GHz resulting in a measured 1-s rms sensitivity of 0.064 K. During aircraft deployment, observations are obtained from a fixed angle relative to the aircraft. During COPE, the blimp installation involved a specially constructed platform that allowed both complete-azimuthal and partial-elevation angle scanning. The elevation angle scans were limited by obstructions from the blimp and were conducted from about 20° from nadir to about 50° in elevation. Another substantial difference from our previous aircraft deployments was the increased time that can be spent from a blimp viewing a scene or a limited area on the surface. For example, at times, almost stationary positions were obtained.

Atmospheric scanning, i.e., scanning at elevation angle angles greater than 0°, was useful in two ways. In the first, scanning through a range of air mass values permitted the "tip cal" technique [7] to be used for absolute calibration of the radiometer. Second, the measured atmospheric brightness temperatures *Tb* could be used to provide information on the downwelling radiance scattered from the ocean surface. In addition, these measurements could also be converted into columnar amounts of vapor and liquid [8] from which radiance at other window frequencies can be calculated. Fig. 3 shows angular scanning data during clear conditions. Note that *Tb*'s at 23.87 GHz are generally warmer than those at 31.65 GHz. For angles from the nadir up to 0°, this behavior is consistent with the increased emissivity at vertical polarization, as predicted by the Fresnel equations; for elevation angles greater that 0°, the increase is due to the stronger clear-air atmospheric component. Emission from clouds, especially scattered clouds, will complicate this simple situation.

Blimp-Borne 37-GHz Polarimetric Radiometer

This instrument was designed by V. Leuskiy of the P.N. Lebedev Physical Institute, Moscow, Russia, and was provided to ETL for use on COPE. The polarimeter and the dual-frequency radiometer shared adjacent platforms on the blimp so that coordinated elevation and azimuthal scans could
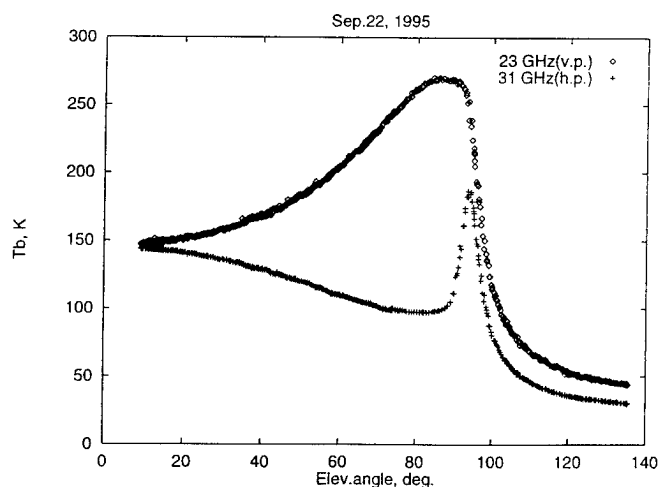
Fig. 3. Brightness temperatures at 23.87 and 31.65 GHz as a function of angle from the nadir taken from a blimp at an altitude of 300 m near R/V *FLIP* off the Oregon coast on September 22, 1995.

be performed. The polarimeter measured polarized emission at the radiometer angles of 0° and ±45° with a corrugated horn whose 3-dB beamwidth was 6.0°. The receiver was a double-sideband type with a frequency range of 0.1 to 1.1 GHz on each side of the local oscillator frequency. Using a measured radiometer noise temperature of 500 K and a target temperature of 298 K, the measured and calculated 1-s sensitivities were 0.02 and 0.018 K.

Fig. 4 shows azimuthal scans observed by the polarimeter at an angle from the nadir of 22°; temporal averages of 10 min were used for these illustrations. The solid curves are produced by least-squares fits of the form

$$Tb(\phi) = B_0 + B_1 \cos(\phi - \phi_1) + B_2 \cos(2\phi - \phi_2) ,$$

where ϕ is the azimuth angle. The sea surface wind, as observed independently from *FLIP* at an altitude of 17 m, had a speed of 7.8 m s^{-1} at 270°. The atmospheric conditions were cloudy. Figs. 4a,b show vertical $Tb(v)$ and horizontal $Tb(h)$
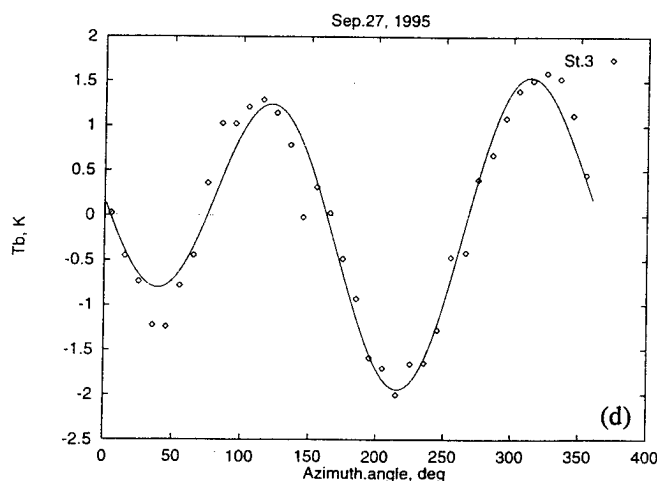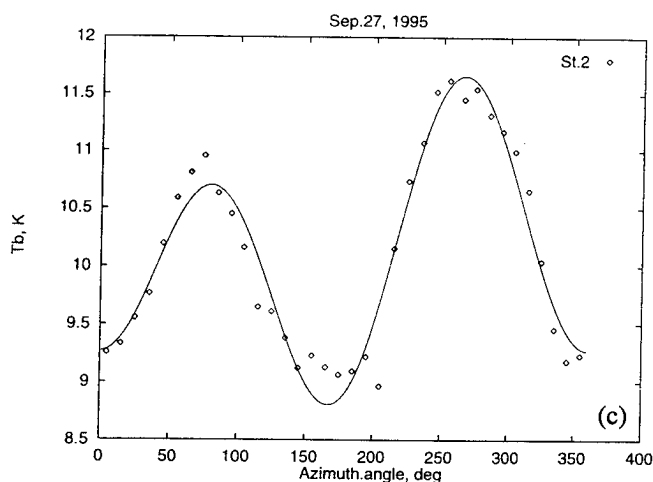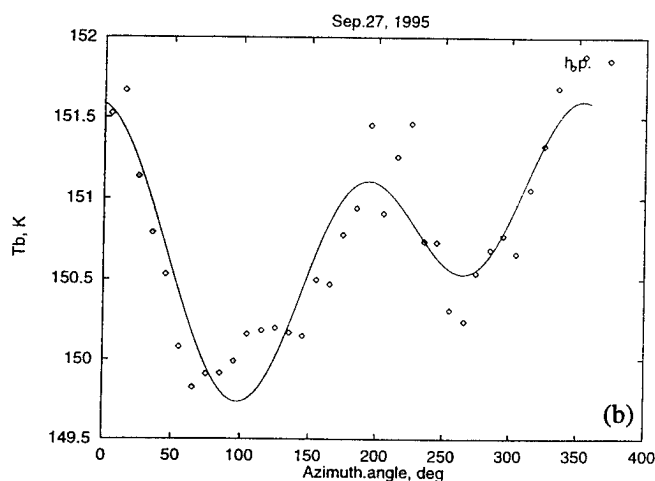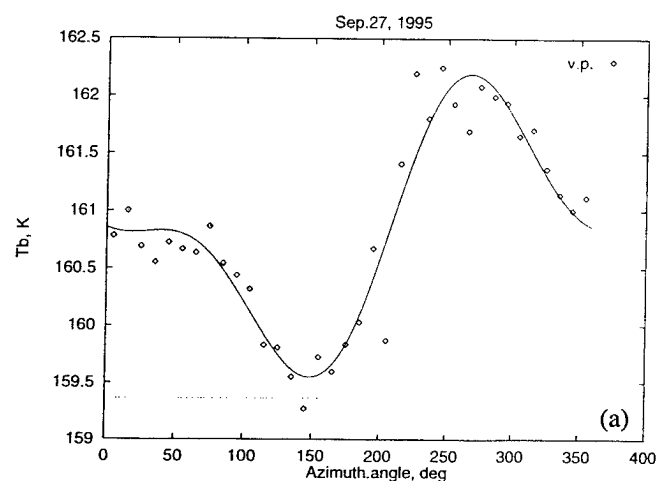
Fig. 4. Brightness temperatures as measured by a blimp-borne 37-GHz polarimeter at an angle from the nadir of 22°. (a) Tb at vertical polarization. (b) Tb at horizontal polarization. (c) Second Stokes component. (d) Third Stokes component. The measured wind speed at 17 m was 7.84 m s^{-1} from the direction of 270°. Clouds were present.

1452

brightness temperatures as a function of φ. As expected, Tb(v) and Tb(h) are out of phase by 90° with Tb(v) having its maximum in the upwind direction at 270°. It is believed that some of the scatter in the data is due to reflected emission from clouds. However, the second [= Tb(v) - Tb(h)] and third [= Tb(+45°) - Tb(-45°)] Stokes vectors are much less affected by clouds, as seen in Figs. 4c,d. In addition, the anisotropy between up- and downwind directions is observed by maximum Tb differences of about 2.5 K. Further examples of polarimetric and radiometric signatures of the ocean, as observed from the blimp platform, are given by Irisov and Trokhimovski [9,10].

DISCUSSION AND CONCLUSIONS

The unique advantages of a blimp as a radiometric platform were exploited during COPE. Using dual-frequency and polarimetric radiometers, the angular dependence of emission from a variety of ocean and atmospheric conditions was studied. Azimuthal angular signatures were clearly evident in the data, were consistent with theory, and provide further evidence that measurements of polarized emission can determine wind speed and direction. Also of interest are the observations of internal waves by blimp-borne polarimeters [10].

The scanning 5-mm radiometer also provided accurate and high temporal resolution measurements of the air-sea temperature difference [3,4]. Work is still in progress to derive low-altitude (<~300 m) temperature lapse-rate profiles. Other work in progress is the analysis of data from the dual-channel radiometer aboard *FLIP*. These data will be used to characterize better the downwelling radiation that was scattered from the ocean surface and observed by blimp-borne radiometers.

ACKNOWLEDGMENTS

REFERENCES

[1] N.M. Pospelov, "Surface wind speed retrieval using passive microwave polarimetry: The dependence on atmospheric stability," Proc., IGARSS'95, Florence, Italy, July 10–14, pp. 1773–1775, 1995.

[2] J.A. Shaw and J.H. Churnside, "Ocean ripple statistics measured with a scanning-laser glint sensor," Proc., IGARSS'96, Lincoln, NE, May 27–31, 1996.

[3] Yu. G. Trokhimovski, E.R. Westwater, and Y. Han, "Air and sea surface temperature measurements using a 60-GHz microwave rotating radiometer," Proc., IGARSS'95, Florence, Italy, July 10–14, pp. 1110–1112, 1995.

[4] Yu. G. Trokhimovski, E.R. Westwater, Y. Han, and V. Ye. Leuskiy, "The results of air and sea surface temperature measurements using a 60-GHz microwave rotating radiometer," unpublished.

[5] L.S. Fedor and V.G. Irisov, "Airborne dual-channel radiometric ocean surface observations during SCOPE'93," Proc., IGARSS'94, Pasadena, CA, August 8–12, pp. 2410–2412, 1994.

[6] L.S. Fedor, E.R. Westwater, and M.J. Falls, "Observations of water vapor and cloud liquid from an airborne dual-frequency radiometer during VORTEX'95," Proc., IGARSS'96, Lincoln, NE, May 27–31, 1996.

[7] Y. Han, J.B. Snider, E.R. Westwater, S.H. Melfi, and R.A. Ferrare, "Observations of water vapor by ground-based microwave radiometers and Raman lidar," *Geophys. Res.*, vol. 99(9), pp. 18695–18702, 1994.

[8] E.R. Westwater, "Ground-based Microwave Remote Sensing of Meteorological Variables," in *Atmospheric Remote Sensing by Microwave Radiometry*, Chap. 4. M.A. Janssen, Ed. New York: J. Wiley & Sons, Inc., 1993, pp. 145–213.

[9] V.G. Irisov and Yu. G. Trokhimovki, "Observation of the ocean brightness temperature anisotropy during COPE," Proc., IGARSS'96, Lincoln, NE, May 27–31, 1996.

[10] V.G. Irisov and Yu. G. Trokhimovski, "Polarimetric observation of ocean internal waves by microwave radiometers during the Coastal Ocean Probing Experiment," Proc., IGARSS'96, Lincoln, NE, May 27–31, 1996.

Surface Wind Measurements by Radiometer-Polarimeters in Frame of Russia Airspace Programs

Yu.A. Kravtsov, A.V. Kuzmin, M.N. Pospelov, A.I. Smirnov

Space Research Institute, Russian Academy of Sciences (SRI RAS)
Profsoyuznaya 84/32 Moscow 117810 Russia
Tel: (7-095) 333-5279; Fax: (7-095) 333-1056; E-mail: kravtsov@asp.iki.rssi.ru

Abstract

Radiometric near surface wind measurements are founded on polarization anisotropy of the thermal microwave emission from ocean. Physical reasons for such an anisotropy for nadir observations were revealed in SRI RAS, in 1978-1979 first theoretically and then experimentally (the so-called "critical phenomena"). The method for wind speed and direction measurements developed in the Space Research Institute is based on nadir radiometer-polarimeter observations. This method provides the accuracy of the wind speed measurements better than 2 m/s, or twice as high if parameters of lower atmosphere stability are known. Nadir-looking surface wind measurements demonstrated their efficiency during long-term Russian experiments in the Barentz sea, in North-West Pacific (near Kamchatka and Sakhalin) and during Joint US-Russia Experiment (JUSREX-92) in Atlantic, near New York coast. Experimental airborne system included polarimetric radiometer at 13.3; 20.0, and 35 GHz and radiometers at 1.6; 3.6; 5.0; 22 and 37 GHz. Polarimetric nadir-looking radiometer IKAR-N (frequency 13.33 GHz) developed by SKB of IRE RAS is to be launched on MIR-PRIRODA module in the spring 1996. Multifrequency and multibeam radiometric-polarimetric system PARK was developed in SRI RAS for another spacecraft of ALMAZ series. Such a system at frequencies 5.0; 13.3; 20 and 35 GHz is supposed to form 8-16 beams using light lowloss metal - ceramic Luneberg lens. The lens provides panoramic image of the sea surface without scanning. Sensitivity of PARK system within a resolution element is 3-4 times higher that of scanning system.

1. Retrieval of Surface Wind Parameters from Polarimetric Data

Surface wind speed is a crucial parameter of atmosphere and sea surface interaction. Wind speed measurements are essential for the needs of marine transport, meteorology, etc. Besides, data on near surface wind vector may be used to correct data on other parameters of the atmosphere-ocean system, above all, sea surface temperature [1].

Theoretical and experimental studies conducted in the SRI RAS under the supervision of Prof. V. Etkin back 1978-1979 [2,3] promoted the method for determination of surface wind speed vector from the sea thermal emission polarization ellipse. An updated theory of critical phenomena, responsible for polarization anisotropy of the sea thermal microwave emission, is outlined in Ref. [4,5].

The directional anisotropy of wind-generated ripples gives rise to the polarizational anisotropy of thermal microwave emission at nadir view angle. The major axis of polarization ellipse coincides with wind direction. The value of anisotropy ΔT_a, i.e. the difference in brightness temperatures, corresponding to major and minor axes of the ellipse, depends mainly on wind speed. Practical algorithms for wind vector parameters retrieval from polarimetric data were reported before [1].

Atmospheric attenuation of microwaves reduces the value ΔT_a, so wind speed under cloudy conditions is underestimated. To compensate for this attenuation, the value of absolute brightness temperature measured by the radiometer may serve as an indicator of the attenuation factor. Our recent investigations have demonstrated that wind speed dependence differs for various states of atmospheric boundary layer stability. The stability correction of wind speed retrieval algorithm allows to almost double the accuracy [6].

2. Airborne Radiometers

The experiments with airborne instruments have some advantages over spaceborne ones, as they usually are carried out under well controlled environmental conditions.

Airborne radiometric system developed by SRI RAS [7,8] incorporates a set of radiometers in the wavelength range from 0.8 to 21 cm, with sensitivity from 0.05 to

0.15 K/s (integration time $\tau=1$ s). Among these are radiometer-polarimeters intended for remote measurements of polarization characteristics of thermal microwave emission [9]. Such a radiometer can measure thermal emission at several linear polarizations using the controlled ferrite gyrator. This allows to reconstruct the polarization ellipse of microwave emission.

3. Airborne experiments

First nadir-looking measurements of microwave polarization anisotropy of sea surface waves were performed as early as 1979 [10]. Later similar experiments were cared out in North-West Pacific [11], in the Barentz Sea and in North Atlantic during JUSREX-92 experiments [5,6]. During these experiments airborne polarimeters were applied to establish the polarizational anisotropy dependence on surface wind and other meteorological and hydrological factors. An example of polarimeter signal record (on Aug. 23, 1988, in North-Western Pacific) is presented at Fig.1.

As a result of more than 50 such circular flights, the anisotropy versus wind speed dependence was plotted for Ku, K and Ka bands [4]. For wind speed below 12 m/s this dependence is described quite reasonably by the quadratic law.

At higher wind speeds, exceeding 12-15 m/s, dependence of ΔT_a on V saturates, because other factors come into the play: foam, white-capping and so on. That is why special experiments are required for calibration anisotropy - wind speed dependence both for nadir-looking method of SRI RAS and for oblique observations method used by JPL [12].

4. Russian Spaceborne Radiometer Projects

Many space agencies including Russian one plan further development of spaceborne radiometer system. The launch of the specialized remote sensing "PRIRODA" module is planned in spring 1996 [13]. It will operate as part of the orbital station MIR. The module will take on board a great variety of scientific instruments of frequencies ranging from visible to microwave, including the IKAR radiometric system IKAR has three main components: the nadir unit IKAR-N, the scanning unit IKAR-D and the panoramic unit IKAR-P. Observation swath of the scanning unit is 400 km, that of the panoramic unit is 700 km.

The Ku-band (13.3 GHz) polarimetric radiometer is part of IKAR-N system. This nadir-looking radiometer with non-scanning horn antenna can measure the value of polarization anisotropy ΔT_a along with azimuthal orientation of polarization ellipse major axis. For wind
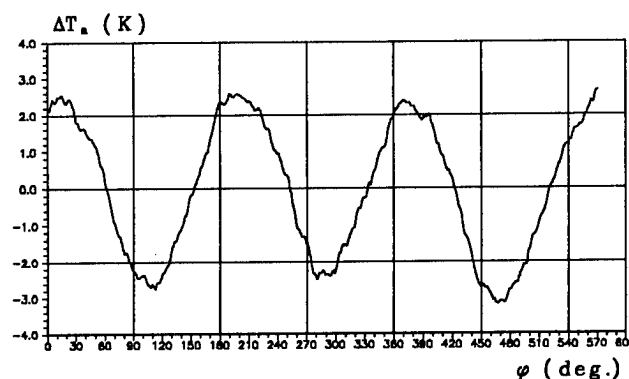
Fig. 1

vector retrieval from these data the SRI RAS algorithm is to be used. This instrument will be the first satellite radiometer of the kind. The realization of MIR-PRIRODA mission may add pros and cons for further use of spaceborne polarimeters.

Panoramic radiometric system PARK was developed by SRI RAS for installation on a spacecraft of ALMAZ series. Such a system at frequencies 5.0; 13.3; 20.0 and 37.0 GHz is supposed to form 8-16 beams using light lowloss metal-ceramic Luneberg lens (Fig.2). Luneberg lens of 0.5 m in diameter and about 50 kg in mass provides panoramic image of the sea surface without scanning (Fig.3). Sensitivity of PARK system within a resolution element is 3-4 times higher that of scanning system. The use of panoramic systems considerably enhances radiometer sensitivity and maintains sufficiently high spatial resolution. This is especially important for the study of mezzo-scale ocean and atmosphere processes. The polarimeters are intended to measure three Stokes parameters of partially polarized emission for wind vector retrieval with the swath of 400 km.

Fig. 2

1455
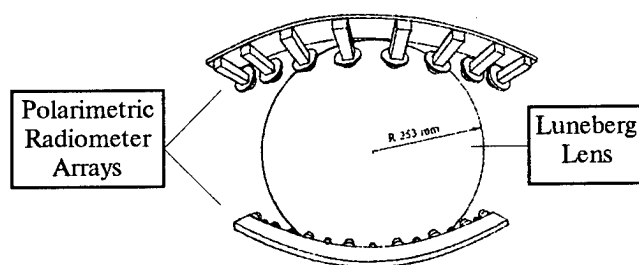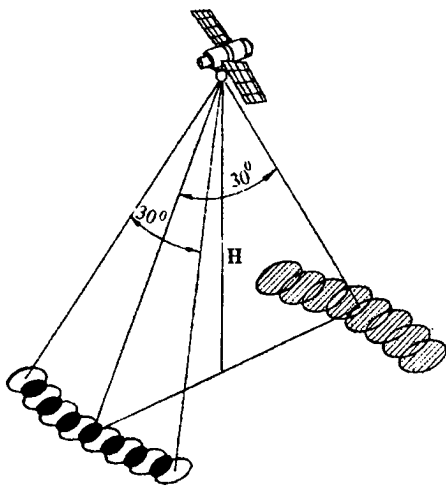
Fig. 3

Conclusion

Polarimetric method of near surface wind vector retrieval proved its efficiency in many airborne experiments performed by Russian and American scientists. This method promises sufficiently high accuracy for spaceborne measurements as well. It can compete with the scatterometric method both in accuracy and in many other characteristics: cost, mass of instrumentation, power supply.

Forthcoming measurements from MIR-PRIRODA module are expected to provide new information about advantages of the prospective polarimetric method.

References

[1] V.S.Etkin, A.V.Kuzmin, M.N.Pospelov, A.I.Smirnov, and Yu.G.Trokhimovskii, "Investigation of Sea Surface Temperature and Wind Fields in Joint US/Russia Internal Waves Remote Sensing Experiment,"— IGARSS'94 Digest, 1994, Vol. 2, pp. 750-752.

[2] Yu.A.Kravtsov, E.A.Mirovskaya, A.E.Popov, I.A.Troitskii, and V.S.Etkin, "Critical effects in thermal radiation of periodically uneven water surface," Akad. Nauk SSSR, Atmospheric and Oceanic Physics, 1978, Vol. 14, No. 7, pp. 522-526 [Translated from: Известия Академии наук СССР, серия Физика океана и атмосферы, 1978, т.14. №7, с.733-739].

[3] V.S.Etkin, N.N.Vorsin, Yu.A.Kravsov et al., "Revealing critical phenomena accompanying thermal microwave emission of periodically perturbed water surface," Radiophysics and Quantum electronics, 1978, Vol. 21, No 3, [Translated from: Известия ВУЗов сер. Радиофизика, 1978, т. 21, № 3, с. 454-456].

[4] V.G.Irisov, A.V.Kuzmin, M.N.Pospelov, Yu.G.Trokhimovskii, and V.S.Etkin, "The Dependence of Sea Brightness Temperature on Surface Wind and Speed. Theory and Experiment,"— IGARSS'91 Digest, vol. 2, pp. 1297-1300.

[5] V.G.Irisov, "Small Slope Approximation for Micro-wave Polarimetric Observation of Sea Surface,"—IGARSS'94 Digest, 1994, Vol. 4, pp. 2421-2423.

[6] M.N.Pospelov, "Surface Wind Speed Retrieval Using Passive Microwave Polarimetry: the Dependence on Atmospheric Stability,"— IGARSS'95 Digest, 1995, pp. 1773-1775.

[7] V.S.Etkin, B.E.Aleksin, V.M.Aniskovich et al., "Multichannel aircraft-based complex for radiohydrophysical research,"—Preprint Space Research Institute, Pr-1279, Moscow, 1987,44p. (in Russian).

[8] V.S.Etkin, M.D.Raev, M.G.Bulatov, Yu.A.Militskii et al., "Radiohydrophysical Aerospace Research of Ocean,"—Preprint Space Research Institute, Pr-1749, Moscow, 1991, 84 p.

[9] M.S.Dzura, A.S.Khrupin, M.N.Pospelov et al., "Radiometers-Polarimeters: Principles of Design and Applications for Sea Surface Microwave Emission Polarimetry," —IGARSS'92 Digest, 1992, vol. 2, pp. 1432-1434.

[10] E.A.Bespalova, V.M.Veselov, A.A.Glotov et al. "Sea-ripple Anisotropy Estimates from Variations in Polarized Thermal Emission of the Sea,"— Oceanology, 1981, vol. 21, pp. 213-215 [Translated from Доклады Академии Наук СССР, 1979 т.246, №6, pp. 1482-1485].

[11] E.A.Bespalova, V.M.Veselov, V.E.Gershenzon et al., "Near Surface Wind Velocity Recovering by Measurements of Polarization Anisotropy Microwave Scattering and Emission,"— Soviet Journal of Remote Sensing, 1982, No. 1, pp. 87-94, [Translated from Исследования Земли из Космоса 1982, №. 1, pp. 87-94].

[12] S.H.Yueh, W.J.Wilson, F.K.Li, S.V.Nghiem, and W.B.Ricketts, "Polarimetric Measurements of Sea Surface Brightness Temperature Using an Aircraft K-band Radiometer", IEEE Trans. Geosci. Remote Sensing, 1995, Vol. 33, No. 1, pp. 85-92.

[13] N.A.Armand, B.G.Kutuza, and V.A.Panchenko, "International Space Project PRIRODA"—III European Symposium on MTPE, Munchen, March, 1992. Nort Holland, Amsterdam, 1992.

Observation of the Ocean Brightness Temperature Anisotropy during the Coastal Ocean Probing Experiment

Vladimir G. Irisov
Cooperative Institute for Research in Environmental Sciences (CIRES),
University of Colorado at Boulder
NOAA/ERL/Environmental Technology Laboratory
325 Broadway, Boulder CO 80303-3328
ph. (303)-497-6549, fax (303)-497-3577, e-mail: virisov@etl.noaa.gov

Yuri G. Trokhimovski
National Research Council Resident Associate
NOAA/ERL/Environmental Technology Laboratory
325 Broadway, Boulder CO 80303-3328

Abstract -- The effect of the brightness temperature anisotropy was investigated by microwave radiometers during the Coastal Ocean Probing Experiment. The radiometers were mounted on rotating platforms on a blimp. The azimuthal dependencies of brightness temperature were measured during 12 flights at different wind speeds and viewing angles. The dependencies of the amplitudes of the first and second harmonic of the azimuthal variations versus wind speed were obtained for viewing angles between 20° and 30° from nadir. The wind speed varied from 2.5 to 9.0 m/s.

INTRODUCTION

The dependence of the microwave brightness temperature of the ocean on wind speed and direction is intensively studied due to its importance for remote sensing of the near-surface wind. The anisotropy of the thermal microwave radiation has been observed many times [1-3], but still there is no satisfactory quantitative description of this effect. One of the purposes of the Coastal Ocean Probing Experiment (COPE) was a study of the azimuthal variations of microwave radiation of the wind-driven sea surface by a sensitive, dual-frequency radiometer (23 GHz (v.p.) and 31 GHz (h.p.)) and a polarimeter (37 GHz). The radiometer at 37 GHz was designed especially for such observations. It was able to measure brightness temperature at three linear polarizations or, in other words, to measure the first three Stokes parameters of the thermal radiation.

EQUIPMENT AND MEASURING PROCEDURE

The observations of the sea surface were conducted from an airship (blimp) near the Pacific coast of Oregon in September-October 1996. The measurements were made preferably close to the Scripps Institute Floating Instrument Platform *(FLIP)* which was equipped with numerous instruments for investigating atmospheric and oceanic parameters. In most cases the wind speed and direction measured from *FLIP* were used for data analysis, although sometimes, when these data were not available, the wind speed and direction were estimated visually from the sea surface state or from the

difference in air and ground velocities of the blimp. The portion of such "unreliable" points does not exceed 14 % from the whole data set. The microwave radiometers were installed on two platforms scanning in azimuth. The sensitivities of the microwave radiometers were about 0.05 K for an averaging interval of 1 s. at 37 GHz and about 0.1 K at 23/31 GHz. Two IR radiometers and a video-camera were mounted on the same platforms for monitoring the sea state and the physical temperature. The orientation of the blimp and scanning platforms was measured by compass, gyroscope, and angle sensors. All the information was collected and stored on a computer with the sample rate of about 1 point per second.

The blimp was also equipped with an X-band radar, altimeter and a high resolution IR-imager operated by the Applied Physics Laboratory, University of Washington. The twelve working flights were made during the COPE for a total duration of about 67 hours.

The platforms provided conical scanning of nearly 360° of azimuthal angle and the elevation angles could vary between 15° from nadir to 50° above the horizon for the polarimeter, and from nadir to 50° above the horizon for the dual-frequency radiometers. The ability to look above the horizon allowed us to calibrate the radiometers using an atmospheric radiation. For a cloudless, uniform atmosphere this is probably the best calibration technique providing accuracy of about 1-2 K of absolute brightness temperature measurements. Note that such high accuracy is not needed for the anisotropy study because it is based on a measurement of relative variations. Nevertheless the absolutely calibrated data is valuable for other studies.

DATA PROCESSING AND RESULTS

An experimental complication was caused by the pitch and roll variations of the blimp. We did not have a mechanical stabilization system so we had to compensate for the effects of pitch/roll in the data processing. First, the variations in brightness temperature caused by pitch/roll variations were filtered from radiometric data. For this purpose we used the regressions obtained during the elevation angle scanning. Fig.1
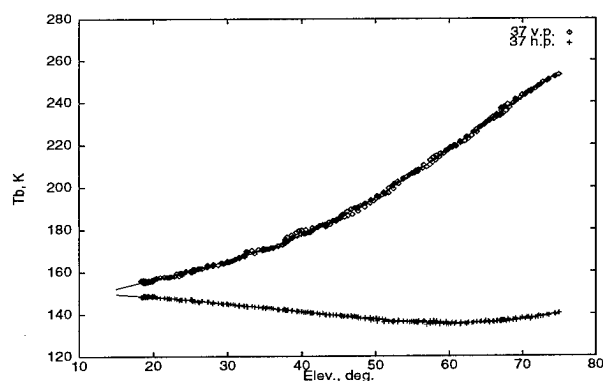
Fig.1. The dependencies of the brightness temperature at vertical and horizontal polarizations versus elevation angle at 37 GHz.

shows a typical experimental regression of the brightness temperature versus the elevation angle along with the polynomial approximation.

After removal of the component related to the fluctuation of the blimp's orientation, the azimuthal dependencies of the brightness temperature were averaged over some period of continuous scanning. The averaging time varied from several minutes to an hour and a half. In this way the azimuthal dependencies were obtained for different frequencies, elevation angles and wind speed. Here we consider only polarimetric data at 37 GHz.

An example of the azimuthal dependencies of the brightness temperature is shown in Fig.2. Fig.2a and fig.2b show the variations at vertical and horizontal polarizations, respectively. Fig.2c and fig.2d show the same dependencies for differences of vertical and horizontal polarizations, and +45° and -45° polarizations, respectively; these correspond to the second and third Stokes parameters. The wind was blowing from a direction about 80°. (the up-wind direction is indicated by vertical dashed line) at 10.5 m/s. The viewing angle was about 18° from nadir. The solid curves represent a best fit to an equation of the form:

$$T_b = B_0 + B_1 * Cos(\phi - \phi_1) + B_2 * Cos(2\phi - 2\phi_2)$$

where B_1 and B_2 are the amplitudes of the first and second harmonics and the phases ϕ_1 and ϕ_2 correspond to the wind direction. Note that for vertical and horizontal polarizations the data looks more noisy than for the second and the third Stokes parameters. This can be explained by the amplitudes for the Stokes parameters being about twice of those for horizontal and vertical polarizations. The noise can be reduced also due to "compensation" of the unpolarized fluctuating component related to atmospheric radiation, foam, etc. Consequently it is more convenient to measure polarization differences directly (using one instrument) than to recover Stokes parameters from independent measurements.

a).

b).

c).

d).
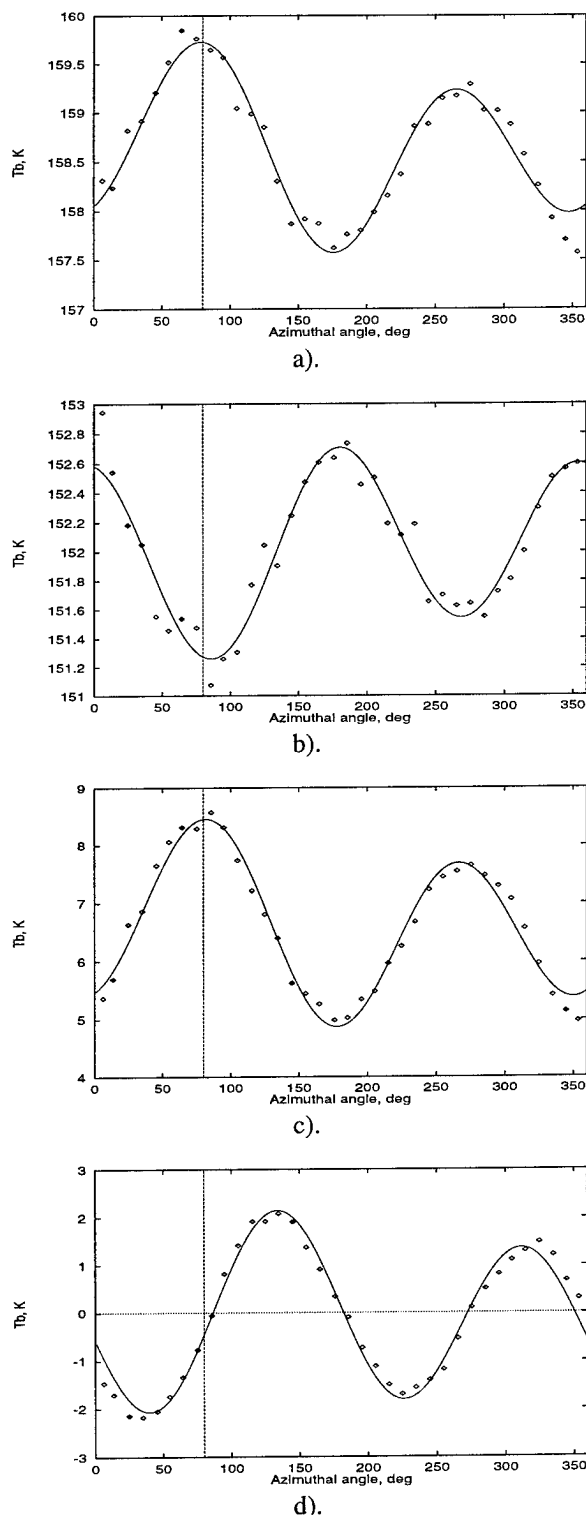
Fig. 2. The azimuthal dependencies of the brightness temperature at vertical and horizontal polarizations (a,b) and the second and the third Stokes parameters (c,d).

Fig.2 illustrates the presence of both harmonics in azimuthal dependencies. On Fig.3 we plot the amplitudes of the first and the second harmonics for the second and the third Stokes

parameters versus wind speed for the viewing angle between 20° and 30° from nadir. Despite unreliable statistics we note that the dependencies are quite different. The amplitude of the second harmonic grows strongly non-linear with the wind speed increasing, but the first harmonic is more or less linear function of wind speed. The non-linear behavior of the second harmonic's amplitude is consistent with [4]. It seems also that the relative scatter of the first harmonic amplitude is slightly higher than that of the second one, although that can be explained by an accuracy of the measurements.

CONCLUSION

During the COPE we studied the anisotropy of the ocean's microwave thermal radiation. We obtained the wind dependencies of the amplitudes of the first and second harmonics of the azimuthal dependencies at viewing angles between 20° and 30° from nadir. It appears that their behavior with the increasing wind speed is very different: the first harmonic amplitude grows approximately as a linear function in contrast to the second harmonic, which can be approximated by a power function of wind speed. Of course it is difficult to reach a final conclusion without measurements at high wind speed, but at least at moderate wind speed one needs to use appropriate approximations for the amplitudes of the first and second harmonic.

To understand the whole picture we need to study the dependencies at high wind speed and at different observation angles and frequencies. Such information on microwave anisotropy is necessary for efficient algorithm development to recover the wind vector from radiometric measurements.

ACKNOWLEDGMENTS

REFERENCES

[1] E.A.Bespalova, V.M.Veselov, A.A.Glotov, *et al.,* "Sea-ripple anisotropy estimates from variations in polarized thermal emission of the sea," *Doklady Akademii Nauk SSSR,* **246,** N.6, 1482-1485, 1979.

a).

b).
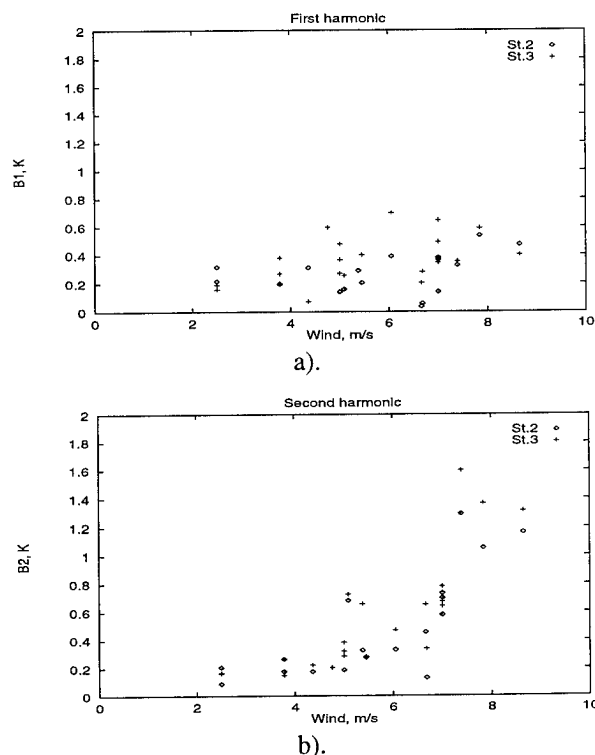
Fig. 3. The wind dependencies of the first (a) and the second (b) harmonics of the Stokes parameters anisotropy.

[2] F.J.Wentz, "Measurement of oceanic wind vector using satellite microwave radiometer," *IEEE Trans. Geosci Remote Sensing,* **30,** N.5, 960-972, 1992.

[3] S.H.Yueh, W.J.Wilson, S.V.Nghiem, F.K.Li, and W.B.Ricketts, "Polarimetric measurements of sea surface brightness temperature using an aircraft K-band radiometer," *IEEE Trans. Geosci. Remote Sensing,* **33,** N.1, 85-92, 1995.

[4] Y.G.Trokhimovski and V.G.Irisov, "Wind speed and direction measurement using microwave polarimetric radiometers," NOAA Tech. Memo. ERL ETL-250, 1995, 35p.

High Altitude Aircraft Mapping of Near Surface Ocean Winds

Robbie E. Hood and Roy W. Spencer

Global Hydrology and Climate Center
NASA/Marshall Space Flight Center CODE: ES41
977 Explorer Blvd.
Huntsville, Alabama 35806

Voice: 205.922.5959 / Fax: 205.922.5788 / e-mail: robbie.hood@msfc.nasa.gov

INTRODUCTION

The Conically-Scanning Two Look Airborne Radiometer (C-STAR) is currently being constructed as a satellite simulator to investigate the feasibility of measuring global ocean vectors with passive microwave instrumentation. The C-STAR will be a total power, four-channel radiometer package remotely sensing 37.1 GHz signatures from a high altitude aircraft platform. The instrument package is being developed by the National Aeronautics and Space Administration (NASA) Marshall Space Flight Center (MSFC) and the Global Hydrology and Climate Center (GHCC) for flight on a NASA ER-2 aircraft during early 1996.

SCIENTIFIC JUSTIFICATION

The importance of surface wind forcing to the ocean circulation, and thus to climate change, necessitates a capability to monitor surface winds over the global oceans. While scatterometers provide some capability to this end, their narrow swath width leads to regional biases which can not be eliminated with even annual averaging. Combined with their high cost in this era of reduced budgets, this encourages the development of new techniques for ocean wind retrieval. There has been increasing interest in the development of passive microwave radiometers which would measure not only wind speed but wind direction as well. The azimuthal anisotropies in surface emission related to near surface ocean wind direction are now being documented with laboratory, aircraft and spacecraft measurements.

A comprehensive overview of these investigations is presented by [1].

C-STAR will provide dual-look, conically scanned imagery of dual linear polarization and polarimetric channels at 37.1 GHz and an Earth incidence angle of 53°. The choice of frequency and view angle for C-STAR was based upon the demonstrated heritage of the Defense Meteorological Satellite Program Special Sensor Microwave/Imager (SSM/I). One goal of the C-STAR investigation is to evaluate the skill with which wind vectors can be retrieved from microwave imagery assuming a baseline instrument configuration like that flown on current satellites.

Another goal is to allow a direct comparison of the two-look microwave radiometric wind direction retrieval technique proposed by [2] and the polarimetric methods of wind direction detection discussed by [1] and [3]. C-STAR information will provide the opportunity to develop oceanic wind speed and direction detection algorithms for each technique as well as a combined algorithm utilizing both techniques which [4] has suggested might be necessary. Although these algorithms will be dependent upon the C-STAR frequency and view angle, they will still provide an useful evaluation of the accuracy and limitations of each method.

INSTRUMENT DESCRIPTION

Instrument Package

The complete C-STAR instrument package will consist of a total power scanning

Table 1: C-STAR Instrument Specifications

Frequency	37.1 GHz
Immediate Frequency Bandwidth	900 MHz
Half-power Beamwidth	7.5°
Number of Feedhorns	2
Number of Channels	4
Measured Polarizations	H, V, P, Q
Temperature Resolution	0.1 Kelvin
Integration Time	0.125 seconds
Total System Mass	120 kilograms
Power	280 watts

radiometer subsystem, a data acquisition system (DAS), and a power distribution unit (PDU). The C-STAR instrument specifications are listed in Table 1. The receiver subsystem will be composed of four heterodyne receivers with diode detectors. One pair of receivers will be matched with one feedhorn to collect horizontal (H) and vertical (V) polarized radiation. The second pair of receivers will be matched to another feedhorn which will be rotated 45° about its view axis compared to the first feedhorn. The polarizations detected with this receiver pair will be P (+45° from V) and Q (-45° from V). By collecting data both fore and aft of the flight vector, the polarimetric method of calculating the ocean wind direction can be tested with fore and aft data separately or together.

The C-STAR antenna subsystem will consist of two 37.1 GHz scalar feedhorns, a reflector, and two calibration loads. In-flight instrument calibration will be performed during each complete scan cycle. The loads will be fabricated as pyramidal cones machined from aluminum stock with Eccosorb coating to ensure a constant return loss. Emissivity will be greater than 0.9999. One load will be cooled to approximately 250K by ambient air at flight level. The other load will be encased in Styrofoam and thermostatically regulated to 330K with heater strips attached to the back side of the load. Calibration of the earth observed scenes will be a simple interpolation (or extrapolation) of the earth viewing measurements from the known cold and warm load measurements. Thus, the measured brightness temperatures are independent of instrument temperature and gain changes, provided that these changes occur on time scales longer than the interval between calibration scans.

The main components of the DAS are a 386SX processor, a twelve bit analog to digital converter, and two 20 megabyte "flash-disk" memory cards to store the digitized data. The data stream will include earth scene measurements, in-flight calibration data, instrument performance characteristics, and aircraft navigation information supplied by the ER-2 Navigation System.

Instrument Operation

The C-STAR will collect earth scene observations +/- 45° of the aircraft flight track in the fore and aft directions. During each complete conical scan, 52 total earth scene observations per channel and eight total calibration samples per channel will be collected. The ten second C-STAR scan rate and the approximate ER-2 air speed of 410 knots at an altitude of 20 kilometers [5] will yield contiguous footprints in both the fore and aft directions. The time lag between viewing a given earth scene pixel in the forward direction and again in the aft direction will be approximately four minutes. Other pertinent operational characteristics of the C-STAR are listed in Table 2.

SUMMARY

The C-STAR will be a low-noise, conically scanning four-channel passive microwave radiometer which will test the feasibility of obtaining a field of ocean surface wind vectors from an aircraft platform. C-STAR will be the only research instrument remotely sensing ocean

Table 2: C-STAR Operational Characteristics

Field of View	+/-45° fore and aft of flight track
Scan Pattern	Conical
Scan Angle	53° from nadir
Scan Rate	6 rpm
Footprint Size from 20 km Altitude	7.3 km x 4.4 km
Number of Data Samples per Scan	21 per channel per direction
Number of Calibration Samples per Scan	2 per channel per load
Data Volume	1 Kilobyte per minute

wind speed and direction from a high altitude aircraft platform. Yet, the information collected will be highly complimentary to research activities being conducted by the Jet Propulsion Laboratory using non-scanning radiometers aboard a medium altitude aircraft. C-STAR will provide a satellite simulation of ocean wind mapping generated from two-look and polarimetric retrieval methods applied to brightness temperature imagery. Evaluation of these two methods will assist the development of future passive microwave spaceborne sensors monitoring global ocean wind circulation and its relation to climate change.

REFERENCES

[1] S. Yueh, W.Wilson, S. Nghiem, F.Li, and W. Ricketts,"Polarimetric measurements of sea surface brightness temperatures using an aircraft K-band radiometer," *IEEE Trans. Geosci. Remote Sensing*, vol. 33, pp 85-92, Jan. 1995.

[2] F. Wentz, "Measurement of oceanic wind vector using satellite microwave radiometers," *IEEE Trans. Geosci. Remote Sensing*, vol. 30, pp 960-972, Sept. 1992.

[3] Y. Trokhimovski, and V. Irisov, "Wind speed and direction measurement using microwave polarimetric radiometers," *NOAA/ERL Tech. Memo.*, 34 pp, 1995.

[4] S. Yueh, R. Kwok, F. Li, S. Nghiem, W. Wilson, and J. Kong, "Polarimetric passive remote sensing of ocean wind vectors," *Radio Sci.*, July/Aug., 1994.

[5] NASA ER-2 Investigators Handbook, Mission To Planet Earth High Altitude Branch, NASA/Ames Research Center, Moffett Field, CA, 1994.

Performance Analysis for the SeaWinds Scatterometer

David G. Long

Brigham Young University
459 Clyde Building, Provo, UT 84602
(801) 378-4383 long@ee.byu.edu

Michael W. Spencer

Jet Propulsion Laboratory
4800 Oak Grove Drive, Pasadena, CA 91109 USA
(818) 354-1175 mws@shiokaze.jpl.nasa.gov

Abstract - The difficulties of accommodating traditional fan-beam scatterometers on spacecraft has lead to the development of a scanning pencil-beam instrument known as SeaWinds. SeaWinds will be part of the Japanese Advanced Earth Observing System II (ADEOS-II) to be launched in 1999. A brief description of the SeaWinds design, signal processing, and backscatter measurement approach is given in this paper. To analyze the performance of the SeaWinds design, a new expression for the measurement accuracy of a pencil-beam system is used which includes the effects of transmit signal modulation. Performance tradeoffs made in the development of Seawinds are discussed.

I. INTRODUCTION

A scatterometer is a radar system that measures the radar backscatter coefficient, σ^o, of an illuminated surface. Multiple measurements of σ^o from different azimuth and/or incidence angles are used to infer the near-surface wind vector over the ocean. While previous wind scatterometers have been based on fan-beam antennas, the SeaWinds scatterometer, to be launched aboard the second Japanese Advanced Earth Observing Satellite (ADEOS-II) in early 1999 as part of the NASA Earth Observation System, will employ a scanning pencil-beam antenna [2, 3, 4].

A scanning pencil-beam scatterometer offers an alternative design concept which is smaller, lighter and has simpler field-of-view requirements [2]. Further, because the antenna illumination is concentrated in a smaller area, a much higher signal-to-noise ratio (SNR) can be obtained with a smaller transmitter. Complicated signal processing is not required and the data rate is small. As a result a pencil-beam scatterometer can be more easily accommodated on spacecraft than a fan-beam.

The issues and tradeoffs encountered in optimizing a pencil-beam scatterometer system are different than those of a fan-beam system. In this paper we describe some of the details of our approach to the analysis and optimization of the SeaWinds scatterometer system.

II. PERFORMANCE EVALUATION

A metric, widely used in scatterometry, for evaluating σ^o error is the "K_p" parameter:

$$K_p = \frac{\sqrt{\text{var}\{\sigma^o_{\text{meas}}\}}}{\sigma^o}.$$

A general objective of scatterometer design is the minimization of K_p. K_p is a function of the signal-to-noise ratio (SNR) which depends on the wind via σ^o. Relating K_p directly to the wind measurement performance can be difficult due to the non-linearity in the wind retrieval process. As a result, we adopt the goal for SeaWinds that K_p should be less than the geophysical modeling error — the percentage variation in σ^o for a given wind velocity (17% at Ku-band). Such a criterion will insure that wind

performance is limited not by the precision of the instrument, but only by our ability to relate the measured σ^o's to wind speed and direction via the model function.

The scatterometer measures the backscattered power. Unfortunately, the measurement is noisy and a separate measurement of the noise-only power is made and subtracted from the signal+noise power measurement to estimate the signal power (see Fig. 1). Ref. [3] presents a derivation of the K_p for a pencil-beam scatterometer. It has the general form

$$K_p = \left\{ A + SB + S^2C \right\}^{1/2} \tag{1}$$

where S is the noise-to-signal ratio, A is the signal variance, B is a signal-cross noise term, and C is the noise variance. For interrupted CW operation (no modulation) and a simplified geometry and antenna pattern it can be shown that $A = 1/T_pB_D$, $B = 2/T_pB_D$, and $C = 1/(T_pB_D) + 1/(T_pB_n)$; where T_p is the pulse length, B_D is the Doppler bandwidth, and B_n is the noise-only measurement bandwidth. This result is equivalent to Fisher's K_p expression [1]. When modulation is employed, A can be expressed as a weighted integral of the radar ambiguity function defined by the modulation function [3]. Proper selection of the modulation function can lead to reduced K_p for some scan angles; however, the K_p can be increased for other scan angles.

To illustrate the tradeoffs in selecting a modulation scheme, K_p for several modulation schemes is computed assuming a high SNR. The modulation schemes include Interrupted CW (ICW) (no modulation), Linear Frequency Modulation (LFM), and Minimum Shift Keying (MSK) with a maximal length pseudo-random data sequence. The results are summarized in Table 1 where values shown are normalized by the $K_p(ICW)$.

Table 1 reveals that K_p is dependent on the measurement geometry as well as the modulation. While K_p for ICW is inversely proportional to the square root of the product of the pulse length and the Doppler bandwidth (the time-bandwidth product of the echo return), K_p for MSK also depends on the bandwidth of the modulation. Though $K_p(MSK)$ is slightly increased at 0°, at 90° it is reduced with $K_p(MSK) \approx K_p(ICW)/\sqrt{B_{msk}T_c}$ where B_{msk} is the bandwidth of the MSK modulation and T_c is the differential time-of-flight over the footprint. Since MSK provides the best overall performance and can be easily generated in hardware, it was chosen for the baseline SeaWinds design [4]. Note that increasing B_{msk} arbitrarily does not always improve K_p since the receiver

Modulation	0°	90°
$K_p(ICW)$	1.0	1.0
$K_p(LFM)$	1.16	0.9
$K_p(MSK)$	1.05	0.43

Table 1. K_p for various transmit signal modulation schemes. Values have been normalized by $K_p(ICW)$.

Parameter	Value
Transmit Frequency	13.402 GHz
Transmit Power	110 Watts
Transmit PRF	185 Hz (92.5 Hz each beam)
Transmit Pulse Length	1.5 ms
Transmit Modulation	MSK, $T_b = 15\mu sec$
Receive Gate Length	2.0 ms
System Noise Temp.	740°K
Signal+Noise Bandwidth	80 KHz
Noise-only Bandwidth	1 MHz
Rotation Rate	18 rpm
Antenna Beamwidth	1.8° × 1.6° (inner)
	1.7° × 1.4° (outer)

Table 2. SeaWinds Radar Electronics Parameters

bandwidth must also be increased to accommodate the signal, requiring a tradeoff between the signal modulation and the receiver bandwidth.

III. SEAWINDS DESIGN AND TRADEOFFS

The SeaWinds measurement geometry is illustrated in Fig. 2. Figure 3 shows a block diagram of the SeaWinds radar electronics. A summary of the key radar parameters is shown in Table 3. A one meter parabolic dish antenna with two offset feeds creates both the "inner" and the "outer" beams. The inner beam makes measurements at 46° incidence angle while the outer beam makes measurements at 54°. The antenna is mechanically spun about the nadir axis to generate a conical scan. Each point within the inner 700 km of the swath is viewed from four different azimuth angles — twice by the outer beam looking forward then aft, and twice by the inner beam in the same fashion. In the outside edge of the swath, between cross track distances of 700 and 900 km, each point on the ocean is viewed twice by the outer beam only. The inner beam is horizontally polarized with respect to the ocean surface while the outer beam is vertically polarized.

Because the σ^o measurements are obtained at favorable high incidence angles over a continuous 1800 km swath, there is no "nadir gap" where wind can not be retrieved. The wide swath will cover 90% of the ocean surface within 24 hours, an improvement over previous scatterometers. The 18 rpm SeaWinds antenna rotation rate and measurement timing were chosen to obtain optimal sampling of the surface σ^o and to meet host spacecraft dynamics requirements.

Due to the motion of the satellite relative to the Earth, a Doppler shift of up to ±500 kHz is imparted to the echo signal, depending on the antenna scan position. In SeaWinds, the Doppler shift is pre-compensated by tuning the transmit carrier frequency to 13.402 GHz $-f_d$, where f_d is the expected frequency shift to be imparted to the return signal. The compensation frequency is computed by the SeaWinds on-board processor using the measured antenna position, orbit location, spacecraft velocity, and Earth rotation. Pre-compensating the transmit pulse for Doppler shift produces an echo signal that always occurs at the same center frequency, simplifying the RF down conversion and detector electronics.

A. Receive Bandwidth Tradeoffs

K_p can be decreased by appropriate modulation of the transmit pulse; however, a tradeoff between the transmit bandwidth and K_p exists due to the need to increase the receiver bandwidth which increases the effects of noise. The bandwidth of the receive signal depends on both the transmit bandwidth and the geometry-dependent Doppler bandwidth. The Doppler bandwidth results from the variation in Doppler shift over the illuminated area. For SeaWinds, the 3 dB Doppler bandwidth, B_{dop}, varies from 9 kHz to 15 kHz depending on the scan angle. We require the receive filter bandwidth B_r to be wide enough to pass at least 90% of the echo energy. A plot of the echo energy versus "filter overhead" $(B_r - B_{msk})$ is shown in Fig. 4 for $B_{dop} = 15$ kHz and various values of B_{msk}.

Nominally, the Doppler shift is perfectly pre-compensated and the echo spectrum is centered in the signal+noise filter. However, antenna position uncertainty and spacecraft attitude uncertainty lead to errors in Doppler tracking. The signal+noise filter bandwidth B_r must be sufficiently wide to accommodate the echo center frequency. The worst-case Doppler pre-compensation error is 10 kHz. Assuming the worst-case error, a plot of the resulting error in the energy detection versus the "filter overhead" is shown in Fig. 5. To minimize Doppler-precompensation induced errors in the measurement of echo return energy, we require the error to be < 0.15 dB.

Applying these criteria to Figs. 4 and 5, we see that they are satisfied for a filter overhead of between 30 kHz and 50 kHz, depending on B_{msk}. Thus, in our trade-off analyses to find the optimum B_{msk} we have used $B_r = B_{msk} + 40$ kHz.

B. Transmit Signal Modulation Tradeoffs

To select B_{msk}, the parameters A, B, and C are computed numerically as a function of antenna scan angle. To optimize K_p over the range of wind speeds, the swath location dependent SNRs corresponding to low wind speeds (3 m/s), moderate winds (8 m/s), and high winds (20 m/s) are used.

In Fig. 6 K_p vs. azimuth angle for a range of B_{msk} is plotted for each beam at three representative wind speeds. Only the azimuth range between 0 and 90 degrees is shown since the performance is symmetry around the scan. Transmit modulation significantly reduces K_p for most of the swath, but offers little improvement for scan angles pointed forward or aft of the spacecraft — near 0 and 180 degrees. At the high wind speeds where S is small (high SNR), the "A" term in Eq. (1) dominates, and a larger B_{msk} leads to lower K_p. Thus, in a high SNR environment, measurement accuracy can be improved by modulating the signal and consequently increasing the effective number of independent samples. At lower wind speeds (which have lower SNRs), however, K_p can actually increase for larger B_{msk}. This is particularly evident for the inner beam. This occurs because the benefit derived from modulating the signal is overcome by the deleterious effect of increasing B_r and passing more thermal noise to the detector.

An evaluation of the curves in Fig. 6 led to the selection of $B_{msk} = 40$ kHz and $B_r = 80$ kHz for SeaWinds. This significantly improves K_p performance over most of the swath and for most wind conditions. Lower values of B_{msk} produced inferior performance at high and moderate wind speeds, in general failing to meet the performance goal of $K_p < 0.17$. Higher values of B_{msk} were judged to produce undesirably large K_p at low speeds. Due to the greater scientific importance of high wind measurements, a degree of performance degradation at low wind speeds, such as that experienced with $B_{msk} = 40$ kHz for the inner beam at 3 m/s, was deemed acceptable. Unfortunately, for the values of S achievable with the SeaWinds design parameters, the goal of $K_p < 0.17$ is not possible at the very lowest wind speeds for any modulation bandwidth. Nevertheless, despite being "K_p limited" rather than "model function limited" in the less critical low wind speed regime, SeaWinds performance simulations indicate that the desired measurement accuracies will still be met [2].

IV. SUMMARY

Because SeaWinds employs a compact dish antenna rather than multiple fan-beam antennas, the instrument is more easily accommodated on spacecraft than previously flown scatterometers. Tradeoffs to select the transmit modulation scheme and filter bandwidths have been described. Modulating the transmit signal results in im-

proved K_p which will result in improved wind measurement accuracy.

REFERENCES

[1] R. Fisher, "Standard Deviation of Scatterometer Measurements From Space," *IEEE Trans. Geosci. Electron.*, Vol. GE-10, No. 2, April 1972.

[2] M.H. Freilich, D.G. Long, and M.W. Spencer, "Sea-Winds: A Scanning Scatterometer for ADEOS II – Science Overview," *Proceedings of the International Geoscience and Remote Sensing Symposium*, Pasadena, California, August 8-12, pp. 960-963, 1994.

[3] D.G. Long and M.W. Spencer, "Radar Backscatter Measurement Accuracy for a Spaceborne Pencil-Beam Wind Scatterometer with Transmit Modulation," submitted to the *IEEE Trans. Geoscience and Remote Sensing*, 1995.

[4] M.W. Spencer, C. Wu, and D.G. Long, "Tradeoffs in the Design of a Spaceborne Scanning Pencil-Beam Scatterometer: Application to SeaWinds," submitted to the *IEEE Trans. Geoscience and Remote Sensing*, 1995.
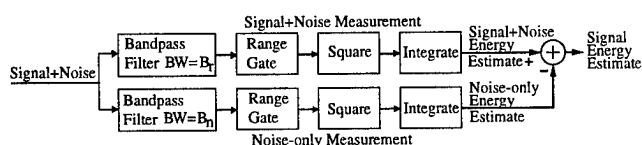
Figure 1. Measurement flow diagram.
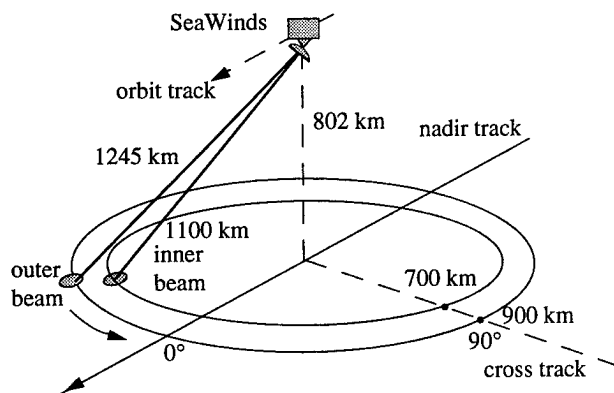
Figure 2. SeaWinds geometry.
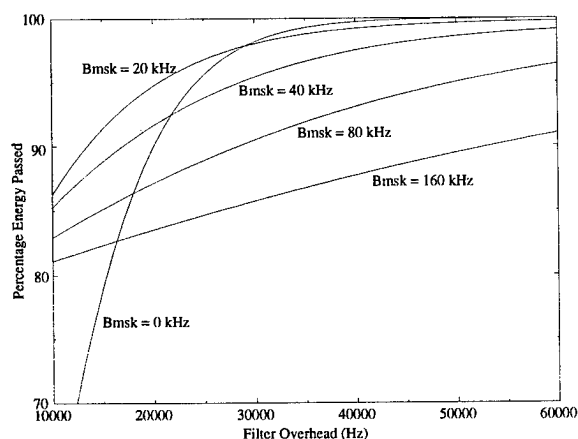
Figure 4. Doppler bandwidth induced energy detection error versus "filter overhead" $(B_r - B_{msk})$.
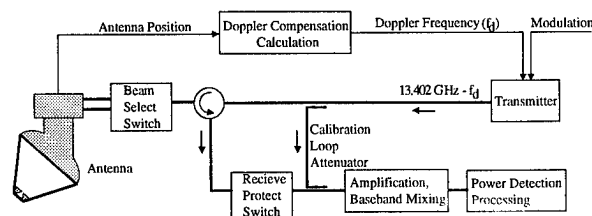
Figure 3. SeaWinds block diagram.
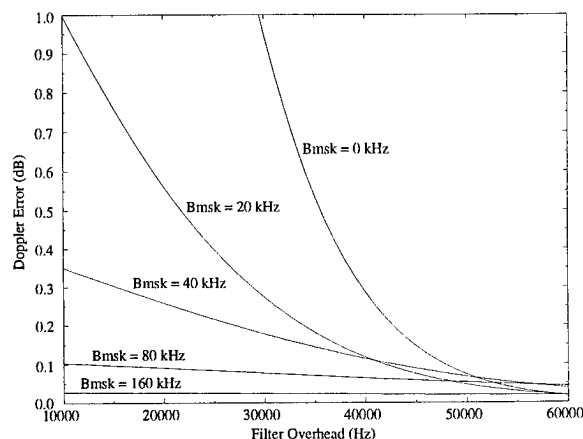
Figure 5. Energy measurement error due to Doppler compensation error versus "filter overhead" $(B_r - B_{msk})$.
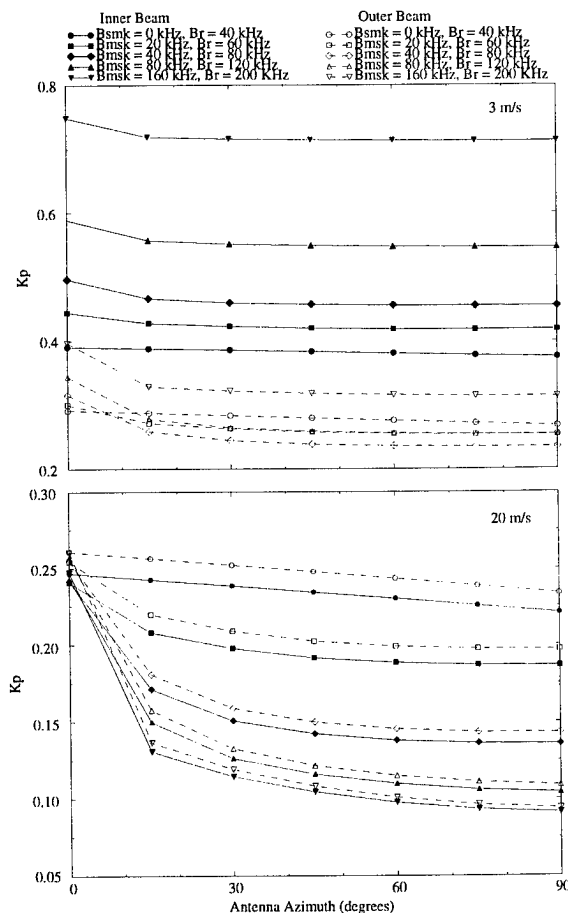
Figure 6. SeaWinds K_p versus scan angle for various B_{msk} and wind speeds.

Remote Sensing of the Near Surface-Ocean Wind Vector Under Low-wind Conditions Using Scatterometry

James Carswell and William Donnelly and Robert McIntosh
Microwave Remote Sensing Laboratory
Dept. of Electrical & Computer Engineering
University of Massachusetts
Amherst, MA 01003
T: 413.545.0779 / F: 413.545.4652 / carswell@dudley.ecs.umass.edu

Abstract— **The University of Massachusetts collected C- and Ku-band ocean backscatter measurements at 21.0°, 31.0°, 41.5° and 52.0° incidence, using a C-band and a Ku-band conical scanning airborne scatterometer. These high spatial resolution backscatter measurements differ significantly, for low-wind cases, from the predicted responses of the CMOD4 and SASS-II model functions. The nulls in the azimuthal backscatter response tend to decrease at a much faster rate than predicted as the winds decrease below 5 m·s⁻¹, the measured backscatter response does not follow a power-law relationship with wind speed nor with wind stress, and a cutoff wind speed, below which the backscatter drops to unmeasurable quantities, is present. These characteristics are predicted by the Donelan and Pierson model, and comparing the measured results with this model shows good agreement. However, when the spatial resolution of the measurements are degraded to an area equivalent to that of satellite-based measurements, the deep nulls and fast fall off rate are no longer present. Such effects may bias the backscatter measurements from satellite-based platforms towards the higher winds within the footprint, and thus overestimate the wind speed.**

I Introduction

Daily monitoring of the global ocean wind vector is essential for many oceanographic and air/sea interaction studies. The near ocean-surface wind vector generates the momentum flux, and thereby affects the ocean circulation and mixing, and plays a significant role in the exchange of moisture and heat between the ocean and atmosphere. Currently, this parameter can be monitored using a satellite-based scatterometer, which measures the electromagnetic backscatter from the ocean surface. At microwave frequencies, the backscatter has been found to be correlated with the ocean wind vector, and empirical models (CMOD4 [1] and SASS-II [2]) have been developed that relate these two parameters.

This technique of estimating the winds, known as scatterometry, works well for moderate winds. However, under low-wind conditions, scatterometer measurements in wave tanks and from platforms and aircraft have disagreed with each other and with the predicted responses of CMOD4 and SASS-II [3][4]. Being able to measure low winds is important since much of the tropical regions of the oceans are dominated by low-wind conditions.

This paper will present low-wind backscatter measurements obtained with two airborne scatterometers, CSCAT and KUSCAT. Section II will describe these instruments and the experiments where low-wind speed data were collected. Section III will present the measurements and their departure from the predicted responses of CMOD4 and SASS-II. Section IV will demonstrate that a power law cannot be used to describe the backscatter response to wind speed or frictional velocity, will compare the measurements to Donelan and Pierson's model to explain the sharp rolloff in the crosswind backscatter measurements and will discuss why these measurements differ from the satellite-based empirical models.

II Instruments and Experiments

The University of Massachusetts Microwave Remote Sensing Laboratory designed and fabricated two airborne pencil-beam scatterometers, CSCAT and KUSCAT. These instruments are vertically polarized pencil beam scatterometers at C-band and Ku-band respectively. Both instruments utilize microstrip-phased arrays to frequency scan their pencil beam from 21° to 52° incidence. These antennas are frequency scaled version of each other, and therefore their patterns are almost identical.

During operation, CSCAT mechanically rotates its antenna in azimuth at 30 rpm, while its pointing angle is fixed at one of four incidence angles: 21°, 31°, 41.5° or 52°. Figure 1 illustrates this measurement technique. KUSCAT operates in a similar fashion except its antenna is rotated at 90 rpm, and its incidence angle is rapidly switched between the four incidence angles at a pulse repetition frequency that results in the maximum number of independent data samples, at all four angles simultaneously, as the aircraft is following its flight line. Thus, the full azimuthal σ° response is measured at all four incidence angles with each conical scan.

These instruments collected low-wind backscatter measurements during two experiments: the Tropical Ocean Global Atmosphere Coupled Ocean-Atmosphere Response Experiment (TOGA COARE), in which CSCAT was flown on the NOAA N42RF P3, and the Ladir Inspace Technology Experiment (LITE), in which KUSCAT was flown on the NASA Wallops P3. In both experiments, the winds ranged from less than 2 m·s⁻¹ to almost 15 m·s⁻¹. During TOGA COARE several buoys were
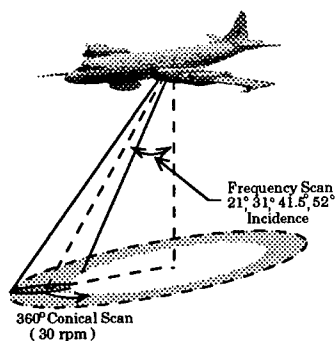
Fig. 1. Conical scan measurement techique.

Fig. 2. Plots five consecutive $\bar{\sigma}^{\circ}$ scans measured with CSCAT and KUSCAT during moderate-wind conditions. The CMOD4 and SASS-II model functions have been overlaid. The wind speed and direction inputs are 7.3 m·s^{-1} and 270° for CMOD4 and 7.3 m·s^{-1} and 330° for SASS-II.

deployed over the warm pool region providing measurements of the surface conditions. In LITE, insitu measurements were not available, but other remote sensing instrumentation, such as the Radar Ocean Wave Spectrometer (ROWS), were installed on the Wallops P3 and provided estimates of the near ocean-surface wind speed.

III Backscatter Measurements

C- and Ku-band ocean backscatter measurements at 31° incidence are presented in this section for moderate- and low-wind speed conditions. The 31° data is representative of data collected at the other angles, and therefore only the 31° data will be shown. Unless otherwise specified, the data is processed in the following manner:

1.) the data from each conical scan are subdivided into seventy-two 5° azimuthal bins,

2.) consecutive conical scans are combined until each azimuthal bin has a minimum of 50 independents samples and

3.) the samples in each azimuthal bin are averaged together on a linear scale.

These averaged results will be referred to as $\bar{\sigma}^{\circ}$ scans. For CSCAT the $\bar{\sigma}^{\circ}$ scans typically are an average of four consecutive-conical scans, and for KUSCAT, six consecutive-conical scans. The difference in the number of consecutive scans averaged is due to different sampling rates and azimuthal scanning speeds between the two instruments.

Figures 2 plots the $\bar{\sigma}^{\circ}$ scans measured by CSCAT and KUSCAT under moderate-wind conditions. The CMOD4 and SASS-II model functions are overlaid; the input wind speed for CMOD4 model is from colocated buoy wind measurements and for SASS-II is from ROWS wind speeds estimates. As can be seen, the models predict the same response as measured by CSCAT and KUSCAT. However for low-wind conditions, the models predict a much different response. Figures 3a and b plot $\bar{\sigma}^{\circ}$ scans observed during low winds. The measured azimuthal modulation differs significantly from that predicted by
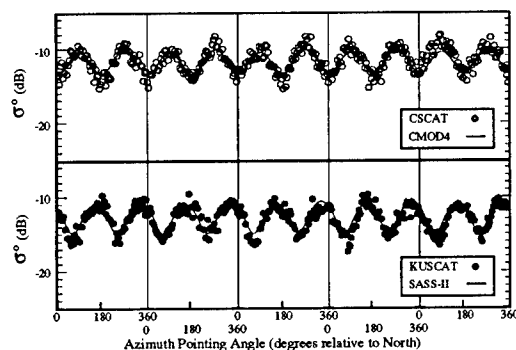
CMOD4 and SASS-II. To demonstrate, the models are fitted to the measurements such that they agree in the upwind direction. The measured crosswind values are more than 10 dB lower than the predicted values of the models, and the measured azimuthal modulation cannot be solely described by a 3-term Fourier cosine series.

IV Discussion

Empirical models, such as CMOD4 and SASS-II, that describe the backscatter response to the ocean surface winds, typically use a power law relationship of the form: $\sigma^{\circ} = \beta \cdot (U)^{\gamma}$, where σ° is expressed in terms of m^2/m^2, U is the neutral stability wind speed at some reference height, and γ is the wind-speed exponent. The backscatter measurements collected with CSCAT and KUSCAT under low-wind conditions, however, do not support a power-law relationship. To demonstrate this, Figures 4 a and b plot the measured crosswind σ° (σ_{cs}°) versus the upwind σ° (σ_{up}°) in dB. If a power law exists, there should be the linear relationship as described below:

$$\sigma_{cs}^{\circ} = \left(\frac{\gamma_{cs}}{\gamma_{up}}\right) \cdot \sigma_{up}^{\circ} + \left[log_{10}\left(\beta_{cs}\right) - \left(\frac{\gamma_{cs}}{\gamma_{up}}\right) \cdot log_{10}\left(\beta_{up}\right)\right],$$

where γ_{up} and γ_{cs} are the upwind and crosswind wind-speed exponents. The data clearly shows that a linear relationship does not hold. Therefore a power-law relationship cannot be used over all winds to describe the backscatter-wind dependence. Additionally, since the above analysis is independent of U, a power law describing the backscatter dependence on any other parameter (ie. frictional velocity) also should not be used for low-wind cases (or low backscatter values).

The departure from a power law seems to be due to the rapid decrease of the backscatter values, especially in the crosswind direction, with decreasing wind speed as
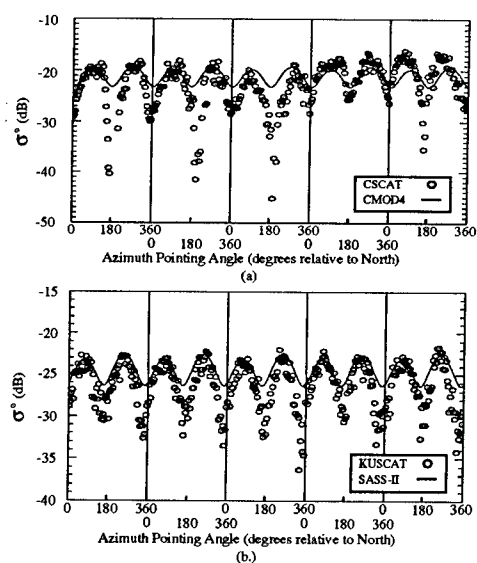
Fig. 3. a and b plot five consecutive $\bar{\sigma}^{\circ}$ scans measured with CSCAT and KUSCAT during low-wind conditions. The CMOD4 and SASS-II model functions have been overlaid and their wind speed and direction inputs to these models were chosen such that they agreed with the upwind direction measurements.

the wind drops below approximately 5 m·s^{-1}. Donelan and Pierson developed a model (DP87) [5] that offers an explanation for this rapid decrease in backscatter and is overlaid on Figures 4 a and b. The model explains that the rapid decrease in the backscatter power is due to viscous dampening. As the wind speed decreases, the dampening forces due to viscosity overcome the wave generating forces of the wind, and as a result, the capillary-gravity waves are suppressed. Therefore, the backscatter due to Bragg scattering from these waves drops off to unmeasurable quantities. The measurements tend to support this model. A polynomial fit to the data shows the same characteristics as the DP87 model. The differences between the fit and the DP87 model can be explained by spatial averaging. At the low winds, the increased temporal and spatial variability of the wind direction smooths out the deep nulls that are shown in Figure 3. If the spatial averaging of the measurements is increased to 25 km, the data in Figure 4 approaches the predicted response of CMOD4 and SASS-II. The effects of spatial averaging are more apparent in the KUSCAT data than the CSCAT data. This is due to the fact that KUSCAT's footprint was almost an order of magnitude larger than CSCAT's since it flew at a much higher altitude, and therefore its backscatter measurements have been smoothed more than CSCAT's.

Although the drop outs noticed in the CSCAT and KUS-CAT data will not be apparent in satellite-based backscatter measurements whose resolution is on the order of 25 km x 25 km or larger, the wind estimates derived from
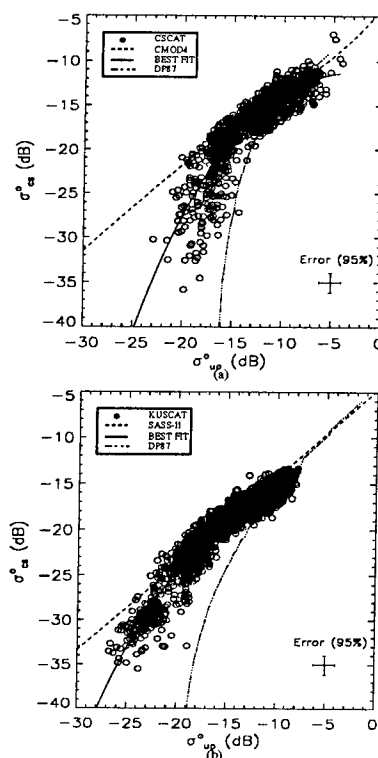
Fig. 4. a and b plot σ^{0}_{cs} versus σ^{0}_{up} measurements from CSCAT and KUSCAT. The predicted response from CMOD4, SASS-II and DP87 models are overlaid. The best fit curves are polynomial fits to the data.

these measurements may be high since the average backscatter values will be biased towards the higher winds in the footprint. To fully understand this problem, high temporal and spatial resolution backscatter measurements under low-wind conditions need to be studied and the effects of spatial averaging better understood.

REFERENCES

[1] European Space Agency, "Cmod4 model description", Electrosciences Report ER-TN-ESA-GP-1120, European Space Agency, 1993.

[2] F. J. Wentz, S. Peteherych, and L. A. Thomas, "A model function for ocean radar cross section at 14.6 ghz", Journal of Geophysical Research, vol. 89, no. C3, pp. 3689, 1984.

[3] M.R. Keller, W. C. Keller, and W. J. Plant, "A wave tank study of the dependence of x band cross sections on wind speed and water temperature", Journal of Geophysical Research, vol. 97, no. C4, pp. 5771–5792, 1992.

[4] J. R. Carswell, R. E. McIntosh, S. C. Carson, F. K. Li, G. Neumann, D. J. McLaughlin, J. C. Wilkerson, and P. G. Black, "Airborne scatterometers: Investigating ocean backscatter under low- and high-wind conditions", Proceedings of the IEEE, vol. 82, no. 12, pp. 1835–1860, 1994.

[5] M. A. Donelan and W. J. Pierson, "Radar scattering and equilibrium ranges in wind-generated waves with application to scatterometry", Journal of Geophysical Research, vol. 92, no. C5, pp. 4971–5029, 1987.

K_u-Band Ocean Backscatter Functions
for Surface Wind Retrieval

S. V. Nghiem, F. K. Li, and G. Neumann

Jet Propulsion Laboratory, MS 300-235
California Institute of Technology
4800 Oak Grove Drive, Pasadena, CA 91109, USA
Tel: 818-354-2982, Fax: 818-393-5285
E-mail: nghiem@malibu.jpl.nasa.gov

Abstract – The accuracy of wind measurements with scatterometer techniques depends on the particular geophysical model function used in the retrieval algorithm. Discrepancies among existing model functions, developed based on a mixture of aircraft and satellite backscatter data acquired two decades ago, will result in differences in retrieved wind fields. The Jet Propulsion Laboratory airborne K_u-band NUSCAT scatterometer was used to obtain an extensive data set over a wide range of wind conditions to provide a more accurate study of ocean radar backscatter signatures. Backscatter was measured during the Surface Wave Dynamics Experiment in an oceanic area off the US East coast. Backscatter data were obtained for both horizontal and vertical polarizations, incidence angles from $10°$ to $60°$, and wind speeds up to $15 \text{ m} \cdot \text{s}^{-1}$. The measured results are compared with calculated values to assess the existing geophysical model functions for applications to ocean surface wind retrieval.

INTRODUCTION

K_u-band scatterometer technology has been demonstrated and will be used to monitor global ocean wind fields from spaceborne sensors such as the NASA Scatterometer (NSCAT) [1]. Algorithms for retrieval of wind speeds and directions from scatterometer data utilize absolute radar returns as well as relative azimuth modulations of backscatter. The accuracy of the wind retrieval depends on the particular geophysical model function used in the algorithm.

Among the existing geophysical model functions are RADSCAT [2], SASS-I [3], and SASS-II [4, 5] developed based on aircraft and satellite backscatter data acquired in the 1970s. With advances in both scatterometer and buoy technologies, an extensive scatterometer data set over a wide range of wind conditions will allow a better assessment of the ocean radar backscatter for the ocean surface wind retrieval.

In this paper, K_u-band backscatter functions of neutral wind are studied based on the NUSCAT-SWADE data base. NUSCAT is an airborne K_u-band scatterometer developed by the Jet Propulsion Laboratory. NUSCAT

was used to measure ocean backscatter during the Surface Wave Dynamics Experiment (SWADE). Ten flights resulted in 30 hours of data collection were conducted on the NASA Ames C130 aircraft during SWADE in February and March of 1991 off the coast of Maryland and Virginia over several ocean buoys. NUSCAT data together with buoy wind speeds and directions are used in this analysis.

AZIMUTH MODULATIONS

A second harmonic function has been adopted to describe ocean aziumth modulations in radar backscatter σ^0 [2, 3, 4, 6]. This function is determined by three different coefficients A_0, A_1, and A_2 as follows

$$\begin{aligned}
\sigma^0(U, \chi, \theta, P) \;=\; & A_0(U, \theta, P) \\
+ \; & A_1(U, \theta, P)\cos(\chi) \\
+ \; & A_2(U, \theta, P)\cos(2\chi)
\end{aligned}$$

where A_0 is the mean backscatter, A_1 is for the upwind and downwind asymmetry, and A_2 is for the difference in backscatter extrema. Each of these coefficients depends on wind speed U, incidence angle θ, and polarization P (HH or VV). Angle χ is the azimuth defined with respect to upwind where $\chi = 0$. In the geophysical model functions, wind speed U is the neutral wind speed $U_N(19.5 \text{ m})$ at the height of 19.5 m above sea surface level [2, 3, 4, 5].

During the NUSCAT flights on the C130, a difference between operational and desired pitch angles of the aircraft caused a tilt of the antenna axis with respect to the nominal incident angle. As a result, the incidence angle was modulated as the antenna scanned through the $360°$ azimuth. Extraneous harmonics were thereby created in the measured signals by the beating between the incidence angle modulations and the physical ocean backscatter modulations. To account for this effect, a harmonic analysis method independent of a priori geophysical model functions is developed, tested, and implemented. This method also finds the upwind backscatter maximum without relying on buoy data for wind direction measurements. In this method, there are two problems need to be considered. First, there exist different solutions for wind directions at azimuth angles with 180° apart. This causes a confusion between upwind and downwind directions. To resolve this problem, we use buoy data for wind directions which need to be known only to within $\pm90°$ for this purpose. The second problem occurs when the wind

direction is parallel to the azimuth direction where the incidence modulation is an extremum. In this situation, the information carried in the backscatter data alone is not adequate to separate the contributions by the ocean modulations and by the incidence modulations to the total first harmonic term. In these cases, significant errors are incurred when the variations in the incidence angle are very close to the sinusoidal form. To avoid the errors, we exclude cases where retrieved wind angles are close to the extremum azimuth angles of the incidence modulation.

OCEAN BACKSCATTER

We apply the above method to the NUSCAT backscatter data to determine azimuth modulations in ocean backscatter over the wind conditions encountered during SWADE. For the results below, we exclude cases with large swells and sea surface temperature differences across the Gulf Stream boundary to avoid complicated air and sea conditions. Buoy measurements at the closest time and location to NUSCAT are selected to correlate with the backscatter data. We will present the results in terms of upwind, downwind, and crosswind backscattering coefficients (σ_u^0, σ_d^0, and σ_c^0, respectively), which determine the coefficients A_0, A_1, and A_2 in the backscatter harmonic function with the following relations

$$A_0 = \frac{1}{4}(\sigma_u^0 + \sigma_d^0 + 2\sigma_c^0)$$

$$A_1 = \frac{1}{2}(\sigma_u^0 - \sigma_d^0)$$

$$A_2 = \frac{1}{4}(\sigma_u^0 + \sigma_d^0 - 2\sigma_c^0)$$

To check the data processing, we examine the result of a case obtained during Flight 1 on 27 February 1991 over buoy 44015 (Discus E), where NUSCAT was less than 10 km from the buoy and within 2.4 minutes from buoy wind measurements and 13.6 minutes from buoy wave data acquisitions. The wind direction obtained by NUSCAT was at 289°, which was very close to the wind direction at 294° measured by Discus E. In this case, the wind direction was almost parallel to the principal wave direction of 292° at the spectral peak. The corresponding directional wave spectrum measured by the buoy showed that most of the wave components propagated in the same direction of the wind. The wind speed from buoy was 9.8 m·s^{-1} at 4-m height corresponding to a neutral wind of 11.7 m·s^{-1} at 19.5 m. Backscatter for this case compares well with SASS-II values.

Fig. 1 presents upwind backscatter at incidence angles from 0° to 60° for the horizontal polarization. The range of wind speeds is from 4 m·s^{-1} to 15 m·s^{-1}. NUSCAT-SWADE results represented by symbols for different incidence angles are compared with RADSCAT results (continuous curves) and calculated valued from SASS-I (dashed curves) and SASS-II (dashed-dotted curves). Discrepancies among RADSCAT, SASS-I, and SASS-II are seen in Fig. 1. Empirical functions obtained from NUSCAT data are also plotted with the dotted curves. In

general, NUSCAT HH data are higher than RADSCAT results. RADSCAT values are the lowest compared to SASS-I and II. Overall, NUSCAT HH backscatter compares best with the SASS-II results as seen in Figure 1. At 10° incidence angle, NUSCAT backscatter is closest to SASS-I; however, the results are insensitive to the wind speed and are quite comparable to each other. NUSCAT, SASS-I, and SASS-II are in good agreement while RADSCAT is low for incidence angles at 20° and 30°. For 40°, NUSCAT fits well with SASS-II at wind speeds higher than 10 m·s^{-1}, where many NUSCAT data are located, while RADSCAT and SASS-I are low. For backscatter cross sections at 50°, NUSCAT, RADSCAT, and SASS-II are in good agreement while SASS-I is low. At 60°, NUSCAT compares well with SASS-II for wind larger than 10 m·s^{-1} while RADSCAT is significantly lower. Backscatter results for downwind and crosswind directions are plotted in Figs. 2 and 3, where similar results are observed. Note that at 50°, NUSCAT agrees with SASS-II, which is higher than both SASS-I and RADSCAT. The analysis presented in this paper is also applied to ocean backscatter with the vertical polarization.

Upwind, H Polarization
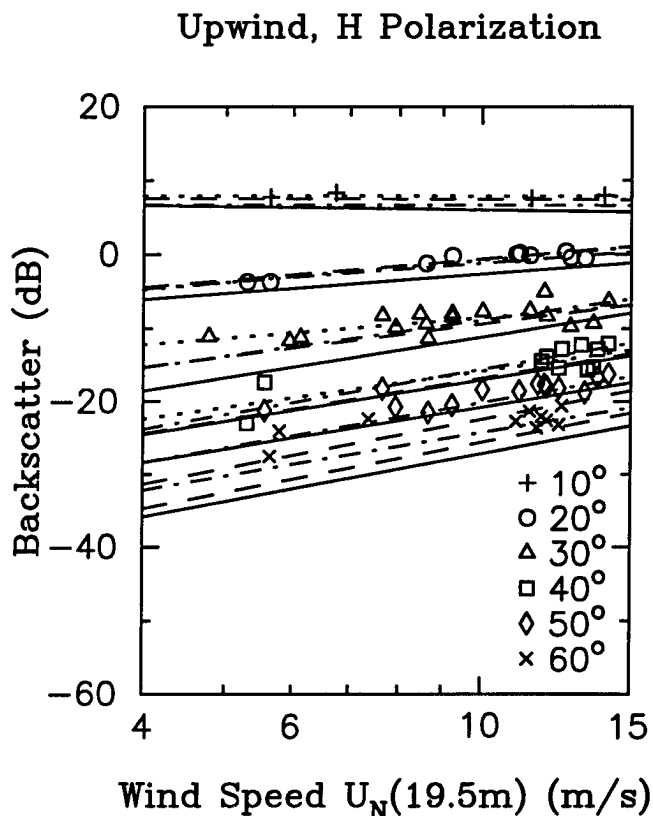
Figure 1. Upwind horizontal backscatter functions of neutral wind speed at 19.5 m. Symbols are for NUSCAT backscatter data, dotted curves for NUSCAT fits, continuous curves for RADSCAT, dashed curves for SASS-I, and dashed-dotted curves for SASS-II.

Downwind, H Polarization
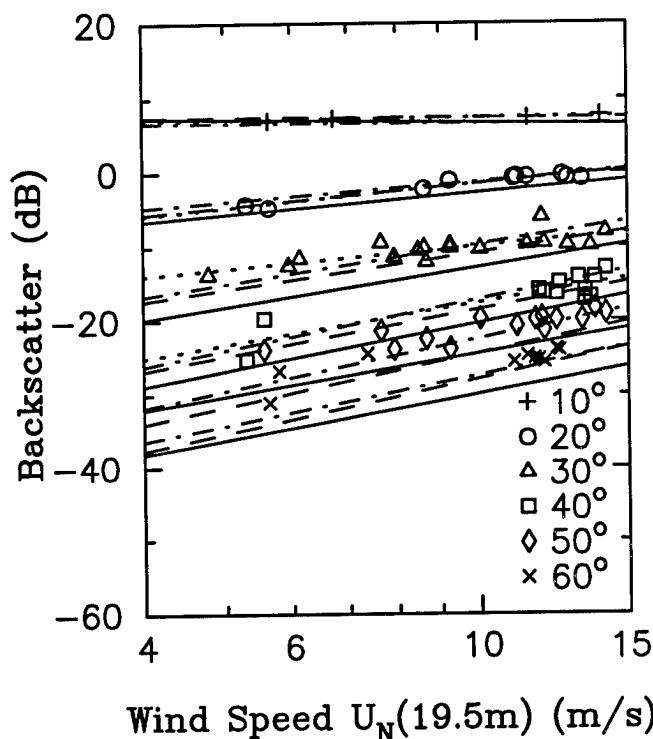
Figure 2. Downwind horizontal backscatter functions of neutral wind speed at 19.5 m. Symbols are for NUSCAT backscatter data, dotted curves for NUSCAT fits, continuous curves for RADSCAT, dashed curves for SASS-I, and dashed-dotted curves for SASS-II.

Crosswind, H Polarization

Figure 3. Crosswind horizontal backscatter functions of neutral wind speed at 19.5 m. Symbols are for NUSCAT backscatter data, dotted curves for NUSCAT fits, continuous curves for RADSCAT, dashed curves for SASS-I, and dashed-dotted curves for SASS-II.

SUMMARY

Ocean backscatter at K_u band was successfully measured by the Jet Propulsion Laboratory NUSCAT scatterometer during SWADE over a wide range of wind speeds. NUSCAT results for ocean backscatter in terms of upwind, downwind, and crosswind radar returns are compared to airborne RADSCAT results and to SASS-I and II geophysical model functions versus neutral wind speed. NUSCAT backscatter is closest overall to SASS-II values, fit best with SASS-I at 10° incidence angle, and are significantly higher than RADSCAT. Empirical relations between backscatter and neutral wind speed are derived for 10° to 40° incidence angles. An error analysis of the derived relations show an overall deviation factor in the order of 1 dB for ocean signatures including uncertainties in surface conditions.

REFERENCES

[1] F. M. Naderi, M. H. Freilich, and D. G. Long, "Spaceborne radar measurement of wind velocity over the ocean – an overview of the NSCAT scatterometer system," *Proceedings of the IEEE*, vol. 79, no. 6, pp. 850-866, 1991.

[2] L. C. Schroeder, P. R. Schaffner, J. L. Mitchell, and W. L. Jones, "AAFE RADSCAT 13.9-GHz measurements and analysis: Wind-speed signature of the ocean," *IEEE J. Oceanic Engineering*, vol. OE-10, no. 4, pp. 346-357, 1985.

[3] L. C. Schroeder, D. H. Boggs, G. Dome, I. M. Halberstam, W. L. Jones, W. J. Pierson, and F. J. Wentz, "The relationship between wind vector and normalized radar cross section used to derive SEASAT-A satellite scatterometer winds," *J. Geophys. Res.*, , vol. 87, no. C5, pp. 3318-3336, 1982.

[4] F. J. Wentz, S. Peteherych, and L. A. Thomas, "A model function for ocean radar cross sections at 14.6 GHz," *J. Geophys. Res.*, vol. 89, no. C3, pp. 3689-3704, 1984.

[5] F. J. Wentz, L. A. Mattox, and S. Peteherych, "New algorithms for microwave measurements of ocean winds: Applications to SEASAT and the Special Sensor Microwave Imager," *J. Geophys. Res.*, vol. 91, no. C2, pp. 2289-2307, 1986.

[6] F. K. Li, G. Neumann, S. Shaffer, and S. L. Durden, "Studies of the location of azimuth modulation minimum for Ku band ocean radar backscatter," *J. Geophys. Res.*, vol. 93, no. C7, pp 8229-8238, 1988.

Scatterometer Measurements of Ocean Surface Stress Magnitude and Direction from Aircraft during SWADE and from ERS-1

David E. Weissman
Department of Engineering
Hofstra University
Hempstead, New York 11550
(516) 463-5564; FAX: (516) 463-4939; E-Mail: eggdew@vaxc.hofstra.edu

Abstract: New results have been obtained from both the K_u-band Scatterometer and from the in-situ, large area estimates of surface wind stress and direction during the SWADE 1991 experiment. These results address the accuracy of the K_u-band model function for estimating the magnitude of the friction velocity, and the ability of the azimuthal scatterometer data to estimate the wind direction. They demonstrate an excellent accuracy for estimating friction velocity magnitude. But they show the potential for frequent errors in estimating wind direction because of small upwind/downwind differences in the radar cross section at the lower incidence angles; however accuracy improves at the higher incidence angles. These results provide useful information in the development of NSCAT/ADEOS algorithms.

INTRODUCTION

Scatterometer model functions which directly estimate friction velocity, have been developed and are being tested with radar and in-situ data acquired during the Surface Wave Dynamics Experiment of 1991. Both K_u-band and C-band scatterometers were operated simultaneously for extensive intervals for each of 10 days during SWADE. The model function developed previously from the FASINEX experiment converts the K_u-band RCS measurements into friction velocity estimates [1]. Each azimuth scan can be analyzed to determine the upwind direction at the angular position of the maximum of the radar cross section. These are compared to in-situ, estimates of surface wind stress and direction across a wide area both on and off the Gulf Stream (for hourly intervals), which were determined from buoy and meteorological measurements during February and March, 1991. The K_u-band estimates of u_* magnitude are in excellent agreement with the in-situ values [2]. The C-Band scatterometer measurements were concident with the K_u-band RCS, whose u_* estimates are then used to calibrate the C-band. The results show the C-band RCS dependence at 20,30, 40 and 50 degrees to be less sensitive to friction velocity than the corresponding cases for K_u-band. The goal is to develop the capability of making friction velocity estimates (and surface stress) from radar cross section data acquired by satellite scatterometers.

IN-SITU MEASUREMENTS

In this study the results from the wave simulation forced by the wind field of Oceanweather, Inc. (OWI) was used. This wind field was derived by intensive manual kinematic reanalysis using all conventional and special SWADE meteorological data. Details of the wind field reanalysis procedures and methodologies is described in Cardone et al. (1995). The intent of the OWI analysis is to resolve the "synoptic scale" wind field at three-hourly intervals on a grid of spacing 0.5 deg in latitude and longitude covering the western North Atlantic or SWADE REGIONAL domain. The accuracy of the wind field was determined by comparing the measured winds in the SWADE array off the middle-Atlantic East Coast with the model winds at the four closest grid points surrounding the buoy location. The surface stress is calculated as a function of both wind speed at 10 meters and the stage of wave development (i.e., a sea-state dependent drag coefficient).

K_U-BAND MODEL FUNCTION STUDIES

These radar cross section measurements were converted into friction velocity estimates using this FASINEX model, at specific locations and times. These u_* estimates will then be compared with the approximately coincident (spatially and temporally) friction velocity estimates developed by Oceanweather, Inc. and University of Miami [4].

The Oceanweather/U.Miami friction velocity estimates were developed into a 0.25° latitude and longitude grid that span the same regions of the ocean over which the aircraft scatterometer operated (100 km x 100 km). The friction velocity maps are among the several variables (significant wave height and dominant frequency, neutral stability wind, drag coefficient and stress direction) that were estimated at hourly intervals as part of the SWADE analysis [5].

Because of the extensive time differences among the radar estimates, a more meaningful comparison was to match acquistion times of the radar data with one of the times at which the Oceanweather/U.Miami u_* maps were created. Each aircraft estimate of u_* represented a 15 km flight path, and it was compared with the closest u_* value (within 0.1° latitude and longitude, and within a one-half hour interval) from this in-situ model. The closer these values agree, the stronger the support for the validity of the FASINEX algorithm. Data from 8 days within this period was combined into a plot of scatterometer-derived u* versus the Oceanweather/ U.Miami derived u_*.

The comparison between the 2 different u_* estimates can be seen in Fig. 1 for 8 days of data. The agreement is very

good. The vertical errorbars represent +/-15%. A probable cause of the error may be a limitation in this model to produce a reliable estimate of the drag coefficient and friction velocity when the sea spectrum of a strong mixture of both wind driven seas and incoming swell, whose propagating directions are at large oblique angles. This condition existed on February 28 and March 6. When the data for these 2 days is omitted from the comparison, the relative agreement was greatly improved. Another possible source of error may be the result of the rapid spatial variablity of u* and steep drops in magnitude, and the limited ability of the meteorological model to precisely position and resolve the rapid variations in these relatively small regions.

Wind direction estimates also were compared. The azimuth scan measurement of the radar cross section by the scatterometer is acquired over a span of about 15 km across a flight track. Past experience with scatterometer studies indicate the azimuthal maximum is usually observed looking upwind. Using this indicator on each scatterometer circular scan to estimate the wind direction, is was compared with the wind direction estimates by the Oceanweather/Univ. Miami group. This comparison can be seen in Figure 2 for 7 days of data for all incidence angles: 20°,30°,40° and 50°. Numerous error can be seen, mostly those due to a 180° ambiguity caused by an inversion of the RCS maximum, causing it to occur when looking downwind instead of upwind. This is more prevalent in Fig. 2(a) for the 20 and 30 degree incidence angle results. Fig. 2(b) shows the same comparion as Fig. 2(a) except this data set is separated into only the 40° and 50° results. Clearly, the 40° and 50° incidence angles have the fewest errors because at these incidence angles, the RCS maximum occurs looking upwind in the large majority of situations. This has important implications for the NSCAT model function.

C-BAND MODEL FUNCTION STUDIES

Development from SWADE Data

This model has the same general structure (a 3 term Fourier series) as the K_u-band function. C-Band RCS data is available at incidence angles from 20° to 50° in 10° steps, and it has been processed to calculate the 3 Fourier coefficients (A0,A1,A2). Each of these coefficients was plotted versus u*, obtained from the simultaneous K_u-band data and FASINEX algorithm.[6] They were then fit to power-law functions, using regression analysis. Only the A0 function was needed with the ERS-1 RCS data to infer the u* magnitude because of the 2 orthogonal azimuth look directions. .

NORCSEX '91: ERS-1 and In-situ Data

The objective of utilizing the NORCSEX '91 (Norwegian Continental Shelf Experiment) data is to continue the evaluation and application of this C-Band algorithm in coordination with the in-situ measurements. This shipboard data was acquired during most of November 1991 from a research vessel (Haakon Mosby) near western Norwegian coast (Haltenbanken) within the footprint of the newly

lanuched ERS-1 scatterometer [3]. The data available for this project spans 8 different days in Nov '91 and consists of spatially and temporally coincident sea surface stress (at the ship locations) and the ERS-1 RCS data. Comparisons with ERS-1 passes produced excellent agreement between the algorithm derived u* and the ship measurements [3].

SUMMARY

The next logical step in evaluating the FASINEX K_u-band model function has been performed. The friction velocity estimates derived from the NRCS measurements were compared with the best available spatial and temporally coincident data on a scale that had not previously possible. The surface conditions; winds, waves and momentum flux, provided by the OWI techniques are the best compromise data set that is available with which to compare the scatterometer results. They represent a major innovation in estimating conditions at the air-sea interface over a wide area. However future extension of these studies are clearly indicated, to continue the development of this technique. Some of the assumptions used in this analysis will be critically re-examined, to see if some of the discrepancies can be reduced.

REFERENCES

[1] D.E. Weissman, K. Davidson, R. Brown, C. Friehe, and F. Li, "The relationship between the microwave radar cross section and both wind speed and stress: model function studies using Frontal Air-S ea Interaction Experiment data" J. Geophys. Res, Vol 99, C5, May 15, 1994

[2] D.E. Weissman, "Scatterometer measurements of ocean surface stress from aircraft and from ERS-1", OCEANS '95 Conference Proceedings, San Diego, CA. (Oct. 9-12. 1995) ISBN No. 0-933957-14-9 (IEEE Service Center)

[3] K.L. Davidson, D.E. Weissman, E. vanHalsema and R. Onstott, "Coastal applications of scatterometer wind algorithms", OCEANS '95 Conference Proceedings, San Diego, CA. (Oct. 9-12. 1995) ISBN No. 0-933957-14-9

[4] V.J. Cardone, H. Graber, R. Jensen, S. Hasselmann, M. Caruso, "In search of the true surface wind field in SWADE IOP-1: ocean wave modeling perspective" (manuscript in review, May 1995)

[5] M.J. Caruso, H.C. Graber, R.E. Jensen and M.A. Donelan, "Observations and Modelling of Winds and Waves During the Surface Wave Dynamics Experiment" Report 2, Intensive Observation Period, IOP-3, US Army Corps of Engineers, Waterways Experiment Station, Technical Report CERC-93-6, March 1994

[6] D.E. Weissman,"Studies of a C-Band Model Function for Friction Velocity Using Coincident, Simultaneous K_u-Band Scatterometer Measurements", OCEANS '94 Conference Proceedings, 13-16 Sept. 1994, Brest, France

Comparison of u* from Scatterometer NRCS with in-situ estimates
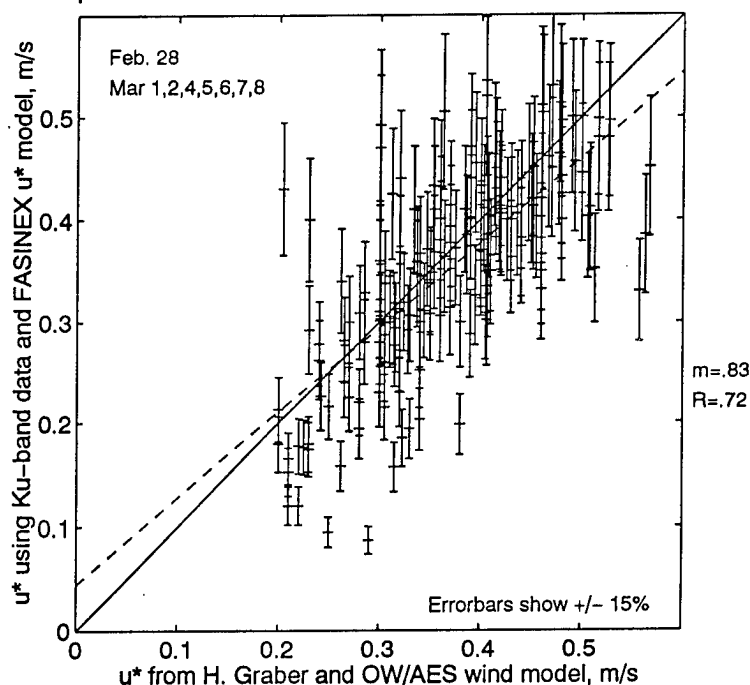
Figure 1. Eight Day comparison from temporally and spatially coincident u⋆ estimates between scatterometer estimates versus those from Oceanweather/Univ. Miami. Solid line represents equality; dashed line represents the regression line.
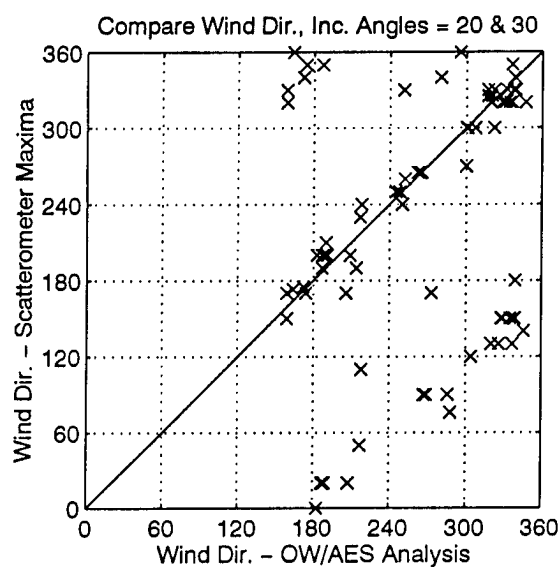
(a)
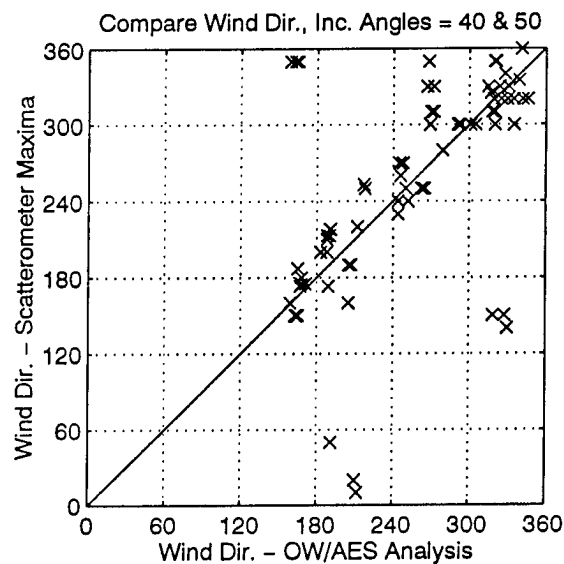
(b)

Figure 2: Separate incidence angle comparisons between scatterometer- derived wind direction and estimates from Oceanweather/Univ. Miami group. (both H & V-polarizations)

Statistics of Radar Backscatter from Wind Waves

David G. Long, Ryan Reed, David V. Arnold

Electrical and Computer Engineering Department, Brigham Young University
459 CB, Provo, UT 84602
(801) 378-4383 fax: (801) 378-6586 long@ee.byu.edu

Abstract - Measurements of wind wave scattering made by the Yscat ultra wide-band radar are used to study the statistics of the sea surface radar backscatter. As a comparison tool, a simple model based on composite Bragg scattering theory is developed and incorporated in a Monte Carlo simulation. The power and velocity distributions are computed from both empirical and simulated data. Comparison suggests that the composite scattering model accurately predicts the qualitative behavior of the radar return for incidence angles between 30° and 50° for both V and H polarization, but that other scattering mechanisms begin to influence the return at 20° and 60° incidence angles. While it has been postulated that additional scattering mechanisms (e.g., wave breaking and wedge scattering) may contribute to the total scattering, our results suggest that such scatterers do not significantly contribute to the total radar cross section for incidence angles between 30° and 50°.

I. INTRODUCTION

The Yscat scatterometer was deployed for six months in 1994 on the Canada Center for Inland Waters (CCIW) Research Tower at Lake Ontario and collected over 3500 hours of data at 2-18 GHz and a variety of wind speeds, relative azimuth angles, and incidence angles. This paper considers the distribution of the radar cross section and the velocity in terms of the composite model. Section II describes the Yscat94 experiment and comparison model. Section III considers the power distribution while Section IV considers the velocity distribution. A summary is provided in Section V.

II. EXPERIMENT AND MODEL

The goal of the Yscat94 experiment was to obtain measurements of the radar cross section under a wide variety of environmental conditions in Lake Ontario. The fetch varies from 1 to 300 km but averages about 6 km. The Yscat instrument is an ultra-wide band (2-18 GHz) Doppler radar. The antenna system provides a nearly constant 5° beam width over most of the operating bandwidth. Ten Hz measurements of the Doppler bandwidth, Doppler centroid, and echo power were made along with 30 s averages of wind speed and direction at 10 m, rain, temperature, and rms weight height [1].

A simple model is used to compare Yscat94 data with scattering theory. The small Yscat antenna footprint (1 m) is on the order of a few "coherence areas," the typical size over which the surface scatterers are correlated. In the composite model the water surface is composed of small independent "patches" whose individual cross sections are given by small perturbation theory. The patches are tilted by underlying long waves or swell which changes the cross section by changing the local incidence angle. The total cross section is the sum of the cross section of the individual patches illuminated by the antenna footprint. The distribution is thus dependent on the distribution of the wave slopes, which is, in turn, dependent on

the wave spectrum. In our simple model the reflection coefficients are given by small perturbation theory [4]. The Donelan wave spectrum [3], which was developed at the same site as Yscat94, is used.

The composite model requires a cutoff between long waves (those that tilt the surface) and very short (Bragg) waves. Since the Yscat footprint size is approximately 1 m, we have computed the slope as the first order fit to a stochastic realization of a 2/3 meter-sized water surface in the simulation. The distribution of slopes is then calculated by forming a random realization of the sea surface with amplitudes from the Donelan spectrum and uniformly-distributed phases, and allowing the various spectral components to propagate through the antenna footprint according to the wave dispersion equation.

The measured velocity of the Bragg waves is affected by wind drift and hydrodynamic modulation by the underlying waves. Each of the small patches in the composite model is tilted and advected by any underlying long waves or swell which changes its cross section by changing the apparent incidence angle and line-of-sight (LOS) velocity. Wedge scatterers and breaking waves are associated with longer wavelength waves and therefore have different phase velocities.

In the simulation the LOS velocity of a point is determined by integrating the LOS velocity over the range of wave frequencies thought to contribute to the velocity of the patch. The patch velocity found by integrating the point velocities over the entire patch. The intrinsic velocity of the Bragg scatterers (both upwind and downwind components) is then added to the LOS velocity of the patch along with the drift velocity. Note that the average centroid velocity measured by a scatterometer will be the weighted average of the upwind and downwind traveling waves plus the superimposed wind drift. While this velocity model is overly simplified, it is useful for comparison to Yscat94 data.

III. POWER DISTRIBUTION

Histograms of empirical and simulated measurements were computed using 0.5 dB bins centered on the mean return power. Each histogram consists of 600 measurements, corresponding to one minute of 1/10 s measurement. Once the individual histograms have been computed, all of the histograms which correspond to the same measurement parameters (e.g. wind speed, direction, frequency) are averaged together to estimate the average histogram. Since we are interested in the average shape of the distribution, the mean of each distribution is first normalized and the corresponding bins averaged together. The mean is then added back in. This was done to minimize the effects of slow changes in system gain or other parameters which aren't relevant to the shape of the distribution. A sample result is shown in Fig. 1.

As long as the range of incidence angles is small, the dependence of the radar cross section on incidence angles is approximately exponential and the resulting distribution is log-normal [2]. The Weibull distribution has also been suggested [7]. The normalized histograms are
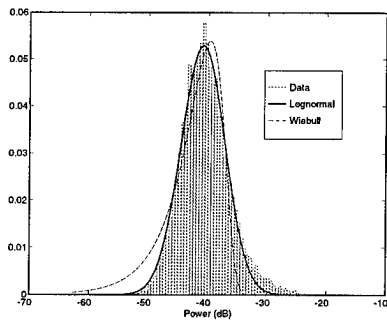
Figure 1. Sample histogram and fitted distributions.

fitted to log-normal and Weibull distributions by minimizing the L2 norm [6] as illustrated in Fig. 1. While the empirical distribution has more of an upper tail than the log-normal, a similar tail is visible in the simulation data and is thus predicted by the composite model. Since the log-normal describes the actual distributions well, the mean and variance of log-normal distribution serve as a compact and useful parameterization of the actual data distribution. In this paper we emphasize the log-variance results summarized in Fig. 2.

The log-variance decreases with increasing incidence angle. This agrees with the composite model which predicts smaller variance as the slope of the incidence angle dependence (m) decreases and the antenna footprint increases. Since the V-pol incidence angle dependence of σ^o is much less for moderate incidence angles [6] the V-pol log-variances should be less than the corresponding H-pol log-variances, a conclusion supported by the data. Note that the V-pol log variances are much less variable than the H-pol.

The log-variances do not appear to change strongly with wind speed. The simulation results have similar log-variance values and exhibit the same incidence angle dependence. However, the simulation results suggest that the log-variance should vary more with wind speed. When viewed in light of the composite model, it is clear that the fluctuations of the local incidence angle, which increase with wind speed, should increase the log-variance of the radar return as in the simulation. However, if the coherence area of the surface decreases with wind speed, the antenna footprint averages over more independent areas, decreasing the variance of the measurements. If the coherence length is decreased by a factor of two over the wind speed range (corresponding to an increase by a factor of four in the number of independent areas) the resulting wind speed dependence in the simulation is similar to that observed in the empirical data. While some empirical work has been done on the size of the coherence area the results were insufficient to determine the wind speed dependence [8]. Our results suggest that coherence area decreases with increasing wind speed.

Representative generalizations can be made by comparing simulation and empirical results. Qualitatively, the simulations compare quite well with the data for most cases. At moderate (30°-50°) incidence angles and wind speeds the distributions are quite log-normal. A distinct upper tail is visible (see Fig. 1) in both the simulation and the empirical data. It has been suggested that the upper tail is caused by additional scatterers such as wave breaking or sea-spikes. However, this cannot be the case in the simulated data since no attempt was made to include wave breaking in the model. There are smaller tails at mid-incidence angles (40° and 50°) suggesting that the source of the tails might be the "nonlinearity" of the slope dependence of σ^o, which is more severe at the extremes of the incidence angle range. Since the tails are visible in both the simulation and empirical data, care must be taken when interpreting the upper tail of the distribution as the result of non-Bragg scattering. At least a por-

tion of this upper tail can be explained by the composite model [6]. At 20° incidence angle, the simulation data shows evidence of quasi-specular scattering as a spike in the distribution suggesting that Bragg scattering alone can not adequately describe this case. The spike is not visible in the empirical data.

At 60° incidence angle a strong lower tail develops in the simulation data due to the steep roll off of the Bragg contribution to the model that occurs at about 70° [6]. However, this tail is absent in the empirical data, suggesting that some mechanism is adding to the incidence angle dependence as the Bragg contribution drops off. It has been noted by several researchers that the mean radar cross section does not drop off with incidence angle as predicted by Bragg scattering [9]. It has also been postulated that either wave breaking or wedge scattering becomes important at high incidence angles [9]. Since breaking waves occur relatively infrequently, the distribution of a combination of wave breaking and Bragg scattering might appear very much like that of Bragg scattering alone, with a few high power events in the upper tail raising the overall mean. On the other hand, the distribution of a wedge scattering plus Bragg scattering model could appear like the Bragg only distribution with the lower tail being truncated by the addition of the low cross section wedge scattering. The lack of a lower tail in the 60° incidence angle data supports this latter description of wedge plus Bragg scattering.

IV. VELOCITY DISTRIBUTIONS

The distribution of the radar return as a function of frequency gives a measure of the range of velocities under illumination by the radar. To compute the Doppler distributions the discrete power measurements are binned according to the velocity estimated for that measurement. Histograms of the Doppler measurements for a given radar parameter set are averaged together and normalized to produce distributions. While slightly skewed, the distributions are nearly normal.

The centroid of the Doppler spectrum is a measure of the effective LOS velocity of the surface as seen by the radar. The LOS velocity predicted by the model is easily determined via the simulation and sheds some light on the qualities of the composite model. At 20° and 30° incidence the model predicts the Doppler centroid velocities quite well for both V-pol and H-pol. Both the magnitude and the measured wind drift are in good agreement between the model and the empirical data. At 40° and 50° incidence the model significantly under-predicts the Doppler centroids at low wind speeds but the difference decreases with increasing wind speed. The wind drift predicted by the model is slightly high. At 60° incidence the model significantly under-predicts the Doppler centroids for all wind speeds by about 50%. This behavior is typical of all the frequencies under consideration.

This latter case points out a significant deficiency in the simple model used here. Several assumptions have been made which affect the centroid calculation. First, the assumption made that the upwind traveling Bragg waves are 1/2 the amplitude of the downwind traveling waves is only tenuously supported by empirical data. Changing the relationship between the upwind and downwind traveling waves has a significant effect on the predicted velocity of the Bragg waves. In addition, the hydrodynamic modulation of the small wave spectrum has been completely ignored in the simple model. Hydrodynamic modulation suggests that an underlying wave "stresses" the small Bragg waves as it passes. The result is a modulation of the amplitude of the Bragg waves which is coherent with the underlying long waves. The ensuing cross section is dependent on the relative phase, φ, of the underlying dominant wave. Adding hydrodynamic modulation to the model would move the peak cross section on the phase of the underlying waves and, hence, change the measured Doppler centroid. Movement of the peak

Bragg spectral amplitude to a faster portion of the wave, might explain the discrepancy between the model and the empirical data.

We note that there is no evidence of high speed scatterers in the Doppler centroid data for incidence angles less than 60°. Although the empirical velocity measurements can be slightly higher than those predicted by the simple simulation, they are on the order of those predicted for Bragg-type scatterers rather than those of breaking waves or of scattering wedges.

The Doppler distribution emphasizes higher-power portions of the return. To study the lower-power portion, the power-velocity histograms are normalized by the total number of measurements in each bin, rather than with the total power in the whole signal. The resulting distributions are called the average cross section velocity distributions. In general, the average cross section velocity distributions are similar for the empirical and simulated data. Though there is an offset in the distribution peaks, the slope of the slow speed dependence, and the general shape of the velocity profile is in very good agreement, suggesting that the composite model of Bragg scattering is in fact valid over much of the range observed by the Yscat radar. However, at 60° incidence angle and to a lesser extent at 50°, the upwind, V-pol empirical distributions are narrower than the predicted distributions.

While the scattering mechanism is the same for both V-pol and H-pol the majority of the power is scattered from a rather narrow region of the wave velocity profile [6]. Because this region is different between V-pol and H-pol, there is some velocity difference between the polarizations. In both the empirical and simulated data the H-pol return is consistently "faster" than the corresponding V-pol return. This difference is likely due to the differences between the slope-cross section relationship, which is steeper for H-pol than V-pol [4]. In any case, the differences between the H-pol and V-pol velocities are consistent with Bragg scattering.

Our results suggest that the composite scattering model accounts for the majority of the characteristics of the velocity statistics [6]. Based on the theoretical velocity of breaking waves, contributions from these events would increase the width of the Doppler distributions. However, if these events occur very infrequently, their effects may not be visible in the average Doppler histogram.

V. SUMMARY

The simplified model used in this paper is based on the composite model. The simulation data appears to agree with the empirical data qualitatively, although the variance of the simulated data shows more wind speed dependence than is evident in the empirical data. It is suggested that a decrease in the coherence area can account for this lack of wind speed dependence in the empirical data.

The composite model accurately predicts the incidence angle dependence of the distribution variance, as well as the differences between the H-pol and the V-pol distributions. Simulations show that the model qualitatively agrees with the shape of the empirical distributions. In particular, the region from 30° to 50° incidence angle seems to be in good agreement with the composite model, with no evidence of additional scattering mechanisms in the empirical data. The simulation also reveals that the upper tail of the observed distribution can be explained within the composite model. Quasi-specular scattering seems to be very important at 20° and wave breaking contributions are evident at 60°.

At 20° - 40° incidence angles, the simulation accurately predicts the observed Doppler centroids. At 50° and 60° the simulation under-predicts the Doppler centroids. This may be due to the hydrodynamic modulation transfer function. The composite model predicts a slight difference in the Doppler centroids of the H-pol and V-pol
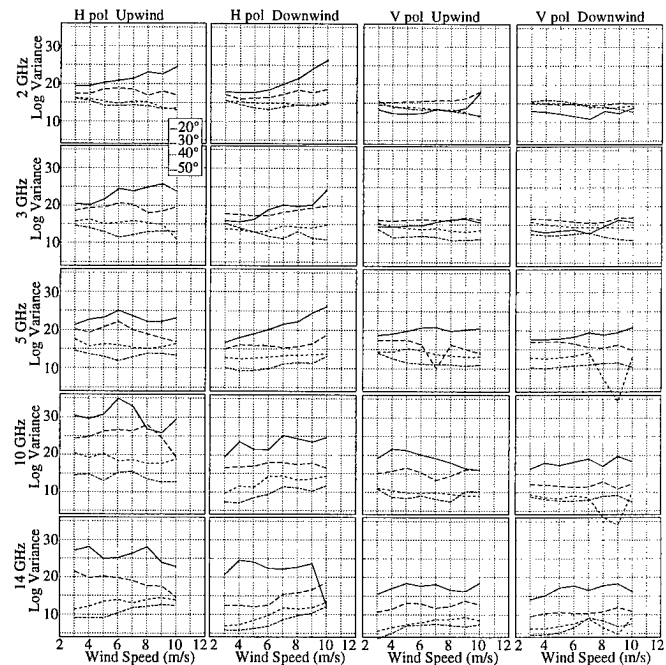
Figure 2. Log variance vs. wind speed.

data, a difference found in the empirical data. No evidence for a significant contribution from fast scatterers is found for incidence angles less than 60°.

REFERENCES

[1] D.G. Long, R.S. Collyer, R. Reed, and D.V. Arnold, "Dependence of the Normalized Radar Cross Section of Water Waves on Bragg Wavelength–Wind Speed Sensitivity," to appear, *IEEE Trans. Geosc. Rem. Sens.*, 1996.

[2] B.L. Gotwols and D.R. Thompson, Ocean microwave backscatter distributions, *J. Geophys. Res.*, vol. c5, no. 99, pp. 9741–9750, 1994.

[3] M.A. Donelan, J. Hamilton, and W.H. Hui, Directional spectra of wind-generated waves, *Phil. Trans. Royal Soc. London*, vol. 315, no. A, pp. 509–562, 1985.

[4] W.J. Plant, A two scale model of short wind-generated waves and scatterometery, *IEEE Trans. Geosc. Rem. Sens.*, vol. 91, no. 9, pp. 10735–10749, 1986.

[5] M.A. Donelan and W.J. Pierson, Radar scattering and equilibrium ranges in wind generated waves with application to scatterometry, *IEEE Trans. Geosc. Rem. Sens.*, vol. 92, no. C5, pp. 4971–5029, 1987.

[6] R. Reed, "Statistical Properties of the Sea Scattered Radar Return," Ph.D. Dissertation, Brigham Young University, Provo, UT, 1996.

[7] D.B. Trizna, Statistics of low grazing angle radar sea scatter for moderate and fully developed ocean waves, *IEEE Trans. Ant. Prop.*, vol. 39, no. 12, pp. 1681–1690, 1991.

[8] W.J. Plant, E.A. Terray, and R.A. Petit, The dependance of microwave backscatter from the sea on illuminated area: Correlation times and lengths, *J. Geophys. Res.*, vol. 99, no. C5, pp. 9705–9723, 1994.

[9] D.R. Lyzenga, A.L. Maffet, and R.A. Schuman, The contribution of wedge scattering to the radar cross section of the ocean surface, *IEEE Trans. Geosc. Rem. Sens.*, vol. GE-21, no. 4, pp. 502–505, 1983.

Study of Katabatic Wind Fields by Using ERS-1 Synthetic Aperture Radar Imagery of the Ocean Surface

Werner Alpers[1], Ulrike Pahl[2], Günther Groß [2], Dieter Etling[2]

[1]Institute of Oceanography, University of Hamburg, Troplowitzstrasse 7, D-22529 Hamburg, Germany
phone: +49-40-4123-5432; fax: +49-40-4123-5713; e-mail: alpers@ifm.uni-hamburg.de

[2]Institute of Meteorology and Climatology, University of Hannover, Herrenhäuserstr. 2, D-30419 Hannover, Germany
phone: +49-511-762-2618; fax: +49-511-762-4418; e-mail: gross@chinook.muk.uni-hannover.de

Abstract – Synthetic aperture radar (SAR) images acquired over the Mediterranean Sea from the First European Remote Sensing satellite ERS-1 showing sea surface manifestations of katabatic wind fields are presented. By using a mesoscale atmospheric model, the wind field associated with cold air flowing from the mountains through a broad valley in Calabria (southern Italy) onto the sea is calculated and compared with the wind field derived from an ERS-1 SAR image.

INTRODUCTION

On synthetic aperture radar (SAR) images of the sea surface often "imprints" of atmospheric phenomena, like atmospheric boundary layer rolls [1], atmospheric convective cells, atmospheric internal waves [2], [3], downdrafts from tropical rain cells [4], meteorological fronts, wakes and vortices behind isolated islands, land and sea breeze, and katabatic wind fields can be delineated. They become visible on radar images because they are associated with a variable wind velocity at the sea surface which modulates the sea surface roughness and thus the radar backscattering. By using a wind scatterometer model [5], one can convert the gray level variations in the SAR image into wind speed variations provided the wind direction is known. The wind direction often can be inferred from "wind streaks" visible on the SAR image. In this paper we discuss sea surface manifestations of katabatic wind fields visible on ERS-1 SAR images acquired over the Mediterranean Sea (Tyrrhenian Sea) off the coast of Calabria (southern Italy). For an ERS-1 SAR image showing a mushroom-type wind field off the coast of Gioia Tauro (Calabria), a numerical simulation with a mesoscale atmospheric model has been carried out which yields - among others - the wind field at the sea surface [6]. It is shown that the calculated wind field agrees reasonably well with the measured one.

ERS-1 SAR IMAGES OF KATABATIC WIND FIELDS

The katabatic wind is a drainage wind current caused by the gravitational flow of cold air off high terrain. Its direc-
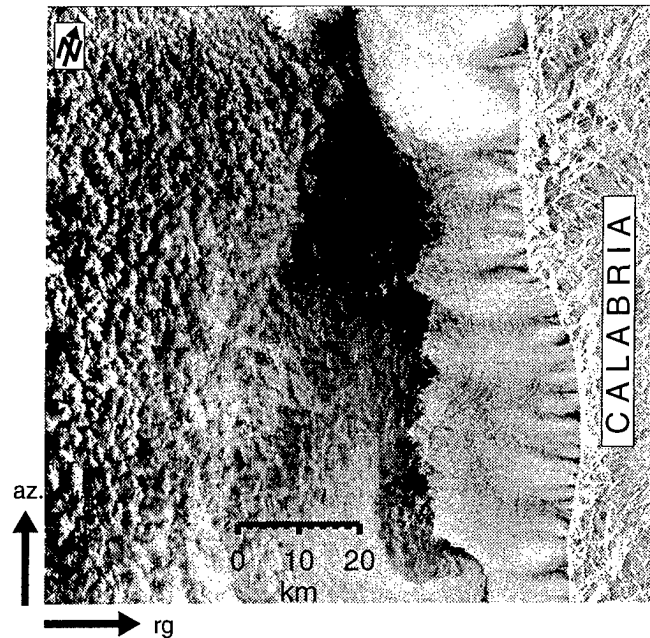
Fig.1: ERS-1 SAR image of a coastal area in the Mediterranean Sea off the western coast of southern Italy showing sea surface manifestations of cold air flowing from the mountains onto the sea (right-hand side) and of atmospheric convective cells (left-hand side).

tion is controlled almost entirely by orographic features. Katabatic winds occur late in the evening and at night when the air in the mountains has cooled down. When the air flow hits the sea surface, it increases its roughness. On the radar images sea surface manifestations of katabatic wind fields appear as white patches whose forms often resemble tongues or mushrooms emanating from valleys. Fig. 1 shows an example of a wind field in the Tyrrhenian Sea off the coast of Calabria associated with cold air flowing down the mountains onto the sea. This image was acquired on February 20, 1995, at 21:13 UTC (22:13 local time), and has center coordinates of 39°26' N, 15°34' E (orbit 18839, frame 783). The wind field has the form of an almost continuous band stretching along the coast. The band has a width of up to 28 km. Note also the sea surface manifestations of atmospheric convective cells in the
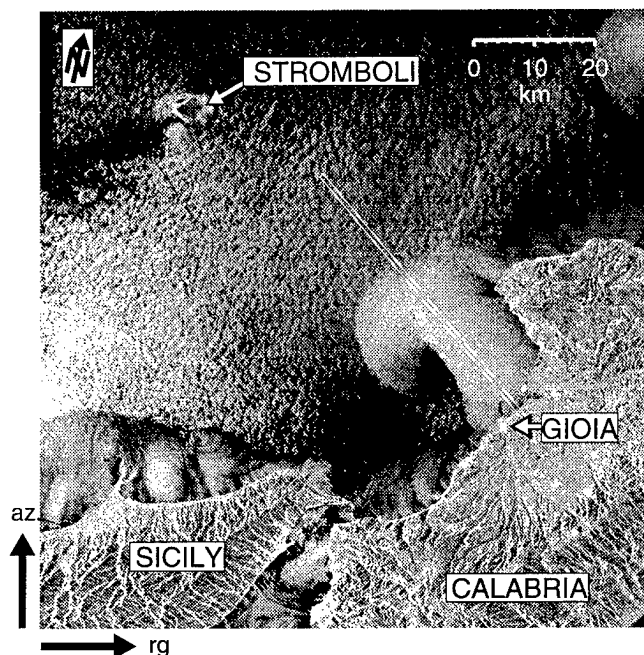
Fig.2: ERS-1 SAR image of the Tyrrhenian Sea north of the Strait of Messina showing sea surface manifestations of a katabatic wind field off the coast of Gioia (white patch NW of Gioia), katabatic wind fields off the coast of northern Sicily, and of atmospheric convective cells (mottled pattern south of Strómboli).

Fig.3: Isolines of wind speed calculated from the mesoscale atmospheric model FITNAH for the area around Gioia. The heavy line denotes the 1.5 m/s isoline of wind speed which extends from the coastline (also marked by a heavy line) onto the sea.

left-hand section of the image. They are formed in calm weather when the air is cooler than the water such that the air is heated from below. A weather station located at the south-east corner of the imaged scene (Lamezia Terme, $38°54'N$, $16°15'E$) reported at 21:00 UTC a wind speed of 2 m/s from 270°, and an air temperature of 9.8°C. A ship cruising in the area reported water temperatures around 16°C. Thus the air-sea interface was highly unstable.

Fig. 2 shows another example of sea surface manifestations of a katabatic wind field which has the form of a mushroom. This image was acquired on Sept. 8, 1992, at 21:13 UTC (orbit 6014, frame 765), also over the Tyrrhenian Sea slightly south of the area shown in Fig. 1 (center coordinates: $38°35'N$, $15°34'E$). At the time of the SAR acquisition the meteorological station at Lamezia reported a wind velocity of 1.5 m/s from 70° and an air temperature of 16.1°C, and no cloud coverage. The water temperature measured at a sea station on the Ligurian islands was 25°C.

NUMERICAL SIMULATIONS

The flow of cold air from the Calabrian mountains (which have heights up to 1800 m) through the valley of Gioia onto the sea has been simulated by using the mesoscale atmospheric model FITNAH of the University

of Hannover [7]. Fig. 3 shows the calculated isolines of wind speed at a height of 15 m. The gray shades denote the height of the topography (white area: sea surface). Note that the 1.5 m/s isoline of wind speed over the sea has a similar shape as the white patch visible on the SAR image. In Fig. 4 the isolines of wind speed in the y, z - plane, where y denotes the horizontal coordinate in the direction normal to the coastline and z the height coordinate, are shown. Note the strong gradient in wind speed at the front of the katabatic wind field. This is the reason why the sea surface manifestations of katabatic wind
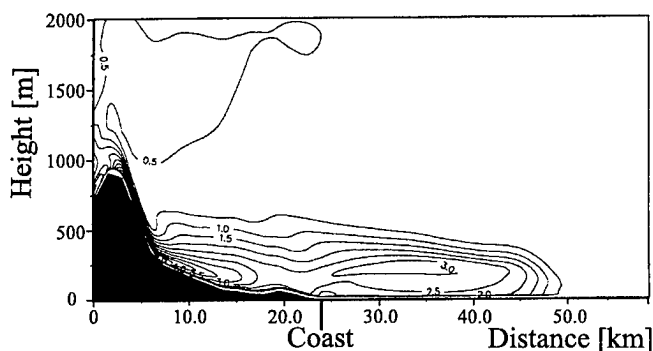
Fig.4: Isolines of wind speed in a vertical plane whose normal is parallel to the coast line as calculated from the FITNAH model.
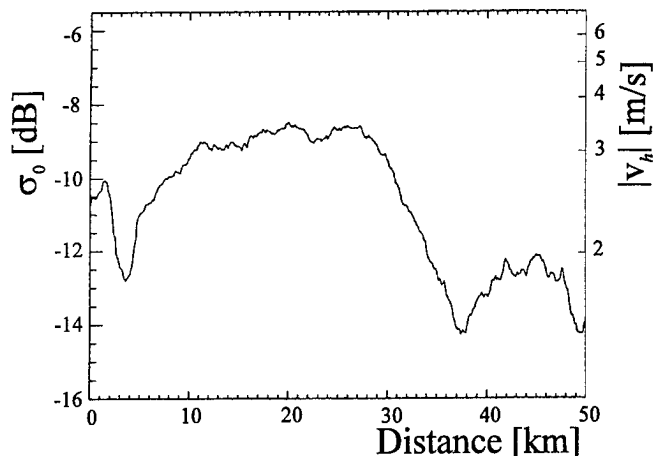
Fig.5: Gray level scan along the line shown in Fig. 2 (starting from the coast). On the left-hand vertical axis the normalized radar cross section (NRCS) is plotted and on the right-hand vertical axis the wind speed calculated from the NRCS values by using the CMOD4 model.

fields usually have very sharp boundaries. We have determined the variation of the normalized radar cross section (NRCS) along the line inserted in Fig. 2 and converted it into variation of wind speed, referenced to a height of 10 m, by using the CMOD4 model [5]. The wind speed variation along this scan line is plotted in Fig. 5. Furthermore, we have calculated the horizontal wind velocity at a height of 15 m from the mesoscale atmospheric model which is shown in Fig. 6. Comparison of both curves shows that their form is very similar, but that the wind speed inferred from the SAR image is slightly higher than the one calculated from the atmospheric model. However, this small discrepancy may be due to the fact that the CMOD4 model overestimates the wind speed when the wind speed is below 3 m/s as noted recently by Rufenach [8].
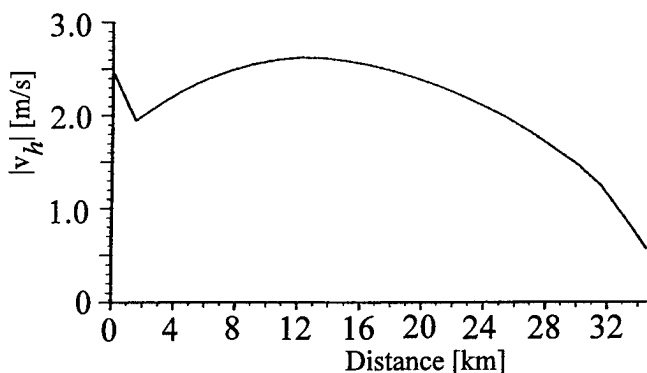
Fig.6: Horizontal wind velocity at a height of 15 m calculated from the FITNAH model as a function of distance from coast.

CONCLUSION

Katabatic winds are mesoscale atmospheric phenomena which strongly affect the micro-climate in coastal regions, the sea current pattern, and the pollutant circulation in the atmosphere as well as in the sea. Although a detailed knowledge of katabatic wind fields would be beneficial to many authorities, they have not been studied well. This and previous studies [1], [2], [3], [9] suggest that SAR can provide valuable information on this and other mesoscale phenomena in the marine atmosphere which are difficult to obtain by conventional meteorological measurements.

ACKNOWLEDGMENTS

REFERENCES

[1] W. Alpers and B. Brümmer, "Atmospheric boundary layer rolls observed by the synthetic aperture radar abaord the ERS-1 satellite," J. Geophys. Res., 99, 1994, pp.12613-12621.

[2] P.W. Vachon, O.M. Johannessen, and J.A. Johannessen, "An ERS-1 synthetic aperture radar image of atmospheric lee waves," J. Geophys. Res., 99, 1994, pp.22483-22490.

[3] W. Alpers and G. Stilke, "Observation of a nonlinear wave disturbance in the marine atmosphere by the synthetic aperture radar abaord the ERS-1 satellite," J. Geophys. Res., 101, 1996, in press.

[4] D. Atlas, "Footprints of storms on the sea: A view from spaceborne synthetic aperture radar," J. Geophys. Res., 99, 1994, pp.7961-7969.

[5] A. Stoffelen, and D.L.T. Anderson, "ERS-1 scatterometer data characteristics and wind retrieval skill," Proceedings First ERS-1 Symposium, Cannes, March 1993, ESA SP-359, pp. 41-47.

[6] U. Pahl, "Numerische Simulationen nächtlicher Kaltluftabflüsse zur Interpretation von SAR Aufnahmen", Diploma thesis, Institute of Meteorology and Climatology, University of Hannover, February 1996.

[7] G. Groß "On the wind field in the Loisach Valley - numerical simulation and comparison with the LOWEX III data," Meteorol. Atmos. Phys., 42, 1990, pp.231-247.

[8] C. Rufenach, "A new relationship between radar cross-section and ocean surface wind speed using ERS-1 scatterometer and buoy measurements," Int. J. Remote Sensing, 18, 1995, pp.3629-3647.

[9] W. Alpers, "Measurement of mesoscale oceanic and atmospheric phenomena by ERS-1 SAR," URSI International Union of Radio Science, Radio Science Bulletin No. 275, 1995, pp.14-22.

A Coupled Wind-Internal Wave System

Andre V. Smirnov

Cooperative Institute for Research in Environmental Sciences,
University of Colorado/NOAA/ETL,
325 Broadway, R/E/ET6, Boulder, Colorado 80303
Tel.: (303)497.3431, Fax:(303)497.6978, E-mail: avs@etl.noaa.gov

Abstract – This paper presents the results of an experimental study of ocean internal waves observed by coastal and airborne radars. The radar modulation of a number of internal waves, as evidenced by surface slicks, is thought to vary, as does the wind direction. A boundary-layer transition study was applied for the explanation of radar signals in X-, K_u-, and K_a-bands from the ocean surface disturbed by internal waves. The study was motivated both by the need to find different wind regimes above a slick smoothed by a current from an internal wave and rough seas around the slick. The most significant results show a strong coupling the transition zone "slick-free sea surface" and a high backscattered signal at the HH-polarized image downstream. There is no comprehensive theory for explaining of the internal-wave radar clutter in all environmental conditions. Backward radio-wave scattering by rough seas at low grazing angles has a number of peculiarities. Field studies disclose that the specific effective scattering surface value is a function of grazing angle, radio wavelength, signal polarization, sea state, and internal-wave aspect relative to the wind direction and a number of other parameters. In this paper we present an aerodynamical model allowing us to validate the high modulation of an observable radar cross section from the internal waves in X- and K-bands.

INTRODUCTION

Internal wave detection is a unique problem in radar-detection theory. The association between internal waves and wind waves has been known and explored by many researchers for many years [1]. Authors [2] describe a classification of radar images obtained under low grazing angles and in different environmental conditions. (This paper is concerned mainly with the air dynamics above a slick and radar observations in the transition zone between a slick and free water.)

The interaction between turbulent air and the free water surface involves complicated physical phenomena. There-fore, the prediction of momentum roughness (z_{0m}) over the sea surface is still subject to some uncertainty. It is generally accepted that, for light winds, the water surface is smooth. In some experiments, the surface has been observed to be "super-smooth." The issue is unresolved. This phenomenon might be due to surface-tension effects resulting from surface films or other impurities [3]. Such discrepancies can be due to the neglect of atmospheric stability. We suggest that "super-smooth" water is observed in the field of a surface slick generated by internal waves. A surface slick is a common feature of the surface manifestation of internal waves. The published data devoted to the observation of the surface manifestation of internal waves in different environmental conditions contain the description of the surface slick. The origin of this slick is so far unknown.

Three possible mechanisms can be involved in the internal-wave slick formation: the currents, turbulence in the upper ocean mixed layer (UOML), the natural films, and surfactants. The positions of the slick relative to the internal-wave phase change greatly. The radar images of the internal-wave slicks both in the visible range and in microwave bands demonstrate reduction of the mean square slopes of wind waves and the suppression of ripples with $\lambda \leq 10$ cm inside the slick. Because there is no data regarding the value of the roughness parameter inside a surface slick generated by ocean internal waves, we suggest using the aerodynamical property of ice. We assume that the roughness length z_0 over the slick is close to one over the ice surface.

SMOOTH-ROUGH TRANSITION

The concept that the surface roughness is affected by only local air flow, which implies conditions of flow reduction downstream from a smooth-rough transition, is in agreement with radar observations of the sea-ice boundary. When air flows from a smooth to a rough surface, the

air flow decelerates in the internal boundary layer (IBL) (Fig. 1).
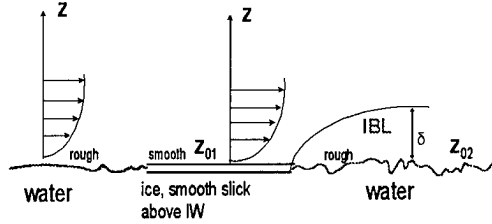
Figure 1: Concept of rough-smooth-rough transition

This results in horizontal convergence and upward motion above the transition zone between the smooth and rough surface. A hydrodynamically smooth surface can be defined by the criterion $Re_0 < 0.13$ approximately, where $Re_0 \equiv (U_*z_0/\nu)$ is the roughness Reynolds number, and ν is the kinematic viscosity. In nature, most surfaces do not satisfy this criterion, but often open water at low wind speeds, snow, and regular ice surfaces are smooth. We chose the sea-ice zone to evaluate the wind structure above the train of smooth-rough transitions. This model might be compared with the situations for internal-wave observation. The value of z_0 depends on the characteristics of the surface. For example, the value of z_0 over ice is 0.001 cm. Over water, the roughness length z_0 is calculated as a function of friction velocity [4] $z_0 = 0.032U_*^2/g + z_{0c}$, where g is acceleration of gravity and z_{0c} is a background value of 10^{-4} m. When a turbulent air flow moves from an icy surface to open water, it experiences a change in turbulent fluctuations that decelerates the mean air flow from a smooth onto a rough surface.

RESULTS

Our experience in observing surface manifestations of internal waves in the ocean shows the great variety of internal-wave signatures with different modulation of radar signals. It was found that the internal-wave modulations depend strongly on wind and other parameters of atmospheric stability. We consider the deformation of wind profile structure above the smooth-rough transition.

According to Blackadar's planetary boundary layer (PBL) model, four dynamical regimes are possible in the near-surface atmospheric layer depending on the stability parameters [5]. The results of the dynamics over ice and water for the height 0.01 m from the surface are presented in Table I.

Table I. *Ratios of $(U_{0.01i} - U_{0.01w})/U_{0.01w}$, where $U_{0.01i}$ is the wind speed above ice and $U_{0.01w}$ is the wind speed above water for four values of U_{10} and for four cases of atmospheric stability.*

Regimes:	2 m/s	4 m/s	7 m/s	10 m/s
-Stable case	2%	N/A	N/A	N/A
-Mechanically driven turbulence	15%	15%	25%	25%
-Unstable (forced convection)	25%	32%	25%	25%
-Unstable (free convection)	42%	59%	30%	26%

In all cases the wind speed at this level over ice is higher than over water, but it is interesting that the differences between regimes is greater when U_{10} is lower. An increment in the friction velocity for sea water-ice surface transition is 20%, and doesn't depend on regimes and U_{10} as well. It is commonly known that in the gravity-capillary region of the surface wave spectrum, there is a linear increase of spectral density with friction velocity.
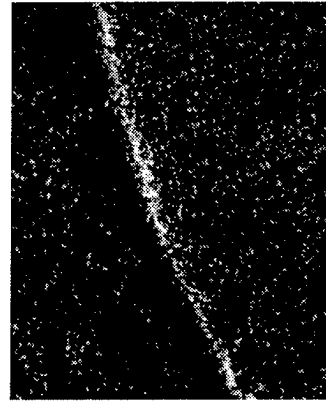
Figure 2: Radar image of internal wave

According to [6] the strongest friction velocity dependence of the spectral density is to be in the region of wavelengths between 1 and 3cm (reaching as high as $U_*^{2.6}$). On the other hand, the initial growth rate of the amplitude of gravity-capillary waves is: $\gamma = k^2 \left(0.1U_*^2/2\pi\omega - 2\nu\right)$, where ω and k are the frequency and the wave number of a surface wave, and ν is the kinematic viscosity of water as presented in [7]. It is seen that the growth rate of the amplitude of gravity capillary waves is a function of the friction velocity, and its small deviations due to change in turbulent fluctuations above a smooth-rough transition affect the growth rate of small gravity-capillary waves. The

radar observations were made in several experiments, using airborne K_u-band radar in the New York Bight experiment in July 1992, and shore-based radars of X-, and K_a-bands in the COPE experiment of NOAA's Environmental Technology Laboratory in September 1995 near the Oregon coast. Figure 2 shows a fragment of the airborne radar image at HH-polarization. The size of the image is 4 × 5.5 km. The horizontal cross section of image intensity throughout the middle part of the radar image given in Fig.2 is presented in Fig.3. The directions of wind and internal-wave propagation are also shown in Fig.3. The presented internal-wave modulation was averaged over 13 realizations. It should be noted that the strong signal enlargement is seen downstream after the area with the weakest signal. The analysis of radar images includes data obtained in atmospheric conditions of variable stability and for a large number of different situations when wind and internal waves interact. Our radar observations show the increased backscatter downwind of a smooth-rough (slick-free water) transition.
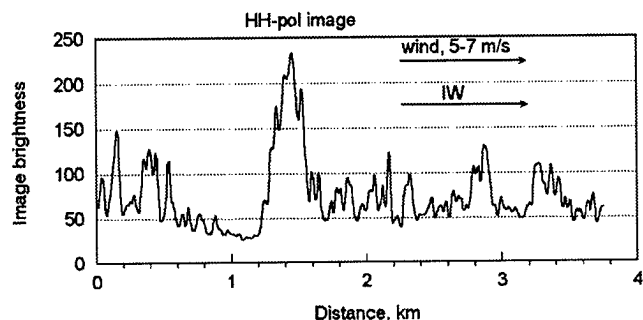
Figure 3: Cross section of radar image intensity

Additionally, we have used a 3-dimensional mesoscale analysis and prediction system (MAPS) developed at NOAA's Forecast Systems Laboratory [8]. The modeled ocean surface with bands of smooth and rough waters had a ratio between roughness parameters of rough-smooth surface $z_{0r}/z_{os} = 10$. The winds flow across this train of bands. This analysis shows that the modulus of vertical mean velocity increases with increasing difference of roughness lengths and the strong upward mean motion above a smooth-rough transition.

CONCLUSION

These results can be appropriate for wind – internal-wave coupling due to the slick formation on the surface of the UOML. A strong modulation of radar returns in the field of internal wave due to friction velocity overshooting in a transition zone of the rough-smooth surface is shown. Field observation of the surface manifestation of internal waves demonstrates that the influences of wind over a sea surface with different roughness properties generating short ripples in a "smooth-rough" transition zone can produce major changes in radar returns. Again, an adequate theoretical treatment demands the use of fully nonlinear numerical methods for describing a delicate balance between two mechanisms: wind waves – internal-wave currents coupling and wind-slick coupling. The first mechanism is very important for interpretation of observable magnitudes of internal-wave signatures in decimetric radars, and the second one might be reasonable for understanding "overshooting" of internal-wave modulation in X-, K- bands.

ACKNOWLEDGMENTS

REFERENCES

[1] B.A. Hughes and H.L. Grant, "The effect of internal waves on surface wind waves. 1. Experimental measurements," *J. Geophys. Res.*, vol.83, pp.443-454, 1978.

[2] A.V. Smirnov and V.U. Zavorotny, "Study of polarization differences in K_u-band ocean radar imagery," *J. Phys. Oceanogr.*, vol.25, pp.2215-2228, 1995.

[3] G.T. Csanady, "The "roughness" of the sea in light winds," *J. Geophys. Res.*, vol.79, pp.2747-2751, 1974.

[4] F. Delsol, K. Miyakoda, and R.H. Clarke, "Parameterized process in the surface boundary layer of an atmospheric circulation model," *Quart. J. Roy. Meteor. Soc.*, vol.97, pp.181-208, 1971.

[5] A.K. Blackadar, "High resolution models of the planetary boundary layer," *Advances in Environmental Science and Engineering*, 1, no.1, Pfafflin and Ziegler, eds., Gordon and Briech Science Publishers, New York, pp.50-85, 1979.

[6] P.A. Hwang, D.B. Trizna, and J. Wu, "Spatial measurements of short wind waves using a scanning slope meter," *Dynamics of Atmos. and Oceans*, vol.20, pp.1-23, 1993.

[7] W.J. Plant and J.W. Wright, "Growth and equilibrium of short gravity waves in a wind-wave tank," *J. Fluid Mech.*, vol.82, pp.767-793, 1977.

[8] R. Bleck and S.G. Benjamin, "Regional weather prediction with a model combining terrain-following and isentropic coordinates. Part I: model description," *Mon. Wea. Rev.*, vol.121, pp.1770-1785, 1993.

A Large-Scale Evaluation of Features for Automatic Detection of Oil Spills in ERS SAR Images

Anne H. Schistad Solberg and Rune Solberg
Norwegian Computing Center, P.O. Box 114 Blindern, N-0314 Oslo, NORWAY
Phone +47 22 85 25 00 Fax +47 22 69 76 60
Email: Anne.Solberg@nr.no Rune.Solberg@nr.no

Abstract We study the performance of automatic methods for oil spill detection in ERS SAR images. The presented algorithm has three main parts: (i) detection of dark spots; (ii) feature extraction; and (iii) dark spot classification. The dark spot detection locates all spots which can possibly be oil slicks in the image. For each slick, a set of backscatter, textural, and geometrical features are extracted. The dark spots are then classified into possible oil slicks and look-alikes based on the extracted features. Based on the current study, we believe that a semi-automatic oil slick identification system which can discriminate between oil slicks and look-alikes can be developed. To achieve this, some new features describing the surroundings of a slick and the slick itself must be defined and tested.

INTRODUCTION

Synthetic aperture radar (SAR) images from the ERS satellites have since the summer of 1994 been used in a pre-operational service for manual identification of oil spills at Tromsø Satellite Station in Norway. In this pre-operational service, SAR images of ocean areas are manually inspected to identify possible oil spills. During this pre-operational phase, a large data set of SAR images containing verified oil slicks and oil slick "look-alikes" has been collected.

In this paper, we study the performance of automatic methods for oil spill detection. A large data set consisting of verified oil slicks and oil slick look-alikes is used. The goal is to develop a semi-automatic system for oil spill detection, in which dark spots with a high probability of being an oil slick are automatically identified. These possible oil slicks are then presented to an operator. Presently, we do not believe that a fully automatic oil spill detection algorithm will be able to correctly discriminate between the most difficult oil slicks and their look-alikes. However, a semi-automatic procedure will greatly reduce the number of SAR images which need to be manually inspected compared to a fully manual detection prodedure.

An algorithm for semi-automatic detection of oil spills is presented. The algorithm has three main parts: (i) de-tection of dark spots; (ii) feature extraction; and (iii) dark spot classification. The dark spot detection locates all spots which can possibly be oil slicks in the image. For each slick, a set of backscatter, textural, and geometrical features are extracted. The dark spots are then classified into possible oil slicks and "look-alikes" based on the extracted features.

OIL SLICKS IN SAR IMAGERY

Oil slicks are visible in SAR imagery because they have a dampening effect on the Bragg waves in the sea (see, e.g., [6]). They will thus appear as dark spots in the SAR images, compared to the surrounding sea. Under strong wind conditions, the oil will be quickly resolved and will not be visible in the image. Under low to moderate wind conditions, dark spots caused by natural phenomena will also be seen in the image. The natural dark spots are termed oil slick look-alikes.

TEST DATA

A data set consisting of 59 ERS-1 SAR low resolution images (LRI) from Tromsø Satellite Station is used to test the performance of the automatic oil spill detection algorithm. These images have been manually inspected for oil slicks by TSS, as part of their manual pre-operational oil spill identification service.

Of the 59 images in the test data set, 29 images contain oil slicks. These 29 images contain a total of 42 oil slicks. These oil slicks can be divided into tree main categories:

- *Thin, linear slicks.* 16 slicks belong to this category. For some of the slicks, a bright object (possibly a ship or an oil platform) can be seen nearby. This type of slick might be caused by a moving ship or a stationary object releasing a small amount of oil under certain wind and current conditions.

- *Thin, piecewise linear slicks.* 15 slicks belong to this category. For some of the slicks, a bright object can be seen nearby. These slicks might be caused by a moving ship changing directions, or by changes in

current or wind directions affecting oil released from a stationary object.

- *Thick/wide slicks.* 11 slicks of this category are found. They can be caused by a stationary object releasing a larger amount of oil. If the oil was released a short time before the image was acquired, the slick will have a regular shape. For an older slick, the wind and current will make the shape of the slick more irregular.

The remaining 30 images in the test data set contain a very large number of dark spots which are not oil slicks. Such dark spots frequently occur in SAR images under low-wind conditions. In many ways, these spots resemble oil spills.

SPOT DETECTION

The developed algorithm for detection of dark spots is based on adaptive thresholding. This thresholding is based on an estimate of the typical backscatter level in a large window. The adaptive threshold is set to k dB below the estimated mean backscatter level in the region. The window is moved across the image in small steps to threshold all pixels in the scene.

SLICK FEATURE EXTRACTION

For each dark spot, a set of features is computed. The features constitute general, standard descriptors often applied for regions, and additional features particularly suited for oil slick detection.

- *Slick complexity:* This feature will in general take a small numerical value for regions with simple geometry, and larger values for geometrical complex regions.

- *Grey level mean*

- *Grey level standard deviation*

- *Mean local area contrast ratio:* a measure describing the contrast between the slick and its surrounding.

- *Sobel mean border gradient [2]*

- *Smoothness contrast locally:* measures the smoothnes of the slick compared to the surroundings.

- *Mean border width:* the average length of the border ramp between the slick and the surroundings.

- *First invariant planar moments [3].*

- *Distance to bright object:* If a bright object (a ship or an oil platform) is detected in the image, the distance from dark spots in the local area to the bright object is used as a feature.

SLICK CLASSIFICATION

Due to the small number of oil slicks available for training, a classifier which utilizes second-order statistics of the data (e.g., a Gaussian classifier) should not be used because the oil class will result in a singular covariance matrix when several features are used simultaneously in a multivariate feature vector. A *K-Nearest-Neighbor* classifier [1] will neither be suited because the number of look-alikes is several orders of magnitude larger than the number of oil slicks. We have chosen to use a hierarchical classifier, a *classification tree.* A classification tree is a nested sequence of partitions of the feature space (see, e.g., [4, 5]). The features are considered one at a time, and each level in the sequence yields a further partition of the feature space.

Training a tree classifier consists of identifying the set of partitions based on a set of n training objects. In constructing the tree, a one-step look-ahead method is used. That is, the next split is selected in an optimal way, without attempting to optimize the performance of the whole tree.

We have used the *S-Plus* implementation of classification trees. A detailed description of the methodology can be found in [5].

CLASSIFICATION PERFORMANCE

Because some of the features describe the shape of the dark spots, we will use several classes of oil slicks during the classification. The following classes are used:

- Class 1: Thin, linear oil slicks

- Class 2: Thick/wide oil slicks with a regular shape

- Class 3: Thick/wide oil slicks with a more complex shape

- Class 4: Thin, piecewise linear oil slicks

- Class 5: Look-alikes.

The classification tree utilized uses the fraction of the classes in the training set to estimate the prior probability of oil slicks vs. look-alikes. When a classification tree is trained on the set of 42 oil slicks and 2471 look-alikes, the resulting performance reflects the effect of using the fraction of the classes in the training set to estimate the prior probability of the classes (indicating a prior probability of look-alikes of 0.98). The implementation of the classification tree does not allow the user to specify proper prior probabilities or alternative loss functions. To overcome this problem, we use a resampling procedure to create a new training data set with a more equal number of oil slicks and look-alikes: from the oil slick classes, $n = 100$ objects are sampled from each class (with replacement), whereas $n = 100$ objects from the look-alike class are sampled at
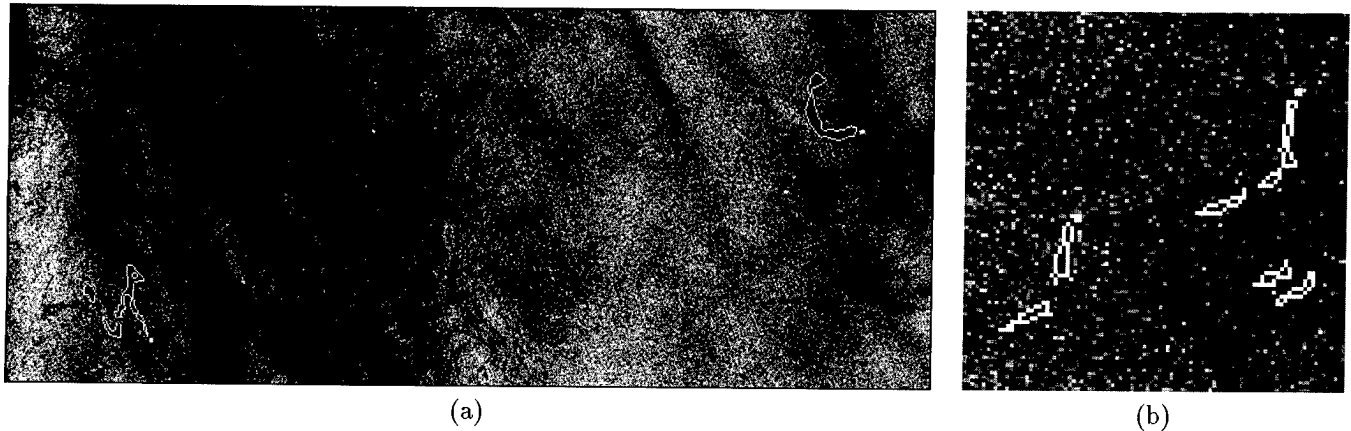
Figure 1: (a) Correctly classified oil slicks. (b) Very low-contrast oil slicks which are misclassified due to fragmentation during spot detection. The borders of the oil slicks are marked in white.

random, creating at new data set with equal prior probabilities.

With this more balanced data set, all oil slicks in the training set were correctly classified, but 3% (87/2516) of the look-alikes were classified as oil slicks.

To evaluate the performance of the classifier on an independent test data set, we use the leave-one-out method for error estimation [1]. In a data set with n oil slicks, $n - 1$ objects are used for training, and the remaining for testing. This procedure is repeated n times. With this procedure, 14% (6/44) of the oil slicks were wrongly classified as look-alikes. 4% of the look-alikes were classified as oil slicks.

If we study the oil slicks which are misclassified, they fall into three main categories: (i) thin, piecewise-linear slicks; (ii) low-contrast slicks in homogeneous sea; and (iii) slicks on a very heterogeneous background where the dark spot detection algorithm fails to define a clear border between the slick and the surroundings. Fig. 1 (a) shows two oil slicks which were correctly classified. The borders of the detected slicks are indicated on the figure. In Fig. 1 (b) two small, low-contrast oil slicks are shown. These two slicks were fragmented during dark spot detection and are misclassified due to this.

Future research will include identification of new features designed particularly for these oil-slick categories. Further prior knowledge of the conditions will also be modelled.

CONCLUSIONS

Based on the current study, we believe that a semi-automatic oil slick identification system can accurately discriminate between oil slicks and look-alikes. To achieve this, some new features must be defined and tested. A classifier which can be guided by a manual operator and learn from experience must be implemented. Refinements of the spot detection algorithm are also desirable.

References

[1] P. A. Devijver and J. Kittler. *Pattern Recognition, A Statistical Approach.* Prentice Hall, Englewood Cliffs, New Jersey, 1982.

[2] R. C. Gonzalez and P. Wintz. *Digital Image Processing, Second Edition.* Addison-Wesley Publishing Company, 1987.

[3] M. K. Hu. Visual pattern recognition by moment invariants. *IEEE Transactions on Information Theory*, IT-8:179–187, 1962.

[4] A. K. Jain and R. C. Dubes. *Algorithms for Clustering Data.* Prentice Hall, Englewood Cliffs, New Jersey, 1988.

[5] W. N. Venables and B. D. Ripley. *Modern Applied Statistics with S-Plus.* Springer-Verlag, New York, 1994.

[6] T. Wahl, T. Anderssen, and Å. Skøelv. Oil spill detection using satellite based SAR, pilot operation phase, final report. Technical report, Norwegian Defence Research Establishment, 1994.

Internal waves in the Strait of Messina observed by the ERS 1/2 synthetic aperture radar

Peter Brandt, Angelo Rubino, Werner Alpers

Institute of Oceanography, University of Hamburg,
Troplowitzstrasse 7, D–22529 Hamburg, Germany;
phone: +49-40-4123-5457; fax: +49-40-4123-5713; e-mail: brandt@ifm.uni-hamburg.de

Abstract – Radar images acquired from 1991 to 1995 by the synthetic aperture radar (SAR) aboard the European Remote Sensing satellites ERS 1 and ERS 2 have been used to study the dynamics of internal solitary waves in the Strait of Messina. Roughness patterns of internal waves which are imaged by the SARs are compared with surface convergence patterns calculated by an one-dimensional, two-layer numerical model which describes the generation and propagation of internal waves in the Strait of Messina.

INTRODUCTION

The Strait of Messina separates the Italian peninsula from the Italian island of Sicily and connects the Tyrrhenian Sea in the north with the Ionian Sea in the south. The strait is a narrow channel, whose smallest cross-section is $0.3 \, km^2$ in the sill region. There, the mean water depth is 80 m. Throughout the year, two different water masses are encountered in the Strait of Messina: the Tyrrhenian Surface Water and the colder and saltier Levantine Intermediate Water. In the vicinity of the Strait of Messina these water masses are separated at a depth of approximately 150 m. During most of the year, a seasonal thermocline is also present in the strait which overlies this weak stratification. In the Strait of Messina large gradients of tidal displacements are encountered, because the predominantly semidiurnal tides north and south of the strait are approximately in phase opposition. This leads to large current velocities in the sill region [1]. The first observation of internal waves generated in the Strait of Messina was made by the synthetic aperture radar (SAR) aboard the American Seasat satellite [2]. In the following years, internal waves propagating northwards as well as southwards have been detected during several oceanographic campaigns [2], [3], [4] and by the thematic mapper (TM) aboard the Landsat satellite [5].

ERS-1/2 SAR IMAGES

In this investigation, we have analyzed ERS 1/2 SAR images acquired during 160 satellite overflights over the sea areas north and south of the sill. On SAR images acquired during 77 satellite overflights sea surface manifestations internal waves could be delineated. Fig. 1 shows
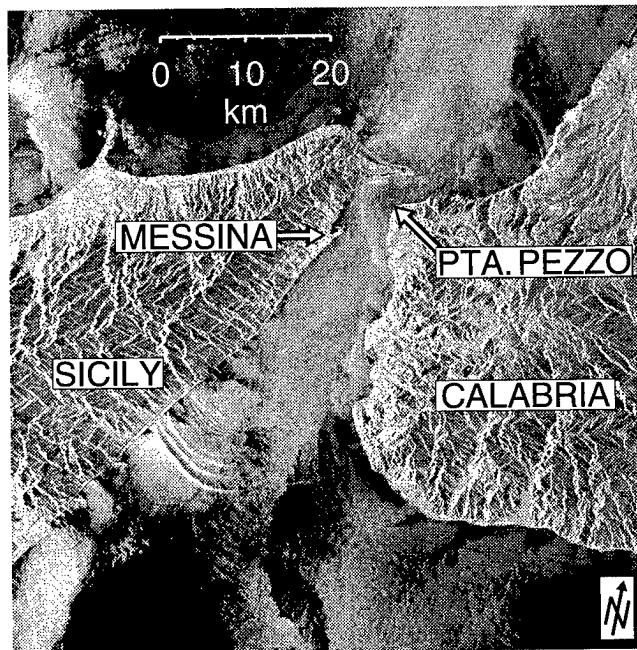
Fig.1: ERS 1 SAR image of the Strait of Messina acquired on August 17, 1995, at 2113 UTC, 12 h 26 min after maximum northward tidal flow at Punta Pezzo.

an ERS 1 SAR image (orbit: 21388, frame: 747/765) on which sea surface manifestations of one internal wave train propagating southwards and one propagating northwards can be seen. The analysis of the available ERS 1/2 SAR images shows that sea surface manifestations of internal waves are observed more frequently during periods where a strong seasonal thermocline is known to be present, i.e. during summer. Furthermore, sea surface manifestations of southward propagating internal wave trains can be delineated on ERS 1/2 SAR images more frequently than those of northward propagating ones. In general, sea surface manifestations of southward propagating internal waves are stronger than those of northward propagating ones. The SAR image depicted in Fig. 1 shows evidence of such north-south asymmetry in the sea surface manifestations of the internal wave field. Fig. 2 shows a time versus distance diagram delineating the propagation of internal bores north and south of the sill as inferred from ERS 1/2 SAR imagery. In this figure, the position of
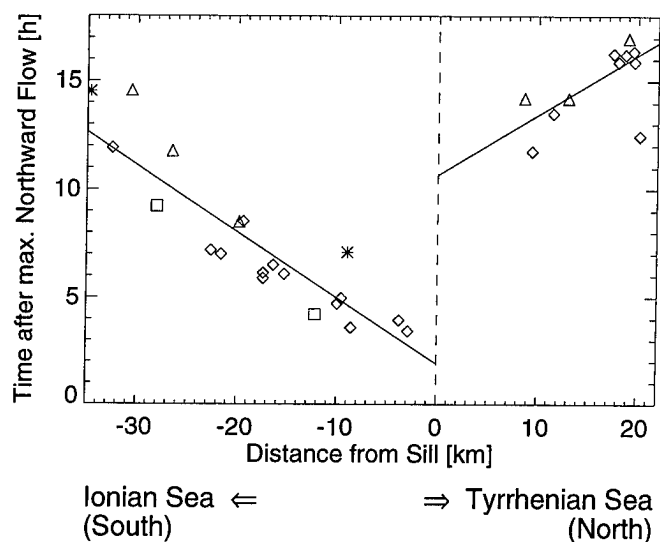
Fig.2: Space-time diagram delineating the northward and southward propagation of the leading edge of internal wave trains in the Strait of Messina as inferred from ERS 1/2 SAR imagery. Diamonds refer to observations made between July and September, triangles to observations made between April and June, squares to observations made between October and December, and stars to observations made between January and March. The lines are least-square fits.

Fig.3: Spatial separation between the first two internal solitary waves of northward and southward propagating wave trains as a function of distance from sill as inferred from ERS 1/2 SAR imagery. Diamonds refer to observations made between July and September, triangles to observations made between April and June, the square refers to an observation made between October and December, and the star to an observation made between January and March.

the leading edge of internal wave trains referenced to the time of maximum northward tidal flow at Punta Pezzo is depicted. The lines are least-square fits which yield for the northward propagating waves an average propagation speed of $1.00\,\mathrm{ms^{-1}}$ and for the southward propagating waves $0.91\,\mathrm{ms^{-1}}$. From this figure, the time of release of internal bores from the sill can be estimated: Southward propagating internal bores are released from the sill between 1 to 5 hours after maximum northward tidal flow at Punta Pezzo, northward propagating internal bores are released from the sill between 8 to 12 hours after maximum northward tidal flow at Punta Pezzo. Fig. 3 shows the spatial separation between the first two internal solitary waves of northward and southward propagating wave trains as a function of the distance from sill as inferred from ERS 1/2 SAR imagery. This plot shows that, in general, the spatial separation between the first two internal solitary waves of southward propagating wave trains is smaller in the period from July to September, where a strong seasonal thermocline is known to be present, than in the period from October to June.

NUMERICAL MODEL

The numerical model is based on nonlinear, weakly non-hydrostatic, shallow-water equations for a two-layer

ocean. It depends on one space variable only, but it retains several features of a fully three-dimensional model by including a realistic bottom topography and a variable channel width. Fig. 4 shows the form of the interface at six different times of the tidal cycle as calculated from this model. At the bottom of this figure the depth profile used in the numerical simulations is shown. We have carried out the simulations with an undisturbed interface depth of 30 m and a relative density difference between the two water layers of 0.0015. These parameters are typical for a well developed seasonal thermocline. During northward tidal flow (Fig. 4a), an interfacial depression develops north and, during southward tidal flow (Fig. 4d), an interfacial depression develops south of the sill. When the tidal flow slackens, internal bores are released from the sill, which propagate in the first case southwards and in the second case northwards. These internal bores then decay into trains of internal solitary waves. However, northward propagating internal solitary waves have, in general, smaller amplitudes than southward propagating ones (see Fig. 4b and 4e). Fig. 5 shows a space-time diagram delineating the evolution of the surface convergence patterns associated with internal waves as calculated from the model. The gray levels indicate the strength of the surface convergence and are, to first order, proportional to the variation of the backscattered radar power. The time of internal bores release from the strait's sill as calculated by the model (Fig. 5) and as inferred from ERS 1/2 SAR
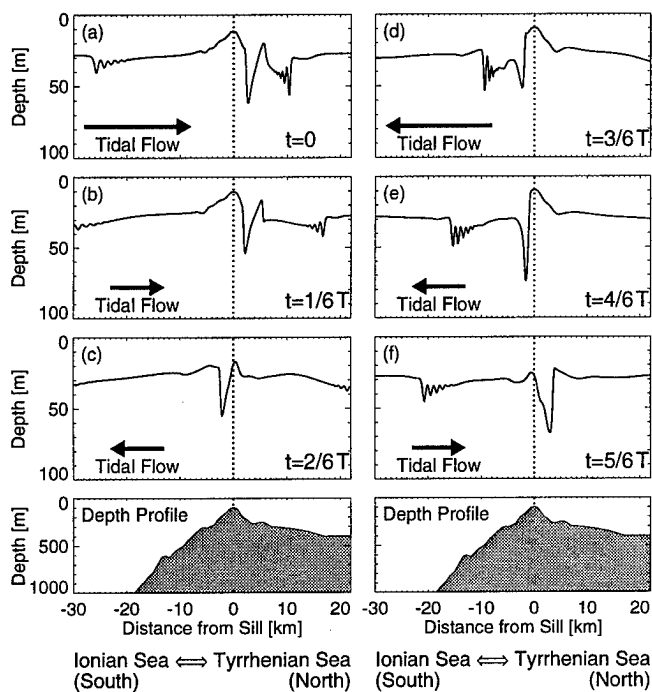
Fig.4: Form of the interface between the two layers at different phases of the tidal cycle as a function of distance from the sill (x=0) as calculated by the numerical model. The time t=0 corresponds to maximum northward tidal flow (T is the tidal period). In the bottom panels the depth profile is depicted. The vertical dotted lines mark the position of the sill.
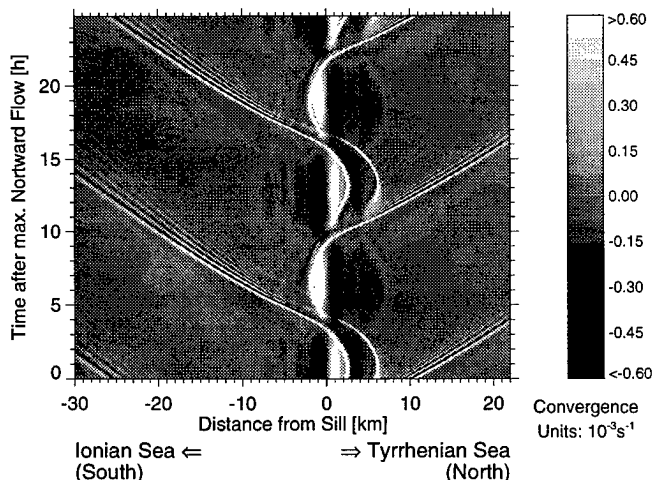
Fig.5: Space-time diagram showing the evolution of internal waves in the Strait of Messina as a function of distance from the sill (x=0) and time after maximum northward tidal flow (t=0) as calculated by the model.

imagery (Fig. 2) agree quit well.

CONCLUSION

The analysis of available ERS 1/2 SAR data of the Strait of Messina and adjacent sea areas show that (1) sea surface manifestations of internal waves propagating northwards as well as southwards are visible on SAR images, (2) sea surface manifestations of internal waves are observed more frequently during periods where a strong seasonal thermocline is known to be present, (3) sea surface manifestations of southward propagating internal wave trains are more often visible on SAR images than those of northward propagating internal wave trains, (4) southward propagating internal bores are released from the strait's sill in the period from 1 to 5 hour, northward propagating internal bores in the period from 8 to 12 hour after maximum northward tidal flow, (5) the spatial separation between the first two internal solitary waves of southward propagating wave trains is smaller in the period from July to September than in the period from October to June.

Numerical simulations, performed with different values for the density difference between the two water layers and for the depths of the undisturbed interface, indicate that most of the time the observed internal wave field is associated with the seasonal thermocline rather than with the interface between the Tyrrhenian Surface Water and the Levantine Intermediate Water in the Strait of Messina. The north-south asymmetry in the internal wave field is a consequence of the asymmetry of the channel topography.

REFERENCES

[1] F. Vercelli, "Il regime delle correnti e delle maree nello stretto di Messina," Commissione Internazionale del Mediterraneo, Venice, Italy, 1925.
[2] W. Alpers, and E. Salusti, "Scylla and Charybdis observed from space," J. Geophys. Res., vol. 88, 1983, pp. 1800-1808.
[3] A. Sapia, and E. Salusti, "Observation of nonlinear internal solitary wave trains at the northern and southern mouths of the Strait of Messina," Deep-Sea Res., vol. 34, 1987, pp. 1081-1092.
[4] L. Nicolò, and E. Salusti, "Field and satellite observations of large amplitude internal tidal wave trains south of the Strait of Messina, Mediterranean Sea," Ann. Geophys., vol. 9, 1991, pp. 534-539.
[5] V. Artale, D. Levi, S. Marullo, and R. Santoleri, "Analysis of nonlinear internal waves observed by Landsat thematic mapper," J. Geophys. Res., vol. 95, 1990, pp. 16065-16073.

Studies of Rainfall Footprints on the Sea
Conducted by Spaceborne SAR "Almaz" and
Shipborne Microwave Radiometers

M.G.Bulatov, M.D.Raev, E.I.Skvortsov.
Space Research Institute, Russian Academy of Science,
Profsouznaya, 84/32, 117810, Moscow, Russia.
FAX:7-095-333-10-56, TEL:7-095-333-35-33
E-mail:bulatov@asp.iki.rssi.ru

Abstract The present paper contains the results obtained in Gulf Stream region under intense rainfall conditions in July-August, 1992. The spaceborne SAR " ALMAZ " images and microwave data of measurements conducted by research vessel " Academic Ioffe " are analyzed. Shipborne active and passive remote instruments were probing the sea surface in 0.6 - 8 cm wave length range of electromagnetic waves. This made it possible to investigate the rainfall influence on a damping of surface waves in different frequency ranges and minimized also the cloud influence on estimates of rain rate with brightness temperature data. Joint analysis of spaceborne SAR observations, microwave shipborne and *in situ* data allowed to explain some SAR images features associate with rainfall and to study radiobrightness and backscattering of sea surface perturbed by rain.

1. INTRODUCTION

Interpretation of rainfall footprints displayed on SAR images of sea surface require an adequate model of rainfall impact on perturbed sea surface. The comprehensive review of the current state of affairs in this area can be found in [1] where a synthetic description of theoretical developments, laboratory experiments over many years of research is presented. Crucial factors of microwave scattering and selfemission characteristics having opposite effects are as follow:

a) damping of wind waves as a result of turbulence induced by rain in boundary layer. The process involves positive feedback effects: short gravity-capillary waves strip an energy of longer waves due to interwave interaction, initial smoothing of roughness eases wind stress, which impedes the growth of longer waves. Smoothing of roughness results in decrease of microwave backscatter cross section at mean incident viewing angles;

b) depth of turbulence layer increases with rain rate and number of bigger rain drops, so wave damping is supposed to be intensified. However, rain drops of large diameters produce splash structures ("stalks", "crowns", ring waves) which increase microwave scattering.

Actual conditions (wind speed, rain duration and rate) determining the dominance of either effect are not specified so far. In a number of laboratory experiments [2, 3] with the increase of rain rate was registered only microwave backscattering increase while several spacecraft observations [4, 5] have shown both decrease and increase of backscattering.

Microwave radar and scatterometer are known to register variations of gravitation-capillary waves which meet the Bragg resonance scatter conditions, while emission peaks registered by radiometers are induced by surface wave components which meet radio emission resonance conditions [6]. Combination of microwave active and passive remote sensing techniques thus offers additional opportunities for the study of sea surface and is expected to turn out most effective in investigation of sea surface under rainfall, in particular [5].

Since rainfall causes changes in surface roughness spatial spectrum over a wide range of wave numbers, sensing should be performed in a wide range of electromagnetic waves and viewing angles using a set of radiometers and scatterometers operating in millimeter, centimeter and decimeter wave length bands. The results of the such sensing are presented in this paper.

2. INSTRUMENTATION

The microwave remote sensing set installed on the research vessel and used to study the sea surface patterns included the radiometers and the scatterometer. The shipborne radiometers provided measurements in the EM-band wave length range of 0.6 to 8 cm at vertical and horizontal polarization with a fluctuation sensitivity better 0.15K. The Ku-band scatterometer was providing
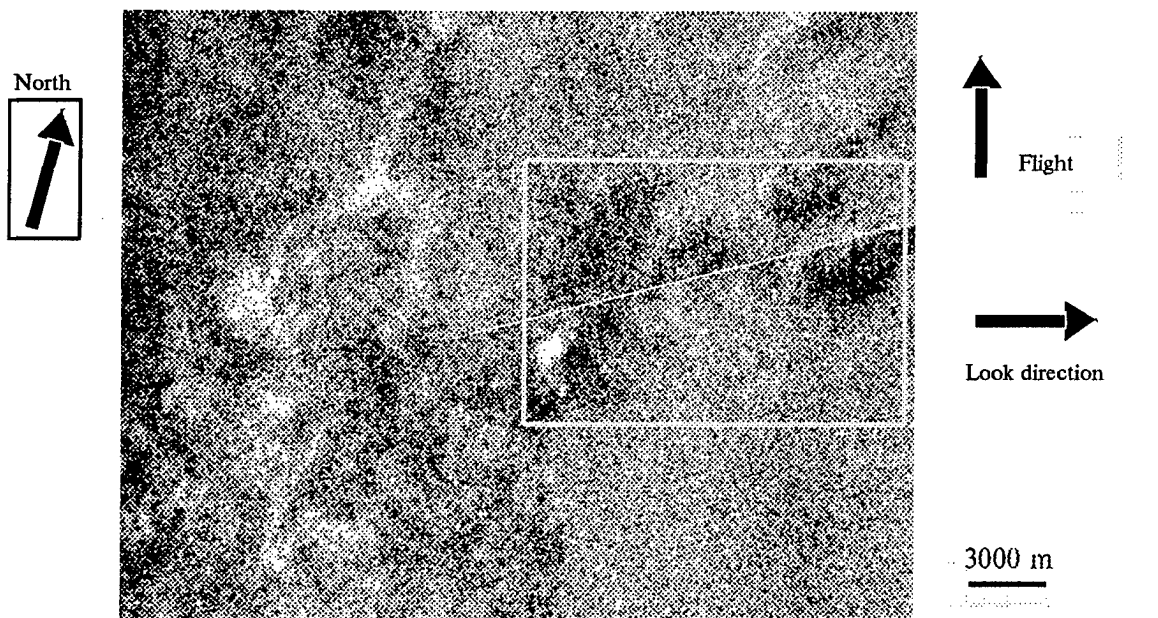
Fig.1. SAR image of the test area

the relative power measurements accurate to 0.2-0.3 dB.

SLAR, installed on the spacecraft "Almaz-1", was operating at EM-wave equal to 9.6 cm, the incident angles were equal to 20°-65°, the resolution was equal to 13 m to azimuth and to 13-19 m to range for the orbit about 300 km.

3. ATMOSPHERIC PROCESSES AT TEST SITE (August 3 to 5,1992)

In early August the polar front passed northward of the test area. Late on August 3 the pressure began dropping down, the wind got stronger, to 10 m/s, cumulonimbus and thick cumulus clouds appeared. The cyclone disturbance formed in the test area. On August 4 heavy rains were falling periodically, the test area found itself within a low-gradient baric field crossed by cold front.

4. RESULTS AND DISCUSSION

The manifestation of this front on SAR image is shown in Fig. 1. The dark band on the left upper part of the image which is an area of reduced backscattering, must be a sea surface manifestation of an atmospheric front. The white ring structure in the central parts of image may be interpreted as the surface manifestation of the wind diverging from the rain core and associated with a dawndraft [1] .

The selected rectangular area includes the ship trace (white line) and the dark spots of strongly reduced backscattering which are the surface manifestations of rainfalls.

Fig.2 displays the SAR signal power variations along the vessel track and corresponding to it shipborne S- band and Ku - band radiometric records. The comparison of these data shows the coincidence of radiobrightness maximums with reduced radar backscattering areas at all channels. The correlation coefficient between S- and Ku - band signals was as high as 0.88. The correlation radar data with radiometric data was about 0.8-0.82.

The straightforward observations and the estimates of rain rates, obtained due to the model calculations with multifrequency radiometric data used, showed that the rain rate was as hight as 30 - 35 mm/hr in this case. As analysis shows, the estimates satisfactory coincide with the measurement results independently of a viewing angle and a probing EM - wave length. This proves that in an area with moderate and moderately-heavy rains, where there is a damping of gravity - capillary waves, the emission of sea surface can be calculated by application of the first-order scattering coefficients for the respective polarization [8].

The radometeric data associate with the bright echo, which is observed in the left lower corner of the selected area and attributes to rain splash
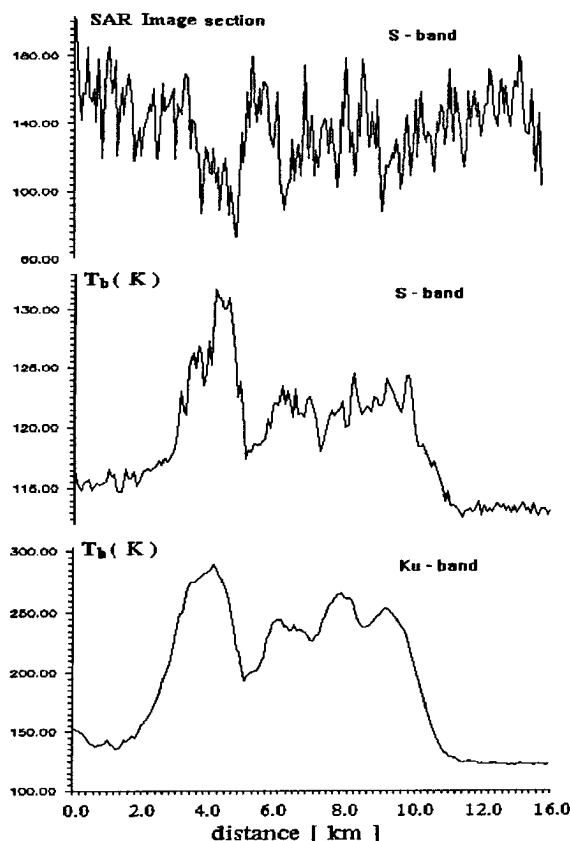
Fig.2 SAR signal power and radiobrightness records along the ship track.

products [1], provide evidence that in the heavy rain are radiobridhtness temperatures are depend on frequently and incident angle. The calculations conducted without considering of splash products influence on an emission pattern of sea surface differ essentially from the experimental data. The joint analysis of data, obtained at incident angles 30° and 70° , make it possible to determine the limiting values of radiobrightness temperatures, caused by wind fluctuations (the slopes of the radiation - wind dependency in S-band are +0.45 and -0.4 respectively) and select the increase due to splash products only. It is equal to 14K at angle 30° and 8 K at angle 70°. These values exceed 2.5-3 times calculated ones for a smooth surface.

5. CONCLUSIONS

The conducted studies show that emission patterns of a sea surface perturbed by rain are different essentially depending on a rain rate. It allows together with active microwave instruments to use microwave radiometers for rainfall perturbation investigations and to improve relevant models.

The results show that an application of the multifrequency radiometric set makes it possible to obtain an additional information to explain the SAR image features of sea surface agitated by rain.

6. REFERENCES

[1] D.Atlas   Footprints of storms on the sea: A view from spaceborne synthetic aperture radar. J. Geoph. Res.,v.99,No.C4, pp.7961-7969, April 15,1994.

[2] P. Sobieski, L. Bliven, H. Branger, J.P.Giovanageli Experimental comparison of scatterometric signatures from a water surface agitated by wind and artificial rain IGARSS'93 - digests, Tokyo, Japan, August 18-21, 1993, v. I, pp.240-242.

[3] T.M.Elfouhaily, B.Chapron, K.Kotsaros, L.Bliven, Microwave scattering distributions from a rain-roughened water surface: Measurements and Modeling. IGARSS94 - digests, Pasadena, USA, August 8-12, 1994, v. I, pp 785-789.

[4] W.Alpers, C.Melsheimer, C. Bruning, R.Schmidt Imaging of Ocean Waves by SIR-C/X-SAR over the North Sea and Atlantic. IGARSS'95 - digests, Firenze, Italy, July 10/14 1995, v.2, pp.1317 - 1319.

[5] M.G.Bulatov, G.A.Bolotnikova, V.S.Etkin, E.I.Skvortsov. Investigation of Microwave Scattering and Emission of Sea Surface Perturbations by Rain Conducted with Space "ALMAZ - 1" SAR and Shipborne Radiometers. IGARSS'95 - digests, Firenze, Italy, July 10/14 1995, v.1, pp.837-838.

[6] Irisov V.G.,Trokhimovsky Ju.G., Etkin V.S., The Radiometric Methods of Diagnostics of the Ocean. -In book "Distansionnye metody izuchenya okeana", Gorky, IPF AN SSSR, 1987, pp.34-59, (in Russian).

[7] Kutuza B.G., Smirnov M.T., Signature of rain microwave emission IGARSS'91-digests, Helsinki, Finland, June 3-6, 1991, v.1, pp.193-194.

[8] Valenzuela, G.R. Theories for the interaction of electromagnetic and oceanic waves - A review, Boundary Layer Meteorol. 13, 61-85, 1978

The Microwave Radar Signal Doppler Spectrum and the Problem of Ocean Surface Slicks Detection

Mikhail B. Kanevsky and Vladimir Yu. Karaev

Institute of Applied Physics, Russian Academy of Sciences
46, Uljanova str., Nizhny Novgorod, 603600, Russia
Tel.: 7 8312 384528, Fax: 7 8312 365976
E-mail: kanevsky@hydro.nnov.su

Abstract – The Doppler spectrum of microwave radar signal backscattered from the ocean surface at intermediate incidence angles ($15^0 \leq \theta \leq 25^0$) is considered. It is shown that Doppler spectrum form and shift at these incidence angles are very sensitive to appearance of the slicks on the ocean surface.

It is known that in case of backscattering of microwave radar signal from the ocean surface, the incidence angle interval $15^0 \leq \theta \leq 25^0$ is intermediate between the specular ($\theta \leq 15^0$) and the Bragg ($\theta \geq 25^0$) areas. If the incidence angle value lies within the mentioned interval both the specular and the Bragg parts are present in backscattered signal. Consequently, the signal Doppler spectrum also consists of two parts:

$$S(f) = \sigma_B^0 \hat{S}_B(f) + \sigma_{sp}^0 \hat{S}_{sp}(f)$$

where f is the temporal frequency, σ_B^0 and σ_{sp}^0 are the Bragg and the specular cross sections, relatively, and $\hat{S}_B, \hat{S}_{sp}$ are the spectrum form factors normalized to unity:

$$\int_{-\infty}^{\infty} \hat{S}_{B,sp}(f)df = 1$$

The formation of two partial spectra is influenced by different mechanisms. The Bragg part is formed by the motion of the resonant ripples in the field of orbital velocity caused by large ocean waves. Its maximum position is determined by the ripple phase velocity, as well as by correlation between the orbital
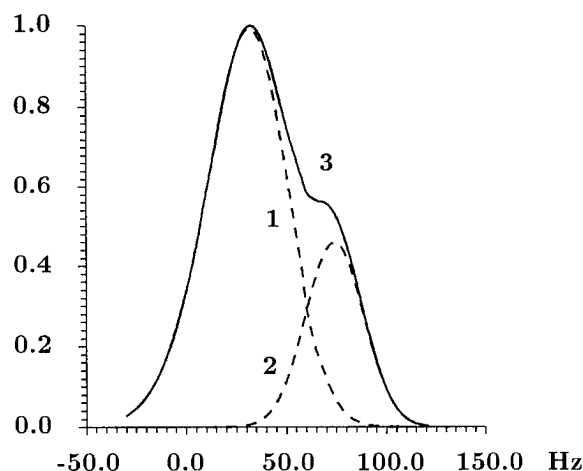
Fig.1. The Doppler spectrum of X-band ($\lambda = 3.2cm$) radar signal backscattered from undisturbed windsea at wind speed 6 m/s. The incidence angle $\theta = 23^0$, the azimuthal angle $\Phi = 180^0$ (upwind observation). The dushed curve 1 is the Bragg part of the spectrum, the dushed curve 2 is the specular one, and the solid curve 3 is the spectrum-sum (full spectrum).

velocity and the tilts of large waves which modulate the amplitude of backscattered signal [1]. As to the specular part, it is formed by the motion of specular points on the large-scale surface. This motion is closely connected with the phase velocity of large ocean waves. (The detailed consideration of specular spectrum parameters can be seen in [2].)

Due to the difference between the values of the large wave phase velocity and the orbital velocity the maxima of the partial spectra are displaced from each other and the spectra are not fully overlapped, as a rule. In Fig.1 the
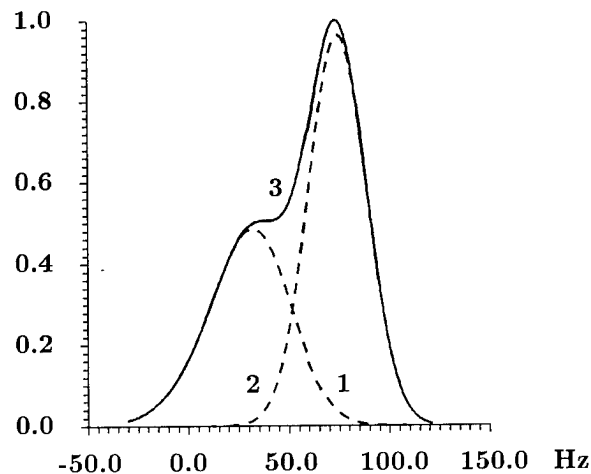
Fig.2. The same that in Fig.2 but at presence of the slick which causes the cross section decrease by 4 dB.

partial spectra and the spectrum - sum for the X-band radar signal are shown. These spectra are calculated for the case of fully developed windsea which is described by the JONSWAP ocean wave spectrum model added with directional factor [3].

The radar platform is assumed to be stationary, the incidence angle $\theta = 23^0$, the azimuthal angle, i.e., the angle between the radar wavenumber horizontal projection and the direction of the ocean wave propagation $\Phi = 180^0$ (upwind observation), the wind speed value is 6 m/s.
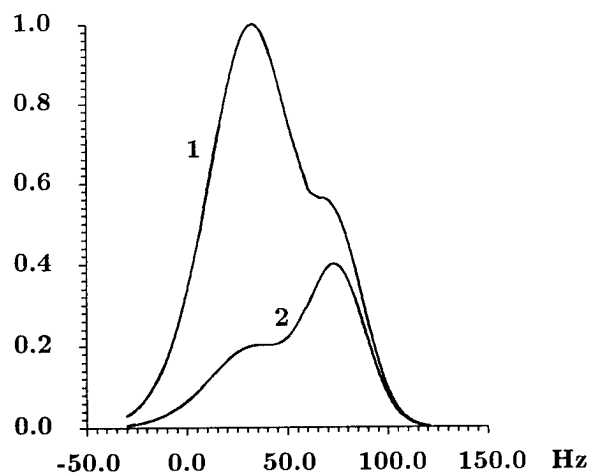
Fig.3. The full spectra for undisturbed windsea (curve 1) and windsea disturbed by the slick (curve 2); all the parameters are the same as in Fig.1 and Fig.2. Here the difference in reflectivity in two cases is taken into account.

Here the Bragg part of cross section exceeds the specular one approximately by 5 dB.

If a slick on the ocean surface appears the Bragg scattering decreases and the spectrum of backscattered signal changes strictly, the correspondent situation is shown in Fig.2. It is assumed here that the specular part of backscattering remains the same, whereas due to the decrease of the Bragg part the full cross section decreases by 4 dB [4]. It is seen that the resulting spectrum changes its form and is shifted approximately by 50 Hz. Really the effect must be even more pronounced since the slick causes some increase of specular backscattering due to the increase of the effective Fresnel coefficient which accounts the ripples influence on the specular backscattering [5]. However, the latter effect is not studied qualitatively yet.

In Fig.3 the solid curves from Fig.1 and Fig.2 are plotted with the difference between the cross section values in two cases taken into account. It is seen that both cross section change and Doppler spectrum form and shift changes are well pronounced. Nevertheless, it should be noted that unlike cross section Doppler spectrum form and shift are not influenced neither by fluctuations of water temperature and salinity nor by radar power stability.

REFERENCES

[1] M.B.Kanevsky and V.Yu.Karaev. "Spectrum of a radar signal backscattered from sea surface" (in Russian). Izv. Vyssh. Ucheb. zav., ser. Radiofizika, v.36, N1, pp.3-15, 1993.

[2] M.B.Kanevsky and V.Yu.Karaev. "On the problem of radar determination of the ocean state parameters", unpublished.

[3] C.Bruening, W.Alpers, and K.Hassellmann. "Monte-Carlo simulation studies of the nonlinear imaging of a two dimensional surface wave field by a synthetic aperture radar", Int. J. Remote Sensing, Vol.11, No 10, pp. 10,695-10,727, 1990.

[4] J.W.Johnson and W.F.Croswell. "Characteristics of 13.9 GHz radar scattering from oil films on the sea surface", Radio Sci., v.17, N 3, pp.611-617, 1982.

[5] G.R.Valenzuela. "Theories for the interaction of electromagnetic and oceanic waves - a review", Boundary Layer Meteorology, 13, pp.61-85, 1978.

Remote Sensing of Ocean Surface in the Frontal Zone

Igor Lavrenov
Arctic and Antarctic Research Institute
St.Petersburg, av. Bering 38, Russia, 199397
Ph: (007)- 812-352-36-04, Fax: (007)- 812-352-26-88, E-mail: Lavren@aari.spb.su

In remote sensing of ocean the study of wind wave field is of interest in its own right, since in a number of cases its spatial inhomogeneity may serve as an indicator of the state of the ocean surface layer - the existence of vortices, fronts, internal waves, surfactant concentration, etc. Wind-driven waves vary under the influence of inhomogeneous flows, which indicates the presence of flows [1,2]. Therefore, the nature of the spatially inhomogeneous spectrum of waves can be the initial information for determining the surface flow velocities [5,6].

EXPERIMENTAL RESULTS

The purpose of the aerial survey was to study the structure of the water flow in a strait between two islands. The aerial survey was subdivided into two types: a survey of the water surface of the strait, and survey of the flows by a float method [7]. The strait was covered by parallel routes across the strait with both ends tied into the island. This allowed us to obtain the spectra of the sea surface image by using the well-known optical method [3,8]. Images of the same part of the sea made it possible to obtain well-transmitted features of the waves and the flow nature. The choppy water regions, foam bands, etc. were clearly evident in the region of the frontal zone.

Current surveys were made by routes along direction, crossing the strait at its narrowest part, which is about 22 km wide. The floats were dropped about every 500m, and then twice with an interval of 15 to 20 minutes a survey was made of the entire "chain" of float. After survey the materials were processed with the well-known procedure in [8], vector schemes were obtained for the movement of the floats for each route. The scheme of the flows shown that value of the flow velocity value was small on the right (0.2 to 0.3 m/s) and large (1.3 to 1.6 m/s) on the left from some boundary. The spatial change in the flow velocity occurred quite sharply in a relatively narrow region, and it corresponds to the position of the front along the strait seen on the camera output. This was the line on which the whitecaps are concentrated, and there was strong wave breaking.

As the boundary between the end of flows was approached, the wind waves change on the following way. On the right side, far from the boundary, a system of ordinary two-dimensional wind driven waves was observed. Fourier spectrum obtained from the image of the water surface is given in Fig.1a as isolines of the intensity on the plane for the wave number k and angle φ (φ - is the angle between the wave vector and a chosen direction). Here it is possible to define a rather clearly of system of wind waves, whose energy-bearing maximum corresponds to a wave of length $\lambda \approx 8.5$ m. The general direction of wave propagation makes an angle $\varphi \approx 160'$ with the horizontal axis across the current flow, which approximately agrees with the direction of the wind velocity, whose magnitude was 5-7 m/s. Near the frontal line the waves consisted of the several system of waves. Figures 1b shows the spectrum at a point located nearer to the front line. It is possible to distinguish two systems of waves whose propagation direction differ by about 120^0. Fig. 1c represents the wave spectrum in the immediate proximity of the frontal zone, where it is difficult distinguish any wave systems with a clear propagation direction. The angular distribution for the waves in the frontal zone is nearly isotropic. Here an intensive choppy water and rips was observed. To the left of the boundary there was clearly seen a system of typical two-dimensional waves propagating to the left. The spectrum (Fig. 1d), once again clearly shows one system of waves, with its direction of propagation making an angle close to 180^0 with the horizontal axis across the current flow.

a	b	c	d
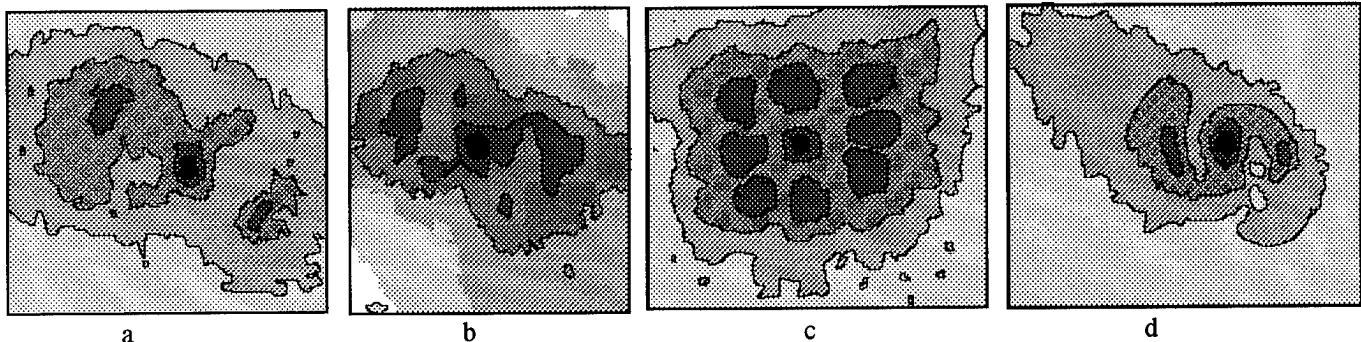
Fig.1 Spectrum of the water surface image

FORMULATION OF THE PROBLEM

To describe the wind wave evolution on nonuniform current we use the spectral wave action balance equation:

$$\frac{d N(\vec{k},\vec{r},t)}{dt} = \frac{\partial N}{\partial t} + \frac{\partial N}{\partial \vec{k}}\frac{d\vec{k}}{dt} + \frac{\partial N}{\partial \vec{r}}\frac{d\vec{r}}{dt} = G \qquad (1)$$

Where $N(\vec{k},\vec{r},t)$ - is the wave action spectral density which depends on the wave vector $\vec{k} = \{k_x, k_y\}$, frequency ω , horizontal co-ordinates $\vec{r} = \{x,y\}$ and time t. G is source function, consisting of physical mechanisms forming wave spectrum. The source function G presents three components: $G = G_{in} + G_{nl} + G_{ds}$, where G_{in} is wind input, G_{ds} is dissipation of the wave energy, G_{nl} - non-linear energy transfer. The characteristics of (1) are the relations:

$$\frac{d\vec{r}}{dt} = \frac{\partial \omega}{\partial \vec{k}}, \quad \frac{d\vec{k}}{dt} = -\frac{\partial \omega}{\partial \vec{r}}, \quad \frac{d\omega}{dt} = \frac{\partial \omega}{\partial t} \qquad (2)$$

where $(\omega - \vec{k}\vec{U})^2 = \sigma^2$, $\sigma = \sqrt{gk}$, $\vec{U}$ is the horizontal flow velocity vector which is a function of $\vec{r}$ and t. Equations (2) describes the propagation of wave packets at the nonuniform current.

In the general case, the problem of wave spectrum determining reduces to the solution of (1)-(2) for the corresponding initial and boundary conditions. To solve the evolution problem we have to define source function G. It is possible to get the value of wind input G_{in} and dissipation G_{ds} functions by using well-known results [4]. But to use the same approximation of non-linear energy transfer function is invalid because it is obtained only for some simple cases of the wave spectrum. That is why we have to compute non-linear transfer by using exact integral which is valid for any form of spectrum. For this purpose we will use the algorithm [5]. The energy spectrum for waves propagation into the computed region is given at the initial boundary as the usual approximation of wave-number angular spectrum [4].

SOLUTION OF THE PROBLEM

In order to solve the problem we use the semi-Lagrangian algorithm which is an combination of the ray method and interpolation algorithm. The method was proposed in [7] for the case of swell propagation at the global distance on spherical surface of the ocean. Now the method is extended to solve equation (1) for the case of wave propagation on nonuniform current and with non-zero source function.

So to construct the complete spectrum at some point $\{x, y\}$ it is necessity to collect here the rays along which all possible wave packet propagate to the point. For this propose we have

to solve (2). Here it is necessary to take into account not only those harmonics which propagate directly from the initial boundary, where their initial values are given, but also those wave packet which at first were able to be reflected from the horizontally non-uniform flow, and only then reached the point $\{x, y\}$. To simplify the problem solution we consider the case stationary of spectrum evolution across the flow velocity $\vec{U} = \{0, U(x)\}$ varying only along the x axis. In such case the component of the wave vector k_y remains constant along the trajectory $k_y = k\sin\varphi = k_0 \sin\varphi_0$. A second integral of the motion is the constant of the frequency ω . These conditions are sufficient to determine the wave number k and the angle φ along the wave trajectory depending on the flow velocity $U(x)$. We note that in the formal case $|\sin\varphi_0| = |\sin\varphi \, k/k_0| \geq 1$ the parameters of the wave packets turn out to be indeterminate in some region, which is the caustic shadow zone [6,7]. In these grid points we admit corresponding spectrum value to be equal zero.

INTERPRETATION OF THE RESULTS

By using the numerical algorithm we calculate the values of the slope spectrum at the different points of the flow velocity profile for the initial general propagation direction $\varphi_0^0 = 160^0$. The results are given on the $\{k, \varphi\}$ plane in the form of isolines for the spectrum of the slopes $S(k,\varphi)k^2$, normalised to its maximum. Note [3] that this relative value is comparable to the optical spectra of the surface image (Fig.1). Thus, Fig.2a gives the spectral density to the right of the boundary between the two flows, where the flow velocity is $U \approx 0.3\,m/s$. As we can see, in the two-dimensional spectrum two clearly defined maxima are observed. The first one is related to the direction of propagation for the initial waves making an angle $\varphi \approx 160^0$ with the axis across the current flow, the second one makes an angle of $\varphi \approx 40^0$. It corresponds to the reflected waves. The isolines of the energy-bearing components of the reflected waves indicate a bending clockwise for wave numbers greater than the wave number the spectral maximum. The angular distribution of the energy for the reflected waves is narrower. A part of spectral components did not undergo reflection and passed to the region of increased flow velocities. Its spectrum is presented at the Fig.2b.

Thus in the experimental and theoretical spectra, we trace a number of common features, which indicates the agreement of the computational results from the suggested model with the field observational data.
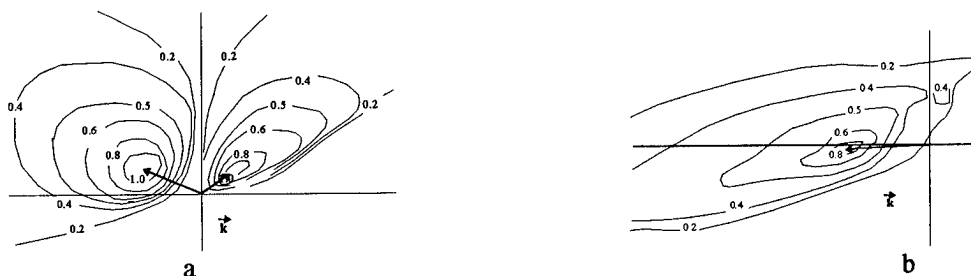
Fig.2 Theoretical spectra of the sea surface slope in two points with different valuye of current speed.

It should be noted that due to the action of dissipation the reflected wave are not able to be observed at large distance from the frontal zone because they propagate against the wind speed. Estimation of deferent source terms in (1) shows that because of the small horizontal scale the role of weak non-linear wave interaction (1) is not so important here as in the simple case of wind wave generation. It makes spectrum smoother then without its action. The most important mechanism in forming the observed wave behaviour is wave interaction with non-uniform current and wave breaking effect.

DISCUSSION

On the basis of the maximum in the direction of the reflected waves spectrum and its corresponding part in the spectrum for the incident waves, it is easy to evaluate the direction and magnitude of the flow velocity on which this reflection occurred. Thus the direction of the flows is determined from the direct reflection conditions, i.e., $\tilde{\varphi} = (\varphi_1 + \varphi_2)/2 \approx 90^0$, where φ_2 is the direction of propagation for the reflected waves, $\varphi_2 \approx 40^0$, $\varphi_1 \approx 140^0$ is the direction of their corresponding incident waves. The magnitude of the velocity at the reflection point for the waves is evaluated as $\Delta U = \sqrt{g/k}(1 - \sin\varphi_1^{1/2})/\sin\varphi_1 = 1.2$m/c. As we see, these estimations are in good agreement with the actual observations, although the accuracy in determining the latter is in the 25% range, which is mainly related to the discreteness in the representation of the spectra, their variability, and the error in determining the angle φ. Figure 2b gives the computed spectrum (Fig. 1d as its corresponding to experimental spectrum) left on the boundary between the two flows, where the difference in the flow velocities reaches $\Delta U \approx 1.2$ m/s. Here the angular spectrum has become narrower. A single general direction is clearly defined that it is oriented across the flow, and the length of the basic system has been increased by nearly a factor of two.

Thus the frontal zone as boundary between two flows is a distinctive wave filter, on which reflection of part of the

spectral components occurs. These components, being superimposed on the waves incident at the boundary, produce the choppy water, In this case, there is strong breaking of waves going in different directions, leads to the isotropic nature of the angular distribution for the spectrum. This is seen the spectra for an agitated surface (Fig.1c). That part of the spectral components, which does not undergo reflection, propagates in fact across the flow and represents a quaziregular system of waves with a clearly defined direction for its own propagation.

REFERENCES

[1] V.A. Dulov and V.N. Kudryavtsev. Imaging of flow inhomogeneities in the state of the ocean. Morsk. Gidrofiz. Zhurn. N 4, 3-13, 1989.

[2] S.A.Grodskiy, V.A. Dulov, V.N. Kudryavtsev and O.V. Shulgin. Experimental research on the evolution of wind waves on inhomogeneous flows. Morsk. Gidrofiz. the Zhurn., N 5, 36-47, 1989.

[3] V.A. Grushin, Yu. L. Ilín, A A Lazarev et al. Synchronous optical and contract studies of the spatial-spectral characteristics of wind-driven waves. Issled. Zemli iz kosmosa, N 2, p.55 -67, 1986.

[4] G.J.Komen et al. Dynamics and modelling of ocean waves. Cambridge University press, 1994, 532p.

[5] I.V.Lavrenov Nonlinear interaction of waves in overfall. Izvestia AN SSSR. Fizika atmosfery i okeana, 27 , N 4, p.438-447, 1991

[6] I.V.Lavrenov, T.V.Belonenko, Yu.D.Sharikov The spatial non-homogeneity of wind wave field as a measure of flow velocity within oceanic frontal zone. Izvestia RAS Phizika atmosfery i okeana, 28 , N 2, p.185-195, 1992

[7] I.V. Lavrenov and J.R.A.Onvlee A comparison between the results of wave energy propagation in the WAM model and the interpolation-ray method.- Meteororolia i gidrologia, N3, 59-76, 1995.

[8] Metody isucheniya morskikh techeiy s samoleta (Methods for studying marine flows from an aircraft) General editor V.G.Zdanovich. Moskva, Iad-vo AN SSSR.1964

The Weather Visualizer: A Java Tool For Interactive Learning

Steven E. Hall, Mohan K. Ramamurthy, Robert B. Wilhelmson, Joel Plutchak,
David Wojtowicz, and Mythili Sridhar

Department of Atmospheric Sciences
University of Illinois at Urbana-Champaign
105 S. Gregory Avenue
Urbana, IL 61801
hall@uiatma.atmos.uiuc.edu

INTRODUCTION

The growing accessibility of the Internet has opened a vast new world of possibilities for K-12 and higher education. From the first version of NCSA Mosaic to current Java-capable web-browsers, these technologies are slowly enhancing the power of the Internet more than ever before. However, this is an ongoing process, and one that is far from being completed. For example, a vast majority of the Web servers on the Internet can be categorized as *information servers* that simply provide access to a collection of documents / products / data / tools to a general audience. Another notable weakness of the so-called first generation Web servers is that they are by and large providers of static information, lacking the ability to let users interact with the information they browse. Nor is the information customized for the end user. This lack of interactivity, dynamic generation and customization critically hinders the effective use of the Web in a classroom setting [2].

In an effort to address this need, the CoVis-Horizon group in the Department of Atmospheric Sciences (DAS) at the University of Illinois Urbana-Champaign (UIUC) has developed a web-based visualization tool known as *The Weather Visualizer* (http://covis.atmos.uiuc.edu/covis/visualizer/) that allows users to generate customized weather images from real-time and archived weather data. This resource is available on our environmental sciences web-server *The Daily Planet* ™ (http://www.atmos.uiuc.edu/). By pointing and clicking, the user has complete control over which features appear on the final product. Hypermedia helper sections have also been incorporated to introduce and explain the importance of meteorological features found on the weather images. *Java*™ development of the Weather Visualizer has significantly increased the user's power to manipulate the data without placing extra strain on the server or having to repeatedly send requests across the network. It is our hope that the Weather Visualizer, coupled with other valuable Internet resources and curriculum, will support the creation of a learning environment, where the user, or student, becomes more actively involved in the learning process through increased interactivity with the data sets.

THE WEATHER VISUALIZER

Several faculty and staff members from UIUC are participating in an NASA-funded project called HORIZON, which seeks to enable greater public access to earth and space science data through enhancements of and innovations in World Wide Web technology [4]. In addition, UIUC is involved in an NSF-funded called CoVis which focuses on; 1) project enhanced science learning (PESL), 2) collaboration and 3) scientific visualization, as a means for creating learning communities and transforming science education as we know it [1]. An important UIUC contribution to these projects was development of the Weather Visualizer; an Internet visualization tool that allows public access to real-time and archived weather data. Users generate customized weather images from a point-and-click interface, increasing the interactivity with the computer by giving the user complete control over which features appear on the final product.

The introductory document of the Weather Visualizer (Fig. 1) consists of a graphical panel of six main categories of weather topics (e.g., Surface Observations, Upper Air Observations, Upper Air Soundings, Radar Summary, Satellite Imagery, and Forecast Data).
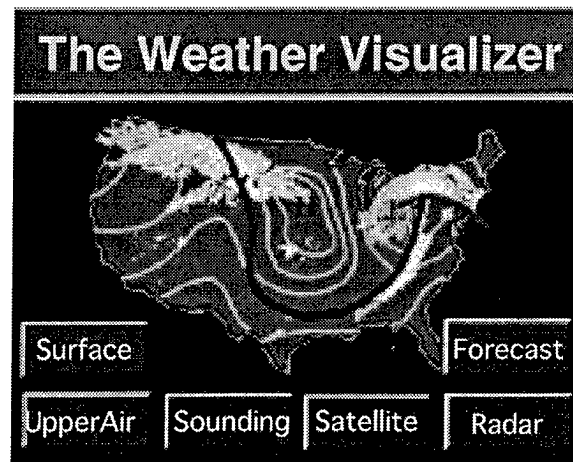
Figure 1. The Weather Visualizer main menu.

We kept several design criteria in mind while developing the Weather Visualizer; 1) to provide reasonably fast access to customized requests, 2) to offer a manageable number of data options to choose from, and 3) to implement this tool in a user-friendly environment accessible to a wide variety of hardware platforms.

Each main section contains one or more subsidiary HTML (HyperText Markup Language) forms or documents that present choices and solicit input as to which meteorological parameters to display. When selection of the parameters is completed, the form is processed, resulting in the return of the image, plot, or textual data requested. Processing of the HTML forms is done using the Common Gateway Interface (version 1.1) in the form of Perl scripts. These scripts interpret the user input from the form, translate that input into the appropriate actions, and format and return custom HTML documents that present the results of the request. Typical end products would be a map of US surface observations, radar echo summary, and frontal analysis superimposed on an infrared satellite image background; a table of forecast model output statistics; or a Stuve thermodynamic diagram. Much of the underlying processing is performed by programs from the WXP package, which was developed at Purdue University and is distributed by the Unidata Project. The server itself runs an up-to-date version of the HTTP daemon developed at the National Center for Supercomputing Applications at the University of Illinois.

An additional feature of the subsidiary pages and forms is the generous use of helper sections, which are accessible by simply clicking on the word in question. For example, if the user clicked on "Frontal Analysis", instructional materials comprised of descriptive text and images would be accessed that introduce the various types of fronts, clarify how to identify fronts on weather maps, and explain their importance in interpreting the weather. The purpose of these helper sections is to equip the user with the knowledge and skills required for valuable and correct interpretation of the images [1]. These resources are a part of a larger collection of instructional modules known as *An Online Guide to Meteorology* (http://covis.atmos.uiuc.edu/guide/). These modules effectively use multimedia technology to introduce and discuss essential concepts in atmospheric sciences (e.g., Pressure, Forces and Winds, Weather Forecasting and Severe Storms).

THE WEATHER VISUALIZER IN THE CLASSROOM

Several faculty from UIUC, along with project partners at Northwestern University and the Exploratorium museum in San Francisco, are participating in an NSF-funded project known as "Collaborative Visualization" or CoVis

(http://www.covis.nwu.edu/). CoVis provides students with the opportunity to work and learn in an environment consistent with that of the scientific community [1]. In this process, we have worked with teachers in the development of activities to transform their classrooms from traditional teacher-centered classes to project-enhanced classes in which students learn about science through personal and group inquiries [3].

With the CoVis community encompassing nearly fifty high schools and elementary schools across the US, UIUC's involvement in CoVis provides a practical testbed for the Weather Visualizer in an everyday classroom environment. In addition to the access of current weather images for classroom discussion, the Weather Visualizer was an integral part of a CoVis Interschool Activity (CIA) that focused on winter storms. In a step-by-step manner, students used instructional materials and weather data to investigate the role of low-level moisture, air masses, and other features in the development of snowstorms.

To successfully complete the CIA, students were asked to construct weather scenarios from archived weather data accessed through the Weather Visualizer. Feedback from participants revealed that the Weather Visualizer, which gave the students complete control of the weather images they accessed, was a highlight of the curriculum. These and other CIA's are found on the *CoVis Geosciences Web Server* (http://www.covis.nwu.edu/Geosciences/index.html), which contains a collection of project based activities that provide teachers with practical applications for data, student mentoring, and other Internet resources [2].

From these activities, we realized there are certain limitations to using the Web to present customized data. Current HTTP daemons seem to be optimized to handle relatively short-lived requests that are not CPU-intensive. However, certain underlying operations of the Weather Visualizer entail fairly intense computations so that initially, a couple dozen simultaneous requests for such data slowed the server down to unacceptable levels. These limitations prompted modifications in the design and implementation of the Weather Visualizer. To this end a few tasks, such as the remapping of satellite imagery as the data was received, substantially raised the number of requests that could be processed simultaneously, while still preserving the interactivity and customizable nature of the Visualizer.

The classroom testing raises an important aspect of the Web, the issue of scalability. In current Web architecture, the bulk of the compute power on a client is left untapped when accessing a server. If the number of clients keeps increasing disproportionate to increases in server capacity, then the clients at some point will have to share in the workload for the load to be sustained.

A *JAVA*™ TOOL FOR INTERACTIVE LEARNING

The recent introduction of the Java environment by Sun Microsystems shows considerable promise in alleviating such scalability-related bottlenecks. In a Java environment, programs, or "Applets", which are written in a C++-like Java language, can be executed on any client that is running a Java-based Web browser. The current Java version (Fig. 2) of the Weather Visualizer (http://covis.atmos.uiuc.edu/java/) provides access to a selected set of meteorological data for the United States (e.g., surface observations, satellite imagery, radar echo summary, frontal boundaries, isotherms and isobars).
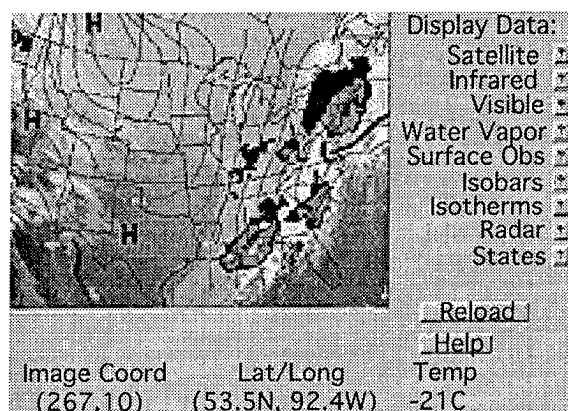
Figure 2. Top half of Weather Visualizer Java page.

Java applets that support highly interactive images are distributed and run locally on the user's machine. Users are able to instantly add and remove various weather fields with a simple click of a button. Since this is accomplished without repeatedly sending requests across the network, the Java environment also relieves some of the strain placed upon Web Server computers.

Several atmospheric variables are computed and displayed on the client side by simply moving the cursor over the image. These include latitude/longitude coordinates, calibrated temperature values from infrared satellite imagery, and reflectivity values from visible satellite imagery. In addition, by pointing and clicking in the weather image, the user is able to access the latest model forecasts from the National Centers for Environmental Prediction (NCEP) for that particular location. This information is also displayed in graphical format for easier interpretation. Finally, hypermedia helper sections are accessible for the available features by simply clicking the help button next to the item in question.

During the coming months, innovative developments of the Weather Visualizer will lead to increased interactivity between user and computer. Since Java distributes a significant portion of the workload to the client, this tool could also be used in schools with slower network connections. As Java becomes more accessible in the classroom, students will have faster and more flexible interaction with meteorological data than previously available using the World Wide Web.

CONCLUDING REMARKS

The challenge of providing interactive educational resources via the Internet is growing. A great number of Web servers provide access to static products (images and text), providing very little interactivity for students. In an effort to address this need, the CoVis-Horizon group at UIUC has developed the Weather Visualizer, a web-based visualization tool that allows users to generate customized images real-time and archived weather data. Hypermedia instructional pages provide valuable content materials, introducing the meteorological features available in the Weather Visualizer while equipping the student with the knowledge necessary for correct interpretation the images themselves. We hope that the Weather Visualizer will become a valuable tool in the creation of an interactive learning environment, both inside and out of the classroom. Java-development of the Weather Visualizer will allow students to actively work with the weather data, instantly adding or removing data fields with a click of a button, promoting an effective and efficient use of the Web in a classroom setting. Much of this can be accomplished without having to repeatedly go over the network and thus reduces the load on the server itself, allowing it to provide weather data to a much larger audience.

REFERENCES

[1] Hall et al., "The Design and Implementation of Multimedia Web-Based Instructional Modules in K-12 Education," Proceedings of the Fifth Symposium on Education. Atlanta, Georgia, American Meteorological Society, 1996.

[2] Ramamurthy et al., "CoVis Geosciences Web Server: An Internet-Based Resource for the K-12 Community," Proceedings of the Fifth Symposium on Education. Atlanta, Georgia, American Meteorological Society, 1996.

[3] Ramamurthy, M.K. and R.B. Wilhelmson, "CoVis: A National Science Education Collaboratory," Proceedings of the Fourth Symposium on Education. Dallas, Texas, American Meteorological Society, 1995.

[4] Wojtowicz et al., "IICE: Bringing Interactivity to Image-Based WWW Products." Proceedings of the Fifth Symposium on Education. Atlanta, Georgia, American Meteorological Society, 1996.

Lessons Learned from Using GIS/RS as an Integrative Tool for Interdisciplinary Learning and Teaching in a Senior-Level Capstone Course on Global Change at Westminster College of Salt Lake City

Robert E. Ford, M.P.H., Ph.D
Chair International Studies
Westminster College of Salt Lake City
1840 South 1300 East
Salt Lake City, UT 84105
Tel. 801-488-1655 FAX 801-466-6916
E-mail: r-ford@wcslc.edu
(Econet): rford@igc.apc.org

OVERVIEW OF THE ESSE PROJECT

Westminster College of Salt Lake City (WCSLC) was awarded in late August 1995 a grant to participate in the USRA (Universities Space Research Association) Cooperative University-based Program in Earth System Science Education (ESSE) along with twenty-one new university members within the consortium. The grant provides about $75,000 over 5 years for interdisciplinary curriculum development and scientific exchange between students and faculty across the US focusing on earth system science and global environmental change. A particular focus is on experimentation with new electronic and multimedia tools for teaching about global change, e.g. the World-Wide-Web on the Internet, GIS/RS and other computer simulation and modeling tools, e.g. STELLA.

Two interdisciplinary courses being developed by Westminster College will be the primary venues for testing and diffusing these innovations. An introductory course entitled: GEOL/BIOL/HON 300 *Earth Systems and Global Environmental Change* and a senior-level course: GEOL/BIOL/HON 400 *Methods of Modeling and Visualizing Global Change*. News about the ESSE collaborating institutions and courses, electronic materials produced, evaluation findings, and other resources will be made available on the Web via the USRA/ESSE server and homepage

URL: *http://www.usra.edu/esse/ESSE.html.*

Several departments at Westminster College collaborate with this interdisciplinary program including the School of Education, Arts and Sciences (via the Physical Sciences Teaching Major), Computer Science, Biology, and Environmental Studies. The Principal Investigator (PI) is Dr. Robert E. Ford, the Kim T. Adamson Chair in International Studies at Westminster College (e-mail: *r-ford@wcslc.edu*).

COLLABORATORS

Dr. Ford is assisted directly in course and lab instruction by James Hipple (e-mail: *james.hipple@geog.utah.edu*) a doctoral student in the Department of Geography at the University of Utah. The University of Utah is an official collaborator with WCSLC on this project--James Hipple is also involved in the design, testing and management of the online Web materials (see following URLs):

http://www.usra.edu/esse/schools/wcslc/wcslc.html

http://www.usra.edu/esse/schools/wcslc/g300/g300hp.html

http://www.geog.utah.edu/~jhipp/models.html

The ESSE project also utilizes and tests new "active learning" modules prepared and tested by the AAG (Association of American Geographers) and the CCG2 (Commission on College Geography II) project which is funded by the National Science Foundation. This project links many other departments of geography across the US to actively test and diffuse active learning modules within a broader series entitled: *Developing Active Learning Modules for Teaching about the Human Dimensions of Global Change* (HDGC). This project is coordinated by Susan Hanson at Clark University (contact: *CCG2@vax.clarku.edu*).

The above project is also closely involved with the new AAG - HDGC / SG (Association of American Geographers, Human Dimensions of Global Change Specialty Group). See that homepage at:

URL: *http://www.geog.utah.edu/~hdgcsg/index.html*

OBJECTIVES OF THE ESSE PROJECT

The central objective of the ESSE program is to broaden and accelerate the development nationally of an academic focus for earth system science and to establish a forum and activities that will motivate and strengthen interdisciplinary earth science education in areas needed to advance NASA's Mission to Planet Earth and other global change research initiatives. Specific objectives include:

- Advance cooperative NASA/university education and research in earth system science.

- Attract students and professional scientists to earth system research and education.

- Provide incentives to stimulate scientific exchange among departments within universities, among universities, and between universities and NASA.

- Increase public awareness of the interactive nature of the earth system.

A key element of the ESSE Program is the development among scientists and aspiring students of the team skills and interdisciplinary perspectives needed for global change research programs. This is accomplished in ESSE through introducing unique educational opportunities and perspectives in the undergraduate curriculum. Under this program students will be introduced to integrated earth system concepts, and will benefit from interaction with visiting faculty and NASA scientists.

RELATED WEB LINKS

Westminster College of Salt Lake City:
   http://risky.wcslc.edu/

Dept of Geography, University of Utah:
   http://www.geog.utah.edu/geography/index.html

AAG Homepage: *http://www.aag.org/index.html*

AAG- HDGC Specialty Group:
   http://www.geog.utah.edu/~hdgcsg/index.html

THE SENIOR-LEVEL CAPSTONE COURSE

The senior-level capstone honors course: GEOL/BIOL/HON 400 *Methods of Visualizing and Modeling Global Change* introduces students and faculty to the tools of GIS/RS (Geographical Information Systems and Remote Sensing) as a new way of "integrating" knowledge graphically and visually in both the sciences and humanities.

Key Objectives:

- Introduce students to the systems approach to learning and doing research in science and technology.

- Develop basic competence in the use of "integrative" computer modeling and mapping tools such as GIS (IDRISI & ArcView).

- Learn-by-doing--in a team setting--how science is done: hypothesis testing and definition, data analysis and collection, critical thinking and written communication / presentation.

- Understand better how the processes of land use / land cover change in their *local* community relates to and impacts *global* environmental change.

The course will be offered in an intensive field course mode during a special session--May Term 1996--when students can focus on one course alone over an entire month without distractions. The class is limited to eight students and provides four semester credits = 1 credit lecture / 3 credits - lab and field activities. Formal lab hours are concentrated over Tuesdays - Thursdays (Mondays and Fridays and even possibly one or two weekends will be used for field trips and community fact-finding).

The only prerequisites are that students must have completed the LE Distribution courses in: Life Sciences and Physical Sciences, as well as have fulfilled the basic skill requirements in: Computer Literacy and Mathematics (or their equivalent). In addition students are encouraged to have completed the ESSE introductory course: BIOL/GEOL/HON *300: Earth Systems and Global Environmental Change* (4 credits) or its equivalent, e.g. Geology, Physical Geography, Environmental Biology. The main criterion, though, is a strong interest in pursuing interdisciplinary study and a willingness to work hard in a team setting--one that bridges the sciences and humanities as well as applied disciplines.

Targeted students are those in the college-wide honors program from various disciplines: business and management information systems, computer science, ecology, biology, physics, education, nursing, and environmental studies. We are particularly targeting students who may pursue K-12 teaching as a career--those students in "pre-service" teachers training programs, e.g. the Physical Sciences Teaching Major.

Students will be teamed-up with faculty from several departments--who also want to learn GIS/RS technology and who have an interest in inter-disciplinary study--to tackle a problem or issue in the local urban or rural area that can be analyzed effectively with GIS/RS. One of the implicit goals is

to get faculty and students working together in manner that is more egalitarian and informal--not the traditional teacher-student role--to encourage innovation, sharing, personal growth and integrative learning.

Each year the problem chosen will change depending on student and faculty interest as well as the expertise and support of collaborators in the community. Field and fact-finding trips will take students to commercial and public agencies using GIS/RS technology so they can see how the "real world" uses it for planning, management, and policy-making. One of the primary community resources will be the statewide Utah AGRC (Automated Geographic Resource Center). During the course teams will also establish links with public interest groups and agencies concerned with the problem/issue chosen for study. Another goal is not only to learn but to serve the community.

THE COURSE PROBLEM FOR MAY 1996

In May 1996 the local problem selected was *urban growth/land use change and its impact on biodiversity* within the city limits of Salt Lake City, particularly within adjacent canyons along Emigration Creek which comes out of the nearby Wasatch Mountains and passes through the WCSLC campus.

BRIEF COURSE OUTLINE / SCHEDULE / TOPICS

Week 1-2   How Humans Alter the Earth's Land Use and Land Cover: What are the Implications?

Primary Resource:

- CCG2 Active Learning Module by Susie Moser and others. *1995. Counting Our Blessings--Guessing Half the Time: Land Use/Land Cover Changes in the Ways of Human Driving Forces.* Clark University, Worcester, MA.

Other Resources and Activities:

- Introduction to Basic Remote Sensing & GIS using the GEOSCOPE Scenario: *Remote Sensing.[1]*

- Tutorials and exercises created for use with IDRISI and ArcView 2.1 (the primary GIS software utilized).

- CD-ROMs such as: *Utah GAP Analysis: an Environmental Information System* and *The UTAH SGID (Utah Geographic Information Database).[2]*

Week 3-4   Faculty-Student Project Implementation and graphical-visual presentation of results--see online materials at URL:

http://www.geog.utah.edu/~jhipp/models.html

OTHER SELECTED RESOURCE BOOKS[3]

Stanley Aronoff. 1995. *Geographic Information Systems: a Management Perspective.* WDL Publications.

Ian Burton, Robert Kates, and Gilbert White. 1993. *The Environment as Hazard.* Guilford Press.

Fred T. Mackenzie and Judith A. Mackenzie. 1995. *Our Changing Planet: an Introduction to Earth System Science and Global Environmental Change.* Prentice Hall.

Brian J. Skinner and Stephen C. Porter. 1995. *The Blue Planet: Introduction to Earth System Science.* John Wiley & Sons.

B.L. Turner II, et al. 1990. *The Earth as Transformed by Human Action: Global and Regional Changes in the Biosphere over the Past 300 Years.* Cambridge University Press.

SUMMARY AND CONCLUSIONS

Examples of the output and "lessons learned" will be presented at IGARSS'96 in Lincoln, Nebraska (May 27-31). Results will be literally "hot off the press" as the course's final day is the previous weekend. Though using GIS as an integrative tool is not new, what we hope to explore and illuminate is how to best use such a tool in the small liberal arts college environment as a mechanism for both teaching science and technology, but more important, how to excite students and faculty with the opportunity and challenge of being integrative.

---

[2] NBS (National Biological Service), the State of Utah (AGRC) and the College of Natural Resources, Utah State University, Dept of Geography and Earth Resources, Logan Utah 84322-5240 Tel. 801-797-3892.

[3] An excellent review of ESS textbooks has been reviewed online by the ESSE project (see "Results from a Short Survey of Textbooks Used by Earth System Science Educators" at URL: *http://www.usra.edu/esse/textlist.html*

---

[1] GEOSCOPE is a DOS-based CD-ROM multimedia learning resource sold/produced by LMSoft of Montreal, Canada. It was originally produced under the auspices of the Canadian Space Agency for UNCED.

Classroom Applications of Marine & Environmental Remote Sensing Data

LCDR M.A. Alfultis and LT M.R. Hicks
Department of Science
US Coast Guard Academy
15 Mohegan Ave.
New London, CT 06320
Phone: (860)444-8633
FAX: (860)444-8627
E-Mail: alfultis@dcseq.uscga.edu

Abstract -- The U.S. Coast Guard Academy teaches Remote Sensing as a capstone course to their junior and senior Marine and Environmental Sciences majors. Students apply knowledge learned in other courses toward the interpretation and analysis of marine and environmental satellite data. The classroom portion of the course first provides an overview of the theoretical aspects of determining geophysical properties from space, and then looks at how remote sensing can be used to study specific ocean and atmospheric processes including stratospheric ozone, phytoplankton, weather, ocean circulation, El Nino, fisheries, and polar sea ice. A lab curriculum also supports the classroom portion of the course. The Remote Sensing laboratory employs data from the Coastal Zone Color Scanner (CZCS), Advanced Very High Resolution Radiometer (AVHRR), Total Ozone Mapping Spectrometer (TOMS), and Special Sensor Microwave Imager (SSM/I). Future plans call for developing a more general classroom/lab curriculum which other educators can readily incorporate into their own classroom, to be placed on the World Wide Web (WWW) and eventually CD-ROM.

COURSE OBJECTIVES

The U.S. Coast Guard Academy teaches Remote Sensing as a capstone course to their junior and senior Marine and Environmental Sciences majors. Upon completion of this course, students will be able to:

1. Demonstrate a working knowledge of the physical radiation principles which form the foundation for measuring geophysical, biological, and chemical processes from space.

2. Comprehend the ability of airborne sensors in various parts of the electromagnetic spectrum to infer biological, chemical and physical processes in the ocean, the atmosphere, and on land

3. Comprehend the methods used to infer ozone concentration, phytoplankton pigment concentration, sea surface temperature, and sea ice concentration from spaceborne observations.

4. Gain a working knowledge on the use of basic image processing techniques to extract quantitative

information from various types of displayed satellite data.

5. Understand remote sensing terms commonly found in the science literature.

6. Gain an appreciation for the multi-disciplinary nature of remote sensing.

CLASSROOM PORTION

There are three goals or aspects of the classroom portion of the course. First, discuss in detail the physical radiation principles for remotely measuring surface processes including Planck's Equation for Blackbody Radiation, Stefan-Boltzman's Law, Wein's Displacement Law, and the Rayleigh-Jeans Approximation. Second, review the following topics which the students have discussed in previous science courses: stratospheric ozone, phytoplankton processes, weather, ocean circulation, El Nino, and fisheries. This review provides the students with the important context (biological, physical, and/or chemical) which they will need when interpreting the satellite data in class and lab. Finally, use satellite data to illustrate the above environmental processes. In this sense, the satellite data is the context/discussion tool to reinforce student comprehension of these environmental processes.

To emphasize the broad spectrum of satellite observations of environmental processes, the course is structured around the electromagnetic spectrum. Measuring ozone concentration using ultraviolet sensors is first discussed, followed by visual observations of phytoplankton pigment concentration, visual and infrared observations of weather systems, infrared observations of sea surface temperature, passive microwave observations of sea ice concentration, and finally active radar observations of sea surface topography and roughness. Again, each environmental process is first reviewed; the method used to study that process from space is discussed; and the satellite data is then examined.

LAB PORTION

There are two goals of the laboratory portion of the course. First, introduce the students to basic image processing techniques, and provide them with hands-on opportunities at applying various contrast and geometric enhancements to

enhance the visual impact of the satellite image for photointerpretation. Second, reinforce student understanding of the environmental processes discussed in class by providing hands-on opportunities to display, manipulate, and interpret satellite data.

Labs have been developed using Total Ozone Mapping Spectrometer (TOMS) Ozone Concentration Observations, Coastal Zone Color Scanner (CZCS) Phytoplankton Pigment Concentration Observations, Advanced Very High Resolution Radiometer (AVHRR) Weather and Sea Surface Temperature Observations, and Special Sensor Microwave Imager (SSM/I) Sea Ice Concentration Observations. Using the National Center for Supercomputer Applications' (NCSA) and the National Institute for Health's (NIH) public domain image display programs, students view animated sequences of satellite images on Macintosh computers to answer questions on the temporal and spatial variability of these oceanographic and atmospheric processes. All lab materials were developed at the Coast Guard Academy from public domain satellite data using public domain Macintosh programs. Examples of these materials will be presented.

FUTURE PLANS

Future plans call for developing lab activities for active radar observations of sea surface roughness and topography, visual and near infrared observations of land vegetation, and infrared and active radar observations of El Nino. In addition, developing a more general classroom/lab curriculum which other educators can readily incorporate into their own classroom, to be placed on the World Wide Web (WWW) and eventually CD-ROM.

A Model For Environmental Earth Science Module Design

Robert J. Myers (bmyers@cotf.edu)
James A. Botti (jbotti@cotf.edu)
Kimberly D. González (kdg@educ.umass.edu)
NASA Classroom of the Future
Wheeling Jesuit College, Wheeling, WV 26003
PH: (304)243-2388, FAX (304)243-2497

INTRODUCTION

The Exploring the Environment (ETE) project team develops problem-based learning modules that engage high school students in authentic environmental Earth Science situations such as biodiversity, sustainability, and deforestation. One of the overarching objectives is to create a multidisciplinary learning environment that emphasizes active student learning, teamwork, and authentic assessment techniques. Addressed here is the design, development, and evaluation of an Environmental Earth Science module with the focus on the use of remote sensing as a research tool.

Satellites, computers, remote sensing, the super information highway—the list of technology and information available to classroom teachers is seemingly endless and growing exponentially. Technology-based applications and their significance are changing the landscape of tools available to science teachers. ETE modules feature essential teacher resources and an effective infusion of remote sensing tools and resources.

This project demonstrates educational applications of NASA's wealth of scientific, remote sensing information. ETE emphasizes preparing teachers to use inquiry-based instructional methods and tools (remote sensing databases delivered over the Internet). ETE scenarios establish classroom environments in which students are involved with environmental topics and issues they regard as useful and connected to their out-of-school experience and lives.

The more vital and real the learning experience, the stronger the material is bonded in children's memory. Research suggests learning is enhanced when material interests students through "live events" in their own ways[1]. Science for all Americans: Project 2061[2] suggests teachers start with interesting and familiar questions, not with abstractions or phenomena outside students' range of perception, understanding, or knowledge. Participating teachers use "real world," relevant activities to engage students in using remote sensing databases,

and to facilitate understanding major environmental Earth Science concepts, big ideas, and general principles.

The model promotes instruction in which students are active, not passive, participants in real-life experiences that replace the less challenging and repetitive "talk and chalk," textbook centered teaching. Project 2061[3] suggests teachers actively engage students—promoting a spirit of healthy questioning. It should be normal practice for science teachers to raise such questions as: How do we know? What is the evidence? What is the argument that interprets the evidence? Are there alternative explanations or other ways of solving the problem that could be better? The aim should be to get students into the habit of posing such questions, examining data, analyzing, and framing possible explanations.

Giving students a piece of the action is an integral part of the ETE. Classrooms. The key to transforming student apathy into student engagement, suggests Kohn [4], "may be as simple as allowing students to make decisions about their learning. Schooling is typically about doing something to children, not working with them." Students need to be encouraged to take charge of their own learning more often by expanding opportunities to explore, participate in meaningful decisions, and become full partners in the learning process. There is nothing new about the belief that students should be able to participate, individually and collectively, in making decisions. This presumption has long played a role in schools described as progressive, democratic, open, free, experimental, or alternative. These tenets also play prominent roles in educational philosophies called developmental, constructivist, holistic, or learner centered; in specific innovations such as whole-language learning, discovery based science, or authentic assessment; and in the classrooms of teachers whose natural intuition is to treat children with respect.

How do we know what students have learned? Does their learning align with our curriculum? Assessment" intricacies can be addressed by replacing lower cognitive level, multiple-choice testing of learning with performance-based evaluations. To test knowledge claims, teachers can provide problem solving opportunities to demonstrate content viability [5]. Any evaluation should reflect how skills are learned, namely through repeated practice over time. ETE teachers apply subjective evaluations that are open to more than one type of response and dependent on the level of competence and the pupil(s) frame of reference. If students were challenged by complex, real and open-ended problems, teachers would look for evidence of understanding such as new generalizations, examples of relationships, and synthesis.

Students need opportunities to look back, to reflect, to debrief, to gather from their experiences what they have felt, thought, and learned. Children do not just receive content; they collect, store and remember the same information in very different ways. The most dynamic learning, separate from what is learned, happens when students self-monitor their thinking [6]. It may be that traditional pencil-and-paper instruments used to assess students' understanding of the nature of science may be an inappropriate (or less than adequate) means of evaluating scientific inquiry learning. When the nature of scientific inquiry is defined in terms of student scientific activities, inquiry, or student directed research, teachers of science may be better able to design activities and employ behaviors consistent with objectives.

ETE students need time for exploring, making observations, taking wrong turns, testing ideas, doing things over, collaboration, collecting data, and constructing physical and mathematical models for testing ideas. They also need time for learning prerequisite mathematics, technology, or science needed to deal with questions at hand; time for asking around, reading, and arguing; time for wrestling with unfamiliar and counterintuitive ideas and for coming to see the advantage in thinking in a different way [7]. Teachers need time too—especially time with technology and the time needed to become comfortable with problem-based environments.

REMOTE SENSING

Teachers may be reluctant to employ instructional technology because of their lack of knowledge concerning technology, or because of the feeling that its use is inappropriate in their disciplines. ETE developers made teachers' lack of time and inexperience with remote sensing technology major issues in the design of materials. A concerted effort was made to provide step by step information concerning the use and utility of satellite images and image analysis software. Self reports from teachers indicated that these materials were the very best part of the project site. One teacher experienced with remote sensing said: "you have to make it easy and understandable to teachers. They don't have the time to develop the skills, so unless you give them small, understandable chunks, it is likely they will not use the materials."

Besides making the modules and technical information understandable and easily accessible, there are other constraints that affect effective classroom use. The first of these is hardware and software. Only a minority of teachers have access to Macintosh or Windows-based machines with both a minimum of 8MB RAM and high speed access to the World Wide Web. Those schools with less than 56KB speed experienced significant delays in receiving graphics and picture-laced materials. To compensate for a minimum of RAM or lower access speeds, the team made an effort to reduce satellite images to 1MB or less in size. We did this by reducing resolution or size—both of which are necessary evils for the time being.

Another constraint dealt with by the team has been a choice of fully featured image analysis software that runs on both the Macintosh or Windows machines. Many teachers have little or no funds to purchase software, so an attempt was made to find inexpensive software. To date the team has used NIH Image for the Macintosh to develop the remote sensing tutorials and problem-based modules. Plans are underway to convert these modules to Windows software. Two candidates high on the list for future development include IDRISI from Clark University and Multispec from Purdue University.

What does formative evaluation tell us after eighteen months of development? Initial results suggest students enthusiastically engage in materials in which they have ownership, tools for analysis, and license to engage in student-centered research. The ETE prototypes have demonstrated "proof of concept." The challenge remains to provide teachers the tools and resources that can help transform their classrooms into centers for enhanced student understanding of science.

REFERENCES

[1] Zemelman, S., Daniels, H., & Hyde, A. Best practice: New Standards for Teaching and Learning in America's Schools. Portsmouth, NH: Reed Publishing. (1993).

[2] American Association for the Advancement of Science (AAAS). Science for All Americans. New York: Oxford University Press. (1990).

[3] Ibid

[4] A. Kohn, Choice for Children: Why and How to Let Students Decide. Phi Delta Kappan, 75(1), pp. 8-20. (1990).

[5] K. Tobin, D. J. Tippins, and A.J. Gallard, Research on Instructional Strategies for Teaching Science in D. L. Gabel (Ed.) Handbook of Research on Science Teaching and Learning (pp. 2-45). New York: MacMillan. (1994).

[6] Kohn, op. cit.

[7] American Association for the Advancement of Science, op. cit.

Remote Sensing and Inner City Youth: A Pilot Collaboration of the Aspen Global Change Institute's Ground Truth Studies and the 4-H After School Programs

John Katzenberger
Aspen Global Change Institute
100 East Francis
Aspen CO 81611
USA
970 925 7376 ofc. 970 925 7097 fax
johnk @agci.org

ABSTRACT

Aircraft, satellite, and Shuttle remotely sensed data are rapidly becoming more available for educational purposes in digital and print form. How can this data be utilized by elementary age students in the inner city while reinforcing existing science framework goals and objectives? The NASA- supported Aspen Global Change Institute's Ground Truth Studies (GTS) program is partnering with the 4-H After School program in Los Angeles to develop and pilot a GTS science kit specifically for use in inner city settings. The kit will include existing and new materials adapted to elementary students in an urban environment. The 4-H After School program in Los Angeles has established 24 after school centers located at elementary schools and public housing communities. 4-H After School Center staff and students will participate in educational workshops conducted by AGCI introducing concepts and tools in remote sensing and in a series of urban ground truth activities designed for youth ages 7-13.

INTRODUCTION

Several challenges converge to create the need for programs such as the one under development between the Aspen Global Change Institute and 4-H After School. Studies such as "A Nation at Risk" and "The 1990 Science Report Card" [1] point sharply to the limitations of our educational system in regard to science. Today's youth often lose the opportunity or interest to pursue science at an early age. The informal educational setting, such as the one created by 4-H After School, is increasingly recognized as an important complement to formal schooling. The National Research Council's *National Science Education Standards* presents "a vision of a scientifically literate populace" that requires a variety of approaches including "the resources of the communities surrounding their schools." The *Standards* specifically calls for "the availability and organization of materials, equipment, media, and technology" and the ability of the science program to "extend beyond the walls of the school to include the resources of the community" [2]. The AGCI and 4-H After School collaboration is designed to serve this niche.

The world is becoming increasingly urban. In 1930 estimates placed the urban percentage at a fifth of the global population [3]. By 1950, the urban environment held 29% of the population and today nearly 47%. This trend is expected to continue with 60% of the global population living in urban settings, 80% in industrialized countries by 2050 [4]. Given this trend, educational programs, such as the Aspen Global Change Institute's Ground Truth Studies,[1] that utilize remote sensing products and focus on anthropogenic change to Earth systems, have a unique role to play.

Inner city youth are particularly at risk of missing out on educational opportunities, and face adversity in many areas of their lives. Often there is considerable disparity between school districts in the amount of resources allocated per student between inner city and suburban districts [5]. Environmental degradation, from the local to the global scale, is of great concern in both industrial and developing countries [6]. Taken together, these challenges provide an opportunity to engage inner city youth in developing their scientific skills and other talents in pursuit of improving their scientific literacy, understanding the role of science in improving local to global environments, and in broadening their career opportunities. Offering these young people a hands-on, minds-on educational experience that fosters their interest in science and the environment can serve multiple purposes in creating positive social change.

4-H After School

The 4-H After School Program was founded in 1988 in Los Angeles. It is a public/private partnership that brings proven 4-H fundamentals to youth, ages 7-13, living in public housing communities in inner city settings. This unique program would provide supportive and challenging after school activities that seek to encourage critical and creative thinking, maximize the strengths of individual children, and motivate them to be lifelong learners and responsible citizens. Older students mentoring younger ones is an important component of the program. Parents and teachers interviewed by evaluators from the S.W. Regional Laboratories reported improvement in students' interest in school, completion of

---

[1] The Aspen Global Change Institute (AGCI) is a Colorado non-profit founded in 1989. Its mission is to further the scientific understanding of Earth systems through interdisciplinary science meetings, publications and educational programs about global change science. Ground Truth Studies is an AGCI educational K-12 program. AGCIs homepage: www.gcrio.org/agci-home.html contains a newsletter for educators and searchable summaries of global change research articles.

homework assignments, problem solving skills, adaptation to new situations, and cooperation with peers. All of the parents interviewed wanted their children to continue in 4-H After School [7]. The resources to initiate and sustain the 4-H After School Program are a blend of US Departments of Housing and Urban Development and Agriculture, corporations and local businesses, local housing authority, land grant universities, cooperative extension and 4-H, the National 4-H Council, and other public and private funding.

Ground Truth Studies

Ground Truth Studies is an interdisciplinary activity-based program that draws on the broad range of social and natural sciences that make up the study of global change and the complementary technology of remote sensing and image analysis. GTS utilizes five unifying global change concepts[2]:

- Change is the norm for the Earth's natural systems
- Recently, humans have become a key agent of change
- Earth systems are linked through interactive processes
- Global change affects all life
- Local changes can have global consequences

GTS emerged from the recognition that increasing quantities of data of different types are being assembled about Earth systems through such efforts as NASA's Mission to Planet Earth. A unique opportunity is present to not only further scientific understanding, but also further education. Applications of this understanding have direct bearing on the rate and nature of anthropogenic change to the biosphere. How students relate to this process and the tools they have available to them are critical in how their understanding will help shape decision making into the next century. A design team consisting of scientists and educators began the GTS project in 1990. An infusion of new ideas into AGCI's educational initiatives takes place each summer during interdisciplinary workshops on topics in global change. These workshops have attracted approximately 400 scholars from 23 countries since 1990 [8]. The activities developed from the design team's work integrate basic and applied science with mathematics and other disciplines such as geography and social studies [9].

An existing set of materials from the Ground Truth Studies program is being adapted and extended to serve the GTS/4-H After School collaboration in Los Angeles. A kit is under development that will include Earth system science and environmental education materials, remote sensing products, and equipment for kit use in the pilot stage of the project. After the pilot stage the goal is to disseminate the GTS kits and hold workshops in each urban environment where 4-H After School becomes established. This unique 4-H program has now expanded to Philadelphia, Oakland and Kansas City with plans for development in other cities.

---

[2] These five unifying concepts were adopted by the GLOBE Program for use in *The GLOBE Program Teacher's Guide*, Pilot Edition, Spring 1995 along with 8 student activities from AGCI's *Ground Truth Studies Teacher Handbook*.

A PERSPECTIVE ON REMOTE SENSING EDUCATION

Even before the Earth was seen whole for the first time, the fascination with the synoptic view has greatly influenced our thinking. In the landmark symposium "Man's Role in Changing the Face of the Earth" held at Princeton in 1955, the lead paper by E. A. Gutkind presented what are now more familiar themes.

"Today we can look at the world with a God's-eye view, take in at a glance the infinite variety of environmental patterns spread over the earth, and appreciate their dynamic relationships...We can see side by side the different scales in time and space and the tensions arising out of the neighborly proximity of seemingly incompatible transformations of the earth's surface" [10].

Gutkind was speaking of the power of aerial photography in shaping the human experience of place some 17 years before the first photograph of the full Earth taken from an Apollo spacecraft. He was also foreshadowing the profound affect human activity has had on the Earth. Astronomer Fred Hoyle predicted that "Once a photograph of the Earth taken from the outside is available, a new idea as powerful as any in history will be let loose" [11]. Interestingly, earlier that same year, 1972, Landsat 1 was launched with the mission of demonstrating the "feasibility of systematic remote sensing from Earth orbit for resource and environmental monitoring" [12].

Since the 1970s there has been a proliferation of programs and materials for remote sensing education. In the 1995 *Report of the NASA Survey of Earth System Science and Remote Sensing Education* [13] over 90 programs and products are listed indicating increased interest by educators in remote sensing and its role in understanding Earth systems.

EDUCATIONAL APPROACH

While there is tremendous advantage in observing Earth from space, maximizing utility from the data obtained requires a blend of *in situ* observations with space-based remote sensing, "for measurement-validation and calibration-reference capabilities" [14]. Bringing this data from the abstract realm to something more concrete for students is critical. Ground observation satisfies this need for the tangible and provides a tremendous opportunity for inquiry-based activities. Analog and digital data of high resolution of territory familiar to students is an excellent way to introduce remote sensing and complementary ground truth concepts and techniques. For example, aerial photographs from programs such as the National Aerial Photography Program offer sufficient spatial resolution for identification of known features by students. In GTS we have found that the aerial photo provides a useful introduction to coarser resolution digital products, such as from Landsat TM & MSS and AVHRR, particularly with elementary age students.

Recognizing the Built Environment

Elementary age students have experienced first hand built

structures and landscape changes that are also observable from space. Towns, cities, farms, parks and large architectural structures such as dams, piers, highways, railways, and bridges are not only evident from space, but also are accessible to students on urban field trips. Familiarity of these features in remotely sensed imagery and by ground observations form a useful basis for introducing surface features that are not typically as accessible to urban students, such as expanses of vegetative cover, snow and ice, or desert. Students bring a considerable amount of prior knowledge to features of the urban landscape based on their own personal experiences.

They have also observed built structures under construction and therefore the sense of change from nothing to something is keen. They have experiences of decay and dissolution of built structures, e.g. abandoned factories, housing developments, and railways. From a temporal and spatial standpoint, cities are a rich laboratory of change and manifest human activity altering the Earth's surface. The transition to data bases concerned with far larger spatial scales such as forest cover of Amazonia or ocean temperatures can build on the student's ability to interpret more familiar imagery. In this way students of the inner city gain skills that enable them to take virtual field trips to any location on Earth's surface given access to the data. An example of this is the introduction to students of synthetic aperture radar data (e.g. for studying mountain gorilla habitat) in the Jet Propulsion Laboratory's CD-ROM titled "Seeing Earth In A New Way: The SIR-C Missions of Endeavour."

Products of remote sensing serve as natural integrators of many disciplines including history, geography, mathematics, science, and social studies. Pattern recognition and problem solving based on remotely sensed imagery contributes to the development of a new visual language that directly relates to "spatial intelligence." In discussing his theory of multiple intelligences, Howard Gardner states, "spatial knowledge can serve a variety of scientific ends, as a useful tool, an aid to thinking, a way of capturing information, a way of formulating problems, or the very means of solving the problem" [15]. Students engaged by GTS activities such as "Where Are You from a Bird's Eye View", "Sand Boxes and Satellites" and "Ground Truthing Your Image" [9] develop a skill in image interpretation along with more general skills such as analysis, description, inference, hypothesizing, observation, computation, synthesis, classification, data representation, and reporting [9].

SUMMARY

Urban areas are growing in importance globally. A better understanding of how cities interact with their surroundings is an important component of global change research. Human activity is changing the biosphere in significant ways. Nowhere is the effect of human activity more prevalent than in cities. The generation of youth now in school will be the next generation making decisions that will impact Earth's air, water, land, and life through the next century. Exposure to and hands-on activities about Earth's natural and human

systems at the elementary level, reinforces the curiosity we have at the earliest ages and provides a practical understanding of how science and technology can be applied in useful ways. The GTS/4-H After School collaboration addresses this opportunity.

REFERENCES

[1] T. Beardlsey, "Teaching Real Science," *Scientific American*, October 1992, p. 100.

[2] National Research Council, *National Science Education Standards* (National Academy Press, Washington DC, 1996) pp. 2, 44, 45.

[3] L. Mumford, "The Natural History of Urbanization," *Man's Role in Changing the Face of the Earth*, Vol. 1, W.L. Thomas, Jr., Ed. (The University of Chicago Press, Chicago IL, 1956) p. 384.

[4] G. D. Ness, "The Long View: Population Environment Dynamics in Historical Perspective," *Population-Environment Dynamics: Ideas and Observations*, G. D. Ness, W. D. Drake, S. R. Brechin, Eds. (The Univ. of Mich. Press, Ann Arbor MI, 1993) pp. 37, 43.

[5] J. Kozol, *Savage Inequalities: Children In America's Schools* (Crown Pubs., Inc., NY, 1991) pp. 236-237.

[6] D. E. Bloom, "International Public Opinion on the Environment," *Science*, Vol. 269, 21 July 1995, pp. 355, 356.

[7] 4-H After School Program, "Vision Team Meeting Minutes" (Los Angeles CA, 6 Dec. 1995) unpublished.

[8] For an example of reporting on these interdisciplinary meetings see: *Elements of Change 1994*, S. Hassol, J. Katzenberger, Eds. (AGCI, Aspen CO, 1995).

[9] *Ground Truth Studies Teacher Handbook 2nd Edition*, S. Hassol, J. Katzenberger, Eds. (AGCI, Aspen CO, 1995) pp. 37-115.

[10] E. A. Gutkind, "Our World from the Air: Conflict and Adaptation," *Man's Role in Changing the Face of the Earth*, Vol. 1, W. L. Thomas, Jr., Ed. (The University of Chicago Press, Chicago IL, 1956) p. 1.

[11] K. W. Kelley, *The Sierra Club Home Planet Postcard Collection: Images From The Home Planet* (Sierra Club Books, San Francisco CA, 1989).

[12] N. M. Short, P. D. Lowman, Jr., S. C. Freden, and W. A. Finch, Jr., *Mission To Earth: Landsat Views The World* (NASA, Washington DC, 1976) p. 1.

[13] *Report of the NASA Survey of Earth System Science and Remote Sensing Education* (NASA, Washington DC, 1995).

[14] Report of the Earth System Sciences Committee NASA Advisory Council, *Earth System Science: A Closer View* (NASA, Washington DC, 1988) p. 120.

[15] H. Gardner, *Frames of Mind: The Theory of Multiple Intelligences* (BasicBooks, 1985) p. 192.

Texas Space Grant Consortium: Educational Opportunities in Earth Science and Remote Sensing

Amy Neuenschwander
Texas Space Grant Consortium
3925 W. Braker Lane, Suite 200
Austin TX, 78759-5321
phone (512)471-3585   fax (512) 471-3585
e-mail: amy@csr.utexas.edu

Abstract

Science education has increasingly been an area of concern for educational leaders in the state of Texas. Many educators are looking for interesting ways to reach students by taking advantage of new technologies. The Texas Space Grant Consortium has begun developing a series of K-12 educational programs focused on using remote sensing for Earth science. These programs include a prototype remote sensing design competition (Sky View) , an Internet based remote sensing program (STARS) and the TOPEX/Poseidon Adopt-a-buoy.

Sky View, in its third year, is a unique and challenging program for secondary students to experience engineering design and to reap the benefits of remote sensing of the environment. The program is centered around a student team designing, building, and operating an aerial photography system to meet an earth science objective. Students must present their results to a panel of judges at a competition held at the University of Texas at Austin. Previous projects include monitoring beach erosion, precision farming, monitoring of prairie dog towns, and drainage capabilities of retention ponds.

STARS (Students and Teachers Accessing Remote Sensing) is a new Internet based program which is focused on using remote sensing for different earth science applications. STARS will serve as an Internet resource for satellite data in conjunction with ground truth data and science curriculum. The primary focus is meteorology, but additional modules are planned in oceanography, land use, geology, and water resources.

TOPEX/Poseidon Adopt-a-buoy is a joint educational outreach program between the University of Texas Center for Space Research (UTCSR) and the Colorado Center for Astrodynamics Research (CCAR). Student teams will design shallow water platforms to be used for calibrating the altimeter measurements of TOPEX/Poseidon.

Introduction

The goal of the Texas Space Grant Consortium (TSGC) is to strengthen the educational foundation necessary for today's students to compete in an ever changing world of technology. This includes giving them the opportunity to become familiar with space and science technologies. The earlier our students are taught the need to protect the environment, the better ability they will have to solve complex issues related to global climate change. The Texas Space Grant Consortium has a mission to increase the educational and career opportunities in science, engineering, and mathematics for young people. TSGC has a number of outreach programs to fulfill this mission. TSGC currently offers several K-12 educational programs focusing on incorporating remotely sensed data into the classroom.

Sky View: Prototype Remote Sensing Design Competition

The goal of Sky View is to promote interest among students in the areas of science, mathematics, and engineering by integrating the fields into an applicable remote sensing project which is both challenging and fun for the students involved. The

idea for this project is based upon a student program in France that uses a camera flown on a kite to take pictures of the ground [1].

Sky View is a design competition which has built upon the idea of an aerial photography platform and expanded to a program where students are tasked with building their own remote sensing system. Schools submit a written proposal to TSGC outlining their environmental application, how remote sensing will aid their environmental studies, and how they foresee the design of such a system. After review by TSGC, initial awards are granted on a competitive basis.

These initial cash grants are used as seed money to cover some of the expenses of the materials. Each selected school is required to design and build a remote sensing system in order to enhance an earth science topic of their choice. The choice of the science application is left open for the schools to decide due to the varying environments and interests across the state. In past years, these topics have included coastal erosion, agriculture, watershed studies, and prairie-dog town monitoring. One of the advantages of this project is the degree of freedom in the design of the system, as well as the selection of individual components. This freedom allows students to experiment with new ideas, designs, alternative materials, as well as begin to understand the basic applications of remote sensing.

On an initial seed grant from the Texas Space Grant Consortium, each student team is left to design the system, collect and analyze the data, and draw conclusions. The remote sensing systems are relatively inexpensive and can be used to study environmental applications, but it is also useful in the engineering, physics, and mathematics that must undergo in order to succeed. After months of work, the student teams arrive at the University of Texas of Austin to present their projects to a panel of judges and their peers. The student designs are judged in three categories; engineering/design, earth science application, and presentation.

STARS: Students and Teachers Accessing Remote Sensing

STARS is designed as an internet based information/curriculum source aimed at providing remotely sensed data for the purpose of studying many environmental topics taught in today's classrooms. Answers to complex questions dealing with environmental issues can be sought with the integration of remote sensing technology and ground truth measurements. Satellites can provide data at the temporal and spatial resolution needed to understand the environment and develop models to predict and understand the future consequences of today's actions. Our research has shown that many teachers are interested and excited about the possibility of bring satellite imagery into the classroom, but they lack the knowledge of interpreting the data and how it can be incorporated into their present curriculum. We are developing curriculum which is written by researchers and engineers, as well as K-12 educators.

Initially, the STARS network will use NOAA AVHRR and GOES satellite imagery for the study of meteorology, atmospheric effects and climate monitoring. As a byproduct, the initial system will also provide a useful resource for computer science classes and hands-on experience with existing and future technologies. The STARS network also includes background information on remote sensing and different applications of sensors. The network will eventually be expanded to provide data for instruction in hydrology, water chemistry, biology, geology, ecology, and land planning.

At the heart of our program is the TEXNET central weather server. TEXNET functions as the state of Texas weather information hub providing current satellite images, ground based weather measurements, nexrad radar and basic weather information for schools and the general public. From the TEXNET database stored on the server, schools are able to download meteorological information for their region. Having such regional weather measurements in combination with NOAA satellite imagery, students will be better able to study and understand regional weather processes.

TOPEX/Poseidon Adopt-a-buoy

The TOPEX/Poseidon Adopt-a-buoy program is a joint education outreach project between the University of Texas Center for Space Research (UTCSR) and the Colorado Center for Astrodynamics Research (CCAR).

The first phase of the TOPEX buoy project is high school student teams designing a buoy capable of operating in the shallow waters of Galveston Bay which will be used to collect GPS positional data[2]. The primary objective of the program is calibration of altimeter measurements from the TOPEX/Poseidon satellite. The secondary objectives include the characterization of bay currents and water properties to better understand the motion and condition of water in the bay. Such measurements will enhance monitoring and prediction of circulation in the bay for understanding the dispersion of pollutants, as well as supporting biological research in Galveston Bay.

In an effort to provide the student design teams with as much information as possible, a World Wide Web (WWW) page has been developed which has detailed information about the TOPEX/Poseidon mission, the use of GPS equipment and data, maps and biological data for Galveston Bay, and basic principles of oceanography. The information published on the WWW is intended as a tool which can be incorporated into classrooms and curriculum. Over the next year, teachers from the Austin LBJ Science Academy will be working with TSGC to develop curriculum using TOPEX/Poseidon altimeter data which will tie into topics such as physical oceanography, climate, and marine biology.

Summary

There is a growing need for not only a steady stream of future scientists and engineers who will be capable of carrying out environmental studies, but also a general public capable of understanding the significance of the results in order to make informed decisions about related public policy and funding. The Texas Space Grant Consortium is continuing its efforts to develop a series of meaningful and usable K-12 educational programs focused on using remote sensing for Earth science. These programs include a prototype remote sensing design competition (Sky View) , an Internet based remote sensing program (STARS) and the TOPEX/Poseidon Adopt-a-buoy and incorporate several data types including NOAA AHVRR, TOPEX/Poseidon altimeter, nexrad radar, surface observations, and GPS positional data.

TSGC World Wide Web Sites

Sky View
http://www.utexas.edu/tsgc/skyview.html

STARS
http://www.utexas.edu/tsgc/stars.html

TOPEX Adopt-a-buoy
http://www.utexas.edu/tsgc/buoy.html

References

[1]. M. Kervadec, G. Pegnolet, N. Bruneau, G. Denis; "Discovering Earth Observation and Image Processing", 43rd Congress of the International Astronautical Federation, 1992.

[2]. G. Born, M. Parke, P. Axelrad, K. Gold, J. Johnson, K.W. Key, D.G. Kubitschek, E.J. Christensen; "Calibration of the TOPEX altimeter using a GPS buoy", Journal of Geophysical Research, Vol. 99, NO. C12, pp. 24,517-24,526, 1994.

The SIMMS'93 SAR Polarimetry Experiment: Combined Surface and Airborne Radar Measurements for Winter Sea Ice

C. E. Livingstone
Canada Centre for Remote Sensing
588 Booth St Ottawa Ontario K1A 0Y7
(613) 998-9060 / livingstone @ccrs.nrcan.gc.ca

D. G. Barber
Centre for Earth Observation Science
Department of Geography
University of Manitoba, Winnipeg Manitoba, R3T 2N2
(204) 474-6918 / dbarber@ccu.umanitoba,ca

F. Spiring
Centre for Earth Observation Science
Department of Statistics
University of Manitoba, Winnipeg Manitoba, R3T 2N2
(204) 474-8162 / fred_spiring@umanitoba.ca

W. Liu
MDA (under contract to CCRS)
588 Booth St Ottawa Ontario, K1A 0Y7
(613) 947-1226 / liu@ccrs.nrcan.gc.ca

Abstract -- Polarimetric SARs promise to be powerful tools for the measurement and investigation of the scattering properties of sea ice. Much of the research done to date is based on a single data set acquired in the western arctic. This paper describes work done with a 1993 central Arctic data set and presents some results for first-year sea ice.

INTRODUCTION

The majority of the published research on the polarimetric signatures of Arctic Sea ice are based on data acquired in March 1988 in the Beaufort, Bering and Chukchi Seas [1] by the JPL AIRSAR. Supporting surface observations for this work were made by researchers at the Applied Physics Laboratory drifting ice station in the Beaufort Sea. Polarimetric analysis of these data and comparisons between observations and model predictions using surface measurements [1,2,3,4] have provided a solid baseline for further polarimetric SAR studies.

In 1993, a complementary polarimetric SAR data set was acquired with a different sensor, the CCRS C-band SAR polarimeter [5], in a different region of the Arctic, the Canadian Arctic Archipelago, under similar environmental conditions to those existing for the 1988 JPL data set. The 1993 data form one component of the SIMMS'93 (Seasonal Sea Ice Monitoring and Modeling Site) set of multidisciplinary field experiments for 1993. An extensive surface measurement program supported the SAR imaging activities.

The results presented in this paper are based on data acquired within Barrow Strait and Resolute Passage, near Cornwallis Island, NWT Canada, during the SAR polarimetry flight on May 3.

THE DATA SET

The polarimetric SAR flight on May 3, 1993 was dedicated to investigating sea ice signatures in the primary measurement areas of the SIMMS'93 program, areas 1 and 2 in figure 1.
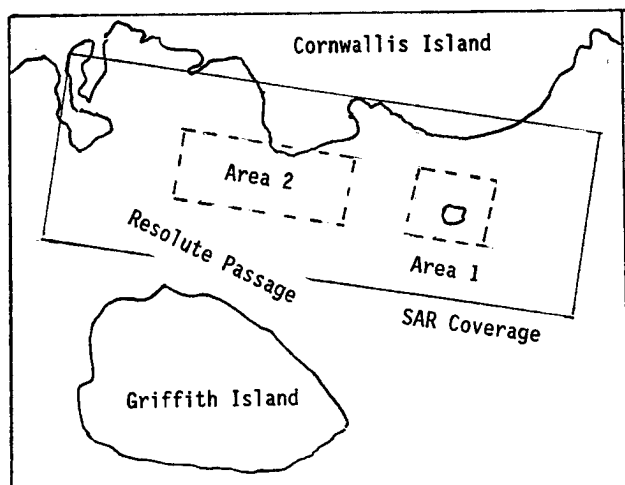
Figure 1 SIMMS'93 experiment area map

The SAR coverage area in this diagram contains four offset flight lines that provided multiple incidence angles angle data at the surface measurement sites as well as multiple aspect angles for the sites clustered near the multi-year floe shown schematically in area 1. The bulk of the polarimetric data presented in this paper were taken from one flight line that imaged areas 1 and 2 at incidence angles from 26^0 to 67^0.

Most of the experiment area was covered by relatively thick (> 1.5 m), mature, first-year ice that contained a few multi-year floes of various ages and origins. The weather conditions over the period of the SAR experiment (April 30 to May 6) were

stable with no precipitation, daily highs near - 15^0 C and daily lows near - 20^0 C. Surface measurements acquired over a seven day block surrounding the May 3 flight can be used with the radar data.

The surface measurement program that supported the SAR investigations consisted of depth profiles of physical and dielectric properties of the snow cover and the upper 30 cm of the underlying ice. These were augmented by crystallographic investigations of the snow cover and thin section micro-structure measurements of ice core samples. The techniques used for snow and ice measurements are reported elsewhere [6,7].

SNOW AND ICE PROPERTIES

The thickness of the snow cover on level first-year ice varied from approximately 12 cm at the intensive site in area 1 to approximately 30 cm in a thick ice region in area 2. Figures 2 and 3 describe bulk physical and dielectric properties of the snow cover on level first year ice at a surface measurement site in area 1.
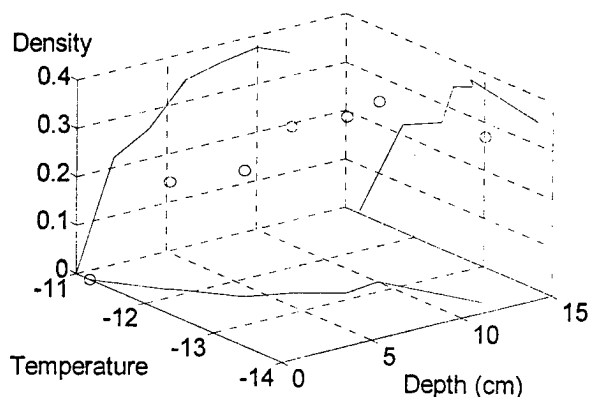
Figure 2　Bulk physical properties of test site 7 snow; density in g/cm^3 , temperature in degrees C, as they vary above the ice surface.

Figures 4 and 5 summarize the bulk physical and dielectric properties of the upper 30 cm at this site.
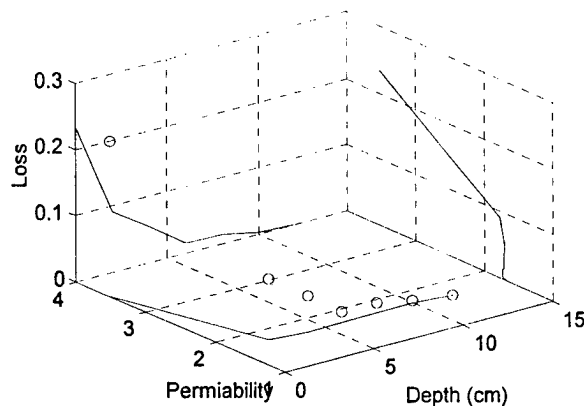
Figure 3 Bulk dielectric properties of the snow at test site 7 as they vary above the ice surface.
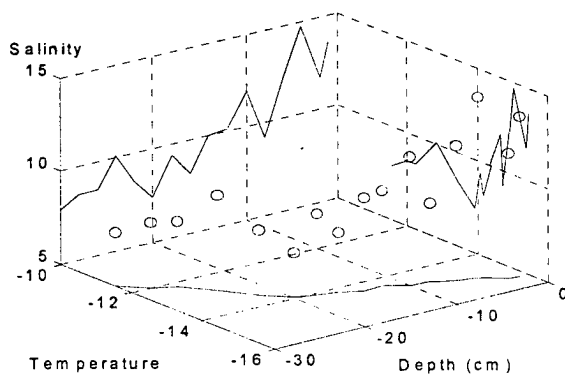
Figure 4 Ice salinity in parts per thousand and temperature (degrees C) variations with depth below the ice surface.
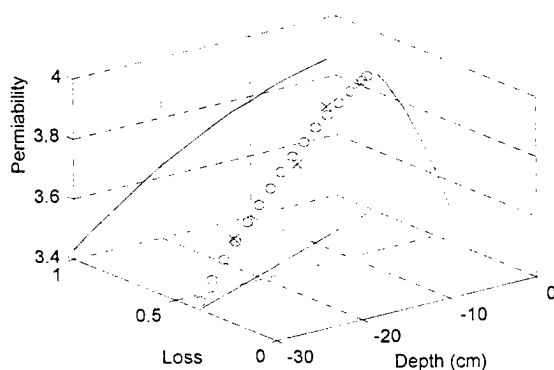
Figure 5 Ice permeability and loss variations with depth below the ice surface at site 7. The crosses are measured points.

THE POLARIMETRIC SAR DATA

The CCRS C-band SAR polarimeter receives time multiplexed, linearly polarized HH, HV and VV, VH channel pairs. The data are range compressed in the receiver and are recorded as base band complex signals for ground processing to registered, calibrated, single look, complex, polarimetric images. Details of the instrument and an outline of the processing can be found in [5]. The processed images have range and azimuth impulse response widths of 0.75 m and 5.7 m respectively and are sampled at 0.43 m azimuth and 4.0 m range. Corresponding samples in the registered image set form single look scattering matrix elements. As the channel isolation in the radar exceeds 35 dB, symmetrization is not required for channel balance or calibration. Where appropriate, azimuth spatial averaging is used to generate polarimetric parameters for analysis and display. 8 look averages are normally used to generate polarimetric parameter images. For polarimetric signature analysis, single look Stokes matrices are generated for each point in the block to be averaged and the averaging is performed on the Stokes matrix elements.

Just prior to the SIMMS'93 flight program, the main transmitter for the CCRS C-band SAR failed and the flight program was conducted with a lower power back-up unit. Analysis of the radar signal to noise ratios shows that the co-polarized channel signal to noise ratios exceed 15 dB for first-year ice returns at incidence angles up to 60^0 for the May 3 data. The cross polarized channel signal-to-noise ratios are approximately 7 dB for first-year ice and these data must be treated with caution. In the results presented here, the HV and VH channel data are coherently averaged to gain 3 dB signal-to-noise ratio.

RESULTS

The polarimetric images generated for areas 1 and 2 show a large range of signatures for undeformed first -year ice. A detailed examination of the full polarimetric image set suggests that the majority of the signature variation results from structure on and near the ice surface that was generated in the early growth stages of the ice.

The systematic dynamic range variation of the incoherent polarimetric variables (radar cross sections, total power, co-polarization ratio and depolarization ratio) over the incidence angles spanned by typical SAR image sets exceeds the

dynamic range of most display media. To view the first year ice returns, 1000 azimuth sample blocks of returns from undeformed first year ice were averaged to model the incidence angle dependence and were expressed as polynomial functions that are valid from 10^0 to 70^0 incidence angle. These were used for image normalization functions and provide a useful description of the mean scattering properties of late winter first-year ice in the experiment area.

The polynomial scattering descriptions are shown in table 1. The independent variable for all functions is the incident wave illumination angle in degrees. In all cases a second order polynomial provides a sufficient description for the data and each function has the form:

$$y = a_2 x^2 + a_1 x + a_0$$

Table 1 polynomial models

	a_2	a_1	a_0	SD
$<\sigma^0_{HH}>$ (dB)	0.0016	-0.2987	0.3608	± 1.6
$<\sigma^0_{VV}>$ (dB)	0.0006	-0.1795	-1.9523	± 1.4
$<\sigma^0_{cross}>$ (dB)	0.0016	-0.2248	-15.870	± 2.0
$<\Sigma\sigma^0_{ij}>$ (dB)	0.001	-0.2310	-1.1402	± 1.6
$<\sigma^0_{VV}/\sigma^0_{HH}>$	0.0	0.0721	-1.1402	± 0.15
Depol. ratio	4.2835 x 10^{-6}	-5.9577 x 10^{-5}	0.01672	± 0.02

The standard deviations in table 1 provide a measure of the signature variations about the polynomial model for the samples selected.

To provide a feeling for the range of variability seen in the SIMMS'93 first-year winter ice signatures, figure 6 describes the polarimetric

signatures of young, smooth first year ice that appears to have formed under calm conditions. The 12 cm snow cover at this site has properties similar to that at site 7 (figures 2 and 3). Figure 7 is the signature of older, thick first-year ice that preserves plates of fractured thin ice at the base of its 30 cm snow cover. Neither of these examples is "typical of the total ice cover but both cases lie within the normal range for first-year winter ice.

Average Stokes Matrix (BSA)			
0.008003	–0.001690	0.000018	–0.000056
–0.001935	0.007430	–0.000025	0.000111
–0.000010	0.000031	0.003981	0.000789
0.000007	–0.000079	–0.000792	0.003910

Incidence Angle (deg) = 61.57
Number of samples = 150 x 400
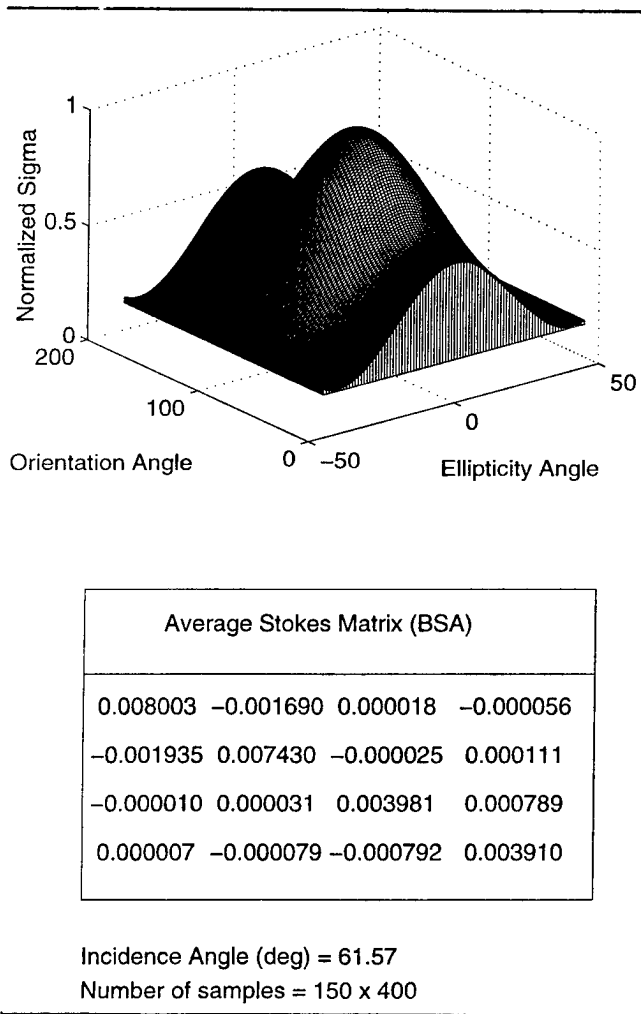
Figure 6 The polarimetric signature of first-year ice formed under calm conditions.
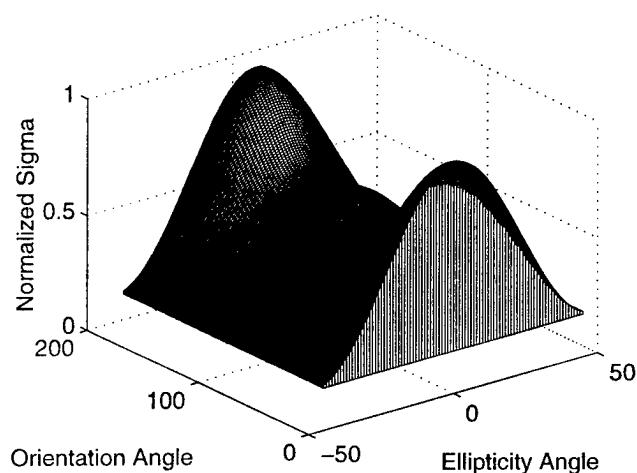
Average Stokes Matrix (BSA)			
0.011551	0.002170	−0.000080	−0.000073
0.002032	0.011031	−0.000069	0.000112
−0.000091	−0.000033	0.006527	0.000125
−0.000031	−0.000113	−0.000136	0.006299

Incidence Angle (deg) = 58.66
Number of samples = 300 x 600

Figure 7 The polarimetric signature of thick first-year ice that has broken thin ice plates at the base of a 30 cm snow cover.

DISCUSSION

The C-band radar signatures of first-year winter sea ice are quite variable and appear to reveal elements of the ice formation history. Quantification of these effects is in progress at the time of writing. The mean polarimetric properties of the ice presented here appear to be consistent with other observations and suggest that the mean characteristics should be retrievable from modeling calculations following the approaches describe in [3]. Future work on this is planned.

REFERENCES

[1] M.R. Drinkwater, R. Kwok, D.P. Winebrenner, and E. Rignot, "Multifrequency synthetic aperture radar observations of sea ice," J. Geophys. Res, vol 96, C11, pp 20679-20698, November 1991

[2] E. Rignot and M.R. Drinkwater, "Winter sea-ice mapping from multi-parameter synthetic aperture radar," J Glaciology, vol 40, 134, pp 31-45, 1994.

[3] S.V. Nghiem, R. Kwok, S.H. Yueh, and M.R. Drinkwater, "Polarimetric signatures of sea ice: 1 Theoretical model," J. Geophys. Res., vol 100, C7, pp 13665-13679, July, 1995.

[4] S.V. Nghiem, R. Kwok, S.H. Yueh, and M.R. Drinkwater, "Polarimetric signatures of sea ice," J. Geophys. Res., vol 100, C7, pp 13681-13698, July, 1995.

[5] C.E. Livingstone, A.L. Gray, R.K. Hawkins, P. Vachon, T.I. Lukowski, M. Lalonde, "The CCRS airborne SAR systems: Radar for remote sensing research," Canadian J. Rem. Sens., vol 21, 4, pp 468-491, December, 1995.

[6] D.G. Barber, T.N. Papakyriakou, and E.F. LeDrew, "On the relationship between energy fluxes dielectric properties, and microwave scattering over snow covered sea ice during the spring transition period," J. Geophys. Res. vol 99, C11, pp 22401-22411, 1994.

[7] M.E. Shokr and N.K. Sinha, "Physical and structural properties of Arctic sea ice observed during the SIMMS'92 experiment," report CARD-95-005, Atmospheric environment Service, Toronto, Canada, 1995

Ice Roughness Classification and ERS SAR Imagery of Arctic Sea Ice: Evaluation of Feature-Extraction Algorithms by Genetic Programming

Jason M. Daida*, Robert G. Onstott**, Tommaso F. Bersano-Begey*, Steven J. Ross*, & John F. Vesecky*

*The University of Michigan, Department of Atmospheric, Oceanic and Space Sciences,
2455 Hayward Avenue, Ann Arbor, Michigan USA 48109-2143. (313) 747-4581 (work). (313) 764-5137 (fax). daida@eecs.umich.edu
**Environmental Research Institute of Michigan, Center for Earth Sciences, Advanced Concepts Division
P.O. Box 134001, Ann Arbor, Michigan 48113-4001

Abstract — This paper describes a validation of accuracy associated with a recent algorithm that has been designed to extract ridge and rubble features from multiyear ice. Results show that the algorithm performs well with low-resolution ERS SAR data products.

1. INTRODUCTION

Roughness in the polar ice cover—like meso-scale features of pressure ridges and rubble fields—is of significant geophysical interest. Pressure ridges and rubble fields help to transfer kinetic energy from meteorological systems to the ice cover. Pressure ridges can significantly increase sea-ice drag coefficients, which subsequently affect sea-ice movement and deformation. Ridges and rubble fields are also of interest because they account for a large portion of the total ice mass.

In ERS synthetic aperture radar (SAR) imagery, pressure ridges commonly appear as filamentary, curvilinear features of variable width. These features have radar backscatter signatures that differ only slightly from those of non-ridged multiyear-ice; pressure ridges subsequently appear as mostly low-contrast features. Rubble fields often form when sea ice undergoes multiple ridging events in the same geographic region. Not surprisingly, rubble fields have backscatter signatures that are similar to that of pressure ridges, except that rubble fields may have shapes ranging from consolidated blobs to interlaced networks of curvilinear features.

The difficulty in extracting such features has been noted in work such as [1]. The problem has been considered untenable for standard image processing algorithms for a variety of reasons. Such reasons include low signal-to-noise ratios, arbitrariness of feature shapes, and radar cross-sections that change depending on the orientation of a feature. The problem, however, has not been considered impossible, since researchers have been able to link the roughness caused by sea ice deformation (like ridges and rubble fields) with ERS SAR backscatter. [4]

This paper evaluates an ice-roughness algorithm that we have developed over the past year. The next section (2) briefly discusses our algorithm. Section 3 describes our procedure for evaluating this algorithm, which involves validation of a derived data product from this algorithm with an area that has ground truth. Section 4 presents and discusses our results. Section 5 summarizes our major conclusions.

2. ALGORITHM NOTES

Our algorithm has been developed by using a relatively new procedure in computer-assisted software design. This procedure, which uses genetic programming, has been developed to help a user to focus more on the problem at hand and less on programming detail. Another paper in this conference highlights some of the salient characteristics of our procedure [2].

We have designed our algorithm to extract ridge and rubble features in multiyear ice. It has been developed for use with low-resolution (ERS) SAR data products, partly because we desired meso-scale distributions and partly because we wanted to track temporal changes. For more information on the development of this particular algorithm (called a switch filter), see [3].

3. PROCEDURE

The image that we have chosen for validation is part of a larger series of temporal ERS-1 SAR data that we have analyzed. The series, which begins in August 1991 and ends in July 1992, describes the synoptic coverage of an area in the Beaufort Sea gyre (roughly 72°N, 140°W). The particular area and dates of coverage overlap with the Lead Processes Experiment (LEADEX) in 1992, which featured both in-situ and ERS-1 observations around a chosen floe.

Figure 1a shows the low-resolution ERS SAR image taken 29 March 1992, while Figure 1b shows the corresponding data product derived with the ice-roughness algorithm. We note that the algorithm was developed using data from a different image (23 April 1992)—the 29 March data is entirely out-of-sample. The boxed area shown in both these figures corresponds to the ice classification map shown in Figure 1c. Classifications for this map were based on ground observations from the LEADEX base camp.

To validate the derived data product, we used a ridge and rubble map that was manually obtained from the high-resolution (nominally 12 m resolution) ERS SAR data product for the same day and area. To ensure accuracy, we limited the extent of this ridge and rubble map to the immediate area (~ one km) around the base camp. The map was verified by personnel present at the base camp at the time the image was taken (i.e., R. Onstott). The boxed area in Figure 1c shows the extent of the manually derived ridge and rubble map.

4. RESULTS AND DISCUSSION

Figures 2a – d show our results. Figure 2a depicts the high-resolution subimage that was used to create the manually derived ridge and rubble map. The image has been enhanced for publication to highlight those features, which show as light gray pixels on a gray background. (Gray generally corresponds to multiyear ice, while dark gray generally corresponds to first-year ice.) The three bright collinear dots in the center of this figure correspond to corner reflectors placed on first year ice. (A fourth dot—another corner reflector—is also visible, but on multiyear ice.)

Figure 2b shows the manually derived ridge and rubble map. (Black denotes ridge and rubble features in multiyear ice, or extreme ridging in first year ice. Note that the three dots have been retained for comparison.)

Figure 2c shows the results from the ice-roughness algorithm.
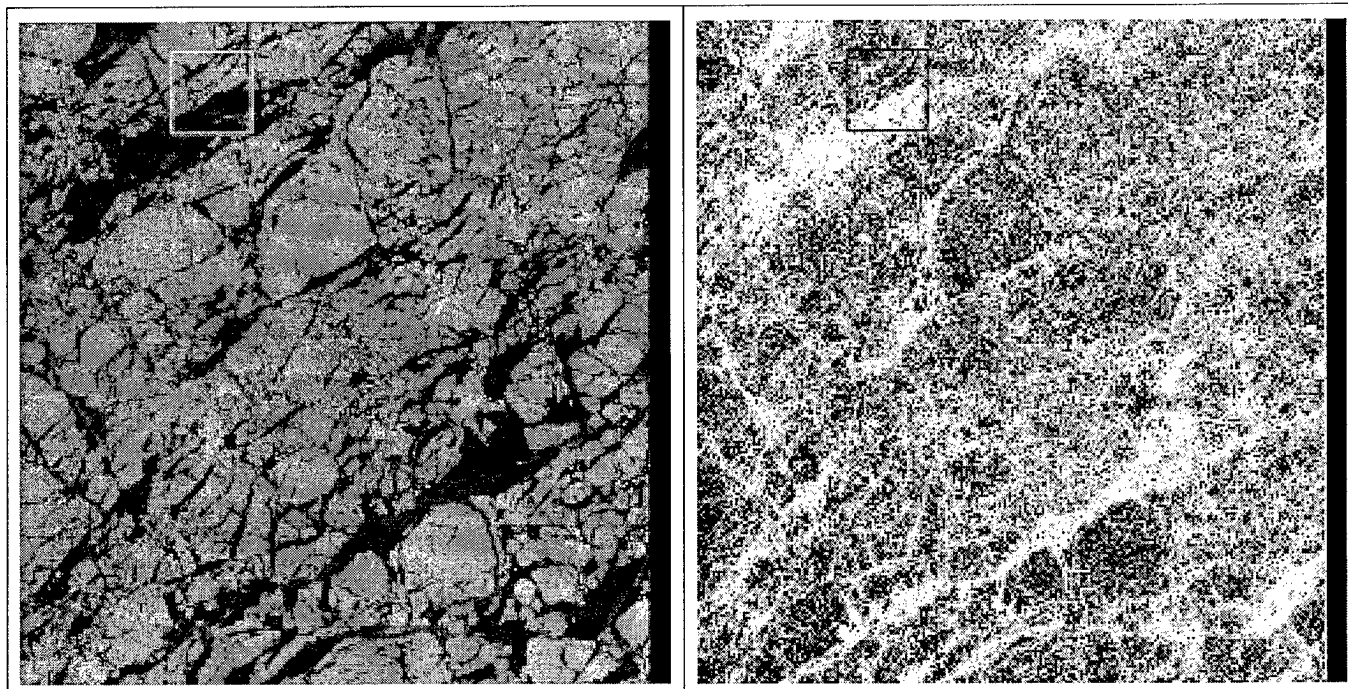
Figure 1. Data and Ground Truth. (a) Top. 29 March 1992 Image (1024 × 1024 pixels) © ESA 1992. (b). Upper right. Derived Data Product. (c) Lower Right. Map of Ground Truth.

Note that the pixels are noticeably larger than those shown in Figures 2a and 2b. This is expected, since the ice-roughness algorithm works on low-resolution data products. (Black and dark grays denote ridge and rubble features.)

Figure 2d shows the results of overlaying the results from the ice-roughness algorithm on the manually derived ridge and rubble map. (Black indicates a high degree of correlation for ridge and rubble features, while white indicates a high degree of correlation for smooth features. Gray without any interior black denotes areas of possible conflict.)

The results show excellent correspondence between the manually derived map and the data product from the ice-roughness algorithm. Much of the identified ridge and rubble features in multiyear ice have been correctly classified in the data product. Tolerance accuracies in the data product are better than ±100 m (± 1 pixel) of a ridge or rubble feature in the high-resolution map.

We note that the data product shows a correct classification of ridge features in an area just below the three collinear dots in Figure 2a. Ground truth corresponding to this area indicates an area of old pressure ridges—worn and smoothed. Radar backscatter signatures corresponding to ridges like these are not much different from non-ridged multiyear ice; such features are difficult to classify.

The ice-roughness algorithm does seem to identify ridges and rubble features regardless of whether such features yield strong or weak signatures in contrast to the mean backscatter values of multiyear ice. If this is the case, such an attribute would help to desensitize the algorithm from ridge orientation effects on radar backscatter.

We further note that the algorithm has classified a series of pixels in the lower right corner of Figure 2c as ridge or rubble features, even though such pixels correspond to areas of first-year ice.
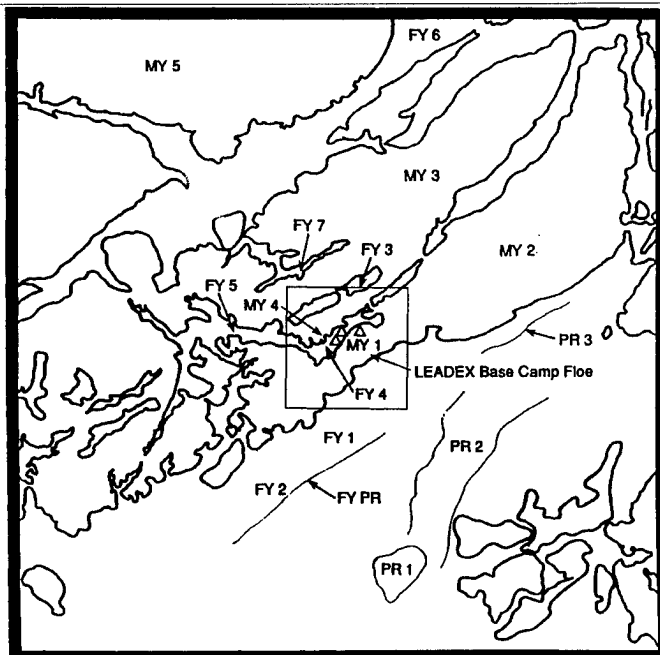
The algorithm apparently identifies a few, but not all the ridge and rubble features in first-year ice. These features do appear in the image data but not in Figure 2a. (As mentioned earlier, we enhanced Figure 2a to show, for publication, ridge and rubble features in multiyear, not first-year ice.) We have found that the few first-year ridge and rubble features that have been identified do show a high correspondence with major stress and deformation patterns in first-year ice. (See [3].)

4. CONCLUSIONS

This paper has evaluated the performance of an ice-roughness algorithm that was developed using a relatively new procedure in

1521
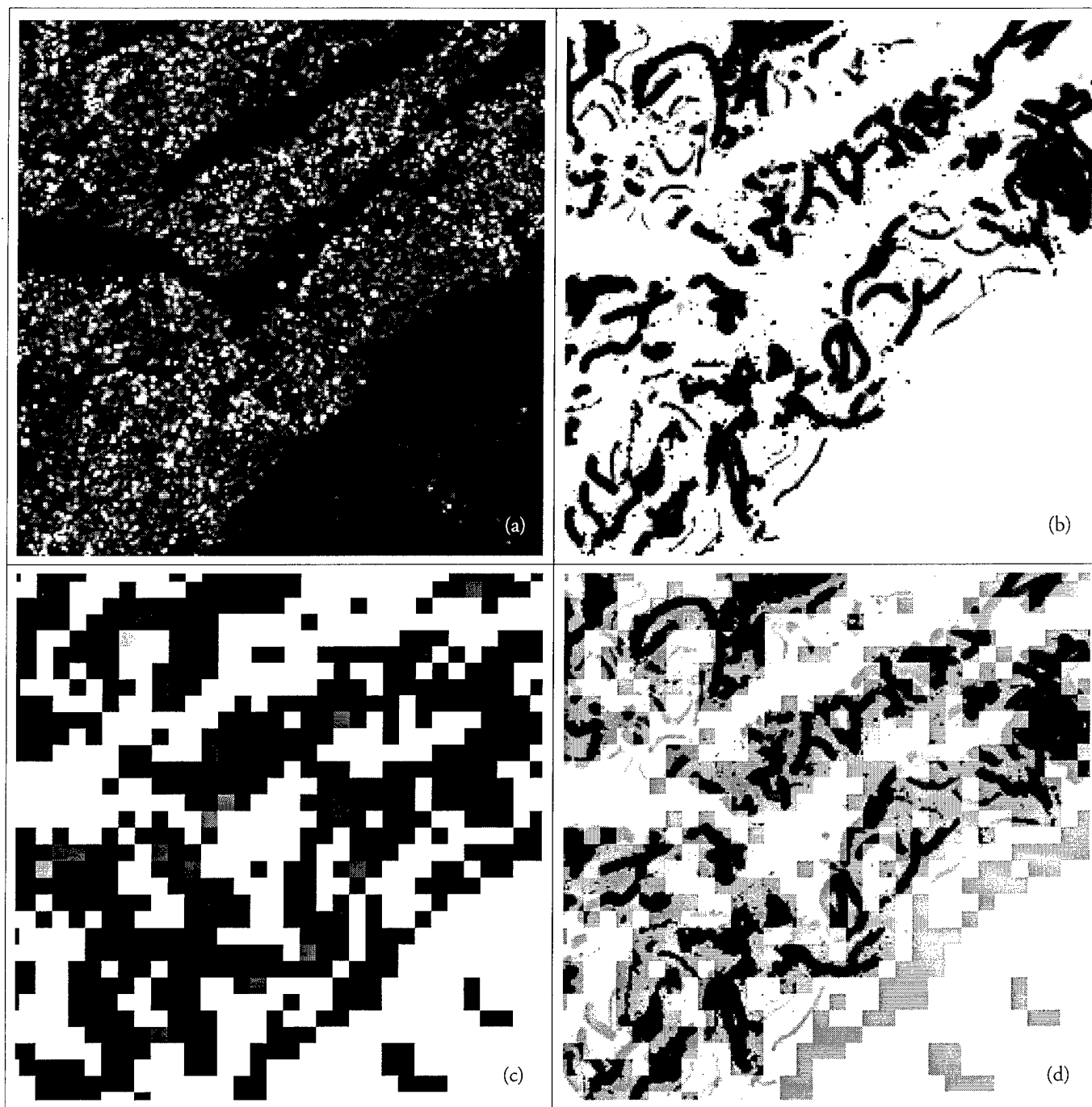
Figure 2. Results. (a) High-Resolution Subimage. (b) Manual Interpretation. (c) Derived Data Product. (d) Comparison.

computer-assisted software design. To evaluate this algorithm, we used ERS SAR image data that coincides with *in-situ* observations obtained during LEADEX '92. The results have shown excellent agreement between the derived data product and a manually interpreted ERS SAR data product. The algorithm has been shown to extract features corresponding to ridges and rubble fields in multiyear ice. We have suggested that the algorithm does extract enough of the ridge and rubble features in first-year ice to show gross deformation patterns. ■

BIBLIOGRAPHY

[1] Burns, B.A., "SAR Image Statistics Related to Atmospheric Drag Over Sea Ice," *IEEE T-GRS*, 28:2, p. 158–65.

[2] Daida, J.M., T.F. Bersano-Begey, S.J. Ross, and J.F. Vesecky, "Evolving Feature-Extraction Algorithms: Adapting Genetic Programming for Image Analysis in Geoscience and Remote Sensing," *Proceedings of IGARSS '96*, IEEE Press. In Press.

[3] Daida, J.M., J.D. Hommes, T.F. Bersano-Begey, S.J. Ross, and J.F. Vesecky, "Algorithm Discovery Using the Genetic Programming Paradigm: Extracting Low-Contrast Curvilinear Features from SAR Images of Arctic Ice," *Advances in Genetic Programming II*, P. Angeline and K. Kinnear (ed.), Cambridge: The MIT Press, 1996. In Press.

[4] Onstott, R.G., D. Miller, and R.A. Shuchman, "Study of the Relationship Between the Scale of Sea Ice Deformation and Radar Backscatter Intensity Using ERS-1 SAR," *Proceedings of IGARSS '95*, IEEE Press, pp. 419–421.

A Microwave Technique for Mapping Ice Temperature in the Arctic Seasonal Ice Zone

Karen M. St.Germain[1] and Donald J. Cavalieri[2]

[1]Department of Electrical Engineering and Center for Electro-Optics
University of Nebraska-Lincoln, Lincoln, NE 68588-0511, USA
Tel: 402-472-9604   Fax: 402-472-4732   Email: kst.germain@unl.edu

[2]Laboratory for Hydrospheric Sciences, Code 971
NASA Goddard Space Flight Center, Greenbelt, MD 20771, USA
Tel: 301-286-2444   Fax: 301-286-1761   Email: don@cavalieri.gsfc.nasa.gov

Abstract— A technique for estimating ice temperature in the Arctic seasonal ice zone from passive microwave radiances has been developed. The algorithm relies on ice concentration and type estimates from a thin ice algorithm to estimate the surface emissivity. Preliminary results have been compared favorably with temperature estimates derived from AVHRR imagery of the Bering Strait.

I. INTRODUCTION

Polar sea ice covers approximately 7% of the world's oceans. In the Antarctic the sea ice spatial extent varies between 4.0 x 10^6 km^2 during summer and 20.0 x 10^6 km^2 during winter, while in the Arctic the variation is significantly less, from 7.8 x 10^6 to 14.8 x 10^6 km^2. This coverage has a tremendous impact on the global climate because the ice changes the planetary albedo. In addition, during the winter, the heat flux from water or thin ice to atmosphere is approximately two orders of magnitude greater than the heat flux through thick ice.

There are many types of sea ice, from the thin ice types (grease ice, nilas, pancake ice, etc.) to thick multi-year ice. The microwave signature of each type is a strong function of dielectric constant. The dielectric constant of ice is dependent on several parameters, most notably salinity and temperature. Because salinity changes over the life cycle of an ice floe, it is possible to classify ice in terms of three broad categories, thin ice, first-year ice and multiyear ice, which are distinguishable from satellite based sensors [1], [2].

Although the heat flux through ice is primarily controlled by ice thickness, reliable estimates of surface temperature are also needed for flux calculations. In the Arctic this information has been inferred from data gathered by buoys drifting on ice floes [3]. The considerable difficulties of this method have encouraged the remote sensing community to develop alternatives. Satellite based infrared sensors such as the Advanced Very High Resolution Radiometer (AVHRR) offer greater Arctic coverage at high spatial resolution, but temperature retrieval is seriously constrained by cloud cover and ice fog contamination [4]. Satellite based passive microwave instruments avoid this problem, but at the cost of ground spatial resolution.

The Scanning Multichannel Microwave Radiometer (SMMR) provided the first opportunity for investigators to attempt to estimate ice temperature from microwave observations. Gloersen et al. [5] proposed a technique to produce ice temperature as a secondary product, and the SMMR radiances were used to calculate sea ice temperature over the nine year lifespan of the instrument. The SMMR algorithm made use of the first order relationship between brightness temperature and physical temperature of an emitting medium. The 6.6 GHz (λ_o = 4.55 cm) channel was used because the emissivity is independent of ice type at this frequency. The extensive comparison of SMMR estimated temperatures with Arctic Ocean Buoy Program (AOBP) data produced encouraging results in the central Arctic. No validation effort was made in the seasonal ice zone.

In this study, the Special Sensor Microwave/Imager (SSM/I) radiances were used to estimate ice temperature. The SSM/I does not have a C-band channel, so a new approach was devised. This study focuses on the seasonal ice zone because it is the most important region for heat flux studies.

II. THEORETICAL CONSIDERATIONS

Radiative transfer theory predicts that the brightness observed by a satellite based sensor will be:

$$T_{B,\lambda,p} = \varepsilon_{\lambda,p} T_S e^{-\kappa_\lambda} + T_{B,\lambda,Up} + \left(1 - \varepsilon_{\lambda,p}\right) T_{B,\lambda,Dn} e^{-\kappa_\lambda}$$
$$+ \left(1 - \varepsilon_{\lambda,p}\right) T_{B,C} e^{-2\kappa_\lambda} \tag{1}$$

where:

$T_{B,\lambda,p}$	=	measured brightness temperature
$\varepsilon_{\lambda,p}$	=	total surface emissivity
T_S	=	physical temperature of the radiating portion of the ice
κ_λ	=	atmospheric opacity
$T_{B,\lambda,Up}$	=	total atmospheric upwelling radiation
$T_{B,\lambda,Dn}$	=	total atmospheric downwelling radiation
$T_{B,C}$	=	cosmic background radiation, 2.7 Kelvin at microwave frequencies

The upwelling and downwelling atmospheric radiation can be approximated as:

$$T_{ATM} = <T> \left(1 - e^{-\kappa_\lambda}\right) \tag{2}$$

where $< T >$ is a constant weighted average atmospheric temperature and $e^{-\kappa_\lambda}$ represents total atmospheric loss.

The atmospheric parameters in (1) depend strongly on such variables as atmospheric pressure, temperature, and vapor profiles.

A. The Atmosphere

Because the temperature and humidity are usually low in the high Arctic, the atmosphere normally contributes little to brightness temperature measurements at most microwave frequencies. This is particularly true over pack ice where the surface emissivity is close to one. However, in the marginal ice zone, higher atmospheric water vapor and clouds are common, and the radiometrically cool surface of open water enhances atmospheric effects on brightness temperature. This becomes more important for SSM/I than SMMR because the lowest SSM/I frequency is 19.4 GHz.

For the Arctic it is reasonable to assume that the atmosphere is saturated with vapor but contains very little cloud liquid water [6]. Under these conditions opacity may be computed as a function only of T_s. At 19.4 GHz the atmospheric attenuation due to water vapor is approximated as:

$$\kappa_{vap} = \frac{e^{0.0878(T_S - 225.8)}}{1000} \text{Np} \quad (3)$$

and the weighted average atmospheric temperature in (2) is approximated as:

$$\langle T \rangle = -27.5 + 1.08 T_S \quad (4)$$

B. The Surface

In the seasonal ice zone (SIZ), the surface emissivity ranges from that of open water to that of thick, first-year ice. In addition, the radiometer field of view may contain a combination of open water and various ice types.

A technique for differentiating between new, young, and first-year ice types in SIZs has been previously developed [4] for use with the SSM/I. The technique utilizes the microwave polarization and spectral characteristics of these three ice types through two microwave radiance ratios: the 19.4 GHz polarization, and the spectral gradient ratio, which is a measure of the spectral difference between the 19.4-GHz and the 37.0-GHz vertically polarized radiance components. The combined use of the spectral gradient ratio and polarization reduces the low ice concentration bias generally associated with the presence of thin ice types. The microwave polarization, which is sensitive to changes in ice thickness and ice surface characteristics, is used to classify new, young, and first-year ice types. The polarization varies from about 0.3 for calm ice-free water, to about 0.15 for new ice, and to 0.03 for thick first-year ice. Based on this parameterization, improved sea-ice concentration maps and maps of new, young and first-year ice type distributions are derived.
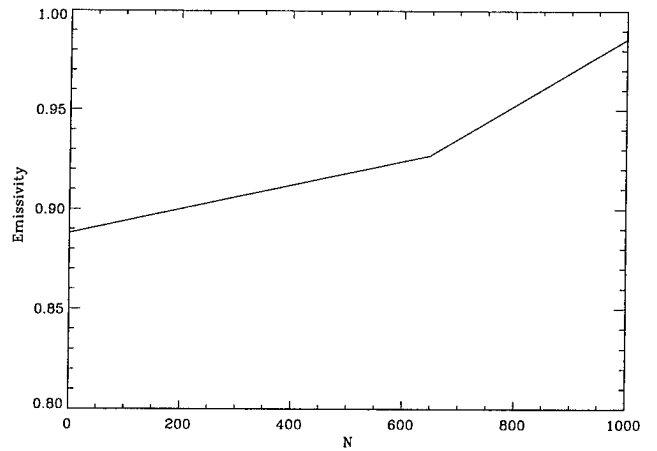
Fig. 1. Emissivity as a function of the thin ice algorithm parameter N. Large values of N correspond to thicker ice, while smaller values of N correspond to very thin ice.

In this study, the effective emissivity of water for the 19.4 GHz SSM/I channel was determined empirically to be 0.67. The emissivity for thin ice is a function of ice type. The thin ice algorithm classifies ice type on a scale from 0-1000. The associated emissivity relationship at 19.4 GHz is shown in Figure 1.

This relationship was determined empirically using AVHRR surface temperature estimates and land station observations.

III. DESCRIPTION OF THE ICE TEMPERATURE ALGORITHM

Following the lead of Gloersen et al. [5], the algorithm takes advantage of the first order relationship between brightness temperature and the physical temperature of the radiating portion of the target. Neglecting the small contribution from the reflected terms in (1), the inclusion of an atmosphere and surface model produce the following equation:

$$T_B = \varepsilon_{tot} T_s e^{-\kappa_{vap}} + < T > (1 - e^{-\kappa_{vap}}) \quad (5)$$

where:

T_B = measured brightness temperature

ε_{tot} = total surface emissivity based on retrieved ice concentrations and type, at 19.4 GHz

$< T >$ = weighted atmospheric temperature as a function of T_s, at 19.4 GHz

κ_{vap} = atmospheric attenuation coefficient as a function of T_s, at 19.4 GHz

Referring to (5), T_B is measured, ε_{tot} is estimated using the output of the thin ice algorithm, leaving T_S as the only unknown. Because of the dependence of κ_{vap} on T_S, (5) cannot be solved directly, so an iterative routine is employed.

The routine begins with a first guess value for surface temperature and calculates an expected $T_{B_{exp}}$. This value is then compared with the actual measured brightness temperature, and the next guess at surface temperature is adjusted accordingly. This routine typically converges in three iterations over the seasonal ice zone.

IV. TEMPERATURE EVALUATION

For obvious reasons reliable ground truth data is rare in the polar regions. Expeditions are few and usually provide only a few point measurements of ice temperature at best. One potential source of surface information is the Arctic Ocean Buoy Program (AOPB), which monitors several buoys drifting freely on ice floes throughout the central Arctic. For this study, however, we focus on the seasonal zone where buoys are rarely found.

We have compared our temperature estimates with those derived previously from AVHRR images [7]. There are several inherent differences between the two techniques. The skin depth of ice and snow is much smaller at infrared frequencies that at microwave frequencies. Therefore, the temperatures derived from IR observations are expected to reflect the air temperature for all but the thinnest ice. The temperatures derived from the SSM/I, on the other hand, will represent the ice temperature, even when there is a snow layer on the ice. For thinner ice and snow covered ice this will usually be significantly warmer than the air temperature.

A typical image from the Bering Straight is shown in Figure 2. This image represents SSM/I derived temperatures on Julian day 95 of 1988.

The trends observed in this image are similar to those previously observed [7]. Differences between the two have several sources. First, one must be careful when interpreting SSM/I pixel that are adjacent to land. These pixels often are "contaminated" by the presense of land and/or fast ice within the antenna footprint. Second, it is very
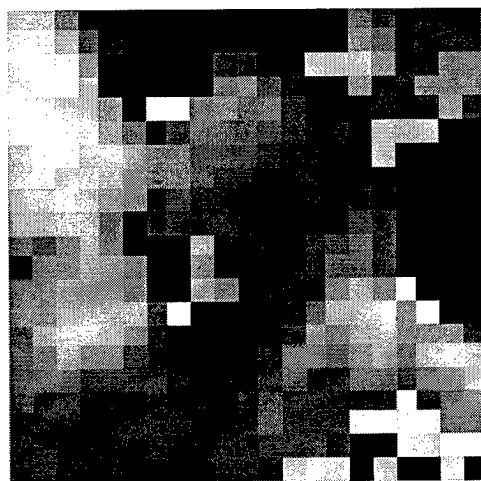
Fig. 2. A typical retrieval in the Bering Sea. Land is masked in black (Alaska to the right, Siberia at the top, and St. Lawrence Island in the middle) The temperature ranges from 250 to 273 Kelvin

difficult to mask clouds and diamond dust in AVHRR images. Regions containing scattered cloud cover in the AVHRR imagery must be viewed with decreased confidence in the retrieved temperature. Finally, because of the differences in penetration depth, we can expect differences between the AVHRR and SSM/I in several regions.

V. CONCLUSIONS

A new technique for estimating ice temperature from SSM/I radiances has been developed. The algorithm uses the ice concentration and type from the thin ice algorithm to estimate the surface emissivity. This emissivity is used to solve a transcendental equation for the surface temperature. Comparisons with temperatures derived from AVHRR observations are encouraging in the seasonal ice zone. Further testing and possible refinement are needed to ensure that this technique will be applicable throughout the freeze-up and winter seasons.

REFERENCES

[1] Parkinson, C.L., J.C. Comiso, H.J. Zwally, D.J. Cavalieri, P. Gloersen and W.J. Campbell. *Arctic Sea Ice, 1973–1976: Satellite Passive–Microwave Observations.*NASA Scientific and Technical Information Branch.Washington, D.C. 1987

[2] Cavalieri, D.J., A Microwave Technique for Mapping Thin Sea Ice, *J. of Geophys. Research*, v 99 (C6),12561–12572, 1994.

[3] Thorndike, A.S. and R. Colony. *Arctic Ocean Buoy data report, 1 January 1979 - 31 December 1979*, University of Washington, Polar Science Center, Seattle, Washington, 1980.

[4] Key, J. and M. Haefliger. Arctic Ice Surface Temperature Retrieval from AVHRR thermal channels, *J. of Geophys. Research*, vol. 97, pages 5885-5893, 1992.

[5] Gloersen, P., W.J. Campbell, D.J. Cavalieri, J.C. Comiso, C.L. Parkinson, H.J. Zwally, Arctic and Antarctic Sea Ice, 1978-1987:Satellite Passive Microwave Observations and Analysis, National Aeronautics and Space Administration, Special Publication 511, Washington, DC, pp.290, 1992.

[6] Climates of the Polar Regions, World Survey of Climatology, ed. Orvig, S., vol. 14, Elsevier Publishing Co., Amsterdam, New York, 1970.

[7] Massom, R. and J.C. Comiso, The Classification of Arctic Sea ice types and the determination of surface temperature using advanced very high resolution radiometer data, *J. of Geophys. Research*, vol. 99, no. C3, pages 5201-5218, 1994.

A Neural Network Sea Ice Edge Classifier for the NASA Scatterometer

Sami M. Alhumaidi, W. Linwood Jones, Jun-Dong Park,
Shannon Ferguson, and Michael H. Thursby
Florida Institute of Technology
150 W. University Blvd.
Melbourne, FL 32901
(407) 768-8000 x6219
(407) 984-8461 fax
alhumaid@ee.fit.edu, ljones@ee.fit.edu
Simon H. Yueh
Jet Propulsion Laboratory
Pasadena, CA 91109
(818) 354-3012

Abstract – The NASA Scatterometer (NSCAT) to be launched in August 1996 is designed to measure wind vectors over ice-free oceans. To prevent contamination of the wind measurements, by the presence of sea ice, an algorithm based on only NSCAT data is described. Results are presented for a neural network trained using dual linear polarized Ku-band backscatter measured by the SeaSat-A Satellite Scatterometer (SASS). These results demonstrate the utility of neural network classifiers to provide this ice flag. Results are presented for both multilayer perceptron (MLP) and a learning vector quantization (LVQ) neural networks. Classification skill is evaluated by comparisons with surface truth and with an independent ice-flagging algorithm.

INTRODUCTION

In August 1996, the NASA Scatterometer (NSCAT) will be launched on Japan's Advanced Earth Observation Satellite (ADEOS) to measure the surface winds over the world's ice free oceans. On each side of the subsatellite track, the NSCAT will measure the ocean normalized radar backscatter (sigma-0) at three azimuths. Further, for one azimuth, the antenna is dual polarized with linear, vertical and horizontal polarization's (V-pol and H-pol). Since land, or ice within the antenna instantaneous field of view (IFOV), will contaminate the ocean wind measurement, it is necessary to identify and remove measurements so affected. For land, the process is relatively simple using land maps and knowledge of the antenna IFOV's. However, because of its dynamic nature, it is difficult to identify the extent of sea ice. Usually, the sea ice

boundary is determined from a variety of satellite remote sensing data e.g., visible, infrared and passive microwave; however the non-simultaneity of these measurements with ADEOS can lead to significant errors as well as increased complexity in the NSCAT data processing. This paper describes a convenient and timely technique for determining this boundary from the NSCAT data alone. The technique involves the use of a neural network algorithm for inferring sea ice cover using sigma-0's from the dual polarized antenna.

SEA ICE SIGMA-0's

To train the neural network, backscatter data collected by the SeaSat-A Satellite Scatterometer (SASS) [1] were used. During the SASS experiment, dual polarized data were obtained for both the Arctic and Antarctic regions; however, because of a premature failure of the satellite, winter sea ice data were only available for Antarctica. Sigma-0's for July 13, 1978 were classified in a two step process. First, they were associated with ocean or sea ice using an independent co-polarized backscatter algorithm by Yueh [2]. Next, they were compared with independent Antarctic ice classification charts from National Snow and Ice Data Center to establish credibility. An example of the sigma-0 data for one revolution is shown in Fig. 1. Data from four even revolutions were used to train the neural network, and data from seven odd revolutions were used as an evaluation set. Because of significant overlap of the SASS swaths, this method provided an excellent means for comparison. For the training set, a conservative approach was adopted whereby data from both the ocean and ice were deleted within about 100 km on both sides of the sea ice boundary. In this manner low ice concentrations (% area coverage) associated with the marginal ice zone were excluded. For the evaluation set,

---

sigma-0 data were subjectively classified using an even more conservative criteria that identified mixed ocean/ice regions as ice. In this way, those sigma-0's classified as ocean were certain to be "not-contaminated".

NEURAL NETWORK CLASSIFIERS

Neural nets have been successfully used for classifying radar backscatter [2-4] and, in particular, to classify SAR images of sea ice [3]. The two most common neural classifiers applied to sea ice classification are the Learning Vector Quantization (LVQ) and the Multilayer Perceptron (MLP) classifiers. The former employs a simple learning rule developed by Kohonon [5]; whereas the latter uses a number of learning rules of which the most common is the backpropagation rule, based on the gradient descent method of optimization.

In this work, we applied the LVQ and MLP neural classifiers to classify sigma-0 measured by the SASS over Antarctica. The sigma-0 values were co-registered V-pol/H-pol pairs from the SASS Global 50-Km binned sigma-0's provided by the Jet Propulsion Lab Physical Oceanography Distributed Active Archive Center.

LVQ Classifier:

First, we used a 6×3 Self Organizing Map [5] neural net to obtain weights to initialize a LVQ net with three input neurons and six output neurons. Each of the output neurons was labeled by a known class (i.e., water or ice). The next step was to train this net with the training set developed using classification criteria as discussed above. The training data was iterated during the learning process for 10,000 epochs. Finally, the resulting net was tested with the evaluation data set which was subjectively classified. The result of the classification is shown in Table 1.

MLP Classifier:

A MLP neural net, with two hidden layers, was used to classify the same training data. The MLP net had three neurons in the input layer, 12 neurons in the hidden layers (six each) and two neurons in the output layer. The net was initialized with random weights and biases. Fig. 2 depicts the architecture of the MLP neural net that was trained using the backpropagation method with momentum term [6] until the total squared error reached a satisfactory level. The resulting weights and biases of the net were used to classify the evaluation data set. The result of the MLP classification is also listed in Table 1.

RESULTS AND DISCUSSION

Although the MLP neural classifier was more difficult to design and stabilize, and took longer time to converge, it performed better than the LVQ classifier. In addition, the MLP classifier was able to generalize better to data that was not presented during training (e.g., mixed ocean/ice).

The MLP had two output categories, namely; ice, and ocean. Whenever the output of the net was -1 and 1, the class declared was ice and vice versa for water. However, when the net can not classify a point, the output will be 0 for both output neurons. In this case, the decision is "mixed".

We compared the neural network (NN) output with the subjective classification (SubC) for the odd revolutions (evaluation data set). Because the objective of this research is to properly classify ice-free ocean, the success criteria was defined as: a match between the NN and SubC for ocean and ice; or data classified by the NN as mixed when the SubC is classified as ice. Further, there were a small percentage (< 1%) of SASS ocean sigma-0's that were anomalous (H-pol > V-pol). For these cases, neural network outputs of mixed were also counted as successful. The rationale for this being that anomalous sigma-0's should be "flagged". Plots of the data classified as ice or mixed are presented in Fig. 4-6.

In conclusion, the classification skill for the two neural networks are excellent which demonstrates the suitability of such algorithms for NSCAT sea ice-edge flagging. Once the designing and learning process is completed, the algorithm can produce reliable ice flags in real time. Future work will include additional input neurons to include multiple azimuth viewing.

REFERENCES

[1] W.L. Grantham, E.M. Bracalente, W.L. Jones, and J.W. Johnson, "The SeaSat-A Satellite Scatterometer", IEEE J. Oceanic Eng., Vol OE-2, No. 2, pp 200-206, April 1977.

[2] S.H. Yueh, R. Kowk, S.H. Lou and W.Y. Tsai, "Sea Ice Identification Using Dual-Polarized Ku-Band Scatterometer Data, IGARSS'96 digest (this issue), May 1996

[3] Y. Hara, R. G. Atkins, R. T. Shin, J. A. Kong, S. H. Yueh, R. Kwok, "Application of Neural Networks for Sea Ice Classification in Polarimetric SAR Images," IEEE Trans. Geosci. Remote Sensing, Vol. 33, pp. 740-748, May 1995.

[4] J. Orlando, R. Mann, S. Haykin, "Radar Classification of Sea-Ice Using Traditional and Neural Classifiers,"

[5] T. Kohonen, Self-Organization and Associative Memory, 2nd ed., Springer, Berlin, 1988.

[6] S. Haykin , Neural Networks A Comprehensive Foundation, Macmillan College Publishing Co., 1994.

Table 1: Classifiers Performance

Classifier Type	Percent Correct
LVQ	96.73
MLP	98.4
Co-Pol	97.16

Fig. 2: A 2-Hidden-Layer MLP Classifier

Fig. 1 : SASS Sigma-0 Time Series
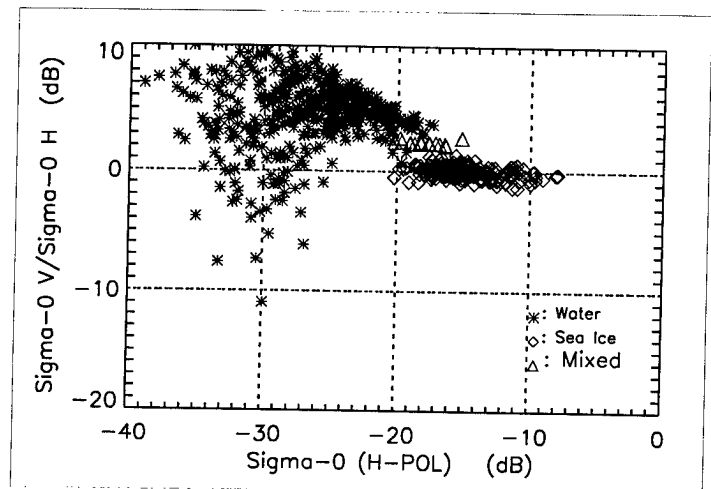
Fig. 3 : MLP Classifier Decision Space
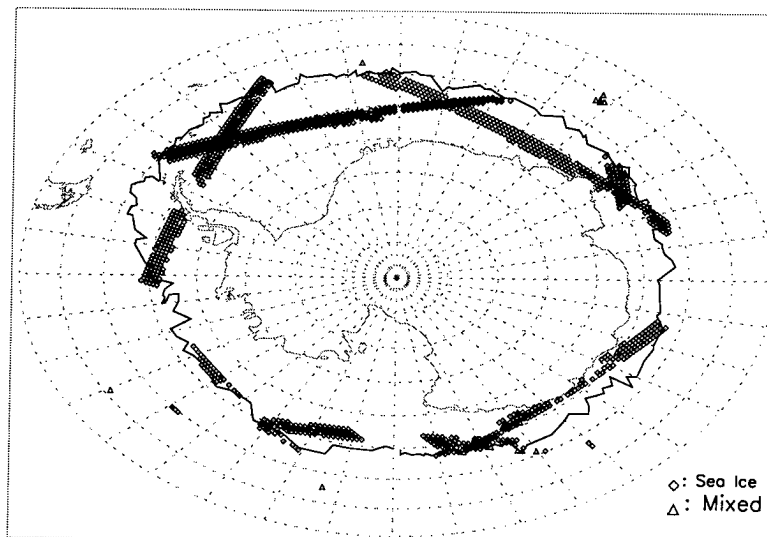
Fig. 4 : SASS - A Swath Showing Classification

Comparison of Open Water and Thin Ice Areas Derived From Satellite Passive Microwave Data With Aircraft Measurements and Satellite Infrared Data in the Bering Sea

T. Markus and D.J. Cavalieri

Code 971, NASA Goddard Space Flight Center, Greenbelt, MD 20771

Tel.:301-286-6808, Fax:301-286-0240, email:thorsten@cavalieri.gsfc.nasa.gov

Absract– For enhanced accuracy in the determination of heat fluxes in the polar regions, estimates of ice thickness are necessary. Only passive microwave sensors provide daily global surface information, but ice thickness is not directly measurable from this data source. Nevertheless, different ice types, associated with a certain thickness, are distinguishable resulting from different emissivities. Two methods using SSM/I data for this discrimination are compared with satellite infrared data and aircraft measurements. The SSM/I results are in good agreement with those data. Therefore, either method should greatly improve heat flux calculations.

INTRODUCTION

Distinction between consolidated first-year ice and areas of thinner ice are needed for ocean to atmosphere heat flux calculations and therefore for a better understanding of polar heat budgets. Only satellite passive microwave sensors can provide daily coverage for monitoring the rapidly changing thin ice areas. Results of two recently published methods ([3],[5]) using data from the DMSP Special Sensor Microwave Imager (SSM/I) are compared with high resolution aircraft data and cloud-free infrared data from the Advanced Very High Resolution Radiometer (AVHRR) over the Bering Sea in spring 1988.

One [3] (hereafter refered as thin ice algorithm) is a modification of the NASA Team ice concentration algorithm [2] which uses a new-ice tiepoint instead of the commonly used multiyear ice tiepoint. This algorithm also corrects for low concentration biases typically associated with the presence of new and young ice. The other method [5], called the Polynya Signature Simulation Method (PSSM), was developed for high resolution (6.25 km) estimates of polynya areas using the polarization ratio at 85 GHz and 37 GHz. The method is applied for the entire Bering sea and extended to discriminate between young and first-year ice.

The wintertime Bering Sea is particularly well suited for testing thin ice algorithms because of the absence of
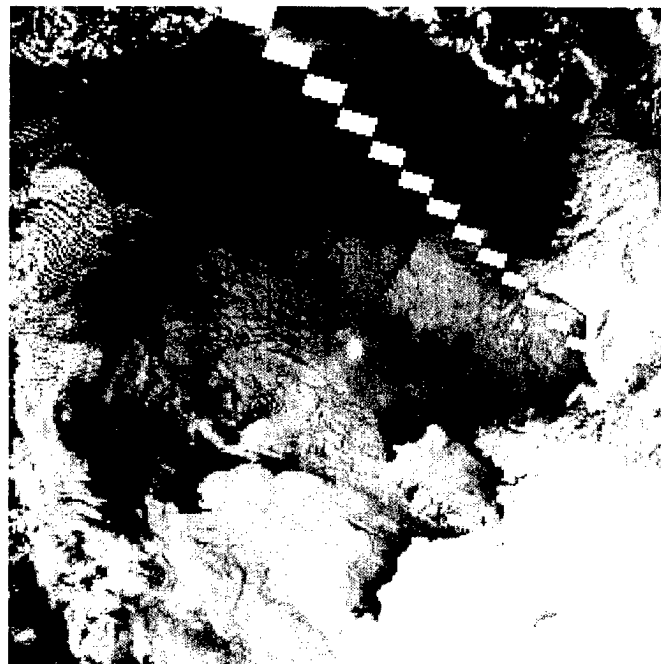
Figure 1: Channel 4,thermal infrared image of the Bering seen in April, 1988, from the AVHRR.

multiyear ice and of the presence of large coastal polynyas which provide extensive areas of new and young ice.

COMPARISON WITH AVHRR

Fig.1 shows the channel 4 AVHRR thermal infrared temperatures of the Bering Sea for April 4, 1988 mapped onto a 6.25 km grid. Fig.2 shows the PSSM results which distinguish between young and first-year ice. One can clearly see the very good agreement between these two data sets. The high resolution ice edge as well as even small areas of thin ice or loose ice pack are identified in the PSSM result. The ice classification using the thin ice algorithm is shown in Fig.3. Although the spatial resolution is lower, the image shows that the polynyas south of St. Lawrence
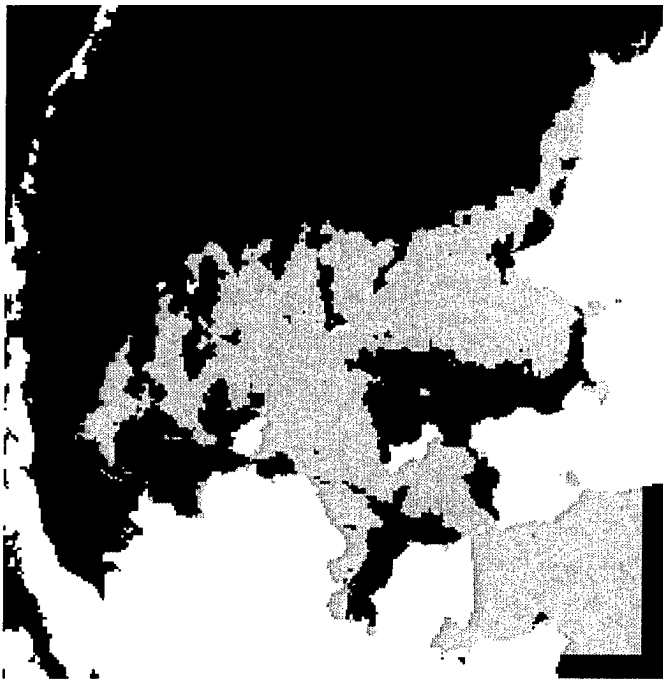
Figure 2: Result of the PSSM (same area as Fig.1). Black is open water, dark grey young or thin ice, grey first-year ice, and white land.

Figure 3: Ice types as derived from the thin ice algorithm. Greyscale as Fig.3, but black-gray indicates new ice.

Island and in Norton Sound are resolved and are in good agreement with the thin ice distribution associated with higher infrared temperatures in the AVHRR data. For a more quantitative comparison, the different ice types determined using the SSM/I algorithms are plotted against the AVHRR temperature (Fig.4) Both the AVHRR temperatures and the PSSM results are degraded into the 25 km SSM/I grid. The ice type versus temperature plot (Fig.4) shows decreasing infrared temperatures with increasing ice thickness as defined from the ice types. The agreement between the average temperatures using the PSSM and thin ice algorithm methods is within 2 K. This difference and also the higher standard deviation for new ice in the PSSM results from the fact, that there is no distinction between new and young ice. The significantly larger temperature difference between open water and new ice than between the other ice types reflects the immediate decrease in heat flux between ocean and atmosphere during the first centimeters of ice growth.

tion on the ice concentration and ice type in the vicinity of St. Lawrence Island [4]. A total of 40 SSM/I pixels over the Bering Sea for March 13 are classified using the two SSM/I algorithms and are compared with the results of the KRMS analysis (see Table 1). Unfortunately on March 13 there was no significant polynya south of St. Lawrence Island so that the vast majority of pixels consists of first-year ice. Almost all of these first-year ice pixels are classified correctly by both methods. Because the resolution of the PSSM is 6.25 km there are four pixels for each 25 km SSM/I pixel. Additionally, ice classification excluding coastal pixels as defined in the high resolution land mask [6] is shown seperately. In addition to the first-year ice pixels, most of the young ice pixels are classified correctly. Those pixels where the KRMS and the thin ice algorithm mismatch (pixels 32, 36) have mixed classes in the PSSM results. The last four pixels are highly contaminated by land. The fact that there are no new ice pixels and that the number of young ice pixels is very small precludes a useful numerical comparison.

COMPARISON WITH AIRCRAFT DATA

The aircraft data were obtained with the Navy Ka-band Radiometric Mapping System (KRMS) during a series of DMSP SSM/I underflights in March 1988 in support of the NASA Sea Ice Validation Program [1]. Analysis of the KRMS data obtained on March 13 provide informa-

CONCLUSIONS

Open water and thin ice distributions derived from DMSP SSM/I radiances using two different methods are compared with aircraft measurements and with AVHRR imagery over the Bering Sea. There is generally a good qualitative agreement in both comparisons. Use of either

Figure and plot

280 ┆ - - PSSM
    ┆ —— Thin ice alg.
275
T(ch4) [K]
270
265
260
    OW   NEW   YG   FY
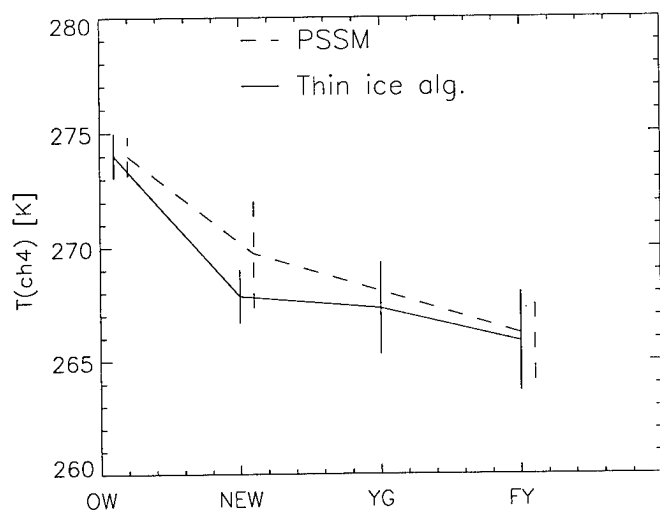
Figure 4: Ice types derived from the two SSM/I algorithms plotted against the AVHRR temperatures. The mean temperatures are plotted as a solid line for the PSSM and dotted for the thin ice algorithm.

Table 1: Classification of surface types using the KRMS aircraft data, the thin ice algorithm and the PSSM. F indicates first-year ice and Y young ice. The PSSM results have the additional flag of land (L). The + indicates the including of the coast and the − the excluded case.

Pixel	KRMS	Thin ice alg.	PSSM+	PSSM−
1	F	Y	Y Y Y Y	Y Y Y Y
2	F	F	F F F F	F F F F
3...31	F	F	F F F F	F F F F
32	Y	F	F F Y Y	F F Y Y
33	Y	-1	Y Y Y Y	Y Y Y Y
34	Y	F	Y Y Y Y	Y Y Y Y
35	Y	Y	Y Y Y Y	Y Y Y Y
36	Y	F	F Y Y Y	F Y Y Y
37	Y	Y	L L L L	Y Y Y L
38	Y	Y	L L L L	Y L L L
39	Y	Y	L L L L	Y Y Y L
40	Y	F	L L L L	L L F F

method should greatly improve heat flux calculations. The choice of method depends predominantly on the spatial scale needed. For large scale analyses (25 km or higher) the thin ice algorithm is easier to use and less sensitive to weather effects. The PSSM has an advantage in small scale studies (6.25 km). Nevertheless, both algorithms are currently limited to seasonal sea ice zones. Application to the entire Arctic region needs further work to eliminate ice-type ambiguities that arise from the presence of multiyear ice.

REFERENCES

[1] Cavalieri, D.J., NASA Sea Ice Validation Program for the Defense Meteorological Satellite Program Special Sensor Microwave Imager, J. Geophys. Res., 96, 21,969-21,970, 1991.

[2] Cavalieri, D.J., Sea Ice Algorithm, D.J. Cavalieri (ed), NASA Sea Ice Validation Program for the Defense Meteorological Satellite Program Special Sensor Microwave Imager: Final Report, NASA Technical Memorandum 104559, 1992.

[3] Cavalieri, D.J., A microwave technique for mapping thin sea ice, J. Geophys. Res, 99, 12,561-12,572, 1994.

[4] Farmer, L.D. and D.T. Eppler, Derivation of the Bering Sea Ice Concentration in Support of NASA SSM/I Thin Ice Algorithm Verification, Final Report, Bronson Hills Associates, Ltd., November, 1994.

[5] Markus, T. and B.A. Burns, A method to estimate subpixel-scale coastal polynyas with satellite passive microwave data, J. Geophys. Res., 100, 4473-4487, 1995.

[6] Martino, M.G., D.J. Cavalieri, P. Gloersen, and H.J. Zwally, An Improved Land Mask for the SSM/I Grid, NASA Technical Memorandum 104625, 1995.

Separating Ice-Water Composites and Computing Floe Size Distributions

Leen-Kiat Soh, Donna Haverkamp, and Costas Tsatsoulis
Department of Electrical Engineering and Computer Science
University of Kansas, Lawrence, Kansas
address: Center for Excellence in Computer-Aided Systems Engineering
2291 Irving Hill Road, Lawrence, KS 66045
tel: (913)864-7767 fax: (913)864-7787 e-mail: lksoh@cecase.ukans.edu

Abstract -- In this paper we describe an image processing technique that separates ice-water composites and determines the floe size distribution and concentration from SAR polar imagery. At marginal ice zones (MIZs), ice dynamics are active, providing important information for climatic indications and polar navigation. Hence, the identification of the ice-water composites and floe size distribution in these areas is of importance to geophysicists and polar navigator. We have designed a multi phase technique that combines Gaussian approximation, Laplacian measurement and structural modeling to obtain ice-water segmentation and floe extraction. With this technique we compute floe size distribution, ice-water composites, and coverage statistics. We have successfully tested our technique on a database of SAR MIZ imagery and established floe distribution and ice coverage maps for the corresponding areas.

INTRODUCTION

At marginal ice zones (MIZs) ice dynamics are active, providing important information for climatic indications and polar navigation. A record of temporally different floe size distributions tell us how floe sizes have changed over time (lateral growth or melt), and hints on the relationship between temperature and melt and freeze dynamics. In addition, a map of floe size distribution helps polar navigators plan an optimal route, for example, to avoid large multiyear ice floes. Also, ice coverage statistics give geophysicists a picture of ice-water composition in the region under analysis.

Given a SAR MIZ image, our technique is able to classify the ice-water composites into three classess: ice, water, and background matrix, using a combination of bi-normal Gaussian curve approximation and Laplacian edgyness measurement. The resultant classes are examined, and features with irregular geometric properties are filtered out. In addition, in most SAR sea ice imagery, adjacent ice floes touch forming a network of conglomerated ice floes, concealing separatedness among ice floes and hindering floe-dependent analyses. We have developed a restricted growing concept, aimed at achieving object separation while maintaining accuracy. Coupling the concept with our classification program, we are able to compute floe size distribution, ice-water composites, and coverage statistics. In the following, we will focus our discussion on the methodology and its results when applied to SAR sea ice imagery.

METHODOLOGY

Our technique consists of five stages: primary image segmentation, floe extraction, floe filtering, secondary image segmentation, and computation of floe size distribution and coverage statistics. A mathematical morphology-based technique that estimated floe size automatically using a disc-like mask to perform morphological operations on the floes was proposed in [1]. However, we see three disadvantages in this scheme. First, the distribution is an estimation since it is based on approximating discs. Second, floes are connected and treated as a piece of large floe. Third, the segmentation technique (a simple binary intensity thresholding) used is not applicable to most SAR sea ice imagery. The objectives of our technique, on the other hand, are to extract floes accurately for their sizes and distinguish background matrix from water regions. Our approach is to first differentiate floe and non-floe regions using intensity-based segmentation, and then distinguish background matrix and water from the non-floe regions using Laplacian edge-based segmentation.

Primary Image Segmentation

This segmentation is based on local dynamic thresholding [2], which has been proven to be able to detect local details of the segmentation and be adaptive to different SAR sea ice imagery across which intensity of similar ice classes vary. The technique was modified to accommodate SAR sea ice imagery composed of floes, background matrix, and water. It first divides the image into smaller regions and then applies Gaussian approximation to each region's histogram. From the resulting best fit curve, an optimal threshold is obtained through maximum likelihood method. The collection of all computed thresholds is further divided into two sets, of which we use only one to segment the image into floes and non-floes. This is because for SAR sea ice imagery that consists of floes, background matrix, and water, background matrix and water regions cannot be directly separated under our implementation of local dynamic thresholding due to their overlapping intensity ranges. This segmentation stage thus produces floe and non-floe regions, and the non-floe region will be further segmented during the secondary segmentation phase.

Floe Extraction

For floe identification in satellite images, a technique that integrated mathematical morphology and principal curve clustering was presented in [3]. The authors used the

erosion-propagation (EP) algorithm to select the potential edge pixels and provide an initial grouping of them into floe outline; and clustering about closed principal curves to determine which floes to be merged. However, we have found that the EP algorithm suffers from two disadvantages. First, preservation of floe size and shape is not satisfactory, and second, the number of iterations needed for the EP algorithm to perform is different for each image, and its determination requires human visual judgment and experimentation. Our technique, based on the restricted growing concept [4], enables extraction of ice floes individually by creating separation among floes while preserving the original size and shape of the floes, retaining small ice floes, and requiring minimal human intervention. Briefly, our floe extraction technique first shrinks (using probabilistic labeling) the floes to their cores, thus creating separation among touching floes. Then, the technique grows the objects back to their original sizes and shapes restricted by the boundary of the original floes, under the guidance of some structural rules that prohibit any growing that will destroy separation of floes.

Floe Filtering

This stage filters out ice features that are not floes, based on an irregularity measure, defined as the ratio of the perimeter over the size of the floe. If this ratio is low, that means the floe is compact and thus accepted; otherwise it is eliminated.

Secondary Image Segmentation

To distinguish background matrix and water, we have designed a Laplacian-based local dynamic thresholding, a variant of Laplacian filtering thresholding [5] and Gradient thresholding [6]. First, floe regions are masked from this phase of processing. Second, for each pixel, its Laplacian value is computed. Third, Laplacian histograms of local regions are analyzed such that only histogram with high "edgyness" value qualify for further processing. Each bin of the histogram represents a gray level value, g_i, of the local region, while its frequency is the sum of the Laplacian values associated with any pixel that has the gray level value g_i. Edgyness is the normalized sum of neighboring differences of the bins of the Laplacian histogram. If the region is homogeneous, its frequencies of Laplacian values will be close and thus its edgyness will be low; otherwise, the measure will be high. Fourth, for each qualified histogram, a threshold is computed by selecting the gray level that maximizes the cumulative probability that its location is in the middle of an edge transition. This is accomplished by selecting the gray level g_i, such that the bin has the largest value among all other bins. Fifth, region interpolation and point interpolation are executed to ensure that each region and pixel have one threshold. Finally, the binary decision is performed to segment the processed regions into background matrix and water.

Floe Size Distribution and Coverage Statistics

Finally, a program is used to generate two types of numerical statistics: 1) distribution of designated floe size bins of the image, by grouping similar floe sizes into the same bin, and 2) ice coverage—distributions of floes, background matrix, and water.

RESULTS

Fig.1 shows an original SAR summer MIZ image, located at the Beufort Sea. As noted, this image contains ice floes that are darker than their surrounding. Water regions appear bright and the background matrix—a composition of slush ice and water mixture—resides at an intensity range close to the water's. Fig.2 shows the floe-water-background matrix segmentation and floe size distribution. The bright regions are water regions. The dark regions are background matrix regions. The other shaded regions are floes. The coverage statistics are: floes occupy 42.05%, background matrix 40.43%, and water 17.52%. The different shaded regions indicate different bins of floe sizes. Table 1 shows the floe size distributions of the image. As we can see from the two images, most of the floes were detected and the floe sizes were preserved nicely, enabling an accurate measurement of floe size distribution. In addition, the water and background matrix regions were separated from each other, completing the final ice-water composition map. In general, we have tested successfully our technique on a database of MIZ data where floe, water, and background matrix regions co-exist.

CONCLUSIONS

We have designed a technique that separates ice-water composites and computes floe size distributions. This technique requires minimal human intervention: one only has to determine which of the two classes generated by the primary image segmentation phase is the floe region. We have applied this technique on a database of SAR sea ice imagery and obtained successful results in generating ice coverage statistics and identifying floes and their sizes. However, this technique does not perform well when one of these regions is missing since the methodology assumes such three classes in the image. In the future, we aim at extending this work to handle different classes of images, and also eliminating the need for inspecting the image for floe intensity identification.

REFERENCES

[1] R. Korsnes, "Quantitative Analysis of Sea Ice Remote Sensing Imagery," International Journal of Remote Sensing, vol. 14, no. 2, pp. 295-311, 1993.

[2] D. Haverkamp, L.-K. Soh, and C. Tsatsoulis, "A Comprehensive, Automated Approach to Determining Sea Ice Thickness from SAR Data," IEEE Transactions

on Geoscience and Remote Sensing, Vol. 33, No. 1, pp. 46-57, 1995

[3] J. Banfield and A. E. Raftery, "Ice Floe Identification in Satellite Images Using Mathematical Morphology and Clustering about Principal Curves," Journal of the American Statistical Association, vol. 87, no. 417, pp. 7-16, 1992.

[4] L.-K. Soh and C. Tsatsoulis, "A Multistage Feature Extraction Technique for Synthetic Aperture Radar (SAR) Sea Ice Imagery, Part II: The Restricted Growing Concept," Technical Report: CECASE TR 9710-03.

[5] J. S. Weszka, R. N. Nagel, and A. Rosenfeld, "A Threshold Selection Technique," IEEE Transactions on Computers, vol. 23, pp. 1322-1326, 1974.

[6] S. Watanabe and CYBEST group, "An Automated Apparatus for Cancer Prescreening: CYBEST," Computer Graphics and Image Processing, vol. 3, pp. 350-358, 1974.

Table 1. The floe size distributions of the image in Fig.1. Six size bins were used. To interpret, for example, there are 1365 pieces ice floes with size less than 100 pixels, covering 6.11% of the image. The image size is 1024×1024 pixels.

size bin (pixels)	# of floes	% of area covered
$x \leq 100$	1365	6.11
$100 < x \leq 500$	685	14.29
$500 < x \leq 5000$	141	16.58
$5000 < x \leq 12000$	1	0.94
$12000 < x \leq 30000$	2	4.10
$x > 30000$	0	0.00
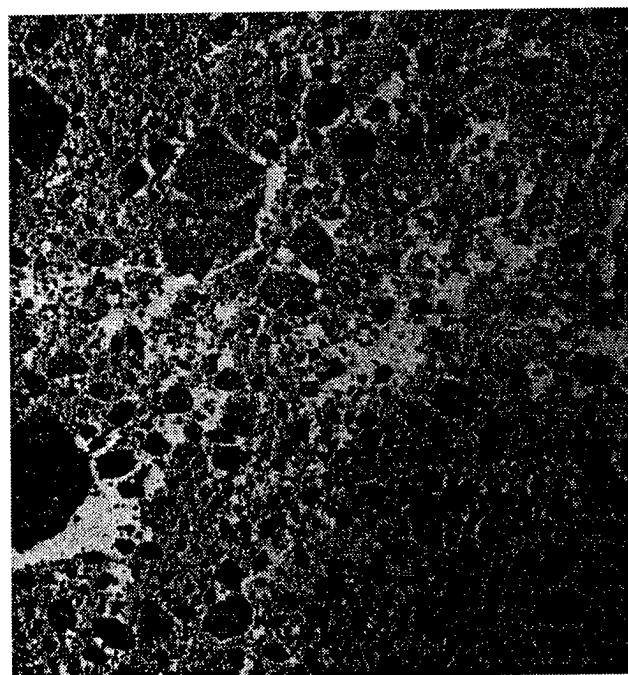
Figure 1. The original of a SAR MIZ image, Aug 17 1991, at 74.43°N, 144.29°W. Bright regions are water regions, floes are dark, and background matrix occupies the middle range.
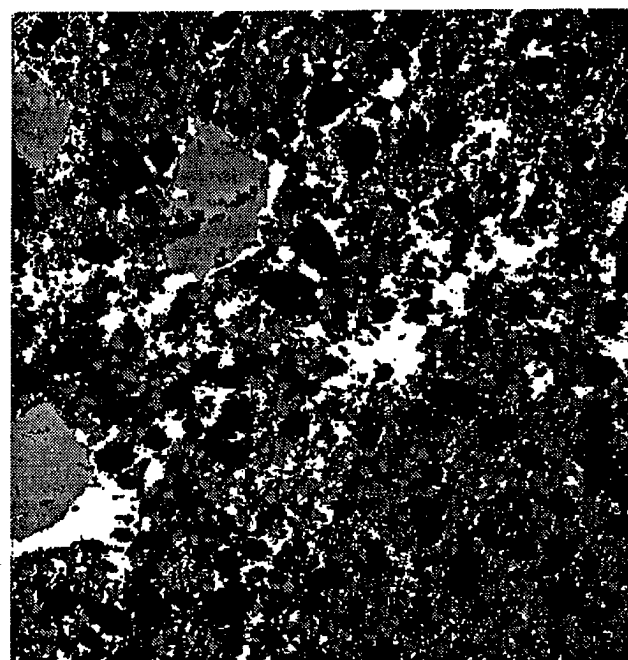
Figure 2. The classified image of Fig.1. Legend: Bright denotes water. Dark denotes background matrix. Different shades denote different bin sizes of floes.

Laser Diode Based New Generation Lidars

J.A. Reagan, H. Liu and J.F. McCalmont
University of Arizona, ECE Dept., Tucson, AZ 85721-0104
Tel (520) 621-6203, Fax (520) 621-8076, reagan@ece.arizona.edu

Abstract -- Recent technological advances in lasers and detectors now permit realization of relatively low cost and eye-safe lidars. Eye safety, even in the visible and near-IR regions, can be achieved by reducing laser pulse energies to a few micro-joules. The reduced signals due to such low transmitted pulse energies can be at least partially offset by operating at higher pulse repetition frequencies (PRF's). Laser diodes as lidar transmitter sources offer advantages of low cost, several available wavelengths and high PRF's, but they have also suffered from limitations of very low pulse energies, spectrally broad pulsed operation and wide beam divergence. However, the development of master oscillator-power amplifier (MOPA) laser diode configurations now offers the possibility of single-mode pulsed operation at microjoule and higher energy levels with reduced beam divergence. High efficiency photon counting avalanche photodiodes (APD's) have also become available which are capable of counting at high rates (~20 MHz), thus permitting effective detection of micro-pulse lidar (MPL) signals. This paper addresses the design requirements of laser diode lidars, based on these technological innovations, to achieve effective aerosol and DIAL water vapor sensing.

INTRODUCTION

Recent advances in laser and detector technology permit development of relatively low cost eye-safe lidars. In particular, GaAlAs diode lasers operating in the ~750 nm to ~950 nm wavelength range have become available which can produce microsecond duration pulses with energies in the micro-Joule (μJ) range at ~10 kHz pulse repetition frequencies (PRF's). Eye safety can be achieved by expanding the laser beam through a collimator to a diameter not greater than about 25 cm. The weak lidar return signal from such low transmitted pulse energies can be sensed by photon counting and summing using new highly efficient photon counting avalanche photodiode (APD) detectors. The high laser PRF permits summing over millions of pulses to achieve large signal-to-noise ratios (SNR's) in fairly short time intervals of several minutes.

The wavelength range spanned by GaAlAs laser diodes is quite effective for aerosol sensing and also presents the opportunity for differential absorption lidar (DIAL) water vapor sensing using the ~830 nm water vapor absorption region [1]. DIAL type water vapor sensing using

pseudorandom-noise modulated cw laser diode has also been demonstrated on a preliminary basis [2]. This paper presents an update on the prospects for laser diode based lidars. Design innovations necessary to achieve effective aerosol and water vapor sensing are discussed. Simulations are also included to demonstrate anticipated system performance.

SYSTEM CONSIDERATIONS

A proposed conceptual design for a laser diode based aerosol and water vapor DIAL lidar is shown in block form in Fig. 1. The laser diode Master Oscillator-Power Amplifier (MOPA) source is the key system component. It provides the means for achieving both spectrally stabilized operation, via frequency lock/control of the cw seed laser diode Master Oscillator, and micro-Joules level output pulses, via current driver pulsing of the laser diode Power Amplifier. A discrete MOPA design, with a fiber optic (FO) coupler/isolator, is required for isolation between the MO and PA in order to achieve pulsed output with the reduced spectral linewidth normally only possible with cw laser diode operation. Frequency control/locking to operate at either on-line (in water vapor absorption line) or off-line wavelengths with linewidths <~50 MHz can be achieved by locking the MO to a water vapor absorption line via feedback through an absorption cell (e.g., [2]), for the on-line, and adding current biasing to shift to the off-line. Laser diode amplifiers are available which have been used to produce outputs of several watts average power and peak powers of ~10 w [3]. Thus, this approach offers a feasible means for producing microsecond duration pulses at ~10 kHz PRF's with energies of several micro-Joules and a combined linewidth/center frequency jitter spread < ~100 MHz. Current bias to achieve on/off-line spectral selection enables use of a single transmitter, reducing system cost but preventing simultaneous on/off-line operation. Sequential switching between on- and off-line operation can be efficiently achieved at 10 to 20 second intervals which should be short enough to avoid significant temporal variation effects. Collimator beam expansion to a diameter of ~25 cm is sufficient to achieve eye-safety and reduce the transmitted beam full-angle divergence to <~200 micro-radians (μ-rad).

The receiver photon counting APD's are the second most important system components. Active quench

photon counting APD's are now available (EG&G SPCM-200-AQ series detectors) which can photon count at rates approaching 20 MHz, have insignificant dark counts (< ~100 counts/sec), and have quantum efficiencies of ~60% in the 830 nm range. An Interference Filter (IF) bandpass filter, now available with FWHM bandwidths < ~0.2 nm, is used for primary filtering of background radiation (significant for daytime operation) at both the on-line and off-line wavelengths (i.e., it is possible to define useable on- and off-line wavelengths separated by ~0.1 nm). Solid Fabry-Perot Etalons (FPE's), with free spectral ranges greater than the IF bandpass, provide additional filtering to reduce the on- and off-line receiver bandwidths to < ~0.02 nm. Such narrow-band receiver filtering is feasible by virtue of the even narrower transmitted pulse linewidths made possible by using the MOPA approach. Receiver primary optics up to about 40 cm in diameter still permit an economical, fairly compact system. The receiver full-angle FOV must be less than the transmitted beam divergence (<~200 μ-rad); hence, it should be <~400 μ-rad. Through careful design, it should be possible to achieve an overall system optical transmission efficiency at the on/off-line wavelengths of > 5%. The transmitter and receiver capabilities defined herein comprise what are considered to be a feasible set of parameters for a lidar based on the MOPA source and APD photon counting detector design innovations.

LIDAR AND DIAL RELATIONS

The received lidar signal for one transmitted laser pulse of energy E_o centered on wavelength λ, expressed in received photoelectrons $n_\lambda(z)$, for backscattering received from a range bin of length Δz centered at a distance z from the lidar may be expressed by

$$n_\lambda(z) = \frac{\lambda \delta_\lambda}{hc} \times \frac{E_o A_R \Delta z \beta_\lambda(z) T_\lambda^2(z)}{z^2} \qquad (1)$$

where δ_λ is the detector quantum efficiency, h is Planck's constant, c is the speed of light, A_R is the effective receiver aperture, $\beta_\lambda(z)$ is the atmospheric unit volume backscattering coefficient at range z for λ, and $T_\lambda^2(z)$ is the atmospheric round-trip transmittance to range z for λ.

If there is negligible background radiation, as occurs at night, the ideal quantum limited SNR(z) is just $SNR(z) = \sqrt{n(z)}$. If the background radiation is signification, as occurs during the day, contributing a count n_B per range bin, the SNR becomes

$$SNR(z) = \frac{n(z)}{\sqrt{n(z) + n_b}} \qquad (2)$$

For M laser pulses, the SNR is increased by the multiplier factor $\sqrt{M}$. While the SNR may be quite low

for only one micro-Joule level laser pulse, the high PRF's of laser diodes make it possible to achieve high SNR's over averaging periods of a few minutes or less.

The DIAL technique is implemented by making lidar measurements at two wavelengths λ_1 and λ_2, where one is on-line (in gaseous absorption region), say λ_1 yielding a signal $n_1(z)$, and the other is off-line at λ_2 yielding a signal $n_2(z)$. For λ_1 and λ_2 quite close together so that the backscattering and non-absorbing transmittances are effectively equal at each wavelength and assuming identical (or normalized) system characteristics for each wavelength, the ratio of the on-line to off-line signals, $Q(z) = n_1(z)/n_2(z)$, reduces to the roundtrip differential absorbing gas transmittance $T_g^2(z)$ through range z; $Q(z) = T_g^2(z)$. Measurements at two closely spaced ranges z_1 and z_2 can be combined to retrieve the number density of the absorbing gas at z, $N_g(z)$, by the well known DIAL retrieval relation

$$N_g(z) = \frac{\ell n \left[Q(z_1)/Q(z_2) \right]}{2(z_2 - z_1)\sigma_g(z)}, \qquad (3)$$

where $z = (z_1 + z_2)/2$ and $\sigma_g(z)$ is the gas per molecule differential absorption cross section. For a practical lidar with a finite transmitter spectral linewidth, $\sigma_g(z)$ becomes a band-averaged cross section weighted by the transmitted spectral energy profile at z. Retrieval accuracy is limited by two major factors. One is the measurement accuracy of $Q_1(z)$ and $Q_2(z)$, which improves with higher SNR's. The other is the accuracy with which $\sigma_g(z)$ can be determined, which depends in part on the spectral width and uncertainty of the transmitted spectral energy profile.

ANTICIPATED PERFORMANCE

Anticipated performance of the proposed laser diode based lidar can be estimated from simulations based on the lidar system parameters and signal relationships given in the preceding two sections. The first step in performing such simulations is to select useable on-line and off-line wavelengths. The water vapor absorption peak at 12,074.57 cm^{-1} (828.1868 nm) is a good candidate for the on-line, and the absorption minimum at 12,073 cm^{-1} (only ~0.1 nm separation) is a good choice for the off-line. Linewidths must then be specified for the lidar transmitted on/off-line wavelengths in order to compute the band-averaged value of $\sigma_g(z)$, including correcting for spectral shift and broadening effects. Trial computations revealed that $\sigma_g(z)$ changed vary little for linewidths up to ~300 MHz; a linewidth of 150 MHz (~0.005 cm^{-1}) was chosen for the simulations.

Example retrievals obtained for daytime simulations,

averaged over 15 minutes, assuming a Summer Mid Latitude U.S. Standard Atmosphere model are shown in Fig. 2. Retrieval uncertainties due to SNR(z) limitations are indicated by +/- one-sigma error bars on the true Ng(z) profile. Aerosol scattering needed to compute $\beta(z)$ was modeled by a relatively clean aerosol profile with aerosol backscattering only 2.5 times the molecular backscatter at a height of 3 km. The simulations assume 5 μJ of laser energy at the on/off-line wavelengths, a 10 kHz laser PRF, a receiver 40 cm in diameter with a 300 μ-rad FOV, on/off-line receiver bandpasses of 0.02 nm, an 8% system optical transmission efficiency, a range bin length Δz=150 m and a background per bin count representative of daytime conditions.

This daytime simulation yields a retrieval uncertainty under ~±0.5 g/kg (under ~25%) up to 3 km, a very functional level of performance for monitoring lower troposphere/boundary layer water vapor profiles. Nighttime performance is better due to the absence of significant background radiation, yielding an uncertainty of about +/- 0.1 g/kg or less up to 3 km. The off-line SNR(z) values are also a few hundred or greater up to 5 km even for daytime, indicating very good aerosol sensing capability. These and other results to be included in the symposium presentation of this paper indicate that laser diode based lidars should be quite effective for aerosol and DIAL water vapor sensing.

Funding is being pursued to develop a prototype laser diode based lidar similar in concept to the one described here under the National Oceanic and Atmospheric Administration (NOAA) Office of Global Programs in a jointly proposed effort involving Investigators from NOAA Environmental Technology Laboratory, the University of Arizona and NASA Goddard Space Flight Center [4].

REFERENCES

[1] J.A. Reagan, T.W. Cooley, and J.A. Shaw, "Prospects for an Economical, Eye-Safe Water Vapor Lidar," *Proc. IGARSS'93 Symposium*, Tokyo, Japan, pp. 872-874, August, 1993.

[2] J.A.R. Rall, J.B. Abshire, D. Reusser, and M. Humphrey, "Measurements of Atmospheric Water Vapor Using a Compact AlGaAs Laser Based DIAL Instrument," *CLEO 94 Conf.*, Anaheim, CA, paper CWD5, May, 1994.

[3] L. Goldberg and D. Mehuys, "21 w broad area near-diffraction limited semiconductor amplifier," *Appl. Phys. Lett.*, vol. 61, pp. 633-635, 1992.

[4] R.M. Hardesty, J.A. Reagan, J.A.R. Rall, and J.B.

Abshire, "Development of a Lower Troposphere Water Vapor Profilier," Proposal to NOAA Office of Global Programs, Silver Spring, MD, August, 1995.
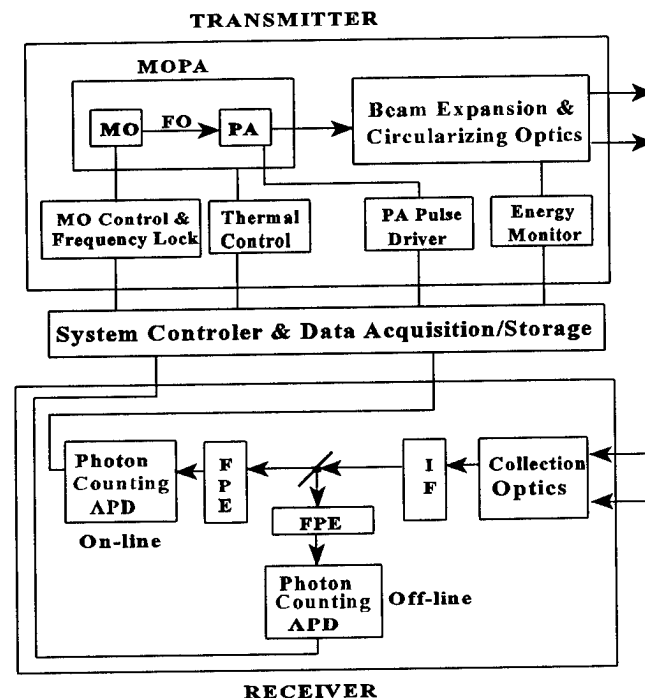
Fig. 1 Lidar system block diagram
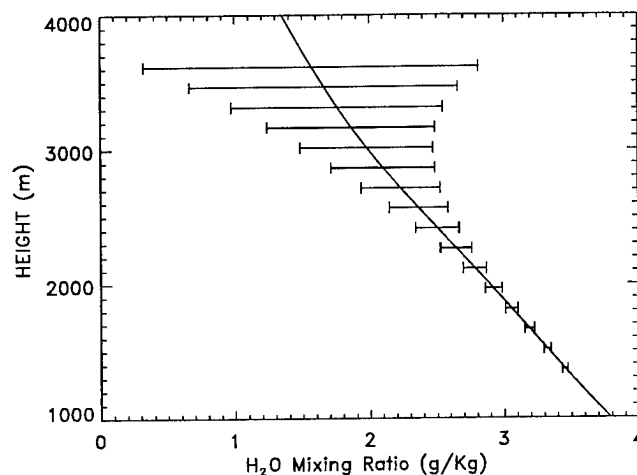
Fig. 2 Simulated water vapor retrieval

Antarctic Miniature Lidar

Jonathan A. R. Rall and James B. Abshire
Laser Remote Sensing Branch / Code 924
NASA Goddard Space Flight Center
Greenbelt, MD 20771
Phone: (301)286-7397 / Fax: (301)286-1761 / email: jarrall@eib1.gsfc.nasa.gov

Abstract - A second Antarctic Miniature Lidar instrument (Ant Lidar II) has been assembled, tested, and deployed to the NOAA Clean Air Facility (CAF) at the Amundsen-Scott South Pole Station. This instrument deployed in February of this year replaces the first Antarctic Lidar (Ant Lidar I) which operated at the South Pole Station from February to July 1995 [1]. The new lidar, as in the first instrument, uses redundant commercially available, single element diode lasers, a 20 cm Schmidt-Cassegrain telescope, and a silicon avalanche photodiode (APD) operated in the photon counting mode. In this paper we present measurements from the Ant Lidar I instrument as well as the design of the Ant Lidar II instrument and measurements made both prior to and following its installation at the NOAA CAF in February, 1996.

INTRODUCTION

Semiconductor (diode) lasers have been used with pseudonoise code (PN) amplitude modulation in previous lidar instruments to remotely sense clouds and atmospheric aerosol distributions at night [2-5]. In addition, a differential absorption lidar (DIAL) based on an externally modulated AlGaAs laser has made night time measurements of integrated path and range-resolved atmospheric water vapor [6].

In 1993, the Experimental Instrumentation Branch at Goddard Space Flight Center was invited to develop a compact, low power, diode laser based lidar as part of the on-going University of Illinois experimental program at the South Pole. The instrument was to be deployable in an Antarctic Geophysical Observatory (AGO), operate continuously during the polar night, and record the occurrence of polar stratospheric clouds (PSC). These clouds form at altitudes from 12 to 27 km and have been implicated in the destruction of polar stratospheric ozone [7,8]. Fig. 1 shows two lidar profiles acquired with the University of Illinois Sodium Lidar during June and July, 1990. The graph depicts backscatter ratio versus altitude; strong PSC returns are evident from 13 to 26 km with the peak backscatter descending over time.

The Ant Lidar I instrument was designed, built, and tested from October 1994 through January 1995 and deployed to the South Pole during February 1995 Figure 2 shows a 30 minute atmospheric profile acquired with Ant Lidar I at the South Pole on July 17, 1995. The data has been range-corrected and a 2-bin smoothing has been performed yielding a vertical resolution of 240 m. Rayleigh scattering is evident from 4-9 km altitude and a prominent cloud return occurs from 10-15 km. The Ant Lidar I instrument failed at this point and no further data was taken.

DESIGN

The Antarctic Lidar II system diagram is shown in Fig. 3 with the system characteristics listed in Table 1.

Redundant 150 mW laser diodes are used and can be operated at either half power or full power, individually or together. At full power, each laser emits 100 mW avg power at a 50% duty cycle. The injected current to the laser is directly modulated with a 2047 bit PN code at a bit rate of 1.25 MHz which yields an effective range resolution of 120 meters in the atmospheric returns.

RESULTS

Ant Lidar II was assembled and tested in early January, 1996. Prior to deployment, the instrument was set-up to run over night acquiring 10 minute data sets continuously. Fig. 4 and Fig. 5 show two ten-minute profiles acquired at Goddard on the night of January 25, 1995. Each profile has been range-corrected. Fig 4 shows a strong night time cirrus layer occurring at 9-10 km altitude. The 10 minute profile in Fig 5 occurs almost 2 hours later and shows that the cirrus layer has almost dispersed. Rayleigh scattering up to ~15 km is evident.

The Ant Lidar II instrument was deployed to the South Pole in early February, 1996. It was set-up and tested in the NOAA Clean Air Facility. The sun was at an elevation angle of ~15° above the horizon which produced a high background count rate on the APD. To limit the high count rate to less than 300 kcounts/sec an adjustable aperture was used which reduced the effective telescope area to only a few square cm. Fig 6 shows a 20 minute profile acquired on Feb. 6, 1996. A cirrus cloud layer is evident at ~4.2 km altitude. Once the sun sets, the telescope aperture will be removed and the lidar can operate continuously.
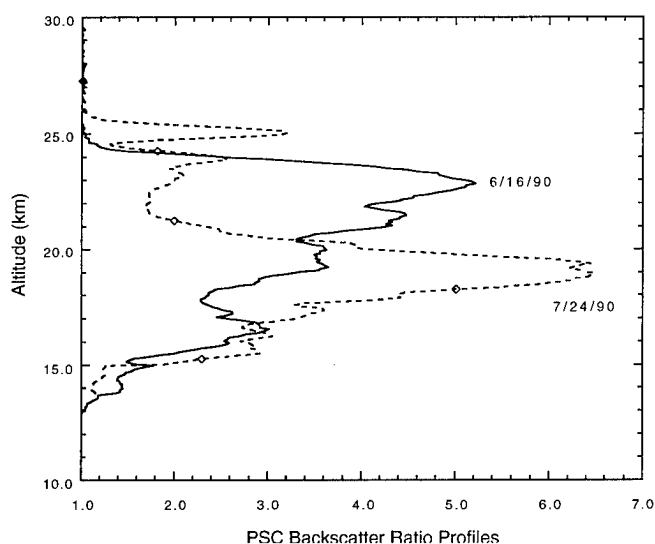
Fig. 1 Stratospheric backscatter ratios measured with the University of Illinois - Sodium Lidar during peak PSC season in June & July 1990. (R. Collins)

Table 1. Antarctic Miniature Lidar system parameters.

Laser Type	AlGaAs laser diode, SDL 5420-G1
Laser divergence	6x beam expander, ~100 urad
PN code	2047 bits, 1.25 MHz bit rate
Telescope	20 cm diam, F/6.3, 200 urad FOV
Bandpass filter	10 nm centered @830 nm
Detector	Si APD, EG&G SPCM-200-AQ

CONCLUSION

The second Antarctic Miniature Lidar has been assembled, tested, and deployed to the NOAA Clean Air Facility at the Amundsen-Scott South Pole Station. Ant Lidar II will operate throughout the austral winter with data being sent regularly to Goddard via the internet for processing. Antarctic Miniature Lidar III is currently being designed for deployment in an Antarctic Geophysical Observatory (AGO) in early 1997.

REFERENCES

[1] Rall & Abshire, Tech. Digest, Vol 20, Semiconductor Lasers Adv Devices & Appl, OSA/IEEE LEOS, 1995.

[2] Takeuchi et al., Appl. Opt. 25(63) 1986.

[3] Abshire, Rall, & Manizade, 16th International Laser Radar Conference, NASA Conf. Pub. 3158, 1992.

[4] Rall, Abshire, & Manizade, IEEE Lasers & Electro Optics Society Annual Meeting, EOS/SSLT/OSM 1.3, 1992.

[5] Abshire & Rall, Technical Digest, OSA - Optical Remote Sensing of the Atmosphere, Paper ThE29, 1993.

[6] Rall & Abshire, Technical Digest -Vol 8, Conference on Lasers and Electro Optics, Paper CWD5, 1994.

[7] McCormick, et. al. J. Atmos. Sci. 39 1982.

[8] Solomon, et. al., Nature 321, 1986.
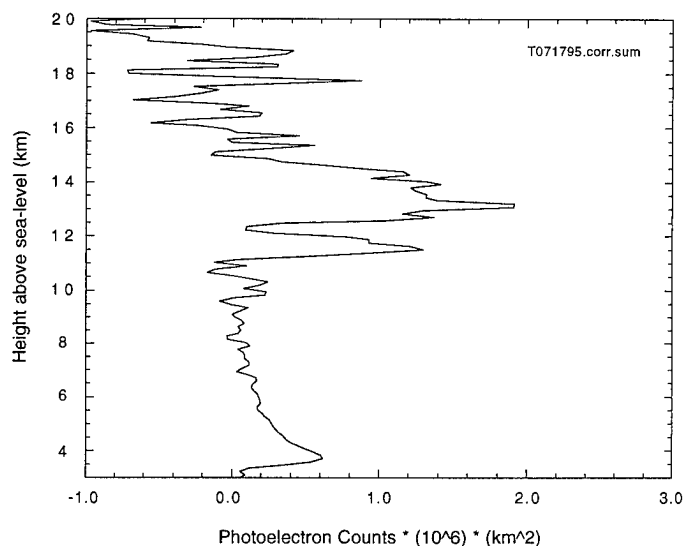
Figure 2. Ant Lidar I atmospheric measurements - July 17, 1995
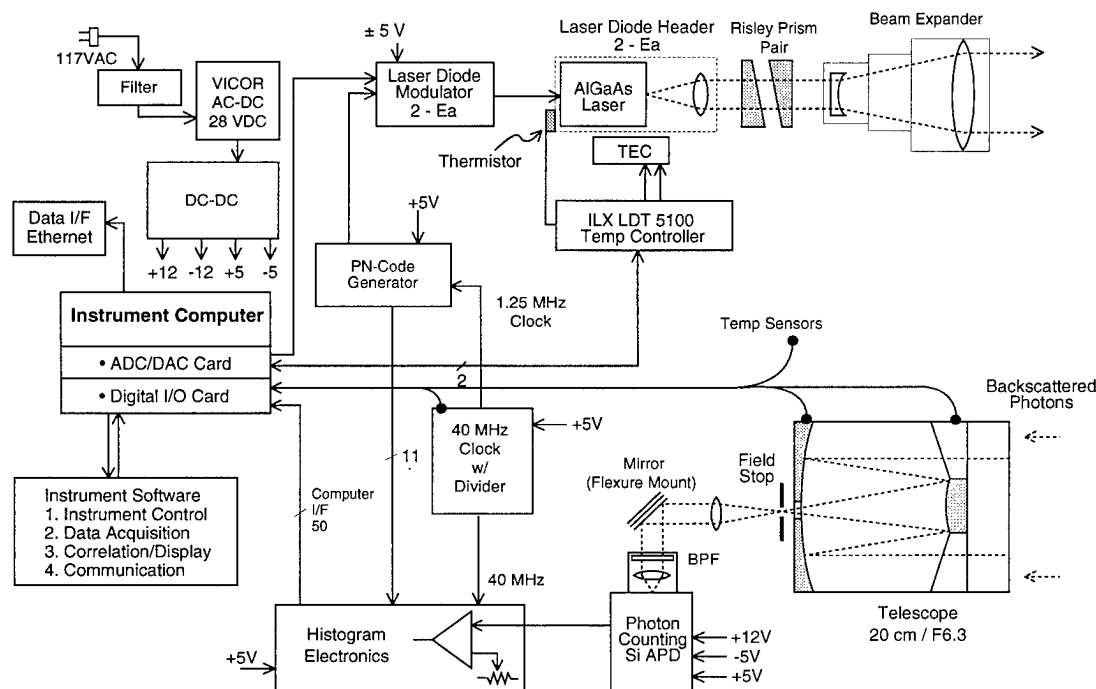
Fig. 3 Antarctic Miniature Lidar II - System Diagram
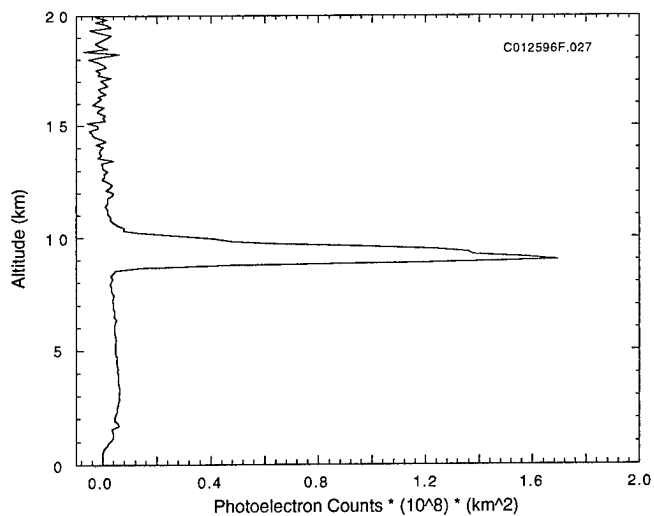
Fig. 4 Prominent cirrus returns at 9-10 km altitude.
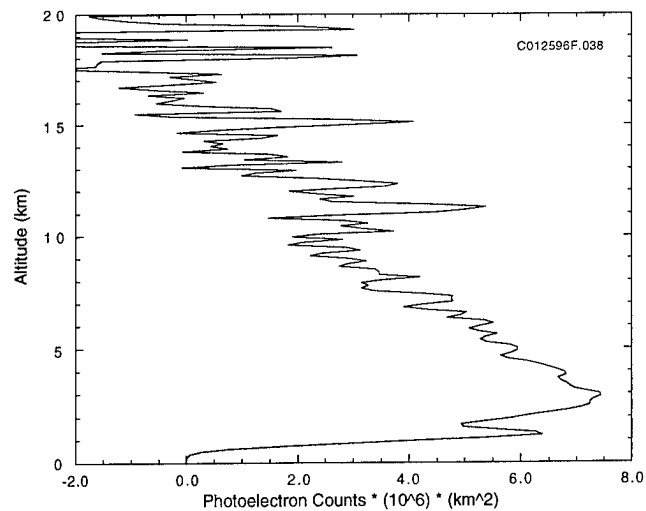
Fig. 5 Rayleigh returns to 15 km, some cirrus at 11-12 km.
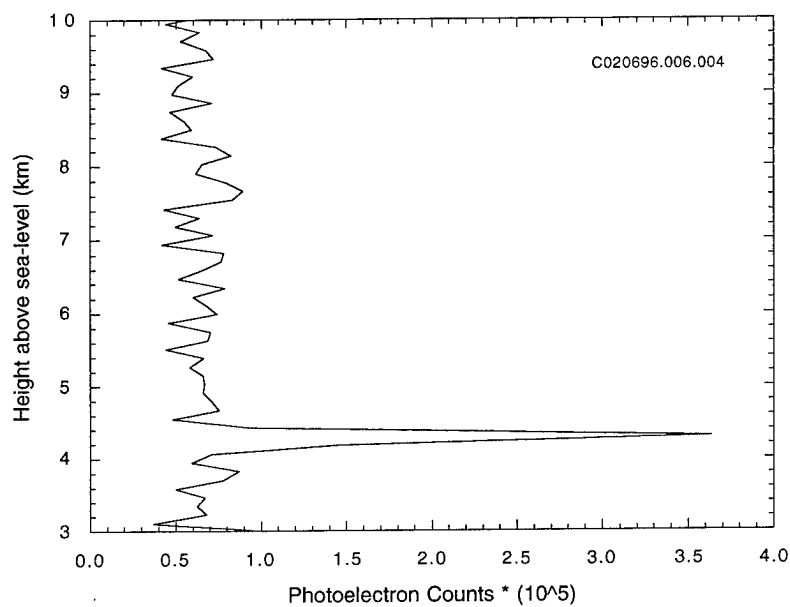
Fig. 6 One 20 minute profile taken at the South Pole on 2/6/96 reveals low altitude cirrus cloud.

Use of FT-IR and UV Spectrometers for Monitoring Multiple Pollutants in the Lower Troposphere

Daniel P. Gibbs and Brendan Krenek
Houston Advanced Research Center
4800 Research Forest Drive
The Woodlands, TX 77381
Tel: 713-364-6008 Fax: 713-363-7923 Email: gibbs@harc.edu

Abstract -- Automated Fourier transform infrared (FT-IR) and ultraviolet (UV) spectrometers have been developed that provide real-time detection of multiple pollutants in the lower troposphere. In "open path" applications, the FT-IR and UV beams are transmitted through the pollution in the open air to a retromirror located up to 500 meters away. A path-averaged concentration is then determined from the total absorbance measured along the entire pathlength. Open path FT-IRs have been applied to urban areas and hazardous waste sites, but the most common application is industrial fence line monitoring of fugitive emissions of hazardous air pollutants. Open path ultraviolet (OPUV) spectrometers have also been developed for monitoring criteria pollutants such as nitrogen dioxide (NO_2), sulfur dioxide (SO_2), and ozone, aromatic hydrocarbons, and carbonyl compounds in urban areas and along industrial fence lines. A description of each system will be given in this paper as well as areas of further development.

INTRODUCTION

A new air pollution monitoring technique is evolving that utilizes optical remote sensing instrumentation for regulatory purposes. Open path FT-IR and OPUV spectrometers are being used to measure path-averaged concentrations of multiple gases simultaneously over pathlengths of between 50 to 1000 m. Open path spectrometers offer several advantages over conventional point monitors: (1) they report spatially-averaged gas concentrations over an extended path length; (2) they are capable of monitoring multiple gases simultaneously and in real time; (3) no canister sampling is required which minimizes sample loss to the walls of the container; and (4) data from open-path monitors provide a spatial resolution that is more appropriate for model comparisons than that of point monitors [1]. A discussion of each technology is given in the remainder of this paper.

FT-IR SPECTROSCOPY

The open path FT-IR is ideally suited for ambient air monitoring of downwind impacts of ground-level sources such as hazardous waste sites and accidental releases of toxic chemicals from industrial facilities. The United States EPA is near completion of a federal reference method, Method TO-16, specifically designed for open path FT-IR monitoring. Years of research and testing using commercially-available FT-IRs went in to the development of Method TO-16. The final completion of this method will underscore the acceptance of open path FT-IR for regulatory use in air quality monitoring.

Many chemical species of importance to air pollution and global monitoring studies have absorbance spectra in two IR atmospheric window regions: 750 to 1200 cm^{-1} (13.3 to 8.3 μm) and 2100 to 3000 cm^{-1} (4.2 to 3.3 μm), where cm^{-1} is a "wavenumber." For example, CO_2 can be detected between 756 and 771 cm^{-1}, O_3 between 1043 and 1064 cm^{-1}, CO between 2100 and 2177 cm^{-1}, N_2O between 2191 and 2224 cm^{-1}, and CH_4 between 2840 and 2930 cm^{-1}. In addition, the FT-IR can detect over a hundred toxic hydrocarbons and biogenic hydrocarbons such as isoprene. FT-IR spectrometers have been used to measure gas concentrations in both the stratosphere and the troposphere [1,2,3]. In the stratosphere, infrared spectrometers are designed with a fine resolution (0.01 cm^{-1}) because atmospheric pressure is low. However, a lower resolution of 0.5 to 2.0 cm^{-1} is commonly used in the troposphere because higher atmospheric pressures broaden absorption lines. Infrared spectroscopic techniques in the troposphere are complicated by water vapor concentrations that are much higher than those in the stratosphere. This strong interference of water vapor is overcome by detecting chemical species in the two spectral regions mentioned above.

The open path FT-IR consists of a transceiver, which includes both the transmitter and receiver, and a retro-mirror. Within the transmitter is the source of infrared radiation and a Michelson interferometer which is used to create the interferogram. Because the interferometer is positioned in the transmitter, the receiver can readily distinguish the transmitted *modulated* beam from unmodulated IR energy emitted from the surrounding background. The transmitted IR beam is directed through the polluted air towards a 46-61 cm (18-24 in) retro-mirror using a 30-36 cm (12-14 in) diameter telescope that also serves as the receiving telescope. A mercury-cadmium-telluride (MCT) detector is used to convert IR energy between 750 and 4000 cm^{-1} into an electronic signal. Finally, an absorbance spectrum is calculated from the measured interferogram using a fast Fourier transform.

A major advance in the use of FT-IR spectroscopy for gas analysis is the automation of quantitative analysis using multicomponent Classical Least Squares (CLS). In the CLS the amount of light absorbed is determined using Beer's Law which is given by

$$I(v)/I_o(v) = e^{-A(v)} \qquad A(v) = \alpha(v)CL,$$

where

I	= measured intensity (sample spectrum),
I_o	= transmitted intensity (background spectrum),
$A(v)$	= absorbance,
v	= wavenumber (cm^{-1}),
$\alpha(v)$	= absorption coefficient,

C = concentration of the absorbing gas,
L = pathlength of the radiation through the gas.

The purpose of the background spectrum is to remove unwanted spectral features from the system itself, such as the spectral features of the source beamsplitter, detector, and system optics. The background spectrum is collected under experimental conditions as close as possible to those for the sample spectrum but with the sample removed. When the above ratio is calculated, spectral features due to the measurement system are removed from $I(v)$, leaving only spectral features due to the pollutants of interest. Note that the absorbance is proportional to the concentration-pathlength product, CL, and that the absorption coefficient contains the unique "fingerprint" shapes of the absorption spectra of the different species.
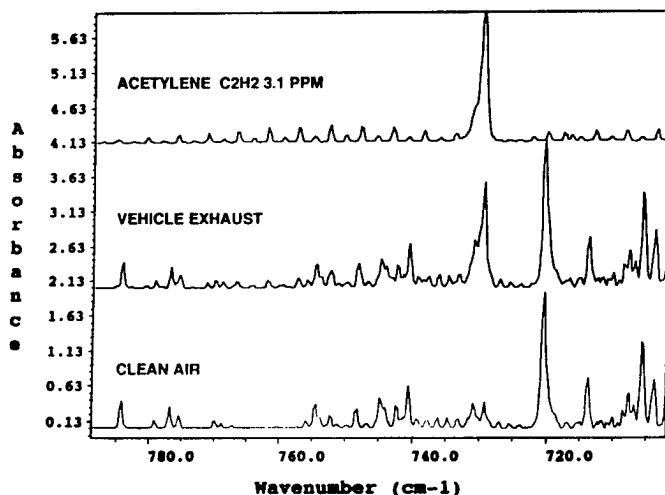
Figure 1   Comparison of absorbance spectra of acetylene (top), vehicle exhaust (middle), and background "clean" air (bottom).

The quantitative analysis routine is automated and can simultaneously detect up to 25 compounds from a spectral library of over 100 compounds. A concentration is determined from a least squares fit of the calibrated reference spectra with the measured spectrum over a specified wavenumber region. As an example, Figure 1 shows a library reference spectrum of 3.1 ppm of acetylene, an absorbance spectrum of vehicle exhaust measured over a pathlength of 180 meters using a 0.5 cm^{-1} resolution FT-IR, and a "clean air" spectrum taken under the same experimental conditions just before the vehicle was started. The presence of acetylene can be confirmed by comparing the unique absorbance peaks of acetylene in the top spectrum to the absorbance peaks associated with the vehicle exhaust (middle spectrum) and the background air (bottom spectrum). The top spectrum is then scaled to fit the peaks in the middle spectrum. The measured concentration is determined by multiplying the scaling factor by the reference concentration of the reference standard, which is 3.1 ppm in

this case. Of course the ratio of the pathlengths used for the measurement and the reference standard must be considered.
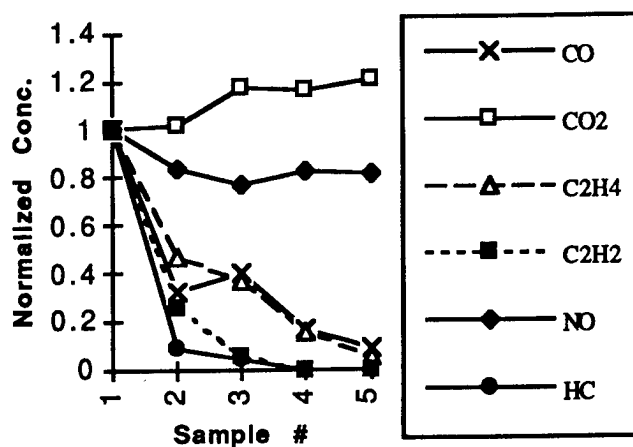
Figure 2   High RPM emissions from the 1992 Chevrolet Truck [3].

Using the FT-IR, the exhaust emissions of a 1992 Chevy operating at approximately 3000 RPMs were measured for five samples as shown in Figure 2. Note that the sample time interval was 47 seconds. The FT-IR detected CO, CO_2, ethylene (C_2H_4), acetylene (C_2H_2), propylene (C_3H_6), the hydrocarbon continuum (HC), methane (CH_4), and nitric oxide (NO). The most noticeable feature of these high RPM emissions is the strong presence of NO, which remained high for all 5 scans totaling nearly four minutes. It is well known that NO_x emissions increase sharply with engine load or speed because of increased combustion temperatures and better mixing of fuel and air (due to more turbulence at higher engine speeds). In addition, the concentrations of C_2H_4, C_2H_2, and HC decrease rapidly with increased engine speed probably because of the higher temperature of the exhaust system. The concentrations of CO and CO_2 decrease and increase, respectively, with sample # instead of remaining relatively flat as observed in the case of idle emissions.

OPUV SPECTROSCOPY

UV spectroscopic techniques complement IR measurements very well, especially in cases where the IR absorbance features of a particular species are lacking or masked by another compound. For example, oxides of nitrogen are quickly masked by strong water vapor lines in the IR as the monitoring pathlength increases beyond about 75 m. Strong absorbance features appear between 340 and 380 nm for NO_2, between 220 and 230 nm for NO, between 280 and 330 nm for SO_2, and between 240 and 300 nm for O_3. In addition, the OPUV can detect aromatic hydrocarbons, such as benzene and toluene, and carbonyls, such as formaldehyde and acetaldehyde.

The capability of the OPUV to detect SO_2, NO_2, and O_3 is well researched. The OPUV received US Environmental

Protection Agency (EPA) approval in mid-1995 for SO_2, NO_2, and O_3 and is now an equivalent method for ambient air monitoring of these compounds. Additional research, however, is needed in order for the OPUV to receive EPA approval for detecting carbonyl compounds, a group of ozone precursors, and aromatic hydrocarbons. Further technological developments that are needed to enable the OPUV to detect these compounds include automated hardware capabilities, advanced quantitative analysis software, and quality assurance/quality control procedures.

Determination of ambient concentrations of carbonyl compounds is a requirement of 40 CFR Part 58, Subpart E, enhanced ozone network monitoring programs [4]. Formaldehyde and acetaldehyde (acetone was removed from the list) are the specific carbonyls that are required to be monitored at this point in time [4]. Formaldehyde and acetaldehyde emissions result from incomplete combustion of hydrocarbons and other organic materials. Major emission sources appear to be vehicle exhaust, waste incineration, and fuel burning (natural gas, fuel oil, and coal). In addition, significant amounts of atmospheric carbonyl compounds can result from photochemical reactions between reactive hydrocarbons and NO_x [4]. In turn, carbonyl compounds can react photochemically to form other products besides ozone, including peroxides and peroxyacetyl nitrate (PAN). States are required to obtain 3-hour and 24-hour integrated measurements of carbonyl compounds at specified collection frequencies ranging from one 24-hour sample every sixth day to eight 3-hour samples every day [4]. The current carbonyl sampling method, Method TO-11, is very costly and requires subsequent laboratory analysis. An automated OPUV would significantly simplify carbonyl monitoring.

A scanning-slit technique has been applied to measuring molecular species in the UV relating to atmospheric photochemistry and smog formation. An alternative to the scanning slit approach is to use a grating or prism spectrometer with a photodiode array as a detector. An important advantage of simultaneous measurement of the desired spectral interval (as opposed to scanning) is the elimination of time dependent changes due to atmospheric scintillation effects that occur during the scan.

The UV source, a xenon arc lamp, can be collimated into a 10 cm beam using an f/10, 100 cm focal length mirror for monitoring pathlengths up to 800 meters. When using a retromirror, the return beam is received through the same f/10 optics and then imaged onto a photodiode array using a spectrometer with a resolution of approximately 0.5 nm. The concentration of each species is determined using a least-squares fit similar to that used for FT-IR data. Note that the fit is carried out over a large portion of the spectral region, instead of at a single pixel, in order to reduce the effect of interfering absorbance features due to other gases.

The capability of the OPUV for detecting nitrogen dioxide is shown in Fig. 3 where an open path spectrum of NO_2 is overlaid on a reference spectrum of NO_2. The detected absorbance peaks represent a path-averaged concentration of 2.5 parts-per-billion (ppb) of NO_2 measured over a 325 meter pathlength. The source of NO_2 was a vehicle being driven

along the length of the monitoring path. This absorbance spectrum was measured in the presence of an ambient NO_2 concentration of 26 ppb. A qualitative analysis of the measured UV spectra revealed absorbance peaks for formaldehyde, toluene, and m-xylene.
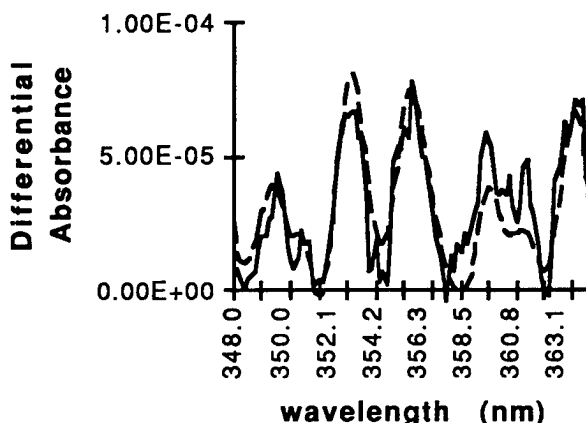
Figure 3 Comparison of an open path absorbance spectrum of NO_2 (—) and a reference standard of NO_2 (---).

CONCLUSIONS

Continued development of open path FT-IR and OPUV spectrometers will provide for improved monitoring techniques and will allow regulatory agencies and industry to obtain more comprehensive and representative data on air pollution. Open path analyzers measure pollutant concentrations over a long path and, thus, are expected to provide better spatial coverage and a better assessment of exposure to air pollution. Such instrumentation will improve upon current capabilities in risk assessment and reduce uncertainties in modeling projections.

REFERENCES

1. Kolb, C.E., "Instrumentation for chemical species measurements in the troposphere and stratosphere", Reviews of Geophysics, Supplement, U.S. National Report to International Union of Geodesy and Geophysics, pp. 25-36, 1991.

2. Grant, W.B., Kagann, R.H., and McClenny, W.A., Optical remote measurement of toxic gases, J. Air Waste Manage Assoc., 42, No. 1, pp. 18-30, 1992.

3. Gibbs, D.P., Betty, C.L., Dolaty, M., and Zepeda, Z., Use of infrared and ultraviolet open-path spectrometers to measure the effect of vehicle emissions on urban air quality, International Symposium on Optical Remote Sensing for Environmental and Process Monitoring, Washington, DC, November 7-10, 1994.

4. Environmental Protection Agency, "Methodology for Determining Carbonyl Compounds in Ambient Air," from Technical Assistance Document for Sampling and Analysis of Ozone Precursors, EPA-600/8-91-215, 1994.

Millimeter Wave Imaging Technology

G. Richard Huguenin
Millimetrix Corporation
Northampton Industrial Park, Northampton, MA 01060
Tel: (413) 665-4416   FAX: (413) 665-4416

Abstract--Millimeter wave video rate focal plane imagers using passive (radiometric) and active (radar) modes of operation are described. These sensors involve compact ("folded") optics and focal plane low-noise receiver arrays. Active optics which utilize load switching and phase shifting twist reflectors are described.

I. INTRODUCTION

This paper describes millimeter wave video rate focal plane array (FPA) imagers developed primarily for concealed weapons detection (CWD) and through-the-wall surveillance (TWS) applications. Both passive (radiometric) and active imagers will be described. The CWD/TWS cameras and the technology employed in these cameras are ideally suited to a wide range of other applications as well.

Traditionally, passive millimeter wave images have been generated using scanned sensors of various types ranging from single elements to line arrays. Scanning imagers, however, cannot meet the frame rate and sensitivity requirements for some applications. The CWD application, in particular, requires a passive, video rate (30 frames per second) imager which we are developing using a patented focal plane array technology we call Millivision™. Similarly, TWS applications demand an active (radar), video rate imager which shares much of the same Millivision™ FPA technology.

Customers always want more resolution, more sensitivity, and a wider field of view all in the smallest possible package. To meet these difficult requirements, the Millivision™ imagers operate near 94 GHz and employ active optics and filled focal plane arrays, both of which will be briefly described. The optimally (electromagnetic) filled FPA is small angle scanned (dithered) relative to the scene in a 4×4 matrix to achieve a 2×2 oversampling of the image. A multiplicative "super resolution" algorithm is then used to digitally enhance the spatial frequency resolution of the resulting image by a factor of approximately 2 in each axis.

II. ACTIVE OPTICS

The Millivision™ camera optics are "folded" for compactness and to provide for convenient active optic processing and rapid refocusing. The primary lens has an f/D of 1.1. Using a transreflector and twist reflector combination, the distance between the lens and the focal plane is reduced by approximately a factor of three as shown in the diagram of Fig. 1. This optics geometry results in a sensor sensitive to one single linear polarization. Since we will be implementing only a single polarization in the focal plane array, this is not limiting for most applications.

The twist reflector in this folded optics scheme is a convenient location for the implementation of active optic wave processing elements. The twist reflector used in the Millivision™ cameras consists of a quarter-wave element backed by a plane mirror. Replacing the plane aluminum mirror in the twist reflector with an active optics plane mirror allows wave processing of the whole scene prior to channelization by the focal plane array.

Two types of active optics twist reflectors are being developed for the Millivision™ family of imagers: a load switching twist reflector (LSTR) and a phase shifting twist reflector (PSTR). These will be briefly described below.

III. LOAD SWITCHING TWIST REFLECTOR

A necessary element of a passive (radiometric) imager design is a comparison scheme to deal with the gain fluctuations of the receiver electronics which can mask the detection of small scene contrast changes. Load comparison is a convenient technique for a staring radiometric imager. In the load comparison mode, the imager alternately compares the scene with a reference load at a rate high enough to overcome the low frequency peak of the receiver gain fluctuation spectrum. The load comparison must also be done in such a manner as to not cause visible blanking of the resulting image. The observation by all channels of the same comparison load also facilitates channel-to-channel gain normalization (flat-fielding).

The component developed to implement load comparison in the Millivision™ passive imagers is the Load Switching Twist Reflector or LSTR which is described in the Huguenin, Bandla, and Moore, 1996 [1]. The plane mirror in the LSTR consists of an array of MMIC tiles that can be electronically switched between reflection and transmission states by the application of external bias. These switchable tile array elements, the front surface of which make up the plane reflector, are backed by a matched millimeter wave load and thermally stabilizing support structure. In the reflecting (scene) state, the insertion loss is only about 0.25 dB. In the load comparison state, the return loss is better than 20 dB.

IV. PHASE SHIFTING TWIST REFLECTOR

It is necessary to microscan (dither) the image relative to the optimally (EM) spaced focal plane array in order to adequately sample the higher spatial frequency components of the image needed to realize the full resolution potential of the diffraction limited optics. The component under development to electronically perform this microscanning function is the Phase Shifting Twist Reflector (PSTR). The subframe rate of the Millivision™ camera is 540 Hz, faster than one can conveniently scan electromechanically.

The PSTR is designed to allow a variable phase gradient to be imposed on the circularly polarized incoming (scene) wavefront upon reflection from the plane mirror component of the compact optics twist reflector. The PSTR plane mirror active optic is an array of tile elements that have a controllable phase shift in reflection. The amount of phase shift is determined by applying an appropriate external bias to the individual tiles. The necessary phase gradients can therefore be programmed into the PSTR array to scan the beam in the desired directions to suitably sample the observed image in the focal plane.

A maximum phase shift of 70 degrees across the PSTR plane mirror is required to scan the image up to one-half power beamwidth. An example of the measured phase shift vs applied bias for a PSTR array MMIC tile is shown in Fig. 2. The insertion loss is measured to be typically between 1 and 2 dB. The PSTR plane mirror substrate and driver board for the M150 camera with four reference tiles mounted to it are shown in Fig. 3.

V. FOCAL PLANE ARRAY

Optimally filled focal plane arrays are required to meet the sensitivity and frame rate requirements for applications such as concealed weapon detection and aircraft landing systems. Optimally filled arrays provide the most dense packing of array elements (and therefore the most dense image sampling) that still has a high electromagnetic coupling efficiency to the focal plane image. Array elements in this configuration produce beams that overlap at the half power (-3 dB) points.

The channel-to-channel pitch in the focal plane array is approximately 4.25 mm for the f/D = 1.1 optics employed in the M300/M150 Millivision™ cameras. The area in the focal plane available to implement a receiver channel is therefore only 4.25 mm × 4.25 mm. The Millivision™ focal plane arrays employ planar, printed, constant width slot antennas (CWSA) that are endfire antennas and launch the signal on a transmission line parallel to the optical axis. The volume available behind the focal plane is therefore readily accessible. Each receiver channel in the Millivision™ passive focal plane array occupies a volume of 4.25 mm × 4.25 mm × 130 mm.

Each receiver channel of the Millivision™ passive array has a superheterodyne architecture with an input amplifier, a mixer, an IF amplifier chain, a detector, a video amplifier, and a sample-and-hold circuit. The local oscillator (LO) is at one-half (47 GHz) of the receiver center frequency (94 GHz). The LO and scene energy are both optically coupled into the CWSA. The input amplifier is both a low-noise amplifier at 94 GHz and an LO amplifier at 47 GHz. The MMIC input amplifier is followed by a single-ended, subharmonic, double sideband mixer. The IF passband is 0.2 to 2.5 GHz resulting in a passband of 5 GHz centered on 94 GHz. FPA receiver noise temperatures are typically 1000°K including all input losses and second stage contributions. A similar homodyne receiver architecture is used for radar FPA receiver channels. The IF in the radar receiver has a passband from 0 to 4 MHz and is multiplexed undetected.

The Millivision™ FPA is made up of individual modules each containing 8 receiver channels, a 1 × 8 video multiplexer, and a video line driver. These 1 × 8 modules are packaged to provide the needed FPA configuration. The individual modules plug into a mother board which enables bias to be distributed and contains the remaining multiplexing and addressing circuitry. The 16 × 16 channel FPA for the M300 series cameras is shown in Fig. 4.

VI. REFERENCE

[1] G.R. Huguenin, S. Bandla, and E.L. Moore, "A millimeter wave monolithic load switching twist reflector for compact imaging cameras," to be published in the 1996 IEEE MTT-S International Microwave Symposium Proceedings.
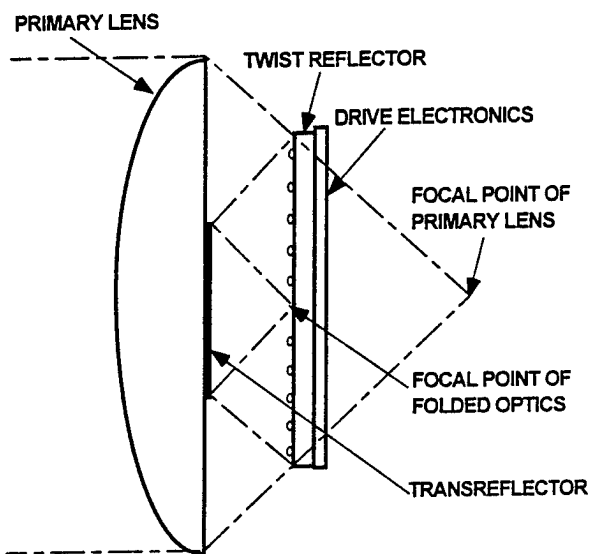
Fig. 1. Folded optics geometry.
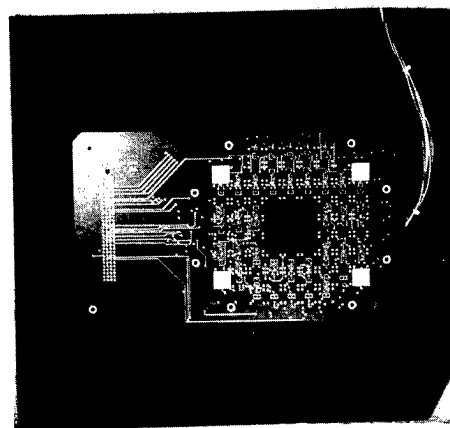
Fig. 3. Four PSTR tiles with driver board.

>S₁₁
REF 30.0 °
1   20.0 °/
∇   −35.818 °

SCALE
20.0 °/div

─ 520V

+ 20V

START   91.999998000 GHz
STOP   97.999998000 GHz
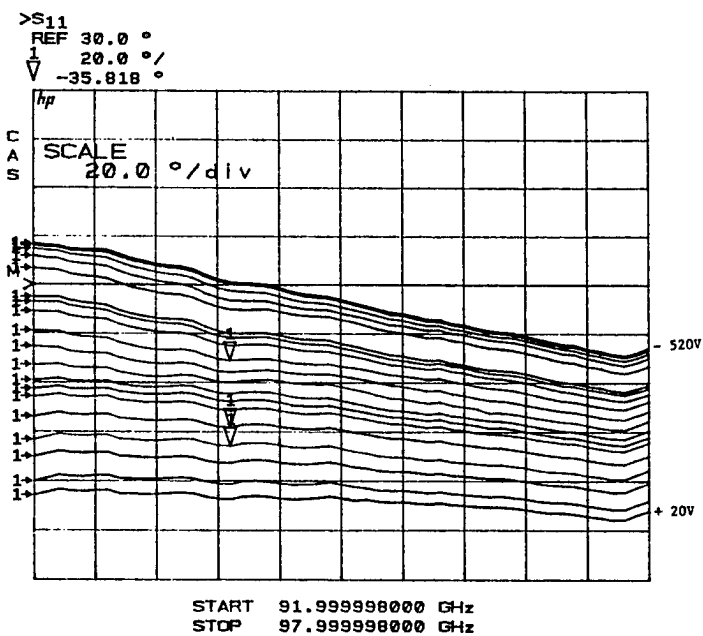
Fig.2. Phase shift characteristics of PSTR array element.

Fig. 4. 16x16 Channel focal plane array.

Synthetic Aperture Radiometers for Microwave Remote Sensing from Space

D.M. Le Vine
Code 975, Goddard Space Flight Center, Greenbelt, Maryland, 20771
Phone: 301-286-8059; FAX: 301-286-1761; email: dmlevine@meneg.gsfc.nasa.gov

C.T. Swift
Department of Electrical & Computer Engineering
University of Massachusetts, Amherst, MA 01003-4410
Phone: 413-545-2136; FAX: 413-545-4652

Abstract: Aperture synthesis is an interferometric technology which could open the way for new applications of passive microwave remote sensing from space. In aperture synthesis pairs of small antennas are used to achieve the resolution of a single larger aperture and a wide field-of-view is obtained without scanning. The technique has been demonstrated from an aircraft (ESTAR) and the technology is ready for implementation in space. To fully enable this technology for future remote sensing from space will require design of antenna and deployment structures, the transition to digital signal processing, the interconnection of many receiver pairs, and optimization of the image reconstruction algorithm.

INTRODUCTION

Aperture synthesis is an interferometric technique in which the product (complex correlation) of the voltage from pairs of antennas is measured at different antenna baselines. In principle, each baseline yields a sample point in the two-dimensional Fourier transform of the scene and an image is obtained by inverting the transform. The technique was first demonstrated for remote sensing of the earth with the L-band airborne prototype, ESTAR, developed at the Goddard Space Flight Center and the University of Massachusetts [1,2]. Research radiometers are now under development in many laboratories around the world. These include a two-dimensional synthetic aperture radiometer (MIRAS) being developed at L-band by ESA/ESTEC in Europe, an ESTAR-like radiometer at 37 GHz developed by Quadrant Engineering with support from the Air Force Phillips Laboratory and the Naval Research Laboratory, and research radiometers developed in Denmark, Germany and Japan [1].

Aperture synthesis addresses a major problem facing passive microwave remote sensing from space -- the size and complexity of the antenna needed to achieve desired spatial resolution. The range of potential applications is illustrated by the following sensor concepts being studied the Goddard Space Flight Center:

o HYDROSTAR: An L-band radiometer based on the ESTAR design (synthesis in one dimension). This sensor is being designed to monitor soil moisture and possibly sea surface salinity from space [3,4]. It consists of 14 stick antennas, and will have horizontal polarization and a resolution at nadir of about 10 km.

o ICESTAR: This sensor also employs synthesis in one dimension but in a conical-scan mode. This sensor is designed to operate at 18 and 37 GHz to monitor sea ice. It will have dual polarization, a resolution at nadir approaching 1 km, and provide complete coverage (of the poles) each day [5].

o WINDSTAR: This is a radiometer to monitor surface winds (magnitude and direction) over the oceans. Unlike the previous concepts, it employs aperture synthesis in two dimensions. It is dual polarized and also measures the cross terms (real and imaginary parts of $E_h E_v^*$) in the Stokes matrix [6,7]. Synthesis in two dimensions permits the sensor to have a wide field-of-view and obtain the equivalent of an instantaneous conical scan to facilitate determining wind direction [6].

o TEMPSTAR: A radiometer designed to profile temperature of the atmosphere from geostationary orbit. The radiometer employs aperture synthesis in two dimensions (antennas arranged in a ring around a central processor) and consists of 10 channels near the oxygen resonance band (50-60 GHz). The goal is 50 km resolution and an image every half-hour.

PERFORMANCE BOUNDS

The list of applications is already demanding of both radiometric sensitivity (ΔT), spatial resolution and coverage (field-of-view). But these are not completely independent parameters. For example, the radiometric sensitivity of synthetic aperture array can be written [8,9]:

$$\Delta T = \frac{T_{sys}}{\sqrt{B\tau}} G$$

where the first term is the sensitivity of a total power radiometer with the same system noise temperature, T_{sys}, the same bandwidth, B, and the same integration time, τ. The additional factor, G, is the penalty paid for thinning the array (i.e. reducing signal-to-noise ratio). In a configuration optimized to use the fewest number of elements for a given maximum baseline, G is roughly the ratio of the area of the equivalent filled array to the area of the thinned array.

In designing the system, one might imagine increasing B and τ to compensate for a G > 1. However, τ is limited by satellite motion (the maximum integration time is approximately the resolution pixel ÷ velocity). Also, the thinned array (aperture synthesis) technique has inherent limits on bandwidth. Synthesis arrays, in essence, measure the difference in path from a point on the scene to pairs of antenna elements in the array, and the larger the bandwidth, the shorter this path difference (time) can be. Hence, in pushing the limits of performance it may be necessary to make a trade between bandwidth and the field-of-view.

Figure 4 illustrates the nature of this trade in the case of a sensor like ICESTAR. It is assumed that the sensor operates at 18 GHz in an orbit at 400 km and in a conical scan mode with an incidence angle (cone angle) of 50 degrees. The required resolution determines the size of the array (maximum baseline) and also determines the maximum available integration time. The solid curve in Figure 4 is the best radiometric sensitivity (ΔT) one can achieve (using the largest permissible bandwidth) when the field-of-view (FOV) is a strip 30 degrees on each side of nadir. For example, suppose a resolution of 2 km is desired (determining the size of the array). Initially, ΔT can be improved by increasing bandwidth, and as the bandwidth is increased the system moves down the dashed line in Figure 4 toward the solid line. The solid line represents the limiting case where the time difference, measured at the longest baseline and associated with signals arriving from the extreme edges of the FOV, can no longer be accommodated by the receiver system. To increase the bandwidth further while keeping the FOV fixed requires a change in the system. One alternative is to decrease the size of the array. Decreasing size (with fixed FOV) slides the system performance to the right along the solid curve. The radiometric sensitivity improves because both bandwidth and integration time can be increased, but at the cost of spatial resolution. The alternative is to move to the left along the solid curve (constant FOV). This improves resolution (the array gets bigger) but at the cost of increasing ΔT because both integration time and bandwidth must decrease.

Figure 4 illustrates the nature of design trades that must be kept in mind in considering thinned array radiometers for a particular measurement. But it may be possible to overcome even such inherent limitations. For example, suppose the bandwidth limitation set by the solid curve in Figure 4 is 50 MHz but 150 MHz of spectrum is allocated for this measurement. One could divide the spectrum into 3 adjacent bands (e.g. with a filter bank at the antenna) and in essence run three radiometers in parallel.

TECHNOLOGY ISSUES

Experience with the aircraft prototype, ESTAR, and studies of systems such as the HYDROSTAR and ICESTAR, have identified some of the technological issues that it will be necessary to address in the design of future sensors in space. These include antennas, the transition to digital processing, the interconnection of a large number of receiver pairs, and optimization of the image reconstruction algorithm.

o ANTENNAS: In principle, resolution depends on how well the Fourier transform space is sampled (i.e. the distribution of the baselines). However, experience with the aircraft ESTAR suggests that the limiting issues are not so much the distribution of antennas, but the antennas themselves which can cause distortion of the basis vectors needed to effect image reconstruction because of coupling and other effects [10].

o DIGITAL SIGNAL PROCESSING: While analogue multiplication works well, digital signal processing affords more flexibility and ultimately will be needed when the required number of products becomes quite large. It is not hard to imagine applications which push existing limits of speed and power. From a practical point of view, experience with digital processing (calibration and effect on ΔT) is needed.

o INTERCONNECT COMPLEXITY: A typical synthetic aperture system requires two receivers (I and Q channels) at each antenna. Local oscillator and calibration signals are needed at for each plus lines for data. This cabling may have to cover large distances (e.g. on the order of 10m in HYDROSTAR) and even for the relatively modest systems envisioned today, the number of receivers can be large. This problem is critical for systems such as TEMPSTAR which would have several hundred receivers.

o IMAGE RECONSTRUCTION: Converting from correlator output to an image of brightness temperature introduces "noise" of its own. The basis functions (impulse

response of each channel) are generally not ideal, further complicating the problem. Optimization which fits the inversion to the scene and instrument errors is needed, especially in applications such as the measurement of sea surface salinity where the dynamic range of brightness temperature is relatively small [3,4].

REFERENCES

[1] Le Vine, D.M., A.J. Griffis, C.T. Swift and T.J. Jackson, "ESTAR: A Synthetic Aperture Microwave Radiometer for Remote Sensing Applications", Proc. IEEE, Vol 82(#12), pp 1787-1801, Dec. 1994.

[2] Le Vine, D.M., M. Kao, A.B. Tanner, C.T. Swift and A. Griffis, "Initial Results in Development of a Synthetic Aperture Microwave Radiometer", IEEE Trans. Geosci. & Remote Sens., Vol 28 (#4), pp 614-619, July, 1990.

[3] Swift, C.T. et al, "ESTAR: The Electronically Scanned Thinned Array Radiometer for Remote Sensing Measurement of Soil Moisture and Ocean Salinity", NASA TM-4523, July, 1993.

[4] Lagerloef, G.S.E, C.T. Swift and D.M. Le Vine, "Sea Surface Salinity: The Next Remote Sensing Challenge", Oceanography, Vol 8, pp 44-50, 1995

[5] Cavalieri, D.J, D.M. Le Vine and J.A. Weinman, "ICESTAR: A Spaceborne Ice and Coastal Environment Surveillance Thinned Aperture Radiometer System to Aid Arctic Navigation", Proc. Internat. Northern Sea Route Prog. Symp., October, Tokyo, Japan, 1995.

[6] Le Vine, D.M., "WINDSTAR: A Synthetic Aperture Microwave Radiometer To Measure Winds Over the Ocean", Proc. OCEANS'95, San Diego, 1995.

[7] Yeuh, S.H., W.J. Wilson, F.K. Li, S.Y. Hghiem and W.B. Ricketts, "Polarimetric Measurements of Sea Surface Brightness Temperatures Using an Aircraft K-band Radiometer", IEEE Trans. Geosci. & Remote Sens., Vol 33 (#1), pp 85-92, 1995.

[8] Le Vine, D.M., "The Sensitivity of a Synthetic Aperture Radiometer for Remote Sensing Applications from Space", Radio Sci., Vol 25(#4), pp 441-453, 1990.

[9] Ruf, C.S., C.T. Swift, A.B. Tanner and D.M. Le Vine, "Interferometric Synthetic Aperture Radiometry for Remote Sensing of the Earth", IEEE Trans. Geosci & Remote Sens., Vol 26(#5), pp 597-611, 1988.

[10] Le Vine, D.M. and D.E. Weissman, "Calibration of Synthetic Aperture Radiometers in Space: Antenna Effects", Proc. IGARSS-96, Lincoln, Nebraska, 1996.
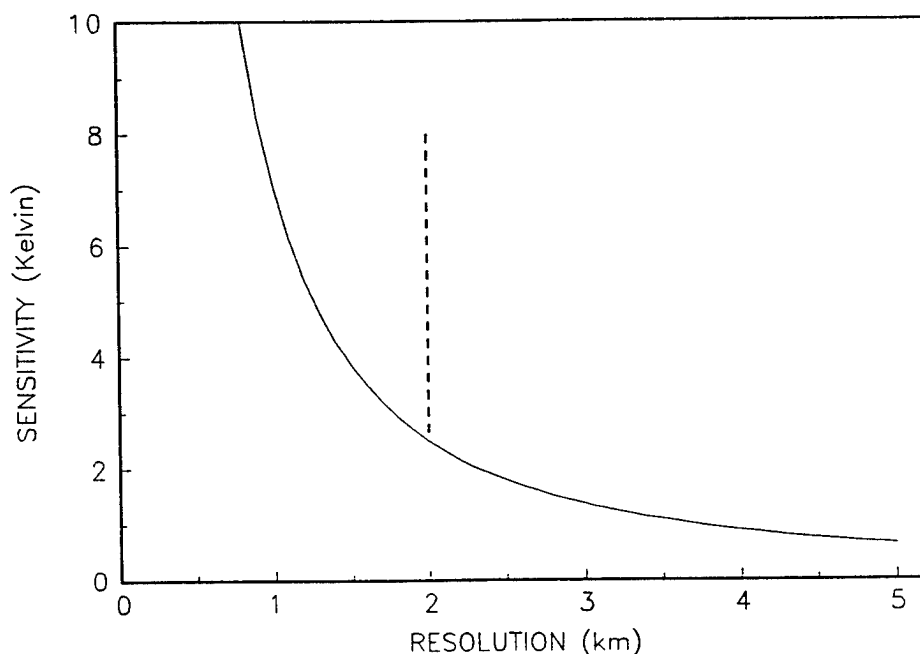
Figure 4: Performance of a conical scan radiometer with frequency = 18 GHz, altitude = 400 km and incidence angle = 50 degrees. The FOV is constant at ±30 degrees and the solid curve is obtained using the maximum permissible BW.

Capabilities and Recent Results from the ER-2 Doppler Radar (EDOP)

S. W. Bidwell[1], G. M. Heymsfield[1], and I. J. Caylor[2]

(1) NASA/Goddard Space Flight Center, Code 975, Greenbelt, MD 20771

(2) Science Systems and Applications, Inc., 2900 Princess Garden Pkwy., Lanham, MD 20706

INTRODUCTION

The ER-2 Doppler Radar (EDOP) is an X-band (9.60 GHz) Doppler radar flown on the high-altitude (nom. 20 km) NASA ER-2 aircraft. A major objective of EDOP is the study of air motions within convective precipitating regions from the strong updraft regions to the cirrus anvil regions. It is common for EDOP to fly with a complement of passive and active precipitation and water vapor instruments on the ER-2. The purpose of this paper is to describe the EDOP instrument specifications and capabilities and to very briefly describe recent data and research activity.

MEASUREMENT TECHNIQUE

The EDOP instrument, with its two antennas, is located in the nose of the ER-2. One antenna is nadir-pointing while the other antenna points 33.5° forward of nadir. Fig.1 depicts the EDOP measurement scheme with data collection at the two look angles. At an altitude of 20 km, above the tallest of thunderstorms, EDOP is provided a complete view of precipitation under the flight path. EDOP is non-scanning and events are profiled as the aircraft cruises at 200 ms^{-1}. With Doppler capability on both antennas hydrometer motion can be evaluated in two radial directions. By careful subtraction of aircraft velocity and with estimates of terminal

Fig.1 EDOP measurements are made from two fixed antennas directed along the ER-2 flight path.

hydrometer fall speed from reflectivity relationships, the air motion can be estimated in the vertical and horizontal directions in the plane of the flight track.

In addition to reflectivity and Doppler capability on the two look angles, the forward channel provides for cross polarization receiving. Combining the forward co-polarization and cross-polarization provides an estimate of the linear depolarization ratio (LDR) which is useful in discriminating the shape and phase of the hydrometers as well as in identifying the melting layer.

INSTRUMENT SPECIFICATIONS AND CAPABILITIES

The specifications of the EDOP transmitter, receiver, antennas, and data processor are detailed in Table 1. A comprehensive description of the instrument and its scientific capabilities can be found in Heymsfield[1]. The transmitter tube is a coherent traveling wave tube amplifier with nominal pulsed output power of 25 kW (74 dBm). This power is split between the two output ports. Typical operation is with a pulse width of 0.5 μs and a pulse repetition frequency (PRF) of 4400 Hz (duty factor 0.22%). Pulse width and PRF are selectable and are set by the data processor. A PRF of 4400 Hz corresponds to an unambiguous range of 34.1 km and an unambiguous velocity of ± 34.4 ms^{-1}.

Since the ER-2 nose is only partially pressurized to 4.5 psia, precautions must be observed for cooling and for prevention of electrical breakdown. A cylinder of pressurized N_2 maintains 16 psia positive pressure within the transmitter, waveguides, and antenna feeds. In addition, the N_2 in these locations prevents condensation or "cold soaking" when the instrument returns to the ground after subjection to the cold (nose air temperature of -20°C) during flight.

The three received signals (nadir co-pol., forward co-pol., and forward cross-pol.) are heterodyned within the receiver to an intermediate frequency (IF) of 60 MHz. Subsequently, the signals are filtered, either 2 MHz or 8 MHz based upon the pulse width, and directed to both linear (coherent) and logarithmic detectors.

The two antennas are an offset feed parabolic reflector type with diameter 0.76 m, gain 36 dB, and beamwidth 2.97°. This beamwidth corresponds to a footprint of 1.2 km at the surface for the nadir pointing antenna. While the
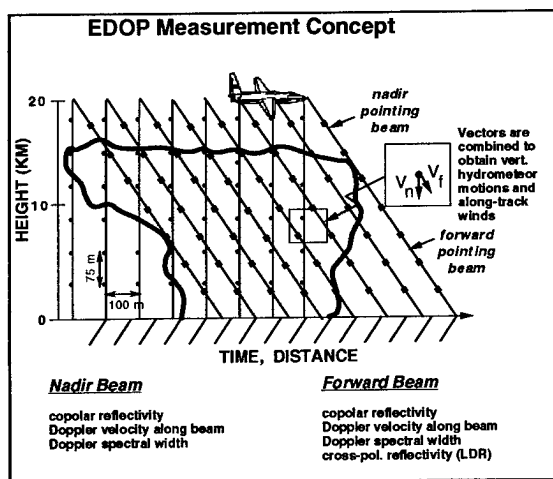
forward antenna is fixed, provision is made for stabilizing the pointing of the nadir antenna. The nadir antenna is attached to a rotatable gimble and motion is controlled with a motorized linear actuator. Nadir stabilization is desired to adjust for aircraft pitch variations. which can vary several degrees during flight due to fuel burnoff as well as random aircraft attitude variation. When fully implemented nadir antenna stabilization will utilize the real-time navigation data stream (ARINC 429) to record pitch and will make the necessary adjustment to the antenna position.

Both antenna feeds include a mode-matching unit to cancel the inherent off-boresight cross-polar coupling associated with offset reflectors. The forward feed includes an ortho-mode transducer to enable the cross-polarization measurement and isolation off boresight is better than 30 dB.

The data system provides for real-time signal processing as well as for radar control. A pulse-pair algorithm is

Table 1 EDOP Instrument Parameters

Transmitter	
Frequency (Wavelength)	9.6 GHz (3.1 cm)
Peak Power	25 kW
Pulse Width	0.25, 0.5, 1.0 μs
	(0.5 μs typ.)
Pulse Repetition	2200, 4400 Hz
Frequency (PRF)	(4400 Hz typ.)
Tube	Litton Traveling Wave
	Tube Amplifier (TWTA)
Receiver	
Intermediate Freq. (IF)	60 MHz
Dynamic Range with Gain	110 dB
Control	
Minimum Detectable	-5 dBz
Signal at 10 km	
Linear Doppler Channels	3
Log. Reflectivity Channels	2
Antennas	
Type	Offset Fed Parabolic
	Reflector with
	"Matched Feed"
Diameter	0.76 m
Beamwidth	2.9°
Gain	36 dB
First Sidelobe Level	<-26 dB
Cross-Polarization Level	<-30 dB
Nadir Transmit/Receive	V/V
Polarization	
Fwd. Transmit/Receive	V/V, V/H
Polarization	
Data Processing	
A/D Converters	7 channels x 12 bits, 2 MHz
Signal Processors	24 AT&T DSP32C
Gate Spacing	75 m, 150 m (75 m typ.)
Gates	436 Reflectivity,
	360 Doppler
Integration Cycle	0.25 - 1.0 s (0.5 s typ.)
Nadir Products	Z_{nvv}, V_n, σ_n, SNR_n
Forward Products	Z_{fvv}, Z_{fvv}, V_f, σ_f, SNR_f
Total System Weight	180 kg
Total System Power	1500 W

implemented for the nadir co-polarization and forward co-polarization coherent channels. The autocovariances are calculated at 0, T, and $2T$, where $T = 1/PRF$, and are averaged over an integration period and then stored to hard disk. Calculation of mean Doppler velocity and mean spectral width is done on the ground in post-flight processing. Reflectivity processing is a simple average of logarithmic detector output. Typically, a 0.5 s integration period (dwell) is employed. At a pulse repetition frequency (PRF) of 4400 Hz, a 0.5 s average corresponds to 2200 pulses. The 0.5 s dwell is based on consideration of independent samples and aircraft translation (100 m).

Signal processing within the data system is based on the AT&T DSP32C digital signal processor (DSP) on Martin-Marietta LUA 200 boards. The system contains three LUA 200 boards, each with 8 DSPs, in a VME 9U backplane. Sixteen of the DSPs are designated for pulse-pair processing while four DSPs perform the reflectivity summing. The remaining four DSPs are reserved for automatic gain control within the receiver and are not implemented at present.

The pulse-pair algorithm is calculated on the first 360 range gates following the transmitted pulse while reflectivity averaging is calculated on the first 436 range gates. This provides viewing to 32.7 km for reflectivity and up to 27.0 km for Doppler. Often this permits viewing the mirror image of the melting layer with the nadir channels and guarantees viewing the surface for the forward channels (forward surface at approximately 24 km). The number of range gates is based upon the upper capabilities of the signal processor.

DATA ANALYSIS

EDOP has participated in three field campaigns since 1993: (1) Convection and Atmospheric Moisture Experiment 1 (CAMEX 1), Wallops Island, VA, Sept. - Oct. 1993, (2) Houston Precipitation Experiment (HOPEX), Houston, TX, Jan. 1995, and (3) CAMEX 2, Wallops Island, VA, Aug. - Sept. 1995. The HOPEX and CAMEX 2 campaigns provided numerous examples of reflectivity and Doppler data over both convective cells and stratiform precipitation. The CAMEX 2 data was collected in conjunction with two scanning precipitation radiometers. The following is a very brief discussion of two research activities involving EDOP data sets.

A preliminary analysis of vertical velocities and relative wind vectors in a convective region is shown in Fig.3. This data is from a rapidly advancing squall line over the Gulf Coast which was overflown on January 13, 1995. A fuller description of this squall line and the methods for deriving the along-track velocity u and vertical velocity w can be found in Heymsfield[3]. In this event the vertical velocity (bottom panel) indicates a strong westward tilted updraft with a maximum core of ~15 ms^{-1} at an altitude of 4-5 km as

well as several regions of strong downdrafts. Weaker vertical velocities exist to the rear of the convective line in the trailing stratiform region.
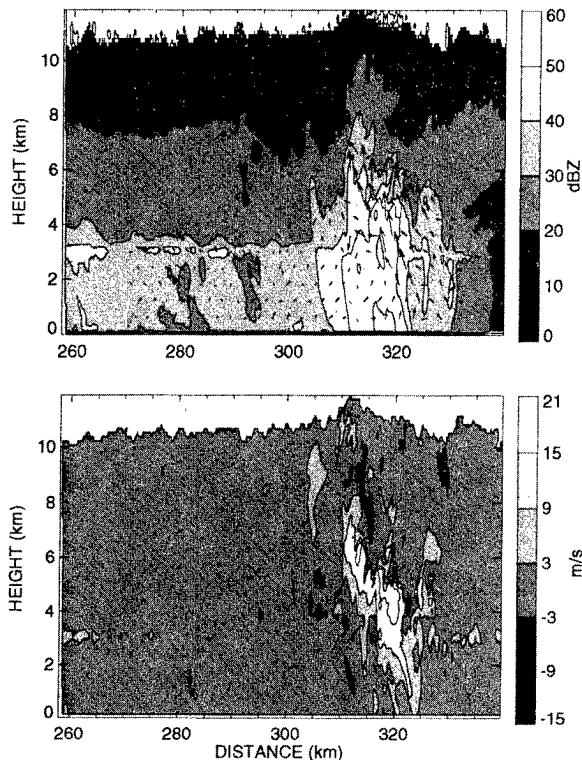
Fig.3 Top: Vertical profile of nadir reflectivity and relative wind vectors. Bottom: Vertical profile of vertical air velocity *w* calculated from nadir Doppler velocity.

A second research activity involves correction for attenuation effects at X-band frequencies. At X-band attenuation can become significant in heavy rainfall events and reflectivity and rainrate estimates will be under estimated if attenuation is not considered. Caylor[4] examined a means[5][6] of correcting for attenuation through use of the ocean surface reflectivity return and from the weaker mirror image. In the surface-reference technique the ocean surface return is examined under convective cells and compared to its value outside of the storm. The assumption is made that the radar cross-section of the ocean surface is nearly identical in the clear air and convection situations. Results indicate that the surface-reference technique works very well, particularly in areas of significant path attenuation. Future efforts include the use of tomography with the EDOP forward and nadir fields which would permit corrected reflectivity and rainrate retrieval without a requirement that the observations be over ocean.

FUTURE INSTRUMENT DEVELOPMENT

Although the present data system has proven its ability to collect real-time reflectivity and Doppler autocovariance products, an upgrade will be initiated in the near future for improved reliability and performance. The new data system will accommodate increased total range gates at a decreased range gate interval (37.5 m). It may employ either a "conventional" system with an analog receiver, as is presently implemented, or a digital IF receiver. A digital receiver would permit replacement of analog hardware within the receiver with its digital counterparts within the data system. In a digital receiver, the IF at 60 MHz is downconverted to 4 MHz and then sampled at 20 MHz. Some advantages over analog receivers include immunity to DC drift of the analog I and Q, reduction of low frequency noise, and better ideal filter approximation. An excellent description of the digital IF technique is found in Randall[2].

CONCLUSION

With its two antennas, coherent operation, and high-altitude platform, EDOP is proving to be a unique tool for studying convective precipitation. Future EDOP deployments are anticipated in support of the Tropical Rain Measuring Mission (TRMM) and other cloud and precipitation measurement objectives over the next several years.

REFERENCES

[1] G. M. Heymsfield, et al, "The EDOP Radar System on the High-Altitude NASA ER-2 Aircraft," in press.

[2] M. Randall, "A Digital IF Processor for Rectangular-Pulse Radar Applications," [AMS 25th Conf. Radar Met., pp. 871-874, 1991].

[3] G. M. Heymsfield, I. J. Caylor, S. W. Bidwell, S. Ameen, and S. Scala, "Structure of Vertical Velocities in a Rapidly Advancing Gulf Coast Squall Line Observed by EDOP," [AMS 27th Conf. Radar Met., pp. 556-558, 1995].

[4] I. J. Caylor, G. M. Heymsfield, S. W. Bidwell, and S. S. Ameen, "Estimating the Rain Rate Profile in the Presence of Attenuation Using EDOP Airborne Radar Observations," [AMS 27th Conf. Radar Met., pp. 783-785, 1995].

[5] T. Iguchi, and R. Meneghini, "Intercomparison of Single-Frequency Methods for Retrieving a Vertical Rain Profile from Airborne or Spaceborne Radar Data", J. Atmos. Oceanic Technol., vol. 11, pp. 1507-1516, 1994.

[6] R. Meneghini, and D. Atlas, "Simultaneous Ocean Cross Section and Rainfall Measurements from Space with a Nadir-Looking Radar," J. Atmos. Oceanic Technol., vol. 3, pp. 400-413, 1986.

Millimeter-wave Radars for Remotely Sensing Clouds and Precipitation

James B. Mead, Andrew L. Pazmany, Stephen M. Sekelsky, Ray Bambha, Robert E. McIntosh
Microwave Remote Sensing Laboratory
Room 113B Knowles Engineering Building
University of Massachusetts
Amherst, MA 01003

Phone: (413) 545-2463   FAX: (413)545-4652
email:mead@alex.ecs.umass.edu

Abstract – Since 1990 the University of Massachusetts
Microwave Remote Sensing Laboratory has been actively
developing innovative millimeter-wavelength radars in-
tended specifically for atmospheric remote sensing. These
instruments take advantage of several major technologi-
cal developments that have only recently become com-
mercially available: 1) Compact, high-power Extended
Interaction Klystron Amplifiers (EIAs) suitable for oper-
ation in the 35 and 95 GHz atmospheric transmission win-
dows; 2) Solid-state, low-loss switches, allowing pulse-to-
pulse polarization agility; 3) commercial data acquisition
and signal processing hardware designed for the industry
standard VXI-bus.

Fig. 1. Photograph of the UMass Cloud Profiling Radar System
(CPRS).

OVERVIEW OF MILLIMETER-WAVE CLOUD RADARS

Since the early 1950s, millimeter-wave radars have been
used for scientific studies of nonprecipitating clouds [1].
These instruments were more sensitive to small cloud
particles than conventional microwave radars and pro-
vided new insights into the rich small-scale structure
of clouds and precipitation. However, there were sev-
eral drawbacks to these early millimeter-wave radar sys-
tems that prevented their widespread use. These prob-
lems included: lack of solid-state, low-noise millimeter-
wave components, such as sources, mixers and ampli-
fiers, which resulted in noisy and unreliable receivers; 2)
scarcity of other millimeter-wave componentry, such as
antennas, switches, and circulators; 3) the lack of devices
and techniques for achieving phase coherence, which lim-
ited cloud radars to backscattered power measurements;
and 4) limited understanding of propagation and scat-
tering at millimeter-wavelengths. These limitations per-
sisted through the 1970s, and prevented millimeter-wave
cloud radars from filling operational needs such as pro-
viding information on cloud top and base height, melting
layer height, and number of cloud layers.

Modern millimeter-wave cloud radars resemble their
predecessors in many respects, but their performance
and reliability are considerably enhanced by advances in

millimeter-wave and digital technology during the past
two decades. Solid-state low phase noise sources, low-
noise mixers, and amplifiers are now widely available from
commercial sources, as well as power tubes, including
magnetron oscillators, commonly used for 35 GHz cloud
radars, and EIAs providing more than 50 dB gain and 1-
2 kW peak power output at 95 GHz. The availability of
low-loss switches and latching circulators has made pulse-
to-pulse polarization agility practical, which now permits
the study of cloud particle shape, orientation and angular
distribution through polarimetric techniques.

CLOUD RADAR DEVELOPMENT AT THE UNIVERSITY OF MASSACHUSETTS

The University of Massachusetts has recently built
two millimeter-wave radar systems, a 95 GHz radar for
airborne and highly portable ground-based applications
[2], and the truck-mounted cloud profiling radar system
(CPRS) that operates simultaneously at 33 and 95 GHz
[3], shown in Figure 1. These instruments are fully po-
larimetric; that is, they are able to measure the complex
scattering matrix of the scene by transmitting a pair a
orthogonally polarized pulses in rapid succession. Covari-
ances of the individual terms of the scattering matrix are
then used to compute meteorological radar parameters
that give insight into cloud-particle orientation, shape,
degree of randomness and anisotropy. In 1992 and 1994

the 95 GHz polarimeter was flown in the University of Wyoming's twin-engine King Air research aircraft. These missions demonstrated that a compact millimeter-wave radar can provide fine-scale reflectivity, polarimetric and Doppler imagery of a variety of cloud types. Since 1993, UMass has carried out measurements of cloud distribution and velocity using the cloud profiling radar system in support of the Department of Energy's Atmospheric Radiation Measurement (ARM) program. These measurements were carried out in conjunction with other remote sensing instruments at ARM's cloud and radiation test site in Northern Oklahoma.

One of the most important technological advance affecting the utility of all cloud radars has been the development of programmable digital signal processors (DSPs). Processor boards are now commercially available for a variety of standard buses, including ISA, VME, VXI, Multi-bus, and others. These boards have as many as five independent floating-point processors, each of which can be configured to execute one or more real-time algorithms. Because cloud radars can easily generate data rates of more than 1 MByte·s^{-1} it is usually desirable to use real-time processing to reduce data rates to a manageable level. Complete data acquisition systems, including analog-to-digital converters, processor boards, radar timing generators, and host computer, are now available for the VXI-bus. VXI's hierarchical architecture greatly simplifies system configuration, programming and debugging. All of these developments have resulted in a substantial reduction in the engineering effort necessary to develop a custom data acquisition and processing system.

During November and December of 1995, CPRS participated in MCTEX (Maritime Continent Thunderstorm Experiment) held along the coast of Northern Austrailia in an effort to study the complex evolution of maritime thunderstorms. The evolution of a typical thunderstorm is seen in Figures 2- 4 where RHI-scans are shown for a period of 34 minutes. Due to the high humidity and high cloud liquid water content, the 95 GHz radar was only effective when pointed vertically. However, the 33 GHz system was often effective to ranges beyond 25 kilometers.

Tornado observations at 95 GHz

The small size and light weight of millimeter-wave systems, which is crucial for airborne operations, also has advantages for land-mobile experiments. Researchers from UMass recently installed the 95 GHz airborne polarimeter in University of Oklahoma's tornado chase van as seen in Figure 5. Days when tornadoes were anticipated, the van was driven as much as 700 miles to try to get close enough to study tornadic activity with the radar. Once the van sped to within 1 to 3 km of an event, less than five minutes were usually available—to start the radar, take data, and then get out of the way of the oncom-
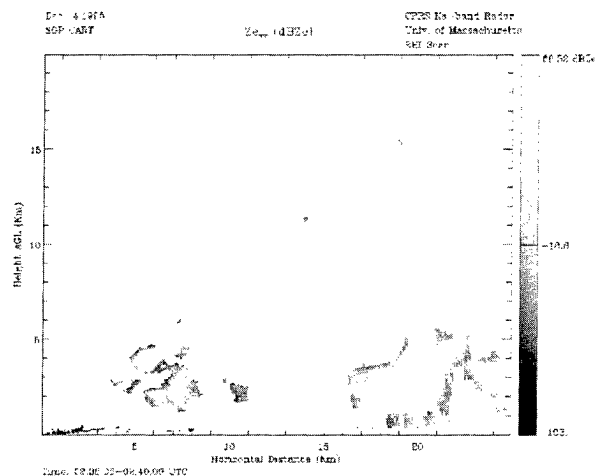
Fig. 2. RHI-scan of reflectivity for vv polarization: early stage of thunderstorm taken at 2:38 pm at 33 GHz.
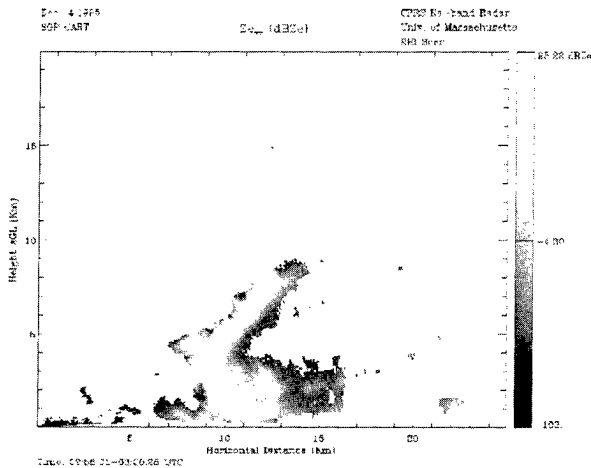
Fig. 3. RHI-scan of middle stage of thunderstorm taken at 2:58 pm at 33 GHz.
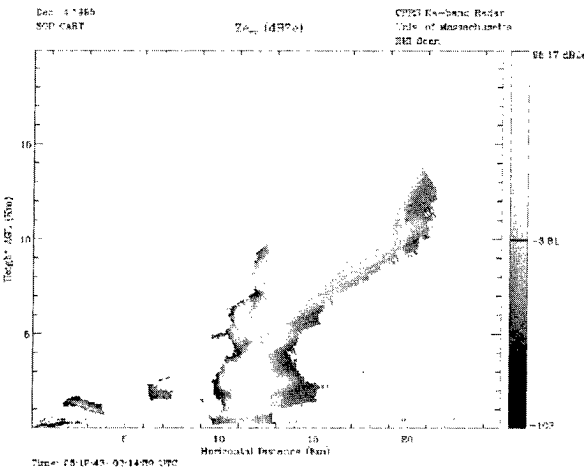
Fig. 4. RHI-scan of late stage of thunderstorm taken at 3:12 pm at 33 GHz.

ing storm. Typical reflectivity data from a pre-tornadic storm is shown in Figure 6, showing a pair of counter-rotating hook echoes at 2 and 2.8 km downrange.

FUTURE APPLICATIONS

In 1995, we began work on a compact, solid-state 95 GHz cloud radar intended for use on an unmanned aerial vehicle (UAV). This system incorporates a 40 W peak-power IMPATT amplifier, a compact lens antenna utilizing folded optics, and a 95 GHz HEMT LNA to achieve sensitivity of approximately -20 dBZ noise-equivalent reflectivity at 1 km range. When completed, the entire system will weigh less than 30 kg and will consume approximately 150 W prime power.

The low power consumption and high sensitivity of millimeter-wave radars make them well-suited for satellite applications. A recent workshop, held under the auspices of the Global Energy and Water Cycle Experiment (GEWEX),[2], assessed the potential for a spaceborne millimeter-wave radar to measure cloud vertical structure over large regions of the atmosphere. The distribution of ice and liquid water in clouds is a critical parameter in understanding the earth's radiation budget but no existing spaceborne instruments are currently available to measure the vertical structure of clouds.

A nadir-looking 95 GHz pulsed radar with a 2 m diameter antenna and 500 m range resolution could detect clouds of approximately -30 dBZ reflectivity from an altitude of 200 km. Such a system would not be able to detect weakly scattering liquid water clouds such as cumulus, stratocumulus and altocumulus but would be capable of detecting a substantial percentage of ice clouds and liquid clouds having larger drop sizes. Potential opportunities for a spaceborne millimeter-wave cloud radar include a Japanese J-1 rocket mission as early as 1997, the Japanese Experiment Module on the Space Station around the year 2000, or a future NASA Delta-class mission [3].

Fig. 5. Photograph of 95 GHz polarimetric radar configured for tornado chasing from the University of Oklahoma tornado chase van.
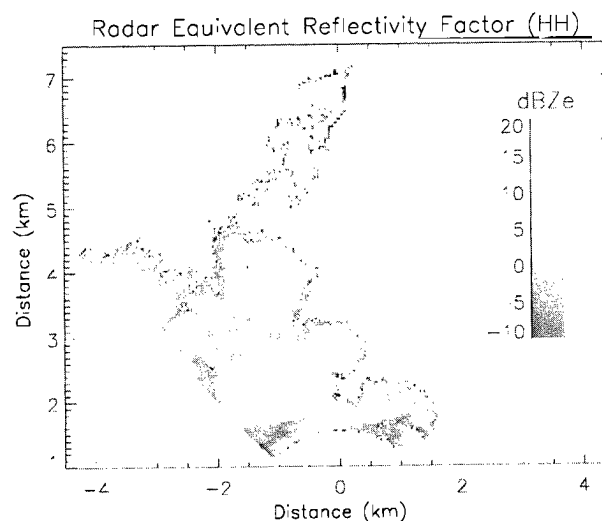
Fig. 6. Horizontal scan of radar equivalent reflectivity factor of a storm feature containing a cyclonic and anticyclonic hook. The image was recorded on May 17, 1995 in northeast Oklahoma. The radar elevation angle was approximately 5o.

BIBLIOGRAPHY

1. J.B. Mead, A.L. Pazmany, S.M. Sekelsky, R.E. McIntosh, "Millimeter-Wave Radars for Remotely Sensing Clouds and Precipitation", *Proc. IEEE*, 82(12), Dec. 1994, 1891-1906.
2. A.L. Pazmany, R.E. McIntosh, R.D. Kelly, G. Vali, "An Airborne 95 GHz Dual-Polarized Radar for Cloud Studies", *IEEE Trans. Geos. Remote Sens.*, 32(4),July, 1994, 731-739.
3. S.M. Sekelsky and R.E. McIntosh, "Cloud Observations with a Polarimetric 33 GHz and 95 GHz Radar", *J. Meteo. and Atmos. Physics,* 58, Jan. 1996, 123-140.
4. H.B. Bluestein, A.L. Pazmany, J.C. Galloway, and R.E. McIntosh, "Studies of the Substructure of Severe Convective Storms Using a Mobile 3-mm-Wavelength Doppler Radar", *Bulletin American Met. Soc.*, 76(11), Nov. 1995, 2155-2169.
5. *Report of the GEWEX Workshop on the Utility and Feasibility of a Cloud Profiling Radar* (Pasadena, CA, June 1993).
6. *Summary of the Second GEWEX Workshop on Cloud Profiling Radar* (Boulder, CO, Feb. 1994).

Polarimetric Image Classification Using Optimal Decomposition of Radar Polarization Signatures*

Yunhan Dong, Bruce Forster and Catherine Ticehurst
School of Geomatic Engineering, The University of New South Wales
Sydney 2052, Australia
Telephone: + 61 2 385 4177, Facsimile: + 61 2 313 7493
Email: yunhan@fatboy.geog.unsw.edu.au

Abstract — The technique of Weighted Least Squares (WLS) is used to obtain the optimal decomposition of radar polarization signatures, in which, backscatter is assumed to consist of odd, double, Bragg and cross scattering mechanisms. The results of the decomposition agree with our understanding of radar backscatter, providing information for polarimetric image classification.

INTRODUCTION

Polarimetric SAR (Synthetic Aperture Radar) data, such as that acquired and processed by NASA/JPL AirSAR system, give more information about ground targets than single channel SAR data. Excellent work has been done on modeling and classification of polarimetric radar backscatter for both built and natural targets in recent years [1–5].

The observed radar polarization signatures are not very similar to the constructed polarization signatures developed using simple scattering mechanisms. It reveals that the observed radar response is a combination of responses from various mechanisms. Since different scattering mechanisms give different polarization signatures, each of them could be separately extracted from the measured Mueller matrix. Statistically, radar measurements for N independent scattering mechanisms can be considered incoherently, as the positions of scatterers are randomly distributed.

In this paper, the backscattering response is assumed to be contributed by four basic scattering mechanisms. The simulated Mueller matrix is a combination of the Mueller matrices of these four scattering mechanisms. A method of optimal decomposition of radar polarization signature is then developed. The technique of WLS is used to find the optimal combination of these four components. The decomposition, in turn, provides information for polarimetric image classification.

BASIC SCATTERING MECHANISMS

Since positions of scatterers are randomly distributed, radar measurements for N independent scattering mechanisms can be added incoherently [6]. That is, the total

Mueller matrix $\mathbf{F}$ for N mechanisms is simply the sum of the N individual Mueller matrices $\mathbf{F}_i$,

$$\mathbf{F} = \sum_{i=1}^{N} \mathbf{F}_i \tag{1}$$

$\mathbf{F}$ can be constructed, therefore, if all $\mathbf{F}_i$ are known. Here only four basic scattering mechanisms are considered.

1. Double Bounce Scattering. This mechanism typically models the scattering from the trunk-ground structure in forested areas and the wall-ground structure in urban areas. The scattering matrix $\mathbf{S}$ can be written as:

$$\mathbf{S}_1 = \begin{bmatrix} S_{hh} & S_{vh} \\ S_{hv} & S_{vv} \end{bmatrix} = \begin{bmatrix} 1 & 0 \\ 0 & 1/\sqrt{\alpha}e^{j\delta} \end{bmatrix} S_1 \tag{2}$$

where $S_1 = S_{hh}$, $\alpha \approx \left| (R_{\perp 1}R_{\perp 2})/(R_{\|1}R_{\|2}) \right|^2$ and $\delta \approx Arg\left\{ -(R_{\perp 1}R_{\perp 2})/(R_{\|1}R_{\|2}) \right\}$, $Arg\{\cdot\}$ denotes the argument of a complex, $R_{\perp 1}$ and $R_{\perp 2}$ ($R_{\|1}$ and $R_{\|2}$) are the horizontally (vertically) polarized Fresnel reflection coefficients for the first and second bounces, which are functions of incidence angle and dielectric constant. α and δ are referred to as PI (polarization index, defined as the ratio of HH to VV polarization responses) and PD (polarization phase difference between HH and VV backscattered fields) values. In the case of perfectly conducting materials, $\alpha = 1$ and $\delta = 180^0$ regardless of incidence angle. Usually, α is about $4 \sim 6$ and δ about $140 \sim 160^0$ for the trunk-ground structure [7].

2. Bragg Scattering. Small perturbation techniques have been successfully used to obtain the polarization dependence from slightly rough surfaces such as bare soil and sea surfaces [8]. The scattering matrix of the first-order Bragg model is,

$$\mathbf{S}_2 = \begin{bmatrix} 1 & 0 \\ 0 & 1/\sqrt{\beta} \end{bmatrix} S_2 \tag{3}$$

where the mean PI value, $\beta = |\alpha_{hh}/\alpha_{vv}|^2$, is generally less than 1, $\alpha_{hh} = (\epsilon - 1)/\left(cos\theta + \sqrt{\epsilon - sin^2\theta}\right)^2$, and $\alpha_{vv} = (\epsilon - 1)[\epsilon(sin^2\theta + 1) - sin^2\theta]/\left(\epsilon cos\theta + \sqrt{\epsilon - sin^2\theta}\right)^2$. θ and ϵ are the incidence angle and the dielectric constant of the surface, respectively. The mean PD value is considered as zero (the Bragg scattering undergoes a single bounce).

3. Odd Bounce Scattering. This mechanism typically models the direct specular reflections from facets of the ground and/or building roofs perpendicular to the incident direction, and big branches whose axes are perpendicular to the incident direction and so on. Since the local incidence angle for such targets is zero degrees, this gives,

$$\mathbf{S}_3 = \begin{bmatrix} 1 & 0 \\ 0 & 1 \end{bmatrix} S_3 \qquad (4)$$

because the PI value is 1 and the PD value zero degrees, for this mechanism. The co-polarized response from forest crown volume backscattering can be included in this mechanism. If the orientations of leaves, twigs and small branches are assumed to be uniformly distributed, the backscattering response will be independent of polarization, giving the same HH and VV response. The backscattering from the trihedral-corner-reflector-like, wall-wall-ground structure can also be classified into this mechanism, since the scattering undergoes odd bounces.

4. Cross Scattering. This is a theoretical model to take account of the cross-polarized response from randomly distributed targets, if we are only interested in the total cross-polarized response. The reciprocity implies $S_{vh} = S_{hv}$ in the backscattering direction. In the case of random mediums, if distributed targets are assumed to be azimuthal symmetry, we have $\langle S_{hh} S_{vh}^* \rangle = \langle S_{vv} S_{vh}^* \rangle = 0$ [9]. Therefore, only the item of S_{vh}^2 is important. The scattering matrix for such a theoretical cross scattering mechanism is,

$$\mathbf{S}_4 = \begin{bmatrix} 0 & 1 \\ 1 & 0 \end{bmatrix} S_4 \qquad (5)$$

ALGORITHM

The total Mueller matrix is the sum of the Mueller matrices for the above individual mechanisms, giving,

$$f_{11} = \frac{\alpha+1}{2\alpha} S_1^2 + \frac{\beta+1}{2\beta} S_2^2 + S_3^2 + S_4^2 \qquad (6)$$

$$f_{12} = \frac{\alpha-1}{2\alpha} S_1^2 + \frac{\beta-1}{2\beta} S_2^2 \qquad (7)$$

$$f_{22} = \frac{\alpha+1}{2\alpha} S_1^2 + \frac{\beta+1}{2\beta} S_2^2 + S_3^2 - S_4^2 \qquad (8)$$

$$f_{33} = \frac{cos\delta}{\sqrt{\alpha}} S_1^2 + \frac{1}{\sqrt{\beta}} S_2^2 + S_3^2 + S_4^2 \qquad (9)$$

$$f_{34} = -\frac{sin\delta}{\sqrt{\alpha}} S_1^2 \qquad (10)$$

$$f_{44} = -\frac{cos\delta}{\sqrt{\alpha}} S_1^2 - \frac{1}{\sqrt{\beta}} S_2^2 - S_3^2 + S_4^2 \qquad (11)$$

$$S_i^2 \geq 0 \qquad i = 1, \cdots, 4 \qquad (12)$$

The left sides of (6)–(11) are the elements of the Mueller matrix measured by the polarimetric radar system [10]. S_i^2

$(i = 1, \cdots, 4)$ are the four unknowns to be determined. The optimal solution of (6)–(12) can be found using the WLS method. Since the optimal solution is found with respect to the combined Mueller matrix, but not just to one or more specific polarizations, the difference between the simulated and measured polarization signatures should be the minimum under the model assumptions. After the unknowns are obtained, the simulated Muller matrix

$$\mathbf{F} = \mathbf{F}_1 + \mathbf{F}_2 + \mathbf{F}_3 + \mathbf{F}_4 \qquad (13)$$

can be reconstructed, and the co- and cross-polarization responses predicted by the model are, $\sigma_{hh}^0 = 4\pi(S_1^2 + S_2^2 + S_3^2)$, $\sigma_{vv}^0 = 4\pi(S_1^2/\alpha + S_2^2/\beta + S_3^2)$ and $\sigma_{vh}^0 = \sigma_{hv}^0 = 4\pi S_4^2$.

DECOMPOSITION AND CLASSIFICATION

To test the model, the NASA/JPL AirSAR P-, L- and C-band data are used. Areas covered by natural targets, such as ocean, unploughed farm grassland, native eucalypts, pine plantations, and by built targets, such as commercial and residential buildings or a mixture, are chosen for the simulation. Table 1 lists the scattering components decomposed for commercial, residential, eucalypts and grassland areas at P-, L- and C-bands, respectively.

Table 1: Scattering components as a percentage of the total backscattering for (a) commercial, (b) residential, (c) eucalypts and (d) grassland areas (Odd + double + Bragg = 100%).

Area	Band	Odd	HH/VV Double	Bragg	Cross
(a)	P	16/29	83/60	1/11	3.2/5.6
	L	14/29	86/71	0/0	2.1/4.4
	C	0/0	94/49	6/51	4.6/4.1
(b)	P	32/54	68/45	0/0	9.8/17.0
	L	34/57	66/43	0/0	11.1/21.8
	C	42/64	58/36	0/0	10.3/18.2
(c)	P	17/30	77/34	6/36	14.1/25.3
	L	24/33	67/23	10/44	20.0/27.8
	C	47/54	44/13	9/33	23.2/27.0
(d)	P	53/54	33/8	14/38	7.1/7.2
	L	63/67	27/7	10/26	10.2/10.8
	C	43/47	42/11	15/42	20.3/27.9

A dominant double bounce scattering from commercial and residential areas is expected. The relative cross-polarized component for residential areas is higher than that for commercial areas, because the vegetation volume scattering is much stronger in the residential areas. It is worth noting that there is little difference between the percentages decomposed from three different bands (it implies that the measured signatures at these three bands are very
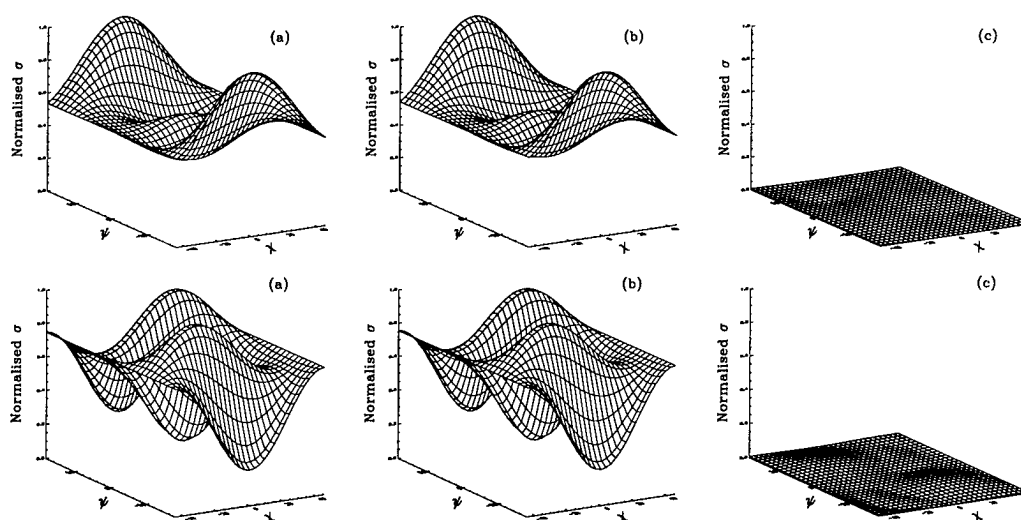
Figure 1: Polarization signature (top: co-polarization and bottom: cross-polarization) comparison using the measured and simulated Mueller matrices for residential areas in Sydney at P-band: (a) measured, (b) simulated and (c) absolute difference.

similar) for either the commercial or residential areas. The situations for forested areas are different. It can been seen that the component of double bounce backscattering decreases from P- to L- and further to C-bands due to the well known effect of foliage attenuation. The foliage attenuation increases with increasing frequency, resulting in a decrease in the double bounce scattering. A dominant component of single (odd) scattering is decomposed for a grassland area at all three bands. It can also be seen from the table that the scattering components for the eucalypts and grassland areas at C-bands are very similar, indicating that C-band has a very limited ability to penetrate in vegetated areas.

Figure 1 shows the measured and simulated polarization signatures for a residential area. Shown in the figure are also the differences of the measured and simulated polarization signatures. In summary, the accuracy of decomposition was found to be more than 95% for linear polarizations (HH and VV polarizations) and more than 85% for any other polarizations, in most cases. A better polarimetric image classification could be achieved using the traditional discriminators (co- and cross-backscattering coefficients, ratios of different backscattering coefficients, and phase difference, etc) as well as the optimal decomposition techniques.

REFERENCES

[1] J.J. van Zyl, "Unsupervised classification of scattering behavior using radar polarimetry data," IEEE Trans. on Geoscience and Remote Sensing, vol. 27, pp. 36-45, 1989.

[2] A. Freeman, and S. Durden, "A three-component scattering model to describe polarimetric SAR data," in H.

Mott, and W.M. Boerner (editors), Radar Polarimetry, July 23-24, 1992, San Diego, Bellingham: SPIE, pp. 213-224, 1993.

[3] L.E. Pierce, F.T. Ulaby, K. Sarabandi, and M.C. Dobson, "Knowledge-based classification of polarimetric SAR images," IEEE Trans. on Geoscience and Remote Sensing, vol. 32, pp. 1081-1086, 1994.

[4] R. Kwok, E.J.M. Rignot, J. Way, A. Freeman, and J. Holt, "Polarization signatures of frozen and thawed forests of varying environmental state," IEEE Trans. on Geoscience and Remote Sensing, vol. 32, pp. 371-381, 1994.

[5] D.A. Evans, T.G. Farr, J.J. van Zyl, and H.A. Zebker, "Radar polarimetry: Analysis tools and application," IEEE Trans. on Geoscience and Remote Sensing, vol. 26, pp. 774-798, 1988.

[6] H.C. van de Hulst, Light Scattering by Small Particles, New York: John Wiley and Sons Inc., 1957.

[7] Y. Dong, and J.A. Richards, "Studies of the cylinder-ground double bounce scattering mechanism in forest backscatter models," IEEE Trans. on Geoscience and Remote Sensing, vol. 33, pp. 229-231, 1995.

[8] C. Elachi, Introduction to the Physics and Techniques of Remote Sensing, New York: John Wiley and Sons Inc., 1987.

[9] S.H. Yueh, R. Kwok, and S.V. Nghiem, "Polarimetric scattering and emission properties of targets with reflection symmetry," Radio Science, vol. 29, 1409-1420, 1994.

[10] JPL, "AirSAR integrated processor documentation: Data formats," version 0.01, JPL, 1995.

A Comprehensive Evaluation of Filters for Radar Speckle Suppression

Yongwei Sheng and Zong-Guo Xia
Department of Environmental Sciences
University of Massachusetts at Boston
100 Morrissey Boulevard, Boston, Massachusetts 02125-3393
Phone: (617) 287 - 5285, FAX: (617) 265 - 7173, E-mail: ysheng@earth.geog.umb.edu

Abstract--This paper presents the result of a comprehensive evaluation of filters for radar speckle suppression. Seven filters in the Radar Module of Erdas/IMAGINE® were evaluated, including the mean filter, the median filter, the Lee-Sigma filter, the Local Region filter, the Lee filter, the Frost filter, and the MAP(Maximum A Posteriori) filter. The performance of these filters was measured in terms of five criteria: speckle suppression index, edge enhancing index, feature preserving index (for both linear features and point features), image detail preserving coefficient, and speckle image analysis. Visual effect of filtered image and its filter theoretical basis were discussed. The relationship between filter performance and speckle patterns was also examined.

INTRODUCTION

Like other types of coherent imagery, all radar images are inherently corrupted by speckle. The presence of speckle in an image reduces the detectability of ground targets, obscures the spatial patterns of surface features, and decreases the accuracy of automated image classification. Thus, it is often necessary to enhance the image by speckle filtering before data can be used in various applications. During the past 20 years, more than a dozen of filters have been developed for speckle suppression. All major commercial image processing systems, such as, ER Mapper®, PCI EASI/PACE® and Erdas/IMAGINE®, include a number of image filters for radar speckle suppression. With the availability of a wide variety of radar image filters, the user needs to know how to pick the best filter for a particular application. Durand[1], Dewaele[2], Shi[3] and Rao[4] carried out comparative studies of radar speckle filters. However, there have been very few studies on the efficiency, range of applicability, the advantages, and disadvantages of different filters. Recently, Lee[5] has given a comprehensive review of the better-known SAR filters. This paper presents the result of a comprehensive evaluation of filters for radar speckle suppression available in the Erdas/IMAGINE® Radar Module.

BRIEF DESCRIPTION OF SPECKLE FILTERS

There are seven filters provided in IMAGINE V.8.2. All of the filters use a $k \times k$ moving window to estimate the central pixel intensity. They are briefly described below.

1. Mean Filter

Radar speckle appears as high frequency component in a radar image. Mean filter, a widely-used low-pass filter, can be used for the speckle suppression purpose.

2. Median Filter

The low-valued and high-valued pixels correspond to destructive and constructive speckle. The use of median value reduces such erratic variations.

3. Lee-Sigma Filter

Based on the Gaussian distribution model, Lee-Sigma filter averages only those pixels within $m \cdot \sigma$ range (e.g., 95.5%, when m=2), i.e.,

$$\hat{R}_0 = \frac{\sum_{i=1}^{n} R_i * \delta_i}{\sum_{i=1}^{n} \delta_i}, \text{ where } \delta_i = \begin{cases} 1, if & R_i \in (R_i - m*\sigma, R_i + m*\sigma) \\ 0, else \end{cases}$$

4. Local Region Filter (LR)

The Local Region filter divides the moving window into eight regions based on angular position. The algorithm compares the variance values of the regions surrounding the pixel of interest. The pixel of interest is replaced by the mean of all values within the region with the lowest variance.

5. Lee Filter

Based on the multiplicative model of speckle noise, the priori mean and variance are computed as follows:

$$\overline{R}_0 = \overline{R}, \quad Var(R_0) = \frac{Var(R) + \overline{R}^2}{\sigma^2 + 1} - \overline{R}_0^2.$$

An estimator of R_0 is obtained by minimizing either the mean square error or the weighted least square estimation:

$$\hat{R}_0 = \overline{R} + k \cdot (R - \overline{R}), \text{ where k is calculated as: } k = \frac{Var(R)}{\overline{R}^2 \sigma^2 + Var(R)}.$$

6. Frost Filter

Like Lee filter, Frost filter is based on the local statistics and the multiplicative model. It differs from the Lee filter in that the scene reflectivity is estimated by convolving the observed image with the impulse response of the SAR system and it averages less in the edge areas to preserve the edge .

7. MAP Filter

MAP is an adaptive speckle filter, which tends to maximize a posteriori probability of the original signal from the speckled signal. MAP filter assumes that the original signal has a Gaussian distribution.

FILTER EVALUATION

A speckle suppression filter is expected to filter the homogeneous areas with reasonable speckle reduction

capability, retain edges, preserve features (linear features and point features), and have reasonable theoretical assumptions. Five indexes are derived for use as the evaluation criteria in this paper:

1. Speckle Suppression Index (SSI):

For homogeneous areas, $\sqrt{Var(R)}/Mean(R)$ is regarded as the measurement of speckle strength. Speckle suppression index (normalized to the original image) is here defined as:

$$SSI = \frac{\sqrt{Var(\hat{R}_0)}}{Mean(\hat{R}_0)} \cdot \frac{Mean(R)}{\sqrt{Var(R)}} \qquad (1)$$

where $\hat{R}_0$ is the filtered value, R is the original value.
For most cases, SSI<1.0, which means speckle is suppressed. The lower the SSI is, the stronger suppression ability the filter has.

2. Edge Enhancing Index (EEI):

For a n-pixel long edge, EEI is defined as

$$EEI = \frac{\sum_{1}^{n}\left|\hat{R}_{01} - \hat{R}_{02}\right|}{\sum_{1}^{n}\left|R_1 - R_2\right|} \qquad (2)$$

where R_1, R_2 are the original values of the one-pixel wide lines on either side of the edge, while $\hat{R}_{01}$, $\hat{R}_{02}$ are the filtered values. Higher EEI represents better edge retaining ability of the evaluated filter.

3. Feature Preserving Index (FPI):

For a one-pixel wide linear feature of n pixels,

$$FPI_{1\_line} = \frac{\sum_{1}^{n}(2 \cdot \hat{R}_0 - \hat{R}_{01} - \hat{R}_{02})}{\sum_{1}^{n}(2 \cdot R - R_1 - R_2)} \qquad (3)$$

where R is the original value of a pixel representing the feature, R_1, R_2 are the pixels on the both sides of the feature, while $\hat{R}_0$, $\hat{R}_{01}$, $\hat{R}_{02}$ are the filtered values.

For a point feature,

$$FPI_{1\_point} = \frac{Mean(\hat{R}_{0point})}{Mean(\hat{R}_{0neighbor})} \cdot \frac{Mean(R_{0neight})}{Mean(R_{0point})} . \qquad (4)$$

Although some filters can preserve features, feature value may change unexpectedly. Thus, FPI_2 is used to describe the ability of feature mean value retention:

$$FPI_2 = \frac{Mean(\hat{R}_{0feature})}{Mean(R_{feature})} \qquad (5)$$

4. Image Detail Preserving Coefficient (IDPC):

Based on speckle identification, the correlation coefficient between the filtered image and the original image shows the filter's ability of preserving the original values of features.

5. Speckle image statistical analysis:

Radar speckle is multiplicative, i.e., $R_{i,j} = R0_{i,j} * SP_{i,j}$. Speckle image can be derived from the original image and filtered image simply by image ratioing. Theoretically, speckle image should have normal distribution with its mean around 1. Thus, the statistics of the speckle image can help us to evaluate filters.

To evaluate the IMAGINE speckle filters by the above criteria, radar image of Flevoland, the Netherlands, acquired by SIR-C/X-SAR system on April 14, 1994, was used for our study. A subimage (600x700) was clipped, where six categories of landuse are identified: built-up area, canal, arable land, meadow, meadow with poplar and forest. There are some linear features (roads and small rivers) and point features in this image. the result of a study on speckle pattern analysis using this image is reported in [6]. Several homogeneous areas of each landuse type were selected to evaluate the performance of filters.

The SSIs of each filter in different homogeneous areas are shown in Tab. 1. In these homogeneous areas, the mean filter performs best and the MAP filter and the median filter also work well, while the Frost filter is the poorest. Comparing the SSI with speckle patterns, we can find some relationship between them. As Fig. 1 shows, the Frost filter almost has no effect in areas with low speckle means(water and meadow); the mean filter performs well in SSI for the more speckled areas (higher speckle density); the median filter gets a high SSI in the areas where the bright and dark speckles are out of balance; the Sigma filter works better when the bright speckle roughness matches the dark speckle roughness; and the Lee filter produces better results in the areas with median speckle strength. From the EEI and FPI (Tab. 2), we can see that the Frost filter is definitely the best in preserving both edges and features, and the Lee filter is favorable. The mean filter blurs edges and features and the median filter causes loss of point features. The IDPC (Tab. 3) and statistics of speckle image (Tab. 4) show that the local region filter changes the original image too much except for speckle. The Frost filter almost keeps the image (excluding sharp speckled pixels) untouched, but the speckle image shows its low ability in speckle suppression. The speckle image processed by the median filter seems to have a reasonable statistical distribution. Comparing the filtered images visually, we can see that the mean filter and the MAP filter blur the image seriously.

CONCLUSION

Several objective normalized evaluation indexes are developed in this paper so that the filter performance can be evaluated for each area of different landuse and speckle pattern. None of the evaluated filters performs well on the basis of all the evaluation indexes. There is always a trade-off between speckle suppression and edge/feature preservation for all the filters. The close relationship between the filter performance and speckle patterns described in this paper indicates that speckle patterns should be considered in filter selection.

REFERENCES

[1] J.M. Durand, B.J. Gimonet, and J.R.Perbos, "SAR data filtering for classification," IEEE Trans. on Geoscience and Remote Sensing, Vol. GE-25, No. 5, pp. 629-637, 1987.

[2] P. Dewaele, P. Wambacq, A. Oosterlinck, and J.I. Marchand, "Comparison of some speckle reduction techniques for SAR images," Proceedings of IGARSS'90 Symposium, pp. 2417-2421, 1990.

[3] Z. Shi and K.B. Fung, "A comparison of digital speckle filters," Proceedings of IGARSS'94 Symposium, pp. 2129-2133, 1994.

[4] P.V.N. Rao, M.S.R.R. Vidyadhar, T.Ch. M. Rao and L. Venkataratnam, "An adaptive filter for speckle suppression in synthetic aperture radar images," Int. J. Remote Sensing, Vol. 16, No. 5, pp. 877-889, 1995.

[5] J.S. Lee and I. Jurkevich, "Speckle filtering of synthetic aperture radar images: a review," Remote Sensing Review, Vol. 8, pp. 313-340, 1994.

[6] Z.G. Xia and Y. Sheng, "Radar speckle: noise or information?" Proceedings of IGARSS'96 Symposium, 1996.

Tab.1 Speckle Patterns and SSIs of Selected Areas

Landcover		Speckle pattern							Filter														
Area No.	Land use	Bright Speckle Mean	Roughness	Dark Speckle Mean	Roughness	Speckle Density	Bright Density	Dark Density	$\frac{Bright\_Density}{Dark\_Density}$	Mean SSI	No.	Median SSI	No.	Sigma SSI	No.	LR SSI	No.	Lee SSI	No.	Frost SSI	No.	MAP SSI	No.
1	Built-up	212.925	43.310	154.828	53.502	0.168	0.026	0.142	0.183	0.653	1	0.773	3	0.769	4	0.829	6	0.737	2	0.904	7	0.769	4
7	....	215.943	26.865	116.419	55.069	0.203	0.057	0.146	0.390	0.634	1	0.735	3	0.793	4	0.849	5	0.849	5	0.880	7	0.676	2
2	Water	61.421	26.865	7.706	10.571	0.291	0.119	0.172	0.692	0.403	1	0.580	2	0.679	4	0.699	5	0.910	6	0.999	7	0.655	3
4	Arable	165.422	32.439	83.601	33.860	0.292	0.112	0.180	0.622	0.550	1	0.621	4	0.633	5	0.719	6	0.606	3	0.786	7	0.554	2
5	......	173.583	35.528	92.026	31.253	0.286	0.103	0.183	0.563	0.544	2	0.597	3	0.621	5	0.705	6	0.617	4	0.748	7	0.540	1
6	......	139.811	35.462	44.265	29.228	0.285	0.111	0.174	0.638	0.528	1	0.631	3	0.738	4	0.742	5	0.792	6	0.940	7	0.556	2
9	......	167.454	33.912	88.491	32.197	0.278	0.102	0.176	0.580	0.578	2	0.639	3	0.661	4	0.719	5	0.725	6	0.783	7	0.575	1
12	......	197.625	35.897	112.181	34.868	0.273	0.102	0.170	0.600	0.504	1	0.554	3	0.587	5	0.707	6	0.634	5	0.717	7	0.514	2
3	Meadow	60.671	52.799	12.310	15.188	0.217	0.099	0.118	0.839	0.688	1	0.876	2	0.939	4	0.958	5	0.964	6	0.995	7	0.862	3
15	......	72.630	39.897	13.882	26.368	0.270	0.101	0.169	0.598	0.659	1	0.796	3	0.853	4	0.836	5	0.926	6	0.992	7	0.773	2
17	Meadow with poplar	219.000	36.530	115.667	42.441	0.193	0.039	0.154	0.253	0.667	1	0.772	4	0.748	3	0.817	6	0.894	7	0.776	5	0.683	2
14	Forest	220.068	26.578	184.131	37.798	0.151	0.012	0.139	0.086	0.655	1	0.810	5	0.707	2	0.799	4	0.983	7	0.845	6	0.753	3
16	......	217.000	25.910	202.663	39.203	0.135	0.005	0.130	0.038	0.753	1	0.825	3	0.844	4	0.708	2	0.942	6	0.981	7	0.909	5
Image	Mixture	138.925	69.264	86.638	71.702	0.226	0.071	0.155	0.458	0.888	1	0.953	4	0.981	7	0.974	6	0.912	2	0.966	5	0.913	3

Tab.2 EEI and FPI

Description of edge or feature	Index type	Mean Index	No.	Median Index	No.	Sigma Index	No.	LR Index	No.	Lee Index	No.	Frost Index	No.	MAP Index	No.
Edge: meadow and arable land	EEI	0.479	7	0.648	5	0.680	4	0.708	3	0.847	2	0.941	1	0.595	6
Edge: meadow and forest	EEI	0.528	7	0.813	3	0.772	4	0.768	5	0.942	2	0.953	1	0.629	6
Edge: canal and built-up area	EEI	0.459	7	0.847	4	0.750	5	0.940	2	0.886	3	0.982	1	0.725	6
Linear feature: small river	FPI_1_line	0.115	7	0.243	6	0.414	5	0.557	3	0.867	2	0.999	1	0.442	4
....	FPI_2	3.602	7	3.302	6	1.813	3	2.482	5	1.514	2	1.000	1	2.157	4
Linear feature: main road	FPI_1_line	0.217	7	0.346	5	0.396	4	0.674	2	0.5982	3	0.877	1	0.241	6
....	FPI_2	0.777	5	0.826	4	0.775	7	0.895	2	0.887	3	0.970	1	0.776	6
Point feature: light tower in canal	FPI_1_point	0.542	6	0.523	7	0.784	4	0.680	5	0.972	2	0.999	1	0.802	3
....	FPI_2	0.525	5	0.379	7	0.525	5	0.551	4	0.968	2	1.000	1	0.653	3

Tab.3 Image Detail Preservation Index

ndex	Mean	Median	Sigma	LR	Lee	Frost	MAP
IDPC	0.949	0.948	0.963	0.920	0.907	0.989	0.960

Tab.4 Speckle Image Statistics

Index type	Mean	Median	Sigma	LR	Lee	Frost	MAP
mean	0.983	1.057	1.092	1.128	0.995	0.997	1.012
std. deviation	0.432	0.784	0.401	1.006	0.469	0.094	0.320

The Relationship of Frost Filter and Speckle Means
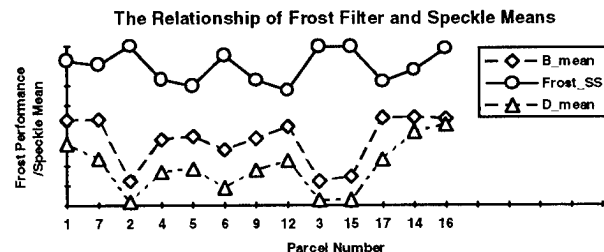
Fig.1 The Relationship Between Frost Filter and Speckle Patterns

SIR-C polarimetric image segmentation by neural network

R. Sergi[1], G. Satalino[2], B. Solaiman[3], G. Pasquariello[2]

[1] GNCB-CNR c/o Dip. di Fisica, Via Amendola, 173 - 70126 Bari - Italy
[2] Istituto Elaborazione Segnali ed Immagini I.E.S.I-C.N.R.
Via Amendola, 166/5 - 70126 - Bari - ITALY
Fax: +39 80 5484311, Phone: +39 80 5481612, E-Mail: satalino@iesi.ba.cnr.it
[3] Telecom Bretagne, Dep. I.T.I., B.P. 832 - 29285 Brest cedex - France

Abstract – In this paper, the results of the segmentation process of polarimetric multiband SAR images are shown. Purpose of the work is the image interpretation in absence of ground-truth. The segmentation process is performed by the Self Organizing Map network which is an unsupervised neural network. The objective of the segmentation is the selection of homogeneous regions on the image and the results are evaluated in terms of grey level statistics on same restricted areas (urban and salina areas).

INTRODUCTION

The use of radar polarimetry is very promising in monitoring terrain parameters. Many SAR systems produce a large amount of measurements for each resolution cell of the polarimetric image and these data must be correctly processed in order to obtain the maximum information of the land characteristics. A supervised approach is normally adopted for classification purposes, however when the ground truth is not available, the image processing can only supply some statistical data. Under these circumstances, a segmentation process can be used to detect homogeneous areas.

In this paper, the results of the segmentation process of polarimetric SAR images are shown. SAR measurements depend on structural and electromagnetic properties of the terrain as the surface roughness and the soil moisture. As first processing step, it is necessary to organize all data into a finite number of clusters. The advantage of a segmentation technique is that it performs a dimensional reduction of the input data; in fact, each multi-dimensional pixel is associated to a scalar value that identifies a cluster. The multi-dimensional pixel is obtained by grouping the polarimetric multiband SIR-C values. The segmentation process is performed by using a Self Organizing Map (SOM)[1] which is an unsupervised neural network and produces a topological map of clusters. This map can be successively used to group in a given class all clusters having similar features. Neural network approaches represent a valid alternative to traditional supervised and unsupervised algorithms [2] and their performances are comparable or slightly better than their analogous conventional methods [3].

The segmentation is evaluated in terms of region homogeneity on same restricted areas. In our case, these references area are identified on the image by a visual inspection as salina and urban areas. Measuring on the segmented images some statistics on the grey levels in correspondence of the above mentioned areas, it are shown how the dispersion of the grey level image changes with the processing of input vector with a different dimensionality.

DATA DESCRIPTION

In this paper SAR images are used. Data have been collected with SIR-C sensor mounted on the Endeavour Space Shuttle which over Italy in October '94. The study area covers 19.5 Km (range direction) · 18.5 Km (azimuth direction) approximately and it is located in a south-eastern region of Italy (Matera site CB 1). The SIR-C is a polarimetric, multifrequency SAR. It measures simultaneously both amplitude and phase of the backscattered signal for each of the four linearly polarized components (HH, HV, VH, VV)(scattering matrix) at C-band ($\lambda \simeq 6$ cm) and L-band ($\lambda \simeq 24$ cm). Assuming reciprocity, the HV component is equal to the VH component [4]. Polarimetric data are the sources of multidimensional feature vectors: in fact, polarimetric measurement can be stored in 3 complex quantities:

$$HH, \quad HV, \quad VV$$

or in 5 real quantities:

$$| HH |, | HV | \cos(\phi_{HV} - \phi_{HH}), | HV | \sin(\phi_{HV} - \phi_{HH}),$$

$$| VV | \cos(\phi_{VV} - \phi_{HH}), | VV | \sin(\phi_{VV} - \phi_{HH})$$

where ϕ_{HH}, ϕ_{HV}, ϕ_{VV} are the phases of HH, HV and VV, respectively [5]. To decrease the effects of the speckle noise, a multilook averaging is usually applied. The averaging is performed on the values of the received power and, considering the covariance matrix of the scattering matrix, the Mueller matrix is obtained finally, taking into account the covariance matrix of the scattering matrix. In this case, we have a feature vector consisting of 6 complex elements [6]:

$$HH \cdot HH^*, HV \cdot HV^*, VV \cdot VV^*,$$

$$HH \cdot HV^*, HH \cdot VV^*, HV \cdot VV^*$$

or 9 real quantities:

$$| HH \cdot HH^* |, | HV \cdot HV^* |, | VV \cdot VV^* |,$$

$$Re\{HH \cdot HV^*\}, Im\{HH \cdot HV^*\},$$

$$Re\{HH \cdot VV^*\}, Im\{HH \cdot VV^*\},$$

$$Re\{HV \cdot VV^*\}, Im\{HV \cdot VV^*\}.$$

The compressed polarimetric radar data were delivered by JPL; for practical purposes a subimage of 512 pixels by 512 lines was extracted from the original scene of 1424 · 9616 pixels. Data are also calibrated. At first, data have been decompressed; then the multilook technique was applied by averaging 2 pixels in range direction and 7 pixels in azimuth direction. This is the optimum multilook to obtain a square ground pixel whose size is approximately of $37 \cdot 37 m^2$. At last, 9 real elements in the Mueller matrix form have been extracted to describe the properties of the polarimetric backscattered signal.

Data suffers of high dispersion. Tab. 1 shows, as example, statistics of data in correspondence of the salina and urban areas that should be the most homogeneous regions that can be found on the image. Fig. 1 a) shows a SAR image.

It should be noted that the absolute maximum value of the images are found on urban areas show a higher dispersion around the mean value. Salina area is characterized by a lower mean and a smaller dispersion of the grey levels.

Table 1: Statistics for salina and urban areas (μ=Mean, σ=Standard Deviation).

Image	Min	Max	μ	σ
Salina area				
$\| HH \cdot HH^* \|$, C	0.002	0.384	0.045	0.040
$\| HV \cdot HV^* \|$, C	0.001	0.053	0.004	0.003
$\| VV \cdot VV^* \|$, C	0.003	0.362	0.049	0.039
$\| HH \cdot HH^* \|$, L	0.001	0.604	0.081	0.065
$\| HV \cdot HV^* \|$, L	0.000	0.019	0.001	0.001
$\| VV \cdot VV^* \|$, L	0.001	0.752	0.170	0.135
Urban area				
$\| HH \cdot HH^* \|$, C	0.055	1.336	0.855	0.416
$\| HV \cdot HV^* \|$, C	0.006	0.134	0.082	0.040
$\| VV \cdot VV^* \|$, C	0.035	0.649	0.412	0.184
$\| HH \cdot HH^* \|$, L	0.025	0.885	0.451	0.293
$\| HV \cdot HV^* \|$, L	0.001	0.056	0.041	0.017
$\| VV \cdot VV^* \|$, L	0.018	0.752	0.344	0.217

data vectors (M(C), M(L), M(C+L), M+P(C), M+P(L)) have been sampled from correspondent images and them have been submitted to a SOM neural network for different experiments of segmentations. The number of output nodes for each network was 16, whereas the number of input nodes was equal to the input vector components. By using all data vectors sampled from images, the SOM training phase is performed without supervision. This phase updates the weight vectors in such a manner that them tend to approach the cluster center of the input data. After training, labelling each multidimensional vector with the cluster code assigned by SOM, a 16-grey level image has been obtained. Each level represents the cluster of all input vectors that are similar in the n-dimensional Euclidean space. The segmented image obtained has the property that close grey levels correspond to similar clusters. As result, the dark and bright areas on the original images are mapped on low and high grey levels on the output image (as the salina and urban areas).

Table 2: Statistics for salina (s) and urban (u) areas on segmented images (μ=Mean, σ=Standard Deviation).

Input images	μ_s	σ_s	μ_u	σ_u
M(C)	1.03	0.28	11.92	4.14
M(L)	3.95	2.79	9.79	4.44
M(C+L)	1.66	1.41	11.66	4.34
M+P(C)	1.05	0.54	9.08	5.03
M+P(L)	1.40	1.04	8.93	4.95

DATA PROCESSING AND RESULTS

Let M(C) and M(L) be the values of $| HH \cdot HH^* |$, $| HV \cdot HV^* |$, $| VV \cdot VV^* |$ in C and L Band, respectively and let M+P(C) and M+P(L) be the 9 components of the Mueller matrix in C and L Band, respectively. These
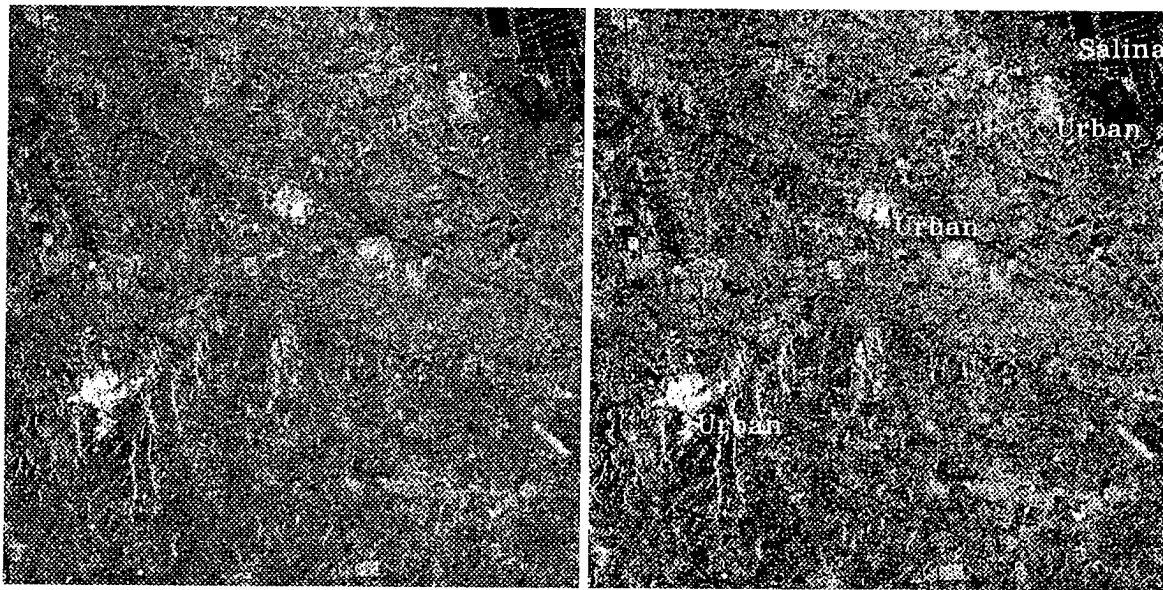
Figure 1: *a) Image* $| HH \cdot HH^* |$*, Band C; b) Segmented image obtained using M(C) input vectors.*

Tab. 2 shows the statistics extracted on the segmented images. It can be noticed that the mentioned areas are peaked on the grey levels indicated by the mean value. The smallest deviations from the mean value occur in the segmentation obtained with the M(C) input vectors. So, this last can be assumed as the more consistent result for the areas of interest (Fig. 1 b)).

CONCLUSIONS

A SOM neural network has been applied for the SIR-C data segmentation in order to detect homogeneous regions on images. The segmented image that has a greater homogeneity respect two areas of interest has been obtained processing the magnitude information. For this purpose, processing also phase informations doesn't improve the result.

ACKNOWLEDGMENTS

REFERENCES

[1] T. Kohonen, *Self-Organization and Associative Memory*, 2nd Edition, Springer Verlag, Berlin, 1987.

[2] R. P. Lippmann, *An introduction to Computing with Neural Nets*, IEEE ASSP Magazine, pp 4-22, 1987.

[3] J. A. Benediktsson, P. H. Swain, and O. K. Ersoy, *Neural network approaches versus statistical methods in classification of multisource remote sensing data*, IEEE Trans. Geosci. Remote Sens., Vol. 28, pp. 540-552, July 1990.

[4] F. T. Ulaby, and C. Elachi, *Radar Polarimetry for Geoscience Applications*, MA:Artech House, 1990.

[5] L. Tsang, J. A. Kong, and R. T. Shin, *Theory of Microwave Remote Sensing*, New York:Wiley-Interscience, 1985.

[6] Y. Hara, R. G. Atkins, S. H. Yueh, R. T. Shin, and J. A. Kong, *Applications of Neural Networks to Radar Image Classification*, IEEE Trans. on Geo. and Rem. Sens., Vol. 32, N.ro 1, Jan. 94.

Determining the Number of Classes for Segmentation in SAR Sea Ice Imagery

Leen-Kiat Soh and Costas Tsatsoulis
Department of Electrical Engineering and Computer Science
University of Kansas, Lawrence, Kansas
address: Center for Excellence in Computer-Aided Systems Engineering
2291 Irving Hill Road, Lawrence, KS 66045
tel: (913)864-7767 fax: (913)864-7787 e-mail: lksoh@cecase.ukans.edu

Abstract -- In this paper, we describe a segmentation technique for SAR sea ice imagery that determines the number of classes in the image without *a priori* knowledge of the characteristics of the image. Image segmentation is important to sea ice research such as classification, and floe and lead analyses. In SAR sea ice imagery, however, backscatter characteristics vary for different seasons, temperatures, wind activity, and geographical locations, etc. As a result, image processing techniques that pre-determine the number of classes could generate segmentation that contains erroneous merging of classes and/or unnecessary separation of a class leading to unrecoverable mistakes during the classification phase. We have designed an image segmentation technique that combines image processing and machine learning methodologies. It computes spatial and textural statistics from the image and determine the number of classes by conceptually clustering these statistics. We have also tested this technique on a large database of sea ice imagery, and it has shown successes in determining the number of classes without human intervention.

INTRODUCTION

In image processing, segmentation is important in isolating objects from the background or separating groups of objects. A segmentation process takes a property derived from the image and classifies that property into two or more groups. One inherent problem that image segmentation faces is the determination of the number of classes. To remedy this problem, many segmentation algorithms have used a pre-determined number of classes, thus producing unnecessary divisions or mergings of classes. Other algorithms required a priori determination of the number of classes by a human operator.

Segmentation in SAR sea ice imagery is a critical part of the classification process. SAR sea ice imagery consists of a wide range of images; for example, a solid pack ice (one class), a lead breaking across a pack ice (two classes), an ice-water composition of different ice types (three or more classes), etc. This characteristic of uncertain number of classes has further complicated the problems as discussed above. Also, conventional segmentation techniques that accommodate different classes and yet require human supervision and parameter (number of classes) adjustments become infeasible when dealing with large amount of data. These problems have motivated the work of this paper.

Our technique determines the number of classes by first generating a second-order statistical texture-contour map of the image, computing a matrix of ordered spatial relationships among local regions of the image, reducing a frequency histogram of the threshold values sequentially, and then clustering the clues computed from the texture map and the spatial matrix (describing the image) into different groups to form a concept hierarchy using a conceptual clustering algorithm.

METHODOLOGY

Our technique is based on two assumptions. First, any segmentation or class-determination technique based on intensity alone is not able to determine the number of classes in SAR sea ice imagery. Different ice types might occupy the same intensity range even though they are different under human inspection, based on size, shape, texture, and other properties. Second, texture is useful in representing different ice features and thus in the investigation of the number of classes in an image. Texture-based classification has been successfully used in sea ice image analysis [1-3]. We believe that combining intensity and textural properties is important in determining the number of classes in an image. In the following, we will discuss our pre-clustering module that processes the image to provide attributes for each selected threshold, and the clustering module that uses the selected thresholds with their attributes for partitioning.

Pre-Clustering Module

This module consists of four components: 1) Generation of raw thresholds, t_r, 2) Generation of significant thresholds, t_s, 3) Generation of spatial matrix, and 4) Generation of textural matrix.

Generation of Raw Thresholds: First, we apply dynamic local thresholding to the image. Dynamic local thresholding is a technique that divides the image into smaller regions and locally computes thresholds for the regions [4]. It is able to capture local details through its localized treatment of the image, and yet maintain the globality of the image through weighted interpolations of the local thresholds to other regions. This thresholding process results in a set of raw thresholds, or t_r.

Generation of Significant Thresholds: The objective of this component is to filter out extraneous threshold values, resulting from the dynamic local thresholding technique, by picking dominant peaks from the histogram of thresholds. As a result, we provide the clustering module only the significant

thresholds and without the residuals, enabling a correct partition during the clustering phase.

Generation of Spatial Matrix: Our spatial descriptor is related to probabilistic relaxation [5]. It computes a *variety* curve for each threshold value. The variety curve measures how a threshold value behaves spatially in relation to its eight immediate neighbors. Each point of the variety curve of a threshold value T_k is the probability of a threshold value being a neighbor to the value T_k. By observing the variety curve, one can tell how frequent two threshold values are in spatial proximity of each other, indicating that whether two threshold values should be merged as one.

Generation of Textural Matrix: To capture sea ice textures, we have used gray-level co-occurrence matrices [6]. This generator uses eight second order statistical, textural features such as energy, contrast, correlation, homogeneity, entropy, autocorrelation, dissimilarity, and maximum probability [6,7], with a multi-displacement co-occurrence matrix implementation [8]. These measurements will then be associated to one of the thresholds in t_s, linking each threshold value with a vector of eight averaged textural features.

Clustering Module

To classify the set of significant thresholds into groups, we employ conceptual clustering [9]. A conceptual clustering system accepts a set of instances, attached with descriptions or attributes, and classifies the data into different clusters based on the attributes. In our work, we use COBWEB/3 [10], a hybrid implementation of COBWEB [11] and CLASSIT [12]. CLASSIT is a descendent of COBWEB; while COBWEB deals with only nominal features, CLASSIT assumes features of normal distributions. Fig.1 shows an example of COBWEB/3's concept hierarchy. There are three instances (N3-N5). Each instance has two attributes: *height*, which is real-valued, and *gender*, which is nominal. N1 and N2 are parent nodes, and their attribute values correspond to their children's. (Note that the default minimum standard deviation value is 0.1 in this example.) These values are used in the *category utility function* that chooses which hierarchy operation (merge, split, incorporate, etc.) to perform given a new instance. We have chosen this program because of its fully automated approach and its simplicity. Its unsupervised learning capability is able to determine the number of classes in the data and assign instances (or in our case, significant thresholds) to these classes, without any human guidance. After obtaining the concept hierarchy, a simple rule is used to collect groups of thresholds: terminals that are at the same level as an immediate neighboring parent node—to resolve the competition between two or more qualified parent nodes—will be absorbed into that parent node.

RESULTS

We have applied our technique to a database of SAR sea ice imagery, and roughly 70% of the results are reasonably correct. We plan to compare our results to other sea ice

classification programs, available ground truth, and human judgment of expert geophysicists. Here we provide an example of an image and the application our technique. Fig.2 shows an original SAR sea ice image. After dynamic local thresholding, we obtained 71 different raw thresholds, ranging between 31 and 109, of a scale of 0-255. Out of the raw thresholds, we extracted 18 significant thresholds. We then proceeded to compute the spatial and textural matrices. Fig.3 shows the concept hierarchy generated by COBWEB/3. Applying our simple rule of clusters collection, we obtained four classes of thresholds: T_0-T_4, T_5-T_9, T_{10}-T_{12}, and T_{13}-T_{17}. Fig.4 shows the final classification result of the image.

CONCLUSIONS

We have designed a technique that determines the number of classes in SAR sea ice imagery automatically without human intervention. This technique combines image processing and machine learning techniques. It is able to hierarchically reduce the number of thresholds into a concept hierarchy representation from which the number of classes in the image can be determined. Our technique has been tested on a database of imagery and has produced reasonable results for more than half of the images. Future work includes handling water-dominated images (MIZ or fast ice regions) where significant difference in water intensities across the image causes the technique to misidentify different classes for the water region.
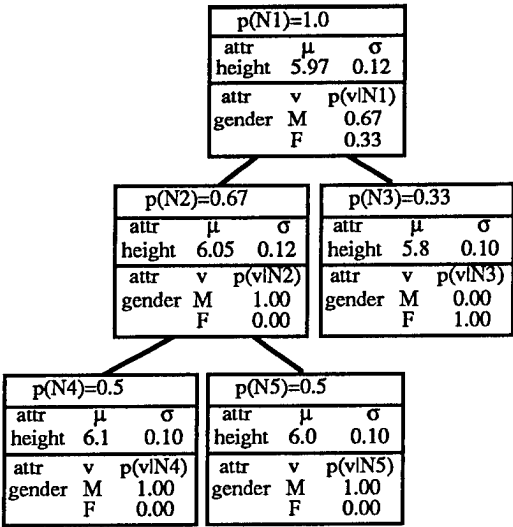
Fig.1 An example of COBWEB/3 's concept hierarchy. Each node contains the mean and standard deviation values for continuous attributes, and conditional probability values for nominal attributes.

REFERENCES

[1] J. Chou, R. C. Weger, J. M. Ligtenberg, K.-S. Kuo, R. M. Welch, and P. Breeden, "Segmentation of Polar Scenes Using Multi-Spectral Texture Measures and

Morphological Filtering," International Journal of Remote Sensing, vol. 15, no. 5, pp. 1019-1036, 1994.

[2] Q. A. Holmes, D. R. Nuesch, and R. A. Shuchman, "Textural Analysis and Real-Time Classification of Sea-Ice Types Using Digital SAR Data," IEEE Transactions on Geoscience and Remote Sensing, vol. 22, no. 2, pp. 113-120, 1984

[3] J. A. Nystuen and F. W. Garcia, Jr., "Sea Ice Classification Using SAR Backscatter Statistics," IEEE Transactions on Geoscience and Remote Sensing, vol. 30, no. 3, pp. 502-509, 1992.

[4] D. Haverkamp, L. -K. Soh, and C. Tsatsoulis, "A Comprehensive, Automated Approach to Determining Sea Ice Thickness from SAR Data," IEEE Transactions on Geoscience and Remote Sensing, vol. 33, no. 1, pp. 46-57, 1995.

[5] A. Rosenfeld and R. C. Smith, "Thresholding Using Relaxation," IEEE Transactions on Pattern Analysis and Machine Intelligence, vol. 3, no. 5, pp. 598-606, 1981.

[6] R. M. Haralick, K. Shanmugan, and I. Dinstein, "Texture Features for Image Classification," IEEE Transactions on Systems, Man, and Cybernetics, vol. 3, pp. 510-521, 1973.

[7] R. M. Haralick, "Statistical and Structural Approaches to Texture," Proceedings of the IEEE, vol. 67, no. 5, pp. 786-804, 1979.

[8] L.-K. Soh and C. Tsatsoulis, "Texture Representation of SAR Sea Ice Imagery Using Multi-Displacement Co-Occurrence Matrices", IGARSS'96.

[9] R. S. Michalski and R. Stepp, "Learning from Observation: Conceptual Clustering," in R. S. Michalski, J. G. Carbonell, and T. M. Mitchell (eds.), Machine Learning: An Artificial Intelligence Approach, San Mateo, CA: Morgan Kaufmann, 1983.

[10] K. Thompson and K. McKusick, "COBWEB/3: A Portable Implementation," Technical Report FIA-90-6-18-2, version 1.4, Ames Research Center, 1993.

[11] D. H. Fisher, "Knowledge Acquisition via Incremental Conceptual Clustering," Machine Learning, vol. 2, pp. 139-172, 1987.

[12] J. H. Gennari, P. Langley, and D. Fisher, "Models of Incremental Concept Formation," in J. Carbonell (eds.), Machine Learning: Paradigms and Methods, pp. 11–61, MIT Press/Elsevier, 1990.

Fig.2 The original SAR image, Mar 26 1992, at 72.86°N, 143.84°W. Copyright ESA.

Fig.4 The classification result: there are four classes. Dark denotes open water. Bright denotes multiyear ice. The two grayish shades denote new ice and first year ice, respectively.

Fig.3 Concept hierarchy of the significant threshold set. N's are parent nodes; T's are terminals. According to our cluster collection rule, we have four classes, as shown by the bubbles.

A Multi-Temporal Classifier for SIR-C/X-SAR Imagery

Kathleen M. Bergen, Leland E. Pierce, M. Craig Dobson, Fawwaz T. Ulaby

The University of Michigan, Radiation Laboratory, EECS Dept.
Ann Arbor, MI 48109-2122 USA
Tel: +1-313-764-0501, FAX: +1-313-747-2106, email: kbergen@eecs.umich.edu

ABSTRACT

Biophysical systems in temperate regions undergo distinct changes in each annual cycle. For forested ecosystems this includes moisture and phenological changes. The dual-flight program (April and October) for the SIR-C/X-SAR instrument aboard the shuttle Endeavor was designed expressly to acquire imagery at different stages of such cycles. This provides new opportunities in terrain classification where phenology and moisture changes may be used as additional information. Given multi-season SIR-C/X-SAR imagery, there are three possible approaches to classifier development: (1) Ignore the multi-season availability and develop independent classifications for each scene using n features, (2) Develop one classification for a set of x scenes using n features, with x times the number of samples per feature, and (3) Develop a true multi-temporal classification where N of features equals n (number of features) times x (number of scenes). Each of these are applied and results for the first two of six selected scenes show the true multi-temporal and the October scene alone to have the highest accuracies (94% and 95% respectively) at a level II classification.

1. INTRODUCTION AND GOALS

Given multi-season (April and October) SIR-C/X-SAR imagery for the Michigan Forests site, there are three possible approaches to classifier development: (1) Ignore the multi-season availability and develop independent classifications for each scene using n features, (2) Develop one classification for a set of x scenes using n features, with x times the number of samples per feature, and (3) Develop a true multi-temporal classification where N of features equals n (number of features) times x (number of scenes). We hypothesize that the first, which is optimized for each scene separately, could result in a best single classification, but does not result in one which is transportable to other scenes, especially over seasonal change. The second attempts to be applicable over more than one image, but does not account for time-dependent changes in phenology/environmental conditions, and the lumping of samples from different scenes inflates the variance of the individual features. Thus this is likely a worse classification. The final approach assumes that environmental and phenologic conditions change with time and in a fashion consistent with what is found on the imagery and so uses phenological differences as additional feature information. This should result in the better or best classification, and one that is transportable across scenes from different seasons. All of these methods are explored and results are compared.

2. METHODOLOGY

2.1. Overview

Most classification procedures, including those developed for the present study, are given some form of training data which are used to statistically define the classes that are to be separated. Training data used here are from permanent test stands in the Michigan Forests test site. The site, centered on 46.394° N. Latitude and 84.885° W. Longitude, is located in the Hiawatha National Forest in the eastern part of Michigan's Upper Peninsula. Training and testing data is available from 70 four-ha forest test stands representing the distribution of forest cover in the test site. Forest communities present are listed in Table 1 as classification categories at three levels (described in the following sections). Detailed measurements were made in each stand to quantify community composition, structure, and biomass. Change information in terms of moisture status and phenology has also been carefully documented.

Six SIR-C/X-SAR images have been selected to test our hypotheses and to develop working classifiers. Two are chosen at $\approx 20°$, and four are chosen at $\approx 32°$ incidence. These scenes represent distinct moisture regimes within each of two seasons of significant phenological difference: spring (April) and fall (October). The present study concentrates on phenologic differences alone and reports on analyses of April and October scenes from datatakes 22.2 $\approx 20°$. Moisture information will be incorporated later by adding the remaining four scenes to the analysis. The typical steps in developing a working classifier are: 1) image pre-processing (filtering, feature extraction), 2) classification, and 3) post-processing (filtering, relaxation methods). During image-preprocessing for this study, SLC data are orthorectified and then averaged to reduce fading. Baseline n of features extracted per image is 11 including 7 power channels and 4 extra channels describing the co-polarized phase difference[5]. In SAR image classification in general, features

Table 1: Classification Categories

Level I	Level II	Level III
surface		
short veg		
tall veg	upland conifer	red pine (low, med, hi BA)
		jack pine (low, med BA)
	lowland conifer	northern white-cedar
		black spruce
	deciduous	northern hardwoods (med, hi BA)
		aspen

may be extracted from the spectral, spatial, and temporal domains. For this project using multi-date imagery we extract features from both the spectral and the temporal domains.

Classifications can be based on a number of different methods. Statistical (supervised and unsupervised), knowledge-based, and artificial neural network are some typical examples. The classifier we have developed is a hybrid consisting of knowledge-based rules for level I, and a supervised Bayesian MLE algorithm for levels II and III. We call this a hybrides hierarchical classifier.

The level I classes used in this classifier are simple structural classes with the same meaning everywhere: urban(if present), tall vegetation (trees), short vegetation, and surfaces. At level II, the next level in the hierarchy, categories are more specific, but equally universal. For example, for tall vegetation, tree architectural forms and the presence of broadleaves or needles for class names are defined, rather than species. In the Michigan Forests test site this includes upland conifers, lowland conifers, and deciduous. At the third level in the hierarchy (level III) level II categories for tall vegetation are further distinguished based on additional or more subtle structural differences, but ones which are still capable of producing significant differences in SAR backscatter. These are two: 1) within form differences (e.g. long vs. short needles on upland conifers), and 2) overall stand structure manifested in age/size. In the Michigan Forests test site the example of long vs. short needles translates into red pine vs. jack pine and illustrates how these simple structural categories can then be matched with local floristic keys. Age and size classes can be defined from the test stands based on known structural measures such as basal area (BA).

At all of these levels the scenes were classified using each of the three methodologies listed in the goals of this paper. Results of the single date, multi-date pooled, and multi-temporal classifications follow.

2.2. Comparison of Classification Methods

2.2.1. Optimized for Each Date Separately

For level I, knowledge-based classification can easily proceed by a simple algorithm and manual optimization. This is done for each image until the training stands are classified well, and then the test stands are evaluated for accuracy. For datatake 22.2 Level I rules are as follows and are the same for both April and October:

IF (L-hv > (-0.91 * L-hh -25.0) trees
   ELSEIF (C-hv > -20.0) shortveg
   ELSEIF (C-hv < -20.0 and L-hv < -20.0) surface
   ELSE shortveg

At level II where tall vegetation is further categorized, the manual procedure outlined above is not viable; classification is too complex and the rules are no longer related as simply to physical principles. Hence, a standard supervised Bayesian maximum-likelihood (MLE) classifier is used. The power data as scaled in dB units presents probability density functions that are closer to normal (as is required by MLE) than if they had been scaled linearly. The above classification procedures were applied to each scene separately for single scene optimization; they were also used in the pooled and multi-temporal classifications and so also apply to the next two sections.

At level III the statistical classification method is the same as that for level II. Physical criteria to differentiate between classes differs as shown in Table 1.

2.2.2. Pooled Classification

Because level I rules can be made the the same for both seasons (a de facto multi-time classification), and because the manually optimized procedure is very simple, it was determined that additional pooled or multi-temporal procedures were unnecessary at this level.

A pooled classification was done at levels II and III. Here all samples were extracted from the images and those of the same feature for SRL-1 and SRL-2 and were merged. The pooled classifier was statistically constructed using Bayesian MLE, and then applied to each scene. While this restricts number of features to that of the single-scene method, because it doubles the number of samples for each feature, it may significantly inflate the within feature variance.

2.2.3. Multi-Temporal Classification

For levels II and III, the samples extracted from the two images/seasons are kept separate and the feature space is doubled. This doubling risks not meeting the statistical requirements for n of samples per feature; the underlying statistical estimations may be underdetermined if the spectral dimensionality is not reduced. On the other hand, this procedure is advantageous as it

keeps the variance within features to the minimum and uses the differences between seasons as additional discriminators. After the multi-temporal classifier is statistically constructed, it is then applied to each of the images at levels II and III.

3. RESULTS

Because SAR is a very good discriminator of the major level I classes, results at level I are predictably high: 99% for datatake 22.2. Because classification rules were the same for both April and October, all types of classifications achieved the same results at this rudimentary stage. In all classifications, accuracies are determined from independent samples from the test stands.

The level II classification accuracy was affected by season. In all classification methodologies, the April scene has slightly poorer results. This is likely due to the combination of deciduous trees with no leaves being confused with sparsely-needled conifers (jack pine) as well as SAR interaction with the snow-covered ground.

Table 2: Level II Multi-Temporal Classification Results: Datatake 22.2 - Training

True Class	Classed As				
	surface	short veg	upland conifer	lowland conifer	deciduous
surface	100	0	0	0	0
short veg	0	99	1	0	0
upland conifer	0	0	98	0	2
lowland conifer	0	0	0	96	4
deciduous	0	0	0	7	93

Table 3: Level II Multi-Temporal Classification Results: Datatake 22.2 - Testing

True Class	Classed As				
	surface	short veg	upland conifer	lowland conifer	deciduous
surface	100	0	0	0	0
short veg	0	99	1	0	0
upland conifer	0	0	94	0	6
lowland conifer	0	0	9	85	6
deciduous	0	0	4	3	93

For the single-season classifications, accuracy achieved for the October scene was excellent (95%) but not as good (75%), for April. Using the same rules for each image (pooled classification), proved the hypothesis that both would be more poorly classified to be correct. This is primarily due to the poorly-distinguished deciduous class from April which lowered the accuracies of the upland conifer and deciduous classes to the low to mid 80%s. The multi-temporal classification did comparable (94%), overall, to that for October alone. It should be noted, however, that each misclassification category in the multi-temporal case is less than the worst-case misclassification in October. Training and testing results are given in Tables 2 and 3. Twice as many features were used in the multi-temporal classification than the October scene alone; as mentioned, further reducing this dimensionality in the spectral domain is expected to increase the certainty of the underlying probability density functions and likely improve classification results.

At level III where categories are at the community and species level and further subdivided by BA, results are preliminary. Using 22.2 as an example, level III accuracy for a single date is 71% October. Pooled and multi-temporal classifications are also in the 70%'s-90%'s.

Results to date in classification have shown the multi-temporal classifier to be superior to either of the others, if results across all seasons are considered, in meeting both the objectives of accuracy and transportability.

4. REFERENCES

[1] Dobson, M.C., L.E. Pierce, F.T. Ulaby, "Knowledge-based land-cover classification using ERS-1/JERS-1 SAR Composites,"*IEEE Trans. Geosci. and Remote Sensing*, Vol. 34, No. 1, pp. 1996.

[2] Dobson, M.C., F.T. Ulaby, and L.E. Pierce, "Land-cover classification and estimation of terrain attributes using synthetic aperture radar," *Remote Sensing of Env.*, vol. 51, no. 1, pp. 199-214, 1995.

[3] Pierce, L.E., F.T. Ulaby, K. Sarabandi, M.C. Dobson, "Knowledge-based classification of polarimetric SAR images," *IEEE Trans. Geosci. and Remote Sensing,* Vol. 32, No. 5, Sept. 1994.

[4] Dobson, M.C., F.T. Ulaby, L.E. Pierce, T.L. Sharik, K.M. Bergen, et al., "Estimation of Forest Biophysical Characteristics in Northern Michigan with SIR-C/X-SAR," *IEEE Trans. Geosci. Remote Sensing*, Vol. 33, No. 4, pp. 877-895, 1995.

[5] Sarabandi, K. "Derivation of phase statistics of distributed targets from the Mueller matrix," *Radio Science*, Vol. 27, No. 5, 1992.

Optimal Multi-look Polarimetric Speckle Reduction and Its Effect on Terrain Classification

Guoqing Liu, Shunji Huang   A. Torre, F. Rubertone

Department of Electronic Engineering   Alenia Spazio S.p.A.
Univ. of Electronic Science and Tech.   Via Saccomuro 24
of China, Sichuang 610054, PR China   00131 Rome, Italy

Abstract -- This paper presents an multi-look polarimetric whitening filtering (MPWF) method to reduce the image speckle using complete multi-look polarimetric SAR data. The amount of speckle reduction achievable by using the MPWF is quantified particularly for nonhomogeneous scenes. Experimental results with NASA/JPL L-band 4-look polarimetric SAR data are given for illustration. With the class separability index, we show how the speckle reduction can improve the terrain classification performance, and the classification results with the speckle-reduced data are also given.

INTRODUCTION

It is well known that coherent SARs produce images with considerable speckle [1]. With the availability of fully polarimetric SAR data, there is the possibility to reduce the image speckle polarimetricly. One of the well-known speckle reduction techniques that use fully polarimetric information is the polarimetric whitening filtering (PWF) proposed by Novak and Burl [2]. This method processes elements in scattering matrix to produce three components that are uncorrelated and have equal average power. This method was, however, only developed for application in single-look polarimetric SAR images. For data compression and preliminary speckle reduction, the polarimetric SAR data are frequently multi-look processed. The multi-look processing makes it impossible to directly use the PWF for speckle reduction because no equivalent polarimetric scattering matrix exits for the average Stokes or covariance matrix.

In this paper, we present an optimal processing method, named the multi-look polarimetric whitening filtering (MPWF), which utilizes complete multi-look polarimetric SAR data to minimizes the speckle, and investigate how the speckle reduction affects the performance of the terrain classification. The amount of speckle reduction which can be achieved by applying the presented algorithm for nonhomogeneous clutter regions is particularly quantified. Experimental results with the NASA/JPL airborne L-band 4-look polarimetric SAR data are provided to demonstrate the algorithm. Then, the effect of the speckle reduction on the terrain classification is analysis. and the classification results with the speckle-reduced data are also given.

POLARIMETRIC MEASUREMENT MODEL AND MULTIPLICATIVE SPECKLE MODEL

The polarimetric scattering matrix measured by a polarimetric SAR consists of four complex elements. For a reciprocal medium, two cross-polarized terms are identical [3], and the polarimetric feature vector, $\vec{y}$, has only three unique complex elements. In a homogeneous scene, the vector $\vec{y}$ is usually considered as having a complex Gaussian distribution [2] with a covariance $\Sigma = E[\vec{y}\,\vec{y}^H]$, here superscript H refers to complex conjugate transpose.

Let Y be the multi-look covariance matrix defined as,

$$Y = \frac{1}{N}\sum_{j=1}^{N}\vec{y}_i\,\vec{y}_i^H \tag{1}$$

where the subscript i means that $\vec{y}_i$ is the i-th polarimetric feature vector, and N is thus the number of looks.

Speckle in the coherent SAR imagery is caused by multi-path interference of coherent waves scattered from a distributed random scene. It has long been regarded as being a kind of multiplicative noise [1]. In case of multi-look polarimetric SAR data, we can approximately expressed the multiplicative speckle model in the multi-look covariance matrix domain [4],

$$Y = t\,X, \tag{2}$$

where X is the multi-look covariance matrix of the speckle, t is the scalar texture variable which is usually assumed to obey a Gamma distribution and to take mean one.

OPTIMAL SPECKLE REDUCTION IN MULTI-LOOK POLARIMETRIC SAR IMAGERY

We now combine the elements of the multi-look polarimetric covariance matrix Y into a unitary variable by

$$w = \text{Tr}[A\,Y] \tag{3}$$

where Tr[·] is the trace of a matrix. Our purpose is to find the optimal matrix A' that leads to the minimum standard-deviation-to-mean ratio (s/m) value for the variable w. When the multiplicative speckle model is considered, substituting (2) into (3), we express the multi-look polarimetric processing procedure as,

$$w = t\,\text{Tr}[A\,X]. \tag{4}$$

The solution for minimizing the (s/m) ratio of variable w can be shown to be [4]

$$A = \Sigma^{-1}. \tag{5}$$

Matrix A is a whitening matrix; The minimum-speckle image is

constructed as

$$w = \mathrm{Tr}\left[\Sigma^{-1}\mathbf{Y}\right], \qquad (6)$$

this is the MPWF filtering equation.

QUANTIFICATION OF SPECKLE REDUCTION

From (2), we can express the (s/m) ratio of variable w as

$$\left(\frac{s}{m}\right)^2 = \frac{1}{N}\left[\left(1+\frac{1}{\alpha}\right)\frac{\sum_{j=1}^{3}\lambda_j^2}{\left(\sum_{j=1}^{3}\lambda_j\right)^2} + \frac{1}{\alpha}\right], \qquad (7)$$

where λ_1, λ_2, and λ_3 are the eigenvalues of the matrix (ΣA), and $\alpha = E^2[t]/\mathrm{var}[t]$ is the nonhomogeneity coefficient of the scene. For the MPWF, $\lambda_1 = \lambda_2 = \lambda_3$, so we have the s/m ratio,

$$\left(\frac{s}{m}\right)_{\mathrm{MPWF}} = \frac{1}{\sqrt{N}}\sqrt{\left(1+\frac{1}{\alpha}\right)\frac{1}{3}+\frac{1}{\alpha}} = \frac{1}{\sqrt{N}}\sqrt{\frac{1}{3}\left(1+\frac{4}{\alpha}\right)}. \qquad (8)$$

The above expression indicates that, the less fluctuation (higher α value) the scene texture has, the more speckle reduction can be obtained by applying the MPWF. In a homogeneous region, the texture variable, t, is a constant indicating that the nonhomogeneity coefficient, α, tends to be infinite, and the MPWF has capability of reducing the image speckle by a factor $\sqrt{3}$ (or 4.77 dB) relative to a multi-look single-polarization-channel intensity image. This quantity can be regarded as an ideal upper bound of the speckle reduction using the MPWF.

If a single-channel intensity image, for instance, the HH-intensity image, is separately discussed, the s/m ratio is

$$\left(\frac{s}{m}\right)_{\mathrm{HH}} = \frac{1}{\sqrt{N}}\sqrt{\left(1+\frac{1}{\alpha}\right)+\frac{1}{\alpha}} = \frac{1}{\sqrt{N}}\sqrt{1+\frac{2}{\alpha}}. \qquad (9)$$

SPECKLE REDUCTION RESULTS AND DISCUSSIONS

A set of NASA/JPL airborne L-band 4-look polarimetric SAR data acquired over San Francisco Bay area is used for illustration. Fig.1 shows a 400x400 pixel section of the HH-intensity image. Testing areas are selected for three kinds of terrain: ocean, park (forest-like), and city. In experiment, we assume the HV return is uncorrelated with the HH and VV returns. A 5x5 moving window centered on the pixel in question is used for adaptively computing Σ, and the MPWF-processed image is multiplied by a factor $(\sigma_{hh}/3)$ in order to match the HH-intensity image.

Fig.2 exhibits the MPWF-processed image. Compared with the HH image, the MPWF image has much better visual effect, distinct speckle reduction can be observed in both the ocean and the park areas, and the edges between streets and buildings and between different features are well retained; The tower and the ships in the

ocean can be more easily differentiated from the background, and the streets in the city area are made more recognizable.

To quantitatively evaluate the MPWF's performance, we calculate the s/m ratios for the HH and the MPWF data in the testing areas, and compare the experimental measurement with the theoretical prediction for the MPWF. With (9), the s/m ratios of the HH data are used for approximately estimating the nonhomogeneity coefficients for each testing area, equation (8) is then used for predicting the s/m ratios for the MPWF data. Table I lists the calculating results.

The MPWF reduces the s/m ratio by 2.08 to 3.45 dB relative to the 4-look HH data. These results are less than the ideal theoretical value (4.77 dB) due to variations of the texture within each testing area. The measurements of the speckle reduction by using the MPWF agree quite well with corresponding predictions. The agreement between theory and experiment is within 5% in all cases. The effect of the nonhomogeneity of the scene texture on the MPWF's performance is also confirmed from the results in Table I. That is, the more homogeneous the clutter region, the higher quality of speckle reduction can be obtained. For instance, the speckle measure is actually reduced by 3.45 dB (prediction 3.34 dB for $\alpha = 3.13$) relative to the 4-look HH-intensity data in the ocean area, but only 2.08 dB (prediction 1.92 dB for $\alpha = 0.15$) in the city area.

EFFECT OF SPECKLE REDUCTION ON TERRAIN CLASSIFICATION

To understand the effect of speckle reduction on the terrain classification and to further evaluate the speckle reduction, we first compute the separabilities between terrain types for the speckle-reduced data. The separability index s between two classes is defined by [5],

$$s = \frac{|\mu_i - \mu_j|}{\sigma_i^2 + \sigma_j^2}, \qquad (10)$$

where μ and σ are the mean and the standard deviation, respectively. It has been previously investigated [5] that the quantity of the separability reflects the accuracy of a Bayesian classification. Table II gives the separabilities of three class pairs, ocean/park, ocean/city, and park/city, for the HH data, and two sets of MPWF data processed with the full multi-look polarimetric SAR data (MPWF 1 as shown in Fig.2) and with only three intensity components (MPWF 2, not shown). These results show that the speckle reduction has considerably improved the class separabilities for all class pairs discussed, and that the MPWF 1 provides higher class separabilities than the MPWF 2. Particularly, the MPWF 1 image can be expected to provide much better classification accuracy in the city area than the HH-intensity image, since the class separability has been enhanced about 45% and 40% for the class pairs ocean/city and park/city, respectively.

Since the mean values of both sets of MPWF data are

approximate to that of the HH-intensity data, the improvements in the separability index are essentially resulted from the decrements of the standard deviation, so it can be understood that the speckle reduction which implies the decrement of the standard deviation for the mean-value-preserved processing algorithm implicitly contributes to the enhancement of the separability between terrain types and therefore to the improvement of the classification performance.

Next, we use a Gamma distribution model to construct an ML classifier to classify the speckled and the speckle-reduced images. Probabilities of correct classification estimated in the training areas are given in Table III, and the maps of classifications based on the HH-intensity data and the MPWF 1 data are shown in Fig.3 and 4, respectively.

The results of the terrain classification based on the speckle-reduced images are very satisfactory. The MPWF processing improves the total classification accuracy by over 7% relative to the HH-intensity image when using complete polarimetric SAR data, and above 5% when only the intensity data are used. Particularly, the probability of correct classification in the city area is increased more than 12% and 9%, respectively. Visually, it is also clear that the classified images based on the speckle-reduced data are better than that using the single-polarization intensity data.

CONCLUSIONS

We have investigated the speckle reduction using ▲e multi-look polarimetric SAR data and its effect on the terrain classification. The presented MPWF algorithm has been quantified particularly for nonhomogeneous regions. The experimental results with the NASA/JPL L-band 4-look polarimetric data demonstrated the effectiveness of the MPWF, the actual reduction inspeckle measureby using the MPWF relative to the multi-look HH-intensity

Table I: Speckle reduction results and comparison

terrain type	HH	α	prediction		measurement	
			s/m	r(dB)	s/m	r(dB)
ocean	0.64	3.13	0.44	3.34	0.43	3.45
park	0.91	0.85	0.68	2.47	0.70	2.28
city	1.88	0.15	1.51	1.92	1.48	2.08

Table II: Class separabilities

data set	ocean/park	ocean/city	park/city
HH-int.	0.84	0.45	0.36
MPWF 1	1.10	0.65	0.50
MPWF 2	1.04	0.57	0.44

Table III: Probabilities of correct classification

data set	ocean	park	city	total
HH-int.	93.75	73.68	69.03	**78.28**
MPWF 1	96.65	80.03	81.19	**86.19**
MPWF 2	95.10	77.95	78.58	**83.86**

data was shown to be consistent well with the theoretical prediction. Further, the analysis of class separability and results of terrain classification using the speckle-reduced data indicated clearly that the speckle reduction does help improve the performance of classification, and the more the speckle is reduced, the higher classification accuracy can be obtained.

REFERENCES

[1] J. S. Lee, "Speckle analysis and smoothing of synthetic aperture radar," Computer Graphics and Image Processing, vol.17, pp.24-32, 1981.

[2] L. M. Novak, and M. Burl, "Optimal speckle reduction in polarimetric SAR imagery," IEEE Trans. Aerosp. Electron. Syst., vol.26, pp.293-305, Mar. 1990.

[3] F. T. Ulaby, and C. Elachi (Ed.), Radar Polarimetry for Geoscience Application, Artech House INC, 1990.

[4] Guoqing Liu, Shunji Huang, A. Torre, and F. Rubertone, "Optimal speckle reduction in multi-look polarimetric SAR image," in Proc. IGARSS'95 Symp., pp.664-666, 1995.

[5] M. C. Dobson, L. Pierce, K. Sarabandi, F. T. Ulaby, and T. Sharik, "Preliminary analysis of ERS-1 SAR for forest ecosystem studies," IEEE Trans. Geosci. Remote Sensing, vol.30, pp.203-211, March 1992.

Fig.1: HH-intensity image   Fig.2: MPWF image

Fig.3: Classification of Fig.1   Fig.4: Classification of Fig.2
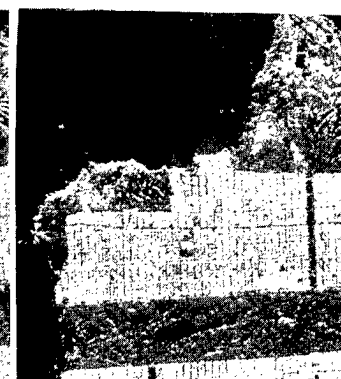
1573

Polarimetric Signature Preservation in SAR Speckle Filtering

J.S. Lee[1], G. De Grandi[2], M.R. Grunes[3] and E. Nezry[2]
[1]Remote Sensing Division
Code 7263, Naval Research laboratory, Washington DC, 20375-5351, USA
Tel/Fax: (202) 767-2004/5599, E-Mail: lee@imsy1.nrl.navy.mil
[2]European Union Commission Joint Research center
Institute of Remote Sensing Applications, 21020 Ispra, (VA) ITALY
Tel/Fax: 39 332 789823/789073
E-Mail: edmond.nezry@jrc.it, gianfranco.degrandi@jrc.it
[3]AlliedSignal Corporation, Columbia, Maryland, USA

Abstract - Current polarimetric SAR speckle filtering algorithms emphasize speckle reduction, but their preservation of polarimetric information and the statistical properties between channels have never been examined. This paper analyzes the existing algorithms for their effectiveness in preserving polarimetric properties, and proposes an algorithm that is effective in both speckle filtering and the preservation of polarimetric properties.

INTRODUCTION

Speckle appears in intensity and also in phase difference images from polarimetric SAR. It causes degradation and makes image segmentation and scene interpretation difficult. Various algorithms has been proposed for speckle reduction. The Polarimetric Whitening Filter (PWF) by Novak and Burl [1] produces a single speckle reduced image which is an optimal combination of all elements from polarimetric SAR data. An alternative implementation of PWF for obtaining speckle reduced HH, HV and VV images has been developed by Lee, et al [2]. They also proposed two other algorithms (i.e.,the vector speckle filter, and the optimal weighing filter) which produced speckle reduced HH, VV and HV images [2]. However, noise in phase difference images was not filtered. Goze and Lopes (JEWA, 1993) generalized the vector filtering to include all complex components of a scattering matrix. Touzi and Lopes (TGRS, 1994) further generalized it for the polarimetric covariance matrix. Other approaches by De Grandi (1992) and by Lopes, Goze and Nezry (IGARSS'92) were also proposed. Like Lee's approach, all these algorithms exploit the degree of statistical independencies between HH, HV and VV channels. The statistical correlations between channels are altered, and the polarimetric properties are somewhat modified. The alteration of polarimetric properties by these filters is experimentally investigated.

An alternative algorithm is proposed based on the principle of spatially filtering of each channel and their phase differences independently. This eliminates the possibility of cross-talk introduced by the existing algorithms. In order to retain polarimetric information along feature boundaries, the refined Lee filter [4] using edge-directed windows is applied. The speckle in phase difference images has the characteristics of additive noise, and its noise level varies with the degree of correlation[3]. Lee's adaptive additive noise filter is applied. The effectiveness of this algorithm in speckle filtering and polarimetric signature preservation is demonstrated using polarimetric SAR data.

SPECKLE FILTERING

NASA/JPL AIRSAR P-Band data of Les Landes (MAESTRO-1) is used for illustration. Fig. 1(A) shows the HH amplitude image of 256x256 pixels. The speckle level of this 4-look polarimetric SAR imagery is effectively 3.0 looks due to the averaging of correlated single look pixels. The optimal weighting filter, the vector speckle filter and the new scheme of filtering each channel separately are applied to this data. The PWF is excluded, since, as previously mentioned, it only produces a single speckle reduced image. The optimal weighting filter produces speckle filtered HH, HV and VV images without using spatial averaging. The results of the optimal weighting filter is shown in Fig. 1(B). The speckle has been reduced to an effective 6.2-look processing. Since no spatial filtering is used, little image smear is observed. However, variations in small features reveals the effect of cross-talk between channels. The vector speckle filter explores spatial information as well as the statistical independence between channels. The amount of filtering depends on the input parameter of estimated speckle level (standard deviation to mean ratio). Less filtering action than normal has been used in the processing result shown in Fig.1(C). The speckle is reduced to an effective 8.4-looks. The cross-talk is less a problem than with the optimal weighting filter.

To maintain statistical correlations between channels, the refined Lee filter is applied to the amplitude of each channel separately. The result shown in Fig.1(D) displays a higher speckle filtering capability with an effective 19-look processing, and also retains edge sharpness. Some minor details have been diminished, because they are near the speckle level. The phase difference image has the characteristics of additive noise. The noise standard deviation is a function of the magnitude of the complex correlation coefficient between the channels. A phase
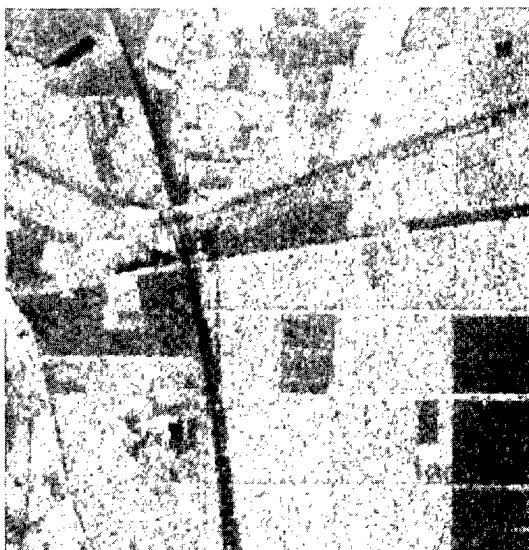
(A) Original HH Image **(B) Optimal Weighting Filtered**
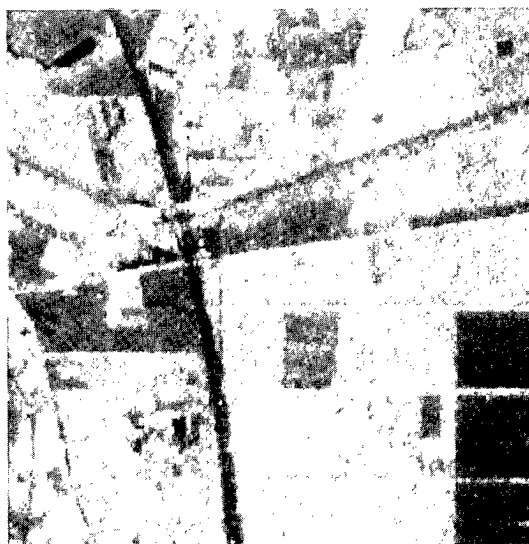
(C) Vector Speckle Filtered **(D) Lee Filtered on HH Only**

Fig. 1 Results of applying polarimetric SAR speckle filters to NASA/JPL AIRSAR P-Band Les Landes scene. Only HH polarization components are shown for comparison. The image has 256x256 pixels.

difference filter can be developed based on the additive local statistics filter and using the coherence map to provide the noise standard deviation.

POLARIMETRY PRESERVATION

To evaluate the preservation of polarimetric information, all three filtered datasets in Fig. 1 are combined with phase differences to form Stokes matrices. The polarization signatures (van Zyl, 1987) and degrees of polarization from these filtered imagery are compared, in homogeneous areas, with those of the original. The preservation of polarization signatures in general are good. Only minor differences are observed. An example is shown in Fig.2 for a forested area. Fig. 2(A) and 2(B) show the co-

polarization signature from the original data in 3-D and contour plots, respectively. The filtered imagery exhibits similar 3-D plots, but minor differences are displayed in the contour plots. All three filtered images have nearly identical contour plots. The degree of polarization are also examined. We find that all filters preserve the degree of polarization well. The difference is within 5% of the original.

However, the difference in polarimetric information could be significantly different at an individual pixel, especially for features with high polarization diversity. This is expected for the optimal weighting filter and the vector speckle filter, because they tend to introduce cross-talk between channels.
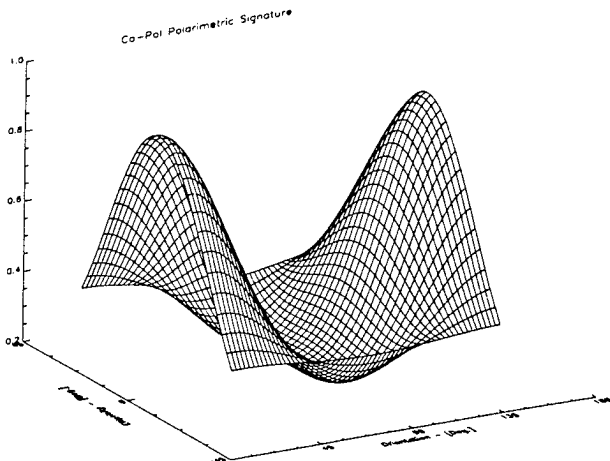
(A) Co-polarization signature of a forested area.
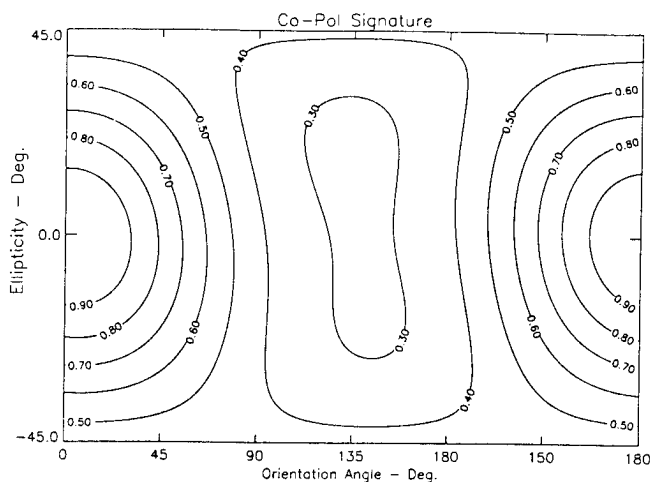
(B) Co-polarization signature using the original data.
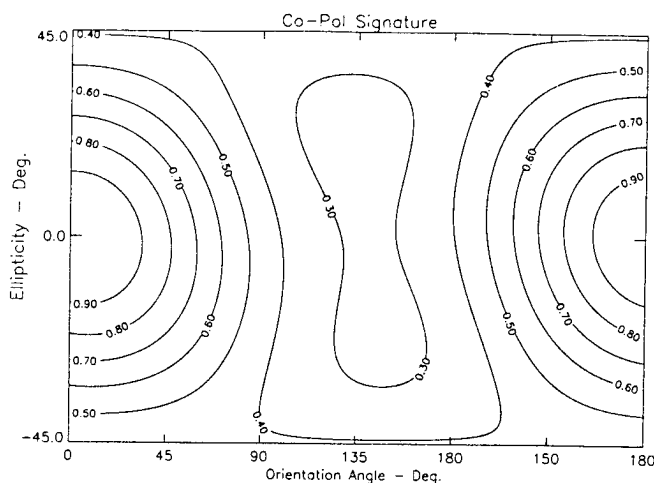
(C) Co-polarization signature using the filtered data.

Fig. 2 Comparison of co-polarization signatures using the original dataset and using the filtered dataset.

STATISTICS PRESERVATION

Since most polarimetric SAR speckle reduction techniques exploit the degree of statistical independence between channels and/or between neighboring pixels, the statistical properties are altered. It has been demonstrated that, based on a circular Gaussian model, the multi-look polarimetric covariance matrix has a complex Wishart distribution[3]. If it is desirable to maintain this statistical property for the filtered imagery, the following items should be carefully monitored: 1) the level of speckle filtering should be the same at all three channels, 2) correlations between channels should be the same as that of the original, and 3) the level of speckle reduction of the phase differences should match the correlation coefficients between channels. These should be tested in homogeneous areas.

In general, all three filters showed good balance in speckle reduction for all three channels as judged by the standard deviation to mean ratios. The correlations between channels, however, were increased significantly by the optimal weighting filter and the vector speckle filter. Theoretically, the optimal weighting filter produces HH, HV and VV images, and they are 100% correlated. The new algorithm of filtering each channel separately maintains the correlations much better.

In filtering the phase difference images, the level of filtering action has to be adjusted to match the correlation coefficient, since, under the circular Gaussian assumption, the standard deviation of the phase difference is directly related to the correlation coefficient and number of looks[3].

CONCLUSION

Polarimetric SAR speckle filtering algorithms have been analyzed for their preservation of polarimetric information and statistical properties. A new algorithm has been proposed that is effective in preserving these properties and also in speckle filtering.

REFERENCES

[1] L.M. Novak and M.C. Burl,"Optimal Speckle Reduction in Polarimetric SAR imagery," IEEE Trans. Aerospace and Electronic Systems, Vol. 26, pp.293-305, march 1990.

[2] J.S. Lee, M.R. Grunes and S.A. Mango,"Speckle Reduction in Multipolarization and Multifrequency SAR Imagery," IEEE Trans. on Geoscience and Remote Sensing, Vol. 29, No. 4, pp. 535-544, July 1991.

[3] J.S. Lee, K.W. Hoppel, S.A. Mango and A.R. Miller,"Intensity and Phase Statistics of Multi-look Polarimetric SAR Imagery," IEEE TGRS, Vol. 32, No. 5, September 1994.

[4] J.S. Lee,"Refined Filtering of Image Noise Using Local Statistics," Computer Vision, graphics and Image Processing, Vol. 15, pp.380-389, 1981.

Reduction of Multiplicative Noise in SAR Imaging by Wiener Filtering

Vito Pascazio[1], Gilda Schirinzi[2]

[1]Istituto di Teoria e Tecnica delle Onde Elettromagnetiche, Istituto Universitario Navale
Via A. Acton 38, 80133 Napoli, Italy. ☎ +(39)-81-5513976 fax +(39)-81-5512884 E-mail: pascazio@naval.uninav.it
[2]Istituto di Ricerca per l'Elettromagnetismo e i Componenti Elettronici, Consiglio Nazionale delle Ricerche
Via Diocleziano 328, 80124 Napoli, Italy. ☎ +(39)-81-5707999 fax +(39)-81-5705734 E-mail: schiri@irece1.irece.na.cnr.it

Abstract -- We present two techniques for multiplicative noise reduction in SAR imaging, based on Wiener filtering. The methods take into account the speckle correlation and allows a drastic speckle reduction, without impairing geometric resolution and preserving edges.

INTRODUCTION

Synthetic Aperture Radar (SAR) is an imaging system widely used for remote sensing of the Earth. It, being a coherent system, produces images affected by speckle noise. This phenomenon gives to the images a granular appearance, From the mathematical point of view, the effect of this interference process can be looked at as a noise (speckle), with exponential probability density function (pdf), multiplicative to the ideal (noise-free) signal. Unlike usual multiplicative noise, it is not only signal dependent but also spatially correlated.

Different techniques can be applied to reduce speckle. One usually applied in SAR applications is multilook [1]; it is based on incoherent summation of independent samples of the same image. Due to practical impossibility to use different full resolution independent images, a certain number of lower resolution images are summed up: the resulting image exhibits better radiometric resolution and worst geometric resolution.. Other speckle reduction techniques are based on adaptive filtering [2].

In this paper we present an alternative speckle reduction technique taking into account speckle correlation. It is based on Wiener filtering of the noisy SAR images. We propose two techniques, the first based on Wiener filtering of multiplicative noise, the latter on Wiener filtering of additive noise obtained after an homomorphic filtering of the SAR image signal [3]. As well known, these processes require knowledge of the power spectra of the involved signals, so that autocorrelation functions of the noise and of the signal must be evaluated. The former one can be analytically computed starting from a mathematical model of the speckle, assumed fully developed. On the contrary, the wanted signal autocorrelation is not known; this lack of knowledge can be circumvented by applying an iterative procedure which makes use as starting point the autocorrelation of the corrupted signal instead of the wanted one.

The presented methods allow drastic speckle reduction without affecting the geometrical resolution.

THE SPECKLE MODEL

The intensity of the SAR image, obtained after raw data processing, can be expressed by [4]:

$$z(x,r) = y(x,r)\,n(x,r) + n_a(x,r), \qquad (1)$$

where $z(\cdot)$ is the noise affected intensity of image, $y(\cdot)$ the corresponding noise-free value estimate of the reflectivity pattern, $n(\cdot)$ the multiplicative noise (speckle), $n_a(\cdot)$ the additive thermal noise, and (x,r) are the azimuth and range coordinates, respectively. It has to be noted that, after the image formation process, the additive noise term $n_a(\cdot)$ is negligible compared to the other term $y(\cdot)\cdot n(\cdot)$. It is noted that the spatial coordinates of the image are sampled in pixels.

In the case of one look images, affected by fully developed speckle, the noise $n(\cdot)$, supposed to be stationary can be statistically represented by the pdf [4]:

$$f_N(n) = \exp[-n], \qquad n \ge 0. \qquad (2)$$

According to Eq. (1) the conditional pdf of the image intensity
$z(\cdot)$, respect to the actual intensity $y(\cdot)$, is given by:

$$f_{Z|Y}(z|y) = \frac{1}{y}\exp\left[-\frac{z}{y}\right], \qquad z,y \ge 0. \qquad (3)$$

Indeed, the noise autocorrelation function is given by [1]:

$$R_{nn}(\bar{x},\bar{r}) = E\left[n(x,r)n^*(x+\bar{x}, r+\bar{r})\right] =$$

$$= \left[1 + \text{sinc}^2\left(\frac{\bar{x}}{\rho_x}\right)\text{sinc}^2\left(\frac{\bar{r}}{\rho_r}\right)\right], \qquad (4)$$

wherein $E[\cdot]$ represents the expected value, and ρ_x and ρ_y are the azimuth and range spatial resolutions, respectively.

According to Eq. (5), the conditional expected value is given by:

$$E[z|y] = \int_0^\infty z\, f_{Z|Y}(z|y)dz = y. \qquad (5)$$

The purpose of filtering out the speckle noise $n(\cdot)$ is to get a new SAR image $s(\cdot)$ whose conditional expected value is equal to $y(\cdot)$, and whose conditional pdf, the actual intensity being $y(\cdot)$, has a variance as small as possible. The implementation of a method providing what above required is described in the following sections.

WIENER FILTERING

For the signal $z(\cdot)$ given by Eq. (1), neglecting the additive noise $n_a(\cdot)$, the two dimensional Wiener filter,

providing the MMSE estimate of $y(\cdot)$, has the frequency domain transfer function:

$$W(\xi, \eta) = \frac{S_{yz}(\xi, \eta)}{S_z(\xi, \eta)} \tag{6}$$

where $S_{yz}(\xi, \eta)$ is the cross-spectral density of the speckled image $z(\cdot)$ and the original image $y(\cdot)$, and (ξ, η) are the Fourier mates of (x, r). For the derivation of $S_{yz}(\xi, \eta)$ and $S_z(\xi, \eta)$ we first evaluate

$$R_{yz}(\overline{x}, \overline{y}) = E\left[y(x, r)z^*(x + \overline{x}, r + \overline{r})\right] = $$
$$= E[n(x, r)] \cdot R_y(\overline{x}, \overline{r}), \tag{7}$$

and

$$R_z(\overline{x}, \overline{y}) = E\left[z(x, r)z^*(x + \overline{x}, r + \overline{r})\right] = $$
$$= R_y(\overline{x}, \overline{r}) \cdot R_n(\overline{x}, \overline{r}), \tag{8}$$

Note that in Eq. (8) we have assumed the noise $n(\cdot)$ uncorrelated with the signal $y(\cdot)$.

By using the Fourier transform of (10) and (11), and substituting into (6), we obtain [5]

$$W(\xi, \eta) = E[n(x, r)]\frac{P^*(\xi, \eta)S_y(\xi, \eta)}{|P(\xi, \eta)|^2 S_y(\xi, \eta) \otimes S_n(\xi, \eta)} \tag{9}$$

where $P(\cdot)$ is a convenient window function. In the case of fully developed speckle $E[n(x, r)] = 1$.

An alternative method acts on the signal obtained after performing an homomorphic filtering of the speckle affected data. In this case, for the signal $z(\cdot)$ given by Eq. (1), neglecting the additive noise $n_a(\cdot)$, we have after the log transformation:

$$z' = \log[z] = \log[y \cdot n] = \log[y] + \log[n] = y' + n'. \tag{10}$$

The noise is now represented by the additive term $n'(\cdot)$, which we assume to be uncorrelated to the signal $y'(\cdot)$. We assume the involved signals to be samples of zero mean stationary processes, or they are set in this condition by subtracting the corresponding mean values [5]. Then, the Wiener filter that provides the MMSE estimation of the signal $y'(\cdot)$ is given, in frequency domain, by [5]:

$$W(\xi, \eta) = \frac{S_{y'}(\xi, \eta) P'^*(\xi, \eta)}{S_{y'}(\xi, \eta) |P'(\xi, \eta)|^2 + S_{n'}(\xi, \eta)} \tag{11}$$

wherein $S_{y'}(\xi, \eta)$ and $S_{n'}(\xi, \eta)$ are the power spectra of the wanted $y'(\cdot)$ and of the noise $n'(\cdot)$ signals, respectively, $P'(\cdot)$ is a convenient window function, and * denotes the complex conjugate.

At the output of the Wiener filter we have:

$$s'(x, r) = \hat{y}'(x, r) = z'(x, r) \otimes w(x, r), \tag{12}$$

where $w(\cdot)$, is the inverse Fourier transform of $W(\cdot)$, $\otimes$ is the two-dimensional convolution, and $\hat{y}'(\cdot)$ is the MMSE estimation of $y'(\cdot)$.

The overall output of the system is given by:

$$s(x, r) = \hat{y}(x, r) = \exp[\hat{y}'(x, r)], \tag{13}$$

thus restoring the multiplicative nature of the input. For the sake of simplicity of notation, in the subsequent analysis we neglect $P(\cdot)$ and $P'(\cdot)$ appearing in Eqs. (9) and (11).

The main problem to be solved in the above mentioned procedure is the implementation of the Wiener filter. The power spectra S_n (or $S_{n'}$) of the noise can be evaluated as the Fourier transform of its autocorrelation functions computed in the previous section (or in [3]). The power spectra S_y (or $S_{y'}$) of the signal to be estimated, is also required, and its *a priori* estimate is not usually available.

With reference to the scheme based on the homomorphic filtering, the evaluation of $S_{y'}$ can be implemented by means of an iterative procedure [6], shortly described in the following. We consider as initial estimate $S_{\hat{y}'(0)}$ of $S_{y'}$ the power spectrum of the original speckled signal z':

$$S_{\hat{y}'(0)} = S_{z'}. \tag{14}$$

Then, we obtain a first estimate of the Wiener filter:

$$W_{(1)} = \frac{S_{\hat{y}'(0)}}{S_{\hat{y}'(0)} + S_{n'}} = \frac{S_{z'}}{S_{z'} + S_{n'}}, \tag{15}$$

and, consequently, a first estimate of the power spectrum $S_{\hat{y}'(1)}$ of $\hat{y}'_{(1)}$ through

$$S_{\hat{y}'(1)} = S_{z'} |W_{(1)}|^2. \tag{16}$$

Now, the power spectrum $S_{\hat{y}'(1)}$ of $\hat{y}'_{(1)}$ is used to calculate $W_{(2)}$, and so on. At the k-th step, we get:

$$W_{(k)} = \frac{S_{\hat{y}'(k-1)}}{S_{\hat{y}'(k-1)} + S_{n'}}, \tag{17}$$

$$S_{\hat{y}'(k)} = S_{z'} |W_{(k)}|^2.$$

Above introduced procedure is convergent. [6].

The final step of the proposed speckle filtering method consists of multiplying the final iteration (the K-th) of the Wiener filter $W_{(K)}$ by the Fourier transform Z' of the original speckled signal z'. The result of this operation, after an inverse Fourier Transform and after taking the exponential, provides the desired speckle filtered estimation $\hat{y}_{(K)}$.

A similar procedure is under study in order to iteratively estimate the unknown power spectrum S_y.

RESULTS

The simulated intensity image of an hypothetical scene characterised by a backscattering coefficient that assumes 4 different values is considered. The speckle free image y and the corresponding speckle affected one z are depicted in Figs. 1 and 2, respectively. The image $\hat{y}$ shown in Fig. 3 is evaluated assuming the power spectrum of the image to be estimated y to be known and using the Wiener filter (9).

This represents the best reconstruction that can be obtained and can be used for reference purposes. The normalized mean square error (NMSE) between the reconstructed image and the ideal one is -27 dB. The image shown in Fig. 4 has been obtained using the one-shot homomorphic filtering, assuming known the power spectrum of y; in this case we obtain an NMSE of -25 dB, a value slightly lower than the one obtained in the previous case, as expected. The image $\hat{y}_{(K)}$, result of the homomorphic iterative procedure after 30 iterations, is shown under Fig. 5. The NMSE is -20 dB, slightly different from the one (-25 dB) appropriate to the ideal (best) case. In Fig. 6 the behaviour of the NMSE with the number of iteration is shown.
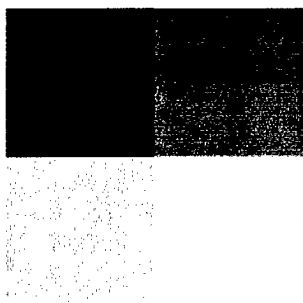
Fig. 1: *Simulated ideal (noise-free) image*
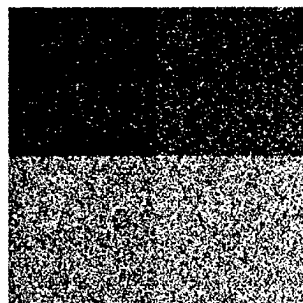
Fig. 2: *Simulated speckled image*
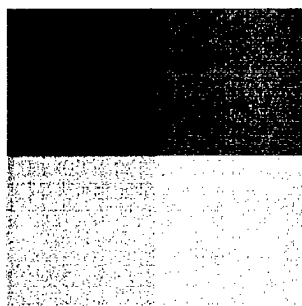
Figure 3: *Image obtained using multiplicative Wiener filter*
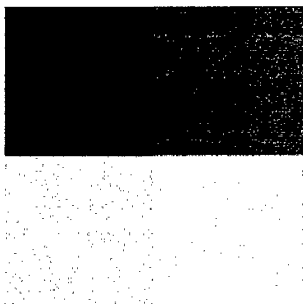
Fig. 4:*One-shot homomorphic-Wiener filtered image*
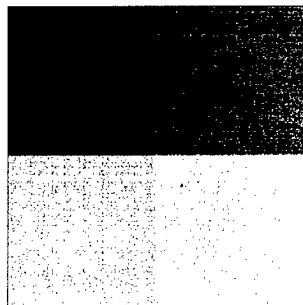
Fig. 5: *Iterative homomorphic-Wiener filtered image after 30 iterations*

As far as radiometric resolution is concerned, a proper quality measure is the ENL, that assumes the following values: 0.999 for the image of Fig. 2, 363 for the image of

Fig. 3, 320 for the image of Fig. 4, and 72 for the image of Fig. 5. Then, according to the ENL, the method exhibits very promising performance. The behaviour of the ENL vs. the number of iterations is plotted in Fig. 7.
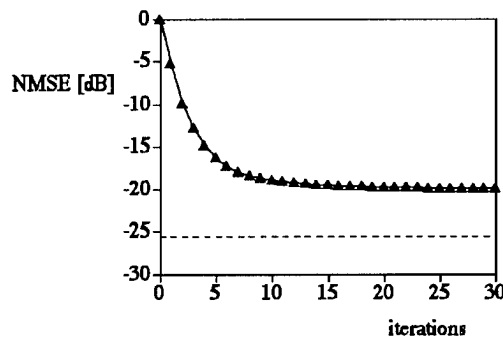
Figure 6: *Behaviour of the normalised mean square error (NMSE) in the iterative homorphic method vs. the number of iterations*

Figure 7: *Behaviour of the ENL in the iterative homomorphic method vs. the number of iterations*

REFERENCES

[1] F. K. Li, C. Croft, D. N. Held, "Comparison of Several Techniques to Obtain Multiple-Look SAR Imagery", *IEEE Trans. Geosci. Rem. Sens.*, **GE-21**, 370-375, 1983.

[2] A. Lopes, R. Touzi, E. Nezry, "Adaptive Speckle Filters and Scene Hetereogenity", *IEEE Trans. Geosci. Rem. Sens.*, **GE-28**, 992-1000, 1990.

[3] G. Franceschetti, V. Pascazio, G. Schirinzi, "An Iterative Homomorphic Technique for Speckle Reduction In Synthetic Aperture Radar Imaging", *Jou. Opt. Soc. of Am.*, *A*, **12**, 686-694, 1995.

[4] J. W. Goodman, "Statistical Properties of Laser Speckle Patterns", in **Laser Speckle and Related Phenomena**, J. C. Dainty ed., 9-75, *Springer Verlag*, 1975.

[5] J. S. Lim, **Two-Dimensional Signal and Image Processing**, *Prentice Hall*, 1990.

[6] A. D. Hillery and R. T. Chin, "Iterative Wiener Filters for Image Restoration", *IEEE Trans. Signal Proc.*, **SP-39**, 1892-1899, 1991.

Statistical Characterization of the Phase Process

in Interferometric SAR Images

M. Di Bisceglie[1], C. Galdi[1], R. Lanari[2]

[1] Università degli Studi di Napoli "Federico II", Dipartimento di Ingegneria Elettronica,
via Claudio 21, 80125 Napoli, Italy. E-mail dibisc@nadis.dis.unina.it, Fax: +39-81-7683149.
[2] IRECE - Consiglio Nazionale delle Ricerche,
via Diocleziano 328, 80124 Napoli, Italy. E-mail lanari@irece1.irece.na.cnr.it Fax: +39-81-5705734.

Abstract— In this paper we consider a statistical model for interferometric SAR images accounting for both the non-Gaussian statistics of the amplitude probability density function and for the most credited model for the interferometric phase distribution. At the basis of the model is the inapplicability of the central-limit theorem for resolution cells composed by a non deterministic number of scatterers. Experimental results carried out on both single-pass and repeat-pass interferometric data show a very good agreement between the theoretically derived phase probability density function and the measured one.

I. INTRODUCTION

Interferometric Synthetic Aperture Radar (INSAR) system is based on the acquisition of data, related to the same area, from two spatially separated antenna systems. The data acquisition can be achieved by using either two antennas physically located on the same platform (single-pass interferometry) or via repeated passes of the same sensor on two nearly parallel trajectories (repeat-pass interferometry). As a consequence of the separation between the two antennas, the phase difference between the data pairs contains information about the surface height. The phase measurements accuracy is limited by several spurious contributes acting as decorrelation sources for the phase at the two sensors. The most important perturbation forms are the spatial decorrelation arising when a resolution cell is viewed at two different angles and the temporal decorrelation due to the change of the surface properties over the time period between the acquisitions [1]. At the basis of both phenomena is the concept of coherent interference occurring inside the single resolution cells. Since the cell size is much greater than the wavelength of the incident radiation, the overall backscattered field is given by the coherent sum of a large number of contributes having random amplitude and phase. Spatial decorrelation arises since different observation angles imply different interference patterns. Temporal decorrelation is more difficult
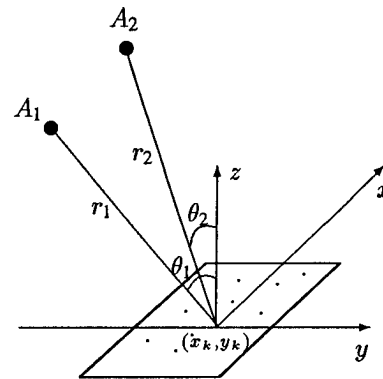
Fig. 1. Geometry of interferometric SAR

to infer and is not easily predictable in advance. Roughly speaking, we can assume that, if the surface properties remain nearly unchanged during the two acquisitions, time lags and space lags produce similar effects.

We introduce in this paper a statistical model for the phase process based on the limit relationship between the random walks with stochastic number of steps and the compound-Gaussian processes. The model stems from the statistical mechanisms incurring among the particles at a subresolution scale and is capable to account for the most credited modulus statistics [2] as well as for the phase distributions [3]. It turns out that the phase statistics are completely determined by the surface intra-pixel characteristics while they are independent on the slowly varying characteristics of the image texture.

THEORY

Let us consider an INSAR system with the geometry of Fig. 1 where the two antennas A_1 and A_2 illuminate the resolution cell with azimuth-range center coordinates (x_k, y_k), at incidence angles θ_1 and θ_2 respectively.

It is usual, for natural scenes, to represent the received signal as the sum of a great number of contributes from the scattering

centres within the resolution cell [4]. Following this model, if the dimensions of the scatterers are small in terms of the cell size but large with respect to the incident wavelength, the complex signal at the ith antenna can be stated as a two-dimensional random walk, i.e.

$$\tilde{\gamma}_i(x_k, y_k) = \sum_{n=1}^{N_i(x_k,y_k)} a_{in} e^{j\phi_{in}} = \sum_{n=1}^{N_i(x_k,y_k)} X_{in} + jY_{in} \qquad (1)$$

where a_{in} is the amplitude of the signal backscattered from the nth scatterer, ϕ_{in} is the corresponding phase assumed to be independent of a_{in} and $N_i(x_k, y_k)$ is the number of scatterers (steps of the random walk) which contribute to the field reirradiated by the resolution cell. The joint statistical characterization of $\tilde{\gamma}_1(x, y)$ and $\tilde{\gamma}_2(x, y)$ requires a more accurate specification of the statistics of the single terms appearing in the above sums. The first reasonable assumption is to consider the scatterers as randomly positioned in the resolution cell; this entails that each sequence $\{a_{1n}\}_{n=1}^{N_1}$, $\{\phi_{1n}\}_{n=1}^{N_1}$, $\{a_{2n}\}_{n=1}^{N_2}$, $\{\phi_{2n}\}_{n=1}^{N_2}$ is composed of independent and identically distributed random variables. On the other hand, since each scatterer is observed at two slightly different viewpoints, some degree of correlation is expected between the complex variables $(X_{1n} + jY_{1n})$ and $(X_{2n} + jY_{2n})$ (see (1)). Such a correlation is accounted through the covariance matrix $\mathbf{K}$ given by

$$\mathbf{K} = \sigma^2 \begin{pmatrix} 1 & 0 & \rho_c & \rho_s \\ 0 & 1 & -\rho_s & \rho_c \\ \rho_c & -\rho_s & 1 & 0 \\ \rho_s & \rho_c & 0 & 1 \end{pmatrix} \qquad (2)$$

where σ^2 is the common variance of the variables $X_{1n}, Y_{1n}, X_{2n}, Y_{2n}$ assumed to have zero mean, ρ_c is the correlation coefficient of the components (X_{1n}, X_{2n}) and of (Y_{1n}, Y_{2n}) and ρ_s is the cross-correlation coefficient of X_{in}, Y_{jn} $i, j = 1, 2$; $i \neq j$. Note that the real and imaginary part of the signal at each antenna have been assumed as incorrelated: this is the result of the underlying hypothesis of circular simmetry of the quadrature component of the received process. Some observations are now in order about the number of interfering elements $N_1(x_k, y_k)$ and $N_2(x_k, y_k)$. When A_1 is close to A_2, the reirradiating scatterers are expected to be the same so we can set $N_1(x_k, y_k) = N_2(x_k, y_k)$; conversely, as the distance between A_1 and A_2 increases, or as a time decorrelation is to be accounted, N_1 is to be actually different from N_2. In this case, a birth and death process can be considered as a model ruling the appearence and disappearence of scatterers and some decorrelation between N_1 and N_2 will arise. We consider in this paper the case $N_1 = N_2$ leaving to further studies the case $N_1 \neq N_2$.

Under such hypothesis it is possible to evaluate the joint statistics of $(\tilde{\gamma}_1(x_k, y_k), \tilde{\gamma}_2(x_k, y_k))$ as the mean number of

contributes, $\overline{N}$ say, diverges; this is in agreement with the previous hypothesis of radar-cell size much greater than the scatterer size. It is possible to demonstrate that the joint characteristic function of $\tilde{\gamma}_1, \tilde{\gamma}_2$ can be cast in the form [5]

$$\Theta_{\tilde{\gamma}_1 \tilde{\gamma}_2}(\mathbf{u}) = E\left[\exp\left(\mathbf{u}^T S \mathbf{K} \mathbf{u}\right)\right] \qquad (3)$$

where $\mathbf{u} = (u_1, u_2, u_3, u_4)$, $\mathbf{K}$ is the previously defined covariance matrix, $E(\cdot)$ denotes expectation and S is a real, non negative random variable whose cumulative distribution function is defined through the limit

$$F_{\sqrt{S}}(x) = \lim_{\overline{N} \to \infty} \Pr\left\{\frac{N}{\overline{N}} \leq x\right\}. \qquad (4)$$

Equation (3) can be regarded as the characteristic function of the product

$$\sqrt{S}(g_1, g_2) \qquad (5)$$

where (g_1, g_2) are complex Gaussian variables, independent of S, with zero mean and covariance matrix $\mathbf{K}$. The model (5) has several interesting properties and is often referred in the literature to as compound-Gaussian model.

As viewed by the two sensors, the scene is described by the stochastic reflectivity patterns $\gamma_1(x, y)$ and $\gamma_2(x, y)$; projecting into the SAR system geometry, the complex images are given by the expression [6]

$$I_i(x', y') = \iint \gamma_i(x, y) \exp(-j2kr_i(y)) h(x'-x, y'-y) dx dy \qquad (6)$$

where $k = 2\pi/\lambda$, $r_i(y)$ is the range from the ith antenna to the scattering point and $h(x, y)$ is the system impulse response function (IRF). We assume now, as usual, that the system IRF is significantly different from zero inside the resolution cell only and we rewrite the integral (6) as the sum of $N(x'_k, y'_k)$ integrals each one extended to the area ΔR_n of the single scattering element within the resolution cell

$$I_i(x'_k, y'_k) = \exp(-j2kr_i(y'_k))$$
$$\sum_{n=1}^{N(x'_k, y'_k)} \iint_{\Delta R_n} \gamma_i(x, y) h(x'_k - x, y'_k! - y) dx dy. \qquad (7)$$

Note that in eq. (7) the reflectivity pattern γ_i includes the overall stochastic properties of the oberved surface depending on both the electromagnetic and roughness characteristics. In other words, it also includes the rapidly varying component usually embedded into the term $r_i(y)$ of the complex exponential in (7). Consequently, $2kr_i(y)$ is a smooth function into the resolution cell whose value can be taken coincident with the cell center range. We also observe that the integral in the above equation represents the complex reflectivity $a_{in} e^{j\phi_{in}}$ of the single scatter including the sensor characteristics. For the points lying inside the region ΔR_n the sensor IRF can be approximated
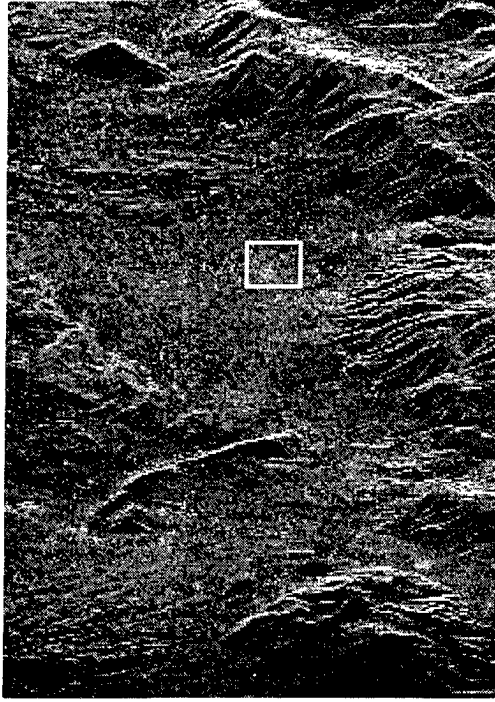
Fig. 2. ERS-1 SAR amplitude image of the Campania region, Italy: area under test marked with a rectangle.
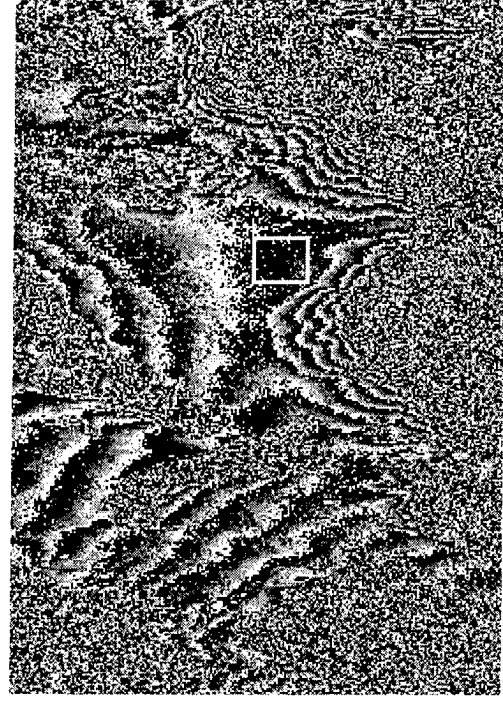
Fig. 3. ERS-1 SAR interferometric image of the Campania region, Italy: area under test marked with a rectangle.

by a constant value which acts as a gain term for the complex reflectivity.

Interestingly, since the sensor IRF is a real function, the phases of the singles scattering terms are not affected by the sensor characteristics. Using (7), (1) and (5) we obtain

$$I_1(x'_k, y'_k) I_2^*(x'_k, y'_k) = |\tilde{\gamma}_1(x'_k, y'_k)||\tilde{\gamma}_2(x'_k, y'_k)|$$
$$\exp(-j\Delta\phi(x_k, y_k)) \exp(-j2k(r_1(x'_k, y'_k) - r_2(x'_k, y'_k))) \quad (8)$$

where $\Delta\phi$ is the phase of $\tilde{\gamma}_1 \tilde{\gamma}_2^*$. The above equation clearly shows that the overall phase is given by the sum of the interferometric component $2k(r_1(x'_k, y'_k) - r_2(x'_k, y'_k))$ containing the height information and a random component $\Delta\phi$ due to the surface roughness. This is exactly the differential phase of the product $\sqrt{S}(g_1, g_2)$ we introduced in (5). Interestingly, since S is a real-values random variable, the probability density function (pdf) of $\Delta\phi(x, y)$ depends on the covariance matrix of the Gaussian component only which, for one-look processing is given by [7]

$$f_{\Delta\phi}(x) = \frac{1 - |\rho|^2}{2\pi} \frac{1}{1 - |\rho|^2 \cos^2(x - \psi)}$$
$$\left[1 + \frac{|\rho|\cos(x - \psi)\arccos(-|\rho|\cos(x - \psi))}{(1 - |\rho|^2 \cos^2(x - \psi))^{1/2}}\right] \quad (9)$$

where

$$\rho = |\rho|e^{j\psi} = \frac{E[g_1 g_2^*]}{E[|g_1|^2]E[|g_2|^2]} = \rho_c - j\rho_s \quad (10)$$

Some remarks are in order. First, the phase pdf is the same as the one derived by other authors [8,9] but it does not require the complex reflectivity to be modelled as a Gaussian process. Second, the amplitude image pdf is ruled by the distribution of the random variate S and is compatible with some well known models such as the K pdf, the Weibull pdf, the Generalized Gamma pdf [10].

ANALYSIS OF THE INTERFEROMETRIC DATA

The theoretical distribution of the random additive term degrading the interferometric phase can be validated by comparison with the statistics estimated from real data sets. According to the theoretical model developed in the previous sections, the interferometric phase pdf is a parametric distribution depending upon the values of $|\rho|$ and ψ. To compare the experimental data pdf with the theoretical one, we need to estimate such parameters. A flat and homogeneous area is necessary in order to obtain a stationary sample and to avoid a bias on the parameter estimates due to topographic variations. Specifically, we consider two different data-sets corresponding to the cases of single-pass and repeat-pass interferometry. The data of the first set were collected by the AIRSAR sensor near Matera, Italy, while the second set refers to data collected by the ERS-1 sensor in the Campania region, Italy. Both sets have been processed to produce single look complex images. The ERS-1 SAR image is shown in Fig. 2 wherein the area under test has been marked

TABLE I

Values of the pdf parameters for the two sensors

	ERS1	AIRSAR
$|\hat{\rho}|$	0.1739	0.8852
$|\rho_{fit}|$	0.1807	0.8763
$\hat{\psi}$ (rad)	−1.788	−1.301
ψ_{fit} (rad)	−1.797	−1.290

with a rectangle. The corresponding interferogram is reported in Fig. 3, where the flatness of the examined region is confirmed by the absence of fringes.
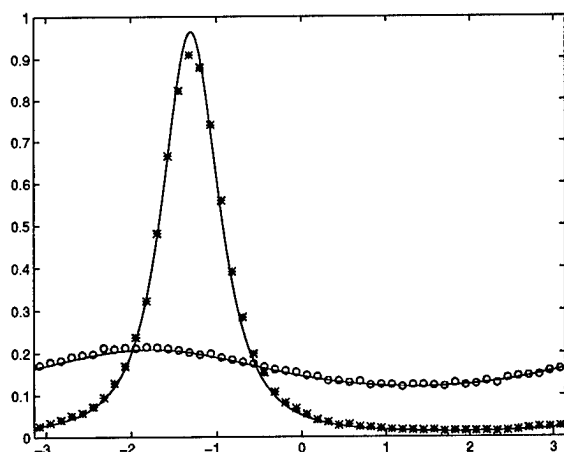
Fig. 4. Comparison between the theoretical pdf and the estimated histogram. Solid: $|\hat{\rho}| = 0.1739$, $\hat{\psi} = -1.788$, circles: ERS1 data, dot-dash: $|\hat{\rho}| = 0.8852$, $\hat{\psi} = -1.301$, stars: AIRSAR data

Fig. 4 shows the histograms of the two data-sets compared with the pdf's corresponding to the estimated values of the parameters. The goodness of fit has been confirmed by the evaluation of the parameters $|\rho_{fit}|$ and ψ_{fit} providing the best fit between the theoretical pdf and the histogram: results are reported in Table I, showing the good agreement between the experimental values of modulus and phase of the correlation coefficient and the same parameters estimated from the complex interferogram.

REFERENCES

[1] H.A. Zebker, J. Villasenor, "Decorrelation in Interferometric Radar Echoes", *IEEE Trans. on Geoscience and Remote Sensing*, Vol. 30, No. 5, September 1992, pp.950-959.

[2] C.J. Oliver, "The representation of correlated clutter textures in coherent images", *Inverse Problems*, No. 4, 1988, pp. 843-866.

[3] I.R. Joughin, D.P. Winebrenner, D.B. Percival, "Probability Density Functions for Multilook Polarimetric Signatures", *IEEE Trans. on Geoscience and Remote Sensing*, Vol. 32, No. 3, May 1994, pp.562-574.

[4] P. Beckmann, A. Spizzichino, *The Scattering of Electromagnetic Waves from Rough Surfaces*, Pergamon, Oxford, 1963.

[5] M. Di Bisceglie, C. Galdi, "Clutter Characterization Based on Random Walks", Submitted to CIE International Conference of Radar, Beijing, October 1996.

[6] F.K. Li, R.M. Goldstein, "Studies of Multibaseline Spaceborn Interferometric Synthetic Aperture Radars", *IEEE Trans. on Geoscience and Remote Sensing*, Vol. 28, No. 1, January 1990, pp.88-97.

[7] W.B. Davenport, W.L. Root *An Introduction to the Theory of Random Signals and Noise*, Mc. Graw-Hill, Tokyo, 1958.

[8] J.S. Lee, K.W. Hoppel, S.A. Mango, A.R. Miller, "Intensity and Phase Statistics of Multilook Polarimetric and Interferometric SAR Images", *IEEE Trans. on Geoscience and Remote Sensing*, Vol. 32, No. 5, September 1994, pp.1017-1028.

[9] D. Just, R. Bambler, "Phase Statistics of Interferograms with Applications to Synthetic Aperture Radar", *Applied Optics*, Vol. 33, No. 20, July 1994, pp. 4361-4368.

[10] E. Conte, M. Lops, G. Ricci, "Generation of Random Sequences with Prescribed Marginal Distribution and Autocovariance Function", *Int'l Symposium on Communication Theory & Applications*, Crieff, Scotland, September 1991.

AEROSOL PROPERTIES FROM BLURRING EFFECT IN REMOTELY SENSED IMAGES

A. Leone, B. Bulgarelli, M. Gabella, G. Perona

Dipartimento di Elettronica, Politecnico di Torino,c.so Duca degli Abruzzi 24, 10129 Torino (Italy)
Tel: ++39-11-5644071, Fax: ++39-11-5644015, E-mail: perona@polito.it

ABSTRACT

The presence of an aerosol layer over a nonuniform surface causes the blurring effect in remotely sensed images.
In principle from the study of this effect it seems to be possible to evaluate aerosol properties.
In this paper an aerosol layer superimposed on a surface with 1-D periodical variation in reflectivity and with half plane reflectivity variation are considered, in the single scattering approximation.

INTRODUCTION

The presence of an aerosol layer over a nonuniform surface causes the radiance from the high reflectivity area to spill over the adjoining low reflectivity pixels, increasing their apparent brightness.
As a consequence of this adjacency effect the remotely sensed images appear blurred.
The adjacency effect has been generally studied with the aim to correct the remote sensed images[1-6,8], only few studies adopted an inverse approach, deducing from the blurring effect aerosol properties [1,7,9].
Some of them [1,5-7]considers cases, such as small-sized nonuniformity, in which it is possible to introduce an average background reflectivity, approach not applicable when a surface reflectivity periodical variation is considered.
Other studies [2,3] consider a general radiance diffused by the atmosphere, path radiance L_p, without distinguishing if it has or not previously interacted with the surface. Others [9] finally do not considers at all the radiance scattered from the background surface of the observed pixel.
Under the following hypotheses: transparent atmosphere with
an aerosol scattering layer of infinitesimal thickness dh at the height h and homogeneous in the coordinate x,y; single scattering approximation; sensor at infinity in nadiral observation; Lambertian surfaces,
a 1-D surface reflectivity periodical variation and a "two-halves" field case study are considered.
For both the cases it is shown how to deduce the height h and the optical thickness $d\tau$ of the aerosol layer directly from the data collected by the sensor.

The radiance directed vertically upward and detected by a sensor moving in the x direction and observing at its nadir a given pixel is given by:

$$L_s = TL_i + L_a + L_b \tag{1}$$

where TL_i is the attenuated radiance directly coming from the observed pixel, with intrinsic ground radiance L_i; L_a is the radiance scattered by the atmosphere before reaching the ground (atmospheric radiance); L_b is the radiance that, after being reflected by the background surface, is scattered by the atmosphere in the observed pixel field-of-view (background radiance).

Assuming for simplicity that the aerosol layer is infinitesimal, no attenuation is considered for the L_a and L_b terms.
While L_a equally affects each pixel radiance, L_b is strictly related to the spatial reflectivity distribution, then only the latest is responsible of the adjacency effect.
Therefore in this paper the attention will be focused only on this term.

Following the approach suggested by Otterman and Fraser [10], the analytical expression for the total background radiance affecting an observed pixel dA(x,y), in the case of an aerosol distribution along h, is here given:

$$L_b(x,y) = \frac{E_g}{\pi} \int_{h_1}^{h_2} h\sigma(h)T_{h,h_2} \, dh \times$$

$$\times \int\int_{-\infty}^{+\infty} \frac{P(\varphi)b(x',y')T_{h_1,h}^{1/\cos\varphi}}{[h^2 + (x-x')^2 + (y-y')^2]^{3/2}} dx'dy' \tag{2}$$

where E_g is the total solar irradiance reaching the ground; b(x,y) is the surface reflectivity; $\sigma(h)$ is the aerosol scattering coefficient at the height h; $P(\varphi)$ is the aerosol scattering phase function; φ is the angle between the direction of the radiation coming from the surface and the sensor line of sight, and where

$$T_{h_1,h}^{1/\cos\varphi} = \exp\left(\frac{-\int_{h_1}^{h}\sigma(h')dh'}{\cos\varphi}\right) =$$

$$= \exp\left(\int_{h_1}^{h} \frac{-\sigma(h')[h'^2+(x-x')^2+(y-y')^2]^{1/2}dh'}{h'}\right) \tag{3}$$

is the aerosol transmittance, in the φ direction, from the ground to the scattering point; finally

$$T_{h,h_2} = \exp\left(-\int_{h}^{h_2}\sigma(h')dh'\right) \tag{4}$$

is the vertical aerosol transmittance from the scattering point to the top.

The atmospheric radiance L_a is instead given by:

$$L_a = E_0 d\tau P(180° - \theta_0) \qquad (5)$$

where E_0 is the direct solar irradiance and θ_0 is the SZA.

1-D GROUND REFLECTIVITY PERIODICAL VARIATION

A single infinitesimal aerosol layer at the height h, characterized by an isotropic scattering phase function $P(\varphi) = 1/2\pi$, normalized to one, is now considered.

Being the phase function isotropic the total solar irradiance reaching the ground is given by:

$$E_g = E_0[\mu_0\exp(-d\tau_0) + d\tau/\pi], \qquad (6)$$

where $\mu_0 = \cos\theta_0$, and $d\tau_0 = d\tau/\cos\theta_0$.

Let $b(x) = b_0(1 + \cos(2\pi/\lambda)x)$ be the surface reflectivity assumed to be known.

Resolving (2) under these conditions (it should be noted that now the problem is only 2-D), the total background radiance L_b affecting the observed pixel dA in x is calculated:

$$L_b(t) = b_0(E_0/4)d\tau[\mu_0\exp(-d\tau_0) + d\tau/\pi][1 + \exp(-2\pi k)\cos(2\pi t)] \qquad (7)$$

where $t = x/\lambda$ and $k = h/\lambda$.

The intrinsic ground radiance L_i is:

$$L_i(t) = b_0(E_0/2)[\mu_0\exp(-d\tau_0) + d\tau/\pi](1 + \cos(2\pi t)). \qquad (8)$$

while the atmospheric radiance L_a is:

$$L_a = E_0 d\tau/2\pi. \qquad (9)$$

So that the total radiance reaching the sensor observing the pixel dA, L_s, is (Fig.1):

$$L_s(t) = (E_0/2)\{b_0[\mu_0\exp(-d\tau_0) + d\tau/\pi]\{\exp(-d\tau)(1 + \cos(2\pi t)) + \\ + (d\tau/2)[1 + \exp(-2\pi k)\cos(2\pi t)]\} + d\tau/\pi\}. \qquad (10)$$

From the mean value of (10),

$$\overline{L}_s = (E_0/2)\{b_0[\mu_0\exp(-d\tau_0) + d\tau/\pi][\exp(-d\tau) + d\tau/2] + d\tau/\pi\}, \qquad (11)$$

it is possible to evaluate the aerosol layer optical thickness $d\tau$; and once $d\tau$ is known, from the amplitude of the signal received by the sensor,

$$\Delta L_s = L_{s,max} - L_{s,min} = b_0(E_0/2)[\mu_0\exp(-d\tau_0) + d\tau/\pi] \times \\ \times [2\exp(-d\tau) + d\tau\exp(-2\pi k)]. \qquad (12)$$

the aerosol layer height can be deduced (Fig. 2).
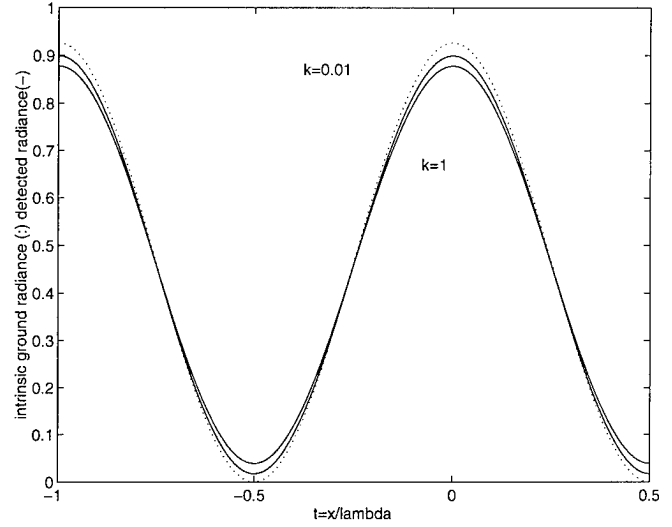
Fig.1. 1-D ground reflectivity periodical variation, with frequency $1/\lambda$: total radiance reaching the sensor L_s (-) and intrinsic ground radiance L_i (--), normalized to the solar irradiance E_0, vs the dimensionless variable $t = x/\lambda$, for different values of the dimensionless parameter $k = h/\lambda$, ($d\tau = 0.1$, $b_0 = 1$, $\mu_0 = 0.99$).
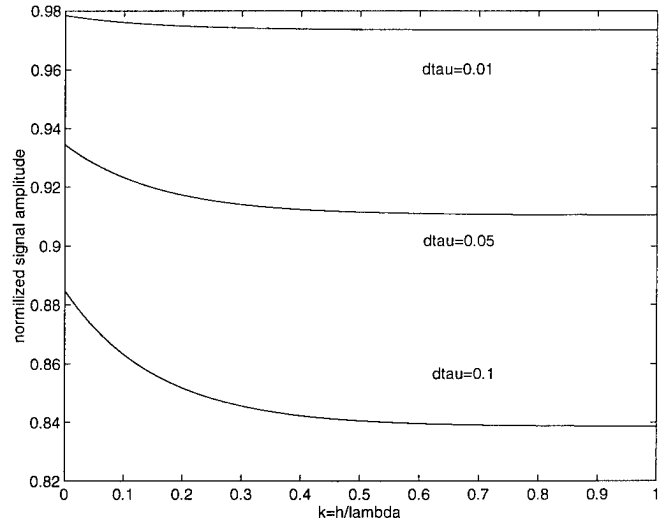
Fig.2. 1-D ground reflectivity periodical variation, with frequency $1/\lambda$: amplitude of the signal received by the sensor ΔL_s, normalized to the solar irradiance E_0, vs the dimensionless variable $k = h/\lambda$, for different values of the aerosol layer optical thickness $d\tau$, ($b_0 = 1$, $\mu_0 = 0.99$).

"TWO-HALVES" FIELD

A single infinitesimal aerosol layer at the height h, characterized by an isotropic scattering phase function $P(\varphi) = 1/4\pi$, normalized to one, is again considered.

Being the problem now 3-D (6) becomes:

$$E_g = E_0[\mu_0\exp(-d\tau_0) + d\tau/2], \qquad (13)$$

Let

$$b(x,y)= \begin{cases} a & \text{when } y<0 \text{ for any } x \\ \\ b<a & \text{elsewhere} \end{cases}$$

be the surface reflectivity.
The total background radiance affecting the radiance of the observed pixel with coordinates (x,y) is given by the solution of (2) under the above conditions :

$$L_b(x,y) = (d\tau/2\pi)(E_0/\pi)[\mu_0\exp(-d\tau_0)+d\tau/2]\times$$
$$\times[(a+b)(\pi/2)-(a-b)\arctan(y/h)], \quad (14)$$

The intrinsic ground radiance is:

$$L_i(x,y) = \begin{cases} a(E_0/\pi)[\mu_0\exp(-d\tau_0)+d\tau/2], & \text{when } y<0 \text{ for any } x \\ \\ b(E_0/\pi)[\mu_0\exp(-d\tau_0)+d\tau/2], & \text{elsewhere.} \end{cases} \quad (15)$$

The atmospheric radiance is:

$$L_a=E_0 d\tau/4\pi, \quad (16)$$

so that the total radiance reaching the sensor observing the pixel dA is:

$$L_{s,y<0}(x,y)=(E_0/\pi)\{[\mu_0\exp(-d\tau_0)+d\tau/2]\{a\times\exp(-d\tau)+$$
$$+(d\tau/2\pi)[(a+b)(\pi/2)-(a-b)\arctan(y/h)]\}+d\tau/4\}$$
$$(17)$$
$$L_{s,y>0}(x,y)=(E_0/\pi)\{[\mu_0\exp(-d\tau_0)+d\tau/2]\{b\times\exp(-d\tau)+$$
$$+(d\tau/2\pi)[(a+b)(\pi/2)-(a-b)\arctan(y/h)]\} +d\tau/4\}$$

The intrinsic ground radiance appears like a step function.
At the sensor a "stretching" of this step is detected, getting larger with the increasing of the aerosol layer height h.
Increasing $d\tau$ the amplitude of the step decreases. Chosen a>b, the aerosol optical thickness can be measured from the difference between the radiance detected in points far enough from the reflectivity edge:

$$L_{s,y<0}(-\infty)-L_{s,y>0}(+\infty)=(a-b)(E_0/\pi)[\mu_0\exp(-d\tau_0)+d\tau/2]\times$$
$$\times[\exp(-d\tau)+d\tau/2] \quad (18)$$

Once $d\tau$ is known, the layer height can be deduced from the radiance reaching the sensor from an area belonging to the brightest zone of the field .

$$\int_{-d}^{0}L_{s,y<0}(y)dy=(E_0/\pi)\{[\mu_0\exp(-d\tau_0)+d\tau/2]\{a\times d\times\exp(-d\tau)+$$
$$+(d\tau/2\pi)[(\pi/2)d(a+b)+(b-a)[(h/2)\log(1+(d^2/h))+$$
$$+d\times\arctan(-d/h)]]\}+d\times d\tau/4\}. \quad (19)$$

CONCLUSION

From the analyses of the adjacency effect caused by an infinitesimal aerosol layer, it has been derived that the background radiance depends on the reflectivity variation on the ground, on the distance between the pixels and on the aerosol layer height and optical thickness.
In the case of a 1-D periodical variation of the ground reflectivity it has been observed that it is possible to obtain the aerosol layer optical thickness from the mean value of the radiance detected by the sensor; hence, the layer height from the amplitude of the received signal.
In the case of the 'two-halves' field, it has been seen that the aerosol layer optical thickness can be obtained from the difference between the radiance detected in points far enough from the reflectivity edge; hence, the layer height can be measured from the radiance reaching the sensor from an area belonging to the brightest zone of the field.
Next steps will be to consider a more appropriate scattering function which better approximates the forward aerosol scattering peak; a realistic atmosphere; and a 2-D variation of the ground reflectivity.

REFERENCES

[1]A.P. Odell, J.A. Weinman,"The effect of atmospheric haze on images of the Earth's surface", J. Geophys. Res. 80, 5035-5040, 1975
[2]S. Ueno, Y. Haba, Y. Kawata, T. Kusaka and Y. Terashita,"The atmospheric blurring effect on remotely sensed Earth imagery", Remote Sensing of Env.: Inversion Methods and Applications, A.L. Fymat and V.E. Zuev, Eds.,(Elsevier, New York), 305- ,1978
[3]R. E. Turner, "Elimination of atmospheric effects from remote sensor data", proc. of 12th Int. Symp. on Remote Sensing of Env., ERIM, 783-793, 1978
[4]Y. Kawata, Y. Haba, T. Kusaka, Y. Terashita and S. Ueno,"Atmospheric effects and their correction in airborne sensor and Landsat MSS data", proceedings of the 12th Int. Symp. on Remote Sensing of the Env., vol.II, Manila, 1241-1257, 1978
[5]J.V. Dave,"Effect of atmospheric conditions on remote sensing of a surface nonhomogeneity", Photogr. Eng. and Remote Sensing, 46, 1173-1180, 1980
[6]D. Tanre, M. Herman and P.Y. Deschamps,"Influence of the background contribution upon space measurements of ground reflectance", Appl. Opt., 20, 3676-3684, 1981
[7]M. Griggs,"Determination of the aerosol content in the atmosphere from ERTS-1 data", proc. of 9th Int. Symp. on remote Sensing of Env., Univ. of Michigan, Ann Arbor, Michigan, 471-481, 1974
[8]Y.J. Kaufman,"The atmospheric effect on the separability of field classes measured from satellite", Remote Sensing of Env., 18, 21-34, 1985
[9] D.H. Williams and J.L.Cogan,"Estimation of visibility from satellite imagery", Appl. Opt., 30, 414-419, 1991
[10]J.Otterman and R.S. Fraser," Adjacency effects on imaging by surface reflection and atmospheric scattering: cross radiance to zenith", Appl. Opt., 18, 2852-2860, 1979

Deriving the Anisotropic Atmospheric Point Spread Function of ASAS off-nadir Images and Removal of the Adjacency Effect

Baoxin Hu, Xiaowen Li, and Alan H. Strahler
Department of Geography and Center for Remote Sensing, Boston University,
725 Commonwealth Avenue, Boston, MA 02215, USA, Tel. +1-617-353-5981,
Fax +1-617-353-3200, e-mail baoxin/wanner/lix/alan@crsa.bu.edu

Abstract–Because of its off-nadir viewing, the Advanced Solid-State Array Spectroradiometer (ASAS) presents a new challenge for atmospheric correction. One of the main differences between the atmospheric effect on nadir and off-nadir observations is the adjacency effect. To remove the adjacency effect on 45° viewing ASAS images, we extracted a first-order analytic approximation of the atmospheric point spread function (PSF) using the relationship between the physical quantities and the geometry of the sensor, target pixel and environmental pixel. The correction results by a Wiener filter based on the PSF demonstrate that this method of removing the adjacency effect is feasible and effective.

INTRODUCTION

Multiangle remotely sensed data provide an opportunity for obtaining quantitative information of the biophysical characteristics of vegetation and albedo. Angular signature information in multiangle remotely sensed data is also expected to be a significant component of improving surface cover classification and characterization. The Advanced Solid-State Array Spectroradiometer (ASAS) [1] was designed by NASA/Goddard Space Flight Center(GSFC) in advance of the EOS era. It is able to track and image a target site through a discrete sequence of fore-to-aft view directions from 45° forward to 45° aftward. ASAS has acquired digital image data of this sort for many terrestrial ecosystem experiments. But a key to further use of ASAS images is the removal of atmospheric effects. Because of its off-nadir viewing, atmospheric correction methods for nadir observations aren't suitable for ASAS images. One of the main differences between nadir remote sensing and off-nadir remote sensing is the adjacency effect. For nadir remote sensing, the adjacency effect depends only on the distance of the environment pixel from the object pixel. However, in off-nadir remote sensing, the effect of the environment pixel on the object pixel varies with both the distance and the direction between them. In this paper, we present a new method to derive the first order analytic approximation of the atmospheric point spread function (PSF) and design a Wiener filter to remove the adjacency effect on ASAS 45° viewing images.

THE ADJACENCY EFFECT

Surface remote sensing through a scattering atmosphere is subject to diffuse illumination into the sensor's field of view (FOV) of radiation originating from surface regions out of the line of sight. This phenomenon is known as the adjacency effect [2]. The adjacency effect cannot be predicted by an atmospheric model based on the assumption of a uniform surface reflectance [3]. It can be computed using 3-D radiative-transfer equations for the coupling the atmosphere and Earth surface system. But both the coupling system and the algorithm are very complicated and extensive numerical computation is needed. Because the spatial scale of the effect of the multiple bouncing between the atmosphere and surface is beyond the FOV of the sensor, we don't include this component in the adjacency effect. Thus the atmosphere can be approximated as a linear medium. The adjacency effect may be viewed as a convolution of the radiation field reflected from the surface with an atmospheric PSF whose shape depends on the geometry of atmospheric single scattering from target toward the sensor.

Vermote et al. [4] used the Monte Carlo simulation method to simulate the adjacency effect to nadir and off-nadir 70° observations. Their results indicated that for nadir remote sensing, the atmospheric PSF was azimuthally isotropic, but in off-nadir remote sensing, it was azimuthally dependent, and the contribution of the background in the direction of the observer was greater than others.

DERIVING THE ATMOSPHERIC PSF

In Fig. 1, points V, O and P represent the sensor, target pixel, environmental pixel respectively; the parallel dashed lines represent the sensor's FOV with a width of $2d$; θ is view zenith angle, and φ and r describe the position of P relative to O (azimuthal angle and distance respectively); and h is the flight altitude. Due to the atmospheric scattering, part of the radiance from P is scattered one or more times and intercepted by the FOV. Here, we just take single scattering into consideration to obtain a first-order analytic approximation of the atmospheric PSF.

From the Fig. 1, we see that only those photons reflected to the directions into the cylinder surrounding the axis, OV, can directly enter the FOV, which is determined by the solid angle Ω subtended at P by the FOV. Here we use α to approximate Ω. The calculation of α is as follows.

$$\cos \beta = \sin \theta \cdot \cos \varphi \qquad (1)$$

$$\alpha_1 = \frac{\pi}{2} - \beta \qquad (2)$$

1587

some characteristics of the observed surface.

Secondly, we select the best-fit model based on the RMSE for every data set and calculate the correlation coefficient between the modeled and the measured values. For most data sets, the correlation coefficient is over 0.8 and the RMSE is smaller than 0.043, which indicates a reasonable agreement between the modeled and observed values. Fig. 1 shows the reflectances in the principal plane in the NIR for some land covers, where the points represent the measured data and the solid lines are the modeled data. These data sets have hotspots, as for field and wheat, and bowl shapes, such as hardwood, demonstrating that the models can fit hotspots and bowl shapes well.

Lastly, we compare the best-fit model for every data set with other semiempirical models, such as Roujean's model [1] and Rahman's model [3]. In Fig.1, dashed lines are for Roujean's model and the dash-dotted lines for the Rahman model. From the plots, we can note that our models fit better than the other models, especially for the dense hardwood canopy.

CONCLUSION

In this paper, we evaluated the ability of linear kernel-driven semiempirical models developed for use with MODIS/MISR data to provide adequate mathematical descriptions of the anisotropic reflectance of a variety of natural surfaces. The results show: 1) different land cover types prefer different models; 2) our models can fit a large variety of vegetation canopies well and they fit better than other semiempirical models, especially for dense forest canopies. This is partially due to the fact that they are based on ellipsoidal crown shapes and the shadow overlapping mechanism is modeled realistically. The fit quality can presumably be further improved by reducing the effect of outlier data on the inversion results by giving the appropriate W_j in (1), and by considering more realistic multiple scattering in the models.

REFERENCES

[1] Roujean, J. L., M. Latoy and P. Y. Deschamps, "A bidirectional reflectance model of the Earth's surface for the correction of remote sensing data", J. Geophys. Res., 97, pp. 20455-20468, 1992.

[2] Wanner, W., X. Li, A. H. Strahler, "On the derivation of kernels for kernel-driven models of bidirectional reflectance", J. Geophys. Res., 100, pp. 21077-21089, 1995.

[3] Rahman, H., B. Pinty, and M. M. Verstraete, "Extracting information on surface properties from bidirectional reflectance measurements", J. Geophys. Res., 96, pp. 2865-2874, 1991.

[4] Strahler, A. H., et al., "MODIS BRDF/ Albedo Product: Algorithm Theoretical Basis Document Version 3.2", NASA EOS-MODIS, 1995.

[5] Kimes, D. S., A. G. Kerber and P. J. Seller, "Dynamics of directional reflectance factor distribution for vegetation canopies", Appl. Opt., 22(9), pp. 1364-1372, 1983.

[6] Kimes, D. S., W. W. Newcomb, C. J. Tucker, et al., "Directional reflectance factor distributions for cover types of Northern Africa", Remote Sens. Environ 18, pp. 1-19, 1985.

[7] Kimes, D. S., W. W. Newcomb, R. F. Nelson, and J. B. Schutt, "Directional reflectance distributions of a hardwood and a pine forest canopy", IEEE Trans. Geosci. Remote Sens. GE-24, pp. 281-293, 1986.

[8] Ranson, K. J., L. L. Biehl and M. E. Bauter, "Variation in spectral response of soybeans with respect to illumination, view and canopy geometry", Int. J. Remote Sens. 6, pp.1827-1842, 1985.

[9] Kim, M. S., "BRDF Infomation System Version M-1, Biospheric Sciences Branch", NASA/GSFC, Software, LGRSS, University of Maryland.

[10] Deering, D. W., S. P. Ahmad, T. F. Eck and B. P. Banerjee, "Temporal Attributes of the Bidirectional Reflectance for Three Boreal Forest Canopies", Proc. Int. Geosci. Remote Sens. Symp. 95, 1239-1241, 1995.

[11] Sellers, P.J., et al., "An overview of the First International Satellite Land Surface Climatology Project (ISLSCP) Field Experiment (FIFE)", J. Geophys. Res., 97, pp. 345-371, 1992.

Fig.1 The BRDF on the Principal Plane in the near infrared band for selected Kimes data (szn=sun zenith angle) dot: observations; solid line: best-fit kernel-driven model dashed: Roujean model; dash-dotted: Rahman model

Quantitative Evaluation of Edge Preserving Noise-Smoothing Filter

Donitson P P

P3TMGB P.O.Box 1089 CJIA

INTRODUCTION

Satellite images are used for lineament analysis , texture analysis and spectral analysis in geology.In order to analyze an image, we should be care to the quality of image. Unfortunately, digital images often include the noise and the effect of noise is frequently eliminated from original images using digital smoothing filter filter of intensities between the neighboring pixels. As pre-processing step commonly used edge preserving noise-smoothing filter for noise reduction. But, most of current digital smoothing filters produced blur image and eliminated the interest features.

For examples, two of edge preserving noise-smoothing filter (averaging and median) have powerful noise reduction in homogenous areas but tend to distort edges in form of blurring, over enhancement or boundaries distortion. Nagao and Matsuyama's edge preserving noise-smoothing filter is able to remove the noise without destroying the details region boundary but sometimes eliminate the interest features such as river, subtle structure, fault and others.

To avoid these problems, my research focus on an evaluation method in order to obtain the best quality of images and the biggest quantitatively calculated of pixel numbers of correct detected edge (signal) and the lowest quantitatively calculated of pixel numbers of false detected edge (noise) through comparison four different kinds of edge preserving noise-smoothing filter techniques. Approximation method of edge preserving noise-smoothing filter have characteristics as follows: enhance subtle structure, edge preserving, and noise cleaning in homogenous/heterogenous areas without distortion of edges, keep topographic features and produce unblur image.

EDGE PRESERVING NOISE - SMOOTH-ING FILTER

Edge preserving noise-smoothing techniques are a class of non-linear noise cleaning filters. These algorithm have been proposed to reduce the effect of random noise. That filters also share the simplicity of local operation and selective use of neighboring pixels in order to approximate the ideal image. Before starting a discussion of qualitative and quantitative evaluation, I present a brief description of the algorithm of edge preserving noise-smoothing filter as follows :

A. AVERAGING FILTER

It is interesting to consider of linearly weigthed (i.e. weght is equal to 1) neighbors averaging for comparison purposes, in non-linear methods of noise reduction. If the noise in an image appears as random,

uncorrelated and additive error that can be reduced by replacing of varions greylevel with local average.

B. MEDIAN FILTER

Median filter is almost similar with the averaging filter in that it uses the local median instead of local mean. The median over a local neighborhood does not respond to an edge, but it is very sensitive to extreem values and it can be concerned to the results confirm its basic characteristics in order to edge preservation and noise reduction.

C. NAGAO AND MATSUYAMA'S EDGE PRESER -VING NOISE - SMOOTHING FILTER

Their filter proposed edge preserving noise-smoothing filter using nine elongated bar mask arround the point instead of five rectangular masks. Their filter can smooth_out the noise from an image by averaging greylevel of the minimum variance area and their filter reportedly that their filter remove the noise without destroying the detail of region boundary.

D. DEVELOPMENT OF EDGE PRESERVING NOISE-SMOOTHING FILTER

This method is similar to median and averaging filter in that it uses the local median instead of the local mean of eight directions point of compass on minimum deviation between median value of each direction and greylevel value at the meet point of eight directions point of compass but deviation at the meet point should not equal to zero. These method over a local neighborhood respond to an edge, and sensitive to extreem values and it can be concerned to the results confirm its basic characteristics in order to reduce the noise and edge preservation. These filter will execute on eight directions point of compass and the operation step as follows :

a. choosing size of window operation (3X3, 5X5,..) then ordering the greylevel value by means sub pixel by sub pixel. The value between two closest pixels is equal to average ve lue of two closest pixels.

b. sequencing the greylevel value by means sub pixel by sub pixel of each direction in ascending order which is available on the window operation.

c. selecting median valueon the middle of sequencing or-der in step b.

d. calculating deviation between median value with grey-level value at the meet point of eight directions point of compass.

e. comparing the results on step d for all directions and - then find the minimum deviation.

f. new greylevel value for new image is equal to median value on the direction which has minimum deviation.

EVALUATION METHOD

To assess the performance of noise reduction algorithm, a specially generated test image from original image used noise signal and noise which are chracterized numerically and was done by assigning the greylevel value where selected randomly from gaussian distribution of means $\mu 1$ and $\mu 2$ respectively and variance $T\wedge 2$. A test image was generated at signal to noise ratio (SNR) equal to 25, 49, 81 and 100. The SNR was defined by Pratt and later used by Kitchen and Rosenfeld in the evaluation of edge detection.

$$SNR = ((\mu 1 - \mu 2)/T)**2 \quad ....(1)$$

EXPERIMENT
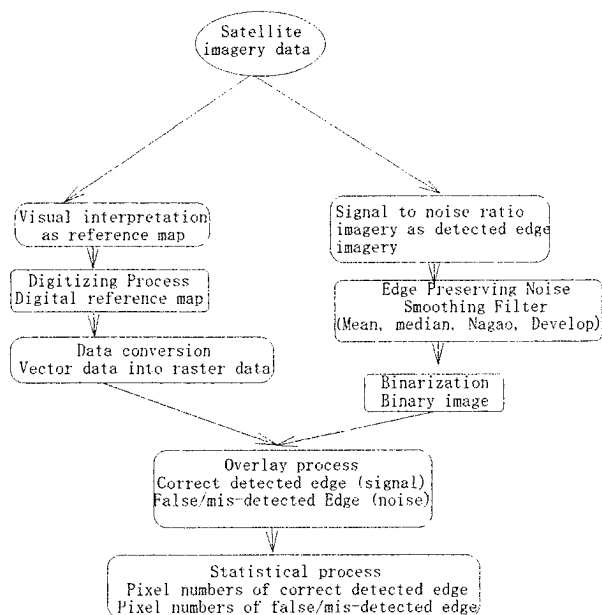
Fig. 1. Flow chart of quantitatively evaluated

DISCUSSION

Noise reduction step as pre-processing is useful in order to smooth_out the noise from original image, preserved the edge, enhance the quality of an image, keep topographic features and enhance the subtle structures.

Firstly, make variation of SNR image by means apply variety of SNR ratio into original image. So, we can see bigger SNR imagery, more clearly extracted of edge. Secondly, applied one by one of edge preserving noise-smoothing filter into SNR image. So, we can see that mean and median filter can reduce noise but produced blur image. Nagao and Matsuyama's edge preserving noise-smoothing filter can reduce not only noise but also reduce interesting features such as river, fault, subtle structures and other, even this filter produce ublur image. On my development of edge preserving noise-smoothing filter can reduce noise similar like mean and median but my filter can enhance subtle structures and keep interesting features. Thirdly, make binary image of each produced image by modification greylevel value and further, will be used as comparison to find the effectiveness of edge preserving noise-smoothing filter.

From greylevel 0 until 103 modify to 0 and from 103 to 255 modify to 1. Finally, overlay between image which produced by human interpretation and binary image. So, by using statistical process we can count the pixel numbers of correct detected edge and false detected edge. From this result and from the quality of image, we can say that development filter will give more better quality of image and more biggest quantitavely calculated. Median filter perform relatively well in both homogenous areas and edge dominated areas, and tend to distort edge in form of blurring. Averaging has powerful noise reduction in homogenous areas but tend to distort edge in form of blurring, over enhancement or boundary distortion. Nagao and Matsuyama's edge preserving noise-smoothing filter can reduce the noise but in this study that filter also reduce the interest features, even this filter do not produce blur image.

CONCLUSION

This paper has presented a method to evaluate the performance advantages of edge preserving noise-smoothing filter algorithm based on objectivity of qualitative and quantitave calculation. The evaluation studies on simulated images were made under the effect of SNR and binary of SNR. Evaluation method were used to compare the effectiveness of four different kinds of edge preserving noise-smoothing filter and the following observation were made median perform relatively well in both homogenous and edge dominated areas, and tend to distort edge in form of blurring. Averaging has powerful noise reduction in homogenous areas but tend to distort edge in form of blurring, over enhancement or boundary distortion. Nagao and Matsuyama's edge preserving noise-smoothing filter can reduce the noise but in this study that filter also reduce the interest features, even this filter do not produce blur image. Development filter produce better smooth_out of noise and better quality than the others because this filter has control for every times processing. That control is different between median value of each direction should be minimum deviation but not equal to zerro.

REFERENCES

1. M. Nagao and T. Matsuyama, "Edge preserving smoothing", CGIP 15, 1981, pp 113-129
2. I.E.Abdou and W.K.Pratt,"Quantitative design and evaluation of enhancement/thresholding edge detectors", Proc. of IEEE, 67, 1979, pp 753-763
3. L.Kitchen and A.Rosenfeld,"Edge evaluation using local edge coherence", IEEE Trans. on SMC 6,1976, pp 845-853

A Constructive Deconvolution Procedure of Bandpass Signals by Homomorphic Analysis

Alvaro L. Marenco and Vijay K. Madisetti

School of Electrical and Computer Engineering
Georgia Institute of Technology
Atlanta, GA 30332-0250, U.S.A.

ABSTRACT

A convolution may be represented as $x(.) = r(.) \star w(.)$. The goal of *deconvolution* is to extract $r(.)$ and $w(.)$ from knowledge of $x(.)$, and finds numerous applications in digital signal processing. Of practical interest in oil exploration, is the case where $w(.)$ is a seismic pressure wavelet, $x(.)$ is the observed seismic response, and $r(.)$ is the reflectivity of the earth. A number of procedures have been proposed, including predictive, deterministic, and homomorphic deconvolution. Homomorphic deconvolution has been found particularly efficient for those cases where $x(.)$ is known to be full-band. This paper presents a robust constructive procedure for efficient homomorphic deconvolution for those cases where $x(.)$ is a bandpass signal. Analysis and comparison with other methods for deconvolving bandpass signals on measured seismic traces (including the Novaya Zemlya event) illustrate the improvement in the deconvolution.

1. INTRODUCTION AND CURRENT WORK

A particular application of deconvolution is in the oil exploration field. In here, the source signal or excitation signal may be a dynamite charge or an air gun, and reflections from the subsurface reflectors are recorded by a seismometer (receiver). Ideally, if the source signal were an impulse, the received signal would be a train of impulses with varying amplitudes. Since the received signal is a convolution of the imprecisely-known source signal with the reflectivity of the reflector, the detection of the individual reflectors becomes a difficult task. The objective, therefore, is to deconvolve the effect of the source from the received signal. Homomorphic signal processing techniques are based on the transformation of a signal $x[n]$

Figure 1: Complex cepstrum transformation

into a signal $\hat{x}[n]$ as shown in Fig. 1. $X(z)$ denotes the Z transform of $x[n]$, and $\hat{X}(z)$ denotes the Z transform of $\hat{x}[n]$ and is defined by the relation

$$\hat{X}(z) = \log X(z) \qquad (1)$$

The signal $\hat{x}[n]$ is defined as the *complex cepstrum*. The complex cepstrum exists if $\log X(z)$ has a convergent power series representation of the form

$$\hat{X}(z) = \log X(z) = \sum_{n=-\infty}^{\infty} \hat{x}[n]\, z^{-n}, \; |z| = 1 \qquad (2)$$

and

$$\hat{X}(z)|_{z=e^{j\omega}} = \log \left| X(e^{j\omega}) \right| + j \arg X(e^{j\omega}) \qquad (3)$$

The sequence of coefficients in (2) represents the actual cepstrum of the signal $x[n]$ [1]. From (3), we observe that both $\log \left| X(e^{j\omega}) \right|$ and $\arg X(e^{j\omega})$ must be continuous functions of ω. Any function that satisfies (2) and the restrictions of continuity is said to be well defined for homomorphic analysis.

Now, suppose that $x[n]$ represents the convolution of two signals $r[n]$ and $w[n]$, i.e $(x[n] = r[n] \star w[n])$. Then, by using both Fourier transform and logarithmic properties, one can easily show that the system of Fig. 1 transforms two convolved signals into the sum of their individual *complex cepstra*. In the cepstral domain, these two signals could be assumed to occupy separate time frames so that deconvolution is simply a subtraction of signals. Consistent with published literature, we may assume that the complex cepstrum of the received signal has two components: a slowly-varying component and a rapidly-varying component. This suggests that the two convolved components of $x[n]$, the source and the reflection coefficient signals, can be separated by applying linear *liftering* [2] or time gating.

However, as seen from (3), homomorphic deconvolution presents some limitations when applied to signals that have bandpass characteristics. This difficulty has proved

difficult to surmount. Tribolet [3] proposed a method called bandpass mapping (BP) that transforms a bandpass signal into a full-band signal via the following transformation:

$$\tilde{\omega} = \frac{\pi(\omega - \omega_1)}{\omega_2 - \omega_1} \qquad (4)$$

where w_1 and w_2 are the cutoff frequencies. Tribolet also showed that this mapping is invertible. After liftering the resulting signal in the full-band domain, we are able to invert back and recover cepstral information pertaining to the bandpass signal. Note that, even though the basic amplitude structure of the deconvolved signal may be preserved, the polarity is not. There is also a limitation with regard to the implementation of the bandpass mapping, when realized by interpolator-decimator structures.

In the next section, we develop the proposed method and then present results of its performance on measured data from seismic records.

2. A NEW PROCEDURE FOR DECONVOLUTION OF BANDPASS SIGNALS

Given a bandpass signal $x[n] = r[n] * w[n]$, where $r[n]$ is an impulse train sequence and $w[n]$ is a pressure wavelet, we define a signal $X_{est}(z) = X(z) + N(z)$, and a signal $Y(z) = X_{est}(z) + S(z)$ ($y[n] = x_{est}[n] + s[n]$), with the following characteristics:

- The signal $N(z)$ is defined as

$$N(z)|_{z=e^{j\omega}} = \begin{cases} 0 & \omega_1 \le |\omega| \le \omega_2 \\ \epsilon & \text{otherwise} \end{cases} \qquad (5)$$

therefore,

$$X_{est}(z)|_{z=e^{j\omega}} = \begin{cases} X(e^{j\omega}) & \omega_1 \le |\omega| \le \omega_2 \\ \epsilon & \text{otherwise} \end{cases} \qquad (6)$$

where ω_1 and ω_2 are the cutoff digital frequencies of the bandpass signal $X(e^{j\omega})$ and ϵ is any constant ($\epsilon \ll 1$).

- The signal $s[n]$, called the *supplemental signal*, is the sum of the original signal $x_{est}[n]$ and a full-band signal $s_i[n]$ with the following characteristics:

  (i) $s_i[n]$ is minimum-phase.

  (ii) $s_i[n]$ is a second-order infinite impulse response (IIR) full-band signal with a smooth spectrum.

  (iii) The locations of the poles of $s_i[n]$ are specified as follows,

$$\omega_c = \begin{cases} \frac{\pi + \omega_2}{2} & \pi - \omega_2 \ge \omega_1 \\ \omega_1/2 & \text{otherwise} \end{cases} \qquad (7)$$

(iv) The bandwidth and maximum bandwidth are given by:

$$BW \approx \frac{2(1-r)}{\sqrt{r}} \ (r \text{ is the radius of the pole})$$
$$BW_{max} = \pi - w_c$$
$$\qquad (8)$$

- In general, $y[n]$ can also be expressed as a linear combination of both $s[n]$ and $x_{est}[n]$, that is

$$y[n] = \beta_1 x_{est}[n] + \beta_2 s[n] \qquad (9)$$

where β_1 and β_2 are any real constants, subject to the condition that

$$\left| \frac{\beta_1 X_{est}(z)}{\beta_2 S(z)} \right| < 1 \qquad (10)$$

- $y[n]$ is full-band signal (transitively, from the full-band nature of $s_i[n]$ and $s[n]$) and suitable for homomorphic analysis.

The objective of this *constructive procedure* is to recover the complex cepstrum $\hat{x}_{est}[n]$, as defined in (1) from the full-band signal $y[n]$.

By taking the z-transform of $y[n]$, we have

$$Y(z) = X_{est}(z) + S(z) = S(z)\left(\frac{X_{est}(z)}{S(z)} + 1\right) \qquad (11)$$

The complex cepstrum $\hat{Y}(z)$ is then given by

$$\hat{Y}(z) = \log(Y(z)) = \log(S(z)) + \log\left(\frac{X_{est}(z)}{S(z)} + 1\right) \qquad (12)$$

Further derivations from (12) lead to

$$\hat{X}_{est}(z) = \log\left(\hat{Y}(z) - \hat{S}(z)\right) + \hat{S}(z)$$
$$- \log\left(\sum_{n=0}^{\infty} \frac{(-1)^n}{n+1} \left(\frac{X_{est}(z)}{S(z)}\right)^n\right), \left|\frac{X_{est}(z)}{S(z)}\right| < 1 \qquad (13)$$

In analyzing our derivation, called Bandpass Transformation (BPT), the following observations can be made:

- One can always construct a function $S(z)$ such that $\left|\frac{X_{est}(z)}{S(z)}\right| < 1$. Consequently, $0 < |\Gamma(z)| < M_r < 1$, where M_r is the radius of convergence and $\Gamma(z) = \sum_{n=0}^{\infty} \frac{(-1)^n}{n+1} \left(\frac{X_{est}(z)}{S(z)}\right)^n$.

- Each term in equation (13) is well defined and suitable for homomorphic analysis.

- This additive approach provides us with a signal in which low power components have been increased to a reasonable degree so that when complex cepstrum analysis is applied, the resulting components do not become either negatively large or unbounded. Moreover, this new constructive procedure uses additional information from the signal that would not be retained if we were to process it directly.

1593
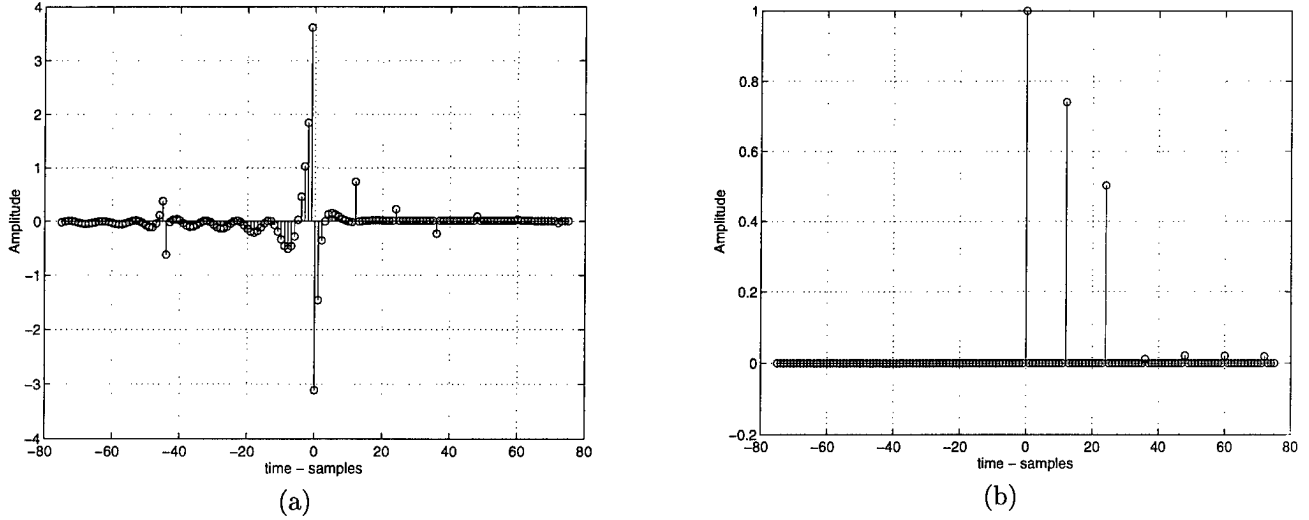
Figure 2: Results for example 1 using the BPT method. (a) cepstrum of $x[n]$ (b) reflection coefficients sequence corresponding to $r[n]$.

3. NUMERICAL RESULTS AND COMPARISON WITH CURRENT WORK

We now present four experimental results that validate the improved performance claimed by the proposed procedure. The signals used for experiments 1-3 are defined as follows:

$$r[n] = r_0\delta[n] + r_M\delta[n - M] + r_{2M}\delta[n - 2M] \qquad (14)$$

and

$$w[n] = \frac{2.51826}{\sqrt{2\pi}}[(0.160n - 3.4641)^2 - 1]$$

$$. \exp(-\frac{1}{2} (0.160n - 3.4641)^2) \quad (0 \le n \le 43) \qquad (15)$$

where $\delta[n]$ is the Dirac delta function, and $w[n]$ is a Ricker wavelet [1] [3, 4]. A seismic wavelet $x[n]$ was generated as $x[n] = r[n] \star w[n]$. The objective is to extract the reflection sequence $r[n]$ from the given seismic trace $x[n]$. Three methods are used in determining the reflection coefficients: our proposed method (BPT), a direct method [2] and Tribolet's bandpass mapping. The waveforms for experiment 4 correspond to a seismic event recorded at the University of Alberta Edmonton Seismological Observatory near Leduc, Alberta. The details of the experiment and its recording information are described in [5].

---

[1] A signal that resembles those recorded in a seismometer and defined as the second derivative of the Gaussian (or error density) function.

[2] Homomorphic analysis is applied directly to the original bandpass signal.

3.1. Example 1 - Ricker Wavelet

The seismic wavelet has the following specifications (assuming a sampling frequency of 250 Hz, $M = 12$, and a 2048-point FFT):

$$\omega_1 = 0, \, \omega_2 = 0.6786 \text{ (both in radians)}, \, \epsilon = 1 \times 10^{-5}$$

Using (7) and (8), a supplemental signal was constructed

$$BW = 20 \text{ Hz}, \quad \omega_c = 1.9101 \text{ (76 Hz)}, \quad F_s = 250 \text{ Hz} \qquad (16)$$

Fig. 2a shows the complex cepstrum $\hat{x}[n]$. Of interest are the impulses at integer multiples of $M = 12$. These are contributed by $\hat{r}[n]$, and correspond to the rapidly-varying component, while the slowly-varying component corresponds to $\hat{w}[n]$. Since the interarrival time of the rapidly-varying component is easily detected, a comb lifter, $g[n]$, was used that can be defined as:

$$g[n] = \sum_{i=1}^{85} \delta[n - 12i], \quad 1 \le n \le 2048 \qquad (17)$$

The signal $r[n]$ is shown in Fig. 2b. This sequence is the approximation to $r[n]$ obtained by homomorphic deconvolution and the proposed BPT procedure. Both amplitudes and delays are accurately determined by BPT. Table 1 shows the numerical results and definition of parameters r_n's.

3.2. Example 2 - Resolution of Overlapping Components

In this example, we use a reflection coefficient sequence with a sample interval $M = 6$. A supplemental signal
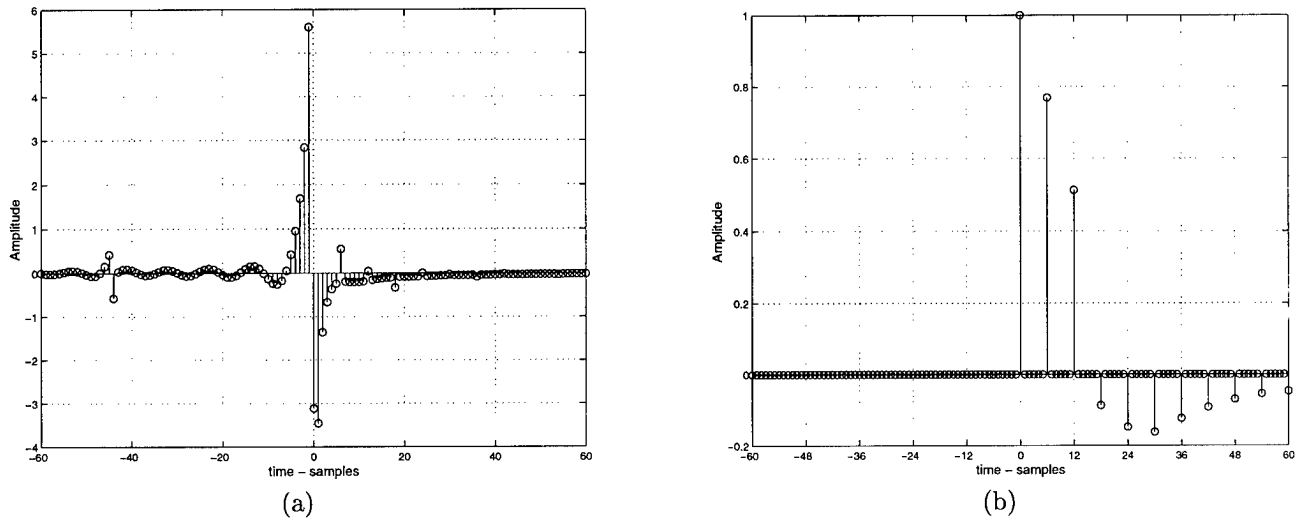
Figure 3: Results of applying homomorphic deconvolution to signal $x[n]$ using the BPT (a) complex cepstrum (b) reflection coefficients sequence.

with a bandwidth of 20 Hz was generated. With regard to frequency content, and values of r_n's, the same specifications from Example 1 were used. The complex cepstrum and the reflection coefficient sequence are both shown in Fig. 3. In this example, we have shown that our proposed method is invariant to the interarrival time of the reflection coefficients. The next example illustrates the robustness of the BPT in which the polarity of the reflection coefficient sequence is changed and the sample interval is kept identical.

3.3. Example 3 - Detection of Signal Polarity

The specifications for Example 3 remain the same as those given in example 1. However, the polarity of the reflection coefficient sequence at $n = 6$ was changed:

$$r[n] = \delta[n] - 0.75\ \delta[n - 6] + 0.5\ \delta[n - 12] \qquad (18)$$

Results for examples 1-3 are summarized in Table 1. We also show the results obtained using the direct method and the BP mapping.

3.4. Example 4 - Novaya Zemlya Experiments

We analyzed the teleseismic wavelet for the Novaya Zemlya explosion. Fig. 4a shows the original seismic waveform as given in [5]. A second waveform that is important for our discussion corresponds to the crustal impulse response of the Leduc crust as calculated by Jensen and Ellis [6] and Sommerville and Ellis [7]. This is shown in Fig. 4b. Similar to the previous examples, we also simulated and compared the performance of the BPT, the

direct method and Tribolet's BP mapping. The goal of the experiments was to extract the source wavelet and the crust impulse response from the seismic signal using the BPT and homomorphic deconvolution. An analysis of the signals of Fig. 4 suggests that our proposed method can be a valuable procedure to detect reflectivity from layers deeper than those detected by the other methods described in this paper. Most of the prolonged oscillatory behavior of the original seismic wavelet is present in our extracted signal, extending up to about 4 seconds, meaning the detection of a longer path or deeper distances.

4. SIGNIFICANCE OF THE RESULTS

In this paper, a constructive procedure for bandpass signals has been applied to solve the limitation that such signals present when analyzed by homomorphic deconvolution. Our additive approach has provided us with a signal in which low power components have been increased to a degree so that when complex cepstrum analysis is applied, the resulting components do not become either negatively large or unbounded. This constructive procedure also uses additional information from the signal that is not retained if it were to be processed directly. We have presented a series of experiments that validate the claim of improvement: (1) increased accuracy and resolution of signal polarity, (2) simplicity (no sampling rate conversion), (3) better estimation from overlapping components, and (4) detection of reflectivity characteristics from deeper layers.

Table 1: Summary of results for experiments 1-3 using the BPT, the *direct method*, and *Tribolet's method*.

Methods	Experimental Results from Seismic Data								
	Ricker Wavelet $M = 12$			Resolution of Overlapping Components $M = 6$			Detection of Signal Polarity $M = 6$		
	n			n			n		
	0	12	24	0	6	12	0	6	12
Expected Results (r_n)	1	0.75	0.5	1	0.75	0.5	1	-0.75	0.5
Proposed Method	1.0000	0.7402	0.5021	1.0000	0.7687	0.5128	1.0000	-0.7410	0.4950
Tribolet's Method	1.0002	0.7604	0.4835	1.0000	-0.2771	0.3404	0.9999	-0.2995	0.5010
Direct Method	1.0000	0.5736	0.3093	1.0000	0.5480	0.1925	1.0000	-0.6186	0.4003

(a) (b) (c)

(d) (e)
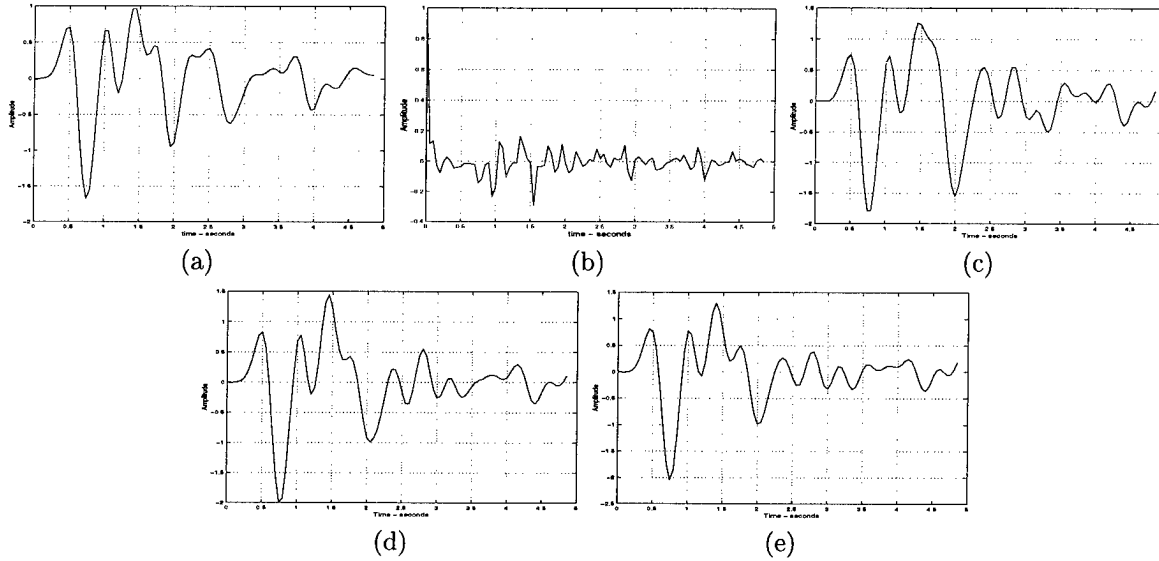
Figure 4: The Novaya Zemlya experiments (a) original seismic wavelet (b) crustal impulse response (c)-(e) results of convolving the crust impulse response of (b) and the extracted source wavelets by using the BPT method, the direct method, and the BP mapping respectively.

5. REFERENCES

[1] A. V. Oppenheim and R. W. Schafer, *Discrete-Time Signal Processing.* Signal Processing, Englewood Cliffs, N.J.: Prentice-Hall, 1989.

[2] B. P. Bogert, M. J. Healy, and J. W. Tukey, "The quefrency alanysis of time series for echoes: Cepstrum, pseudo-autocovariance, cross-cepstrum and saphe cracking," in *Time Series Analysis* (M. Rosenblatt, ed.), ch. 15, pp. 209–213, New York: John Wiley & Sons, 1963.

[3] J. M. Tribolet, *Seismic Applications of Homomorphic Signal Processing.* Signal Processing, Englewood Cliffs, N.J.: Prentice-Hall, 1979.

[4] E. A. Robinson and S. Treitel, *Geophysical Signal Analysis.* Prentice-Hall, 1980.

[5] T. J. Ulrych, O. G. Jensen, R. M. Ellis, and P. G. Somerville, "Homomorphic deconvolution of some teleseismic events," *Bulletin of Seismological Society of America*, vol. 62, pp. 1269–1281, October 1972.

[6] O. G. Jensen and R. M. Ellis, "Generation of synthetic seismogram using linear system theory," *Canadian Journal of Earth Sciences*, vol. 8, pp. 1409–1422, 1971.

[7] P. G. Somerville and R. M. Ellis, "P-coda evidence for a layer of anomalous velocity in the crust beneath Leduc, Alberta," *Canadian Journal of Earth Sciences*, vol. 9, pp. 845–856, 1972.

CUBIC CONVOLUTION FOR ONE-PASS RESTORATION AND RESAMPLING

Stephen E. Reichenbach   *Kevin Haake*
reich@cse.unl.edu   *khaake@cse.unl.edu*

Computer Science & Engineering Department
University of Nebraska – Lincoln
Lincoln, NE 68588-0115

ABSTRACT

This paper describes an efficient filter that implements resampling and restoration of digital images in a single pass. The approach is to derive optimal parameters for a piecewise-cubic, reconstruction function based on a comprehensive model of the imaging process that accounts for acquisition blurring, sampling, noise, and reconstruction artifacts. For many data products produced from remotely sensed images, piecewise-cubic reconstruction is the standard algorithm for resampling. For these products, restoration with the optimal piecewise-cubic function requires virtually no additional processing resources and can significantly improve radiometric fidelity.

1. INTRODUCTION

This paper describes an efficient filter that resamples and restores digital images in a single pass. Resampling involves reconstruction, the process of determining image values at arbitrary spatial locations from the discrete pixels. Reconstruction is required in many imaging applications and is particularly important in remote sensing where images are resampled to correct for geometric distortion and to register, rescale, or otherwise remap. Restoration involves correcting for degradations introduced during the imaging process to obtain more accurate estimates of the scene radiance field. Restoration can yield significant improvements in the accuracy of radiometric measures by accounting for degradations introduced during image acquisition, including

- blurring related to atmospheric transmission, optical components, and the spatial integration of detectors;

- noise caused by the inherent variability of radiance fields, quantization, and various instrument phenomena; and

- artifacts related to aliasing of high spatial-frequency scene components in the sampled image.

In addition to these acquisition degradations, resampling usually is implemented with reconstruction methods that use a local weighted average (e.g., nearest-neighbor or bilinear interpolation) and, as such, involve additional blurring and sampling. Display devices also reconstruct a continuous radiance field by forming a display spot for each pixel — effectively blurring the discrete values to form a continuous image.

Traditional restoration methods have focused on blurring and noise, with the effects of sampling and reconstruction frequently not considered. As Schreiber writes, the effects of these processes "on the overall performance of systems is generally ignored in the literature, but is actually very large.[1, p. *vi*]" Optimal approaches to restoration must be based on a comprehensive system model that adequately accounts for sampling and reconstruction as well as blurring and noise.

The filter developed in this paper is a piecewise cubic reconstruction function. The piecewise cubic function is widely used in resampling to interpolate discrete pixel values, an operation commonly called cubic convolution or, in its one-parameter form, parametric cubic convolution (PCC). The piecewise cubic is efficient because it uses low-order polynomials and has a small region of spatial support. The piecewise cubic requires more computation than simpler nearest-neighbor and linear interpolation functions, but performs much better and can be parameterized for specific systems. For many data products produced from remotely sensed images, piecewise cubic reconstruction is the standard algorithm for resampling. For these products, restoration with the optimal piecewise cubic function requires virtually no additional processing resources and can significantly improve radiometric fidelity.

2. IMAGING SYSTEM MODEL

This paper employs the model of the basic components of the digital image acquisition process presented in [2]. By nature, the model is a simplification of the more complex interactions in real imaging systems, but the model captures the most fundamental effects of the acquisition process. The image acquisition process has three phases: image formation, sampling, and quantization. Mathematically, the process that produces

the digital image p is modeled as:

$$p[n] = \int_{-\infty}^{\infty} h(n - x) s(x) \, dx + e[n] \qquad (1)$$

where s is the scene radiance field, h is the image acquisition point-spread function (PSF), and e is error or noise. Pixels are indexed with integer coordinates $[n]$ and the continuous spatial coordinates (x) are normalized to the sampling interval. Function values are expressed on the digital number scale. This is a fairly modest model, but it is adequate to demonstrate the radiometric issues in resampling and to develop an improved restoration and resampling technique.

Image acquisition can be expressed equivalently in the spatial-frequency domain, where system functions are characterized by their transfer functions and instead of convolution we have the pointwise product. The equivalent frequency domain equation for $\hat{p}$, the Fourier transform of the image, is:

$$\hat{p}(v) = \sum_{\nu=-\infty}^{\infty} \hat{h}(v - \nu) \hat{s}(v - \nu) + \hat{e}(v) \qquad (2)$$

where spatial frequencies (v) are normalized to the sampling frequency, $\hat{s}$ is spatial-frequency spectrum of the scene, $\hat{h}$ is the acquisition transfer function, and $\hat{e}$ is the spatial-frequency spectrum of the noise.

Convolution of the digital image p and the reconstruction PSF f is:

$$r(x) = \sum_{n=-\infty}^{\infty} f(x - n) p[n]. \qquad (3)$$

The corresponding frequency-domain equation for reconstruction is

$$\hat{r}(v) = \hat{f}(v) \hat{p}(v) \qquad (4)$$

where $\hat{f}$ is the reconstruction transfer function.

3. IMAGING SYSTEM ANALYSIS

There is a tradeoff in system design between errors related to blurring and errors related to aliasing. We begin by expressing quantitatively our goal to have the reconstructed image be as accurate a measure of the scene as possible. Linfoot[4] used the expected mean-square error between the scene s and the reconstructed image r

$$S^2 = E\left\{ \int_{-\infty}^{\infty} |s(x) - r(x)|^2 \, dx \right\}$$
$$= E\left\{ \int_{-\infty}^{\infty} |\hat{s}(v) - \hat{r}(v)|^2 \, dv \right\} \qquad (5)$$

to define image fidelity.

The expression for expected mean-square error can be written to make clearer the tradeoff between blurring and aliasing in system design:

$$S^2 = \int_{-\infty}^{\infty} \Phi_s(v) \left| 1 - \hat{h}(v) \hat{f}(v) \right|^2 \, dv$$
$$+ \int_{-\infty}^{\infty} \left(\sum_{\nu=-\infty}^{\infty} \Phi_s(v - \nu) \left| \hat{h}(v - \nu) \right|^2 \right) \left| \hat{f}(v) \right|^2 \, dv$$
$$+ \int_{-\infty}^{\infty} \Phi_e(v) \left| \hat{f}(v) \right|^2 \, dv \qquad (6)$$

where Φ_s is the scene power spectrum and Φ_e is the noise power spectrum. This analysis assumes that the noise is signal-independent and that sidebands of the scene spectrum that alias to the same frequency are uncorrelated.

The first term represents the error associated with blurring the image by both the acquisition PSF h and the reconstruction PSF f. To minimize this term, $\hat{h}$ and $\hat{f}$ should be equal to one at all frequencies (which would mean that the system should not blur during acquisition nor during reconstruction). The second term represents the error associated with the aliasing. To minimize this term, $\hat{h}$ and $\hat{f}$ should be equal to zero at all frequencies (which would mean that the system would eliminate aliasing by not passing any signal). So, there is a clear tradeoff between blurring and aliasing. The final term is associated with system noise. To minimize this term, $\hat{f}$ should be equal to zero at all frequencies (which would mean that the system would eliminate noise by not passing any signal).

4. THE OPTIMAL PIECEWISE CUBIC

The optimal piecewise cubic maximizes radiometric fidelity (i.e., minimize the expected mean-square error in the resampled values relative to the scene radiance field) based on the end-to-end imaging system model presented in Section 2. The spatial support of the piecewise cubic function is between ± 2. A cubic polynomial is defined over each unit interval (with knots at 0, ± 1, and ± 2), so there are 16 degrees of freedom in the general form. To insure a continuous and smooth reconstruction, the following conditions are required for the function derivative and value at each knot:

$$\lim_{x \to k-} f'(x) = \lim_{x \to k+} f'(x) \qquad (7)$$
$$\lim_{x \to k-} f(x) = \lim_{x \to k+} f(x) \qquad (8)$$

for $k = 0, \pm 1, \pm 2$. This leaves six degrees of freedom that can be identified with the function slope and value at the internal knots:

$$\alpha_k = f'(k) \qquad (9)$$
$$\beta_k = f(k) \qquad (10)$$

for $k = 0$ and ± 1. To insure reconstruction does not change the mean, the integral of the cubic must be 1:

$$\int_{-\infty}^{\infty} f(x) \, dx = 1. \tag{11}$$

This constraint removes one of the degrees of freedom, which can be identified with the function value at 0:

$$\beta_0 = 1 - \beta_{-1} - \beta_1. \tag{12}$$

Separating components by parameter, the cubic is

$$f(x) = f_0(x) + \alpha_{-1}f_1(x+1) + \alpha_1 f_1(x-1) + \alpha_0 f_1(x)$$
$$+ \beta_{-1}f_2(1/2 - x) + \beta_1 f_2(x - 1/2) \tag{13}$$

with

$$f_0(x) = \begin{cases} 0 & \text{if } |x| \geq 1 \\ -2x^3 - 3x^2 + 1 & \text{if } -1 \leq x \leq 0 \\ 2x^3 - 3x^2 + 1 & \text{if } 0 \leq x \leq 1 \end{cases}$$

$$f_1(x) = \begin{cases} 0 & \text{if } |x| \geq 1 \\ x^3 + 2x^2 + x & \text{if } -1 \leq x \leq 0 \\ x^3 - 2x^2 + x & \text{if } 0 \leq x \leq 1 \end{cases}$$

$$f_2(x) = \begin{cases} 0 & \text{if } |x| \geq \frac{3}{2} \\ 2x^3 + 6x^2 + 9x/2 & \text{if } -\frac{3}{2} \leq x \leq -\frac{1}{2} \\ -4x^3 + 3x & \text{if } -\frac{1}{2} \leq x \leq \frac{1}{2} \\ 2x^3 - 6x^2 + 9x/2 & \text{if } \frac{1}{2} \leq x \leq \frac{3}{2}. \end{cases}$$

With $\beta_{-1} = \beta_1 = 0$ and $\alpha_0 = 0$, these equations are identical to those in [3]. With $\beta_{-1} = \beta_1$ and $\alpha_0 = 0$, these equations are identical to those in [5].

The Fourier transform of this cubic is:

$$\hat{f}(v) = \hat{f}_0(v) + \alpha_{-1}\hat{f}_1(v) e^{i2\pi v} + \alpha_1 \hat{f}_1(v-1) e^{-i2\pi v}$$
$$+ \alpha_0 \hat{f}_1(v) + \beta_{-1}\hat{f}_2^*(v) e^{i\pi v} + \beta_1 \hat{f}_2(v) e^{-i\pi v} \tag{14}$$

with

$$\hat{f}_0(v) = \frac{3\sin^2(\pi v)}{\pi^4 v^4} - \frac{3\sin(2\pi v)}{2\pi^3 v^3}$$

$$\hat{f}_1(v) = i\left(\frac{1}{\pi^3 v^3} + \frac{\cos(2\pi v)}{2\pi^3 v^3} - \frac{3\sin(2\pi v)}{4\pi^4 v^4}\right)$$

$$\hat{f}_2(v) = i\left(\frac{-3\cos(\pi v)}{2\pi^3 v^3} + \frac{3\cos(3\pi v)}{2\pi^3 v^3} + \frac{6\sin^3(\pi v)}{\pi^4 v^4}\right).$$

The derivation that yields the solution for the optimal piecewise cubic can be expressed as a more general problem. To this end, we generalize the filter as:

$$\hat{f}(v) = \hat{f}_0(v) + \sum_{k=1}^{K} \gamma_k \hat{f}_k(v). \tag{15}$$

For the piecewise cubic function in Equation PCC, there are five parametric components (i.e., parameters α_{-1}, α_0, α_1, β_{-1}, and β_1) and so $K = 5$.

Then, in order to minimize the expected mean-square error, substitute this expression into Equation 6, take the derivative with respect to filter parameters γ_k, and set the result equal to zero. For real-valued imaging systems, this yields the system of linear equations:

$$\sum_{j=1}^{K} \gamma_j \Re\left(\int_{-\infty}^{\infty} \Phi_r(v) \hat{f}_j(v) \hat{f}_k^*(v) \, dv\right) =$$
$$\Re\left(\int_{-\infty}^{\infty} \left(\Phi_{s,r}(v) - \Phi_r(v) \hat{f}_0(v)\right) \hat{f}_k^*(v) \, dv\right) \tag{16}$$

for $k = 1..K$. This is a system of K linear equations with K unknowns. Solving for the values of γ yields the optimal parameters.

5. CONCLUSION

This paper presents the development of an optimal piecewise cubic filter for restoration and resampling. The derivation minimizes the expected mean-square difference between the scene radiance field and the resulting image based on an end-to-end model of the imaging process. Our current work on this filter involves the determination of the optimal values for the planned Landsat 7 Enhanced Thematic Mapper (ETM+) and simulation experiments for the Landsat 7 imaging system using images from the Advanced Solid-State Array Spectro-radiometer (ASAS).

6. ACKNOWLEDGEMENTS

7. REFERENCES

[1] William F. Schreiber. *Fundamentals of Electronic Imaging Systems: Some Aspects of Image Processing.* Springer-Verlag, New York, NY, 1986.

[2] Stephen E. Reichenbach, Stephen K. Park, Rachel Alter-Gartenberg, and Zia-ur Rahman. Artificial scenes and simulated imaging. In *Stochastic and Neural Methods in Signal Processing, Image Processing, and Computer Vision*, pages 422–433. Proc. SPIE 1569, 1991.

[3] Stephen K. Park and Robert A. Schowengerdt. Image reconstruction by parametric cubic convolution. *Computer Vision, Graphics, and Image Processing*, 23:258–272, 1983.

[4] E. H. Linfoot. Transmission factors and optical design. *Journal of the Optical Society of America*, 46(9):740–752, 1956.

[5] Stephen E. Reichenbach and Stephen K. Park. Two-parameter cubic convolution for image reconstruction. In *Visual Communications and Image Processing IV*, pages 833–840. Proc. SPIE 1199, 1989.

Landsat Thematic Mapper Band-to-Band Registration

John L. Barker and Jennifer C. Seiferth
1) Code 923, NASA Goddard Space Flight Center, Greenbelt MD 20771
2) Hughes STX, 4400 Forbes Boulevard, Lanham, MD 20706

ABSTRACT

This paper on Band-to-Band (B-B) registration of Landsat satellite Thematic Mapper (TM) imagery has three objectives. Firstly, it documents a one dimensional (1D) Z-score analytical Fast Fourier Transform (FFT) procedure for measuring along-scan misregistration in raw uncalibrated and unresampled TM imagery to a precision better than ± 0.002 pixels. Secondly, it demonstrates that, with the TDRSS antenna quiet, the largest within-scene coherent changes in B-B sample misregistration (SM) occur at the same 2 Hz frequency as the most significant changes in measured on-orbit scan mirror errors in the instrument for Landsat-4 (L4), and at an additional common 1.2 Hz peak for Landsat-5 (L5). Thirdly, it demonstrates that the cluster of frequency peaks in the FFTs of spacecraft x-axis gyro and Angular Displacement Sensor (ADS) telemetry below 3 Hz are not seen in FFTs of normalized plots of SM versus forward scan number. The 1984 142.7 msec scan time on L5 was observed to increase by 1.5 msec in 8 years.

PURPOSE

This paper is part of a larger study to characterize the geometric stability over time of procedures used to create systematically corrected resampled products from the TM sensors on L4 and L5 that were launched in 1982 and 1984, respectively. This larger study is also designed to provide potential algorithms for the on-orbit characterization of the geometric stability of the Enhanced Thematic Mapper (ETM+) scheduled for launch on Landsat-7 in 1998.

BACKGROUND

Spatial misregistration decreases spectral contrast. Raw satellite imagery is not innately registered. Traditionally, bands are brought into registration during ground processing to a geometrically resampled final product and then resampled again based on use of ground control points and maps of terrain before being reprojected into map compatible formats. This latter process assumes that all within-scene corrections have been made as part of the initial "systematic" processing.

1982-1985 Landsat Image Data Quality Assessment (LIDQA) B-B registration studies were made on raw and

processed imagery with a precision of about 0.02-0.05 pixels [1,2]. Sample misregistration results were reported as single numbers for quadrants, or less frequently, for full scenes, but not for within-scene variation. The primary engineering study documenting observed variations in instrument and spacecraft characteristics attributed the 2 Hz peaks in the gyro and ADS telemetry to cycling of the four spacecraft reaction wheels every 30 seconds over a period of 2 minutes [3]. The assumption is that much, if not all, of this observed within-scene geometric variation is properly corrected out in the resampled systematically corrected products available to the user community.

The TM imagers each have two focal planes. The primary focal plane has three 30 meter (m) bands (B1, B2, and B3) in the visible (0.45 to 0.69 microns (μm)) and one near infrared band (B4 at 0.76-0.90 μm). The cold focal plane has two 30 m bands (B5 and B7) in the shortwave infrared nominally centered at 1.6 and 2.2 μm [4]. Observed changes in the B-B registration of the reflective bands of the TM sensors between pre-launch and on-orbit measurements have been attributed to one-time changes that occurred during the launch phase. Since the ground processing correction algorithms have assumed unchanging registration on-orbit, part of the purpose of the larger study is to establish whether or not there have been any further changes in B-B registration with time.

PROCEDURE

It is necessary to study raw, unresampled imagery with associated telemetry to be able to correlate misregistration results with telemetry. Landsat World Reference System (WRS) Path/Row and acquisition dates for the four images that were used in this study were: L4 41/28-29 (11/24/82) and L5 172/71-72 (6/20/84). The raw Level 0 (L0) imagery and the associated payload correction data (PCD) were obtained from the U.S. Geological Survey's Eros Data Center (EDC).

The authors developed an algorithm to determine the 1D misregistration between bands. This algorithm computed the SM between two bands one line at a time by cross-correlating the center 2048 pixels of each line pair in the frequency domain and then calculating the subpixel misregistration by applying a cubic spline interpolation to the correlation result.

To measure within-scene change in misregistration between two image bands for a single detector, the algorithm was used

to calculate the SM as a function of forward scan number. Fig.1 is an example of the changes in registration for a single detector (16) in B3 relative to the same detector in B5. In order to give all detectors equal weighting, the individual results for each of the 16 detectors were converted to "Z" scores and averaged into a single sample misregistration (SMZ) for each of the 187 forward scans in the scene. The SMZ plot for the B3 to B5 comparison is shown in Fig.2. Six specific band-pairs were calculated. To relate results to telemetry, the FFTs of the SMZ plots were calculated. The resulting misregistration FFT for B3 to B5 is shown in Fig.3. Instrument telemetry was extracted from the image supplementary data file. The handful of single points in the slowly varying telemetry that were dropped out were replaced with averages of adjacent points in order to provide continuous data for the FFT analyses. Examples of telemetry FFTs are shown in Fig.4 and Fig.5.

FFTs of First-Half and Second-Half Scan Mirror errors from the PCD contained identical 1.99 and 1.20 Hz peak patterns as in the SM results, as in Fig.4.

FFTs of L5 telemetry of both scenes revealed nearly reproducible x-axis ADS peaks of decreasing magnitude at 1.95, 2.15, 2.21, 2.03, 0.78 and 0.40 Hz. Peaks in the y- and z-axes ADS FFTs were smaller. The y-axis peaks were at 1.1 and 0.8 Hz, and the z-axis peaks were at 1.95, 0.78, 1.6, and 0.4 Hz. L5 x-axis gyro peaks of decreasing magnitude were at 0.40, 1.95, 2.15, 2.21, 2.03 and 0.78 Hz, as in Fig.5. The y axis did not have peaks and the z-axis had peaks at 0.4 and 0.8 Hz.

FFTs of L4 ADS showed a single 2.27 Hz peak in the x- and y-axes, and smaller amplitude peaks in the z-axis at 0.8, 2.3, 1.8, 1.4 and 1.0 Hz. FFTs of L4 gyro showed no peaks in the y- or z-axes and small x-axis gyro peaks of decreasing amplitude at 2.27, 0.38, 0.8, and 0.6 Hz.

RESULTS

The sixteen detectors in each of the six band pairs for the four scenes showed a relatively similar 2x range of standard deviations (SD) from $\pm$ 0.1 to $\pm$ 0.2 pixels. However, there was within-scene systematic and coherent behavior, as seen in Fig.1 and Fig.2. One measure of the precision of the 1D-Z score procedure is the magnitude of the error bars on each of the points in Fig.2. These SMZ error bars were lowest for the within-focal plane band pairs (B1 to B3 and B5 to B7) at $\pm$ 0.01 and $\pm$ 0.02 for L4 and L5, respectively. Between-focal plane band-pairs (1 to 7, 3 to 7, 1 to 5, and 3 to 5) were up to a factor of 5x and 10x higher for L4 and L5, respectively. Identical SD SMZ results were obtained for each band-pair in adjacent scenes to within $\pm$0.01. The inference is that the repeatable larger changes of registration for between-focal plane band-pairs are real and are either instrument- or scene-based, not procedure limited. The reproducibility of the smallest SMZ SD error bars of 0.01 when combined with the actual observed SD range of 0.1-0.2 pixels indicates a precision for the 1D-Z score procedure of $\pm$0.001-$\pm$0.002 pixels for the band average misregistration. Significance was demonstrated by the 0.7-0.9 correlations between individual detector results within band-pairs and by the 0.9-1.0 correlations between the four average misregistration patterns for between focal plane band pairs. This procedure therefore provides the desired high sensitivity for future studies of the origin of within- and between-scene variability of B-B registration.

FFTs of the SM results showed a single peak at 1.99 Hz for all six band-pair plots in both L4 scenes versus scan number. Plots of all pairs showed the same peak in the two L5 scenes, plus a smaller peak at 1.20 Hz, as in Fig.3.

CONCLUSIONS

A 1D Z-score SM procedure has been demonstrated with a precision of better than $\pm$0.002 30m pixels.

FFTs of Scan Mirror Errors were similar to SM FFTs.

Below 3 Hz, ADS and gyro FFTs were not like SM FFTs.

During the course of this study, it was observed that the average time between forward scans on L5 increased from 142.7 to 144.2 msec from 1984 to 1992. This 0.75 msec increase in a scan is equivalent to about 80 30m pixels.

REFERENCES

[1] E. Malaret, L. Bartolucci, D. Lozano, P. Anuta and C. McGillem, "Landsat-4 and Landsat-5 Thematic Mapper Data Quality Analysis," Photogrammetric Eng. & Remote Sensing, vol. LI, pp. 1407-1416, Sept. 1985.

[2] J. Desachy, G. Begni, B. Boissin and J. Perbos, "Investigation of Landsat-4 Thematic Mapper Line-to-Line and Band-to-Band Registration and Relative Detector Calibration," Photogrammetric Eng. & Remote Sensing, vol. LI, pp. 1291-1298, Sept. 1985.

[3] J Sudey, Jr. and J. Schulman, "In Orbit Measurements of Landsat-4 Thematic Mapper Dynamic Disturbances," 35th Congress of the International Astronautical Federation, Lausanne, Switzerland, October 7-13, 1984.

[4] B. Markham and J. Barker, "Spectral Characterization of the Landsat Thematic Mapper Sensors," Int. J. Remote Sensing, vol. 6, pp. 697-716, 1985.

FIGURES

The illustrative results in the five figures below are derived from a raw uncalibrated unresampled Level-0 Landsat-5 (L5) Thematic Mapper (TM) image and its associated Payload Correction Data. These specific within-scene analyses are derived from a TM scene acquired on June 6, 1984 on Path 172 and Row 71 of the Landsat-4/5 World Reference System. They are almost identical to results obtained on the adjacent Row 72 scene. Results for the two Landsat-4 TM scenes were similar, except for the presence of only a single 2 Hz peak in the equivalent Figs.3 and 4.

Fig. 3. FFT Frequency Spectrum for the B3 TO B5 Plot in Fig. 2, illustrating Peaks at 1.2 and 2.0 Hz

Fig. 1. Scan-by-Scan Sample Misregistration of the same Detector (16) in Landsat-5 Band 3 and Band 5
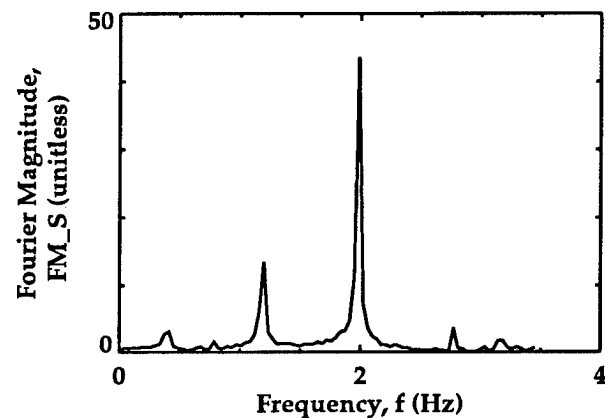
Fig. 4. Row 71 FFT Frequency Spectrum of 1st Half Scan Mirror Errors, illustrating Peaks at 1.2 and 2.0 Hz

Fig. 2. Scan-by-Scan Sample Misregistration of the Average Z-Scores of the 16 Detectors in the L5 B3 TO B5 band-pair (the average SD error bar on each of the 187 points is ±0.13)
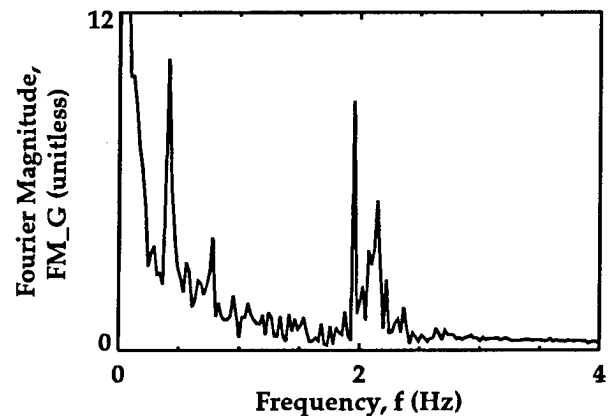
Fig. 5. Row 71 FFT Frequency Spectrum of X-Axis Gyro Telemetry, illustrating Peaks not seen in Fig. 3

1602

DIGITAL RESAMPLING FOR IMAGE PROCESSING AND FUSION OF SSM/I DATA

Pier Franco Pellegrini (IEEE Member), Enrico Piazza (IEEE Member), Alessandro Nervi

University of Florence Dipartimento di Ingegneria Elettronica
Via di S.Marta, 3 - 50139 Firenze - Italy
Tel. +39-55-4796267, Fax. +39-55-494569 E-Mail: labtel@ingfi1.ing.unifi.it

Abstract: Environmental parameters can be extracted from the integration of Remote sensed images data coming from other sensors but they need a geolocation to allow the integration of these data.
The geolocation process depends on several factors: Earth-Satellite geometry, Scanning geometry, mapping projection. Data fusion of preprocessed data can be done in the following ways:
- addition of data of the various sources (overlay) without the same coverage;
- real fusion of data (combination).

Data fusion need data alignment and implies a common time base and a common spatial coordinate system.
Here follows an environment parameter extraction as combination of the data coming from different SSM/I channels and a comparison with the same parameter computed with the IR data coming from Meteosat.

INTRODUCTION

Research trend in future years is oriented towards the development of integrated systems, which collect information coming from various sensors, and distribute it both to ground controllers and to final users.

SSM/I IMAGES CHARACTERISTICS

The Special Sensor Microwave/Imager Instrument (SSM/I), a passive microwaves satellite radiometer, has the advantage over optical and infrared sensors and can observe large portions of the earth's surface trough clouds both during night and day. The first SSM/I was lounched with the Defense Meteorological Satellite Program (DMSP) Block 5d-2 F8 spacecraft on June 19, 1987, and operates in a circular sun-syncronous near polar orbit at an altitude of 860 km with an orbit inclination of 98.8 deg and orbit period of 102 minutes. The orbit produces 14 revolutions every 24 hours [1]. The SSM/I is a conical scanning instrument rotating continuously about the vertical axis and sampling the earth at scan angles ±51.2 degrees about the aft direction of the spacecraft (See Fig. 1)
SSM/I data are not directly available but they have to be gathered from agencies such as NOAA, which submit data to a pre-processing and distribute them to the scientific community. The data used in this work come from the WetNet source and have been extracted in raw format with the McIdas Software [2].
The SSM/I Instrument measures the Top of atmosphere temperature at 19.35, 37.0, and 85.5 GHz both in the

horizontal and vertical polarizations, and at 22.235 GHz channel in the vertical polarization only.
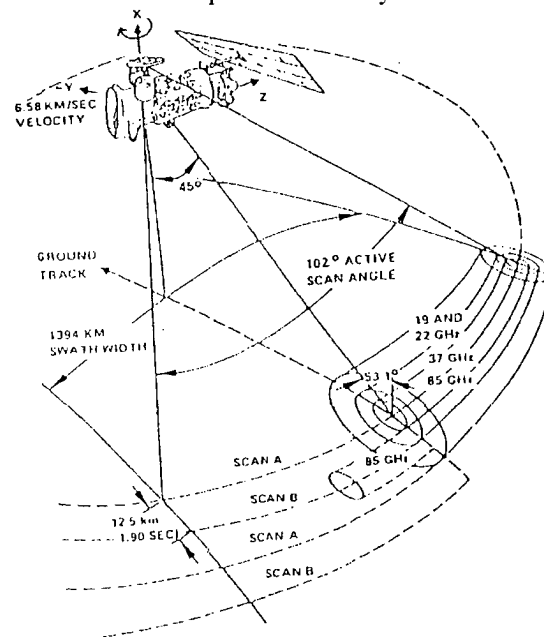
Fig. 1 - SSM/I radiometer Scan Geometry

The spatial resolution of passive microwave sensors depends both on the antenna size and frequency. As the SSM/I instrument uses one parabolic reflector for all frequency [3], [4], the spatial resolution improves with increasing frequency (see Tab. I) [3], [4].
Unfortunately, geolocation errors in eccess of 20-30 km have been routinely observed when comparing SSM/I imagery of coastlines, lakes, and islands to world shorelines and island geolocated points [4].

Table I
Spatial resolution and sampling interval of SSMI channels

Channel Frequency (GHz)	19.35	22.235	37.0	85.5
Polarization v/h	v/h	v	v/h	v/h
Integration time (ms)	7.95	7.95	7.95	3.89
Resolution along track (km)	69	60	37	15
Resolution along scan (km)	43	40	28	13
Sampling Interval (km)	25	25	25	12.5

COMMON MAP PROJECTION

To obtain a map in a common cartographic projection the Mercatore one has been used. It has the advantages of being a conformal transformation with perpendicular grid. The following formula is used:

$$m = a_0 \ln(\tan(\pi/4 + \text{lat}/2)) - a_1 \sin(\text{lat}) - a_2 \sin^3(\text{lat}) + \\ - a_3 \sin^5(\text{lat}) \quad [\text{min}]$$

where the coefficients are computed for an earth eccentricity taken by the Clark ellipsoid.
The coefficients of the Mercatore transformation for e=0.08227185422 are:

$a_0 = 3437.74677078$ [min];
$a_1 = 23.268932$ [min];
$a_2 = 0.0525$ [min];
$a_3 = 0.000213$ [min].
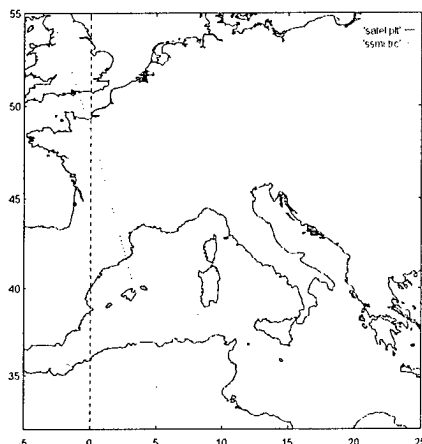
Fig. 2 - Trace of the subsatellite point relative to the analized DMSP orbit superimposed to a map of Europe sampled from a map by Italian Navy Idrographic Institute.

The digital map used was produced by sampling coastlines of the Italian Navy Idrographic Institute, Map Number 340/INT 301 scale 1:2,250,000 (41 deg 30' N) Mercatore projection, Datum ED50. (see Fig. 2)

METEOSAT IMAGE CHARACTERISTICS

The cylindrically shaped spacecraft measures 210 cm in diameter and 430 cm in length, including the apogee boost motor. The primary structural members are an equipment platform and a central tube. The radiometer telescope is mounted on the equipment platform and views the earth through a special aperture in the side of the spacecraft. A support structure extends radially out from the central tube, and is affixed to the solar panels, which form the outer walls of the spacecraft and provide the primary source of electrical power. Proper spacecraft attitude and spin rate (approximately 100 rpm) are maintained by jet thrusters mounted on the spacecraft and activated by ground command. The spin-stabilized, geostationary spacecraft carries a visible-IR radiometer to provide high-quality, day/night cloud-cover data and to take radiance temperatures of the earth/atmosphere system, and a meteorological data collection system to disseminate image data to user stations, to collect data from various earth-based platforms, and to relay data from polar-orbiting satellites.

At the Electronic Engineerig Dept. of University of Florence is operative a primary receiving station for Meteosat PDUS images and NOAA AVHRR HRPT images and Meteosat WEFAX images. Other sensors' image are collected by the means of computer networks. The available images are both in the high resolution digital format and the low resolution WEFAX format.
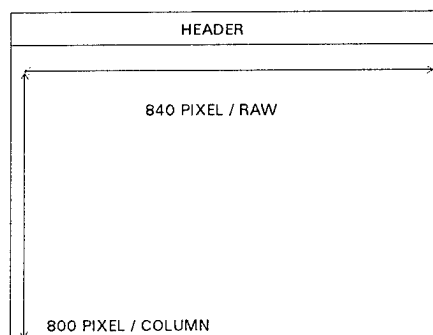
Fig. 3 - Frame of a Meteosat Wefax image. Image dimensions are 840x800x8 bit/pixel

To relate the x,y [pixel] coordinates of the Meteosat Wefax raster image to the λ, ϕ geographical coordinates, the following formulas have been used:

$$k \cdot (x - x_0) = \frac{h_t \cdot \sin\lambda \cdot \cos\phi}{h_t + 1 - \cos\phi \cdot \cos\lambda}$$

$$k \cdot (y - y_0) = \frac{h_t \cdot \sin\phi}{h_t + 1 - \cos\phi \cdot \cos\lambda}$$

where:

x, y : coordinates in pixel of the original image;
λ, ϕ: geographical coordinates;
h_t : height of satellite in Earth radii;
k : scale constant;
x_0 : subsatellite point;
y_0 : subsatellite point.

By the means of the knowledge of four true points it is possible to calculate these parameters as the solution of a linear system. The obtained coefficients are:

$h_t = 5.036$ $k = 6.98 \cdot 10^{-4}$
$x_0 = 399$ $y_0 = -410$

Now it is possible to resample the image on a regular λ, ϕ geographical coordinates grid by a bilinear interpolation using the following formula:

$$T(i, j) = (1 + j - x)(i - y)\left[\phi(i, j) - \phi(i + 1, j)\right] +$$

$$+(j - x)(i - y)\left[\phi(i + 1, j + 1) - \phi(i, j + 1)\right] +$$

$$+(1 - j - x)\phi(i + 1, j) - (j - x)\phi(i + 1, j + 1)$$

RESULTS

To validate the wind speed results obtained by analizing the SSM/I data, a Meteosat image was used (Fig. 4 and 5).

The SSM/I data are relative to the 2 november 1992, 15:58 UTC while the Meteosat images are relative to the same day and sensed at 15:30 and 16:30 UTC [2], [7].
The wind speed is computed from the SSM/I sensor using the D-Matrix formula:

$$W = 147.90 + 1.0969 \cdot T_{B19V} - 0.4555 \cdot T_{B22V} - 1.7600 \cdot T_{B37V} + 0.7860 \cdot T_{B37H}$$

This equation is valid only over open ocean where the wind speed is in m/s referenced to a height of about 20 m above the surface. The hypotesis of open ocean is valid at least 100 km off the shores [6].
The wind speed values are computed from the meteosat IR images with a segmentation and a correlation in different images in the same sequence.

Tab. II
values of wind speed in the open see between Sardinia and Sicily computed from Meteosat IR images

Time UTC	Speed m/s
14:30	25.0
15:30	28.9
16:30	22.2

Tab. II reports the values of wind speed in the open see between sardinia and sicily computed in [7]. The D-Matrix result shows values around 22 m/s that is a quite good match.

REFERENCES

[1] Hollinger J.P., Lo R.C., Poe G.A., Savage R., "Special Sensor Microwave/Imager User's Guide", Naval Research Laboratory, Washington D.C., Sep. 1987
[2] Nervi A., "Telerilevamento Passivo a Microonde in Ambiente Marino. Applicazioni da Piattaforma Satellitare: Stima della Velocità del Vento e di Fenomeni Correlati.", Graduation Thesis, Univ. Firenze, Italy, Mar. 1996
[3] Poe G.A., Conway R.W., "A Study of the Geolocation Errors of the Special Sensor Microwave/Imager", IEEE Transaction on Geoscience and Remote Sensing, Vol. 28, No. 5, Sep. 1990
[4] Cuomo S., Leoncino F., Pellegrini P.F., Piazza E., "Verifica della Georeferenziazione di immagini telerilevate con sensore a microonde SSM/I", Atti della Giornata di Studio su 'il telerilevamento ed i sistemi informativi territoriali nella gestione delle risorse ambientali', Trento, Ott 1994
[5] Col B., Mouchot M.C., "Cloud Classification using passive Microwave Satellite Measurement from the SSM/I Radiometer", IGARSS 95, p. 1889, vol. 3, Florence, 1995
[6] Goodberlet Mark A.,Swift Calvin T,Wilkerson J.C., "Ocean Surface Wind Speed Measurements of the Special Sensor Microwave/Imager", IEEE Transactions and Remote Sensing, vol.28, No.5, pagg. 823-828, Sept. 1990
[7] Leoncino F., Pellegrini P.F., "L'Estrazione di Informazioni da Immagini di Telerilevamento Multitemporali", Rendiconti 95a riunione annuale AEI, pag. 163, Bologna, Italy, 1994
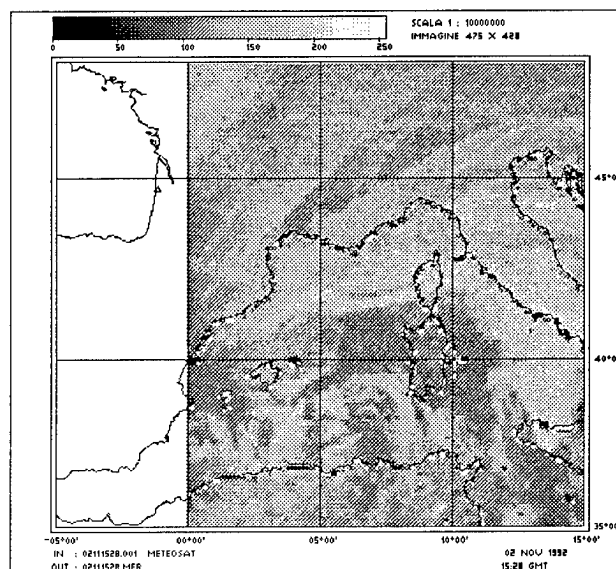
Fig. 4 - Infrared Meteosat Image in Mercatore projection of the 2 november 1992, 15:30 UTC. The lighter pixels represent a greater concentration of clauds, showing a perturbation. The values are brightness temperature [K].
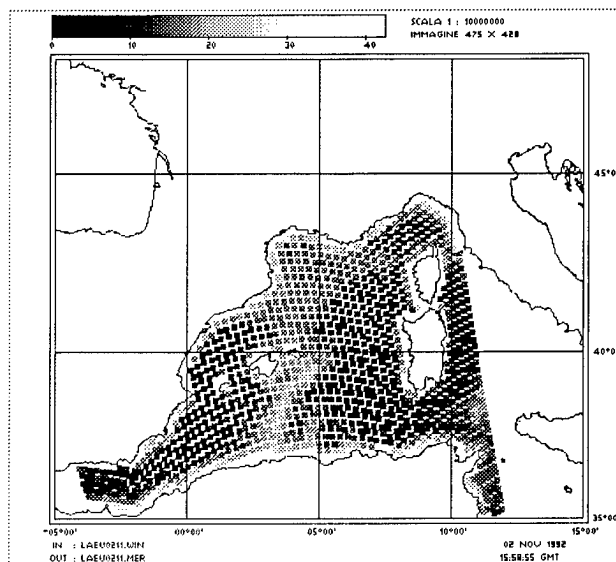
Fig 5 - Resuls of the wind speed computation based upon the SSM/I data superimposed to a map of the mediterranean basin in Mercatore projection. It shows higher speeds where the Meteosat image shows perturbations. The winds closest to the shores result faster due to the presence of the coasts. Values of the wind speed are in [m/s].

Spatial Resolution Enhancement of SSM/I Data: Vegetation Studies of the Amazon Basin

David G. Long, Douglas R. Daum, and Perry J. Hardin

Electrical and Computer Engineering Dept., Brigham Young University
459 CB, Provo, UT 84602
(801) 378-4383   fax: (801) 378-6586   long@ee.byu.edu

Abstract - **The relatively low resolution of the Special Sensor Microwave/Imager (SSM/I) radiometer limits its utility in vegetation studies. However, resolution enhancement techniques can be used to ameliorate this limitation. To this end the Backus Gilbert Inversion (BGI) technique and a modified form of the the Scatterometer Image Reconstruction (SIR) algorithm are investigated as methods to create enhanced spatial resolution images from SSM/I data. A new method for generating cloud-free composite images is presented. The utility of the composite images is illustrated through a tropical vegetation discrimination study of general vegetation classes. An overall discrimination accuracy of 81.4% is achieved for 14 classes with most of the misclassification within broader vegetation categories.**

I.   INTRODUCTION

While microwave radiometer data has wide application in ocean sensing, its relatively low spatial resolution limits its use in vegetation studies. Two spatial resolution enhancement algorithms have been developed for microwave data. The first, based on the Backus-Gilbert Inversion (BGI) method, has been applied to SSM/I data for both resolution enhancement and optimal interpolation [2, 7]. The second, known as the Scatterometer Image Reconstruction (SIR) algorithm [4], originally developed for Seasat-A scatterometer data, has been adapted for use with SSM/I data [3]. In this paper we compare the performance of these algorithms for generating enhanced resolution brightness images over land areas from SSM/I data. Because the images may be adversely affected by spatial variations in the atmospheric profile over the surface we have developed an algorithm to generate cloud-free enhanced resolution composite images from multiple passes of the study region. The vegetation discrimination potential of these composite SSM/I images is then explored in a simple discrimination experiment.

II.   SSM/I RESOLUTION ENHANCEMENT

Ignoring the effects of the atmosphere, an SSM/I antenna temperature measurement can be modeled as the integral of the product of the surface brightness and the antenna pattern. The antenna pattern acts as a low pass filter of the surface brightness, limiting the effective resolution of the measurement. Clouds and precipitation lower the measured brightness temperature with higher frequencies progressively more sensitive. The reduction in brightness temperature can be confused with surface features. Further, the clouds attenuate the polarization differences caused by the geometric or chemical composition of different surface types. This prevents the surface polarization difference from being used to discriminate between vegetation types and/or standing water. Improving the spatial resolution and eliminating clouds can make SSM/I data more useful in vegetation studies.

A.   The Backus-Gilbert Inversion Method

A number of authors have used Backus-Gilbert Inversion (BGI) spatial resolution and/or perform optimal interpolation of SSM/I data to either higher or lower resolution [2, 6, 7]. In resolution enhancement, BGI produces a weighted least squares estimate of the surface brightness on a rectilinear surface grid finer than the intrinsic resolution of the sensor. To estimate the brightness temperature for a given pixel, a linear combination of N "nearby" measurements is used. While there is not a unique solution for the coefficients of the linear combination, regularization permits a subjective tradeoff between noise level in the image and resolution. A noise tuning parameter, γ, which can vary from 0 to π, must be subjectively chosen and controls the tradeoff between resolution. A detailed description of the BGI algorithm is given by [6] and [7]. Following [7] the dimensional BGI tuning parameter ω is set to 0.001.

The resulting image is effected by choice of N and the relative locations and gain patterns of the nearby measurements. Restricting the size of the local region defining "nearby" measurements reduces the computational load at the expense of accuracy. Increasing N to include additional nearby measurements improves the accuracy of the resolution enhancement.

B.   The SIR Algorithm

The Scatterometer Image Reconstruction (SIR) algorithm was originally designed to produce scatterometer images [4] but has been adapted for radiometer measurements [3]. It produces radiometric images via an iterative procedure from an initial brightness estimate. The procedure is non-linear and depends on the antenna pattern dimension, shape, and measurement overlap to obtain resolution enhancement. The SIR algorithm is a variation of the multiplicative algebraic reconstruction technique (MART), a maximum entropy reconstruction method. SIR uses a predicted value of brightness temperature of each measurement and compares that to the actual measurement to generate an update term. When measurements from multiple passes are combined, further resolution enhancement along with noise reduction is possible [4]. Multiple passes cannot be used with BGI due to the occurrence of singular matrices when two measurements fall on top of each other.

C.   Algorithm Comparison

While BGI has previously been applied to SSM/I data [2][6][7], SIR has not been previously applied to radiometer data. Comparisons of the algorithms using simulated measurements suggest that SIR can provide higher resolution but is noisier than BGI [3]. A tradeoff between noise reduction and resolution is possible with BGI while SIR provides objective resolution enhancement.

To compare the performance of the BGI and SIR algorithms with actual data, a 19 GHz V-pol descending pass of F10 SSM/I (September, 1992) was used. The results of SIR and BGI with $\gamma = 0$ are shown in Fig. 1. Subjectively, while SIR exhibits a greater contrast along the

rivers, the BGI and SIR images appear very similar. The BGI image seems a bit smoother but not significantly more. A major difference between the algorithms is processing time. The SIR image required only 1/50 of the computation time of the BGI algorithm.

Since the results are similar for BGI and SIR, and noting the reduced computational load, we have adopted the SIR algorithm for processing the images used in this paper.

III. CLOUD REMOVAL

While multi-channel and/or multisensor algorithms for cloud removal have been developed, we use single channel enhanced resolution images to avoid introducing spurious correlation between the channels. Our algorithm is based on the idea that brightness variations over an area are caused by small-scale, temporal atmospheric effects (clouds) rather than temporal changes in the surface brightness. Using multiple passes over the surface we generate a composite image which represents the effective surface brightness temperature over a two week period. The composite image is generated from enhanced resolution images generated from each descending pass. Two weeks of similar time-of-day SSM/I data[1] (Sept. 1992) are used in the images which follow. During this period each pixel is observed from 5 to 10 times. Extending the observation period increases the number of observations but seasonal brightness variations become a greater concern.

Since the atmospheric distortion (clouds) generally lowers the brightness temperature measurements over land, high pixel values have the least atmospheric influence. Hence, [1] selected the second-highest pixel value from the measurement ensemble as the composite pixel value. To improve the performance of this algorithm, we use a modified maximum average (MMA). This algorithm estimates the cloud-free surface brightness of a pixel by choosing a subset of pixel values from the ensemble of measurements of that pixel and then averaging the selected values together. By properly selecting the subset from the ensemble, the cloud distortion is eliminated. Averaging of the subset reduces the noise and attenuates any residual bias.

In MMA the sample mean of the ensemble is computed. A subset of measurements greater than the mean is selected. The highest value of this subset is then eliminated. The average of the remaining measurements is the composite pixel value. A detailed analysis of this technique is given in [3]. The variance of the MMA estimate is lower than that of the second-highest algorithm. Like the second-highest estimate, the MMA estimate is biased high; however, the MMA bias is less than the second-highest estimate.

IV. VEGETATION DISCRIMINATION EXPERIMENT

Composite images were created for each SSM/I channel with the aid of SIR and MMA (Fig. 2). To illustrate the utility of these images, they are used in a simple tropical vegetation discrimination experiment. With the aid of a large scale vegetation map [8], large homogeneous regions are delimited for 14 different vegetation formations within a study region in central South America. Pixel values from the composite 19H, 19V, 22V, 37H, 37V, 85H and 85V images are extracted for each delimited region. Table 1 summarizes the radiometric values for the 14 vegetation formations sampled.

Generally, the brightness temperature is lower for savanna vegetation classes than for woodland and forest classes. The lack of suitable in situ data to describe the vegetation characteristics in sufficient detail, coupled with the wide range of parameter values within a

---

given vegetation class, preclude developing detailed vegetation emission models for each vegetation class. However, a simple empirical approach can be used to initially evaluate the potential of the composite images for vegetation discrimination. Following [5] radiometric values from the composite images are used to train a simple, non-parametric, supervised classifier for the vegetation class. This approach, in effect, treats any variations of the radiometric response within a vegetation class as noise. The results provide a simple estimate of the performance which could be achieved with more sophisticated techniques or if emission-modifying effects were to be incorporated into the classifier. All 7 SSM/I channels are used in this experiment.

In the experiment one-third of the pixels from each of the vegetation formations constitute the training set for the discriminator with the remaining two-thirds acting as the withheld data set. The assignment of a pixel to a particular set is random. After training with the training set, a common first-nearest neighbor classifier is used to assign test pixels from the withheld set to a predicted vegetation class. The results of this experiment are shown in Table 2. In this table the agreement between each pixel's predicted and actual group is summarized in confusion matrix form. The quality of the supervised classification is shown as a simple percentage accuracy for each of the actual vegetation groups.

Attempts to classify the original 14 classes produced an overall classification accuracy of 81.4%. As shown in Table 2, most of the misclassification is within the broader vegetation categories. In general, the savanna and woodland categories are more accurately classified than the forest categories. The results of this simple experiment suggest that radiometer data can be used for studies of tropical vegetation.

V. CONCLUSION

A comparison of two different methods for improving the spatial resolution of SSM/I images has been presented The best-possible resolution enhancement is similar for the two algorithms. While SIR is objective and maximizes resolution enhancement, BGI permits subjective tradeoffs between resolution enhancement and noise reduction. SIR can be used with multiple passes and requires less computation. A new algorithm, the modified-maximum average (MMA) algorithm, for generating a cloud-free composite image of the surface brightness temperature has also been presented. Using these algorithms, composite images of the Amazon basin have been generated and used in a simple vegetation discrimination experiment.

REFERENCES

[1] B. Choudhury and C. Tucker, "Satellite Observed Seasonal and Inter-Annual Variation of Vegetation Over the Kalahari, The Great Victoria Desert, and The Great Sandy Desert: 1979-1984," *Remote Sensing of Environment*, Vol. 23, pp. 233-241, 1987.

[2] M.R. Farrar and E.A. Smith, "Spatial Resolution Enhancement of Terrestrial Features Using Deconvolved SSM/I Brightness Temperatures," *IEEE Trans. Geosci. Remote Sensing*, Vol. 30, no. 2, pp 349-355, March 1992.

[3] D.G. Long, D.L. Daum, and P.J. Hardin, "Vegetation Studies of the Amazon Basin Using Enhanced Resolution Seasat Scatterometer Data," submitted to the *IEEE Trans. Geosci. Remote Sensing*, 1995.

[4] D.G. Long, P.J. Hardin, and P.T. Whiting, "Resolution Enhancement of Spaceborne Scatterometer Data," *IEEE Transactions on Geoscience and Remote Sensing*, Vol. 31, No. 3, pp. 700-715, May 1993.

[5] D.G. Long and P.J. Hardin, "Vegetation Studies of the Amazon Basin Using Enhanced Resolution Seasat Scatterometer Data," *IEEE Trans. Geosci. Remote Sensing*, Vol. 32, No. 2, pp. 449-460, March 1994.

---

[1]Courtesy of Dr. Frank Wentz of Remote Sensing Systems

[6] G.A. Poe, "Optimum Interpolation of Imaging Microwave Radiometer Data," *IEEE Trans. Geosci. Remote Sensing*, Vol. GE-28, pp 800-810, Sept. 1990.

[7] W.D. Robinson, C. Kummerow, and W.S. Olson, "A Technique for Enhancing and Matching the Resolution of Microwave Measurements from the SSM/I Instrument," *IEEE Trans. Geosci. Remote Sensing*, Vol. 30, no. 3, pp 419-429, May 1992.

[8] UNESCO, *Vegetation Map of South America* (1:5,000,000, two sheets) and *Vegetation Map of South America Explanatory Notes*, United Nations Education, Scientific and Cultural Organization, Paris, France, 1980 and 1981.
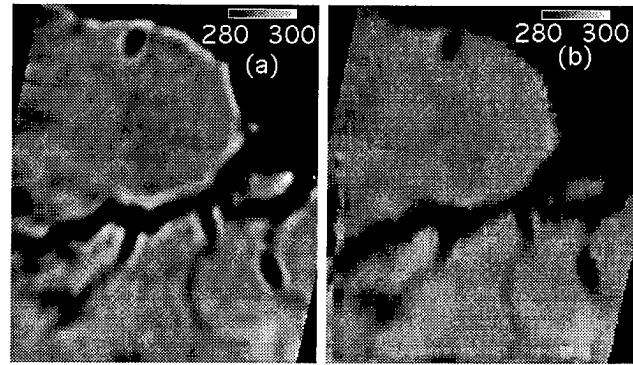
Figure 1. 19 GHz V-pol Images of Amazon Delta Region. (a) SIR. (b) BGI with $\gamma = 0$ and minimum N.

Vegetation Formation	pixels	19H (K)	19V (K)	22V (K)	37H (K)	37V (K)	85H (K)	85V (K)
Forest formations								
Extremely moist ombrophilous forest (Emf)	105	7.6	8.5	7.0	3.8	4.2	6.1	6.5
Very moist ombrophilous forest (Vmf)	2365	7.8	9.0	7.0	4.0	4.8	6.1	6.4
Moist evergreen seasonal forest (Msf)	969	8.1	9.3	8.0	4.5	5.4	7.2	7.6
Ombrophilous submontane forest (Sf)	137	4.7	7.0	5.4	1.5	2.9	4.4	5.1
Degraded forest and crops (Dfc)	48	1.3	2.2	2.8	1.8	1.0	2.6	3.8
Tropical (seasonal) evergreen lowland forest (Tse)	126	9.0	11.0	8.7	5.8	7.1	7.1	7.8
Woodland formations								
Degraded woodland and crops (Dwc)	234	10.3	12.6	9.8	6.7	8.6	8.8	9.4
Chaco (Ch)	1225	3.4	4.9	4.2	1.6	2.8	3.8	4.3
Caatinga (Ca)	414	3.8	8.0	6.9	2.8	5.7	6.1	7.2
Degraded Caatinga (Dca)	72	4.6	10.3	8.5	3.2	7.2	6.3	7.9
Savanna formations								
Campo cerrado north (Ccn)	900	6.0	12.1	9.1	4.0	8.4	6.4	8.1
Degraded campo cerrado (Dcc)	162	-1.8	3.9	2.1	-3.1	0.7	0.0	0.3
Campo cerrado south (Ccs)	408	-0.5	5.0	3.1	-1.5	2.0	0.6	1.7
Campos sujo / limpo (Csl)	472	6.0	13.0	9.3	5.5	8.5	8.7	9.1

Table 1. Mean brightness temperature for vegetation formations. Actual temperatures are obtained by adding 280 K to the tabled values.

Predicted Class		Forest Emf	Vmf	Msf	Sf	Dfc	Tse	Woodland Dwc	Ch	Ca	Dca	Savanna Ccn	Dcc	Ccs	Csl
Forest	Emf	18	25	16	—	—	—	—	1	1	—	—	—	—	9
	Vmf	27	1280	153	12	7	23	6	48	10	—	—	—	—	16
	Msf	14	165	466	—	—	13	1	—	17	—	1	—	—	13
	Sf	2	33	—	66	1	—	—	9	7	1	—	—	—	—
	Dfc	—	1	—	—	17	—	—	—	—	—	—	—	—	—
	Tse	—	14	4	—	—	14	11	—	1	—	—	—	—	7
Woodland	Dwc	—	2	—	—	—	11	134	—	—	—	—	—	—	12
	Ch	—	48	—	2	7	—	—	741	4	—	—	—	1	—
	Ca	—	4	7	6	—	—	—	4	214	6	2	—	—	4
	Dca	—	—	—	—	—	—	—	—	12	26	4	—	—	2
Savanna	Ccn	—	—	—	—	—	1	4	—	4	13	574	—	—	21
	Dcc	—	—	—	—	—	—	—	—	—	—	—	92	16	—
	Ccs	—	—	—	—	—	—	—	—	—	—	—	13	245	—
	Csl	4	31	8	—	—	—	6	—	1	1	11	—	—	238
Total		65	1603	654	86	32	62	162	804	271	47	592	105	262	322
Percentage Correct		27.7	79.9	71.3	76.7	53.1	22.6	82.7	92.2	79.9	55.3	97.0	87.6	93.5	73.9

Table 2. Confusion matrix produced from the vegetation classification experiment. Class abbreviations are defined in Table 1.

19V   19H   37H   37V

19H 19V 275-295 K
22V 275-290 K
37H 37V 275-290 K
85H 85V 280-290 K

22V   85H   85V
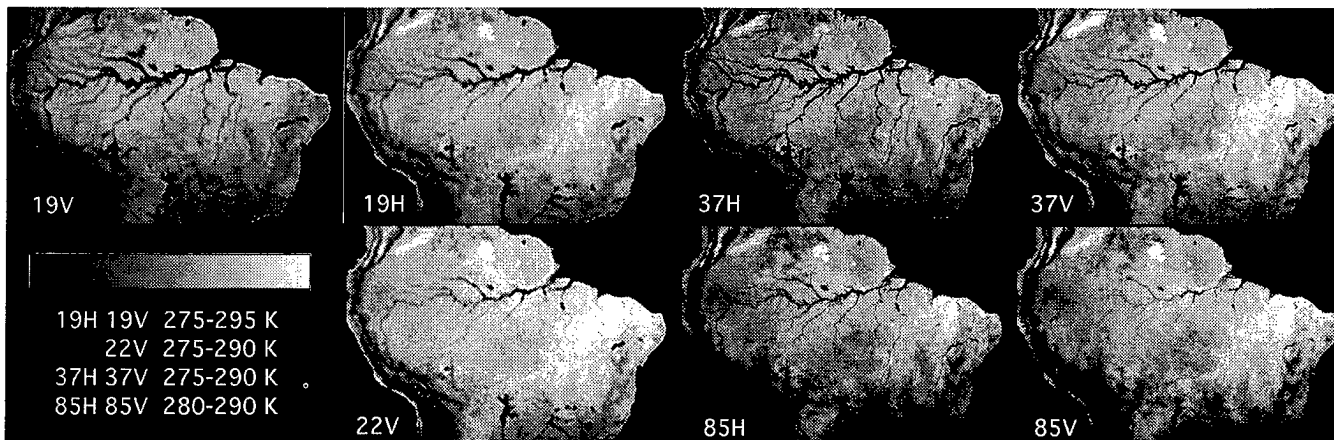
Figure 2. Composite Images of Amazon Basin for 1-15 September, 1992.

Automated Image Registration for Change Detection from Landsat Thematic Mapper Imagery

Xiaolong Dai[1], Student Member, IEEE
Siamak Khorram[2,3], Member, IEEE
Heather Cheshire[1]

[1] Computer Graphics Center, Campus Box 7106, North Carolina State University, Raleigh, NC 27695 -7106
[2] Director, Computer Graphics Center, Campus Box 7106, North Carolina State University, Raleigh, NC 27695 -7106
[3] Dean of International Space University, Parc d'Innovation, Communaute Urbaine de Strasbourg
Blvd. Gonthier d'Andernach, 67400 Illkirch, France
Telephone: (919)515-3430   FAX: (919)515-3439   E-mail: xiaolong_dai@ncsu.edu

ABSTRACT— Image registration is a critical operation in digital change detection to correct for spatial image-to-image displacement. One challenging problem in this area is the automated registration with higher levels of accuracy. In this paper, we explored the basic elements for an automated image registration system based on image segmentation. The technique used region boundaries and strong edges as the matching primitives, and chain-code correlation as the similarity function. A mapping between the two images was formed by interpolation and used to resample the images. The method is automatic and computationally efficient.

I. Introduction

Image registration is an inevitable problem arising in many image processing applications whenever two or more images of the same scene have to compared pixel by pixel [1]. In digital change detection, it is an essential precursor to the use of remotely-sensed data for change detection purpose [2]. Almost all the existing change detection algorithms depend considerably on reasonably accurate image registration to be workable. The research in [2] indicates that in the absence of any actual changes to the land surface, the consequences of misregistration were very marked even for subpixel misregistrations, which strongly suggests that higher levels of image registration must be achieved for an operational change detection system to accurately detect changes on the ground.

Existing image registration techniques fall into three broad categories: manual registration, semiautomatic registration, and automatic registration. Manual registration techniques have been extensively used in practical applications. However, these techniques are subject to inconsistency, limited accuracy, and, in some instances, lack of availability of reference data. Also manual registration is a repetitive and labor-intensive task, especially when several Thematic Mapper (TM) scenes (over 6000×6000 pixels for each TM scene) are involved in change detection implementation. Therefore, it is necessary to introduce automated procedures when higher accuracy is desired and image analysis is subject to time constraints [1].

There are mainly two classes of automated registrations: the area-based and feature-based methods [3], [4]. In the area-based method, a small window of points in the base image is statistically compared with windows of the same size in the reference image. Feature-based methods extract and match the common structures from two images [3]. In this paper, the basic elements for an automated image registration protocol based on [3] are explored. This procedure consists of the following steps: (1) image segmentation; (2) contour Match and control point selection; and (3) transformation parameter estimation.

II. Image Segmentation

Points, straight lines, arcs, and closed contours are four basic matching primitives [7]. All of these primitives are edge points. Therefore, image segmentation is the first task in automated image registration implementation. Since convolution is an associative and accumulative operation, the Laplacian of Gaussian (LoG) operator combines smoothing and second derivative operations into one operation. For these reasons, we used the LoG zero-crossing operator as the edge detector in our experiments. The operator can be expressed as:

$$\text{LoG}(x, y) = \frac{\partial^2}{\partial x^2} G(x, y) + \frac{\partial^2}{\partial y^2} G(x, y) \qquad (1)$$

where G(x,y) is Gaussian. Taking the second derivative of the G(x,y), we obtain the Laplacian of Gaussian operator as follows:

$$\text{LoG}(x, y) = \frac{1}{2\pi\sigma^4}\left(\frac{x^2 + y^2}{\sigma^2} - 2\right)\exp\left(-\frac{x^2 + y^2}{2\sigma^2}\right) \qquad (2)$$

where σ is the variance of the Gaussian. The central negative area of the resultant kernel is a disk of radius $\sqrt{2}\sigma$. Therefore, the domain of the LoG kernel must be at least as large as a disk of radius $3\sqrt{2}\sigma$.

Based on the image obtained by convolving the original image with the LoG, edges are found at zero-crossing points.

Because of the discrete nature of data representation, the determination of zero-crossings is not without problems [7]. A method suggested in [4] uses a threshold to remove weak edge points. An edge-strength-based two-threshold scheme was proposed in [3] to choose the strongest edge points. For simplicity, we used a method that we called virtual zero-plane fitting to find the zero-crossing points, i.e. the edge points. This ensures closed contours and correct connections at T-junctions. The starting points were picked up when they were first scanned by a raster scan search, and the pixels on the boundary were flagged as zero crossings. In the contour refinement process, short contours and weak edges were discarded before the match process was applied. The segmentation results after contour refinement are shown in Fig. 1 (c) and (d). In our analysis, the standard deviation of the LoG operator is 2.5, and the digital LoG filter is 15×15 pixels.

III. Contour Match and Control Point Selection

The next step is to find a technique to efficiently represent the edge points for matching the corresponding contours. One of the efficient representations of digital curves is chain code. Chain code uses a sequence of integer values 0-7 to represent the angle change, from 0° to 315° (-45°), of the current edge pixel relative to its previous edge pixel. A five-point Gaussian filter {0.0545, 0.2442, 0.4026, 0.2442, 0.0545} was used to smooth the chain code for further correlation evaluation. Example image contours and their smoothed chain codes are shown in Fig. 2 (a) through (d). A normalized correlation measure from [3] was used to derive the similarity function. We simply summarize as follows: for N-point chain code $\{a_i\}$ of contour A and M-point chain code $\{b_i\}$ of contour B, a similarity function is defined as the maximum correlation between two n-point segments with different starting points k and l:

$$S_{AB} = \text{Max}\left\{ \frac{1}{n} \sum_{j=0}^{n-1} \cos\frac{\pi}{4} (a'_{k+j} - b'_{l+j}) \right\}_{k \in N, l \in M} \quad (3)$$

where a'_{k+j} and b'_{l+j} are the jth normalized chain code components from starting point k and l for A and B respectively. Normalization was done by removing the means of $\{a_i\}$ and $\{b_i\}$. For detailed descriptions, the reader is referred to [3]. Based on the similarity values, the contours were matched to each other. Their centroids were then used as the control points for the use in the estimation of transformation parameters.

IV. Estimation of Registration Parameters

Given a number of corresponding control points from two
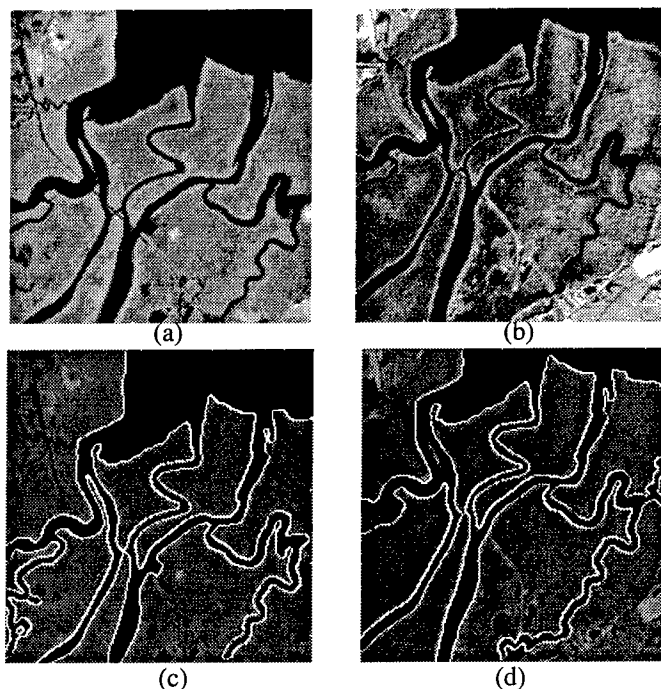
Fig. 1. (a), (b) Two Landsat TM test windows from North Carolina Coastal Plain acquired in the Summer and Winter 1993 respectively; (c), (d) Image segmentation results for (a) and (b) respectively.
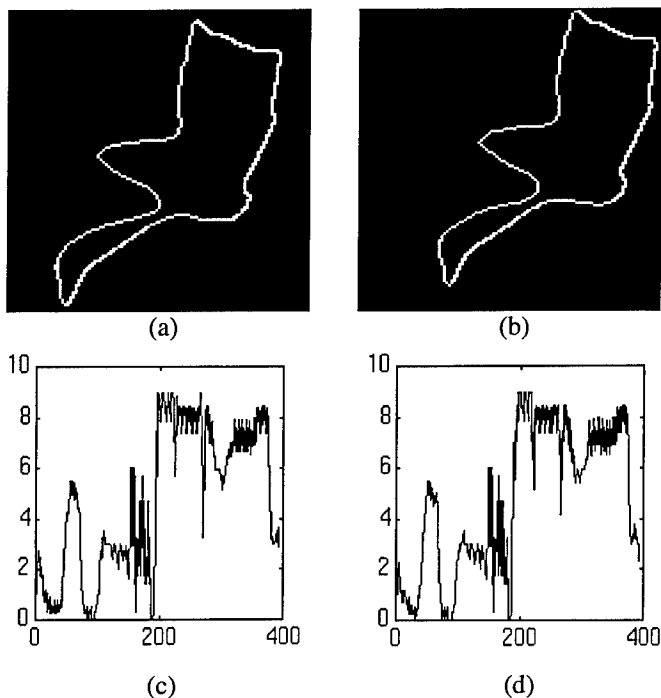
Fig. 2. (a), (b) Sample image contours detected from Fig. 1 (a) and (b) respectively; (c), (d) The smoothed chain code representations.

images, the transformation parameters can be estimated for the images. The registration of images with rotational, translational, and scaling differences can be expressed as the following relationship:

$$\begin{bmatrix} \hat{X} \\ \hat{Y} \end{bmatrix} = s \begin{bmatrix} \cos\theta & \sin\theta \\ -\sin\theta & \cos\theta \end{bmatrix} \begin{bmatrix} X \\ Y \end{bmatrix} + \begin{bmatrix} \Delta X \\ \Delta Y \end{bmatrix} \quad (4)$$

where $(\hat{X}, \hat{Y})$ and (X, Y) are two corresponding points in the transformed image and reference image respectively; and $(s, \theta, \Delta X, \Delta Y)$ are the transformation parameters and correspond to scaling, rotational, and translational differences [3]. The above equation can be expressed as follows by substitution $u = s\cos\theta$ and $v = s\sin\theta$:

$$\begin{bmatrix} \hat{X} \\ \hat{Y} \end{bmatrix} = \begin{bmatrix} u & v \\ -v & u \end{bmatrix} \begin{bmatrix} X \\ Y \end{bmatrix} + \begin{bmatrix} \Delta X \\ \Delta Y \end{bmatrix} \quad (5)$$

A least square approach was used to determine these four transformation parameters (u, v, X, Y) from matched control points. The scaling factor s and rotation angle θ can be obtained from u and v: $s = \sqrt{u^2 + v^2}$, and $\theta = \arctan(v/u)$ for $-\frac{\pi}{2} < \theta < \frac{\pi}{2}$. The image to be transformed was resampled based on the transformation parameters. The matched image after registration is shown in Fig. 3.

V. Conclusions and Discussions

In this paper, we explored the basic elements for an automated image registration procedure using Landsat TM imagery. These elements include image segmentation, contour match and control point selection, and transformation parameter estimation. In image segmentation, we used the LoG operator zero-crossing edge detector. Chain code correlation, smoothed and normalized, was used as a similarity measure between two contours. The transformation parameters were estimated based on the matched control points. The first stage

Fig. 3. Registration of two test windows after transformation.

experimental results were presented. Based on our study, the technique discussed is promising in terms of its computational efficiency, robustness, and usefulness in digital change detection. We must also point out that there are many problems, such as noise and low contrast problems in the image segmentation process, to be solved for an automated image registration system to be operational in practice.

References

[1] Anna Della Ventura, Anna Rampini, and Raimondo Schettini, "Image Registration by Recognition of Corresponding Structures," IEEE Transactions on Geoscience and Remote Sensing, Vol. 28, No. 3, pp. 305-314, May 1990.

[2] John R. G. Townshend, Christopher O. Justice, Cahrlotte Gurney, and James McManus, "The Impact of Misregistration on Change Detection," IEEE Transactions on Geoscience and Remote Sensing, Vol. 30, No. 5, pp. 1054-1060, September 1992.

[3] Hui Li, B. S. Manjunath, and Sanjit K. Mitra, "A Contour Based Approach to Multisensor Image Registration," IEEE Trans. Image Proc., Vol. 4, No. 3, pp. 320-334, March 1995.

[4] Robert M. Haralick, and Linda G. Shapiro, Computer and Robot Vision, Volume I, Reading, MA: Addison-Wesley, 1993.

[5] Ardeshir Goshtasby, George C. Stockman, and Carl V.Page, "A Region-Based Approach with Subpixel Accuracy," IEEE Transactions on Geoscience and Remote Sensing, Vol. GE-24, No. 3, pp. 390-399, May 1986.

[6] Qinfen Zheng, and Rama Chellappa, "A Computational Approach to Image Registration," IEEE Transactions on Image Processing, Vol. 2, No. 3, July 1993.

[7] Toni Schenk, Jin-Cheng Li,and Charles Toth, "Towards an Autonomous System for Orienting Digital Stereopairs," Photogrammetric Engineering & Remote Sensing, Vol. 57, No. 8, pp. 1057-1064, August 1991.

[8] Eric J. M. Rignot, Ronald Kowk, John C. Curlander, and Shirley S. Pang, "Automated Multisensor Registration: Requirements and Techniques," Photogrammetric Engineering & Remote Sensing, Vol. 57, No. 8, pp. 1029-1038, August 1991.

[9] John Canny, "A Computational Approach to Edge Detection," IEEE Trans. Pattern Analysis and Machine Intelligence, Vol. PAMI-8, No. 6, pp. 679-698, November 1986.

NASA/JPL AIRBORNE THREE-FREQUENCY POLARIMETRIC/INTERFEROMETRIC SAR SYSTEM

Y. Kim, Y. Lou, J. van Zyl, L. Maldonado, T. Miller, T. Sato, and W. Skotnicki

Mail stop 300-243
Jet Propulsion Laboratory
California Institute of Technology
4800 Oak Grove Drive
Pasadena, CA 91109
Tel: (818) 354-9500
Fax: (818) 393-5285
e-mail:ykim@delphi.jpl.nasa.gov

ABSTRACT

The NASA/JPL airborne SAR system (popularly known as "AIRSAR") has been flown aboard the NASA Ames Research Center DC-8 since 1987. AIRSAR is a three frequency (P-, L-, and C-bands) polarimetric radar with the interferometric capability. Even though various modes of operation are possible with the AIRSAR system, it has three basic operational modes (polarimetric, across track interferometry, and along track interferometry).

The AIRSAR hardware consists of RFE (RF Electronics), digital electronics, antenna, control computer, on-board processor, and power distribution subsystems. A single DCG (Digital Chirp Generator) generates the chirp waveform and it is up-converted to L-band. Subsequent up- and down- conversions produce C- and P- band chirp signals, respectively. The return echo is amplified by LNA (Low Noise Amplifier) and digitized by 8-bit ADC (Analog-to-Digital Converter). The digital data from six channels are multiplexed and stored on tape using the high density digital recorder.

During the AIRSAR mission, a real time correlator produces low resolution imagery to assess the general health of the radar and to verify that the correct area has been imaged. Data processing to produce high quality image products happens in the weeks and months following a flight campaign after proper calibration parameters are generated. The current integrated processor can process both polarimetric and interferometric data. In this talk, we will present detailed mission description, hardware configuration, and data processing.

INTRODUCTION

The NASA/JPL airborne SAR (AIRSAR) system became operational in late 1987 and flew its first mission aboard a DC-8 aircraft operated by NASA's Ames Research Center in Mountain View, California. Since then, the AIRSAR has flown missions every year and acquired images in North, Central and South America, Europe and Australia.

The AIRSAR system can operate in the fully polarimetric mode at P-, L-, and C-band simultaneously. Both ATI (Along-Track Interferometry) and XTI (Cross-Track Interferometry) modes are available at L- and C-bands. In the following sections, we will briefly describe the instrument characteristics and performance. In addition, we will discuss data processing and calibration of the radar.

INSTRUMENT CHARACTERISTICS

To achieve polarimetric capability, the AIRSAR system transmits the H- and V- polarized signals. Receive polarization diversity is accomplished by measuring six channels of raw data simultaneously, both H and V polarizations at all three frequencies. The video data are digitized using 8-bit ADCs, providing a dynamic range in excess of 40 dB. This raw data together with navigation data is stored on tape using high density digital recorders. The AIRSAR system also includes a real-time processor capable of processing any one of the 12 radar channels into a scrolling image. In addition to checking the health of the radar, the scrolling display is also used to ensure that the correct area has been imaged. Table 1 provides a summary of the AIRSAR system characteristics. AIRSAR can be operated in many different modes due to the complexity and flexibility of the instrument.

Parameter	Value
Chirp Bandwidth (MHz)	20 (40)
Chirp Center Freq. (MHz)	P: 438.75 (427.5) L: 1248.75 (1237.5) C: 5298.75 (5287.5)
Peak Transmit Power (dBm)	P: 62 L: 67 C: 60
Antenna Gain (dBi)	P: 14 L: 18 C:24
Azimuth Beamwidth (deg)	P: 19.0 L: 8.0 C: 2.5
Elevation Beamwidth (deg)	P: 38.0 L: 44.0 C: 50.0
ADC Sampling (MHz)	45 (90)
Data Rate (MB/s)	10
NE σ_0 (dB)	P: -45 L: -45 C: -35
Nominal Altitude (m)	8000
Nominal Velocity (Knots)	450
Slant Range Resolution (m)	10 (5)
Azimuth Resolution (m)	1
Ground Swath	10 -15

Table 1. Summary of AIRSAR system characteristics. The parameters in ( ) apply to 40 MHz chirp bandwidth configuration.

In addition to three frequency polarimetric mode, both ATI and XTI modes are available. ATI mode was successfully used to image ocean currents and waves moving in the radar line-of-sight direction. With addition of more antennas and antenna switching networks, AIRSAR is capable of taking XTI data (known as TOPSAR). TOPSAR was successfully used to generate topographic maps of areas of interest. Since 1995, we have been experimenting with alternating the transmit antenna between the top and the bottom antennas (known as ping-pong mode). This effectively doubled the baseline and initial data analysis showed that the longer baseline produced DEMs (Digital Elevation Models) with reduced RMS height error as expected. In addition, the newly added L-band XTI mode produced DEMs of slightly higher RMS height error due to shorter baseline length (scaled by wavelength) compared with those of C-band XTI mode.

To produce accurate DEMs, we need to know the baseline precisely. To do this, we have also upgraded the Inertial Navigation System (INS) and the Global Positioning System (GPS) receiver in order to acquire more accurate knowledge of the location and attitude of the antennas. The original navigation system of AIRSAR consisted of a Honeywell INS with a ring laser gyro that determined the

attitude of the aircraft and a Motorola Eagle 4-channel GPS receiver that provided the positioning information (latitude and longitude) of the aircraft. As technology advanced and our need for more accurate positioning and attitude information became more stringent, we purchased a new Motorola Six-Gun GPS receiver and a new Honeywell Integrated GPS and INS (IGI) in 1994. The Six-Gun GPS receiver has six channels and a much more stable clock compared to the old unit and provides positioning accuracy of 100 m using CA code. This receiver was integrated in the radar in 1994. The Honeywell IGI has a smaller and more sensitive ring laser gyro integrated with a GPS receiver capable of receiving the more accurate but restricted Precise Positioning Service (PPS) data. The specifications on this unit are: 0.02° heading accuracy, 0.01° roll and pitch accuracy, 0.03 m/s velocity accuracy per axis, and 16 m positioning accuracy with PPS. The IGI was installed on the DC-8 in 1994 but the data were recorded off-line and were not available in the radar header until the 1995 flight season. In addition, we have also experimented with differential GPS by using a Turbo Rogue GPS receiver on the aircraft in conjunction with another Turbo Rogue receiver on the ground to obtain positioning accuracy of better than 1 m.

DATA PROCESSING

A variety of processors and processing techniques are utilized to process AIRSAR data to imagery. A real-time correlator is part of the AIRSAR radar flight equipment (the Aircraft Flight Correlator) and is used to produce low resolution (approx. 25 meter) two look survey imagery. The same on-board equipment is used to generate a slightly higher resolution (15 meter), 16 look image of a smaller area (12 km x 7 km) within 10 minutes of acquisition using the quick-look processor. These on-board processors are useful for assessing the general health of the radar and the success of data taking in real-time.

Final processing of selected portions of the data to high quality, fully calibrated image products happens in the weeks and months following a flight campaign. Currently, users may request images from two different operational processors, the synoptic processor and the frame processor. In the synoptic processor, the user specifies three data channels to be processed. About five minutes of raw data from each of the three selected channels are processed to 16 looks and amplitude-only image strips, covering about 40 km along track. In 40 MHz mode, the image strips would be 8 looks and 20 km long. These image strips cover about 9 km in the slant range direction for the 20 MHz mode and 4.5 km for the 40 MHz mode.

In terms of frame processing, we currently support two processor versions: the AIRSAR processor and the new integrated processor which is still under development. The new integrated processor was developed mainly to process XTI data since XTI mode has become increasingly popular.

In order to do so, we needed a new processor that tracks and compensates for the motion of the aircraft since uncorrected motion translates into baseline error between the two antennas, which results in height error in the DEM.

The integrated processor processes one minute of raw data of all available data channels into absolutely calibrated images in compressed Stokes matrix format that contains all the polarization information. If C-band cross-track interferometer data are available for the data take, the integrated processor will generate a digital elevation model and a local incidence angle map. By using the local incidence angle map, all output images will be geometrically and radiometrically corrected taking the topography into account and resampled to ground range with a 10 m by 10 m pixel spacing. The output images cover about 10 km in the range direction by about 10 km in the along-track direction for the 40 MHz mode, and about 20 km in the range direction by about 10 km in the along-track direction for the 20 MHz mode. Although the radar data rate allows us to image about 20 km in range swath for the 20 MHz mode, the increasing phase noise due to decreasing SNR as a function of incidence angle reduces the correlation between the two antenna channels. As a result, the RMS height error can be quite large in far swath due to poor SNR.

DATA CALIBRATION

The calibration of polarimetric data is well understood. Briefly, with the calibration tone in the receive chain and corner reflector verification, we are able to consistently produce polarimetric images with better than 3 dB absolute accuracy, better than 1.5 dB relative accuracy amongst the 3 radar frequencies, and better than 0.5 dB between the polarization channels. The relative phase calibration between the HH and VV channels is better than $10°$.

The calibration of XTI data is much more challenging because various parameters, such as baseline vector, are involved in the XTI data processing. The absolute phase must be known in order to derive height information from the interferometric data without 2π ambiguity. The differential phase (between two channels) of the radar can be a function of system temperature. Therefore, we need to determine both absolute and differential phase for each data take. In addition, accurate knowledge of the baseline between the two antennas is necessary to generate accurate DEMs Using the Rosamond Dry Lake data, we are currently working on calibration of XTI data. In addition to usual calibration, we implemented the phase screen to remove systematic range dependent height errors which can be caused by multipath.

ACKNOWLEDGMENT

Hughes Integrated Synthetic Aperture Radar

Robert W. Bayma
Hughes Aircraft Company, Radar and Communications Systems
RE/R7/P581, PO Box 92426, Los Angeles CA 90009-2426
(310) 334-2723, FAX: (310) 334-4665, email: rbayma@msmail4.hac.com

ABSTRACT

This paper describes the low cost Hughes Integrated Synthetic Aperture Radar (HISAR™) which provides real-time high resolution imagery with precise Ground Moving Target (GMTI) overlays.

INTRODUCTION

Based on a long history of development of multi-mode airborne radars for weapon control and reconnaissance, Hughes Aircraft Company has developed a low-cost X-band Synthetic Aperture Radar (SAR) for real-time airborne reconnaissance and surveillance. The Hughes Integrated Synthetic Aperture Radar (HISAR) uses Commercial-Off-the-Shelf hardware combined with standard High-Order programming languages for software development.

HISAR has the capability to rapidly switch between pre-planned or operator-selected imaging modes. These include a 24-meter resolution Wide Area Search Mode with a 60 degree azimuth sector and 74 km range swath, a 6-meter resolution Strip Map Mode with a 37 km range swath, and a 1.8-meter resolution Spot Mode with a 4.8 by 2.8 km patch.

The wide area search and strip modes use multiple looks for speckle reduction and are interleaved with Ground Moving Target Indicator (GMTI) overlays for activity display. The high resolution Spot map has the capability of squinting ± 45 degrees from broadside. All modes operate to ranges of 110 km from either side of the aircraft.

This paper addresses some of design solutions for efficiently implementing these modes using the programmability features of the airborne transmitter and receiver/exciter and the on-board image formation processor. In particular, the image processing makes use of general, parameter-controlled software kernels, which are programmed to adapt to the varying modes and collection geometries. The algorithms and software are adapted from those used on military programs and include highly advanced autofocus algorithms needed to insure high quality fine resolution imagery at long ranges.

HISAR is currently being demonstrated in a Beech Super King Air 200 aircraft.

HISAR SYSTEM DESCRIPTION

Fig. 1 is a simplified block diagram of HISAR. Data collections are controlled by the operator workstation using either preplanned missions or operator selected imaging modes. The Embedded Global Positioning System (GPS) Navigator sends aircraft attitude, position and velocity to the Processor Control Unit (PCU) which in turn, sends aircraft position data back to the workstation. The mission planning software monitors and displays the aircraft location and automatically tasks the radar to collect the preplanned scenes. The operator can modify the collection plan and also use the processed image display to immediately designate and command high resolution Spot scenes using a cursor.

The PCU sets the mode-dependent timing and control parameters; accepts the navigational data, and continuously computes the dynamic motion parameters required for processing and antenna pointing. The Exciter generates the required chirp waveform and the coherent reference frequencies for the receiver and A/D converter.
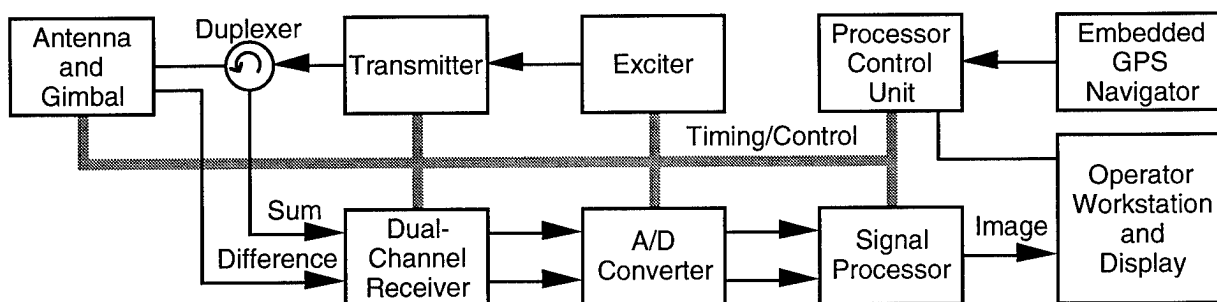
Figure 1. Simplified HISAR Block Diagram

The received sum and difference signals are sent to the dual-channel receiver where they are down-converted to inphase and quadrature (I and Q) baseband signals which are then sampled and quantized by four matched Analog-to-Digital (A/D) converters and stored in a large high-speed buffer for processing.

The sampled radar data is then read from the buffer into the signal processor where the data is compressed in range and azimuth to form imagery which is sent to the workstation display. The resultant image sizes are much larger than the display format. Therefore, the operator is given the option to collapse the imagery to obtain a full scene overview, or to selectively roam over the entire image at full resolution.

The antenna is stabilized in elevation and azimuth using a Hughes-designed gimbal and servo having both position and gyro feedback loops. The antenna includes an azimuth monopulse channel which is used for the GMTI modes.

Aircraft attitude, position and velocity, which are used for antenna pointing and radar motion compensation, are obtained from a commercial Embedded Global Positioning System and Inertial Navigation System (GPS/INS) .

The Pulse Repetition Frequency (PRF), transmit pulse width, A/D converter sampling rate, and the range gate sampling interval are programmable. This permits a wide selection of chirp waveforms and range swath widths which can be used to match the varying requirements for a multi-mode radar.

The radar control and on-board image formation processing use standard commercially available signal processing boards. These processors are controlled by a commercial work station which the radar operator uses for on-board mission planning, control, image display and initial exploitation. Images are digitally recorded for further exploitation.

HISAR PERFORMANCE

Fine Resolution Spot Mode

The finest range resolution of 1.8 meters is used for the Spot Mode. It was initially designed for a nominal image size of 2.5 by 2.5 km and later increased in size to fully utilize the available signal processing power required for the continuous strip map mode. This mode uses the most general sequence of processing kernels. Each of the kernels are controlled by mode- and geometry-dependent constant parameters which are computed at mode initialization and sent to the signal processors. In addition, certain kernels perform motion compensation functions requiring dynamic parameters which vary pulse-by-pulse and are computed from the navigational data.

In HISAR, the received data is subdivided into contiguous range subswaths which are processed independently. This is done for two reasons. First, the required azimuth correlation function is a function of range, so this permits focusing each range interval with its corresponding reference function, including the effects of aircraft line-of-sight motion which

can vary with range. Second, this provides a convenient method for subdividing the data among parallel signal processing elements to achieve the required throughput.

After subswath focus, the data is compressed in range using a Fast Fourier Transform (FFT). Now, except for unmeasured motion errors, the final image can be formed using an azimuth FFT over all compressed range bins. However, for high resolution images at long range, even very small errors from the navigator and atmospheric inhomogenieties can result in large azimuth phase errors. Therefore, autofocus is generally required to achieve the desired azimuth resolution with low sidelobes. HISAR uses proprietary parametric and nonparametric autofocus algorithms, as needed, to obtain high quality imagery for all modes and collection geometries.

After azimuth compression, the complex image is square-law detected. Gain corrections are applied to compensate for antenna shading and range and processing filter passband rolloff. The image is then encoded for recording and display.

Continuous Strip Map Mode with GMTI Overlay

The continuous Strip map mode collects an image having 6 meter resolution over a 37 km range swath simultaneously with a Ground Moving Target Indicator (GMTI) overlay for activity indication. This is the most demanding mode in terms of processor loading since the processing rate must keep up with the airborne collection rate. Moreover, the required Strip and GMTI waveforms are substantially different: the Strip map mode uses a low PRF chirp waveform while the GMTI modes uses multiple PRF's for Doppler ambiguity resolution. The two modes are interleaved as follows: first, a short array of GMTI pulses are used to set the receiver gain; next, a sequence of GMTI arrays are collected for each of the PRF's; and finally, the Strip mode waveform is generated and data is collected for the synthetic array length required to attain 6-meter azimuth resolution at the far edge of the mapped range swath. Image formation uses the same processing kernels as the Spot mode.

Wide Area Search Mode with GMTI Overlay

The Wide Area Search (WAS) mode is used to rapidly obtain maximum area coverage for cueing the higher resolution modes and for ocean surveillance. This was easily done by using the flexibility inherent in the HISAR design. This mode uses the same waveform as the Strip modes, but collects data over twice the range swath. However, instead of operating with a fixed squint angle, the antenna is scanned over ± 30 degrees from broadside forming an image consisting of a mosaic of azimuth patches as shown in Fig. 2. For this mode, azimuth processing is changed to Doppler Beam Sharpening (DBS) using a fixed array length to provide constant angular rather than constant cross-range resolution.
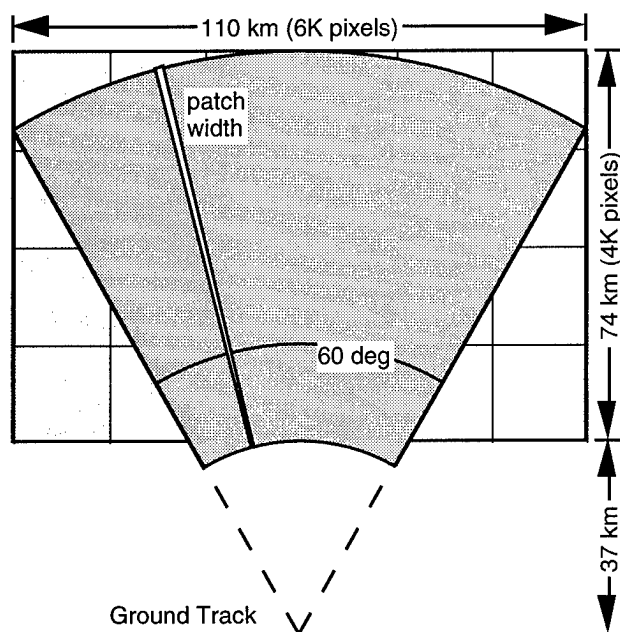
Figure 2. Wide Area Search Map Formation

The Wide Area Search image data is noncoherently collapsed in range by a factor of four in the conversion from range-angle to Cartesian display coordinates while preserving point target amplitudes. This provides the multilook desired for speckle reduction, while the original higher resolution range processing provides a better signal-to-clutter ratio for target detection. At the display, the image will have a nominal resolution of 24 meters. The GMTI mode is interleaved with the Wide Area Search collection to provide an overlay for activity detection.

The nominal rectangular display buffer size required to circumscribe the entire Wide Area Search image is 6K by 4K pixels, where K = 1024 is the nominal display raster size. Hence, to display the entire scene, the image is collapsed by 4:1 in the workstation, thus providing additional smoothing with a pixel spacing of 72 meters. The operator can then switch to full resolution and roam over a selected 18.5 by 18.5 km area having a pixel spacing of 18 meters for examination of potential areas to be designated for higher resolution maps.

EARTH RESOURCES APPLICATIONS

While HISAR is designed primarily for reconnaissance and surveillance, it is also capable of outstanding performance in earth resources applications by taking advantage of its stability, sensitivity and flexibility.

HISAR is all-digital beginning with a state-of-the-art wide-band direct digital synthesized chirp waveform generator and wide dynamic range analog-to-digital converters. Pulse compression, motion compensation and azimuth compression are done using 64-bit floating-point

arithmetic throughout image formation. The Embedded GPS Inertial Navigation System and high performance antenna positioning system guarantee accurate position and pointing measurements. The entire system can be calibrated and operated with an essentially unlimited dynamic range. This data can then be used for relative and absolute terrain reflectivity measurements in post-processing classification algorithms.

Sensitivity, in terms of noise-equivalent backscatter (σ_N), at a ground speed of 180 kts and 110 km slant range is better than -37 dB in Spot and -42 dB in Strip mode.

HISAR has a dual-channel receiver which is used for azimuth monopulse for GMTI. By using alternate antenna configurations, the second channel can be used for single-pass Interferometry or Polarimetric SAR applications. Multispectral imaging can be done by multiplexing with additional transmiters.

SUMMARY

The nominal radar system parameters and constraints which bound the performance of HISAR are given in Table 1. A summary of the perfromance parameters of the mapping modes is given in Table 2. These are used for the initial demonstration and can be easily modified, subject to bandwidth and antenna illumination constraints, to obtain alternate cove ages and resolutions to match specific applications.

Table 1. HISAR Radar Parameters

Center Frequency	9.35 GHz
Azimuth Beamwidth	1.75 deg
Elevation Beamwidth	6.90 deg
Peak Transmit Power	3500 Watts
Maximum Transmit Duty Cycle	10 percent
Transmit Waveform	Linear FM
Maximum Transmit Pulse Length	100 μs
Maximum Transmit Bandwidth	100 MHz
Maximum A/D Sampling Rate	100 MHz
A/D Converter Word Size	8 bits I and Q

Table 2. HISAR Performance Parameters

	Spot	Strip	WAS
Resolution	1.8 m	6.0 m	24 m
Pixel Spacing	1.3 m	4.5 m	20 m
Range Looks	1	1	4
Azimuth Looks	1	1-4	1
Range Swath	4.8 km	37 km	74 km
Azimuth Patch	2.8 km	continuous	60 deg
Squint Angle	±45 deg	±15 deg	±30 deg
σ_N @ 110 km	-37 dB	-42 dB	

Ingara: An Integrated Airborne Imaging Radar System

N.J.S. Stacy, M.P. Burgess, M.R. Muller and R. Smith
Microwave Radar Division, Defence Science and Technology Organisation,
PO Box 1500, Salisbury SA 5108, Australia
Phone: +61-8-2597191, Facsimile: +61-8-2595200, Email: Nick.Stacy@dsto.defence.gov.au

Abstract -- The Ingara airborne imaging radar system is a technology demonstrator aimed at evaluating the application of multi-mode radar to broad area land surveillance. An integrated system has been developed that includes an X-Band radar with SAR and MTI modes, real-time signal processing system, air-to-ground data link, automated target detection algorithms and a simple image analysis geographical information system.

INTRODUCTION

Broad area surveillance of the Australian mainland and littoral regions are problems being addressed by the Australian Defence Forces (ADF). The basic requirement is to frequently survey large areas, detect the presence of either small vehicles or vessels and, where possible, provide identification of these man made objects. High resolution imaging radar with synthetic aperture radar (SAR) and moving target indicator (MTI) modes is a remote sensing sensor suitable for the detection layer of a broad area surveillance system. These modes have the advantage of providing high resolution images of scene backscatter in all weather and day/night operations. Though acquired in an oblique geometry, the SAR images provide a plan view of the scene with constant resolution independent of standoff distance. Man made objects typically have backscatter greater than the natural terrain providing a contrast suitable for their detection. This detection information from an imaging radar can be used to cue other sensors for identification.

In its role of providing technical advice to the ADF, the Microwave Radar Division (MRD) of the Defence Science and Technology Organisation (DSTO) has developed over the last six years a low-cost airborne imaging radar technology demonstrator called Ingara (formerly called AuSAR). The aims of the Ingara project are to evaluate multi-mode imaging radar technology in the broad area surveillance application and to provide the scientific and remote sensing communities access to an in-country imaging radar sensor. The Ingara system has participated in several ADF exercises that have exposed it to operational broad area military surveillance activities. In addition the system has collected an extensive database of calibrated scene backscatter measurements of the Australian terrain.

SYSTEM DESCRIPTION

The Ingara system, shown in Fig. 1, consists of airborne and ground components joined by a C-Band data link. The system currently operates in a stripmap SAR mode where a swath of constant width and standoff from a defined aircraft data acquisition track is progressively imaged as the aircraft flies along the track. Spotlight SAR and moving target indicator (MTI) modes are being implemented and preliminary test data have been acquired in these new modes. The parameters, given in Table 1, show that the Ingara system is capable of acquiring and processing in real-time the wide swaths required for broad area surveillance. Radar echo data acquired as the aircraft passes a point on the ground is processed onboard in the real time signal processor (RTP) and then transmitted to the ground station over the bi-directional C-Band data link. The delay between data acquisition and viewing the image on the ground is approximately thirty seconds due to the delayed nature of the processor and data link.

The airborne components of the system are installed on a Royal Australian Airforce (RAAF) Research and Development Unit C-47 aircraft which is unpressurised and so is restricted to a maximum operating altitude of 3,000 m. This limits the minimum incidence angle (the angle between the radar wave and the local vertical) with a reasonable swath width to approximately 60°. Each flight is pre-planned with a graphical user interface (GUI) mission planning tool that permits the organisation of image swath and aircraft track icons overlaid on a scanned map. The user will typically let the requirements of data collection determine the aircraft flight path with the mission planning output being a series of aircraft position and radar activation waypoints that are navigated to during the flight using an onboard global positioning system (GPS).

The radar data acquisition component has a digital subsystem that is primarily based on commercial off the shelf (COTS) equipment with several custom hardware cards that perform radar timing and data handling functions. Motion compensation for aircraft drift from the data acquisition track is performed in real time using aircraft position measurements from an inertial navigation unit (INU). Because the INU has a low frequency offset that results in a error in the absolute position of the aircraft, a differential GPS is also employed to record aircraft position. This provides the necessary information for accurate geocoding of the image data. The
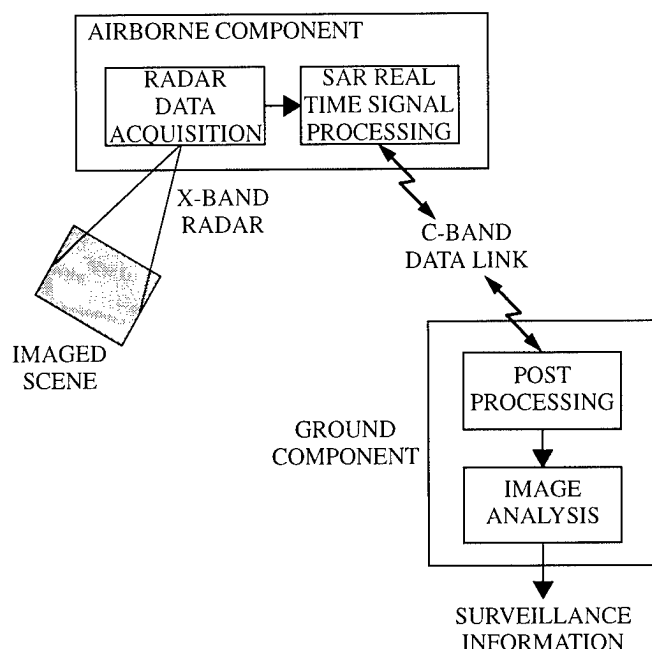
Figure 1: The Ingara system airborne and ground based components.

Table 1: Ingara System Parameters

C-47 Aircraft altitude & velocity	3000 m, 75 m/sec
Radar Freq. & Polarization	X-Band (9.375 GHz), HH
Maximum ADC Sampling	16384 samples of I and Q data at 100 MHz, 8 bits
Stripmap Parameters:	
Finest Resolution	3 m 1.5 m
Number of Looks	4 2
Max. Acquisition Swath Width	48 km 24 km
Max. RTP Swath Width	30 km 15 km
Swath Standoff Distance	5 km - 36 km
Typical Incidence Angles, θ	60° - 86°
Pulse Repetition Frequency:	
Typical in SAR mode	150 Hz
Range	120 Hz - 2000 Hz
Antenna Size	1.46 m by 0.16 m
Peak Transmit Power	1 kW
Sensitivity	$\sigma_0 < $ -35 dB (3 m resolution at 24 km standoff)
Radar Control Processor	VME bus computer & dedicated hardware cards
Radar Operator Interface	SUN Workstation with Openlook GUI
Real Time Signal Processor	CSPI RTS-860 System with twenty eight Intel i860 processing nodes
C-Band Data Link:	
Downlink Bandwidth	8 Mbits/sec
Uplink Bandwidth	1 Mbits/sec
Maximum Range	200 km

transmit signal is generated by a commercial digital waveform generator that can be programmed with a mathematical function or an arbitrary waveform. The radio frequency subsystem is custom built and utilises a two stage up and down conversion process that provides a potential future L-Band capability. A recent upgrade extended the data sampling capability to 16384 range bins which achieves a wide swath capability of 48 km at 3 m resolution or 24 km at 1.5 m resolution. Prior to this upgrade a wide swath capability was demonstrated through the interlaced acquisition of several narrower swaths displaced in range at a higher total pulse repetition frequency [1]. The echo data is combined with auxiliary information from the radar into a raw data stream that is sent to the RTP and recorded onto a high speed tape system.

The real-time SAR signal processor is a COTS vector processor with twenty eight Intel i860 processing nodes and a SUN SparcStation host computer. The vector processing elements are CSPI SuperCard-4XL and SuperCard-2XL cards that have 16 MBytes of memory per node and additional data buses for raw data input and the sharing of intermediate processing results. The range-Doppler algorithm [2], which is programmed in C, is implemented in a scalable fashion to cope with the different processing loads associated with different data acquisition swath widths and standoffs. For example, all processing nodes are required for real-time processing of a 30 km-wide swath at 3 m resolution with a standoff of 10 km from the aircraft ground track (i.e. the swath is the region 10 km to 40 km from the ground track). The processed SAR image data

is saved to disk and tape on the SUN host computer.

The data link utilises a small omni-directional antenna on the aircraft and a COTS tracking satellite TV antenna on the ground. It supports the TCP/IP protocol which is limited in the current implementation to a sustained data throughput of approximately 2.5 Mbits/sec even though the data link can support 8 Mbits per second. This protocol has the advantage of a lossless data transfer and has automatic link re-establishment if the aircraft flies out of range or if multipath causes a deep signal fade. The uplink capability permits the transfer of new mission plans or other information from the ground station.

The ground component post processing function currently includes radiometric correction, fine geocoding and data formatting for the image analysis software. The geocoding process uses the aircraft GPS and INU position information to model the actual data acquisition trajectory and extracts ground topographic information from a digital elevation map to resample the image pixels onto a map grid [3]. The image swath, which can be up to 100 km in length, may be placed at any angle with respect to north. To save storage space the geocoded image does not have north oriented to the top of the image (which is common in many geographical information systems), but uses a rotated map grid that fits the orientation of the acquired image. After geocoding the information content of the image has been maximised through two mathematical

Figure 2: An Ingara image of an area to the south of Darwin with a zoom of an orchard area.

used as an icon overlay in a simple geographical information system. The image analyst can sort the automated detections into unlikely and probable categories. The probable detections can be reported as surveillance information in a text format that includes imaging time and geographic location. The ground component has been implemented as a mobile caravan with several computer workstations that include a computational and image server, and image analysis stations.

An example of an Ingara real-time processed image is shown in Fig. 2.

FUTURE WORK

Future work for the Ingara project includes the full implementation of the MTI mode, a finer-resolution Spotlight mode and participation in military exercises where the full multi-mode aspects of the system can be demonstrated. The RTP algorithm may be modified to include the radiometric and geometric corrections to remove the post-processing function from the ground component. The automated target detection algorithms are an area of continued work that may include the incorporation of other geographic information into the process.

CONCLUSION

The Ingara system has successfully demonstrated the stated aims of the project through developing and evaluating an integrated multi-mode imaging radar surveillance system. Results from the Ingara concept demonstrator will be used to specify a system that may be in service with the ADF at the turn of the century.

ACKNOWLEDGMENTS

relationships that are saved in the image header: the pixel image x-y coordinate to real world latitude-longitude; and the pixel greyscale value to real world backscatter cross-section.

A challenge with a broad area imaging surveillance system is to transform the copious quantity of image data into surveillance information (e.g. the Ingara system can collect over 3 GBytes of 1.5 m imagery per hour). Significant levels of ground clutter and obscuration of man-made objects by trees further complicates the application of imaging radar to land surveillance. The DSTO has taken the approach of using automated target detection tools to cue human analysts to regions of interest in an image. To date, threshold detection algorithms that look for unnaturally bright objects in the image data and change detection algorithms that analyse the difference of two images of the same area, have been developed. The later process requires acquisition of repeat imagery from a similar viewing geometry and automated fine alignment of the images to better than a pixel accuracy. The automated detection information is stored in a database and

REFERENCES

[1] N.J.S. Stacy and M.P. Burgess, "Ingara: The Australian Airborne Imaging Radar System", Proc. IGARSS'94, Pasadena USA, pp. 2240-2242, 1994.

[2] J.R. Bennett, I.G. Cumming, and R.A. Deane, "The digital processing of Seasat synthetic aperture radar data", IEEE Int. Radar Conf., pp. 168-174, 1980.

[3] N.J.S. Stacy, G.G. Nash, D.H. Howard and T.G. Miller, "Quantitative measurements with Ingara Airborne SAR data", Proc. 8th Australasian Remote Sensing Conference, Canberra, Australia, 1996.

The Canadian Airborne R&D SAR facility: The CCRS C/X SAR

C.E. Livingstone, A.L. Gray, P.W. Vachon, M. Lalonde, R.K Hawkins, T.I. Lukowski
Canada Centre for Remote Sensing
588 Booth St., Ottawa Ontario, K1A 0Y7
(613) 998-9060, [last_name]@ccrs.nrcan.gc.ca

K. Mattar, J.W. Campbell
Intermap (under contract to CCRS)
588 Booth St., Ottawa Ontario, K1A 0Y7
(613) 998-9060, [last_name]@ccrs.nrcan.gc.ca

Abstract -- The CCRS C- and X-band SAR systems have evolved continuously since their commissioning in 1988. This paper summarizes the present state of the radar system and outlines its capabilities.

INTRODUCTION

The CCRS SAR sytstem, as it was commissioned in 1988 [1], was composed of two radars, one operating at C-band (5.66 cm) and the other operation at X-band (3.24 cm). The radars were designed as an open system and their architecture permitted the addition and reconfiguration of system modules to create operating capabilities that were not considered in the initial design.

The system has evolved continuously since 1988 as new functions were added and existing functions were upgraded. The added capabilities include:

- increased control of imaging geometry;
- a C-band polarimeter mode;
- a C-band spatial interferometer mode;
- a C-band temporal interferometer mode;
- efficient software processors for generating outputs from the new modes;
- complex signal recording of four, 4096 range cell channels;
- Exabyte recording of real time processed data;

The details of the radar system as it existed at the end of 1995 are discussed elsewhere [2]. This paper provides a condensed summary of the system properties and key parameters.

SAR SYSTEM MODULES AND ARCHITECTURE

The C- and X- band radars each have a transmitter and a two channel receiver. The receiver electronics are dedicated to the radar frequency and have identical control and two channel signal processing subsystems that differ only in frequency specific software elements. Either digital subsystem can be operated with software specific to either frequency. Each control subsystem is the master control for its radar and commands the system functions with control parameters computed from function-based operator inputs. Functions controlling imaging geometry, resolution, channel / polarization assignment, motion compensation, real-time processing, and signal recording respond to operator commands.

The antennas for the two radars share a three axis drive that is steered by the radar control system. Both inertial navigation and global positioning satellite receivers provide attitude, position and motion information. The interferometric antenna system mounted on the right side of the aircraft is adjustable for roll and pitch, but dynamically steerable only in azimuth.

A fast polarization switch, and signal distribution interface to the C-band transceiver, allows the four digital channels to be assigned for the polarimetry and interferometry modes.

MAJOR SYSTEM PARAMETERS

The following tables present the key system parameters that combine to define the radar system capability.

Table 1: The C-band Transceiver

Wavelength	5.66 cm	
Transmitter power	16, or 1 KW peak	
RF gain control (CG)	42 dB, 6 dB steps	
IF gain control (FG)	63.5 dB, 0.5 dB steps	
Receiver 1 gain	FG-CG+25.0 dB	
Receiver 2 gain	FG-CG+21.2 dB	
STC attenuator range	38 dB	
Resolution modes	high	low
CHIRP length	7 ms	8 ms
Compressed pulse length	38 ns	120 ns
3 dB range resolution	5.7 m	18 m
SAW plus electronic delay	13.29 ms	16.7 ms
Receiver noise figure	5.2 dB	3.7 dB
Receiver noise bandwidth	34 MHz	10 MHz
Master clock rate	150 MHz	

Table 2: The X-band Transceiver

Wavelength	3.24 cm	
Transmitter power	6 KW peak	
RF gain control (CG)	none	
IF gain control (FG)	63.5 dB, 0.5 dB steps	
Receiver 1 gain	FG+44.9 dB	
Receiver 2 gain	FG+44.2 dB	
STC attenuator range	38 dB	
Resolution modes	high	low
CHIRP length	15 ms	30 ms
Compressed pulse length	32 ns	134 ns
3 dB range resolution	4.8 m	20.1 m
SAW plus electronic delay	19.6 ms	39.0 ms
Receiver noise figure	5.3 dB	5.2 dB
Receiver noise bandwidth	37 MHz	11.4 MHz
Master clock rate	150 MHz	

Table 3: The Digital Signal Parameters

Along-track pulse spacing	V/prf = 0.43 m or 0.39 m
A to D converters: number	4 for each radar (I,Q pairs)
dynamic range	33 dB
quantization	6 bits I and Q
... after motion compensation	8 bits I and Q
signal data recording	4096 range cells both channels
sampling in range (high res)	4 m (16.38 km slant range)
sampling in range (low res)	15 m (61.44 km slant range)

Table 4: Real-time processing parameters

Real-time processors	2 (1 per radar)	
channels processed per radar	1 full swath, 2 @ 1/2 swath	
number of looks	7	
C-band	high res	low res
processed beamwidth	1.9 deg	1.2 deg
azimuth resolution (nominal)	6 m	10 m
pixel spacing (V/prf = 0.43)	4.31 m	6.89 m
(V/prf = 0.39)	3.90 m	6.23 m
sub-sampling factor	10	16
look separation (in looks)	0.881	0.881
X-band		
processed beamwidth	1.25 deg	0.85 deg
azimuth resolution (nominal)	6 m	10 m
pixel spacing (V/prf = 0.43)	3.45 m	5.17 m
(V/prf = 0.39)	3.12 m	4.67 m
subsampling factor	8	12
look separation (in looks)	.908	.908
image recording	4096 one channel, or 2048 both channels, for each radar	

In the CCRS Polarimetric SAR mode, the isolation between raw data channels exceeds 35 dB for all channel combinations and, thus, the radar distortion matrix is diagonal to within measurement limits. Also, test results show that the antenna phase centres for all polarizations have no differential separation as a function of radar illumination angle, and there are no range dependent phase corrections after post-flight motion compensation.

Table 4: InSAR Parameters

Frequency and polarization	5.3 GHz, HH polarization
Peak power	16 KW
Pulse length	7 μs
Cross-track InSAR	
pulse spacing	0.389 m
Azimuth beamwidths	3.1°, main; 3.0°, InSAR
Baseline (nominal)	2.8 m
Baseline off nadir direction	41 deg
Slant range swath	16.4 km
Along-track InSAR	
Pulse spacing	0.0195 m
Along-track antenna separation	0.46 m
Radial velocity sensitivity	24° per m/sec
Processed azimuth beamwidth	4°
Unambiguous azimuth range	8.3°
Unambiguous velocity range	-7.5 m/sec to +7.5 m/sec

DATA OUTPUTS

Available directly off the aircraft after a flight are:
- dry silver paper, hard-copy imagery;
- Exabyte 8500 tapes of all the real-time processed data in CEOS format;
- range-compressed signal data on helical scan tape recorder on D1 cassettes;
- NTSC video tapes of reduced resolution imagery;
- Exabyte 8200 tapes of all inertial navigation and radar parameters;
- GPS data files in PC compatible format; and
- radar operator logs and hard copy flight records and maps.

Post-flight, on-ground processing (for example, using differential GPS to improve post-flight motion compensation and mapping) can provide digital data files of:
- radiometrically calibrated data [5];
- geocoded (eg. UTM projection) SAR imagery from the cross-track InSAR mode, as well as a registered digital terrain model [3,4];
- geocoded SAR imagery and digital file of radial velocity derived from the along-track InSAR mode [4]; and

- calibrated 4 channel complex SAR image files for the 4 linear polarizations. Additional software generates images of derived amplitude and phase products, various polarimetric signature sets and appropriate scaling for colour display of the data.

SUMMARY

This paper provides some information and description of the CCRS SAR system flown by CCRS from the mid-eighties through to the termination of the program in March 1996. Many more details of this radar, including data processing etc., are contained in reference [2].

ACKNOWLEDGMENTS

The crew and sensor operators who have made possible the delivery of SAR data and imagery, and thus the scientific results from the system, are gratefully acknowledged.

REFERENCES

[1] C.E. Livingstone, A.L. Gray, R,K. Hawkins, and R.B. Olsen, "CCRS C/X-Band Airborne Synthetic Aperture Radar: An R&D Tool for the ERS-1 Time Frame," IEEE Aerospace and Electronic Systems Magazine, vol. 3. (10), pp 11-20, 1988.

[2] C.E. Livingstone, A.L. Gray, R.K. Hawkins, P. Vachon, T.I. Lukowski, and M. Lalonde, "The CCRS Airborne SAR systems: Radar for Remote Sensing Research," Canadian J. Rem. Sens., vol. 20. (4), pp. 468-491 Dec. 1995.

[3] Gray, A.L., K.E. Mattar, and P.J. Farris-Manning, "Airborne SAR interferometry for terrain elevation", Proc. IGARSS '92, pp. 1589-1591, 1992.

[4] Gray, A.L., K.E. Mattar, and M.W.A. van der Kooij, "Cross-track and along-track interferometric SAR at CCRS", Proc. Can. Symp. Remote sensing, V 1, pp. 232-235, 1995.

[5] Hawkins, R.K. and P.S. Daleman, "Calibration implementation for the CCRS airborne SAR", CCRS report DMD-90-724, 63 p, 1990.

The DLR Airborne SAR Project E-SAR

Ralf Horn

Institut fuer Hochfrequenztechnik
Deutsche Forschungsanstalt fuer Luft- und Raumfahrt (DLR)
P.O.Box 11 16, D-82230 Wessling, Germany
Tel.: +49-8153-28-2384, Fax: +49-8153-28-1449, Email: ralf.horn@dlr.de

Abstract -- Microwave remote sensing is a main area of research of the German Aerospace Research Establishment (DLR). Especially the Institut fuer Hochfrequenztechnik is engaged in this field by making use of synthetic aperture radar systems (SAR) on both air- and spaceborne platforms. The institute's engagement in the international projects ERS-1 and SIR-C/X-SAR initiated the design and development work, which lead to the well-known Experimental airborne SAR, E-SAR. It is used for testing new technologies and signal processing algorithms. In recent years it has advanced to a main research tool for remote sensing applications in geology, agriculture, forestry and military reconnaissance.

INTRODUCTION

Microwave remote sensing at wavelengths ranging from 1 cm to 1 m has gained a lot in importance over the last decade with the availability of active radar imaging systems for a wide range of scientific applications. Especially synthetic aperture radars mounted on airborne or spaceborne platforms proved to be of great benefit, due to their day and night capabilities and weather independence. In comparison, optical sensors are strongly dependent on weather conditions, where, on average, only 10% of the data collected over Europe throughout a year proves to be useful. Modern technology in RF and digital electronics allows the development of complex imaging radars, not just single frequency, single polarization, but multispectral, polarimetric systems. Interferometry has entered the 3rd dimension into radar imagery. The user today may extract terrain height information at the same time while imaging the scene using specially configured SAR systems.

THE SYNTHETIC APERTURE RADAR E-SAR

Systems dedicated to microwave remote sensing have a long tradition in the Institut fuer Hochfrequenztechnik of DLR. In the past the performance of multispectral imaging radiometers and X-Band real aperture radar systems operated on airborne platforms was demonstrated and analyzed. Today, airborne SAR forms a major subject in the institute, not only to show its technological feasibility, but to exploit its benefits to a range of applications, such as agriculture and forestry.

The decision to develop an airborne SAR system was initially taken to gain sufficient Know-how in SAR sensor design and data processing to support the space missions ERS-1 and SIR-C/X-SAR. The system was purely meant to be a testbed for new technology and processing algorithms. Especially problems induced by small airborne platforms, which are subject to heavy air turbulence at low flight altitudes (< 3000 m), should be tackled and solved. The aim was to obtain high resolution imagery (2 m x 2 m) even under platform manœuvres.

However, as soon as we published our first C-Band imagery in 1989, we received a strong request for SAR data from user groups in Europe. It initiated our campaign work and it also pushed the applications work in the institute. In recent years the system was extended to other frequency bands. It was not only used during SIR-C/X-SAR preparatory campaigns together with the AIRSAR system of the Jet Propulsion Laboratory (JPL), but it also supported the two shuttle radar lab missions in 1994.

THE E-SAR SYSTEM DESIGN

The E-SAR is a multi-frequency SAR system mounted on board a Dornier DO 228 aircraft, which is owned and operated by DLR. At present the radar is operational in P-, L-, C- and X-Bands with selectable vertical or horizontal antenna polarizations. System extension to P-Band (450 MHz centre frequency) operation was completed in 1994. A L-Band multipolarization capability was realized in 1995. SAR interferometry and SAR polarimetry are new functional modes of the radar, which are on their way to be integrated during 1996.

The photo in Fig.1 shows a DLR research aircraft of type Dornier DO 228 with the E-SAR radar installed onboard. Antenna installations are visible under the nose and in the back of the aircraft. The cigar-like pod under the nose contains the P-Band antenna. Beneath the cargo door in the back a radome covers both the C- and X-Band antennas. The L-Band antenna, splitted into two individual arrays, one for each polarization, is attached to the tail of the aircraft and carries the aircraft's ID.

A special feature of the system are small, fixed mounted antennas. The associated wide azimuth beam avoids having to steer the antenna to compensate for yawing of the platform. A small antenna also permits very high azimuth resolution (< 100 cm) to be achieved under favourable flight conditions. Depending on the Doppler offset used during processing of the SAR data, scenes can be imaged under different azimuth viewing angles (squint mode, spotlight mode). These characteristics consequently lead to a very high data amount to be recorded at high data rate.
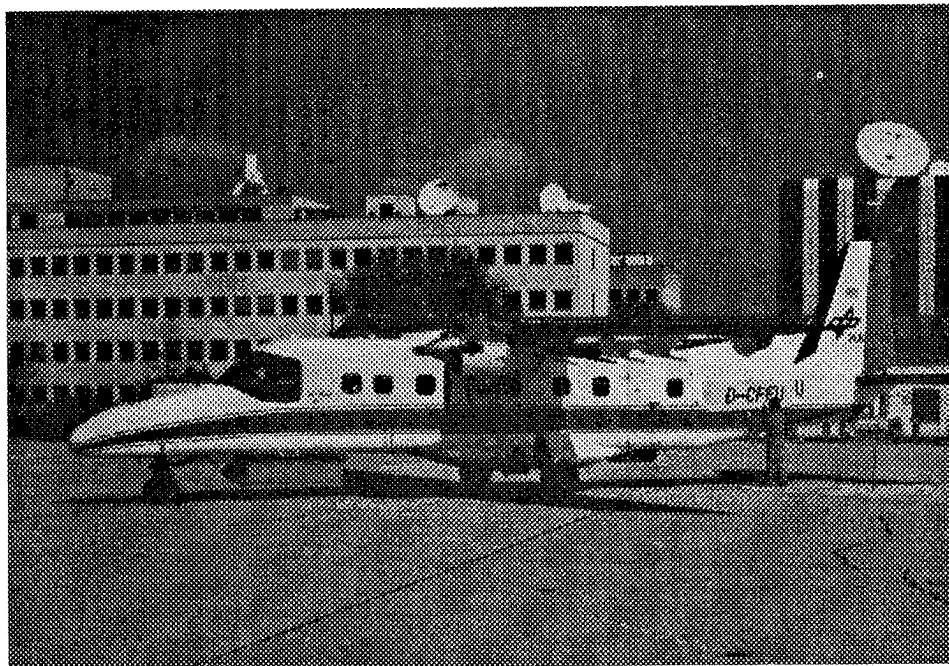
Figure 1: The E-SAR radar installed onboard a DLR DO 228 aircraft.

The conditions set mainly by the system platform require special signal processing algorithms. Therefore an extensive effort for the development of a dedicated SAR processing system at DLR was necessary.

Today, the SAR off-line data processing chain consists of three major steps:

Transcription. The data must be transferred from HDDT to CCT, i. e. an Exabyte tape. One high density Exabyte contains the complete information required for calibrated SAR processing of the data.

SAR Processing with compensation for platform motion errors [3]. The algorithm is phase preserving and, hence, also suitable for SAR interferometry. A number of image output products is available: single look complex (SLC), single and multi-look detected imagery in slant range as well as in ground range geometry.

The received SAR raw data is recorded on HDDT. Tapes of 9200 ft length allow a maximum recording time of 15 minutes at the nominal data rate of 28 Mbit/s on 14 parallel tracks. The tape speed is slaved to the pulse repetition frequency (PRF), which may vary by +/- 30% of its nominal value of 952 Hz. The sensor operates with a constant PRF setting according to wavelength and antenna azimuth beamwidth. Azimuthal sampling criteria limit the maximum forward speed of the platform. Speed variations are compensated for off-line in the processor. Typical PRF values are 670 Hz (P- and L-Band), 952 Hz (C-Band) and 1200 Hz (X-Band).

In flight a Real-Time 'Multi-Look'-SAR-Processor converts the raw data to high resolution imagery of good quality, which is recorded on Exabyte tape. A subaperture algorithm is implemented for range and azimuth processing. A new, unique approach has been developed to allow for processing at squint angles of up to 12° [1]. The real-time imagery is used as a survey product, which allows the selection of a particular scene to be processed off-line to maximum image quality.

The DO 228 is a twin-engine STOL-aircraft (short take-off and landing). Its nominal flight level is 12000 ft above sea level (3600 m). Radar flights may be performed at altitudes ranging from 1000 m to 6000 m. A typical mission lasts 3 h, but can be extended to 5 h under good conditions. The maximum mission range is in the order of 400 to 500 nm. The nominal ground speed for SAR operation ranges from 70 to 95 m/s (140 to 190 kt), the cruising speed is about 100 m/s. The relatively low ceiling and airspeed means that the aircraft is subject to turbulence, placing special requirements (motion compensation) on the SAR processor to avoid defocusing and distortion of the imagery [2].

Radiometric calibration. Being part of the SAR processor this routine corrects for antenna diagram and geometry related effects on the image. It compensates for platform attitude error induced intensity variations in range and azimuth. E-SAR imagery is absolutely calibrated as the radar system transfer function of each spectral channel is included with the processing. The accuracy achieved in all four bands is better or equal 3 dB. Calibration flights are performed on a regular basis to maintain the performance of the complete system [4].

A standard image reflects the radar brightness relation in slant range geometry, as in (1).

$$\sqrt{\beta_0} = \sqrt{\sigma_0/(\sin\Phi_{Inc.})} \qquad (1)$$

Each image pixel is encoded as 16 bit signed integer. Standard images are processed with 8 looks in X- and C-Band and with 4 looks in L- and P-Band. L-Band, 8 look is optional.

Each E-SAR image is distributed on a 8200 Exabyte cassette (low tape density) in a simple data format, which is easy to handle. The format is referred to as *E-SAR Image Data Format*.

The E-SAR image tape contains radar system and processing parameters, a browse image and a precision SAR image file, where the user may choose among a number of products.

E-SAR TECHNICAL CHARACTERISTICS

The E-SAR sensor system is characterized by a modular design. A radar signal, i.e. a short FM coded pulse of 5 µs duration, with a bandwidth of up to 100 MHz centred around an

intermediate frequency of 300 MHz can be easily converted into any other frequency band. In recent years front-ends have been realized in P-, L-, C- and X-Bands. Today we put effort into the development of a new S-Band radar segment.

Antenna technology was exploited to its limits to obtain more than 10% bandwidth from a microstrip patch array in P-Band. This is also the design goal in S-Band. The present P-Band dual-polarized antenna has a multi-layered, high dielectric array element design. The antenna is a 2 by 4 element array, 0.5 m high and 1.3 m long. Measurements on DLR's antenna range showed satisfactory results, so that radiometric calibration of the data is possible. All relevant E-SAR technical parameters are given in Table 1.

Further, motion compensation for L-Band and even more for P-Band represents a difficult task, rather than in X- and C-Band. For example, to obtain a P-Band image with four looks and 4 m azimuth resolution the total integration time would be in the order of 25 to 40 seconds. Hence, the platform motions must be considered critical. GPS augmenting an inertial measurement system is our solution to this problem. We have solved it for L-Band. In P-Band, however, imagery of reasonable quality can only be obtained today at lower azimuthal resolution. The standard P-Band product features 4 looks and 12 m resolution in both azimuth and slant range directions.

The E-SAR radar involves antenna technology ranging from a pyramidal horn (X-Band) over microstrip patch arrays (C- and P-Band) to passiv microstrip phased arrays (L- and S-Band). Transmitter power is generated by pulsed TWTAs (X, S) and solid state devices (C, L, P). The radar pulse is generated either by a digital or analogue signal generator (DSG or SAW), where the digital subsystem provides higher flexibility in terms of pulse bandwidth and pulse duration. The receiver incorporates a fast gain control including a STC for signal adaptation to two 6-bit A/D-converters, which digitize the inphase (I) and quadrature (Q) signal components. Three different coherent sampling frequencies (100 MHz, 60 MHz and 20 MHz) allow the implementation of three swath modes (narrow, wide and super wide).

Representative radar results recently obtained are shown in Fig. 2, 3, and 4. The selection intends to demonstrate the advantages of a multi-frequency SAR system.

Figure 2: E-SAR image of the Oberpfaffenhofen airfield showing the DLR research centre beneath the runway. (X-Band, narrow swath, 8 looks, 3 m x 3 m resolution.)

A simple comparison of the images shown in Fig. 2 and 3 reveals differences in the radar signatures typical for X- and L-Band. The visibility of a gras runway in Fig. 3 demonstrates the volumetric scattering characteristics in L-Band. Surface roughness, on the contrary, is better reflected in X-Band. Also apparent is the rather low image contrast in X-Band.

Fig. 4 shows a test area for agriculture applications in Southern Germany imaged in P-Band with horizontal polarization. The image reveals the typical high contrast between wooded

Table 1: E-SAR Technical Key Parameters

RF-Band	X-Band	C-Band	S-Band	L-Band	P-Band
RF-centre frequency	9.6 GHz	5.3 GHz	3.3 GHz	1.3 GHz	450 MHz
Transmit peak power	2500 W	50 W	2000 W (goal)	360 W	180 W
Receiver noise figure	3.5 dB	5.0 dB	tbd	8.0 dB	4.5 dB
Antenna gain	17.5 dB	17 dB	tbd	17 dB	12 dB
Azimuth beamwidth	17°	19°	20° (goal)	18°	30°
Elevation beamwidth	30°	33°	35° (goal)	35°	~ 60°
Antenna polarization	H and V	H and V	H and V	H and V	H and V
System bandwidth	120 MHz	120 MHz	120 MHz	100 MHz	25 (or 60) MHz

Figure 3: E-SAR image of the Oberpfaffenhofen airfield showing the DLR research centre beneath the runway. (L-Band, narrow swath, 8 looks, 3 m x 3 m resolution.)

Figure 4: E-SAR image showing agricultural fields and woodlands located north of the city of Weilheim. The river Ammer is visible along the image centre line. (P-Band, wide swath, 4 looks, 12 m x 12 m resolution.)

areas and graslands. The amount of radio interference is low. In general we have about 20 dB less distortion with horizontal as with vertical polarization.

E-SAR IMAGING GEOMETRY

The E-SAR is able to collect raw data in three different swath modes, narrow (3 km), wide (5 km) and super wide swath (15 km), with accordingly reduced slant range resolution. One range line consists of 2k complex samples, which is fixed by the present onboard data recording system. Thus, a larger coverage in range can only be obtained by increasing the slant range sample spacing, narrow swath (1.5 m), wide swath (2.5 m) and super wide swath (7.5 m).

E-SAR's imaging geometry is ruled by flight altitude, swath width and antenna footprint. Flight operations, which require maximum endurance of the platform, can only be performed at altitudes up to 3600 m above mean sea level (flight level FL 120). The off-nadir angle ranges from 25° to 60° (narrow swath) or 70° (wide swath). At an altitude of 5700 m (FL 190) the off-nadir angle in far range is reduced to 55° (narrow swath) and 65° (wide swath). The endurance, however, is reduced by approx. 20%, because additional equipment providing oxygen has to be installed in the aircraft.

Narrow and wide swath imagery of land surface can be obtained in all spectral bands with a ground range coverage of 3.5 to 4 km and 5.5 to 6 km, respectively. Sea surface must be imaged in narrow swath mode only, due to limited available si-

gnal power, especially at low sea state. The off-nadir angle range in this case is reduced to 25° to 55°.

At the present we do not offer the super wide swath mode, because the processing is not yet fully operational. Flight tests showed, that this mode is useful in L-Band over land surface.

CURRENT AND FUTURE ACTIVITIES

Our current development work on the E-SAR system is mainly aimed at a new digital control and data recording unit. The final goal is the capability of recording 4 channels quasi-simultaneously at full data rate. This allows polarimetric measurements in one frequency band or multispectral measurements at one polarization carried out on a pulse-to-pulse basis. The use of two parallel receiver chains in each radar RF module is not intended at the moment.

Multi-channel Operation

As an intermediate step we realized in 1995 the possibility to obtain multi-polarization data in L-Band with the present M14LR recording system. As the Doppler bandwidth in L-Band equals only 266 Hz at a ground speed of 75 m/s the radar records a frame of 4 samples with switched polarization (HH, HV, VH, VV) at an nominal PRF of 300 Hz (per frame). Each range line carries a special ID to allow for proper separation before off-line SAR processing. First results of successful flight trials are expected soon to be released. Consequently we

are now modifying the P-Band section of the radar in order to obtain multi-polarization data sets as well.

P-Band SAR Processing

During EMAC'94 and '95 remote sensing campaigns we recognized, that P-Band image quality is suffering badly from TV/MobileCom interference especially in vertical polarization. At the present the radar segment reveals its full potential only over areas with no telecommunications facilities. We have taken steps so far in reducing the radar's bandwidth to 25 MHz (or 60 MHz) at the input to the low noise preamplifier. However, it is still necessary to implement adaptive interference filtering in the off-line processing to remove distortions.

SAR Interferometry

Much effort was put into the realization of a radar front-end for both across and along track single-pass SAR interferometry in X-Band. Additional antenna mounts were attached to the right hand side of the aircraft for both configurations. The mechanical baselines are approx. 150 cm (across track) and 80 cm (along track). Switched from pulse to pulse both antennas are transmitting and receiving radar signals.

In 1995 flight trials resulted in useful data sets obtained in the across track configuration and off-line SAR processing has provided first interferometric phase information. However, the system performance is not yet fully satisfactory. New antennas featuring higher bandwidth and higher gain will be integrated to improve SNR and resolution.

The evaluation of one data set resulted in the successful generation of an interferometric phase image shown in Fig. 5 with the flat Earth removed. Fig. 6 finally shows the derived digital elevation model of a Munich city garbage dump with a hight resolution of approximately 1 m and an absolute accura-
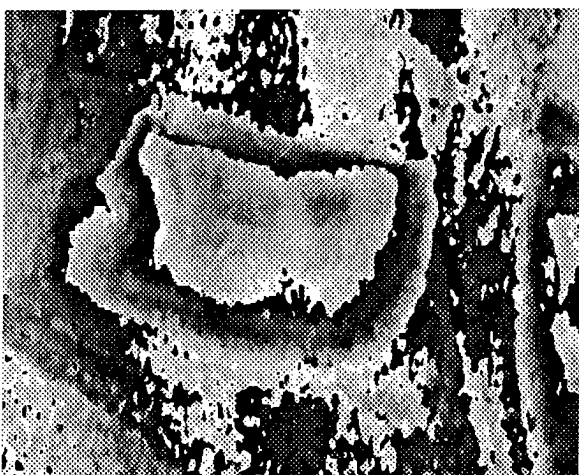
Figure 5: E-SAR X-Band interferometric SAR phase image with the flat Earth removed. Site: City garbage dump located north of the city of Munich, Germany.
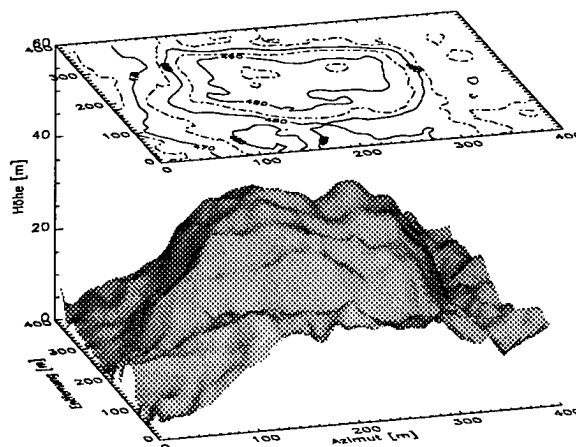
Figure 6: Digital elevation model (DEM) of the Munich City garbage dump obtained by E-SAR in across track interferometric SAR mode. Hight accuracy: ~ 5 m. Resolution: ~ 1 m.

cy of approximately 5 m. This is our first result obtained with X-Band across track single-pass SAR interferometry.

REFERENCES

[1] A. Moreira, R. Spielbauer, W. Pötzsch, "Conceptual Design, Performance Analysis and Results of the High Resolution Real-Time Processor of the DLR Airborne SAR System", Proceedings of IGARSS'94, Pasadena (USA), 1994.

[2] St. Buckreuss, "Motion Compensation for Airborne SAR based on Inertial Data, RDM and GPS", Proceedings of IGARSS'94, Pasadena (USA), 1994.

[3] R. Horn, J. Moreira, E. Meier, "A Refined Procedure to generate Calibrated Imagery from Airborne Synthetic Aperture Radar Data", Proceedings of IGARSS'92, Houston (USA), May 1992.

[4] M. Zink, P. Olivier, A. Freeman, "Cross-Calibration between Airborne SAR Sensors", IEEE Transactions on Geoscience and Remote Sensing, Vol. 31, No. 1, pp. 237-245, January 1993.

EMISAR: C- AND L-BAND POLARIMETRIC AND INTERFEROMETRIC SAR

E. Lintz Christensen, J. Dall, N. Skou, K. Woelders, J. Granholm, and S. Nørvang Madsen
Danish Center for Remote Sensing, DTU, Dept. for Electromagnetic Systems[1]
B. 348, Technical University of Denmark, DK-2800 Lyngby, Denmark.
Phone: +45 4588 1444. Fax: +45 4593 1634. E-mail: lintz@emi.dtu.dk

ABSTRACT

EMISAR is a C- and L-band fully polarimetric (i.e. 4 complex channel per frequency) synthetic aperture radar designed for remote sensing with high demands for resolution (2 m), polarization discrimination, and absolute radiometric and polarimetric calibration. The present installation has one 3-axes stabilized antenna (C- or L-band) and two flush mounted C-band antennas providing the system with cross track and repeat track interferometric capabilities.

INTRODUCTION

Electromagnetics Institute (EMI) began operating its C-band, vertically polarized, Synthetic Aperture Radar (SAR) in 1989. The radar has a 100 MHz bandwidth and an 80 km range. A full swath, full resolution real-time processor was completed in 1992. The C-band system has since been upgraded to fully polarimetric capability, and the first test flights took place in the fall of 1993. An additional L-band system with full polarimetric capability and the same resolution and image quality was completed and tested early 1995. The system was upgraded to interferometric capability in 1995 and the work on perfecting the installation and the processing software is ongoing.

The major application of the system is data acquisition for the research of the Danish Center for Remote Sensing (DCRS) which has been established at EMI with funding from the Danish National Research Foundation. The upgrade to polarimetry has been supported by the Joint Research Centre (JRC) of the European Community with the intention that EMI will operate the polarimetric SAR for JRC in connection with the intended EARSEC (European Airborne Remote Sensing Capabilities) campaigns. During 1994 and 1995 the SAR system has been used to acquire polarimetric data for EMAC (European Multi-sensor Airborne Campaigns) organized and sponsored by ESA [1].

SAR SYSTEM RADAR HARDWARE

The SAR consists of an airborne system (the SAR sensor including 2 sensors with antennas), and a ground segment (the off-line processing facility). Figure 1 gives an overview of the complete system while Table 1 summarizes the more important performance parameters of the sensor.

AIRCRAFT

The EMISAR is operated on a Gulfstream G–3 aircraft of the Royal Danish Air Force (RDAF). The G–3 is a twin engine jet, with a 6000 km range. The radar is usually operated at an altitude of 41,000 ft. but lower altitudes are used in some modes.

The size, weight, and power consumption allows the complete dual frequency system to be transferred to a smaller jet aircraft of the size of a Falcon 20 but the large range and high ceiling of the G-3 has advantages with regard to data acquisitions at distant sites and flexibility in imaging geometry. The G-3 can reach most sites in Europe, carry out the mapping, and return to the home base within one or two days.

The aircraft flight director gets its navigation information from an inertial navigation system and thus has a limited accuracy which is sufficient for normal flights. The SAR control computer gets navigation information from the aircraft P-code GPS receiver and emulates an instrument landing system (ILS) receiver which is connected to the aircraft flight director computer. In this way the actual flight track during mapping can be kept within a few meters of the desired track.

ANTENNA POD INSTALLATION

A polarimetric antenna system and the radar INU are installed in a pod mounted below the fuselage, which facilitates rapid system installation and dismount. The pod installation includes a 3-axes stabilized antenna that allows zero Doppler

Table 1. EMISAR performance parameters

Frequency	5.3 GHz	1.25 GHz
Polarization	Polarimetric	Polarimetric
Antenna cross polarization	< -30 dB	< -35 dB
Azimuth ambiguity	< -30 dB	< -30 dB
Resolution in slant range	2, 4 or 8 m	2, 4 or 8 m
Resolution in azimuth	2, 4 or 8 m	2, 4 or 8 m
Swath width	12 or 24 km	12 or 24 km
Range (at noise equivalent σ_{on} < -20 dB)	Max. 80 km	Max. 64 km
PSLR (In azimuth only at good flight conditions)	30 dB	25 dB
ISLR (In azimuth only at good flight conditions)	25 dB	25 dB
Intrinsic cross-talk terms	< -30 dB	< -35 dB
Calibrated cross-talk terms	< -35 dB	TBD
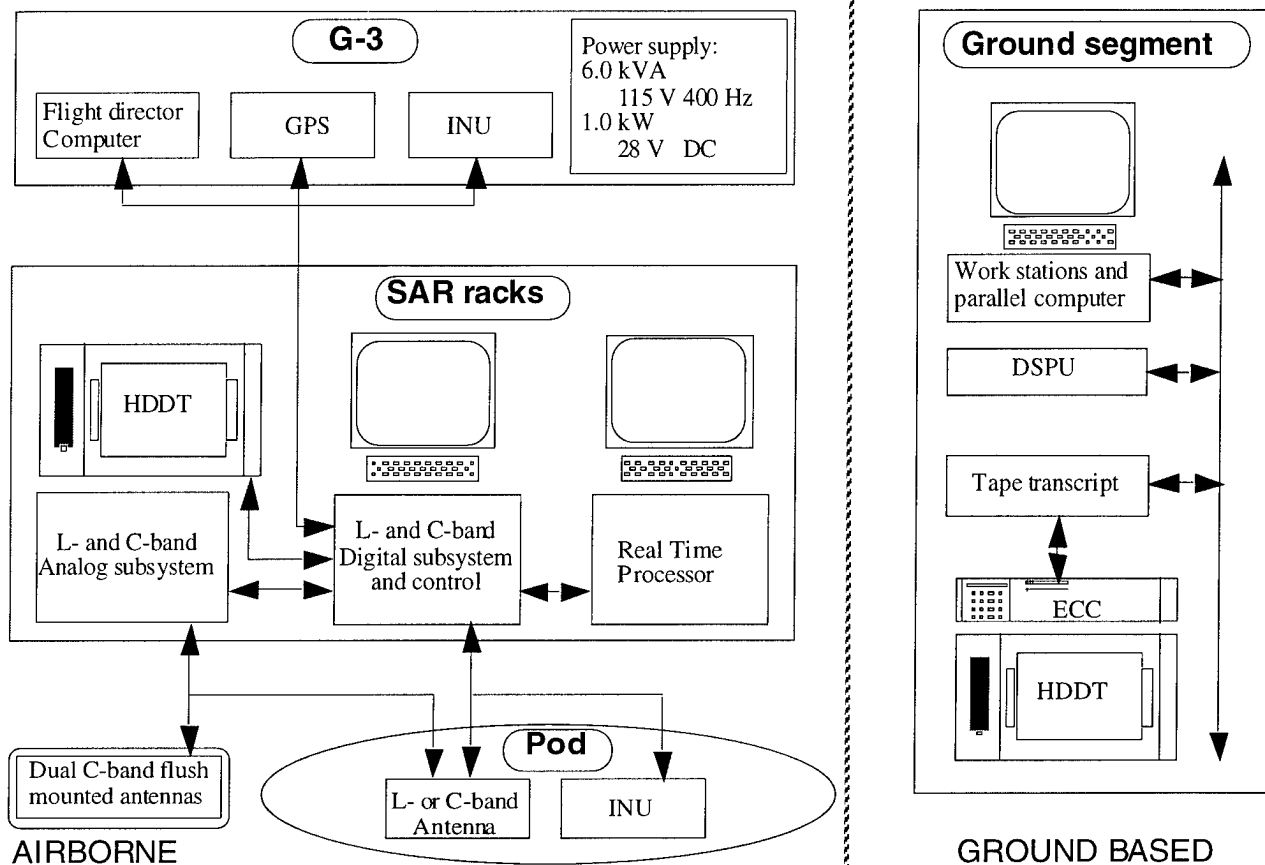
Figure 1. EMISAR C- and L-band SAR system overview with airborne and ground based segments.

mapping. However, the present pod has only room for one antenna, i.e. either L- or C-band. The radar electronics has been designed for simultaneous L- and C-band operation.

DUAL FREQUENCY AND INTERFEROMETRY

In 1995 one RDAF Gulfstream aircraft was augmented with two flush mounted antennas primarily intended for interferometric SAR applications. However, both antennas are fully polarimetric thus this installation offers a possibility for simultaneous dual frequency operation, although not at zero Doppler. The data rate needed for the squinted operation with the present hardware does not permit full resolution/swath dual frequency operation with full polarimetry.

The flush mounted installation presently has a physical baseline of 1.1 m and topographic mapping (aiming at producing digital elevation models) with this system has already been demonstrated [2]. The complete installation, having one antenna in the pod and two flush mounted antennas, also has the capability of along track interferometry although that feature has not yet been tested.

The system has been extended to support repeat track interferometry (RTI) but this mode is still under development. Very accurate track geometry is possible by the SAR control computer emulating an ILS receiver making actual tracks deviate only a few meter from the desired. Very high resolution

topographic mapping and change detection are possible although the method does require a challenging off-line processing [3].

ANTENNAS

The antenna for C-band is a dual polarized 32x7 element microstrip antenna designed to approximate a modified cosec-squared elevation radiation pattern for optimum illumination of the ground. The design has achieved high polarization discrimination, [4], [5].

The L-band antenna is a dual polarized 8x2 element microstrip antenna with even better high polarization discrimination. In order to obtain the required bandwidth the elements are stacked microstrip patches [6].

The antenna designs have furthermore been optimized to improve the system azimuth sidelobe performance [7]. Some of the more important antenna parameters are listed for both frequencies in Table 1.

The antenna attitude is automatically controlled. The antenna depression is set-up before each mapping to give the appropriate illumination of the target area. The aircraft attitude is measured by an inertial navigation unit (INU) located next to the antenna, and the antenna pointing is continuously updated to compensate for aircraft motion during mapping.

THE SENSORS

The two sensors, one for C-band and one for L-band are identical except for the microwave subsystems.

Digitally generated modulation waveforms are converted to an I, Q pair of baseband signals which are upconverted, amplified, and then guided to the antennas. The signals received by the antennas are amplified and downconverted to an I, Q pair of baseband signals. The analog subsystems are temperature regulated to assure high stability.

The I, Q baseband signals are digitized to 8 bit samples at 100 Mhz and the received baseband signals is range pre-filtering (if reduced bandwidth and wider swath has been requested), double buffered, first order motion compensated, and azimuth pre-filtered and decimated to the requested pixel spacing. The pre-processed data are sent to the high density digital tape recorder (HDDT) which has sufficient capacity for the necessary ancillary information plus the output of both sensors at 1.5 m pixel spacing (240 Mbit/s). The data are also sent to the real time processor, [8], [9], which performs the SAR processing at full swath and resolution of one channel (although with some limitations at L-band and for squinted data).

The HDDT can accept all 8 channels at 1.5 m pixel spacing which is sufficient only when the signals are recorded at zero Doppler (a limitation of the existing azimuth pre-filter). With the present installation one sensor will use the flush mounted antennas and thus simultaneous dual frequency polarimetric operation is not yet supported at the highest resolution with a full swath.

ABSOLUTE CALIBRATION

The SAR system has been designed and thoroughly tested to provide absolute radiometrically and polarimetrically calibrated data. This is accomplished by 1) having a very stable system, 2) performing internal calibration of this system immediately before and after each data take, and 3) by performing an absolute calibration at each mission using external standards.

EMISAR employs a unique internal calibration system which greatly relieves the dependence on external calibration targets: by measuring system parameters via internal signal loops just before and after mapping a scene, a calibrated image can be generated assuming knowledge and stability of a few passive components [10], [11], [12].

The internal calibration procedure comprises channel amplitude- and phase-imbalance correction, absolute radiometric calibration, and it has a potential for range delay calibration, STC calibration, and noise estimation, as well. Furthermore, the built-in calibration paths allow the pulse-based procedure to calibrate almost the complete system, including both the transmitter and the receiver, but not the antenna.

A 3-axes stabilized antenna has been chosen for both frequencies (the flush mounted antennas are not used for polarimetric calibrated modes) to avoid the calibration uncertainty otherwise caused by temporal variation of the antenna pointing error. The antenna is pointed perpendicular to the desired

track to permit zero Doppler processing. The antennas which are not included in the internal calibration loops have been calibrated to an accuracy of 0.1 dB on the directivity and 0.2 dB on the absolute gain by using the ESA-TUD Spherical Near-Field Antenna Test Facility [13]. The cross polarization terms of the antenna gains have not been included in the calibration.

To facilitate the absolute (external) calibration, a calibration test site (with 3 trihedral and 4 dihedral corner reflectors) has been established in cooperation with Research Centre Foulum which is also collaborating with DCRS on research in mapping soil and plants. This site is mapped on all missions and a very significant number of calibration data sets are available.

The results obtained for the 3 dB resolution, the peak side lobe ratio (PSLR) and the integrated side lobe ratio (ISLR) using the co-polar trihedral responses are summarized in Table 2.

The calibration stability has been examined based on a three day campaign where first two C-band calibration scenes were acquired, then four L-band scenes, and finally two additional C-band scenes, i.e. the antenna was dis-mounted and re-mounted between the two C-band missions. Using internal calibration only, the standard deviations of the absolute calibration and the channel imbalance was calculated, Table 3. Obviously a single external calibration per mission suffice.

For absolute calibration and channel imbalance correction, the internal calibration is complemented by corrections derived from external calibration results. These corrections are small and vary little from mission to mission. They were determined in an initial calibration experiment, and on most missions they are checked and adjusted if necessary by external calibration.

Cross-talk calibration may be carried out using distributed targets for which the true co- and cross-polarized returns are uncorrelated. This requirement is met by natural targets with azimuthal symmetry. Unlike most other algorithms, the Quegan algorithm [15] is non-iterative, and since it has previ-

Table 2. L-band and C-band impulse response statistics based on 2.0 m trihedrals (average ±standard deviation).

L-band		azimuth	range
3 dB resolution	(m)	2.05 ± 0.02	1.98 ± 0.02
PSLR	(dB)	-25.2 ± 2.0	-25.8 ± 1.3
ISLR	(dB)	-25.1 ± 2.4	-22.8 ± 1.7

C-band		azimuth	range
3 dB resolution	(m)	1.97 ± 0.01	2.09 ± 0.01
PSLR	(dB)	-31.9 ± 2.4	-30.9 ± 2.1
ISLR	(dB)	-30.8 ± 0.8	-29.0 ± 1.2

Table 3. Standard deviation of residual calibration errors after internal calibration..

Frequency	TX imbalance	RX imbalance	Absolute cal.
L-band	0.12 dB 1.1°	0.20 dB 2.2°	0.51 dB
C-band	0.07 dB 1.2°	0.14 dB 1.6°	0.05 dB

ously shown good results for AIRSAR data, it has been used - in an enhanced version providing 4 channels - to estimate the rather small residual cross-talk from the EMISAR data [1]. Recent results seem to question that natural targets in general can be assumed to have sufficient azimuthal symmetry. Therefore EMISAR data, considering their low intrinsic cross talk (Table 1), are usually not cross-talk corrected.

PROCESSING CAPACITY

The processing of SAR data to quality images used to be a very time consuming task for standard computers. However, with 3 of todays fast RISC work stations with adequate RAM the computer capacity for processing polarimetric SAR data is in excess of 1000 fully polarimetric (i.e. 4 channels, 12 by 12 km, 2 by 2 m resolution) scenes a year. With the recent acquisition of a parallel computer facility the computer capacity is not the problem.
However, bottlenecks during HDDT transcription, lack of automated set-up in parts of the processing chain and output product generation presently limits the actual throughput to a somewhat lower number. The HDDT reliability is a weak link. Presently the actual processing throughput is around 10 polarimetric scenes per week. Work on automating the entire processing chain is in progress and further improvements of the capacity is expected during the summer of 1996.

REFERENCES

[1] J. Dall, S. Nørvang Madsen, H. Skriver, S. Savstrup Kristensen, and E. Lintz Christensen, "EMISAR Deployment in the EMAC '94 Campaign", Electromagnetics Institute, The Technical University of Denmark, Lyngby, Denmark, R 600, Sept. 1994.

[2] S.N. Madsen, N. Skou, J. Granholm, K. Woelders, E.L. Christensen, "A System for Airborne SAR Interferometry", European Conference on Synthetic Aperture Radar, EUSAR '96, Königswinter, Germany, 26-28 March, 1996, and in the International Journal of Electronics and Communication, Germany (AEÜ), March 1996. Both in press.

[3] J.J. Mohr and S. Nørvang Madsen, "Parametric Estimation of Time Varying Baselines in Airborne IFSAR", International Geoscience and Remote Sensing Symposium, IGARSS '96, Nebraska, USA, 27-31 May 1996, In press.

[4] K. Woelders and J. Granholm, "Design and Performance of a Dual-Linearly Polarized C-band Microstrip Array Antenna", Second International Workshop on Radar Polarimetry, Nantes, France, Sept. 1992, pp. 369-378.

[5] J. Granholm, K. Woelders, M. Dich and E. Lintz Christensen, "Microstrip Antenna for Polarimetric C-band SAR", IEEE AP-S International Symposium and URSI Radio Science Meeting, Seattle, Washington, June 19-24, 1994

[6] N. Skou, J. Granholm, K. Woelders, J. Rohde, J. Dall, and E. Lintz Christensen, "A high Resolution Polarimetric L-Band SAR - Design and First Results", IGARSS '95, 1995 International Geoscience and Remote Sensing Symposium, Firenze, July 10-14, 1995, Vol. 3, pp 1779-1782.

[7] E. Lintz Christensen and M. Dich, "SAR Antenna Design for Ambiguity- and Multipath Suppression", IGARSS '93, 1993 International Geoscience and Remote Sensing Symposium, Tokyo, August 18-21, 1993, Vol. 2, pp 784-787.

[8] J. Dall, J. Hjelm Jørgensen, E. Lintz Christensen and S. Nørvang Madsen, "Real-Time Processor for the Danish Airborne SAR", IEE Proceedings Part F, Special part on Remote Sensing, pp 115–121, April 1992.

[9] J. Dall, J. Hjelm Jørgensen, A. Netterstrøm, N. Vardi, E. Lintz Christensen, and S. Nørvang Madsen, "The Danish Real-Time SAR Processor: First Results", IGARSS '93, 1993 International Geoscience and Remote Sensing Symposium, Tokyo, August 18-21, 1993, Vol. 3, pp 1401-1403.

[10] A.L. Gray, P.W. Vachon, C.E. Livingstone, and T.I. Lukowski, "Synthetic Aperture Radar Calibration Using Reference Reflectors", IEEE Transactions on Geoscience and remote Sensing, Vol. 28, No 3, pp. 374-383, May 1990.

[11] N. Skou, "The Danish Polarimetric SAR System", Second International Workshop on Radar Polarimetry, Nantes, France, 8-10. September 1992, pp 525-533.

[12] J. Dall, Niels Skou, E. Lintz Christensen, "Pulse-based Internal Calibration of Polarimetric SAR", IGARSS'94, 1994 International Geoscience and Remote Sensing Symposium, California, USA, 8-12 August 1994.

[13] J.E. Hansen (Ed), "Spherical Near Field Antenna Measurements", Peter Peregrinus, London, 1988

[14] Henning Skriver, Jørgen Dall, Søren Nørvang Madsen, "External Polarimetric Calibration of the Danish Polarimetric C-band SAR", IGARSS'94, 1994 International Geoscience and Remote Sensing Symposium, California, USA, 8-12 August 1994

[15] S. Quegan, "A Unified Algorithm for Phase and Cross-Talk Calibration of Polarimetric Data - Theory and Observations", IEEE Transaction on Geoscience and Remote Sensing, Vol. 2, No. 1, pp. 89-99, January 1993.

First Results and Status of the PHARUS Phased Array Airborne SAR

H. Greidanus, P. Hoogeboom, P. Koomen
TNO Physics and Electronics Laboratory
P.O. Box 96864, 2509 JG Den Haag, The Netherlands
tel. +31-70-3740000, fax +31-70-3280961, e-mail greidanus@fel.tno.nl

P. Snoeij
Delft University of Technology, Lab. for Telecom. and Remote Sensing Technology

H. Pouwels
National Aerospace Laboratory NLR

Abstract -- PHARUS is an airborne fully polarimetric C-band SAR. It uses a compact phased array antenna with electronic beam steering. Its design provides for a flexible and robust system concept, suited for operational use on small aircraft. PHARUS was developed in The Netherlands to cater for both the military and civil markets. Its development was initiated in 1987 and has now resulted in completion of the system, which made its maiden flight in September 1995.

In the paper, the particulars of PHARUS will be discussed, with special attention to the antenna, followed by the SAR processing, use of the system, its history and status, and foreseen future developments.

INTRODUCTION

PHARUS ("Phased Array Universal SAR") is an airborne, fully polarimetric C-band SAR. Its special characteristic is the use of an electronically steerable phased array antenna, with each (individually replaceable) antenna element consisting of a dual polarized patch mounted on a T/R module based on (M)MIC technology. This antenna design results in a system concept that is compact, robust and flexible, making it suitable for economic use on small aircraft. Furthermore, it is the technology envisaged for future spaceborne radars.

The current antenna contains 48 (2×24) elements with a total peak power output of 475 W (in tapered mode) at 5.3 GHz (chirped). The beam is steerable over −/+15° in elevation and −/+20° in azimuth. The compact design necessitates pumped liquid cooling. The next section will provide some more information on the PHARUS antenna. Concerning other characteristics of PHARUS, it uses motion compensation as recorded by a cascade of motion sensors with increasing precision (GPS and lasergyro-IRS systems in the aircraft, and an Attitude Reference Assembly in the antenna itself); its current platform is a Cessna Citation II operating at a speed of around 150 m/s up to large (14 km)

altitudes; the radar data are digitally recorded with a maximum rate of 100 Mbyte/sec on a DCRSi; and the system is operated through a console, on which gain, beam pointing, image mode, swath location (up to 26 km out) and other imaging parameters can be set. Possible image modes are 4, 8 or 16 m resolution (at 3 - 20 looks), 1, 2 or 4 polarization channels (the latter being fully polarimetric, i.e. including phase information) and swath width between 3 and 20 km. The single look azimuth resolution is 1 m. The data rate actually being the limiting factor, it is, however, not possible to combine full polarimetry at the highest resolution with the widest swath.

ANTENNA

Given the C-band frequency, the scan range of the beam mentioned above dictates an antenna element spacing of 41 × 44 mm. This is also the size of the T/R modules, which are in addition 160 mm deep. The necessary miniaturization is attained by the use of MMIC technology. The top of each T/R module is a radiating square patch positioned in the antenna plane. The patch is fed from two adjacent sides by a hybrid ring ("rat race"); both sides are excited with the same amplitude for each transmit polarization (H or V), but either in phase or anti-phase. With this arrangement a polarization decoupling of better than 25 dB is reached within the main (−3 dB) beam, necessary for accurate polarimetric measurements. The T/R module further contains a power amplifier (PA), two low-noise amplifiers (LNA) and two vector modulators. In dual polarization transmit mode, the 20 W PA is connected to alternately the H- and V-channel; in receive mode, both channels operate simultaneously using their own LNA. Microwave switching is controlled by digital timing and control circuits. Total transmit gain of each T/R module is 55 dB, total receive gain 30 dB.

The setting of the vector modulators (4 bit in amplitude and 7 bit in phase) is generated using two look-up tables

(LUTs) per T/R module. The values of the first LUT have been assigned by calibration after construction of the T/R module, to make all T/R modules behave identically. The second LUT, associated not with a specific T/R module but with a specific position in the antenna plane, has been calibrated after construction of the complete antenna in order to produce the desired full antenna pattern. Each T/R module is also equipped with a separate calibration channel, enabling an internal calibration procedure. This autocalibration can be performed in-flight, as often as needed to correct for electronic drift.

PROCESSING

On board the aircraft, a real-time quick-look SAR processor will be available for immediate verification. The ground segment of the PHARUS system consists of the Generic SAR Processor (GSP), a UNIX-based processor that can handle not only PHARUS data but also SAR data from other air- or spaceborne sources. It has been used for ERS-1 and JERS-1 data. For aircraft, it is able to use the recorded platform motion data for motion compensation; it also has an autofocus capability for automatic Doppler centroid and Doppler rate estimation. The GSP accommodates polarimetric calibration (including e.g. cross-talk removal and the use of external calibrators such as corner and active reflectors) and quality control functions (beam width, side lobe level, ENL, etc.). Output of the GSP are images in several formats of choice, to be ingested into commercial image processing packages.

USE

The characteristics of the PHARUS system make it an economically viable option, particularly suitable for operational use. It can be flown, affixed with a rigid mounting, on small (hence economic) aircraft; its modular design results in robustness, since failure of one (or even several) of the individual T/R modules only slowly degrades the performance, and not totally aborts operation. Broken modules may be quickly replaced, and the pre-defined- and auto-calibration bring the system immediately up to specs. Its ability to fly high (and fast) provides efficient and stable operation, also in mountainous areas and turbulent skies.

PHARUS' system parameters make it suitable for many applications, including mapping, land use inventory (including forestry and agriculture), but also maritime applications such as ship traffic monitoring, oil spill detection and ocean wave measurements. The polarimetric capability provides additional discerning power, enhancing possible

military uses of the system (object recognition, etc.). In these applications, PHARUS can be used in addition to satellite data on account of the complementary resolution and polarimetric and revisit capabilities of an airborne system. Performance in many of these areas has already been proven by PHARUS' predecessor and testbed "PHARS" (next section). In addition, the (M)MIC active phased array concept and the high maximum operating altitude of 14 km enable PHARUS to be deployed as an ASAR demonstrator.

The flexibility of the PHARUS concept is not only found in its operation, but also in its design. On the same base design, different actual systems can be built combining more or less T/R modules, resulting in systems with a range of performances and corresponding costs. Together with the ground segment and the transfer of knowledge concerning construction, maintenance and operation of the system, the PHARUS concept can provide an autonomous airborne SAR capability for its user.

HISTORY AND STATUS

The PHARUS project is a cooperation between the TNO Physics and Electronics Laboratory (TNO-FEL), the National Aerospace Laboratory (NLR) and the Delft University of Technology (TUD). It is sponsored by the Netherlands' Remote Sensing Board (BCRS) and the Ministry of Defense, and program management is carried out by the Netherlands' Agency for Aerospace Programs (NIVR).

The start of the program can be traced back to 1987, after work in the Netherlands with airborne SLAR and scatterometers. An important milestone was reached in late 1990, when the testbed PHARS produced its first airborne images [1]. In PHARS, the new technology was tried out and experience for the full system was gained. PHARS has a somewhat lower resolution (5 m) and only one polarization channel (VV); otherwise it shares many traits with PHARUS. The PHARS system has been used for many applications and is still available today. Development of the actual PHARUS system was begun in 1991, and has culminated in its first, and successful, flight in September 1995.

The first test flights have so far demonstrated achievement for a number of the design criteria. All four polarimetric channels have been used, and the multi-look resolution goal of 4 m has been reached. One particular aspect that worked according to expectation was the limited pre-summing, resulting in the relatively wide Doppler filter that is necessary to accommodate the Doppler spectra over the full swath. The Doppler filter needs to be wide because the Doppler centroid is a function of range, due to the fact that the electronic beam

steering takes place in other planes than the aircraft motions (the antenna being mounted with its normal at 57.5° incidence angle). One unexpected result of the tests pointed to a relatively high sidelobe level when using the combination of large microwave bandwidth and highly skewed beam pointing, a matter currently being investigated.

FUTURE

The near future will bring an extensive test and familiarization program, in which PHARUS will be tried at numerous applications, ranging from crop classification to sea bottom topography imaging. For the somewhat longer term, extensions are foreseen toward interferometric capability for DEM-generation, surface current mapping and moving target indication. Also, future activities will be aimed at design and (cooperative) construction of dedicated systems for specific users based on the PHARUS concept, including technology transfer.

REFERENCES

[1] P. Hoogeboom, P. Snoeij, P.J. Koomen, H. Pouwels, "The PHARUS project, results of the definition study including the SAR testbed PHARS", IEEE Trans. on Geosc. and Rem. Sens., vol. 30, no. 4, pp. 723-735, July 1992
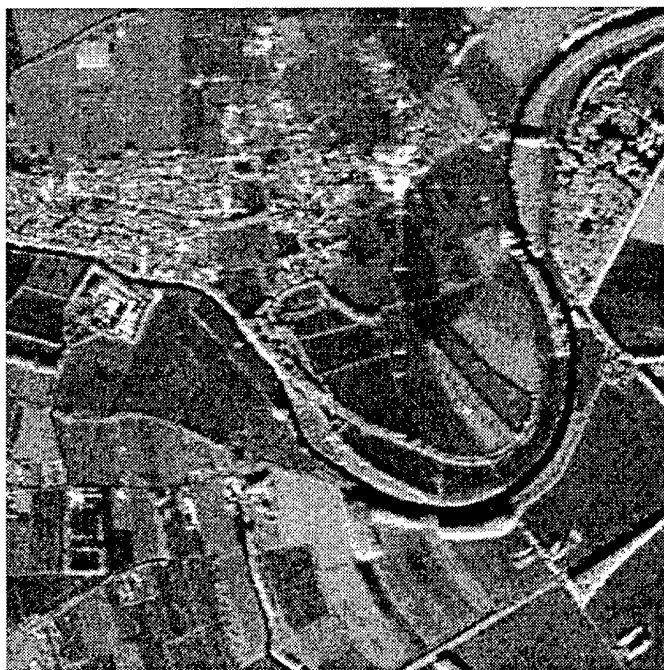
Figure 1. Scene from the first test flight, containing agricultural fields, forest patches, a river, roads and built-up areas. Resolution is 4 m at 3 looks, scene size 2.4 km, taken from 5 km altitude at around 45° incidence angle. One co- and one cross-pol image have been added, after bringing to the same average value.

Figure 2. Same scene as Fig. 1, now displaying the absolute difference between co- and cross-pol. It can be seen that, with the average cross-pol backscatter level scaled to the average co-pol level, mostly the built-up structures in the image become highlighted. Also a few of the fields have a slightly deviating co/cross-pol signature.

Development of the NASDA Airborne Synthetic Aperture Radar (NASAR-1)

Masanobu Shimada, Hiromi Oaku, and Masato Yamanashi
Earth Observation Research Center, National Space Development Agency of Japan (NASDA)
Roppongi First Bldg. 13F, 1-9-9 Roppongi, Minato-ku, Tokyo-to, Japan, 106
81-3-3224-7056(Tel), 81-3-3224-7052(Fax), e_mail:shimada@eorc.nasda.go.jp

Abstract -- NASDA has been developing a full polarimetric L band airborne Synthetic Aperture Radar (NASDA Airborne SAR-1: NASAR-1) since the beginning of 1995, in order to establish the complementary system to calibrate the spaceborne SAR and to understand the backscattering characteristics of the targets in this frequency. NASAR-1 onboard Gulfstream II provides the high resolution images of 3 m x 3 m for 20 km of imaging swath. NASAR-1 will be completed by the end of August 1996, and the various experiments will be conducted for CAL/VAL and science purposes. This paper describes the performance and the development status of the NASAR-1.

INTRODUCTION

The needs for the radar remote sensing using the Synthetic Aperture Radar (SAR) is increasing since the operational spaceborne SARs have been in service from the beginning of 1990. JERS-1, ERS-1/2, and newly settled Radarsat are those satellites for the earth remote sensing utilizing several SARs. JERS-1 SAR was developed by NASDA and Ministry of International Trade and Industry(MITI). It was launched on Feb. 11 1992 and has been in operation in L band HH polarization. As the results of the four years operation and data analysis, it is shown that L band SAR is suitable for the monitoring of forest change, sea ice discrimination, topography, surface deformation, etc., especially for interferometry because of less scene decorrelation and longer baseline criterion. Although JERS-1 may be in service for six years more from the point of remained fuel, the need for the follow-on SAR is raised to be improved the image quality, such as SNR, orbit determination error, orbit recurrence, etc. Then the new satellite "Advanced Land Observation Satellite(ALOS)" was planned which will carry SAR with the same fequency with JERS-1, in order to preserve the data continuity of the L-band SAR. As the preparation for the calibration and validation of ALOS data, development of the airborne SAR was decided in 1994. Since then, the basic designing of NASAR-1 was started, and the manufacturing is underway. This paper introduces the characteristics and the features of the NASAR-1.

SYSTEM CONFIGURATION

System performance

The representative system performances are as follows;
-High resolution SAR imaging capability of 3 m x 3 m geometric resolution and radiometric accuracy of less than 0.1 dB (expected).
-Full polarimetric observation.
-Repeat pass interferometry
-Digital chirp generation technique to allow the various transmission pulses.
-24 hours' all weather observation capability with the shortest installation time.
-synchronous operation with X band SAR, which is under development by Communication Research Laboratory (CRL).

Description of the each subsystem

NASAR-1 consists of five subsystems to be assembled on the aircraft. (see Figure 1 for the simplified block diagram and Table 1 for the spcification)
1) Antenna subsystem (ANT)
ANT is composed of two planner array antennas for H and V polarizations, made of carbon fiber of honeycomb structure. Among two operation modes, mode 1 offers the wider imaging swath in either of H and V polarization signal. Mode 2 offers the full polarized signals HH, HV, VH, and VV. Antenna pattern is of two dimensional pencil beam type. Antenna subsystem is contained within the radome made of the carbon honeycomb structure.
2) Trans receiver subsystem(TRX)
TRX is composed of original signal generator, chirp signal generator, high power amplifier, transmitter, and the receiver. Pulse modulated chirp signal is generated by the digital chirp generator. AGC (Automatic Gain Control) and MGC (Manual Gain Control) are selective, sensitivity time control (STC) can be used on request in order to well sit the received signal within the dynamic range of the receiver and the signal processor. Although NASAR-1 has its own original signal generator, the original signal of X-SAR can be ingested. The synchronous L and X band SAR operation is available and the co-registered X-L SAR images can be obtained.

3) Signal processing subsystem(SIGP)
Detected I and Q videos are digitized in two 8 bit streams. They are reformatted with SAR telemetry data, aircraft data, INS data and GPS data, then sent to high data rate data recorder (HRDR).
4) Controlling unit(CNT)
CNT is composed of system controller and signal monitoring unit and controls TRX, SIGNAL, and HRDR, in order to govern the whole NASAR system. It contains the function to save the log information on some certain frequency in order to read the ingested commands or the filed commands, and to display their contents to enable the operator to verify. GPS information (location, timing and velocities of the air craft) and INS information (angular velocity and acceleration in roll/pitch/yaw) is read and output to the signal processor.
5) High data rate data recorder(HRDR)
Observation data are recorded onto HRDR. When the data is recorded with 32 Mbytes/sec, 50 mins observation data will be stored on a tape.

GULFSTREAM II

As the carrier for the NASAR-1 and the X-SAR, Gulfstream II was selected from the following point of view, 1) to enable the stable flight at the altitude of more than 10,000 m, where the air stream is relatively stable than the lower altitude. This need is raised from that the motion compensation unit is not developed for these SARs, 2) to be able to carry two SARs and two operators within the four hours experiments, 3) the vibration of the aircraft should be as small as possible, 4) to contain the big enough power reservoir to enable two SARs' experiments, 5) the operation fee should be as cheap as possible. Diamond Air Service(DAS) is the commercial company to conduct the airplane SAR experiments. The outside view is shown in Fig. 2. G-II is the dual jet aircraft sized with 24 .3 meter long and 21 meter width and 7.5 m height. It can fly with the maximum speed of 900 Km/hour and upto 13,100 meter altitude. The maximum take off weight is 28.182 kg and maximum carry weight is 2.480 kg.

OPERATION

Calibration

Calibration of NASAR-1 will be conducted as the first priority task after the completion of the NASAR-1 at the end of Aug 1996. Two Active Radar Calibrators(ARC) will be used for the inflight calibration of NASAR-1 as deployed at NASDA's test sites, Hatoyama and Niigata, which exist as the calibration sites for JERS-1 SAR. The history of the incoming pulse intensity received by ARC may estimate the

azimuth antenna pattern at one off nadir angle. Repeat measurements with the different incidence angle will provide the whole the elevation and azimuth antenna pattern. Noise equivalent sigma zero will be estimated from the noise measurement data and natural data which are supposed to out of radar signal (Layover). Image quality of the standard product will be evaluated in terms of signal to noise ratio, peak to sidelobe ratio, integrate sidelobe ratio, signal to ambiguity ratio, etc. Calibration flight are planned in this fall.

Data take

Each flight pass normally acquires the 100 minutes data. Depending on the flight speed, the image length varies from 600 km to 1300 km. The standard processor defines the image size as 13.7 km * 13.7 km. Due to too much data volume for each image, it is estimated that the an image data processing may take 80 minutes. The data processor is under development for those work stations of SGI and SUN, expecting the completion by the end of August 1996. Raw data, single look complex, detected image, polarimetric images will be generated by this processor.

Data take plan

Each flight takes normally four hours including the ferry time to the test site. As the activity of '96, four to six passes are planned. Currently, it is planned that those flights focus on the agriculture, calibration, interferometry, ocean spectrum monitoring, forest monitoring, ice sheet monitoring, disaster monitoring, etc.

CONCLUSION

This paper introduces the development status of the NASDA Airborne synthetic aperture radar system (NASAR-1), which will be completed in the summer 1996. NASAR-1 is expected as the reference data source for the L band SAR science, and also to offer some basement for the coming spaceborne SAR remote sensing technology.

ACKNOWLEDGEMENT

Table 1 NASAR-1 Specification

1	Center frequency	1.27149 GHz
2	Band width	<= 50 MHz
3	Polarization	mode 1 HH or VV mode 2 HH, HV, VH, VV
4	Phase accuracy	<= 5 deg (after correction)
5	Off nadir angle	40 deg
6	Imaging swath	>= 16 Km at 12000 of cruising altitude

7	Resolution
	  Range direction
	
	  Azimuth direction
		
		3, 5, 10, 20 m(at 60 deg of incidence angle)
		3 m at three looks processing

8	Noise equivalent sigma zero	- 30 dB at SNR = 10 dB
9	S/A	>= 30 dB at off nadir of 20 - 60 deg.
10	calibration accuracy	0.6 dB
11	pulse duration	10 micro sec(nominal)
12	PRF	variable and <= 1 KHz

13	Data
	  ADC bit number
	  data rate
		
		8bit / I and Q channel
		256 Mbps

14	power consumption	<= 3.5 KW

15	total weight	450 Kg.

16	Antenna
	  gain
	  beam width
	
	  sidelobe
	
	  cross pol.
	  dimension
		
		>= 18 dB
		38 +- 4 degree in elevation
		9.8 +- 1.0 degree in azimuth
		< - 20 dB in elevation
		< - 25 dB in azimuth
		< - 25 dB
		1.7 m x 0.6 m

17	Transmission
	transmission pulse
	  duration
	  chirp band width
	
	  peak power
	  noise figure
		
		10 micro sec +- 0.1 micro sec.
		50MHz/45MHz/22.5MHz/11.3 MHz
		3 kW
		< 1.5 dB

18	Signal processor sampling frequency	 61.7 MHz/30.9 MHz

19	data recorder
	  media
	  data rate
	  data capacity
		
		D-1 cassette(L size)
		max. 32 Mbytes/sec.
		96 Gbyte

Fig.1 NASAR-1 Block Diagram
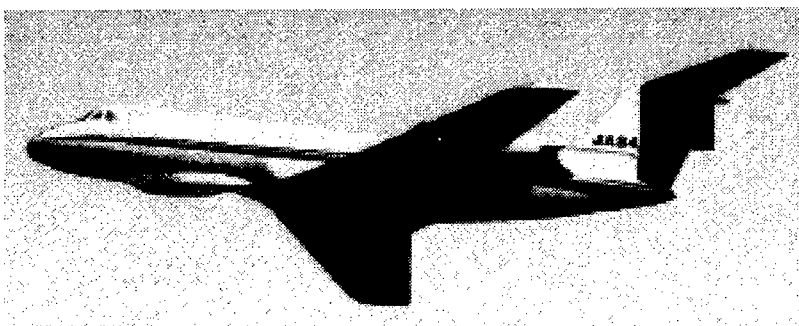
Fig.2 Outside View of Gulfstream II

The NEC Interferometric SAR system "NEC-SAR"

Hidefumi Nagata, Hiroshi Shinohara, Minoru Murata, Masonori Miyawaki, Hajime Shinme, Mamoru Sugawara, Hideharu Totuka, Yoshitaka Ohura, Hitoshi Nohmi

NEC Corporation

1-10, Nisshin-cho, Fuchu-city, Tokyo 183

tel.: 81-423-33-1146, fax: 81-423-33-1886, e-mail: NAGATA_23-24560@aladdin.nec.co.jp

Abstract

In this paper, we describe the "NEC-SAR" system outline, and data processing, and the summary of evaluation of interferometric images.

Introduction

NEC airborne SAR (NEC-SAR) system installed in a Cessna 208 has been evaluated since 1992, and have obtained many useful results [1]. This system was a conventional SAR system and used for earth resources detection and 2-D mapping.

Recently, we have experienced many big disasters, earthquakes, volcano eruptions. So, interferometric SAR [2],[3] are noticed as the promising techniques for geophysics.

So, we improved the system to extract the displacement field of earthquake and to generate DEM in high-speed. Then, this new system has been evaluated.

System outline

In NEC-SAR system, all units except the image processor are installed in a Cessna 208. This system has two antennas for interferometric SAR, that are separated in cross truck direction, and are installed inside the fuselage toward outside at a removed door. Fig. 1 shows a Cessna 208 with NEC-SAR installed.

Fig. 2 shows the system block diagram. This system is composed of a transmitter, a receiver, a signal processor, a system controller, a digital data recorder.

Onboard navigation systems in the Cessna 208 are VOR, ADF, and DME. Their is not inertial navigation system (INS). Altitude data, ground speed data, and drift angle data are very important for SAR image processing. The airplane installs no instrument which can output those to SAR system. A GPS and an 1-axis gyro compass are installed in this system and they are independent of navigation instruments. Their data is recorded to digital data recorder with SAR raw data.

To realize interferometric SAR, the antenna 1 is used for both transmission and reception. The antenna 2 is used for only reception. Receiving data to receiver are switched from the antenna 1 and the antenna 2 alternatively by every PRF. Main characteristics of this system are shown in Table 1.

Table 1   System characteristics

Altitude:	3000 m (nominal)
Frequency:	9.53 GHz (X-Band)
Resolution:	5 m
Polarization:	Linear polarization (H-H)
PRF:	1200 MHz (nominal)
Data rate:	32 Mbps

SAR data processing

SAR data processing for this system is based on the range-doppler algorithm [4]. All parameters for SAR processing are derived from GPS data and 1-axis gyro compass data. This outline are as follows:

(1) The doppler power spectrum is calculated using raw data. The highest power point will be considered as the doppler center frequency (Fd).

(2) The Fd derived from (1) includes ambiguities of PRF. To determine true Fd, a wind direction, a drift angle is calculated using GPS data.

(3) To improve this image quality, the auto focus is used to make adjustment. This method is using pixel shifts among look images, that is caused by mistaken doppler rate.

In processing SAR image for interferometry, one of important things is to compensate for the changes of distance from both antennas to a ground target. That is mainly caused by airplane roll motion, and they introduce phase changes on interferometric SAR images, and they influence height error in the altitude map. An example of airplane roll motion data detected by onboard 1-axis gyro compass is shown in Fig. 3. To remove phase changes

caused by this roll motion, new phase compensation algorithm to range compressed data is developed.

The series of these processing algorithm has been developed on engineering work station "EWS4800", and processed on this work station. The SAR data processing, the interferometric phase processing, and the phase unwrapping have been done this work station also.

Results of this processing are shown in Fig. 4, 5. For processing data, we used Mt. Sakurajima data, that is an active volcano in Kagoshima prefecture, Japan, in July 1993, and the top of the mountain is 1117 m above sea level.

Fig. 4 shows a SAR power image of processing area that is synthesized 6 look images. This scene size is 4.5km (Az) × 4.5km (Rng) approximately. The flight direction is right to left on the image. Two craters of this mountain are bottom in the image.

Fig. 5 shows a contour map derived from interferometric SAR data. This contour interval is 10 m. The geometric correction is processed for this map.

Evaluation

The evaluation of the height error by interferometric SAR is carried out by comparing to 1/50,000 altitude map. Table 2 shows the evaluation results. The height error from this table is 6.5 m rms. approximately. In the best case, height error is 2-3 m rms. This difference must be examined carefully.

Table 2 Evaluation of height error

No.	height of altitude map[m]	height error [m]
1	0.0	− 0.4
2	0.0	− 4.9
3	85.0	+ 6.3
4	373.0	− 7.2
5	563.1	+ 8.7
6	1060.0	− 5.5
7	1109.8	+ 5.5

Conclusion

We improved a NEC-SAR system of conventional SAR and achieved to interferometric SAR image. At the result of the estimation of the altitude map made by interferometric SAR image, height error is 6.5 m rms. approximately, and in the bast case, height error is 2-3 m rms.

Commercial products based on this system have been developed, and will be delivered in this summer.

Reference

[1] Hiroshi Shinohara, Hideharu Totuka, Hidefumi Nagata, Yoshitaka Ohura, Hitoshi Nohmi, "AN X-BAND SAR SYSTEM FOR A LIGHT AIRPLANE", Technical report of IEICE, Vol.92, No. 353, SANE92-53, pp.7-14, November 1992.

[2] Soren N. Madsen, Howard A. Zebker and Jan Martin, "Topographic Mapping using Radar Interferometry: Processing Techniques," IEEE Trans. Geosci. Remote Sensing, vol. 31, No. 1, January 1993.

[3] Didier Massonnet, Marc Rossi, César Carmona, et al, "The displacement field of the Landers earthquake mapped by radar interferometry", Nature, Vol. 364, pp.138-142, July 1993.

[4] J. R. Bennett and I. G. Cumming, "A digital processor for the production of Seasat synthetic aperture radar imagery", in Proc. SURGE Workshop, Frascati, ESA-SP-154, 1979.
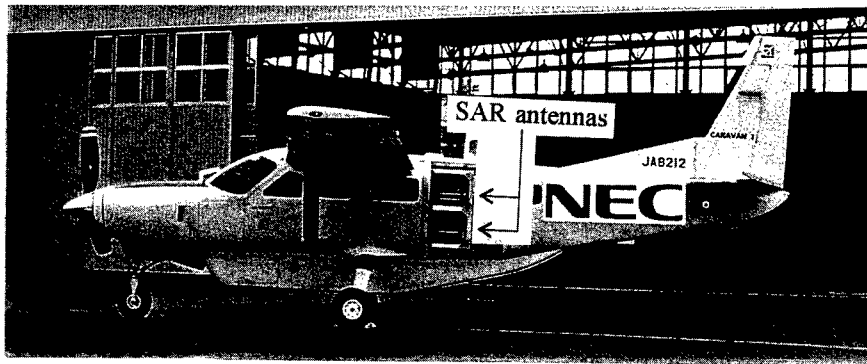
Fig. 1   Cessna 208 with NEC-SAR installed
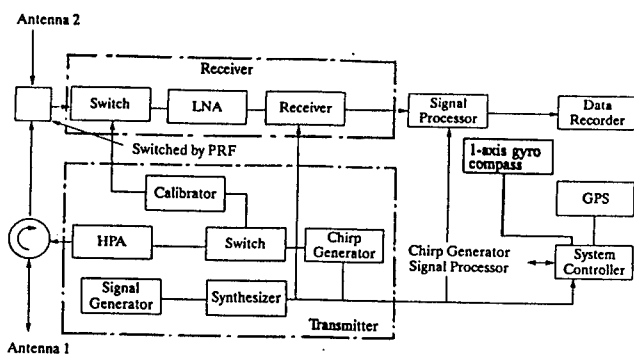
Fig. 2   NEC-SAR Block Diagram
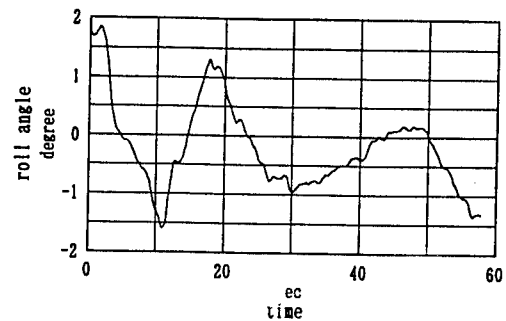
Fig. 3   Airplane Roll Motion
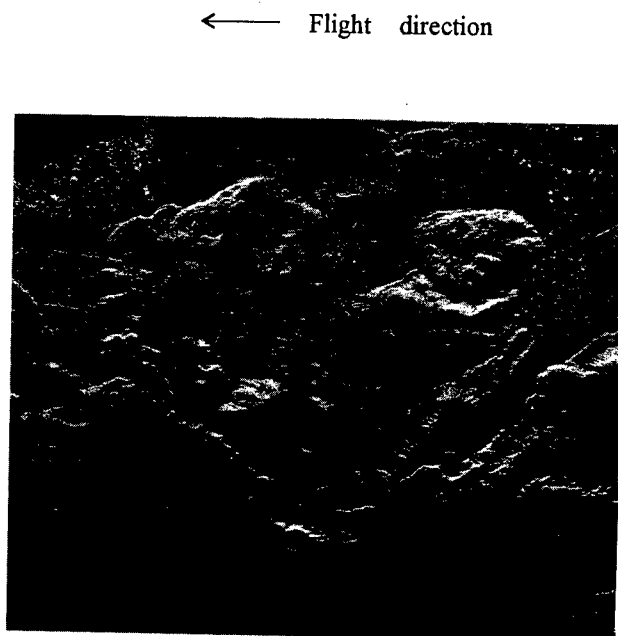
Fig. 4   SAR power image

CONTOUR INTERVAL 10m
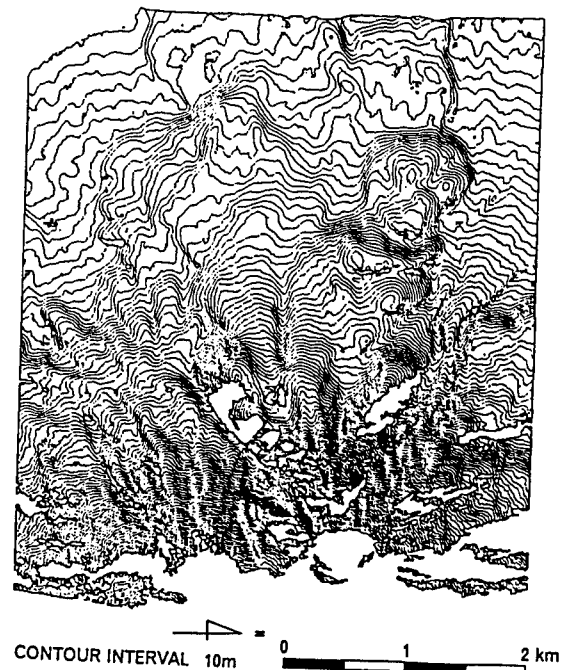
Fig. 5   Contour Map

Angular Signatures, and a Space-borne Measurement Concept

Siegfried A.W. Gerstl
Los Alamos National Laboratory, NIS/RS, MS-C323,
Los Alamos, New Mexico 87545, USA
Phone: (505)667-0952, Fax: (505)667-3815, e-mail: sig@lanl.gov

ABSTRACT

The nature and value of angular signatures in remote sensing are reviewed with emphasis on the canopy hot-spot as a directionally localized angular signature and an important special case of a BRDF. A new concept is presented that allows hot spot measurements from space by using active (laser) illumination and bistatic detection. The detectors are proposed as imaging array sensors that are circulating the illumination source (or vice versa) and are connected with it through tethers in space which also provide the directional controls needed so that the entire system becomes pointable like a search light. Near infrared or IR operation in an atmospheric transmission window is envisioned with night-time data acquisition. Detailed feasibility and systems analyses have yet to be performed.

INTRODUCTION

Every remote sensing instrument measures radiation that is expected to be related to a physical feature of the remotely sensed object; the data is then called a signature. Typically, when a surface scene is the object of the remote measurement, the measured radiance is the result of reflected or emitted radiation which may vary with the wavelength of the radiation and is then called a spectral signature. Similarly, spatial, temporal, angular and polarization reflectance signatures can be identified [1], as shown in Fig. 1.

An angular signature requires observations from different view directions. Airborne and satellite remote sensing systems that operate only at nadir, for example, are incapable of recording angular signatures. Some developmental instruments, such as ASAS and PARABOLA, and future EOS detectors, such as MISR, do measure angular signatures requiring that models are developed that relate the measured data to the physical surface feature [2].

ANGULAR SIGNATURES

All structured (three-dimensional) surfaces, such as vegetated surfaces or sloped terrain with varying elevations within a scene, exhibit angular signature effects. A Bidirectional Reflectance Distribution Function (BRDF) may be considered the most general form of an angular signature. BRDF's of vegetated surfaces, whose architecture always is three-dimensional in nature and where the reflected radiation is therefore dominated by internal shadowing effects, usually show large variabilities in their values across the
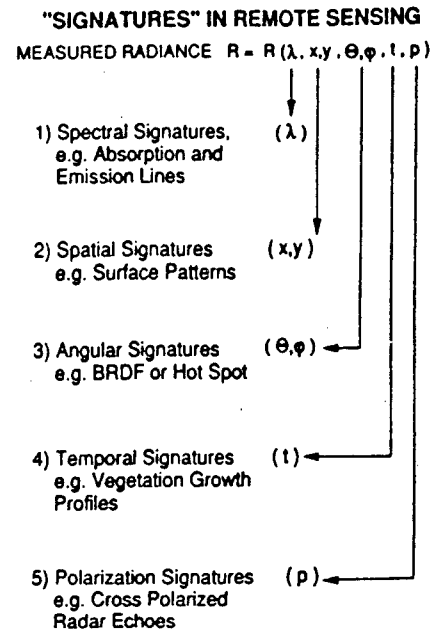
Figure 1: Five characteristic reflectance signatures in remote sensing.

hemisphere. A typical example is reproduced from BRDF measurements taken by Kriebel [3] from an aerial platform over grasslands, which are probably the earliest fairly complete angular signature data taken of that kind. The data for 3 different BRDF slices through the principal plane under 3 different solar illumination conditions, are shown in Figure 2 as an illustration.

THE CANOPY HOT SPOT

A prominent component of every BRDF of a structured surface is its internal shadowing that depends on illumination and observation directions, and on the internal structure (architecture) of the 3D surface. The structural information about a vegetation canopy, e.g., is not expressed in either the spatial or spectral signatures of the canopy, but solely in its angular signature. It has been shown that leaf size and canopy height can be retrieved from a special/local angular signature, the canopy hot spot, in particular from its angular width [4]. Figure 3 shows 2 examples of hot spot photographs taken from an airplane with standard panchromatic film in the visible. Additional such data are shown in [4].
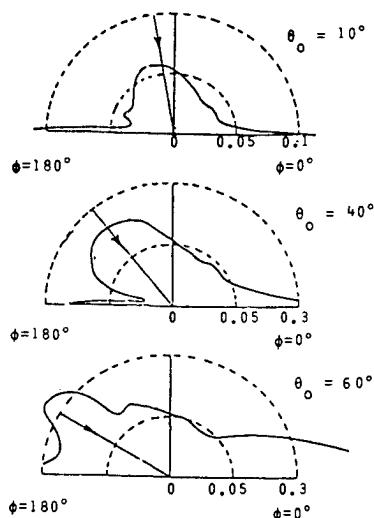
Figure 2: BRDF slices as angular signatures for pasture at 520 nm in the principal plane for 3 different solar illumination angles of 10, 40, and 60 degrees .
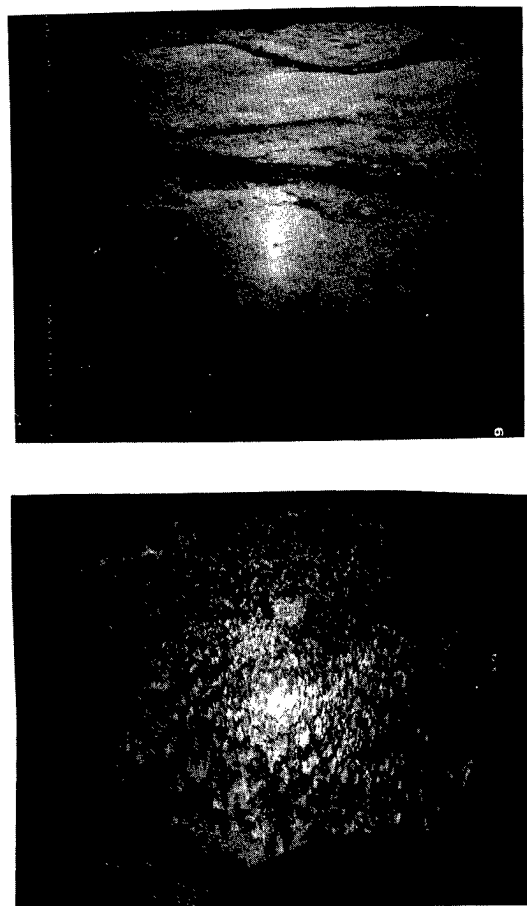
Fig. 3: The Canopy Hotspot photographed from about 300m altitude, over grass land (top photo) and coniferous forest (bottom).

Hot spot angular distribution measurements have been reported from aircraft data [4] and [5], but not from satellites. In fact, most scanning satellite detectors are excluding the hot spot direction from their field of view.

A SPACE-BORNE HOT SPOT MEASUREMENT CONCEPT

Taking hot spot data from an aerial platform with an imaging camera is fairly simple as is demonstrated by the photographic images. Recently, large goniometers have been used at the Joint European Research Center in Ispra, Italy, and at the Changchun Institute of Optics and Fine Mechanics in China, to perform laboratory measurements of complete BRDF's of small patches of vegetation targets. In every case the almost unlimited pointing capabilities of these instruments and platforms have been exploited, which is not a given for today's space-based sensors. Two fundamentally possible conical scanning techniques that allow hot spot angular signature measurements have been described in [2] and [6] and are graphically summarized in Fig. 4. Replacing the solar illumination with an active and pointable illumination source allows us to present a new concept enabeling space-borne measurements of hot spot angular signatures.
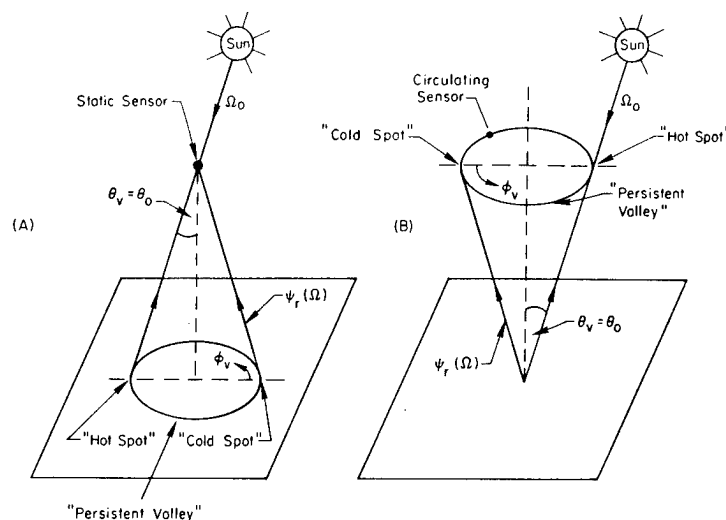
Fig.4: Two possible conical scan patterns that allow hot spot angular signature measurements.

Our new concept for canopy hot spot measurements from space envisions active illumination and bistatic detection that would allow hot spot angular distribution measurements from space in a search light mode. The concept includes a pointable illumination source, such as a laser, coupled with a number of high spatial-resolution detectors that are tethered to the source and are rotating around the illumination source receiving photons nearly

coaxial with the retroreflection direction, see Fig. 5. This measurement concept is an extension to the conical scan pattern described in [6] and depicted on the right side of Fig. 4; it will allow measurements of the intensity wings of the hot spot angular distribution, especially its angular width.

Tethered satellite systems have been tested in recent space shuttle missions [7], demonstrating the technical viability of up to 20 km long tethers operating in space. A circular path of the illuminating laser circulating around the sensor (or vice versa) at a radius of 20 km at a nominal satellite altitude of about 500 km above the earth will allow the hot spot angular distribution to be investigated out to about 5 degrees full angle, which is sufficient to characterize most agriculturally important vegetation by its hot spot angular signature.

The illumination wavelength has to be selected so as to minimize atmospheric interference, i.e. within the atmospheric transmission windows in the near infrared, or the 8 to 14 micrometer IR region. Such selection will make night-time observations possible, which will increase the signal-to-noise ratio due to reduced or nearly eliminated solar background radiation. Since the tethers can be made of conducting material, they can be used to carry control signals between the illumination and sensor components to direct the laser beam and the look angle so that they cover the same area on the ground. Orienting the direction of both components simultaneously would allow the entire system to function like a search light, providing it with almost unlimited pointing capabilities. Engineering systems analyses and feasibility studies have yet to be performed.

CONCLUSIONS

Angular signature measurements can provide information about vegetation surfaces, e.g. about their canopy architecture, which is not otherwise accessible by today's remote sensing methods. A new concept is presented that may allow angular signature measurements from a space-borne platform involving active laser illumination, bi-static observation, and would operate at night. Potentially most useful applications of the concept are to measure canopy hot spot parameters from space. Hot-spot angular signatures are expected to be quantified and parameterized in sufficient detail to extract relevant information content on plant architectures.

The HOT-SPOT SEARCH LIGHT

SATELLITE CONCEPT
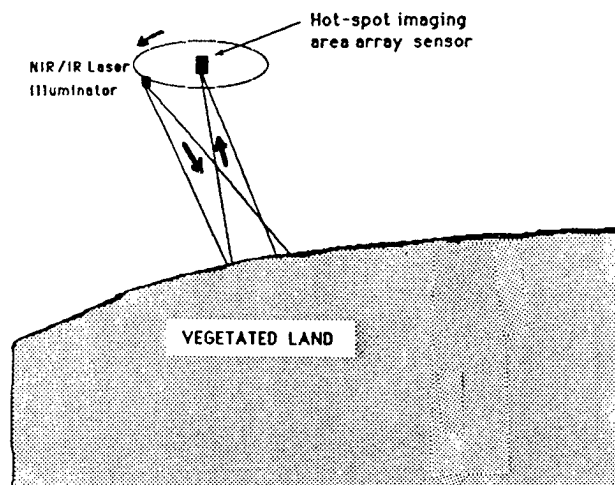
Fig. 5: The Hot-Spot Search-Light Concept for Angular Signature Measurements from Space.

REFERENCES

[1] S.A.W. Gerstl, "Physics Concepts of Optical and Radar Reflectance Signatures, Int. J. Remote Sensing, 1109-1117, 1990

[2] S.A.W. Gerstl and C. Simmer, "Radiation Physics and Modelling for Off-Nadir Satellite-Sensing of Non-Lambertian Surfaces", Remote Sensing of Envir. 20:1-29, 1986

[3] K. T. Kriebel, "Measured Spectral Bidirectional Reflectance Properties for four Vegetated Surfaces", Appl. Opt. 22: 1364, 1978

[4] S.A.W. Gerstl, "The Angular Reflectance Signature of the Canopy Hot Spot in the Optical Regime", 4th Intl. Coll. on Spectral Signatures of Objects in Remote Sensing, Aussois, France, 18-22 Jan. 1988, ESA Report SP-287, 129, 1988

[5] J. L. Privette and E.F. Vermote, "Fitting Remote Sensing Data with Linear Bidirectional Reflectance Models", SPIE Symposium on Satellite Remote Sensing II, Paris, 25-28 Sept., 1995

[6] S.A.W. Gerstl, "Off-Nadir Optical Remote Sensing from Satellites for Vegetation Identification", IGARSS'86 Symposium, Zurich, 8-11 Sept. 1986. ESA Report SP-254, 1457 - 1460, 1986

[7] H. F. Smith et al, "Flight results of the Small Expendable Deployer System", NASA Marshall Space Flight Center, and other presentations at Fourth Intl. Conf. on Tethers in Space, Washington, DC, 10 - 14 April, 1995

Estimation of Leaf Size from Hotspot Observations

Wenhan Qin, Narendra S. Goel and Bingquan Wang
Department of Computer Science, Wayne State University
431 State Hall, Detroit, MI 48202
Tel (313) 577-3310   Fax (313) 577-6868
Email: wenhan@epic.cs.wayne.edu

Abstract–The feasibility of estimating leaf size from canopy reflectance in the hotspot region is investigated for both homogeneous (leaf) and heterogeneous (rowed crops and trees) canopies. We specify optimal sun-view geometry, wavelength and index which can minimize the impacts of other structural parameters (e.g., LAI, leaf angle distribution (LAD) and inter-plant spacing) for most accurate estimation.

INTRODUCTION

Leaf size has the potential to discriminate vegetation types. The canopy reflectance in the hotspot region is known to depend on the leaf (scatterer's) size and hence in principle this size can be estimated from hotspot canopy reflectance. However, optical and other structural parameters also contribute to the canopy hotspot, which will induce uncertainties into the estimation. We investigate the relationship between canopy hotspot and canopy parameters through calculation of radiation regime in computer generated vegetation canopies. This relationship is used to assess the feasibility of estimating leaf size from hotspot reflectance and the optimal conditions for most accurate estimation.

CANOPIES GENERATED AND APPROACH

Three kinds of vegetation canopies are generated/used:

(1) Leaf canopies consisting of randomly dispersed rectangular scatterers (leaves) [1]. Three LAIs–0.5, 2.0 and 5.0–representative of three densities of the canopy, are considered. For each LAI, canopies with seven LADs (horizontal, planophile, two plagophiles (mean leaf angle of 30° and 60°), spherical, erectophile and vertical) are used. For a given set of LAI and LAD, canopies with four leaf sizes are generated.

(2) Row-planted heterogeneous crop canopies, with each plant consisting of long, thin leaves attached on a vertical stalk, like a corn or a wheat plant, with three typical LAIs (0.5, 2.0 and 5.0). Canopies for each LAI have three row spacings (SPCs): small ($0.5h$, h is the canopy height); medium ($1.0h$) and large ($1.5h$), and in-row spacing is equal to $0.25 \cdot SPC$. The leaf and soil properties are the same as for the random

canopies. Stem reflectances in red and near-infrared (NIR) regions are taken as 0.1 and 0.5, respectively and the transmittances are set to zero. When canopy LAI increases, the plants grow in a natural way–the length, width and number of leaves increase; the mean canopy height increases from 50cm to 220cm and the mean leaf inclination angle changes from about 65° to 40°. For a given LAI when SPC increases, both the canopy height and number of leaves increase.

(3) Architecturally realistic aspen-like tree canopies, with low (0.6) and high (5.5) LAIs (the corresponding canopy (tree) height (h) is about 7.0m and 11.5m). For each LAI, canopies with a spherical LAD but three different spacings between trees (as for crop canopies) or canopies with a medium SPC but three LADs (planophile, spherical and erectophile) are generated. For a canopy for a given LAI, LAD/SPC three typical leaf sizes, equal to $0.029h$, $0.064h$ and $0.112h$ on average, respectively are used. The optical properties of tree canopy components and the underlying soil are given in Table 1 in [2].

To calculate canopy reflectance, we use a model Diana [3], a computer graphics-radiosity based model for calculating radiation regime in a canopy. For a given view direction, we use four spectral indices: reflectance (R) and normalized reflectance (RN), normalized by hotspot reflectance, in both red and NIR regions. To understand the effects of various canopy parameters on the relationship between hotspot reflectance and leaf size, a signal-to-noise (STN) method [2, 4] is employed. The "signal" is referred to as the value of one of the indices mentioned above. The "noise" factors here are LAI, LAD and SPC, which affect the relationship between leaf size and "signal" intensity. The view directions with highest STN are the optimal sampling domain (OSD) for leaf size estimation.

RESULTS AND ANALYSIS

Three view planes–PP, the principal plane; PC, the principal cone and CP, the plane perpendicular (cross) to PP and two solar zenith angles (SZAs)–low (10°) and high (60°), are considered. In each view plane, the view zenith/azimuth angles are varied around the hotspot direction by ±0.2° (in the PP) or ±0.5° (in the PC) interval if the view angle is within ±20° off the hotspot direction or by ±2° (in the PP) or ±5° (in the PC)

elsewhere. In most cases, RN is the best index for leaf size estimation. There seems to exist an exponential relationship between RN and the relative leaf size ($l^*_L = l_L/h$, l_L is characteristic leaf dimension):

$$l^*_L = \exp[-(a-RN)/b] \qquad (1)$$

where coefficient a fluctuates around 1.0 and b varies from 0.01 to 0.15, depending on vegetation type. The OSD, best index and wavelength for every case, and results of fitting (1) (using the value of the best index under the optimal sun-view geometry) are summarized in Table 1.

Leaf Canopies

Normally the major "noise" factors in a leaf canopy are LAI and LAD. If LAI is known, the possibility to estimate leaf size is quite high (large STN values) if RNs in the hotspot region ($\pm 4°$ in the PP or $\pm 8°$ in the PC) in either red or NIR region at a high SZA (e.g., 60°) are used. The smaller the LAI, the higher are the values of STN. If both LAI and LAD are unknown (Fig.1), this possibility is reduced. Only when LAI is not too high (say, no more that 3.0), can an acceptable estimation be made from RNs in the PP (within $\pm 3.0°$ off the hotspot direction) at a high SZA.

Row Planted Crop Canopies

For such a kind of canopy, we only consider the general case —neither LAI nor SPC is known (i.e., we combine all three cases for LAI and SPC together) since here leaf size is different from case to case. Because of the strong influence of row structure on the hotspot distribution, we select three typical values of RSA (the relative solar azimuth to the row direction). We find that the reflectance (only for the CP) or RN in NIR at a high SZA are most preferable, but the optimal view plane depends on RSA. For example, when RSA=0°, the best view plane is the CP (in which the highest value of STN is larger than that in the PC and PP); whereas when RSA=45° or 90°, the optimal plane changes to the PC or PP. But the result in the CP or PP is not stable and strongly depends on RSA. Since only the result in the PC is relatively least sensitive to changes in RSA, PC is the optimal view plane for leaf size estimation for row planted crops, even if RSA is unknown either (Fig.2, combining the three cases for RSA). The effective azimuth range is within $\pm 3.0°$ off the hotspot direction (Table 1).

Tree Canopies

For such canopies if only LAD is unknown and LAI is low, one may have several options to select, such as view plane (PP or PC); RNs in red or NIR; and even different SZAs (low or high). But if LAI is high, only RNs at a high SZA are useful. If neither LAI nor LAD is known, the possibility of such an

estimation exists only if RNs at a high SZA in the PC is used (Fig.3), but the OSD is quite narrow, only about $\pm 1°$ off the hotspot direction (Table 1).

In the case where only SPC is unknown, if LAI is low, the two indices in NIR at a low SZA are useful, and the result in the PC is slightly better than others. The OSD is different in different view planes. For a high LAI, only RNs in NIR in the PP are useful. When LAI is also unknown, although values of STN in the PP within 1° off the hotspot direction are the highest, they are still below the limit of significance. Thus, it seems highly unlikely to estimate leaf size in such a case (Fig.4).

CONCLUSIONS

In this study, we investigate the feasibility of estimating leaf size from reflectance in the hotspot region and the nature of optimal observations for most accurate estimation.

In most cases, the normalized reflectance at a high SZA is the best index for the estimation. A universal negative exponential relationship (1) between this index and the relative leaf size can be established for all applicable cases for the three vegetation types.

The possibility and OSD to estimate leaf size vary with canopy type (increasing as it changes from leaf, crop to tree canopies) and architecture (decreasing as LAI increases or canopy becomes more spatially heterogeneous). For leaf canopies, RNs in both red and NIR and both view planes (PP and PC) are useful; for crops, only RNs in NIR in the PC can yield a reliable estimation; and for a tree canopy with unknown LAD the opportunity is larger than that with unknown spacing. Therefore, if neither LAI nor spacing is known, one does not seem to have a chance to estimate leaf size from canopy reflectance.

REFERENCES

[1] W. Qin an N.S. Goel, "An evaluation of hotspot models for vegetation canopies," Remote Sens. Rev., vol. 13, pp. 121-159, 1995.

[2] N.S. Goel and W. Qin, "Influences of canopy architecture on relationships between various vegetation indices and LAI and FPAR: a computer simulation," Remote Sens. Rev., vol. 10, pp. 309-347, 1994.

[3] N.S. Goel, I. Rozehnal and R.L. Thompson, "A computer graphics based model for scattering from objects of arbitrary shapes in the optical region," Remote Sens. Environ., vol. 36, pp. 73-104, 1991.

[4] C. Leprieur, M.M. Verstraete, and B. Pinty, "Evaluation of the performance of various vegetation indices to retrieve vegetation cover from AVHRR data," Remote Sens. Rev., vol. 10, pp. 265-284, 1994.

Table 1

Results of fitting (1) for the three types of vegetation canopies. r^2 is the square correlation coefficient and σ^2 is the residual mean square. The values in the second column are for LAI except for crops where they represent RSA in degrees. "??" stands for unknown. Subscripts 1 and 2 respectively, are for red and NIR wavebands.

veg. type	LAI or RSA	optimal index & OSD	a	b	r^2	σ^2 x10^{-4}	index & view geo. for fitting
Leaf LAD ??	0.5	RN₁ & RN₂ SZA=60° PP (±4°) PC (±8°)	1.16	0.117	0.97	0.76	RN₁ 61° (PP)
	2.0		1.08	0.094	0.94	1.08	RN₂ 58.6°(PP)
	5.0		0.92	0.084	0.79	0.74	RN₁ 56° (PP)
	<3.0		1.21	0.134	0.91	3.41	RN₁ 58.5°(PP)
Crops LAI, SPC & LAD ??	0	RN₂ SZA=60° PC (±3°)	1.05	0.109	0.88	2.76	1.2°
	45		1.12	0.159	0.94	2.91	1.4°
	90		1.02	0.074	0.83	1.88	-1.6°
	??		1.06	0.114	0.79	5.23	1.0°
Trees LAD ??	0.6	RN₁ & RN₂ PC, PP(±2°)	1.04	0.025	0.96	0.11	RN₂ 0.2°(PC)
	5.5	RN₁ & RN₂ SZA=60° PC, PP(±2°)	1.09	0.072	0.94	1.42	RN₁ 59.4°(PP)
	??	RN₁(PP) & RN₂(PC) SZA=60° PP, PC(±1°)	1.04	0.025	0.89	0.26	RN₂ 0.2°(PC)
Trees SPC ??	0.6	RN₂ or NIR CP(-5°, 5°) SZA=10° PC, PP(±2°)	1.01	0.011	0.81	0.11	RN₂ -0.8°(PC)
	5.5	RN₂ PP (±2°)	1.04	0.020	0.93	0.13	60.2°
	??	RN₂ SZA=60° PP (+1°)	1.03	0.020	0.64	0.81	59.8°
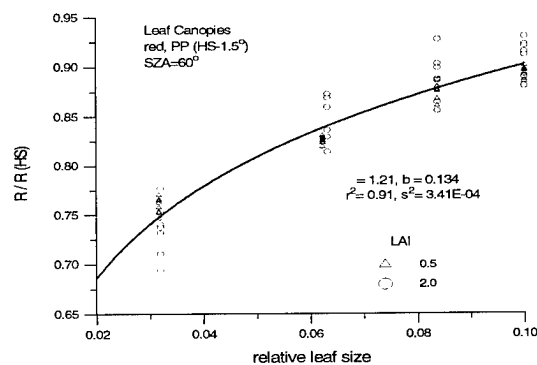
Fig. 1 The results of fitting (1) for leaf canopies. "HS" stands for the hotspot direction.
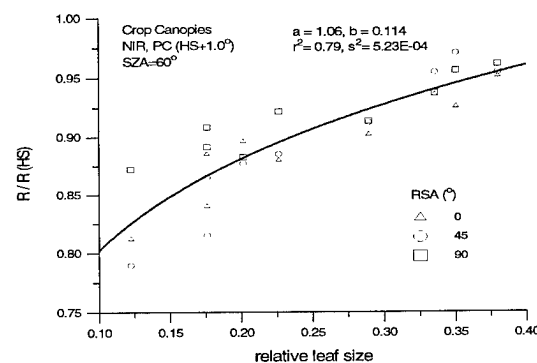
Fig. 2 As Fig.1 except for crop canopies.
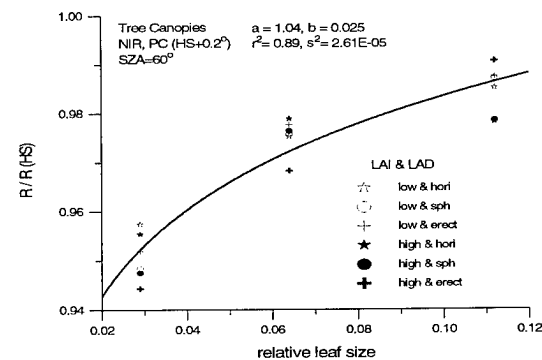
Fig. 3 As Fig.1 except for tree canopies with different LADs.
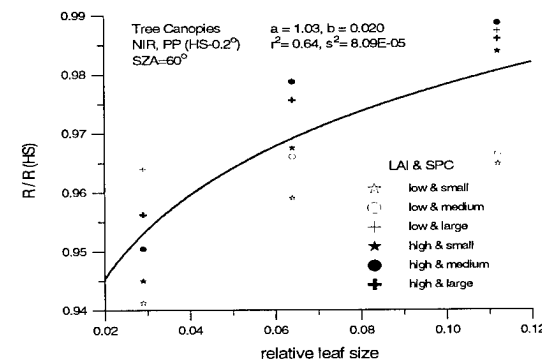
Fig. 4 As Fig.3 except for different spacings.

Multiple Scattering Approximations and Coherent backscattering Theory for Soil Bidirectional Reflectance

Shunlin Liang

Laboratory of Global Remote Sensing Studies
Department of Geography, University of Maryland,
College Park, MD 20742, USA

Abstract -- Soil radiative transfer has been poorly investigated, compared to canopy radiative transfer modeling. This paper summarizes our recent studies on this subject. The well-known Hapke model is improved and a new approximation is developed for the multiple-scattering calculations. Soil hot spot effects are evaluated using coherent backscattering theory, rather than the shadowing theory that has been widely used for calculating soil and canopy hot spots.

INTRODUCTION

Easy invertibility of a soil BRDF model is highly desirable, if we wish to retrieve various environmental parameters from remotely sensed imagery. Other applications such as atmospheric correction or atmosphere-biosphere models need simple soil models as the boundary conditions. For these purposes, a parametric model is preferable. Few approximate directional-reflectance soil models based on radiative transfer theory have been published [1][2][3]. The differences among different approximate radiative transfer models depend on their problem formulations and approximations for the multiple-scattering component. Most analytical radiative transfer models that simplify multiple scattering are based on the two-stream approximation or its variants. Two-stream approximation has been widely used because of its simplicity, but its accuracy is questionable. Approximation approaches for the calculation of multiple scattering are still quite limited. A widely used soil bidirectional reflectance model is the Hapke model [1][2], which originally was developed for planetary surface reflectance. Several inversion experiments have been carried out to retrieve soil physical parameters using the Hapke model [4][5]. One of the approximations made in the Hapke model is that multiple scattering is isotropic regardless of the actual phase function of the medium. In a recent study, we improved the Hapke model by formulating the soil radiation field with three components: single-scattering radiance, double-scattering radiance and multiple-scattering radiance [6]. Although multiple-scattering radiance is approximated by the same isotropic H-function expressed in the original Hapke model, the modified Hapke model is much more accurate than the original

Hapke model because of the exact inclusion of the double-scattering component.

A new multiple-scattering formula based on the four-stream approximation is presented for the soil bidirectional reflectance [7]. An arbitrary directional distribution of the sky radiance has been incorporated. Comparisons among the present model, the Hapke model and DISORT code indicates that the present model is much more accurate than the Hapke model and also works better than the modified Hapke model [6]. The effect of the present model accuracy on parameter inversion is also evaluated.

One of the pronouncing phenomena of the soil bidirectional reflectance is the hot spot. The Hapke's empirical hot spot function based on the shadowing theory [8] has been widely used for soils. According to the shadowing theory, particles in a medium that are large compared to the wavelength and/or opaque cast shadows on the neighboring particles. When the viewing direction matches the illumination direction, all shadows are hidden by the particles that cast them and thus the local brightness reaches its maximum. When the viewing direction moves away from the illumination direction, shadows can be seen and the detected brightness sharply decreases. However, the shadowing theory is not valid for soils composed of fine particles that do not have well-defined shadows. In a recent study, coherent backscattering theory has been used for calculating the soil hot spot [9].

AN IMPROVED HAPKE MODEL

The Hapke model for soil bidirectional reflectance has been modified. The radiation field is divided into three rather than two components. The multiple-scattering component is approximated by the original formula with appropriate modification, while single-scattering and double-scattering components are exactly calculated.

A numerical code DISORT based on the discrete-ordinate algorithm is used for accuracy verification. When the soil asymmetry parameter is small, where scattering by a soil is close to isotropic or

when the single-scattering albedo is small, implying that multiple scattering is weak, both the modified model and original Hapke model work quite well. When the soil scatters anisotropically or multiple scattering dominates, the modified model works much better than the original Hapke model (Fig. 1).

If the parametric model is not accurate enough, estimated parameters may be far from "true" values. An inversion experiment shows that the modified model can yield more accurate estimation of parameters than the Hapke model. It is also demonstrated that a good satisfactory fit between the simulated radiance or reflectance does not mean that the model can consistently retrieve correct physical parameters.

FOUR-STREAM APPROXIMATION

Because the multiple-scattering radiance of the soil medium cannot be explicitly calculated, we use instead a four-stream approximation. A numerical discrete-ordinate algorithm is used for the validation of this present model. The results indicate that this approximate model is much more accurate than the widely used Hapke model.

Many soil directional reflectance models do not account for sky radiance directly. However, the sky radiance is usually not negligible. One of the common practices is the use of the following formula for the upwelling radiance at the top of the soil due to sky radiance $I^s(\Omega)$

$$I(\Omega) = \int_{2\pi^-} I^s(\Omega')f(\Omega',\Omega)|\mu'|d\Omega'$$

where $2\pi^-$ denotes the downward hemisphere, $f(\Omega',\Omega)$ is the soil BRDF at the viewing direction Ω given the diffuse illumination at the directions Ω'. If Gaussian quadrature is used, the above integration can be replaced by the sum over M (zenith angle) by N (azimuth angle) discrete directions. Obviously, this requires MN calculations of the parametric soil model, which may take longer than a numerical code. The parametric model has explicitly incorporated the sky radiance distribution, and it does not require multiple runs of the code.

SOIL HOT SPOT EFFECTS

The soil hot spot effect is characterized by the magnitude enhancement factor ξ and the the half-width at half-maximum (HWHM) for the angular width of the hot spot. Coherent backscattering theory is used to calculate the magnitude and angular width of the soil hot spot. The soil particle size is assumed to follow the power distribution and gamma distribution, the individual particle is assumed as spheroidal. The T-matrix approach is used to calculate the optical properties (e.g., single-scattering albedo, scattering matrix, differential scattering cross section, etc.) of the medium for non-spherical particles. The soil structure is characterized by the filling factor, percentage of the particle occupancy. The vector radiative transfer equation is solved by the fast invariant imbedding method. The variables are also linked to the coefficients of the Hapke empirical hot spot function based on the shadowing theory.

Because the mechanisms between the coherent backscattering theory and the shadowing theory are completely different, the calculated results reveal different behaviors. (1). The predicted soil hot spot based on coherent backscattering theory primarily depends on multiple scattering, therefore the magnitude of the soil hot spot peak increases as the reflectance increases which is a strong function of the wavelength (Fig.2). Conversely, the predicted magnitude of soil hot spot peak based on the shadowing theory decreases as the reflectance increases since shadow hiding is important only for singly scattered light. (2). The angular width of the coherent backscattering peak is a function of the wavelength (precisely the ratio of the particle radius to the wavelength), whereas the shadow hiding peak is independent of the wavelength.

The numerical calculations in this study show that the magnitude of the soil hot spot is insensitive to the solar zenith angle. It is demonstrated that the soil hot spot is sensitive to the particle shape and the filling factor. Theoretically, those important soil properties may be retrieved from hot spot observations. Practically, the current radiometers used for remote sensing have much larger fields of view, which may largely change the angular shape and the magnitude of the soil hot spot. The soil refractive index is an another parameter controlling the hot spot shape. We need to examine how variable this parameter is. Another problem is that the hot spot may be caused by other factors, for example, the surface roughness. Further theoretical and experimental studies are highly required.

Present soil radiative transfer models still cannot account for soil moisture content, organic matter and other biochemical substances which may have significant effects on soil bidirectional reflectance [10]. More investigations are needed.

REFERENCES

1649

[1]   Hapke, B. W., Bidirectional reflectance spec-
       troscopy 1. Theory, *J. Geophys. Res.* vol. 86, pp.
       3039-3054, 1981.

[2]   Hapke, B., *Theory of reflectance and emittance
       spectroscopy,* Cambridge University Press, New
       York, 1993.

[3]   Ahmad, S. P., and Deering, D. W., A simple ana-
       lytic function for bidirectional reflectance, *Jour-
       nal of Geophysical Research,* vol. 97, pp.
       18,867-18,886, 1993.

[4]   Pinty, B., Verstraete, M. M., and Dickson, R. E.,
       A physical model for predicting bidirectional
       reflectance over bare soil, *Remote Sens. Environ.*
       vol. 27, pp. 273-288, 1989.

[5]   Jacquemoud, S., Baret, F., and Hanocq, J. F.,
       Modeling spectral and bidirectional soil
       reflectance, *Remote Sens. Environ.* vol. 41, pp.
       123-132, 1992.

[6]   Liang, S., and Townshend, J. R. G., A modified
       Hapke model for soil bidirectional reflectance,
       Remote Sensing of Environment, in press.

[7]   Liang, S., and Townshend, J. G. R., Parametric
       soil BRDF model : A four-stream approxima-
       tion, *Int. J. Remote Sens.* in press.

[8]   Hapke, B., Bidirectional reflectance spectros-
       copy 4: The extinction coefficient and the oppo-
       sition effect, *Icarus,* vol. 67, pp. 264-280, 1986.

[9]   Liang, S., and Mishchenko, M. I., Calculation of
       soil hot spot effects using coherent backscatter-
       ing theory, submitted to *Remote Sens. Environ.*

[10]   Irons, J. R., Weismiller, R. A., and Petersen, G.
       W., Soil reflectance, in *Theory and applications
       of optical remote sensing,* ed. G. Asrar, (John
       Wiley & Sons, New York, USA), 66-106, 1989.

Fig. 1 Model comparisons.
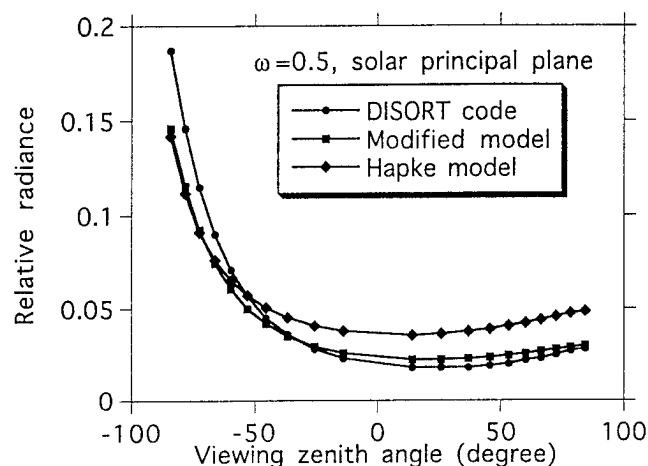
Fig. 2 Hot spot enhancement factor of fine silt soils.
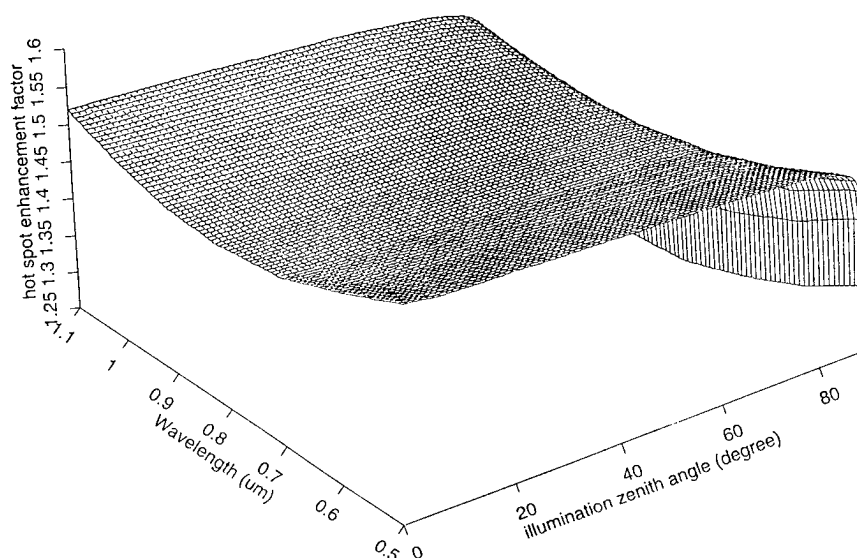
A Four-Level Bidirectional Reflectance Model Based on Canopy Architecture and its Inversion

Jing M. Chen and Sylvain G. Leblanc

Applications Division, Canada Centre for Remote Sensing

588 Booth Street, Ottawa, Ontario, Canada K1A 0Y7

Tel. (613)947-1266 / Fax. (613)947-1406

Email: chen@ccrs.nrcan.gc.ca / http://www.ccrs.nrcan.gc.ca/ccrs/general/ems/ems.html

Abstract - Open boreal forests present a challenge in understanding remote sensing signals acquired under various solar and view geometry. Much research is needed to improve our ability to model the bidirectional reflectance distribution (BRD) for retrieving the surface information using measurements at a few angles. The geometric-optical bidirectional reflectance model outlined in this paper differs from Li-Strahler's model [4], [5], [7] in the following respects: i) the assumption of random spatial distribution of trees is replaced by the Neyman distribution which is able to generate the clumpiness of a forest stand; ii) the multiple mutual shadowing effect among tree crowns is considered using the combination of the negative binomial and the Neyman distribution theory; iii) the probability of observing the sunlit background is modelled using a canopy gap size distribution function which is shown to affect the size and width of the hotspot; iv) the branch architecture of conifer trees affecting the directional reflectance is simulated using a simple angular radiation penetration function; v) the tree crown surface is treated as a complex surface with small structures which themselves generate mutual shadows and a hotspot. All these levels of canopy architecture are shown to have important effects on the directional distribution of the reflected radiance from boreal forests. The model results compare well with a data set from a spruce forest. The model after validation is used as a tool to retrieve the leaf area index of plant canopies according to a vegetation index (NDVI) calculated from the modelled red and near infrared bidirectional reflectance factors at various solar and view angles. The importance of canopy architecture (tree density and distribution, and branch and shoot structure) in the retrieval of LAI will be demonstrated.

INTRODUCTION

In previous geometric-optical models, a forest stand is assumed to consist of randomly distributed objects containing leaves as turbid media. These two-level models mark a major advancement in simulating radiation regimes in forest stands compared with the one-level turbid-media models. However, two-level models can only be considered as much simplified mathematical descriptions of the physical reality. First, trees are generally not randomly distributed in space. They are clustered at large scales due to variations in the soil and topographic conditions. They are also not randomly positioned at small scales because of the natural re-

pulsion effect. Second, leaves are not randomly distributed within tree crowns. In conifer trees, for example, leaves are grouped into shoots, branches and whirls. The 4-level directional reflectance model outlined in this paper includes these two additional levels of canopy architecture.

TREE DISTRIBUTION

Tree distributions are commonly modeled by the Poisson theory. Measurements from a boreal forest shown in Fig. 1 indicate a clear departure from the random case. Based on Neyman [8], and Getis and Boots [3], it is assumed that trees are clustered in groups and the size of a group follows a Poisson process, centred around a certain size. This group must be confined into a quadrat. The probability of having a group inside a certain domain also follows a Poisson distribution. This process is a double Poisson distribution, better known as Neyman type A:

$$P_N\left(i;m_1;m_2\right)=e^{-m_1}\frac{m_2^i}{i!}\sum_{j=1}^{\infty}\frac{\left(m_1e^{-m_2}\right)^j}{j!} \quad \text{for } i=0,1,2,... \quad (1)$$

where m_1 is the mean number of group per quadrat and m_2 is the cluster mean size. The mean number of trees in a quadrat is $m=m_1 \cdot m_2$. When the quadrats are small, or when the grouping is large compared to m, a Neyman process is more likely to give empty quadrats and create patchiness than the Poisson process. In Fig. 1, a Neyman with grouping of 3 gives results closer to the measurements than the Poisson theory. The measurements are taken from an area of 100×100 m^2 in a mature jack pine stand located near Candle Lake, Saskatchewan.

TREE CROWN

The present model is first used to simulate a black spruce forest. The top of a tree is modeled by a cone, and the lower part by a cylinder "on a stick." This situation occurs when the lower part of a tree has a trunk without much foliage. We denote S_g as the shadow on the ground surface and V_g the viewing shadow, i.e. the ground area blocked by trees in the viewing direction. The illuminated area on one tree crown is calculated according to the crown shape.
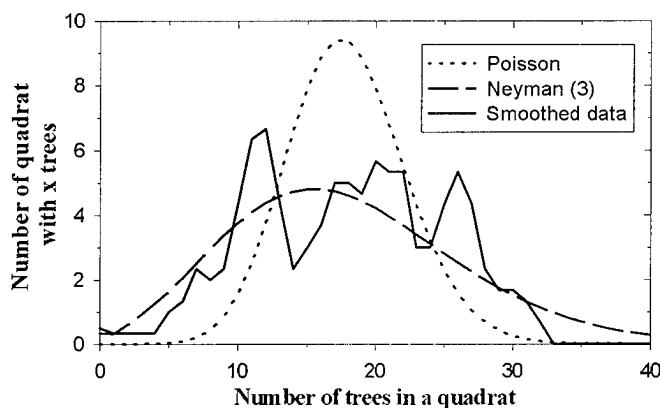
Fig. 1 Comparison between Poisson, Neyman and measurements of a Jack Pine forest

CANOPY GAP FRACTION AND THE HOTSPOT

The probability of seeing the ground is used for estimating the contribution of the underlying surface. If the trees are clustered, and overlapping is allowed we have:

$$P_{sg} = \sum_{j=0} P_{tj}(V_g) \cdot P_{gap}^j(\theta_v) + P_{to} \qquad (2)$$

where $P_{gap}^j(\theta_v) = \prod_1^j P_{gap}(\theta_v)$ is the gap probability within j tree overlaping, θ_v is the view zenith angle, and P_{tj} (V_g) is the probability of j overlapping:

$$P_{tj}(V_{gi}) = \sum_{i=0} P_N(i; m_1; m_2) \left[\frac{(i+j-1)!}{(i-1)! j!}\right] \left[1 - \frac{V_{gi}}{A}\right]^i \left[\frac{V_{gi}}{A}\right]^j \qquad (4)$$

In real forests, trees found in clusters are usually smaller than the average tree size. We have m trees on average in one quadrat. The model assumes that for the probability of having more than m trees in a quadrat, the size of the projection will decrease as $V_{gi} = V_g \cdot m/i$. The gap probability $P_{gap}(\theta)$ from Nilson [9] is used for a continuous medium. For a discontinuous canopy, we use a similar equation [7]. It has the advantage of being usable for any form of trees:

$$P_{gap}(\theta_v) = \exp\left(-\frac{G(\theta_v)\Omega}{DV_g \cos(\theta_v)}\right) . \qquad (5)$$

Additional equations are used to describe the foliage projection coefficient $G(\theta)$ and the clumping index Ω depending on the crown architecture. D is the density of trees. Similarly, the probability of having an illuminated ground surface (P_{ig}) can be found by replacing θ_v with θ_s in (2). Using (4), mutual shadowing of trees can be computed. The model assumes that the cone part is not affected by overlapping. The canopy gap size (λ) distribution [1] is used to model the hotspot. For an illuminated area on the ground, the viewer needs

a minimum gap size, λ_m, to see the ground area through the same gap. The process is done on the crown level for the ground hotspot, and at the shoot and branch levels for the tree crown hotspot. The resulting hotspot function is:

$$f(\Delta\theta) = \frac{\int_{\lambda_m}^{\infty} [1 - \Delta\theta / \theta_m] \cdot N(\lambda) d\lambda}{\int_{\lambda_m}^{\infty} N(\lambda) d\lambda} \qquad (6)$$

where $\Delta\theta$ is the angular difference between the viewer and the sun, θ_m is the minimum angle difference required to see an illuminated area on the ground for a gap size of λ_m which can be predicted [1]. $N(\lambda)$ is the number density of a gap with size λ. Equation (6) is used as a hotspot kernel which equals one at the hotspot and zero where the viewing and illumination processes become independent. The reflectance is found by multiplying the proportion of illuminated and shaded tree crown or ground surface seen by the viewer, by their respective reflectivity in red or near-infrared wavelengths.

MODEL RESULTS

The model first computes the canopy gap fraction. Measurements from a black spruce forest were used as a validation. A density of 2800 trees per hectare, divided into 20 quadrats, a LAI of 4, a tree height of 13 m, a radius of 0.45 m, and an apex angle of 13° were assumed. To give an validation of the effect of the grouping, Fig. 2 shows the gap probability from (2) for values of grouping of 1, 5, 10, and 20. Because the stand is very open, the Neyman grouping effect becomes relatively small in the gap fraction near the vertical direction. The best curve is for $m_2 = 10$. With the same parameters, the reflectance in the red band is computed for 4 different solar zenith angles (Fig. 3). The model is able to simulate the measurements reasonably well. Compared with measured data points, the modelled curves show sharp
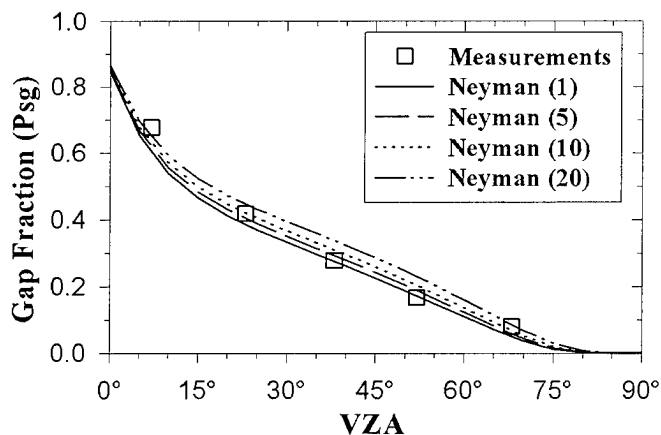
Fig. 2 Measured gap probability and different grouping factor output of the model.
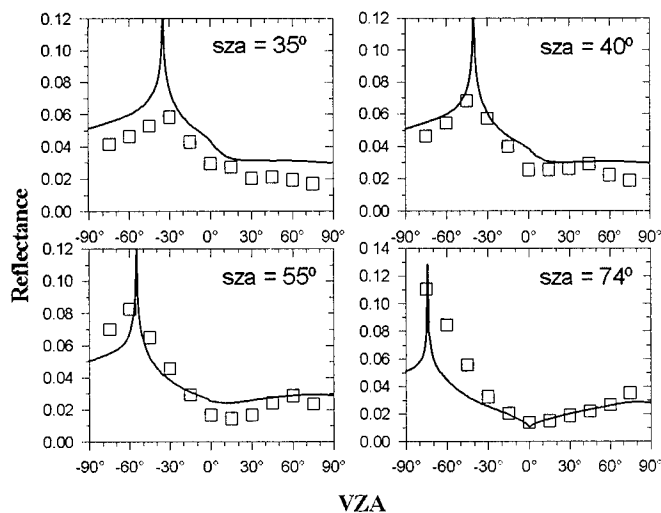
Fig. 3 Comparisons of boreal black spruce reflectance measurements in the red (□) with the model (—) in the principal plane.

spikes at the hotspot. The difference may be partly due to the small angular resolution (15°) in the measurements, which effectively average out the peak of a hotspot. The subtle differences in other angle ranges suggest that further improvements in the mathematical description of the sub-canopy architecture are needed.

INVERSION

The model offers enough variability to be used to retrieve forest canopy parameters. It can be used to estimate LAI from NDVI calculated from red and near-infrared reflectance. The NDVI found in Fig. 4a for the forwardscattering side is larger than that on the backscattering side. This is in agreement with measurements in black spruce forest [2]. The difference between the LAI-NDVI relationship at various view angles is largely determined by within-crown structures. The effect of the grouping is plotted in Fig. 4b for the forwardscattering side, showing how the NDVI changes with different Neyman grouping. The effect of Neyman grouping depends on the quadrat size. Larger effects are found in
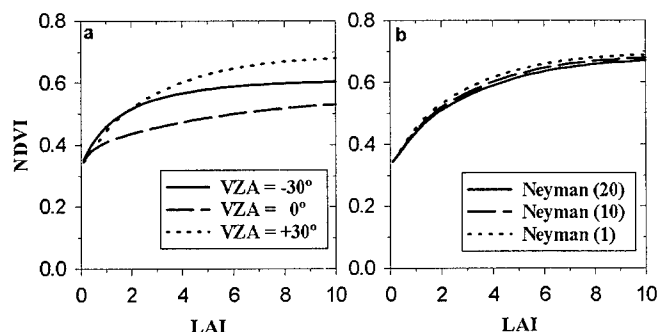
Fig. 4 Effect of different levels of the model on the inversion process.

larger quadrats with larger Neyman groups, suggesting that in coarse resolution remote sensing data, the grouping effect would be more important.

CONCLUSION

The four-level model represents a significant improvement over previous two-level geometric-optical models in its capability to simulate the directional reflectance behavior for complex plant canopies. Such a model provides the needed flexibilities in inversion for a wide range of plant canopy types.

REFERENCES

[1] J. M. Chen and J. Cihlar, "Quantifying the effect of canopy architecture on optical measurements of leaf area index using two gap size analysis methods," IEEE Trans. Geosci. Remote Sensing, vol. 33, pp. 777-878, 1995.

[2] D. W. Deering, S.P. Ahmad, T. F. Eck and B. P. Banerjee, "Temporal attributes of the bidirectional reflectance for three boreal forest canopies," IEEE Trans. Geosci. Remote Sensing, pp. 1239-1241, 1995.

[3] A. Getis and B. Boots. Models of Spatial Processes. Cambridge University Press, Cambridge, 1978.

[4] X. Li and A. H. Strahler. "Geometric-optical modeling of a conifer forest canopy," IEEE Trans. Geosci. Remote Sensing, vol. GE-23, pp. 705-721, 1985.

[5] X. Li and A. H. Strahler, "Geometric-optical bidirectional reflectance modelling of a coniferous forest canopy," IEEE Trans. Geosci. Remote Sensing, vol GE-24, pp. 906-919, 1986.

[6] X. Li and A. H. Strahler. "Modeling the gap probability of a discontinuous vegetation canopy," IEEE Trans. Geosci. Remote Sensing, vol. GE-26, 1988.

[7] X. Li and A. H. Strahler. "Geometric-optical bidirectional reflectance modelling of the discrete crown vegetation canopy: Effect of crown shape and mutual shadowing," IEEE Trans. Geosci. Remote Sensing, vol. GE-30, 1991.

[8] J. Neyman. "On a new class of 'contagious' distribution, applicable in entomology and bacteriology," Ann. of Math. Stat. vol. 10, pp. 35-57, 1939.

[9] T. Nilson, "A theoretical analysis of the frequency of gaps in plant stands," Agric. Meteorol., vol. 8, pp. 25-38, 1971.

Validation of a BRDF Model for Boreal Forest

P.R. North[1], S.E. Plummer[1], D.W. Deering[2] and M. Leroy[3]

1. British National Space Centre
Remote Sensing Applications
Development Unit
Monks Wood, Cambridgeshire
PE17 2LS,UK
Tel: 44 1487 773381
Fax: 44 14877 773277
Email: P.North@nerc.ac.uk

2. Code 923
NASA/GSFC

Greenbelt, MD 20771

3. CESBIO
bpi 2801

18 Av. E. Belin

31055 Toulouse

France

ABSTRACT

This paper presents validation of a method for estimation of forest bi-directional reflectance for an example of boreal forest. The method employs Monte Carlo solution of a hybrid geometric optical / radiative transfer model. The model output is compared with ground and airborne measurements of a mature jack pine site collected during BOREAS.

INTRODUCTION

Accurate models of light interaction with the land surface are required to derive the parameters needed for climate and vegetation studies from remotely sensed data. The problem has received much recent attention given the demand for spatial estimates of inputs to models to predict the effects of climate change, and the need to maximise the potential of new instruments capable of detailed sampling of land surface reflectance [1] [2]. Forests present a particularly complex case, where both small and large scale structural heterogeneity make it difficult to model the many scattering events contributing to reflectance.

This paper presents validation of a method for estimation of forest bi-directional reflectance for an example of coniferous forest. The method employs Monte Carlo solution of a hybrid geometric optical / radiative transfer model [3] [4]. Hybrid models attempt to combine the geometric-optical representation, which captures large scale structure well, with a radiative transfer approximation of the volume scattering and extinction occurring within the geometric boundary. While single scattering and light penetration have previously been accurately modelled [5], calculation of bi-directional reflectance has been limited by the difficulty in evaluating the angular distribution of multiple scattering. Applied to photon transport, the Monte Carlo method involves simulation of the chain of scattering events incurred by a photon in its path from the source to the receiver or to its absorption [6] [7]. The technique has the advantage that only the single scattering properties need be explicitly modelled. The method developed here allows accurate treatment of multiple scattering within and

between crowns, trunk and ground, and is applicable to forests of arbitrary density.

MODEL DESCRIPTION

Representation

Forest macro-structure is represented by a set of geometric primitives, positioned in three dimensions above a horizontal plane. The primitives define crown shape and size, and may overlap. Crown positions may be directly specified for an individual scene, or estimated from a statistical distribution or growth model. All non-understory foliage is considered to lie within the crown boundaries. Within each crown, foliage is approximated by structural parameters of area density, angular distribution and size, and optical properties of reflectance and transmittance. These parameters are approximated as homogenous within each boundary, but may vary between crowns. In the examples given for coniferous forest, a cone is used to approximate crown shape and a second cone is used to represent the trunk.

Evaluation

The paths of individual photons are traced through successive interactions from illumination source to viewer. An individual photon may undergo interactions within a number of distinct crowns and with the ground surface before reaching the upper boundary. At each interaction a photon may be either absorbed or scattered in a new direction. This is simulated by approximating aggregate photon intensity at each wavelength with a continuous probability density function, allowing all paths traced to contribute to the reflectance estimate. The accumulated exiting intensity allows calculation of reflectance for view directions quantised over a hemisphere.

The scattering phase function for an individual leaf has been approximated using a bi-Lambertian reflectance model. The remaining phase functions are approximated by a Lambertian scattering model for reflectance from the trunk, and by Hapke's equations [8] [9] for ground

reflectance, normalised to bark and understory reflectance estimates respectively.

The discontinuous nature of the forest canopy complicates the simulation of photon trajectory. Within a crown, scattering is evaluated by Monte Carlo solution of the radiative transfer approximation, modified to include consideration of the effect of finite sized foliage scattering elements[10]. External to the crowns, simulation of photon trajectory proceeds by deterministic ray-tracing.

RESULTS

Bidirectional reflectance predicted by the model has been compared with ground and airborne measurements using data collected during BOREAS. The site considered is dominated by mature jack pine (Pinus banksiana), located in the BOREAS Southern Supersite Area (53.916° N, 104.692° W) near Candle Lake, Saskatchewan. Structural and optical measurements were obtained from both the BORIS database and [11].

To estimate bi-directional reflectance, a representative volume enclosing 50 trees was modelled. Each tree crown was approximated by a cone defining its crown boundary and a second defining its trunk. The three-dimensional positions of the crowns were generated using a modified Poisson model based on forest structural statistics. Bidirectional reflectance factors (BRFs) were estimated over a hemisphere in 5° bins, by simulating 1.5×10^7 photon trajectories.

The model output was compared with reflectance factors derived from PARABOLA [12] and POLDER [13] [14] measurements. The PARABOLA measurements were taken from a tram track 13-14 m above the canopy on 5/31/94, and calibrated using a $BaSO_4$ reflectance panel. The measurements were resampled to bins with angular width 5° in zenith and 30° in azimuth at wavelengths centered on $662nm$, $826nm$ and $1656nm$. The POLDER instrument was flown above the canopy 5/26/94, sampling directional radiance over a wide area of forest at five wavelengths ($445nm$, $550nm$, $670nm$, $864nm$, $910nm$). The radiances were atmospherically corrected using the 6S code [15] and in situ measurements of aerosol optical depth to estimate ground BRFs. The solar zenith angle for both sets of data was ~45°.

Figures 1 and 2 show reflectance in the principal plane predicted by the model (solid line) at $670nm$ and $870nm$ respectively. PARABOLA measurements in the principal plane are shown as crosses and POLDER measurements lying close to the principal plane (r.a. ≈ 19°) as diamonds. Positive values of the view zenith angle indicate reflectance in the back-scattering direction. Comparison of the model with PARABOLA measurements for the cross principal plane is shown in figures 3 and 4.

Error bars show standard deviation of the PARABOLA data where a number of measurements lie within the same angular bin.

The model BRDF shows a clear hotspot peak at both wavelengths, with markedly lower reflectance in the forwards scattering direction. In comparison to the measured data, reflectance at 670 nm appears to be underestimated by the model, while reflectance at 865 nm is overestimated. However there is agreement in overall shape of the BRDF in both principal plane and cross-principal plane directions.

CONCLUSION

A model of forest bidirectional reflectance was compared with field measured reflectances for an example of mature coniferous forest. Agreement was seen in overall BRDF shape although there was some difference in absolute reflectance. The results should be considered preliminary as there are some differences between the model and the two sets of measurements in spectral and angular sampling.

ACKNOWLEDGMENTS

REFERENCES

[1] D.J. Diner et al. "MISR: A multiangle imaging spectroradiometer for geophysical and climatological research for EOS," IEEE Trans. Geosci. Remote Sens., vol. 27, pp. 200-214, 1989.

[2] C. Godsalve, "Bidirectional reflectance sampling by ATSR-2 - a combined orbit and scan model," Int. J. Remote Sens., vol. 16(2), pp. 269-300, 1995.

[3] P.R. North and S.E. Plummer, "Estimation of conifer bi-directional reflectance using a Monte Carlo method," in Proceedings, International Geosciences and Remote Sensing Symposium: IGARSS'94, Pasadena, CA, IEEE, New York, NY, pp. 114-116, 1994.

[4] North, P.R., "Three-dimensional forest light interaction model using a Monte Carlo Method", to appear in IEEE Trans. Geosci. Remote Sens., 1996.

[5] X. Li, A.H. Strahler and C.E. Woodcock, "A hybrid geometric optical - radiative transfer approach for
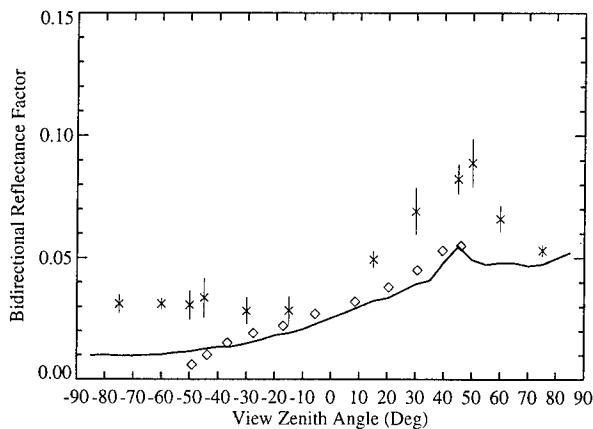
Figure 1
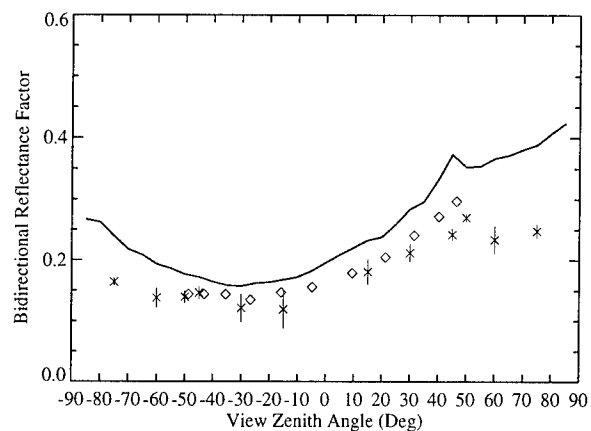
Figure 2
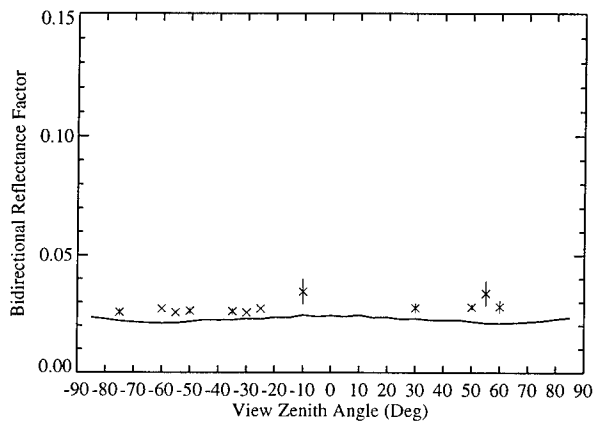
Figure 3
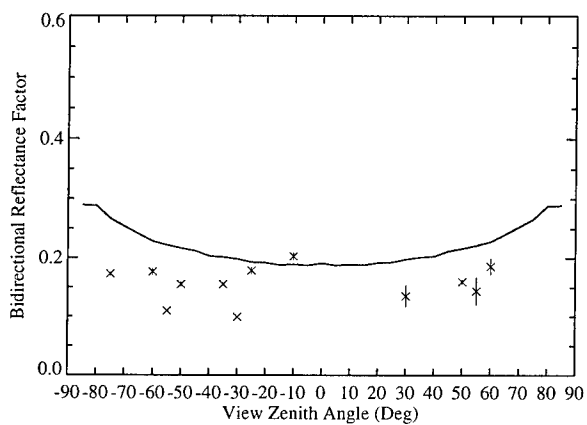
Figure 4

modeling albedo and directional reflectance of discontinuous canopies," *IEEE Trans. Geosci. Remote Sens.*, vol. 33, pp. 466-480, 1995.

[6] J.K. Ross and A.L. Marshak, "Calculation of canopy bidirectional reflectance using the Monte Carlo method," *Remote Sens. Environ.*, vol. 24, pp. 213-225, 1988.

[7] V.S. Antyufeev, and A.L. Marshak, "Monte Carlo method and transport equation in plant canopies," *Remote Sens. Environ.*, vol. 31, pp. 183-191, 1990.

[8] B. Hapke, "Bidirectional reflectance spectroscopy: 1. Theory," *Journal of Geophysical Research*, vol. 86, pp. 3039-3054, 1981.

[9] B. Hapke, "Bidirectional reflectance spectroscopy: 3. Correction for macroscopic roughness," *Icarus*, vol. 59, pp. 41-59, 1984.

[10] D.L. Jupp and A.H. Strahler, "A hotspot model for leaf canopies," *Remote Sens. Environ.*, vol. 38, pp. 193-210, 1991.

[11] J.M. Chen, P.M. Rich, S.T. Gower, J.M. Norman and S.E. Plummer, "Leaf area index of boreal forests: theory,techniques and measurements", *in prep.*

[12] D.W. Deering and P. Leone, "A sphere-scanning radiometer for rapid directional measurements of sky and ground radiance," Remote Sens. Environ., 19:1-24, 1986.

[13] J. L. Deuze, F. M. Breon, P. Y. Deschamps, C. Devaux, M. Herman, A. Podaire, and J. L. Roujean, "Analysis of the POLDER (POLarization and Directionality of Earth's Reflectances) airborne instrument observations over land surfaces," *Remote Sensing of Environment*, vol. 45, pp. 137-154, 1993.

[14] P.-Y. Deschamps, F.-M. Breon, M. Leroy, A. Podaire, A. Bricaud, J.-C. Buriez, and G. Seze, "The POLDER mission: instrument characteristics and scientific objectives," *IEEE Transactions on Geoscience and Remote Sensing*, vol. 32, pp. 598-615, 1994.

[15] J.L. Deuze, M. Herman, J.J. Morcrette, D. Tanre and E. Vermote, "Second simulation of satellite signal in the solar spectrum", Fortran Computer Code Version 3.0.

1656

Assessing Canopy Biomass and Vigor by Model-Inversion of Bidirectional Reflectances: Problems and Prospects

Thomas W. Brakke
Biospheric Sciences Branch, Code 923, NASA/GSFC, Greenbelt, Maryland 20771
TEL: 301-286-3851, FAX: 301-286-0239, tbrakke@ltpmail.gsfc.nasa.gov

Joseph Otterman
Land-Atmosphere-Ocean Research
Code 910.4, NASA/GSFC, Greenbelt, Maryland 20771
TEL: 301-286-1312, FAX: 301-286-1757

James R. Irons
Biospheric Sciences Branch, Code 923, NASA/GSFC, Greenbelt, Maryland 20771
TEL: 301-286-8978, FAX: 301-286-0239, jim_irons@gsfc.nasa.gov

Forrest G. Hall
Biospheric Sciences Branch, Code 923, NASA/GSFC, Greenbelt, Maryland 20771
TEL: 301-286-2974, FAX: 301-286-0239, fghall@ltpmail.gsfc.nasa.gov

ABSTRACT

Determining the biomass of an incomplete canopy by inversion of a plant/soil model depends upon assessing the separate contributions of the soil and the leaves to the overall surface reflectance. The factors affecting the relative importance of these two surface components are: 1) the canopy optical thickness, 2) the canopy architecture (these first two factors control the gap function), 3) the magnitude and anisotropy of the leaf reflectance (which control single-scattering backscattering), 4) the magnitude and anisotropy of the leaf transmittance (which control forward scattering), and 5) the magnitude and anisotropy of the soil reflectance. An appropriate inversion is made more problematic by the fact that these factors can change over time in response to environmental influences. Applying a simple model, we present and discuss bidirectional reflectances for an incomplete canopy/soil surface. Isotropic leaf and soil reflectances produce quite different overall reflectance patterns than those based on measured leaf and soil reflectances.

INTRODUCTION

Assessing canopy vigor and biomass, and predicting yield, constitute important tasks for remote sensing of vegetated surfaces. Because of the wide-ranging importance of these tasks, the number of pertinent studies is very large, with results ranging from the ordinary to the superior. We do not intend to summarize the various techniques used for inversion, or survey the record of successful characterizations of canopies. We do point out that different characterization approaches range widely from the point of view of i) mathematical complexity and ii) dependence upon background information about the reflectances of the surface components.

An extreme example of simple inversion is the determination of the grass-blade reflectance and transmittance for prairie, when the canopy can be assumed to be dense (essentially complete) and the structure predominantly vertical. The inversion under these assumptions can be a one-parameter inversion, in which grass-blade reflectance is determined from measurements in the backscatter direction, and the grass-blade transmittance is determined from canopy reflectances in the forward-scatter region [1]. The other extreme, which we regard as difficult, is the determination of biomass [through leaf area index (LAI) assessment] for a rather thick canopy of not closely-determined structure and unknown plant-element reflectances, transmittances, and underlying soil reflectances. Thus, we are impressed by the results of [2], who estimated LAI for a soybean canopy with an error level of 7.7%.

Leaf and soil reflectances have been shown to be anisotropic [3],[4]. In our short study, realistic leaf and soil reflectances will be incorporated into a canopy model originally designed for Lambertian reflectances.

ANISOTROPIC SOIL AND LEAF REFLECTANCES

For our analysis, we select the laboratory measurements made by [5] of the bidirectional reflectance from Elkton silt loam. Fig. 1a and b show the fractional reflectances (i.e., the reflectance factor times the cosine of the view zenith angle; see [6]) for incidence zenith angles of 0° and 60°, respectively.

The leaf facet reflectance data is taken from laboratory measurements described by [7]. Fig. 2 shows the scattering from red oak (*Quercus Rubra* L.) leaves in June at two incidence angles.

HORIZONTAL FACET CANOPY MODEL

To illustrate the importance of anisotropic leaf and soil reflectance, we apply here a simplified vegetated surface model consisting of horizontal facets over a soil plane as given by [8]. The reflectance r is given by

$$r = r_i\, e^{-2u} + r_u \frac{1 - e^{-2u}}{2} \qquad (1)$$

where r_i is the reflectance factor of the soil plane, r_u is the reflectance factor of a leaf facet (both assumed Lambertian in [8]), and u is the projected area of the facets on a horizontal plane. r does not vary with view angle when r_i and r_u are Lambertian. We insert the non-Lambertian reflectance factors for the Elkton silt loam and red oak leaves into (1) to obtain the surface reflectance factors shown in Fig. 3. The surface reflectance now varies with view zenith angle, and the pattern is different for the two incident angles.

For nadir illumination, the reflectance is close to that of the Lambertian case. Increasing LAI lowers the reflectance. However, for an incidence angle of 60°, there is a change with view angle. There is a back-scatter peak that is damped by increasing LAI, and a forward scattering peak that is enhanced by increasing LAI. Model inversion for determining leaf reflectance should be done in the forward scattering direction where the model is sensitive to leaf reflectance and insensitive to LAI.

DISCUSSION AND CONCLUSIONS

Incorporation of realistic (measured) leaf reflectances strongly changes (as compared to the isotropy assumption) the bidirectional reflectance pattern of a complete or incomplete canopy. In addition, the pattern for an incomplete canopy depends on the actual reflectance of the underlying soil. Information about soil and leaf reflectances thus constitutes important background information for interpreting (or inverting) bidirectional reflectances for canopy characterization.
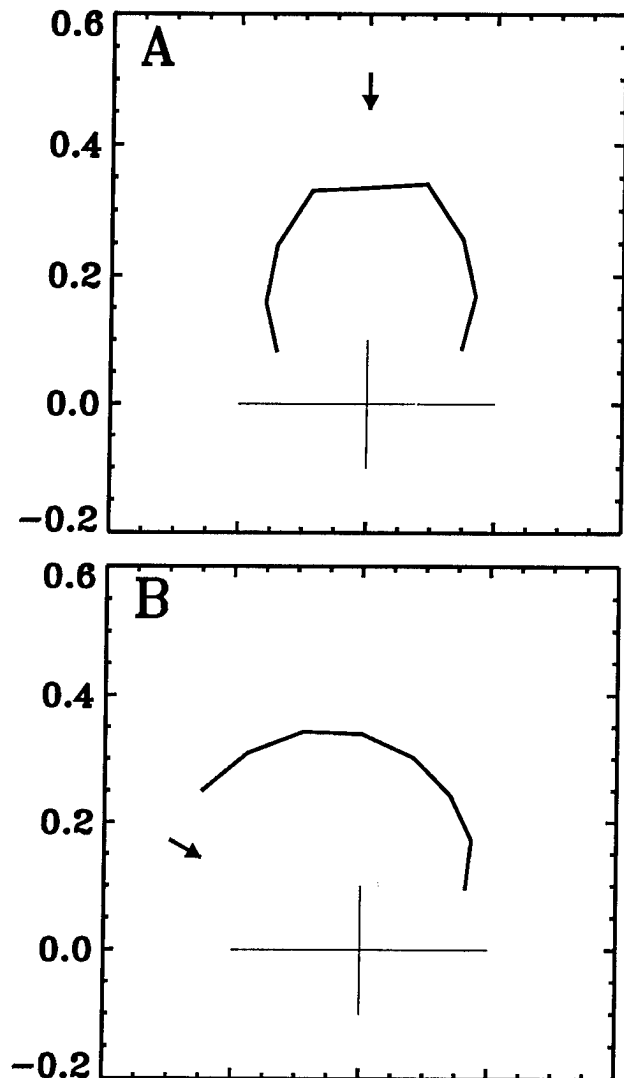
Figure 1. Bidirectional fractional reflectance at 0.65μm in polar coordinates in the principal plane for Elkton silt loam. The incident zenith angles are 0° for (A) and 60° for (B) as indicated by the arrows.

Figure 3. Surface reflectance as given by (1) versus view zenith angle for solar zenith angles of 0° (———) and 60° (— — —) and LAI's of 0.0 (+), 0.5 (✳), 1.0 (◊), and 4.0 (Δ).

Figure 2. Bidirectional fractional reflectance and transmittance (above and below the plane of the leaf, respectively, in polar coordinates) for visible (0.59μm; –●–●) and near-infrared (0.91μm; ———) radiation incident upon the adaxial surface of a red oak leaf (average of six leaves). The incident zenith angles are 0° for (A) and 60° for (B).

REFERENCES

[1] J. Otterman, T. Brakke, and J. Smith, "Effects of leaf-transmittance versus leaf-reflectance on bidirectional scattering from canopy/soil surface: an analytical study," Remote Sens. Environ., vol. 54, pp. 49-60, 1995.

[2] N. S. Goel, and R. L. Thompson, "Inversion of vegetation canopy models for estimating agronomic variables. V. Estimation of leaf area index and average leaf angle using measured canopy reflectances," Remote Sens. Environ., vol. 16, pp. 69-85, 1984.

[3] T. W. Brakke, "Specular and diffuse components of radiation scattered by leaves," Agric. For. Meteor., vol. 71, pp. 283-295, 1994.

[4] J. R. Irons, G. S. Campbell, J. M. Norman, D. W. Graham, and W. M. Kovalick, "Prediction and measurement of soil bidirectional reflectance," IEEE Trans. Geosci. Remote Sens., vol. 30, pp. 249-260, 1992.

[5] J. R. Irons, "Solar radiation scattering by soils," Ph.D. Dissertation, University of Maryland, College Park, MD, 1993.

[6] J. T. Woolley, "Reflectance and transmittance of light by leaves," Plant Physiol., vol. 47, pp. 656-662, 1971.

[7] T. W. Brakke, "Goniometric measurements of light scattered in the principal plane from leaves," IGARSS'92, Houston, TX, pp. 508-510, May 26-29,1992.

[8] J. Otterman, "Bidirectional and hemispheric reflectivities of a bright soil plane and a sparse dark canopy," Int. J. Remote Sens., vol. 6, pp. 897-902, 1985.

Retrieval of Forest Biophysical Parameters
from Remote Sensing Images with the DART Model

Pinel V., Gastellu-Etchegorry J.P., Demarez V.

Centre d'Etude Spatiale de la **BIO**sphère
C.N.E.S. - C.N.R.S. - U.P.S., BPI 2801, 31055 Toulouse Cedex - France
Tél.: (33) 61.55.66.70. Fax: (33) 61.55.85.00. E-mail: pinel@cesbio.cnes.fr

ABSTRACT: This paper presents a quantitative analysis of the sensitivity of textural information of high resolution remote sensing images of a forest plantation (Les Landes, France) with a number of biophysical characteristics: tree cover, crown diameter, distance between rows and leaf area index (LAI). The influence of spatial resolution and viewing and illumination configurations are also assessed. The work is conducted with directional images simulated with the DART (Discrete Anisotropic Radiative Transfer) model, whereas textural information is quantified by means of variograms. Finally, actual 1.67m resolution spectral images provide a partial validation of the approach and results.

I - INTRODUCTION

Image spatial structure: Spatial structure in remote sensing images plays a very important role in visual interpretation of high resolution imagery. Here, we consider images of a forest plantation (Les Landes, France). Detection of spatial variations within images is often essential for a better understanding of stand and landscape structure and dynamics, and for improving inventory and mapping. We quantified the spatial variability of pixel values P in images with variograms [1]:

$$V(h) = \frac{1}{2} E\left\{ [P(r_i + h) - P(r_i)]^2 \right\} = \frac{1}{2n} \sum_{i=1}^{n} [P(r_i + h) - P(r_i)]^2$$

where r_i is the pixel location, h the lag over which V(h) is computed and n the number of couples of pixels with a lag h.
Studies [2] already stressed that variograms tend towards image variance with large h. So, the asymptote or sill is related to tree cover through image variance. The shape of the variogram and lag to the sill, the range, are related to the area of objects within the image; *e.g.* tree crowns. Coarsening the spatial resolution of the imaging system results in lowering the sill, increasing the range, and increasing V(1). Variograms presented here are computed along directions parallel to tree rows.

Physical modeling for simulating images: The lack of understanding of the nature and causes of spatial variations in images explains that presently their use is mostly limited to empirical relationships between scene information and the structure of necessarily limited sets of remote sensing images. Physical modeling may greatly improve the situation if models are realistic enough for accurate image simultaions. For example, the symplifying hypothesis of [3, 2], *i.e.* totally opaque crowns and no actual atmosphere, may lead to erroneous textural characteristics [4]. Here, we use a more accurate model: the DART model [5]. The latter operates on realistic discrete scene representations. The scale of analysis is selected with the discretization scheme value. Radiation propagation is tracked with the discrete ordinate method. Major electromagnetic interaction mechanisms (*i.e.* single and multiple scattering, specular reflectance, variable sky conditions, etc.) of soils, leaves, trunks and water are simulated.
We coupled the DART model with a 3-D scene model [4]. So, images were simulated with different canopy structural characteristics (tree cover, clumped, random or regular tree distribution, etc.) and experimental conditions in order to assess their impact on textural information. This paper presents quantitative results about the influence of distance between trees, crown diameter, LAI, illumination and viewing directions, and spatial resolution on textural information. All our results are not shown here.

II - IMAGE STRUCTURE AND FOREST PARAMETERS

The sensitivity of the textural information of DART images to forest structural parameters was analysed. Here, images are simulated in the visible domain with a 50cm spatial resolution, a soil layer (ρ_s=10%) and a grass layer (ρ_g=τ_g=15% - LAI_g=3). Trees are 14.5m height and 4.5m apart with a 90% probability of presence at the nodes of a rectangular grid; crowns are homogeneous and ellipsoidal ($\varnothing$=3.5m - ρ_l=τ_l=10%). Canopy LAI is 2.92 and sun direction is θ_s=31.2° and ϕ_s=330°.

Sensitivity of texture (variogram) to tree cover.

This is evaluated by means of two structural parameters: (1) space between trees and rows and (2) crown diameter.

(1) Space between rows and trees (Δr). Figure 1 shows simulations with four Δr (4.5/5.5/6.5/7.5m). Tree cover varies from 10.5% to 36.3%.
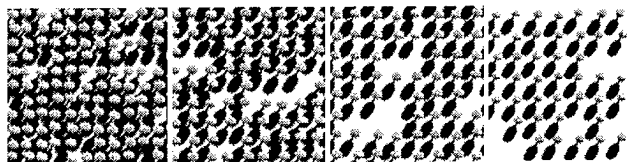
Fig. 1: DART simulations. Δr = 4.5/5.5/6.5/7.5m.

Associated variograms (Fig. 2) show that:

- variograms oscillate with a period equal to Δr.

- the larger Δr the larger the oscillations amplitude. This is correlated to the difference of reflectance Δρ between tree crown and vegetation between tree rows. Δρ decreases because tree crown shadows overlap less when Δr increases.

- sills vary as the image variance. They increase with Δr, up to Δr=6.5m and then decrease. This non monotonous variation is logical. Indeed for very large and very small Δr the image is homogenous (*i.e.* nil sill/variance).

So, the sensitivity of variograms to Δr and thus tree cover, can be quantified. Δr can be assessed with their period.
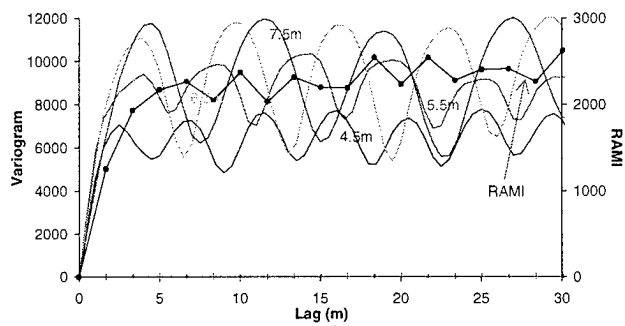
Fig. 2: Variograms of simulations. $\Delta r = 4.5/5.5/6.5/7.5m$.

(2) Crown diameter (∅). The size of ∅ directly influences tree cover. Figure 3 shows simulations in the visible with four ∅ (1.5m, 2.5m, 3.5m et 4.5m). Variograms show that:

- a period equal to Δr appears systematically.

- the sill/variance of the images decreases with the increase of the diameter, *i.e.* images become more homogeneous.

- oscillations are more marked for smaller ∅, because this corresponds to a better periodic and equidistribution of the illuminated and shaded areas.
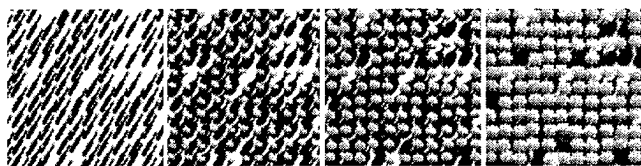
Fig. 2: DART simulations. ∅ = 1.5/2.5/3.5/4.5m.
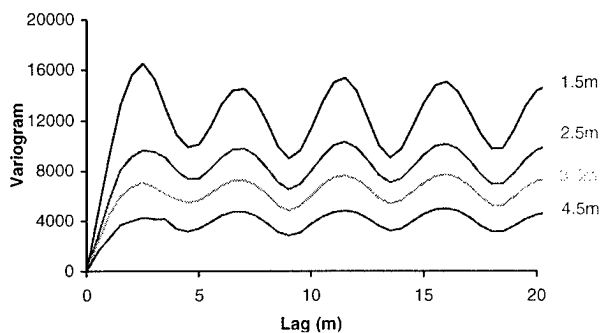
Fig. 3: Variograms of simulations. ∅ = 1.5/2.5/3.5/4.5m.

Sensitivity of texture (variogram) to LAI.

Simulations were conducted with LAI between 1 and 10, and (1) direct sun only (SKYL=0%) and (2) SKYL=50%.

(1) Direct sun. The sill and the amplitude of variogram oscillations increase with LAI. They saturate for LAI>4-5:

- illuminated area reflectance (Table 1) decreases with LAI increase. Indeed, whereas the 1st order (It1) contribution of direct sun radiation is constant with LAI, multiple order scattering contribution (Itn-It1) decreases with LAI.

- shaded area reflectance decreases with LAI increase due to the increasing opacity of tree crowns.

- the reflectance of tree crowns decreases with LAI increase due to a decrease of the transmission of soil reflected radiation through the crowns.

(2) SKYL (50%). Variograms show that the sill/ variance of the variograms increases up to LAI=3 and then decreases. This tendancy is related to:

- the illuminated area reflectance decreases with LAI<5 and increases for LAI≥5. Variations are larger than for the case (1). Indeed, crown transmitted radiation is larger than leaf scattered radiation for LAI<5 and smaller for LAI>5. It is always smaller with SKYL=0.%

- reflectances of shaded surfaces decrease strongly with LAI. Reflectances of tree crowns decrease also. Similarly to the case of illuminated areas, the contribution of the diffuse atmospheric radiation explains the slight increase with LAI≥5.

The interval of variability of the sill is more limited than for SKYL=0% due to the reduced difference between the reflectance of sunlit and shaded surfaces.

	Refl illuminated areas			**Refl** shaded areas			**Refl** crown		
SKYL	**0**%		**50**%	**0**%		**50**%	**0**%		**50**%
LAI	**It1**	**Itn**	**Itn**	**It1**	**Itn**	**Itn**	**It1**	**Itn**	**Itn**
1	6.95	7.53	5.50	2.31	2.56	3.04	4.98	5.45	5.75
2	6.94	7.49	4.91	0.77	0.91	1.62	4.70	5.15	5.58
3	6.94	7.47	4.63	0.26	0.34	1.08	4.53	4.93	5.43
4	6.94	7.45	4.52	0.09	0.14	0.86	4.43	4.80	5.38
5	6.94	-	4.17	0.03	-	0.61	4.38	-	5.00
7	6.94	-	4.34	0.00	-	0.66	4.34	-	5.31
8	6.94	-	4.32	0.00	-	0.64	4.34	-	5.31
10	6.94	7.43	4.28	0.00	0.02	0.61	4.33	4.57	5.32

Table 1: Illuminated, shaded and crown area with LAI=1 to 10, and SKYL=0% and 50%.
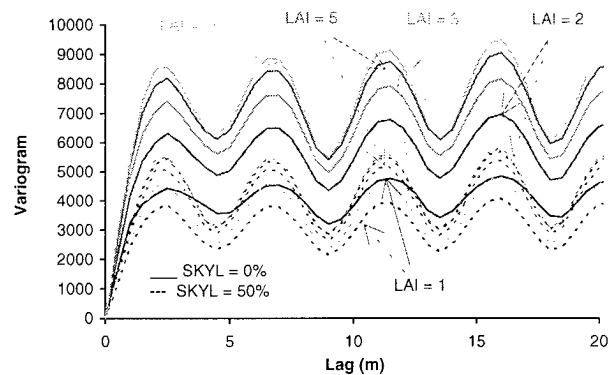
Fig. 4: Variograms of simulations. LAI=1/2/3/5/10.

In short, LAI strongly influences image texture. Its complex role is well quantified with the DART model.

III - INFLUENCE OF THE VIEWING CONFIGURATION

The proportions of the illuminated and shaded areas strongly influence textural information through the geometric configuration of observation. This aspect is analysed here with images simulated in the azimuthal plane ($\phi_v=50°$) with $\theta_v=0°/14.4°/31.2°/48°$: a single DART simulation produces these images.

The along-row variograms allow us to note that:

- the period decreases when θ_v increases. Indeed, the space between tree rows seems to decrease.

- the sill and oscillations of variograms decrease with large θ_v, *i.e.* the cover becomes apparently more homogeneous.
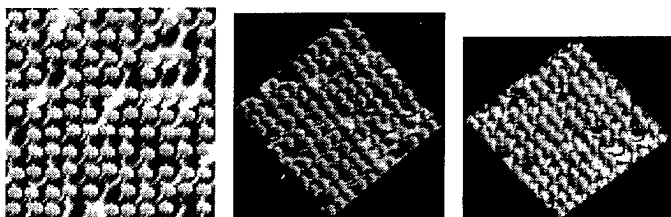
Fig. 5: DART directional images($\phi_v=50°$, $\theta_v=0°/14.4°/31.2°$)
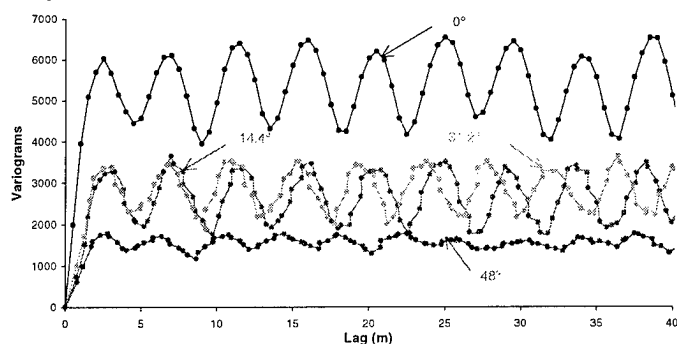
Fig. 6: Variograms of simulations. ($\phi_v=50°$, $\theta_v=0°/14.4°/31.2°/48°$).

IV - INFLUENCE OF THE SPATIAL RESOLUTION

Spatial resolution influences a lot the capability to retrieve forest parameters from textural information. This point is analysed with DART visible simulations at 50cm and 1.5m spatial resolutions. Images at 1/1.5/2/2.5/3m spatial resolutions were simulated with block averaging the 0.5m resolution scene simulation (Fig. 7). It appears that:

- periodic oscillations associated to Δr are visible up to 2m spatial resolution, *i.e.* a lower limit of $\varnothing$ and Δr. If the size of the averaging block is larger than the dimension of scene objects, averaged pixels come from different objects and the periodic pattern 'grass-tree' disappears.

- sills decrease with the decrease of spatial resolution. Indeed, block averaging decreases image variance.

- oscillations decrease with the larger homogeneity degree of images that arises from block averaging..
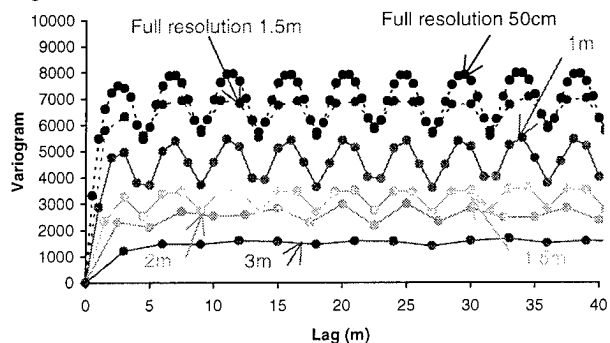
Fig. 8: Variograms of 0.5/1/1.5/2/3m resolution images.

We also compared the variograms derived from the block averaged 1.5m resolution image with the image directly simulated with a 1.5m resolution scene model.

- the amplitude of the oscillations are very similar in spite the block average process.

- the sill from the 1.5m resolution scene is much larger.

In fact, block averaged images, from larger spatial resolution, are more comparable to remote sensing images than images simulated directly with final resolution.
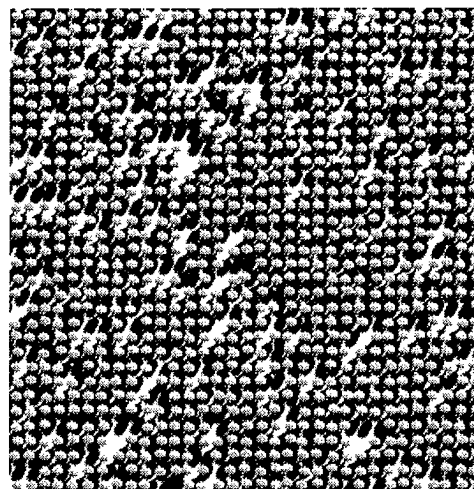
Fig. 7: Simulation of a 0.5m resolution scene. 1/1.5/2m resolution images are derived with block averaging.

V - CONCLUSION

DART images were compared with 1.67m resolution images of the RAMI airborne radiometer [4]. The capability of the DART model for simulating reliably (radiometry and texture) remote sensing images was well verified. Fig. 2 shows the variogram of a RAMI image of a pine stand with $\Delta r \approx 4m$. Although attenuated oscillations appear clearly, similarly to the oscillations of the 1.5m-2m resolution image of Fig. 7. This confirms our theoritical result: 2-3m is the larger spatial resolution of visible remote sensing systems for retrieving Δr from images. Finally, we stress that a realistic reflectance model such as DART is a reliable and practical tool for assessing the capability of remote sensing images for retrieving parameters of a forest plantation, under various illumination and viewing configurations.

VI - REFERENCES

[1] Curran P. J., 1988, 'The Semivariogram in Remote Sensing: An Introduction', *Remote Sensing of Environment*, Vol. 24, p. 493-507.
[2] St-Onge B. A. and Cavayas F., 1995, 'Estimating forest stand structure from high resolution imagery using the directional variogram', *International Journal of Remote Sensing*, Vol. 16, N°11, p. 1999-2021.
[3] Woodcock, C. E., Stralher, A. H., Jupp, D. L., 1988, 'The Use of Variograms in Remote Sensing: II. Real Digital Images', *Remote Sensing of Environment*, Vol. 25, p.349-379.
[4] Pinel V., 'Modélisation physique multi-echelle et télédétection des systèmes forestiers', Dec. 96, PhD, Univ. Paul Sabatier, Toulouse, France.
[5] Gastellu-Etchegorry J.P., Demarez V., Pinel V., Zagolski F., 1996, 'Modeling Radiative Transfer in heterogeneous 3-D Vegetation Canopies', *Remote Sensing of Environnent*, in press.

Extracting Sub-pixel Vegetation Endmember Bidirectional Reflectance for Canopy Model Inversion Using NOAA AVHRR Satellite Imagery

Gregory P. Asner

Department of EPO Biology and Cooperative Institute for Research in Environmental Sciences (CIRES)
University of Colorado. Campus Box 216, Boulder, CO 80309-0216
Tel: (303) 492-5130, Fax: (303) 492-5070, Email: asner@cses.colorado.edu

Jeffrey L. Privette
Department of Geography, University of Maryland, College Park, MD 20740

Carol A. Wessman
Department of EPO Biology and CIRES, University of Colorado, Boulder, CO 80309-0216

C. Ann Bateson
CIRES, University of Colorado, Boulder, CO 80309-0216

ABSTRACT

Biophysical parameter retrieval via BRDF inversion over heterogeneous regions is highly affected by the spatial resolution of the angular reflectance data. An AVHRR unmixing methodology is presented which utilizes high resolution imagery and a geometrical-optical model inversion to recover reflectances of individual land-cover types in savanna regions. Results of a sensitivity study are discussed.

INTRODUCTION

Inversions of bidirectional reflectance (BRDF) models with remote sensing data allow accurate retrieval of surface biophysical information [1]. The success of these inversions depends on the spatial, spectral, angular, and temporal resolution of the data. Since most current BRDF inversion methods utilize 1-dimensional models, surface homogeneity within an image pixel is necessarily implied. In addition, most inversions require an angularly diverse set of data gathered over a temporally- and spatially-invariant landcover. The NOAA Advanced Very High Resolution Radiometer (AVHRR) is one of the few spaceborne sensors capable of acquiring radiometric data over a range of view angles required for BRDF inversions [2]. However, its coarse spatial resolution (1.1~4.3km) often results in measurements of mixed landcovers. Our goal is to resolve the inconsistency between the models and data by deconvolving the angular AVHRR data into single landcover reflectances.

Spectral mixture analysis allows for sub-pixel classification of cover types (endmembers) within a remotely sensed image, providing information on spatial heterogeneity inaccessible to coarse-scale sensors [3]. However, unmixing AVHRR data is tenuous due to its relatively low spectral resolution and large ground instantaneous field-of-view. Reference [4] successfully addressed this issue by spatially unmixing AVHRR imagery using classified Landsat TM data. However, they assumed that endmembers did not cause shadows, that endmembers were homogeneous at TM (30m) scales or larger, and that endmember reflectances were Lambertian. All of these factors are important for sampling the surface BRDF in heterogeneous landscapes.

Therefore, we have developed a technique that utilizes spectrally-unmixed high resolution imagery and a geometrical-optical shadow model to decompose an AVHRR signal into multiple land-cover reflectances. This unmixing technique is specifically planned for savanna-like ecosystems. Savannas cover more than one-fourth of the global vegetated land surface [5], and are principally composed of a continuous layer of grasses with scattered trees which vary in density at high spatial frequency. In an effort to evaluate and monitor changes in savanna ecology over large regions, spectrally-unmixed angular reflectances are required to retrieve biophysical parameters via BRDF model inversions.

MODEL DESCRIPTION

Our approach employs a two-step unmixing method. First, a high spatial/spectral resolution image is reduced to component fractions using a manual endmember selection method [3,6]. Endmembers are constructed from a principal components analysis of the image spectral space. This step captures fine scale heterogeneity (i.e. TM: sub-30m) and has been shown to work well in tallgrass and woodland landscapes [3]. A full description of the high resolution unmixing will not be discussed here, and the derived high resolution endmember fractions will be considered inputs to the AVHRR unmixing model. For purposes here, we consider TM data as the high resolution imagery.

For savanna ecosystems, typical TM endmembers obtained from spectral unmixing include tree, grass/herbaceous, and shade fractions. Differences in sun-sensor geometry between

TM and AVHRR data result in different shade fractions between images. To correct the problem. we use a geometrical-optical (G-O) canopy shadow model for vegetation covers consisting of discrete plant crowns [7]. G-O model input parameters include areal density of tree stems (λ), the ratio of crown vertical to horizontal radius (b/r), the ratio of tree height (ground to crown center) to vertical crown radius (h/b), view and solar zenith angles (VZA, SZA), and relative azimuth angle. The model computes areal fractions of sunlit crown, and sunlit and shaded background.

The G-O model was numerically inverted to retrieve the input parameters for a given set of high resolution sunlit and shaded endmembers and sun-sensor geometry. In savanna ecosystems. tree stem density spatially varies at a higher frequency than crown dimension ratios. and these ratios are relatively constant amongst dominant savanna tree species (Northrup and Archer. unpublished data). Thus. b/r and h/b can be averaged over a 4 TM pixel grid (60m x 60m). Each TM pixel within this grid provides 2 parameters (a sunlit crown and shaded background fraction) for a total of 8 known parameters. Six unknown parameters for each grid include 4 tree stem densities (λ). and an average b/r and h/b. Inversion of the model for each grid is accomplished with an optimization routine (E04JAF. NAG) which minimizes the merit function:

$$\varepsilon^2 = \Sigma \left[(c_j - c_{jm})^2 + (b_j - b_{jm})^2 \right] \qquad (1)$$

where c_j and b_j are the actual sunlit canopy and shade background fractions. and c_{jm} and b_{jm} are the modeled sunlit canopy and shade background fractions. The retrieved canopy parameters (4 λ's. 1 b/r. and 1 h/b) are then used in a forward G-O model simulation. but with the appropriate AVHRR sun-sensor geometry for each 4-pixel grid, to produce corrected high resolution sunlit and shade fractions.

Corrected endmember fractions are then individually convolved to the AVHRR spatial resolution using a 2-D Gaussian representation of the AVHRR point spread function (PSF) [4]. Here. the Gaussian filter is independently scaled in the along- and across-track directions based on sensor VZA and earth curvature.

For a set of 3 x 3 AVHRR pixels. a system of equations is now constructed:

$$\text{AVHRR } \rho_k = \Sigma\Sigma \, PSF_i \cdot W_{ij} \cdot \rho_j, \; k = (1 \dots 9) \qquad (2)$$

where W_{ij} refers to the endmember fraction (j) in TM pixel (i) weighted by the AVHRR PSF and multiplied by endmember reflectance ρ_j. This system of equations is solved for the bidirectional endmember reflectances (ρ_j) using singular value decomposition of the independent endmember concentration matrix and the dependent AVHRR pixel reflectances (ρ_k). Thus the mean reflectances for tree and grass canopy are obtained for a 9-pixel AVHRR sub-scene.

MODEL EVALUATION

A landscape simulation was developed to produce realistic TM and AVHRR images for testing the unmixing model. A 1-D turbid medium BRDF model based on the discrete ordinates solution to the radiative transport equation was used to simulate tree and herbaceous canopy reflectance separately [8]. Input parameters for the BRDF model are listed in Table 1. Tree and grass leaf optical properties were obtained in a Texas savanna (Texas A&M's La Copita Research Area) using a field spectrometer (ASD Inc.. Boulder. CO) and integrating sphere. Other parameters were chosen to realistically represent the vegetation characteristics in savanna ecosystems.

The G-O model was used to compute shade fractions based on input tree canopy and sun-sensor geometry parameters (Table 1). Tree canopy characteristics were permitted to randomly vary within a realistic range for common savanna tree species. Sunlit tree and grass areal fractions were multiplied by tree and grass canopy BRDF reflectances. The shadow endmember was simulated using:

$$\rho_{shade} = W_{shade} \cdot \rho_{sb} \cdot e^{(-L \cdot l / \cos\theta)} \qquad (3)$$

where W is the shade fraction. ρ_{sb} is the sunlit background reflectance. and the tree canopy transmission function depends on tree leaf area index (LAI) and solar zenith angle (θ).

The three endmembers were linearly summed to produce TM mixed reflectances for a 300 x 300 pixel image. Similarly. 105 AVHRR images. each with a unique sun-sensor geometry (Table 1). were created with the G-O model canopy parameters used in creating the TM image and the AVHRR PSF. All simulations were constrained to the solar principal plane.

Table 1. BRDF and geometrical-optical model parameters for savanna landscape simulations.

BRDF Parameters	Trees		Grasses	
	RED	NIR	RED	NIR
Leaf reflectance	0.063	0.304	0.095	0.333
Leaf transmittance	0.078	0.426	0.059	0.458
Leaf angle orientation	planophile		erectophile	
Leaf area index	1.0 - 3.0		0.5 - 2.0	
Geometrical-Optical Model Parameters				
Tree density	Random: 0.0 - 1.0			
b/r	Random: 0.3 - 0.7			
h/b	Random: 4.0 - 10.0			
Image Parameters	GIFOV	SZA (deg)	VZA (deg)	
TM	30m	30	0	
AVHRR	1.1~4.3km	0-60; 15incr.	0+/-50; 5incr.	

UNMIXING RESULTS

The AVHRR endmember reflectances were spatially unmixed using the simulated TM cover fractions. and the relative error between retrieved and actual endmember reflectances was calculated. Random Gaussian mean-zero noise was added in 5. 10. and 15% increments to the TM

cover fractions to assess the sensitivity of our method to potential errors in high resolution endmembers (Table 2). Errors in the no-noise case are very low (< 1.5%) for all geometries. cover types, and wavebands. thus demonstrating the stability of the model. Errors increase as TM endmember noise increases for each AVHRR SZA.

To illustrate bidirectional reflectance effects that arise when coordinating data from multiple satellite instruments, the AVHRR images were unmixed using the TM cover fractions but without the G-O model inversion. Fig. 1 shows the relative error along the principal plane when AVHRR SZA = TM SZA = 30° (i.e. errors only due to view geometry). Errors are high for tree and herbaceous canopy, but decrease at nadir (coincident with TM sun-sensor geometry). in the extreme forward- and back-scattered directions, and at the hotspot (VZA = -30°). True tree canopy reflectances are greatly underestimated at |VZA| < 35° (excluding nadir) since the projected normal area of sunlit tree canopy and shaded background in the AVHRR direction is incorrect, resulting in reflectances that are too high for shade and too low for tree cover. The herbaceous layer endmember is less sensitive since a much greater proportion of any pixel contains this cover type, thus dampening small errors in fractional shade cover. Errors decrease at large VZA since both tree and shade projected areas are low, and uncorrected cover fractions approach the corrected values. In addition, SZA differences between images produce even larger errors in retrieved endmember reflectances when bidirectional geometry is not taken into account (data not shown). These combined factors are the focus of current and future study.

Table 2. Relative error between actual and retrieved tree and herbaceous endmember reflectance with random noise added to TM images. Mean percent relative error for all AVHRR view angles is given with standard deviation in parentheses.

Noise Added	AVHRR SZA	Tree		Herbaceous Layer	
		RED	NIR	RED	NIR
0 %	0	0.8(0.5)	0.3(0.1)	0.2(0.2)	0.3(0.2)
	15	1.4(0.7)	0.4(0.3)	0.4(0.3)	0.4(0.3)
	30	1.1(0.7)	0.5(0.3)	0.5(0.3)	0.4(0.3)
	45	1.3(1.0)	0.7(0.5)	0.6(0.3)	0.6(0.3)
	60	1.2(0.9)	0.8(0.5)	1.0(0.4)	1.1(0.5)
5 %	0	3.3(1.5)	1.5(1.2)	0.4(0.4)	0.5(0.4)
	15	2.6(1.5)	1.8(1.1)	0.3(0.2)	0.5(0.4)
	30	2.2(1.3)	1.4(0.9)	0.7(0.6)	0.7(0.7)
	45	4.7(2.6)	2.8(1.8)	1.0(0.6)	1.2(0.8)
	60	12.2(5.2)	8.2(3.7)	3.0(1.0)	4.0(1.4)
10 %	0	2.4(1.5)	3.4(1.2)	0.7(0.6)	0.9(0.6)
	15	3.6(2.6)	3.4(2.1)	1.1(0.7)	1.0(0.7)
	30	3.6(2.7)	3.4(2.1)	1.1(0.7)	1.5(1.0)
	45	6.6(2.7)	4.7(2.1)	1.1(0.8)	1.5(0.9)
	60	13.1(4.4)	8.7(4.4)	1.9(1.2)	2.7(1.5)
15 %	0	5.6(3.4)	4.6(1.8)	1.8(0.8)	1.1(1.0)
	15	6.1(2.4)	4.5(1.9)	2.2(1.0)	1.0(0.8)
	30	6.1(4.4)	5.5(2.4)	2.1(0.7)	1.2(0.8)
	45	9.2(2.0)	7.4(3.4)	2.3(0.9)	1.8(0.9)
	60	16.4(4.3)	12.2(4.0)	2.8(1.4)	2.8(1.5)

Fig. 1. Comparison of relative error between true and retrieved reflectances without (top) and with (bottom) G-O model inversion for TM and AVHRR SZA = 30°. Red band only.

ACKNOWLEDGMENTS

REFERENCES

[1] J.L. Privette, R.B. Myneni, C.J. Tucker, and W.J. Emery, "Invertibility of a 1-D discrete ordinates canopy reflectance model," Remote Sens. Environ., vol. 48, pp.89-105, 1994.

[2] M.J. Barnsley, A.H. Strahler, K.P. Morris, and J-P. Muller, "Sampling the surface bidirectional reflectance distribution function: 1. Evaluation of current and future satellite sensors," Remote Sens. Rev., vol. 8, pp. 271-311, 1994.

[3] C.A. Wessman, C.A. Bateson, and T.L. Benning, "Detecting fire and grazing patterns in tallgrass prairie using spectral mixture analysis." Ecol. Applic., in press.

[4] K.W. Oleson, S. Sarlin, J. Garrison, S. Smith, J.L. Privette, and W.J. Emery, "Unmixing multiple land-cover type reflectances from coarse spatial resolution satellite data. Remote Sens. Environ., vol. 54, pp. 98-112, 1995.

[5] W.M. Hao and M. Liu, "Spatial and temporal extent of tropical biomass burning." Global Biogeochem. Cycles. vol. 8, pp. 495-503, 1994.

[6] C.A. Bateson and B. Curtiss, "A tool for manual endmember selection and spectral unmixing." Remote Sens. Environ., in press.

[7] X. Li and A. Strahler. "Geometrical-optical modeling of a coniferous forest canopy," IEEE Trans. Geosci. Remote Sens., vol. GE-23, pp. 207-221, 1985.[8] K.S. Shultis and

[8] R.B. Myneni, "Radiative transfer in vegetation canopies with anisotropic scattering," J. Quant. Spectrosc. Radiat. Transfer, vol. 39, pp. 115-129, 1988.

Estimation of Bidirectional Reflectance Distribution Function from Land Surfaces Using Airborne POLDER Data

Kazuya Takemata, Tetsuya Yonekura* , Masamitsu Asae* and Yoshiyuki Kawata*

Kanazawa Technical College, 2-270 Hisayasu, Kanazawa, Ishikawa 921, Japan

81-762-48-1080 ext. 2892; 81-762-48-5548 (FAX); takemata@infor.kanazawa-it.ac.jp (Internet)

*Kanazawa Institute of Technology, 1-1 Ogigaoka, Nonoichi, Ishikawa 921, Japan

81-762-48-1100 ext. 2594; 81-762-48-7753 (FAX); kawata@infor.kanazawa-it.ac.jp (Internet)

Abstract -- This paper shows the estimation of the Bidirectional Reflectance Distribution Function (BRDF) using the airborne POLDER image data. The BRDF is an intrinsic measurement of directional properties of the earth's surface. The estimation of BRDF requires many remote sensing measurements of a given surface target from different viewing angles. The airborne POLDER sensor has a capability of measuring successively reflected radiation by terrestrial surfaces in a framed image from different viewing angles during a single airplane pass.

In this study we have analyzed a subset of the airborne POLDER data over lands obtained in the so-called La Crau campaign conducted by Centre National d' Etudes Spatiales (CNES), France in 1990 by using the multiple scattering theory. The airborne POLDER data is converted into the albedo data by using our atmospheric correction scheme and then the accurate BRDFs for selected surface covers are estimated. The estimated BRDFs show an anisotropic reflection law is valid for vegetated surfaces at 850 nm and fitting parameters for their BRDFs are presented in this paper.

INTRODUCTION

The Bidirectional Reflectance Distribution Function (BRDF) is an intrinsic measurement of directional properties of the earth's surface. However, it is difficult to measure the BRDF of target surfaces directly by the scanning type remote sensor. The estimation of BRDF requires many remote sensing measurements of a given surface target from different viewing angles. In addition, it is needed a good atmospheric correction scheme to retrieve intrinsic informations from remote sensing measurements.

The airborne POLDER instrument was built by Centre National d' Etudes Spatiales (CNES) and Universite des Sciences et Technologies de Lille, France [1],[2]. We have analyzed the airborne POLDER measurements to estimate the BRDFs [3]. The accurate atmospheric correction is a prerequisite for such analysis. And then we presented the atmospheric correction algorithm applicable the airborne POLDER measurements, by using the multiple scattering theory [3],[4]. In this study, a empirical model is used to assess the BRDF of surfaces. Then we apply our atmospheric correction scheme for the airborne POLDER measurements and retrieve the fitting

parameters that describe the shape of the BRDFs for each surfaces.

ATMOSPHERIC CORRECTION FOR AIRBORNE FRAMED IMAGE DATA

For the atmospheric correction of the airborne remote sensing measurements, we need to evaluate the internal radiation field. To deal with the internal radiation field, let us assume an incident solar flux πF illuminates a plane parallel atmosphere from the direction of (μ_0, ϕ_0), where μ_0 and ϕ_0 are the cosine of the solar zenith angle θ_0 and the solar azimuth angle , respectively. The earth's atmosphere is divided two layers at the aircraft altitude. And the atmosphere above the aircraft is denoted by Layer 1 and the atmosphere below the aircraft is denoted by Layer 2. Each layer is assumed to be horizontally homogeneous atmosphere, respectively. In this study land surfaces are assumed to be characterized by a target albedo A_t, and a mean background albedo $\overline{A}$. And Lambert's low is assumed for surface reflection. Let the atmospheric optical thickness, reflection and transmission functions of Layer 1 be τ_1, R_1 and T_1, respectively. Similarly, let those of Layer 2 be τ_2, R_2 and T_2, respectively. The internal radiance I_u at POLDER aircraft level in the direction of (μ, ϕ) can be written as (1), in terms of the upwelling diffuse radiation U at the aircraft altitude,

$$I_u(\mu, \mu_0, \phi - \phi_0) = \mu_0 U(\mu, \mu_0, \phi - \phi_0) F . \qquad (1)$$

For given atmospheric parameters, such as the optical thickness, single scattering albedo and the turbidity factor of the atmospheric layers, we can compute U by using the doubling and adding method [5]. Computing U in terms of R_1, T_1, R_2 and T_2 and A_t, $\overline{A}$ were given by kawata et al. [4].

Considering a single reflection by a target with an albedo of A_t and up to double reflections by the background with a mean albedo of $\overline{A}$, the internal radiance I_u can be expressed approximately in terms of A_t and $\overline{A}$ by (2),

$$I_u = (s \cdot \overline{A} + t)A_t + (p-s)\overline{A}^2 + (q-t)\overline{A} + r, \qquad (2)$$

where p, q, r, s and t are radiance coefficients. Then, the mean

internal radiance $\bar{I}_u$ can be given by assuming $A_t = \bar{A}$ in (2) as follows,

$$\bar{I}_u = p \cdot \bar{A}^2 + q \cdot \bar{A} + r. \qquad (3)$$

These radiance coefficients can be expressed in terms of R_1, T_1, R_2 and T_2 and computed by the doubling and adding method for each pixel in a framed image. However, they can be computed without difficulty by applying a least square method in (2) - (3), using pre-computed values of I_u and $\bar{I}_u$ for various values of $\bar{A}$ and A_t from (1). In this study we used the latter approach to compute them.

AIRBORNE POLDER DATA ANALYSIS

The airborne POLDER sensor measures successively the reflected radiation by terrestrial surfaces in a framed image form. The angular coverage of the POLDER is $\pm 51°$ in the cross-track direction and $\pm 41°$ in the along-track direction. Several airborne POLDER measurements over lands and seas have been made since 1990 in France and other countries. The La Crau campaign was conducted in the southeast of France on June 17 by CNES [2]. In this paper we have analyzed a subset of a large La Crau data set. Our data consists of 55 sequential framed images. Both the reflectance and polarization data at 550 nm, 650 nm and 850 nm were included, and only the reflectance data were used to yield the directional reflectance properties of the land surfaces.

Atmospheric model in this study

The estimation of the surface albedos requires information on atmospheric parameters at the time of the observation. In La Crau campaign, the air - truth data, such as aerosol optical thickness, the refractive index of aerosols and the aerosol size distribution, were measured before and during the airborne flight [2]. We adopted these data in our atmospheric correction. Because values of the molecular optical thickness were not given in [2], we adopted the optical thickness values based on the standard model atmosphere of Lowtran6 (Midlatitude, Spring - Summer model) [6]. Since we found the slope of the observed size distribution is similar to that of Junge type aerosol model with $v = 3$, we adopted Junge type aerosol with $v = 3$ as an appropriate aerosol model. And the aerosol model is given by (4),

$$n(r) = C \cdot 10^{v+1} \quad \text{for } 0.02\mu m \leqq r \leqq 0.1\mu m$$
$$n(r) = C \cdot r^{-(v+1)} \quad \text{for } 0.1\mu m \leqq r \leqq 10\mu m \qquad (4)$$
$$n(r) = 0 \qquad \text{for } r < 0.02\mu m \text{ and } r > 10\mu m,$$

where $n(r)$ is the number of particles of radius r per unit increment in radius r. The optical parameters in our atmospheric model are listed in Table 1.

Estimation of BRDFs at 550 nm

In this study we selected 22 target areas (each consisting of 5×5 pixels) which are identified by consulting the local geographic map with a scale of 1/25,000. The theoretical reflectance curve in the principal plane is presented for the atmospheric model with a Lambertian surface of $A_t = 0.15$ and $\bar{A} = 0.15$ in Fig.1, together with observed reflectance value of "Forest01" and "Rice Field01". The reflectance is defined as ($\pi I_u / \mu_0 \pi F = I_u / \mu_0 F$). Positive and negative signs in the zenith viewing angle correspond to cases of the surface reflection occurred in the backward and forward scattering directions, respectively. In Fig.1 we found a good between theoretical and observed reflectance values. This suggests that the assumption of Lambert's law for the these covers is acceptable at 550 nm.

Estimation of BRDFs at 850 nm

In a similar manner at 550 nm, we estimated the surface BRDF for "Forest01" at 850 nm. "Forest01" is one of vegetated surface covers. However, The Lambertian assumption was not acceptable for that target in the backscattering direction. Then a empirical BRDF model was introduced for surface covers. Empirical models of the BRDF of a surface cover do not dependent on physical parameters, but instead characterize the shape of the BRDF function using fitting parameters. In this study, we adopted a empirical model proposed by Deuzé et al. [2]. This model is expressed by the sum of an isotropic contribution, a function accounting for the brightening to the limb viewing ($c1$), and a function accounting for the maximum in the sun's direction (c2).

$$\hat{A}_t = k_0 + c_1 \cdot k_1 + c_2 \cdot k_2, \qquad (5)$$

where,

$$c_1 = 1 - \mu\mu_0,$$
$$c_2 = [\text{Min}(0, \cos\Theta)]^2 - 1,$$

and $\hat{A}_t$ is the model albedo, Θ is a scattering angle. The coefficients k_0, k_1 and k_2 are obtained with a least square fit on estimated target albedo values for different viewing angles. Table 2 shows the result of the empirical model fitting against each surface cover.

Fig.2 shows simulated reflectance curves in the principal plane for "Forest01" by assuming the atmosphere with the model fitted BRDF. At 850 nm the observed reflectance increase in the backscattering direction (hot spot) are approximately reproduced by the simulations, allowing for a systematic bias by about 10 %. In the adding and doubling method we assumed a homogeneous surface layer with the same model fitted BRDF. Thus the bias may originate from our assumption in dealing with the bottom surface layer.

CONCLUSIONS

In this paper, the BRDFs for selected land covers was found by using the airborne POLDER image data. The main results in this study can be summarized as follows:

1) We estimated the BRDFs by using successive albedo images at 550 nm and 850 nm. The BRDFs for vegetated surfaces showed non-Lambertian reflection at 850 nm, while the assumption of Lambertian surface was generally valid at 550 nm. And then empirical fitting parameters were given for vegetated surfaces at 850 nm.

2) Then, studies on physical BRDF models for vegetated surfaces are necessary to understand fully reflection characteristics by vegetations. The airborne (spaceborne) POLDER measurements over lands will be increasingly important for such studies.

REFERENCES

[1] Deschamps, P.M. , Bréon, F. M. , Leroy, M. , Podaire, A. , Bricaud, A. , Buriez, J.C. , and Séze, G. , "The POLDER mission: instrument characteristics and science objectives", IEEE Trans. Geosci. Remote sensig, vol.32, no.3, pp.598-615, 1994.

[2] Deuzé, J. L. , Bréon F.M. , Deschamps, P.Y. , and Herman, M., "Analysis of the POLDER Airborne Instrument Observations over Land Surfaces", Remote. Sens. Environ., no.45, pp.137-154, 1993.

[3] Takemata, K. and Kawata, Y. , "Estimation of land surface bidirectional reflectance distribution function by using airborne POLDER image data", IEICE Trans. Commun. vol.E78-B, no.12, 1591-1597, 1994.

[4] Kawata, Y. , Yamazaki, A. , Kusaka, T. , Ueno, S. , and Smokty, O. , "Atmospheric correction algorithm for remote sensing data with multi-viewing angles", Proc. 14th IGARSS , pp.1113-1115, 1993.

[5] Hansen, J. E., and Travis, L.D. , "Light scattering in planetery atmospheres", Space Sci. Rev., vol.13, pp.527-610, 1974.

[6] Kneizys, F. X. , Shettle, E. P. , Gallery, W. O. , Chetwynd, J. H. Jr. , Abreu, L. W. , Selby, J. E. A. , Clough, S. A. , and Fenn, R. W. , "Atmospheric Transmittance/Radiance : Computer code Lowtran-6", Air Force Geophys. Laboratory , Hanscom AFB, MA, Rep. AFGL-TR-83-0187, 1983.

Table 1. Optical Parameters in the Atmospheric Model

Band[nm]		τ_{total}	ω	f_r
550	Layer1	0.092	0.711	0.699
	Layer2	0.434	0.951	0.121
650	Layer1	0.058	0.643	0.618
	Layer2	0.309	0.931	0.088
850	Layer1	0.018	0.942	0.422
	Layer2	0.234	0.814	0.045

τ is the total optical thickness, ω is the scattering albedo of the atmosphere, and f_r is molecule gas - aerosol mixing ration for each layer.
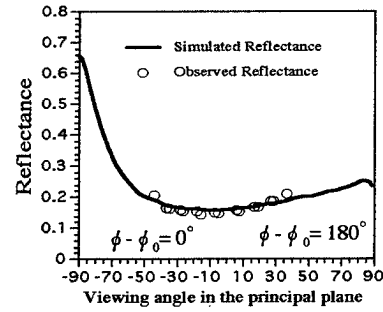
Fig.1 The reflectance variation at 550 nm against the zenith viewing angle in the principal plane for vegetated surface covers("Forest01" and "Rice Field01"). The "○" represents the observed reflectance. Lambertian surface of A_r = 0.15 and $\overline{A}$ = 0.15 is assumed. The incident solar zenith angle θ_0 =43°is alos assumed.
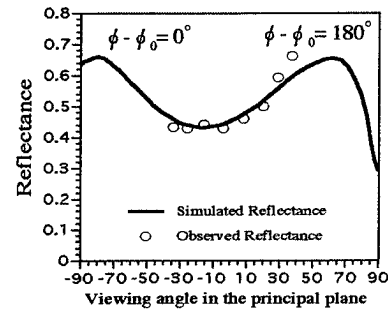
Fig.2 The same as Fig.1, except for "Forest01" and at 850 nm. The simulated reflectance based on an anisotropic surface reflection (the model fitted BRDF) corrected for a 10% bias is also assumed.

Table 2. Result of the Model Fitting against the Target Observations

Surface	N_{obs}	k_1	k_2	k_3	RMS	R^2
River01	13	0.179	-0.070	0.002	0.015	0.038
River02	13	0.191	-0.114	-0.010	0.020	0.158
Pond01	16	0.188	-0.126	-0.010	0.019	0.227
Pond02	12	0.229	-0.204	0.004	0.030	0.094
City01	15	0.294	0.454	0.197	0.010	0.958
City02	18	0.376	0.343	0.150	0.011	0.915
Road01	17	0.414	0.206	0.156	0.014	0.850
Road02	12	0.276	0.335	0.097	0.006	0.954
RiceField01	15	0.537	0.278	0.096	0.023	0.554
RiceField02	17	0.422	0.970	0.095	0.018	0.884
RiceField03	16	0.674	0.530	0.188	0.025	0.797
Forest01	14	0.392	0.808	0.201	0.017	0.939
Forest02	19	0.407	0.301	0.147	0.010	0.932
Forest03	19	0.350	0.471	0.192	0.045	0.635
Orchard01	17	0.310	0.812	0.190	0.031	0.795
Orchard02	13	0.365	0.309	0.123	0.031	0.492
Orchard03	19	0.377	0.455	0.184	0.017	0.902
Vineyard01	7	0.443	0.304	0.139	0.004	0.967
Vineyard02	9	0.295	0.661	0.210	0.011	0.950
Vineyard03	18	0.522	0.312	0.186	0.017	0.915
Marsh01	18	0.295	0.211	0.047	0.008	0.356
Marsh02	8	0.088	0.682	0.185	0.007	0.954

"Surface" gives the target surface type. N_{obs} is the number of reflectance data used for the fit. $K_0, K_1,$ and K_2 are the retrieved model's fitting parameters. RMS is a root mean square difference between the estimated albedo and modeled albedo at 850 nm. R^2 is the ditermination coefficient.

Validation of Kernel-Driven Semiempirical BRDF Models for Application to MODIS/MISR Data

Baoxin Hu, Wolfgang Wanner, Xiaowen Li, and Alan H. Strahler
Department of Geography and Center for Remote Sensing, Boston University,
725 Commonwealth Avenue, Boston, MA 02215, USA, Tel. +1-617-353-5981,
Fax +1-617-353-3200, e-mail baoxin/wanner/lix/alan@crsa.bu.edu

Abstract–Increasing emphasis on global monitoring makes global modeling of bidirectional reflectance of vegetation an important issue. We study four linear kernel-driven semiempirical models for use in operational production of the BRDF/albedo product for the Moderate Resolution Imaging Spectroradiometer (MODIS) instrument of NASA's Earth Observing System (EOS). In this paper, we use a variety of multiple angle surface reflectance data sets from field and airborne measurements to evaluate these models. The results show that our semiempirical BRDF models provide a good mathematical description of the bidirectional reflectance of the land covers tested.

INTRODUCTION

With the development and wide use of coarse and medium-resolution multiangle sensors especially in global monitoring, the analysis of the BRDF (Bidirectional Reflectance Distribution Function) of each pixel in a remotely sensed image becomes more and more important. It can be used not only to compare observations obtained at different angles or standardize observations to a common geometric situation, but also to provide surface physical parameters and the boundary condition for the atmosphere-earth system. Linear kernel-driven semiempirical models based on physical models were developed [1,2] to meet the needs of global modeling of bidirectional reflectance. Rahman et al. [3] developed a semiempirical model of another type. These models can be applied to inhomogeneous land covers and are readily invertable, making them suitable for low and moderate spatial-resolution remote sensing.

KERNEL-DRIVEN SEMIEMPIRICAL MODELS

Kernel-driven semiempirical models describe the BRDF as a linear superposition of a set of kernels that describe basic BRDF shapes. These kernels are derived from physical models, thus providing a physical basis to the retrievals. The coefficient given to each kernel is determined empirically by fitting to a specific set of observed reflectances. Thus it is the weights of the physically-based kernels that are retrieved, not a set of physical parameters as in physical models. Linear BRDF models scale linearly in space if adjacency effects are assumed to be small, which allows for mixed pixel cases. This advantage is especially important in global processing. Roujean et al. [1] derived the Ross-thick and Roujean kernels, and Wanner

et al. [2] the Ross-thin, Li-sparse and Li-dense kernels. For the MODIS/BRDF product [4], we employ four models, Ross-thin–Li-sparse, Ross-thin–Li-dense, Ross-thick–Li-sparse and Ross-thick-Li-dense, based on these kernels.

Like all linear models, these four models can be inverted analytically through matrix inversion, avoiding costly numerical inversion problems. For a given data set in a specific band, a set of model parameters is so selected that

$$\sum_{j=1}^{N} \frac{(R_{obs_j} - R_{model_j})^2}{W_j} \qquad (1)$$

is minimal. Here, N is the number of observation, W_j is a weight which determines the contribution of each measurement to the model inversion, and R is reflectance. Two popular values for W_j are 1 and R_{obs}^2. At present, we set the weight W_j at 1.

VALIDATION OF THE MODELS

We use Kimes' data [5,6,7], Ranson's soybean data [8], soil data from the BRDF Information System [9], PARABOLA data from a boreal forest [10], FIFE data [11] and POLDER data to perform the validation of the kernel-driven semiempirical models. These data sets include a large variety of land cover types with various coverage and leaf area indices.

To evaluate the 4 models, we firstly use them to fit all data sets and to calculate the root mean square error (RMSE) between the predicted and observed values based on all available bands. The results show that all data sets are fit well by at least one of the models. As anticipated, in a number of cases different land cover types prefer different models. For example, bare soil and sparse vegetation are fitted better by models with the Li-sparse kernel than those with the Li-dense kernel. For thick vegetation canopies, such as orchard grass and irrigated wheat (Kimes data), volume scattering is dominant. Thus the selection of Li-sparse and Li-dense kernels in these models does not make much difference. But the models containing the Ross-thick kernel fit better than those with the Ross-thin kernel. A dense forest canopy, such as hardwood (Kimes data), is fitted better by models containing the Li-dense kernel than those with the Li-sparse kernel, because the Li-dense kernel can model the shadow overlapping mechanism which determines the bidirectional reflectance of dense crown canopies. So the relative RMSE of each of the four models can indicate

some characteristics of the observed surface.

Secondly, we select the best-fit model based on the RMSE for every data set and calculate the correlation coefficient between the modeled and the measured values. For most data sets, the correlation coefficient is over 0.8 and the RMSE is smaller than 0.043, which indicates a reasonable agreement between the modeled and observed values. Fig. 1 shows the reflectances in the principal plane in the NIR for some land covers, where the points represent the measured data and the solid lines are the modeled data. These data sets have hotspots, as for field and wheat, and bowl shapes, such as hardwood, demonstrating that the models can fit hotspots and bowl shapes well.

Lastly, we compare the best-fit model for every data set with other semiempirical models, such as Roujean's model [1] and Rahman's model [3]. In Fig.1, dashed lines are for Roujean's model and the dash-dotted lines for the Rahman model. From the plots, we can note that our models fit better than the other models, especially for the dense hardwood canopy.

CONCLUSION

In this paper, we evaluated the ability of linear kernel-driven semiempirical models developed for use with MODIS/MISR data to provide adequate mathematical descriptions of the anisotropic reflectance of a variety of natural surfaces. The results show: 1) different land cover types prefer different models; 2) our models can fit a large variety of vegetation canopies well and they fit better than other semiempirical models, especially for dense forest canopies. This is partially due to the fact that they are based on ellipsoidal crown shapes and the shadow overlapping mechanism is modeled realistically. The fit quality can presumably be further improved by reducing the effect of outlier data on the inversion results by giving the appropriate W_j in (1), and by considering more realistic multiple scattering in the models.

ACKNOWLEDGMENTS

REFERENCES

[1] Roujean, J. L., M. Latoy and P. Y. Deschamps, "A bidirectional reflectance model of the Earth's surface for the correction of remote sensing data", J. Geophys. Res., 97, pp. 20455-20468, 1992.

[2] Wanner, W., X. Li, A. H. Strahler, "On the derivation of kernels for kernel-driven models of bidirectional reflectance", J. Geophys. Res., 100, pp. 21077-21089, 1995.

[3] Rahman, H., B. Pinty, and M. M. Verstraete, "Extracting information on surface properties from bidirectional reflectance measurements", J. Geophys. Res., 96, pp. 2865-2874, 1991.

[4] Strahler, A. H., et al., "MODIS BRDF/ Albedo Product: Algorithm Theoretical Basis Document Version 3.2", NASA EOS-MODIS, 1995.

[5] Kimes, D. S., A. G. Kerber and P. J. Seller, "Dynamics of directional reflectance factor distribution for vegetation canopies", Appl. Opt., 22(9), pp. 1364-1372, 1983.

[6] Kimes, D. S., W. W. Newcomb, C. J. Tucker, et al., "Directional reflectance factor distributions for cover types of Northern Africa", Remote Sens. Environ 18, pp. 1-19,1985.

[7] Kimes, D. S., W. W. Newcomb, R. F. Nelson, and J. B. Schutt, "Directional reflectance distributions of a hardwood and a pine forest canopy", IEEE Trans. Geosci. Remote Sens. GE-24, pp. 281-293, 1986.

[8] Ranson, K. J., L. L. Biehl and M. E. Bauter, "Variation in spectral response of soybeans with respect to illumination, view and canopy geometry", Int. J. Remote Sens. 6, pp.1827-1842, 1985.

[9] Kim, M. S., "BRDF Infomation System Version M-1, Biospheric Sciences Branch", NASA/GSFC, Software, LGRSS, University of Maryland.

[10] Deering, D. W., S. P. Ahmad, T. F. Eck and B. P. Banerjee, "Temporal Attributes of the Bidirectional Reflectance for Three Boreal Forest Canopies", Proc. Int. Geosci. Remote Sens. Symp. 95, 1239-1241, 1995.

[11] Sellers, P.J., et al., "An overview of the First International Satellite Land Surface Climatology Project (ISLSCP) Field Experiment (FIFE)", J. Geophys. Res., 97, pp. 345-371, 1992.

Fig.1 The BRDF on the Principal Plane in the near infrared band for selected Kimes data (szn=sun zenith angle)
dot: observations; solid line: best-fit kernel-driven model dashed: Roujean model; dash-dotted: Rahman model

A Scanning 60 GHz Radiometer to Measure Air-Sea temperature Difference: Recent Results During COPE

Yuri G. Trokhimovski
NRC Resident Associate, NOAA/ERL/ETL
325 Broadway, Boulder, Colorado 80303

Ed R. Westwater and Vladimir G.Irisov
Cooperative Institute for Research in Environmental Sciences (CIRES), University of Colorado/NOAA
Boulder, Colorado 80309-0216

Vladimir Ye. Leuskiy
Astro Space Center of the Lebedev Physical Institute, Russian Academy of Sciences
Profsoyuznaya St.,84/32, Moscow, 117810, Russia

Abstract -- During September-October in 1995, the Environmental Technology Laboratory (ETL) conducted the Coastal Oceans Probing Experiment COPE off the Oregon coast. During this experiment, a 5-mm scanning radiometer was deployed on a research vessel. In this report, a summary of the obtained results is presented.

METHOD

The 60 GHz radiometer is designed for precise, continuous measurements of air-water temperature difference and for recovery of air temperature profiles (h = 0-300 m). This device was first used from a research vessel during the Joint US-Russia Internal Waves Experiment (JUSREX) in July 1992 [1].

The main idea of the technique is to measure oceanic and atmospheric emission in a wavelength band that exhibits relatively high atmospheric attenuation. In this case, the radiation in the horizontal direction can be used as a reference level since the brightness temperature is nearly equal to the air temperature at the measurement height. Radiometric measurements are made in a scanning mode and the radiometer measures brightness temperature relative to the air temperature.

The radiometer is a total power system with automatic compensation of the direct current in the output signal (a compensation-type radiometer). No additional modulation, except for the antenna beam rotation, is done in the radiometer. The scanning mirror of the radiometer rotates at 1.3 Hz.

We used radiometric measurements at wavelengths in the 5- mm oxygen absorption band. This wavelength band is usually employed for recovery of atmospheric temperature profiles [2,3]. The same technique can be used at infrared or short millimeter wavelengths. The COPE data presented below have confirmed that the technique recovers air-water temperature difference to an accuracy of about 0.1 K (or 5-7%) and can provide long, continuous observations. It is simple and can be used not only from a ship but also from low-altitude airborne platforms.

In addition to the water-air temperature difference, the same measurements provide information about air temperature profiles in the lower atmosphere. Thus, it is possible to compare different parameters that are related to heat and momentum fluxes and to check predictions of surface layer models. We suggest that the proposed technique could be deployed widely in the investigation of ocean - atmosphere interactions.

MEASUREMENT TECHNIQUE AND CALIBRATION

During COPE, 5-mm radiometric measurements were performed with an instrument slightly modified from the one used during JUSREX. First, the local oscillator in the radiometer was shifted to a higher frequency. The total band was estimated as 58.5 - 62.5 GHz. Note that this shift of central frequency does not change the ocean skin depth, which is still 0.3 mm. Next, the polarization of the radiometer was changed. During COPE the antenna received horizontal polarization (in JUSREX - vertical polarization). Near nadir, the water surface was observed at vertical polarization, at grazing angles, at

horizontal polarization. Such an installation provides better agreement between air temperature and brightness temperature in the horizontal direction.

The calibration of the radiometer output and antenna beam orientation was performed before COPE on the Boulder Atmospheric Observatory research tower during August 18-19, 1995. Scale calibration was performed from five different tower altitudes: 10, 50, 100, 200, and 300 m. Radiometric measurements were accompanied by radiosonde measurements and direct measurement of air temperature from sensors on the tower platform. Comparisons between calculated and measured brightness temperatures were used for the determination of calibration coefficients.

RESULTS OBTAINED FROM R/V *FLIP*

The 5-mm radiometer was mounted on the south side of the port boom at a distance about 10 m from *FLoating Instrument Platforms's* main structure. The altitude of the radiometer relative to the water surface was about 6 m. On the same boom were located the flux packages of Chris Fairall (ETL/NOAA).

Preliminary retrievals of air-water temperature were based on the brightness temperature measurements at angles 48-57 degree from nadir and with an averaging time of 12 min. During COPE, both stable and unstable conditions were encountered. These conditions were simultaneously observed by both radiometric (see Fig. 1a) and in situ instruments (Fig. 1b). We consider the common agreement between in situ and 5-mm data as very good.

Fig. 1c presents the air temperature gradient from 10 to 50 m retrieved from the upper part of the radiometric scan. In general, our data allow us to retrieve the air temperature profile in the layer 0-200 meter and this part of analysis will be performed soon. Note that the air temperature gradient has good correlation with air-water temperatures derived from the down-looking part of 5-mm measurements (Fig. 1a) and with in situ measurements (Fig. 1b). We used an averaging time of 12 min to provide about the same time resolution as the *in situ* measurements. Next, we averaged data for 36.29 seconds. Fig. 2 shows an example of air-water temperature difference obtained at the higher time resolution. This example indicates that the the variance of the air-water temperature difference is large under stable atmospheric conditions (at least during COPE). During COPE, the wind flow from shore to FLIP occurred during periods of stable stratification. The same conclusion can be made from all available data. Fig. 3a and Fig 3b show power spectral density under unstable and stable

conditions calculated from high resolution data set. We have used the Julian Day time intervals 261.6 - 263.3(Fig.3a) and 263.8 - 265.5 (Fig.3b). Each spectrum was calculated using a 10.3 h data set.

SUMMARY

Our 5-mm radiometer operated continuously about 12 days during COPE. The retrieval of air-water temperature difference was performed for two averaging times: 12 min and 36 sec. The results are in good agreement with in situ measurements. It was also noted that measurements of downwelling radiation (brightness temperature above horizon) predict the same sign of stability as analysis based on upwelling radiation (sea surface brightness temperature).

The results indicate that the variability of air-water temperature difference in time increases during stable atmospheric conditions

REFERENCES

[1] Yu. G. Trokhimovski, E.R. Westwater, Y. Han, and V. Leuskiy, " The results of air and sea surface temperature measurements using a 60 GHz microwave rotating radiometer", submitted to *IEEE Trans. Geosci. Remote Sensing*.

[2] E. R. Westwater, J. B . Snider, and A. V. Carlson, "Experimental determination of temperature profiles by ground-based microwave radiometry," *J. Appl. Met.*, vol. 14, no. 4, pp. 524-539, 1975.

[3] E. R. Westwater, "Ground-based Microwave Remote Sensing of Meteorological Variables," in M. A. Janssen, Eds., *Atmospheric Remote Sensing by Microwave Radiometry*, New York: J. Wiley & Sons, Inc., 1993, pp. 145-213.
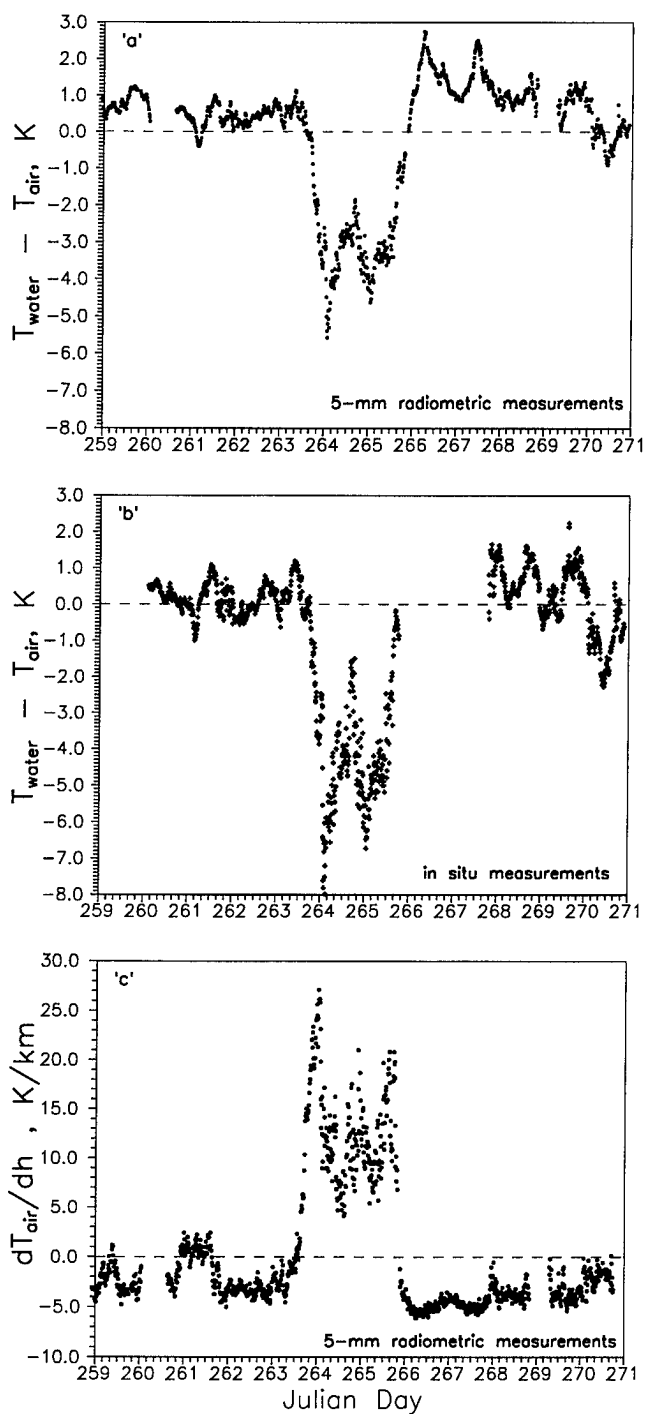
Fig. 1. Water-air temperature difference retrieved from 5-mm radiometric measurements (a) and in situ measurements(b). Radiometrically-retrieved air temperature gradient from 10 to 50 m (c).
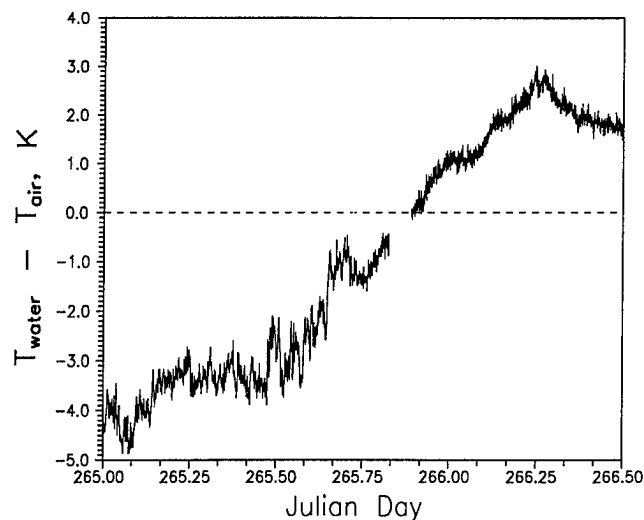
Fig. 2. Time series of radiometrically-retrieved water-air temperature difference obtained every 36 seconds
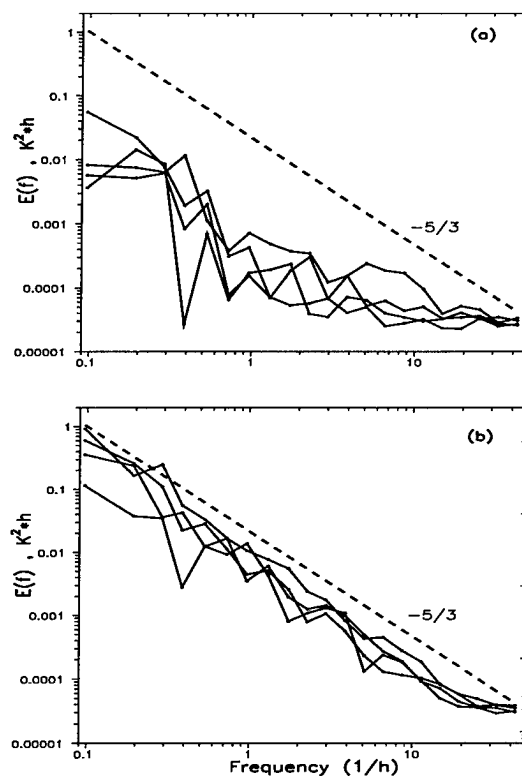
Fig. 3. Power spectrum calculated from radiometrically-measured water-air temperature difference. 'a' - unstable conditions, 'b' - stable conditions.

1674

Measurements of Integrated Water Vapor and Cloud Liquid Water from Microwave Radiometers at the DOE ARM Cloud and Radiation Testbed in the U.S. Southern Great Plains

J. C. Liljegren
Pacific Northwest National Laboratory[1]
Battelle Boulevard
Richland, WA 99352
telephone: 509.372.6136
facsimile: 509.372.6168
e-mail: jc_liljegren@pnl.gov

B. M. Lesht
Argonne National Laboratory
9700 S. Cass
Argonne, IL 60439
telephone: 708.252.4208
facsimile: 708.252.5498
e-mail: bmlesht@anl.gov

Abstract -- The operation and calibration of the ARM microwave radiometers is summarized. Measured radiometric brightness temperatures are compared with calculations based on the model of [1] using co-located radiosondes. Comparisons of precipitable water vapor retrieved from the radiometer with integrated soundings and co-located GPS retrievals are presented. The three water vapor sensing systems are shown to agree to within about 1 mm.

INTRODUCTION

In order to quantify the spatial and temporal variations of water vapor and clouds, the U. S. Department of Energy's Atmospheric Radiation Measurement (ARM) Program has deployed five dual-frequency microwave water radiometers at its Cloud and Radiation Testbed (CART) in Oklahoma and Kansas, as illustrated by the map in Fig. 1.

The microwave radiometers are used to derive the integrated ("precipitable") amount of water vapor and cloud liquid water overhead of the instrument as defined by

$$PWV = \int \rho_v(z)\,dz \qquad (1)$$

$$LWP = \int w(z)\,dz \qquad (2)$$

where $\rho_v(z)$ is the vertical distribution of water vapor density and $w(z)$ is the vertical distribution of cloud liquid water content. It is common practice to normalize these by the
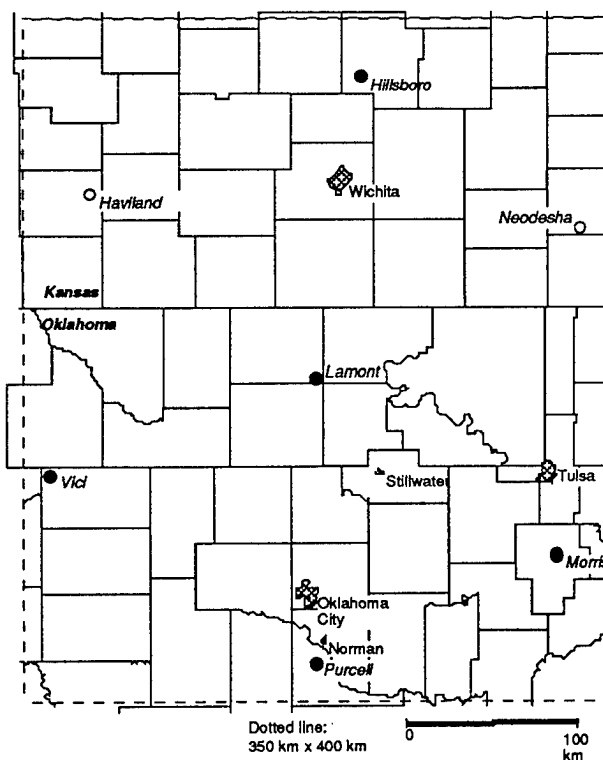
Fig. 1. The ARM Cloud and Radiation Testbed (CART). Filled circles indicate the locations of the CART Boundary Facilities plus the Central Facility near Lamont, OK. Microwave radiometers and balloon-borne sounding systems are co-located at each of these facilities; NOAA wind profilers and GPS receivers are located within a few kilometers. Open circles indicate the locations of additional NOAA wind profilers at Haviland and Neodesha, KS.

nominal density of liquid water, 10^6 g/m^3, and to express precipitable water vapor or PWV in centimeters and the liquid water path or LWP in millimeters.

THE MICROWAVE RADIOMETERS

The microwave water radiometers (MWRs) that ARM has deployed are Radiometrics™ model WVR-1100. These instruments have a vapor-sensing channel at 23.8 GHz and a liquid-sensing channel at 31.4 GHz. The instruments use a common antenna and waveguide for both channels with individual Gunn diode oscillators for each frequency. Consequently the beamwidths are unequal: 5.5° at 23.8 GHz and 4.6° at 31.4 GHz.

Radiometric Measurements

At the beginning of each 20-second observing cycle the radiometer first measures the microwave sky signal V_{sky} at each frequency for a 1-second integration period. Its elevation mirror is then rotated to measure the signal from an internal blackbody target V_{ref}. The target temperature T_{ref} is also measured. The signals are converted to a sky brightness temperature T_B using the radiometer equation

$$T_B = X\left[T_{ref} + \overline{G}\left(V_{sky} - V_{ref}\right)\right] + (1-X)T_{ref} \quad (3)$$

where the factor $X = 1+\varepsilon$ accounts for the contribution of the Teflon™ foam window that protects the mirror. While viewing the blackbody target a noise injection source is energized and the corresponding signal V_{ref+n} measured at each frequency. The instantaneous gain G is then determined according to

$$G = \Delta T_n / \left(V_{ref+n} - V_{ref}\right) \quad (4)$$

where ΔT_n is determined by prior calibration. The instantaneous gain is then low-pass filtered to yield the central tendency $\overline{G}$.

Calibration

Calibration of the noise injection is achieved using "tipping curves" [2]. Using the true zenith brightness temperature from each tipping curve, (3) and (4) are combined and solved for ΔT_n. We use ten angles on both sides of zenith (cosec(elev) = 1, 1.5, 2, 2.5, 3) and reject tips for which the correlation coefficient of the fit is less than 0.998. We can acquire a tip curve every 60 seconds; we typically acquire about 1000 tips in a calibration period. We use a robust fitting scheme to regress ΔT_n on T_{ref} to account for a slight dependence on ambient temperature. The calibration of S/N 10 in effect 5 January - 12 September 1995 differed by less than 1% from that in effect 12 September - 30 November 1995.

COMPARISON WITH RADIOSONDES AND GPS

In Fig. 2 we compare brightness temperatures measured with MWR S/N 10 against those calculated using co-located radiosondes and a radiation transfer model [3] based on the microwave absorption model of [1]. ARM uses Vaisala Balloon-Borne Sounding Systems (BBSS) and RS-80 radiosondes with H-Humicap® relative humidity sensors. The MWR T_B values are 40-minute averages centered on the time of sonde launch.

To assure a valid comparison we included only those cases for which the 40-minute standard deviation of T_B was less than 0.3 K in the liquid sensing channel (clear sky) and less than 0.35 K in the vapor channel (homogeneous sky). These values are twice the RMS noise level of the instrument. As
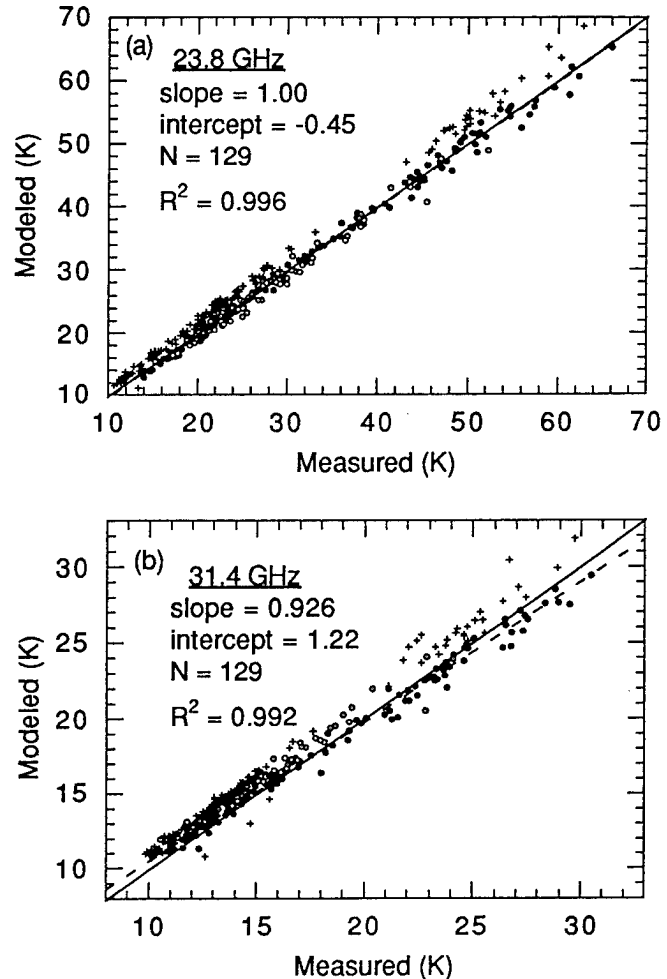
Fig.2. Model-calculated and measured brightness temperatures at (a) 23.8 GHz and (b) 31.4 GHz. The regressions (– – –) apply to the period 5 Jan-12 Sep 1995 (•). (o) indicate the period 12 Sep-30 Nov 1995. Incorrectly calibrated radiosondes are also indicated (+).

shown in Fig. 2 we identified many soundings for which the manufacturer's calibration appeared incorrect; this finding was later confirmed by Vaisala.

We use a statistical retrieval [4] to obtain the precipitable water vapor (PWV) and liquid water path (LWP) from the measured brightness temperatures. Because the retrieval is based on the radiation transfer model [3], we must apply the regression of modeled T_B on measured T_B as a correction or tuning function to the measured T_B values in order to obtain accurate estimates of PWV and LWP with the retrieval.

A histogram of LWP for cases where the standard deviation of the liquid sensing channel was less than 0.3 K (i.e. "clear sky") is presented in Fig. 3. This indicates the accuracy with which LWP can be determined by the system; it reflects the limiting accuracy of the instrument as well as the retrieval.

The comparison of PWV from the MWR and the BBSS for clear and cloudy sky conditions is presented in Fig. 4.. Although the agreement is good both for clear sky cases and for cloudy skies with LWP < 0.5 mm (50 g/m²), as LWP increases above 0.50 mm the difference between the PWV reported by the two systems is essentially uncorrelated.

Retrievals of PWV are now possible using the Global Positioning System (GPS) [5]. In Fig. 5 we present comparisons of 30-minute averaged PWV from the MWR and GPS for clear sky conditions. Because the GPS measurement represents an average over nearly the entire sky, whereas the MWR has a relatively narrow field of view (~5°), cloudy sky comparisons show considerably more variability.

REFERENCES

[1] H. J. Liebe and D. H. Layton, "Millimeter-wave properties of the atmosphere:laboratory studies and propagation modeling," Nat. Telecom. and Inform. Admin., Boulder, CO, NTIA Rep. 87-24, 1987.

[2] M. T. Decker and J. A. Schroeder, "Calibration of ground-based microwave radiometers for atmospheric remote sensing," NOAA Tech Memo ERL WPL-197, 1991.

[3] J. A. Schroeder and E. R. Westwater, "User's guide to WPL microwave radiative transfer software," NOAA Tech. Memo. ERL WPL-213, 1991.

[4] E. R. Westwater, "Ground-based microwave remote sensing of meteorological variables," *Remote Sensing by Microwave Radiometry*, M.A. Janssen, ed. John Wiley & Sons, 1993.

[5] Christian Rocken, *et al.*, "GPS/STORM - GPS sensing of atmospheric water vapor for meteorology," J. Atmos. Sci., vol. 12, pp. 468-478, 1995.

Fig. 3. Distribution of LWP for clear sky conditions (standard deviation of T_B at 31.4 GHz less than 0.3 K).
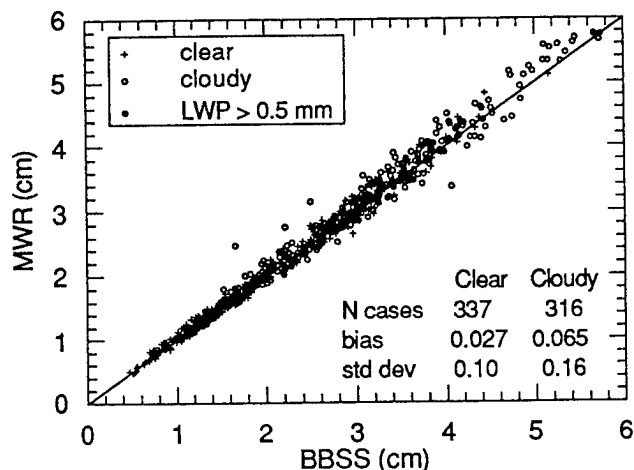
Fig. 4. Comparison of precipitable water vapor measured by microwave radiometer (40-minute averages) and balloon-borne sounding system at Lamont, OK for 5 Jan-30 Nov 1995.
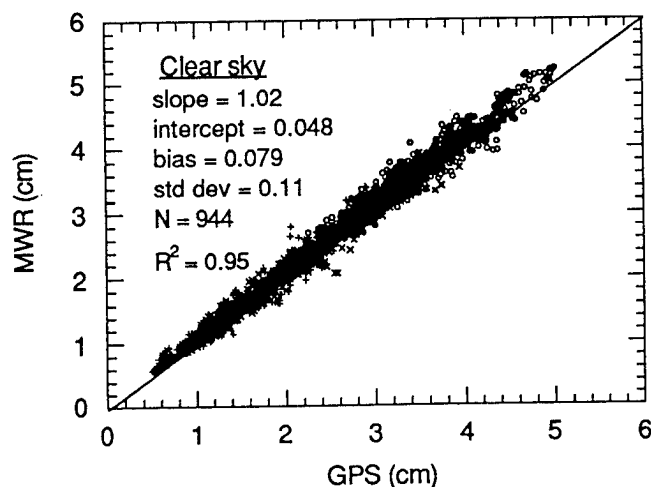
Fig. 5. Comparison of 30-minute averaged precipitable water vapor from microwave radiometer and Global Positioning System at Lamont, OK for clear sky conditions (LWP < 0.004 mm) during April, May and July 1995.

Performance Evaluation of a Spinning Flat Reflector for Millimeter-Wave Radiometry

Mark D. Jacobson[1] and William M. Nunnelee[2]

[1]NOAA/ERL/ETL, R/E/ET1, 325 Broadway, Boulder, CO 80303-3328 USA, Voice: (303)497-6497, FAX: (303)497-3577, email: mjacobson@etl.noaa.gov

[2]NOAA/NWS, Goodland, Kansas, 67735 USA

I. INTRODUCTION

For more than a decade, the Environmental Technology Laboratory (ETL) of the National Oceanic and Atmospheric Administration (NOAA) has been successful in operating dual-channel (20.60 and 31.65 GHz) radiometers (see Fig. 1) for measuring water vapor and cloud liquid [1]. These radiometers routinely produce brightness temperatures with an absolute accuracy of about 1 K and a rms sensitivity of about 0.05 K for a 2-minute data average. Data from ground-based microwave radiometers are also commonly used to derive attenuation statistics [2] useful to communication engineers.

These radiometers are particularly useful in winter storm experiments for measuring supercooled liquid water (SLW) in clouds [3]. As a result, dual-channel radiometers have been used in the WISP experiments [4] along Colorado's Front Range. The primary goals of the WISP experiments are to improve our understanding of the processes involved in the production and depletion of SLW in winter storms and to develop improved aircraft icing forecasts on local, regional, and national scales. In particular, a principal objective of the program was to determine the utility of unattended millimeter-wave radiometers in detecting SLW and providing input to forecasts of aircraft icing.

The most recent WISP experiment was conducted from 25 January through 25 March 1994. This experiment is referred to as WISP94 for the rest of the paper. During this period, two collocated dual-channel millimeter-wave radiometers were operated at the Platteville, Colorado, site. This period was selected for a careful intercomparison of the performance of these two radiometers. The radiometers are identical in design except that one was equipped with a spinning reflector to disperse precipitation particles through centrifugal force, while the other's reflector was fixed. A dry reflector surface is required during precipitating conditions to avoid contamination of the atmospheric data [5]. The Desert Research Institute (DRI) in Reno, Nevada, and the Commonwealth Scientific and Industrial Research Organization (CSIRO) Division of Atmospheric Research in Melbourne, Australia, have implemented spinning disks on their radiometric systems. DRI has found that the spinning reflector has been effective in shedding liquid water and snow [6]. The spinning reflector radiometer [7] is referred to as the SPIN radiometer, and the fixed reflector radiometer is referred to as the FIX radiometer for the remainder of the paper.

II. CONTROLLED SPINNING FLAT REFLECTOR MEASUREMENTS

Before this spinning reflector was deployed for unattended operation, a controlled experiment to simulate moderate to heavy rainfall was performed on this radiometer to determine how well the spinning reflector sheds water. A rainstorm was simulated by postioning a nozzle upward so the water would fall onto the entire spinning flat's surface. Radiometric data were recorded at 5-s averages as the spinning reflector's speed was set, and the water spray was directed onto the flat for a few minutes and then stopped. This process was repeated for different flat speeds and water-flow rates.

An informative parameter contained in these measurements is called the decay time. The decay time is a measure of how long it takes the spinning wetted reflector to disperse the water on it. This is found by measuring the difference between the time when the water is shut off and when the reflector is dry. Another useful quantity is called the decay brightness temperature, decay T_b, which is the difference between the brightness temperature before and after the water is turned off. These two quantities, plotted versus reflector (disk) speed for a water-flow rate of about 150×10^{-6} m^3 s^{-1} are shown in Fig. 1. This water-flow rate can be converted into an approximate rain rate of 68 mm hr^{-1}, a moderately intense rainfall rate. The decay time plots show that there is essentially no improvement in decay time for disk speeds above 250 rpm. The decay T_b plots show a general trend of decreasing decay brightness temperatures with increasing reflector speeds up to about 250 rpm; i.e., the water-layer thickness on the disk is reduced with increasing spin speed.

The operating speed of the ETL's spinning reflector was chosen to be 300 rpm because of three criteria. The first was that the spinning disk should disperse the water quickly (see

Fig. 2. Scatter plots of SPIN- versus FIX-measured values of brightness temperature at 31.65 GHz. These measurements were taken when the integrated liquid-water content is ≥ 0.05 mm.

Fig. 1. (a) The time required for the spinning disk to disperse the light water spray (decay time) versus disk speed, and (b) the difference between the brightness temperatures before and after a water-flow rate of 150×10^{-6} m^3 s^{-1} (approximate rain rate of 68 mm hr^{-1}) is turned off (decay T_b) versus disk speed.

Fig. 1a). The second criterion was that the spinning disk minimize the water-layer thickness (see Fig. 1b). The last criterion was that the spinning disk structure be mechanically stable during operation, i. e., flat speeds less than 500 rpm.

III. RADIOMETER COMPARISONS

A. Scatterplots and Statistics of Radiometer Data

Recovery of the amounts of atmospheric water vapor and liquid water from dual-channel radiometer measurements involves a statistical inversion [1]. On the other hand, the total atmospheric attenuations are computed from the brightness temperatures measured by the radiometer [2].

The integrated liquid-water measurements were used to categorize the data into three groups: pairs obtained when integrated liquid water was measured (integrated liquid-water content ≥ 0.05 mm), and pairs obtained when little or no integrated liquid water was measured (integrated liquid-water content < 0.05 mm).

Fig. 2 shows scatter plots of the 31.65 GHz brightness-temperature data when integrated liquid-water content is ≥

0.05 mm. There are about 6 000 paired data points. The large brightness-temperature deviations from the 45° line indicate periods when the FIX radiometer was likely to have had more liquid on its exposed surface than did the SPIN radiometer. The low correlation coefficients and large rms values illustrate the large effect that these conditions can have on the comparison statistics when the integrated liquid-water content is ≥ 0.05 mm. Fig. 2 shows that almost all of the instances of anomalous FIX 31.65 GHz brightness temperature measurements occur for very light cloud or cloudless conditions, i.e., the SPIN 31.65 GHz brightness temperature measurements < 20 K imply less than 0.2 mm of cloud liquid. This means that almost all of the FIX failures occurred during snow events, i.e., melting snow on the stationary reflector.

B. A Wet Reflector Case Study

A wet snow storm on 28 February to 1 March 1994 provided an excellent test for the spinning reflector. The precipitation detector, located next to the radiometers, was activated from 2100 to 0000 UTC while the surface temperature was about 0°C. A zenith-viewing, narrowband, 10.6-μm infrared (IR) radiometer measured a temperature of about 0°C, indicating the presence of a low, solid cloud deck. Fig. 3a shows that the FIX radiometer's measured 31.65 GHz brightness temperatures, and consequentely the derived precipitable water vapor (see Fig. 3b) were much more adversely affected by the snow than the SPIN radiometer's measured parameters. Four CLASS radiosondes were launched before, during, and after this wet snow storm as
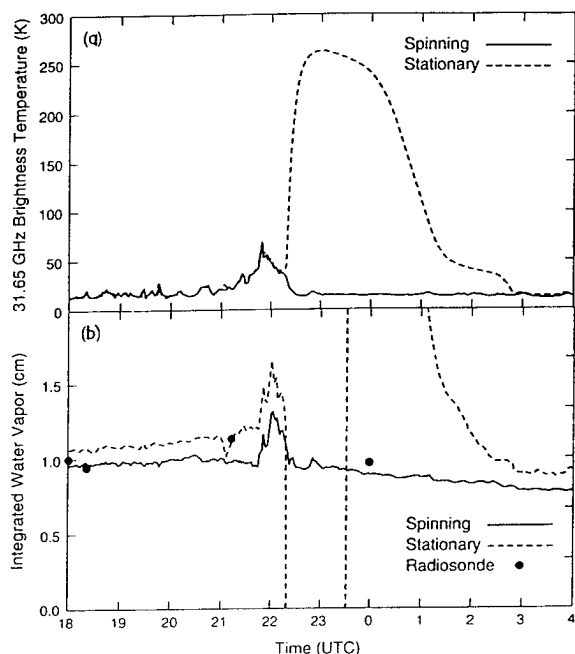
Fig. 3. Time series plots of the Platteville measurements from the (a) 31.65 GHz brightness temperatures, and the (b) precipitable water vapor, where solid lines are from the SPIN radiometer and dashed lines are from the FIX radiometer, during a wet snow storm on 28 February 1994. The precipitation detector was on from about 2100-0000 UTC.

shown in Fig. 3b by the solid dots. The first three pairs of radiosonde and radiometer water-vapor measurements (1800, 1822, and 2113 UTC) yield a maximum difference of 0.15 cm. This result was obtained just before and just after the wet snow storm began. However, near the end of this storm, at approximately 0000 UTC March 1, 1994, the radiosonde and FIX vapor difference is almost 13 cm, whereas the radiosonde and SPIN integrated water-vapor difference is only about 0.08 cm. These results clearly show that the SPIN radiometer successfully measured the atmospheric vapor accurately at these times, whereas the FIX radiometer did not. Other snow storm cases from WISP94 show similar results.

V. CONCLUSION

These results and other snow events during the WISP94 show that the spinning-reflector system prevented contamination of brightness temperature data during snow conditions. Consequently, the system with the rotating reflector provides accurate derived values of precipitable water vapor, vertically-integrated liquid water, and zenith attenuation at 20.60 and 31.65 GHz during snow conditions in WISP94. In summary, these results show that a spinning-

reflector system can produce accurate radiometric data for certain, perhaps all, snowing conditions.

REFERENCES

[1] D. C. Hogg, F. O. Guiraud, J. B. Snider, M. T. Decker, and E. R. Westwater, "A steerable dual-channel microwave radiometer for measurement of water vapor and liquid in the troposphere," J. Appl. Meteor., vol. 22, pp. 789-806, 1983.

[2] E. Fionda, M. J. Falls, and E. R. Westwater, "Attenuation statistics at 20.6, 31.65, and 52.85 GHz derived from emission measurements by ground-based microwave radiometers," IEE Proc.-H, vol. 138, pp. 46-50, 1991.

[3] T. Uttal, J. B. Snider, R. A. Kropfli, and B. W. Orr, "A remote sensing method of measuring atmospheric vapor fluxes: Application to winter mountain storms," J. Appl. Meteor., vol. 29, pp. 22-34, 1990.

[4] B. B. Stankov, E. R. Westwater, J. B. Snider, and R. L. Weber, "Remote measurements of supercooled integrated liquid water during the WISP/FAA aircraft icing program," J. Aircraft, vol. 29, pp. 604-611, 1992.

[5] M. D. Jacobson, D. C. Hogg, and J. B. Snider, "Wet reflectors in millimeter-wave radiometry: Experiment and theory," IEEE Trans. Geosci. Remote Sens., vol. 24, pp. 784-791, 1986.

[6] B. B. Demoz, A. W. Huggins, J. A. Warburton, and R. L. Smith, " Field performance of a spinning-reflector microwave radiometer, " J. Atmos. Ocean. Technol., vol. 10, pp. 420-427, 1993.

[7] M. D. Jacobson and W. M. Nunnelee, "Design and performance of a spinning flat reflector for millimeter-wave radiometry," to be published in IEEE Trans. Geosci. Remote Sens..

OBSERVATIONS OF WATER VAPOR AND CLOUD LIQUID
FROM
AN AIRBORNE DUAL-FREQUENCY RADIOMETER
DURING VORTEX '95

L. S. Fedor and E. R. Westwater
Cooperative Institute for Research in
Environmental Sciences (CIRES)
University of Colorado/NOAA
Boulder, Colorado 80309
Tel: (303) 497-6440
email: lfedor@etl.noaa.gov

Michael J. Falls
Environmental Technology Laboratory
NOAA
325 Broadway
Boulder, Colorado 80303
Tel: (303) 497-6536
Fax: (303) 497-3577

Abstract -- The fine-scale horizontal variations of water vapor and cloud liquid water are of importance to climate, meteorology, and satellite validation/calibration. The Environmental Technology Laboratory of NOAA has developed a dual-frequency upward- (and downward-) looking radiometer at 23.87 and 31.65 GHz to measure the integrated amounts of water vapor and cloud liquid above an aircraft. Two experiments involving the NOAA WP-3D (tail number N43RF) were conducted in the Oklahoma-Texas region during April 1 to June 15, 1995. The first, the Verification of the Origin of Rotation in Tornadoes Experiment (VORTEX), focused on obtaining detailed observations of mesocyclones and their potential for developing into tornadoes. The second, sponsored by the Department of Energy's Atmospheric Radiation Program, was to obtain detailed aircraft observations of cloud liquid and water vapor to correlate with short- and long- wave radiation measurements. The almost mutually exclusive goals of the two experiments allowed shared use of NOAA WP-3D aircraft throughout the entire April-June period. During VORTEX, the radiometer was operated on all WP-3D flights; of particular interest were several flights flown in zig zag flight patterns through mesoscale moisture fronts known as "dry lines". Through the sharp boundaries of dry lines, strong horizontal gradients in moisture can occur. Several of the dry line cases were observed, and examples will be shown.

INSTRUMENTS

The Environmental Technology Laboratory (ETL) developed a dual-channel radiometer at 23.87 and 31.65 GHz for deployment on aircraft platforms [1],[2]. The two frequencies share a common antenna (offset parabola), have equal beamwidths (3.6° at half-power), and are orthogonally polarized. Each channel has a double-sideband receiver with a total bandwidth of 1 GHz resulting in a measured 1-s rms sensitivity of 0.064 K. The primary function of the instrument is to measure the precipitable water vapor (PWV) and integrated cloud liquid (ICL) above an aircraft; hence, it is designated as the Airborne Water Substance Microwave Radiometer (AWSMR). During the ETL San Clemente Ocean Probing Experiment it was deployed on the NOAA King Air aircraft for both atmospheric (up-looking) and oceanographic (down-looking) measurements [3]. The Coastal Ocean Probing Experiment was conducted during September-October 1995. For this experiment the AWSMR was one of the instruments mounted on a US LTA blimp to look downward at surface phenomena [4].

Three probes for in situ measurements of cloud liquid were installed on the W.-3D aircraft for these experiments. One, the Johnson-Williams probe (J-W), has been a standard instrument for field programs for many years. Data from this hot wire instrument will be presented in this paper. The second instrument, a Particle Measuring Systems King probe was not available for the flight shown here. A new instrument, the Gerber probe was installed on the NOAA WP-3D aircraft for the first time on this experiment. This instrument, PVM-100A, measures the cloud liquid content (LWC), the integrated particle surface area (PSA), and the effective droplet radius r_e of cloud droplets. These real time in situ measurements are simultaneous, sample a cloud volume of 1.25 cm^3, and have a maximum bandwith of 5 KHz [5].

Other instruments used for this study were for the standard meteorological parameters of pressure, temperature, dew point, and wind plus the location provided by the Global Positioning System.

DRY LINE FLIGHT

A preferred area for thunderstorm development over the Great Plains is near a dry line - defined as the surface boundary between maritime tropical air masses from the Gulf of Mexico and dry air masses from the desert southwest [6]. The process by which convective storms form along the dry line is not well understood [7],[8]. During the spring and early summer months

these storms frequently spawn tornados that endanger life and property. On May 6, 1995 the NOAA WP-3D aircraft made a joint flight with the NCAR Electra to document supercell development in the Texas Panhandle. It is fairly common for the dry line to develop here due to the presence of the Caprock Escarpment [6]. Indeed the dry line was found on the cap rock at 101.2 W.

The dry line was traversed at three levels (500 ft, 3000 ft, and 5000 ft AGL) by the NOAA aircraft along a line defined by the 34.5 N latitude. Later sets of traverses were made at 35 N. A total of six sets of traverses of the dry line were made on this flight. In Fig. 1 we show PWV measured by the AWSMR as a function of time during the first three passes. Fig. 1a is for the pass at an altitude of 500 ft. Fig. 2 shows the corresponding

Fig. 1c. Precipitable water vapor traverse of a dry line at an altitude of 5000 ft.

is to the left and east of the dry line is to the right. The change in PWV across the boundary is more than 0.5 cm in less than 1.5 km horizontal distance. At 3000 ft (Fig. 1b) the variation of PWV across the boundary is smaller, 0.3 cm, while at 5000 ft (Fig. 1c) the variation across the boundary may be as much as 0.2 cm but it is difficult to distinguish. On the other traverses of the dry line at 5000 ft (not shown here) there is no boundary indicated by the PWV variations. Thus this dry line is confined to the lowest part of the atmosphere. At all three levels the dry line crossing occurred at 101.2 W longitude, i. e., the boundary is vertical.

Clouds above the aircraft were measured by the AWSMR on the 500 ft traverse (see Fig. 2). The maximum of 0.13 mm is indicated by the horizontal arrow. Fig. 3 shows the temperature and dew point as the aircraft traversed the dry line. The dew point is the most sensitive parameter to dry line characteristics. The time has been reversed so that west is to the left side of the figure and east is to the right. To demostrate further the atmospheric effects as the aircraft traversed the dry line we show in Fig. 4 the variation in the geopotential altitude of the

Fig. 1a. Precipitable water vapor traverse of a dry line at an altitude of 500 ft.

Fig. 1b. Precipitable water vapor traverse of a dry line at an altitude of 3000 ft.

plot of ICL. The vertical arrow in Fig. 1a marks the dry line boundary determined by the change in dew point (Fig. 3). Note that time decreases from right to left so that west of the dry line
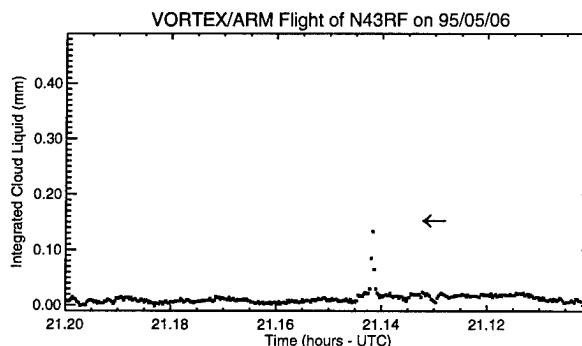
Fig. 2. Liquid water traverse of a dry line at an altitude of 500 ft.

aircraft. This height variation is indicative of the convective activity that is well to the east of the dry line itself (see Fig. 3). Superimposed on the altitude vs. time plot are wind barbs indicating the wind measurements at altitude. Although the wind is generally southerly we see that there is a divergence of wind at the boundary shifting from south-south-westerly on the east side to south-south-easterly on the west side.

Statistics for some of the variables measured in flight were calculated on either side of the dry line boundary. The change in average dew point across the boundary is 9 K. The change in mixing ratio is 4.5 g/kg over a horizontal distance of less

Fig. 5. Aircraft altitude while in the last 15 minutes of its landing pattern into Will Rogers airport.

Fig. 3. Temperature (upper) and Dew Point (lower) during the traverse across the dry line at 500 ft.
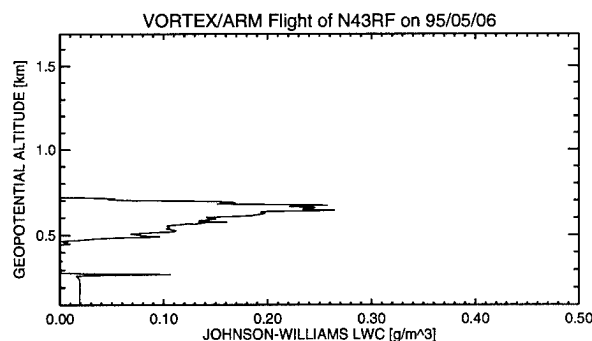
Fig. 6. Cloud liquid content estimated by the Johnson-William probe for the descent shown in Fig. 5.

Fig. 4. Aircraft altitude during the traverse across the dry line at 500 ft. Wind barbs are superimposed on the trace

than 1.5 km. Current mesoscale models define dry line environments by east-west gradients of moisture on the order of 10 g/kg per 100 km [8].
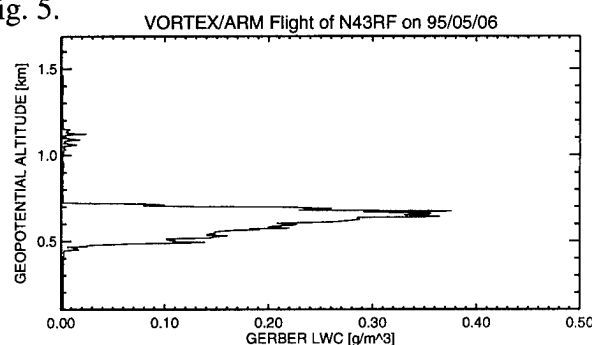
Fig. 7. Cloud liquid content estimated by the Gerber probe for the descent shown in Fig. 5.

DESCENT INTO WILL ROGERS AIRPORT

The flight was successful for its documentation of the dry line. As the aircraft maneuvered to return to Will Rogers airport, it flew through and beneath clouds to provide an opportunity to measure both horizontal and vertical structure. In Fig. 5 we show the aircraft altitude variations of the final 15 minutes of flight. Figs. 6 and 7 show the measurements made

by the two water probes as a function of altitude (the timesequence is the same). In Figs. 8 and 9 we show the PWV and ICL measured by the AWSMR.

There are three time sections of interest. The first is in the altitude descent from 1.5 km to 0.9 km just before 01:00 UTC. The aircraft passes through a cloud that is detected by the Gerber probe, above 1.0 km, but not by the J-W probe.

The amount is slight, 0.02 g/m^3 at maximum. The AWSMR also measures the cloud, but with an amount that is less than 0.04 mm. After 01:00 and before 01:06 UTC the aircraft is in level flight below a cloud layer. The AWSMR measures about 11 peaks in this sequence with a maximum of 0.11 mm. On the final descent the aircraft passes through a stratus layer that is measured by both probes. The J-W probe measures the same structure as the Gerber probe but is significantly reduced in magnitude, 0.26 g/m^3 versus 0.37 g/m^3 at maximum. The AWSMR also measures the cloud as the aircraft passes through it (after 01:06 UTC) showing some structure with a maximum of 0.08 mm of liquid. Upon landing the instrument was still measuring cloud liquid up to 0.10 mm and PWV of 3.0 cm.

CONCLUSION

We have presented a sample of data collected during the VORTEX/ARM 95 experiment. The 26 flights by the NOAA WP-3D aircraft provide a wealth of atmospheric information. Our immediate activities will focus on the details of retrieving PWV and ICL as a function of altitude for the experiment. We also will compare ground- and aircraft-based measurements of PWV and ICL.

ACKNOWLEDGMENTS

Fig. 8. Precipitable Water Vapor estimated by the AWSMR during the descent shown in Fig. 5.

REFERENCES

[1] L.S. Fedor, M.D. Jacobson, A.J. Bedard Jr., E.R. Westwater, D.C. Hogg, R.T. Nishiyama, "Dual-Channel Microwave Radiometer for Airborne Meteorological Applications", NOAA Tech. Memo. ERL WPL-157, 20 pp., December 1988.

[2] M.D. Jacobson, L.S. Fedor, D.A. Hazen, W.B. Madsen, M.H. Francis, and D.P. Kremer, "A Dual Frequency mm-Wave Radiometer Antenna for Airborne Remote Sensing of Atmosphere and Ocean," Microwave Journal, vol. 37, pp 24-29, September 1994.

[3] L.S. Fedor and V.G. Irisov, "Airborne Dual-Channel Radiometric Ocean Surface Observations During SCOPE '93," Proc. IGARSS'94, Pasadena, CA, August 8-12, pp. 2410-2412,1994.

[4] V.G. Irisov and Yu.G. Trokhimovski, "Observation of the Ocean Brightness Temperature Anisotropy During the Coastal Ocean Probe Experiment," Proc. IGARSS'96, Lincoln, NE, May 27-31, 1996.

[5] H. Gerber, B.G. Arends, and A.S. Ackerman, "New Microphysics Sensor for Aircraft Use," Atmos. Res. vol. 31, pp. 235-252, 1994.

[6] J.O. Rhea, "A Study of Thunderstorm Formation Along Dry Lines," J. Appl. Met., vol 5, pp. 58-63, February 1966.

[7] H.B. Bluestein and S.S. Parker,"Modes of Isolated, Severe Convective Storm Formation Along the Dryline," Mon. Weather Rev., vol 121, pp. 1354-1372, May 1993.

[8] C.L. Ziegler, W.J. Martin, R.A. Pielke, and R.L.Walko, "A Modeling Study of the Dryline," J. of the Atmos. Sci., vol. 52, no. 2, pp. 263-285, 15 January 1995.

Fig. 9. Integrated Cloud Liquid estimated by the AWSMR during the descent shown in Fig. 5.

Applications of Kalman Filtering to Derive Water Vapor Profiles from Raman Lidar and Microwave Radiometers

Y. Han and Ed R. Westwater
Corporation Institute for Research in Environment Science (CIRES)
University of Colorado/NOAA, 325 Broadway, Boulder, CO 80303
R. A. Ferrare
Hughes-STX Corporation, Lanham, Maryland

Abstract -- Water vapor profiles are derived from data provided by a Raman lidar and a microwave radiometer, as well as other instruments. We demonstrate that this system can provide accurate profiles at altitudes above which the Raman lidar technique is limited.

INTRODUCTION

In ground-based remote sensing of atmospheric water vapor, Raman lidars and microwave radiometers have been used in routine operations and field investigations. The most significant advantage in microwave radiometry is the capability to measure water vapor and liquid water in almost all non-precipitating weather conditions. The ability to profile water vapor by microwave radiometers has also been investigated theoretically and experimentally [1]. Because of insufficient profile structure information in the measurements themselves, retrieving accurate profiles requires application of constraints. Raman lidars have the capability to profile water vapor up to 7 km or higher with vertical resolutions of better than 100 meters [2] in cloud-free and nighttime environments. Under cloudy conditions, the lidar beams are attenuated by clouds and usually can not probe through liquid clouds. During daytime conditions, contaminations by sun light limit lidar measurements to the lowest 3 or 4 km.

In this investigation, we derive water vapor profiles by integrating data from a Raman lidar, a microwave radiometer, a radio acoustic sounding system (RASS) and surface *in-situ* instruments. A Kalman Filtering technique is applied to derive profiles from the integrated system. The data collected during the FIRE II experiment, conducted in November and December 1991 in Coffeyville, Kansas, are used for our preliminary test. The set of instruments was described in [2][3][4]

RETRIEVAL ALGORITHM

The measurements, from which water vapor mixing profiles are derived, consist of water vapor mixing ratio profiles from Raman lidar, surface temperature, pressure and humidity from *in-situ* sensors, and integrated water vapor from the microwave radiometer. The measurements of RASS virtual temperature profiles are used to derive integrated water vapor and liquid and also used to convert water vapor between different units. Cloud base height, derived from Raman or another lidar, is also used in retrievals. The vertical coordinate of the profile vector **x** starts at the surface level. The second level is set at the lidar's first range gate. The remaining levels have adjacent intervals of 75 m, to be consistent with lidar's range gates. The top level is set at 10 km, a height above which the total amount of water vapor is negligible.

Under conditions when **x** is partially measured by the lidar, surface instruments and microwave radiometer, the retrieval of **x** is an ill-posed mathematical problem. Additional information is required for such retrievals. In our retrieval algorithm, we introduce two such sources. One is the information contained in previous lidar measurements and the other is the statistical information obtained from an *a priori* water vapor profile ensemble. The algorithm is a two-stage retrieval that is outlined in the following.

In the first stage, a Kalman Filtering (KF) technique [5] is applied to derive a state vector **s**, which has the same vertical coordinates as **x** but less range coverage. The measurement vector **d**, on which the filter operates, comprises a vapor mixing ratio at the surface and a lidar profile. The number of the elements in **d** varies depending on the lidar measurements. The error of the surface vapor mixing ratio is estimated from the errors in the measurements of surface air temperature, pressure and relative humidity. The error profile of lidar measurements is related to the statistics of the Raman water vapor return signal and is given with each lidar vapor mixing ratio profile. The measurement error covariance consists of these errors and it is assumed that the off-diagonal elements are zero, which is equivalent to the assumption that the errors are uncorrelated with each other. The dimension of **s** depends on the following situation: when the maximum height of current lidar measurements is lower than those of all previous measurements, the dimension is the

same as the previous; otherwise, the dimension is reset to that equal to the dimension of the new measurement vector and the KF is re-initialized. Thus, the state vector s describes atmospheric water vapor from the surface to the maximum lidar range in the history of lidar measurements. In the first situation, the portion that is not measured by current observation is actually predicted from the past and the new measurements. d is linearly related to s (corrupted by errors) with coefficients contained in the so-called observation matrix.

The evolution of s is assumed to be a first-order Markovian process and is characterized by a time-dependent transition matrix, which linearly relates the s vectors at two different times, and by the errors (assumed white noise) in the transition model. In our system, the time interval of the transition is two minutes. Since the variation of the atmospheric water vapor in two minutes is usually small in comparison with the estimated errors in the retrievals, we approximate the transition by advancing s without modification, which is equivalent to set the transition matrix to unity. The transition errors may be estimated using a historic profile data base. The Raman lidar itself may provide part of such a data base if a large number of nighttime clear lidar measurements are collected. For this experiment, however, the collection of clear-sky lidar measurements was not statistically sufficient. The data base we used is a collection of three-hourly radiosonde profiles from five observation stations at the DOE CART site during the Intensive Observation Period (IOP) conducted in April and May, 1995. Over 700 radiosonde profiles are used for the error estimation. Assuming that the transition errors are time invariant and time uncorrelated, we estimated the errors by advancing each profile three hours, calculating the mean square difference between the advanced profiles and the profiles measured at that time, and then dividing the difference by the number of two-minute intervals in the advanced time period. In general, a certain time correlation between errors is expected. Assuming a correlation time greater than three hours, in the time intervals concerned, the correlations are likely to be positive, causing the estimate of the transition errors to be larger than those when the correlations are counted. Larger transition errors result in a larger error covariance of an a priori estimate, which is propagated from the last estimation. This effectively gives more weight to current measurements in the profile estimation. Existence of the correlation is also inconsistent with the assumption that the transition errors are white noise. However, our testing results have shown that our KF technique under this assumption works well for our system.

The recursive KF starts at an initial state and its error covariance. We use the first arrival of measurements and error covariance as the initial state. The state vector s and its

covariance are propagated, according to the transition system, to the point when new measurements arrive. The propagated state vector and its covariance are seen as an a priori estimate. Using the error covariance matrices as weights, the a priori estimate is linearly combined with the new measurements that have been mapped to the s space by using the observation matrix. The error covariance of the new estimate is also calculated. The newest estimate and its covariance are used, on one hand, in the second stage of the retrieval process described in the following, and, on the other hand, in the next process of KF estimation.

In the second stage, the estimate and error covariance of the profile obtained from KF as well as integrated water vapor and its error from the microwave radiometer comprise a new measurement vector and error covariance matrix. The measurement vector again is related linearly to the unknown profile by a new observation matrix. From an a priori ensemble of radiosonde data, a climatological mean of water vapor profile and its covariance were derived. The climatological mean serves as an a priori estimate of the unknown profile. A covariance-weighted averaging is performed to combine the measurement vector and the statistical data. The result is our final estimate of the water vapor profile.

In the nighttime clear sky cases in which the lidar covers the range close to the top of the retrieval vertical coordinate, the estimate from KF usually yields a much small error covariance in comparison with the statistical covariance. Hence, the averaging performed in the second stage is in favor of KF, resulting an estimate differing little from that of KF. In other cases in which lidar measures only a portion of a profile, for the same reason as that in the clear sky cases, the two-stage retrieval yields a profile with that portion similar to the lidar measurements. The other part of the retrieved profile is a result of a balance among previous and current measurements and statistical data.

EXPERIMENT RESULTS

During the FIRE II experiment, the Raman lidar observed the atmosphere only during night. There were a total of 14 nights of observations, out of which there were 4 nights when low level clouds with cloud base at about 2 or 3 kilometers were observed. Unfortunately, during the cloudy periods when the lidar operated, there were no vapor profile observations by other instruments, such as radiosondes. Therefore, a direct comparison of retrievals with "ground-truth" is not available. In order to demonstrate the system performance, we created "clouds" by extending existing cloud bases into clear periods. The Raman lidar soundings during these periods were then truncated at the artificial cloud bases and used as cloudy measurements. The original

lidar soundings were used as "ground-truth". We show here examples, which were obtained during the artificial cloudy period on November 24. Figure 1 shows a retrieval compared with ground-truth, 16 min after the start of the cloudy period. As anticipated, the retrieved profile below the cloud base resembles the lidar measurement and above the cloud base, the influence of the previous lidar measurements is obvious. Figure 2 shows an example in a situation when there are no historic lidar measurements available above cloud base height. This situation is likely happen when clouds persist for a long period or in daytimes. The information for the profile above the cloud base is supplied by the statistical data and integrated water vapor, as well as the lidar measurement below the cloud through the correlations characterized by the error covariance matrix. In general, under such conditions, the profile above the lidar range is smoothed.

SUMMARY

The technique optimizes the use of information contained in past and current lidar measurements, surface *in-situ* measurements, measurements of integrated water vapor, and statistical data. We have shown that this technique extends our capability to profile water vapor during cloudy and daytime conditions.

Under nighttime clear conditions, retrievals differ little from lidar measurements. Under cloudy or daytime conditions, the low portions of the retrieved profiles differ also little from the lidar measurements that cover those portions. The upper portions are constrained by the integrated water vapor measurements and the profile structures are shaped by the previous lidar measurements and statistical data.

ACKNOWLEDGMENTS

REFERENCES

[1] Skoog, B. G., J. I. H. Askne, and G. Elgered, "Experimental determination of water vapor profiles from ground-based radiometer measurements at 21.0 and 31.4 GHz," *J. appl. Meteor.*, vol. 21, pp 394-400, 1982.

[2] Melfi, S. H., D. N. Whiteman, and R. A. Ferrare, "Observation of atmospheric fronts using Raman lidar moisture measurements," *J. Clim. Appl. Meteor.*, Vol. 28, pp 789-806, 1989.

[3] Han, Y., J. B. Snider, E. R. Westwater, S. H. Melfi and R. A. Ferrare, " Observations of water vapor by ground-based microwave radiometers and Raman lidar," *J. Geophys. Res., Vol. 99, pp18695-18702, 1994.*

[4] Martner, B. E., et al., "An evaluation of wind profiler, RASS, and microwave radiometer performance," *Bull. Amer. Meteor Soc.*, Vol. 74, pp 599-613, 1995.

[5] A. Gelb, et al., "Applied optimal estimation," *The M. I. T. Press,* pp 107-110, 1988.
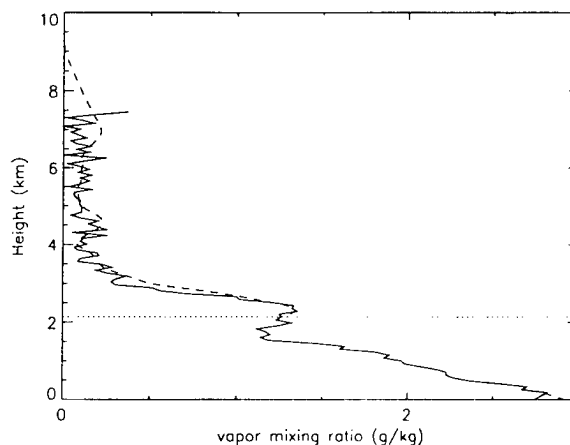
Figure 1. An example of retrieval using the technique described in the text. Dashed line - retrieval; solid line - ground-truth (from lidar); dotted line - artificial cloud base. Data were collected during FIRE II. The cloud base is created by extending the existing cloud base into the clear period. The lidar sounding is truncated at the artificial cloud base and used as cloudy measurements. The original lidar sounding is used as ground-truth.
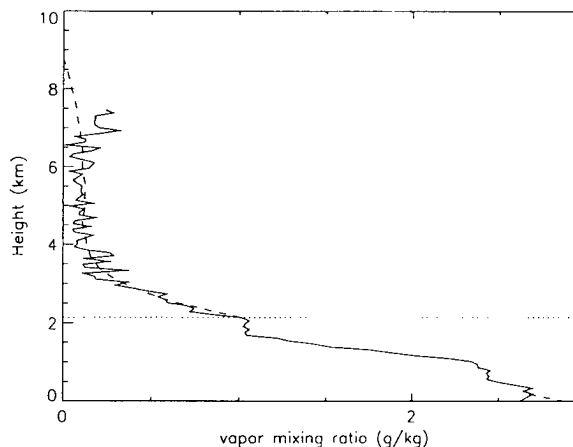
Figure 2. An example of retrieval when lidar provides no historic measurements for the portion above the cloud base. Other notations are explained in Figure 1.

Application of Neural Nets to Rain Rate Retrieval from Simulated Multichannel Passive Microwave Imagery

A.J. Gasiewski, G.A. Showman, and G.M. Skofronick
School of Electrical and Computer Engineering
Georgia Institute of Technology, Atlanta, GA 30332-0250
(404) 894-2984; (404) 894-2934; FAX (404) 894-4641
ag14@prism.gatech.edu ; gt7418d@prism.gatech.edu ; gail@cem1.ee.gatech.edu

Abstract — The retrieval of precipitation parameters from passive microwave imagery requires the use of a nonlinear statistical estimation technique operating on a multichannel data stream. We describe here the application of a feed-forward neural net to the estimation of precipitation parameters from noisy, multispectral brightness temperature imagery. A comparison of the neural net retrieval technique vis-à-vis a nonlinear statistical technique shows that with proper training the neural net achieves slightly better performance. The neural net technique developed here has been used to study the tradeoffs associated with using various microwave channel sets and sensor resolutions. Initial calculations using simulated nadir-viewing imagery for a MIMR-compatible set of six channels are presented.

1. INTRODUCTION

Nonlinear retrieval techniques using either model-based iteration or supervised high-order curve fitting have been shown to be useful for precipitation parameter retrieval (e.g., [1]). Recently, neural nets have seen increasing use in remote sensing studies as classifiers and (to a lesser extent) as continuous parameter retrieval operators. The advantages of neural nets for the latter application include the ability to capture relevant high-order statistical information in the underlying data set and the capability to form highly nonlinear muldimensional mapping functions. These are both essential attributes for many geophysical sensing problems. In addition, neural nets exhibit flexibility in adding weakly correlated information from additional sources [2] and are simple to implement. While a review of neural nets for parameter estimation is beyond the scope of this paper, a sufficient background is developed in [3, 4, 5].

We report here the development of a neural network technique appropriate for rain rate (RR) retrieval using multichannel passive microwave brightness imagery at 6.0, 10.7, 18.7, 23.8, 36.5, and 89.0 GHz. The imagery was computed using the Georgia Tech Microwave Radiative Transfer (MRT) model [6] for five time values of the Goddard Cumulus Ensemble (GCE) microphysical stormcell model [7] over an ocean background. Two spatial resolutions were used in this study: (1) full resolution (FR) imagery consisting of 64 x 64 pixels sampled on a 1.5 km grid, and (2) degraded-resolution (DR) imagery consistent with the imaging capabilities of a diffraction-limited aperture antenna of diameter 1.6 m at 705 km altitude. DR imagery was obtained by convolving the FR imagery with the gain pattern of a circular antenna with quadratic field amplitude taper (Figure 1). Pseudorandom Gaussian noise appropriate for the observation geometry and scan rate were added to the convolved imagery to simulate the radiometric imaging process.

Brightness imagery sampled at five storm temporal stages (126, 138, 174, 210, and 234 minutes) were used, thus providing a total of 20,480 multispectral pixels. The data set was identical to that used in [1]. Training and test sets of equal size were derived from this set by pseudorandom partitioning.

2. NETWORK ARCHITECTURE AND TRAINING

Two-layer (i.e., one hidden layer) neural nets were trained on the MRT/GCE data using a variety of node numbers (from two to eight), training algorithms, weight initialization, and input prefiltering methods. The hidden layer perceptrons used the hyperbolic- tangent sigmoid as . their activation transfer function, while the single perceptron of the output layer used a pure-linear transfer function. Both Karhunen-Loève (KL) and non-KL prefiltering was used.

The nets were implemented using the MATLAB Neural Net Toolbox backpropagation software which allows the option of using an adaptive learning rate (ALR) and momentum term in the training rule. Together ALR and momentum facilitate net training by increasing the likelihood of escaping shallow local minima in error space while rapidly traversing regions characterized by relatively gradual error descent slopes. These features reduced training and test RMS errors by 20-30% for a fixed number of training epochs. In order to negotiate the deep er-

ror troughs encountered in the error landscape, an adaptive hard-limit (ALR-AH) algorithm was developed. The salient feature of this modification is an adaptive limit on the maximum value of the learning rate.

Both uniform pseudo-random and Nguyen-Widrow initialization of the net weights and biases were studied. Net performance did not appear to be affected by the type of initialization. Nets were trained until RMS training errors stabilized; nets with six nodes in the hidden-layer were typically trained for 3000 epochs, and nets with 4 nodes for 2000 epochs. These limits reflect good compromises between complete convergence and reasonable training times. Since nets that are trained on the same data but randomly initialized will inevitably result in differing final weights and RMS errors, an ensemble of nets were trained for the case studies described below. Training of the net using the KL modes of the input data was also tested. Using only the highest energy modes for training and testing offers the possibility of reducing net complexity without compromising retrieval performance.

3. NEURAL NET RETRIEVAL PERFORMANCE

To compare the retrieval performance of a neural net to that of the nonlinear statistical retrieval (NSR) algorithm in [1], a number of nets with four and six hidden nodes were trained on the entire ensemble of data, i.e., without partitioning. The nets were trained with both brightness temperature and KL-transformed data. The retrieval performance of nets using KL data was comparable to nets trained with brightness temperatures. However, the training on KL data occasionally resulted in nets with very large RMS errors. Similarly poor performance were not observed for any of the nets using brightness temperatures, thus, brightness temperature-based retrievals are used in the comparison.

The results for retrievals of RR and integrated ice content (IIC) at both full and degraded resolution using the NSR algorithm and neural net are summarized in Table 1 (see also Figures 2a and b). The better of the KL or brightness temperature (BT) retrievals from [1] appear in the table. The retrieval performance of 6-node nets was slightly better than for the 4-node nets. However, the 4-node nets have approximately the same number of degrees of freedom as does the NSR algorithm, so these results are used in the comparison.

The first measure of performance in the table is the standard deviation of the retrieval error. The second is unconstrained accuracy (a_u), defined as the percentage of pixels with retrieval errors less than 1.0 mm/hr RR or 0.5 kg/m^2 IIC. The final measure is a constrained accuracy (a_c), and is the same as a_u, except that only those pixels

with true RR greater than 0.01 mm/hr or IIC greater than 0.001 kg/m2 are included in the calculations. The neural nets always have a smaller error standard deviation, and in three of the four cases have higher values of a_u and a_c.

Table 1. Rain rate (RR) and integrated ice content (IIC) retrieval performance comparisons between a nonlinear statistical and neural net algorithm.

	FR		DR (1.6m)	
RR	NSR(BT)	NN(4-node)	NSR(KL)	NN(4-node)
σ_e (mm/hr)	1.93	1.63	6.20	5.33
a_u (%)	90.7	92.5	88.9	88.6
a_c (%)	46.2	56.2	36.6	35.6
IIC	NSR(BT)	NN(4-node)	NSR(KL)	NN(4-node)
σ_e (kg/m^2)	0.91	0.34	1.36	0.93
a_u (%)	92.2	94.5	90.4	91.0
a_c (%)	87.2	90.1	84.2	85.2

4. SENSOR TRADEOFF SIMULATION

The neural net retrieval operator was used to study the tradeoffs in rain rate retrieval accuracy for specific channel sets and sensor resolutions. To this end, equal-size training and test data sets were created by pseudo-random partitioning of the entire five-frame data set. Figure 3 shows plots of the standard deviation of the net output error and a_c for FR and DR 4-node RR retrievals. The abscissa indicates the particular channel case: 0 denotes the use of all 6 channels, 1 denotes the use of only the 6.0 GHz channel, etc..., 6 denotes the use of only the 89 GHz channel. Retrieval performance on the training set is shown with solid lines, and test set with dashed lines. The error bars reflect the use of two realizations for each condition to provide a measure of the simulation noise inherent in the use of neural nets.

Using only the 6.0 GHz channel results in a FR retrieval error not too much greater than those achieved by the nets trained on all channels. The worst retrieval is obtained using the 36.5 GHz channel alone, a consequence of the bimodal nature of the brightness variations over oceanic convection for this channel. The 6.0- and 10.67 GHz channels are the most useful in the FR single-channel case. For the DR case, the most useful channel is at a higher frequency (e.g., 18.7 or 89 GHz). This conclusion is expected since the higher frequency channels provide better spatial resolution, and hence better accuracy at any given pixel.

The training rate on a 100 MHz 486 computer for a net with 6 hidden nodes and training on all of the available data (20480 pixels with 6 brightness temperatures each) was about six seconds per epoch; machine usage was approximately six million flops per epoch. In general

the training time and total operation count were found
to scale well to the number of hidden nodes and the size
of the training set and weakly with the number of input
channels or modes, as expected fom complexity calcula-
tions.

5. SUMMARY

Feedforward multilayer neural nets were trained on
brightness temperatures from simulated brightness im-
ages of a tropical convective storm. Data was available
for five stages of the storm's development. The nets were
trained to retrieve rain-rate (RR) and integrated ice con-
tent (IIC) using the backpropagation algorithm. The re-
trieval performance of these nets was compared to that
of a nonlinear statistical retrieval algorithm. The results
suggest that the neural net estimators will be at least
as accurate in precipitation parameter retrieval as con-
ventional nonlinear statistical methods, and that KL pre-
filtering can potentially improve net performance. Neural
net retrieval operators were also used to determine the
importance of individual single radiometric channels and
sensor spatial resolution to rain rate retrieval accuracy.
The reduced spatial resolution available when observing
with low-frequency microwave channels in low-Earth orbit
(i.e., 6.0 and 10.7 GHz) makes these channels significantly
less useful for precipitation parameter retrieval than cer-
tain higher frequency channels (e.g., 18.7 and 89 GHz).

REFERENCES

. [1] G.M. Skofronick-Jackson and A.J. Gasiewski, "Non-
linear statistical retrievals of ice content and rain rate
from passive microwave observations of a simulated
convective storm", *IEEE Trans. Geosci. Remote Sens-
ing*, vol. 33, no. 4, pp. 957–969, July 1995.

[2] M.S. Spina, M.J. Schwartz, D.H. Staelin, and A.J.
Gasiewski, "Application of multilayer feedforward
neural networks to precipitation cell-top altitude esti-
mation", in *Proceedings of the 1994 International Geo-
science and Remote Sensing Symposium (IGARSS)*,
Pasadena, CA, 1994, vol. 4, pp. 1870–1872.

[3] R. P. Lippmann, "An introduction to computing with
neural nets", *IEEE ASSP Magazine*, April 1987.

[4] B. Widrow and M. A. Lehr, "30 years of adaptive neu-
ral networks: Perceptron, madaline, and backpropa-
gation", *Proc. IEEE*, vol. 78, no. 9, pp. 1415–1440,
1990.

[5] R. Beale and T. Jackson, *Neural Computing: An In-
troduction*, Adam Hilger, New York, 1990.

[6] A.J. Gasiewski and D.H. Staelin, "Numerical analy-
sis of passive microwave O_2 observations over precip-
itation", *Radio Science*, vol. 25, no. 3, pp. 217–235,
May–June 1990.

[7] R.F. Adler, H.-Y.M. Yeh, N. Prasad, W.K. Tao, and
J. Simpson, "Microwave simulations of a tropical rain-
fall system with a three-dimensional cloud model", *J.
Clim. Appl. Met.*, vol. 30, pp. 924–953, 1991.

FIGURES
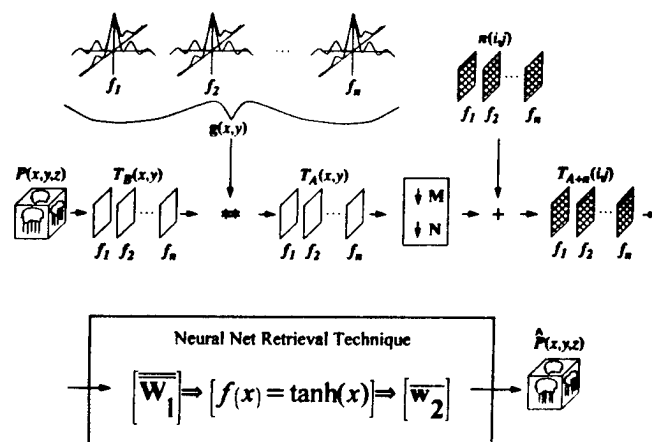
Figure 1: Block diagram of the passive microwave simula-
tion and retrieval process. The neural net estimator was
used in the retrieval stage.
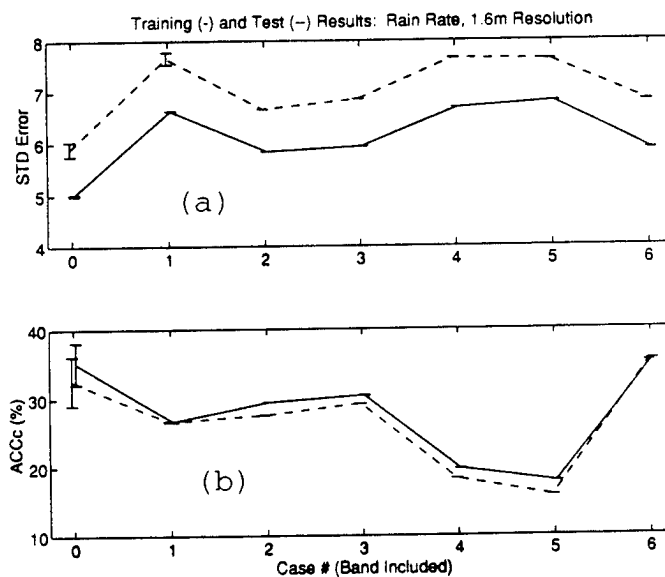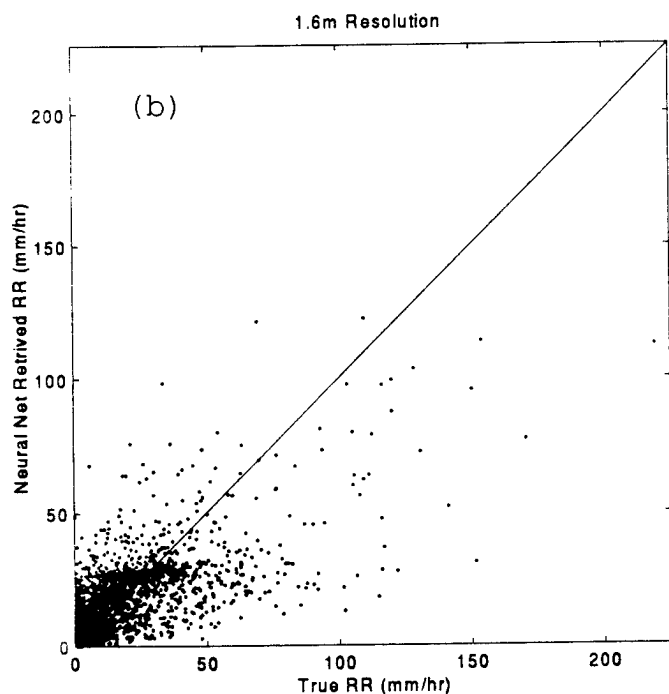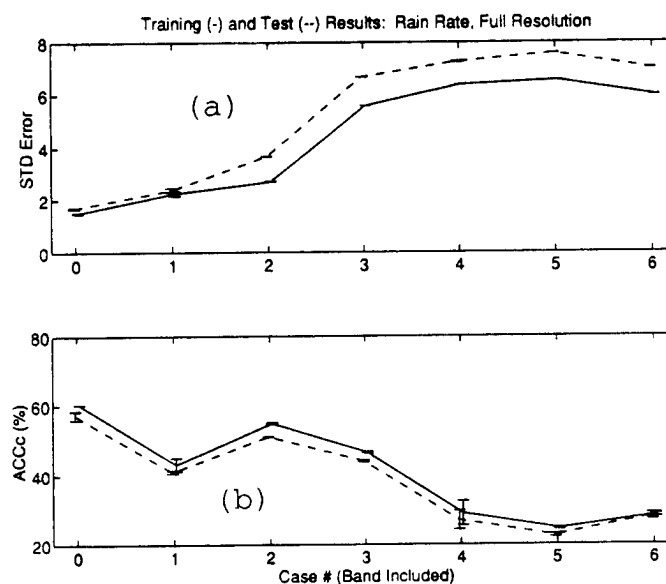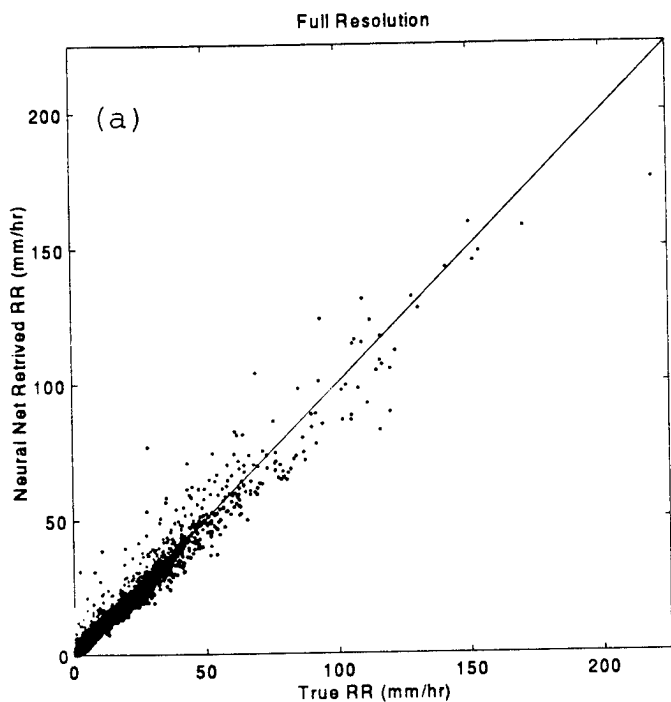
Figure 2: Scatter plot of rain rate retrieved from (a) FR imagery and (b) DR imagery using a six node neural net and six radiometric channels (6.0, 10.7, 18.7, 23.8, 36.5, and 89.0 GHz).

Figure 3: Plots of the (a) standard deviation of the net output error and (b) constrained accuracy a_c for FR and DR (1.6m) neural net rain rate retrieval. A 4-node net was used.

Prediction of Water Vapor Scale Height from Integrated Water Vapor Measurements

Justin P. Bobak and Christopher S. Ruf
Communications and Space Sciences Laboratory
The Pennsylvania State University
323 Electrical Engineering East
University Park, PA 16802
(814) 865-6452/FAX: (814) 863-8457/bobak@rufece.psu.edu

Abstract -- A method for estimating the 10% height of water vapor in the atmosphere is presented. This 10% height is the altitude below which 10% of the atmospheric water vapor vertical distribution occurs. The estimation is based on a time series of ground-based measurements of integrated water vapor, and results from the behavior of the turbulence structure function for water vapor outside of the outer scale of tropospheric turbulence. This behavior is demonstrated by a model which expands on earlier work by Treuhaft and Lanyi on the behavior of atmospheric turbulence in a "frozen" atmosphere. The model integrates statistics of the climatological average water vapor profile with wind and integrated water vapor measurements. Microwave water vapor radiometer, radar wind profiler, and radiosonde data from the Continental Stratus campaign have been processed and the results are presented in support of the model. It is shown that, through the combination of integrated water vapor data from a microwave radiometer, wind profile data from a tropospheric radar, and a realistic model created with local radiosonde launches, the water vapor 10% height in the atmosphere can be successfully predicted with a simple algorithm.

INTRODUCTION

Treuhaft and Lanyi Model

Much work has been done towards the modeling of turbulence in atmospheric water vapor with varying degrees of success. In particular, the work of Treuhaft and Lanyi [1] served as a basis for the ideas presented here.

Assumptions of the Treuhaft and Lanyi Model: The model used by Treuhaft and Lanyi had several important assumptions. Treuhaft and Lanyi modeled atmospheric water vapor as a flat slab, which had a constant mean density of water vapor from the ground to some height, h, and no water vapor for altitudes greater than h. Their model assumed a "frozen" atmosphere, which is one in which the wind speed is high enough that no appreciable change occurs in the turbulence structure in the time necessary for the turbulence structure to flow over some fixed point on the

ground. This assumption allows the transformation of a temporal series of measurements into an apparent spatial series if an effective wind, which can be seen as driving the turbulence structure over the ground site, can be determined. Treuhaft and Lanyi also assumed perfect Kolmogorov turbulence within their slab.

Kolmogorov turbulence: This model of turbulence is characterized by the behavior of a structure function

$$D_f(\bar{r}) = \left\langle \left(f(\bar{x} + \bar{r}) - f(\bar{x}) \right)^2 \right\rangle \tag{1}$$

of some constituent present in the turbulent field. This structure function will have a power law behavior [2] in a range of separations called the inertial subrange

$$D_f(\bar{r}) = C^2 \left(|\bar{r}| \right)^{2/3} \tag{2}$$

which divides the microscale of turbulence from the outer scale of turbulence. Equation (2) assumes local isotropy in the turbulent structure, which leads to the structure function being only a function of the magnitude of the separation. For atmospheric turbulence, the inner scale of turbulence is on the order of magnitude of a few millimeters, while the outer scale is in the tens of meters [3].

Conclusions of Treuhaft and Lanyi: Treuhaft and Lanyi found that the power law exponent in (2) varied when a local fit to the structure function of integrated water vapor with separation distance was performed. This exponent assumed a value of 1.67 for small separations and decreased to 0.67 for separations much greater than the thickness of the water vapor slab. When the separation was approximately equal to the thickness of the water vapor slab, the exponent was approximately 1, and the rate of change of the power law exponent with separation was greatest there.

Our Improved Model

Model Description: A new model for modeling the effects of turbulence on atmospheric water vapor has been created

based on this work. This improved model includes a more realistic water vapor profile as well as some measure of the cross-correlation of water vapor variability at different altitudes. The water vapor profile used in the improved model is taken directly from radiosonde measurements. This should provide more realistic results than a slab model. The cross-correlations between heights, which were calculated from 18 radiosonde launches over a two month period, were included in the model to more accurately portray the apparent lack of interaction between the boundary layer, which is the well-mixed portion of the atmosphere extending from the ground to a few kilometers, and the free atmosphere, which is the portion of the atmosphere above the boundary layer. The free atmosphere is characterized as a more laminar flow than the boundary layer. The variability in the free atmosphere is relatively independent of those in the boundary layer. The cross-correlation we calculated is fairly strong within the boundary layer and the free atmosphere, but is weak between these two regimes. The equation describing the model is included in the next section.

Method of estimating the 10% water vapor height: In the new model, the 10% water vapor height can be estimated by noting that the power law exponent in (2) appears to be related to some measure of the thickness of the water vapor distribution. Based on this, we sought a relationship between the height of the water vapor and the power law exponent in the structure function at a specific separation. The separation that we picked was the 10% water vapor height of the average profile created by averaging the water vapor density of each of the 18 radiosondes.

MODEL

The model used to calculate the integrated water vapor structure function follows Treuhaft and Lanyi's derivation, with two major changes. The first change is the use of real water vapor profiles from radiosonde observations in place of the slab profile. The second modification is the inclusion of cross-correlations between water vapor densities at different altitudes. These cross correlations are used to modify the turbulence model used from one which is purely Kolmogorov to one which closely approximates Kolmogorov within either the boundary layer or the free atmosphere (where the cross correlations were relatively high) and approximates independence when the heights are on opposite sides of the dividing line between these two regimes (where the cross correlations were relatively low). Factoring in the cross-correlation effectively makes our model into two slabs, one representing the boundary layer and one representing the rest of the atmosphere, but gives us a mathematical way to

calculate a structure function across the boundary layer and into the free atmosphere.

The final improved model is

$$D_{IWV}(r) = C^2 \int_0^\infty \int_0^\infty w(z)w(z')r^2(z,z') \cdot$$
$$\left\{ \left(\sqrt{r^2 + (z-z')^2} \right)^{2/3} - (z-z')^{2/3} \right\} dz dz' \quad (3)$$

where C is a structure function constant, w(z) is the water vapor at height z, $r^2(z, z')$ is the correlation coefficient between heights z and z', and r is the horizontal separation. The structure functions and local power law exponents from this model are in similar to the results in Treuhaft and Lanyi.

DATA

The data used here were collected during spring 1995 in State College, Pennsylvania, which has a continental mid-latitude climate. Integrated water vapor measurements were made every 5 seconds by the Penn State University Meteorology Department's microwave radiometer. The water vapor profiles were measured by Vaisala RS-80 radiosondes, which were launched from the radiometer location. The wind profiles were from the Penn State stratosphere-troposphere radar, which is located approximately 20 km south of the radiometer location. These measurements were a part of the Continental Stratus intensive field operations Phase II.

PROCESSING

Using the "frozen" atmosphere assumption, profiler measured winds at an altitude of 1 km above ground level were used to create a spatial series of integrated water vapor from a 2 hour temporal series of radiometer data around each radiosonde launch. The structure functions for each period were calculated, and for each period the structure function value at a separation of one sample (5 seconds) was subtracted from the structure function at all separations. This value was assumed to primarily result from radiometer ΔT noise. This noise can be shown to corrupt the structure function calculation. Some question as to the correct value to remove remains as the value subtracted is somewhat larger than the ΔT noise calculated for the radiometer. The resulting structure function was smoothed by a 5-point triangular filter.

From the resulting structure functions, the respective local power law exponents were calculated by doing a 3-

point linear fit to the common logarithm of the structure function versus the common logarithm of the separation
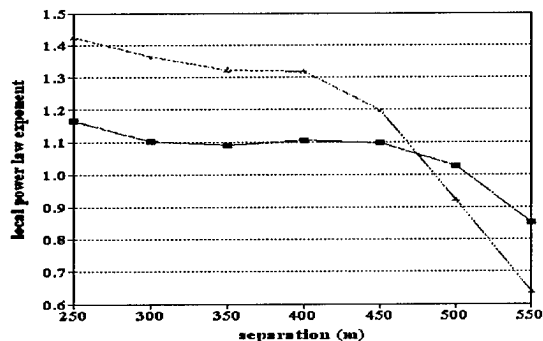
Figure 1. Power law exponents for two sample structure functions from radiometer data.

distance. The analytical derivative of the linear fit at each point was taken to find the slope which is the local power law exponent.

The power law exponents of two sample structure functions are shown in Fig.1. The data indicated by the filled squares is from a period with a 10% height of 132 meters, while the data represented by filled triangles is from a period with a 10% height of 280 meters. It is because of the difference in power law exponent, which is evident in Fig.1, that we are able to estimate the 10% height. As shown in Fig.1, the exponent for the 132 meter data should be smaller than that for the 280 meter data due to the decrease of exponent with increasing separation to height ratio.

RESULTS

The 10% height of the average water vapor profile is 335 meters. In order to estimate the 10% height of the individual profiles, we calculate the power law exponent at 335 meters. The power law exponent of each structure function calculated from the model (using the individual radiosonde profiles rather than the average profile) is shown in Fig.2 versus the individual 10% water vapor heights. The power law exponent of each structure function calculated from the radiometer data was then compared to the 10% water vapor height, as shown in Fig.3. The smaller number of points in Fig.3 is due to equipment dropout and sampling problems due to the variations in wind speed while the sampling rate of the radiometer remained constant.

The match between Fig. 2 and Fig.3 appears to be fairly good, and leads one to suspect that one could estimate 10% water vapor height from only integrated liquid water vapor and wind data.
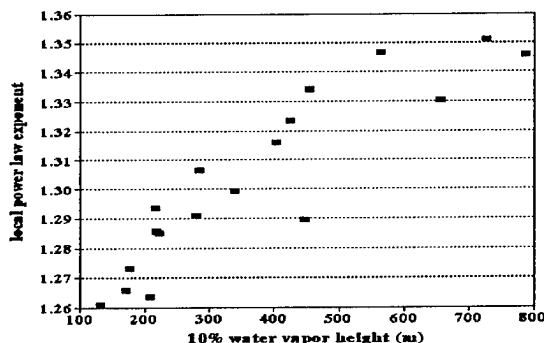
Figure 2. Comparison of exponent at fixed separation with 10% water vapor height. Results from the model.
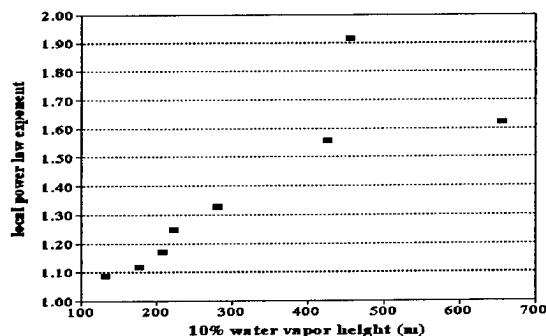
Figure 3. Comparison of exponent at fixed separation with 10% water vapor height. Results from radiometer data.

REFERENCES

[1] R.N. Treuhaft and G.E. Lanyi, "The effect of the dynamic wet troposphere on radio interferometric measurements," Radio Science, vol. 22, no. 2, pp. 251-265, March-April 1987.

[2] V.I. Tatarskii, Wave Propagation in a Turbulent Medium, New York: Dover, 1961, pg. 32.

[3] A. Ishimaru, Wave Propagation and Scattering in Random Media, vol. 2. New York: Academic Press, 1978, pg. 369.

Feasibility of A New Ground-based Microwave Measurement Method
for the Atmospheric Water Vapor

Shinobu Hashimoto, Nariharu Yamashita and Takayoshi Mikami

Marine Production System Science, Faculty of Fisheries, Hokkaido University

Minato-machi 3-1-1, Hakodate, Hokkaido 041, Japan

Tel. 0138-40-8520, Fax 0138-40-8849

Abstract - Our method for the atmospheric water vapor measurement assums quasi-stable nature of the atmospheric water vapor absorption. To determine the effect of the fractional instability on the integrated water vapor estimation, computer simulations are carried out using radio sonde data at Yonago station of Japan Meteorological Agency in 1993. The results show that the errors are less than 5 % for the cold and dry weather conditions in February, when the error is generally increased. Further improvement of the measurement accuracy are discussed.

INTRODUCTION

Authors have proposed a new ground-based microwave measurement of the atmospheric water vapor using solar extinction measurement [1], which consists of the following major points: (1) utilization of the quasi-stable nature of theweighting function of the absorption $W(f,z)$, or the functionof the absorption coefficient divided by water vapor density, (2)the relative intensity between two frequencies in the 22 GHz absorption spectrum is used as the measure of the water vapor concentration, and (3) a multifrequency radiometer having two different beamwidth antennas continuously measures the antenna temperature difference relating the solar extinction, and the relative intensity of the water vapor absorption. The output is free from the fluctuation of the solar radiation and the thermal emission of the atmosphere.

The fractional variation of the weighting function for a wide variety of variation of atmospheric conditions determines theoretical accuracy limit of the measurement. The resolution of the relative intensity measurement is also dependent on the atmospheric conditions for a given radiometer resolution .

The aim of this investigation is to estimate possible errors due to the residual variation of the weighting function and the radiometer measurement errors for the

various atmospheric conditions by computer simulation using the radio sonde data at Yonago Station, Japan Meteorological agency, in 1993.

EFFECTS OF VARIATION OF WEIGHTING FUNCTION

The weighting function $W(f,z)$ of the atmospheric water vapor absorption is a stable function which has the unique altitude variation for each frequency. Variation of the water vapor density and the temperature affects small second order effect on the weighting function. These fractional variations of the weighting function are dependent on the frequency, and approximately symmetrical in both sides of the absorption center frequency. Therefore, in our method using relative intensity of the absorption, further suppressed effects of the weighting function variation on the water vapor estimation can be expected by the selection of the frequency pair of the measurement.

Radiometer measures water vapor absorption in terms of the relative intensity, and then produces the difference of opacity of the atmosphere by the following steps:

(1) Radiometer having two different beamwidth antennas measures the antenna temperature difference $Tm(f, \theta)$ $=TA2(f, \theta)-TA1(f, \theta)$, where $TA1$ and $TA2$ are the temperatures of each antenna, and Tm is the temperature difference. θ is the solar zenith angle. The thermal emission component is canceled out in the antenna temperature difference.

(2) The relative intensity of the absorption at frequency $f1$ and $f2$, $R(f1/f2)=Tm(f1, \theta)/ Tm(f2, \theta)$, is used to estimate the opacity difference [$\tau (f2)- \tau (f1)$]. The opacity difference is free from fluctuation of the solar radiation.

The opacity difference, on the other hand, is given in

terms of the composite weighting function, $[W(f2,z)-W(f1,z)]$, and water vapor density $\rho(z)$ as

$$[\tau(f2) - \tau(f1)] = \int_0^\infty \rho(z)[W(f2,z) - W(f1,z)]dz \qquad (1)$$

Frequency pair is selected so as to have a quasi-constant value of the composite weighting function along the altitude, the opacity difference becomes proportional to the integrat-ed water vapor.

In estimation of the integrated water vapor, we define the weighted mean of the composite weighting function $\overline{W}$ using the standard exponential decay of water vapor along altitude as the weight.

The estimated integrated water vapor V* is given by

$$V^* = [\tau(f2) - \tau(f1)] / \overline{W} \cdot \qquad (2)$$

Cloud add a nonresonant absorption that is proportional to the square of frequency over the whole region of 22 GHz water vapor spectrum [2]. Cloud contribution in opacity $\tau_{cl}(fi)$ at any frequency can be related as

$$\tau_{cl}(fi) = \left(\frac{fi}{fk}\right)^2 \tau_{cl}(fk) \cdot \qquad (3)$$

From the symmetrical property of the weighting function, we can select two pairs of composite weighting functions which are approximately proportional to each other by a constant A,

$$[W(fi,z) - W(fk,z)]_{H2O} = A[W(fm,z) - W(fn,z)]_{H2O} \quad . \qquad (4)$$

The opacity difference due only to the water vapor and cloud absorption can be separately estimated using the opacity difference measured at two pairs of frequency points (fi, fk) and (fm, fn) and using (3) and (4).

The Pairs of composite weighting functions used in (1) and (4) should have approximately equal dependence on the variation of atmospheric conditions. The residual variations of these composite weighting functions determine the error in estimation of integrated water vapor.

RADIOMETER RESOLUTION AND OPACITY DIFFERENCE ERROR

Radiometer resolution ΔT in the measurement of the antenna temperature difference determines the estimation error of the relative intensity and the opacity difference in (2).

Assuming the radiometer resolution of each frequency is equal ΔT, and the diameters of two antennas are $D1$ and $D2$, respectively, the measurement errors in the relative intensity and the opacity difference are given by [3]

$$\varepsilon_R = \Delta T \left[\frac{1}{Tm(fk,\theta)} + \frac{1}{Tm(fi,\theta)} \right] , \qquad (5)$$

$$\varepsilon_\tau = \frac{\varepsilon_R}{\left[\tau(fi) - \tau(fk)\right]\sec\theta} \cdot \qquad (6)$$

These are also depended on the atmospheric conditions.

ESTIMATION OF ERRORS USING RADIO SONDE DATA

To determine errors in estimation of the integrated water vapor due to the residual variation of the composite weighting functions for the possible variation in the real atmosphere, computer simulations were carried out using radio sonde data at Yonago Station of Japan Meteorological Agency in 1993.

The altitude, pressure, temperature and water vapor density data on each day (twice a day) are used to calculate the antenna temperature difference, the relative intensity, the opacity difference and separation of cloud contribution for the frequency pairs of (23.9-20.6) GHz and (24.5-18.0) GHz, with and without uncertainty of radiometer 0.1 K.

The integrated water vapor V^* in (2) are estimated using the opacity difference and the weighted mean of composite weighting function $\overline{W}$ for the frequency pair of (23.9-20.6) GHz, and compared with the true values V obtained by integrating the density profiles of the sonde data.

In the above calculations, $\overline{W}$ in (2) is decided for the standard atmosphere with temperature of 283 K, water vapor density of 10 g/m^3 at ground level, and the radiometer antenna diameters are assumed $D1 = 30$ cm, $D2 = 200$ cm.

Two typical examples of the results are shown in Fig. 1 and Fig. 2 for the dry and cold weather condition in February, and for the hot and humid condition in August, respectively. X and ●marks in both figures show errors in

estimation of integrated water vapor due to weighting function variation for the sonde data at 8:30 a.m. and at 8:30 p.m., respectively. The vertical bars show the uncertainty due to the radiometer resolution.

DISCUSSIONS

The data scatter in Fig. 1 and Fig. 2 are considered due to the residual variation of real composite weighting function, and the deviation from the weighted mean $\overline{W}$ used for estimation. Comparably large deviations of data in Fig. 1 are understood due to large deviation from the weighted mean $\overline{W}$ for the cold and dry atmosphere in February. It is considered that the relatively large dependence of the (24.5-18.0) GHz composite weighting function on the temperature variation is one of the error source.

For further improvement of the estimation accuracy, it would be expected to select other frequency pair having less residual variation, and more effectively, to use

different weighted mean $\overline{W}$ from the known atmospheric parameters at ground level.

REFERENCES

[1] S. hashimoto, "A New Simplified Water Vapor Measurement Using a Multifrequency Microwave Radiometer with Two-Different-Beamwidth Antennas," Trans. GRS, vol. 30, no. 4, pp. 832-837, July 1992.

[2] D. H. Staelin, "measurements and Interpretation of the Microwave spectrum of the Terrestrial Atmosphere Near 1-centimeter Wavelength," J. Geophys. Res., vol. 71, no. 12, pp. 2875-2881, June 1966.

[3] S. Hashimoto, "Estimation of Errors in the Two-Beamwidth-Antenna Method for Microwave Measurement of Atmospheric Water Vapor," in Microwave Radiometry and Remote Sensing of the Environment, D. Solimini, Ed. Utrecht: VSP, 1995, pp.53-63,
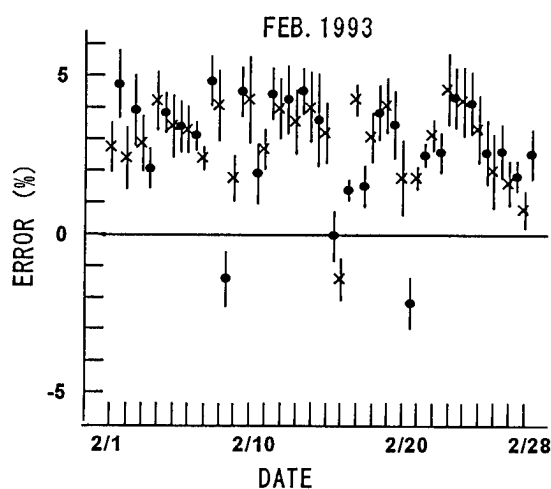
Fig. 1 Estimation erroe of integrated water vapor. Computer simulation using radio sonde data at Yonago in February 1993.
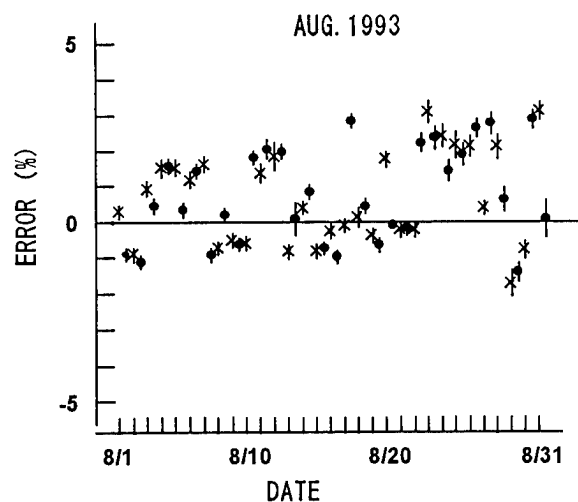
Fig. 2 Estimation erroe of integrated water vapor. Computer simulation using radio sonde data at Yonago in August 1993.

Determination of humidity profiles from measurements of upgoing radiation at wavelengths 0.3 cm and 1.35 cm.

N.N.Markina, A.P.Naumov
Radiophysical Research Institute
B.Pecherskaya st., 25, Nizhniy Novgorod, Russia, 603600
Phone:(097 8312) 367294, Fax:(097 8312) 369902
E-mail: nau@nirfi.nnov.su

Abstract - The possibilities to restore of humidity profiles from satellite data in the atmosphere transparency window 0.3 cm and water vapour resonance 1.35 cm have been investigated. Numerical simulations have been carried out and the accuracy of determination of humidity profiles have been discussed.

1. INTRODUCTION

One of the actual problems of remote sensing is the restoration of humidity height profiles from the measurements of upgoing radiation of the atmosphere- underlying surface system in the microwave range. Usually this problem has been studied in the water vapour resonant regions [1,2]. However, we have found that some atmosphere transparency windows have a sufficiently high sensitivity of radio brightness temperatures to the variation of specific humidity height profiles. In this work we investigate the possible retrieval of atmosphere humidity profiles from the measurements of upgoing radiation both at the resonant region 1.35 cm and the atmosphere transparency window 0.3 cm.

2. PHYSICAL SETTING OF AN INVERSE PROBLEM

An initial integral equation to determine humidity profiles from radiometric measurements is a relation for variations of radio brightness temperatures of upgoing radio emission $\delta T_B \uparrow$ [3]:

$$\delta T_B \uparrow = \int_0^H \delta T(h) \gamma^{av}(h) \exp(-\tau^{av}(h,H)) \, dh +$$

$$+ \int_0^H \delta\gamma(h)[T(h) - T_B\uparrow(h)] \exp(-\tau^{av}(h,H)) \, dh +$$

$$+ \{(1-R^{av})\delta T_o + [T_B^{av}\downarrow(0) - T_o]\delta R +$$

$$+ R\delta T_B\downarrow(0)\} \exp(-\tau_m^{av}),$$

$$(1)$$

where $\delta T_B\downarrow = \int_0^H \delta T(h) \gamma^{av}(h) \exp(-\tau^{av}(0,h)) \, dh +$

$$+ \int_0^H \delta\gamma(h) [T(h) - T_B\downarrow(h)] \exp(-\tau^{av}(0,h)) \, dh,$$

$\delta T(h) = T(h) - T^{av}(h)$, $\delta\gamma(h) = \gamma(h) - \gamma^{av}(h)$ and etc. The temperature $T^{av}(h)$, absorption coefficient $\gamma^{av}(h)$ etc. are related to the standard atmosphere. In (1) $\tau(h_1,h_2) = \int_{h_1}^{h_2} \gamma(h) dh$ is the optical depth of the atmospheric layer (h_1,h_2), $\tau_m(0,H)$ is the total optical depth of the atmosphere, H is the upper boundary of the atmosphere.

The physical basis of setting the inverse problem given is the existence of significant variations of radio brightness temperatures caused by variations of humidity height distribution at a constant content of water vapour mass in a vertical atmospheric column.

The estimations of radio brightness temperatures were carried out for different models of specific humidity distributions with fixed values of the total water vapour mass of a vertical atmosphere column [4]:

$$q(h) = \begin{cases} q_o \exp(-\alpha h), & 0 \le h \le 16\text{км} \\ q(16), & 16 \le h \le 80\text{км} \end{cases} \quad (2)$$

Parameters α were taken equal to α^{av}, $\alpha^{av}+\sigma_\alpha$ and $\alpha^{av}-\sigma_\alpha$, where σ_α are rms deviations of α. Notations $q_{+\alpha}$ and $q_{-\alpha}$ correspond to profiles with $\alpha = \alpha^{av}+\sigma_\alpha$, $\alpha = \alpha^{av}-\sigma_\alpha$, and q^{av} to profile $\alpha = \alpha^{av}$. The variations of radio brightness temperatures were calculated using meteorological data for middle -latitude (zone 1) and near-equatorial (zone 2) climatic zones [5]. In these zones the values of α^{av} are respectively 0.336 km^{-1} and 0.331 km^{-1}; σ_α=0.1 km^{-1}. The values q_o together with values α for profiles q, $q_{+\alpha}$ and $q_{-\alpha}$ at fixed values of total water vapour mass Q equal to 2.29 g/cm^2 (zone 1) and 5.14 g/cm^2 (zone 2) are given in Table 1.

The estimations of $\delta T_B\uparrow$ variations were made for the cases of satellite nadir soundings over a smooth water surface for the variations of humidity profiles:

Table 1.

Zone	Parameters	$q_{+\alpha}$	q^{av}	$q_{-\alpha}$
1	α, km^{-1}	0,436	0,336	0,226
	q_o, g/g	0,0103	0,00826	0,0062
2	α, km^{-1}	0,431	0,331	0,231
	q_o, g/g	0,02386	0,0192	0,0145

$$\delta q_{+\alpha}(h) = q_{+\alpha}(h) - q^{av}(h)$$

$$\delta q_{-\alpha}(h) = q_{-\alpha}(h) - q^{av}(h) \qquad (3)$$

Variations of $\delta T_B\uparrow$ at the resonance 1.35 cm attain values of 7.5 K for humidity variations $\delta q_{-\alpha}$ and -2.4 K for $\delta q_{+\alpha}$ in the middle-latitude zone. In the near-equatorial zone these values attain respectively 6.6 K and -2.5 K. For the radiometer bandwidth δv=400-600 MHz the brightness temperature variation at 1.35 cm decrease cor-respondingly to 1.7 - 1.3 K. Variations $\delta T_B\uparrow$ at 0.3 cm do not practically depend on the reception bandwidth and are equal modulo 1.2 - 3.5 K for the given humidity profile variations.

We investigated as well the influence of the surface temperature and the atmosphere temperature profile on the variations of radio brightness temperature. The numerical simulation of a radiometric experiment has shown that the change of surface temperature T_o by 1 K leads to the variations of the radio brightness temperature at 1.35 cm and 0.3 cm within 0.3 K. If the temperature profile over the whole height changes by 1 - 2 K brightness temperature will change by 0.5 - 0.9 K at the wavelengths considered.

3. RESULTS OF HUMIDITY PROFILE RESTORATION

In this section we study the possibilities to restore specific humidity profiles q(h) (inverse problem) at the given wavelengths on the basis of a numerical simulation for an ensemble of aerological atmospheric profiles above equatorial ocean areas obtained onboard the research ship (80 realization).

The equation to solve an inverse problem of humidity sounding for the known temperature profile and reflection coefficient for nadir observations has the following form according to (1):

$$\delta T_B\uparrow(v) = \int\limits_0^H K(v,h)\, \delta q(h)\, dh , \qquad (4)$$

where the kernel of integral equation

$$K(v,h) = \delta\gamma^{sp}(h)\{[T^{av}(h) - T_B\uparrow(h)]\exp(-\tau^{av}(h,H)) + \qquad (5)$$
$$+ R^{av}\exp(-\tau_m^{av})[T^{av}(h) - T_B\downarrow(h)]\exp(-\tau^{av}(0,h))\}$$

and $\qquad \delta\gamma^{sp}(h) = \delta\gamma_{H2O}/\delta q .$

We carried out the computation simulation of the experiment to retrieve humidity profiles from radio brightness temperature values at 1.35 cm and 0.3 cm for the errors of radiometric measurements δT_r= 0.5 - 2.0 K. RMS variations of brightness temperature for ensembles of radio sonde humidity profiles above equatorial ocean areas are respectively 14.7 K and 8.8 K for the given wavelengths. The retrieval was made by the statistical regularization method [6,7]:

$$(K' W K + B_{qq}^{-1})\delta q = K'W \delta T_B\uparrow , \qquad (6)$$

where K, δq, $\delta T_B\uparrow$ - are the matrices and vectors of corresponding values obtained for a piecewise difference approximation of equation (4), sign ' denotes transposition, W is the diagonal matrix of the measurement errors, B_{qq} is correlation matrix of the specific humidity. Here we used B_{qq} and q^{av} obtained for the given ensemble of aerological data. The elements of matrix K depend on the humidity, so equation system (6) is solved by the iteration method. At the first iteration the matrix elements are calculated using values $T_B\uparrow(h) = T_B^{av}\uparrow(h)$, $T_B\downarrow(h) = T_B^{av}\downarrow(h)$. For the next and following iterations these values are calculated using values of the specific humidity. The numerical simulations have shown that it is quite enough to have three iterative loops.

Table 2 gives the results of numerical simulation to retrieve $q(h)$ from simulated measurements with error δT_r= 0.5 K for different frequencies over the given aerological ensemble. The results obtained show the improvement as a result of restoration as compared with a priori uncertainty. It is seen from the results of Table 2 that the humidity in lower atmospheric layers (h ≤ 3 km) is restored better from measurements at λ = 0.3 cm than from those at λ = 1.35 cm and vice versa the humidity in the layers h > 3 km is restored better at λ = 1.35 cm. The best results are obtained for atmospheric sounding at two frequencies. The results of numerical simulation for two reception bandwidths (δv = 400 - 600 MHz) differ very little from each other.

Table 2

Relative rms climatic variations of the specific humidity σ_q/q^{av} and relative rms errors of retrieval of humidity profiles $\sigma_q{}^r/q^{av}$ at δT_r=0.5 K for different heights (λ_1=1.35 cm, λ_2=0.3 cm) .

h,km	σ_q/q^{av}, %	$\sigma_q{}^r/q^{av}$, %		
		λ_1 , λ_2	λ_1	λ_2
0.0	13.2	6.1	7.6	6.8
0.5	17.3	6.9	9.0	7.8
1.0	19.4	6.7	9.3	7.7
1.5	23.1	8.2	9.6	8.0
2.0	29.5	12.1	13.1	11.6
2.5	33.5	13.8	14.0	12.8
3.0	31.5	13.4	13.2	13.2
3.5	32.9	14.0	13.7	15.2
4.0	35.4	16.4	16.4	18.7
4.5	37.6	16.7	17.8	20.6
5.0	37.8	16.0	18.3	21.4
6.0	44.1	19.5	28.1	32.1
7.0	50.5	27.6	38.1	41.9
8.0	54.7	31.5	41.9	45.7
9.0	55.6	33.2	42.1	45.8
10.0	56.4	34.9	43.5	46.9
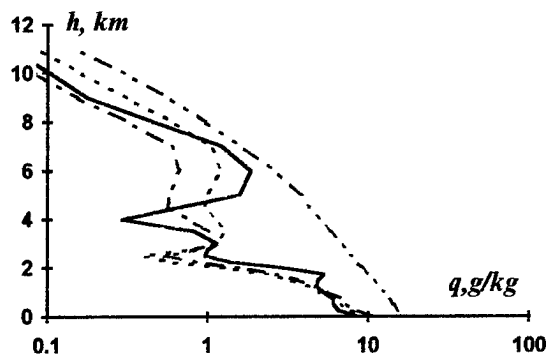
Fig. 1.
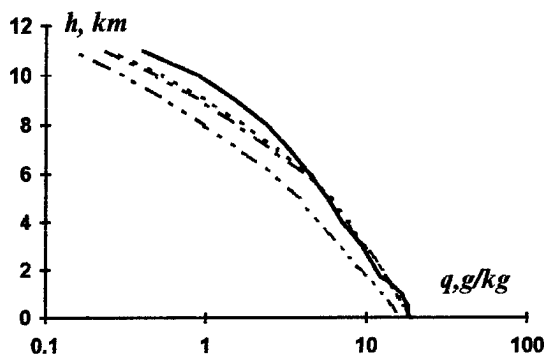
Fig. 2.

For errors of radiometric measurements $\delta T_r=2$ K the relative rms errors of profile restoration $q(h)$ increase from 1 per cent to 8 per cent within height interval 0 - 10 km.

A very noticeable improvement in profile determination $q(h)$ from retrieval results is obtained in the case of a stronger contrast of the desired profile from the averaged one , i. e. when the absolute value of radio brightness temperature variations of a given profile exceeds rms variations of radio brightness temperature over an

ensemble. Such examples of the retrieval are given in Fig.1 and Fig.2. Fig.1 corresponds to the case of humidity distribution $q(h)<$ $q^{av}(h)$ and Fig.2 corresponds to that when $q(h) >q^{av}(h)$. The following designations are used in the figures: solid curve - sonde values of the specific humidity profile; double dot-and-dash line - mean ensemble values of the specific humidity; dashed line - restored values $q(h)$ for radiometric measurement error $\delta T_r = 0.5$ K, dot-and-dash line - restoration results for $\delta T_r = 2.0$ K.

4. REFERENCES

[1] G.Schaerer, T.T.Wilheit, "A passive microwave technique for profiling of atmospheric water vapour," Radio Science, vol.14, no.3, pp. 371-375, 1979.

[2] N.N.Markina, "Retrieval of height humidity profiles by the measurements of upgoing radio emission of the atmosphere in MM wave band". Abstracts of All-Union Conference "The use of satellite data in ocean and atmosphere exploration". Moscow, p. 101, April 1989.

[3] N.N.Markina, A.P.Naumov, M.I.Sumin. "On equations for radio brightness temperature variations of the atmosphere," Radiotekhnika i Electronika, vol. 30, no.5, pp. 851-859, 1985.

[4] A.P.Naumov, V.A.Rassadovskij. "On some statistical characteristics of the atmosphere water content". Preprint N 96. Gorky : NIRFI, 1976.

[5] U.S.Standard Atmosphere Supplements. Washington: Printed covernment Office, 1966.

[6] V.F.Turchin, "The solution of Fredholm integral equation of the first kind in a statistical ensemble of smooth functions" Zhurnal vychislitelnoj matcmatiki i matcmatichcskoj fiziki, vol.7, no.6, pp. 1270-1278, 1976.

[7] O.N.Strand, E.R.Wcstwatcr, "Minimum rms estimation of the numerical solution of a Fredholm integral equation of the first kind," SIAM J. Numer. Anal., vol.5, no.2, pp. 287-295, 1968.

Recovering of Atmospheric Water Vapor and Liquid Water Contents by Multifrequency Radiometer: Experiments and Modeling

Yu.P.Perfiliev

Space Research Institute, Russian Academy of Sciences
Profsoyuznaya st. 84/32, Moscow 117810, Russia
Phone (7-095) 333-5078, Fax (7-095) 333-1056, EMail:KUB@asp.iki.rssi.ru

ABSTRACT

The optimal pair of frequencies for dual-frequency radiometer presuming the presence of clouds and accounting on the possible accuracy of the instrument are investigated. The water vapor and liquid water contents retrieved from microwave measurements with dual-frequency radiometer were averaged over various types of clouds. To reduce the influence of strong cloud conditions the third frequency band is proposed. Optimal frequency set is estimated in the case of zenith-looking observation.

INTRODUCTION

Microwave remote sensing of the atmosphere by means of radiometers usually includes obtaining the water vapor and, if necessary, liquid water contents of clouds. The radiative transfer equation in case of receiving of atmospheric emission by ground-based zenith-viewing radiometer for brightness temperature is as following:

$$T_{br}(\nu) = \int_0^\infty T(h)\gamma(\nu,h)\exp\left(-\int_0^h \gamma(\nu,z)dz\right)dh \qquad (1)$$

where:
ν - frequency,
$T(h)$ - thermometric temperature profile of the air,
$\gamma(h)$ - total absorption coefficient of the atmosphere at an altitude h.

This equation can be written as:

$$T_{br}(\nu) = T_{air}[1-\exp(-\tau(\nu))] \qquad (2)$$

where:
T_{air} - averaged atmospheric temperature,

$$\tau(\nu) = \int_0^\infty \gamma(\nu,h)dh -$$

- total atmospheric transmittance due to H_2O vapor, liquid H_2O, and O_2.

For microwave range the transmittance can be approximated as:

$$\tau(\nu) = a(\nu)Q + b(\nu,T_{cl})W + c_{O_2}(\nu) \qquad (3)$$

where:
$a(\nu)$, $b(\nu,T_{cl})$, and $c_{O_2}(\nu)$ - absorption coefficients due to

vapor, liquid water and oxygen respectively,
T_{cl} - effective cloud temperature,
W - integrated liquid water content,
Q - integrated water vapor content.

Two techniques for water vapor recovering are used. First approach is based on the measurements in several wavelengths and then on solution of inverse problems. Spectral features of atmospheric emission permit to restrict oneself to two frequencies near 22.23 GHz and 37 GHz to derive W and Q parameters. The second technique considers the regression between water vapor content and brightness temperatures difference in the frequencies near the 22.23 GHz (at the center of water vapor absorption line and on its slope). This difference is measured by microwave dual-frequency radiometer [1,2], using frequency band modulation.

DUAL-FREQUENCY RADIOMETER

To estimate the optimal pair of frequencies for using in dual-frequency radiometer the calculations were made over the range of 10-30 GHz. The accuracy of each frequency channel was supposed to be $\delta T = 0.2K$. Combining the equations (2) and (3) the simplified expression can be obtained:

$$Q = (a_{\nu2}\exp(-c_{\nu2}) - a_{\nu1}\exp(-c_{\nu1}) + \sqrt{S})/D, \qquad (4)$$

where:
$S = [a_{\nu1}\exp(-c_{\nu1}) - a_{\nu2}\exp(-c_{\nu2})]^2 - 2[\exp(-c_{\nu2}) - \exp(-c_{\nu1}) - \Delta T_{br}/T_{air}] \times D$,
$D = a_{\nu2}^2\exp(-c_{\nu2}) - a_{\nu1}^2\exp(-c_{\nu1})$,
$a_{\nu1}$, $a_{\nu2}$ - absorption coefficients due to water vapor in frequencies ν_1 and ν_2,
$c_{\nu1}$, $c_{\nu2}$ - absorption coefficients due to liquid water and oxygen,
$\Delta T_{br} = T_{br}(\nu_1) - T_{br}(\nu_2)$.
The RMS water vapor retrieval errors

$$1/\xi = (1 - Q_0/Q)^2,$$

where Q_0 - calculated water vapor content without taking into account clouds,
were computed for all set of frequencies. The water vapor absorption coefficients were calculated on the base of Van

Vleck-Weiskopf formula. The normalized coefficients were averaged over 500 MGz bandwidth. In the range of 5-40 kg/m^2 for Q and 0.1-1.5 kg/m^2 for W optimal pair proves to be 22.23 GHz and 20.20 GHz which agrees with results obtained in [3]. This is illustrated in Fig.1 for $Q=20$ kg/m^2 and $W=0.5$ kg/m^2. In this connection we have developed dual-frequency radiometer described in [1] and operated in frequencies 22.23 and 20.20 GHz. The radiometer construction gives possibility to obtain simultaneously both the absolute level of brightness temperatures and their difference due to adjustable dual-frequency pass-band filter. The difference measurements in the center of water vapor absorption line 22.235 GHz and on its slope 20.20 GHz provide us directly the water vapor path.

OBSERVATIONAL RESULTS

The complex experiments were made as onboard research aircraft (Winter 1992) as from ground-based platform (Summer 1994) to verify the proposed scheme of dual-frequency K-band radiometer. They demonstrated the device reliability as well as the possibility to measure difference of brightness temperatures with high accuracy. However to obtain the water vapor content under heavy cloud conditions one had to use additional channel as it was shown in [2]. The results of water vapor and liquid water contents recovering using the method described in [2] and summarizing the data obtained during June 1994 experiment in Zvenigorod

Table 1. Cloud properties.

Date	Time	Cloud type	Cloud height, km	Averaged Q, kg/m^2	Maxim W, kg/m^2
15.06	14.00-17.00	Ac	3060-3320	17.3	0.20
20.06	17.00-18.00	Sc	1440-1780	23.5	0.50
21.06	15.30-17.30	Ac,Cu	1800-3445	16.6	0.47
22.06	15.15-16.15	Ac,Cu	1970-2190	15.8	0.73
23.06	11.00-12.30	Cu, Cufr	1325-1870	16.6	0.67
28.06	13.30-14.00	Ac,Cu Cufr	-	13.7	0.60
29.06	16.00-18.00	Sc	1740-2010	19.3	0.35

(Moscow region) over various types of clouds are shown in Table 1. The heights of the bottom boundary of clouds were taken from lidar measurements.

THREE FREQUENCY SET SIMULATION

The need of adding third frequency for difference measurements and so obtaining two difference brightness temperatures $\Delta T_1 = T_{br}(\nu_1) - T_{br}(\nu_2)$ and $\Delta T_1 = T_{br}(\nu_1) - T_{br}(\nu_3)$ to compensate the influence of heavy clouds have been demonstrated in [2]. All possible combinations of three frequency bands in the range of 10-30 GHz were computed by method described above for two-frequency set optimization. Fig.2 shows the effectiveness of two frequency band choice when third frequency is fixed in the 22.23 GHz. The strong peak can be seen at the values of 20.20 and 24.45 GHz. This pair of frequencies lay in opposite slopes of the center 22.235 GHz H$_2$O water vapor absorption line. Fig.3 shows the choice of third frequency provided two other ones are kept in 20.20 and 22.23 GHz. It was plotted for two different values of liquid water W. The effectiveness ξ_3 has its maximum in 24,45 GHz and increases as liquid water in clouds augments. To illustrate it, Fig.4 depicts the behavior of effectiveness of using third frequency ($\nu_3 = 24.45$ GHz) as a function of W. So the accuracy of water vapor content retrieving may be improved in 2-3 times under heavy cloud conditions when comparing dual-frequency difference measurements.

CONCLUSIONS

The chosen pair of frequencies was demonstrated to be optimal for using in dual-frequency radiometer. The experimental results proved the reliability and high accuracy of difference method to determine water vapor content. The values of water vapor and liquid water contents along with the cloud parameters collected by ground-based instruments were averaged over various types of clouds. On the other hand the influence of heavy clouds on the accuracy of difference measurements indicated the need in using a third frequency band to reduce this effect. Optimal frequency set was estimated in the case of zenith-looking observation. It proves to be the same pair of frequencies as before plus additional frequency band centered to 24.45 GHz.

REFERENCES

[1] V.S.Etkin, M.S.Dzura, Yu.P.Perfiliev, and Yu.G.Trokhimovsky, "The determination of atmospheric water vapor content using dual-frequency radiometer," IGARSS'94, pp.436-438,1994.
[2] Yu.P.Perfiliev, V.S.Etkin, M.S.Dzura, "The retrieval of water vapor content under various cloud conditions as

measured by the dual-frequency radiometer during the Zvenigorod-94 experiment," IGARSS'95, 1995.

[3] A.G.Gasiewski, "Channel-ranking in passive microwave wet-path delay measurements," IGARSS'94, pp.1765-1767, 1994
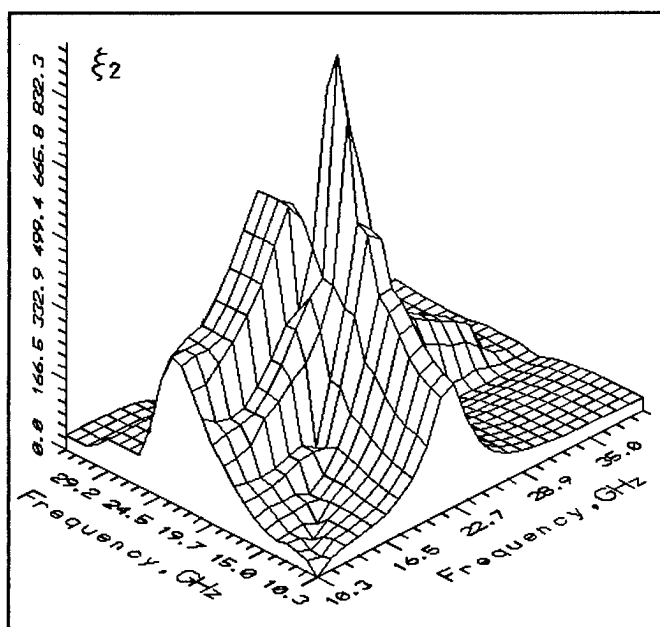
Fig.1 The effectiveness of two-frequency set for dual-frequency radiometer
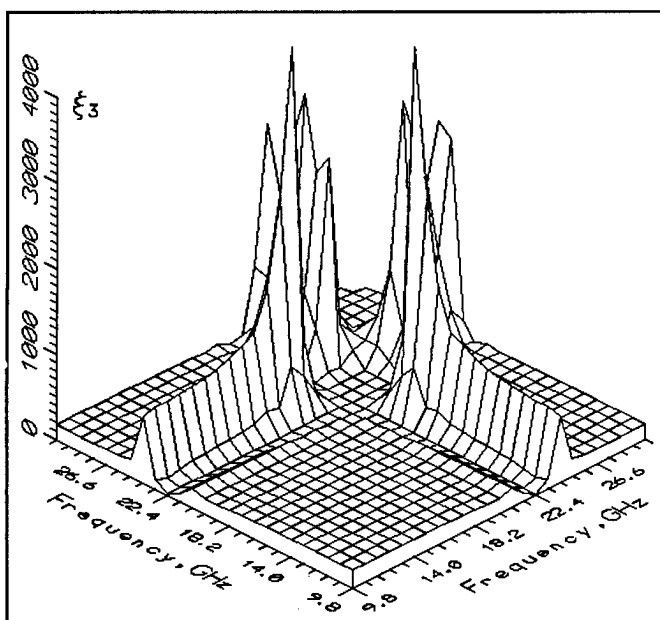
Fig.2. The estimation of the effectiveness of two frequency set assuming third frequency $\nu_1 = 22.23$ GHz
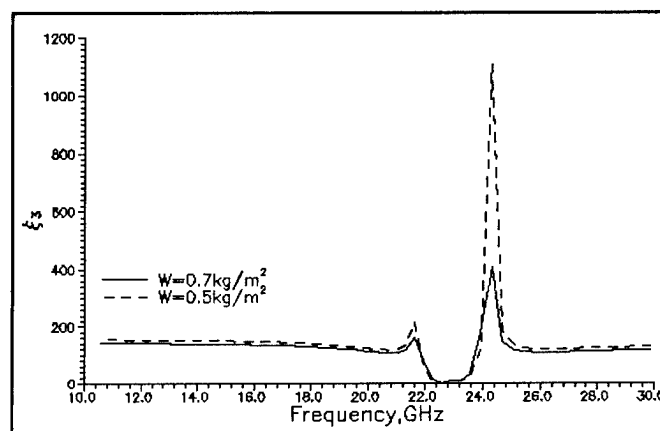
Fig.3 Optimal frequency choice when fixing $\nu_1 = 22.23$ GHz and $\nu_2 = 20.20$ GHz
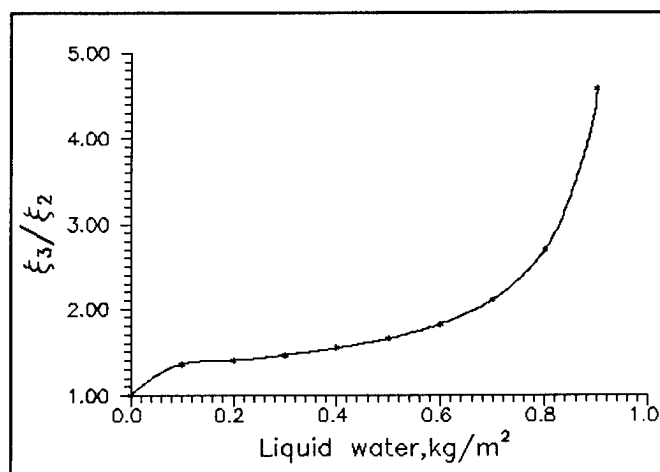
Fig.4 The effectiveness of using third frequency as a function of W of clouds for difference zenith-viewing observations

A Simple Model For Deriving Ocean Surface Wind Direction From The DMSP Special Sensor Microwave Imager (SSM/I)

Donald J. Boucher, Bruce H. Thomas, Kenneth N. Ricci, and A. Megumi Kishi
DMSP Environmental Applications Center
The Aerospace Corporation
P.O. Box 92957
Los Angeles, CA 90009
(310) 336-3327
boucher@aero.org

INTRODUCTION

The Special Sensor Microwave Imagers (SSM/I) currently flying on the DMSP polar orbiting spacecraft derive relatively high resolution surface wind speeds over the oceans. These wind speed retrievals are used as input to; (1) numerical weather prediction models, (2) Dvorak analysis of tropical cyclones, and (3) map the climatological distribution of global ocean winds and wind stress. The SSM/I is limited, however, to ocean surface wind speed only. Recently, techniques to infer wind direction from passive microwave measurements have been developed. Polarimetric measurements are currently of interest and researchers are beginning to develop airborne instruments as a proof of concept. Active devices such as microwave scatterometers are now flying that produce very high quality vector wind measurements. Some scatterometer measurements do, however, require that directional ambiguities be resolved. It is the goal of this paper to discuss a simple technique that could be used in conjunction with polarimetry and scatterometry to augment the complete description of boundary layer winds. We will discuss a simple technique first developed by T.S. Yu (1987), that yields a closed form solution to the horizontal momentum equations for the boundary layer vector wind field using in-situ satellite measurements as a source of wind speed data, and surface pressure gradient data from state-of-the-art numerical weather prediction models. The SEASAT scatterometer and altimeter data were originally used as a proof of concept for this technique. We will be describing an implementation using the SSM/I as the source of wind speed data, and the Air Force Global Weather Central (AFGWC) HIgh Resolution Analysis System (HIRAS) as the source of boundary layer pressure analysis. We will calculate a wind field at the resolution of the SSM/I, with time and space interpolation of the model surface pressure analysis to match the satellite measurements. It should be noted that

the HIRAS resolution is much coarser than the SSM/I data, therefore we are relying on the general smoothness of the surface pressure during the interpolation process. For future work, we will be evolving to MM5 (Grell, 1995) which is a very high resolution nested grid model originally designed by Penn State and modified by NCAR.

SSM/I DERIVED SURFACE WIND SPEED

The DMSP SSM/I's provide operational ocean surface wind speed retrievals using relatively simple multiple linear regression. There are a host of newer techniques being evaluated as a replacement for the simple regression schemes including neural nets (Stogryn, 1994), and physically-based retrievals. For the purposes of evaluating the following wind vector retrieval scheme for the SSM/I, we will use the globally applicable original Calibration and Validation wind speed algorithm (Hollinger, 1991), namely

$$S(m/s) = a_0 + a_1 T_{b19v} + a_2 T_{b22v} + a_3 T_{b37v} + a_4 T_{b37h}$$

where

$$a_0 = 147.9$$
$$a_1 = 1.0969$$
$$a_2 = -0.4555$$
$$a_3 = -1.76$$
$$a_4 = 0.786$$

There are a set of test criteria on the brightness temperatures that serve to screen pixels for rain contamination. We have included these tests in our algorithm implementation, and only run the model on uncontaminated SSM/I pixels. In the next section, we will briefly describe the model that we are using to extract vector information

using the SSM/I derived wind speed, and the AFGWC HIRAS numerical weather prediction model derived surface pressure analysis.

SSM/I DERIVED SURFACE WIND DIRECTION

The set of equations to be solved are the classic Ekman balances between the horizontal pressure gradient forces, the Coriolis force, and frictional forces. We will follow precisely the formalism of Yu, and write down the horizontal momentum equations

$$-fv = -\frac{1}{\rho}\frac{\partial p}{\partial x} + \frac{\partial}{\partial z}(K_m \frac{\partial u}{\partial z})$$

$$fu = -\frac{1}{\rho}\frac{\partial p}{\partial y} + \frac{\partial}{\partial z}(K_m \frac{\partial v}{\partial z})$$

(1)

where f is the Coriolis force, p is atmospheric pressure, u and v are the zonal and meridional components of the wind field. It is assumed that momentum fluxes in the boundary layer are proportional to the surface wind speeds, and that the fluxes vanish at the top of the boundary layer

$$K_m \frac{\partial}{\partial z}(u,v) \propto C_D |S|(u,v)$$

where K_m is the eddy diffusion coefficient for momentum, S is the SSM/I derived wind speed (i.e. $S = (u^2 + v^2)^{1/2}$), and C_D is the surface drag coefficient. We next integrate (1) from 10 meters to the top of the marine boundary layer (h). It is assumed that an "equivalent depth (σ)" exists independent of wind components that scale the surface contribution of the integral to represent the entire boundary layer

$$\int_{10m}^{h} (\frac{1}{\rho}\frac{\partial p}{\partial x} - fv)dz = \sigma(\frac{1}{\rho}\frac{\partial p}{\partial x} - fv)_{10m}$$

$$\int_{10m}^{h} (\frac{1}{\rho}\frac{\partial p}{\partial y} + fu)dz = \sigma(\frac{1}{\rho}\frac{\partial p}{\partial y} + fu)_{10m}$$

Equation (1) is now written with respect to quantities at the 10 meter level as

$$-fv = -\frac{1}{\rho}\frac{\partial p}{\partial x} - \hat{C}_D |S|u$$

$$fu = -\frac{1}{\rho}\frac{\partial p}{\partial y} - \hat{C}_D |S|v$$

(2)

where $\hat{C}_D$ is defined as C_D / σ. (2) now represents a very simple set of coupled differential equations that can be solved for the zonal and meridional wind components as follows

$$u = \frac{-1}{\rho f^2 + \rho \hat{C}_D^2 S^2}(f\frac{\partial p}{\partial y} + \hat{C}_D S\frac{\partial p}{\partial x})$$

$$v = \frac{1}{\rho f^2 + \rho \hat{C}_D^2 S^2}(f\frac{\partial p}{\partial x} - \hat{C}_D S\frac{\partial p}{\partial y})$$

$$\hat{C}_D = \frac{1}{S^2}\left[(\frac{1}{\rho}|\nabla p|)^2 - f^2 S^2\right]$$

This completes the model for calculating the directional information from the SSM/I wind speeds (S), and the model derived horizontal pressure gradients (∇p). This simple model is computationally robust even when the Coriolis parameter tends to zero. This technique relies on the HIRAS model surface pressure gradients to specify the boundary layer bulk flow with cross isobar tendencies provided by the surface drag paramaterization.

INITIAL RESULTS

We have analyzed a number of SSM/I derived versus model analyzed wind fields that closely agree both in magnitude and direction. The case that we present here represents a stressing condition in that the SSM/I generated wind field, and the model wind field strongly disagree. Fig. 1 represents the boundary layer flow in the Indian Ocean southeast of Madagascar as characterized by the AFGWC operational HIRAS. A very weak area of convergence is identified by the dashed line where the model wind field is in the range of a 2-3 m/sec. Fig. 2 is the corresponding SSM/I generated wind field analysis where we have assigned direction to each of the non-rain contaminated pixels. The SSM/I identified several sub-grid scale (to the analysis model) wind events with speeds approaching the upper limit of SSM/I validity at ~20 m/sec. The

SSM/I model identified strong areas of convergence (but no rain cells were flagged) in approximately the same location as the HIRAS analysis of weak convergence near -35S. A new area of convergence is identified in the SSM/I analysis at approximately -28S. The SSM/I wind field suggests the potential for strong convection in these areas that are not identified by HIRAS. We continue to investigate how well the SSM/I model performs under the conditions whereby the HIRAS boundary layer pressure field is not in balance with the observed SSM/I wind speeds.

SUMMARY

A simple model for calculating ocean boundary layer vector winds from a combination of SSM/I in-situ wind speeds, and numerical weather prediction model analysis of the surface pressure distribution has been presented. This technique can be used as an additional source of high resolution marine winds for typhoon forecasting, ship route planning, and climatological mapping of wind stress. In addition, this technique could be used to de-alias scatterometer data, and validate polarimetric measurements. We will be in the process of quantitative evaluation of this simple technique using the ERS-1 scatterometer data, buoys and ship reports at times that are coincident with the overpass of the DMSP spacecraft.

REFERENCES

[1] G. Grell, J. Dudhia, and D. Stauffer, "A Description of the Fifth Generation Penn State/NCAR Mesoscale Model (MM5)", NCAR TN-398, June 1995.
[2] J. Hollinger, "DMSP Special Sensor Microwave Imager Calibration/Validation", Naval Research Laboratory Final Report, July 1989.
[3] A. Stogryn, "Ocean Surface Wind Retrievals From SSM/I Data With Neural Networks", JGR, Vol.99, pg.981-984, January 1994.
[4] T.S. Yu, "A Technique For Deducing Wind Direction From Satellite Microwave Measurements of Wind Speed", Monthly Weather Review, pg. 1929-1939, September 1887.
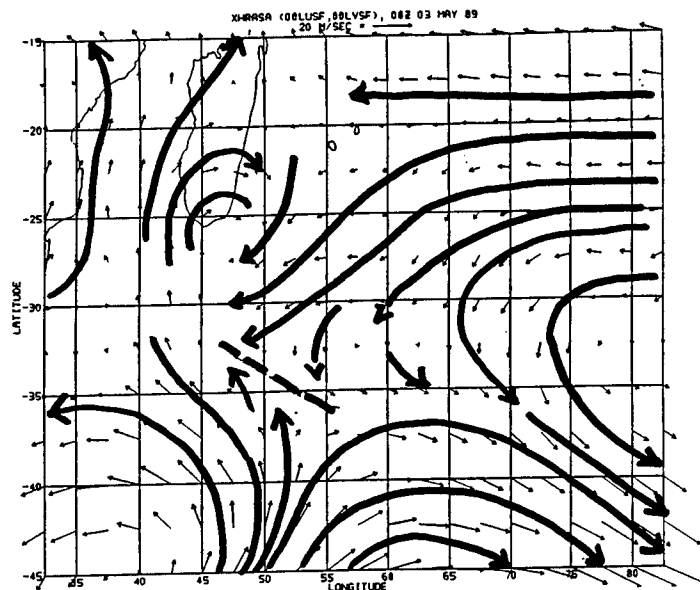
Fig. 1 AFGWC HIRAS Surface Wind Analysis
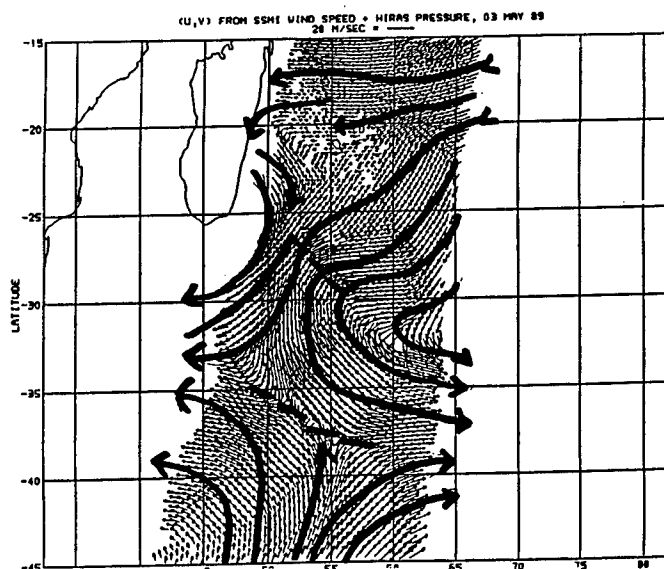
Fig. 2 SSM/I Derived Surface Wind Analysis

1706

Ocean Surface Wind Speed and Direction Retrievals from the SSM/I

Li Li[2], and Paul Chang[1]

[1]NOAA/NESDIS/Office of Research and Applications
NOAA Science Center, Room 102, E/RA13;Camp Springs, MD 20746
Phone:(301)763-8231 FAX:(301)763-8020
Email: pchang@orbit.nesdis.noaa.gov WWW: http://manati.wwb.noaa.gov/

[2]Caelum Research Corporation; Silver Spring, MD 20901
Email: lli@orbit.nesdis.noaa.gov

Abstract— A semi-empirical model is developed that permits retrieval of ocean surface wind direction information in addition to improved wind speeds from SSM/I measurements. With two SSM/I instruments currently providing operational ocean surface wind speed fields, the addition of wind direction information and improved wind speed retrievals will enhance its impact in weather prediction models and analysis.

I. INTRODUCTION

Accurate and timely measurements of the global ocean surface wind speed and direction are essential information for short-term weather forecasts and warnings and for seasonal and interannual climate forecasts. Current operational spaceborne sensors that can retrieve ocean surface wind information are the Special Sensor Microwave/Imagers (SSM/I) aboard the Defense Meteorological Satellite Platform (DMSP) and the Active Microwave Instrument (AMI) aboard the European Environmental Remote-Sensing Satellite (ERS). The AMI is a scatterometer system that provides ocean surface wind speed and direction, while SSM/I is a multi-channel radiometer that provides ocean surface wind speed information operationally. However, unlike the AMI scatterometer, the SSM/I system provides almost complete daily global coverage utilizing two satellites and a larger measurement swath.

The operational wind retrieval algorithms for AMI and SSM/I are empirical, derived from match-ups between buoy and satellite measurements. The accuracy of the remotely measured ocean wind speed and direction greatly influences its impact on numerical weather prediction (NWP) models. The current operational wind speed retrieval algorithm [1] for the SSM/I sensors have an rms error of more than 2 m/s. This error is partly due to the wind direction influence on the measured brightness temperature, which is not accounted for in the operational wind speed retrieval algorithm. While the brightness temperature of the ocean surface is not a strong function of the wind direction, it will limit the wind speed retrieval accuracy if it is not accounted for.

Since SSM/I is only a dual-polarization (vertical and horizontal) microwave radiometer, it cannot uniquely determine the wind direction. In a companion paper, we demonstrate that an airborne polarimetric microwave radiometer can retrieve wind direction without ambiguity. The airborne experiments also show that the ocean wind direction with two ambiguities can be determined from a dual-polarization radiometer. In this paper, a new semi-empirical SSM/I model is developed that can retrieve ocean wind speed with improved accuracy in addition to wind direction information. This model was derived and tested using match-up data sets between the SSM/I and NOAA National Data Buoy Center (NDBC) buoys. An accuracy of approximately 1 m/s is achievable if the wind direction effects on the measured brightness temperature are removed.

II. IN SITU MEASUREMENTS

In situ observations are crucial in the development and validation of all remote sensing retrieval algorithms. The operational SSM/I ocean wind retrieval algorithm is based on match-ups between buoys and satellite observations, however, these original match-up data sets do not contain satellite position information which is necessary to infer the satellite azimuth looking direction and its angle relative to the wind direction. Therefore, a new in situ match-up data set was created using 14 buoys located in the Northeast Pacific and the Gulf of Mexico. For this initial study, data was collected only for the month of April 1993, and therefore, a full range of wind speed cases (no data at speeds greater than 15 m/s) and any seasonal to interannual variations are not included. Other in situ data were also utilized, and included wind speed W_b, wind direction ϕ_b, air temperature T_a and sea surface temperature T_s. The temporal and spatial match-up windows were set at 1 hour and 30 km, respectively. Furthermore, the data set only considered data that met the operational rain flag 0 criteria, which is defined as $Tb37v - Tb37h > 50K$ and $Tb19h < 165K$. Two independent match-up data sets were constructed for the operational DMSP satellites F10 and F11. Since the wind direction signal is not clearly defined at low wind speeds, buoy wind speeds less than 2 m/s were excluded from the match-up data sets.

III. RADIATIVE TRANSFER

The microwave brightness temperature measured over the ocean surface is a function of the ocean surface conditions, primarily ocean surface wind speed and direction, and sea surface temperature. The atmosphere also contributes significantly

to the measured brightness temperature. However, since the atmospheric brightness temperature contributions are unpolarized (i.e., the vertically and horizontally polarized brightness temperatures are equal), the atmospheric contributions can be removed from the ocean surface signal. Following the approach of [4], a radiative transfer model is developed for the two SSM/I 37 GHz channels. The brightness temperatures observed by SSM/I can be calculated using simple radiative transfer equations [4],

$$T_{37v} = T_{Bu} + \tau[E_{37v}T_s + (1 - E_{37v})(1 + \omega_{37v}W)(T_{Bd} + \tau T_{Bc})] \tag{1}$$

$$T_{37h} = T_{Bu} + \tau[E_{37h}T_s + (1 - E_{37h})(1 + \omega_{37h}W)(T_{Bd} + \tau T_{Bc})] \tag{2}$$

where T_{37v} and T_{37h} GHz are the vertically and horizontally polarized brightness temperatures at 37 GHz. E_{37v} and E_{37h} are the vertically and horizontally polarized ocean surface emission as a function of wind speed which were derived by [4], [5] based on collocated Seasat microwave radiometer and scatterometer measurements. τ is the atmospheric transmittance along the viewing path of the radiometer. The product ωW is a correction factor for reflected atmospheric radiation contributions due to surface multiple scattering. T_{Bu} and T_{Bd} are the atmospheric upwelling and downwelling brightness temperatures, and T_{Bc} is the cosmic radiation background. T_s is the sea surface temperature, which can be obtained from the monthly optimum interpolation sea surface temperature fields in a one-degree grid [3].

In summary, the radiative transfer approach models the brightness temperature as a function of wind speed, sea surface temperature, atmospheric transmittance and satellite viewing angle. On the other hand, given SSM/I brightness temperatures at the 37 GHz channels, sea surface temperature and satellite viewing angle, an iterative approach, such as Newton's method, used with the radiative transfer function can retrieve wind speed and atmospheric transmittance [4].

IV. WIND SPEED AND DIRECTION RETRIEVAL

It has been demonstrated that the vertically and horizontally polarized brightness temperatures are both even functions of the relative wind direction, which is defined as the angle between the radiometer look angle and the wind direction [6], [4]. SSM/I data analysis by [4] and an airborne radiometer experiment by NRL and JPL indicate that vertical and horizontal brightness temperatures can be adequately approximated by truncating the harmonic series after the second term,

$$T_v = T_{v0} + T_{v1}\cos(\phi) + T_{v2}\cos(2\phi) \tag{3}$$

$$T_h = T_{h0} + T_{h1}\cos(\phi) + T_{h2}\cos(2\phi) \tag{4}$$

where ϕ is the relative wind direction. The first harmonic is related to the upwind/downwind asymmetry of ocean gravity waves and whitecaps, while the second harmonic is related to the capillary waves on the gravity waves [2]. The amplitude of each harmonic is a function of the ocean surface wind speed, sea surface temperature and atmospheric transmittance. Since T_v and

T_h are both even functions, the wind direction can not be detected uniquely from SSM/I measurements. Nevertheless, the wind direction signal is well represented by $cos(\phi)$ and $cos(2\phi)$, which, if considered in the retrieval scheme, will enhance the wind speed accuracy by reducing the "noise" from the wind direction signal in the measured brightness temperatures. And, wind direction information is retrieved in the form of $cos(\phi)$.

Wind direction signals in the SSM/I brightness temperatures are not considered in the radiative transfer wind retrieval model used in this study. As a result, wind speed retrievals from such an iterative radiative transfer model will contain errors which are correlated to the relative wind direction [4]. Therefore, using buoy reports as ground truth, the difference between SSM/I retrievals, W, and buoy reported windspeed, W_b, are used to determine the brightness temperature perturbations caused by the wind direction through radiative transfer model. Wind speed and direction signals can then be easily separated for each buoy and SSM/I match-up. This separation procedure readily handled using neural networks. To avoid the ambiguity of retrieving wind direction from dual-polarization radiometer observations, the wind speed from buoys W_b, wind direction $cos(\phi)$ and $cos(2\phi)$ are included in the neural network training targets. The atmospheric transmittance obtained from iterative radiative transfer model is also used as an approximation. This combined neural network retrieval model couples iterative radiative transfer model with neural network techniques.

V. MODEL VALIDATION AND PRELIMINARY RESULTS

The two operational SSM/I satellites, F10 and F11, have similar characteristics, but because of residual system biases, each satellite data set needs to be individually calibrated with buoy match-ups. After calibration, wind speed and direction retrieval algorithms are derived using the iterative radiative transfer approach and the combined neural network inversion technique. F11 SSM/I data and buoy match-ups were used for the model development, and F10 SSM/I data and buoy match-ups for the model evaluation. Table 1 lists the error statistics for three different wind speed retrieval algorithms: Goodberlet algorithm [1], iterative radiative transfer model, and the combined neural network model. Table 2 lists the error statistics of $cos(\phi)$ and $cos(2\phi)$ retrievals using combined neural network model. Figure 1 plots the buoy wind speed against the retrieved wind speed values from F10 measurements. The small circles are the wind speeds obtained from the combined neural network model, and the dots are the winds speed from Goodberlet algorithm. The combined neural network model performs better than the Goodberlet algorithm. Figures 2 plots $cos(\phi)$ derived from buoy wind direction against $cos(\phi)$ derived from SSM/I F10 measurements. $cos(2\phi)$ is plotted in figure 3. As seen in figures 2 and 3, the retrieved wind direction signals, $cos(\phi)$ and $cos(2\phi)$, show good agreement with buoy measurements.

VI. CONCLUSIONS

These results clearly indicate that a substantial improvement can be realized for wind speed retrievals, and that wind direc-

TABLE I
STATISTICS ON WIND SPEED RETRIEVAL

	Operational	Iterative RT	Combined
Training (F11)	2.30	1.72	0.969
Testing (F10)	2.24	1.72	0.965

TABLE II
STATISTICS ON WIND DIRECTION RETRIEVAL

	First Harmonic	Second Harmonic
Training (F11)	0.1982	0.2309
Testing (F10)	0.2433	0.2782

Fig. 2. Scatter plot of buoy $cos(\phi)$ versus retrieved $cos(\phi)$ from the combined neural network model.

Fig. 3. Scatter plot of buoy $cos(2\phi)$ versus retrieved $cos(2\phi)$ from the combined neural network model.

tion information can be retrieved using the combined neural network approach. Future work will include extending the matchup data set to cover a larger range of wind conditions to validate this model on a global scale, and then demonstrate its operational implementation.

REFERENCES

[1] Goodberlet, M.A. and C.T.Swift, Improved retrieval from the DMSP wind speed algorithm under adverse weather conditions, IEEE Trans. Geoscience Remote Sensing, 30, 1076–1077, 1992.

[2] Kunkee, D.B., and A.J. Gasiewski, Airborne passive polarimetric measurements of sea surface anisotropy at 92 GHz, International Geoscience and Remote Sensing Symposium, IEEE, Pasadena, 1994.

[3] Reynolds, R.W. and T. M. Smith, 1994: Improved global sea surface temperature analysis using optimum interpolation. J. climate, 7, 929-948.

[4] Wentz, F.J., measurement of oceanic wind vector using satellite microwave radiometers, IEEE Trans. Geoscience and Remote Sensing, 30(5), 960-972, 1992.

[5] Wentz, F.J., A model function for ocean microwave brightness temperatures, J. Geophy. Res., 88(C3), 1892-1908, 1983.

[6] Yueh, S.H., R. Kwok, and S.V. Nghiem, Polarimetric scattering and emission properties of targets with reflection symmetry, Radio sci., 29(6), 1409-1420, 1994.

[7] Yueh, S.H., W.J. Wilson, F.K. Li, W.B. Richetts, and S.V. Nghiem, Polarimetric measurements of sea surface brightness temperatures using an aircraft K-band radiometer, IEEE Trans. Geoscience and Remote Sensing, 1995.

Fig. 1. Scatter plot of buoy wind speeds versus retrieved wind speeds from the combined neural network model.

Assessing the Ocean Surface Vector Wind Signal in SSM/I Data Using Neural Networks

John Bates
NOAA/ERL Climate Diagnostics Center
325 Broadway
Boulder, CO 80309
(303)497-6646(voice) (303)497-7013 (fax) bates@cdc.noaa.gov

K. ChesleyMcColl
Cooperative Institute for Research in Environmental Studies
Campus Box 449
Boulder, CO 80309
(303)492-7304 voice) (303)497-7013 (fax) chesley@cdc.noaa.gov

INTRODUCTION

Minimization techniques have long been used by the remote sensing community to obtain relationships between observed radiances and retrieved geophysical quantities. Originally, special sensor microwave imager (**SSM/I**) passive microwave wind observations were regressed against coincident wind speed observations from buoys. More recent research has shown that a wind direction signal may also be present in SSM/I observations. This wind direction signal, however, is not very large, meaning that accounting for the error characteristics of this signal is very important, and it is believed that the signal is somewhat non-linear. Thus, more advanced minimization techniques are required to extract this wind direction signal. Neural networks (**NN**) are a non-linear minimization technique and they can be used either in simulation mode, where the net is trained using simulated radiances assumed to be the truth, or in observation mode, where the observed radiances are matched with in situ observations.

BACKGROUND

Surface wind speed retrievals have been modeled successfully using neural networks [1]. It was shown that the NN had advantages over empirical algorithms, for 3< wind speeds <15 m/s. The accuracy of the low and high wind speed (**WS**) calculations were affected by not having sufficient SSM/I vs buoy matched data. In the case of wind direction, empirical algorithms, using just SSM/I retrievals, are insufficient.

DATA

In this study we first considered simulated vector wind data. Because the wind direction signal is larger for higher wind speeds, we limited our simulated study to wind speeds of 7 - 20 m/s, and because of the symmetry of the change in brightness temperature with wind direction, we limited our simulated study to wind directions of 0-180 degrees. The test and training sets were generated by parametrically varying wind speed (**WS**), wind direction, and Sea Surface Temperature (**T_s**).

An empirical model of the wind direction dependence (1) and specular emissivity (2) were employed [2].

$$T_B = B_1 \cos\phi + B_2 \cos 2\phi \qquad (1)$$

$$E_0 = (s_0 + s_1 t + s_2 t^2 + s_3 t^3 + s_4 q + s_5 tq + s_6 q^2 + s_7 t^2 q)/T \qquad (2)$$

$$T = T_s - 273.16$$

$$q = \Theta_i - 51°$$

Where B_i is a function of wind speed, and sea surface temperature, the coefficients for both equations can be found in [1]. The inputs, Tb19v(19 GHz vertically polarized brightness temperature), Tb19h (19 GHz horizontally polarized brightness temperature), wind speed, and T_s where then rescaled to obtain values ranging from 0 to 1. The learning and training sets were created such that the wind direction and T_s were statistically homogeneous, same number of samples in each direction and T_s.

NEURAL NETWORKS

A network consists of units, input units, hidden units and output units. In this study we had four inputs, (Tb19h, Tb19v, wind speed, T_s), 10 hidden units, and 19 outputs (wind direction in 10 degree bins). The network was fully connected, and a standard backward propagation method was used. The activation function, or squashing function, used was the logistic function.
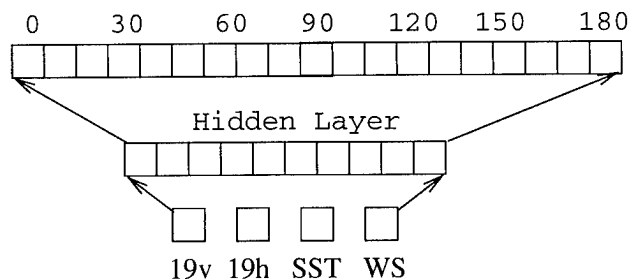
Fig 1. An example of the neural network architecture used in this study. This is a fulling connected network, all units are connected to all other units.

For the simplest case of using a single $T_s = 290K$, ie brightness temperature, the NN performs very well, +/- 10 degrees for all wind directions (**Fig. 2**). When adding the complexity of many different sea surface temperatures, the NN doesn't perform as well, yet still can determine the wind direction to within +/- 30 degrees (**Fig. 3**).

The mean square error for this NN was 0.4331, this is the criteria for adequacy of the true model in the population, when the sample size >> number of hidden units.
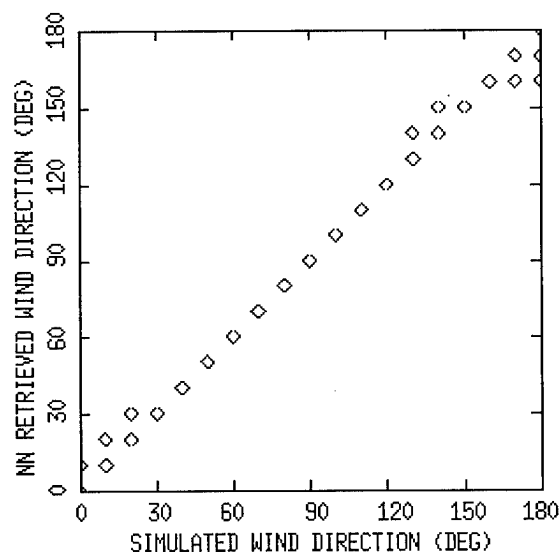
Fig 2. When using only a sea surface temperature of 290K, the NN solves for wind direction extremely well.
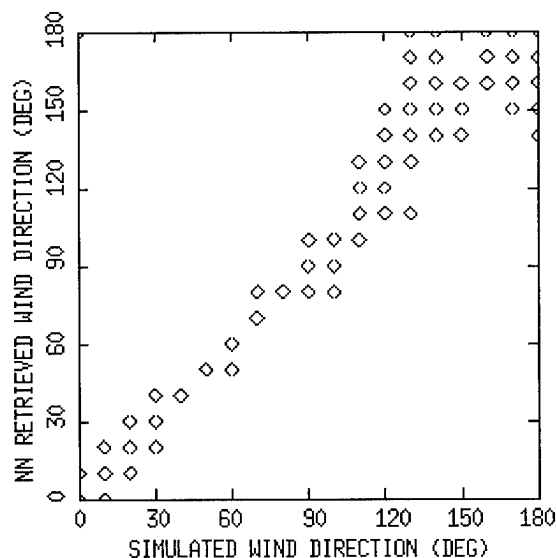
Fig 3. When using a range of sea surface temperatures from $290 < T_s < 304K$, the NN solves for wind direction to within +/- 20 degrees.

FUTURE WORK

Although we have demonstrated that the NN can be trained to retrieve wind direction reasonably well using simulated data, we have not been successful as of yet in training the NN to retrieve wind direction using a matched SSM/I versus buoy observational data set. We believe this may be due to inadequate quality control of this observational data set, since we initially have tried only a minimum level of quality control. In addition, we are evaluating improved radiative transfer models to better account for the atmospheric influences on microwave brightness temperatures. We are also examining different averaging techniques in a attempt to isolate the SSM/I wind direction signal from other variability in the SSM/I brightness temperatures. Additional results will be presented at the Conference.

[1] V. M. Krasnopolsky, L. C. Breaker, and W. H. Gemmill, "A neural network as a nonlinear transfer function model for retrieving surface wind speeds from the special sensor microwave imager," Journal of Geophysical Research, Vol. 100, pp. 11033-11045, June 1995.

[2] F. J. Wentz,"Measurement of Oceanic Wind Vector Using Satellite Microwave Radiometers," Remote Sensing Systems Technical Report 051591, May 1991.

Surface Winds from the SSM/I Using Neural Networks

V. M. Krasnopolsky[1], L.C. Breaker and W.H. Gemmill
Environmental Modeling Center, National Centers for Environmental Prediction
W/NMC21, Room 207, 5200 Auth Rd., Camp Springs, MD 20746
Phone: (301)763-8133, Fax: (301)763-8545, e-mail: kvladimir@sgi78.wwb.noaa.gov

Abstract -- An improved neural network (NN) wind speed retrieval algorithm which covers the entire range permitted for retrievals both with respect to moisture and wind speed is presented. Improvements in the NN approach have permitted the development of a wind speed retrieval algorithm which can retrieve wind speeds up to ~25 m/sec for LWP concentrations ≤ 0.5 kg/m^2, with a bias of ~0.2 m/s and an rms error of ~1.75 m/s. Also, results are presented which demonstrate significant correlation (correlation coefficient ~0.75) between wind directions retrieved, using a NN, and buoy wind direction. Although the F10 SSM/I data set which was used in this study was noisy, higher quality data are now being used to develop a prototype for a NN wind direction retrieval algorithm for the SSM/I.

INTRODUCTION

Retrieving surface winds from the SSM/I instrument has two primary limitations: (I) the level of moisture in the intervening atmosphere, and (ii) the extent of whitecaps and foam (WF) over the surface of the ocean. The geophysical transfer function becomes significantly nonlinear when liquid water path (LWP)≥ 0.1 kg/m^2, and little or no information reaches the SSM/I from the surface when LWP ≥ 0.5 kg/m^2 [1]. Secondly, the WF restriction also gives rise to an upper limit in terms of the maximum wind speed which may be retrieved (~25-30 m/sec [2]), using microwave radiometry, and to nonlinearity in the transfer function at wind speeds higher than about 7-10 m/sec.

The fact that the empirical transfer function for the SSM/I wind retrieval problem is essentially nonlinear is compounded by the problem that the types of nonlinearity are not known a priori. Thus, linear and nonlinear regression approaches, which are routinely used to model such empirical transfer functions, have only limited success. NNs are well-suited to serve as flexible nonlinear models for a very broad class of nonlinear transfer functions [1].

NN algorithms which were initially developed [1,3] to retrieve wind speeds from the SSM/I were both moisture and high wind speed limited. Subsequently, a single, extended-range (SER) NN algorithm was developed [1] which covered the entire domain of moisture levels ($0 \leq$ LWP < 0.5 kg/m^2). However, this algorithm was still wind speed limited, with the accuracy of retrievals dropping off significantly at wind speeds

higher than 14-15 m/sec and in no case could generate wind speeds higher than ~18 m/sec. Further improvements in the NN approach, particularly at higher wind speeds, led to an improved NN retrieval algorithm [2] which covers the entire retrieval range both with respect to moisture and wind speed.

The existing of wind directional signature in the SSM/I data has been established both theoretically and empirically [4,5]. However, in retrieving wind direction from the SSM/I, two problems must be addressed, (1) the amplitude of the signal is very small and (2) an ambiguity may exist in the wind direction retrievals. Because of these problems, an SSM/I wind direction retrieval algorithm has not yet been developed. We proceed to show that the NN approach which is sensitive to even small systematic signals may provide a practical tool for wind direction retrievals from the SSM/I.

WIND SPEED

To develop a new NN algorithm which is capable of generating higher wind speeds than our previous SER NN algorithm, we have initially examined the sensitivity of the different SSM/I channels to changes in wind speed, and then developed a new training strategy, followed by a correction for the expected systematic residual error. As a result, a new NN architecture has been developed which differs significantly from that used previously [2,3].

We have found that in addition to the original four channels [19GHz(V), 22GHz(V), and 37GHz(H,V)] that have been used in most previous SSM/I wind speed retrieval algorithms, the 85GHz(V) channel can further improve wind speed retrievals (especially at higher wind speeds) and, consequently, it has been included in the development of a new retrieval algorithm.

Because there are very few matchups available at higher wind speeds (w > 15 m/sec), the distribution of wind speeds in the training set is highly nonuniform . If we use the standard cost function in NN training, where all of the data are equally weighted, the few matchups that do exist at high wind speeds become completely obscured in the training process. This problem can be reduced if a weighted cost function is used for training instead of the standard cost function. A weighted cost function can be expressed as (1), where, N is the number of matchups in the training set, the W_i are the wind speeds obtained during the training process, the w_i are the observed buoy wind speeds, and the α_i are the weights.

$$E = \frac{1}{N} \sum_{i=1}^{N} \alpha_i \, (W_i - w_i)^2 \qquad (1)$$

Because a uniform data distribution is clearly preferable for training, the distribution of the α_i can be chosen to compensate for the inherent nonuniformity of wind speeds in our training set. A distribution which is inversely proportional to the square root of the wind speed distribution was found to be an acceptable choice. For such a weighting scheme, the highest wind speeds are emphasized and the NN is forced to learn more from these few cases. The penalty, of course, is that any errors at high wind speeds will be amplified during the training process.

Weighting the error function as indicated in (1), improves performance of the NN significantly for wind speeds in the interval from ~12m/s to 20m/s where little data exist; however, it does not improve the performance of the NN significantly for wind speeds higher than ~20m/s. In this high wind speed region the transfer function is clearly not supported by the empirical data. The only way to improve the NN empirical transfer function in this region is to introduce an empirical correction. We examined the bias of the NN model and found that the bias as a function of wind speed (binned and calculated as the difference between the buoy and the NN-generated wind speeds) for the training set has a systematic trend which we approximate by the following expression,

$$b(w) = a + b \, (w - c)^3 \, (1 - exp(-dw)) \qquad (2)$$

By applying the bias correction $b(w)$ to the wind speed w generated by the NN algorithm as

$$w = NN \, (T), \; where \; T = [t19v, \, t22v, \, t37v, \, t37h, \, t85v] \qquad (3)$$

we obtain the wind speed w_c, which is now corrected for the systematic error as

$$w_c = w + b(w) \qquad (4)$$

In these calculations, the same training set has been used for developing the NN and for calculating the bias correction, $b(w)$.

Equations (3) and (4) together constitute an algorithm called the OMB algorithm. Table 1 shows summary statistics for the multiple linear regression (MLR) algorithm [6], our original SER NN [1] and the OMB NN algorithms [2] which were tested on the same independent test set. The upper part of Table 1 shows the total statistics and the lower part shows the high wind speed statistics for wind speeds $w > 15$ m/s. The weather conditions correspond to the clear plus cloudy case [3] or to 0. $< LWP < 0.5$ kg/m^2. Maximum wind speeds are also shown for comparison. We have started testing of the OMB NN on data from the currently operational F10 and F13 instruments. Our

Table 1. Total and high wind speed statistics.

Total	Max w	Bias	RMS
Buoy	21.2	N/A	N/A
MLR	28.8	-1.42	2.69
SER NN	16.1	-0.01	1.56
OMB NN	22.0	0.17	1.74
$w > 15 \; m/s$			
MLR	25.3	-1.5	2.84
OMB NN	22.0	0.28	2.27

initial results show that the OMB NN outperforms the MLR algorithm; however, both of these algorithms have lower retrieval accuracy than for F8 instrument. It means that the OMB NN algorithm must be modified for new satellites (NNs should be retrained and new bias corrections obtained).

WIND DIRECTION

Is has been shown empirically [4] and theoretically [5] that the SSM/I brightness temperatures (BTs) contain a low amplitude wind directional signal. Because the amplitude of this signal (~ 2 - 4° K) is weak, neither empirical no theoretical approaches have yet to succe·d in developing an algorithm for retrieving SSM/I wind direction. Only two components (Q and U) of the Stokes vector S (5) contain information on wind direction [5], where

$$S = \begin{bmatrix} I \\ Q \\ U \\ V \end{bmatrix} = \begin{bmatrix} T_v + T_h \\ T_v - T_h \\ T_p - T_m \\ T_l - T_r \end{bmatrix} \qquad (5)$$

Here $T_{v,h}$ corresponds to the vertical and horizontal polarizations, $T_{p,m}$ to the $\pm45°$ polarizations, and $T_{l,r}$ to left- and right-hand circular polarizations. However, only Q is available from the SSM/I. Even if a low amplitude wind direction signal could be extracted from the BTs, there would still be an ambiguity in the retrieved wind vectors since Q depends only on $cos(\theta)$ and $cos(2\theta)$.

To examine the possibility that NNs can retrieve a wind directional signal from SSM/I, we applied a NN to a small data set from the F10 instrument. This data set is limited in that: (1) F10 has an elliptical orbit, (2) there is no information about satellite viewing geometry, (3) only less than 300 matchups are

within 25 km and 0.5 hours of the buoy data. For testing, we ~1,000 matchups which were within 50 km and 0.5 hours of the buoy data.

Two NNs were trained   The first one has been trained to retrieve $cos(\theta)$ and $cos(2\theta)$, and the second one, $cos(\theta)$ and $sin(\theta)$. All seven BTs were used as NN inputs. Using the test set, both NNs were able to retrieve $cos(\theta)$ with an rms error of ~0.5. The correlation coefficient (CC) between the buoy $cos(\theta)$ and the NN-generated $cos(\theta)$ was ~0.76. For $cos(2\theta)$ the first NN gives an rms error of ~0.59 and a CC of ~0.52; for $sin(\theta)$, the second NN gives an rms error of ~0.5 and a CC of ~0.61.

For $cos(\theta)$, the correlation between the NN retrievals and the buoy data is considered significant, and our results suggest that NNs can retrieve $cos(\theta)$. Using better matchup data and additional information (such as satellite viewing angles, SST, and moisture concentration), both the rms error and the correlations may be improved. Regarding $cos(2\theta)$ and $sin(\theta)$, our calculations demonstrate better statistics for $sin(\theta)$, an unexpected result according to the theory; however, the high noise level in our data prevents us from considering these correlations as significant.

DISCUSSION AND CONCLUSIONS

A new OMB NN algorithm has been developed using only the SSM/I F8 database. This database has many limitations; it does not have a sufficient number of matchups at high wind speeds, high latitudes are poorly represented, and matchup uncertainties could be reduced. The OMB algorithm was tested on matchup data for the F10 and F13 SSM/I instruments and showed significant improvements both in the accuracy of the retrievals and in providing increased areal coverage as compared with the current operational algorithm [6]. The OMB algorithm has been applied to extratropical cyclones in both hemispheres at mid-latitudes characterized both by significant moisture and high wind speeds. Wind speed retrievals from both the F10 and F13 instruments based on the new algorithm, showed major improvements in resolving details in surface wind speed patterns. However, the absolute errors which the OMB NN (and the current operational MLR algorithm) demonstrated for F10 and F13 were higher than for the original F8 data set. Taking into account these limitations, the OMB algorithm will be re-evaluated and improved when a more representative matchup database is produced.   The creation of such a database is presently underway.

Regarding the possibility of retrieving wind direction, our results demonstrate that even our relatively simple approach (no information except BTs was used for the NN training) enabled us to retrieve $cos(\theta)$. Thus, the NN is sensitive enough to recognize the weak wind direction signal in the SSM/I BTs and to retrieve this signal. If no signal of significant amplitude which is proportional to odd functions of wind direction exist in the BTs, wind direction retrievals will be ambiguous ($\pm \theta$ ambiguity) and a future SSM/I wind direction retrieval algorithm must include an ambiguity removal procedure.

Overall, the NN approach is a useful tool in addressing the SSM/I wind retrieval problem.   It has a great potential as a generic tool for the empirical solution of inverse problems in remote sensing.   It is very flexible and can also be used in combination with theoretical approaches.

REFERENCES

[1] V. Krasnopolsky, L.C. Breaker, and W.H. Gemmill, A neural network as a nonlinear transfer function model for retrieving surface wind speeds from the special sensor microwave imager, *J. Geophys. Res, 100,* 11,033-11,045, 1995.

[2] V. Krasnopolsky, L.C. Breaker, and W.H. Gemmill, Improved SSM/I wind speed retrievals at higher wind speeds, *submitted to J. Geophys. Res*, 1995.

[3] A.P. Stogryn, C.T. Butler, and T.J. Bartolac, Ocean surface wind retrievals from special sensor microwave imager data with neural networks, *J. of Geophys. Res., 90,* 981-984, 1994.

[4] F.J. Wentz, Measurement of oceanic wind vector using satellite microwave radiometers, *IEEE Trans. Geosci. Remote Sens., GE-30,* 960-972, 1992.

[5] S.H. Yueh,,S.V. Nghiem, R. Kwok, W.J. Wilson and F.K. Li, Polarimetric thermal emission from periodic water surfaces", *Radio Science,* vol. 29, pp. 87-96, 1994

S.H. Yueh, W.J. Wilson, F.K. Li, S.V. Nghiem and W.B. Ricketts, Polarimetric measurements of sea surface brightness temperatures using an aircraft K-band radiometer, *IEEE Transactions on Geoscience and Remote Sensing,* vol. 33, pp. 85-92,1995

[6] M.A. Goodberlet, C.T. Swift, and J.C. Wilkerson, Remote sensing of ocean surface winds with the Special Sensor Microwave/Imager, *J. Geophys. Res., 94,* 14,574-14, 555, 1989.

Development of a Statistical Method for Eliminating Improbable Wind Aliases in Scatterometer Wind Retrieval

Travis E. Oliphant and David G. Long
Brigham Young University
459 CB, Provo, UT 84602
801-378-4884, FAX: 801-378-6586, e-mail: oliphant@newt.ee.byu.edu

Abstract -- Wind velocities over the ocean can be estimated using measurements from spaceborne scatterometers by inverting the Geophysical Model Function (GMF) which relates normalized backscatter to wind velocity. Current estimation procedures employ maximum-likelihood techniques. Unfortunately, there are several local maxima of the maximum-likelihood function. As a result, several (2-6) wind estimates are returned as possible solutions at each wind vector cell. An ambiguity-removal step is required to determine a wind field. In this paper, we develop a statistical test to distinguish among the maxima of a maximum likelihood equation, and apply it to wind estimation. An upper bound is derived on the probability of error if a lower likelihood wind estimate is discarded. This bound is used to eliminate improbable wind solutions. Using this procedure we show that for most ERS-1 wind vector cells the number of wind estimates can be reduced to two. This reduces the complexity of the ambiguity-removal step while at the same time increasing the confidence in the entire retrieved wind field.

INTRODUCTION

Spaceborne scatterometers are a proven method of estimating wind velocities over the earth's oceans. A wind scatterometer makes indirect measurements of the normalized radar backscatter coefficient, σ^o, of the ocean's surface. The backscatter is then related to the wind velocity over the surface by inverting an empirical relationship called the Geophysical Model Function (GMF). Wind retrieval algorithms are based on the optimization of a maximum-likelihood (ML) objective function which is based on a statistical model of the σ^o measurements.

Unfortunately, in general there are multiple wind velocities, or ambiguities, which give maxima of the likelihood function. Current techniques keep all of the local maxima of the likelihood function for further processing by an ambiguity-removal algorithm which uses correlation in adjacent cells or other techniques to determine a wind field.

However, keeping all the wind vectors which give local maxima of the likelihood function does not adhere to the general philosophy of a maximum likelihood estimate: pick the wind velocity which gives the largest probability that the measurements would have been observed. It is hard to statistically justify retaining a wind velocity estimate that has a distinctly lower likelihood value than the maximum value. The problem is determining how much lower the likelihood value should be before the wind velocity solution is eliminated as a

possible wind vector. A solution to this problem is to formulate a probabilistic question, and then place a probability threshold for eliminating wind vectors at a statistically satisfying level.

It is important to note that the technique developed below for resolving maxima in a ML equation with multiple maxima can be employed in any ML estimation procedure. The notation given in developing the technique is convenient for wind estimation but the technique is general.

STATISTICAL TEST

To establish notation, let z be a vector of σ^o measurements, and let w be the wind vector. Let z_0 be a particular vector of measurements and w_0 and w_1 particular wind vectors associated with the maxima of the log-likelihood function, i.e., w_0 and w_1 are two ambiguities, where w_1 is the most-likely ambiguity of the set of ambiguities resulting from point-wise wind retrieval. In addition, let $M_{k,i}$ be the value of the Geophysical Model Function (GMF) when the wind is w_i and the measurement is taken with the incidence and azimuth angles corresponding to the σ^o measurement z_k. Furthermore, $\sigma_{k,i}^2$ is the variance of the measurement z_k assuming a wind of w_i.

We want to develop a statistical test to determine if we should retain ambiguity w_0 for further processing. To do this we evaluate the probability that the observed ratio of likelihood values would be as large if w_0 is the true wind. In other words we want to evaluate the probability that $p_z(z|w_1) \geq \mathcal{K} p_z(z|w_0)$ given that w_0 is the true wind. The constant $\mathcal{K}$ is the observed likelihood ratio, $\mathcal{K} = p_z(z_0|w_1)/p_z(z_0|w_0)$. In other words, define

$$\alpha_0(\mathcal{K}) = \text{Prob}[p_z(z|w_1) \geq \mathcal{K} p_z(z|w_0)|w_0], \quad (1)$$

α_0 is then the probability that the likelihood ratio, $\mathcal{K}$, would be observed if the lower-ranked ambiguity (w_0) is the true wind. A small value of α_0 suggests that w_0 is not a reasonable wind estimate and can thus be discarded.

To simplify the calculation of α_0 we use the log-likelihood ratio $\log \mathcal{L}(z)$ where

$$\log \mathcal{L}(z) = \log[p_z(z|w_1)/p_z(z|w_0)]$$

and calculate the probability that $\log \mathcal{L}(z) \geq \log \mathcal{K}$ given w_0 is the true wind. This ratio can be written as

$$\log \mathcal{L}(z) =$$
$$\sum_{k=1}^{N} \left[\log\left(\frac{\sigma_{k,0}}{\sigma_{k,1}}\right) + \frac{(z_k - M_{k,0})^2}{2\sigma_{k,0}^2} - \frac{(z_k - M_{k,1})^2}{2\sigma_{k,1}^2} \right], (2)$$

where again $M_{k,i}$ denotes the value of M_k assuming a wind of $\mathbf{w}_i$ and $\sigma_{k,i}$ is the value of σ_k assuming a wind of $\mathbf{w}_i$. Note that in this paper the CMOD-FDP GMF is used [1].

We define several variables useful in simplifying this expression and obtaining the probability density function in order to evaluate the probability.

$$a = \sum_{k=1}^{N} \log\left(\frac{\sigma_{k,0}}{\sigma_{k,1}}\right), \qquad b = \sum_{k=1}^{N} \frac{(M_{k,0}-M_{k,1})^2}{2\sigma_{k,1}^2},$$

$$c_k = \frac{1}{2}\left(1 - \frac{\sigma_{k,0}^2}{\sigma_{k,1}^2}\right), \qquad d_k = \frac{\sigma_{k,0}(M_{k,0}-M_{k,1})}{\sigma_{k,1}^2},$$

$$x_k = \frac{(z_k) - M_{k,0}}{\sigma_{k,0}},$$

and the random variable l,

$$l = \log\mathcal{L}(\mathbf{z}) - a + b = \sum_{k=1}^{N}\left(c_k x_k^2 - d_k x_k\right). \tag{3}$$

Note, that assuming $\mathbf{w}_0$ is the true wind implies that each x_k is a zero-mean, unit-variance, Gaussian random variable. Now, α_0 can be computed as the probability that l, a random variable which is a function of the measurements, is greater than or equal to $y = \log\mathcal{K} - a + b$ given that $\mathbf{w}_0$ is the true wind. Thus,

$$\alpha_0(\mathcal{K}) = \int_y^{\infty} p_l(l|\mathbf{w}_0)dl. \tag{4}$$

Calculating the probability function of l is a difficult task in general. However, the moment-generating function can be obtained in a fairly straightforward manner since the measurements are independent. The result is

$$\Phi_l(s) = \prod_{k=1}^{N} \frac{1}{\sqrt{1-2c_k s}} \exp\left(\frac{d_k^2 s^2}{2 - 4c_k s}\right) \tag{5}$$

The central limit theorem guarantees that as N gets large (corresponding to more measurements) the distribution of l approaches a normal distribution with mean $\eta = \sum_{k=1}^{N} c_k$ and variance $\sigma^2 = \sum_{k=1}^{N}(d_k^2 + 2c_k^2)$. For large N this makes calculation of α_0 a trivial task. For small N the distribution of l is more complicated but can be expressed asymptotically as a normal density plus an error term. The error term can be written in terms Hermite polynomials and moments of the density function [2]. These moments can be obtained, in principle, from the moment-generating function of l. Thus, a series solution for α_0 can be found. Defining $v = (y - \eta)/(\sqrt{2}\sigma)$ we obtain.

$$\alpha_0 = \frac{1}{2}\left[1 - \mathrm{erf}(v)\right] + \sum_{k=3}^{\infty} \frac{C_k}{\sqrt{\pi}} e^{-v^2} H_{k-1}(v) \tag{6}$$

where

$$C_k = \sum_{m=0}^{\left[\frac{k-3}{2}\right]} \frac{(-1)^m \left(E\left[(l-\eta)^{k-2m}\right] - L_{k,m}\right)}{m!(k-2m)!\sigma^{k-2m}2^{k/2+m}} \tag{7}$$

$$L_{k,m} = \begin{cases} 0 & k \text{ odd,} \\ \sigma^{k-2m}(k-2m-1)!! & k \text{ even.} \end{cases} \tag{8}$$
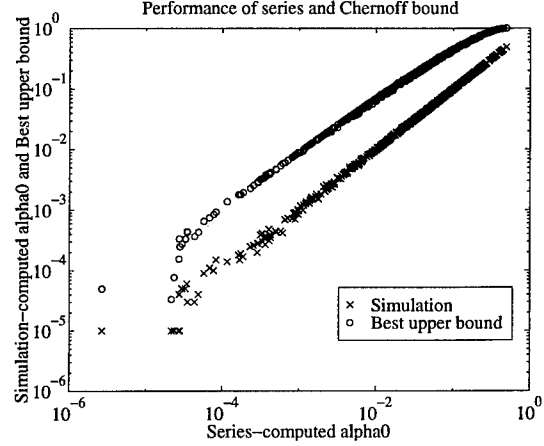
Figure 1: *Plot of α_0 estimated from simulation versus α_0 estimated from four terms of series in (6). Also a plot of the best Chernoff bound versus the series calculation of α_0.*

Simulation suggests that more than four terms are required to get an accurate value of α_0 when there is large variance in the measurements due to large modeling error. Since the moments of l become increasingly cumbersome to calculate, an alternative approach may be used which involves only an easily computable upper bound on the value of α_0.

By establishing an upper bound on α_0, a conservative decision can be based on the value of the upper bound rather than the exact value. A relatively tight upper bound is the Chernoff bound which states that for arbitrary $s > 0$,

$$\alpha_0 \le e^{-sy}\Phi_l(s) \tag{9}$$

where $\Phi_l(s)$ is the moment generating function of l.

The tightest Chernoff bound is obtained by finding the value of s that minimizes $e^{-sy}\Phi_l(s)$, or $-sy + \log(\Phi_l(s))$. Such a value is a positive real root of a polynomial of order $2N$, restricted to ensure a real value of $\Phi_l(s)$. Thus, the minimum value of the bound can be found in a computationally tractable way. However, to speed computation a single value of s for global use is often used. Testing using ERS-1 orbit parameters shows that $e^{-sy}\Phi_l(s)$ is extremely flat around the minimum value near $s = 1$. Thus, $s = 1$ is a satisfactory choice for obtaining a useful upper bound. Numerically evaluating this bound provides a value to be used in the probability test given in (1). Remembering that α_0 is the probability of discarding an ambiguity which is the true wind, a threshold for this probability is selected. The Chernoff bound ($s = 1$) is then computed. Any ambiguities with probability bounds less than the threshold can be discarded with confidence since the probability that the discarded ambiguity is the true wind is less than the chosen threshold.

Since it is desirable to throw out as many aliases as possible without removing the true wind, it is advantageous to evaluate how tightly the Chernoff bound approaches α_0 for various wind vector cells and wind estimates. Fig. 1 shows the relationship

between Monte-Carlo calculation of α_0 and a four-term series calculation using (6) for all of the aliases in 500 wind vector cells. Actual measurements are used.

Two distinct relationships are shown in Fig. 1. The first is a plot of simulation-calculated α_0 versus series-calculated α_0 which shows excellent agreement between simulation and series calculations. The second is a plot of the best Chernoff upper bound versus the series calculation of α_0. Note that for a given upper bound the actual value of α_0 for that likelihood ratio is consistently a factor of 10 lower. This implies that the upper bound selected for thresholding can be about 10 times larger than the acceptable probability of throwing out the correct wind. Thus if a 10^{-4} probability of throwing out the correct wind is desired, a threshold of 10^{-3} can be selected.

PERFORMANCE

The utility and performance of the method of eliminating wind aliases described in this paper can be illustrated with the aid of Fig. 2. In part (a), all wind aliases returned by a ML wind retrieval algorithm for a particular region within an ERS-1 swath are kept. In part (b) only the ambiguities greater than a threshold of 10^{-3} are shown. Note how the resulting "most probable ambiguities" field clearly enables determination of the wind streamline.

To further analyze the performance of upper-bound thresholding on removing wind aliases, we use simulated measurements based on known wind fields and ERS-1 orbit parameters. For this simulation only communication noise is added. The results are in summarized in Fig. 3 where a comparison is made between using the thresholding scheme and not using it. When all wind aliases are kept, there is an average of 3.4 aliases per cell. Applying an upper-bound- probability threshold of 0.001 reduces this number to 2.3 aliases per cell with a large majority of the cells having only 2 aliases. This reduction is obtained without ever erroneously discarding the alias closest to the true wind.

As a final demonstration, actual σ^0 measurements are used

Figure 3: *Histograms of the number of cells with a given number of aliases when thresholding is applied versus when it is not applied using simulated measurements.*
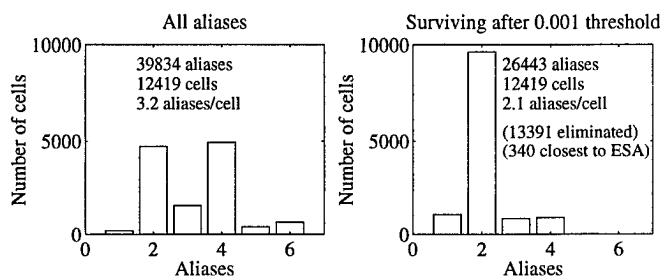
Figure 4: *Histograms of the number of cells with a given number of aliases when thresholding is applied versus when it is not applied using real measurements from ERS-1 revolution 7220 ascending.*

from the ascending portion of ERS-1 revolution 7220. A graph similar to Fig. 3 is shown in Fig. 4. As in the simulations, the scheme eliminates all but two aliases for nearly all of the wind vector cells. Since the true wind is unavailable, a count is made of how many times the alias closest to the wind selected by the European Space Agency (ESA) for that cell is discarded.

CONCLUSION

We have developed a statistical test which can be used to effectively to distinguish between solutions in inverse problems in which maximum likelihood estimation results in multiple maxima. The technique is applied to eliminating improbable wind solutions arising in point-wise wind estimation using scatterometer data. Evaluation of the technique suggests that it can be used effectively to support ambiguity removal by eliminating all but two wind aliases for nearly all of the wind vector cells in a swath.

REFERENCES

[1] M.H. Freilich and R.S. Dunbar, "A preliminary C-band scatterometer model function for the ERS-1 AMI Instrument," Proc. First ERS-1 Symp., Cannes, France, ESA SP-359, pp. 79-84, 1993.

[2] A. Papoulis, *Probability, Random Variables, and Stochastic Processes*, 3rd ed., McGraw-Hill, 1991, pp. 214-218.

Figure 2: *Comparison plot suggesting that eliminating improbable wind aliases can aid ambiguity removal. Data taken ascending part of revolution 7220.*

Advanced Techniques for Improving Wind Direction Ambiguity Removal in Scatterometry

James N. Huddleston, Richard D. West, Simon H. Yueh, & Wu-yang Tsai
Jet Propulsion Laboratory
California Institute of Technology
M/S 300-319
4800 Oak Grove Drive
Pasadena, California 91109-8099
Tel: 818.354.1748, Fax: 818.393.5184, Email: hudd@warukaze.jpl.nasa.gov

Abstract -- Ocean surface winds, which drive the ocean currents and momentum flux exchanges, are critical for numerous atmospheric and oceanographic studies. Ocean surface winds also generate small capillary waves which affect the normalized radar cross section (σ^0) of the ocean surface. A scatterometer is a microwave radar that measures ocean surface σ^0 values which, in turn, can be used to determine the driving wind speed and direction through the inversion of an empirical model function relating σ^0 to wind speed and direction. Unfortunately, for a given value of measured σ^0, there is not a unique wind vector solution. Multiple σ^0 measurements of the same ocean area using different viewing geometries and/or polarizations can be used to reduce the number of possible wind vector solutions.

Seasat-A was launched in 1978 to perform global mapping of ocean surface wind fields using scatterometry. Following the success of the Seasat mission, the NASA Scatterometer (NSCAT) was designed and built to be launched on ADEOS in August of 1996. Whereas Seasat only measured σ^0 from two different viewing geometries producing four equally likely wind vector solutions, NSCAT will have improved instrument skill by measuring σ^0 from three different viewing geometries with one of the antennas making dual-polarization measurements. The NSCAT configuration provides additional information to assist in the selection of a wind vector solution. The process of selecting one of the wind vector solutions to represent the true wind vector is referred to as ambiguity removal or dealiasing.

The ambiguity removal algorithm currently planned for NSCAT utilizes a simple median filter. From simulations, it has been determined that the median filtering technique will have an average skill of about 87.6%, i.e. it will select the wind vector nearest to the true direction about 87.6% of the time. The errors remaining in the wind field after ambiguity removal tend to be clustered together, span the width of the swath (600 km), and extend in the along track direction for several hundred kilometers. Errors also tend to produce sharp discontinuities in the retrieved wind field where there are no such discontinuities in the true wind field. We will discuss techniques of ambiguity removal and outline two new algorithms which can be used to improve ambiguity removal performance without the inclusion of additional wind field information. The techniques are applied to simulated NSCAT
data but can be generalized to other scatterometer instruments such as the ERS-1 and ERS-2 scatterometers, and SeaWinds to be launched aboard ADEOS-II in 1999.

INTRODUCTION

A scatterometer system indirectly determines the speed and direction of wind near the ocean's surface via measurements of the normalized radar cross section (σ^0). As wind blows over the ocean, it creates small ripples on the ocean's surface. These ripples affect the radar cross section of the ocean through resonant Bragg scattering [1]. Empirical model functions have been developed which describe σ^0 as a function of wind speed, relative azimuth wind direction, incidence angle, and polarization. A scatterometer measures the ocean surface σ^0 from several different viewing geometries and/or polarizations. For each measurement of σ^0, there is a continuous curve of possible wind speed/direction pairs. Using multiple measurements of σ^0 from different azimuth angles and/or polarizations reduces the set of solutions to a handful of possible wind vectors. In the case of NSCAT, which utilizes three vertically polarized measurements at different azimuth angles and one horizontally polarized measurement, there are generally four unique wind vector solutions for each 50 km x 50 km wind vector cell [2]. The wind vector solutions are commonly referred to as aliases or ambiguities, and the process of selecting one of the vectors as the solution vector is referred to as dealiasing or ambiguity removal.

MEDIAN FILTERING

An effective technique for selecting a solution vector out of the set of ambiguities for a wind vector cell is to use median filtering (MF) [3]. The median filter selects the ambiguity which has the minimum summed vector difference between itself and the selected vectors of the neighboring wind vector cells in an NxN region. In essence, the median filter selects the ambiguity that makes a wind vector cell "most similar" to its neighbors. In order to start the median filtering process, an initial wind field must be chosen. In NSCAT science data processing, the initial wind field is determined by employing a maximum likelihood estimator to the ambiguities of each wind vector cell. The ambiguity with the highest likelihood of being nearest to the true wind direction is called the first

ranked vector and is used to initialize the wind vector cell. Once an initial wind field is determined by selecting the first ranked vector from each wind vector cell, the median filter is repeatedly applied to the wind field until it converges.

To a certain extent, the median filter imposes continuity on the wind field and consequently relies on the first ranked vectors generally pointing in the correct direction. A metric called skill has been devised which indicates the percent of selected ambiguities which are closest to the true wind direction. Simulations indicate that the first skill, i.e. the skill of the first ranked ambiguity, is about 57.8% for NSCAT.

There is a technique, called "nudging," which uses a model wind field to select the initial wind vector cell directions rather than simply using the first ranked vectors. This technique tends to improve the overall skill of the retrieved wind field. However, there are instances in which the model wind field has missed a feature, such as a cyclone, and consequently causes systematic dealiasing errors in the retrieved wind field. The techniques presented in this paper are aimed at dealiasing scatterometer data without relying on additional information.

SIMULATED NSCAT DATA

An NSCAT simulation, called SuperSim, has been developed at the Jet Propulsion Laboratory. SuperSim simulates the operation of NSCAT in a highly detailed fashion including employing orbit propagation algorithms, using measured antenna gain patterns for power calculations, and incorporating expected errors in both measurements and the model function. We have simulated the flight of NSCAT over 39 high resolution (1° x 1°) ECMWF wind fields resulting in 546 orbits worth of σ^0 data using SuperSim. The ECMWF wind fields have a time resolution of six hours and the 39 wind fields used were selected from data acquired between December 26, 1991 and September 30, 1992 so that the selected fields were spaced approximately a week apart. For each wind field, 14 orbits of NSCAT were simulated, producing about 23.5 hours worth of σ^0 data for each wind field. The σ^0 data was then processed into wind vector ambiguities using NSCAT science data processing software.

ERROR DECORRELATION

The median filtering technique tends to create clumps of incorrectly selected vectors because it favors the local direction as specified by the neighboring selected vectors. Thus, if a majority of the selected wind vectors in the median filter window are pointing in the wrong direction, the median filter will tend to align the central vector with these incorrect vectors creating a cluster of errors. Median filtering is generally successful if the skill of the initialized wind field (in our case, the first skill) is high and the erroneous vectors are randomly distributed. It is expected, however, that errors in the first ranked vector wind field for NSCAT will not be randomly distributed. In generating our simulated data, we have made some assumptions about error correlation. Model

function errors were correlated within 50 km by 50 km regions, while receiver errors were correlated along the entire beam for 50 km in the along track direction. These correlation assumptions produced a clustering effect in the first ranked vectors.

The objective of the error decorrelation plus median filtering algorithm, as the name suggests, is to break up clumps of errors in the initial first ranked wind field. To decorrelate the errors, a pair flip operation is applied to the initial wind field prior to median filtering. The pair flip operation flips the directions of two wind vector cells by approximately 180 degrees if they satisfy the following three criteria: (1) the two wind vector cells are adjacent to each other; (2) the first ranked vectors of the two cells are approximately opposite in direction; (3) neither vector has previously been pair flipped. We assume that two adjacent wind vector cells are unlikely to have nearly opposite wind directions. Thus, one of the two cells is probably wrong, and the other is correct. By flipping the directions of both cells, the location of the incorrect selection is moved (hopefully away from neighboring incorrect vectors) but the number of incorrectly selected vectors remains the same. This has the effect of redistributing errors in the first ranked wind vectors without degrading the overall first ranked skill. Once the pair flip operation has been applied, standard median filtering is employed.

Fig. 1 shows a skill density comparison of error decorrelation plus median filtering (ED+MF) and median filtering (MF). The average skill increases from 87.6% for median filtering alone to 89.2% when error decorrelation is applied. The actual performance improvement will depend on the nature of error correlation in actual NSCAT data.

SKILL GUIDED MEDIAN FILTERING

The median filtering technique applied to NSCAT data involves initializing the solution wind field with the first ranked ambiguities from each wind vector cell and applying the median filter to the entire wind field. A problem with this approach is that all regions of the wind field are allowed to influence the median filtering process equally. Ideally, we want to begin the median filtering process in areas where we expect to have a large number of correctly selected vectors.
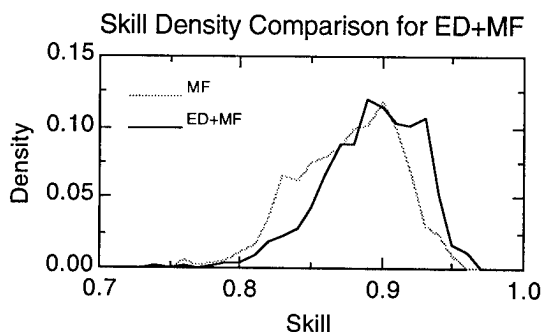
Fig. 1. Skill Density Comparison for ED+MF

As correctly disambiguated areas "grow" via median filtering, they would influence neighboring areas. This is the basic concept behind Skill Guided Median Filtering (SGMF).

Using the simulated NSCAT data, we have found that the following parameters affect the skill of the first ranked vector: the speed of the first ranked vector, the direction of the first ranked vector relative to the antenna beams, and the cross track distance (incidence angle) of a wind vector cell. The first skill was calculated as a function of these parameters and are plotted, in an average sense, in Fig. 2.

In the SGMF algorithm, this first skill information is used
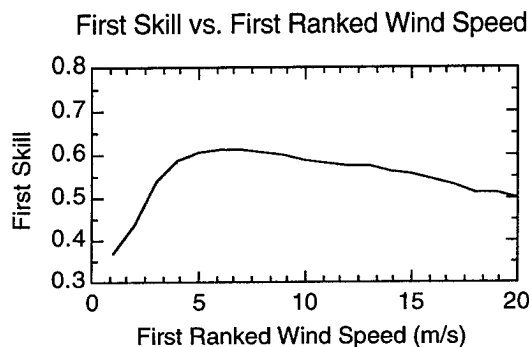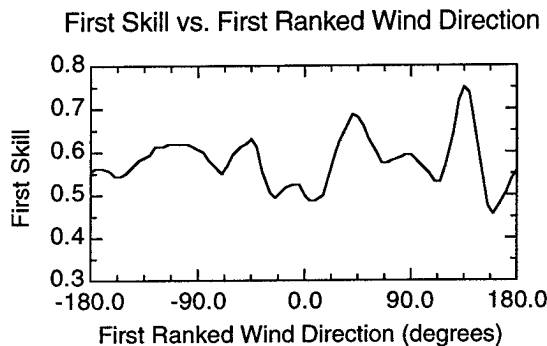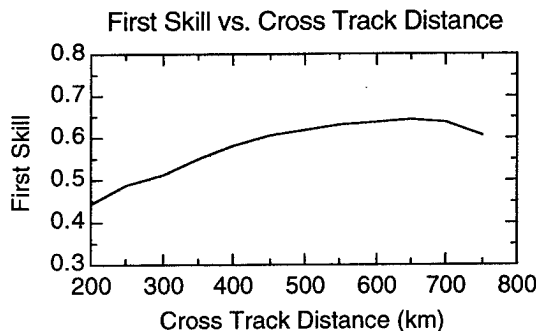
Skill Density Comparison for SGMF
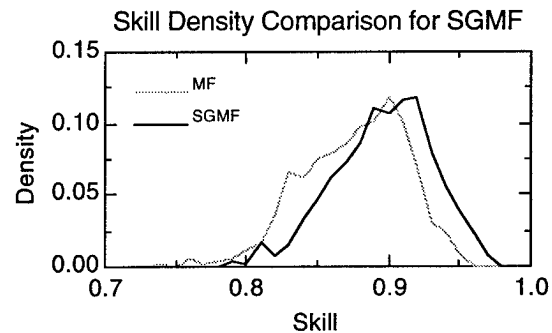
Fig. 3. Skill Density Comparison for SGMF

to guide the median filtering process via selective filtering and weighting. The algorithm steps are as follows: (1) Initialize the wind field with the first ranked vectors (as in standard median filtering); (2) Calculate an expected skill for each wind vector cell based on the empirical skill function; (3) Calculate an average, or local, skill for each NxN region, where NxN is the size of the median filter to be applied; (4) Apply the median filter (weighted by the expected skill) only to wind vector cells which have a local skill above some threshold. Exclude third and fourth ranked vectors from being selected; (5) Repeat step 4 multiple times while reducing the local skill threshold until all wind vector cells have been filtered; (6) Apply the median filter (weighted by the expected skill) to all wind vector cells and allow third and fourth ranked vectors to be selected; (7) Repeat step 6 until the retrieved wind field converges.

The SGMF algorithm increases the average skill from 87.6% for median filtering alone to 89.6%. A plot of the skill densities for median filtering and SGMF is shown in Fig. 3.

SUMMARY

Standard median filtering has proven to be a robust approach to ambiguity removal. However, algorithms such as ED+MF and SGMF can be used in conjunction with median filtering to improve its performance.

REFERENCES

[1] F. T. Ulaby, R. K. Moore, and A. K. Fung, "Microwave Remote Sensing, Active and Passive," Artech House Inc., vol. I (1981), vol. II (1982)

[2] F. M. Naderi, M. H. Freilich, and D. G. Long, "Spaceborne Radar Measurement of Wind Velocity Over the Ocean -- An Overview of the NSCAT Scatterometer System," Proc. IEEE, vol. 79, pp. 850-866, June 1991

[3] S. J. Shaffer, R. S. Dunbar, S. V. Hsiao, and D. G. Long, "A Median-Filter-Based Ambiguity Removal Algorithm For NSCAT," IEEE Trans. Geosci. Remote Sens., vol. 29, pp. 167-174, Jan. 1991

(a)

First Skill vs. First Ranked Wind Speed

First Ranked Wind Speed (m/s)

(b)

First Skill vs. First Ranked Wind Direction

First Ranked Wind Direction (degrees)

(c)

First Skill vs. Cross Track Distance

Cross Track Distance (km)

Fig. 2. (a) First Skill vs. First Ranked Wind Speed; (b) First Skill vs. First Ranked Wind Direction; (c) First Skill vs. Wind Vector Cell Cross Track Distance

Geophysical Modeling Error in Wind Scatterometry

Paul E. Johnson, David G. Long and Travis E. Oliphant
Brigham Young University
459 CB, Provo, UT 84602
801-378-4884, FAX: 801-378-6586, e-mail: johnsonp@newt.ee.byu.edu

Abstract--Scatterometer wind retrieval is based on the relationship between the wind over the ocean and the resulting scattering cross section of the surface; this relationship, termed the "geophysical model function," maps the wind speed, relative wind direction (relative to the antenna azimuth angle), antenna incidence angle, polarization and frequency band to the scattering cross section. The sea surface temperature, salinity, long waves, wind variability within a scatterometer footprint, etc., lend variability to the backscatter. A particular observation of the wind-dependent backscatter can be viewed as a random variable with mean given by the geophysical model function and variability due to unmodelled effects and measurement errors. Little is known about the variability due to unmodelled effects, or the statistics of this variability; this paper presents some considerations and simulations to estimate the magnitude of the model function error.

INTRODUCTION

The geophysical model function relates the wind over the ocean surface, along with parameters characterizing the way the radar looks at the surface, to the normalized radar cross section, σ^o. However, there are many unmodelled factors affecting the relationship between the wind and the radar cross section; these can be viewed as terms causing variability in the true value of the backscatter for given wind and satellite conditions. For example, CMOD4 doesn't account for temperature or salinity [1], which [2] suggests affect the backscatter. Understanding the magnitude and effect of this variability improves our understanding of the model function and the scatterometer measurement process.

In this paper, a measurement model is expressed, describing how the model function value of the backscatter is corrupted by thermal noise and unmodelled parameters; this leads to an equation for the variance of the model function. Then, simulated results demonstrate that this technique provides a means to estimate the model function error from scatterometer data. Data from the ERS-1 satellite is then examined to study the general behavior of the model function error.

THE MEASUREMENT MODEL

Several sources introduce uncertainty into scatterometer measurements; in this paper we consider two: the communication error and the modeling error. The communication error, due to the thermal noise in the measurement process itself, is well understood [3]. Other causes of variability in the observed
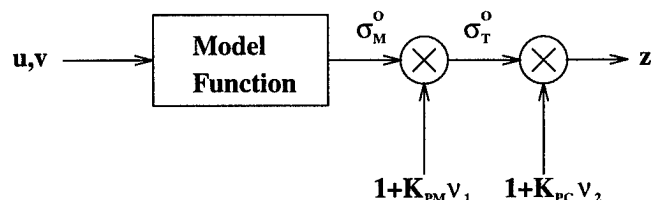
Figure 1: The model for scatterometer measurements. The wind is mapped through the model function to the model function backscatter; variability is introduced through K_{PM}, the effect of unmodelled parameters. The resulting "true" backscatter is corrupted by communication error (i.e., thermal noise) in the measurement process, which yields the measured value of the backscatter, z.

backscatter with respect to the surface wind are lumped into the term "model function error."

Fig. 1 shows a block diagram of the measurement model. The model function maps the surface wind, along with the parameters of the scatterometer, to the model function backscatter, σ^o_M. This value is perturbed by unmodelled parameters to yield the true backscatter coefficient of the surface, σ^o_T. The measurement of the true backscatter, σ^o_T, is corrupted by thermal noise. The actual measurement, z, is modeled as

$$z = (1 + K_{PM}\nu_1)(1 + K_{PC}\nu_2)\sigma^o_M, \qquad (1)$$

where, for simplicity, ν_1 and ν_2 are assumed to be independent, zero mean, unit variance, Gaussian random variables. K^2_{PM} and K^2_{PC} are the normalized variances for the modeling error and the communications error, respectively.

The expected value of the measurement, z, is σ^o_M, and the variance of z is:

$$\text{var}(z) = (K^2_{PM} + K^2_{PC} + K^2_{PM}K^2_{PC})\sigma^o_M{}^2. \qquad (2)$$

To understand the effect of the modeling error, we examine the second moment of the measurement and solve for K^2_{PM}:

$$K^2_{PM} = \left[\text{var}\left(\frac{z}{\sigma^o_M}\right) - K^2_{PC}\right]\frac{1}{1 + K^2_{PC}}. \qquad (3)$$

The model function backscatter, σ^o_M, and the communication error, K_{PC}, depend on several parameters, including wind speed, wind direction, and radar incidence angle. Equation (3) further requires knowledge of the variance of the measurements for a given set of these parameters. Assuming that K_{PM} is
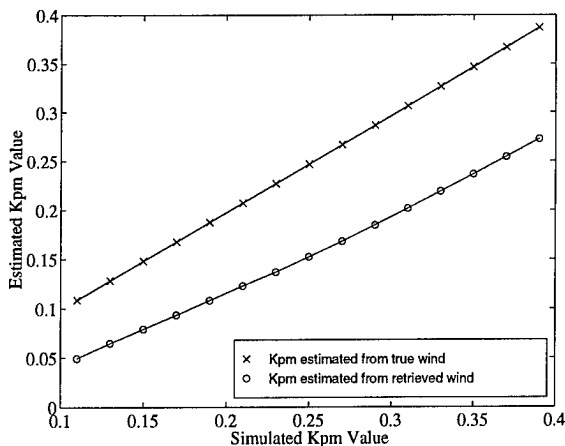
Figure 2: The estimate of K_{PM} based on the true wind provides a good reconstruction of the true value of K_{PM}, while that based on the retrieved wind (Median Filter De-aliasing) is consistently low.

a constant (at least over a sufficiently small range of the parameters) allows us to average over measurements with similar sets of the parameters to yield an estimate of the average value of K_{PM}^2:

$$\langle K_{PM}^2 \rangle = \frac{1}{L} \sum_{k=1}^{L} \left[\mathrm{var}\left(\frac{z_k}{\sigma_{M,k}^o} \right) - K_{PC,k}^2 \right] \frac{1}{1 + K_{PC,k}^2}. \quad (4)$$

For some oceanic region and set of parameters, the variance of the measurements is estimated, yielding a sample value for K_{PM}; taking the average over many regions provides an estimate of the magnitude of the model function error.

SIMULATIONS TO ESTIMATE K_{PM}

A simulated wind field, along with simulated ERS-1 measurements for several revolutions provides a test case for the estimation procedure. Values of K_{PM} are introduced in the simulation to add uncertainty about the backscatter and (4) is used to see its ability to estimate the value of K_{PM}.

Equation (4) requires knowledge of σ_M^o, the model function backscatter. If the true wind (which is known in the simulation) is used to evaluate the model function to generate this, then a very good estimate of K_{PM} is obtained. In actual data, the true wind is not known. The wind is retrieved with maximum likelihood estimation [4] and de-aliased using a median filter based approach [5]; an estimate of the model function backscatter is obtained from the geophysical model function using the retrieved wind. The estimate of the model function error based on the retrieved wind is consistently low, as shown in Fig. 2. This is due to a difference in statistics of the model function when driven by true wind as opposed to retrieved wind.
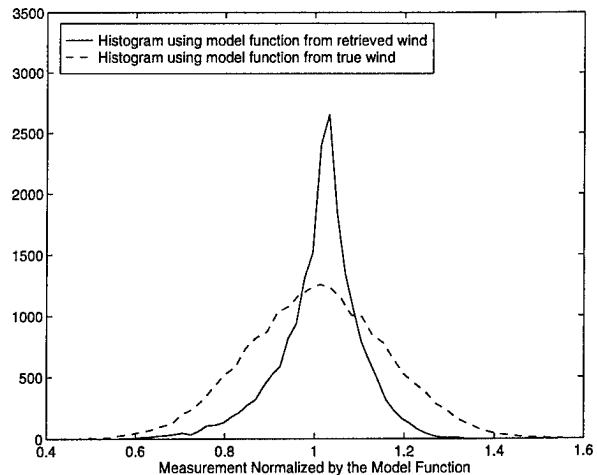
Figure 3: The backscatter measurement normalized by the model function based on the retrieved wind, $\sigma_{M,retrieved}^o$, yields a much smaller variance than that based on the true winds of the simulation, $\sigma_{M,true}^o$. This causes the estimate of the model function error, K_{PM}, to be low when the retrieved winds are used.

The statistics of the model function backscatter due to the true wind are much different from those due to the retrieved wind. Fig. 3 compares the terms $z/\sigma_{M,true}^o$ and $z/\sigma_{M,retrieved}^o$. Normalizing the measurements by the backscatter that results from the retrieved wind, yields a much smaller variance than when the measurements are normalized by the backscatter based on the true wind.

Fitting a quadratic equation to the data displayed in Fig. 2 suggests that a simple functional form relates the estimate of the K_{PM} based on the retrieved wind, to that resulting from the true wind:

$$K_{PM}(true) = -0.77 K_{PM}^2 + 1.50 K_{PM} + 0.03. \quad (5)$$

Simulating additional wind fields and estimating the model function error with (4), and then using the correction of (5) results in accurate estimation of the value of K_{PM} used in the simulation.

ESTIMATES BASED ON ERS-1 DATA

Binning the ERS-1 data according to various parameters reveals the behavior of the model function error. In this section, rough estimates of K_{PM} are found, appropriately adjusted for use when the backscatter is based on the retrieved wind using (5). Representative values of the model function error are found, and its sensitivity to incidence angle and wind speed are observed.

Fig. 4 plots the value of K_{PM}, against the number of revolutions used to estimate it for several values of incidence angle. The estimate of the model function error for near-swath measurements (low incidence angles) is greatest; the
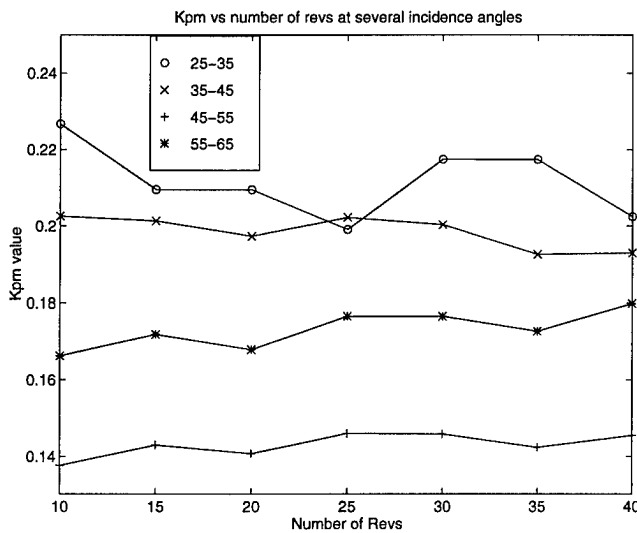
Figure 4: The estimate of K_{PM} varies between about 0.14 and 0.22, depending on the incidence angle.

Figure 5: The estimate of K_{PM} depends on the wind speed. This plot was produced by binning K_{PM} values estimated for ERS-1 satellite data observed at incidence angles between 45 and 55 degrees (mid-swath), with different wind speeds.

variability of the 25 to 35 degree incidence angle bin is due, in part, to the relatively few measurements in each rev at this bin---this decreases the confidence in the estimate of the measurement variance, yielding less consistent estimates of the model function error. The mid-swath measurements (45 to 55 degree incidence angles) yields the lowest value of K_{PM}, at about 0.14, and the far-swath yields values about 0.17.

The model function error is also quite sensitive to speed. Fig. 5 plots the estimate of K_{PM} for the mid-swath measurements (incidence angles of 45 to 55 degrees) against wind speed. Other incidence angle bins follow similar trends. Moderate wind speeds yield K_{PM} near the average value, while lower wind speeds have lower K_{PM} and higher wind speeds have higher K_{PM}.

DISCUSSION

Unmodelled effects in the geophysical model function and the wind retrieval process contribute variability to the backscatter of the ocean surface. In this paper, we have found an expression for the model function error based on a simple model.

Simulations show that if the true surface wind is known, then the value of K_{PM} can be accurately estimated. Using retrieved wind, instead, the estimated model function error is consistently less than the actual value of K_{PM}. The correction function, found from simulations using independent, Gaussian random variables to introduce both communication noise and model function error, permits accurate estimates of K_{PM} based on the retrieved wind.

Examining ERS-1 data indicates the general behavior of the model function error. Low incidence angles have high model function errors, moderate incidence angles have low K_{PM}, and high incidence angles experience moderate values. K_{PM}
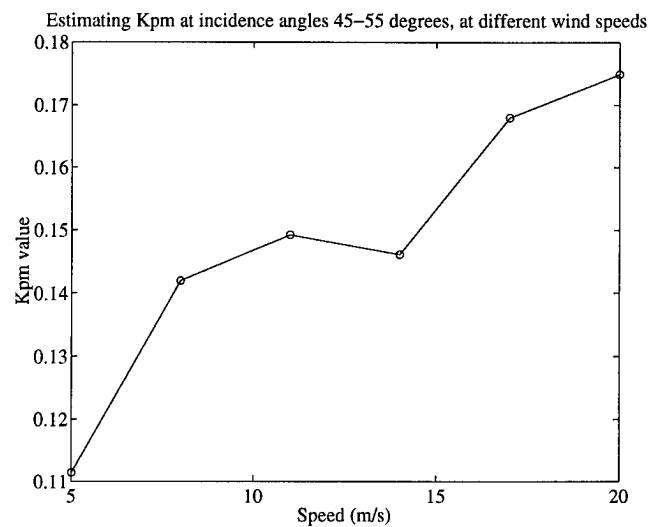
is also sensitive to wind speed, varying about 20% above and below its average value for moderate incidence angle.

These results indicate that the model function error is appreciable, particularly when compared to the communication noise inherent in the scatterometer. These uncertainties limit the confidence that can be placed in the geophysical model, and need to be further understood to enhance the wind retrieval process.

REFERENCES

[1] P. LeComte, "CMOD4 model description," Tech. Rep. ER-TN-ESA-GP-1120, European Space Agency, March 1993.

[2] M. Donelan and W. Pierson, "Radar scattering and equilibrium ranges in wind-generated waves with application to scatterometry," *IEEE Journal of Geophysical Research*, vol. 92, pp. 4971--5029, 1987.

[3] R. E. Fischer, "Standard deviation of scatterometer measurements from space," *IEEE Transactions on Geoscience and Electronics*, vol. GE-10, no. 2, pp. 106--113, 1972.

[4] S. J. Shaffer, R. S. Dunbar, S. V. Hsiao, and D. G. Long, "A median-filter-based ambiguity removal algorithm for NSCAT," *IEEE Transactions on Geoscience and Remote Sensing*, vol. 29, pp. 167--174, Jan 1991.

[5] C.-Y. Chi and F. Li, "A comparative study of several wind estimation algorithms for spaceborne scatterometers," *IEEE Transactions on Geoscience and Remote Sensing*, vol. GE-26, pp. 115--121, March 1988.

Cramer-Rao Bound for Wind Estimation from Scatterometer Measurements

Travis E. Oliphant and David G. Long
Brigham Young University
459 CB, Provo, UT 84602
801-378-4884, FAX: 801-378-6586, e-mail: oliphant@newt.ee.byu.edu

Abstract -- A wind scatterometer makes measurements of the normalized radar backscatter coefficient, σ°, of the surface. To retrieve the wind, a Geophysical Model Function (GMF), which relates σ° to the near-surface wind, is used. The wind vector is estimated using maximum likelihood techniques from the σ° measurements. The probability density of the measured σ° is assumed to be Gaussian with a variance that depends on the true σ° and therefore the wind through the GMF. The measurements from different azimuth angles are assumed independent in estimating the wind. Given this model for wind estimation, the Cramer-Rao bound is derived for wind estimation, and its implications for wind retrieval are discussed. As part of this discussion, the role of geophysical modeling error is considered and shown to play a significant role in the performance of near surface wind estimates.

INTRODUCTION

Scatterometer wind retrieval is a non-linear estimation process: the wind vector is estimated from the σ° measurements based on a statistical model for the σ° measurements. To better understand the accuracy of the wind estimate, the Cramer-Rao (C-R) bound can provide a useful tool since it gives the minimum achievable variance based on the assumed statistical model for the measurements. In this paper we derive the C-R bound for scatterometer wind retrieval. Since the C-R bound depends on the statistical model, the scatterometer measurement model is briefly presented.

Neglecting possible errors in the radar equation parameters, a scatterometer σ° measurement z can be modeled as

$$z = \sigma_t^\circ(1 + K_{pc}\nu_1) \qquad (1)$$

where σ_t° is the true value of σ° from the ocean surface and ν_1 is a zero-mean, unit-variance, Gaussian random variable representing communication noise. K_{pc} is in general a function of σ_t° and the instrument design [1].

Experiments have shown that for a given polarization and frequency the true value of σ° is a function of wind speed, U, antenna incidence angle, θ, and relative wind direction $\chi = \psi - \phi$, where ψ is the antenna azimuth angle, and ϕ is the wind direction. This relationship is called the Geophysical Model Function (GMF). Unfortunately, σ_t° is also influenced by other unmodeled parameters such as sea surface temperature, local salinity, and long waves. As a result the GMF must be interpreted as the expected value of σ_t° for a given set of parameters θ, U, ψ, and ϕ over all the values of the unmodeled parameters.

Without any further information regarding error in the GMF, we model a particular σ_t° from the ocean surface as $M(1 + K_{pm}\nu_2)$ where M is the σ° predicted by the GMF for the given wind conditions and radar parameters, and ν_2 is another zero-mean, unit-variance, Gaussian random variable which accounts for modeling error. Very little is known about K_{pm}, and in general it is a function of θ, U, and χ. Later it will be shown to have a significant effect on the reliability of wind estimates and should thus be investigated further. Reference [2] gives some estimated values of K_{pm} for the CMOD-FDP GMF [3] used in ERS-1 scatterometry.

With this background a σ° measurement can be modeled as

$$z = M(1 + K_{pm}\nu_2)(1 + K_{pc}\nu_1) \qquad (2)$$

where the modeling error ν_2 and the communication error ν_1 are independent random variables. We make one other simplifying assumption and let K_{pc} be a function of deterministic M instead of random σ_t°. This latter assumption guarantees that z is normally distributed with

$$
\begin{aligned}
E[z] &= M & (3)\\
\mathrm{Var}[z] = \sigma_z^2 &= M^2(K_{pm}^2 + K_{pc}^2 + K_{pm}^2 K_{pc}^2) \\
&\approx M^2(K_{pm}^2 + K_{pc}^2) & (4)
\end{aligned}
$$

To estimate the wind, multiple measurements of σ° from different azimuth angles are required. These measurements are assumed independent. With this model, wind retrieval is performed using traditional maximum-likelihood (ML) estimation [4].

THE CRAMER-RAO BOUND

The C-R bound gives a lower bound on the mean squared error (MSE) of any unbiased estimator. Since a ML estimate is used in wind retrieval, the wind estimate variance approaches this lower bound asymptotically. The wind estimate is also "strongly consistent" meaning that the estimate converges to the true value with probability one for all parameter values. Since only a small number of measurements are used in obtaining wind estimates ($N = 3$ for 25 km wind vector cells or $N = 12$ for 50 km wind vector cells), it is questionable whether the variance of the wind estimate actually reaches this lower bound. Simulations can help to resolve this question. Regardless, the C-R bound is useful in determining how accurately wind can be estimated from a space-borne scatterometer given the communication noise and modeling error.

Let $\hat{\mathbf{w}}$ be an unbiased estimate of $\mathbf{w} = [U, \phi]^T$. The Cramer-Rao Theorem states that the error covariance matrix of an

unbiased estimator is bounded by the inverse of the Fisher information matrix:

$$\mathbf{C} = E\{[\hat{\mathbf{w}} - \mathbf{w}][\hat{\mathbf{w}} - \mathbf{w}]^T\} \geq \mathbf{J}^{-1} \qquad (5)$$

where J is the Fisher information matrix,

$$\mathbf{J} = E\left\{\frac{\partial L(\mathbf{z}, \mathbf{w})}{\partial \mathbf{w}} \left[\frac{\partial L(\mathbf{z}, \mathbf{w})}{\partial \mathbf{w}}\right]^T\right\}. \qquad (6)$$

In this expression, L is the log-likelihood function.

Using the assumed measurement model, it can be shown that

$$J_{ij} = \sum_{k=1}^{N} \left[\frac{\partial M_k}{\partial w_i} \frac{1}{\sigma_{z_k}^2} \frac{\partial M_k}{\partial w_j} + \frac{\partial \sigma_{z_k}^2}{\partial w_i} \frac{1}{2\sigma_{z_k}^4} \frac{\partial \sigma_{z_k}^2}{\partial w_j}\right]. \qquad (7)$$

The partial derivatives of the GMF must be obtained numerically. Then (note that $J_{12} = J_{21}$)

$$\mathbf{C} \geq \mathbf{J}^{-1} = \frac{1}{J_{11}J_{22} - J_{12}J_{21}}\begin{bmatrix} J_{22} & -J_{21} \\ -J_{12} & J_{11} \end{bmatrix}. \qquad (8)$$

RESULTS

In the following, ERS-1 geometry and noise variance with the CMOD-FDP GMF are used [3], though the results are qualitatively similar for other model-functions and fan-beam scatterometers.

The C-R bound for a representative far swath wind vector cell of ERS-1 as a function of the true wind speed and direction is plotted in Fig. 1 where the modeling error is zero ($K_{pm} = 0$). Note that both the wind direction error and wind speed error are peaked at particular directions. While this behavior has been previously attributed to problems with using the correct model function in wind retrieval, the C-R bound suggests that this behavior is intrinsic to the wind estimation problem. The larger MSE can be attributed to the shape of the model function and the relative azimuth angles of the observations: in effect, there is less information in the measurements about the wind at these particular directions. For comparison, MSE estimates from a simple compass simulation [4] with the ML wind retrieval algorithm are given in Fig. 2. In the simulation, the wind error is for the ambiguity closest to the true wind direction. The two plots are nearly identical, suggesting that the wind retrieval algorithm is efficient at far swath and zero GMF error.

The C-R bound resulting from increasing K_{pm} or changing the cross-track location of the cell is qualitatively similar to the far swath result. To observe, quantitatively, how the error bound changes as cross-track location and K_{pm} are varied, consider Figs. 3 and 4. In these figures, a true wind direction corresponding to a maximum in Fig. 1 is used.

First consider Fig. 3. Note that for high values of K_{pm} the error bound is more sensitive to K_{pm} than for lower values. Note, also the dramatic decrease in precision of the wind estimate for reasonable values of K_{pm} suggested by [2]. For example, for $K_{pm} \approx 0.2$, the C-R bound suggests that at

Far swath speed error (Kpm = 0)

Far swath direction error (Kpm = 0)
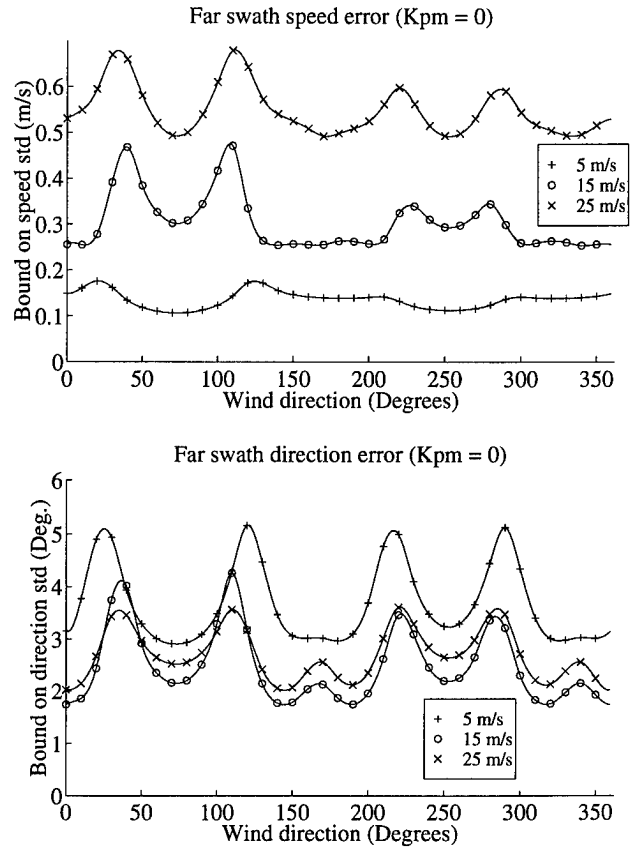
Figure 1: *C-R bound for various wind speeds, and wind directions at far swath for the ERS-1 geometry and noise variance with $K_{pm} = 0$ using the ML estimator and the CMOD-FDP GMF.*

moderate wind speeds of 15 m/s the wind direction error is at least $\pm 12°$. This emphasizes the importance of understanding the GMF modeling error in order to report reliable error estimates for wind from scatterometers.

Now consider Fig. 4. No modeling error is assumed in this figure. Note, that the nearer to the satellite the wind vector cell the worse the wind estimate becomes, especially for low wind speeds. This is not a surprising result since it is well known that the GMF is less sensitive to wind direction at lower incidence angles. Therefore, even with low modeling error, wind direction estimates from near swath cells are less precise than those from far swath cells. Another interesting result from this plot, is that beyond cross cell track location 8, the error on the wind estimate is nearly constant.

CONCLUSIONS

In this paper, we have derived the C-R bound for wind retrieval using scatterometer measurements. The results show that certain wind directions have less sensitivity to error than others depending on the particular azimuth angles of the measurements. In addition, the C-R bound demonstrates that the

wind estimator performance is sensitive to the modeling error and to cross track location of the wind vector cell. Thus, the bound can be useful in understanding the performance of the wind retrieval algorithm.

REFERENCES

[1] R.E. Fischer, "Standard deviation of scatterometer measurements from space," *IEEE Trans. Geosci. Electron.*, Vol. GE-10, No. 2, pp. 106-113, April 1972.

[2] P.E. Johson, D.G. Long, T.E. Oliphant, "Geophysical Modeling Error in Wind Scatterometry," IGARRS 1996.

[3] M.H. Freilich and R.S. Dunbar, "A preliminary C-band scatterometer model function for the ERS-1 AMI Instrument," Proc. First ERS-1 Symp., Cannes, France, ESA SP-359, pp. 79-84, 1993.

[4] C-Y. Chi and F.K. Li, "A comparative study of several wind estimation algorithms for spaceborne scatterometers," *IEEE Trans. on Geo. and Rem. Sens.*, Vol. GE-26, No.2, pp. 115-121, March 1988.

Figure 3: *Lower bound on speed and direction error standard deviation versus K_{pm} for far swath location.*

Figure 2: *Compass simulation MSE estimates for various wind speeds and wind directions at far swath for the ERS-1 geometry and noise variance with $K_{pm} = 0$ using the ML estimator and the CMOD-FDP GMF.*
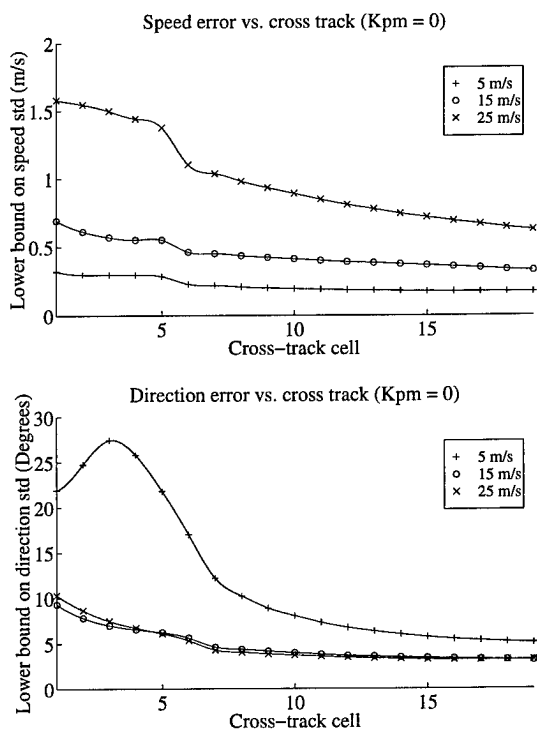
Figure 4: *Lower bound on speed and direction error standard deviation versus cross-track cell location for $K_{pm} = 0$*

1726

Atmospheric Effects on the Wind Retrieval Performance of Satellite Radiometers

Richard D. West and Simon H. Yueh

Jet Propulsion Laboratory
California Institute of Technology
4800 Oak Grove Drive
Pasadena, California 91109-8099
Phone: 818-354-6025, Fax: 818-393-5184, Email: richw@stokes.jpl.nasa.gov

Abstract – Atmospheric emission contributes to radiometer measurements meant to study the ocean surface. The relative importance of this contribution depends on the amount of water (vapor and liquid) in the air column, and on the frequency and polarization used. For vertical and horizontal polarization, the atmosphere contributes a significant bias to observed brightness temperatures. The U stokes parameter, however, is relatively insensitive to the atmosphere, and is therefore a more reliable measure of surface conditions.

I. INTRODUCTION

Ocean winds are important to weather prediction and global climate studies. They drive ocean currents which can transport thermal energy over large distances, and they provide clues about the nature of the atmospheric circulation patterns which affect weather all over the planet. A satellite borne radiometer can be used to measure the surface winds over the oceans because the winds affect the emissivity of the surface. Small scale roughness generated by surface winds modifies the emissivity by scattering the emitted radiation over a range of directions. Since the small scale roughness is aligned with the local wind, it is possible to infer the wind speed and direction by measuring emission from several different azimuth directions.

The radiation emitted by the ocean surface is also affected by absorption and radiation in the atmosphere before it reaches the satellite radiometer. In the microwave frequency range, the most important factors are water vapor and liquid water in clouds. Thus, the atmosphere represents a source of bias and noise in the surface emission signal. In this paper, we will examine the impact of the atmosphere on multi-frequency aircraft radiometer data obtained by the JPL WindRad experiment. In particular, we will look at how atmospheric absorption affects the azimuthally varying signal from the ocean surface, and how it affects the overall radiometric brightness level.

II. MULTILAYERED ATMOSPHERE MODEL

The atmosphere is modelled as 100 meter thick layers with different temperatures, humidities, and pressures. The

attenuation rate of each atmospheric layer is derived using a millimeter wave propagation model (MPM) described by H. Liebe [1]. In this paper, we will concentrate on rain-free cases, therefore scattering is not included.

The brightness temperature observed by a radiometer looking down at the ocean surface through an absorbing and radiating air column is given by the following radiative transfer equation [2],

$$
\begin{aligned}
T_\alpha(f,\theta,\phi) = \ & T_{au}(f,\theta)\,(1-\beta(f,\theta)) \\
& + T_{ad}(f,\theta)\,(1-\beta(f,\theta))r_\alpha(f,\theta,\phi)\,\beta(f,\theta) \\
& + T_{\mathrm{sky}}\beta(f,\theta)^2 r_\alpha(f,\theta,\phi) \\
& + T_s\beta(f,\theta)(1-r_\alpha(f,\theta,\phi)),
\end{aligned} \tag{1}
$$

where $T_\alpha(f,\theta,\phi)$ is the brightness temperature at polarization α as a function of frequency f, incidence angle θ, and radiometer azimuth angle ϕ. β is the net transmissivity of the atmosphere along the look direction. It is determined by multiplying together the transmissivities of each atmospheric layer. T_{au} and T_{ad} are the upward and downward effective air temperatures respectively. They are determined by summing the upward and downward emission from each atmospheric layer (appropriately attenuated), and dividing by the overall absorption. T_{sky} is the isotropic background brightness temperature of cold space, and r is the surface reflectivity function. The layers of air are assumed to be azimuthally isotropic, therefore β, T_{au}, and T_{ad} are independent of ϕ.

III. SURFACE EMISSION MODEL

The surface emission model is contained in the surface reflectivity function r. We assume that the wind-roughened surface has an effective emissivity that determines both its reflection and emission characteristics. The surface emissivity is computed from a two-scale rough surface model [3] which determines all four stokes parameters (T_v, T_h, U, and V) [4] as functions of wind speed, frequency, incidence angle, and the relative azimuth angle between the wind and the radiometer look direction. The two-scale model is tuned to fit SSM/I data [2], and WindRad data collected in 1994 [5].

IV. DATA

In this paper, we present WindRad data collected in 1995, and show how the model described above compares with the data. The atmospheric profiles needed by the
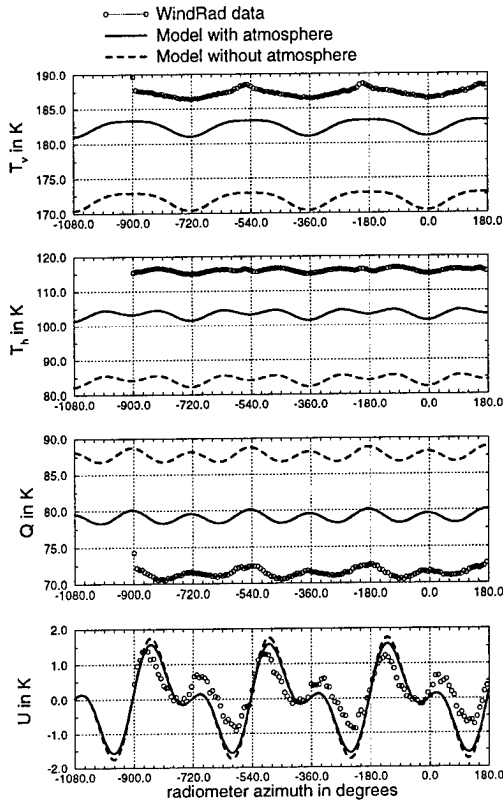
Figure 1. WindRad data and model results for 19 GHz at an incidence angle of 55° on March 30, 1995. The buoy groundtruth is: wind speed = 10.0 m/s, wind direction = 175 deg. (from), sea surface temperature = 10.6°C. Sky conditions: clear. Aircraft altitude: 7010 meters.

Figure 2. WindRad data and model results for 37 GHz. Other parameters match those used in the preceeding figure.

radiative transfer model are obtined from Daily Global Analyses supplied by the National Meterological Center (NMC). This data is available by anonymous ftp from ftp.cdc.noaa.gov. We extracted the temperature, pressure, and relative humidity profiles for the dates and locations of the WindRad flights in 1995. The profile data is interpolated onto the 100 meter height spacing using cubic splines. The wind speed, wind direction, and sea surface temperature were obtained from National Data Buoy Center (NDBC) buoys moored off the coast of northern California and Oregon. Brightness temperatures were measured at vertical polarization, horizontal polarization, +45° linear polarization, and −45° linear polarization. The stokes parameter Q is $T_v - T_h$, and the stokes parameter U is $T_{+45} - T_{-45}$. The stokes parameter V can be measured using circular polarization, but it was not always obtained and is not shown in the figures.

V. ANALYSIS

Figs. 1 and 2 show WindRad data and model predictions for March 30, 1995 at 43.1° N, 128.2° W. NDBC buoy 46002 supplied the surface conditions. The NMC profiles for this time and location indicate a fairly dry atmosphere with a relative humidity around 50% near the surface, and dropping at middle altitudes. Observers on the aircraft

reported clear sky conditions. Fig. 2 shows very good agreement between the model (solid lines) and WindRad data (open circles) at 37 GHz. At 19 GHz, there is more bias in the model predictions for T_v (6 K), T_h (13 K), and Q (8 K) because the close proximity to the water vapor absorption line at 22 GHz leads to greater sensitivity to errors in the NMC water vapor profile. The prediction for U, however, remains very close to the data, and the azimuthal modulation of all the model curves follow the corresponding modulation in the data. For comparison, model results without any atmosphere (dashed lines) are also shown. The biases are more than twice as large (except for U) indicating the importance of the atmosphere in determining observed brightness temperatures.

Figs. 3 and 4 show WindRad data on the same day, but at a slightly different time and location (42.5° N, 130.3° W). Again, NDBC buoy 46002 supplied the surface conditions. Observers on the aircraft reported cloudy conditions, indicating that more water was actually present than indicated by the NMC profile. Consequently, the biases in the model predictions for T_v, T_h, and Q are larger than in the clear case (20 K for T_v and Q, and 40 K for T_h). Furthermore, the azimuthal modulation is somewhat obscured by heterogeneous cloud structure. The signal in U, however, is still in good agreement with the theoretical prediction.

These results can be understood by looking at the relative importance of the four terms in (1). Using the clear

1728
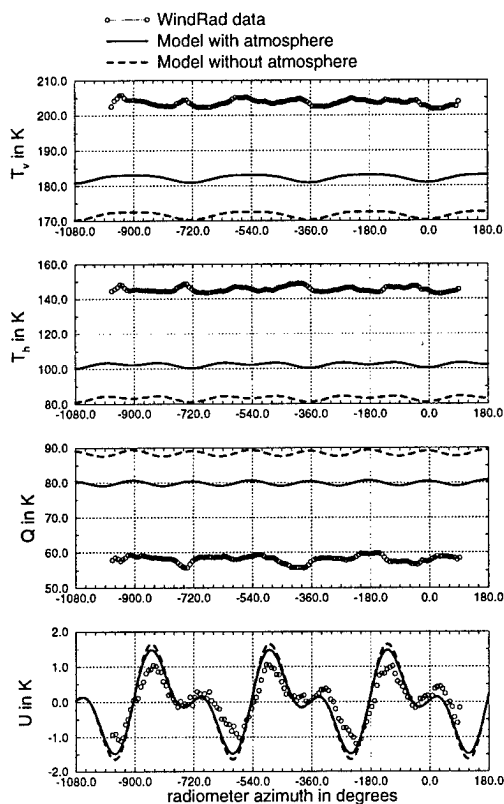
Figure 3. WindRad data and model results for 19 GHz at an incidence angle of 55° on March 30, 1995. The buoy groundtruth is: wind speed = 9.6 m/s, wind direction = 175 deg. (from), sea surface temperature = 10.5°C. Sky conditions: cloudy. Aircraft altitude: 7010 meters.

sky case at 37 GHz, we have the following relative contributions. The largest contribution (85%) comes from surface emission which is modulated by wind. The second largest contribution comes from upward atmospheric emission (11.3%), and the third largest comes from reflected downward atmospheric emission (3.4%). Reflected sky brightness supplies a very small offset. T_v and T_h incorporate all four terms, and are subject to biases in T_{au} and T_{ad} caused by errors in the atmospheric profiles. Q is less sensitive to the atmosphere because the upward atmospheric emission term subtracts out. There can still be some atmosphere induced bias in Q, however, because the surface reflectivity is very different for V-pol vs H-pol. Thus, the level of Q is partly determined by the polarization contrast in reflected downward atmospheric emission. U is insensitive to the atmosphere for two reasons. First, the upward atmospheric emission term cancels out (as with Q), and second, the reflected downward atmospheric emission term almost cancels out because there is little difference in the surface reflectivity at +45° and −45° linear polarization.

VI. CONCLUSIONS

The atmosphere can cause significant biases in T_v, T_h, and Q. These biases can be removed accurately for dry
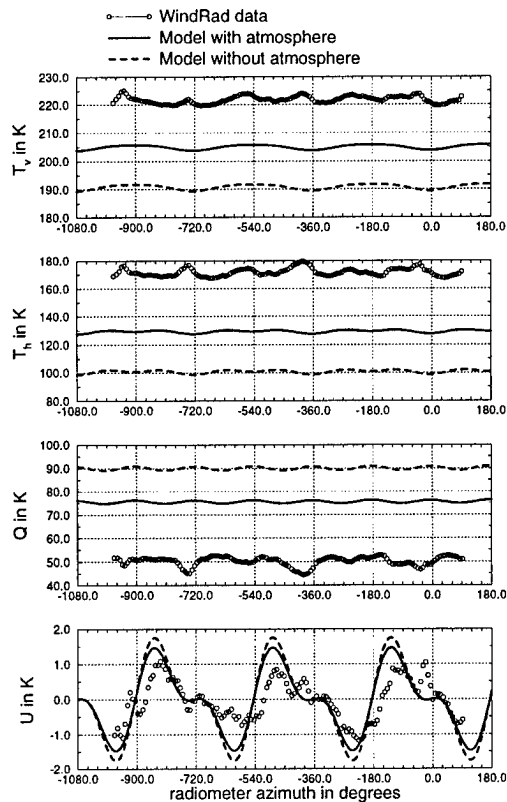
Figure 4. WindRad data and model results for 37 GHz. Other parameters match those used in the preceeding figure.

atmospheric conditions when the frequency isn't close to a water vapor line. When more water vapor or clouds are present, an accurate profile of the atmosphere is needed before the bias can be removed. The wind induced azimuthal modulation of brightness temperatures is unaffected as long as the atmosphere is reasonably homogeneous. The signal in U, however, is relatively insensitive to the atmosphere, and gives a reliable indication of surface emission even when clouds are present.

REFERENCES

[1] H. J. Liebe, "An updated model for millimeter wave propagation in moist air," Radio Science, vol. 20, no. 5, pp. 1069-1089, September-October 1985.

[2] F. J. Wentz, "Measurement of oceanic wind vector using satellite microwave radiometers," IEEE Trans. on GeoScience and Remote Sensing, vol. 30, no. 5, pp. 960-972, September 1992.

[3] S. H. Yueh, "Modelling of wind direction signals in polarimetric sea surface brightness temperatures," unpublished.

[4] L. Tsang, J. A. Kong, and R. T. Shin, Theory of Microwave Remote Sensing, New York, Wiley-Interscience, 1985, Ch. 3.

[5] W. J. Wilson and S. H. Yueh, Ocean wind direction measurements using passive polarimetric radiometers, JPL Internal Document, February 1996.

Nonlinearities and Reverse Travelling Energy Observed in Wavenumber-Frequency Spectra of X-Band Ocean Backscatter

Stephen Frasier and Robert McIntosh
Microwave Remote Sensing Laboratory
University of Massachusetts, Amherst, MA 01003
T: 413.545.0779 / F: 413.545.4652 / frasier@alex.ecs.umass.edu

Abstract— Wavenumber-frequency spectra of microwave backscatter from the sea surface occasionally show harmonics of the expected linear gravity wave dispersion in both backscattered power (AM) and Doppler velocity (FM) modulations. Harmonics are confined to the peak wave direction, and the ratio of fundamental to second harmonic energy in the velocity modulation indicates increasing nonlinearity with wavenumber, peaking at a wavenumber consistent with observed wave group modulations. Under higher sea state conditions where whitecapping was evident, spectra show weak reverse travelling waves – opposite to the dominant wave direction. Space-time filtering of the image data suggests breaking events are a source for these waves.

I Introduction

Fourier analysis of ocean wave radar image sequences provides a complete representation of the ensemble average wavenumber-frequency characteristics of ocean surface backscatter. Because vertically polarized microwave backscatter is dominated by a distributed (Bragg) scattering mechanism over moderate to large incidence angles, modulations of the backscatter can be useful for observing the dispersion properties of ocean waves.

In this paper we show two examples of dispersion characteristics observed with the FOPAIR imaging radar system [1]. In the first case, harmonics of the linear gravity wave dispersion curve are evident in directional slices through 3-D spectra of backscattered power and Doppler velocity. Though expected in the power spectrum, the presence of harmonics in the velocity data may indicate the level of nonlinearity in the ocean surface waves. In the second case, obtained under whitecapping conditions, we observe low energy wave components travelling directly opposed to the dominant wind waves. It is suggested that breaking events are the source for these waves.

II Dispersion Harmonics

Fig. 1 shows a snapshot of X-band radar imagery obtained on March 24, 1994 from the end of the USACE research pier at Duck, NC. The range direction in the images corresponds to 8° true North, or 62° north of the pier axis. While winds were 7.4 m/s from 199°, the images show wind waves propagating towards the upper left of the image (316° true North). The misalignment of wind
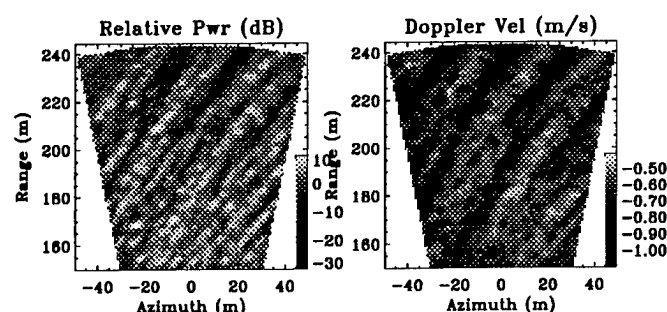
Fig. 1. Radar image snapshot of the ocean surface obtained on March 24, 1994. The left image is proportional to σ° while the right image shows mean Doppler velocity over 0.25 s averaging time.

and waves is due primarily to the progressive shoaling of the developing wind waves as they travel up the coast. Water depth at the radar site was approximately 6.6 m.

Three dimensional wavenumber-frequency spectra were calculated from an 8 minute image sequence, processed in overlapping 32-second blocks, and a slice through the three dimensional volume along the peak wind wave direction is shown in Fig. 2. The three panels in this figure show the variance spectra of the backscattered power (AM signal), the mean Doppler velocity (FM signal), and their coherence defined as the norm of the cross-spectrum divided by the product of the auto-spectra. We use the coherence as a filter to identify backscattered power fluctuations that can be attributed to detectable surface motions. Rejecting energy that is incoherent between power and velocity removes much of the variance due to speckle as well as spatial power modulations induced by the antenna pattern and range rolloff, and low frequency variations in the surface roughness. A coherence threshold of 0.3 is used.

These spectra show most of the signal variance following the dispersion curve for linear gravity waves. In the power modulation spectrum, three harmonics of the fundamental are discernable while only one is evident in the velocity modulation spectrum. The coherence spectrum, however, indicates the presence of the second and third harmonics, with the second harmonic persistent out to the limiting wavenumber of the instrument where auto spectral densities are low. Energy in the harmonics approaches a limiting phase velocity of approximately 5
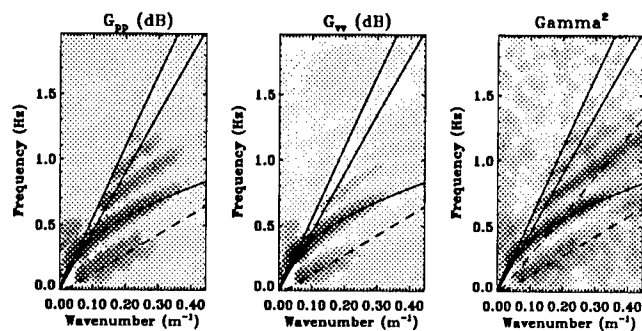
Fig. 2. Slices through the power (left), velocity (center), and coherence (right) spectra along the dominant wind-wave direction. The grayscale represents a 40 dB range for auto-spectra and a linear [0,1] scale for coherence. Steep solid lines mark phase velocities between 4.5 and 5.5 ms^{-1}. The dashed line is a fit to nondispersive energy with slope 1.5 ms^{-1}.

ms^{-1} as indicated by the steep lines in the dispersion diagrams. The stronger relative appearance of harmonic energy in the power modulation spectrum is expected because of the nonlinear relation between radar backscatter and local incidence angle (wave slope) at near-grazing angles. In this case about 5% of the total power modulation is contained in harmonics compared to 0.3% for the Doppler velocity modulations.

Spectral energy falling below the dispersion curve in Fig. 2 has been attributed to modulations in backscatter induced by the group modulation of the waves [2]. Such modulations would include effects such as non-Bragg scattering from breaking waves and from features bound to wave crests including Bragg-type scatterering from bound capillary waves. This energy is therefore usually associated with the portion of the wave spectrum most actively breaking. A linear fit to this energy indicates a group velocity of 1.5 ms^{-1} corresponding to a wave group centered at K=.17 m^{-1}.

In upper panel of Fig. 3 we have plotted the energy in each of the harmonics as a function of wavenumber by bandpass filtering along the individual dispersion curves with a 0.2 Hz wide filter and integrating over frequency. To compare properties between harmonics it is appropriate to consider wave components that travel at the same phase speed. Assuming a rigid, propagating wave profile, energy at a given wavenumber in second harmonic travels with the phase speed of the fundamental wave of half the wavenumber. Proper comparison is therefore achieved by normalizing the wavenumber axis for each harmonic by its harmonic index as shown in the lower panel of Fig. 3.

The relative levels of harmonic energy in the Doppler velocity spectrum show increasing nonlinearity with wavenumber. The dash-dot line in the lower right panel of Fig. 3 is the ratio of energy in the first and second harmonics which peaks at -20 dB between K=.16-.20 m^{-1} (beyond .20 m^{-1}, second harmonic energy exceeds the
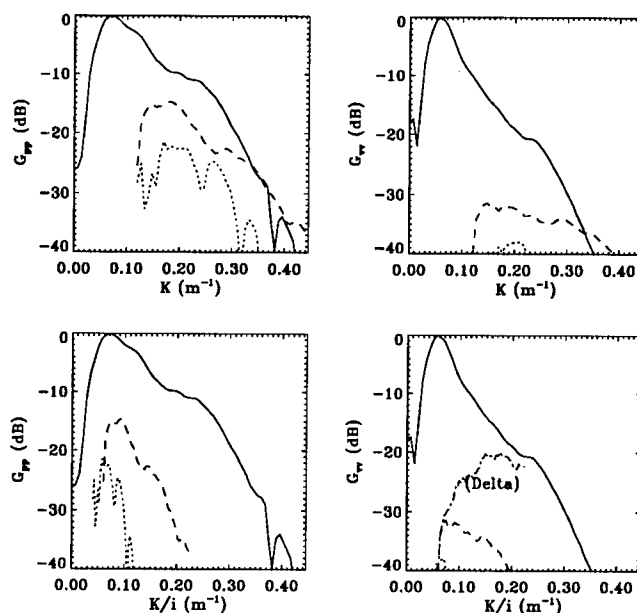
Fig. 3. Upper panel: Profiles of the variance spectral density of power (left) and Doppler velocity (right) along dispersion curves for the fundamental (solid), second (dashed), and third (dotted) harmonics. Lower panel: Same as above with wavenumbers referenced to the fundamental. The dash-dot lines indicates the ratio of second second harmonic energy to the fundamental.

Nyquist wavenumber of the radar). The relative harmonic energy is well above that attributable to radar receiver distortion,[1] and its location in the wavenumber spectrum is in general correspondence with the nondispersive energy. Assuming that Doppler velocity is a linear detector of wave orbital velocity components, the ratio of peak powers in the first two harmonics is consistent with a long wave slope, AK, of 0.1, or a fundamental wave amplitude, A, of 8 cm for a 5 m wave. These values appear plausible given the measured significant wave height of 36 cm.

III   REVERSE TRAVELLING WAVES

Figure 4 shows an iso-frequency slice at 0.4 Hz of a wavenumber-frequency Doppler velocity spectrum obtained under whitecapping conditions (upwind, upwave radar look, windspeed of 8.2 ms^{-1}). The majority of spectral energy is confined to the linear gravity dispersion shell which is distorted in this case due to a southbound surface current (towards the radar). The dominant wave energy in advancing wavenumbers is shown in the lower half of the diagram. Of particular interest is the

[1]Receiver harmonic distortion is dominated by the 3rd harmonic measured at -32 dBc from a CW test signal at maximum power (worst case). Such distortion can induce 2nd harmonics in AM and FM modulations at about the same level. Third harmonic distortion at the power level corresponding to the ocean radar data is below -40 dBc, however.
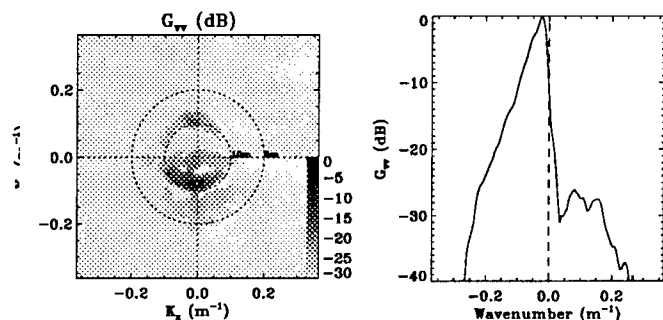
Fig. 4. Left: Iso-frequency (F=0.4 Hz) slice through the 3-D velocity spectrum showing dominant advancing waves ($K_y < 0$) and weaker receding waves. Right: The range-wavenumber spectrum (a slice along $K_x = 0$) integrated over frequency shows the relative energy in advancing and receding waves.

Fig. 5. Top: Space-time diagram of Doppler velocity of range travelling waves. Bottom: The same data set filtered for receding waves with frequency of $0.5 \pm .1$ Hz only.

energy propagating opposite to the dominant wave direction which, though much lower in intensity, is clearly discernable.

Logical sources for such waves are localized disturbances caused by breaking waves. Wavetank measurements have demonstrated that such reverse travelling waves do follow breaking events [3] suggesting that energy contained in such waves could provide a quantitative measure of the amount of breaking. Although energy levels are low, such measurement of a distributed feature may be inherently easier to perform than the tracking and counting of individual transient events.

To test this hypothesis, we applied spatio-temporal filtering to Doppler velocity image data. The upper panel of Fig. 5 shows a space-time diagram of range-only travelling waves. Advancing wave structure is clearly evident through the negative-sloped ($\Delta r/\Delta t < 0$) features. High velocity excursions appear periodically with the passing of wave group peaks. The largest of these excursions are likely to be associated with wave breaking.

The lower panel of the figure shows the same data segment filtered for receding waves with frequency of 0.5 ± 0.1 Hz. This frequency band was chosen because it corresponds to short gravity waves near the spatial sampling resolution limit of the radar. Short waves are desirable as they dissipate more rapidly, increasing the likelihood that they may be easily associated with their source. The diagram shows significant variations in the phase velocity of the receding waves which are due to the space- and time-varying current (due to the orbital velocity of the wave field) through which these short waves propagate.

The linear phase FIR filter used has a group delay of 4 seconds, so the signature of interest is enhanced modulation of the filtered wave envelope peaking about 4 seconds following, and at ranges larger than, a given high-velocity event in the unfiltered data. In the two minute segment shown, one such signature is evident between 35 and 40
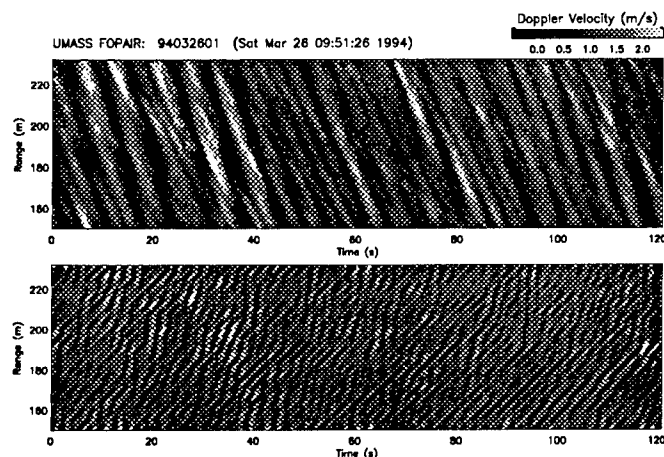
seconds at 200 m range in the filtered data. It may be associated with the the high velocity event at 32 seconds. Similar signatures occur beyond 220 m range around 12 seconds. High velocity events near the 80 second mark generate little if any modulations in the filtered data, indicating that these events may represent peaks in the wave group envelope without breaking. Elsewhere in the diagram, the amplitude of the 0.5 Hz waves is generally lower. A receding wave group is evident starting at 90 seconds at the nearest range. This short data segment is representative of the remainder of the record, and appears to support the hypothesis of breaking events as a source for reverse travelling waves. Further investigation is warranted.

REFERENCES

1. McIntosh, R.E., S.J. Frasier, J.B. Mead, "FOPAIR: A Focused Array Radar for Ocean Remote Sensing", *IEEE Trans. on Geoscience and Remote Sensing*, 33(1), pp. 115-124, Jan 1995.

2. Smith, M.J, E.M. Poulter, J.A. McGregor, "Doppler Radar Measurements of Wave Groups and Breaking Waves", *Journal of Geophysical Research*, in-press, 1996.

3. Melville, W.K., A. Rozenberg, "Measurements of Wave Breaking and Microwave Scattering in the Laboratory", presented at *Fourth SIO Workshop on Capillary Wave and Remote Sensing Phenomena*, Scripps Institute of Oceanography, La Jolla, CA, Oct 4, 1995.

Observed Space-Time Structure of Radar Backscatter from the Ocean Surface

Vahid Hesany, William J. Plant, William C. Keller, Kenneth Hayes
Applied Physics Laboratory, University of Washington
1013 NE 40th Street, Seattle, WA 98105
hesany@apl.washington.edu

ABSTRACT

Space-time radar images of the ocean surface were collected from an airship off the Oregon coast in the fall of 1995, using a coherent, short pulse, HH-polarized X-band system. The radar successfully mapped wind waves, long swell waves and internal wave features. The radar images are converted to two-dimensional spectra of microwave backscatter and the surface velocity field. These spectra are used to examine space-time properties of surface waves. Examples of the radar maps and their corresponding spectra are presented. It is demonstrated that the linear dispersion relation gives the relationship between the time and spatial dependence of the long gravity waves. Also, evident in the spectra are features that don't obey the linear wave theory.

INTRODUCTION

Measurements of ocean microwave backscatter were performed from an airship off the Oregon coast in September and October of 1995. The radar used in the experiment was a coherent, short pulse, X-band system with a range resolution of 7.5 m. It was equipped with a fan-beam antenna with beamwidths of 2° in azimuth and 23° in elevation. The backscattering measurements were horizontally polarized and obtained at incidence angles ranging from nadir to approximately 65°. Although the system was designed as a rotating beam radar, the examples presented here are with the antenna fixed at a constant azimuth angle. In this mode space-time images of the surface were produced. The majority of measurements were conducted at an altitude of 150 m, although measurements at altitudes as low as 50 m and as high as 300 m were also performed. The swath width was on the order of 400 to 500 m, and data records were typically 10 to 20 minutes long. The missions included flights over specific sites near the research vessel FLIP, which was in the area conducting surface and atmospheric measurements. Images of received power, Doppler offsets gave the cross-section and line-of-sight component of the ocean surface velocity field at each image pixel. These images were processed to obtain the two-dimensional spectra of the backscattered signal and surface velocity field as functions of wavenumber and frequency.

EXPERIMENTAL OBSERVATIONS

Figure 1 shows a set of radar images. The vertical axis is the slant range to surface, and the horizontal axis is time. The top panel, Fig. 1a, is the backscattered power image corrected for the antenna pattern and range variations across the image. The image was obtained line by line from left to right, and the time difference between two lines is 1 second. The wind was steady at about 11 to 12 m/s from 180° T, and the antenna was facing the wind at a center incidence angle of 45°. The airship was pointed into the wind, hovering above the sea surface at less than 1 m/s ground speed. The first return from the surface occurs at 330 meters (airship altitude). The surface return is from 330 m to 600 m in range, with the corresponding surface coverage of about 500m. The surface footprint for each image pixel at the beam center is roughly 11 m (range) by 14m (across beam).

Waves of various scale are evident in the image. The inclination of each wave crest corresponds to phase velocity. Crests with positive slope are waves moving toward the antenna. Fig. 1a is a particularly interesting image since it shows the effect of rain on the microwave backscatter. Normally, any return before nadir is dominated by the receiver noise. Here, however, the rain signature at close ranges is clearly visible in the image, particularly where the rain had intensified. Notice the corresponding increase in the surface backscatter; the latter half of the image is brighter than the first half of the image. This enhanced scattering from the surface is presumably due to an increase in surface roughness caused by rain-induced ripples.

Fig. 1.b shows the corresponding line-of-sight velocity image. Although the airship was relatively steady, small variations in airship speed appear as vertical streaks in the image and were removed by de-trending each vertical line in the image. This procedure is effective in bringing out the surface wave patterns in the velocity image. Unfortunately, It also removes the rain drop velocity signature, which is why it is not visible in the image at close ranges.

WAVENUMBER-FREQUENCY SPECTRA

Wavenumber-frequency spectra were computed by interpolating both power and velocity images of Fig. 1 to evenly spaced points on the surface. The images were divided into 64×64 segments with 50% overlapping and padded with zeros to produce 29 128×128 segments. Each segment was multiplied by a two-dimensional Hanning window, and the mean of each section was removed. Finally, two-dimensional Fourier transforms were applied and the resulting 29 spectra were averaged.

Normalized Received Power (dB) -- 9/29/95 18:26 UTC

Relative Line-of-Sight Velocity (m/s) -- 9/29/96 18:26 UTC
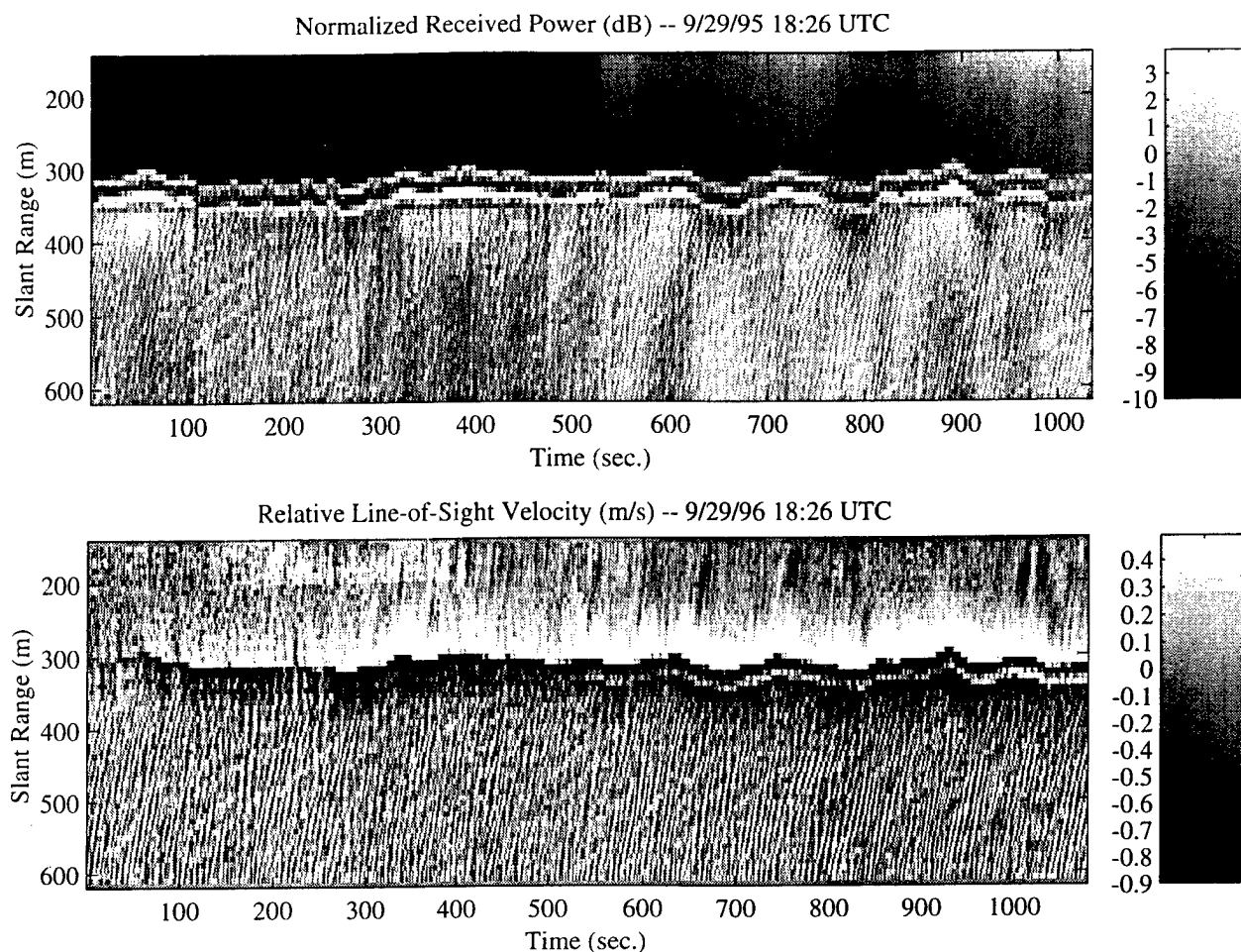
Figure 1. (a) Space-time image of backscattered power, corrected for the antenna and range variations. The signal at close ranges is due to rain. Note enhanced surface backscattering where the rain has intensified,(b) corresponding line-of-sight velocity image.

Normalized Line-of-Sight Velocity PSD -- 9/26/95, 18:26 UTC

Normalized Backscattered Signal PSD -- 9/26/95, 18:26 UTC

Mag. @ (0.11,0.16)=1 $\theta = 70°$
Mag. @ (0.02,0.98)=0.5
Mag. @ (-0.02,0.12)=0.13
Mag. @ (0.11,0.03)=0.12

Mag. @ (0.11,0.16)=1 $\theta = 70°$
Mag. @ (0.02,0.98)=0.21
Mag. @ (-0.02,0.12)=0.11
Mag. @ (0.11,0.03)=0.23
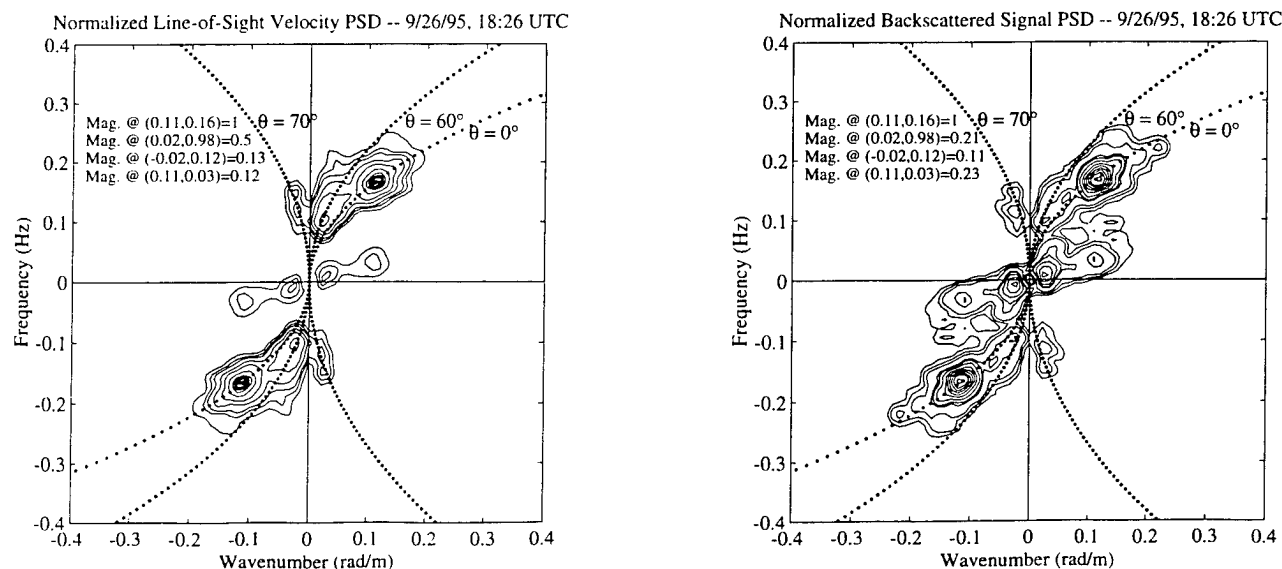
Figure 2. Wavenumber-frequency spectra obtained by Fourier Transformation of the images in Figure 1. (a) velocity spectrum, (b) bacscattered power spectrum. The horizontal axis is wavenumber in the antenna look direction. The dotted line is the linear dispersion curve for waves traveling at angle θ to the radar beam.

1734

Figure 2 shows contour plots of the resulting spectra. Due to the nature of the FFT transform, there is a two-quadrant symmetry in the spectrum, and the lower part of the spectra is redundant. However, full display of the spectra helps identify features that are near the zero frequency axis. For positive frequencies, positive wavenumbers correspond to waves traveling toward the antenna, and negative wavenumbers correspond to waves moving away. The dispersion relation for various propagation directions are also plotted as dotted lines. For waves traveling at angle θ to the radar beam, the dispersion curve is $2\pi f = \sqrt{g k_a / \cos(\theta)}$, where k_a is wavenumber in the antenna look direction, f is frequency, and $g = 9.8$ m/s^2. Wave direction relative to the antenna axis is determined by adjusting θ so the dispersion curve crosses the particular peak in the spectrum. The 180° inherent ambiguity in swell direction is resolved by assuming that these long waves are always propagating toward the shoreline.

Figure 2.a shows the velocity spectrum. Four dominant features identified as peaks in the spectrum are evident. The relative amplitude of each peak and its corresponding location is shown in the upper left corner. The dominant peak in the velocity spectrum is at frequency 0.16 Hz and wavenumber 0.11 rad/m (6 second period, 57 m long), which corresponds to waves propagating in the direction of the wind and nearly straight down the beam (wind is from 180°T and the antenna is facing the wind). Therefore, the wave energy is accordingly concentrated around the dispersion curve $\theta = 0°$.

The dominant swell is at 0.98 Hz and 0.02 rad/m, and its peak falls on the $\theta = 60°$ dispersion curve, indicating a swell propagating toward the antenna from 240°T. A weaker system also exists (0.12Hz,-0.02 rad/m) that is moving away from the antenna at an angle of 70° to the beam, which translates to a swell direction of about 290°T. A vector plot, summarizing the various azimuth angles is shown in Fig. 3.

The bow-shaped pattern in both the velocity and backscattered spectra near the zero frequency axis (well below the dispersion curve) doesn't conform to linear wave theory. Its peak occurs at 0.03 Hz, and 0.11 rad/m, nearly the same wavenumber as the wind waves but at about 1/5 their frequency. This feature appears in the velocity image of Fig. 2.a as occasional bright streaks (large line-of-sight velocity) moving almost diagonally from upper left to lower right. Probable causes include wave breaking events or wave-wave interactions between wind waves and swell.

All of the peaks in the velocity spectrum have a corresponding peak in the backscattered power spectrum, as a comparison of Figures 2.a and 2.b clearly indicates. Wind waves and swell appear in the backscattered power spectra primarily due to their modulation by the gravity waves. Note the peak at the swell frequency is considerably smaller than the wind wave peak, indicative of the lower level of

modulation by azimuthally traveling waves. The radar backscattered spectrum also shows considerable low-frequency clutter below 0.1 Hz, with no clear corresponding signature in the velocity spectrum.

N

Swell @ 290°T

E

Swell @ 240°T

Antenna

Wind 11m/s, from 180°T
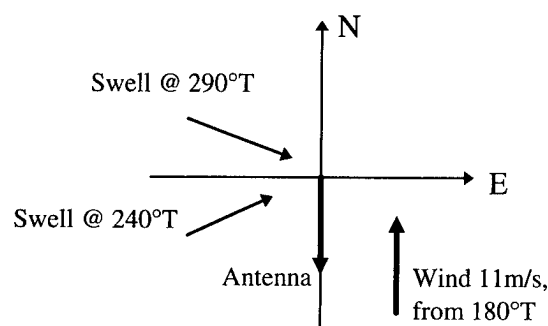
Figure 3. Vector plot of various quantities relevant to images of Fig. 1. Swell directions were obtained by fitting linear dispersion curves to the peaks in the velocity spectrum.

CONCLUSION

The complicated ocean surface evolves both in time and space. Waves of various amplitude, wavelength and period cover the ocean surface. Waves often interact with each other, and nonlinear intermittent processes such as wave breaking also occur. In this paper, it is demonstrated through an example that the long gravity waves follow linear wave theory. However, there are also features on the surface that do not conform to linear theory. Point measuring systems that measure in either time or space provide insufficient information for exploring these observed anomalies. Since ocean surface features manifest themselves in surface velocities, simultaneous measurements of the spatial and temporal variations of the ocean velocity filed provide valuable information about the ocean surface dynamics.

Optical, Radar and *In Situ* Measurements of Internal Wave Dispersion

B. L. Gotwols[1], E. Aarholt[2], R. D. Chapman[1], and R. E. Sterner II[1]

[1]Johns Hopkins Univ., Applied Physics Lab., Johns Hopkins Rd., Laurel, MD 20723
Tel.: 301-953-600, FAX: 301-953-5548, E-mail: gotwols, chapman, sterner @tesla.jhuapl.edu
[2]PFM, Storgaten 6, PO Box 89,N-2001 Lillestrom, Norway
Tel.: +47 638 92660, FAX: +47 638 92670, E-mail: Eldar.Aarholt@pfm.no

Abstract -- A deep draft fishing boat was used to generate internal waves in a glacially-fed Norwegian fjord during August 1995. Data from a CCD camera, and X-band delta-K radar were used to compute the internal wave dispersion relation. The optically derived dispersion relation agreed with theoretical calculations based on nearby CTD casts. The radar observations also showed good agreement with the CTD casts but in addition exhibited a nondispersive feature which may be attributed to nonlinear scattering of the radar signal from the surface roughness.

INTRODUCTION

Internal waves cause currents at the surface of the ocean which interact with wind waves and thus modulate the surface roughness. This modulated surface roughness can be monitored optically, since a change in rms roughness causes a change in reflected sky radiance, which shows up as bright and dark bands propagating on the water surface. A time sequence of optical images can be Fourier analyzed to yield a direct measurement of the internal wave dispersion relation. Similarly, the propagating roughness patterns can be monitored by radar. A coherent multi-frequency radar known as delta-K radar is particularly useful for investigating dispersion relations. Here a series of closely spaced frequencies are transmitted, and the complex return signals multiplied together in pairs. The signal can be thought of as the return from those Fourier components on the surface which obey the resonant Bragg scattering relation, where the resonant frequency corresponds to the *difference* in the two transmitted frequencies. By carefully choosing the transmitted frequencies, a large number of unique difference frequencies can be generated, allowing the dispersion relation to be carefully mapped out.

An experiment was done in a large glacially-fed fjord in Norway in the summer of 1995, where the pycnocline was typically at a depth of 5 m. A deep draft fishing vessel was used to generate internal waves. A delta-K radar and bore-sighted video cameras were located on a cliff 820 m above the water. *In situ* measurements of currents were made at several depths from a platform near the optical/radar footprint, and periodic CTD casts were used to characterize the stratification. The dispersion relation measured directly with the delta-K radar and the video systems are compared below with theoretical predictions based on the *in situ* data.

OPTICAL MEASUREMENTS

Two Charge Coupled Device (CCD) video cameras were carefully boresighted with the delta-K radar. Both cameras were rotated 90° from their usual orientation in order to maximize coverage in the radar look direction. One camera provided an overview of ship activity in the fjord, while the coverage of the second camera was matched with the radar. Both cameras had their IR blocking filters removed and were equipped with a Kodak number 23A red filter and horizontal polarizer. These steps greatly improved the image quality, particularly in the early morning when visibility was often reduced by fog. The images from each camera were recorded
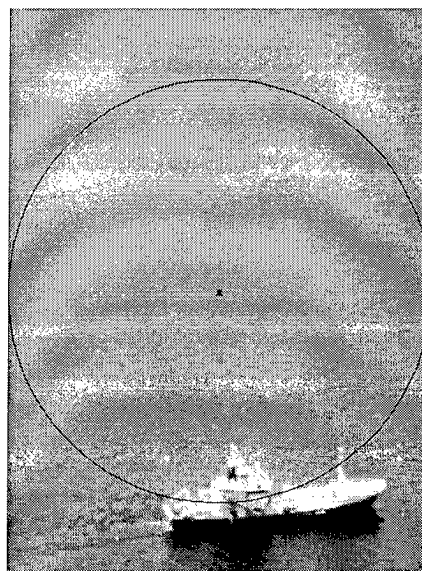
Fig. 1. — CCD image showing the 7 m draft fishing boat Fiskebas used to generate internal waves. The delta-K radar beam is shown as an inscribed circle.

digitally with a period of 10 s throughout the daylight hours. Fig. 1 is a video image from the higher resolution camera showing the deep draft (7 m) Norwegian fishing boat Fiskebas, which was used to generate internal waves. Fiskebas was run in a racetrack pattern passing the near and far edges of the radar beam, on a course calculated to provide internal waves propagating precisely toward or away from the radar. In fact, early in the experiment the racetrack orientation was adjusted slightly based on the video images. The delta-K radar antenna one-way (3dB) beamwidth of 2.1° is shown inscribed on the video image in Fig. 1. The center of the beam is at an incidence angle of 70.4°. When the circular beam is projected onto the water surface it becomes an ellipse with major and minor axes of 268 m x 89 m.

Theoretically, in order to calculate the dispersion relation from a time sequence of two dimensional images it is necessary to compute the 3-D spectrum $S(\omega, k_x, k_y)$. This was the approach adopted for the study of wind wave dispersion in [1]. However, since the internal waves under study were propagating along the y axis, all we really want to compare with the delta-K radar is a cut through the 3-D spectrum, $S(\omega, k_x = 0, k_y)$. This was obtained by averaging the video data in the cross-look direction [2], correcting for foreshortening, and constructing a space-time image. Computing the 2-D spectrum of this image yields $S(\omega, k_x = 0, k_y)$. Note that S is the spectrum of image radiance, not the wave height spectrum, but it should nevertheless provide information on the propagation velocities of the underlying internal waves. Had we computed the full 3-D spectrum it would have been possible to estimate the average vector current present [1], a calculation we plan to carry out in the near future.

Fig. 2a shows the space-time image computed for run 1101 on 11 Aug. 1995. Large gradients in brightness were removed in order to improve feature recognition. In this run, Fiskebas passed on the far side of the video image, hence the ship itself does not appear in any of the images. Starting slightly after 05:03 the lead internal wave entered the top of the video image with a phase velocity of approximately 0.74 m/s. As expected for a dispersive wave system, the internal waves gradually decreased in wavelength while simultaneously weakening (see Fig. 2a at 05:30). A 2-D Fast Fourier Transform (FFT) was computed after windowing the image with a 10% cosine taper. The resultant spectrum shown in Fig. 2b shows a very clearly defined peak in the spectral density lying slightly below the dashed theoretical curve. The theory curve is the simplified dispersion relation given by Barber [3], with a Brunt Vaisala frequency of 0.0398 Hz, and maximum phase velocity of 1.09 m/s, both measured by a CTD cast nearby in time. We plan to incorporate a correction for the mean current flow into the theoretical calculation in the near future.

11 August 1995

(a)

(b)
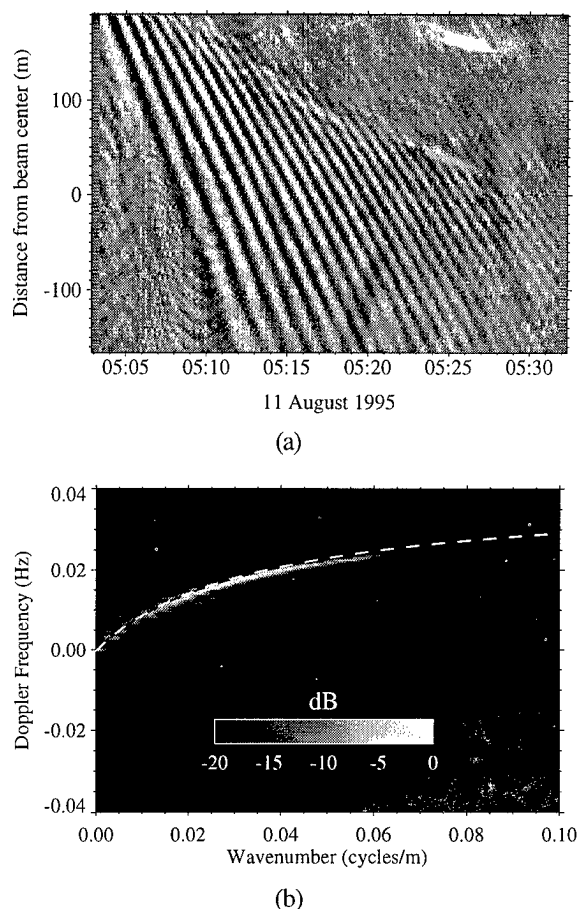
Fig. 2 — Run 1101 optical data. (a) Space-time image, (b) Wavenumber-frequency spectrum.

DELTA-K RADAR MEASUREMENTS

The delta-K radar was a coherent horizontally polarized X-band multi-carrier radar system equipped for transmission of 32 simultaneous interrupted CW carriers from a circular aperture 0.9 m diameter antenna. The 32 frequencies were chosen to give evenly spaced difference frequencies from 0.63585 MHz to 148.789 MHz. Separate transmit and receive antennas were used. The transmitter and receiver pulse lengths were set to 3.1 μs, with a repetition interval of 9.4 μs. The complex (I/Q) time series were simultaneously sampled at 500 Hz.

The algorithm for computing wavenumber-frequency spectra consists of multiplying the various pairs of raw complex time series together, correcting for gain differences, smoothing and subsampling to a 10 Hz rate, and finally computing the spectrum of each of the 496 delta-K time series over an interval of 200 s. Redundant spectra corresponding to the same difference frequency are ensemble averaged together.

Fig. 3a shows a frequency-wavenumber spectrum which has been ensemble averaged over 1200 s, corresponding to the entire period of significant internal wave activity. Difference frequencies to approximately 16 MHz were used in constructing this figure. The peak in the spectrum at approximately 0.015 cycles/m lies on the dashed theoretical curve, but there is a progressive deviation at higher wavelengths. When each of the spectra that went into the ensemble average are viewed separately, it is apparent that the spectral peak in each one lies on the theoretical dispersion curve, with a linear feature extending toward higher wavenumbers. The reason for the apparent linear trend in the ensemble averaged spectrum is due to the dominance of the spectra early in the event when the internal waves are significantly stronger. Fig. 3b shows a single 200 s spectrum near the end of the event. Here the spectral peak again lies on the theoretical curve at a wavenumber of approximately 0.04 cycles/m. The linear feature is missing, possibly because the signal has become so small that the weaker linear feature has fallen below the noise floor.

We can only speculate at this time as to the cause of the linear features in the wavenumber-frequency spectra from the delta-K radar. At the beginning of the event, when the lead wave begins to intrude into the antenna beam, there are not enough cycles to "resonate" with the delta-K processing, hence the spectra respond as if there is a non-dispersive target moving through the beam with the phase velocity of the lead wave. However, this period ends fairly soon as the beam fills. The data we have inspected to date indicate that the linear feature (which is not present on all runs) persists long after the beam has filled. An alternate explanation, suggested to us by K. Ward, is that nonlinear scattering of the radar signal from the water surface gives rise to the linear dispersion.

(a)

(b)

Fig. 3 — Wavenumber-frequency spectra from the delta-K radar. (a) Averaged over the entire event, (b) Averaged over 200 s near the end of the event.

CONCLUSIONS

The dispersion relation for ship generated internal waves has been measured optically and with a delta-K radar. Both techniques compared favorably with theoretical calculations based on the measured *in-situ* data. However the radar derived spectra also exhibit a linear feature which may be caused by a strong nonlinear scattering mechanism.

REFERENCES

[1] Keller, M. R., B. L. Gotwols, W. J. Plant and W. C. Keller, "Comparison of optically-derived spectral densities and microwave cross sections in a wind-wave tank", J. Geophys. Res., Vol. 100, pp. 16,163-16,178, 1995.

[2] Irani, G. B., B. L. Gotwols, and A. W. Bjerkaas, "The 1978 ocean wave dynamics experiment", in Wave Dynamics and Radio Probing of the Ocean Surface, O. M. Phillips and K. Hasselmann, eds., Plenum Press, New York, pp. 165-179, 1986.

[3] Barber, B. C., "On the dispersion relation for trapped internal waves", J. Fluid Mech., Vol. 252, pp. 31-49, 1993.

The Coastal Ocean Probing Experiment: Further Studies of Air-Sea Interactions with Remote and In-Situ Sensors

Robert A. Kropfli[1] and Steven F. Clifford[2]
NOAA/Environmental Technology Laboratory
325 Broadway, Boulder, Colorado 80303

[1]*Corresponding Author*
ph: 303-497-6235
fax: 303-497-6978
email: rkropfli@etl.noaa.gov

[2]*Collaborating Author*
ph: 303-497-6291
fax: 303-497-6020
email: sclifford@etl.noaa.gov

INTRODUCTION

A comprehensive multi-sensor experiment on air-sea interactions was held off the coast of northern Oregon during September and October of 1995. The experiment, called the Coastal Ocean Probing Experiment (COPE), utilized the Environmental Technology Laboratory's (ETL) two shore-based microwave radars, one at x-band and the other at k_a-band, and a full complement of in-situ and other remote sensors. Sensors were mounted on the Scripps Institute Floating Instrument Platform (FLIP) to measure properties of the air-sea interface including wind, wind stress, air/sea temperatures, wave characteristics, and profiles of current, temperature, and density. Scatterometers at k_u-band and x-band, a laser wave slope device, and microwave and IR radiometers were also operated from FLIP. Other active and passive remote sensors were deployed from a blimp, and a small complement of in-situ and atmospheric sensors were operated from a 65 ft boat, the Snowgoose. A moored array consisting of thermistor chains and an inverted echo sounder was also operated within view of the radars. Additionally, a Doppler lidar was operated near the shore to measure winds within a few meters of the ocean surface and a Coastal Ocean Dynamics Radar (CODAR) system was used to monitor larger scale ocean currents in the area.

The northern coast of Oregon was selected for its wide variety of atmospheric and oceanic conditions and particularly for the frequency and intensity of tidally-forced internal waves (IW) in that area. The proximity of a 744 m-elevation radar site within 4 km of the shoreline satisfied another important observational requirement.

As expected, a wide variety of wind and wave conditions were experienced during COPE with swell varying from less than 1 m to over 3 m and winds up to 17 ms^{-1}. Nearly all sensors observed manifestations of the tidally-forced internal waves, often during conditions of high wind and waves when such signatures would not seem to be expected.

Preliminary results of radar observations will be stressed here, particularly regarding observations of the naturally-occurring internal wave fields. The large amount of high-quality, in-situ atmospheric and oceanic measurements available during the experiment will be useful in helping to interpret the various polarimetric, Doppler, delta-k, and multi-wavelength radar data obtained during COPE.

THE EXPERIMENT

The IW packets in the experimental area are caused by tidal flow over a well-defined shelf break about 70 km offshore and the nearby source of fresh, warm water from the Columbia River that produces a strong density gradient at a depth of ~15 m. SAR imagery such similar to that shown in Fig. 1 (courtesy of John Bates, NOAA/Climate Diagnostics Center) gave us good reason to believe that this region would be active with internal waves.

Two instruments critical to the success of COPE were the ETL x-band and k_a-band Doppler radars which were operated together from the 744 m level near Onion Peak, 4 km from the shoreline and 50 km south of the Columbia River. This high site allowed the radars to observe backscatter from the ocean to 50 km range and covered the entire region sampled by FLIP, the blimp, the Snowgoose, the moored array, the lidar, and the CODAR as shown in Fig. 2.

The radars operated in a variety of modes, usually on a two hour cycle. These modes included surveillance scanning to cover the entire region in relatively coarse detail, higher resolution but limited-area scans, and fixed azimuth/variable elevation scans for observing radar cross-section as a function of grazing angle. Other radar data that were collected as conditions allowed were 1) fixed beam (FB) data to allow wave fronts to propagate through and allow ω vs. k plots to be constructed from two dimensional

Fig. 1. SAR imagery off the northern Oregon coast at 0625 Z on Sept. 11, 1995.

Fig. 2. COPE experimental layout. Grazing angles are shown at each range mark

FFTs of the range/time images, 2) FB delta-k data to observe surface currents at high resolution, 3) FB Doppler spectra data to examine spectrally-resolved details of the echo at different polarizations, and 4) repeated sweeps of the antenna at fixed elevation over several hours to observe the wave temporal evolution. These data modes allowed for measurements of the spatial/temporal characteristics of HH, VV, HV, and Doppler velocity to be observed at the two radar wavelengths. Radar parameters are given in Table 1.

The overall objectives of COPE are threefold: 1) to determine the extent to which environmental conditions affect our ability to observe the surface strain rate field with active and passive microwave techniques, 2) to improve our ability to retrieve ocean surface layer fluxes, stability and winds with active and passive microwave sensors, and 3) to increase our overall understanding of scattering and emission from the ocean under all atmospheric conditions. COPE was organized and coordinated by NOAA/ETL, but it benefited greatly because of major contributions by researchers from the Naval Post Graduate School, University of Washington Applied Physics Laboratory, Johns Hopkins University Applied Physics Laboratory, Woods Hole Oceanographic Institute, the Canadian Institute for Oceanographic Sciences, and the University of Washington. It differed significantly from the San Clemente Ocean Probing Experiment (SCOPE) conducted by ETL two years earlier in that it was located in an active field of naturally-occurring IWs, it experienced a much wider variety of wind and wave conditions, there was a stronger emphasis on measuring inhomogeneous flows and density profiles with a better complement of in-situ meas-

urements, there were significant enhancements to ETL remote sensing instrumentation, and there was wider external involvement which brought to the experiment important instrumentation such as scatterometers, thermal imaging devices, CTDs, thermistor chains, acoustic Doppler current profilers and laser wave measurements from other organizations.
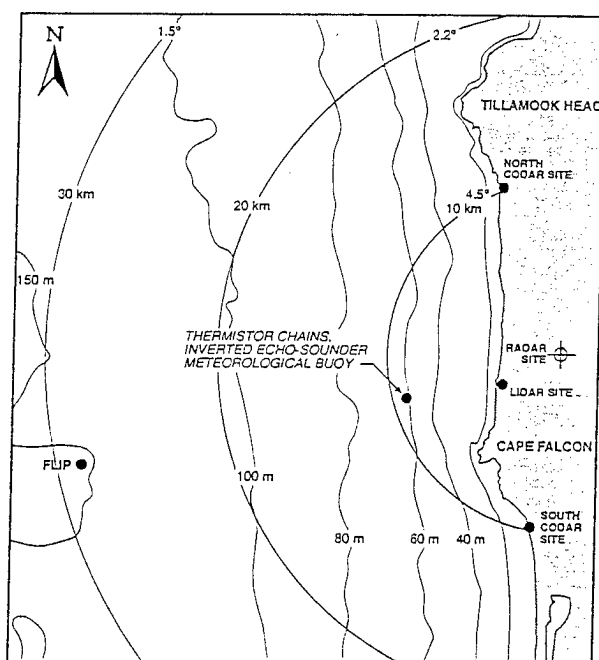
Table 1. Characteristics of ETL Ocean Radars

Parameter	X-band	K_a-band
Peak Power (KW)	20	100
Pulse Width (m)	7, 37, 150	37
Beamwidth (deg)	1.0	0.5
H/V Pol Switching	fast, ferrite	slow, mechanical
No. Gates	328	328
Doppler	yes	yes
Delta-k Bandwidth	35 MHz	N.A.

INITIAL RADAR RESULTS

Internal waves were observed on nearly all of the 24 days of radar operations. The contrast with which they

1740

could be seen (defined as the peak-to-peak amplitude of the return signal) varied with wind speed, polarization, radar wavelength, and other factors. The effect of surface layer stability is currently being investigated. Fig. 3 shows an image of the IW field when the wind was 11 ms^{-1} from the north, i.e., approximately along the wave front. Radar echo is shown from 22 to 30 km and the leading edge of IW appears at 26.5 km from the radar. Its contrast is seen to be greater at HH (right frame) than at VV. FLIP is seen at a range of 29 km and an azimuth of 257°.
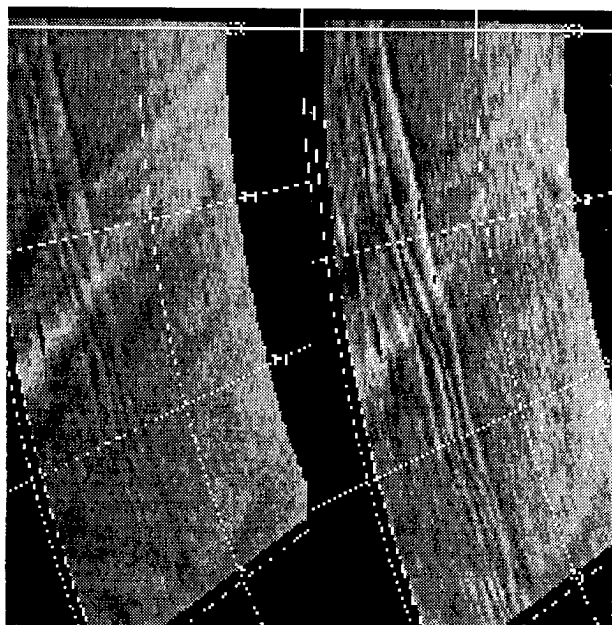
Fig. 3. X-band radar images of IW field at 2226 Z on Sept. 19, 1995. Grazing angle is approximately 1.7 degrees. HH and VV images are in right and left frames respectively.

An average of data from 247° to 253° is shown in Fig. 4 and clearly shows the increased contrast in HH over VV. HH shows peak-to-peak swings of about 9 dB whereas VV is less than 4 dB. This was generally the case as shown in Table 2 where the IW peak-to-peak amplitudes are shown for both polarizations on other days having light, moderate and strong winds. It is noted that the IW signature was evident at HH even when the winds were very high (17 ms^{-1}) and the sea was rough. The leading edge of IW packets as viewed with the radars during COPE generally propagated at about 0.9 ms^{-1} and crest-to-crest distances near the leading edge were typically about 800 m. Detailed radar observations, including time lapse imagery of IW packets and radar wavelength differences, will be discussed during the presentation.

A wide variety of delta-k observations (Plant and Schuler, 1980) were also taken during COPE with the intent of measuring surface current gradients at a measurement
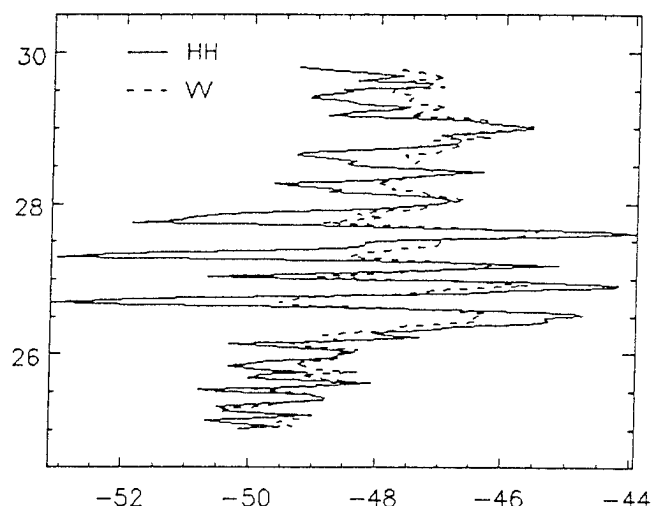
Fig. 4. Average of X-band radar signals at VV and HH within azimuth sector from 247° to 253° at 2226 on Sept. 19, 1995.

Table 2. Contrast for each polarization for various wind speeds during COPE.

Wind Speed (ms^{-1})	VV	HH
1	8 dB	>8 dB
5	7 dB	>19 dB
8	6 dB	19 dB
15	**	8 dB

resolution of 150 m in the vicinity of an IW. Improvements in delta-k processing algorithms have been found since SCOPE which, under many conditions, significantly improve the signal-to-noise ratio. These results will also be discussed.

ACKNOWLEDGEMENTS

REFERENCES

[1] Kropfli, R.A., and S.F. Clifford. "The San Clemente Ocean Probing Experiment: A study of Air-Sea Interactions with Remote and In-Situ Sensors." IGARSS '94, Pasadena, CA, IEEE, NY, NY, 2407- 2409 (1994).
[2] Plant, W.J., and D.L. Schuler. "Remote sensing of the sea surface using one- and two-frequency microwave techniques." *Radio Sci.* 15 (1980): 605-615

The Estimation of Ocean Current from ω-k Analysis of Radar Data

T. Lamont-Smith
Defence Research Agency
St. Andrew's Road, Malvern
Worcestershire, WR14 3PS
phone: (01684) 894007
e-mail: tlsmith@taz.dra.hmg.gb

Abstract -- 2D Fourier transform analysis was carried out on radar sea clutter data. It was found that the gravity wave dispersion relation and its harmonics were clearly visible in the ω-k images. The dispersion curve and its harmonics were found to be distorted and rotated from their expected positions due to the existence of ocean currents. Measurements are made from the dispersion curves of both advancing and receding waves, and a significant difference is observed between the two measurements.

INTRODUCTION

An experiment was carried out jointly by DRA Malvern and DRA Southwell from the 5th to the 28th October 1994 from a cliff-top site at Portland, on the south coast of England. A high resolution (1.5m), dual polarisation and multi-frequency radar was positioned on the cliff-top (60m above sea level). Either 10GHz and 16GHz, or, 10GHz and 3GHz, were measured simultaneously with both vertical and horizontal polarisation. The range to the middle of the swath was around 2.5km, thus there was a grazing angle of 1-2°. The beam width of the radar was around 1°.

The depth of the sea was between 35-40m over the area of observations. The position of the site was such that large swell waves, presumably from the Atlantic, were present.

Several environmental buoys were fielded that collected directional wave spectra, ocean current, wind speed, as well as a number of other parameters.

Remote sensing measurements of ocean currents have been made for many years by researchers using HF radio measurements [1,2]. At the microwave frequencies used in this experiment, the Bragg peaks in the Doppler spectra are not distinct enough for accurate measurement. A technique similar to that used by Young and Rosenthal [3], is more effective.

In an ω-k image, we would expect most of the spectral energy to lie along a line along a line defined by the gravity wave dispersion relation,

$$\omega_0^2 = kg \tanh(kd)$$

(1)

Where ω_0 and k are the wave frequency and wave vector respectively, g is the acceleration due to gravity and d is the depth of the water.

A current represents a transport of the water mass, and can be thought of as a translation of the entire coordinate frame of the waves. So that if there is a current **V** relative to the observer then there will be an additional Doppler shift **k.V** superimposed on the Doppler spectrum seen in the ω-k image. The final Doppler shift is given by,

$$\omega = \omega_0 + \mathbf{k.V}$$

(2)

where ω_0 is the frequency of the gravity waves in the absence of a current, and ω is the frequency observed for a particular wave of wave vector k in the presence of a current.

DATA ANALYSIS

Fig. 1 shows Range-Time-Intensity (RTI) images produced from data that has been averaged to 1 second per pixel. There are two different frequency bands, I-band (10GHz) and F-band (3GHz), and two different polarisations. The most obvious difference visible between the images is that the H-pol data is spikier than the V-pol.

Fig. 2 shows the corresponding ω-k images of the data shown in Fig. 1. The gravity wave dispersion curve, both positive and negative, can be observed. The negative curve comes from waves receding from the radar, and away from the shore, against the predominant wind direction.

A harmonic of the dispersion curve may also be seen. If we use the deep water approximation, where we neglect the $\tanh(kd)$ term because it tends to 1 for sufficiently large d, then we may write,

$$\omega' = 2\omega_0, \quad k' = 2k,$$
$$\omega'^2 = 2k'g .$$

(3)

In general the harmonics take the form $\omega_0^2 = nkg$, where $n=2,3,4,..$

It is obvious in Fig. 2 that the curves are not symmetric, and that they have been affected by the presence of an ocean current. Equation (2) was used to simulate what we would expect to see in the ω-k image. Fig. 3 shows the effect on the positive dispersion curve only, for currents between +2.5ms⁻¹ to -2.5ms⁻¹ in steps of 0.5ms⁻¹. Fig. 4 shows the effect for both positive and negative

sides of the dispersion curve, when there is a current of 1ms^{-1} towards the radar. Even quite modest currents produce a significant distortion to the ω-k images.

Fig. 5 shows a slice taken at a constant value for k through one of the ω-k images shown in fig. 2. The scale of the ω-k image is in fact frequency, f and wave vector $1/\lambda$, so we get $1/\lambda=0.0625$m^{-1} and $f=0.2676$Hz. Using the value of λ and g (9.81ms^{-2}) to calculate f_0, we may then by using (2) calculate the current towards the radar, V. For the advancing waves the current is measured to be -0.71ms^{-1}, but for the receding waves (negative dispersion curve), $V=-0.88$ms^{-1}.

It is possible to make these measurements with different radar look angles. The results are summarised below. The error for each of the measurements is around +/-0.04ms^{-1}.

Table 1

Radar look direction	Current measured (m/s)	
	Adv. waves	Rec. waves
into wind	-0.68	-0.91
45^0 to wind	0.45	0.25
across wind	0.90	0.73

The current for advancing waves appears to be consistently greater (more positive) than that for the receding waves by around 0.2ms^{-1}. Further measurements from data collected into wind over two days, show that although the current varies substantially through the period due to tides, there is still a nearly constant 0.2ms^{-1} difference.

Wave Resolution and Spatial Selectivity

We can make an approximation that waves of a particular wavelength are not resolvable if there are many peaks and troughs for those waves in each range cell. Fig. 6 shows the geometry used to estimate limits for the minimum wavelength resolvable for a given angle of entry. We assume that there should be only one wave crest of a wavelength λ in a range cell at any time, and that all the waves are long-crested. Thus,

$$\lambda/2 > R\phi \, |\sin\theta| + w|\cos\theta|,$$

(4)

where θ is the entry angle of the wave into the range cell, R is the range from the radar and ϕ is the beam width. The length of the long axis of the range cell is given by $R\phi$ (~80m), and the width of the short axis is w (1.5m). So for a wavelength of 5m, the entry angle is restricted to around +/-2^0. Manasse [4] produces very similar results for the same radar system by using Fourier transform theory.

Fig. 7 shows a simulation of what we would expect to see in the ω-k image if there were waves present of every wavelength and travelling in every direction. There is some broadening of the curve for long wavelengths. A comparison of the simulation with any of the ω-k images in fig. 2 shows good agreement, if the effect of current is ignored.

Conclusions

From ω-k analysis of high resolution, narrow beam width radar, it is possible to see the gravity wave dispersion relation and its harmonics. There is slightly less line resolution for H-pol than V-pol, but otherwise the results are very similar for both frequency bands and polarisations.

The curves are effected by the presence of currents. Advancing and receding waves appear to be effected in a different way, or else there is a slightly different imaging mechanism that is causing the difference.

It is apparent from the ω-k images that a high degree of spatial selectivity must exist in order for the dispersion curves to be so sharply defined. We would expect to see a solid cone if there were no spatial selectivity.

ACKNOWLEDGMENTS

REFERENCES

[1] R. H. Stewart, J. W. Joy, "HF radio measurements of surface currents", Deep-sea Res., 21, pp1039-1049, 1974

[2] D. E. Barrick, M. W. Evans, B. L. Weber, "Ocean surface currents mapped by radar", Science, 198, pp138-144, 1977

[3] I. R. Young, W. Rosenthal, "A 3D analysis of marine radar images for the determination of ocean wave directionality and surface currents", J. Geophys. Res., 90(C1), pp1049-1059, 1985

[4] R. Manasse, "Pencil beam radar selectivity of ocean wave spectra", Lawrence Livermore Nat. Lab. internal report, UCRL-ID-118533,1994
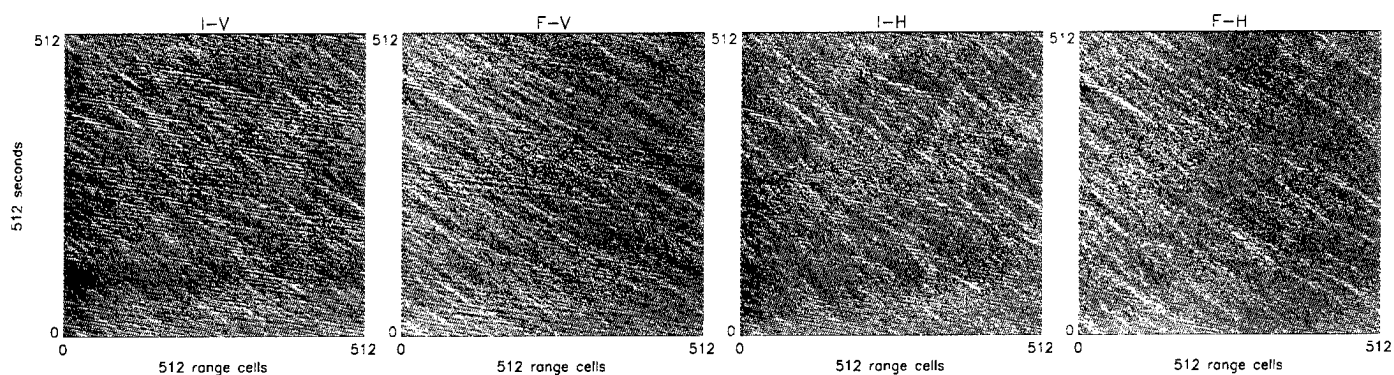
Figure 1: Range–Time–Intensity images, 512 seconds of data and 768 metres range swath.
Wind speed 9.8m/s, blowing towards the radar
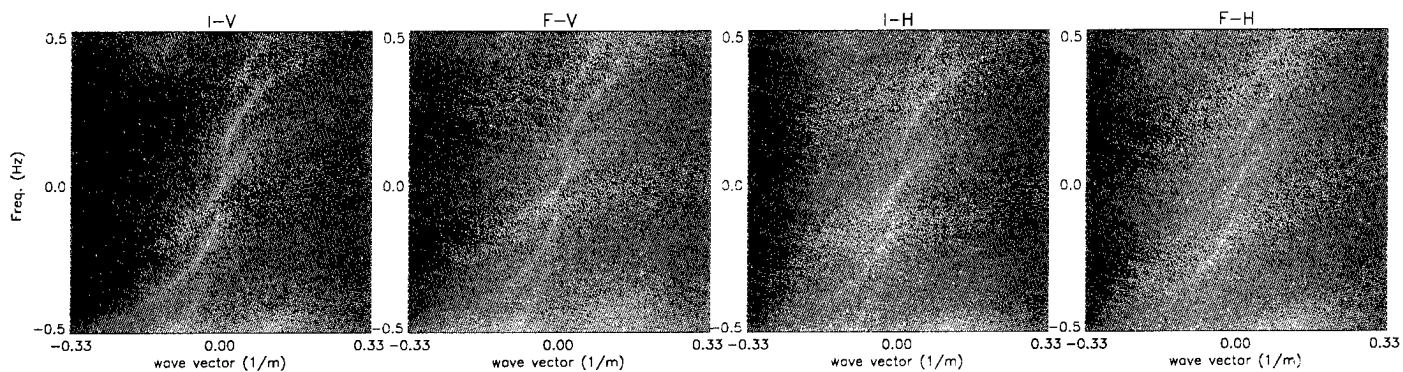
Figure 2: 2D Fourier transforms of images in fig. 1
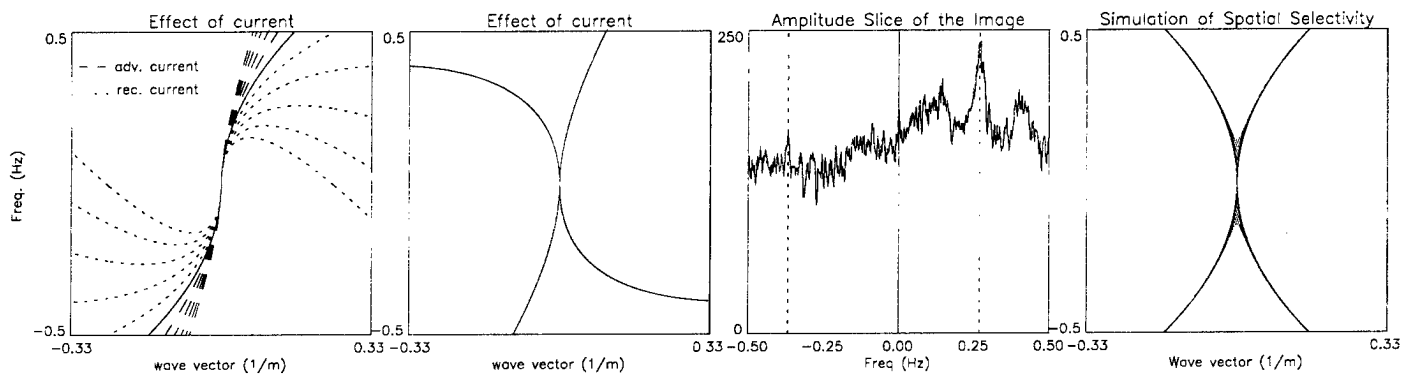
Figure 3: Effect of current from +2.5m/s to −2.5m/s

Figure 4: Effect of current, 1m/s towards the radar

Figure 5: Slice of I−V image at const. wave vector

Figure 7: simulation with spatial selectivity

Radar line of sight
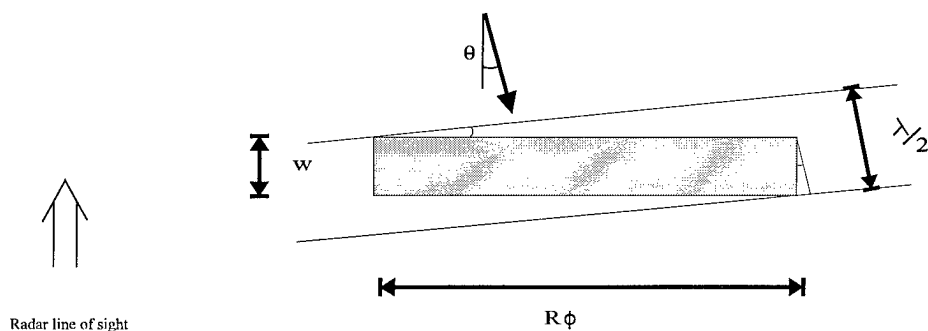
Figure 6: Sketch of geometry for waves entering a range cell at some angle

High Resolution Polarimetric Radar Scattering Measurements of Low Grazing Angle Sea Clutter

E.M. Twarog and D.J. McLaughlin
ECE Department
Northeastern University
Boston, MA 02115 USA
(617) 373-2032/2117

N. Allan
Sachs-Freeman Inc.
Landover, MD 20785 USA

Abstract - This paper presents fully polarimetric radar scattering measurements of low grazing angle sea clutter. The measurements were obtained at a three degree grazing angle using a high range resolution (1.5 m) X-Band polarimeter operated from a shore site overlooking the Chesapeake Bay. Analysis of these measurements indicates that "sea spike" radar echoes are caused by a combination of two or more independent scattering mechanisms, such as a population of non-Bragg scatterers at breaking wave crests, superimposed on a background of distributed Bragg resonant waves. The experimental data are compared with theoretical polarimetric scattering models based on Bragg scattering as well as Bragg scattering augmented with scattering from wedges and plumes. Polarization signatures for the composite Bragg+plume model are shown to more closely predict the experimental data than the Bragg model alone or the composite Bragg+wedge scattering model.

I. INTRODUCTION

Radar systems operating from ship and shore-based platforms tend to view the ocean surface at grazing angles below a few degrees. Microwave radar backscatter from the ocean at these low grazing angles (LGA) is more complex and less-well understood than ocean scattering at higher grazing angles. A striking characteristic of LGA sea scatter is the presence of "sea spikes" - large amplitude scattering events, of ~ 1 second duration frequently observed in high-resolution (~10 m) horizontally polarized (HH) microwave sea echoes. Sea spikes exhibit cross-section values, polarization ratios (ratio of HH to VV normalized radar cross section) and Doppler shifts significantly larger than be explained by a distributed Bragg-resonant surface scattering model. The occurrence of sea spikes is generally associated with the passage of breaking wave crests through the radar resolution cell, but the scattering mechanism or mechanisms responsible for these echoes are presently unknown.

Examination of dual polarized (VV and HH) amplitude statistics [1,2], Doppler spectra [3,4], and polarization signatures [5] of LGA radar echoes from the ocean suggests that a combination of Bragg resonant waves and non-Bragg scatterers are contributing to the sea spike events.

Scattering structures associated with breaking wave crests, such as wedges [6] and plumes [7], have been suggested as being responsible for the non-Bragg component of the sea spike echo. In this paper, we examine the Stokes scattering matrix descriptions of wedge, plume, and Bragg-wave scatterers and compare these descriptions with the fully polarimetric scattering measurements of sea spikes reported in [5].

II. POLARIMETRIC SCATTERING FROM SEA SPIKES

Polarimetric scattering measurements of ocean waves were performed during August 1992 from a shore site overlooking the Chesapeake Bay. The X-band (9.3 GHz) radar was installed on a cliff, 35 m above sea level, with the antenna beam directed into the incoming wind and waves. Visually, the wave field was composed of trains of regularly-spaced wind waves propagating perpendicular to the shore line, with occasionally breaking crests. Measurements were obtained at a distance of approximately 700m from shore at a three degree grazing angle in 7 m deep water. The radar had 1.5 m range resolution. The radar, experiment design, and signal processing are described in detail in [5].

A. Polarization Signatures of Sea Spikes

A Stokes scattering operator representative of sea spike echoes was computed by averaging individual Stokes operators for fifteen different sea spike events resulting in the 4x4 matrix (using the notational convention from our earlier paper [5]):

$$\begin{bmatrix} 1.0000 & -0.2209 & 0.0540 & 0.0224 \\ -0.2008 & 0.7642 & 0.0698 & 0.0186 \\ 0.0417 & 0.0591 & 0.2544 & 0.0008 \\ -0.0079 & 0.0058 & -0.0586 & -0.0343 \end{bmatrix}$$

The "polarization signature" calculated from this matrix is shown in Fig 1. Salient features of this plot include: large cross-section values at both horizontal (orientation angles of ±90°, ellipticity angle of 0°) and vertical (orientation angle 0°, ellipticity angle 0°) polarizations, a large "pedestal" value of ~0.4 on which the wavy signature surface sits, and a "coefficient of variation" (ratio of the minimum to

maximum cross-section values for a polarization signature plot) of 0.31, indicating that sea spike scattering events are not highly sensitive to radar polarization. The last row of Table 1 summarizes the VV and HH normalized radar cross section (NRCS) values in dB for the sea spikes as well as the polarization ratio (the dB difference of HH to VV NRCS, denoted by χ_{hhvv}) and the coefficient of variation, υ, for the signature plot of Fig. 1. The quantity ρ_{vvhh} in the Table is a normalized covariance coefficient describing the correlation between vertically and horizontally copolarized scattering components. The low value of 0.17 for this coefficient indicates that the VV and HH scattering coefficients are dominated by different, independent scattering mechanisms. (The remaining three rows of Table 1 contain the same set of parameters for three other scattering models to be discussed below.)

Table 1: Parameters for Models and Measured Data

Model	σ°_{vv}	σ°_{hh}	χ_{hhvv}	ρ_{vvhh}	υ
Bragg	-55.7	-27.5	-28.2	1.00	1.3e-4
Bragg + Wedge	-25.1	-22.2	-3.0	0.86	0.05
Bragg + Plume	-25.2	-25.7	0.5	0.60	0.19
Sea Spike data	-25.1	-27.2	2.4	0.17	0.31

B. Bragg Scattering Model

The complete set of six scattering matrix elements required to calculate the Stokes scattering operator for second-order Bragg scattering can be found in [8]. For a zero degree tilt angle, the Stokes scattering operator for the Bragg model based on a saturated capillary wave spectrum is given by:

$$\begin{bmatrix} 1.0000 & 0.9968 & 0 & 0 \\ 0.9968 & 0.9999 & 0 & 0 \\ 0 & 0 & 0.0758 & 0.0218 \\ 0 & 0 & 0.0218 & -0.0758 \end{bmatrix}$$

and the corresponding polarization signature is shown in Fig. 2. In contrast to the signature of sea spikes, the polarization signature for Bragg scattering is characterized by a strong vertically polarized response, weak horizontally polarized cross-section (polarization ratio of -28.2 dB), low coefficient of variation of $1.3 \cdot 10^{-4}$, and negligible pedestal. These quantities are listed in the first row of Table 1. Bragg scattering predicts VV cross section levels within one dB of the measured sea spike data. However, the Bragg model significantly underpredicts both the measured HH cross section levels and the polarization ratio, by nearly 30 dB.

C. Composite Bragg+Wedge Scattering Model

Ref. [6] suggested that scattering from wedge-shaped surface elements whose radii of curvature are small with

respect to the radar wavelength may become important scattering mechanisms for breaking waves at low grazing angles. They showed that by incoherently superimposing scattering from a population of normally-aligned wedges onto a Bragg scattering background, the resulting composite model can predict both VV and HH NRCS values close to measured LGA data. The wedge scattering cross section dominates the predicted HH cross section values for LGA, whereas the Bragg and wedge scattering contributions are compatible with one-another for the VV polarized case.

The RCS contribution from the wedges is calculated as a function of local grazing angle and an external wedge angle. A value of 240° for the exterior wedge angle was suggested by [6] based on the predicted interior angle for a wave at the onset of breaking and will be used for the results presented here.

The normalized Stokes scattering operator for the wedge scattering model is given by:

$$\begin{bmatrix} 1.0000 & 0.1687 & 0 & 0 \\ 0.1687 & 1.0000 & 0 & 0 \\ 0 & 0 & 0.9856 & 0 \\ 0 & 0 & 0 & -0.9856 \end{bmatrix}$$

The corresponding polarization signature is shown in Fig. 3. The polarization signature for the wedge exhibits nearly equal VV and HH cross sections (polarization ratio -1.48 dB), a negligible pedestal, and extremely low coefficient of variation (υ=0.006).

To incorporate a wedge contribution to into a composite Bragg plus wedge model, an average length L and number N of the wedges per unit area must be estimated. The wedge cross section component is proportional to $L^2 N$, and the total cross section is obtained by incoherently adding this wedge contribution to the Bragg model. *A value of $L^2 N = 0.12$ is used in this paper to match the measured sea spike cross section at HH polarization.* The normalized Stokes scattering operator for the combined Bragg plus wedge model is given by:

$$\begin{bmatrix} 1.0000 & 0.3278 & 0 & 0 \\ 0.3278 & 1.0000 & 0 & 0 \\ 0 & 0 & 0.8108 & 0.0042 \\ 0 & 0 & 0.0042 & -0.8108 \end{bmatrix}$$

and the corresponding polarization signature is shown in Fig. 4. The composite signature exhibits large HH and VV levels but lacks the large pedestal that characterized the experimental sea spike polarization signature. Furthermore, the VV and HH polarized components predicted by this composite model are highly correlated, in contrast to the measured data. These results are tabulated in Table 1. This high correlation results from the wedge contribution yielding high cross section values for both VV and HH elements of the polarization scattering matrix.

C. Composite Bragg+Plume Scattering Model

Wetzel [7] proposed a model based on scattering from "plume" water masses generated at breaking wave crests. In the open sea, breaking waves tend to be of the "spilling" type, where the crests sharpen until the interior crest angle reaches the point of instability, and the plume water masses then break from the crest and slide down the front face of the wave due to gravity. Wetzel modeled a plume as a conducting half cylinder sitting on an inclined flat plane. The electromagnetic field incident on the plume is composed of a direct field reflected from the cylindrical surface in addition to a multipath field forward-reflected from the smooth water surface ahead of the cylinder. Resulting cross section values are highly sensitive to changes in local grazing angle, plume diameter and position, due to the varying interference between the direct and forward-reflected propagation paths. The results are also highly polarization sensitive due to the substantially different LGA Fresnel reflection coefficients for sea water at horizontal and vertical polarizations.

The RCS contribution from the plumes is calculated as a function of local grazing angle and a ka plume size parameter, where electromagnetic wavenumber k is 2 cm^{-1} at X-band and a is the plume's cylindrical radius. The model is highly sensitive to values of ka, the number of oscillations in the predicted HH and VV cross sections versus grazing angle curve increasing with increasing ka. The normalized Stokes scattering operator for a plume scatterer with $ka = 40$ is given by:

$$\begin{bmatrix} 1.0000 & -0.5303 & 0 & 0 \\ -0.5303 & 1.0000 & 0 & 0 \\ 0 & 0 & 0.7104 & -0.4628 \\ 0 & 0 & -0.4628 & -0.7104 \end{bmatrix}$$

and the corresponding polarization signature is shown in Fig. 5. The signature shows a large HH response, significantly weaker VV response, no overall pedestal, and a coefficient of variation υ of 0.002.

The plume contribution to a composite scattering cross section is proportional to L^2N which, in the following, *is chosen to match the measured sea spike HH cross section level for a given value of ka.* The normalized Stokes scattering operator for a composite Bragg+plume scattering model having plume parameters $ka = 40$ and $L^2N = 4.5 \cdot 10^{-5}$ is given by:

$$\begin{bmatrix} 1.0000 & -0.0556 & 0 & 0 \\ -0.0556 & 1.0000 & 0 & 0 \\ 0 & 0 & 0.5131 & -0.3122 \\ 0 & 0 & -0.3122 & -0.5131 \end{bmatrix}$$

and the corresponding polarization signature is shown in Fig. 6.

The polarization signature shows a shape similar to that of the measured sea spike data, exhibiting large VV and HH cross sections and a copolarization ratio of 0.5 dB. The pedestal of ~0.25 is somewhat lower than the pedestal value for the sea spike measurements (0.45), however it is substantially higher than the pedestal value predicted by the Bragg+wedge model. The coefficient of variation is 0.19. The VV and HH scattering components are less highly correlated in this than in the previous model. This is the result of a high fraction of the total VV echo being caused by the Bragg waves in the Bragg+plume model, whereas the HH echo is entirely caused by the plume scatterer.

III. SUMMARY AND DISCUSSION

Large pedestals and coefficients of variation observed in the measurement polarization signature of Fig. 1 suggest that sea spikes are caused by a multiplicity of independent scattering mechanisms. The low value of the correlation coefficient $\rho_{vvhh} = 0.17$ indicates that vertically and horizontally co-polarized scattering measurements are each dominated by a different type of scatterer.

The Bragg scattering mechanism produces VV cross section values in close agreement with the measurement data but it significantly underpredicts the measured HH cross sections. A combination of Bragg and non-Bragg scatterers may explain the measured data. To reproduce the salient features of the measured polarimetric data, namely, similar VV and HH cross section values, ~ 0 dB polarization ratio, large pedestal, large coefficient of variation, and weak VVHH correlation, the non-Bragg scatterer must produce a large HH echo and a weak VV echo. Wedge scattering produces large VV and HH components and thus does not predict the features of the sea spike polarization signature reported here. Plume scattering, based on a multipath propagation factor model, is more polarization sensitive than wedge scattering. Plume parameters chosen to produce a large HH and weak VV cross section value, when combined with a Bragg scattering contribution, more closely predicted the data measured in this experiment than the wedge-based model.

IV. REFERENCES

[1] I.D. Olin, "Amplitude and temporal statistics of sea spike clutter," IEE Conf. Publ., 216, pp. 198-202, 1982.

[2] D.B. Trizna," Statistics of low grazing angle radar sea scatter for moderate and fully developed waves," IEEE Trans. Antenn. Propagat., vol. 39, pp. 1681-1690.

[3] E.G. Eckert, C.L. Rino, A. Siegel, and T. Webster, "Ocean microwave backscatter from the LOGAN experiment," in Proc. Int. Geosci. Remote Sensing Symp. (IGARSS-1994), Los Angeles, CA, 1994, pp. 815-817.

[4] P.H.Y. Lee, J.D. Barter, K.L. Beach, C.L. Hindman, B.M. Lake, H. Rungaldier, J.C. Shelton, A.B. Williams, R. Yee, and

H.C. Yuen, "X-band microwave backscattering from ocean waves," J. Geophys. Res., vol. 100, pp. 2591-2611, 1995.

[5] D.J. McLaughlin, N. Allan, E.M. Twarog, and D.B. Trizna, "High Resolution Polarimetric Radar Scattering Measurements of Low Grazing Angle Sea Clutter," IEEE Journal of Oceanic Engineering, Vol. 20, No. 3, July 1995, pp. 166-178.

[6] D.R. Lyzenga, A.L. Maffett, and R.A. Shuchman, "The contribution of wedge scattering to the radar cross section of the ocean surface," IEEE Trans, Geosci. Rem. Sens., vol. 31, pp. 502-505, 1983.

[7] L.B. Wetzel, "Models for electromagnetic scattering from the sea at extremely low grazing angles," Naval Research Laboratory, Washington, DC, Memorandum Report #6098, Dec. 1987, available from NTIS as ADA 190-472.

[8] D. Schuler, "Polarimetric SAR image signatures of the ocean and gulf stream features," IEEE Trans. Geosci. Remote Sens., vol. 31, pp. 1210-1221, 1993.
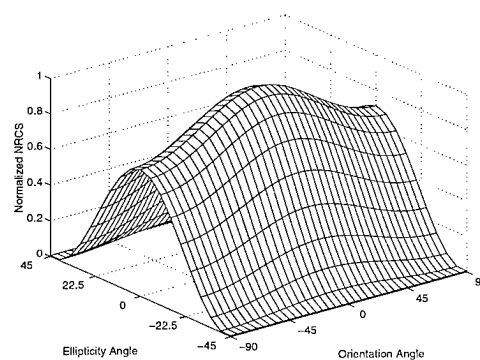
Fig. 3. Wedge model polarization signature
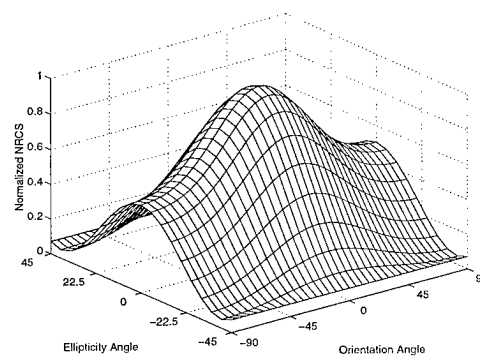
Fig. 4. Bragg+wedge model polarization signature
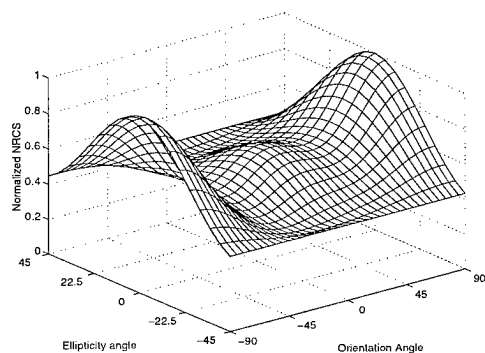
Fig. 1. Spike polarization signature
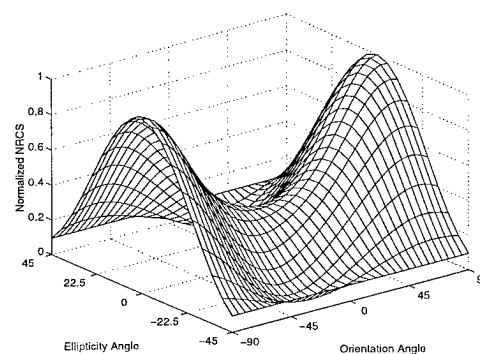
Fig. 5. Plume model polarization signature
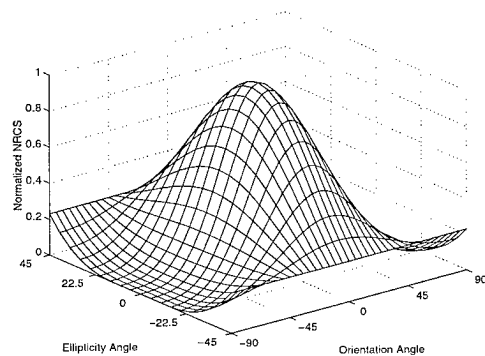
Fig. 2. Bragg model polarization signature
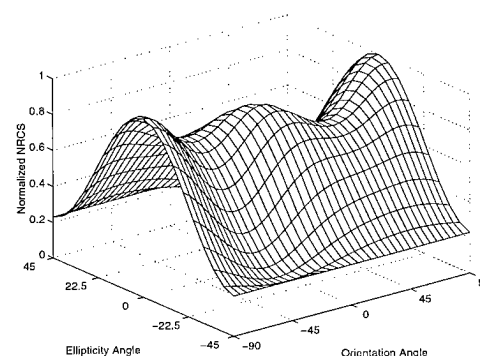
Fig. 6. Bragg+plume model polarization signature

Simultaneous CODAR and OSCR Measurements of

Ocean Surface Currents in Monterey Bay

Daniel M. Fernandez
University of California, CE/CIS Dept.
225 Applied Sciences Bldg.
Santa Cruz, CA 95064
Phone: (408) 459-4099, FAX: (408) 459-4829, e-mail: dan@cse.ucsc.edu

Jeffrey D. Paduan
Naval Postgraduate School, Code OC/Pd
Monterey, CA 93943
Phone: (408) 656-3350, FAX: (408) 656-2712, e-mail: paduan@oc.nps.navy.mil

Abstract – Presently, three Coastal Ocean Dynamics Applications Radars, or CODARs, which are ocean surface current measuring radars, are operated around Monterey Bay, California and provide data hourly to an ONR-funded real time environmental monitoring system operated through UC Santa Cruz known as REINAS. CODARs operate using Bragg scatter of high frequency (HF) radio waves from the sea surface to infer radial surface currents. They use direction finding techniques applied to compact, co-located antennae to determine the bearing angle of the measurements.

During 4-8 May 1995, a pair of high frequency radar units called Ocean Surface Current Radars, or OSCR's, were deployed within close proximity of two CODAR systems. Unlike the CODAR units, OSCR units rely on standard beam forming techniques using a long (80 m) phased array to determine bearing angle. The purpose of this demonstration was to highlight the capabilities of the OSCR systems. The presence of the CODAR network also provided a unique opportunity to compare measurements from the two types of HF radars to each other and to the suite of in situ instrumentation available in the Monterey Bay area.

This study focuses on comparisons of radials measured from each radar system along the corresponding radar baselines and comparisons of radial measurements from each radar site to the near-surface ADCP measurements.

INTRODUCTION

The potential for high-frequency (HF) radar instruments to measure ocean surface currents was first explored in the early 1970's [1, 2]. Since that time, various versions of high-frequency radar instruments have been used throughout the world for characterization and measurement of ocean surface circulation, as well as ocean wind and wave parameters.

The physical mechanism that allows all HF radars to generate ocean surface current measurements has been well documented in the literature. See, for instance [3, 4]. One major practical factor that affects the performance of off-the-shelf high-frequency radars is the technique that is used to determine the bearing angle for a given measurement. Techniques used by the systems described herein are beam steering and direction finding. Discussions on the implementations of both techniques may be seen in [5].

The CODAR systems that are stationed in the Monterey Bay area utilize a broad beam system and a direction finding technique to determine the bearing angle. The Marconi OSCR systems, on the other hand, use a narrow beam, which is steered to the desired bearing angle.

EXPERIMENT

Figure 1 illustrates the three sites in Monterey Bay at which the CODARs are located (two of which were also sites for the OSCRs during this period) along with averaged vector data derived from both the CODAR and OSCR units. The newer version of CODAR is called a CODAR SeaSonde and these units exist at Point Pinos and Santa Cruz. The CODAR SeaSonde at Santa Cruz operated at a frequency of 12.2 MHz, the Point Pinos CODAR SeaSonde and operated at 13.7 MHz, and the Moss Landing CODAR operated at 25.6 MHz during the experiment. Both CODAR SeaSondes (at Santa Cruz and Points Pinos) ran continuously, and produced new radials hourly. The Moss Landing CODAR, an older vintage machine, ran for about 40 minutes out of each two hour period and produced radials only every two hours. The OSCR sites were located at Moss Landing and Santa Cruz, and they produced new radials every 20 minutes based on 5 minutes of operation during each twenty minute period. Both OSCRs operated at about 25.4 MHz. The

OSCR at Moss Landing operated with a receive phased array of 16 whip antennas. The Santa Cruz OSCR site had less space available, and thus a receive array of only 11 antennas. The OSCR at Moss Landing operated at a frequency close enough to the CODAR that the OSCR data collected when the CODAR was turned on was very noisy. Similarly, at the Santa Cruz site, although the SeaSonde and the OSCR operated at different frequencies, the proximity of the two units resulted in interference, which required the CODAR SeaSonde to be turned off while the OSCR collected data. Since the SeaSonde requires a full hour to collect data, both units could not be operated simultaneously from this site.
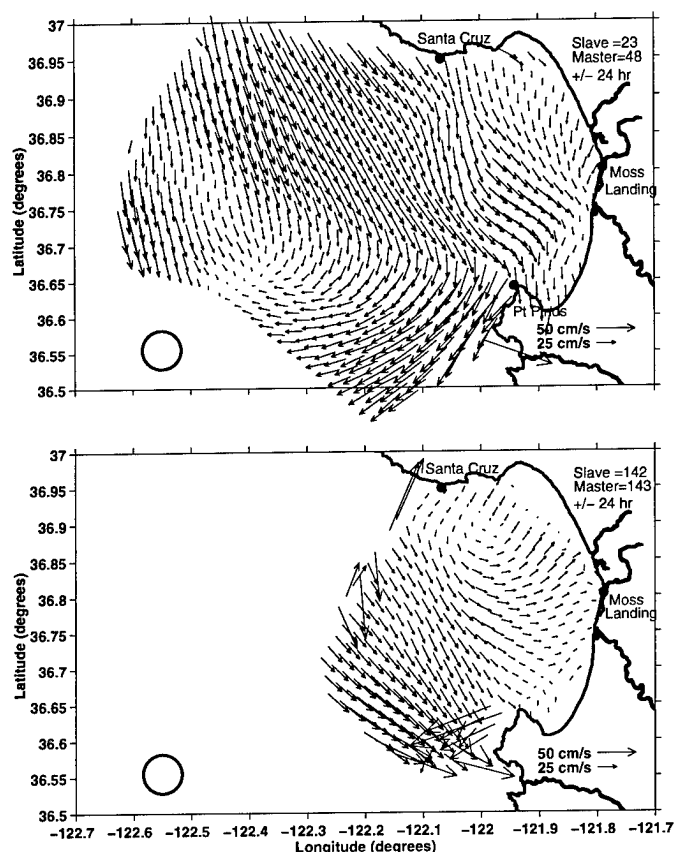
Figure 1: Monterey Bay with sites and with two day averaged derived current vectors from both the OSCR and CODAR deployments (averaging periods were separated by two days)

BASELINE COMPARISONS

Validation of the radial ocean surface current measurements made by HF radar is not straightforward. The measurement is rather unique in terms of its large swath and near-surface depth. Past comparative studies have often used data from a limited number of drifters, a moored current meter, or perhaps a moored ADCP [1, 6, 7]. No open literature to date has that we are aware of, however, has examined the performance of HF radar systems for current measurement by comparing radial measurements

made along the baseline that joins the two sites. Under ideal conditions, radial current measurements from one of the radar systems would be equal and opposite to the measurements made from the opposite site, within the combined error bars of each system's performance. Such measurements, of course, cannot be made unless both radar sites have a large body of water within their field of view. Both the CODAR and the OSCR setups in Monterey Bay offer this geometry.

CODAR Baseline Comparison

Baseline tests were performed on CODAR radial data collected between August-December, 1994 [8]. The three sites for which baseline pairs were made are shown in Figure 1. Results, which are shown in Figure 2 for the Santa Cruz - Moss Landing comparison, indicate that the lowest RMS differences seen between the time series of radials collected from any of the sites is between 14 cm/s and 17 cm/s, depending on the two sites chosen for the comparison. Furthermore, the angle at which the RMS difference is minimized (and at which the correlation is maximized), is 5 to 10 degrees off the angle that represents the baseline direction.
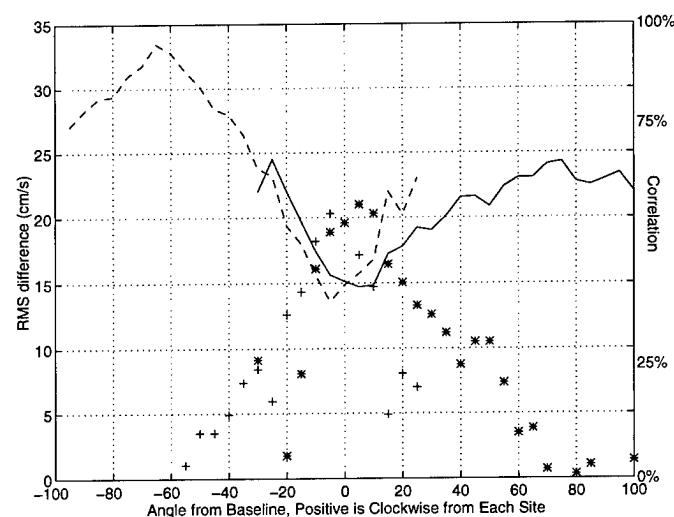
Figure 2: Correlations (* represents measurements from the Santa Cruz site at various angles and + the same for the Moss Landing site) and RMS differences (solid line represents Santa Cruz measurements) for CODAR time series data from the two sites. Angles shown represent the angle steered from the baseline direction for the corresponding site, positive is clockwise.

OSCR Baseline Comparisons

Baseline tests were performed on the OSCR data for the two days during which both OSCR sites operated without interference from the nearby CODAR systems (May 6 - May 8, 1995). Analysis was done by first fixing points at which the Santa Cruz site collected radials along the baseline. Correlations and RMS differences were then computed for time series collected from

the Moss Landing OSCR from points that lie on the same range but at different angles from the baseline. This was done for all of the points along the baseline. This process was then repeated by fixing points along the baseline at which the Moss Landing OSCR collected radials and steering the Santa Cruz site off the baseline. Resulting correlations and RMS differences as a function of look angle, when averaged over all points at all the ranges, are shown in Figure 3. Some of the most striking features of this analysis for the OSCR radials are that the minimum RMS difference is about 6 cm/s, which is nearly the same as one would expect the measurements to be based on the statistics of HF scatter [9, 10].
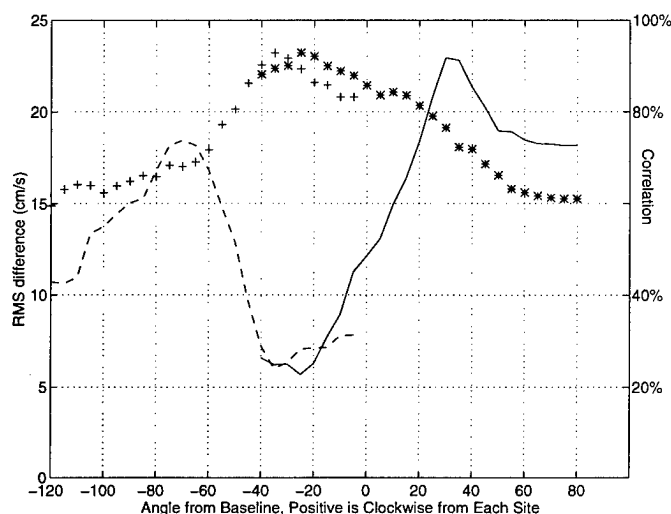
Figure 3: Same as Figure 2, except for OSCR units at Santa Cruz and Moss Landing. Observe the lower RMS differences between the sites, but the much larger difference in the perceived and actual baseline angle than with the CODARs. Also, observe the well-defined maximum and then significant decrease in the RMS difference vs. angle. This may be attributable to sidelobe effects.

Similarly, for the OSCR data, the maximum correlations are over 90%, which is ideally what one would expect to see along the baseline between the two HF systems. The optimal values, however, do not occur at the baseline angle, but, at about 35 degrees south of the baseline (for the Moss Landing site) and about 20 degrees north of the baseline angle for the Santa Cruz site. Furthermore, unlike the CODAR, the values of the RMS difference for the OSCR data reach maxima 30 degrees (for the Moss Landing site) to 55 degrees (for the Santa Cruz site) away from the angle of minimum RMS difference, and then they creep back down at further angles. The correlation shows a much less obvious increase at angles further from the baseline direction. The non-monotonic behavior of the RMS difference is a concern, since it is very unlikely that the radial ocean surface currents themselves exhibit coherence in the pattern depicted by Figure 3. A likely candidate for these effects, therefore, is that

they are system generated and possibly related to the sidelobes and nulls in the array patterns of the master and slave sites. The angle between the minimum RMS difference and the peak of the RMS difference is larger for the Santa Cruz site, which is consistent with the fact that the distance between nulls in the antenna pattern will be larger, since the phased array at Santa Cruz was shorter than the phased array at Moss Landing. Ideally, such effects would have been characterized during this experiment by conducting transponder runs, however, this was not possible during the short demonstration period of the OSCR system.

The apparent offsets of 20 and 35 degrees for the Moss Landing and Santa Cruz sites in the minimum RMS difference and the maximum correlation are potentially caused by alignment errors in the setup of the OSCR Santa Cruz and/or Moss Landing phased arrays, or they could have been caused by distortion in the array patterns themselves. Such effects could also be characterized by transponder runs at the outset of the experiment.

CODAR and OSCR Baseline Comparisons

One day of overlap occurred when valid data from the Point Pinos CODAR was collected and processed during the OSCR demo. For this day, radials from the CODAR were generated along the baseline that joins Point Pinos and Santa Cruz. There were a total of 108 samples of overlapping coverage between the two systems. The RMS difference between the CODAR and OSCR along the baseline was 10 cm/s and the correlation coefficient was 0.69, which is significant above the 95% confidence level. This result is consistent with the OSCR-OSCR and CODAR-CODAR comparisons in that it is intermediate between the values determined in those cases.

ADCP TO HF RADAR COMPARISONS

An acoustic Doppler current profiler (ADCP) deployed on board MBARI's M1 buoy was located within the beam coverage of both the OSCRs and the CODARs. This provided some in situ ocean current data (though at about a 9 meter depth) to compare to the radars. Correlations of the OSCR radials from the Santa Cruz and Moss Landing sites over the two days from May 6, 1995 to May 8, 1995 yielded 0.72 for the Santa Cruz site and 0.58 for the Moss Landing site. This may be compared with the correlation of the u- and v- components of the ocean current vectors derived from CODAR radials correlated to the u- and v- components of the ocean current collected from the ADCP. These yielded a correlation coefficient of 0.40 for the u-components and 0.66 for the v-components [8]. Note that the difference between these two comparisons is (1) their temporal extent and (2) the formation (and reduction) of HF ocean current vectors in the CODAR case and direct use of radials in the OSCR case. All of these results are significant above the 95% confidence level.

RMS differences were calculated about the linear regression

of the CODAR u- and v- components to the ADCP u- and v-components. In this case, they were found to be 8.5 cm/s for the u-component and 9.5 cm/s for the v-component [8]. Similar RMS errors were computed for the OSCR Santa Cruz and Moss Landing data and the radial component of the ADCP currents extracted in the direction of the corresponding OSCR site. In this case, the RMS errors for the regression were found to be 5.7 cm/s for the Santa Cruz site and 6.4 cm/s for the Moss Landing site. These results appear to be consistent with the smaller errors associated with the baseline comparisons of the OSCR units.

CONCLUSIONS

Measurements of CODAR/SeaSonde and OSCR data made in Monterey Bay as part of the UCSC REINAS project provided some interesting results concerning the operation of both types of HF radar. The baseline RMS differences associated with the OSCR units were typically quite low (about 5 - 6 cm/s), which is approximately the stated accuracy of radial current measurements with these units. On the other hand, the apparent skewed baseline direction for the OSCR units at Santa Cruz and Moss Landing as well as the reduction in the RMS differences between measurements from the sites as the sites are steered far off the baseline direction, indicate problems often associated with phased array systems, such as phase steering inaccuracies at both sites, antenna pattern distortions, or else simply misaligned arrays. Transponder measurements would have detected such difficulties at the outset and are highly recommended for future data collection with these systems.

CODAR/SeaSonde measurements made over a several month period showed lower correlations and higher RMS differences between baseline pairs than were found for the short-term OSCR data. These values are higher than would have been anticipated based on the expected accuracy of the system. The differences, however, were fairly monotonic and typically increased with angle away from their peak values, but the best correlations and lowest RMS differences were observed slightly offf the baseline, again indicating possible antenna problems.

ADCP runs and OSCR-CODAR comparisons all supported the conclusions stated above regarding the accuracy of both systems. Although the baseline differences were lower for the OSCR than for the CODAR, the length required for the OSCR array makes it less feasible in many coastal situations where current measurements are desired. For this reason, it is also important to improve the direction finding algorithms used by the CODAR to assess bearing for individual current measurements extracted from the data.

ACKNOWLEDGEMENTS

References

[1] R.H. Stewart and J.W. Joy, "HF radio measurements of surface currents," *Deep Sea Research*, vol. 21, pp. 1039-1049, 1974.

[2] D.E. Barrick, J.M. Headrick, R.W. Bogle, and D.D. Crombie, "Sea backscatter at HF: interpretation and utilization of the echo," *Proc. IEEE*, vol. 62, pp. 673-680, 1974.

[3] D.M. Fernandez, J.F. Vesecky, C.C. Teague, and J.D. Roughgarden, "Use of High Frequency for the Measurement of Ocean Surface Currents," *IGARSS'90 Conference Proceedings*, vol. 1, pp. 715-717, 1990.

[4] D.E. Barrick, M.W. Evans, and B.L. Weber, "Ocean surface currents mapped by radar," *Science*, vol. 198, pp. 138-144, 1977.

[5] B.L. Lipa and D.E. Barrick, "Methods for extraction of surface currents from CODAR data," *IEEE Journal of Oceanic Engineering*, vol. OE-8, No. 4, pp. 226-253, October 1983.

[6] D. Prandle, "A new view of near-shore dynamics based on observations from HF radar," *Progress in Oceanography*, vol. 27, pp. 403-438, 1991.

[7] J.D. Paduan and L.K. Rosenfeld, "Remotely sensed surface currents in Monterey Bay from shore-based HF radar (CODAR)," unpublished.

[8] D.C. Melton, "Remote sensing and validation of surface currents from HF radar," M.S. Thesis, Naval Postgraduate School, September, 1995.

[9] D.M. Fernandez, "High-frequency radar measurements of coastal ocean surface currents," Ph. D. Dissertation, Stanford University, August, 1995.

[10] D.E. Barrick, "Accuracy of parameter extraction from sample-averaged sea-echo Doppler spectra," *IEEE Transactions on Antennas and Propagation*, vol. AP-28, pp. 1-11, 1980.

A Multitemporal Land-Cover Change Analysis Tool Using Change Vector and Principal Components Analysis.

Guillermo Alfonso Parra, Marie-Catherine Mouchot, Christian Roux
Ecole Nationale Supérieure des Télécommunications de Bretagne
Image and Information Processing Department
BP 832 29285 Brest, France
Telephone (+33) 98 00 13 58 Fax (+33) 98 00 10 98
e-mail parra, mouchot, roux@gti.enst-bretagne.fr

Abstract. Scientists are devoting a lot of energy to monitor and to assess the impact of fires and to mesure the evolution on land cover in tropical savannas. A key element in a monitoring system is the land cover changes analysis tool. While some land cover changes are caused by natural processes, such as long term changes of the climate or shorter-term vegetation successions, human activity modifies surface cover through direct actions, such as deforestation, farming activities, or indirectly, through man-induced climatic change.

This paper presents a method that applies Principal Components Analysis for land-cover change detection with multitemporal SPOT data.

INTRODUCTION

The purpose of principal components analysis (PCA) is to define the number of dimensions presents in a data set and to fix the coefficients which specify the positions of the set of uncorrelated orthogonal axes which point in the directions of greatest variability in the data. The first principal component accounts for the maximum possible proportion of the variance of the original data set, and succeeding components account for decreasing proportions of the unexplained residual variance.

When the transformation coefficients are developed by computing the principal eigenvectors of the variance/covariance matrix we refer to a Unstandardized PCA (UnS-PCA). When the eigenvectors are computed from the correlation matrix we refer to a Standardized PCA (S-PCA).

From the 80's authors have applied PCA to the problem of detecting and classifying temporal changes in remotely sensed imagery. Byrne and Crapper use in their work two four-channel Landsat MSS scenes of the same area, and different date. They propose in [1] to use UnS-PCA for decomposing the four-plus-four correlated MSS channels into eight orthogonal axes. UnS-PCA of this array resulted in the gross differences associated with overall radiation and atmospheric changes appearing in the low order component images and statiscally minor changes associated with local changes in land cover appearing in the higher order, the third,

fourth and fifth component images. This is a direct outcome of the high correlation that exists between dates for regions that are relatively constant and the low correlation associated with regions that are quite different on time.

Richards in [6] uses UnS-PCA to detect regions of localized change associated with bushfire damage and with vegetation regrowth following fire burns. He uses the same method that [1] but applies a classification procedure to the higher components. Ingebritsen and Lyon [4] showed that the method proposed by [1] often leads to specific types of change related PC, which they referred to as 'Δbrightness' and 'Δgreenness' in analogy to Kauth and Thomas 'brightness' and 'greenness' indices.

Fung and LeDrew examine in [2] the effect of using a UnS-PCA versus UnS-PCA approach on total area and subset area data. As in [1] and[6] they use a single 8-channel as input. They found that S-PCA provides more accurate information for change detection that the UnS-PCA approach. They noted also that PCA is a scene dependant technique. Gong in [3], instead of applying UnS-PCA to a merged data set of original multispectral images, apply this transformation to difference band pair images. In this approach, change information is always accumulated in the low order principal component images.

THE STUDY AREA AND DATA DESCRIPTION

The study area named Carimagua is located aproximately N 04 03'latitude and W 71 20' longitude in the middle of East Savannas (Llanos Orientales) in Colombia, close to one of the International Investigation Center in Tropical Agriculture (CIAT) research sites.

In this region it is important to monitor the evolution of different types of fields, ranging from natural savannas to improved or introduced pastures. It is also very important to estimate the environmental consequences of burning natural savannas during the hot dry summer season. Three multispectral SPOT images (91-02-21, 91-03-20, 91-09-02) centered over CIAT-Carimagua Research Center are studied. However, the total study area is an extracted image set of 1400 x 1000 pixel. Also, to examine the effect of using total

versus subset area statistics, several subwindows are chosen from the total study area. Assumptions about atmospheric and climatic homogenity are maintained for all images.

SOURCES OF VARIANCE

In general, each image data set may be considered as a set of points ,i.e. pixels, in m-dimensional space. The effect of change on the position of these pixels in the m-dimensional space may be anticipated as follows [1]:

- Changes in atmospheric conditions might be expected to affect all pixels similarly.
- Changes in soil humidity would have a similar effect but confined to those pixels which represent vegetated surfaces or bare soil.
- Changes in land cover would presumably produce a significant change in the position of the relevant pixels, but these would be fewer in number.

Thus, differences, i.e., variance between the two images will typically be of two kinds. First, there are those that extend over a substantial part of the scene such as those arising from changes in atmospheric conditions or soil water status. These would presumably be a substantial source of variance, since they involve all the pixels. Second, there are those that are restricted to parts of the scene such as the clearing of forest, savanna fires, or agricultural works. Variance in the latter category would be orthogonal to that of the first category.

DATA ANALYSIS

We have evaluated all the approaches presented in the introduction, using the total study area and several subwindows. Particularly, we have chosen to work with two subwindows. The first represents a natural savanna where a scar fire appears on the second date. The second subwindow is centered over a set of special lots where the age and the type of the pastures growing, and the type of land cover change that has occured is known.

It is well known that in temporal change detection using PCA, both the surface proportion and the magnitude of changed area in an image determine which principal component images will contain change information. Rigorously speaking it is the relative amount of variance between the changed area and the unchanged part in an image that determines which particular PCs contain change information. Small magnitude changes may come out in low order components if they affect large areas. Conversely, large effects may come out in high order components if they occupy only a small portion of the analyzed area.

The same constrain has been frequently observed: it is unusual to know *a priori* both, the magnitude and the surface

dimension of the changed area. It is thus difficult to determine which particular PCs contain change information and what is their true meaning. Certainly, loadings and eigenvalues give an idea of the type of land cover change but the information is obviously merged. Only the approach presented by Gong [3] gives a better result.

The following method, allows us to retrieve the knowledge of the source or the nature of land cover change.

METHOD

The change detection procedure proposed can be described in the following steps:

- Apply standardized principal components analysis to every image band pair, to obtain, two principal component images by band.
- Apply a fuzzy set membership function to all second principal component images. The land cover change information detected by the corresponding band is contained in it. Use a sigmoidal function centered over the mean value of each principal component.
- Create a binary image choosing a threshold level, often close to the meanvalue of the image defined with the membership function. The changed and unchanged areas coming from each band are obtained.
- After filtering thresholded image with a median filter, combine the relevant change information into one image.
- As the method allows us to feedback, the nature of the change can be derived from the original band.
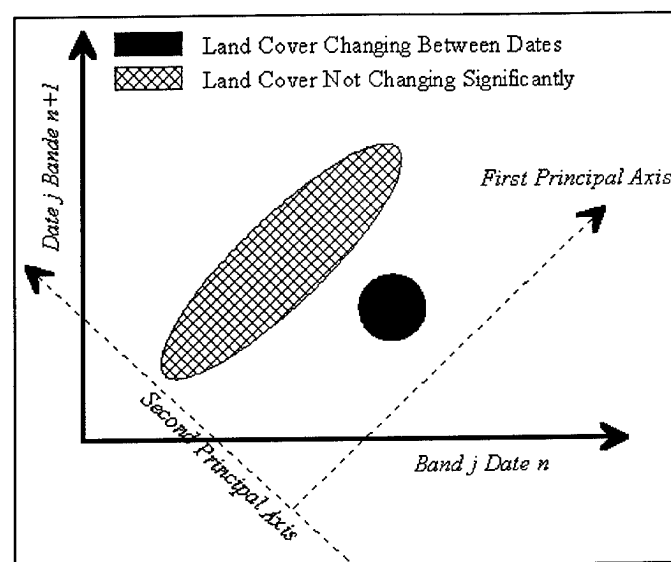
Fig 1. Pixels corresponding to unchanged land cover cluster about an elongate area as indicated. Pixels corresponding to change in land cover show a major departure from that area.

1754

Run in a first time the method just described, over a large scene, making possible to define some series of smaller regions where a land cover change has taken place. But for the principal components technique to be useful, it is also necessary that the subscene containing the change region of interest also includes a substantial region of relatively no change. In consequence, choose a subwindow with 50% minimum of no change zone. Then, repeat the method over the chosen subwindow. Each specific problem will guide us choosing the stopping criteria in the analysis.

RESULTS

For illustrating purposes the same subwindows set employed in the previous data analysis are chosen. 2. In Fig 2 (a) and (b) the original infrared bands, date 1 and date 2, of a set of supervised lots are shown. The second principal component of infrared image pair contributes with a 6.06% of land cover change information and the second component of red image pair contributes with a 4.38%. After superposition, it is found that SPOT infrared band contributes really with near of 70% of change land cover information as is shown in Fig 2 (c). It is due to the agricultural nature of the tested area. Because the CIAT has provided all the data in relation with the age and the type of the pastures growing in supervised lots, it has been possible to verify the results of our approach.

(a)   (b)

(c)   (d)
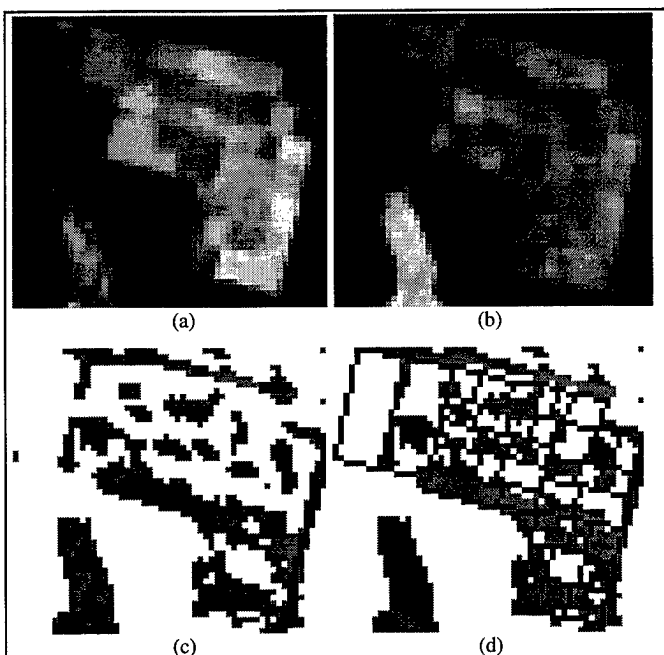
Fig 2. (a.) and (b.) date 1 and date 2 Infrared Spot bands XS3. (c.) combination of the thresholded second principal components of red and infrared bands. (d.) the final change map superposed with the lots boundaries.

The final results are shown Fig 2 (d) were the grid describing the boundaries has been superposed.

This approach has been integrated with a change vector analysis method [5] into a Land Cover Change Analysis Module. The purpose is to detect, at spatial and temporal scale, subtle and abrupt change types due to ecological and human events as: floods, forest clearing, accidental or provocated fires, etc. Two output formats are derived. The first of these formats is based on a pixel by pixel approach and the second uses a vector map oriented aproach.

CONCLUSIONS

Generating and combining principal components images from bands image pair is a valid approach for enhancing and extracting land cover change information. The origin of change information is always conserved and easily retrieved. The importance of mapping, quantifying and monitoring changes on land-cover in tropical savannas have been widely recognized in the scientific community. It is a key element in the study of global change that help us to conserve natural resources for coming generations.

Further research is needed to find how adjust the method to detect land-cover change in not predominantly agricultural regions.

REFERENCES

[1] BYRNE. G. F., CRAPPER. P. F., MAYO. K. K., 'Monitoring Land-Cover Change by Principal Component Analysis of Multitemporal Landsat Data'. *Remote Sensing of Environment.* N° 10, 1980, pp 175-184.

[2] FUNG. T, LE DREW E.,' Application of Principal Components Analysis to Change Detection'. *Photogrammetric Engineering & Remote Sensing.* Vol 53, N° 12, December 1987, pp 1649-1658.

[3] GONG. P, ' Change Detection Using Principal Component Analysis and Fuzzy Set Theory'.*Canadian Journal of Remote Sensing.* January 1993. Vol 19, N° 1, pp 22-29.

[4] INGEBRITSEN. S. E., LYON. R. J. P., ' Principal components analysis of multitemporal image pairs'. *International Journal of Remote Sensing.* 1985. Vol 6, N° 5, 687-696.

[5] LAMBIN. E. F., STRAHLER. A. H., 'Change- Vector Analysis in Multitemporal Space: A Tool to detect and Categorize Land-Cover Change Processes Using High Temporal-Resolution Satellite Data'. Remote Sensing Environment 1994. Vol 48, pp 231-244.

[6] RICHARDS. J.A., ' Thematic Mapping from Multitemporal Image Data Using the Principal Components Transformation'. *Remote Sensing of Environment.* N° 16, 1984, pp 35-46.

Monitoring land cover of the desert fringes of the eastern Nile Delta, Egypt.

Hashem M., El-Khattib[1], Nabil M., El-Mowelhi[2] and Fetoh Hawela[1]
1- Professor Dr. (Chief Researcher)
2- Director of SWERI
Remote Sensing Unit, Soil, Water Environment Research Institute SWERI,
Mailing address: 2 El-Nokali st., El-Nadi El-Riadi st., El-Haram post code, 12111, Giza, Egypt.
Tel: 5687421   Tel: 5720608   Fax: 5720608

Abstract -- Remote sensing provides a possibility to significantly speed-up mapping of natural resources and to establish an efficient system for monitoring of their changes. Resource manages are now able to monitor changes in vegetation cover and land use patterns over large areas. The objective of the current investigation is to asses capability of multitemporal analysis of LANDSAT data through comparisons with ground based observation, to identify land cover changes and monitoring vegetation of the new reclaimed areas in the extension of the eastern part of the Nile Delta of Egypt. LANDSAT MSS and TM data of the summer seasons 1976 and 1994, respectively were available for the land cover studies. On the basis of the spectral reflectance characteristics, simple ratio, normalized difference vegetation index and ground truth data are possible to determine the main parameters to monitor the changing in the vegetation covers under the Egyptian condition. Seven different approaches land cover/land use classes are distinguished; three classes of which are for agricultural use, one class represent desert and sandy soils areas, one class is for water, while two classes are occupied by built-up areas. Multi-temporal comparison have been undertaken, the changes of the land cover and land use patterns are distinguished. The result indicate that the variation in land cover reflectance is a function of soil characteristics.

INTRODUCTION

It is a fact that soil resources and their management are the key factor in agricultural and rural development in Egypt. Development and imp-rovement of agriculture pattern is of prime import-ance for food supply. For this reason it has been decided to execute a land cover/land use survey of the eastern Nile Delta region outside the old culti-vated land to attain thorough information from this large area about the agriculture development condi-tions after the last thirty years. Since then different governmental authorities apply great effort in land reclamation and put large areas under cultivation.

Much progress has been made in analyzing land use and in classifying land cover and vegetation types using LANDSAT, SPOT and AVHRR data. The level in detail that can be identified and the accuracy of such analysis depend on the nature of the region to be analyzed as well as the spectral, spatial, temporal, and radiometric resolution of the sensor. Single and multidate LANDSAT data have been used routinely to classify vegetation community types with approximately 70-90 % accuracies, [1].

The objective of the current investigation is to assess the capability of LANDSAT TM data and the vegetation indices, through comparisons with ground based observation, to identify land cover changes and monitoring vegetation in a relatively large area of the desert fringes of the Eastern Nile Delta, Egypt.

MATERIALS AND METHODS

The new reclaimed areas in the extension of the eastern part of the Nile Delta boarded by Manzala Lake from the north and Suez Canal from the east and Ismailiya-Cairo desert road from the south and the old alluvial cultivated land of the Nile Delta from the west have been selected as the test site. Two LANDSAT Multispectral Scanner MSS and Thematic Mapper TM images of the summer season dating during August 1976 and 1994 were available for this study. This corresponds to path 176, row 39 in the LANDSAT World Reference System. The LANDSAT data are geometrically and radiometri-cally corrected. EASI (Engineering and Scientific Interface) / PACE (Picture Analysis correction and Enhancement) PCI software for image processing system in the Remote Sensing Unit within Soil, Water and Environment Research Institute,

Ministry of Agriculture was used for image interpretation and analysis. Furthermore, because multiple images were needed to identify ground features, standard change detection techniques which compare just two images, were applicable. For calculating Vegetation Indices the simple Ratio (SR) of nearinfrared (NIR) to visible portion (red) Eq.(1) and normalized difference vegetation index Eq.(2) are the most common ratio transformations used as vegetation measurements.

$SR = NIR(TM4)/red(TM3) \ldots (1)$

$NDVI = IR(TM4)-IR(TM3)/NIR(TM4)+IR(TM3) \ldots (2)$

Fig.1: LANDSAT MSS data for 1976.

RESULTS AND DISCUSSION

A trial was undertaken to present the vegetation cover for an area in the eastern site of the Delta using LANDSAT data. According to definition, a land cover type is a geographer's term which denotes a class describing vegetational natural and artificial as well as constructions covering the land surface in contrast to land use type, which refers to man's activities which are directly related to the land.

LANDSAT are composed of a mosaic of land cover units, shaped by differences in topography, microclimate, substrate characteristics, and disturbance or management history. Remote sensing have proved to be a fundamental research tool for the landscapes and land cover. The LANDSAT MSS data illustrated and identified the land forms in the study area, the vegetation cover for the eastern desert fringes of the Nile Delta which are the old alluvial cultivated land and very few of scattered vegetated areas adjacent at Ismailya Canal. Most of the land use / land cover areas are desert nature, Fig. 1.

The presented digital land cover study based on recent LANDSAT TM data and the change detection of TM & MSS acquired over the eastern part of the Nile Delta of Egypt, the change detection for TM and MSS which was processed to determine the possibilities of applying data for land cover study. The processing data is based on the limited ground truth data, which represent the main summer field crops which were planted in 1994 namely corn, cotton, rice, peanuts, sunflowers, fruits and vegetables, in addition to the desert area in the

eastern site; water, urban and industrial areas.

On the basis of the spectral characteristics, the magnitude of the sum of reflectance of the electromagnetic radiance in all TM channels, ratios (SR and NDVI) and ground truth data, it is possible to determine some parameters to identify the vegetation cover; namely, green vegetation, density of the vegetation, chlorophyll content, phenological stages of plant, soil moisture, to identify non-vegetated and water areas and the degree with which the spectral contribution of non-vegetation components (soil) and canopy leaf area.. Each Land cover type or class is characterized by its own characteristic signature, which may be sufficient to be identified. However, the shapes assumed by a type or class may be also necessary for the identification. As a result of the above discussion and after detected the changes between the data dated in 1976 and 1994, four main land cover types have been separated, Fig. 2:

1. **Water:** Suez Canal has salty water, while Ismailiya Canal and El-Saidia Canal are the main canal having their water from Nile Damietta Branch for irrigating the old cultivated land. Ismailiya Canal as the main Canal in the middle of the investigated area.

2. **Built-up areas:** These classes have been discriminated within this group showing medium to low values of NDVI. Which could be separated into :

a) Urban areas: representing the cities and villages distributed within the eastern part of old cultivated land.

b) Industrial areas: represented by the city of Tenth of Ramadan in the Eastern Desert having also medium values of NDVI.
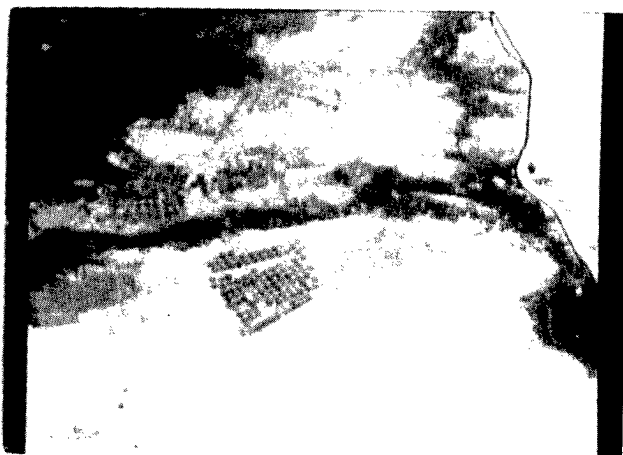
Fig.2: LANDSAT TM data for 1994.

c) **Roads**: Ismailiya- Cairo Desert Road.

3. Desert and Sandy Soils Areas: They show different values of spectral signatures; the highest is represented by the main wadis around the city of Tenth of Ramadan El-Gafra plain and the big wadi which is divided by Ismailiya Cairo desert road. The rest of the desert areas having medium values of magnitude; this is mainly due to the different size and colour of gravel and sand which could be considered the main factor responsible for their spectral signature.

4. Agricultural Areas: Remote sensing of agricultural and other resources involves the detection of electromagnetic energy that is reflected or emitted from the complex assemblage of biological, geological and hydrological features at the earth's surface. The differences in their reflectivity allow discrimination of plant species or vegetation types which can be traced due to their leaf and canopy characteristics.

NDVI ratio has been considered to be more sensitive to low vegetation cover to detect and separate green vegetation and to monitor its changes than the Simple Ratio SR which is relatively less sensitive to sparse vegetation, [2]. The NDVI is a bounded ratio with values between 1.0 and + 1.0 over land surfaces. The negative value of NDVI is mainly due to the very low vegetation densities the composite reflectance almost the soil background (the red reflectance from soil may be greater than the nearinfrared reflectance), [3]. The agricultural areas have been distinguished and separated to:

a) **Old cultivated land:** which has a darker green colour, characterized by high NDVI values. The summer field crops which were grown in this area during 1994 : cotton,corn, rice, soybean, sunflower, vegetables and fruits.

b) **New extension areas:** represent the adjacent areas to the old land as well as the scattered areas in the Eastern Desert showing light green colour and are characterized by low to medium NDVI values. The summer field crops which were grown in these areas are peanut, corn, cotton, sunflower, vegetables and fruits.

c) **The center Pivot areas:** which represents El-Shabab and El-Salhia areas and some scattered pivot in the Eastern Desert, showing different green and yellow tones colour (light and dark). This is mainly due to the different values of NDVI (low to high) according to the plant condition and the phenological stage of the plant. The main field crops which were grown in 1994 under the pivot system were corn, sunflower, peanut, vegetables, and fruits; in between the center pivot Guava trees were planted.

Generally, it could be said in this concern that NDVI is a suitable measure for land cover assessment and monitoring under the Egyptian conditions. The satellite data provide us with a quantitative assessment of the percentage of vegetation within a heterogeneous pixel assuming similar soil brightness and spectral conditions.

REFERENCE

[1]   L.A. Morrissey, L.L. Strong, and D.H. Card, (1986). "Mapping permafrost in the boreal forest with TM Satellite data," Photogramm. Eng. & Remote Sens. 52(9): 1513-1520.

[2]   D.W. Deering, J.W.Jr. Rouse, R.H. Haas, and H.H. Schell, (1975). "Measuring forage production of grazing units from LANDSAT MSS data," Proc. of the Tenth Int. Symp. of Remote Sens. of Env., ERIM, Ann Arbor, Michigan, PP. 1169-1198.

[3]   C.O. Justice, J.R.G. Townshend, B.N. Holben, and C.J. Tucker, (1985). "Analysis of phenology of global vegetation using meteorological satellite data," Int. J. of Remote Sens., 6, 1271.

RETRIEVAL OF FOREST PARAMETERS FROM MULTITEMPORAL SPACEBORNE SAR DATA

Lauri Kurvonen, Jouni Pulliainen*, Martti Hallikainen* and Petri Mikkelä**
Joint Research Centre of European Commission
Institute for Remote Sensing Application
TP 272, I-21020 Ispra (Va), Italy
Tel: +39-332-785194, Fax: +39-332-785469, email: lauri.kurvonen@jrc.it
*Helsinki University of Technology, Laboratory of Space Technology
**Finnish Forest Research Institute

Abstract-- The aim of the study is to develop inversion methods for spaceborne SAR images of the boreal forests. The parameters of interest are stem volume (biomass), forest and land-cover types, soil and vegetation moisture. The previously developed forest stem volume/soil moisture retrieval algorithm was tested by producing soil moisture maps for large test areas. The textural information of a seasonal set of ERS-1 SAR images was studied with the first and second order statistical measures. These measures had a higher information value than intensity values (or their principal components) for the forest and land type classification. The multitemporal approach was beneficial for the application of textural measures and the textural parameters significantly improved the classification of land-use and forest types.

INTRODUCTION

We are developing inversion methods for spaceborne SAR images of the boreal forests. The parameters of interest are stem volume (biomass), forest and land-cover types, soil and vegetation moisture. Previous studies have shown that seasonal effects in boreal forests (such as soil freezing and thawing, snow cover and soil wetness) may drastically change the level of the total backscatter. Nevertheless, these seasonal effects may benefit the inversion if suitable methods are used with a multitemporal data set.

The effect of soil and forest canopy moisture on the backscattering coefficient is higher than that of the forest biomass at the C-band [1,2]. Hence, the applicability of ERS-1 SAR for soil moisture mapping is investigated in this paper.

Previous studies [3] have shown that water, bogs and forested areas can be separated from multitemporal ERS-1 SAR images. A set of ERS-1 SAR images (intensity) was compressed with the principal component analysis from which the first three components were used in the classification. Now, the texture of the multitemporal SAR data set is explored to improve the land-use and forest type classification.

SAR DATA AND GROUND TRUTH

Over 40 ERS-1 and 7 JERS-1 SAR images are acquired for two test sites in Finland. The northern test site is in Finnish Lapland (Sodankylä) while the other test site is in southern Finland (Porvoo).

The Sodankylä test site (centre coordinates N67° 41'N; E26° 58') consists of sparsely forested areas where the average stem volume is only about 50 m³/ha. National Board of Survey has provided a digital land-use map of the area which has 23 land-use classes. The forest information of the land-use map was complemented with a timber volume map produced by Finnish Forest Research Institute. In Sodankylä the main forest types are pine, mire and mixed while open areas consist of bogs, lakes and clear-cuts. The total size of the Sodankylä test site is 1600 km².

The size of the Porvoo test site is 5000 km² (centre coordinates N60° 30'; E25° 30'). The area includes various land classes: forests, mires, fields, urban areas and water areas. The forests are conifer-dominated mixed forests. The most usual species are Norwegian spruce and Scots pine. The overall relief is low (elevation well below 100 m), but not flat (small hills are usual). The Porvoo test area reference data include National Forest Inventory (NFI) sample plot characteristics, ground-based forest stand data for selected test sites, LANDSAT TM-based land use map and stem volume estimates, in situ soil moisture measurements in selected areas, and daily hydrological model-based soil moisture estimates covering the whole Porvoo area.

METHODOLOGY

Soil and vegetation moisture estimation

The estimation of soil moisture is carried out by employing an inversion algorithm for ERS-1 SAR data. The retrieval algorithm is based on the previously developed semi-empirical forest backscattering model that describes the backscattering coefficient as a function of stem volume (biomass), soil moisture and forest canopy moisture. The algorithm requires the use of pixel- or forest stand-wise stem volume data (LANDSAT TM-based stem volume estimates were used in this study). The algorithm fits the forest backscattering model into ERS-1 SAR results obtained for a certain forest district and the outcome is the estimate for the average soil moisture and the average vegetation (forest canopy) moisture. In this study, the estimates were calculated for a 1 km by 1 km grid covering a 40 km by 50 km subarea of the Porvoo test area. In near future, a similar method is tested with JERS-1 SAR data for biomass retrieval.

Land and forest type Classification

The first and the second order texture statistics are explored to define the textural information in the multitemporal SAR images. The first order statistics (such as mean and variation) describe the probability density function of a local set of pixels. The second order statistics (such as the autocorrelation function) describe the relationships between a pixel and its neighbours [4].

In this paper the coefficient of variation (CV) is used as the measure for the first order statistics:

$$CV = \frac{STD_{local}}{mean_{local}} \qquad (1)$$

The local STDs and means are calculated with a moving window (7 by 7 pixels was used for results presented in this paper).

Due to practical reasons, the second order texture statistics are calculated from normalized gray-level co-occurrence (GLC) matrices [5] and not from autocorrelation functions. The following second order texture measures were used [5]:

$$Contrast = \sum_{i,j}(i-j)^2 p_{ij} \qquad (2)$$

$$Inverse\ Moment = \sum_{i,j} \frac{p_{ij}}{1+|i-j|} \qquad (3)$$

$$Maximum\ Probability = \max_{ij} p_{ij} \qquad (4)$$

$$Uniformity = \sum_{i,j} p_{ij}^2 \qquad (5)$$

where p_{ij} are probability values of a GLC-matrix. The local GLC-matrices are calculated with a moving window (7 by 7 pixels was used for results presented in this paper).

The separability of different land-use and forest type classes was studied with Jeffries-Matusita (JM) Distance [6]. The distance predicts the results of a maximum likelihood classification. JM-distance is scaled between 0 and 1414 and a distance of zero means that the signatures are inseparable. The maximum likelihood decision rule was used in the test classifications.

RESULTS AND DISCUSSION

Soil and vegetation moisture estimation

The soil moisture estimates, as well as the forest canopy moisture estimates, were determined for a 40 km by 50 km subarea of the Porvoo test area for four dates (summer 1993). The estimates were determined for a 1 km by 1 km grid (the hydrological model-based soil moisture maps are also available for a 1 km by 1 km grid size). The comparison of ERS-1 SAR-based estimates with the reference predictions is not yet performed.

Land and Forest type Classification

The land type classification was first studied with the Sodankylä data set (all the results below are for that test site). A set of eight ERS-1 SAR (PRI) images were picked from the set of

23 ERS-1 images to present the seasonal variation. Two smaller test areas (about 20 km² each) were selected for the experiment. For these test areas following images products were calculated from each SAR image, 1) Principal components, 2) Coefficient of Variance (CV), 3) Contrast, 4) Inverse Moment, 5) Maximum Probability and 6) Uniformity images.

In general, there was a large seasonal variation in the textural images and the correlation was low between images of same type from different times. Table 1. Shows the average of correlation (from the 8 different dates) between the different images types. Correlation is low between intensity, CV and the second order statistical images, which predicts that these measures are differently related to the target area. Nevertheless, some relatively high correlations are found among the second order statistical images which was expected.

The separability of different land-use classes was studied with the test area 1. The amount of land use classes was reduced to 10 (see Table 2, exclude Urban area). JM-distances were calculated between all class pairs (45) for each image (intensity, CV, contrast, inv. Moment, max. probability and uniformity) from each date. Figures 1 and 2 show the mean separabilities of the 45 pairs for each date and measure. In general, the separability is very sensitive for the seasonal factors like snow and moisture. In mid-winter all the measures have the lowest separability when there was about 80 cm of dry snow. Moreover, the order of the second order measures is reversed in mid-winter. Uniformity and inverse moment have also large changes between the summer and fall images when the soil moisture changed. In most cases intensity had the lowest separability while uniformity had the highest. In both Figures 1 and 2, the top line shows the separability when all the measures are used together.

All the textural images (40) and the first three principal component images were merged into an image which had 43 layer. The benefit of combining the data from different dates was studied with this image. Figure 3 shows the mean (of 10 classes = 45 pairs), maximum and minimum separability as a function of channels (layers) used. In each case of Figure 3, the set of layer was selected so that it gives the maximum mean separability. The results of Figures 1, 2 and 3 confirm that textural parameters have a significant effect on the separability and the multitemporal approach even increases their usefulness.

The classification accuracy was tested with both test areas. Ten (area 1) and eleven (area 2) signatures were taught with 20 % of pixels and the remaining pixels were classified. All textural measures and the first three principal component (a total 43 channels) were used. The overall accuracy for the test area 1 was 65 % and that for the test area 2 was 48 %, respectively. The results for test area 2 are summarized in a confusion matrix in Table 2. Five classes (water, urban area, Bare mountain top, Forested bog and mixed forest) had an accuracy of over 90 %. Agricultural land, clear-cut, pine and deciduous had the lowest accuracies. Some agricultural areas were classified into pine, deciduous or clear-cut. All agricultural areas of the land-use map are not in active cultivation. In this class there are meadows

Table 1.   Average correlation coefficients between intensity and textural measures.

	CV	Contrast	Inverse Moment	Maximum Probability	Uniformity
Intensity	-0.10	0.30	-0.32	-0.24	-0.25
CV		0.29	0.05	0.19	0.09
Contrast			-0.73	-0.38	-0.46
Inv. Moment				0.76	0.79
Max Probability					0.92

Table 2.   Confusion matrix for land-use and forest type classification of test area 2 in Sodankylä. The rows present the results of the classification in percent and the columns are from the land-use map.

	Water	Urban area	Bare Mountain top	Gravel	Agri-cutural land	Clear-cut	Open bog	Forested bog	Pine	Deciduous	Mixed
Water	90	0	0	0.7	2.7	0.9	0	0	2.8	0.7	0
Urban area	0.4	86	0	0	1.0	0	0	0	0.1	0.2	0
Bare mountain top	0	0	96	7.1	3.3	1.8	0.5	0.1	3.2	1.7	0
Gravel	0.2	0	0.6	77	8.5	1.7	0.2	0	1.8	0.1	0
Agricultural land	2.6	0	0	0.2	31	1.7	0	0	1.6	0.9	0
Clear-cut	2.0	3.6	0	3.4	13	31	2.4	1.3	4.6	2.7	0
Open bog	0.3	0	0.6	3.4	8.5	12	78	4.7	13	12	0
Forested bog	0	0	2.3	2.6	3.0	25	12	90	16	20	4.2
Pine	1.3	8.0	0	2.9	13	12	2.6	0.8	33	11	0.8
Deciduous	2.7	2.2	0.2	2.3	16	13	3.3	2.5	17	46	0.4
Mixed	0	0	0	0.2	0	0.9	0.6	0.2	7.1	4.0	95
Total of samples	1144	138	649	1327	1536	3529	2834	2044	15687	4759	474

which grow bushes and small trees which may partially cause the errors. Clear-cuts were found in right places, but they were smaller than in the land-use map. It can be expected that new forest is already growing in these areas. The errors of pine and deciduous classes were mainly with other forest classes. Some of these errors may due to the fact that all the forests in the area are natural and they consist of several species to some extend.

CONCLUSIONS

The previous work has shown that ERS-1 SAR has a considerable potential in the soil moisture retrieval [1,2]. This aspect was further continued in this investigation by producing ERS-1 SAR-based soil moisture maps.

Due to resampling and averaging, ERS-1 PRI images are expected to have a low textural information. Nevertheless, the application of textural parameters significantly improved the classification of land-use and forest types. If only one image was used at a time, the textural and/or intensity information was not adequate for a satisfactory classification. However, the multitemporal approach was beneficial especially for the textural measures. Thus, encouraging classification results were achieved.

REFERENCES

[1] Pulliainen, J., Mikkelä, P., Hallikainen, M., Tomppo,. E. (1995) "Estimation of forest biomass and soil moisture in boreal forests employing ERS-1 SAR data", Digest IEEE International Symposium on Geoscience and Remote Sensing (IGARSS'95), Firenze, Italy.

[2] Pulliainen, J., Heiska, K., Hyyppä, J., Hallikainen, M, (1994) "Backscattering properties of boreal forests at the C- and X-bands", IEEE Trans. Geosci. Remote Sensing, vol. 32, no. 5, pp. 1041-1050.

[3] Koskinen, J., Kurvonen, L., Jääskeläinen, V., Hallikainen, M. (1994) "Capability of radar and microwave radiometer to classify snow types in forested areas", Digest IEEE International Symposium on Geoscience and Remote Sensing (IGARSS'94), Los Angeles, USA.

[4] Ulaby F., F. Kouyate, B. Brisco, T. Lee Williams (1986) "Textural Information in SAR Images", IEEE Trans. Geosci. Remote Sensing, vol. 24, no 2, pp. 235 - 245.

[5] Haralick, R. (1979) "Statistical and structural Approaches to texture", Proceedings of IEEE, vol. 67, no. 5, pp. 786 - 804.

[6] Swain, P., Shirley M. (1978) Remote Sensing: The Quantitative Approach. McGraw-Hill Book Company, New York.

Separability of land cover types with 2. order textural measures

Figure 2. Average separability of contrast, inverse moment, maximum probability, uniformity and all the measures together.

Separability of land cover types with Intensity and CV

Separability of land cover types with optimum channels combination for mean separability

Figure 1. Average separability of intensity, CV and all the measures together.
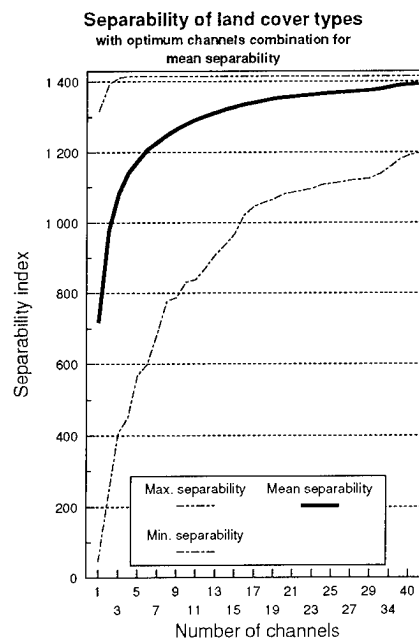
Figure 3. Maximum, average and minimum separability as function of different measures (channels).

Monitoring of the Change of Vegetative Conditions Using Multitemporal SAR Data

Yuzo Suga*, Shoji Takeuchi**, Hiroji Tsu***
*Hiroshima Institute of Technology
2-1-1, Miyake, Saeki-ku, Hiroshima 731-51, Japan
**Remote Sensing Technology Center of Japan
1-9-9, Roppongi, Minato-ku, Tokyo 106, Japan
***Earth Remote Sensing Data Analysis Center
3-12-1, Kachidoki, Chuo-ku, Tokyo 104, Japan

Abstract -- SAR data have higher potential for monitoring than optical sensor data because of its capability for data acquisition in any weather condition. The authors studied the applicability of SAR data for monitoring the change of vegetative conditions caused by seasonal variation, flooding and biomass burning. As to the biomass burning, the authors investigated the change of SAR backscatter due to the forest fire. Through these experimental studies, the authors suggested the possibility of L-band SAR data by JERS-1 for practical monitoring of several types of changes of vegetative conditions.

INTRODUCTION

Land cover change monitoring using multitemporal data is one of the important and practical applications in remote sensing fields. However, the observations by conventional optical sensors are much affected by weather conditions and actually the observation in a winter season or rainy season has been almost impossible using optical sensors. On the other hand, the Synthetic Aperture Radar (SAR) can observe in any weather condition and the SAR data can be used practically to monitor the land cover change which occur in the season of bad weather conditions. The authors studied the applicability of the SAR data for the monitoring of the changes of vegetative conditions caused by seasonal variation between dry and rainy weather conditions, by flooding in rainy season and by biomass burning.

RELATION BETWEEN SAR BACKSCATTER AND VEGETATION COVERAGE

The authors have conducted the preliminary analysis of the multitemporal SAR data at the Central Plain in Thailand and the results suggested that those data contain much information about the seasonal variations of vegetation. The upper two images in Fig.1 show seasonal changes of L-band SAR backscatter between dry season (March 16th)

and rainy season (September 8th). The change of SAR backscatter is represented by the Normalized Radar Cross Section (NRCS) which can be derived from the SAR level 2.1 product using the calibration coefficient given by NASDA.

Regression analysis was performed between SAR backscattering intensity and Perpendicular Vegetation Index (PVI), one of the parameters indicating the vegetation coverage conditions, using JERS-1 SAR and Landsat TM images pair acquired on the same day (April 29th, 1993). The PVI can be estimated in the two dimensional plane composed by the intensity of TM band 3 (visible-red) and band 4 (near infrared). It is defined as the line perpendicular to the soil line and indicates the degree of vegetation coverage. The maximum value of PVI corresponds to the averaged value of PVI for the areas fully covered by vegetation. The two images were co-registered each other and twenty pairs of the averaged values in 5 x 5 window areas for SAR and TM images which were sampled from the bare soil areas and the vegetated areas were used for the regression respectively.

Fig.2 shows the result from the regression analysis between SAR-NRCS and PVI. The result indicates positive correlation between SAR backscatter and vegetation coverage, although there are seen relatively large variations of NRCS for large PVI samples, which is one of the factors decreasing correlation between PVI and NRCS. This variation is considered to be caused by the differences of vegetation types, that is, the SAR backscatter for grasses is lower than that for trees even the area is fully covered by vegetation.

SEASONAL CHANGES OF SAR BACKSCATTER IN PADDY FIELD

The authors studied the actual changing patterns of SAR backscatter concerning to the change of vegetative

conditions in the paddy field at the same test site as Fig.1. For the monitoring of seasonal change of paddy fields, three temporal SAR data were acquired on March 16th, April 29th and September 8th, in the middle and final stage of the dry season and in the middle of the rainy season respectively.

As the result of the analysis, several kinds of paddy fields were identified which seasonal changes were different each other. The graph in Fig.3 shows the changing patterns of NRCS for eight land cover classes obtained from the classification using above three multitemporal SAR data. The solid lines (C2, C3, C4, and C6) in the graph correspond to the patterns of paddy fields. The change of C4 and C6 between March/April and September was proved to be caused by the difference between bare soil condition and the rice growth from the ground survey. The change of C2 was considered due to the planting of second rice in the dry season. The change of C3 between March and April was estimated to be caused not by the change of paddy, but by the change of soil moisture by the combined analysis of SAR and TM described above. Natural levee which distributes widely in the test site was easily identified as the class C8, which always resulted in high backscatter.

CHANGES OF SAR BACKSCATTER BY FLOODING

The authors studied the change of SAR backscatter in paddy fields when they were flooded. The lower image in Fig.1 shows the SAR image taken on September 26th, 1995 when a big flood occurred in the Central Plain of Thailand. This image can be compared with the middle image in Fig.1, which was taken almost in the same rainy season but in non-flood condition.

According to a ground survey at the same time of SAR observation, the SAR data were proved to result in very low backscatter in the flooded areas as shown in Fig.4. Therefore, the flooded areas in the paddy fields were extracted by subtracting NRCS values from those of the data in non-flooded conditions, namely the data in September, 1993. According to all weather characteristics of SAR, the SAR data is considered to be effective data source for the detection of flood in the rainy season.

CHANGES OF SAR BACKSCATTER BY FOREST FIRE

The authors investigated the change of SAR backscatter caused by a forest fire occurred in Okayama Prefecture in Japan to assess the applicability of JERS-1/SAR data for the detection of biomass burning. Vegetation in burnt forest is mainly occupied with the secondary forest including Querco glaucae - Pinetum densiflorae which height are about 5 to 8m. The difference of backscatter between before and after the fire is 3.2 dB in NRCS at the slope area of burnt forest. And also, the difference of backscatter between burnt and non-burnt forest is 12.0 dB as shown in Fig.5. It was proved that the decrease of biomass by forest fire can be detected from the decrease of SAR backscatter. However, it is considered that the remained standing trees in burnt forest caused less decrease of backscatter. If the forest fire is larger-scale, it is considered that the damage by forest fire will be detected more clearly as the change of SAR backscatter.

SUMMARY

Regression analysis using JERS-1 SAR and Landsat TM data acquired on the same day suggested that the change of SAR backscatter is related to the change of vegetation coverage conditions with positive correlation. Several case studies concerning to the change of vegetative conditions by season, flooding and burning proved that these changes can be detected as the change of SAR backscatter. The result of these case studies indicates the effectiveness of L-band SAR data by JERS-1 for the monitoring of several types of changes of vegetative conditions in which data acquisition is necessary even in bad weather conditions.

REFERENCES

[1] S. Takeuchi and R. Suwanwerakamtorn, "Analysis of the Influence of Land Cover Conditions on SAR Backscatter Using Simultaneous SAR and TM Data", J. of JSPRS, vol. 34, no. 5, pp.45-48, 1995.

[2] S. Takeuchi and R. Suwanwerakamtorn, "Monitoring of Land Cover Conditions in Paddy Fields Using Multitemporal SAR Data", RESTEC news letter, no 18, 1995.
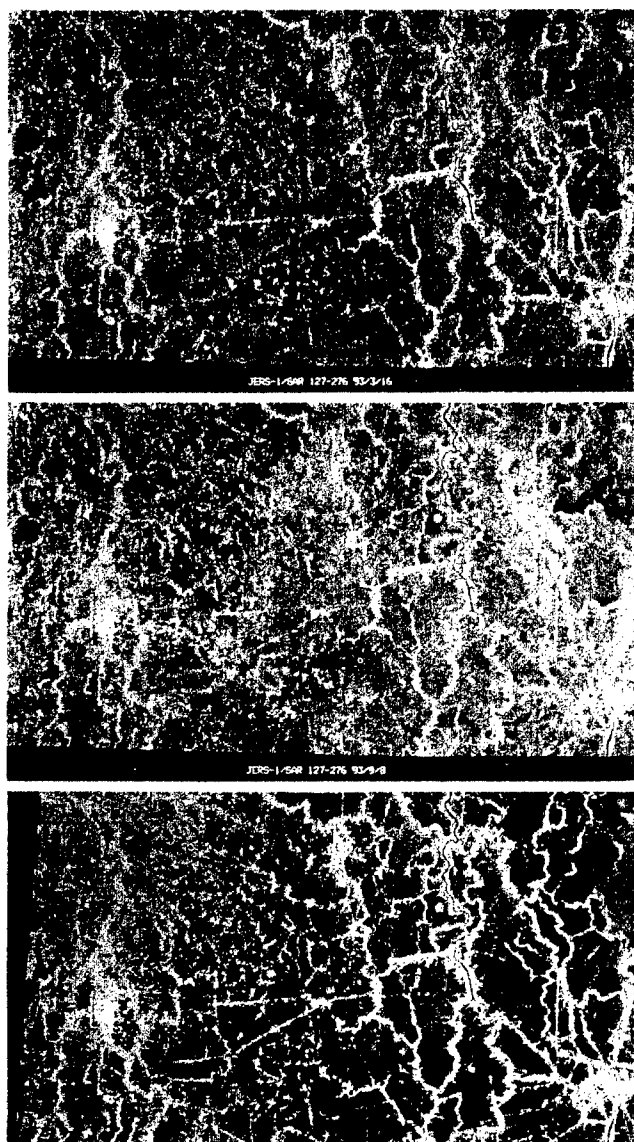
Fig.1 Three temporal JERS-1/SAR images.(Upper: Mar.16,'93, Middle:Sep.8,'93, Lower:Sep.26,'95)
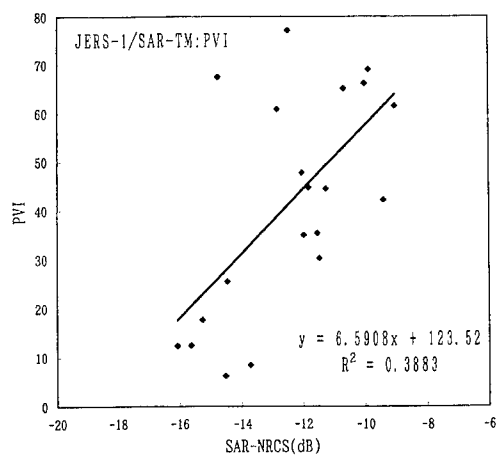
Fig.2 Result of the regression analysis between SAR backscatter (NRCS) and PVI.
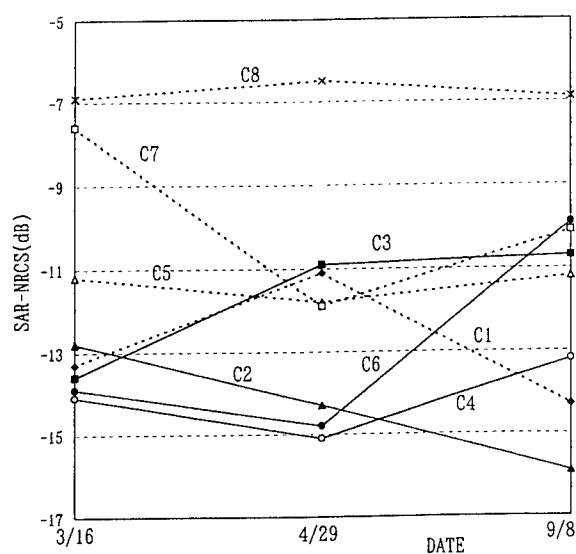
Fig.3 Seasonal changes of SAR backscatter for eight land cover types including paddy and natural levee.
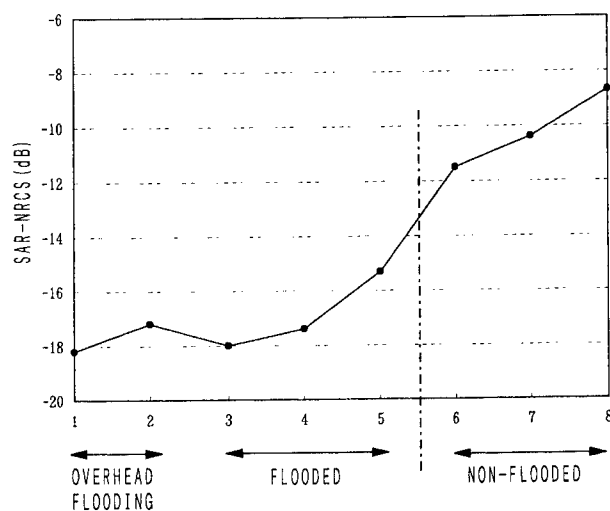
Fig.4 SAR backscatter in flooded and non-flooded paddy field.
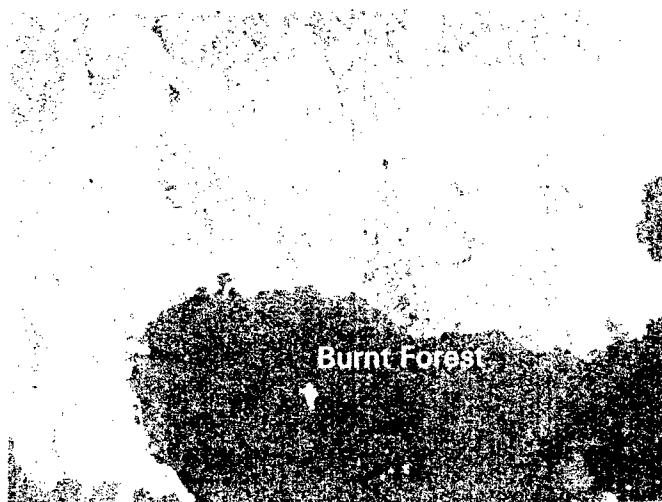
Fig.5 SAR image of burnt forest area.

C- and L-Band Multi-Temporal Polarimetric Signatures of Crops

Henning Skriver[1], Flemming Nielsen[2], and Anton Thomsen[2]

[1]Danish Center for Remote Sensing, Dept. Electromagnetic Systems
Technical University of Denmark, Building 348, DK-2800 Lyngby, Denmark
Phone: +45 45 88 14 44, Fax: +45 45 93 16 34, E-mail: hs@emi.dtu.dk

[2]Danish Institute of Plant and Soil Sciences
Research Center Foulum, DK-8830 Tjele, Denmark

Abstract -- Polarimetric SAR-data of agricultural fields have been acquired by the Danish polarimetric SAR (EMISAR[1]) during a number of missions[2] at the Danish test site Foulum during 1994 and 1995. EMISAR has operated in a fully polarimetric mode at C-band since the fall of 1993 and at L-band since the beginning of 1995. The SAR system is installed on a Danish Air Force Gulfstream aircraft, and a significant amount of polarimetric SAR data have been acquired on various missions. Polarimetric parameters for a number of different agricultural crops are shown, and the advantage of having polarimetric, multi-frequency, and multi-temporal data for crop discrimination is clearly seen.

INTRODUCTION

A research and development project initiated in 1986 at the Department of Electromagnetic Systems (EMI) of the Technical University of Denmark resulted in a C–band VV-polarized airborne SAR first flown in 1989 [1]. The Danish airborne polarimetric SAR (EMISAR) has since then been extended to an L- and C-band fully polarimetric and interferometric SAR [2]. The polarimetric extension of the system has been co-sponsored by the EU's Joint Research Centre (JRC). The EMISAR is used for scientific experiments conducted by the Danish Center for Remote Sensing (DCRS) which was established early 1994 at EMI by the Danish National Research Foundation, and it is expected to be utilized by JRC for its European Airborne Remote Sensing Campaign (EARSEC). Also, EMISAR has been used for the European Multisensor Airborne Campaign (EMAC) arranged by ESA.

The SAR system is installed on a Danish Air Force Gulfstream. The SAR system is normally operated from an altitude of approximately 12.500 m, the spatial resolution is 2 m by 2 m, the ground range swath is approximately 12 km and typical angles of incidence range from $35°$ to $60°$. The processed data from this system are fully calibrated by using an internal calibration and a test area is equipped with a number of reference targets thus enabling the verification of system performance. The radiometric calibration is better than $±0.5$ dB, and the channel imbalance is less than $±0.5$ dB in amplitude and $±5°$ in phase. The cross polarisation contamination is generally suppressed by more than 30 dB.

The DCRS conducts research in collaboration with science partners within areas related to remote sensing techniques and Earth science, such as agriculture, environment, geology, glaciology, hydrology and sea ice. The research within agriculture, i.e. on crop monitoring and soil moisture mapping, is carried out in co-operation with Research Center Foulum (RCF). The RCF is a research centre under the Danish Ministry of Agriculture, with intensively monitored farm land, ideally suited for studying the application of remote sensing to agriculture. The research is primarily aiming at studying the application of radar remote sensing techniques to monitor agricultural crops, biomass, and soil physics. The primary observational technique is SAR polarimetry, and results from this study will be presented in this paper.

DATA ACQUISITION

The test site used for the agriculture study is located in the northern part of Jutland around RCF at Foulum. At RCF, spectral reflectance measurements in the visible and near infra-red spectral bands are routinely used to monitor biomass and canopy structure (leaf-area-index, foliage distribution and orientation). The primary instruments are mast mounted and portable dual band (visible red and near infra-red) radiometers. Digital analysis of false-color aerial photography is used for field variability mapping. Instrumentation and laboratory facilities are also available for the measurement of water content of canopy elements, soil composition, micro relief, and water content.

A large number of acquisitions with both the C- and L-band polarimetric SAR was carried out in 1995, for instance on March 22 (L-band), March 24 (C-band), April 27 (C-band), June 8 (L-band), and July 4 (C- and L-band). The data acquisitions have been co-ordinated with extensive in-situ measurement campaigns, where e.g. soil moisture, soil roughness, a multitude of plant parameters and crop types were measured.

VEGETATION SIGNATURES

It is well known that the canopy development of different crops with time causes variation of the backscatter, and it is the basis for e.g. multi-temporal classification of ERS-1 SAR data (e.g. [3]). Also, for polarimetric SAR data multi-temporal acquisitions may contain additional and important information (see e.g. [4]). Below examples of backscatter coefficients for different crop types will be shown, that is winter wheat, winter barley, winter rape, and spring barley.

The polygons picked for the crop types contain at least 2000 pixels, where the pixels are sampled with 1.5 m pixel spacing. The pixels are of course correlated, and using homogenous areas in the image, the equivalent number of looks for an 2000 pixel area is estimated to at least 300. This results in a standard deviation for the backscatter coefficients due to the speckle noise of less than 0.2 dB. The variance caused by the speckle noise will consequently have a very small effect on the results from the polygons used, and it is ignored below.

The polygons are picked in the full range of incidence angles from about $39°$ to $58°$. The polygons are then grouped according to their incidence angle in $4°$ intervals, and the mean and standard deviation are computed for each of these intervals, so that error bars may be estimated. Examples of these results are shown in <u>Figs. 1 and 2</u>, where the angular dependence of the γ_{vv} backscatter coefficient for the L- and C-band acquisitions in March is shown. The γ backscatter coefficient is used because it has a slightly weaker dependence on the incidence angle than the σ backscatter coefficient. For the actual incidence angle interval the decrease with incidence angle is about 1.5 dB larger for σ than for γ. In a crop discrimination application the weaker dependence is an advantage, because fewer classes are necessary to cope with the variation.

The largest variation between near- and far-range is observed for these early spring acquisitions (about 4 dB at L-band and about 2 dB at C-band), whereas the variation is well below 2 dB for the later acquisitions. These observations correspond with the fact that the backscattering in the early spring is dominated by surface scattering from the bare fields, whereas volume scattering from the vegetation is contributing at the later acquisitions. Furthermore, we have the largest variation at L-band because the same surface appears rougher at C-band than at L-band.

As mentioned above the incidence angle dependence is weak especially for the larger incidence angles. Therefore, fields with incidence angles larger than $45°$ are used to compute the multi-temporal signatures and their standard deviation. The multi-temporal γ_{vv} backscatter coefficients for L- and C-band are shown in <u>Figs. 3 and 4</u>, respectively, and the multi-temporal γ_{xp} backscatter coefficients for L- and C-band are shown in <u>Figs. 5 and 6</u>, respectively. The γ_{xp} backscatter coefficient is computed by averaging the

scattering matrix elements S_{HV} and S_{VH} for thermal noise reduction, where reciprocity has been implied.

We observe, that the variation indicated by the error bars is relatively large, especially at the early spring acquisitions. The standard deviation is from 2 to 3 dB for the latter acquisitions, probably caused by the sensitivity of the backscattering to the plowing direction. For the later acquisitions the standard deviation is smaller, e.g. less than 1 dB in most of the cases, probably caused by the backscatter contribution from the vegetation. The standard deviation for the L-band data is slightly larger than for the C-band data.

All the curves for the spring barley, the winter barley and the winter wheat are constant or decreasing from the March to the May acquisition and then increasing for the later acquisitions. The increase is correlated with the measurements of the Leaf Area Index (LAI) (c.f. [5]), where the LAI increases from 1.5 at Julian Day 137 to 3.3 at Julian Day 178. We observe a more distinct increase at L-band. The backscattering from the winter rape differs significantly from the others, because of the very different structure and larger biomass.

The importance of multi-temporal acquisitions for classification applications is clearly seen from the results. Using the acquisitions in May and in July of the C-XP channel it will be possible to discriminate between the crops. Furthermore, it is obvious that the discrimination capability is larger for the C-band than for the L-band.

CONCLUSIONS

Multi-temporal and multi-frequency vegetation backscatter results measured by the Danish L- and C-band polarimetric SAR have been presented. We observed a relatively large variation of the backscattering from fields at approximately the same incidence angle. This variation is probably coarse by the sensitivity of the backscattering to e.g. the plowing and sowing directions, and the local incidence angle. The multi-temporal signatures showed correlation with LAI and thereby biomass. Finally, C-band has larger discrimination capability than L-band.

REFERENCES

[1] Madsen, S.N., E. L. Christensen, N. Skou, and J. Dall: The Danish SAR System: Design and Initial Tests, IEEE Trans. Geosc. Rem. Sens., vol. 29, 1991, pp. 417-476.

[2] Christensen, E. L., J. Dall, N. Skou, J. Granholm, K. Woelders, and S.N. Madsen,: EMISAR: C- and L-band Polarimetric and Interferometric SAR, Proc. IGARSS 96, *this issue*.

[3] Schotten, C. G. J., W. W. L. van Rooy, and L. L. F. Janssen: Assessment of the capabilities of multi-temporal ERS-1 SAR data to discriminate between agricultural crops, Int. J. Remote Sensing, 1995, vol. 16, pp. 2619-2637.

[4] Baronti, S., F. Del Frate, P. Ferrazzoli, S. Paloscia, P. Pampaloni, and G. Schiavon: SAR polarimetric features of agricultural areas, Int. J. Remote Sensing, 1995, vol. 16, pp. 2639-2656.

[5] Ulaby, F. T., C.T. Allen, G. Eger III, and E. Kanemasu, 1984,: Relating the Microwave Backscattering Coefficient to Leaf Area Index, Remote Sening Environ., vol. 14, pp. 113-133.
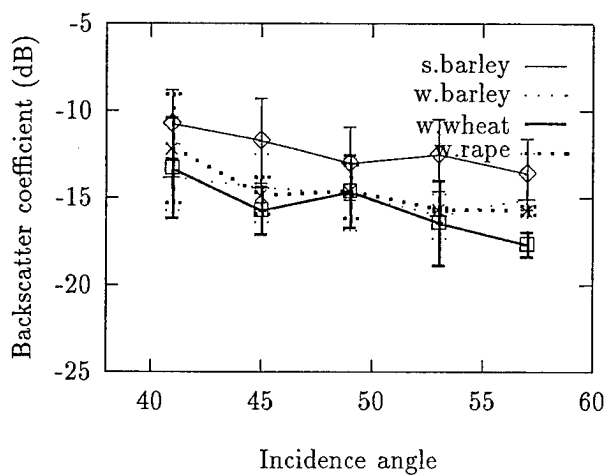
Fig. 1 The γ_{vv} backscatter coefficient for L-band acquired March 22, 95.
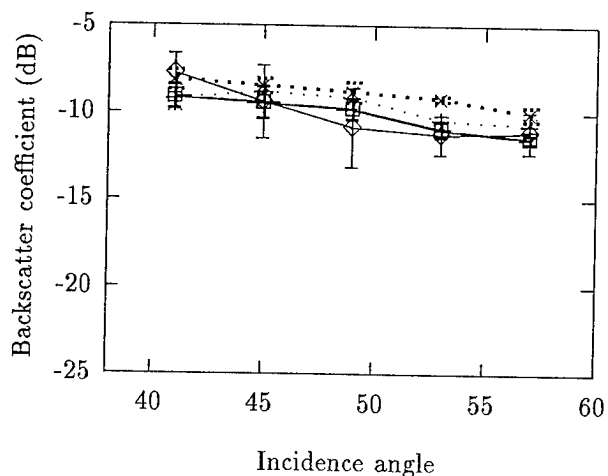
Fig. 2 The γ_{vv} backscatter coefficient for C-band acquired March 24, 95.
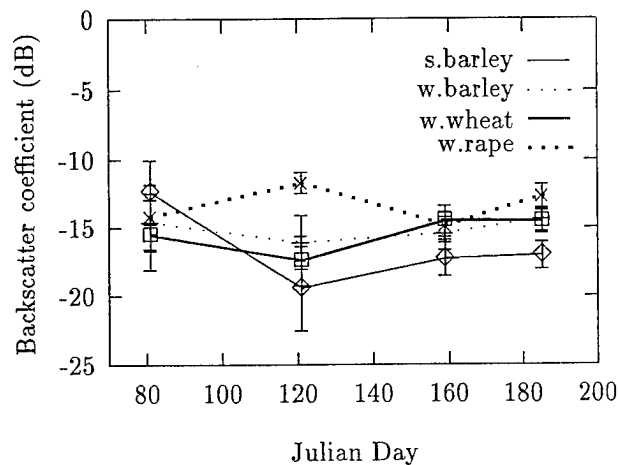
Fig. 3 The multi-temporal γ_{vv} backscatter coefficient for L-band acquired 95.
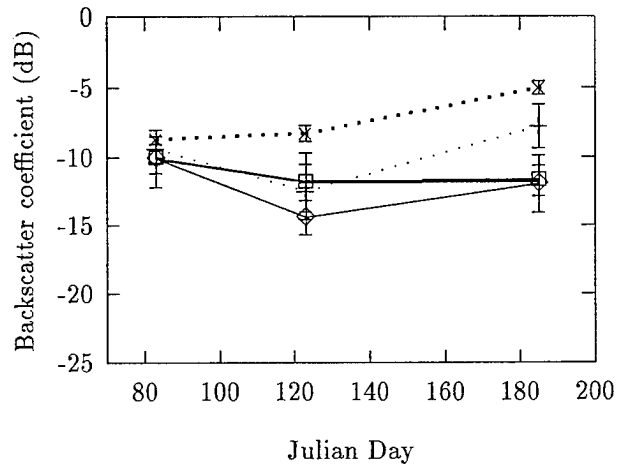
Fig. 4 The multi-temporal γ_{vv} backscatter coefficient for C-band acquired 95.
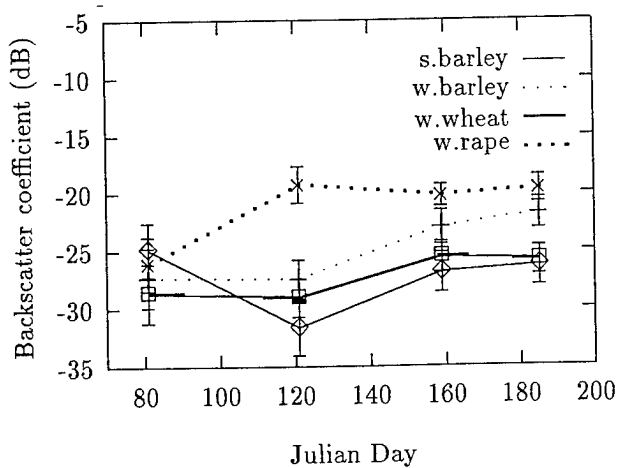
Fig. 5 The multi-temporal γ_{xp} backscatter coefficient for L-band acquired 95.
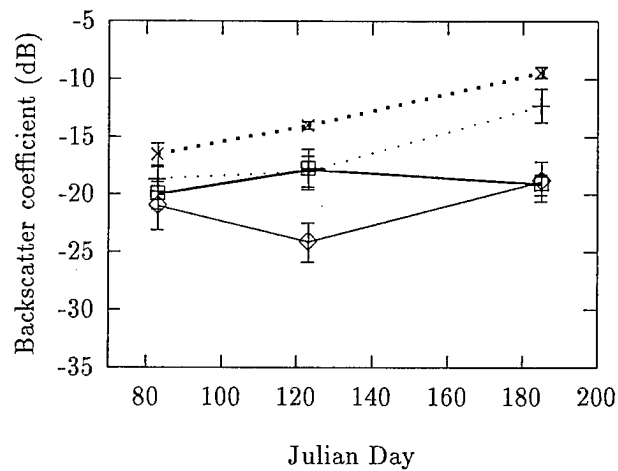
Fig. 6 The multi-temporal γ_{xp} backscatter coefficient for C-band acquired 95.

Characterization of Oklahoma Reservoir Wetlands For Preliminary Change Detection Mapping Using IRS-1B Satellite Imagery

John Mahlke

Department of Geography, University of Oklahoma, Norman, OK 73019
Telephone: (405) 325-5325 / (405) 325-3148 / JMahlke@uoknor.edu

INTRODUCTION

The multifaceted nature of wetlands in recent years have attracted the attention of a variety of different interests. From land developers and agriculturists, to conservationists and planners, the debate over definition and delineation of wetlands has been a point of contention.

In the 1970's and 1980's wetlands gained attention as being fragile landscapes that required suitable delineation and monitoring. Aerial photography had a decisive role in the delineation process with such agendas as the National Wetlands Inventory, and the mapping of Tennessee Valley Authority (TVA) wetlands [1]. However, more recently the economy and efficiency of remote sensing to carry out these mapping responsibilities have gained more attention [2]. Ducks Unlimited was one of the first non-governmental private company applications of extensive wetland monitoring with LANDSAT 4 and LANDSAT 5 products to determine extent and phenology of upper great plains prairie potholes [3]. Even with the greater accessibility and variety of sensors available today wetland mapping is still done from a somewhat static basis.

Multidate imagery has been used to improve classification accuracy's and to provide more of a dynamic basis of analysis in a variety of applications. The use of an extensive amount of time series AVHRR satellite data to measure metrics within a vegetation phenology [4] and to explain spatial and time series change with the use of principal components [5] are two studies that represent the value of moving beyond single date remote sensing analysis. The use of the Landsat Thematic Mapper to create a dynamic multidate land cover classification scheme showed improved accuracy for land cover classification of agricultural areas [6]. The use of multidate imagery from the MSS and SPOT satellite systems were used in a change detection analysis to explain an increase in the amount of cattails, and the decrease in the amount of sawgrass, over an eighteen year period in the Florida Everglades [7].

The purpose of this paper is to discuss the use of using multidate satellite imagery, to characterize the exoatmospheric reflectance phenology of five wetland plant communities

Prior knowledge of the size and bearing of the wetland communities were known from visits to various sites. Some very broad knowledge of the wetland plants and their cycles were extracted from a limited amount of aerial photographs.

STUDY AREA

Canton Lake Reservoir, a flood control measure to meet recreational and municipal water needs erected during the 1940's, is located on the North Canadian River in northwest Oklahoma. The lake's flood control facilities are maintained by the U.S. Army Corps of Engineers and water is drawn down annually during the winter season prior to one of Oklahoma's two maximum rainfall peaks.

Comparisons between historical aerial photography of the Canton system reveals that at the western end of the lake, circa the 1950's, there was the beginning of the growth of various Cowardin wetland types [8]. The results have been a uniquely manmade series of wetland communities.

- Common Reed *(Phragmites australis)* a member of the grass family found at Canton Lake in abundance in several different areas. For this study, the area around where the North Canadian River empties into the lake was sampled.

- Curlytop Smartweed *(Polygonum lapathiform)* a member of the Buckwheat family (Polyonaceae) located in highly discernible beds around the Common Reed beds of the North Canadian River emptying point into the lake

- Southern Cattail *(Typha domingesis)* a cattail variety that is found throughout the United States. It is present in several extensive beds in the Canton Lake watershed.

- Eastern Cottonwood (*Populous deltoides*) is a tree variety found in developed stands along the North Canadian River leading into the lake. Cottonwoods are also found surrounding the wetlands at the farthest extent of Canton Lake [9].

METHODS

By choosing three wetland plant community types made up of three distinctly different plants and two other wetland plant communities made up of the same plant type growing under two varying hyd˙ ˙ogic environments, it was determined that sampling pixels from each of these domains would yield separate exoatmospheric reflectance value ranges at distinct times during the year. Areas of homogeneous stands of common reed, southern cattail, and eastern cottonwood were determined. In addition two environmentally different sample domains of curlytop smartweed were chosen. The first smartweed sample (referred to as Smartweed 'A' in Figure 1) is characterized by a moderate amount of submersion during the year. The second smartweed sample (referred to as smartweed 'B' in Figure 1) was chosen from an area characterized by longer periods of submersion in comparison to the first smartweed sample.

The five indicator wetland plant communities were sampled over a thirteen month time period from June 8, 1994 - July 9, 1995. All data consisting of eleven IRS-1B and 1 IRS-P2 scenes were collected at the EOSAT Norman Ground Station at Norman, Oklahoma. All image processing was accomplished using ERDAS software. A band-by-band normalization algorithm was run on all four bands individually to account for sun angle, earth/sun distance, and spectral radiance values to convert the raw data to absolute reflectance. Unified four band image sets were produced. A minimum of 12 ground control points were maintained for each image, digitized to National Wetlands Inventory (NWI) maps, with an RMS error of .33 and then resampled with the use of the nearest neighbor resampling algorithm. A subset, of no more than 36 square miles, was devised to include all of the sample areas resampled with the use of the nearest neighbor resampling algorithm. A subset, of no more than 36 square miles, was devised to include all of the sample areas. Homogeneous sampling of each of the vegetation communities were outlined using the onscreen GIS capabilities of the ERDAS software. Sample exoatmospheric reflectance values were recorded for each wetland plant community. The minimum number of sampling units totaled 6 pixels. The maximum number of sampling units totaled 9 pixels. Exoatmospheric reflectance was also

IRS Satellite Spectral Ranges

IRS Band	Spectral Range	
Band 1	Blue	0.45 - 0.52 μm
Band 2	Green	0.52 - 0.59 μm
Band 3	Red	0.62 - 0.68 μm
Band 4	Near I.R.	0.77 - 0.86 μm

sampled and recorded for the NDVI of each of the sampled 12 images. Mean sampling values were determined for each sample type for each image date. The NDVI is particularly useful in determining and mapping various environmental effects on vegetation [10]. For the scope of this paper just the NDVI values were graphed and appear in Figure 1. The U.S. Army Corps of Engineers retains detailed records on the lakes they maintain that include precipitation data and lake pool elevation data. These hydrologic data were plotted on a daily basis from June 8, 1994 to July 9, 1995 and appear in Figure 2.

Figure 1

Figure 2

1770
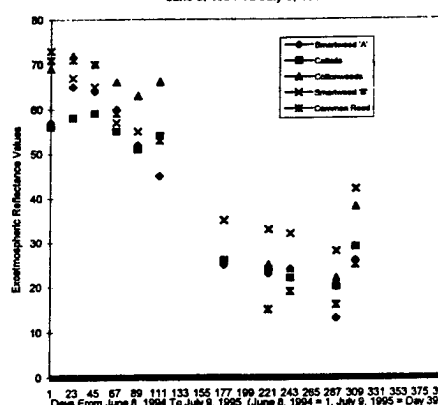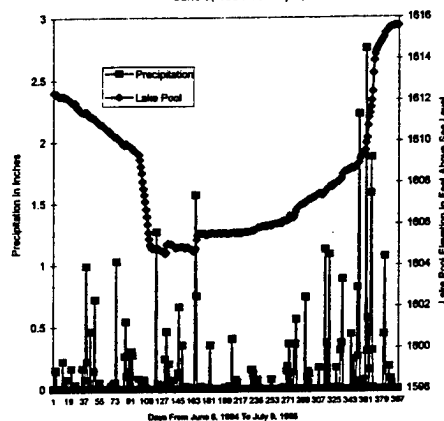
RESULTS

The overall phenological trends exhibited by the wetland plant communities indicates that exoatmospheric reflectance is highest in the late spring and summer months and diminishes to the lowest level of average exoatmospheric reflectance sometime in March of 1995.

Generally the best time of year to distinguish between all of the plant communities is springtime. The two best dates for discrimination between plant community types are March 24, 1995 (Day 289) and July 9, 1995 (Day 397). March has the lowest average exoatmospheric reflectance and July of 1995 has some of the highest average exoatmospheric reflectance. It appears that July 9, 1995 has better discrimination between plant communities than July 22, 1994 (Day 45) partly as a function of lake level and precipitation. Prior to July of 1995 there was a greater amount of precipitation and a higher lake level than both attributes a year earlier in July 1994 and this caused a greater discrimination between all of the wetland community types for that date (see Figures 1 and 2).

The worst time of the year for the plant community discrimination was December 1, 1994 (Day 177). Four of the of the five community types clump together and are indistinguishable on that date. From December on there appears to be an improvement in community discrimination. Smartweed 'B' appears to be the wetland plant community easiest to distinguish from the other plant communities almost year round. Other plant community types exhibit optimal times of the year to distinguish them from other types. An example of this is the eastern cottonwood which appears to be most distinguishable from the other community types in late summer and fall (Days 67, 89 and 111).

The three images that merit further investigation for the basis of an annual change detection map (using two or more images) are:

December 1, 1994
The image expresses the lowest lake level of the 12 images used.

March 24, 1995
The image shows good separation between NDVI exoatmospheric reflectance for all five wetland plant communities, expresses low lake pool elevation level, and represents the lowest exoatmospheric reflectance for the majority of the communities.

July 9, 1995
The image shows good separation between NDVI exoatmospheric reflectance for all five wetland plant communities, expresses nearly the highest lake pool

elevation level, and represents one of the highest levels of exoatmospheric reflectance for the majority of the communities.

REFERENCES

[1] Carter, Virginia. (1982) : Application of Remote Sensing to Wetlands. In Introduction of Remote Sensing of the Environment. Dubuque, IA: Kendall/Hunt Publishing Company.

[2] Luman, D.E. (1990) : The Potential For Satellite-Based Remote Sensing Update Of The Illinois Portion Of The Ntional Wetlands Inventory. Quarterly Report, submitted to the Illinois Department of Conservation.

[3] EOSAT Application Notes 1987, Earth Observation Satellite Company, Lanham, MD.

[4] Reed, B. C., Jesslyn F. Brown, D. VanderZee, T. R. Loveland, J. W. Merchant, and D. O. Ohlen. (1994) : Measuring Phenological Variability From Satellite Imagery. Journal of Vegetation Science, 5: 703-714, 1994.

[5] Eastman, R.J. and M. Fulk. (1993) Long Sequence Time Series Evaluation Using Standardized Principal Components. Photogrammetric Engineering and Remote Sensing, Vol. 59, No. 8, August 1993, pp. 1307-1312.

[6] Egbert, S. L., K. P. Price, M. Duane Nellis, and Re-Yang Lee. (1995) Developing A Land Cover Modelling Protocol For The High Plains Using Multi-Seasonal Thematic Mapper Imagery. ACSM/ASPRS '95 Annual Convention and Exposition, Charlotte, North Carolina, February 27-March 2.

[7] Jensen, John R., Ken Rutchey, Marguerite S. Koch, and Sunil Narumalani. (1995) : Inland Wetland Change Detection In The Everglades Conservation Area 2A Using A Time Series Of Normalized Remotely Sensed Data. Photogrammetric Engineering and Remote Sensing, Vol. 61, No. 2. February 1995, pp.199-209.

[8] Cowardin, Lewis. (1979) Classification of Wetlands and Deepwater Habitats of the United States. U.S. Fish and Wildlife Service.

[9] Hoagland, B. W. and F. L. Johnson. (1994) Emergent Wetland Vegetation Of Western Oklahoma: Final Report. Norman, OK: University of Oklahoma.

[10] Hardisky, M.A., M.F. Gross, and V. Klemas. (1986) Remote Sensing Of Coastal Wetlands. BioScience, Vol. 36, No. 7.

RADARSAT Antarctica Mapping System: System Overview

Lynne Norikane[1], Bob Wilson[1], and Ken Jezek[2]

1. Vexcel Corporation 2477 55th Street Boulder, Colorado 80301
(303) 444-0094, Fax: (303) 444-0470, lynne@vexcel.com
2. Byrd Polar Research Center, Ohio State University, Columbus, Ohio 43210

Abstract -- In October 1996, RADARSAT will map the entire Antarctic continent from space, presenting scientists with an unprecedented snapshot of the entire continent in the microwave spectrum. NASA has charged the Byrd Polar Research Center with the goal of producing a full continental map using this data, subject to a number of constraints to maximize the utility of the data to the scientific community. To meet these requirements, a number of SAR data processing techniques shall be applied including orthorectification processing, block adjustments for ephemeris refinements, simulation techniques and radiometric balancing for automated image seam removal. These techniques shall be implemented in the RADARSAT Antarctica Mapping System being developed by Vexcel Corporation for the Byrd Polar Research Center. In this paper, we will provide an overview of the system.

OVERVIEW

Over the course of 18 days in October of 1996, at least 12 hours worth of data will be collected by the Canadian RADARSAT sensor, completely mapping the continent of Antarctica. These data in turn will be processed by the Alaska SAR Facility (ASF) into no less than 3600 image frames, all to be ultimately assembled into a single digital mosaic by the Byrd Polar Research Center (BPRC). To form this mosaic, Vexcel Corporation is developing the RADARSAT Antarctica Mapping System (RAMS) which is specifically designed to handle the large data volumes and demanding processing requirements for this project.

RAMS consists of a combination of hardware and software solutions. It resides on one or more Unix platforms. The choice and number of platforms used is highly dependent on the desired overall throughput for map formation. The data processing software are accessible via graphical user interfaces (GUIs) which are written in X. Both data processing software and GUIs interface to a database and operate on other files such as images.

PROCESSING STRATEGY

The overall processing strategy for map formation is designed to handle both large data volumes (more than can be stored on disk simultaneously) and to allow map formation to begin prior to all data being processed into images by ASF. To do so, we process the data in "blocks" or groups of overlapping images. Each block is processed individually and then archived. After all blocks for the map have been processed, they are geometrically and radiometrically adjusted so as to remove block-to-block seams, and the final map product is formed. The phase during which individual blocks are being

processed is called the Block Processing Phase. The final map product is formed during the Tile Processing Phase.[1]

By using this strategy, only enough disk space is required to store data for one or two blocks simultaneously. In addition, not all data for the map are required to be processed by ASF before map formation can begin. An overview of the system is shown in Figure 1. Each of the data processing steps shown are described in more detail later.
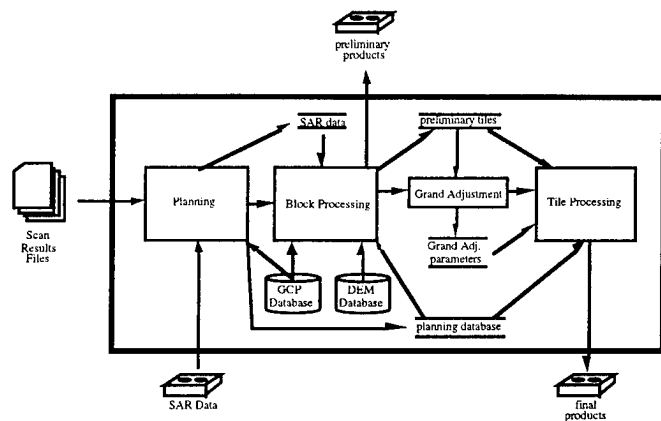
Figure 1: RAMS Data Processing Overview

PLATFORM

The overall performance and number of platform(s) needed are a function of the overall throughput requirement for map formation. Using today's mid-range computing systems, it is clear that multiple platforms or CPUs are required to meet BPRC's requirement to form one map within 15 months.

In addition to one or more computer platforms for RAMS, a variety of additional peripheral devices are required. A large disk array is needed to store input and output images, digital elevation maps (DEMs) and ground control points (GCPs), intermediate products, and the RAMS database. 64 GB is currently planned for RAMS. To backup and restore data to the disks, a backup system is required (such as a digital linear tape,). To ingest ASF products, an 8-mm tape drive is required and to form output products a CD-ROM mastering capability is also required. X-terminals or other computers may be used as displays.

SOFTWARE

---

[1]The actual map product consists of approximately 90 individual tiles which are each divided into 75-115 smaller sub-tiles.

The software components of RAMS are best described in relation to the overall data processing flow. The first step in map formation is processing planning.

Processing Planning

The entire map formation process requires that an overall processing plan be formulated. The primary purpose of this planning is to divide the map into blocks (groups of overlapping images) and to choose the order in which blocks will be processed. Given this, data processing requests may be submitted to ASF in the proper sequence. After the first data have been received, Block Processing may begin.

A good block is considered to having the following characteristics. At least 2 radar-visible ground control points must be contained within its boundaries. Blocks should consist of long contiguous swaths of data, overlapping each other in the cross-track direction.

Block Processing

Once all data for a given block have been received, block processing may begin. The overall objective is to combine all image frames for the block into preliminary map tiles. The result must satisfy geometric and radiometric accuracy requirements and must be seamless in appearance.

The first objective is to compute a block adjustment or correction to all orbits contained within the block. To do so, we require the collection of ground control points and tie points between frames within the block.

Tie Points Tie points are collected in both an automated fashion and a manual fashion. Tie points are collected in the along-track direction through an automated process. Cross-track tie points (i.e. tie points collected between frames in different orbits) are also collected in an automated fashion using estimates on locations of overlap regions and an image automatcher.

The operator may choose to verify or correct the automatcher results and may choose to manually select new tie points.

GCPs Ground control points must be manually located by the operator. If the operator is unable to locate at least 2 GCPs within the block, then a radar simulation technique may be used to form a synthetic GCP.

Radar Simulation In an area of "sufficient" terrain, a small synthesized SAR image may be formed using a backscatter model and the terrain itself. This synthesized SAR image is then automatched to the actual SAR image resulting in a single tie point for the pair. Given that the geolocation of the synthesized image is known, we then convert the tie point into a ground control point with known latitude, longitude, and elevation and its corresponding location in the SAR image.

Block Adjustment Given a sufficient number of tie points and located ground control points within the block, the block adjustment may be computed. In this step, the block adjustment corrects all orbits within the block such that tie points are reconciled as closely as possible and GCPs are

geolocated as accurately as possible. The overall goal is to greatly exceed the 300 meter geolocation accuracy requirement for the map.

Orthorectification Once the block adjustment has been computed, all image frames are resampled into a map grid, taking into account geometric distortions due to terrain. Radiometric corrections due to slope effects are also applied in this step.

Radiometric Balancing The next step is to remove radiometric seams between images in an automated fashion. This is done by taking advantage of our already having tie points between images. At each tie point, local image statistics are computed and a target value assigned. Using actual and target values at each tie point, a radiometric balancing function may be computed as a function of image position. One such function is computed for every image in the block.

Preliminary Tile Formation The final step in block processing is to apply the radiometric balancing functions to the orthorectified images and form preliminary map tiles. Having done so, image chips are extracted around the block edges for later use during the Grand Adjustment. The operator may also choose to create preliminary products. Otherwise, the data is archived, the disk is cleaned, and data loaded for the next block.

Options If data were collected for the purposes of filling in areas of layover or shadover, a steps are required to reset these areas and merge the orthorectified data collected for that purpose.

Grand Adjustment

Once all blocks have been processed individually, the Grand Adjustment is performed. In this step, the radiometric and geometric seams between blocks are removed. To do so, the block-to-block image chips collected during block processing are used to compute tie points and their local image statistics.

The radiometric balancing approach is essentially the same as that used for individual blocks. The geometric adjustment computes an offset and rotation for each block. based on the block-to-block tie points.

Tile Processing

The formation of the final map products are done during the tile processing phase. In this phase, the results of the Grand Adjustment are applied to each block in turn. These data are then merged into final tile products which can then be prepared for CD-ROM mastering. In addition, overview or lower-resolution map products may be formed for areas of larger extent.

OPERATOR INTERFACES

Throughout RAMS, the operator initiates processing and can view and often modify intermediate results through graphical user interfaces. RAMS is an exceptionally flexible system. The operator can be guided through the various processing steps or may choose to beat his or her own path.

BATCH PROCESSING

RAMS relies on overnight batch processing to meet overall throughput requirements for map formation. An intelligent program dispatcher is used to control both the order in which programs are run and the number of programs which may run simultaneously on one or more different platforms. The dispatcher has its own GUI which provides the operator with a list of pending jobs, jobs currently being run, and jobs completed. Access to error logs is also provided.

SUMMARY

RAMS is a complete end-to-end processing system for the formation of large-scale maps from synthetic aperture radar imagery. It utilizes the techniques of block adjustment for improving geolocation accuracy, orthorectification for terrain distortion removal, automated radiometric balancing for image seam removal, as well as other techniques to improve the overall quality of the final product, at the same time, providing the operator with a large degree of control over each step to ensure the formation of the best product possible.

REFERENCES

[1] Jezek, K. C., and F. D. Carsey, 1993. Radarsat: The Antarctic Mapping Project. Byrd Polar Research Center Report no. 6, 24.

RADARSAT: The Antarctic Mapping Project

K.C. Jezek[1], J. Curlander[2], L. Norikane[2], F. Carsey[3], J.P. Crawford[3], C. Wales[4], J. Muller[5]

1. Byrd Polar Research Center, The Ohio State University, 1090 Carmack Road Columbus, OH 43210
Tel: 614) 292-6531, Fax: 614) 292-4697, e-mail: jezek@iceberg.mps.ohio-state.edu
2. Vexcel Corporation, Boulder, Colorado
3. Jet Propulsion Laboratory, California Institute of Technology, Pasadena, California
4. The Alaska SAR Facility, Fairbanks, Alaska
5. Canadian Space Agency, Saint-Hubert, Quebec, Canada

I. Introduction

On November 4, 1995, the Canadian RADARSAT was carried aloft by a NASA rocket launched from Vandenberg Air Force Base. RADARSAT is equipped with a C-band Synthetic Aperture Radar (SAR) capable of acquiring high resolution (25 m) images of Earth's surface day or night and under all weather conditions. Along with the attributes familiar to researchers working with SAR data from the European Space Agency's Earth Remote Sensing Satellite and the Japanese Earth Resources Satellite, RADARSAT will have enhanced flexibility to collect data using a variety of swath widths, incidence angles and resolutions. Most importantly, for scientists interested in Antarctica, the agreement for a U.S. launch of RADARSAT includes a provision for rotating in orbit the normally right-looking SAR to a left-looking mode. This 'Antarctic Mode' will provide for the first time a nearly instantaneous, high resolution view of the entirety of Antarctica on each of two proposed mappings separated by 2 years. This is an unprecedented opportunity to finish mapping one of the few remaining uncharted regions of the Earth. The completed maps will also provide two important benchmarks for gauging changes of Antarctica's ice cover (Jezek and Carsey, 1993).

II. Project Plan

The preparation of a digital mosaic of Antarctica is being conducted by the Byrd Polar Research Center of The Ohio State University under a NASA Pathfinder Project. The primary goal of the project is to compile digital SAR mosaics of the entire Antarctic continent using a combination of

Figure 1. The area of Antarctica to be mapped is equivalent to that of the United States and Mexico combined.

Radarsat Antarctic Mapping Coverage
Ascending Standard and Extended Beam Segments

Figure 2. Map showing 3 days of standard beam 2 coverage. Mapping to the South Pole will be completed with extended beam 4. Ascending swaths will be used to compile the mosaic.

standard and extended beams during the "Antarctic Mode" of the RADARSAT Mission (figure 2). Preliminary plans

call for the first Antarctic Mapping Maneuver to occur in October, 1996. A mission plan to coordinate that complex acquisition and downlinking of Antarctic data is being developed by NASA's Jet Propulsion Laboratory and the Canadian Space Agency. The plan indicates that a minimum of 18 days are required to completely image the continent using standard beams 2 through 7 and extended beam 4 for imaging the Pole (figure 2). Contingency plans are in preparation in the event of unforseen complications during the data acquistion.

The Alaska SAR Facility (ASF) will be used as the primary data collection site supported by collections at the Canadian Gatineau and Prince Albert Ground Stations. ASF will process data into images which will be sent to OSU for compositing into map products using equipment under design by Vexcel Corporation of Boulder, Colorado. Final products will be distributed through the ASF and the National Snow and Ice Data Center which are both NASA Distributed Active Archive Centers (DAACs). The mosaics and ancillary information will be prepared on CDROM and will be made available to the science community through NASA DAACs.

III. Science Opportunities

The international research community is providing guidance through the Antarctic Mapping Advisory Group. AMAG is tasked with helping assure that science opportunities envisioned for the program (as summarized on table 1) can be achieved with the mission plan, data reduction algorithms and final product suite. These opportunities include studying the dynamics and variability of the Antarctic Ice Sheet including studies of regions like the Wordie Ice Shelf and the Larsen Ice Shelf which have recently experienced unexplained and very rapid retreat. Geologic applications include large scale mapping of faults, volcanic features, and studies of mountain building processes (particularly the Transantarctic Mountains). Data are also expected to assist in the development and implementation of policies for managing the Antarctic environment (Jezek and Everett, 1995). Finally, there is simply the unprecedented opportunity to use these digital maps in studies of many previously unexplored areas of the Southern Continent.

Table 1

RADARSAT: THE ANTARCTIC MAPPING PROJECT
SCIENCE OPPORTUNITIES

GLACIOLOGY
* Ice sheet/stream flow regimes (fast glacier flow, relict
features, outlet glaciers)

* Stability of West Antarctic Ice Sheet (grounding lines, surface velocities)
* Ice sheet mass balance (calving rates, ice sheet margins, topography)
* Surface melt regimes

GEOLOGY
* Uplift of the Transantarctic Mountains (Fault and lineament mapping)
* History of subduction beneath the Antarctic Peninsula
* Geologic mapping (Sirius Formation)
* Vulcanology

GEOMORPHOLOGY
History of glaciation (moraines, raised beaches)

ENVIRONMENTAL MONITORING
* Fuel spills
* Camp and airstrip construction

Figure 3. This JERS-1 scene of Ross Island, Antarctica (center) illustrates the kind of imagery that will be incorporated into the RADARSAT digital mosaic. Shear lines appear diagonally across the Ross Ice Shelf (lower right). The bright finger of ice (left center) extending from Ross Island is the Erebus Ice Tongue. McMurdo Station is located on the tip of Hut Point Peninsula (left center). The bright patch of intersecting lines just to the lower right of McMurdo Station is the Williams Field airstrip.

IV. References

1. Jezek, K.C., and F.D. Carsey, 1993. RADARSAT: The Antarctic Mapping Project. Byrd Polar Research Center Report no. 6, 24p .

2. Jezek, K.C., and L. Everett, 1995. Managing the Antarctic Environment: From Observations to Policy. Byrd Polar Research Center Report no. 12, 42 p.

The McMurdo Ground Station (MGS): Ready for SAR Acquisition

Carl Wales
Director, Alaska SAR Facility
Geophysical Institute
P.O. Box 757320, University of Alaska Fairbanks
Fairbanks, AK 99775-7320
phone (907) 474-7848; fax (907) 474-5567
cwales@iias.images.alaska.edu

Abstract.—The McMurdo Ground Station (MGS), a satellite receiving facility on Ross Island, Antarctica, was installed in December 1994 by the Ground Networks Division of NASA in concert with the Office of Polar Programs of NSF. Its original purpose was to acquire synthetic aperture radar (SAR) data from the Canadian RADARSAT spacecraft, which was launched in November 1995. To test the system, SAR data from the European ERS-1 spacecraft was successfully acquired by MGS in January 1995 and processed at the Alaska SAR Facility (ASF). The role of the MGS has expanded to include other SAR missions, and its first major role is to support the ERS-1 and ERS-2 tandem mission. The tandem mission should collect three complete coverages of the McMurdo mask during the first half of 1996. In late spring MGS will start receiving and recording SAR data from RADARSAT. Data recorded in summer is expected to be shipped every two weeks; all winter data will be shipped on the first flight out in the spring. Electronic transfer of the data out of the Antarctic is desirable, but the large quantity of data—as much as 30–40 GBytes per day—makes this a challenge. Efforts to develop such a capability continue.

INTRODUCTION

In 1990 the need for a ground station to receive synthetic aperture radar (SAR) data from satellites at a high southern latitude was recognized. SAR satellites were scheduled to come on-line soon. Some of those planned did not have on-board recorders sufficient to accommodate storage of SAR data collected over Antarctica. Therefore, it was decided to collect Antarctic data on the continent via a direct downlink. To cover a large portion of the Antarctic, a station at McMurdo was proposed. In December of 1994 NASA-Wallops and NSF staff, aided by contractors, installed a receiving facility at McMurdo Station on Ross Island, Antarctica (77.8°S, 166.7°E) for reception of data streams from satellites; it is called the McMurdo Ground Station (MGS).

While the primary interest initially was in having a receiving site for the Canadian RADARSAT spacecraft, the first satellite data received was for test purposes from ERS-1. The test data was successfully received and processed in early 1995. ERS-1 and ERS-2 reception for research purposes has commenced. RADARSAT data will be received after the completion of the spacecraft's commissioning phase. All of these spacecraft have data rates in the 100 megabits per second (Mbs) range.
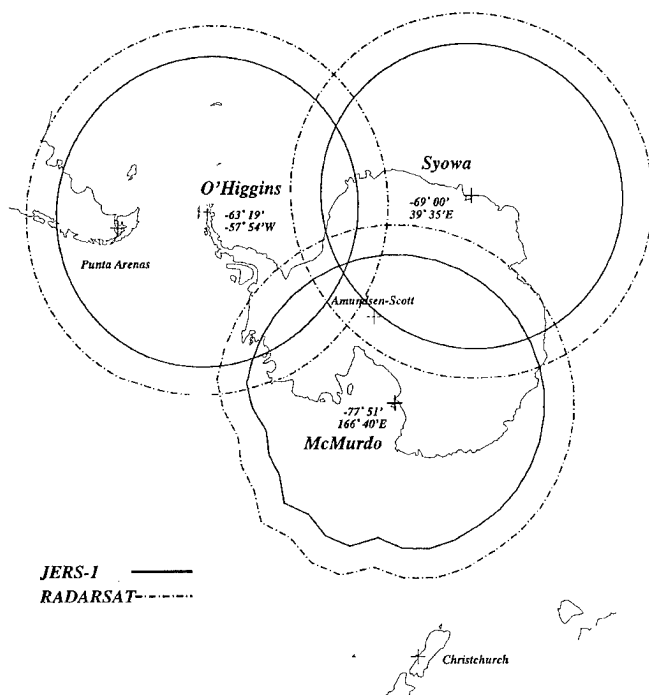
Fig.1. Antarctic receiving stations.
Graphic by John Crawford, JPL.

The SAR reception at MGS will mean that real-time down-link data from SAR satellites is now possible for all of Antarctica, as shown in Fig.1, because of the coverage afforded by three receiving stations: one at O'Higgins Station on King Island, operated by the University of Chile, Santiago, for the Deutsche Forschungsanstalt für Luft und Raumfahrt (DLR); one operated by the Japanese National Institute for Polar Research at Syowa; and MGS. Only MGS will be operational for 12 months per year, but depending on the success of a satellite data link, austral winter data may of

necessity be stored at McMurdo until it can be removed in spring, according to current data-handling capabilities. The SAR signal data is stored on Ampex DCRSi cassettes which will be flown to the Alaska SAR Facility (ASF) where they will be processed into images and distributed to approved users[1].

In 1992, NASA and NSF agreed that it would be beneficial and feasible to construct a ground station capable of receiving satellite SAR and other high data rate signals at NSF's McMurdo Station in Antarctica. These discussions led to a Memorandum of Agreement (MOA) between NSF and NASA for spacecraft tracking and data acquisition there. The MOA stipulates the shared responsibilities for the installation and operation of the MGS. NASA Wallops Flight Facility, with the assistance of the NSF, installed the ground station and radome during the 1994/95 Antarctic summer season (October 1994–February 1995).

DESCRIPTION OF THE MCMURDO GROUND STATION

The McMurdo Ground Station consists of the antenna site, located on a hilltop 2 km north of McMurdo; a control room, located in the Crary Science and Engineering Center (CSEC) in central McMurdo Station; and a boresight antenna verification system, located on Observation Hill. The antenna site includes a 10 meter autotracking antenna system (see Fig.2), housed in a radome (see Fig.3); and a control building which contains the receiving equipment, a local control computer system, and three High Density Data Recorders (HDDRs) capable of recording serial data at rates up to 107 Mbps. The antenna system receives downlink telemetry and can autotrack signals in either S-Band or X-Band. Acquisition is usually done with S-Band and autotracked in X-Band once tracking consistency is established.

The control room is connected to the antenna site via fiber optic lines. The Crary facility is designed as the operations center; access to the antenna site is required only occasionally.

The HDDRs are used to record two copies of every downlink (one as a back-up). The primary copy is shipped and the back-up copy held until receipt of an acknowledgment and readability of the prime copy. The Data Quality Monitor is an on-site determination of the quality of the data being recorded. Given that tape shipment may have to wait through an entire winter season, assurance that good data is being recorded is important.

The CSEC control room includes a computer control system, three HDDRs, a Data Quality Monitor system, and a Store and Forward system.

---

[1]*ERS-1, ERS-2, and RADARSAT data handled by the Alaska SAR Facility can be distributed only to approved Users. To initiate the process of becoming an approved User contact ASF User Services at uso@eosims.asf.alaska.edu.*
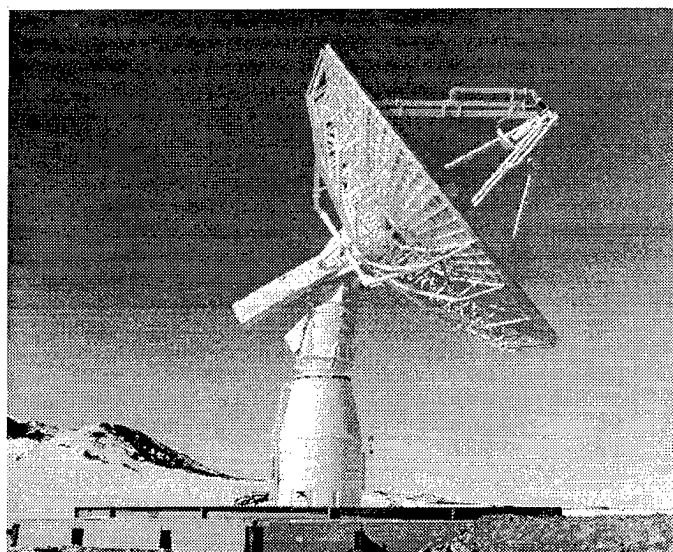
Fig.2. 10 meter antenna at McMurdo Station, before installation of radome.
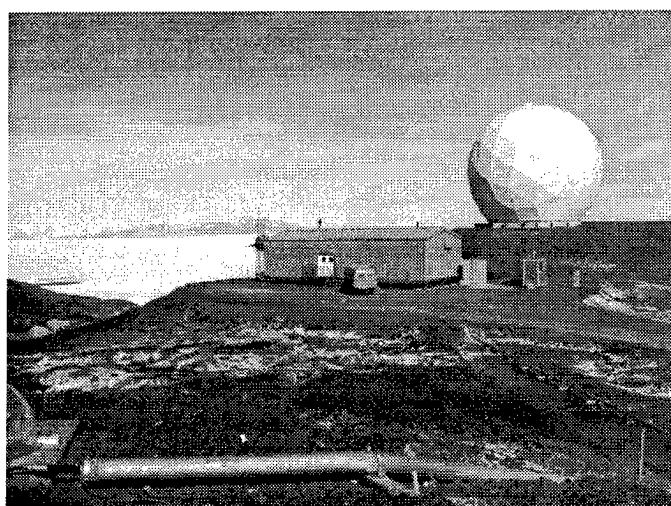
Fig.3. Radome at McMurdo Station. Photo by Frank Carsey.

RADAR DATA

NSF and NASA plan to operate MGS on a 24-hour availability basis. In operation MGS is expected to receive, record, and send (to ASF) SAR signal data from ERS-1 and ERS-2, and RADARSAT. The acquisition of ERS-1 and ERS-2 data is particularly interesting as the two satellites are currently flying in the same orbit in a 1-day separation so that radar interferometry for topography and change studies will be possible. RADARSAT data reception is anticipated by late spring after the usual satellite commissioning period.

SCHEDULING

ASF will provide the scheduling for the SAR acquisitions at MGS. ASF, as the prime contact with other national space agencies for SAR remote sensing, will establish spacecraft instrument schedules for user data requests such that any conflicts with other MGS activities are reconciled.

FUTURE

The MGS has a bright future to provide a wide range of data acquisition and spacecraft tracking services, owing largely to its high latitude location.

Clearly, the present system of mailing data cassettes to Fairbanks after being flown from McMurdo to New Zealand is only one approach to data transfer; it was selected because electronic transfer for the anticipated data acquisition schedule would be a significant expense.

The McMurdo Ground Station is functioning and seems to be a very satisfactory source of data. It stands as a good example of interagency collaboration.

Calibration of Data From the Antarctic Mapping Mission

Jason Williams

Alaska SAR Facility, Geophysical Institute, University of Alaska
P.O. Box 757320, Fairbanks, AK, 99775-7320
phone (907) 474-6715, FAX (907) 474-5567
jason@conan.gi.alaska.edu

Abstract — In October of 1996 the RADARSAT SAR will acquire high resolution C-band radar data over the entirety of Antarctica. The mission will last for a period of about 18 days, during which 12 hours of data or approximately 3300 SAR images will be acquired. A substantial effort will be undertaken at the Alaska SAR Facility to ensure that all downlinked data is successfully acquired. To support calibration of the dataset, two transponders have been built and deployed in Antarctica. These transponders, together with other calibration targets in Alaska, Canada and Brazil will be used to calibrate the data.

INTRODUCTION

The RADARSAT Antarctic Mapping Mission (AMM) represents the first effort to generate a high resolution radar map over 100% of Antarctica from space. RADARSAT, a Canadian satellite launched in November 1995, carries a single-polarization right-looking SAR. In October of 1996 the spacecraft will be turned around in orbit to produce a left-looking SAR which, through use of the RADARSAT programmable beams, will image the entire Antarctic landmass.

Over a period of 18 days, roughly 12 hours of SAR data, representing over 3600 100 x 100 km scenes will be acquired. The data from the SAR will be recorded on tape and downlinked to the Alaska SAR Facility (ASF) in Fairbanks, Alaska, and to the Gatineau and Prince Albert stations in Canada. The data downlinked at the Canadian stations will be shipped to Alaska via courier.

All of the AMM data will be calibrated and processed at ASF. This data will then be provided to the staff at the Byrd Polar Research Institute at the Ohio State University, where the RADARSAT Antarctic Mapping System will be used to synthesize the actual digital mosaic. The mosaic is expected to be an important dataset in the fields of Glaciology, Geology and Geomorphology in Antarctica.

All spaceborne SARs have orbital inclinations of 97° to 98°, with sensors looking sideways on the north side of the satellite track. For this reason, there is a large region around the south pole where no data has ever been acquired. To accomplish the mapping, the RADARSAT spacecraft will actually rotate around to point the SAR antenna in the south-looking mode.

VALIDATION OF DATA DURING THE AMM

During the 18-day mission, it is critical that any lost data be re-acquired while in the south-looking mode if possible. For this reason an extensive validation will be performed on all data at ASF. The data will be scanned to produce detailed scan results files. These files outline the location and quality of the data. The files will be analyzed for any sensor problems and forwarded to Ohio State to verify that the correct coverage was obtained. Selected scenes around the perimeter of the continent will be Quick Look processed to verify overlapping coverage. All mapping data is expected to be scanned within 36 hours of arrival at ASF.

CALIBRATION OF ASF DATA

Calibration requirements for AMM data processed at ASF can be inferred from the science requirements [1] placed on the output map. The quality of the output map is dependent upon both the quality of the SAR images produced by ASF and the RAMS resampling algorithms. Without proper calibration, synthesis of the map becomes difficult, and some kinds of quantitative analysis would be impossible with the map.

TABLE I
CALIBRATION REQUIREMENTS FOR THE ANTARCTIC MAP

Georeferencing	±300 m
Distortion	±50 m in 100 km
Absolute Radiometric	±2 dB
Relative Radiometric	±1 dB

The Alaska SAR Facility is an end-to-end system of data reception, archive, processing and distribution. The SAR Processing System consists of multiple SAR processors, a central controller and the Product Verification Subsystem. The Product Verification Subsystem generates a calibration parameter file for each RADARSAT beam mode, which is in turn used by the SAR processors to process calibrated data.

The calibration parameter files are created after analysis of a sufficient number of images to achieve the desired accuracy. Images analyzed consist of two target types: point targets such as corner reflectors, and distributed targets such as the Amazon tropical rainforest. Point targets are used to verify

geometric and radiometric quality and to set the absolute and relative radiometric calibrations. Distributed targets are used mainly to verify the in-flight antenna patterns of the instrument.

The primary concern with calibration of AMM data is with the SAR antenna itself. The sun will be striking the side of the antenna which is normally always in shade. This, coupled with the maneuver itself, could result in slight physical deformation of the antenna. If not properly compensated for in the processor, this could introduce significant errors into the dataset. Therefore, the antenna patterns will be verified immediately following the attitude change to the left-looking configuration. This verification will be accomplished by imaging selected sites in the Amazon basin where the normalized radar cross section profile is well characterized. Measurements made at various points in the antenna pattern using precision transponders provide a second method of verifying the antenna patterns.

AMM TRANSPONDERS

The Environmental Research Institute of Michigan (ERIM) built and deployed two active transponders to support the AMM. The transponder characteristics [2] are presented in Table II. Location of these transponders in Antarctica helps to tie down sensor calibration and orbit determination in the southernmost portion of the orbit. A total of approximately 120 images will be acquired over these two devices.

TABLE II
DESIGN CHARACTERISTICS FOR THE ERIM AMM
TRANSPONDERS

Frequency	5.3 GHz
Antenna Type	Planar Cavity-Backed Spiral
Antenna Polarization	Circular
RF Bandwidth	300 MHz
Incidence Angle Range	0° to 60°
RCS Stability	±0.5 dB
RCS Accuracy	±1 dB
Operating Temperature	-60°C to +50°C
External Power	115 VAC @ 3A

Current plans for the acquisition of the map call for the use of beams Standard 1 through Standard 7 and Extended-High 4. Together, these beams represent an incidence angle range from 20° to 57°. To support long periods of unattended operation, the ERIM transponders were designed using wide beamwidth antennas which eliminated the need to align the transponder with the SAR antenna. The calibration requirements for these devices are met using look-up tables for temperature correction and transponder antenna pattern.

One transponder is located at McMurdo station, the other at the south pole station. Initial testing has been done with ERS-1 and ERS-2, and will be extended to RADARSAT once the spacecraft is deemed operational. The McMurdo transponder will be operated year around to support the McMurdo receiving ground station. The transponder at the south pole station will only be operated in support of the AMM.

In addition to the ERIM transponders, the Canadian Space Agency has agreed to provide use of their four precision transponders. These devices provide relative and absolute accuracies of ±0.15 and ±0.25 dB respectively [3]. There is also an array of eleven 2.4 m corner reflectors located in Alaska which provide relative and absolute accuracies of ±0.4 dB and ±1.2 dB respectively [4]. Two more ERIM-built transponders may be deployed in Alaska by the time the mapping occurs.

Due to restrictions on tape recorder use, the datatakes over the two transponders in Antarctica will be downlinked directly to the McMurdo ground station. Logistical problems prevent full validation of those datatakes until long after the AMM. To guarantee a successful mapping, datatakes scheduled over calibration devices in Canada and Alaska will be sufficient to perform the calibration even if all the Antarctic transponder datatakes are lost.

Fig. 1. One of the ERIM transponders deployed for testing at McMurdo. Photo by Kenneth Jezek.

REPORTING OF RESULTS

Following the 18-day mission, a brief report summarizing the passes acquired, any passes lost and data quality for the dataset will be produced. After the entire AMM dataset has been analyzed and calibrated, a report will be published summarizing the results. Analysis of the output map will be performed to ensure that the radiometric calibration was preserved.

REFERENCES

[1] Kenneth C. Jezek, "RADARSAT: The Antarctic Mapping Project," NASA Pathfinder Proposal NRA-94-MTPE-06, March 1995.

[2] Robert G. Onstott, "ERIM Active Radar Calibrator for RADARSAT and ERS-1 SAR," ERIM Proposal ERIM-606265, November 1995.

[3] Hawkins, R.K. et al, "External Calibration Transponders for RADARSAT," Proceedings of the SAR Calibration Workshop, University of Michigan, Ann Arbor, Michigan, September 1994.

[4] Freeman, A., "SIR-C Ground Calibration Plan," JPL D-6999, Jet Propulsion Laboratory, Pasadena, CA, February 1990.

A Robust Threshold Retracking Algorithm
for Extracting Ice-Sheet Surface Elevations from
Satellite Radar Altimeters

Curt H. Davis
Electrical & Computer Engineering
University of Missouri - Columbia/Kansas City
5100 Rockhill Road
Kansas City, MO 64110 USA
T: 816/235-1276 F: 816/235-1260 Email: curt@polar.cuep.umkc.edu

ABSTRACT: A threshold retracking algorithm for processing ice-sheet altimeter data is presented. We performed extensive comparisons between the threshold algorithm and three other ice-sheet retracking algorithms. The algorithm comparisons were made using Seasat and Geosat datasets comprised of over 30,000 crossover points. Our results show that the threshold retracking algorithm produces ice-sheet surface elevations that are more repeatable than the elevations derived from all the other retracking algorithms. For analysis of long-term change in ice-sheet surface elevations, it is critical that a retracking algorithm produce repeatable elevations. The more consistent an algorithm is in selecting the retracking point the less likely that biases will be introduced by the retracking scheme in the elevation change measurement. For this reason, the robust threshold retracking algorithm has been adopted by NASA/GSFC as an alternative to their existing algorithm for production of ice-sheet altimeter datasets under the NASA Pathfinder program. The threshold algorithm will be used to re-process existing ice-sheet altimeter datasets and to process the datasets from future altimeter missions.

INTRODUCTION

All altimeter data over the ice sheets must be post-processed to produce accurate surface elevation measurements. This post-processing is called "retracking" and is required because the leading edge of the ice-sheet return "waveform" deviates from the on-board altimeter tracking gate, causing an error in the telemetered range measurement. A return "waveform" is the received power sampled at the satellite and results from the interaction of the altimeter's transmitted pulse with the scattering surface or volume directly beneath the altimeter. Retracking altimetry data is done by computing the departure of the waveform's leading edge from the altimeter tracking gate and correcting the satellite range measurement (and surface elevation) accordingly. Fig. 1 illustrates this concept.

Martin *et al.* [1] developed the first retracking algorithm for processing altimeter waveforms from the continental ice sheets. This algorithm, hereafter referred to as the NASA

algorithm, was used by Zwally *et al.* [2] to measure the growth of the Greenland ice sheet. The NASA algorithm fits a 5 or 9 parameter function to return waveforms that is based upon Brown's surface scattering model [3]. The European Space Agency (ESA) uses an empirical Offset Center of Gravity (OCOG) technique to produce ice-sheet data products from the ERS-1/2 satellites [4]. The ESA algorithm computes a rectangular box with the same area as the altimeter waveform. The ESA retracking point is determined using a threshold crossing of 25% of the rectangle's amplitude. Davis [5] developed the S/V retracking algorithm using a model based upon a combination of surface and volume scattering. This was the first retracking algorithm to include a volume scattering term to describe ice-sheet altimeter waveforms.
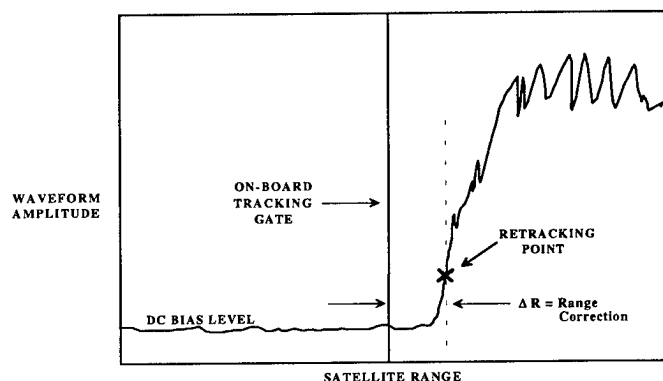
Figure 1. Typical ice-sheet altimeter waveform illustrating the retracking correction, ΔR, that must be applied to correct for deviation of the waveform's leading edge from the on-board altimeter tracking gate.

Given the wide variety of retracking algorithms available for processing ice-sheet data, it is a daunting task for data users who are not well versed in the fundamentals of altimetry to select from these various methods. All the algorithms have their own unique advantages and disadvantages, and it is generally accepted that no single algorithm can meet the diverse needs of all ice-sheet altimetry data users. Recently, by comparing the

repeatability of surface elevations from the various retracking algorithms, Davis [6] demonstrated that the NASA algorithm introduced significantly larger errors into the ice-sheet elevations than the other three algorithms used in the study. In addition, the NASA algorithm was shown to produce ice-sheet growth estimates that were 30-55% larger than the other three algorithms, which all produced nearly identical results.

Another important result from this study was that a simple thresholding scheme could perform as well or better than all the other retracking algorithms from a repeatability standpoint. In attempting to measure ice-sheet elevation change it is extremely important to use an algorithm that is consistent in its selection of the waveform retracking point. The more consistent an algorithm is in selecting the retracking point the less likely that biases will be introduced by the retracking scheme in the elevation change measurement.

THRESHOLD RETRACKING ALGORITHM

In this section we develop a threshold retracking scheme that is primarily intended for use in measuring ice sheet elevation change. It is therefore important to ensure that the algorithm produces consistent elevation measurements, and this will be addressed in the following section.

For basic threshold retracking, the position on the leading edge of the return waveform is found by locating the first range bin to exceed a percentage of the maximum waveform amplitude. For Seasat and Geosat altimeter data this is complicated by the fact that a DC bias exists in the range bins preceding the location of the actual return waveform (see Fig. 1). The magnitude of the DC bias is different for the two satellites and is also known to vary with location and time in a given satellite dataset. These variations cause the leading-edge retracking point to vary considerably if the threshold level is referenced only to the maximum waveform amplitude. To overcome this problem, the threshold retracking scheme adopted here is referenced to a percentage of the maximum waveform amplitude above the pre-leading edge DC level. Fig. 2 illustrates this concept.

The mathematical formulation of the threshold algorithm is very straightforward. Let the array of waveform data samples be WD_n, where n is the range gate number (e.g. 0-59 for Seasat/Geosat data). First, the maximum amplitude of the waveform data array, A_{max}, is found, where

$$A_{max} = max(WD_n). \qquad (1)$$

Next, an estimate of the pre-leading edge DC level is obtained. This estimate is computed using the first five unaliased waveform samples

$$DC = \frac{1}{5} \sum_{n=\tilde{n}}^{\tilde{n}+4} WD_n, \qquad (2)$$
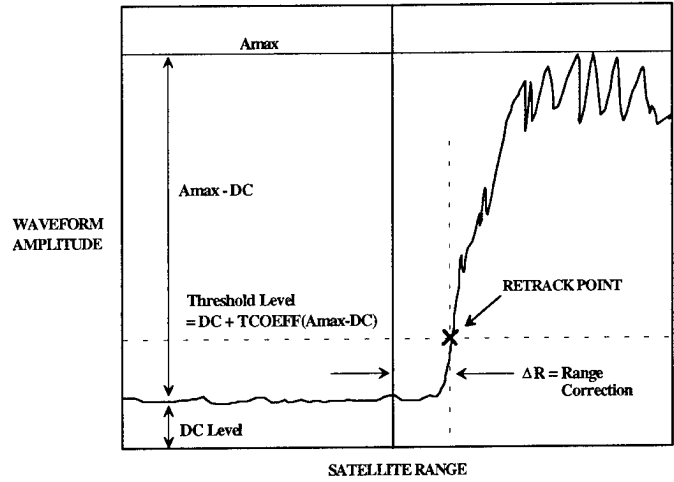
Figure 2. Ice-sheet altimeter waveform illustrating the threshold retracking method. Note that the threshold level is referenced to a percentage of the maximum waveform amplitude above the pre-leading edge DC level.

where $\tilde{n}$ is the location of the first unaliased waveform sample. For Seasat and Geosat data there are no aliased waveform samples, consequently $\tilde{n} = 0$. However, for ERS-1/2 data, the first 4 to 6 waveform samples (approximately) contain aliased amplitudes that should not be used in the estimation of the DC level. It should be pointed out that, unlike Seasat/Geosat data, the DC level in ERS-1/2 data is very small and believed to be, for the most part, inconsequential in its effect on the variability of the threshold retracking level. However, the DC level estimation is included for the ERS data to ensure that the retracking scheme is consistent for all the satellite datasets. Once the DC level estimate is obtained, the threshold level is then set to be

$$TL = DC + T_{COEFF} (A_{max} - DC), \qquad (3)$$

where T_{COEFF} is the percentage of the maximum waveform amplitude above the DC level. In order to provide greater precision, the retracking location on the leading edge of the waveform, n_{ret}, is linearly interpolated between the bins adjacent to the threshold crossing using

$$n_{ret} = (\hat{n} - 1) + \frac{TL - WD_{\hat{n}-1}}{WD_{\hat{n}} - WD_{\hat{n}-1}}, \qquad (4)$$

where $\hat{n}$ is the location of the first gate to exceed the threshold level. Note that the second term in (4) can become undefined when $WD_{\hat{n}} = WD_{\hat{n}-1}$, and in this case the retracking location is set equal to the first term, $n_{ret} = \hat{n} - 1$. Finally, the correction to the telemetered altimeter range measurement (and surface elevation) is given by

$$\Delta R = G_{2m} (n_{ret} - n_{tr}) \text{ (m)}. \qquad (5)$$

where n_{tr} is the on-board altimeter tracking gate (see Fig. 1) and G_{2m} is the conversion factor from gates to meters. For Seasat and Geosat, $n_{tr} = 29.5$ and $G_{2m} = 0.4684375$ m/gate.

THRESHOLD LEVELS

Because of the wide range of applications for ice-sheet altimetry data, several different threshold levels are used to retrack the altimeter waveforms and generate the corresponding range/elevation corrections. Advantages and disadvantages for each of the threshold levels are discussed to help the user identify the correction that is best suited for their specific application.

10% Level

As mentioned before, the threshold retracking algorithm was primarily developed for measuring ice-sheet elevation **change** using altimeter crossover datasets. Crossover datasets are comprised of the altimeter waveforms immediately adjacent to sub-satellite crossing points of successive altimeter orbits. The more consistent an algorithm is in selecting the retracking point, the less likely that biases will be introduced by the retracking scheme in the elevation change measurement.

In order to determine the optimum threshold level for elevation change detection, we created three different crossover datasets: Seasat x Seasat (SxS), Geosat-GM x Geosat GM (GM x GM), and Geosat-ERM x Geosat-ERM (ERMxERM). Each of the datasets contained crossovers where the time difference between the successive altimeter orbits was less than 30 days. The standard deviation (SD) of the elevation differences for these datasets is used as a measure of the algorithm's repeatability or consistency. For each of the datasets, the SD was computed for threshold levels from 5 to 25 %. Fig. 3 shows a plot of the SD vs. threshold level for the SxS dataset.

We see from the plot that the smallest SD's occur for threshold levels from 8 to 13% for this dataset. In evaluating all the datasets, the 10% threshold level was found to consistently produce the lowest SD values. The 10% level produces low SD values because it is not affected by a) the noisy nature of the higher amplitude waveform values and b) the wide variety of complex waveform shapes that are typical of ice sheet waveforms. The repeatability of the threshold algorithm steadily worsens as the level is increased above the 10% mark for these very reasons.

Once the optimum threshold level was determined for elevation change analysis, we then compared the performance of the threshold retracking algorithm with the other ice-sheet retracking algorithms. The SD's of the various retracking algorithms were computed for each of the datasets described above, and these results are summarized in
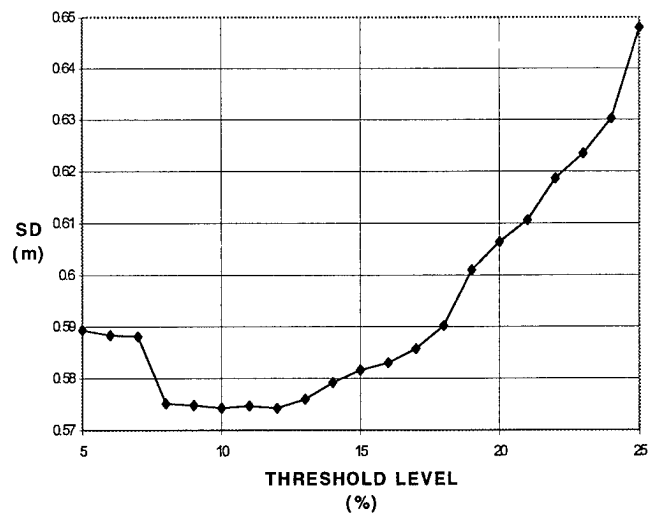
Figure 3. Standard deviation vs. threshold level % for the Seasat x Seasat crossover dataset.

Table I. The results show that the NASA algorithm produces significantly larger SD's than the ESA, S/V, or 10% threshold algorithms. This was shown by Davis [6] to be caused by a mixing of the 5 and 9 parameter functional forms of the NASA algorithm. The SD's of the 10% threshold level are the lowest in all three datasets, indicating that this algorithm is more consistent than any of the other retracking algorithms. Thus, the 10% threshold algorithm is best suited for obtaining reliable estimates of ice-sheet elevation change.

Table I. Retracking Algorithm SD Comparison

Algorithm	Seasat x Seasat σ_{SxS} (m)	GMxGM σ_{GxG} (m)	ERMxERM σ_{GxG} (m)
NASA	0.77	0.81	1.27
ESA	0.58	0.51	1.21
S/V	0.59	0.51	1.22
10% Thresh.	0.57	0.45	1.13
# of Xovers	1,022.00	27,184	5,479

20% Level

Over the continental ice sheets, it is widely accepted that variations in the scattering properties of the surface and near-surface snow affect the shape of the altimeter return waveform. This has important implications for proper selection of the retracking point when the primary motivation is to obtain accurate estimates of the true ice-sheet elevation. If a waveform is completely dominated by surface scattering, the half-power point (50%) best represents the mean surface elevation within the altimeter's pulse limited footprint. As

the strength of the surface scattering return is reduced, the importance of the sub-surface volume scattered return is increased. This, in turn, causes the location of the mean-surface retracking point to decrease from 50% as the volume-scattered signal begins to increasingly dominate the waveform shape.

The relative importance of the volume-scattered return depends upon the depth that the altimeter's incident pulse penetrates the surface of the ice sheet. The depth of penetration, d_p, is determined by physical properties of the ice-sheet surface and near-surface snow like snow wetness, grain size, and density. Studies have shown that over the Greenland ice sheet d_p can vary anywhere from 0 to 10 m. Over the vast majority of the Antarctic ice sheet the depth of penetration varies from 5 to 10 m. The larger variation of d_p in Greenland is due to extensive surface melting that takes place in the lower elevations and latitudes of the ice sheet during the summer. Water is an excellent reflector and absorber of electromagnetic energy, and its presence prevents the altimeter energy from significantly penetrating the surface. In addition, surface melting and refreezing will cause ice layers and ice lenses to form, both of which will tend to concentrate the scattering near the ice-sheet surface, thereby reducing signal penetration. The surface conditions of the Antarctic ice sheet are typically much colder and drier than the Greenland ice sheet, so consequently the variation in d_p is less.

It should be pointed out that, in general, altimeter-derived profiles of a sloping ice-sheet surface will always overestimate the true elevation along the profile because of the wide antenna beamwidths of radar altimeters. This is why slope corrections must be applied to the altimeter elevations when absolute measurement of the surface elevation is required. For the purpose of the following discussion on the affect of the threshold level for measuring absolute ice-sheet elevation, we will assume that valid slope corrections have already been applied to the altimeter data.

For absolute measurement of ice-sheet elevation, the 10% level will overestimate the true elevation over areas of the ice sheet where surface scattering or combinations of surface and volume scattering determine the altimeter waveform shape. The 10% level would only be appropriate in instances where the altimeter data were in a region of the ice sheet known to be completely dominated by volume scattering, e.g. the higher latitude and higher elevation areas of the interior portion of the ice sheet. The majority of the Greenland ice sheet, south of 72° N, experiences combinations of surface and volume scattering so the 10% level would not be a very good choice for a large amount of this data. Following the same arguments, the 50% threshold level will underestimate the true elevation for the most of the Greenland ice sheet and would only be appropriate in areas where surface scattering dominated the return signal. When surface scattering dominates (no signal penetration), the 10% level can

overestimate the true elevation by 0.5 to 1.5 m (typically), and this depends primarily on surface roughness. When volume scattering dominates, the 50% level can underestimate the true elevation by 1 to 3 m (typically).

Corrections based upon a 20% threshold level are included for use in areas of the ice sheet where combinations of surface and volume scattering contribute to the shape of the altimeter waveforms. This represents a compromise between the extreme cases of waveforms solely dominated by either surface or volume scattering, and is suitable for obtaining a first-order estimate of the true surface elevation for the majority of Greenland ice sheet data. In addition, one study using averaged waveform data from a portion of the East Antarctic plateau concluded that a retracking point very similar to the 20% threshold level closely corresponded to the mean ice-sheet elevation in this area. It should be pointed out that the 20% retracking point provides a reasonable estimate of the true ice-sheet elevation in only an average sense. This is true because the shape of individual altimeter waveforms can and will differ significantly from a regional average for a variety of reasons. However, this approach is a reasonable first-order solution to this complex problem.

50% Level

As discussed in the previous section, when the shape of an altimeter waveform is dominated by surface scattering the half-power point represents the mean surface elevation within the altimeter's pulse limited footprint. Thus, retracking corrections are provided using a 50% threshold level to give reasonable estimates of the absolute elevation for this case. Examples of areas where the 50% level would be appropriate include many of the ice shelves in Antarctica as well as the southern dome region of the Greenland ice sheet. Both of these areas are known to experience periodic melting and refreezing in the summer season. The melting/refreezing enhances snow-grain size and produces ice layers and lenses, all of which tend to concentrate the scattering from the ice-sheet surface or near surface.

It should again be pointed out that the vast majority of ice-sheet altimeter waveforms exhibit a combination of surface and volume scattering. Consequently, the use of the 50% threshold level over large areas of the ice sheets is discouraged. As mentioned in the previous section, the 50% level can underestimate the true elevation by up to 3 m when used in areas of the ice sheet where surface scattering does not dominate.

For elevation change measurements, the use of the 50% threshold level is also discouraged for the reasons discussed previously, namely the inherently noisy nature of the higher amplitude waveform values. The repeatability of the 50% retracking point is severely compromised by the waveform noise. The 10% or 20% levels are much more consistent in

the retracking point selection, with the 10% level being the most repeatable.

THRESHOLD LEVEL ELEVATION DIFFERENCES

It is useful to provide some insight into the magnitude of the elevation differences resulting from selection of the different threshold levels. Because of the wide variety of ice-sheet altimeter waveform shapes only approximate ranges for the elevation differences can be given. In general, as the width of the leading edge of the altimeter waveform increases the magnitude of the elevation difference between the different threshold levels will also increase. Factors like surface roughness, surface geometry, and the amount of sub-surface signal penetration all can affect the waveform's leading-edge width.

Differences on the order of 0.1-0.9 m between the 10% and 20% threshold levels can be expected, and in isolated instances this can approach 2 or 3 m. The 20% level will produce larger satellite range values and therefore lower surface elevations with respect to the 10% level. Differences of 0.5-4.5 m between the 10% and 50% threshold level are typical, and in some cases this can be as high as 6 or 7 m. Obviously the 50% level will also produce lower surface elevations with respect to the 10% level. These typical values were found by comparing the different threshold levels on approximately 885,000 altimeter waveforms from the Greenland ice sheet. The statistics from this comparison are summarized in Table II, and it should be noted that the distribution of the differences are approximately Rayleigh. The approximate ranges for the threshold level differences were found using the 10 to 90% range in their cumulative distribution functions (CDF).

Table II. Statistics for Threshold Level Differences

Threshold Level Differences	Mean (m)	St. Dev. (m)	10%-90% CDF Range (m)
20%-10%	0.50	0.60	0.10 - 0.90
50%-10%	2.50	1.97	0.50 - 4.65
50%-20%	2.00	1.65	0.35 - 3.85

CONCLUSIONS

A threshold retracking algorithm for processing ice-sheet altimeter waveforms was presented. The primary application of the threshold algorithm is for measuring ice-sheet elevation change. The 10% threshold level was shown to produce the most repeatable elevation estimates when compared to three other ice-sheet retracking algorithms. This is the first time an ice-sheet retracking algorithm has been

developed specifically for measurement of ice-sheet elevation change.

The 20% and 50% threshold levels are provided as alternative retracking points. These levels are intended for users interested in obtaining realistic estimates of the absolute ice-sheet elevation. The 20% level is appropriate when combinations of surface and volume scattering are expected, while the 50% level is appropriate only when surface scattering dominates the return waveform shape.

The threshold retracking algorithm has been adopted by NASA/GSFC as an alternative method to their existing retracking scheme. Range/elevation corrections for all three threshold levels will be made available on the ice-sheet altimeter datasets. The threshold algorithm will be used for reprocessing existing Seasat and Geosat datasets, as well as the processing of new datasets from the ERS-1/2 and GFO satellites. The new datasets are being produced under the NASA Pathfinder program, whose purpose is to provide research quality datasets for the study of global change.

REFERENCES

[1] Martin, T.V., H.J. Zwally, A.C. Brenner, and R.A. Bindschadler (1983), "Analysis and retracking of continental ice sheet radar altimeter waveforms," *J. Geophys. Res.*, Vol. 88, pp. 1608-1616.

[2] Zwally, H.J., A.C. Brenner, J.A. Major, R.A. Bindschadler, and J.G. Marsh (1989), "Growth of Greenland ice sheet: measurement," *Science*, Vol. 246, pp. 1587-1589.

[3] Brown, G.S. (1977), "The average impulse response of a rough surface and its applications," *IEEE Trans. Antennas & Propagation*, Vol. 25, pp. 67-74.

[4] Wingham, D.J., C.G. Rapley, and H. Griffiths (1986), "New techniques in satellite altimeter tracking systems," *IGARSS '86 Symposium Digest*, Vol. 1, pp. 185-190, Zurich, Switzerland, 8-11 Sept 1986.

[5] Davis, C.H. (1993), "A surface and volume scattering retracking algorithm for ice sheet satellite altimetry," *IEEE Trans. on Geoscience & Remote Sensing*, Vol. 31, No. 4, pp. 811-818.

[6] Davis, C.H. (1995), "Growth of the Greenland ice sheet: a performance assessment of altimeter retracking algorithms," *IEEE Transactions on Geoscience & Remote Sensing*, Vol. 33, No. 5, pp. 1108-1116.

Individual Weather Correction for Antarctic Sea-Ice Concentrations from SSM/I

Christian H. Thomas, Georg C. Heygster
Institute of Environmental Physics, University of Bremen, 28334 Bremen, Germany
Tel.:+49 421 218-4726/Fax:-4555/E-mail: cthomas@diana.physik.uni-bremen.de

Abstract – Sea-ice concentration as determined from the brightness temperatures of passive microwave sensors is affected frequently by high values of atmospheric water vapour, cloud liquid water, rain and sea surface roughening by surface winds. A correction scheme for SSM/I taking these influences into account is presented. Over open water, water vapour, liquid water and wind determined from the SSM/I signal serve to reduce the brightness temperatures to clear sky conditions using a radiative transfer model. When applied to a sample scene, the procedure results in reduced mean value for sea-ice extent, sea-ice area and open water, but increased ice concentration.

INTRODUCTION

Measurements obtained from the SSM/I are suitable to explore sea-ice-concentration and ice extent. A problem in calculating the sea-ice covers has been the false indication of sea-ice over the ice free ocean and at the ice edge resulting from the presence of atmospheric water vapour, cloud liquid water, rain and sea surface roughening by surface winds.

Therefore a weather filter for SMMR NASA-Team algorithm based on spectral information of the 18 and 37 GHz channels has been previously developed but a similar filter for the SSM/I sensor [2] is less successful because the 19.35 GHz SSM/I channels are closer to the center of the 22.2 GHz atmospheric water vapour line [6].

Except for a few case studies completed during the development of the weather filters discussed above it is unknown to which extent they eliminate low ice concentrations in the Antarctic in different seasons. Also unconsidered are the weather effects on the ice-concentration calculation in the marginal ice zone (MIZ). Therefore the influence of the meteorological parameters over the ice free ocean and on the ice concentration of the MIZ is corrected by a new scheme based on the results of radiative transfer model calculations.

RADIATIVE TRANSFER CALCULATIONS

The brightness temperature (T_B) data were generated with a radiative transfer model developed by [7]. Model radiances are calculated for a multilayered plane parallel atmosphere using Eddington's second approximation to the equation of radiative transfer. The model includes the effects of single scattering from precipitating hydrometeors with the Mie calculation of the extinction coefficients being carried out assuming the Marshall-Palmer drop size distribution and that from [10] for the solid phase. Drops of cloud liquid water are assumed to
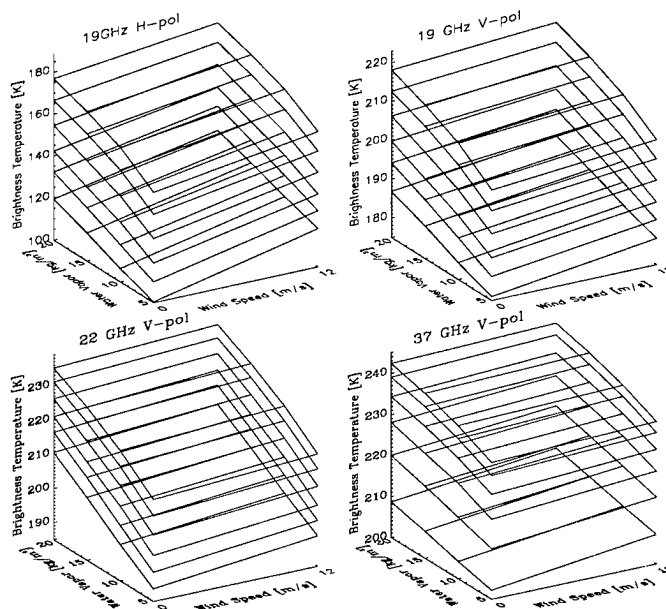
Figure 1: Model T_B for ice-free water. Each level represents a constant LWP content from 0 (lowest level) up to $0.5\,\text{kg/m}^2$ (highest level).

be too small to produce scattering at microwave frequencies so that only Rayleigh absorption is accounted for. Absorption coefficients for water vapour and atmospheric oxygen are also included in all levels; these are the sole contributors in levels not having cloud as well as in the clear sky case.

Model calculations produce top-of-atmosphere T_B for the geometry and frequency/polarization channels of the SSM/I instrument. Accuracies of 2–3 K in T_B (not including errors due to cloud effects) are expected with this model.

The temperature and emissivity of the surface (water and sea-ice types) was directly given. The variable surface emissivity through the sea surface roughening by surface wind was further taken into the algorithm. For this statistically and empirically computed wind induced emissivity changes the near surface wind algorithm by [4] were used. First radiative transfer computations were carried out over open water under clear sky conditions, and the algorithm was fitted until the results corresponded with the open water tie-points of [1].

The influence of integrated water vapour, liquid water path and wind on the T_B of the SSM/I channels was calculated. Fig. 1 shows three dimensional plots of the SSM/I channel T_B over open water dependent on the atmospheric parameters. Similar plots for T_B over 50 % sea-ice are presented in [6].

Coefficients describing the dependences of the T_B of the different channels were determined from multiple regression analysis.

The ice concentration fluctuations in the MIZ are greatest at ice concentrations below 50 %, above this value the high emissivity of the sea-ice is most dominant. Thus the fluctuations are low within the ice-pack.

ALGORITHMS FOR THE ATMOSPHERIC PARAMETERS

The amount of microwave energy being emitted from the ocean surface depends on the wave structure and foam coverage [13] which are, in turn, influenced by the ocean surface wind speed. Therefore by measuring the ocean surface microwave emission, the SSM/I is able to predict ocean surface wind speed. Microwave emission at the SSM/I frequencies which is coming from the ocean surface is effectively masked by the emission and attenuation characteristics of the rain and large amounts of water vapour in the atmosphere. Therefore different rain flags for different accurate wind speed retrievals are used [4]. The D-matrix wind speed retrieval algorithm developed by Environmental Research and Technology, Inc. has the following form [8]:

$$SW = C_0(j) + C_1(j)T_B(19H) + C_2(j)T_B(22V)$$
$$+ C_3(j)T_B(37V) + C_4(j)T_B(37H)$$

The wind speed SW is given in meters per second and refers to a hight of 19.5 meters above the surface. $C_i(j)$ are the D-matrix coefficients, where j is the climate code index given by [8]. The good performance of the validated wind speed algorithm by [4] is based on a climate code which contains different seasons and latitude zones.

In the SSM/I wavelength range, the radiometer signal is directly influenced by cloud and rain microphysical properties. The liquid water path (LWP) estimation is based on the emission of the cloud droplets over the radiometrically cold ocean surface. A retrieval algorithm by [5] was implemented and is defined as:

$$LWP = D_0 + D_1 T_B(19V) + D_2 \ln(280 - T_B(22V))$$
$$-D_3 \ln(280 - T_B(37V)) + D_4 \ln(280 - T_B(37H))$$

Values above $0.5 \, \text{kg/m}^2$ LWP are masked out since they are influenced by rain droplets [5, 12]. The arising data-gaps are filled by interpolation.

For the retrieval of water vapour an algorithm by [11] is used. This algorithm has also been derived using radiosonde measurements and radiative transfer calculations:

$$W = E_0 - E_1 T_B(22V) - E_2 T_B(37V)$$

LWP and W are given in kg/m^2.

IMPROVED ICE CONCENTRATION ALGORITHM

This correction scheme is useable only for SSM/I data, since the 21 GHz V-pol channel data of SMMR were noisy and therefore not included in the CD-ROM data. In order to provide a similar correction scheme for SMMR, the algorithms for liquid water path, water vapour and wind speed would have to be derived without using the 21 GHz channel.

Ice Concentration[%]

0   10   20   30   40   50   60   70   80   90   100
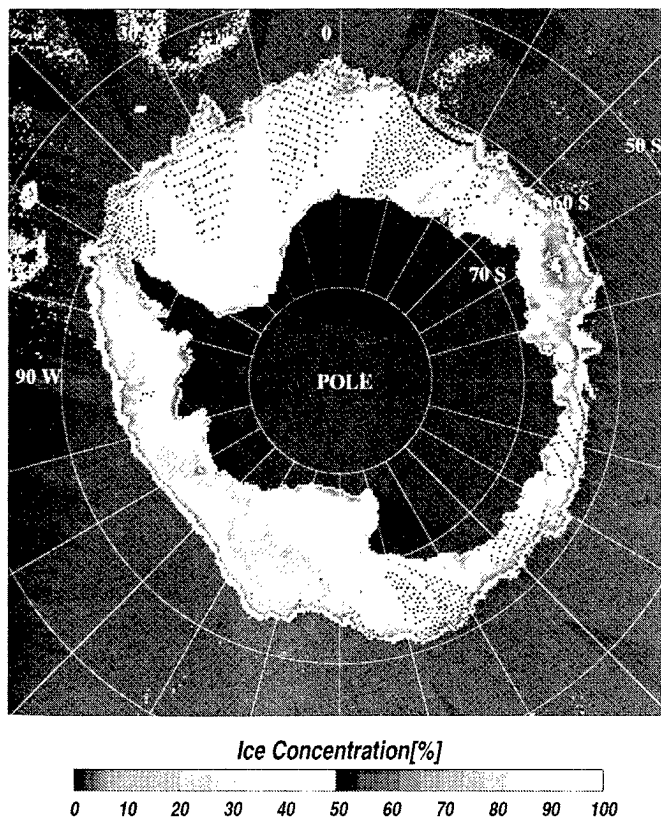
Figure 2: SSM/I sea-ice concentration map for NASA-Team on 17 July 1995.

In the first step, uncorrected sea-ice values are computed with the NASA-Team algorithm. The Southern Hemispheric tie-point set and both weather filters are used. These filters merely mask out the pixels, which are recognized as weather effect pixel with ice concentrations below approximately 20 %, without taking into account the weather caused offset on the T_B of the ice pixel.

Since the calculation of the atmospheric parameters can be done over open water only, it is necessary to separate the pixel containing ice in the field of view of the sensor from those containing weather effects. This separation is realized through a number of thresholds and arising data-gaps are filled by interpolation. The determined meteorological fields are then extrapolated over all regions containing ice concentrations less than 50 %.

This procedure allows us to determine corrected ice concentrations on the basis of reduced T_B dependent on the individual atmospheric parameters.

RESULTS

The procedure was applied to the averaged Southern Ocean data of 17 July 1995 as distributed by [9]. Fig. 2 shows the ice concentration resulting from the NASA-Team algorithm including the fixed-threshold weather filters of [2]. In the upper part three regions of low ice concentration far apart from the ice pack are to be seen. The maps of liquid water path, water

Table 1: Sea-ice extent, sea-ice area, open water (OW), and mean ice concentration derived with the NASA-Team algorithms for 17 July 1995 in the Antarctic. And the differences between the algorithms.

	Ice (pixel) # Observ.	extent [10^3 km^2]	area [10^3 km^2]	OW area [10^3 km^2]	mean ice conc.
Old	27500	17187	13151	4036	76.52
New	24893	15558	12462	3096	80.10
Diff	2607	1629	689	940	

vapour, and wind (not shown here) allow to indentify them as active weather systems. Many weather effects are masked out by the fixed-threshold weather filters, e. g. the inner region of the low in the middle.

In the results of the same ice concentration algorithm, but including the individual weather correction (not shown here), these systems are completely suppressed. Fig. 3 shows the difference of the two algorithms. While over the ice pack the results are identical, over open water and over the MIZ there are considerable differences. Here the new filter leads to lower ice extents. This is confirmed by Tab. 1: When applied to this sample scene, the individual weather correction scheme results in reduced mean values for sea-ice extent (91%), sea-ice area (95%), and open water (77%), but increased mean ice concentration (80% instead of 77%).

Further insight into the role of the weather effects in the determination of sea-ice from passive microwave data will be gained when applying the filter to a time series of SSM/I data. This study which is currently in work will furthermore allow a better understanding of the role of sea-ice for the heat exchange between ocean and atmosphere.

Difference in Ice Concentration [%]

0.0   3.3   6.7   10.0   13.3   16.7   20.0   23.3   26.7   30.0

Figure 3: Difference in ice concentrations between NASA-Team and NASA-Team with correction scheme.

REFERENCES

[1] D. J. Cavalieri, J. P. Crawford, M. R. Drinkwater, D. T. Eppler, L. D. Farmer, R. R. Jentz, and C. C. Wackerman, "Aircraft active and passive microwave validation of sea ice concentration from the DMSP SSM/I," J. of Geophys. Res., vol. 96, pp. 21989–2008, 1991.

[2] D. J. Cavalieri, "A microwave technique for mapping thin sea ice," J. of Geophys. Res., vol. 99, 1994.

[3] D. T. Eppler et al., "Passive microwave signatures of sea ice," In: Carsey, pp. 47–71, 1992.

[4] M. A. Goodberlet, C. T. Swift, and J. C. Wilkerson, "Remote sensing of ocean surface winds with the special sensor microwave/imager," J. of Geophys. Res., vol. 94, pp. 14547–55, 1989.

[5] U. Karstens, C. Simmer, and E. Ruprecht, "Remote sensing of cloud liquid water," Met. and Atm. Phys, vol. 54, pp. 157–71, 1994.

[6] Heygster et al., 1996 G. C. Heygster, L. Toudal Pedersen, H. Schottmüller, C. Thomas, J. Turner, T. Viehoff, "PELICON: Project for Estimation of Long-term variability of Ice Concentration", final report to EC contract E V5C-CT93-0268 (DG 12 DTEE), Bremen, 1996.

[7] C. Kummerow, and L. Giglio, "A passive microwave technique for estimating rainfall and vertical structure information from space," Part I: Algorithm Description, J. Appl. Met., vol. 33, pp. 3–18, 1994.

[8] R. C. Lo, "A comprehensive description of the emission sensor microwave imager SSM/I environmental parameter extraction algorithm", NRL Memo. Rep., 5199, 1983.

[9] National Snow and Ice Data Center (NSIDC), "DMSP SSM/I Brightness Temperature and Sea Ice Concentration Grids for the Polar Regions on CD-ROM," User's guide, NSIDC Special Report-1, Cooperative Institute for Research in Environmental Sciences, Boulder, CO, USA, 1992.

[10] R. S. Sekon, and R. C. Srivaastava, "Doppler radar observations of drop size distributions in a thunderstorm," J. of Atm. Sciences, vol. 28, pp.983–94, 1971.

[11] Simmer 1994 C. Simmer, "Satellite remote sensing of hydrological parameters of the atmosphere with microwaves," Hamburg, Verlag Dr. Kovac, 1994.

[12] C. H. Thomas, "Comparison of rain algorithms for the Special Sensor Microwave Imager," Master thesis, Institute for Marine Research, University of Kiel, Germany, 1993.

[13] Ulaby et al., 1986 J. Ulaby, R. K. Moore, and A. K. Fung, "Microwave remote sensing, active and passive," Volume 1: Microwave remote sensing fundamentals and radiometrie. London: Addison Wesley Publication, 1986.

The effect of the grounded tabular icebergs in front of Berkner Island on the Weddell Sea ice drift as seen from satellite passive microwave sensors

Thorsten Markus

NASA Goddard Space Flight Center, Code 971, Greenbelt, MD 20771

Tel.:301-286-6808,FAX:301-286-0240, email:thorsten@cavalieri.gsfc.nasa.gov

Abstract– The huge grounded tabular icebergs in the southern Weddell Sea might have a significant influence on the sea ice drift, because they form a barrier to the clockwise circulation. The influence of these icebergs on the sea ice distribution is studied with ice concentration analyses from satellite passive microwave sensors over an eleven year period. Besides total ice concentration the fractions of the two different types distinguished in the NASA Team algorithm are studied. One is attributed to first-year ice and the other to deformed ice or ice with heavy snow cover. Results show that the ice coverage east of the icebergs has changed from 40% to between 80 and 90% in summer. This happens because the southward drifting sea ice is trapped between the continent on the right and the icebergs on the left. Therefore less ice formation in this area results in less heat exchange and brine release, which might effect the oceanic processes in front and under the ice shelfs.

Figure 1: OLS image of the southern Weddell Sea durng April 1992. The icebergs are located between the boxes I and II. The boxes indicate seperately studied regions along the coast.

INTRODUCTION

In 1986 a large portion of the Filchner Ice Shelf in the southern Weddell Sea broke off and grounded in front of Berkner Island. This of the grounded icebergs prevents the sea ice from drifting clockwise along the coast. Fig.1 shows the southern Weddell Sea as measured from the thermal infrared channel of the operational linescan system (OLS) onboard of the DMSP satellite series in April 1992. The Antarctic continent is masked out in white. The icebergs are located between boxes I and II (see Fig.1). Although the surface is partially hidden from cloud cover, the consolidated ice east of the icebergs (box I) and the area of thinner ice west of the icebergs (box II) can be clearly seen (the darker area in the nothern part of box I results from fog or low clouds which have a warmer top temperature than the surface). Another interesting feature is the streams along the peninsula (boxes III and IV) indicating northward drift parallel to the coast. The icebergs additionally shelter the coast of the Ronne Ice Shelf (Box II) from the drifting sea ice which is necessary for polynya development [1]. Therefore, lower ice concentrations are expected in this region.

Satellite measurements offer a good opportunity to study the long-term changes in ice conditions in the southern Weddell Sea. Passive microwave data, because of their insensitivity to clouds and global coverage, are operationally used to give estimates of areal ice cover fraction, i.e. ice concentration, and also, although limited, information of ice type. The period of study are the years 1984 through 1994. Because the icebergs gounded at the end of 1987, we have four years before and seven years after the grounding.

DATA

Ice concentration from satellite passive microwave data is derived with the NASA Team algorithm [3]. This algorithm makes use of both the polarization ratio of the 19 GHz channels (PR) and the spectral gradient ratio of the 19 and 37 GHz channels at vertical polarization (GR). As PR gives predominantly a measure of ice concentration, GR gives predominantely the fraction of two ice types, which are in the Arctic first-year and multiyear ice. In the Antarctic the types are referred to as type A and type B because of the absense of a multiyear ice sig-
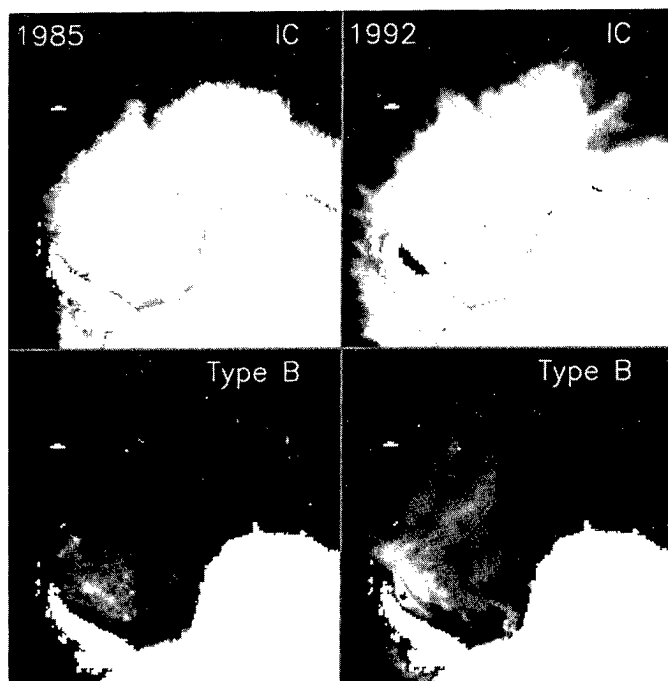
Figure 2: Total and ice type B concentration in July before (1985) and after (1992) the grounding of the icebergs.

nature in the microwave data. Ice type A is attributed to first-year ice whereas ice type B has a lower GR because of enhanced scattering resulting from the ice deformation or snow cover. Deformed ice indicates areas of convergence and deep snow snow cover indicates older ice.

For the years 1984 through July 1987 the brightness temperatures from the scanning multichannel microwave radiometer (SMMR) onboard the Nimbus 7 satellite were used. After the shutdown of the SMMR, data from the special sensor microwave imager (SSM/I) were used in this study. Tiepoints for open water, ice type A and ice type B are published in [4] for the SMMR and in [2] for the SSM/I. Fig.2 shows typical winter (July) total ice concentration for the years 1985 and 1992 (top) and only ice type B concentration (bottom). Whereas there is little difference in the total ice concentration, there is a stream of high ice type B concentration in 1992 visible which progresses from the icebergs towards the main area of high ice type B concentration. Normally ice type B is mostly present along the peninsula in fall which then forced by the Weddell Gyre drifts northward during the winter season. In 1992 there is also an amount of ice type B accumulated east of the icebergs which is then also draged along with the general sea ice drift.

RESULTS

Fig.3 presents the total ice concentration as well as the
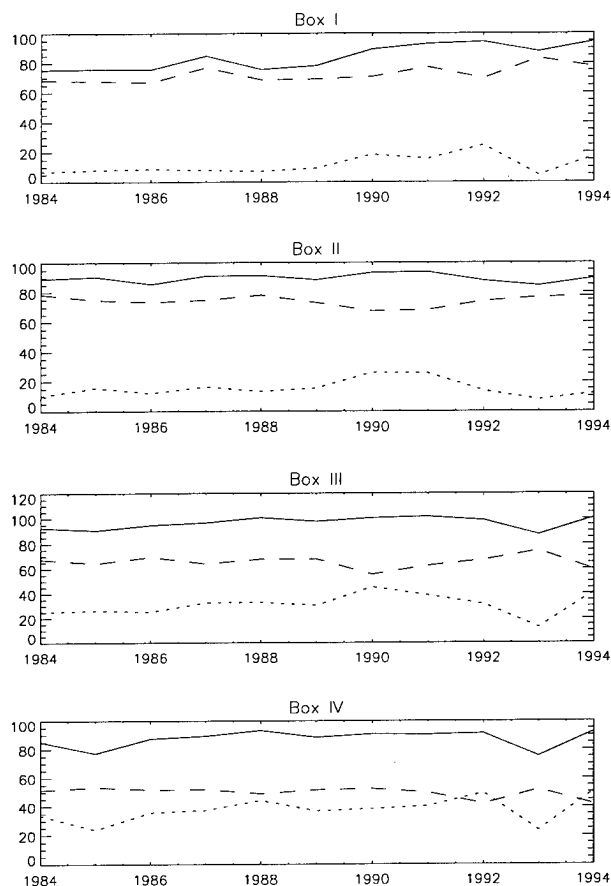
Figure 3: Yearly average total ice concentration (solid line) as well as for ice type A (dashed line) and ice type B (dotted line).

concentration for the individual ice types averaged over each year. In Box I the abrupt change in total ice concentration and in concentration of ice type B is clearly visible after 1988, confirming the expected accumulation of ice in front of the Filchner Ice Shelf. There is also a slight increase in ice type A detectable, which results from general higher ice concentrations during summer. Fig. 4 presents the averages in total ice concentration for the summer (January through March) and the winter (July through September) seasons. One can clearly see the almost constant summer ice concentration until 1989 of about 40% and afterwards of about 80 to 90%. Of course there is the natural annual variability overlain in the signal, e.g. summer of 1987 and 1993. Especially in the summer of 1993 the ice coverage in the Weddell Sea was significantly lower than in the other years, resulting in distinct minima in ice concentration for all boxes. The less ice coverage, however, is compensated during the freeze-up period showing no such signal for the winter months. Expect for Box I there is no influnce of the icebergs seen in the ice
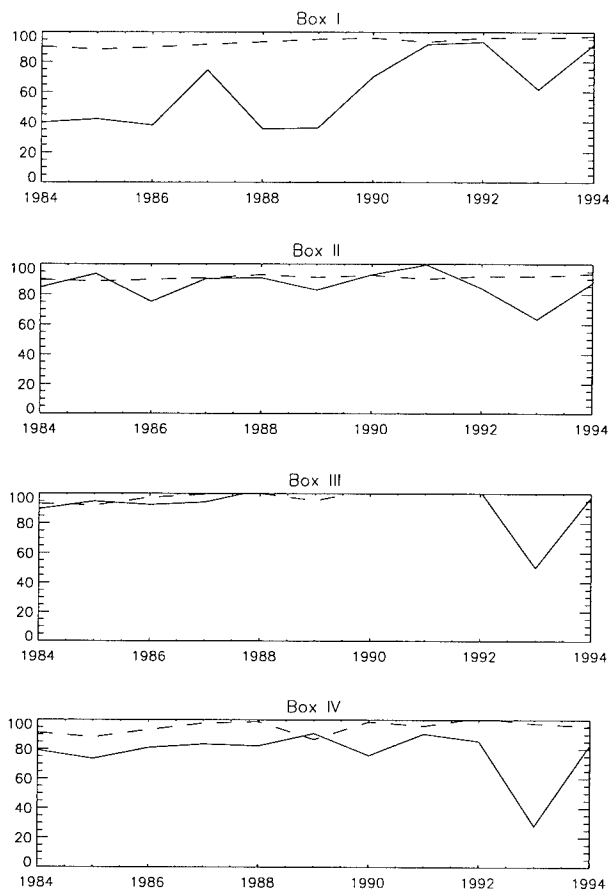
Figure 4: Average ice concentration for months January through March (solid line) and July through September (dashed line).

Table 1: Trends in % ice concentration per year for the individual boxes, ice types, and seasons.

	Box I	Box II	Box III	Box IV
Year:				
A	1.1	-0.2	-0.2	-0.8
B	1.0	0.1	0.6	1.1
A+B	2.1	-0.1	0.4	0.4
Summer:				
A	2.9	-1.5	-1.9	-2.4
B	2.3	1.0	1.1	1.1
A+B	5.2	-0.5	-0.8	-1.3
Winter:				
A	0.2	0.4	0.8	-0.4
B	0.6	-0.1	0.1	1.2
A+B	0.8	0.3	0.9	0.7

90% after the grounding. Because this area is mostly ice covered during the freezing period, less ice formation will occur there, which might have an effect on the complicated oceanic processes in front of and under the ice shelfs. It is also expected that more or larger polynyas would develop in front of the Ronne Ice Shelf because the icebergs prevent the sea ice from drifting in front of the ice shelfs. This could not be measured.

Acknowledgments

REFERENCES

[1] Bromwich,H.B. and D.D., Kurtz, Katabatic winds forcing of the Terra Nova Bay polynya, *J. Geophys. Res., Vol.89, No.63, 3561-3572, 1984.*

[2] Cavalieri, D.J., Sea ice algorithm, *D.J. Cavalieri (ed.) NASA Sea Ice Validation Program for the Defense Meteorological Satellite Program Special Sensor Microwave Imager: Final Report, NASA Technical Memorandum 104559, 1992.*

[3] Cavalieri, D.J., P. Gloersen, and W.J. Campbell, Determination of sea ice parameters with the NIMBUS 7 SMMR, *J. Geophys. Res., 89, 5355-5369, 1984.*

[4] Gloersen,P., W.J. Campbell, D.J. Cavalieri, J.C. Comiso, C.L. Parkinson and, H.J. Zwally, Arctic and Antarctic Sea Ice 1978-1987: Satellite Passive-Microwave Observations and Analysis, *NASA Spec. Publ. SP-511, 1992.*

concentration results. Table 1 presents the trends for the individual boxes, ice types, and seasons derived from a linear fit. The only larger trend is seen in box I with an average yearly increase of 2.1%. But of course this is not a long term trend but just reflects the change in ice concentration because of the icebergs. Therefore, a constant summer ice concentration in box I between 80 and 90% is expected for the following years. No enhanced polynya development is observed in front of the Ronne Ice Shelf. Also, the ice conditions along the peninsula have not notably changed. The negative trends of between -1.5 and -2.5% for the boxes II through IV result from the little summer ice coverage in 1993.

CONCLUSIONS

Passive microwave ice concentration analyses have shown that the grounded tabular icebergs significantly influence sea ice conditions in front of the Filchner Ice Shelf. The yearly average ice concentration has changed from 75 to

Mueller Matrix Associated with Diffuse Scattering from Two-Dimensional Random Rough Surfaces - Full Wave Analysis

Bom Son Lee* and E. Bahar

* Department of Radio Science and Engineering, Kyung Hee University
1 Seocheon-ri, Kihung-eup, Yongin-gun, Kyungki-do, Korea

Department of Electrical Engineering and Center for Electro-Optics
University of Nebraska, Lincoln, NE 68588-0511, USA
T: 402.472.1966   F: 402.472.4732   EMail: bahar@dragon.unl.edu

Abstract—In earlier work, it is shown that there is good agreement between the full wave results and experimental data or numerical results based on Monte Carlo simulations for one dimensionally random rough surfaces [1], [3]. In this work, the full wave solutions for the diffusely scattered fields from two-dimensional random rough surfaces [2] are used to evaluate elements of the 4×4 Mueller matrix. The modified Mueller matrix elements are related to the like and cross polarized radar cross sections as well as to the relative phase of the vertically and horizontally polarized waves. The 4×4 Mueller matrix elements completely characterize electromagnetic scattering from targets (rough surfaces, in this case). The full wave solution presented here can be applied to surfaces with a wide range of roughness scales. Computation time for the full wave Mueller matrix elements is significantly less than the numerical results based on the Monte Carlo simulations even for one-dimensional random rough surfaces.

Formulation of the Problem

The 4×4 Mueller matrix relates the incident Stokes vector to the scattered Stokes vector. In this work, the modified Mueller matrix elements are evaluated. The upper left-hand 2×2 elements are the conventional like and cross polarized scattering cross sections. The lower right-hand 2×2 elements contain relative phase data. The modified Stokes vector is given by

$$
G_m = \begin{bmatrix} G_{m0} \\ G_{m1} \\ G_{m2} \\ G_{m3} \end{bmatrix} = \begin{bmatrix} \langle |E_1|^2 \rangle \\ \langle |E_2|^2 \rangle \\ 2\text{Re}\langle E_1 E_2^* \rangle \\ 2\text{Im}\langle E_1 E_2^* \rangle \end{bmatrix} \tag{1}
$$

where the subscript 1 and 2 denote the vertical and horizontal polarizations, respectively. For isotropic random rough surfaces, the modified Mueller matrix elements in the backscatter direction are given by

$$
M_m = \begin{bmatrix} M_{m11} & M_{m12} & 0 & 0 \\ M_{m12} & M_{m22} & 0 & 0 \\ 0 & 0 & M_{m33} & M_{m34} \\ 0 & 0 & M_{m43} & M_{m44} \end{bmatrix} \tag{2}
$$

where

$$
M_{m11} = \rho \left\{ S^{VV} S^{VV^*} \right\} \tag{2a}
$$

$$
M_{m22} = \rho \left\{ S^{HH} S^{HH^*} \right\} \tag{2b}
$$

$$
M_{m33} = \rho \left\{ \text{Re} \left(S^{VV} S^{HH^*} + S^{VH^*} S^{HV} \right) \right\} \tag{2c}
$$

$$
M_{m12} = \rho \left\{ S^{VH} S^{VH^*} \right\} \tag{2d}
$$

$$
M_{m34} = -\rho \left\{ \text{Im} \left(S^{VV} S^{HH^*} - S^{VH^*} S^{HV} \right) \right\} \tag{2e}
$$

$$
M_{m43} = \rho \left\{ \text{Im} \left(S^{VV} S^{HH^*} + S^{VH} S^{HV^*} \right) \right\} \tag{2f}
$$

$$
M_{m44} = \rho \left\{ \text{Re} \left(S^{VV} S^{HH^*} - S^{VH} S^{HV^*} \right) \right\} \tag{2g}
$$

The quantities $\rho \left\{ S^{PQ} S^{RS^*} \right\}$ are defined in a manner analogous to the definition of the incoherent diffuse normalized scattering cross sections (per unit area A_y) as follows

$$
\rho \left\{ S^{PQ} S^{RS^*} \right\} = \frac{4\pi r^2}{A_y} \left[\langle S^{PQ} S^{RS^*} \rangle - \langle S^{PQ} \rangle \langle S^{RS^*} \rangle \right] \tag{3}
$$

where the symbol $\langle \rangle$ denotes the statistical average. For isotropic random rough surfaces, the upper right 2×2 elements and lower left 2×2 elements vanish. For backscatter, $M_{m12} = M_{m21}$ and $M_{m34} = -M_{m43}$. For isotropic random rough surfaces, the full wave expression for $\rho \left\{ S^{PQ} S^{RS^*} \right\}$ in (3) is given by [2]

$$
\rho \left\{ S^{PQ} S^{RS^*} \right\} = \frac{k_0^4}{\pi v_y^2} 2\pi \iiint f_{RS}^{PQ}(\bar{n}) \left\{ |\chi(v_y)|^2 \right.
$$
$$
\left[\exp \left(\frac{\sigma_s^2}{2} v_y^2 r_d^2 \exp \left(-\frac{2r_d^2}{l_c^2} \right) + \langle h^2 \rangle v_y^2 \exp \left(-\frac{r_d^2}{l_c^2} \right) \right) \right.
$$
$$
\left. J_0 \left(v_{xz}' r_d \right) - J_0 \left(v_{xz} r_d \right) \right] - \chi(v_y)
$$
$$
\left[\exp \left(\frac{\sigma_s^2}{2} v_y^2 r_d^2 \exp \left(-\frac{2r_d^2}{l_c^2} \right) \right) \right.
$$
$$
\left. \left. J_0 \left(v_{xz}' r_d \right) - J_0 \left(v_{xz} r_d \right) \right] \right\}
$$
$$
p(h_x, h_z) r_d dr_d dh_x dh_z \tag{4}
$$

where k_0 is the free space wave number, χ is the surface height characteristic function, $\langle h^2 \rangle$ and σ_s^2 are the mean square height and slope, respectively, $l_c = 2\left[\langle h^2 \rangle/\sigma_s^2\right]^{1/2}$ is the correlation length, r_d is the distance variable,

$$\bar{v} = \bar{k}_0^f - \bar{k}_0^f = v_x \bar{a}_x + v_y \bar{a}_y + v_z \bar{a}_z, \tag{5}$$

$$\bar{k}_0^f \equiv k_0 \left(\sin\theta_0^f \cos\phi^f \bar{a}_x + \cos\theta_0^f \bar{a}_y + \sin\theta_0^f \sin\phi^f \bar{a}_z \right) \tag{6}$$

$$\bar{k}_0^i \equiv k_0 \left(\sin\theta_0^i \cos\phi^i \bar{a}_x - \cos\theta_0^i \bar{a}_y + \sin\theta_0^i \sin\phi^i \bar{a}_z \right), \tag{7}$$

$$f_{RS}^{PQ}(\bar{n}) = D^{PQ}(\bar{n})D^{RS^*}(\bar{n})P_2(\bar{n}^f, \bar{n}^i | \bar{n}), \tag{8}$$

$$v_{xz} = \sqrt{v_x^2 + v_z^2}, v'_{xz} = \sqrt{(v'_x)^2 + (v'_z)^2}, \tag{9}$$

$$v'_x = v_x + v_y h_x \exp\left(-\frac{r_d^2}{4l_c^2}\right),$$

$$v'_z = v_z + v_y h_z \exp\left(-\frac{r_d^2}{4l_c^2}\right). \tag{10}$$

In (4), $p(h_x, h_z)$ is the probability density function for the large scale slopes in x and z directions (assumed here to be Gaussian). In (8), $\bar{n}$ is the unit vector normal to the large scale rough surface, P_2 is Sancer's shadow function [6], and $D^{PQ}(P, Q = V, H)$ is the surface element scattering coefficient which depends on the incident and scatter angles, the large scale slopes of the rough surface, and electromagnetic characteristics above and below the rough surface [1], [3]. element scattering coefficient which depends on the incident and scatter angles, the large scale slopes of the rough surface, and electromagnetic characteristics above and below the rough surface [1], [3]. The full wave expression in (4) which accounts for surface height/slope correlations [1], [3] have been shown to reduce to the physical/geometrical optics solution [4] in high frequency limit (when the root mean square height and radii of curvature are large compared to the wavelength) and to the small perturbation solution [5] in low frequency limit (when the surface height and slope are of the same order of smallness). The full wave solutions have been used for a wide range of rough surface scales.

ILLUSTRATIVE EXAMPLES

In the following figures, the incident angle is 20°. Elements of the Mueller matrix for backscatter are plotted as functions of $k_0 h$ (h is the rms height). The electric permittivity of the medium below the surface is assumed to be $\epsilon_r = 5-i0.07$.

In Fig. 1, the Mueller matrix element M_{m11} is plotted as a function of rms surface height ($0 \le k_0 h \le 1$), and correlation length ($1 < k_0 l_c \le 10$). In this broad range of rough surface scales, M_{m11} is largest when $k_0 h \approx 1$ and $k_0 l_c \approx 6$. For surfaces with small slopes $\left(\sigma_s^2 = 4\langle h^2 \rangle/l_c^2\right)$,
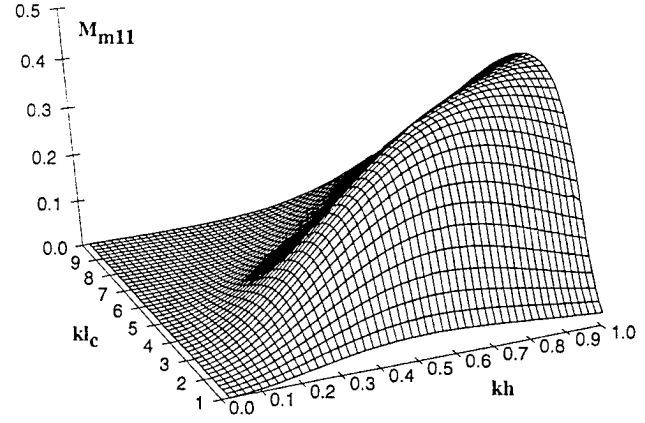
Fig. 1. Modified Mueller matrix element M_{m11} in the backscatter direction for $\theta_0^i = 20°$, as a function of kh and kl_c, $\epsilon_r = 5-i0.07$
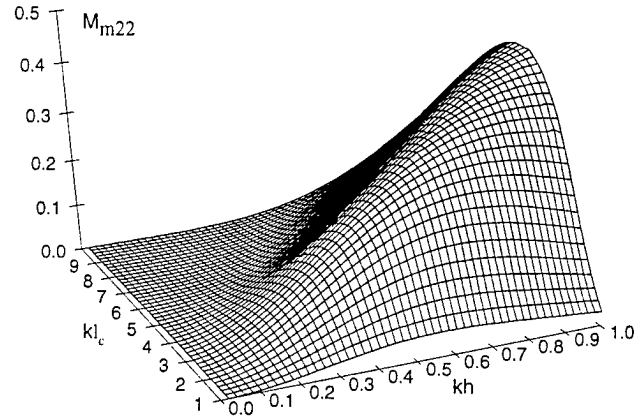
Fig. 2. Modified Mueller matrix element M_{m22} in the backscatter direction for $\theta_0^i = 20°$, as a function of kh and kl_c, $\epsilon_r = 5-i0.07$

M_{m11} is very small because the waves are essentially scattered coherently in the specular direction. For root mean square heights $kh = 0.5$, M_{m11} is largest when $kl_c \approx 3$. For both cases, ($kh = 1$, $l_c = 6$ and $kh = 0.5$, $l_c = 3$) this corresponds to an rms slope $\sigma_s = 0.33$ (multiple scatter is significantly smaller than single scatter for $\sigma_s < 0.3$).

In Fig. 2, M_{m22} exhibits similar results except that its magnitudes are smaller than those shown in Fig. 1.

Consider the plots of M_{m33} in Fig. 3. Since the order of magnitude of $|S^{PQ}|^2$ ($P \ne Q$) is usually $10^{-2} \sim 10^{-3}$ times $|S^{PP}|^2$, $M_{m33} \approx M_{m44}$ are primarily related to the cosines of the phase difference between S^{VV} and S^{HH}. For near normal incidence, S^{VV} and S^{HH} are approximately equal in magnitude and 180° out of phase. Thus, the results for M_{m33} are similar to the results for M_{m11} and M_{m22} except for the negative sign.

In Fig. 4, M_{m12} (related to the cross polarized cross section) is plotted as a function of kh and kl_c. It also peaks in the intermediate region where $\sigma_s = 0.33$. For small slopes there is little depolarization. While Figs. 1, 2 and 4 (for M_{m11}, M_{m22} and M_{m12}) are similar in shape, the level of M_{m12} is about 20 db lower than the level of M_{m11} and M_{m22}.
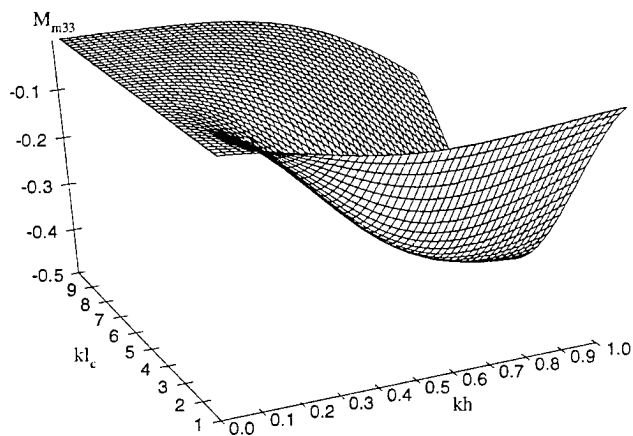
Fig. 3. Modified Mueller matrix element M_{m33} in the backscatter direction for $\theta_0^i = 20°$, as a function of kh and $kl_c, \epsilon_r = 5\text{-}i0.07$
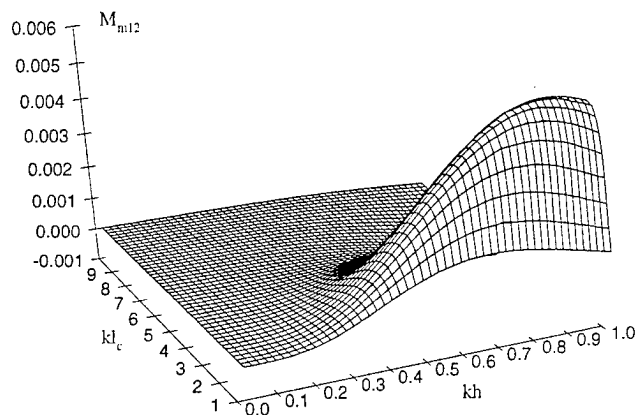
Fig. 4. Modified Mueller matrix element M_{m12} in the backscatter direction for $\theta_0^i = 20°$, as a function of kh and $kl_c, \epsilon_r = 5\text{-}i0.07$

In Fig. 5, $M_{m34} = -M_{m43}$ (for backscatter) is plotted as a function of kh and kl_c. Since S^{VV} and S^{HH} are approximately 180° out of phase, for near normal incidence $Im\ (S^{VV}S^{HH^*})$ is very small compared to $Re\ (S^{VV}S^{HH^*})$ and $M_{m34} = -M_{m43} \ll M_{m33} \approx M_{m44}$ (backscatter). Thus, in this example, for remote sensing at near normal incidence, data related to M_{m11} (or M_{m22}), M_{m33} (or M_{m44}) and $M_{m12} = M_{m21}$ (only if the instrument is sufficiently sensitive) is most useful.

ACKNOWLEDGMENTS

CONCLUSION

The Mueller matrix elements for the fields scattered from two-dimensional random rough surfaces have been
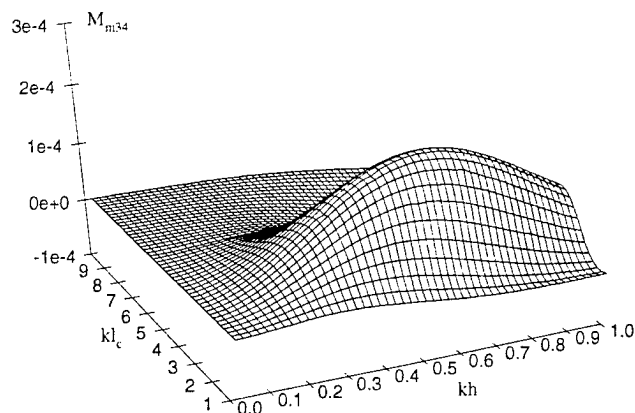
Fig. 5. Modified Mueller matrix element M_{m34} in the backscatter direction for $\theta_0^i = 20°$, as a function of kh and $kl_c, \epsilon_r = 5\text{-}i0.07$

evaluated using the full wave soution. The full wave solution can provide a reliable database of the Mueller matrix elements for two-dimensional random rough surfaces over a broad range of rough surface parameters in a timely manner. It can be used to identify the most useful Mueller matrix elements, optimal incident (and scatter) angles and frequency, for effective remote sensing purposes.

REFERENCES

[1] E. Bahar and B.S. Lee, "Full wave solutions for rough surface bistatic radar cross sections - Comparison with small perturbation, physical optics, numerical, and experimental results," Radio Science, vol. 29, pp. 407-429, 1994a.

[2] E. Bahar and B.S. Lee, "Full wave scatter cross sections for two-dimensional random rough surfaces using joint conditional surface height characteristic functions," Proceedings of International Geoscience and Remote Sensing Symposium, pp. 1638-1640, 1994b.

[3] E. Bahar and B.S. Lee, "Full wave vertically polarized bistatic radar cross sections for random rough surfaces - Comparison with experimental and numerical results, IEEE Trans. Antennas Propag., vol. 43, pp. 205-213, 1995.

[4] P. Beckmann and A. Spizzichino, The Scattering of Electromagnetic Waves from Rough Surfaces, Macmillan, New York, 1963.

[5] S.O. Rice, Commun. Pure Appl. Math., vol. 4, pp. 251-378, 1951.

[6] M.I. Sancer, "Shadow corrected electromagnetic scattering from randomly rough surface," IEEE Trans. Antennas Propag., vol. SP-17, pp. 577-585, 1969.

Development and Present Configuration of the NASA GSFC/WFF Helicopter-based Remote Sensing System

C. L. Walthall
USDA-ARS
Remote Sensing and Modeling Laboratory
008 BLDG. 007, BARC-West
Beltsville, MD 20705
301-504-6074/FAX 301-504-5031/Email cwalthal@asrr.arsusda.gov

D. L. Williams
B. L. Markham
J. E. Kalshoven
R. F. Nelson
NASA
Goddard Space Flight Center
Laboratory for Terrestrial Physics
Greenbelt, MD 20771

Abstract -- There is a need for calibrated remote sensing data from airborne platforms emphasizing spatial, spectral, temporal, bidirectional and polarization information domains. A system developed by NASA Goddard Space Flight Center and Wallops Flight Facility utilizing a helicopter as the platform has proven to be a versatile means of acquiring such data. As the system evolved, it was used for the acquisition of data supporting field measurement campaigns such as an acid deposition effects study, the First International Satellite Land Surface Climatology Project (ISLSCP) Field Experiment (FIFE), the Forest Ecosystems Dynamics Project (FED), and the BOReal Ecosystem Atmosphere Study (BOREAS) among others. The data collected with the helicopter system have been used to develop relationships between vegetative parameters and remotely sensed measurements, validate atmosphere and vegetation models, address scaling issues, and provide low altitude data for instrument calibration studies. Off-the-shelf field and experimental instrumentation have been flown as part of the system. Most recently, gyro-stabilized, pointable mounts and an automatic sun-tracking sun photometer were specifically designed and fabricated for the system. The stages of development of the helicopter system over a twelve year period are described and illustrate the advantages and limitations afforded to investigators using helicopter-based systems.

USE OF HELICOPTERS IN MACs

Helicopters have proven to be versatile platforms for remote sensing with unique deployment and mission characteristics. A helicopter remote sensing system has been developed by scientists, engineers and flight personnel at NASA Goddard Space Flight Center (GSFC) and NASA Wallops Flight Facility (WFF). This system has played a critical part of interdisciplinary multi-sensor aircraft campaigns (MACs) such as the First International Satellite Land Surface Climatology Project (ISLSCP) Field Experiment (FIFE) [1], the Forest Ecosystems Dynamics Project (FED) [2] and the BOReas Ecosystem Atmosphere Study (BOREAS), [3] among others. The data collected with the system during these deployments have been used to develop relationships between vegetative parameters and remotely sensed measurements, to validate atmosphere and vegetation models, and to provide data for studies on instrumentation correction and calibration.

DESIGN PHILOSOPHY

The first configuration of the GSFC/WFF optical remote sensing helicopter system was developed to acquire spectra of forest canopies [4]. Engineering of the system was guided by: 1) the use of off-the-shelf field instruments, 2) real-time feedback of data to the operator, 3) downward-looking photographic camera(s) boresighted with the radiometric instrumentation, 4) the use of instruments located on the ground for calibration data, and 5) minimal alteration to the airframe and use of standard rack mounts where possible. Adhering to these criteria allowed construction of the system for minimal

costs and made modifications possible. Additionally, the data from this system were considered comparable with data taken using ground-based platforms mounting the same instrumentation. As technology developed, opportunities for additional investigators with prototype instrumentation were available, often simultaneously with the primary, passive optical sensor instrumentation.

EARLY CONFIGURATIONS

The primary instruments were the Barnes Engineering[1] eight channel Modular Multiband Radiometer (MMR), and the Spectron Engineering SE-590 visible/near infrared spectrometer. A 35mm photographic camera with a 700 frame film back was also included. The mounting surface for the instrumentation sensors consisted of a brace beneath the cabin of a Bell UH-1B helicopter. Field of view (FOV) optics for the MMR and the SE-590 were 1 degree. A 50mm focal length lens was used on the 35mm camera.

The microcassette of the SE-590 controller was used for data logging SE-590 spectra and an Omnidata Polycorder provided data logging and analog to digital conversion (A/D) for the MMR. An intervalometer with a manual switch triggered the photographic camera. Power was supplied to the SE-590 controller via an invertor on the aircraft and portable, sealed, rechargeable batteries were used for the MMR. The camera and its controls used aircraft power (28 volts DC). Real-time data display from the SE-590 was provided by an oscilloscope while selected MMR channels were displayed by the Polycorder screen. Internal clocks of each system were manually synchronized and each instrument was triggered by a separate operator. This system provided the rudimentary capabilities for collecting spectral data using the helicopter platform.

Early modifications included re-mounting the sensors on a flat plate hung on existing hard points on the nose of the aircraft for easier handling and maintenance. A video camera with a Beta format VCR and a second 35mm camera with a telephoto lens were added. A signal from the SE-590 designed for coincident firing of a 35 mm camera was used to trigger the MMR. This reduced the size of the aircrew by one person, thereby saving fuel and increasing flight time for data collection.

The microcassette data logging of the SE-590 was slow, sometimes unreliable and required a considerable amount of time to offload data for processing and analysis. The audio tracks of the VCR were used to record conversations among the aircrew and a time/date stamp was encoded on the image. Computer data logging was initiated when portable PCs became available using the RS-232 port of the SE-590. Later use of A/D cards in the PC expansion slots to log the MMR data and modifications to the SE-590 by the manufacturer allowed computer control of the data collection and logging sequence. A single keyboard stroke of the computer triggered the SE-590, the MMR, the photographic camera and inserted an audible tone on the VCR sound track. A video monitor was located so that the pilot could see the area in view by the instruments which helped the pilot keep the aircraft located over a target while hovering. This configuration was used during a project to study the effects of acid deposition [5].

Off-nadir viewing in the direction of the aircraft nose was addressed by mounting an electrically-controlled actuator behind the aircraft nose mounting plate which could be used to vary the view angle of the sensor package. Inexpensive bubble inclinometers were located on top of the mounting plate to provide the front left seat crew member with an indication of the angle. This configuration was used for the 1987 FIFE deployment.

Calibration procedures initially had been using another SE-590 and MMR on the ground set to automatically measure reflected irradiance off a calibrated halon or barium sulphate panel. Laboratory measurements from the SE-590s were used to develop procedures to match the spectral bands between the airborne and ground-based units. Calibration procedures were updated to recent developments [6] while still retaining the ground-based calibration panel.

LATER MODIFICATIONS

Two-degree-of-freedom pointability was provided by mounting an inverted radar pedestal on side mounts such that it could be lowered into position below the level of the skids after takeoff. This assured that the landing skids did not restrict the view. The pointable mount was kept on the starboard side of the helicopter to insure that the primary instrument operator/mission manager and the pilot had similar views. An infrared thermometer (IRT) was also added to the system to provide thermal infrared data to complement that of the MMR. This configuration was used for the

1989 FIFE deployment and the FED deployments.

CURRENT CONFIGURATION

The UH-1B helicopter was replaced with a larger UH-1H aircraft during 1994 for the BOREAS deployment. Gyro-stabilized pointable mounts, the use of off-the-shelf software for an industrial-quality PC-based A/D and data logging system, lighter instrument racks that allow an additional bay, a temperature control box for the SE-590 optical sensors, the ability to add additional sensors (such as a pyranometer, photosynthetically active radiation (PAR) sensor, and barometric pressure transducer), and a sun-tracking photometer specifically designed for use with helicopters [7] were added. The Beta-format VCR was replaced with a super-VHS format VCR. Some additional changes to enhance the operating environment for the aircrew were also been made such as foot switch controls for microphones. The two most critical changes, that of the pointable mounts and the sun photometer are such that the attitude of the instruments is now independent from that of the aircraft, and the system is no longer dependent on a calibration panel located on the surface at a fixed location. The sun photometer also provides a means of atmospheric corrections for the radiometric data sets.

CONCLUDING REMARKS

The use of off-the-shelf and some specialized components within the framework of a simple and flexible design have provided unique data collection capabilities with a helicopter platform. The present configuration of the system creates a mobile, self-contained, flexible system for the acquisition of calibrated and atmospherically corrected remotely sensed data. Opportunities for other investigators to mount their instruments are such that there would be no interference with existing systems.

ACKNOWLEDGMENTS

The development and deployments of the NASA GSFC/WFF helicopter optical remote sensing system has been through the efforts of numerous individuals. Chief among them are Frank Wood, Charles Smith, Sam Goward, Moon Kim and John Schafer.

REFERENCES

[1] P.J. Sellers, F. G. Hall, G. Asrar, D.E. Strebel, and R. E. Murphy, "An overview of the First International Satellite Land Surface Climatology Project (ISLSCP) Field Experiment (FIFE)," Jour. Geophy. Res., Vol. 97, no. D17, 18,345-18,371, 1992.

[2] E. R. Levine, K. J. Ranson, J. A. Smith, D. L. Williams, R. Knox, H. H. Shugart, D. L. Urban, and Lawrence, W.T., "Forest ecosystem dynamics: linking forest succession, soil processes, and radiometric models," Ecol. Model. 65:199-219, 1993.

[3] P. J. Sellers, P.J., F. Hall, D. Baldocchi, J. Cihlar, P. Crill, J. Den Hartog, B. Goodison, R. Kelly, D. Lettenmeier, H. Margolis, J. Ranson, M. Ryan (ed.), 1994. BOReal Ecosystem Atmosphere Study (BOREAS) Experiment Plan. Version 3.0. NASA, GSFC. 4 Vols.

[4] D. L. Williams, C.L. Walthall and S.N. Goward, "Collection of in-situ forest canopy spectra using a helicopter: A discussion of methodology and preliminary results," Proceedings of 1984 Symposium on Machine Processing of Remotely Sensed Data, Purdue Univ., West Lafayette, IN. pp. 94-106, 1984.

[5] B. N. Rock, D.L. Williams and J.E. Vogelmann, "Field and airborne spectral characterization of suspected acid deposition damage in red spruce (Picea Rubens) from Vermont". Proceedings of the 1985 Machine Processing of Remotely Sensed Data Symposium, 1985.

[6] B. L. Markham, F. Wood, and S.P. Ahmad, "Radiometric calibration of the reflective bands of NS001-Thematic Mapper Simulator (TMS) and Modular Multispectral Radiometers (MMR)," in Recent Advances in Sensors, Radiometry, and Data Processing for Remote Sensing, Proc. SPIE, 24, 96-108, 1988.

[7] C. L. Walthall, R. N. Halthore, G. Elman, J. Schafer and B. L. Markham, "An airborne sun photometer for use with helicopters," Proceedings of 2nd International Airborne Geoscience Symposium, ERIM, 1996.

[1]Manufacturer names are given for information purposes only and do not imply endorsement by USDA or NASA.

System Requirements for Active Optical Search and Rescue

Christopher T. Field
Electrical and Computer Engineering
The Johns Hopkins University
34 th and Charles St.
Baltimore MD 21218
301-286-6119
ctf@light.ece.jhu.edu

Pamela S. Millar
NASA Goddard Space Flight Center
Laser Remote Sensing Branch
Greenbelt MD 20771
301-286-3793
pam@eib1.gsfc.nasa.gov

ABSTRACT

This paper describes an lidar remote sensing system for searching for lost planes and watercraft. We present a simple expression for the average laser power required to search at a particular rate given a required ground level energy density. The required ground level energy density is determined by the target characteristics and background light which has a solar component. While several important parameters are not well known, active probing for lost planes and boats may be practical.

1. INTRODUCTION

Current downed airplane search methods rely on remote detection of an emergency beacon and passive optical remote sensing. The emergency beacon is a radio designed to transmit in response to an accident. Unfortunately they operate in less than 25% of all aircraft crashes due to crash damage or poor maintenance [1]. Civil Air Patrol search efforts then resort to visual search from single or twin engine planes using ambient light. Night searches are ineffective. Searcher fatigue also reduces search effectiveness. The best probability of detection of a downed plane is less than 30% with typical values between 15% and 20% [2].

There is interest in using lasers to perform active searching for downed planes and distressed watercraft. A remote sensing system mounted in a plane would fly over the search area. Suitable material on the plane or boat reflect and modify the incident laser light so that a detector on the search plane is able to distinguish the ground return from the target material return. The material may change the incident light's polarization or wavelength spectrum. This paper describes search systems based on Stokes shifted returns using fluorescent dyes or Laser Paint™.

The following requirements have been set for a realistic automated search system. It must perform significantly better than the present visual search method and be usable during day and night. It must provide a significantly higher probability of detection than current methods with search speeds and ground coverage comparable to or better than the current values of about 180 km^2/hr with 50% ground coverage. It ought to be usable under most conditions in which planes can be flown. It must not require more electrical power than is available on the small planes used by the Civil Air Patrol, about 1 kW.

Two approaches are considered in this paper. The first, proposed and build by Richard S. Hughes of the U.S. Naval Weapons Center [3], uses broadband fluorescence from a laser dye. The second system, proposed by Nabil M. Lawandy, of Spectra Sciences Corporation and Brown University, uses the emission line narrowing of Laser Paint™ to increase the contrast between background photons and the target material emission [4].

2. SYSTEM DESCRIPTION

A model of a lidar remote sensing search method has three major statistical components: the probability of a target being visible to the search plane, the probability of correct detection of a visible target illuminated by a laser beam, and the probability that a laser beam will strike (illuminate) a visible target. The probability of a target being visible depends on the object size and the size distribution of gaps in the plant canopy as applied in the case of wooded areas. These statistics are not well known for crash sights. Since plane crashes tend to leave rather large holes in the tree canopy, we will assume for this study that some part of the plane is visible. The probability of correct detection of an illuminated, visible target depends on the statistics of optical detection and the background light level. This has been the major thrust of the study. The probability of target illumination depends on the laser beam size, the fraction of ground illuminated by the laser (ground coverage), and again on the target size.
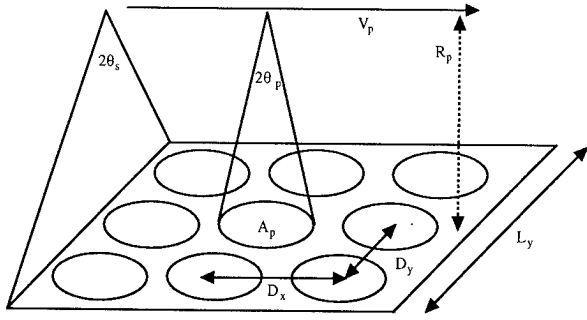
Figure 1: Search model geometry. Plane at altitude R_p flies with speed V_p. The pump had full angle divergence $2\theta_p$ and illuminates ground area A_p.

Fig. 1 shows the configuration of the system parameters used in the model. A search plane flies at altitude R_p with velocity V_p. A downward directed pulsed laser beam (the pump beam) with wavelength λ_p is swept perpendicular to the flight direction. The laser pulse hits a ground area $A_p = \pi R_p^2 \theta_p^2$, where θ_p is the beam half angle divergence. The illuminated area may or may not contain the fluorescent target. Assuming the beam has a top hat profile, the ground level energy density, E_g, is given by

$$
\begin{aligned}
E_g &= E_p \eta_{atm}/A_p & \text{(1a)} \\
&= E_p \exp(-\alpha_{atm}R_p)/\pi(R_p\theta_p)^2 & \text{(1b)}
\end{aligned}
$$

where E_p is the total pulse energy, η_{atm} is the atmospheric transmission efficiency, and α_{atm} is the atmospheric attenuation coefficient.

The field of view of a photo-detector is swept to coincide with the laser beam. If no fluorescent target material is present in the pump beam, the receiver collects only noise photons. An optical bandpass filter with bandwidth $\Delta\lambda$ centered at the target fluorescence peak of λ_r limits the collected noise photons. For a Lambertian surface the average number of collected noise photons is given by

$$
\begin{aligned}
n_n &= \eta_D \eta_{atm} \frac{I_s \lambda_r}{hc} \rho \frac{\cos(\theta)}{\pi} \Delta\lambda \frac{A_r}{R_p^2} \\
&\quad \times \pi \left(R_p \theta_{FOV}\right)^2 \Delta t & \text{(2a)} \\
&= \eta_D e^{-\alpha_{atm}R_p} \frac{I_s \lambda_r}{hc} \rho \cos(\theta) \Delta\lambda A_r \\
&\quad \times \theta_{FOV}^2 \Delta t & \text{(2b)}
\end{aligned}
$$

where η_D is the receiver efficiency including the detector quantum efficiency, I_s is the downward solar energy flux density, ρ is the surface albedo, θ is the observation angle, A_r is the receiver area, θ_{FOV} is the receiver half angle field of view, and Δt is the observation window time.

If present and illuminated, the fluorescent target emits signal light at wavelength λ_r, longer than the pump wavelength λ_p. The total fluorescent energy emitted in the

receiver passband is given by

$$
E_f = \eta_f E_g A_t \qquad \text{(3)}
$$

where η_f is the fluorescence efficiency and A_t is the total area of fluorescent material illuminated and visible. Assuming that the receiver field of view is larger than the target material, the fluorescent energy detected is

$$
E_r = \eta_{atm} E_f A_r / R_p^2. \qquad \text{(4)}
$$

Equations (1) through (4) can be combined into one "radar range equation" [5].

The receiver compares the number of detected photons, n, to a threshold, n_{th}, and decides that target fluorescent material is present if $n > n_{th}$ and no target is present if $n < n_{th}$. The threshold must be selected so that the probabilities of a miss and false alarm are sufficiently small. The probability of miss, P_M, is the probability of deciding the target is not present when it is in fact present. The probability of false alarm, P_F, is the probability of deciding the target is present when it is not.

Photon detection is properly described by Poisson statistics. However, because many photons are collected, Gaussian statistics may be used with the standard deviation equal to the square root of the mean. In the absence of the target, the average number of noise photons detected, n_n, is given by (2). When the fluorescent material is present, the average number of detected photons is given by $n_s + n_n$, where n_s is the number of detected signal photons given by

$$
n_s = \frac{E_r \lambda_r}{hc}. \qquad \text{(5)}
$$

At noon the sea level solar flux at 600 nm is $150\,\mathrm{mW/cm^2/\mu m}$ [7]. Using a conservative surface albedo of 0.5 there are 10^5 noise photons detected by a receiver with 10% detection efficiency, bandwidth of 10 nm, collection diameter of 20 cm, field of view half angle of 4 mrad, and observation time 100 ns. Assuming $P_F = 10^{-6}$, the threshold must be more than 4.75 standard deviations greater than the mean noise, $n_{th} > n_n + 4.75\sqrt{n_n}$ [8]. For $P_M = 10^{-3}$ the threshold must be less than 3.1 standard deviations below the mean signal plus noise, $n_{th} < (n_s + n_n) - 3.1\sqrt{n_s + n_n}$. Solving these two equations, the mean detected signal must be greater than 2600 photons. For a plane altitude of 3 km, using the receiver parameters above, and neglecting atmospheric attenuation, the target material must emit 1.5×10^{14} photons, $51\,\mu\mathrm{J}$ at 600 nm.

3. FLUORESCENCE MODELS AND LASER POWER

Fluorescent dyes have an emission peak red shifted 30 to 100 nm from the pumping wavelength. The emission

spectrum can vary from 50 to 100 nm across [6]. The total quantum yield between incident and emitted light is higher than 50%, however much of the emitted light is outside the receiver passband. We assume that the conversion efficiency of pump light into signal light within the receiver band is a modest 5%. A square meter of target material will emit the required 51 μJ of light when the incident intensity is 100 nJ/cm^2. The maximum safe exposure for the eyes to a single pulse of visible light is 500 nJ/cm^2 [9] which is five times the required pump level. While a factor of five is not great, it shows that an eye safe system is feasible at 532 nm.

Nabil M. Lawandy has found that when a mixture of laser dye and scattering centers, such as the paint pigment TiO$_2$, is illuminated by intense light pulses, the mixture will emit narrow band light. This mixture is trademarked Laser Paint^{TM}. The emission spectrum is only 2 to 5 nm wide when pumped by a 3 mJ/cm^2 pulse 7 ns long. The slope efficiency is about 25% so the pump energy only has to barely exceed threshold to yield the required received signal. The eye safe power level for visible light is 6000 times lower than this value. Either the threshold energy must be lowered by four orders of magnitude or the pump can be shifted to wavelengths shorter than 400 nm where the eye safe limit rises to more than 3 mJ/cm^2. However, as shown next the average power required to search the ground is a more stringent requirement than eye safely.

The required average laser power can be written as

$$P_{av} = S_s C_f E_g \qquad (6)$$

where $S_s = V_p L_y$ is the search rate given by the product of the plane's forward speed and the width of the transverse scan, $C_f = A_p/(D_x D_y)$ is the ground coverage factor which expresses the fraction of ground actually illuminated by the pump laser, and E_g is the ground level energy density given above. As described before, current search speeds are about 180 sqkm/hr which will be used for S_s. The desired coverage factor depends on the size of the laser spots and the size of the lost object but will range from $0.50 \leq C_f \leq 2$ where values greater than 1 indicate the some spots are hit multiple times. A coverage factor of unity will be assumed. Equation (6) applies regardless of the plane's altitude, laser spot size or repetition rate. It states simply that to place a given amount of energy density on a given area per unit time requires a specified average power.

The ground level energy density depends on whether spontaneous fluorescence or stimulated fluorescence is being used. For spontaneous fluorescence, $E_g =$ 100 nJ/cm^2. The average laser power is 13 W, which is a feasible amount of power. For the Laser Paint^{TM}, stimulated fluorescence, $E_g = 3$ mJ/cm^2 and the required *average* optical power is 1.5 MW which is clearly unrealistic.

4. DISCUSSION AND CONCLUSIONS

There are several open questions which must be resolved before a practical system can be built. Most importantly, plants also fluoresce. Although there are several proposals to distinguish plant fluorescence from target material fluorescence, it is not known how much of a problem this will be. However, plant fluorescence is inefficient and is not believed to present a major problem for a 532 nm pump and 600 nm receiver wavelength. There also is uncertainty about the probability of the plane being visible through the plant canopy. Work is currently underway to measure the size distributions of holes in tree canopies. Finally the atmospheric scattering is expected to degrade the performance but it is not known by how much.

We have shown that active probing for downed planes marked with fluorescent dye seems practical. By designing the system to identify one square meter or more of target material, the system can be built eye safe in the visible, capable of day and night time operation, and requires reasonable power levels from the search plane.

5. REFERENCES

[1] *Search and Rescue Synthetic Aperture Radar SAR^2*. NASA, Goddard Space Flight Center. Search and Rescue Mission.

[2] Warren Vest, Director of Flight Operation for the Maryland Civil Air Patrol. Personal conversation.

[3] Richard S. Hughes, Automatic Night Search and Rescue System., U.S.Patent #3839639, 1 Oct 1974

[4] N.M. Lawandy, R.M. Balachandran, A.S.L. Gomes, and E. Sauvain, "Laser action in strongly scattering media" in Nature, vol 368, pp 436–438, 1994

[5] Raymond M. Measures, *Laser Remote Sensing,* John Wiley & Sons, Inc., (1984)

[6] Karl H. Drexhage, "Structure and Properties of Laser Dyes," in *Dye Lasers,* Topics in Applied Physics, Springer-Verlag, 3rd edition, F. P. Schafer Ed. (1990) p155

[7] *The Infrared Handbook.* William L. Wolf and George J. Zissis Ed. Environmental Research Institute of Michigan 1989 section 3

[8] *Handbook of Mathematical, Scientific, and Engineering Formulas, Tables, Functions, Graphs, Transforms.* Research and Education Association. New York 1984

[9] *American National Standards for Safe Use of Lasers* (1993)

Shortwave Infrared Spectral Reflectance of Plant Litter and Soils

P. L. Nagler [1], C.S.T. Daughtry[2], S. N. Goward[1]

[1]University of Maryland, College Park, MD 20742 USA, (301) 405-4050

[2]USDA ARS Remote Sensing and Modeling Lab., Beltsville, MD 20705-2350 USA, (301) 504-5015

Acquiring and understanding the spectral reflectance of two non-photosynthetically active materials, plant litter and soils, is important for interpreting vegetative landscapes. The goal of this research is to develop robust remote sensing techniques to discriminate plant litter from soils. Spectral reflectance of wet and dry soil and litter (crop, forest, and grass) in the 0.4-2.5 μm wavelength range was measured. An absorption feature at 2.1 μm in the spectrum of dry litter, associated with cellulose, was not present in soils. Water absorption dominated the spectral properties of both soils and litter, but discrimination of wet litter from wet soil was possible. Plant litter reflectance is a verifiable component in vegetative landscapes and should be labeled and modeled separately from soils in landscape studies.

INTRODUCTION

Spectral measurements can provide information on land processes. The influence of plant-litter reflectance has generally not been recognized in canopy spectral measurements [4]. Litter affects not only surface energy balance, but also spectral estimates of primary productivity because the green vegetation spectra are altered by the background reflectance. Identification of these background materials will permit landscape models to evaluate the condition and yield of vegetation correctly. Discrimination of litter from soils will allow the quantification of crop residue cover which is important in protecting soils from erosion. Quantification of residue cover is necessary to evaluate the effectiveness of conservation tillage practices.

Visible and near-infrared (VIS-NIR, 0.4-1.1μm) wavelengths do not produce absorption features that can be used to discriminate soils from litter because litter may be brighter or darker than a particular soil depending on many factors, including soil moisture and age of the litter [1]. Although fluorescence techniques were less ambiguous and better suited for discriminating litter from soils than VIS-NIR reflectance methods, several potential problems inhibit the implementation of the fluorescence technique [1]. Elvidge [3] showed cellulose and lignin absorption features at 1.9-2.2 μm in the spectra of dried plants. Subsequent work with spectral reflectance has indicated that these features may be useful for discriminating litter from soils [2].

Thus, defining the reflectance spectra for litter is necessary to describe the vegetative landscape further and to model the terrestrial environment accurately. This research was conducted to (i) provide reflectance signatures for plant litter and soils, and (ii) improve the terminology currently used to define non-green background spectral components.

MATERIALS AND METHODS

Spectral reflectance data over the 0.4-2.5 μm wavelength region were acquired with an IRIS Mark IV[1] (GER Corp., Millbrook, NY) spectroradiometer at 2-4 nm intervals. Samples were illuminated by sixteen 62 W quartz-halogen lamps in a hemisphere painted with $BaSO_4$. The hemisphere provided nearly uniform illumination over an area larger than the field of view of the spectroradiometer. Although the spectroradiometer has dual 2x6° fields of view, it was operated as a single beam instrument, i.e., both sample and reference channels viewed different areas of the same target. The spectroradiometer was positioned at a zenith view angle of 30° resulting in views of two areas approximately 2x7 cm each.

Corn (Zea mays L.) and soybean (Glycine max Merr.) residues were collected from agricultural fields near Beltsville, Maryland on four dates, representing <1, 6, 8, and 10 months after harvest. Tree litter samples included seven samples of conifer (i.e. six pine and one hemlock), and seven samples of deciduous (i.e. two white oaks, two sweetgum, and three mixed canopies of primarily maple, poplar, and sassafras). Samples were collected from forested land near Beltsville, Maryland on four dates, representing aged litter: 1 month, 8 months, 1 year and >1 year. Two samples of grass, tall and short, were collected for three ages. All plant litter samples were dried at 70°C and stored at room temperature. Sample trays (45x45x2 cm) were filled to a depth of 3-5 cm with oven-dried intact residues and the spectral reflectance of the dry samples was measured. Samples were immersed in water for 2 hours, drained and measured wet.

Six U.S. cropland soils (i.e. Barnes, Codorus, Othello, Portneuf, Cecil, Houston Black Clay) and a sand were acquired to represent a wide range of colors and textures. Each soil was oven-dried, crushed to pass a 2-mm screen and placed in the sample tray. Spectral reflectance data were recorded for the dried samples. Soils were then saturated with water and allowed to drain overnight before acquiring spectral data for wet samples.

Nine pairs of spectral data were acquired at different locations on each sample. Reflectance factors were calculated using a Spectralon (Labsphere, Inc., North Sutton, NH) reference panel. Reflectance factors (R) were plotted as a function of wavelength for each sample. A minor discontinuity in the spectra at 1772 nm was associated with a change in

---

[1]Company and trade names are given for the benefit of the reader and do not imply any endorsement of the product or company.

detectors and/or a change in the diffraction gratings. The data surrounding the discontinuity were deleted rather than forced to match.

RESULTS AND DISCUSSION

Plant litter and soils reflectance spectra were measured for the 0.4-2.4 µm wavelength range; however, the first part of the spectrum (0.4-1.1 µm) cannot be used to discriminate between plant litter and soils reflectance spectra [1]. Only the spectra for the 1.6-2.4 µm range are presented in Fig.1. Although 82 litter and 7 soil samples were measured, only representative spectra of three types of litter (Fig.1a) and three soils (Fig.1b) are shown. For each litter and each soil, a pair of spectra is shown; the upper curve is the spectrum of the sample and the lower curve is the spectrum of the wet sample.

A water absorption band at 1.9 µm can be seen in the reflectance spectra of both litter and soils. The cellulose/lignin absorption feature that Elvidge [3] noted in the spectra of dried plants can be seen at 2.1 µm in the dry litter spectra. This absorption feature is not present in the spectra of soils. The difference between litter and soils reflectance spectra is pronounced when the peaks to either side of the cellulose absorption are considered. These shoulder peaks are visible in the litter spectra at 2.0 and 2.2 µm.

For both litter and soils samples, moisture reduced reflectance by approximately 20% (absolute units). For litter, the reflection peak at 2.0 µm, *i.e.* the shoulder of the cellulose absorption, was nearly obscured by the effects of water absorption. This altered the shape of litter spectra; it appears similar to the spectra of wet litter. However, the concavity of the cellulose absorption exists in the litter spectra regardless of moisture.

Five spectral bands (50 nm wide) are indicated along the x-axis of Fig. 1. The water absorption band at 1.9 µm provides information on sample moisture content. The mean spectral reflectance was used to calculate a cellulose absorption index (CAI) as follows:

$$CAI = 0.5 \ (R_{2.0} + R_{2.2}) - R_{2.1}$$

where $R_{2.0}$, $R_{2.1}$ and $R_{2.2}$ are the wavebands centered at 2023 nm, 2100 nm, 2215 nm, respectively.

In Fig.2, CAI for plant litter and soils is plotted as a function of reflectance in the water absorption band (1.9 µm), which is related to sample moisture content. Plant litter samples produced positive CAI values. The soils samples lack cellulose; thus the absence of the cellulose spectral feature in soils is depicted by negative CAI values.

Sample moisture content is implicitly recorded in Fig.2; wet samples had reflectances <25%, while dry samples had >25%

Fig. 1: Mean reflectance spectra of three representative types of litter and soils. The upper curves of litter and soils represent dry samples and the lower curves represent wet samples. Litter spectra are for deciduous trees (dt), coniferous trees (ct), and corn (c). Soil spectra are for Codorus (c), Portneuf (p), and Barnes (b).

Fig. 2: CAI as a function of water band reflectance (1930 nm). Cellulose absorption index (CAI) is calculated as 0.5 $(R_{2.0} + R_{2.2}) - R_{2.1}$, where $R_{2.0}$, $R_{2.1}$ and $R_{2.2}$ are the wavebands centered at 2023 nm, 2100 nm, 2215 nm, respectively.

Table I. Mean percent reflectance in five-50 nm wide bands of wet and dry samples of litter and soils. Cellulose absorption index (CAI) is also presented.

| TYPE | n | Waveband Centers (μm) | | | | | |
		1.6	1.9	2.0	2.1	2.2	CAI
DRY							
CORN	12	50 a[1]	36 ab	42 a	35 ab	39 a	4.89 a
SOY	12	40 b	28 c	32 c	28 c	30 b	3.56 b
CONIF	25	40 b	32 bc	33 c	27 c	29 b	4.06 b
DECID	27	52 a	41 a	44 a	37 a	39 a	3.77 b
GRAS	6	49 a	33 bc	38 ab	31 bc	34 a	4.88 a
SOILS	7	40 b	35 b	38 ab	39 a	37 a	-1.58e
WET							
CORN	12	32 cd	12 d	17 d	18 d	21 c	0.90 c
SOY	12	28 de	12 d	16 de	17 d	19 c	0.80 c
CONIF	25	26 de	9 d	12 de	14 d	16 c	0.50 c
DECID	27	36 bc	12 d	16 d	18 d	21 c	0.26 c
GRAS	6	28 de	10 d	13 de	14 d	17 c	0.66 c
SOILS	7	23 e	7 d	10 e	14 d	16 c	-0.72d
RMSE (df=132)		5.3	4.4	4.7	4.4	4.6	0.54

[1]Within each column, means followed by the same letter are not significantly different according to Duncan's Multiple Range test (∝=0.05).

reflectance. For wet soils, reflectances were <10%, with the exception of the sand which was very bright even when wet. Dry soils samples had reflectance values in the water absorption band >25% with the exception of Houston Black Clay, which held more mo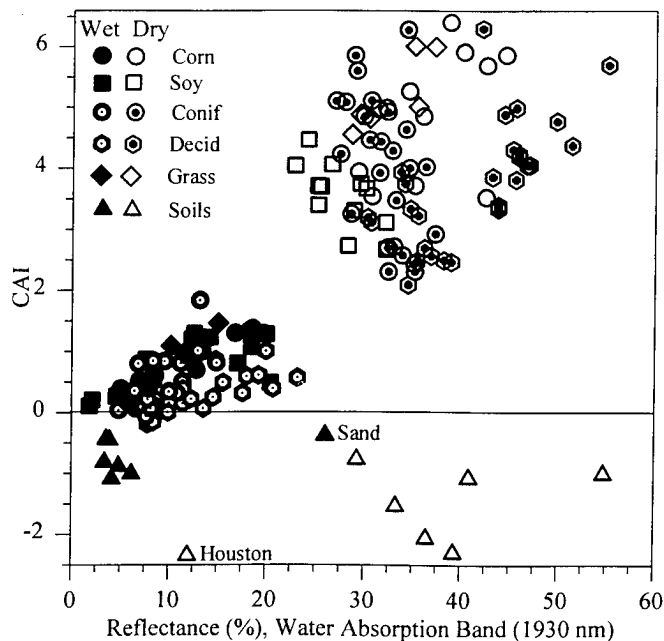isture when air-dried than other soils. For litter, a CAI threshold of approximately 2.0 separated the dry litter from the wet litter. Since reflectance at 2.0 μm is reduced by moisture, CAI is reduced; thus, the CAI range for wet samples is reduced. Moisture makes discrimination of litter and soils more difficult.

All soils had negative CAI values; however, there were five litter samples that also had negative CAI values. The cellulose absorption feature was lacking for three wet deciduous samples and one wet pine sample that were all greater than one year old. These samples were sufficiently decomposed so that the absorption due to cellulose or lignin fibers were easily masked by moisture. A fifth sample with a negative CAI value, >1yr old hemlock, contained soil particles because the decomposed,

1-cm-long needles made the layers difficult to separate from the underlying soil. Excluding these samples made separation of litter and soils possible regardless of moisture content.

A subtle clustering of five dry litter sample types, representing mean reflectance, can be detected from the symbols in Fig.2. For crop residues, the brighter samples are generally the older ones, whereas for tree litter, the brighter samples are generally the younger ones. The reflectance of litter was not significantly different from the reflectance of soil in the five bands in Table I. In some cases, the litter was brighter than the soil and in other cases, the litter was darker. Only CAI consistently discriminated litter from soil; the values were positive for litter and negative for soils. Dry samples had significantly higher reflectance and CAI values than the wet samples.

CONCLUSION

Forest litter, crop residues, senesced grass, and soils spectra provided data on background spectral reflectances. Information about the spectral behavior of the cellulose feature in the shortwave infrared wavelengths provided a way to index the reflectances and distinguish most litter from soils. The ability to discriminate plant litter from soils using CAI will allow background components to be identified and will provide a more accurate spectral green vegetation estimate. CAI may also be used to distinguish crop residues from soils and may be used to quantify crop residue cover.

REFERENCES

[1] C.S.T. Daughtry, J.E. McMurtrey III, E.W. Chappelle, W.P. Dulaney, J.R. Irons, and M.B. Satterwhite. 1995. Potential for Discriminating Crop Residues from Soil by Reflectance and Fluorescence. Agronomy Journal 87: 165-171.

[2] C.S.T. Daughtry, P.L. Nagler, M.S. Kim, J.E. McMurtrey III, and E.W. Chappelle. 1995. Spectral Reflectance of Soils and Crop Residues. Proc. 7th Int. Symposium on Near Infrared Spectroscopy, Montreal, Quebec, Canada.

[3] C.D. Elvidge. 1990. Visible and Near Infrared Reflectance Characteristics of Dry Plant Materials. International Journal of Remote Sensing 11: 1775-1795.

[4] S. N. Goward, K.F. Huemmrich, and R.H. Waring. 1994. Visible-Near Infrared Spectral Reflectance of Landscape Components in Western Oregon. Remote Sensing of Environment 47: 190-203.

Using Laser Echo Recovery and a Scannable Field-of-View Telescope to Determine Vegetation Structure and Sub-canopy Topography over Wide Swaths

J. Bryan Blair

Laser Remote Sensing Branch, Code 924, NASA Goddard Space Flight Center
301-286-9809, 301-286-1761(FAX), bryan@eib2.gsfc.nasa.gov

David J. Harding

Geodynamics Branch, Code 921, NASA Goddard Space Flight Center

D. Barry Coyle

Physics Department, The American University

ABSTRACT

Building upon several years of aircraft laser altimetry development, a system capable of mapping surface height distributions across wide, nadir-centered swaths has recently been developed at NASA/Goddard Space Flight Center. The Laser Vegetation Imaging Sensor(LVIS) system (Fig. 1) can be used to construct maps of precise surface elevations and three-dimensional vegetation canopy structure. The quality of the derived data products as well as satellite-like footprint sizes are maintained using novel laser output and receiver Field of View (FOV) scanning techniques.

The sensor concept is based on rapidly scanning a laser beam and the telescope FOV across the flight track of the aircraft using small, galvanometer-controlled mirrors. The laser transmitter was custom designed and built in-house to achieve 10% wall-plug efficiency in a compact, rugged package. The laser output pulse is 2 nsec full-width at half-max (FWHM), with a 500 Hz pulse repetition rate and 6 mJ output energy evenly split into 1.064 nm and 0.532 nm wavelength channels. A multiple pass pump scheme along with diamond substrates at electrically isolated interfaces reduce the amount of heat coupled to the laser enclosure through variable conductance heatpipes (VCHPs). The VCHPs maintain the pump diodes at their optimum temperature to 2 C in an external temperature range of 5-35 C. The passive operation of the VCHPs imposes none of the excessive power draw normally associated with thermal control systems. The telescope was custom designed to have an efficiency of > 85%, a 20 cm aperture, a 6° potential FOV, and 0.5° instantaneous FOV that is movable to any position within the potential FOV within 2 msec. The telescope aft optics allow the use of bandpass filters and dichroics in collimated light, thus permitting multiple channels. The system as built has 1.064 nm and 0.532 nm receive channels with the capability of adding multiple polarization channels. The return echo from each channel in the system is recorded using a 500 MHz, 8-bit waveform digitizer and stored. The instantaneous FOV is focused to a 1 mm spot allowing the use of low noise, high bandwidth detectors. The data products that this system can produce range from simple topographic mapping swaths (i.e. dense grids of x,y,z data)to 3-dimensional vegetation structure

mapping. Using the waveform digitizer to capture the return echo from each channel allows us to reconstruct the surface height distribution(SHD) from within each laser footprint. Tree heights, canopy architecture, and surface elevation and roughness beneath canopies can be extracted from the return echo. Adding the 2-color capability allows normalized difference vegetation index (NDVI) measurements through the entire depth of the canopy with 30 cm vertical resolution, thus providing a measure of leaf surface area height distributions. The raster scan pattern of contiguous footprints resulting from positioning the laser beam and telescope FOV across the aircraft flight track covers 100% of the underlying terrain. The 100% coverage greatly simplifies the map making process with assurance that no area was unsampled. Statistical analysis of derived SHDs, local surface slopes, and roughness data can thus be performed without making any a priori assumptions about the nature of the slope/height distributions.
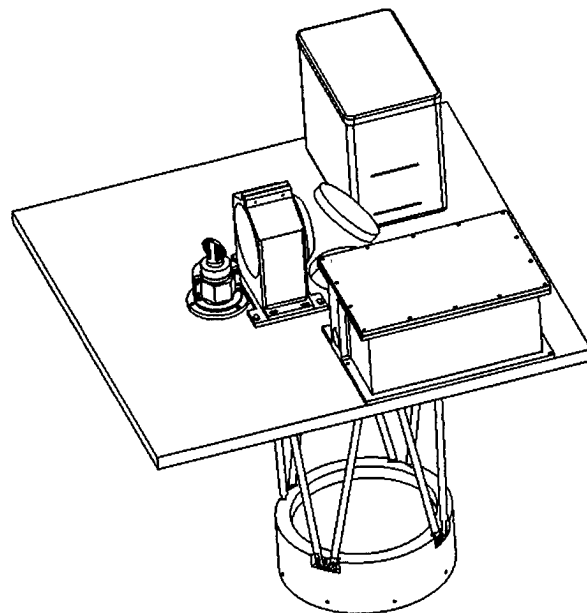

Fig. 1 LVIS Instrument

INTRODUCTION

Laser altimetry provides a unique method of directly measuring vegetation vertical structure and sub-canopy topography over large areas. By recording the entire return echo for each pulsed laser shot, the distribution of intercepted surfaces within each laser footprint can be directly determined. Over vegetated topography, such surfaces include leaves, needles, branches and any underlying open ground surface. With this instrument, LVIS, we measure this distribution of surfaces for each laser footprint at a rate of 500 Hz while rapidly scanning the laser footprint in a raster pattern across the aircraft flight track. The telescope FOV is simultaneously scanned to follow the laser footprint. Galvanometers, provided by Cambridge Technology Inc. Watertown, MA., are used to scan the output laser pulse and the receiver FOV. An added advantage of randomly positionable scan mirrors is the ability to compensate for aircraft roll motion to center the data swath beneath the aircraft flight line in real-time. The final data set is a nadir-centered, 3-dimensional volume representation of the scanned surface. From this data we can remove the vegetation to reveal only the underlying terrain or provide a map of canopy architecture and height.

MEASUREMENT CONCEPT

An important feature of this system is the high temporal resolution digitization of the return echo from each channel, allowing the surface height distribution (SHD) within each footprint to be reconstructed. By performing simple analysis on each laser return echo, vegetation extent and density as well as the elevation of the underlying terrain can be extracted. Applications for this data range from precise mapping of surface elevation of unvegetated surfaces such as sand sheets, glacial flows, and sea ice to determining three-dimensional forest canopy structure and individual tree architecture. Each return echo is a data set in itself in that it provides a sampling of the vegetation height or vertical roughness in that area. By combining many of these samples into an image with 100% areal coverage, one can generate an image of the underlying ground surface for use in hydrologic studies as well as the topography of both the top and bottom of the tree canopy. This data can then be used in model-based studies of the aerodynamics of energy exchange between the atmosphere and the earth's surface. The LVIS instrument can reliably and simultaneously measure all three of the surfaces needed for this critical boundary condition data product, i.e. the top and bottom of canopy and the ground surface.

INSTRUMENT

In the design of this new type of scanning laser altimeter, maintaining instrument performance levels equivalent to
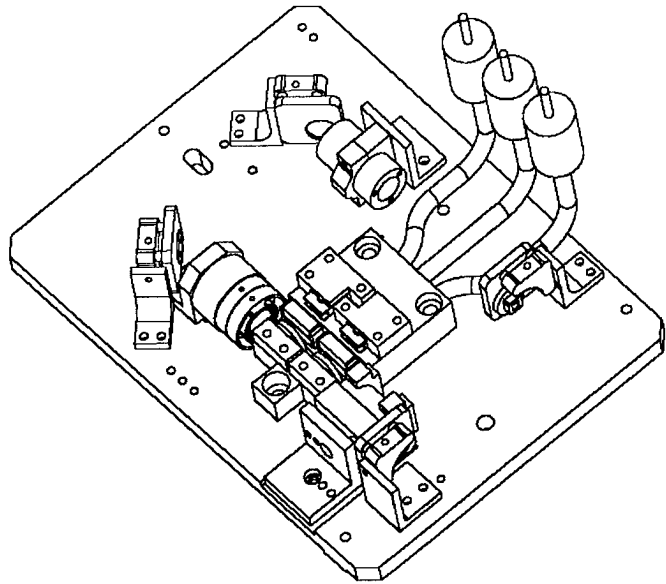

Fig. 2 Laser Cavity (note: VCHPs)

previous profiling vegetation sensing systems [1] was a critical driver. Signal-to-noise ratios had to be maintained and specifications such as detector bandwidth and digitization rate were modified to increase the performance. The quality of the data product is strongly linked to the quality of the recorded return echo. Throughout the system, modifications were engineered to reduce input paths for noise sources and to maximize the SNR of the return signal. The output power of the laser has been significantly increased and the output pulse width has been reduced by a factor of two (i.e. from 4 down to 2 nsec FWHM). The most difficult aspect of the receiver design was combining the large aperture, large FOV telescope with the small, ~1 mm, detector into a single package. The solution that we arrived at was to scan the FOV of the telescope to create an instantaneous FOV over the laser footprint. To keep up with scan rates approaching 500 Hz, the size of the scan mirror and the full sweep scan angle were both minimized.

SCANNING FOV TELESCOPE

The receiver system consists of a 20 cm telescope mounted to the bottom surface of a light-weighted interface plate. On the top surface rests the 10 cm turning mirror, an eyepiece, galvanometer, beamsplitters, condenser optics, and detectors. The 10 cm turning mirror is at 45 degrees to the plate surface in order to bring the light into the plane of the interface plate. This is followed by the eyepiece that collimates the desired FOVs into 2.5 cm beams and then by the beryllium scan mirror mounted to the galvanometer. The galvanometer is mounted such that the shaft is pointed upwards to allow access to the scan mirror after assembly. The scan mirror selects a collimated beam from the selected FOV to image onto the detector face. The different images are distinguished by their incident angle to the scan mirror.

The width of the scan mirror is 2.5 cm/cos[max scan angle]. To minimize the size of the scan mirror, the center scan angle at which the mirror is mounted is ~32°. Since the total FOV of the telescope is 6° and it has a magnification of 8X, the mirror must move ±12° (i.e. ±3 x 8 / 2 (mirrors double the angle) = ±12). If the mirror were centered at 45 degrees then it would have to be large enough to redirect the entire 2.5 cm beam even at an angle of 57°. With the scan centered at 33°, the maximum angle is 45°. A smaller angle could be used, but the reflected beam begins to impinge on the eyepiece assembly at smaller angles.

HIGH-EFFICIENCY LASER TRANSMITTER

To investigate how to meet all the unique requirements of the laser transmitter (Fig. 2) for LVIS, a complex computer model of laser cavities was utilized [2]. The design was optimized for efficiency, while meeting the pulse-width, mode shape, pulse rep-rate, and output power requirements. Some of the general parameters of the laser are: 500 Hz, 6 mJ (3 mJ at 1.064 um and 3 mJ at 532 nm), 2 nsec FWHM pulsewidth, ~10% wall-plug efficiency. Passive thermal control allows operation at ambient temperatures between 10 C and 40 C. To achieve the desired 10% efficiency, several aspects of the laser design were optimized. First, to allow the use of passive thermal control, laser diodes that could operate efficiently at high temperatures (~45 C) were selected. The thermal path for removing the waste heat was optimized by using diamond substrates to electrically isolate the diodes (i.e. diamond has a thermal conductivity 3X that of copper) and then heat pipes were implemented to act as a thermal short, transferring waste heat to the laser enclosure. Since the diodes need to be temperature controlled to maximize the absorption in the YAG crystal, variable conductance heat pipes(VCHPs) were used. With VCHPs, the evaporator(diodes) temperature can be maintained over a wide range of condenser(enclosure) temperatures. This is achieved by attaching a reservoir of gas to the condenser end of the heat pipe. The gas expands and contracts with the evaporator temperature, thereby changing the pressure inside the heat pipe. Due to the fact that the efficiency at which the heat pipe transfers the heat from the condenser to the evaporator is related to the pressure in the heat pipe, the higher the pressure, the more efficient the heat pipe. Therefore, at higher ambient temperatures there is less of a temperature gradient across the heat pipe and at lower temperatures there is a greater gradient. By tuning the amount of gas and working liquid in the heat pipe for a specific amount of waste heat and ambient temperature range, the heat pipe can passively maintain the condenser at a set temperature to within ±2° passively. In building a single-mode, short-pulsed laser, relatively few laser pump diodes are used, thus making the absorption of diode light in the YAG crystal highly temperature dependent. To lessen this temperature dependency while at the same time
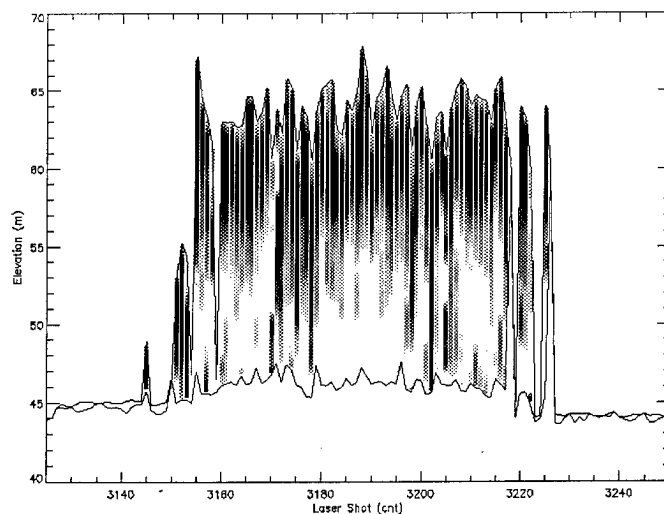
Fig. 3   Example Data from 5 Beam Laser Altimeter

increasing the absorption in the crystal, a 4-pass pumping scheme was devised. Each pump pulse from each diode passes through the YAG crystal 4 times. This greatly increases the total absorption and reduces temperature dependency.

SUMMARY

This system, LVIS, has been developed to produce high accuracy, geolocated topographic mapping data as well as 3-dimensional vegetation volume data sets. . LVIS will be especially useful in determining tree canopy structure (Fig. 3), but future applications will include topographic mapping of ice sheets and glaciers, volcanoes and coastal erosion.

ACKNOWLEDGMENTS

REFERENCES

[1] J.B. Blair, D.B. Coyle, J.L. Bufton, and D.J.Harding, "Optimization of an Airborne Laser Altimeter for Remote Sensing of Vegetation and Tree Canopies" Proceedings of IGARSS'94, Vol. II, p. 939-941(1994).

[2] B. Coyle, D. Guerra, D. Kay, "An Interactive Numerical Model of Diode-Pumped, Q-Switched / Cavity Dumped Lasers" Journal. Phys. D, 28, pp. 452-462 (1995).

An Active Optical Remote Sensing System for Vegetation Index Determination

James E. Kalshoven[*] and David P. Rosten[+]

[*]NASA Goddard Space Flight Center, Laboratory for Terrestrial Physics/924, Greenbelt, MD 20771
Voice: (301) 286-8506, FAX: (301) 286-1757, Kalshoven@gsfc.nasa.gov
[+]Ressler Associates, Inc., 14440 Cherry Lane Court #212, Laurel, MD 20707
Voice: (301) 206-3232, FAX: (301) 953-7622

Abstract -- An airborne hyperspectral remote sensing system, initially for use to verify theories for rapid, accurate determination of vegetation indices, is described. The system, called AVIS (Airborne Vegetation Index Sensor), is mounted on a helicopter and employees a Xenon flash lamp to illuminate the Earth's surface. The backscattered radiation is measured with better than 10 nm resolution in the visible and near-IR over a shiftable 400 nm bandpass. Background subtraction is used for daytime flights. By its nature, AVIS measures the hot spot, resulting in no shadowing. It is a versatile system, minimizing atmospheric effects and eliminating view angle variables and other ambiguities and assumptions associated with general algorithm development and verification which arise when using the sun as a test source.

INTRODUCTION

Although being introduced at a slower pace in a tighter fiscal environment, new technology and techniques to collect the data needed in parameterizing the Earth's various biomes continue to be proposed and adopted. Assumptions used in some earlier, now archived, data sets often limit or prevent their use. To meet the demand for developmental data, with minimal restrictive assumptions, an active, hyperspectral optical airborne instrument has been developed: AVIS, the Airborne Vegetation Index Sensor, was funded by the NASA Small Business Innovative Research (SBIR) Program because of potential commercial application. Among other applications, AVIS' measurements can verify and complement space borne measurements for NASA's Mission to Planet Earth,

Straight forward in its technology, AVIS was conceived as a remote sensing instrument by the first author in 1992 after reviewing a paper by Curran [1] on problems arising in the determination of green leaf area index (GLAI). During the design of AVIS under the SBIR grant, enhancements were made to meet criteria for higher resolution, total bandwidth, and sensitivity to make the system specifically applicable to measurements proposed by Hall, Huemmrich and Goward [2]. Their proposal for measuring the fraction of absorbed photosynthetically active radiation, f_{apar}, and leaf area index uses second order derivatives of the spectrum to reduce the effects of non-photosynthetically active material bene th the canopy.

SYSTEM

AVIS provides its own light source and spectrograph receiver. It is shown in Fig. 1 mounted on the side of the NASA UH-1D stationed at Wallops

Figure 1. AVIS mounted on NASA helicopter.

Flight Facility. The system is rather large, primarily due to the telescope optics needed to direct and focus the lamp energy. From its vantage point in flight, the data is acquired far enough above ground that the view angle is effectively 0°. This results in no shadowing by leaf material.

The system consists of a Xenon flash lamp driven at 2 Hz to give 2 Joules per pulse. A 65 cm, f /3.6 parabolic reflector directs the light from the Xenon lamp. It gives a measured divergence of about 15 x 35 mrad, which translates to a surface spatial resolution of 2.5 x 5.25 meters from an altitude of 150 meters. The spectrograph is a grating type feeding a 512 element intensified linear CCD detector array. Alignment was made using a calibration source to give a working spectral range from about 460 to 840 nm. This total range can be shifted. For reference, a color video camera is used to record the scene. Fig 2. shows a frame taken from that video over a soybean field near a road. The 2 cm glow in the center is the flash. (A monochrome image reproduction is used here.)

Data acquisition is done using a basic DX 486 PC with appropriate A/D conversion of the CCD data stream. The data is permanently stored in binary format in real time. Custom software is then used to

Figure 2. Flash, in center, as recorded on video over soybean field near a road. Time is given to seconds, with the last two digits being video frame count.

convert this data as needed, with various user selectable options, to standard space, comma, or tab delimited text with identifying headers for use in any spreadsheet or scientific analysis program.

OPERATION

In order for an active optical remote sensing system to be effective, proper calibration is necessary. While the outgoing flash is monitored by photodiodes at different wavelengths, initially it was thought that specular reflection off of the surface of a body of water would be ideal for measuring the flash characteristics. However, the weight of the AVIS platform, about 150 kilograms, and its location on the side of the helicopter, caused the helicopter's normal to point slightly off nadir in flight. This resulted in a flash irradiance that was, typically, not backscattered off the surface directly back to the helicopter. The signal that was received arose from backscatter from below the water surface. This was immediately apparent when the data was examined and a spectral effect in the near-IR was observed due to flora in the water (see below).

It was therefore decided, in order to get a convenient yet reliable calibration, to use the somewhat lambertian runway tarmac at Wallops as the calibration reference. The tarmac's actual reflectivity was acquired using the Field Spec FR spectroradiometer from Analytical Spectral Devices and a barium sulfate reference plate. Once an in-flight flash reflectivity was taken over the tarmac and corrected for the tarmac spectral response as measured on the ground with the spectroradiometer, a calibration curve was produced and stored for each flight.. Sometimes curves were taken before and after a flight, but the system proved stable enough to make this unnecessary. The repeatability of the tarmac reflectivity at different locations at the air field is so good that it can be represented in general by a spectral response with increasing reflectivity from 450 to 850 nm, an increase of about 25%. Measurements made on concrete had similar response, so that AVIS can be well calibrated out at
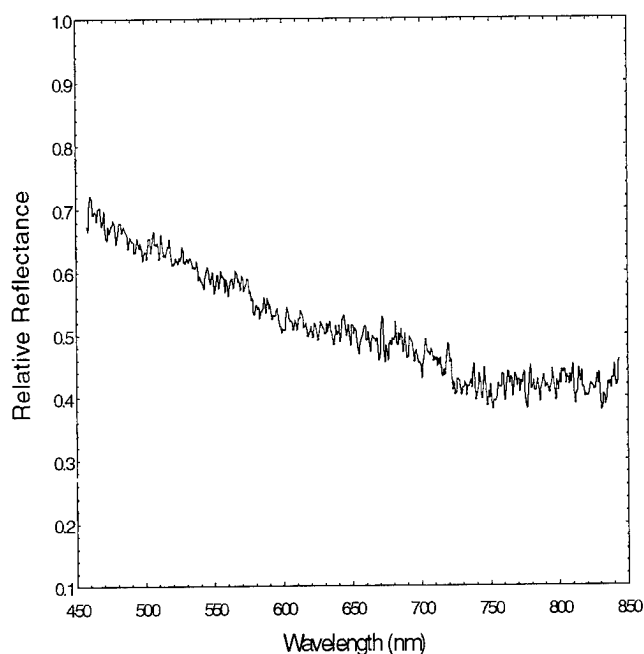
1810

Figure 2 Spectral response of shallow water. Note compensating response above 700 nm due to underwater plant material.

any location without custom ground measurements of the local airport tarmac spectral response. A flight over the tarmac itself is still necessary, of course, to allow for possible flash lamp spectral
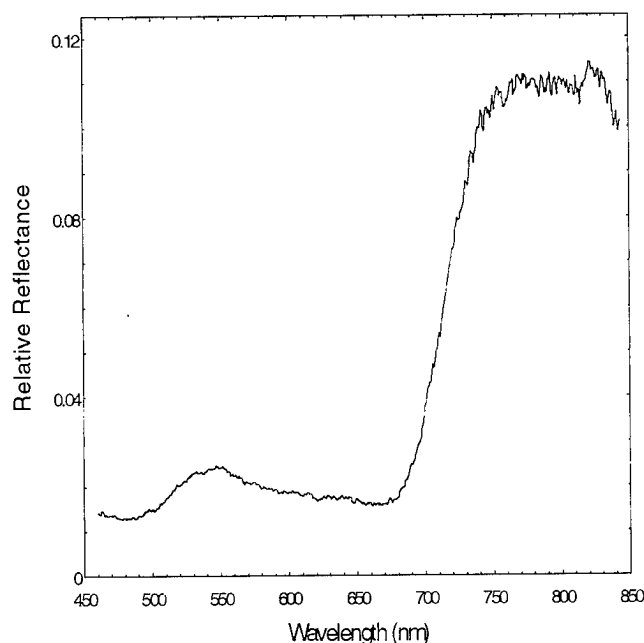

Figure 3. Spectral response from flash backscatter off pine tree canopy.

shifts with age and mechanical vibration over time during and between flights.

Background readings of the surface are made between flashes and used to normalize the flash energy. Using the calibration curve developed with the tarmac, the response of shallow water near the Wallops Flight Facility is shown in Fig. 2, which is from a single flash. As can be seen, the spectral response falls off with wavelength up to about 700 nm where it levels off. This is due to plant material in the water and the increased reflectivity in the near-IR. This is illustrative of the inappropriateness of using water for calibration.

APPLICATIONS

Fig. 3 shows the spectral response obtained over a coniferous tree with a single flash. The higher noise in the near IR is due to the fall off in energy at those wavelengths by the Xenon lamp. Applications to agriculture are also being investigated with the USDA's Remote Sensing and Modeling Laboratory at Beltsville, MD, while the next major application planned for AVIS will involve blocking the Xenon flash energy at wavelengths longer than about 500 nm for fluorescence studies of the surface biomass in the red and near-IR. In addition, AVIS' origins in NASA's SBIR program also speak to a desire to commercialize this system or its equivalent. Overall, AVIS is a conceptually simple, but a scientifically and technically effective new remote sensor.

REFERENCES

[1] P.J. Curran, "Multispectral remote sensing for the estimation of green leaf area index," Phil. Trans. Roy. Soc. London, vol. 309, pp. 257-270, 1983.
[2] F.G. Hall, K.F. Huemmrich, and S.N. Goward, "Use of narrow-band spectra to estimate the fraction of absorbed photosynthetically active radiation," Remote Sens. Environ., 32, 47-54, 1990.

OPTIMAL FLUORESCENCE EXCITATION WAVELENGTHS FOR DETECTION OF STRESS IN VEGETATION

L. A. Corp[1], J. E. McMurtrey[2], E. W. Chappelle[3], M. S. Kim[1], and C. S. T. Daughtry[2]

[1]Science Systems and Application Inc., 5900 Princess Garden Pkwy., Lanham, MD 20706
Phone: (301) 504-6616   Fax: (301) 504-5031
email: moonk@ltpmail.gsfc.nasa.gov

[2]Remote Sensing and Modeling Laboratory, ARS, United States Department of Agriculture
Beltsville, MD 20705, U.S.A.

[3]Laboratory for Terrestrial Physics, NASA/GSFC, Greenbelt MD 20771

Abstract - Considerable efforts are being directed by many research groups toward the development of instrumentation to excite and remotely sense fluorescence of vegetation at the field and forest canopy levels. Green vegetation when exposed to appropriate wavelengths of light, dissipates a portion of the absorbed energy as light emissions (fluorescence) in several broad areas of the spectrum. Currently, leaf level fluorescence emissions have been broken down into five primary regions of the spectrum, namely; ultraviolet (UV), blue, green, red, and near-infrared (NIR). Optimal excitation wavelengths for the UV, blue, and green fluorescent areas are bands centered at 284 nm, 340 nm, and 380 nm respectively. The red and NIR fluorescent emissions can be excited within the broad wavelength region from 250 to 675 nm with excitation peaks at 430 nm, 470 nm, 600 nm, and 660 nm. The ratio of red to NIR fluorescence excitation spectra produced a ratio spectrum. The relative differences between these two emission bands are not constant and depend on the wavelength of excitation. Fluorescence sensing systems based on the above emission bands are being developed for ground based mobile vans, helicopters, and small aircraft. The goals of these efforts were to determine the optimal regions of the spectrum to excite vegetation in order to differentiate plant stress condition based on fluorescence emission bands.

INTRODUCTION

Vegetation, when exposed to long wave ultraviolet (UV) radiation of sufficient energy, dissipates a portion of the absorbed light energy as fluorescence with emission maxima near 450, 525, 685, and 740 nm [1]. The broad blue-green fluorescence band ranges from 360 to 650 nm with a principal maximum at 450 nm and a shoulder near 525 nm. The blue-green fluorescence is a convolution of emissions corresponding to several plant constituents. Part of the dynamic portion of the blue band fluorescence has been attributed to the water soluble compound nicotinamide-adenine dinucleotide phosphate in the reduced form (NADPH) with the more static portion due to relatively inert structural compounds such as polyphenolics and lignin [2].

A UV band of fluorescence with an emission maximum near 335 nm results when vegetation is excited with 280 nm radiation and is primarily due to proteins containing the aromatic amino acid tryptophan (TRP)[3,4]. Pure ribulose 1,5-bisphosphate carboxylase (rubisco), which constitutes up to 70% of the soluble plant proteins, exhibits fluorescence characteristics in accordance with a TRP containing plant protein and is believed to have a significant contribution to the UV band fluorescence. Furthermore, it has been established that the fluorescence emission emanating from intact vegetation is proportional to the nitrogen fertilization level [3].

Under optimal growth conditions the majority of light absorbed by plant chlorophylls and carotenoids is utilized in photosynthesis with less than 3% of the absorbed light energy being dissipated as heat or fluorescence emissions near 685 (red) and 740 nm (NIR). The magnitude of these fluorescence emissions on exposure of a plant to light are governed by chlorophyll concentration and photosynthetic activity. The primary roles played by certain nutrients in photosynthesis and chlorophyll synthesis suggest that nutrient deficiencies could be detected on the basis of changes in these fluorescence emissions [1]. The majority of red fluorescence emission has been attributed to chlorophylls associated with photosystem II (PS II) while the NIR fluorescence emission has been attributed to antenna chlorophylls of Photosystem I (PS I) [5]. The fluorescence ratio 685/740 nm could relate to changes in the distribution of excitation energy between the two photosystems and has been extensively studied as an indicator of chlorophyll content and stress condition in plants [6]. In addition, several studies have demonstrated that linear and curvilinear relationships exist between certain ratios of fluorescence maxima to pigment concentrations and rates of photosynthesis [2,7].

The goals of this study were to; define the optimal excitation wavelength or wavelengths to maximize emissions from the five primary fluorescent areas, identify regions of the spectrum which are best suited for excitation of multiple fluorescent emission bands, and identify excitation and the corresponding emission bands best suited for the detection of nitrogen stress in vegetation.

METHODS

A spectrofluorometer was used to collect fluorescence excitation and emission spectra from greenhouse grown soybean plants. The spectrofluorometer utilizes two 0.22m double monochrometers. The excitation monochrometer was attached to a 450 W xenon lamp that allowed variation of the excitation radiation. The emission monochrometer was attached to a photon-counting photomultiplier tube corrected to obtain linearity throughout the emission wavelength range of 290 to 850 nm while voltage readings were converted to photon counts per second (cps). Fluctuations in lamp intensity were corrected by a beam splitter that delivered a portion of the excitation radiation to a rhodamine dye cuvette. The fluorescence response of rhodamine dye was monitored by a silicon photo diode. This response was used to generate correction factors for minimizing the effect of changes in lamp intensity as a function of wavelength. Excitation spectra were acquired by fixing the emission wavelength (usually at the fluorescence emission maximum) and recording emission intensities while stepping through a shorter wavelength region of the spectrum. Conversely, emission spectra were obtained by fixing the excitation wavelength and recording emission intensity while stepping through a longer wavelength region of the spectrum. Both excitation and emission spectra were acquired at a 1 mm slit width yielding 1.7 nm resolution. Leaf samples were held in place by an anodized aluminum solid sample holder.

RESULTS AND DISCUSSION

UV Emission Band

Illumination of a healthy soybean leaf with 280 nm radiation produced multiple fluorescent emissions in the UV, blue, green, red, and NIR regions of the spectrum (fig. 1). The excitation spectrum shown in fig. 1 indicates dual excitation maxima the first centered at 232 nm and the second centered at 284 nm. The symmetry and location of these two excitation maxima closely resemble the absorption maxima of TRP (in aqueous solution) which is the primary chromophore within proteins for this fluorescence emission [4].

UV band fluorescence decreases in intensity with nitrogen deficiency while the excitation distribution remains much the same. Selection of excitation wavelengths near 284 nm will maximize the fluorescence emission at 335 nm while providing additional information in the remaining four bands of fluorescence. The ratio of the UV band maximum to the blue band maximum when excited near 284 nm has proven useful in assessing nitrogen fertilization level [3].

Blue/Green Emission Bands

Illumination of the same leaf material with 340 nm light yields multiple fluorescent bands (fig. 2) with maxima in the blue, green, red, and NIR consistent with those reported by other scientists [1]. The blue band emission maximum when excited at 340 nm, was 20 % more intense than when excited

at 280 nm. Some of the compounds that are suspected to contribute to the convoluted blue band fluorescence when excited at 340 nm also exhibit absorption characteristics at 280 nm. Although not optimally excited, these compounds are believed to contribute to blue band fluorescence when excited at 280 nm. The excitation spectra shown in fig. 2 indicates that the optimal excitation for in vivo blue fluorescence was 340 nm with more subtle features at 284 and 232 nm. The distribution of the blue fluorescence excitation spectra are not symmetrical and skewed toward shorter wavelengths. This rise in blue fluorescence when excited within the wavelength range of 220 to 300 nm originates from the added intensity by the broad tail of UV band fluorescence. Hence the lack of symmetry in the blue fluorescence excitation spectra is due to the convoluted nature of the UV and blue emission bands of fluorescence.
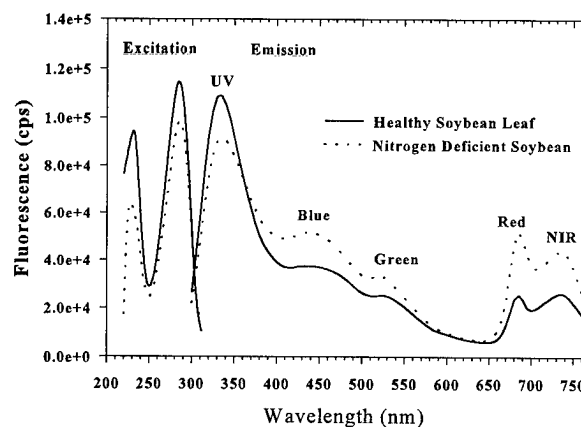
Fig. 1 Healthy vs. nitrogen-deficient soybean leaf fluorescence characteristics. Excitation spectrum was obtained at a fixed emission wavelength of 335 nm (UV band emission maximum). Emission spectrum was obtained at a fixed excitation wavelength of 280 nm.
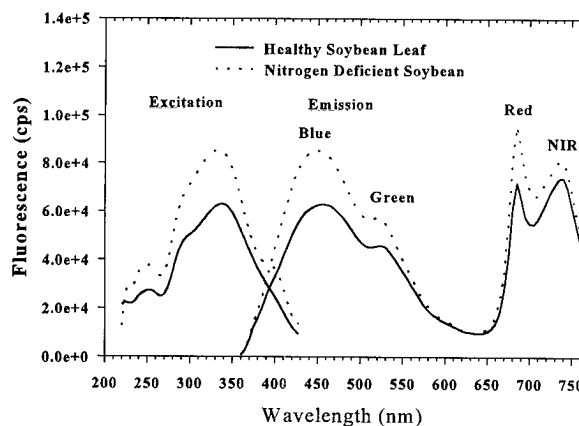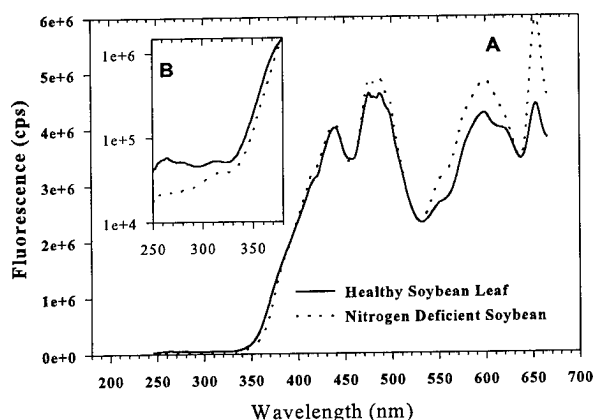

Fig. 2 Healthy vs. nitrogen-deficient soybean leaf fluorescence characteristics. Excitation spectrum was obtained at a fixed emission wavelength of 450 nm (blue band emission maximum). Emission spectrum was obtained at a fixed excitation wavelength of 340 nm (blue band excitation maximum).

Previous research [2] indicated a significant relationship between the fluorescence ratio 440/600 nm and rates of photosynthesis. These studies utilized a nitrogen laser emitting at 337 nm as an excitation source. Our studies would indicate that the nitrogen laser optimally excites blue fluorescence while shifting the excitation wavelength from 337 nm to 380 nm decreases the blue band fluorescence emission by ~43% while increasing; the green emission by ~10%, and both the red and NIR emissions by ~95%. The excitation characteristics of the blue band are similar to the UV band in that with nitrogen deficiency the intensity varies while the distribution remains nearly constant.

Red and NIR Emission Bands

Illumination of vegetation from 250 nm to 675 nm produced multiple fluorescent emissions in the red (~685 nm) and NIR (~740 nm) regions of the spectrum. Excitation spectra for each of these fluorescence emissions are shown in fig. 3 and fig. 4 respectively. Each curve has multiple peaks which relate to the combined absorption of light by plant pigments and its subsequent use in energy transfer reactions of photosynthesis. The intensity of the fluorescence emission as a function of excitation wavelength was directly related to concentrations of plant pigments and inversely related to the efficiency of energy transfer in photosynthesis.

Fig. 3 Healthy vs. nitrogen-deficient soybean leaf fluorescence characteristics. Excitation spectrum was obtained at a fixed emission wavelength of 685 nm (red band emission maximum). The inset in this figure was plotted on a log scale to better display treatment differences.

When assessing fluorescence information in the red and NIR bands independently the greatest differences due to nitrogen fertilization level occur at excitation wavelengths ranging from 560 to 670 nm. The most significant differences occur when these bands are excited at or near 600 nm and 660 nm. Information in the red and NIR bands of fluorescence are influenced by short term fluctuations in the rate of photosynthesis and as a result are highly variable. Whereas information received in the UV, blue, and green bands of fluorescence relate to compounds whose concentration tend to

vary over a much longer time frame.
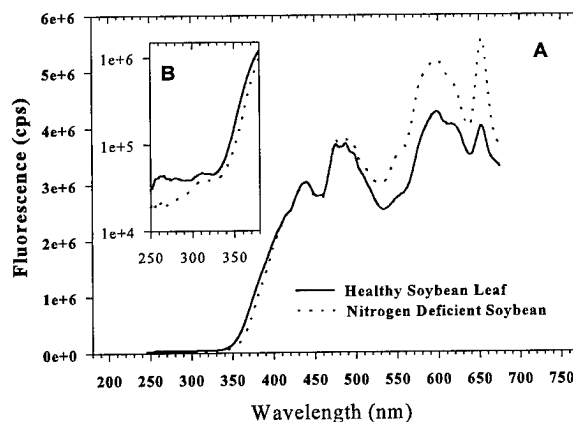
Fig. 4 Healthy vs. nitrogen-deficient soybean leaf fluorescence characteristics. Excitation spectrum was obtained at a fixed emission wavelength of 740 nm (NIR band emission maximum). The inset in this figure was plotted on a log scale to better display treatment differences.

Relative differences between these excitation spectra are better seen through the ratio spectra where the red excitation spectrum was divided by the NIR excitation spectrum (fig. 5, and 6). The distribution of peaks and valleys in this ratio spectrum yield striking similarities to the action spectrum of photosystem I and II (data taken from [9]) (fig. 5). We believe that some of the variation in the ratio spectrum is due to the distribution of pigments between these two photosystems. From the ratio spectra it is apparent that relative differences between the fluorescence emission intensity at 685 nm to that of 740 nm are not constant and depend on the wavelength of excitation.
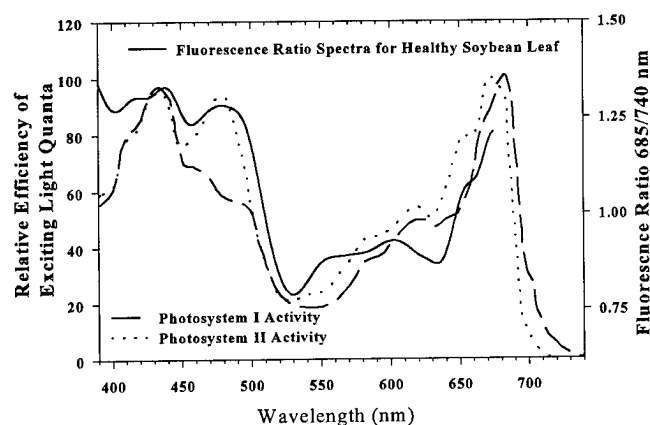
Fig. 5 Comparison between the fluorescence ratio spectrum of a healthy soybean leaf and the action spectra for each of the two photosystems (data taken from [9]).

Substantial differences are noted in the ratio spectra between the control and nitrogen-deficient soybean leaf in the excitation wavelength region from 250 nm to 300 nm. However, emission

intensities are extremely low in this area and may not be detectible at the canopy level. Excitation areas to avoid include regions where the two curves in fig. 6 converge. From these data it would appear that an excitation area at or near 380 nm would yield substantial differences in the red to NIR fluorescence emission ratio in addition to providing information in the blue and green fluorescent regions.
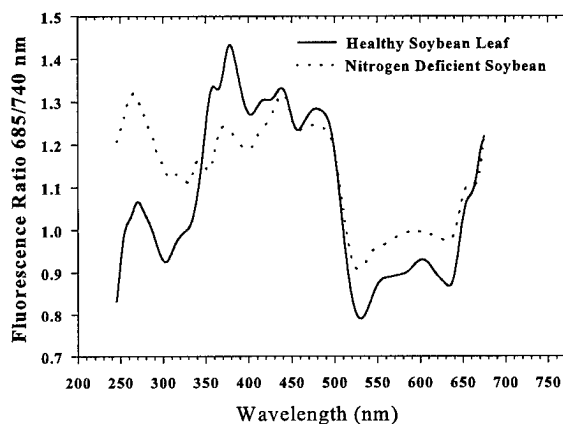
Fig. 6 Healthy vs. nitrogen-deficient soybean leaf fluorescence characteristics. Ratio spectrum was obtained by dividing the 685 nm excitation spectrum by the corresponding 740 nm excitation spectrum.

CONCLUSIONS

Instrumentation for the remote assessment of the UV fluorescence band would be limited in so far as aerial observation due to safety considerations using lasers emitting near 280 nm. Portable ground based instrumentation could easily be fabricated and prove useful in assessing plant vigor. A rapid quantitative measure of nitrogen status would prove useful to many farming systems where substantial investments are made in the application of nitrogen fertilizers.

Important relationships between parameters that influence plant physiology such as rate of photosynthesis and chlorophyll concentration, and optimal excitation region for the 335, 450, 525, 685, and 740 nm fluorescence emissions in vegetation were found. These studies aid in defining the necessary parameters for the development of field instrumentation based on currently available lasers as excitation sources which will maximize fluorescence ratio differences as a function of stress condition. Similar studies need to be undertaken to assess plant stress in species other than soybean and for plant stress resulting from different origins.

The preferred choice for excitation of fluorescence for most field applications is laser light. In the past excitation wavelengths for fluorescence instrumentation have been limited by the availability of lasers. With recent advances in laser technology, the choices of laser emission wavelengths are rapidly increasing. These kinds of studies will aid in the development of new field instrumentation based on laser excitation sources that will maximize fluorescence differences due to stress condition.

REFERENCES

[1] E. Chappelle, F. Wood, J. McMurtrey, and W. Newcomb, "Laser induced fluorescence (LIF) of green plants. II: A technique for the remote detection of plant stress and species differentiation," Appl Optics, 23: 134-138, 1984.

[2] E. Chappelle, J. McMurtrey III, and M. Kim, "Identification of the pigment responsible for the blue fluorescence band in the laser induced fluorescence (LIF) spectra of green plants, and the potential use of this band in remotely estimating rates of photosynthesis", Remote Sens. Environ., 36: 213-218, 1991.

[3] L. Corp, E. Chappelle, J. McMurtrey, M. Kim, "A New Fluorescence Band Obtained by the Excitation of Plants at 280 nm and its Implications to the Remote Assessment of Vegetation", Proc. Internat. Geoscience and Remote Sensing Symp., 2: 986-989, 1994.

[4] Wetlaufer, D. B., "Ultraviolet spectra of proteins and amino acids", Adv Protein Chem 17: 303-390, 1962.

[5] S. Bose, "Chlorophyll Fluorescence in Green Plants and Energy Transfer Pathways in Photosynthesis", Photochem. Photobiol., 36: 725-731, 1982.

[6] H. Lictenthaler, U. Rinderle, "Role of chlorophyll fluorescence in the detection of stress conditions of plants", CRC Critical Rev Anal Chem, 19: 29-85 1988.

[7] H. Lichtenthaler, F. Stober, M. Lang, "Laser-Induced Fluorescence Emission Signatures and Spectral Fluorescence Ratios of Terrestrial Vegetation", Proc. Internat. Geoscience and Remote Sensing Symp., 3: 1317-1320, 1993.

[8] J. McMurtrey, E. Chappelle, M. Kim, J. Mesinger, and L. Corp, "Development of algorithms for detecting nitrogen fertilization levels in field corn (Zea mays L.) with laser induced fluorescence", Remote Sens of Environ, 47: 36-44, 1994.

[9] A. Ried, "Proc. 2nd Int. Congr. Photosynthesis Res.", F. Forti, M. Avron, and A. Melandri, edition, 763-772, 1972.

An Improved Aircraft Underflight Instrument for the Derivation of Band Gains in Satellite Sensors

Peter Abel[1] and Balu Subramanya[2]

[1] NASA/ Goddard Space Flight Center, Code 920.2, Greenbelt, MD 20771
Office: (301) 286-6829, Fax: (301) 286-1757, peter.abel@gsfc.nasa.gov

[2] Hughes STX Corporation, Greenbelt, MD 20771
Office: (301) 286-6439, Fax (301) 286-1757, balu@carnival.gsfc.nasa.gov

ABSTRACT

There is an increasing need for improved in-flight calibration of visible and near-IR satellite sensors to gather reliable information on global climate mechanisms and climate change. Satellite instruments for the near future, such as MODIS and SeaWiFS, require accurate calibration throughout their lifetimes on orbit, and represent a challenging task. Flying a calibrated transfer spectroradiometer on a high altitude aircraft above most of the atmosphere over a uniform and extended radiance target near the subsatellite track during satellite overpass provides the most direct method of independently calibrating satellite sensors. The "High Altitude Underflights to Calibrate Satellite Sensors" (HAUCSS) system, developed by NOAA and NASA under various acronyms since 1980, is described here with emphasis on recent improvements in the system, along with an outline of the satellite instrument calibration method, performance, uncertainty analysis and planned improvements.

The HAUCSS system has recently been used to underfly the GOES-8 imager and NOAA-14 AVHRR sensors. An in-flight radiance calibration source is expected to be used in the future. Future plans also include real time ground station links through an aircraft-TDRSS link for instrument control from ground and real time data viewing.

INTRODUCTION

Satellite radiometry at performance levels useful for earth sciences applications demands technologically challenging levels of long-term absolute accuracy, and in particular must be corrected for normal, but radiometrically significant, changes in sensor radiometric gain on orbit. In spectral regions other than the visible and near-infrared, on-board calibration systems using either an on-board radiometric source or (in the UV) the sun as a source have been used for many years, and for the most part with great success, to address the problem of sensor gain correction. Visible and near-infrared (VISNIR) band on-board calibration has been slow to develop, and the MODerate resolution Imaging Spectroradiometer (MODIS) will be the first sensor with full primary on-orbit calibration capability for these bands when it is launched on the Earth Observing System (EOS) AM platform in 1998 [1].

Vicarious (ground and aircraft-based) calibration has been found necessary to adequately calibrate sensors with VISNIR bands in the past [2]. With the use of sensors in the near future to evaluate long-term Global Change, and the concomitant requirements for higher gain stability, it is clearly necessary to continue such measurements into the future for VISNIR sensors without on-board calibration. Plans are now being developed to validate the performance of the as yet unproven MODIS on-orbit VISNIR calibration technology both during its introduction to the space environment and other critical periods and, at a less intense level, throughout the lifetime of the sensor.

Applications for measured VISNIR radiance and target reflectance data sometimes require only band-to-band relative knowledge (rather than absolute knowledge) of sensor gain changes. An example is the uncorrected Normalized Difference Vegetation Index (NDVI). But absolute sensor gains are required to maintain internal calibration consistency between identical sensors launched on a series of satellites, or between different sensors in orbit at the same time, and for other applications. Relative sensor gain can be established through several related vicarious methods [3, 4, 5] using well characterized surface or cloud targets and radiative transfer modeling; absolute sensor gain can be derived through some of these methods, but is most directly and arguably more accurately measured through congruent path observation of a

surface target with a well characterized sensor on a high altitude aircraft.

This paper describes the design and performance of a dedicated aircraft system, the High Altitude Aircraft Underflights to Calibrate Satellite Sensors (HAUCSS) system, which is the latest evolutionary state of equipment in use by NASA and, before 1989, by NOAA to measure the absolute value of satellite sensor band gain. The method has been described earlier [6], and only a brief summary is given here. HAUCSS is a calibrated spectroradiometer flown on an ER-2 aircraft at an altitude near 20 km, capable of scanning from 0.43 μm to 1.04 μm with a spectral resolving power of approximately 200 and a scan time of a few

typically has an absolute uncertainty of approximately ± 3.8%.

INSTRUMENT DESCRIPTION

The HAUCSS system is a fully automated 1/8m f/4.8 zero dispersion double Fastie-Ebert monochromator, with suitable foreoptics, second order suppression filter mechanism, silicon detector, and a pointing mechanism, flown in a NASA ER-2 aircraft at an altitude of 20 km. A schematic of the spectrometer configuration is shown in Fig 2.
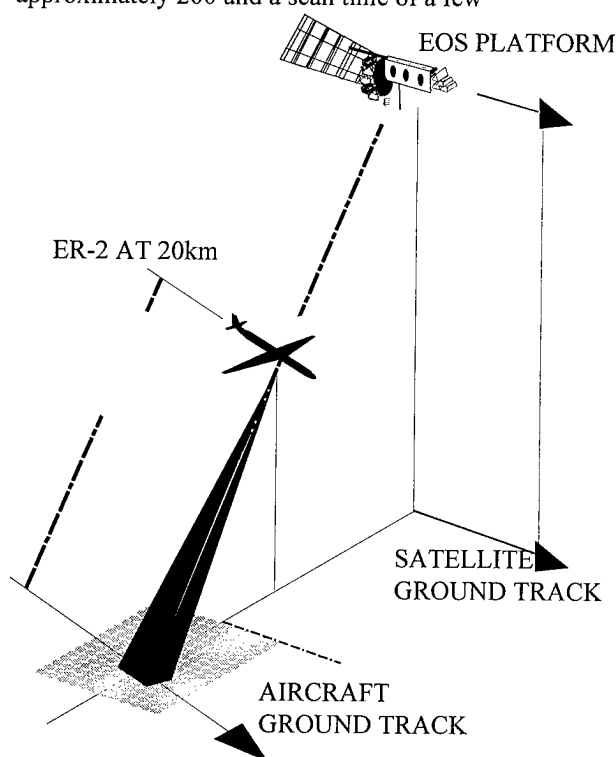
Figure 1: Observation geometry

Figure 2: Schematic of the HAUCSS spectroradiometer.

seconds. It is mounted on a gimbal system that can be aligned (Fig.1) along an overflying satellite's view vector to a suitable sunlit target on the surface. Knowing the satellite sensor band's spectral response from pre-launch measurements, the equivalent satellite target radiance at the aircraft is calculated, and the small correction to satellite altitude (usually <2% for AVHRR bands 1 or 2) is calculated and applied using results from the LOWTRAN code. Spatial correlations between the aircraft and satellite data are used to align the navigation, and corrections are applied to give equivalent HAUCSS and satellite sensor footprints. The result for sensor gain assumes the validity of sensor observations of space view radiometric offset levels, and
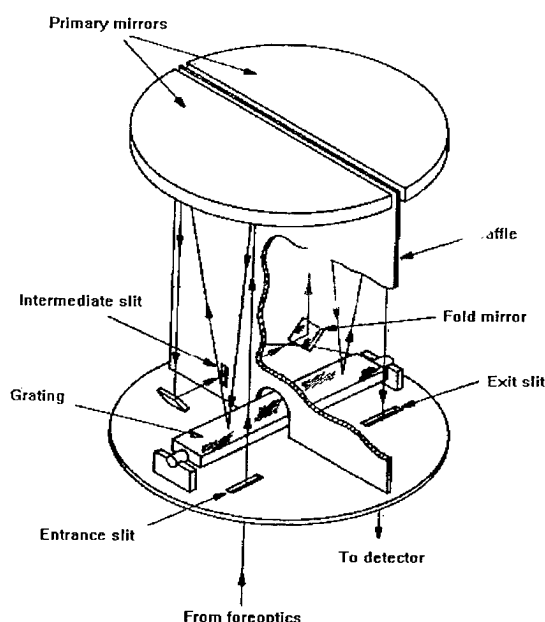
The instrument is mounted on a gimbal in the Q-bay (Fig.3) of an ER-2 aircraft, and observes the surface target through an uncoated quartz window. The Q-Bay is partially environmentally controlled at altitude, maintaining air temperatures between 12-15°C and a pressure altitude around 33k ft, but instrument mounting surfaces can reach temperatures below 0°C. This means that instrument temperatures must be actively controlled. The foreoptics include a telescope using crossed confocal cylindrical lenses to obtain a circular footprint of diameter 2 km on the ground at nadir, a quartz depolarizing element, and a source wheel that can be rotated to introduce a beam blocking plate, a small integrating sphere source, or surface target radiation into the

instrument.. The entrance and exit slits widths are currently set to 0.25mm (x 4 mm high) to obtain the desired resolution of 3.5 nm for GOES/AVHRR calibration. The median slit width is set to 0.5 mm. The detector, along with a thermo-electric controller and amplifier assemblies, is housed adjacent to the exit slit. An EG&G HUV-4000B detector with built-in preamplifier stage in a hermetically sealed windowed package is used. The single grating (1200 g/mm blazed at 500 nm) is controlled by a 4 wire 3 phase stepper motor-driven cam assembly. The system uses a cut-on filter near 380 nm and a switchable second order filter with a cut-on near 700 nm.

Upper hatch
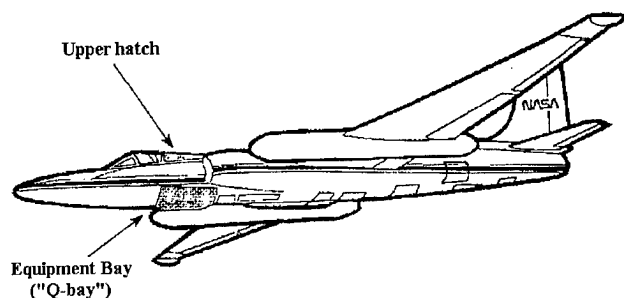
Equipment Bay ("Q-bay")

Figure 3: ER-2 equipment bay location

A chain drive connects the stepper motor assembly to the cam which drives the grating in a linear relationship between cam rotation angle and wavelength. The grating scans the range 430-1040 nm in 320 degrees of cam rotation and is quickly reset during the remainder of a complete cam rotation. The stepper motor is driven with the torque ranges of 70 to

85% of maximum torque at 650-700 sps to minimize mechanical jitter. The residual jitter is insignificant considering the 3.5 nm spectral resolution of the instrument and is not observable in any line source scans. An optical rotational encoder with a resolution of 3600 steps/revolution is also driven by the cam.

ELECTRONICS DESCRIPTION

The system electronics digitizes and stores system data and controls the mechanical subsystems. These functions include digitizing the detector output, controlling the grating and the second order filter mechanism, pointing the spectrometer view axis as a function of time, temperature stabilizing the spectrometer, collecting and storing all system data including aircraft navigation data, and interfacing with the pilot's control console. A diagram of the electronics is shown in Fig 4. Though the Q-Bay is partially environmentally controlled, it still offers a rather hostile environment for the operation of precision instrumentation. Large temperature gradients and electronic noise sources are present in the Q-Bay environment.

Several shortcomings of the previous electronics system have now been removed and additional capabilities added to improve the accuracy and reliability of the measurements. Additional enhancements presently in progress are discussed later in this paper
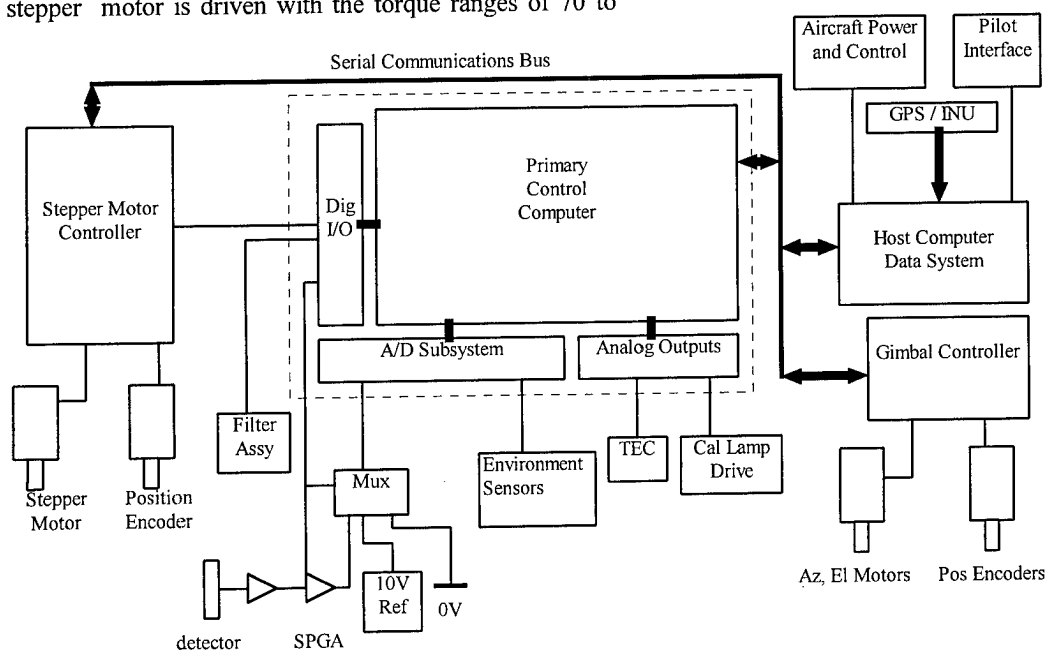

Figure 4: HAUCSS electronic system

The electronics subsystem in its earlier versions suffered from insufficient signal-to-noise ratio and preamplifier bandwidth, bulky cabling (raising aircraft safety and reliability issues), no access to in-flight navigational data and a reliability problem in the filter switching mechanism.

The electronics were redesigned and built to eliminate these problems and to add new capabilities. The present electronics features a low noise pre-amplifier and analog-to-digital converter (A/D) utilizing more efficient signal integration to improve the signal to noise ratio, distributed control to eliminate bulky cabling, a modified second order filter mount with contact sensors for independent position verification, an electronic interface with the aircraft's Global Positioning System (GPS) based navigation system for in-flight navigation data, a optical rotational encoder for the grating for accurate spectral registration and robust hardware with redundancies for critical systems to improve reliability.

In addition, the system provides enhanced diagnostics with flags to indicate many types of system failures and error recovery procedures for each failure, redundancy in diagnostics and data storage for improved reliability, on-the-fly programmable grating motion control, reduced scan times from 10s to about 3.8s, software-programmable A/D integration times, software-programmable amplifier gains for more dynamic range and flexibility, removable data storage media, and an improved information and control display for the pilot in the unlikely event that direct pilot control of the instrument is necessary. An in-flight calibration integrating sphere source and lamp drive electronics have also been added. After passing appropriate tests to assess stability this device will be used in future flights.

The stepper motor controller consists of a dedicated 8751 microcontroller-based embedded controller with onboard non-volatile storage, serial communications link and power drive electronics. This provides on-the-fly programmable variable resolution micro-stepping motion control of the stepper motor.

The detector assembly, consisting of the detector, thermoelectric controller (TEC), and two amplification stages, is housed behind a window at the exit aperture of the spectrometer. The detector has a 100 mm^2 surface area, overfilling the beam exiting the spectrometer. The integration time constant of the amplifier stages is about 1 ms. The second amplification stage is a software programmable gain amplifier with programmable gains of 1, 2, 4, 8 and 16. The signal from the detector amplification stage is fed into the input of the A/D subsystem located outside the spectrometer housing. This consists of a unity gain amplifier, analog multiplexer and an integrating A/D with programmable integration times. The A/D subsystem is located on the primary instrument control computer (PCC)

which is an Analog Devices RDAS 1060 board with a 80188 microprocessor, onboard battery backed RAM, Analog and Digital I/O and EPROM storage with operational and dynamic link routines.

The TEC is mounted on the back of the detector case. The second order filter is mounted at the entrance slit, and is driven by a solenoid which provides the rotational motion to switch the filter into the optical path. A coil spring mechanism switches the filter out to its default position. Contact sensors are positioned to independently verify filter position at both the 'in' and 'out' positions.

With a typical A/D integration time of 10 ms, the effective resolution of the A/D is 17 bits. Though currently the instrument is being flown over bright land targets, there will be a need in the future to observe other types of targets such as dark cloud-free ocean scenes, or ocean with scattered clouds. The system is designed to operate over a wide dynamic range of target radiance levels. Depending upon the target brightness, required signal to noise ratio and required spectral resolution, a slit size will be selected and installed pre-flight to provide adequate energy at the detector along with the gain setting for the programmable amplification stage. Typically the detector is operated at less than 5% of its saturation level. For high contrast scenes the gain of the software programmable gain amplifier can be changed on-the-fly to increase the dynamic range, but this is not being used currently for land targets. The programmable amplifier is controlled by the PCC.

With a 10 ms integration time, the A/D can be sampled at about 80 samples per second. In a typical scan of 3.8 second, the data window is about 3.0 second, with 0.8 second overhead time to switch filter and reset grating position. This gives about 240 data samples per scan or a sample every 2.5 nm.

The PCC has two analog outputs, one of which is used to set the current through the TEC. The PCC monitors this current using a stable shunt resistor and adjusts the current using a proportional-integral algorithm with a time constant of 40 seconds. A 2 pole relay is used to switch the polarity of the thermoelectric controller depending whether it is heating or cooling. The TEC is usually set to control the detector at 14 ± 0.1 °C. This is the expected temperature of the spectrometer chassis in-flight and minimizes temperature gradients in-flight without introducing any danger of condensation near or on the detector.

An 8052-based embedded controller controls the gimbal movement. The gimbal controller and motor drive electronics are located on the side of the gimbal itself. This minimizes the cabling between the host and the gimbal

reducing risk of the cable getting caught in aircraft hardware or snapping. The gimbal azimuth and elevation shafts are attached to optical angle encoders which are interfaced to the gimbal controller. The gimbal controller has all its routines stored in EPROM and battery-backed RAM and starts to move upon command from the host. The bi-directional precision, or repeatability, of azimuth and elevation measured 2.5 and 1.5 degrees respectively. To minimize positioning errors, the azimuth and elevation are always moved from the reset position in the same direction. The unidirectional precision of the azimuth and elevation control measured 0.75 and 0.5 degrees respectively. A large gear ratio in the azimuth and elevation drives ensures that there is no movement in idle mode and makes 'locking' the gimbal with hold currents unnecessary.

The host computer is a 80486-based industrial PC using the industry standard STD-32 backplane. The host computer is interfaced to the aircraft GPS based navigation system using a serial link. Another serial link from the host computer is used for the system serial bus. The host computer is rack mounted at the top of the ER-2 Q-Bay. Also on the rack mount are circuitry to control power from the aircraft 28 V DC bus, a 110 V 60 Hz inverter, ±12V and 5V power supplies for the system power bus and cabling for aircraft interface. The parallel port data lines of the host computer and error input lines are used for pilot interface I/O . The host computer uses a solid state and a PCMCIA hard disk to store software and data. A monitor and keyboard is easily connected to the host on ground when manual operation of the host data system is desired.

The stepper controller, PCC, gimbal controller and the host computer all communicate through the serial bus. The host computer listens to the stepper controller, PCC and gimbal controller and vice versa.

SYSTEM TESTING

It is necessary for the spectrometer's field of view (FOV) to be characterized to be able to determine the ground track footprint and appropriate footprint model in computing equivalent satellite pixel space. It is also necessary to measure the system gain and spectral stability under all operational conditions. For these purposes the FOV was mapped in the laboratory and the spectrometer was tested in a thermal vacuum chamber (T/V) for stability of system gain and spectral response to simulate aircraft flight conditions.

The FOV pattern measured at 632 nm is shown in Fig 5. System gain results showed less than 0.1% variation in gain over the whole range in the region below 550 nm and less than 0.5% variation in the rest of the spectrum with the

system at a pressure altitude of 40 k ft and temperatures of mounting surfaces between 0 and 25 °C. The exact source of this relatively small dependence is not known at this point and is being investigated. No measurable shift in wavelength calibration was observed.

HAUCSS FOV Measurement
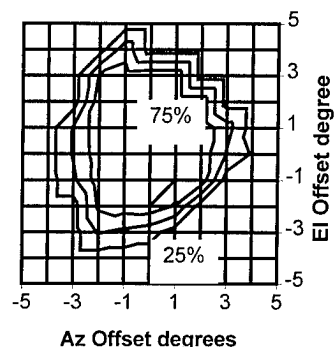
Figure 5: HAUCSS FOV Measurement.

SOFTWARE

The previous data system including all operational and analysis software was redesigned and replaced to accommodate the new electronics and to provide the additional features discussed earlier. The low level and system services routines on the PCC are stored in EPROM. An embedded C compiler from Aztec Corporation was used to compile high level C programs to dynamically link to the EPROM routines. This improves system performance and reduces program size, enabling most of the RAM use for data storage and buffering. The PCC, gimbal controller and the stepper controller have their programs stored in non-volatile programmable storage areas and start up upon applying power. However, the host computer has the capability to download the programs again in-flight or before flight if any errors are detected. Upon power-up all the subsystems perform independent self checks and diagnostics and report to the host computer. Two levels of diagnostics are used. Upon power-up detailed diagnostics are performed once, which takes up to several minutes and in-flight a smaller subset of tests are performed to determine the health of the instrument. If the host computer fails or if the host is not able to reset any of the embedded controllers, a pilot fault signal initiating manual reset by the pilot is generated. Also upon power-up each time, the host computer searches for and reads the most recent configuration from the hard disk or floppy drive. The configuration file contains information like flight leg timings, view vectors, etc., and the host transmits the information to the embedded controllers. This allows for

quick configuration setup and changes before flight. The real time clocks on the host and the PCC are reset to synchronize with the GPS clock upon power up.

The software on the PCC stores the data from 1 data leg, which can be of any reasonable length, in battery backed memory. This is to have a backup of the mission-critical data in case of a host computer storage failure. In addition the data from the aircraft INS is obtained through an asynchronous serial link at the host computer. This data is obtained once a second with a delay of one second. The time reference of this data is incremented by one second and the data is integrated along with the spectrometer scan data.

INSTRUMENT OPERATION

The spectrometer is calibrated before flight using a 76 cm (30") diameter spherical integrating sphere which itself is calibrated using a NIST standard lamp and a transfer spectrometer [6]. This calibration is performed usually 4-6 hours before flight, in the detached Q-bay hatch at the planned flight azimuth and elevation, with the aircraft window in place. The hatch is then integrated with the aircraft and the configuration file loaded. Manual check of cabling and system operation is performed. The window and the hatch are cleaned each time before flight to remove contaminants that may affect the signal.

Typically three data legs are flown for each satellite contact, with the center of one of the legs coinciding within a few seconds of the satellite overpass. Each data leg at present takes about 20 minutes, centered on about 5 minutes of data collection. The remainder of the time is required for the pilot to get into position and turn around at the end of the leg. Before the data legs, the host commands the gimbal controller to set the desired azimuth and elevation angles. The host then starts and stops the data collection at the preset times. Zero radiance baseline data is collected before, after and in between the data legs with the entrance slit blocked by the turret wheel.

The data is stored on the PCMCIA hard disk which is easily removed when the aircraft lands for analysis and archival. Data from the contact leg is also stored on the battery backed RAM as a backup in case there is a hard disk or host computer failure in flight.

The spectrometer is purged with dry nitrogen a few minutes before take off to minimize the chances of water vapor condensation on the optics A hatch heater and heat-wrap around the spectrometer chassis are used to provide additional heating. After the flight typically within a few hours of landing, the Q-Bay hatch and the instrument

subsystems are removed from the aircraft and the calibration procedure is repeated in the same configuration as in the aircraft with the aircraft window in place.

FUTURE IMPROVEMENTS

Several improvements to the system are being currently implemented and planned for the future. A new detector manufactured by Hamamatsu Corporation, S6204, is proposed. In addition to having a built in 2 stage TEC which enables lower detector operating temperatures, the detector has higher detectivity than the current detector at the same temperature. This will allow a combination of increased spectral resolution and greater sensitivity over low radiance targets.

An in-flight radiance calibration source, (an 8W quartz-halogen lamp in a 5 cm diameter integrating sphere), has been added to the turret wheel and will be tested during the next calibration mission. An in-flight wavelength calibration source is also desirable, and suitable designs are being evaluated.

Replacing the existing gimbal mechanism, which has unidirectional repeatability of 1 degree and maximum slew rate about 15 degrees/minute by a commercially available gimbal system with 0.05 degree precision and slew rate of 60 degrees /sec is being investigated.

An ER2-TDRSS link is being established for data downlinking and control command uplinking. Thie link is planned to be tested during the next mission and will enable the manual monitoring and control of the instrument in-flight.
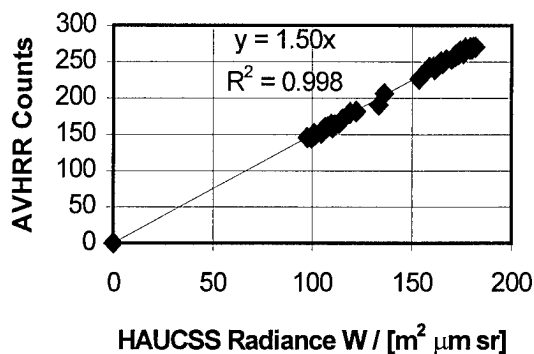
AVHRR Ch1 Counts Vs. Radiance

Figure 6: NOAA 14 AVHRR Band 1 result, July 1995

1821

RESULTS

In its present form, HAUCSS has been used to calibrate GOES-8 Imager in Oct 1994 and NOAA-14 AVHRR in July 1995. Good data quality was achieved on both missions. Fig.6 shows HAUCSS radiance corresponding to AVHRR band 1 (extrapolated to TOA) plotted against NOAA-14 AVHRR band count difference (averaged over the HAUCSS footprint), for the spatial translation corresponding to maximum correlation between the two data sets. The slope of this line represents the HAUCSS solution for the gain of this band. Comparison of these results with those of Rao and Vermote shows agreement within one sigma uncertainty estimates in band 2, but at the 2 sigma level in band 1. Causes for this apparent discrepancy are currently being investigated.

A series of underflights of GOES-9 imager and NOAA-14 AVHRR is planned for April, 1996, at Railroad Playa, NV.

AVHRR Ch2 Counts Vs. Radiance

$y = 2.08x$
$R^2 = 0.99$

x-axis: HAUCSS Radiance W/ [m² μm sr]
y-axis: AVHRR Counts
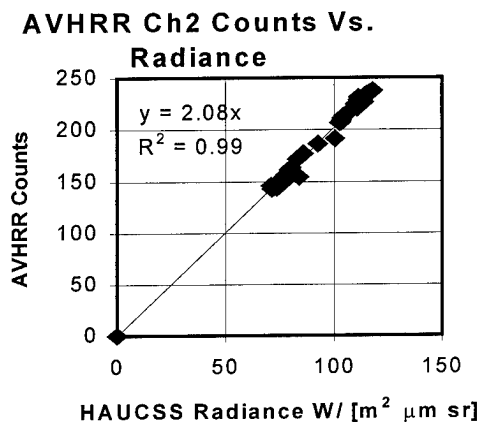
Figure 7: NOAA 14 AVHRR Band 2 result, July 1995

REFERENCES

[1] B.Guenther, et al., "MODIS level 1B Algorithm Theoretical Basis Document (ATBD), April 1995, obtainable though http://spso.gsfc.nasa.gov/atbd.

[2] C.R. Nagaraja Rao (Editor), "Degradation of the visible and near-infrared channels of the Advanced Very High Resolution Radiometer on the NOAA-9 spacecraft: assessment and recommendations for corrections", NOAA Technical Report NESDIS 70, U.S. Department of Commerce, June 1993.

[3] P.M. Teillet, P.N. Slater, Y. Ding , R.P. Santer, R.D. Jackson, and M.S. Moran, "Three methods for the absolute calibration of the NOAA AVHRR sensors in-flight", Remote Sens. Environ. 31: 105-120 (1990)

[4] C.R. Nagaraja Rao and Jianhua Chen, "Post-launch calibration of the visible and near infrared channels of the Advanced Very High Resolution Radiometer on the NOAA-7, -9, and -11 spacecraft", NOAA Technical Report NESDIS 78, U.S. Department of Commerce, August 1994.

[5] E.Vermote and Y.J.Kaufman, "Absolute calibration of AVHRR visible and near-infrared channels using ocean and cloud views", Intl.J. Remote Sensing 16: 2317-2340 (1995).

[6] Peter Abel, B. Guenther, Reginald N. Galimore and John W. Cooper, "Calibration results for NOAA-11 AVHRR channels 1 and 2 from congruent path aircraft observations", J. Atmos. and Oceanic Tech., 10: 493-508 (1993)

Radiometric Corrections of Visible/Infrared Satellite Data Over Terrestrial Environments: Angular, Atmospheric and Topographic Effects

Jose F. Moreno[(*)]

Jet Propulsion Laboratory, MS 300-243, 4800 Oak Grove Drive, Pasadena, CA 91109-8099
Tel. 818-3543865, Fax: 818-3936943, Email: moreno@blacks.jpl.nasa.gov
[(*)] on leave from: Remote Sensing Unit, Faculty of Physics, University of Valencia, 46100 Burjassot, Valencia, Spain

Abstract -- Monitoring ground conditions through land-surface reflectance retrieval from satellite data in the solar spectrum requires accurate radiometric corrections. Such corrections have been usually decoupled in atmospheric, topographic and intrinsic angular corrections. Actually, the decoupling is only possible when the effects are described at the first order of approximation, and the actual coupling introduces non-linear terms which must be also accounted for. In a full description of the effects, inversion of surface reflectance from measured radiance values becomes almost impossible, unless some assumptions are made. In this paper, a review is made of the different alternative formulations, and a complete model is proposed to simultaneously account for spatially varying atmospheric, topographic and angular effects in such a way that practical application to actual remote sensing data (model inversion) is possible while still keeping consideration of all the major intervening effects.

INTRODUCTION

The derivation of land-surface reflectance from satellite data in the solar spectrum (visible/infrared) requires accurate removal of radiometric distorsions, including atmospheric effects, topographic effects and intrinsic angular effects due to non-Lambertian behaviour, particularly when comparisons are done with varying illumination/viewing geometry. Horizontal variability of atmospheric parameters in the case of flat surfaces, horizontal/vertical variability in the case of mountainous terrain, and intrinsic atmospheric angular effects must be taken into account. Topographic effects change the local illumination conditions, and introduce additional multiple reflection terms. A realistic (non-Lambertian) model for the surface reflectance must also be taken into account. Although angular effects due simply to non-Lambertian behaviour are important in the case of sensors with off-nadir viewing capabilities, topographic effects play a major role and are the most important distorsion for quantitative interpretation of the data, mainly because they introduce significant 'relative' differences among pixels of an image, then difficulting application of techniques like classification or physical parameters retrievals. The actual correction of topographic effects will not be possible in a systematic way until we have a full accurate Digital Elevation Model (DEM) of the Earth surface, but methods can already be derived and tested over pilot areas.

ATMOSPHERIC EFFECTS

Atmospheric effects in remote sensing are currently very well known, and accurate description of such atmospheric effects is possible by using Modtran [1] or other similar codes. For practical purposes, some assumptions are required [2][3]. First, usually the atmospheric structure is not precisely known, so that we can not run sophisticate radiative transfer models with uncertain inputs. Also, the use of explicit full radiative transfer calculations is computationally inadequate for our purposes. The basic assumption made in the model adopted in this case is that all the atmospheric effects can be described after defining five major terms:

- direct 'down' transmittance: $T_{dir}^{\downarrow}(\vartheta_s)$
- diffuse 'down' transmittance: $T_{dif}^{\downarrow}(\vartheta_s)$
- direct 'up transmittance: $T_{dir}^{\uparrow}(\vartheta_v)$
- diffuse 'up' transmittance: $T_{dif}^{\uparrow}(\vartheta_v)$
- intrinsic reflectance: $\rho_{atm}(\vartheta_s,\vartheta_v)$
- spherical albedo: S

Such terms are calculated by using a radiative transfer model. A modified version of the 6S code [2] is used in the present study for computing all the parameters. Accuracy of the transmittance/radiance terms is evaluated by means of the Modtran-3 code [1], especially when data within the atmospheric gaseous absorption bands have to be considered for a particular sensor, due to the poor description of the scattering/absorption coupling effects in the 6S code.

A major problem is the derivation of the required atmospheric inputs. If not available as external information, they can be retrieved from the image itself, provided a pre-knowledge of the surface reflectance for some reference surfaces. In the adopted implementation, once a reflectance value (for each one of all the available spectral channels) is assumed for a reference surface, the atmospheric parameters are derived by numerical non-linear inversion of the full atmospheric model (with compensation for target altitude and multiple scattering terms). Five atmospheric parameters are inverted from the available surface reflectance information in order to describe the atmospheric structure: column integrated water vapor amount, aerosol concentration (visibility), two effective parameters for aerosol-type characterization and one parameter describing the dominant scattering/absorption coupling behaviour.

Once such parameters are derived from several reference points in the image, interpolation to the image continuum is done by a topographic-compensating technique, assuming that topography is driving the vertical profile. Analysis of the outputs of mesoscale meteorological model calculations for the spatial distribution of atmospheric water vapor shows that this approximation would require incorporation of mesoscale atmospheric circulation in order to better describe water vapor distribution, especially over large areas, like those

included in a full AVHRR scene. The effects become insignificant for small areas (like Landsat or Spot scenes).

TOPOGRAPHIC EFFECTS

Topographic effects play a major role in disturbing observation from space. On the one hand, they produce a vertical geometric distorsion in the images introducing horizontal displacement due to relief, especially significant for off-nadir looking sensors. But the most important effects are radiometric: variation of the atmospheric (optical) properties with height, and mainly the relative changes in slope and orientation which introduce variations in local illumination conditions. Pixels can now be illuminated or in shadowed areas (including self-shadowed areas and cast-shadowed areas due to local horizons over solar elevation). Also, diffuse radiation can not be longer considered simply as isotropic, and modeling of directional distribution of diffuse irradiance is necessary, as well as the corresponding (local) sky view factors for each type of direct/diffuse illumination components. The surface reflectance model must also be considered as realistically non-Lambertian, with explicit treatment of direct/diffuse illumination components as varying local illumination conditions. Finally, topography also changes the adjacency effects of the surroundings over the apparent reflectance of a target, as well as introduces additional terms related to multiple reflections with adjacent slopes, including slopes-target and slopes-atmosphere-target contributions.

Of course, not all the terms have the same importance, but none can be neglected in the general case. The key question is how to take into account all the major effects while still have a mathematically tractable model which could allow model-inversion. For that objective, the definition of the local horizon line, and the radial distance target-horizon for each relative orientation with the Sun, plays the basic role in defining a simple parameterization.

INTRINSIC SURFACE ANGULAR REFLECTANCE EFFECTS

The intrinsic angular effects are due to the fact that even in the case of flat areas and horizontally homogeneous atmosphere, the measured reflectance over the same surface types under different illumination/viewing geometry can be different due to the general non-Lambertian behaviour. For accurate description of such angular effects, a detailed knowledge is required of each type of surface, due to the different quantitative and also qualitative behaviours. For practical purposes, the only possible alternative is a 'normalization' procedure which allows reduction of the spatially varying measured radiances to a common reference illumination/viewing geometry. Such normalization procedure implies that we are no longer dealing with directional reflectance, but with surface albedo. In multitemporal studies, the relative albedo must be also normalized to a reference Sun angle for quantitative comparisons. In any case, a model of the surface reflectance is required to allow such normalizations.

The particular reflectance model used here has been derived from more general methods already used for AVIRIS data [4]. The new model has been still limited to six parameters as a minimum compromise. Although more sophisticate models can be used, the reflectance model required for topographic/angular normalization must be very simple, because at this level no pre-information about the surface has to be assumed, and then any method depending on particular surface types must be avoided. The 'normalization' of N different images (acquired at N different illumination/viewing angles) is then achieved by inverting the bidirectional surface reflectance model for the N available angular measurements. Once the surface intrinsic parameters are retrieved, a final output image can be generated representing a 'normalized' surface property, typically surface (spectral) albedo (after angular integration) for a reference Sun angle (nadir reference illumination conditions). Of course, no time variation is assumed in surface conditions for such approach. In the cases where surface changes are to be monitored over also changing illumination and viewing conditions, the alternative modeling requires additional parameters accounting for surface changes. Otherwise, a reference illumination is used for normalization, without attempts to correct intrinsic surface bidirectional effects. The output illumination-corrected reflectance images must then be interpreted by additional processing to separate the changes due to different viewing angles from the actual changes in the surface, because in such cases only the relative illumination can be accounted for in a general case.

COMBINED MODELING FOR APPLICATION TO REMOTE SENSING DATA BY INCLUDING COUPLING EFFECTS

After consideration of different alternatives and looking for a complete but efficient reflectance formulation, the apparent reflectance at the sensor can be written, after some simplifications and assumptions, as

$$\rho' = \rho_{atm} + T^{\downarrow}_{dir}(\vartheta_s)\left[\rho_c\,\Theta\,\frac{\cos\vartheta_i}{\cos\vartheta_s}\right]T^{\uparrow}_{dir}(\vartheta_v) +$$

$$+ T^{\downarrow}_{dir}(\vartheta_s)\left[<\dot{\rho}>\right]T^{\uparrow}_{dif}(\vartheta_v) +$$

$$+ T^{\downarrow}_{dif}(\vartheta_s)\left[\bar{\rho}_c^{cis}\,\frac{\cos\vartheta_i}{\cos\vartheta_s}\,V_d^{cis}\,F_d^{cis}\right]T^{\uparrow}_{dir}(\vartheta_v) +$$

$$+ T^{\downarrow}_{dif}(\vartheta_s)\left[\bar{\rho}_c^{iso}\,V_d^{iso}\,F_d^{iso}\right]T^{\uparrow}_{dir}(\vartheta_v) +$$

$$+ T^{\downarrow}_{dif}(\vartheta_s)\left[\bar{\rho}_c^{hor}\,V_d^{hor}\,F_d^{hor}\right]T^{\uparrow}_{dir}(\vartheta_v) +$$

$$+ T^{\downarrow}_{dif}(\vartheta_s)\left[<\overset{*}{\rho}>^{cis}<V_d^{cis}>F_d^{cis}\right]T^{\uparrow}_{dir}(\vartheta_v) +$$

$$+ T^{\downarrow}_{dif}(\vartheta_s)\left[<\overset{*}{\rho}>^{iso}<V_d^{iso}>F_d^{iso}\right]T^{\uparrow}_{dif}(\vartheta_v) +$$

$$+ T^{\downarrow}_{dif}(\vartheta_s)\left[<\overset{*}{\rho}>^{hor}<V_d^{hor}>F_d^{hor}\right]T^{\uparrow}_{dif}(\vartheta_v) +$$

$$+ T^{\downarrow}_{dif}(\vartheta_s)\left[<\hat{\rho}_{slp}>P^{slp}\,V^{slp}\,\bar{\rho}_c^{slp}\right]T^{\uparrow}_{dir}(\vartheta_v) +$$

$$+ T^{\downarrow}_{dif}(\vartheta_s)\left[<\hat{\rho}_{slp}>^{cis}\,\frac{<\cos\vartheta_i>_{slp}}{\cos\vartheta_s}<V_d^{cis}>_{slp}\,F_d^{cis}\,V^{slp}\,\bar{\rho}_c^{slp}\right]T^{\uparrow}_{dir}(\vartheta_v) +$$

$$+ T_{dif}^{\downarrow}(\vartheta_s)\left[<\hat{\rho}_{slp}>^{iso} <V_d^{iso}>_{slp} F_d^{iso} V^{slp} \bar{\rho}_c^{slp}\right] T_{dir}^{\uparrow}(\vartheta_v) +$$

$$+ T_{dir}^{\downarrow}(\vartheta_s)\left[<\overset{*}{\rho}_{slp}> P^{slp} <V^{slp}> <\overset{*}{\rho}>^{slp}\right] T_{dif}^{\uparrow}(\vartheta_v) +$$

$$+ T_{dif}^{\downarrow}(\vartheta_s)\left[<\overset{*}{\rho}_{slp}>^{cis} \frac{<\cos\vartheta_i>_{slp}}{\cos\vartheta_s} <V_d^{cis}>_{slp} F_d^{cis} <V^{slp}> <\overset{*}{\rho}>^{slp}\right] T_{dif}^{\uparrow}(\vartheta_v) +$$

$$+ T_{dif}^{\downarrow}(\vartheta_s)\left[<\overset{*}{\rho}_{slp}>^{iso} <V_d^{iso}>_{slp} F_d^{iso} <V^{slp}> <\overset{*}{\rho}>^{slp}\right] T_{dif}^{\uparrow}(\vartheta_v) +$$

$$+ \left[\left(T_{dir}^{\downarrow}(\vartheta_s)<\rho> + T_{dif}^{\downarrow}(\vartheta_s)\left\{<\overline{\rho}>^{cis}<V_d^{cis}>F_d^{cis} + <\overline{\rho}>^{iso}<V_d^{iso}>F_d^{iso} + \right.\right.\right.$$

$$\left. + <\overline{\rho}>^{hor}<V_d^{hor}>F_d^{hor}\right\}\right)\frac{S}{1-S<\overline{\rho}>^{iso}}\left(T_{dir}^{\uparrow}(\vartheta_v)\overline{p}_c^{iso} + T_{dif}^{\uparrow}(\vartheta_v)<\overline{\rho}>^{iso}\right)\right] +$$

$$+ \left[\left(T_{dir}^{\downarrow}(\vartheta_s)<\overline{\rho}_{slp}> + T_{dif}^{\downarrow}(\vartheta_s)\left\{<\overline{\rho}_{slp}>^{cis}<V_d^{cis}>_{slp} F_d^{cis} + <\overline{\rho}_{slp}>^{iso}<V_d^{iso}>_{slp} F_d^{iso}\right\}\right)\right.$$

$$\left.\frac{S}{1-S<\overline{\rho}>^{iso}}\left(T_{dir}^{\uparrow}(\vartheta_v)\overline{p}_c^{iso} + T_{dif}^{\uparrow}(\vartheta_v)<\overset{*}{\rho}>^{iso}\right)\right]$$

where the terms within brackets labeled by ρ represent different surface reflectance-type contributions, describing the bidirectional behaviour of the target, the surrounding environment and adjacent slopes, as coupled to the different atmospheric terms. The remaining symbols are effective geometric parameters to be derived from the DEM in order to account for topographic effects (local horizon, sky view factors, effective local roughness, etc.). An additive modeling is adopted, still keeping description of all major non-linear effects due to multiple reflections. Details and particular expressions of the different terms involved are given in [3].

This rather complicated formula is however the result of a series of approximations, the main of which is the decoupling between geometric-shape terms (derived from a DEM for the surroundings of each pixels, after determining the local horizon line) and the actual bidirectional (angular) reflectance terms of the surroundings of the central target. The actual contributions can be accurately evaluated in a 'forward' mode (theoretical simulations), by using Montecarlo techniques, for instance, but they can never be resolved is a 'backward' mode (reflectance model inversion) when starting for actual reflectance measurements. The resulting expression is a compromise between simple formulation and retention of the major present effects, still allowing model inversion by iterative techniques.

The major limitation is the computational time required. Note however that the most time-consuming calculations are done only once for a given area (for each DEM), and many intermediate calculations can be sped-up by using pre-calculated look-up-tables for typical situations. The spatial resolutions at which we are actually working and the availability of accurate digital models of the surface topography is currently representing a challenge for existing simple formulations of topographic corrections.

The effects, however, are not only significant when working with high spatial resolution. Even at scales of 1-5 km resolution (like data from AVHRR, Meteosat, GOES, etc.) topographic effects play a major role, not only for the derivation of surface reflectance and albedo, but also for cloud screening techniques due to the influence of bright

surfaces illuminated with low local incidence angles in topographically structured areas.

CONCLUSIONS

A general algorithm for describing and correcting atmospheric/topographic/angular effects in optical remote sensing data has been developed, by including the coupling of the three types of intervening effects as they actually appear in natural surfaces with topographic structure.

Most of the algorithm has been developed as a modification/enhancement of the existing 6S code [2]. In order to make the code computationally efficient and to introduce the required additional capabilities, it has been significantly changed, allowing for a better description of the scattering/absorption coupling terms, as well as the coupling surface BRDF/botton boundary conditions in the atmosphere, and mainly to introduce full account for topographic effects.

The formulation is fully sensor-independent. Actually, the same model has been applied to extreme spectral cases, like AVHRR (satellite) and AVIRIS (aircraft), by changing only the spectral filter functions applied to the output terms to derive the corresponding spectral values for each sensor channel, and also to two extreme spatial cases: high resolution Landsat TM data with a 10m resolution DEM, and low resolution AVHRR data with a 900m resolution DEM. The importance of the effects in both high and low resolution data has been analyzed, and the accounting for the different radiometric effects is proven to be consistent for both very different resolution data because of the generality of the developed algorithms. A general formulation of radiometric corrections is required for inter-sensor comparisons and multi-sensor studies, in order to guarantee compatibility in treatments at the same order of accuracy.

ACKNOWLEDGMENTS

REFERENCES

[1] A. Berk, L.S. Bernstein, and D.C. Robertson, "MODTRAN: a moderate resolution model for Lowtran 7", Rep. GL-TR-89-0122, Air Force Geophys. Lab., Bedford, MA, 1989.

[2] E. F. Vermote, D. Tanré, J. L. Deuzé, M. Herman, and J. J. Morcrette, "Second Simulation of the Satellite Signal in the Solar Spectrum (6S): User Manual", University of Maryland-Laboratoire d'Optique Atmospherique, 1994.

[3] J. Moreno, "Radiometric corrections of satellite remote sensing data in the solar spectrum: angular, atmospheric and topographic effects", submitted to IEEE Trans. Geosci. Remote Sens., 1996.

[4] J. Moreno and R.O. Green, "Surface and atmospheric parameters retrieval from AVIRIS data: the importance of non-linear effects", Proceedings of the Sixth Annual JPL Airborne Earth Science Workshop, March 1996, in press.

Comparison of Lidar Water Vapor Measurements
Using Raman Scatter at 266 nm and 532 nm

Ronnie Harris, Franz Balsiger, C. Russell Philbrick
Applied Research Laboratory / Pennsylvania State University
P.O.Box 30, State College, PA 16804
Phone: +814 863 8340 Fax: +814 863 8783 Email: fxb9@psu.edu

ABSTRACT

Raman lidar measurements at different wavelengths have become a well-established technique to obtain water vapor profiles. Measurements of the atmospheric distributions of water vapor have been made with the LAMP lidar (Laser Atmospheric Measurement Program) during the 1995 Case I measurement program on Wallops Island, VA. The simultaneous measurements obtained from the vibrational Raman technique at night using the visible signal ratio of 660/607 nm and the ultraviolet signal ratio of 295/285 nm were compared in order to validate the Raman technique for the UV channel. Correlations of the water vapor between the visible and UV channel were made, producing an overall average correlation of 0.94. Data sets with detailed vertical night time profiles from the surface to 4 km are presented. In addition, daytime vertical profiles from the surface to about 1 km are also shown.

INTRODUCTION

Water vapor, one of the most variable constituents in the atmosphere, has a major influence on the Earth's energy budget and climatic system. For instance, changes in the Earth's climate may occur when tremendous amounts of energy are transferred into the atmosphere in the form of latent heat as water evaporates and when energy is extracted from the atmosphere in the form of sensible heat as water vapor condenses [1]. Also, water vapor participates as a dominant "greenhouse" gas by absorbing and trapping the radiation that is remitted by the Earth particularly in the 5 to 7 μm spectral region [2]. Because of water vapor's important role, an understanding of its spatial and temporal distribution in the atmosphere is needed to obtain knowledge of many of Earth's atmospheric processes. Some of the most commonly used methods of measuring water vapor are radiosondes, satellite observations, meteorological towers, and remote sensing instruments, such as DIAL and Raman lidars [3].

In particular, the Raman lidar technique has exhibited the ability to produce high spatial and temporal resolution measurements of water vapor, however, most of these measurements are limited to nighttime operations. Daytime operations are difficult because of the high background of solar radiation. A solution to this problem is to operate with wavelengths in the "solar blind" spectral region between 230 and 300 nm [4]. This technique is based on the principle, that stratospheric ozone absorbs most of the solar radiation between 230 and 300 nm in the Hartley band and wavelengths in the Higgins bands which extend to 340 nm [5]. A disadvantage to

operation in this spectral region is that absorption by tropospheric ozone and strong molecular scattering will limit the transmission path of the laser light. Therefore a correction for the attenuation of the laser light by ozone absorption must be applied when operating with wavelengths between 230 and 300 nm.

In this paper, we will discus the correction that is applied to the water vapor measurements to account for the attenuation of the laser light due to the wavelength dependence of molecular (Rayleigh) scattering. In addition, there will also be a discussion about the correction that is needed for the UV channel because of the difference in absorption of the water and nitrogen lines due to ozone in the Hartley band. Then, simultaneous measurements of water vapor profiles for visible and UV channels will be compared. Finally data sets showing daytime vertical profiles obtained from the UV channel will be displayed and analyzed.

INSTRUMENTATION

A multi-wavelength Rayleigh/Raman lidar was built at the Pennsylvania State University in the summer of 1991. The Laser Atmospheric Measurement Program (LAMP) was developed to study the properties of the middle and lower atmosphere (0-80 km). LAMP utilizes a Nd:YAG laser that has a pulse repetition frequency of 20 Hz and a fundamental wavelength of 1064 nm. The Nd:YAG laser is doubled and quadrupled by nonlinear crystals. The laser's output energy per pulse is 1.5 J at 1064 nm, 0.6 J at 532 nm and 80 mJ at 266 nm. LAMP transmits both the 532 nm and the 266 nm wavelengths. The system contains a f/15 Cassegrain telescope which collects the backscattered signal and sends it over a fiber optic cable to a detector box. LAMP's detector box measures the vibrational Raman backscatter return from H_2O, N_2 and O_2 in the UV at 295 nm, 284 nm and 277 nm, respectively, with photon counting photo multiplier tubes (PMT). In the visible it measures the vibrational Raman return of H_2O and N_2 at 660 nm and 607 nm, respectively, and the rotational Raman return at 528 nm and 530 nm with photon counting PMT's and the Rayleigh backscatter return at 532 nm with an analog detector. LAMP's coaxial configuration allows for near field as well as far field measurements.

From September 9 to September 22, 1995, LAMP participated in the CASE I program on Wallops Island, VA. During the program, coincident measurements of atmospheric structure properties and water vapor and ozone distributions were made by several different instruments. The NASA/GSFC (Goddard Space Flight Center) Raman water vapor lidar was among those instruments which were included in the measurement program. There were also a series of radiosondes and ozone sondes

launched by the staff at NASA Wallops. Also the NASA/LSFC aircraft water vapor lidar experiment, LASE, had overflights on several occasions during the campaign. The data from each of these instruments is intended to be used in cooperative investigations between the various groups.

DATA ANALYSIS

The water vapor content of the atmosphere can be expressed as the ratio of its mass to the mass of ambient dry air, known as water vapor mixing ratio (g/kg). In lidar measurements of water vapor in the visible channel, the mixing ratio is expressed as

$$w(z) = \frac{n_{H_2O}(z)}{n_{dryair}(z)} \frac{M_{H_2O}}{M_{dryair}} = K_{vis} \frac{S_{H_2O}(z)}{S_{N_2}(z)} \qquad (1)$$

where n is number density, M is molecular mass, K_{vis} is the calibration constant and S_{H_2O} and S_{N_2} are the Raman backscatter count rates for water vapor and nitrogen in the visible, respectively [6]. The nitrogen signal is used because nitrogen represents a constant portion of dry air. Taking the ratio of two neighboring wavelengths eliminates many of the unknown factors within the lidar equation, such as telescope form factor, absolute detector sensitivity and transmitted power. However, parameters that are wavelength and altitude dependent such as molecular scattering and ozone absorption, are not canceled in the ratio and must therefore be eliminated via a correction procedure.

The strength of Rayleigh scatter is proportional to the atmospheric density. As light passes though the atmosphere the loss of light due to molecular scattering over a distance z can be expressed as

$$I_\lambda(z) = I_{\lambda,0} e^{-\sigma_\lambda \int_0^z n(r)dr}, \qquad (2)$$

where n is the number density of air and σ_λ is the Rayleigh scattering cross section for air at the wavelength λ, given by

$$\sigma_\lambda = \frac{(3.93 \pm 0.05) \times 10^{-28}}{\lambda^{3.916 + 0.074\lambda + 0.05/\lambda}} cm^2, \qquad (3)$$

where λ is in μm [7]. This form takes the variation of the refractive index of air into account. For altitudes well below 5 km, an analytical calculation of the optical thickness can be made using (2), given the temperature T_0 and the pressure P_0 at the ground and assuming the temperature T(z) decreases linearly with altitude. Integrating the hydrostatic equation

$$\frac{dP}{dz} = -\frac{gM}{kT(z)} P(z), \qquad (4)$$

where g is the acceleration due to gravity, M is the mean molecular mass of a air molecule, and k the Boltzmann's constant, yields the atmospheric pressure P(z). Treating the air as an ideal

gas, the integral of the optical thickness is given by

$$\kappa(z) = \int_0^z n(r)dr = \frac{P_0}{gM}\left[1 - \left(\frac{\alpha z}{T_0} + 1\right)^{-\frac{gM}{k\alpha}}\right] \qquad (5)$$

where α is the temperature gradient. Therefore, assuming that the molecular scattering is the only wavelength dependent attenuation, the corrected water vapor mixing ratio is given by

$$w(z) = K_{vis} \frac{S_{H_2O}(z)}{S_{N_2}(z)} e^{(\sigma_{H_2O} - \sigma_{N_2})\kappa(z)}. \qquad (6)$$

We know also that the particle/aerosol attenuation can add a wavelength dependent term, however this contribution is difficult to estimate and its contribution is generally less significant.

In the UV spectral region the absorption due to ozone must also be considered. By measuring the Raman back scatter of N_2 and O_2 it is possible to obtain the integrated ozone column density for the altitude range of interest. Similar to (1) the expression for the ozone column density is found by taking the ratio of the O_2 and N_2 Raman back scatter signal in the UV region. Applying the Beer-Lambert law leads to the following expression [8] for the integrated ozone column density

$$\frac{S_{O_2}(z)}{S_{N_2}(z)} = \frac{O_2}{N_2} e^{-(\sigma_{O_2} - \sigma_{N_2})\int_0^z O_3(r)dr}. \qquad (7)$$

Because the ratio of O_2 to N_2 is constant in the lower atmosphere (7) can be used to determine the ozone column density. The water vapor is then given for the UV channel as

$$w(z) = K_{uv} \frac{S_{H_2O}(z)}{S_{N_2}(z)} \left[\frac{S_{O_2}(z)}{S_{N_2}(z)}\right]^{-\frac{\sigma_{H_2O} - \sigma_{N_2}}{\sigma_{N_2} - \sigma_{O_2}}}, \qquad (8)$$

where S_X are the count rates at the corresponding wavelength already corrected for the losses due to molecular scattering as discussed above. K_{uv} is the calibration constant for the visible channel.

The count rates S_X at the different channels are given as the difference between the measured signal returns and the background counts for each of the channels. These quantities follow a Poisson distribution. For the calculation of measurement error we treat them as Gaussian distributed variables. This simplification leads to reasonable estimates of the measurement error. In (6) and (8) the only critical term in the error propagation is the division by S_{N_2}. For $S_{N_2} < 5$ counts larger differences between the exact and the simplified technique would occur in the error estimation. Since we only look at data were S_{H_2O} is bigger than 1 count and S_{N_2} is more than one order of magnitude larger

1827

than S_{H_2O} the critical condition never occurs.

The two calibration constants K_{uv} and K_{vis} can be obtained by comparing the uncalibrated lidar profile with a profile from a balloon sonde. For each lidar range bin we ratio the balloon water vapor with uncalibrated lidar value and take their weighted average.
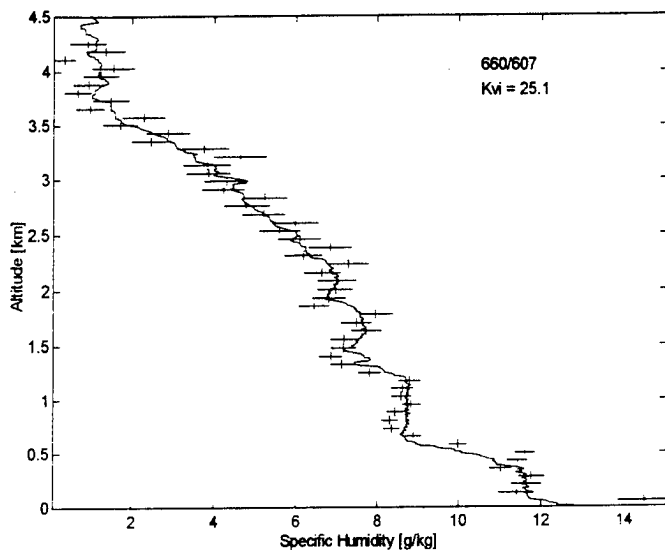
Figure 1. Vibrational Raman lidar water vapor profile together with a concurrent radio sonde profile.

MEASUREMENTS

Figure 1 displays a comparison water vapor mixing ratio measurements obtained by LAMP and a concurrent radiosonde

released 3 km away from the lidar site on September 18, 1995 at Wallops Island around 02:45 UT. The lidar profile was integrated over 30 min and has a height resolution of 75 m. A comparison of the lidar and the radiosonde profiles show that their fine structures have similar characteristics, thereby, showing that measurements between both instruments are consistent. Between ground and 2.5 km both instruments reveal the same detailed layer structure.

The left panel of Figure 2 provides examples of water vapor profiles measured by both the UV and the visible channels integrated over 60 min starting at 01:20 UT on September 16, 1995. On the right panel the correlation between the two measurements is displayed. Both the profiles are in good agreement up to 2 km. The correlation coefficient of the two measurements is 0.97. The good correlation between the two methods validates the data analysis for the UV channel and shows that the technique can be used for daytime measurements.

Figure 3 shows an example of a UV water vapor daytime measurement and a concurrent radiosonde profile. The lidar profile was taken on September 20,1995 at 19:25 UT using 30 min integration. The balloon was released at 19:38 UT, 3 km away from the laser site. The reduced range of the daytime measurement is due to difficulties in aligning the laser beam in the field of view of the telescope when the daylight background was present. In the present setup of the LAMP instrument we have to rely on the alignment of the prior night. Due to the low background level in the UV, one can expect to have a similar performace during daytime as during nighttime (see Figure 2) with a correct alignment.
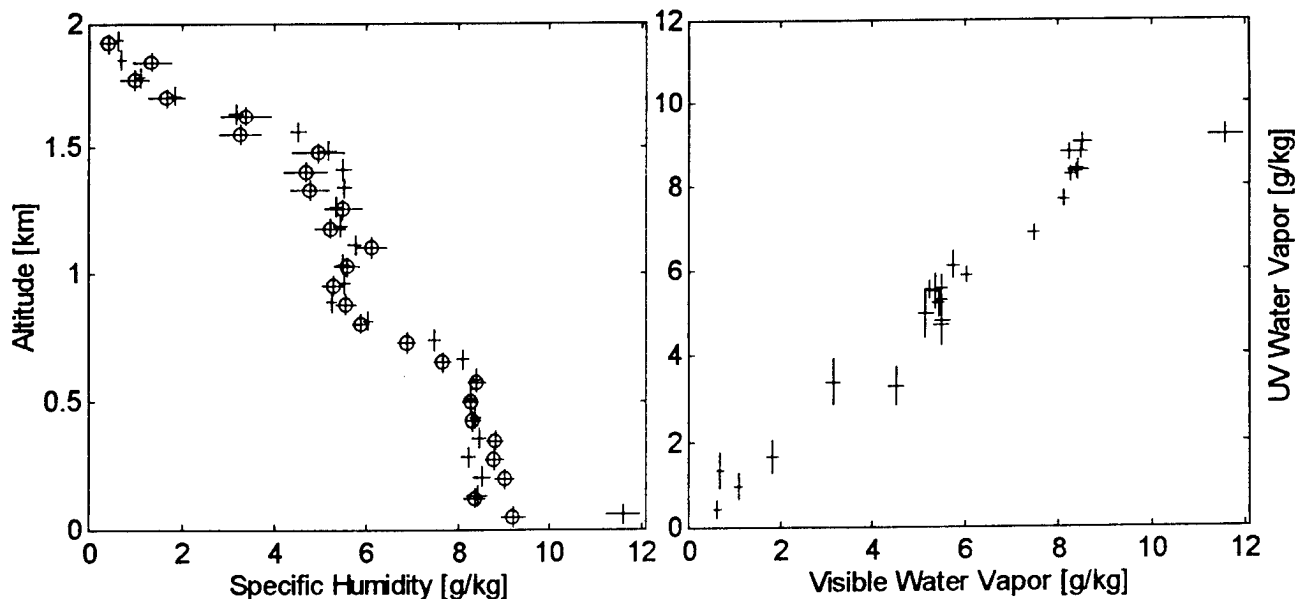
Figure 2. Comparison of a visible and a ultraviolet (circles) profiles. The bars indicate the measurement uncertainty. The right panel showa the correlation between the two, the correlation coefficient is 0.97.

1828
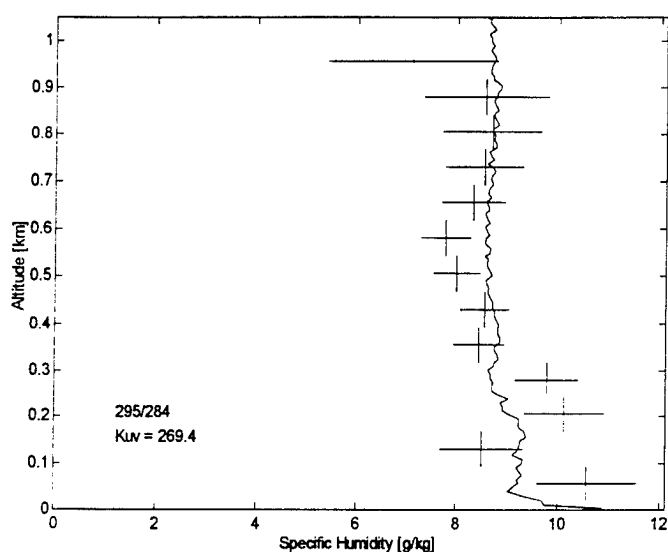
Figure 3. Daytime vibrational Raman water vapor profile from the UV channel togther with a concurrent radio sonde profile.

CONCLUSIONS

The methods of using corrections for the molecular scattering wavelength dependence and the corrections of the profile for tropospheric ozone scattering have been demonstrated. We have shown that using the vibrational Raman return from a 266 nm pulsed beam at 295 nm, 284 nm and 277 nm provides a valid technique to measure water vapor profiles in the lower troposphere. Daytime measurements were performed with this technique. However, to improve the daytime measurements it is necessary to make the system's alignment more stable with respect to time.

ACKNOWLEDGMENTS

REFERENCES

[1] J. P. Peixoto, and A. H. Oort, Physics of Climate, American Institute of Physics, New York, 1992.

[2] S. C. McKinley, Water Vapor Distribution and Refractive Properties of the Troposphere, MS Thesis, The Pennsylvania State University, 1994.

[3] S. H. Melfi and D. Whiteman, "Observations of Lower Atmospheric Moisture Structure and Its Evolution Using Raman Lidar", Bulletin American Meteor. Society, vol 66, no 10, pp 1288 - 1292, 1985.

[4] R. M. Measures, Laser Remote Sensing, John Wiley and Sons, New York, 1990.

[5] T. G. Kyle, Atmospheric Transmission, Emission and Scattering, Pergamon Press, Terrytown NY, 1991.

[6] S. Rajan, T. J. Kane, and C. R. Philbrick, "Multiple-wavelength Raman Lidar Measurements of Atmospheric Water Vapor", Geophysical Research Letters, vol.21, no. 23, pp 2499-2502, 1994.

[7] M. Nicolet, R. R. Meier, and D. E. Anderson, Jr. "Radiation Field in the Troposphere and Stratosphere II. Numerical Analysis", Planet. Space Sci., vol. 30, no. 9, pp 935-981, 1982.

[8] D. Renault, J. C. Pourny, R. Capitini, "Daytime Raman-lidar measurements of water vapor", Optics Letters, vol. 5, no. 6, pp 233-235, 1980.

Vladimir P.Lukin

Institute of Atmospheric Optics, Siberian Branch of RAS,
av.Academicheski, 1, 634055,Tomsk, Russia
tel.(382-2)25-9606, fax:(382-2)25-9086, E-mail:ZUEV@IAO.TOMSK.SU

Abstract - Numerical simulation on a computer is one of the main methods used for studying the possibilities of adaptive correction of turbulent distortions of imaging forming in the atmosphere.

FOUR-DIMENSIONAL COMPUTER DYNAMIC MODEL OF ATMOSPHERIC OPTICAL SYSTEMS

The scientists of the Institute of Atmospheric Optics have the experience in creation of computer codes describing different components of an adaptive system. The models of these elements have been checked solving the atmospheric problems. We are working under creation of 4D computer codes for calculations of optical waves parameters propagating in a layer-inhomogeneous and random-inhomogeneous stratified media.

At present we laid the groundwork for creation of 4-dimensional (three spatial coordinates and time) computer system simulating the optical radiation propagation in the atmosphere under conditions of adaptive phase control of the optical radiation parameters. In particular, we created the numerical models of both the separate components and the whole channel of adaptive optical system. Nowadays we have the operating programs which simulate the following parameters: a) optical radiation propagation when forming the images through the refraction and turbulent atmosphere. b) low-frequency part of spectral density of turbulent atmosphere for ground layer (atmosphere) and for the whole atmosphere, c) different schemes and algorithms of operation of wave front sensors of interference and diffraction types, d) quantum fluctuations of optical radiation beam are actual under conditions of optical system operation at weak emission flux. e) at last. different active and adaptive control elements of optical wave phase. so-called multi-element segmented and deformable controlled mirrors.

As has been shown and proved in our papers we managed to make the following on the basis of the Programs a) to calculate correctly the statistical characteristics of optical wave intensity fluctuations propagating in the turbulent atmosphere. The calculation of the mutual coherence function is possible. The given program can provide the calculation of statistical characteristics of the optical wave phase fluctuations form the wave equation directly. Program b) represents the models of low-frequency range of spectrum of atmosphere turbulence. In contrast to intensity fluctuations, phase fluctuations appear to be more sensitive to low-frequency spectral range of atmospheric turbulence. When calculating phase characteristics of optical waves we use the models of turbulence spectrum with finiteness outer scale of turbulence both for ground layer and for the upper layers of the atmosphere. Program c) consists of some subprograms simulating the work of interference and Harttmann wave front detectors. We investigate the algorithms of optical wave phase restoration using the interferometers with reference wave and shift as well as some versions of Hartmann detector. By comparing the wave front phase restored using one or another method from the optical measurements and phase obtained when solving the wave equation we hope to find a correct and adequate to problem description of optical wave phase in the mode of speckle-structures formations. Programs d) and e) permit modeling of conditions of natural optical experiment and estimate of efficiency of application of adaptive phase control for correction of distortions in optical wave including atmospheric refraction. turbulence. We are going to investigate different atmospheric paths, different regimes of adaptive control.

DEVELOPMENT OF MODELS OF TURBULENCE SPECTRA

This chapter deals with the theoretical and experimental studies of optical waves fluctuations for comparing different models of the atmospheric turbulence spectra. Using the experimental data we have investigated behavior of spectral density of atmospheric turbulence in the region of large spatial scales. Special efforts will be done to detect the variability of large optical inhomogeneities as manifestation of the influence of thermodynamic instability of the atmosphere. In the practical calculations of fluctuations of the optical waves various models are used to describe the spectrum in the region of large scales: von Karman, Greenwood-Tarazino, and Russian model. These models have already had two parameters, one of which was the so called outer scale of turbulence.

Our simultaneous measurements of the structure function of phase in the "saturation" region and of the turbulence intensity allow one to estimate the outer scale Lo corresponding to the horizontal transport of the optical inhomogeneities. Since the scales Lo were measured under different meteorological conditions. an attempt has been undertaken to classify the results of optical measurements of Lo depending on the degree of thermodynamic stability of the atmosphere. It was found that the values of exceeding

the mean value are realized under the conditions of neutral stratification.

Together with the dependence of the outer scale of turbulence on variations of meteorological parameters of the atmosphere, there exists anisotropy of the atmospheric properties, in other words, inhomogeneities with dimensions exceeding several meters possess the properties that depend on direction. As a consequence, the correlation characteristics of some parameters of optical waves appear to be direction-dependent. For example, random displacements of an image, which is formed by the optical radiation passed through atmospheric layers, exhibit such properties. The so-called coefficient of anisotropy K, being obtained immediately in the experiment, varied in the interval from 0.62 to 2.57 with the mean value K = 1.57 that indirectly indicated that the temperature induced optical inhomogeneities, which produce the phase fluctuations, were anisotropic in the large-scale region. The relationship is quite obvious between the K value and the instability parameter. Let us compare the measured variances (and their ratios) with those calculated. In the numerical calculations we use the model of the turbulence spectrum that makes it possible to introduce two scales for the outer scale of turbulence. The calculations will be performed under the assumption of uniform optical paths. It follows from our calculations that the measured K values can be explained with the help of the spectrum as a model with two different projections of the outer scale of turbulence into the vertical and horizontal directions.

Let us finally analyze the our data on the astroclimatic characteristics obtained in the region of the Elbrus mountain. These measurements were conducted at the Special Astrophysical Observatory. In our analysis of the experimental data we assume that the atmosphere is stratified and its inhomogeneities have the shape of elongated ellipsoids of revolution. This implies that: (1) In the case of vertical propagation the image jitter must be practically isotropic. (2) The anisotropy of the jitter of an optical source image must be maximum for the case of horizontal propagation and will be determined by the atmospheric instability. In the experiment we have used the measurer of fluctuations of the angles of arrival of the optical waves based on the telescope, which was manufactured based on the soviet TV tube. The parameters of the telescope and the measurer ensure the determination of angular position of the center of gravity of the focal spot with the accuracy of about 0.08" and the measurements of its deviation in the frequency range from 0.01 to 100Hz. As a result we have obtained the values of the variances of an image jitter and of the orthogonal components. Under the near-surface conditions one can expect a strong anisotropy of the turbulence that leads to the anisotropy of the jittering process. Based on the experimental data it was revealed that: (1) In the ground atmospheric layer the outer scale of turbulence is comparable to the height above the underlying

surface. (2) The value of this outer scale appears to be dependent on the atmospheric stability. (3) In the ground atmospheric layer the most large-scale inhomogeneities of the atmospheric turbulence are anisotropic. (4) From the standpoint of vertical distribution of the atmospheric inhomogeneities one can introduce the average integral spectrum.

NEW RESULTS WITH ADAPTIVE OPTICS IMAGING SYSTEMS IN THE ATMOSPHERE

The special attention will be concentrated on the investigation of efficiency of different active and adaptive algorithms for compensation of atmospheric aberrations. The simulation will be made taking into account the finite rate of control, with the use of artificial beacons, and on the base of forecast of propagation conditions. The requests to the quality of radiated laser beams, parameters of a wave-front sensor, parameters of a ground-based telescope, etc. will be determined. During the optical experiments a complex system has been developed and designed for measuring meteorological parameters. The average values of temperature and wind velocity, as well as temperature and wind velocity fluctuations, are measured at fixed levels above the ground. As a result, each optical experiment is accompanied by the data on meteorological measurements. i.e., we calculate the intensity characteristics of turbulence, the parameters characterizing the atmospheric instability. The structure of wind velocity in the ground layer is studied. To analyze the atmospheric turbulence along vertical optical paths we use an optical meter of stellar image "tremor" constructed on the basis of a mirror telescope. It is well known that the atmospheric turbulence limits to a great extent the performance of the optical telescopes operating from the ground surface. We may introduce the traditional, determined by the atmosphere, parameters: spatial scale of coherence of an optical wave or the Fried's radius, dimension of isoplanatic angel of visual field for the layer of turbulent atmosphere, "life-time" of phase distortions in an optical wave.

These characteristics of atmospheric turbulence determine the structure of phase distortions at the telescope aperture and technical parameters of telescope as the optical transfer function, the point spread function (PSF), the integral resolution, the Strehl parameter. These and other atmospheric characteristics for the systems of image formation can be calculated both on the basis of atmospheric sounding at a point of location of telescope and on the basis of atmospheric models. We are developing the methods and setups for sounding of optically-active atmospheric layer as well as the models of the atmosphere. In the previous years we have developed the models for various regions of the former Soviet Union. It is of interest to compare our models with the models for "good", from the view-point of astroclimate, place in the world.

We present the data of calculations of atmospheric parameters for different models of the atmosphere with deformable and segmented mirrors. The PSF determination was determined for the visible spectral range at the wavelength 0.55mm. The calculations were made for a segmented corrector whose number of elements varied between 1 (3 degrees of freedom) and 16 (48 degrees of freedom) and for a deformable corrector (20 degrees of freedom).

From the our results with the parameters of real optical telescopes we conclude that the most of large designed and put into operation astronomic telescopes can be attributed to the class of active telescopes. Moreover, that we realize that the total adaptive correction is difficult for large telescopes. For this reason we pay much attention to partial adaptation by means of correction of lower aberrations and to the use of the methods of post-detection processing. To understand the processes of image formation with partial correction the structure phase function provides a useful guide. The real measurements of the structure phase function in the atmosphere are few in number: in the ground layer our measurements and in USA are well known, for the entire thickness of the atmosphere are our measurements in Zelenchuk, the measurements at MMT, and those at NTT. Their results speak in favour of inapplicability of the Kolmogorov-Obukhov model [1-4]. This is also confirmed by measurements in New Mexico region and of group of scientists from Japan. The corrected model of the turbulent atmsophere results in greater contribution of high-frequency aberrations, and also in anisotropy of atmospheric-induced phase distortions. Taking into account these problems we have studied the possibilities of adaptation for large telescopes with the use of a secondary mirror [5-9].

It is pertinent to note that the applications of adaptive optics for implementation of the total potential of such a high-power Russian telescope-project as AST-10 imposes heavy demands on the quality of production, adjustment and phasing of a primary mirror (PM). The atmospheric turbulence was a controlling factor of the image quality for previous generations of telescopes. We shall consider some results of carried out calculations of the PSF of the telescope-atmosphere system. To investigate the effect of AST-10 aperture dephasing we gave the optical wave phase within each PM segment accidentally with the use of a program data sensor unit of random numbers with normal distribution. Here shows the PSF for different values of dephasing.

It concerns the operation of adaptive telescope under of image formation from a large number of speckles. A phenomenon of the wavefront dislocations of the optical irradiance propagating through the turbulent atmosphere. Using the numerical simulation method, the effects of the wavefront dislocations on the adaptive optical system performance have been investigated. We have found a connection between instability of the phase conjugation

efficiency and the reference wavefront dislocations. When optical wave propagates through an inhomogeneous medium the finite number of points occurrence is possible, where irradiance intensity equals to zero as consequence of partial waves interference. The phase of the wave can not be defined in these points and in their vicinity the phase surface can be described either as a multi-list three-dimensional surface or as a broken two-dimensional surface. In the last case the branch cuts connect the pairs of the screw dislocations with opposite sign. The classical description of the phase fluctuations as a value proportional to eikonal becomes invalid in this situation and mathematical formulation of the phase conjugation algorithm, used in adaptive optics, is ill-posed.

We have investigated formation of the wavefront dislocations in the optical wave propagated through the turbulent atmosphere. We used the computer code that allows us to simulate coherent irradiance propagation in the atmosphere in paraxial approximation of the wave optics and the main elements of an adaptive optical system, such as the Hartmann wavefront sensor and various types of the wavefront correctors.

I am pleased to Mr.B.Fortes for numerical calculations for this paper.

REFERENCES

1. V.P.Lukin. "Optical measurements of the outer scale of the atmospheric turbulence", Atmospheric and Oceanic Optics, Vol.5, No.4, 1992.
2. V.P.Lukin and V.V.Pokasov, "Optical wave phase fluctuations", Applied Optics, Vol.20, pp.121–135, 1981.
3. V.P.Lukin, "Investigation of some peculiarities in the structure of large scale atmospheric turbulence", Atmospheric and Oceanic Optics", Vol.5, No.12, 1992.
4. V.P.Lukin. Atmospheric adaptive optics, Nauka, Novosibirsk. 1986 (translation will publish in SPIE, 1966).
5. V.P.Lukin, B.Fortes, F.Kanev, "Adaptive forming beams and images simulation through the atmosphere". Photonics West'95, San Jose, USA, Proc.SPIE, Vol.2375 .1995 ·
6. V.P.Lukin, B.Fortes, P.Konayev, "Adaptive beaming high-power laser on vertical and slant atmospheric paths". Photonics West'95, San Jose, USA, Proc. SPIE, Vol. 2376, pp.244-254 .1995
7. V.P.Lukin. B.Fortes, "Effects of wavefront dislocations on atmospheric adaptive optical systems performance". AeroSense, Orlando, USA, Proc. SPIE. Vol.2471, 1995.
8. V.P.Lukin, "Investigastion of the anisotropy of the atmospheric turbulence spectrum in the low-frequency range". AeroSense, Orlando, USA, Proc. SPIE. Vol.2471, 1995.
9. V.P.Lukin.B Fortes. F Kanev. "Adaptive forming of beams and images through the atmosphere. Numerical simulations". Internat. Geoscience and Remote Sensing Symposium, Firenze, Italy, July. 1995.

Integration of SIR-C/X-SAR and Landsat TM Data for Geologic Mapping and Resource Exploration

T. Wever & M. Frei

Department for General and Applied Geology
Working Group Remote Sensing
University of Munich, LMU
Luisenstr. 37, 80333 Munich, Germany
Tel: ++49 89 5203 238
Fax: ++49 89 5203 393
Email: uk10103@iaag.geo.uni-muenchen.de

Abstract --The synergetic approach of optical and microwave remote sensing data has established a new dimension in remote sensing due to the availability of different sensor systems for earth observation. For the here presented investigation TM data as well as multifrequency and multipolarization SIR-C/X-SAR data were used. On the basis of the Timna Complex in Israel, a copper - manganese - uranium ore deposit, the advantage of this synergetic approach shall be demonstrated exemplarily. The study area is located North of Elat and West of the Dead Sea Rift. Due to the fact that the mineralization is controlled mainly by well-defined horizonts and structures, the integrated utilization of Landsat TM and SIR-C/X-SAR data allows a far-reaching verification of this deposit. While different rocks can be seperated with optical data by their spectral signatures as well as their albedo, the tectonic inventory can be detected by SAR data. Besides structural information multifrequency SAR data provide also important physical information about the surface roughness and the dielectricity as well as the morphology. These parameters can be used also as additional parameters for the mapping of geologic units.

INTRODUCTION

The investigations in the Timna Valley are part of an international research program in geology and remote sensing carried out along the Dead Sea Rift system. Due to the fact that in the Timna Valley the mineralization has a synsedimentary as well as a tectonic history it is an ideal object for the synergetic use of optical and microwave remote sensing data (SIR-C/X-SAR, TM).

The reasons for the investigation with different remote sensing techniques are the spectral ranges and spatial resolutions describing the same target from the point of view of surface chemistry (reflective optics) and physical quantities (SAR) in a different way. Several types of sensors do not just lead to a sum of individual facts, but there is a considerable synergy which helps to interprete the remote sensing data more reliable and more detailed.

The here presented synergetic approach provides complementary information and improves the verification of the geolocical setting clearly by utilization of spectral bands in the visible and infrared region on the one side and in the microwave region on the other side.

GEOLOGY

The Timna Valley is situated on the western margin of the Dead Sea Rift, and north of the junction with the Tamad fault, an E-W regional fault running from the Gulf of Suez to the Arava Valley. The Tamad fault is probably a Precambrian structure rejuvenated in the Miocene predating the Dead Sea Rift. The Dead Sea Rift is a strike-slip fault with a left-lateral movement, where the eastern Jordanian block moved about 100 km northward.

The geologic setting of the test area is characterized by a magmatic Precambrian massif surrounded by Paleozoic and Mesozoic sediments. The magmatic core (Har Timna) can be classified into basic/ultrabasic peridotite and norite, intermediate diorites and monzonites as well as asidic granites and syenites. The sediments consist esentially of sandstones, limestones, dolomites and subordinately of silty shales. Since the Timna Fm. has the greatest potential for metallic mineralizations, especially Cu and Mn, its units are dealed with in detail. The deposition of this formation marks the first Phanerozoic marine transgression in the Middle East onlapping the cristalline basement of the Timna Valley. The Timna Fm. can be subdivided into the Hakhlil Mbr. and the Sasgon Mbr. The Hakhlil Mbr. is composed of base conglomerates, laminar sandstones, dolomites and sandy dolomites and silty shales in the upper part. The Sasgon Mbr. can be separated into the lower dolomitic, middle sandy and upper shaly lithofacies, the mineralization of Cu and Mn is disseminated in the upper parts.

MINERALIZATION

Mineralizations occur as beds, veins and nodules of secondary hydroxides of copper and manganese minerals accompanied by phosphate lenses with uranium, mainly associated with the Cambrian Timna Fm.. The enriched source rocks are of sedimentary origin, the final and major enrichment was caused by hydrothermal activity along faults and joints of the late Cenozoic rifting or rejuvenated faults [1]. The indications for hydrothermal epigenetic activity are veins of manganese, copper, phosphate with uranium cross cutting the whole stratigraphic section from the Precambrian to lower Cretaceous mainly along the NNW-SSE and NE-SW directions. The mineralized veins can also be found along NNW trending fault lines penetrating sediments of a

recent terrace. The dolomites of the Timna Fm. are leached along NNW and ENE trending faults [2].

DATA PROCESSING

For the study and verification of the geological setting and the mineralization of the Timna Valley optical (Landsat TM) as well as microwave (SIR-C/X-SAR) data were used. Both data sets were processed in the way to enhance their information content with regard to the presented considerations.

For geoscientific applications of multisensor data the transformation in a consistent reference geometry is a unalterable requirement. For SAR-data a parametric geocoding on the base of a DTM was necessary, which uses carthographic image transformations as well as sensor specific transformations for the correction. For that reason the geometric correction has to consider the sensor as well as processor characteristics, and therefore had to be based on a rigorous range-Doppler approach [3], [4], [5].

For signature extraction the SIR-C/X-SAR data were additionally radiometric corrected on the base of the local resolution and the local incidence angle. Especially in mountainous areas like the Timna Valley these two parameters can vary in a wide range which reduces the geophysical interpretation of backscatter phenomena dramatically. For correction of the relief induced distortions the SAR data has to be normalized to an uniform local resolution and incidence angle [4], [5].

Taking into account a spatial resolution of 25 x 25 m referring to the DTM the great scale relief distortions can be removed very well while the smaller relief cannot be corrected. Beside this texture information induced by the small scale relief now the surface roughness is the dominant part influencing the variance of the SAR images.

In a first step the TM-data were transformed to the common reference geometry presented by the geologic map via a simple polynom rectification. For the assessment of the spectral features the data had to be radiometric corrected, in this case a simple haze correction was carried out [6]. The concept of the following image processing was to combine and extract the diagnostic spectral information of the most suitable TM band for validation of the geologic setting and especially the mineralization of the Timna Valley.

The Sasgon Member of the Timna Formation consisting of sandy dolomites and limestones contains the highest enrichment in copper and manganese. Due to the high content of Mn and Fe this horizon appears in very dark brown, grey to black colours with a very low albedo. Many authors (e.g. [7], [8]) are favouring the TM band combination 1-4-7 in B-G-R in arid regions for the presentation of geological features. Most of the important spectral absorption features of iron and hydrothermally altered minerals are covered by the TM bands 4 and 7 [9]. At last band ratioing was performed to emphasize spectral differences between the different surfaces. In this case the object was to elaborate the mineralized Timna Fm. on the base of their spectral features. This formation is characterized by iron crusts due to weathering. Especially the ratio of TM band 4/3 enables the separation of this formation due to the absorption features of iron in this spectral range.

An approach was carried out to combine the different information levels of the two sensors in one single image. The objectiv was the visualization of the different physical and chemical information of the surfaces on the base of their spectral signatures and backscattering. For this purpose the TM image 1-4-7 was transformed into the IHS space and the orginal intensity from the TM image was replaced by the first principal component (PC) of the multifrequency and multipolarisation SAR image. Finally the image was transformed back into the RGB space. Now the image contains the the intensity of the SAR data and hue and saturation of the TM data. Due to the fact that within the IHS space only the intensity was replaced by the SAR data in the resulting image the spectral information of the 1-4-7 combination was conserved. The effect of replacement of the intensity by SAR data however leads to an improved illustration of structural and textural phenomena together with the spectral information derived from the TM data.

RESULTS

The lithological and structural interpretation of the Landsat-TM and the SIR-C/X-SAR data bases on the geological and structural map of the Timna Valley [10]. In a first step the complementary data sets of TM and SIR-C/XAR were investigated and studied separately to demonstrate the potential of each system. The multispectral Landsat-TM data were analysed using the decorrelated TM channels 1-4-7 and the ratio image 1/3-4/3-7/5 coded in B-G-R. Both objectives the discrimination between the sedimentary and magmatic rocks as well as the delimitation of the mineralized Timna Fm. on the base of their spectral features were successful.

To define the individual properties of each frequency the SAR bands were elaborated separately. Additionally the investigation of the SIR-C/X-SAR date based on the processing of multifrequency and multipolarization color images (X-, C- and L-Band). A combination of the enhanced SAR bands shows a distinct significance of multifrequency and multipolarized SAR for structural investigations. Compared with the single bands the color image X/VV-C/HH-L/HH coded as B-G-R enhances the inerpretation of the structural inventory clearly . The combination of X/VV and the cross polarized bands C/HV and L/HV offers a better differentiation of the lithological units compared to the like

polarizations, due to their higher sensitivity in surface roughness and microrelief.

In a last step the different data of the optical and microwave part of the electromagnetic spectrum were merged to illustrate the complementary information content of the data sets in only one image. The data show clearly that the general geological scenery is well documented, due to the different spectral behaviour derived from the TM data and the shape, the texture and the structural components of the different lithological units derived from SAR data.

CONCLUSIONS

- The integrated use of optical (TM) and SAR data (SIR-C/X-SAR) improves the geologic interpretation capability of remote sensing data clearly.
- The additional use of SAR data establishes the new dimensions of surface roughness and small scale relief information which improves the discrimination significantly especially in areas with a very uniform petrography.
  These parameters offer a new possibility to derive information about the state of weathering, age and e.g. sedimentary sequence.
- The SIR-C/X-SAR system is very suitable for geologic investigations due to its multifrequency (X-, C- and L-Band) and multipolarization capabilities.
- The TM data show distinct spectral features which allow a good verification of different petrographical compositions related to the geological units.
- The multifrequency and multipolarization SIR-C/X-SAR data offer a new dimension in structural interpretation in contrast to conventional SAR Systems like the ERS-1/2 with only one frequency and one fixed polarization.
- The complementary of optical and microwave data demonstrated in all discussed investigations can be used for an enhanced interpretation of the geology.
- For geoscientific applications of multisensor data the transformation in one consistent reference geometry is an unalterable requirement.
- A far-reaching verification of the mineralization is possible:
  - The mineralized Timna Fm. is detectable due to its spectral features Fe^{2+}/Fe^{3+} with the TM.
  - The mineralization controlled by structures is mainly detectable by the SIR-C/X-SAR system.

ACKNOWLEGMENTS

REFERENCES

[1] BEYTH M., 1987, Mineralizations related to Rift systems: Examples from the Gulf of Suez and the Dead Sea Rift. Tectonophysics, 141, pp. 191-197.

[2] SEGEV A., BEYTH M. & BAR-MATTHEWS M., 1992, The Geology of The Timna Valley with Emphasis on Copper and Manganese Mineralization-Updating and Correlation with the Eastern Margins of the Dead Sea Rift. Geological Survey of Israel, Report G.S.I/14/92.

[3] HÄFNER H., HOLECZ F., MEIER E., NÜESCH D. & PIESBERGER J., 1994a, Geometrische und Radiometrische Vorverarbeitung von SAR-Aufnahmen für Geographische Anwendungen", Zeitschrift für Photogrammetrie und Fernerkundung (ZPF), Bd. 4/94, pp. 123-128.

[4] HÄFNER H., HOLECZ F., MEIER E., NÜESCH D. & PIESBERGER J., 1994b, Capabilities and Limitations of ERS-1 SAR Data for Snowcover Determination in Mountainous Regions. Proceedings of 2nd ERS-1 Symp., Hamburg, pp. 971-976.

[5] MEIER E., FREI U. & NÜESCH D., 1993, Precise Terrain Corrected Geocoded Images. Editor: Schreier G. , SAR Geocoding: Data and Systems, Wichmann Verlag, Karlsruhe.

[6] JASKOLLA F. & HENKEL J., 1989, A New Concept of Digital Processing of Multispectral Remote Sensing Data for Geological Applications. Proceedings of the 7th Thematic Conf. on Rem. Sens. for Exploration Geology, ERIM, Calgary, Canada, pp. 877-890.

[7] KAUFMANN H., 1988, Mineral Exploration along the Aqaba-Levant Structure by Use of TM-data- Concepts, Processing and Results. International Journal of Remote Sensing, 9, 10-11, pp. 1639-1658.

[8] FREI M. & JUTZ S., 1989, Use of Thematic Mapper Data for the Detection of Gold Bearing Formations in the Eastern Desert of Egypt, *Proceedings of the 7th Thematic Conf. on Rem. Sens. for Exploration Geology*, ERIM, Calgary, Canada, pp.1157 - 1172.

[9] DRURY S.A. & HUNT G.A., 1988, Remote Sensing of Laterized Archaean Greenstone Terrains: Marshall Pool Area, Northeastern Yilgard Block, Western Australia. Photogrammetric Engineering and Remote Sensing, 54, 12, pp. 1717-1725.

[10] SEGEV A. & BEYTH M., 1986, Timna Valley, Geological Map, Geological Survay of Israel.

Retrieval of Man-Made Structures in Siberia with INSAR Techniques using ERS-SAR Data

C. Streck * & O. Hellwich **

* Kayser-Threde GmbH, Department of Environmental Monitoring
Wolfratshauser Str. 48, 81379 Munich - Germany
Tel: +49-89 72495-217, Fax: +49-89 72495-291, E-Mail: sc@kayser-threde.de
** Chair for Photogrammetry & Remote Sensing, Technical University Munich
Arcisstr. 21, 80290 Munich - Germany

Abstract -- The potential of the interferometric correlation (coherence) is investigated for the mapping and monitoring of man-made structures in the Nadym region, Siberia. The area is located in the West Siberian Lowlands and most of the region is underlaid by discontinous permafrost. Man-made structures such as pipelines are undergoing yearly heave displacements by thawing and freezing of the active permafrost layer. The dimension of the displacement varies depending on the underground and surface cover. Man-made structures are embedded in a mosaic of boreal forest, bogs, rivers, small tundra lakes and tundra which impedes their detection. ERS SAR data acquired during the ERS-1/ERS-2 tandem mission have been used for interferometric processing. The coherence information, along with intensity and intensity change information, is demonstrated to be useful for the detection of man-made structures in varying environments.

INTRODUCTION

For remote and inaccessible areas such as parts of the West Siberian lowlands spaceborne radar remote sensing with its allweather capacity and illumination independance offers a valuable tool for mapping and monitoring man-made structures. Especially in this taiga biome where permafrost is underlying most of the region, land surfaces and their man-made structures undergo up- and downward displacements due to thawing and freezing of the active permafrost layer. A spaceborne radar-based detection and monitoring of structures like pipelines and roads which helps to allocate these impacts and to assess the potential hazards is of major interest for the local authorithies.

The Active Microwave instruments on board of the launched ESA satellites ERS-1 and ERS-2 offer data for this mapping task. A promising technique is the Synthetic Aperture Radar Interferometry (INSAR), where the ERS-SAR data of two passes are combined to derive terrain height information. The availability of data from the tandem phase of ERS1 and ERS2 with a one day acquisition interval favours the INSAR technique. Usually, this technique is applied to generate height and height displacement maps; however, it has been shown that SAR interferometry also has a large potential for the mapping of land surfaces. Examples have shown that an interferometric data analysis can strongly improve the potential of SAR data for landuse mapping [1], [3], [4]. The interferometric correlation is an additional parameter for the retrieval of land use classes. Color composites such as those created by [3] using interferometric correlation, backscatter intensity and backscatter intensity changes demonstrate the use of the correlation parameter. In this paper the information content of such an RGB composite for the mapping of man-made structures is evaluated for a testsite in Siberia. The study is part of an ESA Pilot Project for the "Detection of Man-Made Structures in Natural Environment", supported by DARA. Direction for future work is the measurement of the yearly permafrost heave displacement by differential radar interferometry.

TEST SITE AND DATA SETS

The area of investigation is located in the northern part of the West Siberian lowlands. It is situated at latitude of 65°30'N and a longitude of 73°15'E in the circumpolar taiga biome. The man-made structures such as gas pipelines, roads, power lines and buildings are embedded in a mosaic of vegetation composed by forest, grassland, shrub, bog and tundra and embraced by rivers and lakes. Discontinuous permafrost underlies most of the region. A ground truth campaign has been carried out during August 1995; for additional verification a Landsat TM scene of the 26/07/95 has been acquired. The investigated region covers approximately 25 km by 50 km. The test site is located in a river floodplain with a terrace level varying up to 25 m and is considered as relatively flat. The first available interferometric pairs from the tandem phase of ERS-1 and ERS-2 (descending orbits) have been analyzed. The scenes are listed in Tab. 1.

Tab.1   Scene Parameters

Orbit/ Frame	Acquisition Date
E1-22839/2277-SLC2	27/11/95
E2-03166/2277-SLC2	28/11/95
E1-23340/2277-SLC2	01/01/96
E2-03667/2277-SLC2	02/01/96

According to long-term meteorological observations at the aquisition times the area is snowcovered and the monthly temperature mean is about -20°C which indicates freezing conditions.

DATA PROCESSING

The two images have been coregistered to a subpixel accuracy. The baselines are 83 m for the 22839/3166 pair

and 107 m for the 23340/3667 pair. The short baselines did not require common-band spectral filtering in range. A common-band spectral filtering in azimuth was not applied. The coherence was computed for subareas of 11 single look pixels in azimuth direction and 3 single look pixels in range direction which covers an approximate ground area of (4.3 x 11 m) by (19 x 3 m). The interferometric phase trend of the flat surface has been subtracted which, according to [4], is a neccessary step for an accurate phase and coherence estimation. The SAR image intensities have been Frost-filtered with a 5 x 5 window and averaged over 5 looks in azimuth direction. For the RGB composite, a ratio of the intensity images 22839/2277 and 23340/2277 was calculated. To enhance image features two principle component analyses have been conducted for the four intensity images and the two coherence images. Figs. 1 to 3 show these channels for particular subareas of the test region: Figs. 1a, 2a and 3a show the first principle component of the two coherence images; Figs. 1b, 2b and 3b show the first principle component of the four intensity images; and Figs. 1c, 2c and 3c display the intensity ratio images.

DATA INTERPRETATION

Figs. 1b (raster square A/2,3), 2b (D/2,3), and 3b (E/1,2) display a north-south transect of a 1 km wide pipeline track including 9 subsurface sandcovered gas pipelines. The pipeline track crosses various natural environments such as open boreal forest, bogs, grassland, river channels, tundra and lakes. The detectability of the pipeline track depends on the surface cover.

Fig. 1b (A,B/2,3) displays the 1 km broad pipeline track interrupted on the left side of the track by a strip of open forest. It is easily detected mainly due to the shape of the sandcover of the pipelines, whereas the coherence information in Fig. 1a (A,B/2,3) does not allow a differentiation. This is due to the high coherence of both the pipeline tracks and the open boreal forest.

The ratio images do not help at all to differentiate between pipelines and surrounding cover types. The stable climatic conditions during winter time cause hardly any intensity changes on the four dates. Following the pipeline track in southern direction, it is easier to detect them in the coherence image (Fig. 1a; C,D,E/2,3) than in the intensity image (Fig. 1b). This may be due to a different surface cover type.

A compressor station (Fig. 1a and 1b; D/3) and the settlements (C/3) are clearly visible in the intensitiy image due to the strong corner-reflection effects at buildings, and do in general have a high coherence with high spatial variability.

Another interesting phenomenon is the detectability of small tundra lakes (Figs. 1a and b; A/1,2, C/2, and E/3) in the coherence images. The lakes are not visible in the intensity images due to the frozen surface and the snow coverage. The size and the location of these lakes have been verified with the help of the summer Landsat image. Low coherence may be obvious for the rivers. Temporal

intensity changes and a low signal to noise ratio are the main reasons. The low coherence of ice and snow covered lakes cannot be explained as easily. The coherence image clearly favours the detection of rivers and small tundra lakes.

The next subarea (Fig. 2) shows the pipeline track crossing dense mixed floodplain forest and tundra environment with small ponds. The track of the pipeline in the intensity image (Fig. 2b; A,B/2) is almost invisible due to intensities similar to those of the dense floodplain forest. This is not the case for the coherence image; here the effect of low coherence of the forest due to volume scattering and temporal decorrelation along with the higher coherence of the pipeline areas allows the detection of the pipeline track. In the environment of small tundra lakes the pipeline track is almost invisible in the coherence image (Fig. 2a, D/2,3), whereas the intensity image shows the single pipelines. This may be due to the snowcovered frozen tundra which has low intensities contrasting increased intensities of the pipeline which does not have a sandcover in this area. The small tundra lakes (Figs. 2a, 2b, and 2c; D,E/1,2,3) are clearly visible in the coherence image due their low coherence. The ratio images indicate intensity changes for some of the lakes.

The last subarea (Fig. 3) shows the pipeline track crossing the floodplain of the river Nadym. The coherence image (Fig. 3a; B,C/2,3) indicates it more clearly than the intensity image (Fig. 3b).

Creeks are visble in the coherence image (Fig. 3a) and invisible in the intensity image (Fig. 3b).

The coherence image (Fig. 3a; D/1,2) also shows a road due to its comparatively low coherence which my be caused by car traffic (tracks in the snow) between the passes of the satellites. It cannot be detected in the intensity image [2].

REFERENCES

[1] J. Askne and J. Hagberg, "Potential of Interferometric SAR for classification of land surfaces," Proc. IGARSS 93, Tokyo, Japan, pp. 985-987, 1993.

[2] O. Hellwich and C. Streck, "Linear Structures in SAR Coherence Data," in press.

[3] U. Wegmüller, C. L. Werner, D. Nuesch and M. Borgeaud, "Land surface analysis using ERS1/SAR interferometry," ESA Bulletin, No. 81, pp.30-37, Feb. 1995.

[4] U. Wegmüller and C.L. Werner, "SAR Interferometric Signatures of Forest," IEEE Trans. Geosci. Remote Sensing, Vol. 33, No. 5, pp. 1153-1161, Sept. 1995.

[5] E. Rignot & J. B. Way, "Monitoring Freeze and Thaw Cycles along North-South Alaskan Transects Using ERS-1 SAR," in Remote Sens. Environ. 49, pp.131-137, 1994.
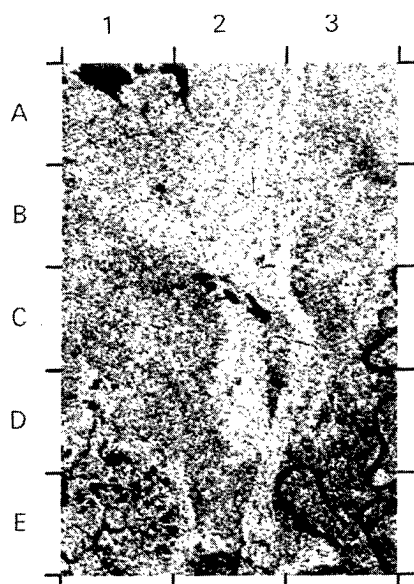
Fig. 1a 1. PC of Coherence Images

Fig. 1b 1. PC of Intensity Images
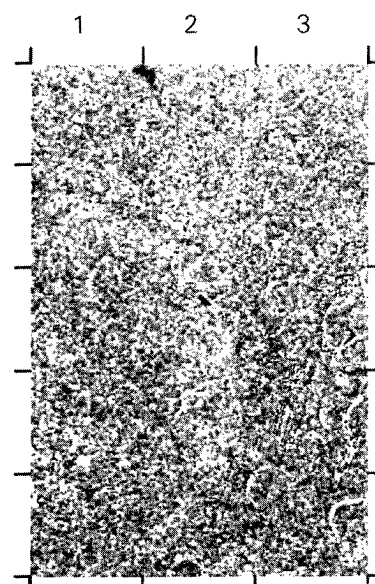
Fig. 1c Ratio of Image Intensities
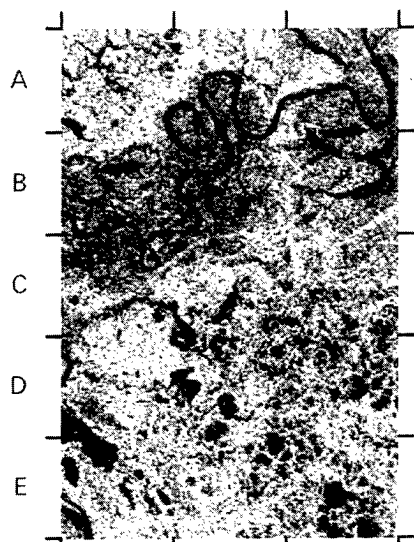
Fig. 2a 1. PC of Coherence Images

Fig. 2b 1. PC of Intensity Images
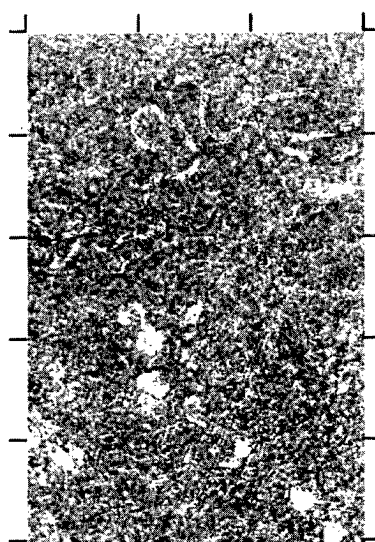
Fig. 2c Ratio of Image Intensities
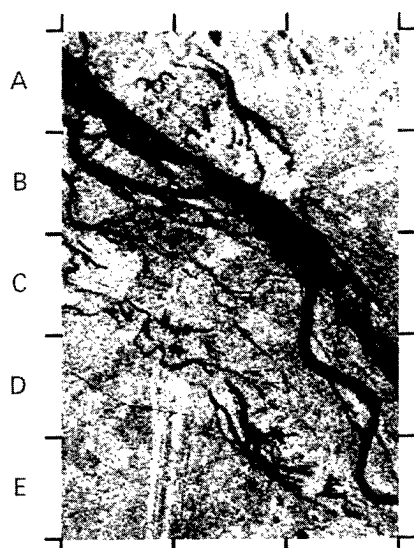
Fig. 3a 1. PC of Coherence Images

Fig. 3b 1. PC of Intensity Images
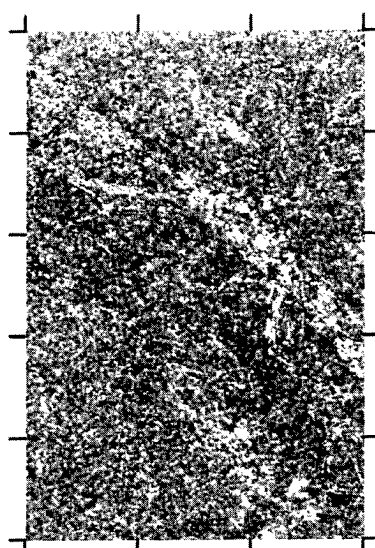
Fig. 3c Ratio of Image Intensities

Angular dependence of SAR backscatter around Mt Taranaki, New Zealand

David Pairman, Stella Belliss and Stephen McNeill
Landcare Research - Manaaki Whenua
PO Box 38 491, Wellington Mail Centre, New Zealand
Ph: 64 4 569 0182 Fax: 64 4 569 0181 Email: PairmanD@Landcare.cri.nz

Abstract -- An L-band SAR image from the Japanese JERS-1 satellite has been analysed for the effects of local surface orientation relative to the viewing angle. A high resolution digital terrain model is used to determine the local surface orientation and to orthorectify the SAR imagery. It is shown that the major variation in backscatter due to local incidence angle is accurately corrected for over a wide variety of slopes by simply accounting for the expected change in distributed scatterer density. Residual orientation effects are found to be dependent on the ground cover class. Backscatter from the indigenous forest was more isotropic than that from the farmland. Accurate registration was required for this study and a method of identifying control points in the rectified imagery is described.

INTRODUCTION

Synthetic aperture radar (SAR) has been available from aircraft instruments for over forty years and from space since the Seasat experiment in 1978. It has numerous unique properties including its ability to see through cloud and its sensitivity to physical target characteristics, making it of great interest to the remote sensing community. Despite this interest, much of the interpretation is still done manually. The difficulty is that there are many competing physical, electromagnetic, and orientational properties all affecting the radar backscatter. Along with speckle noise and geometric distortions, these make it difficult to routinely automate the analysis of radar imagery.

Although the mechanisms for strong angle dependence are generally well recognised, adequate characterisations for particular target classes are often not available. In this paper we explore the topographical effects on radar backscatter from a natural scene containing a variety of cover classes. The aim is twofold. Firstly, we wish to confirm that the theoretical adjustment of radar brightness for variation in local incidence angle does produce reasonable results over a useful range of such angles. Secondly, we wish to identify any secondary slope and aspect effects and determine if these are dependent on the ground cover class.

SAR processors form images from the returned backscatter, using Doppler shift to identify a point's origin in the along track (flight) dimension, and time to determine it's across track or range position. The range dimension is often resampled to convert to ground range. However, the range dimension of an image pixel is basically a slant range increment. Consequently, the radar brightness of a pixel is highly dependent on local incidence angle. Raney [1] illustrates that, due to the increase in distributed scatterers falling into a unit range increment, for a local incidence angle of θ_i, the slant range increment is scaled by $1/\sin\theta_i$ when projected onto the local geoid.

Other phenomena such as Bragg scattering, specular reflectance and the orientation of major scatterers in the target all have the potential to cause radar energy to be scattered in a non-uniform manner. Scene orientation effects can be characterised using electromagnetic theory and models of the target or by measurements of real targets. Two areas where there has been particular emphasis on modelling have been; backscatter from water surfaces under varying wave conditions [2] and backscatter from forests [3].

Direct measurements of Seasat data were used by Rauste [4] to analyse topographic effects from four different forestry classes. Rauste was able to identify significantly (statistically) different topographic effects in his four classes over a 10 degree incidence angle variation. It is this approach that is taken here to analyse our particular ground cover classes.

TEST SITE AND DATA

The test site chosen is the Taranaki region, dominated by the stratovolcano, Mt Taranaki/Egmont, and two older eroded volcanoes to the NNW - Pouakai and Kaitake. This area was chosen for two reasons. Firstly, the methodology relies on natural topography to provide a range of slope and aspects and a volcanic cone to provide a uniform range of angles. Secondly, the vegetation cover is reasonably homogenous around the volcano and the boundary of the Egmont National Park clearly delineates natural forest (mainly beech) from the surrounding dairying farmland.

JERS-1 L-band SAR data of Taranaki taken 3 February 1994 was provided by NASDA/ MITI. The image is level 2.0 data, that is, not geocoded and without geocoding information, but including range information. It is a three look product with nominal ground resolution of 18m. In addition, a SPOT multispectral image of Taranaki taken 26 May 1988 was used to assist in ground cover class identification.

Digital contours at 20m intervals, as used in 1:50 000 scale maps, were used to generate a detailed digital elevation model (DEM) of the study area on a 10m grid.

PROJECT METHOD

Before any angle effects can be analysed the SAR data must be orthorectified to a regular map projection. Ground control points identified in the SAR image and on 1:50 000 maps were used along with the DEM and range information provided with the image, to define the warping process. An in-house

orthorectification technique was used based on polynomial warping and explicit modelling of foreshortening/layover effects. The SAR image was orthorectified onto a 10m grid in the NZ map projection as illustrated in Fig.1.

It was found extremely difficult to identify points in the unrectified data in steep terrain. An alternative approach employed identified these points in an initial rectified image and then calculated the raw line/pixel values using the current warping models. The refined set of control points was then used to regenerate the models and re-rectify the data.

A variety of angles relating to the local surface were generated as images from the DEM. These included: surface slope, slope azimuth (from north), view direction to surface normal, azimuth of surface normal projection as viewed from the sensor, and view direction to component of surface normal in the direction of the sensor. This last angle is often referred to as local incidence angle.

IDENTIFICATION OF GROUND COVER CLASSES

The JERS-1 SAR image was separated into three major ground cover classes for analysis as shown in Fig.1. This was done with the aid of SPOT data and the known altitude dependence of vegetation cover based on surveys by Clarkson [4]. The zones identified were;

Zone 1 (farmland) predominantly containing introduced grasses. The park boundary, which describes a near-perfect circle around the mountains, is at between 350 and 500m altitude above sea level.

Zone 2 (forest), the vegetation within the park and up to 1100m, is indigenous forest proper. Tree heights are up to 25m

at the base of this zone, seldom exceed 15m above the 760m line, and become even shorter as the altitude increases.

Zone 3 (bare), from 1100-1300m, vegetation is a more or less continuous cover of shrubs no more than 2.5 m high. With increasing altitude, shrubs are replaced by tussocks, herbfield, mossfield, and finally bare ground above 1650m. A snow and icefield are almost permanent features of the summit.

RESULTS

In collecting class dependent information on, for instance, radar brightness vs. incidence angle, the pair of images are sampled within the appropriate mask area on a regular grid in order to achieve at least 10,000 sample pairs. These can then be plotted (not shown) or used in a standard regression analysis to determine any dependence between the variables and the significance of this dependence.

As expected, the analysis of this information shows a characteristic increase in brightness as the local surface becomes more perpendicular to the radar beam. The noise appears to be greater at lower incidence angles. Several factors may be contributing to this:

- speckle noise is multiplicative and therefore larger in the brighter areas;
- the small angles tend to come from steep and rough areas on the ground where the DEM is likely to be less accurate.
- errors in registration are most apparent at sharp terrain boundaries which, as noted above, are often where low incidence angles are achieved;
- vegetation cover may be less homogeneous in areas of rapid terrain variation.
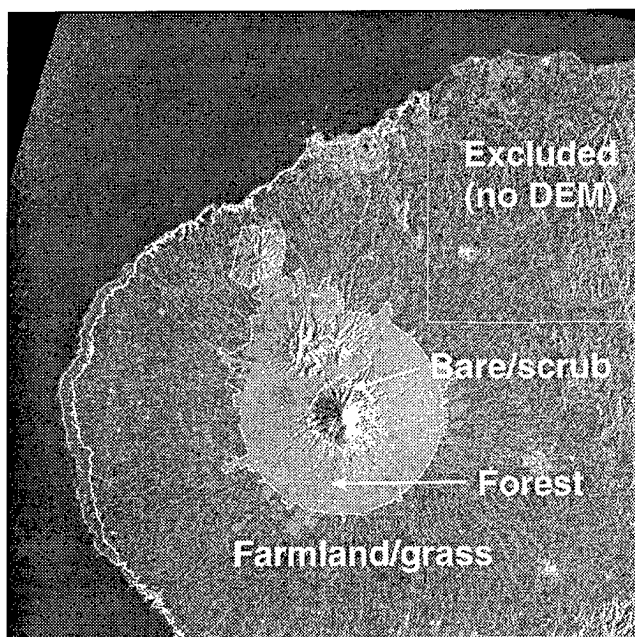
Figure 1 Orthorectified JERS-1 SAR
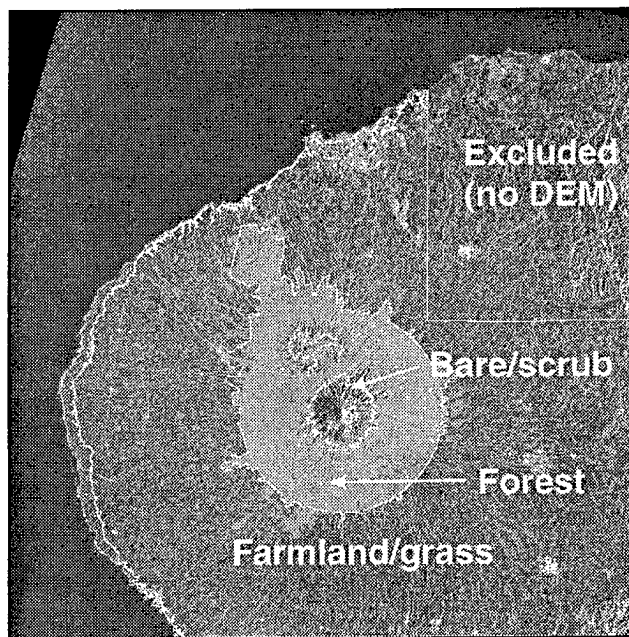
Figure 2 Corrected for scatterer density

The first step in normalising for terrain is to scale the backscattered power by $\sin\theta_i$ where θ_i is the local incidence angle, or the component of the angle between the surface normal and viewing direction projected onto the vertical plane passing through both the sensor and the target. This scaling accounts for the additional area of distributed scatterers contributing within a pixel's range increment [1]. In the present study where amplitudes are being used $\sqrt{\sin\theta_i}$ is the appropriate scaling factor. Fig.2 illustrates the effect of this correction where it can be seen that the image appears much flatter and the differences in cover class are enhanced. The success of the correction can be seen most clearly on the two lower volcanoes to the NNW, Pouakai and, in particular, the more northerly Kaitake. A close inspection indicates that the correction is performing better than may appear in Fig.2, even over quite steep terrain found in the "bare" region.

Once corrected as described above, any remaining angle dependency of the backscatter is expected to be a function of the radar frequency and the particular target. The corrected backscatter was compared to the angle between the viewing direction and the local surface normal. Straight lines were fitted to the data (about 60,000 samples/class) using the parameters listed in table 1. It is clear from these parameters that the grass cover class is significantly different in its mean backscatter for a nominally flat surface (35° incidence). This is borne out by the general appearance of the imagery where the farmland appears darker than the area within the National Park boundary.

y = a + b*x	a	b	σ	mean @ 35°
Bare	947	-4.5	405	791
Trees	764	-0.3	238	755
Grass	914	-6.6	266	683

Table 1. Parameters of lines fitted to corrected data.

DISCUSSION

Apart from the means for a level surface (35° incidence), it can also be seen in table 1 that the three cover classes have significantly different dependence on viewing geometry. Farmland has a negative slope indicating it has a tendency reflect in a specular sense. Supporting this is the fact that most of the farmland around Mt Taranaki/Egmont is pasture and would be relatively smooth compared to the 23cm JERS-1 wavelength.

Likewise the bare class has a negative slope although of a smaller magnitude. This result appears less reliable, as seen by the standard deviation in table 1, and is probably a result of the factors mentioned in the previous section. None the less, there are many large scree slopes and moss covered areas at the lower

altitudes of this class that may appear smooth compared to the radar wavelength.

After correction, the trees class has an flatter response to viewing angle indicating that it is scattering energy evenly in all directions. Unlike plantation forestry, this native forest will be much more irregular in the distribution of trees and the angle of their trunks. It would seem from this result that the canopy is reasonably dense and that there is no specular component in the backscatter at all.

CONCLUSION

A JERS-1 SAR image has been analysed using a high resolution (10m) DEM in order to detect viewing angle dependencies. It was found that the theoretical correction for local incidence angle worked well over a wide range of angles. The residual dependence appears to be sensitive to the ground cover class. In this study both farmland and bare ground/low level vegetation show a fall off in backscattered radiation as the target facet points away from the sensor. On the other hand the native forest class had a flatter response and even showed a tendency to scatter more strongly at shallower angles to the target facet.

ACKNOWLEDGEMENTS

REFERENCES

[1] R.K.Raney, T.Freeman, R.W.Hawkins, and R.Bamler, "A plea for radar brightness," *Proc. IGARSS'94, Pasadena, August. 8-12 1994*, vol. I, pp. 1090-1092.

[2] E.Robin, and A.Guissard, "A parametric study of the trunk-ground corner effect in forest remote sensing," *Proc. IGARSS'94, Pasadena, August 8-12 1994*, vol. I, pp. 100-102.

[3] R.W.Jansen, T.L.Ainsworth, R.A.Fusina, S.R.Chubb, and G.R.Valenzuela, "Modelling of surface features observed in Gulf Stream boundary regions," *Proc. IGARSS'94, Pasadena, August 8-12 1994*, vol. I, pp. 460-462.

[4] Y.Rauste, "Incidence-angle dependence in forested and non-forested areas in Seasat SAR data," *IJRS.*, vol 11 (7), pp. 1267-1276.

[5] B.D.Clarkson, *"Vegetation of Egmont National Park New Zealand,"* DSIR Science Information Publishing Centre, Wellington. National Parks scientific series no. 5. 95 p.

Edge Detection in Speckled SAR Images Using the Continuous Wavelet Transform

Marie CHABERT, Jean-Yves TOURNERET and Gilles MESNAGER

ENSEEIHT/GAPSE, 2 rue Camichel 31071 Toulouse, France

Tel: (33) 61 58 83 67 - Fax: (33) 61 58 82 37

e-mail: chabert@len7.enseeiht.fr

Abstract— This study presents an original method to detect edges in Synthetic Aperture Radar images corrupted by speckle. We show that the Continuous Wavelet Transform (CWT) allows to accurately detect edges embedded in speckle. Edges give rise to a conic signature in the CWT. Furthermore, the Signal to Noise Ratio (SNR) increases with the scale of the CWT. The optimal wavelet maximizing the SNR is derived and two wavelet based detectors are proposed. Both are 2D detectors and so take advantage of information redundancy in the scale-space plane.

I. INTRODUCTION

This paper addresses the problem of edge detection in Synthetic Aperture Radar images corrupted by speckle. As shown in a previous study [1], the SPECAN concept, combined with parametric spectral estimation, offers spatial resolution improvement and speckle noise reduction. We show that a post-processing stage, based on the Continuous Wavelet Transform (CWT), allows an accurate detection of edges embedded in speckle. The case of a step in the image is studied. In this case, there exists an optimal wavelet maximizing the signal to noise ratio. Two wavelet based detectors are proposed, both providing jump date and amplitude estimators.

II. MODEL OF SPECKLED IMAGES

Speckle is produced by imaging systems using coherent radiation such as laser and radar systems. We denote by μ the average intensity of the image in a uniform region containing no object (for instance a quiet sea or a cultivated field). The image intensity $I(x,y)$ after the conventional SAR processor (e.g. chirp matched filter followed by modulus operator) is a random stationary variable with mean μ and variance μ^2 :

$$I(x,y) = \mu.s(x,y) \tag{1}$$

where $s(x,y)$ denotes the speckle. The speckle is modeled as a stationary multiplicative noise with unit mean and variance. It is assumed to have a Rayleigh distribution.

An ideal edge process $e(x,y)$ is modeled by a step of amplitude A located at position x_0:

$$
\begin{aligned}
e(x,y) &= 1 && \text{for } x < x_0 \\
&= 1 + A && \text{for } x \geq x_0
\end{aligned}
\tag{2}
$$

A step in the image represents for instance two fields of different reflections and, in general, piecewise constant backgrounds. The resulting process is:

$$\zeta(x,y) = I(x,y).e(x,y) \tag{3}$$

For the sake of simplicity, we consider an azimut processing of the image. The image is then studied line by line (for fixed y). The azimut line is denoted by:

$$\zeta(x) = I(x).e(x) = \mu.s(x).(1 + A.U(x - x_0)) \tag{4}$$

where $U(x)$ is the unit step. $\zeta(x)$ is a random process with piecewise constant mean value and variance. Figure 1 represents a realisation of a step of amplitude $A = 1$ on an azimut line of average intensity $\mu = 1$:
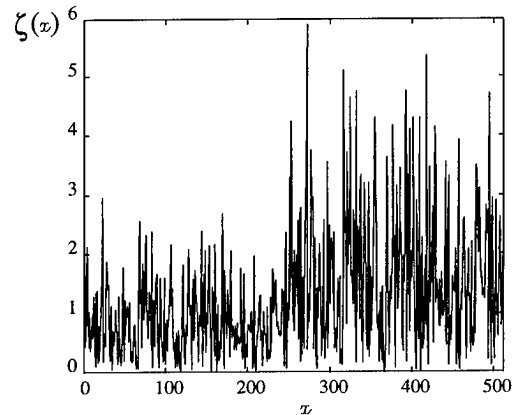
Figure 1: 512 samples of $\zeta(x)$ with $A = 1$, $\mu = 1$ and $x_0 = 250$

III. DETECTION USING CONTINUOUS WAVELET TRANSFORM

A. Edge signature in the scale-space plane

The detection consists in determining the jump location x_0. Our strategy uses the Continuous Wavelet Transform. For a 1D signal $f(x)$, it is defined as:

$$C_f(a,b) = \frac{1}{\sqrt{a}} \int_{\mathbb{R}} f(x)\psi^*\left(\frac{x-b}{a}\right) dx \tag{5}$$

where $\psi(x)$ is an L^2 normalized wavelet. It must verify several well-known so-called admissibility conditions

among which the following:

$$\int_{\mathbb{R}} \psi(x)dx = 0 \qquad (6)$$

Owing to the transform linearity, $C_\zeta(a,b)$ can be expressed as:

$$C_\zeta(a,b) = \frac{1}{\sqrt{a}} \int_{\mathbb{R}} \mu.s(x).e(x)\psi^* \left(\frac{x-b}{a}\right) dx \qquad (7)$$

$$= \mu.(C_s(a,b) + C_{e'}(a,b)) \qquad (8)$$

with:

$$e'(x) = s(x).A.U(x-x_0) \qquad (9)$$

Let us define the "signature" of the multiplicative jump by $E[C_\zeta(a,b)]$. According to (6):

$$E[C_s(a,b)] = 0 \qquad (10)$$

Finally, the signature is expressed as:

$$E[C_\zeta(a,b)] = \mu E[C_{e'}(a,b)] = -\sqrt{a}\mu A I_\psi^* \left(\frac{x_0-b}{a}\right) \qquad (11)$$

with $I_\psi(x) = \int_{-\infty}^x \psi(u)du$. Considering a wavelet of bounded support $\left[-\frac{\Delta x}{2}, +\frac{\Delta x}{2}\right]$, an edge results in a conic signature in the scale-space plane. This conic signature stems from the mean value jump of the signal. The variance jump gives rise to a variance jump in the scale-space plane at the same location [3].

As an example, figure 2 represents the CWT modulus of the signal defined above. It is computed with the Haar wavelet of support 20 for scales equal to [1, 6, 11]. The cone points to the edge location $x_0 = 250$ and its maximum amplitude at fixed scale a, obtained for $b = x_0$, is proportional to the jump amplitude A.
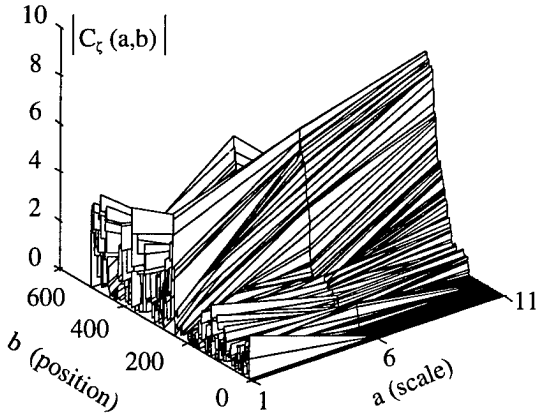
Figure 2: Conic jump signature modulus

The signature depends on the local regularity of the signal. Indeed, according to Mallat [4], the evolution of wavelet transform across scales depends on the Lipschitz exponent of the signal. The study of maximum amplitude variation across scales allows to distinguish different kinds of jumps. Fig. 3 shows a contour plot of the jump signature.
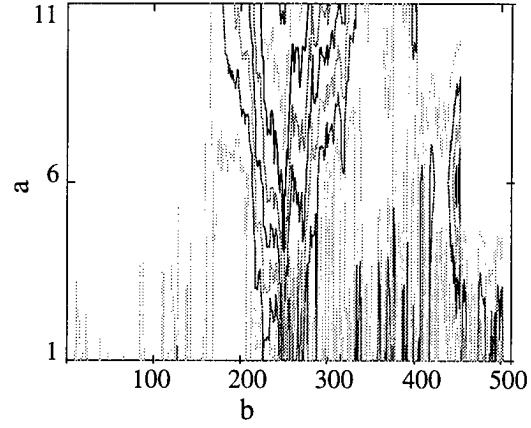
Figure 3: Conic signature contours

B. Signal to Noise Ratio

According to the speckle model, the signal to noise ratio is constant everywhere on the radar image [2] and is equal to unity when no noise reduction has been performed. An important advantage of working in the scale-space plane is that the SNR increases with the scale of the CWT. We consider the CWT in the region of the scale-space plane defined by the conic edge signature. When the scale a tends to infinity, the variance of the CWT is asymptotically constant, whereas the signature amplitude increases continuously with a. This can be summarized by expressing the signal to noise ratio:

$$\gamma(a,b) = \frac{|E[C_\zeta(a,b)]|^2}{Var[C_\zeta(a,b)]} \sim \frac{2\mu^2 A^2 a}{A^2+1} \frac{|I_\psi(0)|^2}{S_{s'}(0)} \qquad (12)$$

$$\text{when } a \longrightarrow +\infty$$

with $s' = s - m_s$.

The SNR is proportionnal to the scale. However, this property, valid not only for a step, depends on the evolution across scale of the maximum value and so on the local regularity of the edge. Equation (12), with some weak hypotheses regarding the d.d.p. of $e'(x)$, allows to compute the detection and false-alarm probabilities.

C. Optimal wavelet

An optimal wavelet, maximizing the SNR, can be derived in the case of an ideal edge process [5]. We consider the SNR for large scale a: the optimal wavelet maximizes $|I_\psi(0)|^2$. For a real wavelet of bounded support $\left[-\frac{\Delta x}{2}, +\frac{\Delta x}{2}\right]$:

$$|I_\psi(0)|^2 = \left(\int_{-\Delta x/2}^0 \psi(u)\, du\right)^2 \qquad (13)$$

The Cauchy-Schwartz inequality leads to:

$$|I_\psi(0)|^2 \leq \int_{-\Delta x/2}^0 \psi^2(u)\, du \int_{-\Delta x/2}^0 du \qquad (14)$$

$$|I_\psi(0)|^2 \leq \frac{\Delta x}{2} \int_{-\Delta x/2}^0 \psi^2(u)\, du. \qquad (15)$$

The Cauchy-Schwartz inequality becomes an equality when ψ^2 is a constant over the interval $\left[-\frac{\Delta x}{2}, 0\right]$ and so when ψ is a binary wavelet. Consequently, the symmetrical Haar wavelet belongs to the class of optimal solutions for a bounded support wavelet and an abrupt multiplicative jump.

D. Wavelet based algorithms

The matched filter is the optimal detector in the sense that it maximizes the SNR. Unfortunately, the noise is not white in the scale-space plane. This complicates the computation of the filter and leads us to study the performance of two wavelet based sub-optimal detectors. The wavelet based algorithms developed for the case of an additive noise [3] can be used for multiplicative noise models, if the signal is not zero mean on either side of the edge. This condition is always satisfied in radar images since a zero reflection value cannot be encountered.

The first approach consists in computing the CWT correlation with 2-D signature (see fig. 4):

$$\Gamma_1(b) = \iint_{\mathbb{R}^2} C_\zeta(a, b)\, C_s(a, b - c)\, da\, dc \qquad (16)$$

This approach implies that the edge shape is known. It is equivalent to the 2D matched filter when the noise is white in the scale-space plane.
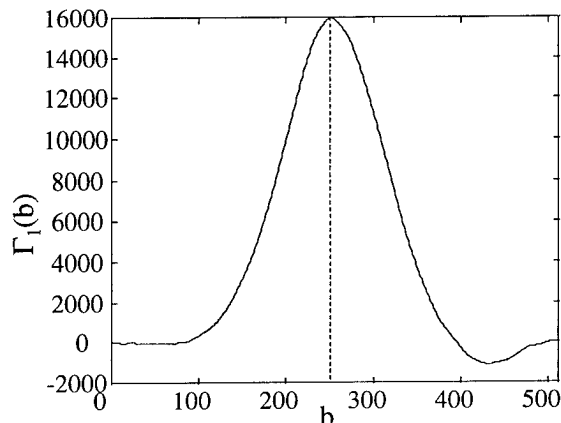
Figure 4: Maximum at $\widehat{x_0} = 251$

The second detector uses the modulus of a sum along n fixed scale slices of the CWT (see fig.5):

$$\Gamma_2(b) = \left| \sum_{i=1}^{n} C_\zeta(a_i, b) \right| \qquad (17)$$

Considering the sum of n fixed scale slices amounts to taking the average, and so reduces the noise of the CWT. Moreover, it takes into account the information available at each computed scale.
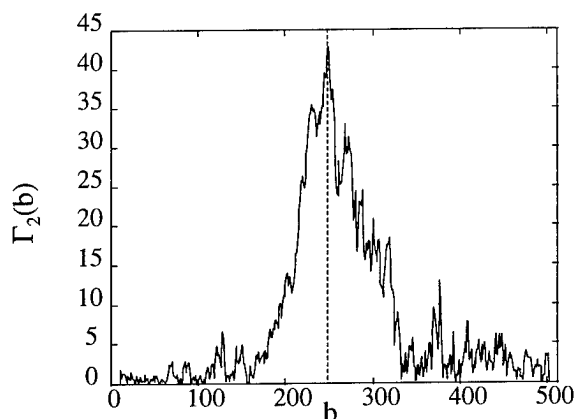
Figure 5: Maximum at $\widehat{x_0} = 250$

For these two detectors, the edge location and amplitude estimation in the scale-space plane amounts to a maximum search. An edge location estimator $\widehat{x_0}$ can be derived as follows:

$$\Gamma_i(\widehat{x_0}) = \underset{b}{Max}\, \Gamma_i(b) \qquad i = 1, 2 \qquad (18)$$

The maximum value is proportionnal to the edge amplitude. This provides a jump amplitude estimator.

Both are 2D detectors and thus take advantage of information redundancy in the scale-space plane. The qualitative behavior of the two detectors is very similar: they show good performance.

The problem of edge detection can also be solved with zero-crossing algorithms [4]. The zeros of the second-derivative of a smoothed version of the signal correspond either to minima (slow change in the signal) or maxima of the first-derivative (abrupt change). These algorithms are capable neither of estimating the jump amplitude nor of dinstinguishing between an abrupt and a slow change.

IV. CONCLUSION

This paper proposes two wavelet-based methods to detect abrupt edges immersed in speckle. The jump properties (amplitude and location) can be determined from the jump signature in the scale-space plane. The case of an abrupt edge is detailed, but the detectors can also be applied to other edge shapes. The signature, as well as the optimal wavelet, will then be different.

REFERENCES

[1] G. Mesnager, C. Lambert-Nebout and F. Castanié "Spatial resolution improvement using a SPECAN approach in SAR data processing", proc. IGARSS'95, July 1995.
[2] A.C. Bovik, "On detecting edges in Speckle Imagery", IEEE Trans. on Acoustics, Speech, and Signal Processing, October 1988.
[3] M. Chabert, J.-Y. Tourneret and F. Castanié, "Additive and Multiplicative Jump Detection using Continuous Wavelet Transform", Proc. ICASSP'96, Atlanta, to appear.
[4] S. Mallat and S. Zhong, "Characterization of signals from multiscale edges," IEEE Trans Pattern Analysis and Machine Intelligence, vol.8, pp.679-698, 1986.
[5] A. Denjean and F. Castanié, "Mean Value Jump Detection: a Survey of Conventional and Wavelet Based Methods," in Wavelet Theory, Algorithms and Applications,C. K. Chui, L. Montefuso and L. Puccio (eds.), Academic Press, Inc., 1994.

Removing RF interferences from P-Band airplane SAR data.

G. Cazzaniga, A. Monti Guarnieri.
Dipartimento di Elettronica - Politecnico di Milano.
Piazza L. da Vinci, 32 - 20133 Milano - Italy
Fax: +39-2-23993585, e-mail: monti@elet.polimi.it

Abstract – This paper approaches the problem of canceling the disturbs due to *RF* interferences in P-band, airborne SAR missions. Two techniques are introduced: one exploits *MUSIC* to estimate the interferences' frequencies, and then performs notch filtering at that frequencies; whereas the other adaptively estimate the interference contributions and cancel them by means of in-phase subtraction. Both techniques have been successfully tested on the data acquired by the *DLR E-SAR* sensor [1] over urban areas.

INTRODUCTION

Airplane SAR sensors that operate in the P-Band (~450 MHz) can be affected by interferences due to earth transmitters, like *RF* beacons, telephone carriers and so on. As a consequence, artifacts appears in the focused image (filtered by the SAR compression reference), moreover that disturbs can prevent the proper extraction of motion and Doppler parameters by raw data, necessary for a fine focusing [2,3]. The degradation of the image quality is marked. For example, these interferences were observed in the data acquired by the *DLR* airplane when flying in the area close to Munich (Germany). The azimuth power spectrum shows several peaks, caused by the interferences, in the plot of Fig.1.
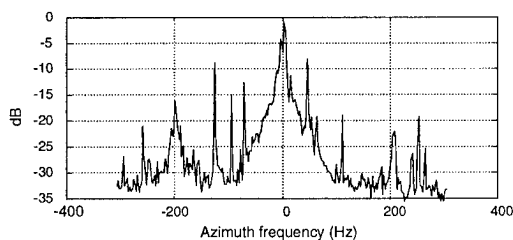
Figure 1: *Azimuth spectrum of Airplane P band SAR data.*

These carriers are caused by interfering sources that can be located anywhere in the very wide beam of the *SAR* antenna, $30^0 \times 60^0$ (azimuth, elevation). As an example, the focused energy of a 25 m^2 scatterer with reflectivity coefficient $\sigma_0 = -20$ dB, located in the closest range ($r_0 = 4$ km), is the same of a 10 W interfering transmitter located at the farthest range in the 3 dB antenna beam ($r_0 \simeq 50$ km). The effect of such interferences is quite visible in the range compressed data image of Fig.2 and in the focused image of Fig.3.
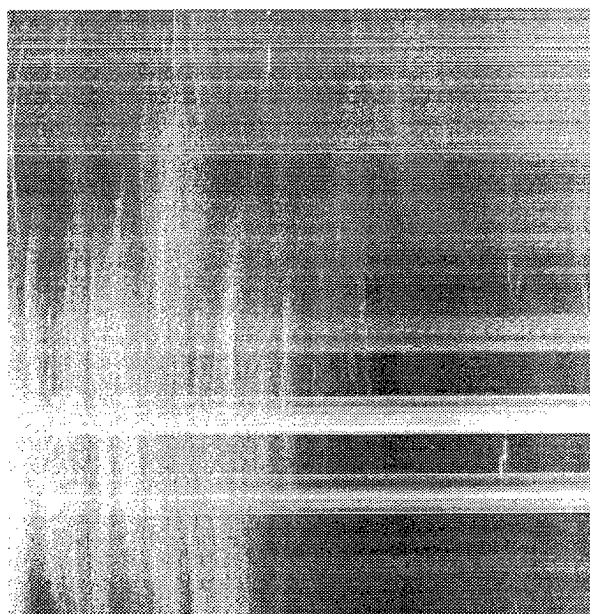
Figure 2: *P-band range compressed E-SAR data acquired in the area of Munich. Note the artifacts due to RF interferences.*

INCOHERENT INTERFERENCES ESTIMATE AND CANCELLING

The first technique implemented to cancel the interferences is by means of power spectrum estimate and notch filtering. The P band raw data can be modeled as a white signal (e.g. coming from backscattering) + sinusoidal interferences, as the short time periodograms sequence of Fig.4 shows.

A monodimensional *MUSIC* estimates was assumed, since it provides a robust, fast and very accurate power spectrum density estimate for the assumed model, the variance of the frequency estimate being close to the Cramer Rao bound [4]. The estimate and removal of interferences was performed after 3:1 azimuth presumming,

in order to cancel the contribution of interfering sources out of the data bandwidth (see Fig.1). Increase in efficiency and accuracy were gained by operating on range-compressed data: a $M = 32^{th}$ order covariance matrix was computed by exploring the darker areas (e.g. the data portion with the minimum backscattering, usually close to the far range), to enhance the contribution of the interferences.
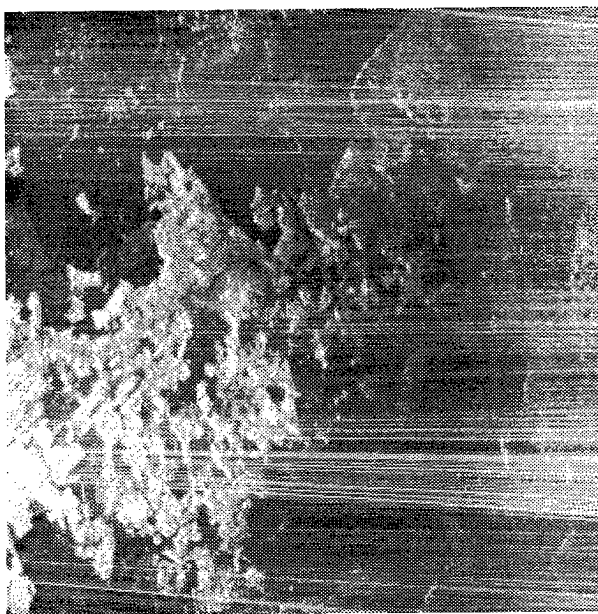
Figure 3: *The same dataset of Fig.2 after focusing.*

A few adjacent range lines were averaged to increase statistic accuracy. The interferences could be easily identified by the corresponding eigenvalues: $\lambda_i \gg \sigma^2 = \lambda_M$, (being λ_M being the minimum eigenvalue, and σ^2 the estimated variance of scene reflectivity), we currently assumed a threshold $\lambda_i \geq 3 \cdot \lambda_M$ to detect interfering peaks. Usually $3 \div 6$ interfering sources were found within the azimuth presummed data spectrum. Each of the interferences was then canceled by means of the zero-phase non causal notch filter:

$$H(z) = \frac{1 - z_o z^{-1}}{1 - z_p z^{-1}} \cdot \frac{1 - z_o z^{-1}}{1 - z_p^* z^{-1}} \qquad (1)$$

The zeros of the filter, $z_0 = \exp(j\hat{\omega})$, were located in correspondence of the estimated interfering frequency, whereas the poles, $z_p = \rho_p \exp(j\hat{\omega})$ were fixed in order to give a canceled bandwidth: $B_{3dB} \simeq 3(\rho_p - 1)$ some times larger that the standard deviation of the estimated frequency, $\sigma_{\hat{\omega}}$, derived in [4]. In the explored datasets, the accuracy achieved in the estimate of interfering frequencies (and the frequency stability of the carriers) allowed the use of a notch filter (1) with a bandwidth B_{3dB} always smaller than 1/100 of sampling rate. As an example, Fig.5

shows the same range compressed data of Fig.2, after canceling interferences; the focused image, shown in Fig.6, is to be compared with Fig.3.
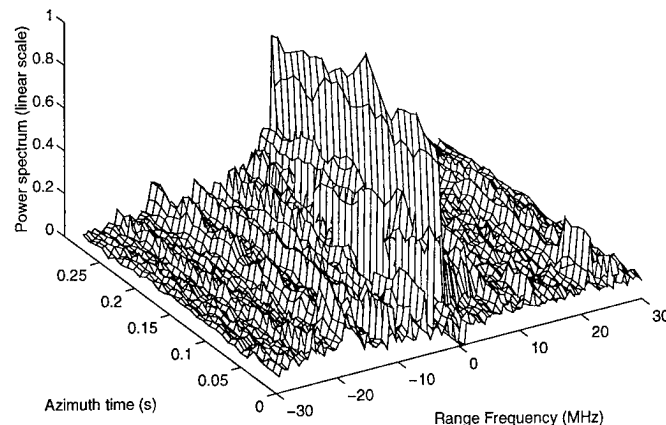
Figure 4: *Time-varying power spectrum estimates of raw data. The peaks due to interferences appear at almost constant frequencies.*

The complete removal of interferences has been checked by an accurate periodogram analysis.
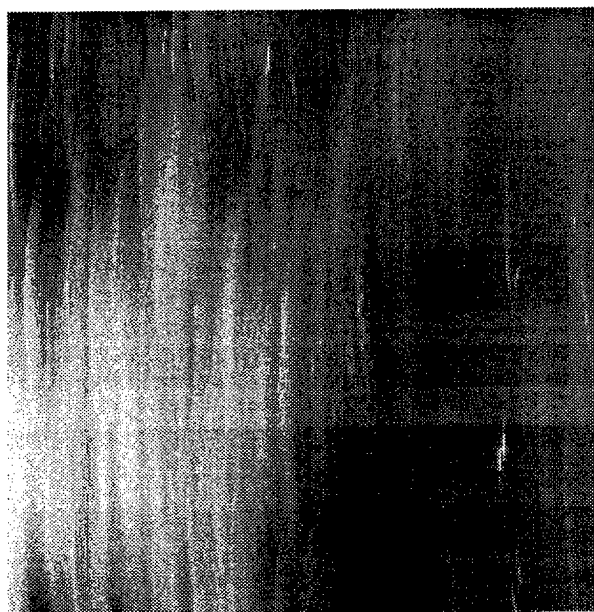
Figure 5: *The same data-set of Fig.2 after removing interferences.*

COHERENT ESTIMATION AND CANCELLATION

An alternative approach to the incoherent interference canceling consists in a coherent estimation and in-phase subtraction of the disturbing sources. We can assume that

1846

M interferences, due to beacons or mobile telephone systems as carrier, eventually amplitude modulated with a very small bandwidth ($\ll f_s = 60$ MHz, see Fig.4):

$$n(t) = \sum_{k=1}^{M} a_k(t) \exp(\omega_k t + \varphi_k) \qquad (2)$$

superimposed to the SAR signal.

Figure 6: *The data-set of Fig.5 after focusing.* The frequencies ω_k can be coarsely estimated as shown before, e.g. by *MUSIC* algorithm. Next, a sort of *PLL* is implemented by bandpass filtering (around ω_k): fine estimates of ω_k, φ_k can be retrieved by fitting a linear phase (that corresponds to the MLE estimator [5]), and the amplitude is estimated by coherent amplitude demodulation. The estimated signal, $\hat{n}(t)$ (see (2)), is then subtracted, and the interferences removed. This was usually carried on presummed data for efficiency. However if performed on the raw data (sampled every 15 cm), the estimate of the phases at the beginning of each range line, $\varphi_k(x)$ (where x is azimuth), allows for a precise tracking of the airplane motion:

$$\varphi_k(t) = \frac{\omega_k}{c}(r(x) - r_o) \qquad (3)$$

being $r(x)$ the distance between airplane and the transmitter. This allows to locate the position of the transmitter: its range is found by the measuring the curvature of $\varphi_k(t)$, and its azimuth is found by exploring the averaged interference amplitude. As an example, Fig.7 shows the amplitude and part of the unwrapped Doppler phase history of an interference due to a transmitter that should be located ~ 43 km far from the airplane, i.e. at the edges of the antenna beam.

CONCLUSIONS

Two techniques, both capable of removing RF interferences on P-Band airplane SAR data has been presented. The incoherent approach, that exploits $MUSIC$ for estimating fringes frequency and second order pole-zero notch filtering, has been proven simple, fast, and robust: its canceled bandwidth is modest. On the other hand, the coherent in-phase canceling gives superior performances since - theoretically - it does alter the "good" signal, however its computational cost is higher (actually more than doubled). Yet, it can provide useful information e.g. to track the airplane motion.
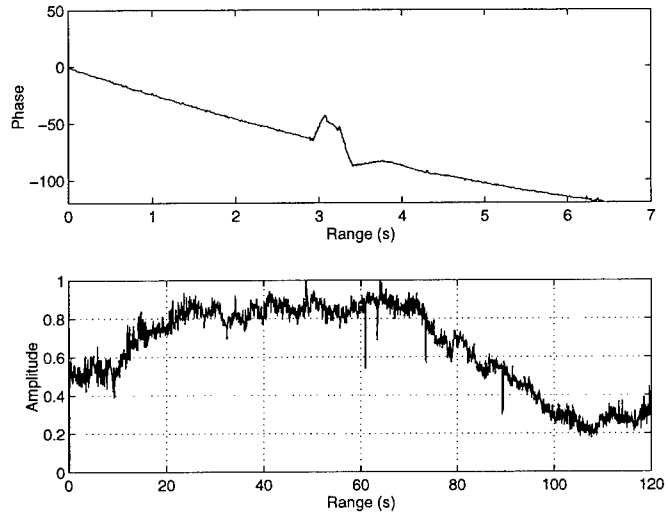
Figure 7:*Doppler phase and amplitude of one of the interfering sources.*

REFERENCES

[1] *Statusbericht 1995* Deutsche Forschungsanstalt für Luft und Raumfahrt e.V. Institut für Hochfrequenztechnik, Jan. 1995

[2] J. R. Moreira*A New Method of Aircraft Motion Error Extraction From Radar Raw Data For Real Time Motion Compensation*, in *IEEE Trans. Geosci. and Remote Sensing*, Vol. 28, No. 4, pp. 620–626, Jul. 1990.

[3] A. Moreira, *Real-Time Synthetic Aperture Radar (SAR) Processing with a New Subaperture Approach*, in *IEEE Trans. Geosci. and Remote Sensing*, vol 30, no. 4, pp 714–722, 1993.

[4] P. Stoica, A. Nehoray *MUSIC, Maximum Likelihood, and Cramer-Rao Bound*, in *IEEE Trans. Acoust. Speech and Sig. Proc.*, vol ASSP-34, pp 331–341, Apr. 1986.

[5] D. C. Rife, R. Boorstyn, *Single-Tone Parameter Estimation form Discrete-Time Observation*, in *IEEE Trans. on Inf. Theory*, vol IT-20, no. 5, pp. 591–598, 1974.

HYBRID CONSENSUS THEORETIC CLASSIFICATION[1]

Jon Atli Benediktsson[†], Johannes R. Sveinsson[†] and Philip H. Swain[‡]

[†]Engineering Research Institute
University of Iceland
Hjardarhaga 2-6, 107 Reykjavik, Iceland
E-mail: benedikt@verk.hi.is
[‡]School of Electrical and Computer Engineering
Purdue University
W. Lafayette, IN 47907, U.S.A.

ABSTRACT

Hybrid classification methods based on consensus from several data sources are considered. Each data source is at first treated separately and classified using statistical methods. Then weighting mechanisms are needed to control the influence of each data source in the combined classification. The weights are optimized in order to improve the combined classification accuracies. Both linear and non-linear methods are considered for the optimization. A non-linear method which utilizes a neural network is applied and gives excellent experimental results. The hybrid statistical/neural method outperforms all other methods in terms of test accuracies in the experiments.

1. INTRODUCTION

In multisource classification different types of information from several data sources are used for classification in order to improve the classification accuracy as compared to the accuracy achieved by single-source classification. Conventional statistical pattern recognition methods are not appropriate in classification of multisource data since such data cannot, in most cases, be modeled by a convenient multivariate statistical model. However, statistical methods based on consensus theory have shown potential in classification of multisource data [1].

In this paper, hybrid statistical/neural consensus theoretic classification is discussed and applied in classification of multisource data. First, consensus rules are introduced in Section 2. Weight selection schemes for consensus rules are then discussed in Section 3. Finally, experimental results are given in Section 4.

2. CONSENSUS RULES

Several consensus rules [1],[2] have been proposed. Probably the most commonly used consensus rule is the linear opinion pool (LOP) which has the following (group probability) form for the information class ω_j if n data sources are used:

$$C_j(Z) = \sum_{i=1}^{n} \lambda_i p(\omega_j | z_i) \qquad (1)$$

where $p(\omega_j | z_i)$ is a source-specific posterior probability and λ_i's $(i = 1, \ldots, n)$ are source-specific weights which control the relative influence of the data sources. The weights are associated with the sources in the global membership function to express quantitatively the goodness of each source [2].

Another consensus rule is the logarithmic opinion pool (LOGP) which can be described by

$$\log(L_j(Z)) = \sum_{i=1}^{n} \lambda_i \log(p(\omega_j | z_i)). \qquad (2)$$

3. WEIGHT SELECTION SCHEMES

It is needed to define a function

$$Y = f(X, \Lambda) \qquad (3)$$

where X contains source-specific posteriori discriminative information and Λ corresponds to the source-specific weights in (1) or (2).

In the case when f is non-linear a neural network can be used to obtain a mean square estimate of the function. Here, the consensus theoretic classifiers with equal weights can be considered to preprocess the data for the neural networks. Then, the neural network learns the mapping from the source-specific posteriori probabilities to the information classes. Therefore, the neural network is used

to optimize the classification capability of the consensus theoretic classifiers. If $Y = D$ is the desired output for the whole classification problem, the process can be described by the equation

$$\Lambda_{nlopt} = \arg\min_{\Lambda} \|D - f(X, \Lambda)\|^2. \tag{4}$$

The update equation for the weights of the neural network is

$$\Delta\Lambda = \eta\|D - f(X, \Lambda)\|\nabla_{\Lambda} f \tag{5}$$

where η is a learning rate.

If, on the other hand, f is linear, the combined output response, Y, can be written in matrix form as

$$Y = X\Lambda \tag{6}$$

and the optimal linear weights can be determined by using the pseudo inverse of X.

4. EXPERIMENTAL RESULTS

Classification was performed on a data set consisting of the following 4 data sources:

1. Landsat MSS data (4 spectral data channels).

2. Elevation data (in 10 m contour intervals, 1 data channel).

3. Slope data (0-90 degrees in 1 degree increments, 1 data channel).

4. Aspect data (1-180 degrees in 1 degree increments, 1 data channel).

Each channel comprised an image of 135 rows and 131 columns, and all channels were spatially co-registered. The area used for classification is a mountainous area in Colorado. It has 10 ground-cover classes which are listed in Table 1. One class is water; the others are forest types. It is very difficult to distinguish among the forest types using the Landsat MSS data alone since the forest classes show very similar spectral response [1]. Reference data were compiled for the area by comparing a cartographic map to a color composite of the Landsat data and also to a line printer output of each Landsat channel. By this method 2019 reference points (11.4% of the area) were selected comprising two or more homogeneous fields in the imagery for each class. Approximately 50% of the reference samples were used for training, and the rest were used to test the algorithms.

Three statistical methods were used to classify the data [3]: the minimum Euclidean Distance (MED) classifier, the linear opinion pool (LOP), and the logarithmic opinion pool (LOGP). For the LOP and LOGP, ten data classes (corresponding to the information classes in Table

Table 1: Training and Test Samples for Information Classes in the Experiment on the Colorado Data Set.

Class #	Information Class	Training Size	Test Size
1	Water	301	302
2	Colorado Blue Spruce	56	56
3	Mountane/Subalpine Meadow	43	44
4	Aspen	70	70
5	Ponderosa Pine 1	157	157
6	Ponderosa Pine/Douglas Fir	122	122
7	Engelmann Spruce	147	147
8	Douglas Fir/White Fir	38	38
9	Douglas Fir/Ponderosa Pine/Aspen	25	25
10	Douglas Fir/White Fir/Aspen	49	50
	Total	1008	1011

1) were defined in each data source. The multispectral remote sensing data sources were modeled to be Gaussian but the topographic data sources were modeled by Parzen density estimation [4] with Gaussian kernels.

Several different versions of the LOP and LOGP were tried. These included: 1) versions with equal weights, 2) weights based on reliability factors [1], 3) optimal linear weights, and 4) non-linear versions based on (4). For the non-linear versions, two and three layer conjugate-gradient backpropagation (CGBP) neural networks [5] were utilized with different numbers of hidden neurons (0, 15, 25, 35, and 45 hidden neurons). For each implementation, the neural networks were trained six times with different initializations. Then, the average accuracy for these six experiments was computed (see Figures 1 and 2).

The conjugate-gradient backpropagation (CGBP) algorithm with two and three layers was also trained on the same data with different numbers of hidden neurons (0, 15, 30, and 45 hidden neurons). Each version of the CGBP network was trained six times with different initializations and the overall average accuracies were computed in each case.

The overall classification accuracies for the different methods are summarized in Table 2. In the table the average result for the best implementation of the neural network based methods is shown in each case. From the results in Table 2 it is interesting to note that very similar results were achieved in terms of classification accuracies of test data with both the LOP and LOGP when they were optimized by the neural networks. These methods outperformed all other methods in terms of test accuracies. It is noteworthy that the CGBP optimization increased the accuracies of the equally weighted LOGP by 11.61% (training) and 3.83% (test). In comparison

Table 2: Overall Training and Test Accuracies for the Classification Methods Applied to the Colorado Data Set.

Method	Training Accuracy	Test Accuracy
MED	40.28%	37.98%
LOP (equal weights)	68.06%	66.67%
LOP (source-specific weights from [1])	75.89%	74.09%
LOP (optimal linear weights)	80.26%	80.42%
LOP (optimized with CGBP, 30 hidden)	83.49%	82.22%
LOGP (equal weights)	79.76%	78.44%
LOGP (source-specific weights from [1])	81.65%	79.03%
LOGP (optimal linear weights)	79.66%	80.02%
LOGP (optimized with CGBP, 30 hidden)	91.37%	82.27%
CGBP (0 hidden neurons)	84.15%	79.70%
CGBP (40 hidden neurons)	96.26%	78.34%
Number of Samples	1008	1011

Figure 1: Training Accuracies as a Function of the Number of Iterations for the Methods that Utilize the CGBP.
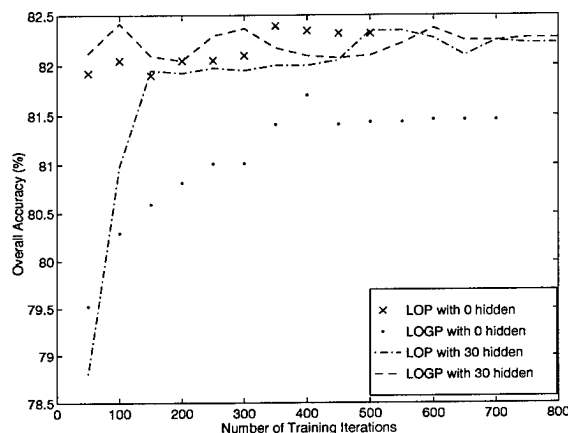
Figure 2: Test Accuracies as a Function of the Number of Iterations for the Methods that Utilize the CGBP.

the CGBP optimization increased the accuracies for the equally weighted LOP by 15.43% (training) and 15.55% (test). Both CGBP optimized methods outperformed the best neural network classifiers in terms of test accuracies by more than 2.5%. This indicates the significant results that the discriminative information provided by LOP and LOGP are effective preprocessors for neural networks.

5. CONCLUSION

Hybrid consensus theoretic classification has been discussed. The approach is based on using a neural network as an optimizer for statistical methods which use consensus from several data sources in classification. The hybrid approach outperformed all other classification methods used, in terms of test accuracies. The results suggest that the discriminative information provided by the equally weighted LOP and LOGP can be effective preprocessors for neural networks. Based on the results, the proposed hybrid statistical/neural consensus theory has potential to be applied successfully for many difficult classification problems.

6. REFERENCES

[1] J.A. Benediktsson and Philip H. Swain, "Consensus Theoretic Classification Methods," *IEEE Transactions on Systems Man and Cybernetics*, vol. 22, no. 4, pp. 688-704, July/August 1992.

[2] C. Berenstein, L.N. Kanal and D. Lavine, "Consensus Rules," in *Uncertainty in Artificial Intelligence*, L.N. Kanal and J.F. Lemmer (eds.), North Holland, New York, 1986.

[3] P.H. Swain, "Fundamentals of Pattern Recognition in Remote Sensing," *Remote Sensing - The Quantitative Approach*, edited by P.H. Swain and S. Davis, New York: McGraw-Hill 1978.

[4] B.W. Silverman, *Density Estimation for Statistics and Data Analysis*, Monographs on Statistics and Applied Probability, Chapman and Hall, New York, 1986.

[5] E. Barnard, "Optimization for Training Neural Nets," *IEEE Transactions on Neural Networks*, vol. 3, no. 2, pp. 232-240, March 1992.

A Framework for Multi-date Multi-sensor Image Interpretation

A. Murni[1], A.K. Jain[2], and J. Rais[3]

[1] Computer Science Department, Michigan State University, A714 Wells Hall, E. Lansing, MI 48824, USA
[2] Computer Science Department, Michigan State University, A714 Wells Hall, E. Lansing, MI 48824, USA
[3] Geodesy Department, Bandung Institute of Technology, Jl. Ganesha 10, Bandung 40132, Indonesia
aniati@ogah.cs.ui.ac.id (Indonesia) murniani@cps.msu.edu (Michigan)

ABSTRACT

This paper describes a methodological framework for multi-date multi-sensor remotely-sensed image interpretation. The framework was built based on an integrated multi-sensor classification scheme. The classification scheme considers a remotely-sensed input image to consist of *homogeneous* and *textured* regions. This approach allows flexibility in performing digital image mosaicking and data fusion for the purpose of cloud cover removal and a more consistent scene interpretation. We have determined that both in optical and radar images the land cover types can be grouped into *homogeneous* and *textured* regions. Using our classification scheme, the discrimination between land cover types in each group can be enhanced. It was found that better classification accuracy can be obtained by not assuming that the input image is fully *homogeneous* where a classifier based on image tone or spectral features is applied or fully *textured* where a classifier based on texture features is applied. Several results on digital image mosaicking and data fusion using the proposed classification scheme are presented.

INTRODUCTION

Integration of different and complementary sensor images such as optical and radar remotely-sensed images has been widely used for cloud cover removal [1] and achieving better scene interpretation accuracy [2, 3]. The integration may be done by image mosaicking or data fusion which are accomplished either at the preprocessing stage [4] or the postprocessing stage [2]. Sensor-specific classifiers are commonly used. For example, classifiers based on image tonal or spectral features are used to classify optical images [2]. In other cases, classifiers based on texture features are used for recognizing cloud types [5] and improving the urban area classification result for optical images. For radar image interpretation, classifiers based on various texture models were used [6, 7, 8], but problems may arise if *homogeneous*-region land cover objects exist in the radar image [9].

We have observed that both optical and radar images consist of *homogeneous* and *textured* regions. A region is considered as *homogeneous* if the local variance of gray level distribution is relatively low, and a region is considered as *textured* if the local variance is high. Our further investigations found that land-cover objects can also be grouped into homogeneous and textured land cover objects which offers better discrimination in each group. Based on this findings we have proposed an integrated multi-sensor classification scheme [1]. The same procedure can be used for classifying optical or radar input images. We use the multivariate Gaussian distribution to model the homogeneous part of an image, and use the multinomial distribution to model the gray level co-occurrences of the textured part [9]. We apply a spectral-based classifier to the homogeneous part and a texture-based classifier to the textured part of an image. These classifiers use maximum-likelihood decision rule which work concurrently on an input image.

We propose a methodological framework which uses the integrated multi-sensor classification scheme. The framework is facilitated by performing digital image mosaicking and data fusion at the preprocessing (low-level) stage and at the postprocessing (high-level) stage. The following sections present the aim of this study, the discussion on the proposed methodological framework, and experimental results. Finally, a conclusion is drawn from this study.

OBJECTIVES OF THIS STUDY

Indonesia is a tropical country where the use of optical remotely-sensed image for land cover mapping is confounded by the cloud cover problem. Microwave radar images are cloud-free images but their use is hampered due to the limited availability of the image interpretation system. To solve these problems we have proposed an integrated multi-sensor image classification scheme whose performance should at least be comparable to the standard or common procedure for optical and radar image interpretation. The synergestic approach of optical and

radar remote sensing data has become important for solving cloud cover problem and obtaining a more consistent scene interpretation. We propose a complete methodological framework for multi-date multi-sensor image interpretation scheme.
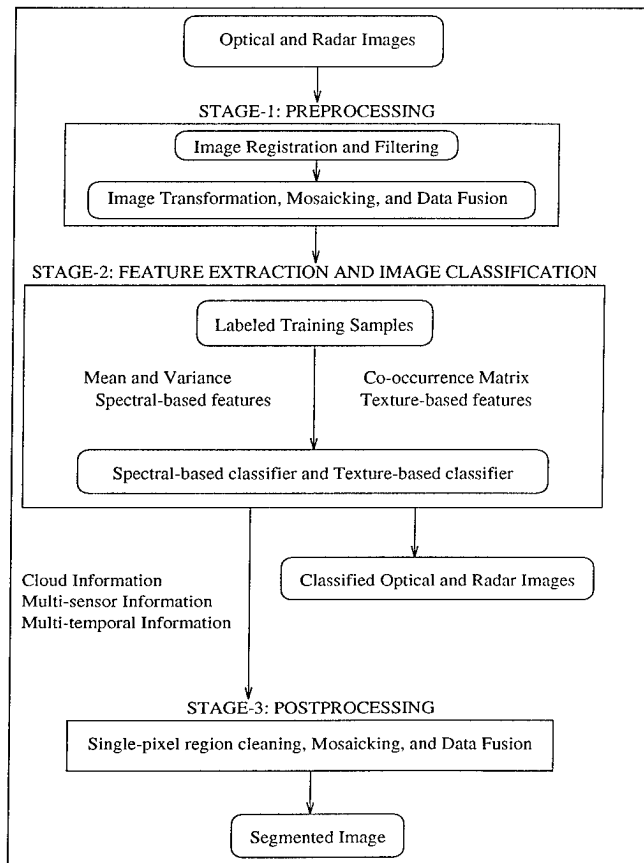
Fig.1: A methodological framework for multi-date multi-sensor image interpretation.

METHODOLOGICAL FRAMEWORK

The diagram of the methodological framework is shown in Fig. 1. Digital image mosaicking at the low-level may use multitemporal optical images with complementary cloud cover. We have utilized the algorithm proposed by Soofi *et al.* [10]. In case the multitemporal optical images are not fully complementary in terms of cloud cover, we propose a technique to remove the cloudy areas with the aid of the corresponding classified radar image by setting the cloudy pixel intensity to the mean intensity value of the corresponding pixel class. An example of low-level image mosaicking is shown in Fig. 2.

Low-level data fusion may be done to improve radar image classification accuracy or to exploit the synergy of multi-sensor information. The data fusion method may include algebraic operations, the principal compo-

nent transformation or the Karhunen-Loeve transform, FCC or IHS tranformation, augmented vector classification, and hierarchical data fusion. We have utilized the intensity transformation based on the Karhunen-Loeve transform [11] and hierarchical data fusion [4].

An example of high-level image mosaicking and data fusion is shown in Figs. 2(e) and 2(f). The image mosaicking is done between classified optical and radar images. The data fusion is an intermediate data fusion which is done at feature level, and can be applied to multi-sensor images or multi-date single-sensor images. We have compared the use of decision combination function based on the *a posteriori probability* [12, 13] and the highest rank method [14].

The classification scheme was discussed in [1]. Basically, there are three parameters that control the proposed classifier: (i) a threshold value that decides if a pixel belongs to either the homogeneous or the textured region, (ii) type of each land cover object (homogeneous, textured, or both), and (iii) the window size over which the texture measures are computed. The threshold value can be tuned so that we can even have a fully spectral-based classifier or a fully texture-based classifier if it is necessary. The type of each land cover object can be determined based on the labeled training samples. We can use a window size as small as 3x3 if there are roads or other line-shaped objects, or a window size of 9x9 if larger objects are contained in the image.

An optical Landsat TM image in Fig. 3(d) shows that the water and forest classes are homogeneous regions while urban, village and agriculture areas are textured regions. In a SPOT panchromatic image we found that only the cloud and open areas are textured regions. For radar image STAR-1 in Fig. 4(b) the water and forest classes occupy the homogeneous regions while the village and agriculture areas are textured regions. In an airborne radar image we found that all land cover objects are textured regions except for the water class.

RESULTS AND DISCUSSIONS

Fig. 2 shows simulated multitemporal SPOT panchromatic images with cloud cover. Low-level image mosaicking is done between images in Figs. 2(a) and 2(b). The remaining cloudy areas are removed with the aid of its classified radar image in Fig. 2(c). The cloud-free mosaic image is classified and shown in Fig. 2(d). Figs. 2(e) and 2(f) compare the results of high-level image mosaicking and high-level data fusion of optical and radar images, respectively. The data fusion gave a better result where the cloud shadow area at the lower left corner is correctly classified as the forest class while in the mosaic image it is classified as the water class.
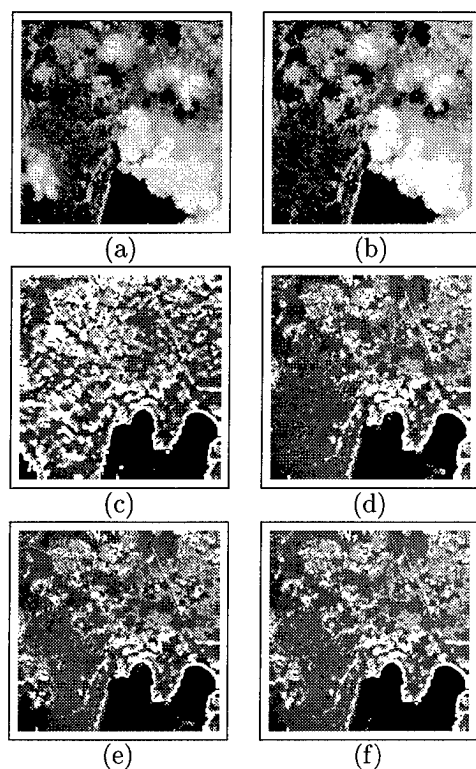
Fig. 2: SPOT panchromatic (simulated multitemporal) and airborne radar images of Sumatra area; (a) and (b) simulated multitemporal SPOT panchromatic images; (c) Classified radar image; (d) Cloud-free SPOT classified image (low-level mosaicking); (e) SPOT and radar mosaic classified image (high-level mosaicking); (f) Segmented image as a result of SPOT and radar data fusion.

Fig. 3: Landsat TM images of Jawa area; (a) Band-1 image; (b) Band-4 image; (c) Principal component transformed image of Band-1 and Band-4 images; (d) Binary image of (c): black=homogeneous and white=textured; (e) Classified image using the proposed scheme; and (f) Clustered and classified based on ground truth and using all the seven bands of Landsat TM images.

Fig. 3(e) shows an example of using our classifier with Landsat TM visible Band-1 and infrared Band-4 input images. The classification was applied to the principal component transformed image of the Band-1 and Band-4 images. This classification result is compared to another classified image in Fig. 3(f). The classified image in Fig. 3(f) was created based on clustering and ground truth class association using all the seven bands of the Landsat TM. The two results are comparable except that the urban areas, village and agriculture areas in Fig. 3(f) are not as well separated as in Fig. 3(e).

Fig. 4 compares the classification result of a STAR-1 radar image using our classifier which is shown in Fig. 4(c) and the classification result using the augmented vector approach based on three texture models which is shown in Fig. 4(d). The two classified images show comparable good results except that in Fig. 4(d) the village and agriculture areas along the river are classified into the forest class.

Fig.4: STAR-1 radar image of Kalimantan area; (a) Original image; (b) Binary image: black=homogeneous and white=textured; (c) Classified by the proposed scheme; and (d) Classified using augmented vector approach based on three texture models.

1853

CONCLUSIONS

In general, our classification scheme performs slightly (about 2%) better than the standard procedure based on image tonal or spectral features. The improvement occurs in the textured regions (urban areas, village and agriculture areas). There is also an improvement in radar image classification accuracy of up to 6% if we compare our results to those reported in [15, 6]. Radar image transformation using the corresponding optical image can also improve the radar image classification. We found that in some cases, data fusion result is better than image mosaicking result. We also found that the decision combination function based on the highest rank method is more fair than the function based on the joint *a posteriori* probability. We are continuing our investigation on using the classifier for second-level land cover mapping in forestry applications.

ACKNOWLEDGMENTS

REFERENCES

[1] A. Murni, A.K. Jain, and J. Rais. An Integrated Multisensor Image Classification Scheme for Land-cover Mapping. In *Proc. 2nd Asian Conference on Computer Vision*, pages III–92 – III–96, December 1995.

[2] A.H. Schistad Solberg, T. Taxt, and A.K. Jain. A Markov Random Field Model for Classification of Multisource Satellite Imagery. *IEEE Transactions on Geoscience and Remote Sensing*, 34(1):100–113, 1996.

[3] R. Loizzo, G. Sylos Labini, M. Pappalepore, P. Pieri, G. Pasquariello, and M. Antoninetti. Multitemporal and Multisensor Signatures Evaluation for Lithologic Classification. In *Proc. International Geoscience and Remote Sensing Symposium*, pages 2209–2211, 1995.

[4] Y.T. Zhou. Multi-sensor image fusion. In *Proc. 12th Int. Conference on Pattern Recognition, Jerusalem*, pages 193–197, October 1994.

[5] J.L. Lee, R.C. Weger, S.K. Sengupta, and R.M. Welch. A Neural Network Approach to Cloud Classification. *IEEE Transactions on Geoscience and Remote Sensing*, 28(5):846–855, September 1990.

[6] A.H. Schistad and A.K. Jain. Texture analysis in the presence of speckle noise. In *Proc. International Geoscience and Remote Sensing Symposium*, pages 884–886, May 1992.

[7] A. Murni, N. Darwis, M. Mastur, and D. Hardianto. A texture classification experiment for SAR radar images. In *Pattern Recognition in Practice IV, E.S. Gelsema and L.N. Kanal (eds), North Holland*, pages 213–225, 1994.

[8] D.R. Peddle and S.E. Franklin. Image Texture Processing and Data Integration for Surface Pattern Discrimination. *Photogrammetric Engineering and Remote Sensing*, 57(4):413–420, April 1991.

[9] G. Lohmann. Co-occurrence-based Analysis and Synthesis of Textures. In *Proc. 12th Int. Conference on Pattern Recognition, Jerusalem*, pages 449–453, October 1994.

[10] K.A. Soofi, R.S.U. Smith, and R. Siregar. A Planimetrically Accurate SPOT Image Mosaic of Buton Island, Sulawesi, Indonesia. *Photogrammetric Engineering and Remote Sensing*, 57(9):1217–1220, September 1991.

[11] R.Y. Wong. Sensor transformations. *IEEE Transactions on Systems, Man, and Cybernetics*, SMC-7(12):836–841, December 1977.

[12] P.H. Swain. Bayesian Classification in a Time-Varying Environment. *IEEE Transactions on Systems, Man, and Cybernetics*, SMC-8(12):879–883, December 1978.

[13] J.A. Benediktsson, P.H. Swain, and O.K. Ersoy. Neural Network Approaches Versus Statistical Methods in Classification of Multisource Remote Sensing Data. *IEEE Transactions on Geoscience and Remote Sensing*, 28(4):540–551, July 1990.

[14] T.K. Ho, J.J. Hull, and S.N. Srihari. Decision Combination in Multiple Classifier Systems. *IEEE Transactions on Pattern Analysis and Machine Intelligence*, 16(1):66–75, 1994.

[15] C. Schmullius and J. Nithack. Crop Monitoring with Multi-temporal Airborne DLR E-SAR Images. In *Proc. International Geoscience and Remote Sensing Symposium*, pages 719–721, July 1995.

AUTOMATED TRAINING SAMPLE LABELING USING LABORATORY SPECTRA

Pifuei Hsieh
School of Electrical and Computer Engineering
Purdue University
West Lafayette, IN 47907-1285
Phone (317) 494-1743
Fax (317) 494-3358
hsieh@ecn.purdue.edu

David A. Landgrebe
School of Electrical and Computer Engineering
Purdue University
West Lafayette, IN 47907-1285
Phone (317) 494-3486
Fax (317) 494-3358
landgreb@ecn.purdue.edu

Abstract--This paper presents a method for automatically labeling training samples in mineral identification problems. A previous work showed that an experienced human operator can successfully identify training samples by visually comparing the strong absorption features of the laboratory spectra to those of the adjusted remotely sensed spectra. However, it is obviously a time-consuming process. The purpose of this research is to automate the labeling process. The method proposed in this paper consists of a data preprocessor and correlation detection. This data preprocessor is used for shape adjustment and scale unification. It includes three parts: (1) the log residue method; (2) reference level setting; (3) signal normalization. The desired number of training samples can be specified to guarantee that enough training samples are drawn from the data set. After training samples are labeled, a series of statistical pattern recognition analysis methods are applied to the original remotely sensed data set to do classification. The data set used in the paper is Airborne Visible/Infrared Imaging Spectrometer (AVIRIS) data taken over the Cuprite mining District, Nevada in 1992. The result is compared to a previous work that requires a human operator to visually label training samples and a rough geologic ground truth map. It shows that this automated labeling method not only saves human laboring but also achieves a fair performance of classification.

INTRODUCTION

Conventionally, a ground truth map is needed to label training samples when pattern recognition methods are used for classifying remote sensing data. In [1], it is shown that with no ground truth map, training samples in mineral classification problems can be labeled if laboratory reflectance spectra are available. It is due to the fact that many minerals have unique and diagnostic absorption characteristics in their reflectance spectra. In [1], after remotely sensed radiance spectra were adjusted to resemble reflectance spectra by using the log residue method [2], the adjusted spectra were visually compared to laboratory reflectance spectra by a human operator. A sample was labeled as a training sample if its absorption features in the adjusted spectrum and laboratory reflectance spectrum appeared to be adequately similar.

In this paper, a technique of signal detection is used to replace the visual comparison. The comparison criterion remains the same -- the absorption features of spectra. Note that the laboratory reflectance spectra used in [1] lack scaling units. While a human operator has no difficulty comparing absorption features with no scaling units available, it is more

difficult for any automatic comparison method to compare signals without any quantity information. A normalization approach is proposed to set up a common comparison background without any loss of absorption features of spectra. The laboratory reflectance spectra and all adjusted signal are normalized to be of zero mean responses and unit energies.

BACKGROUND

If an absorption feature is regarded as a spectral band where a local minimum of the spectrum occurs, then the absorption features of a spectrum are conserved with the following two operations:

(i) The spectral function is multiplied by a scalar, and
(ii) A constant is added to the spectral function.

Assume that a signal has a spectral function $p(\lambda)$. Let

$$s(\lambda) = \frac{p(\lambda) - \mu}{E}, \quad \text{where} \quad \mu = \frac{1}{n}\sum_{i=1}^{n} p(\lambda_i), \quad \text{and}$$

$$E = \sqrt{\sum_{i=1}^{n}(p(\lambda_i) - \mu)^2}, \text{ then } s(\lambda) \text{ and } p(\lambda) \text{ have the same}$$

absorption features.

Observe that $\sum_{i=1}^{n} s(\lambda_i) = 0$, and $\sum_{i=1}^{n}\left(s(\lambda_i)\right)^2 = 1$, so $s(\lambda)$ is a signal with zero mean and unit energy. The zero mean response provides a comparison reference level and unit energy eliminates the effect of the energy on the detection.

For the sake of convenience, each spectral response is expressed by a vector in a feature space $\underline{x} = [x_1 \; x_2 \; x_3 \; ... \; x_n]^T$. For the case at hand the wavelengths of the laboratory reflectance spectra represent only 31 bands covering the range 2.05-2.35 μm, so n=31 is used for the following discussion. The spectra comparison problem can be modeled as an m-hypothesis problem as below.

LABELING TRAINING SAMPLES

Assume that m laboratory spectra are normalized to $\underline{s}_1, \underline{s}_2, ..., \underline{s}_m$ ($\underline{s}_i^T \underline{s}_i = 1$). Therefore there are m hypotheses [3] for each normalized remotely sensed pixel $\underline{r}$ ($\underline{r}^T \underline{r} = 1$),

$$H_i : \underline{r} = \underline{s}_i + \underline{w}, \quad i = 1, 2, ..., m$$

where $\underline{w}$ is assumed to be a white Gaussian noise vector with a mean vector $\underline{0}$ and an identity covariance $\underline{I}$. To insure that the labeled samples are representative, thresholds are set. If H_i is true and the pixel $\underline{r}$ passes the threshold test, then $\underline{r}$ is labeled as a training sample of class i (i = 1,..,m).

Under H_i, the probability density of $\underline{r}$ is

$$p_{\underline{r}|H_i}(\underline{r}|H_i) = (2\pi)^{-n/2} exp[-\frac{1}{2}(\underline{r}-\underline{s}_i)^T(\underline{r}-\underline{s}_i)].$$ Assume that *a priori* probabilities are equal, then the decision rule based on the Bayes criterion is

$$\text{If } \underline{s}_k^T \underline{r} = \max_i(\underline{s}_i^T \underline{r}) \quad \text{say } H_k$$

That is called correlation detection. A threshold d is set to reject those pixels with little correlation with signal $\underline{s}_k$.

$$\text{If } \max_i(\underline{s}_i^T \underline{r}) < d, \text{ Do not label the pixel}$$

A more convenient way is to set a minimum training sample size so that a desired number of training samples is guaranteed. The labeling flowchart for known laboratory spectra is shown in Fig. 1.

For those minerals which do not have known or identifiable absorption features, their training samples were selected by the same technique as [1]. It was suggested that training samples were located in the low likelihood areas of a preliminary likelihood map, which was produced after the discriminant analysis feature extraction [7] and a maximum likelihood classifier for m classes were run on the original remotely sensed radiance data.
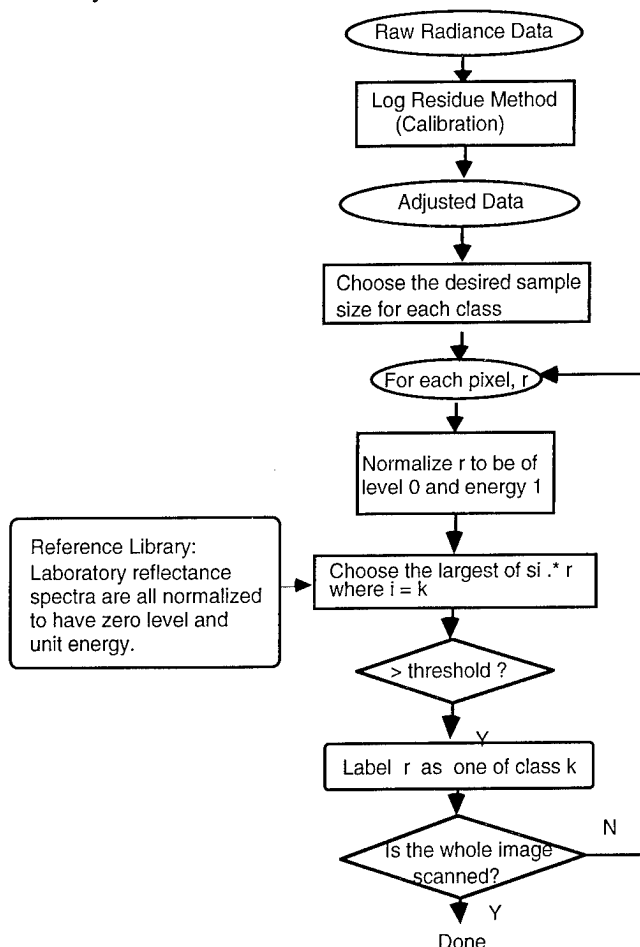
Figure 1. The flowchart of the automatic labeling process

CLASSIFICATION

The data set used is from the 1992 AVIRIS flight over the Cuprite Mining District in southwestern Nevada. The complete data set consists of 220 spectral bands covering the wavelength range 0.4 to 2.5 μm. This site has very little vegetation and several exposed minerals. Among these minerals, the laboratory reflectance spectra of alunite, buddingtonite, kaolinite and quartz are available [4]. As for other minerals such as argillized, tuff, alluvium and playa, their training samples were determined by comparing the preliminary likelihood map to the geologic maps from [5] and [6].

After the training samples of all eight classes were obtained, the discriminant analysis feature extraction method [7] was used to transform the data to a lower dimensional space so that classification could be done faster while the separability of the classes was maintained For an eight-class problem, the maximum number of features that discriminant analysis can extract is seven. In our experiment, all seven features were used for classification. A maximum likelihood classifier was designed based on the statistics of training samples in the 7-dimensional feature space.

To estimate the performance of the classifier, the resubstitution method and the hold-out method are used to bound the Bayes accuracy [7]. When the number of training samples is very limited, it is hard to apply the hold-out method so the leave-one-out method is often used instead to provide the lower bound on the accuracy.

Table1. The number of training samples and the classification accuracy

	Previous work	Threshold = 0.85	min. training sample size = 220
Alunite	729	3345	978
Buddingtonite	71	380	380
Kaolinite	232	698	227
Quartz	385	28	411
Alluvium	689	689	689
Playa	252	252	252
Tuff	293	293	293
Argillized	93	93	93
Accuracy (resubstitution, leave-one-out)	99.6% 99.6%	98.2% 98.0%	98.3% 98.2%

Although the experiment with threshold 0.85 and the experiment with minimum size 220 achieve comparable accuracies, the number of training samples for Quartz is too small (only 28) in the experiment with a threshold 0.85. Thus, the training samples obtained from the experiment with minimum setting were used to design a classifier and its classification result was compared to the previous work.

CONCLUSION

The thematic maps in Fig. 2 show that the result (min size=220) is similar to the previous work[1]. From the viewpoint of pattern recognition, using laboratory spectra to label training samples is a way in which the means of classes in the subspace (31 features) are utilized to identify training samples. Without the second order statistics information, the noise in the hypotheses is assumed a white noise. That is, all classes are assumed to have the same covariance matrices in the 31-dimensional subspace. After training samples are collected, a classifier is designed from data in the whole space.

When a ground truth map is not available, it is necessary to use other knowledge to train a classifier. In mineral identification, the strong absorption features of laboratory reflectance spectra are generally considered helpful in classification. For other ground types, photo interpretation or clustering techniques may be useful for labeling training samples.

REFERENCES

[1] Hoffbeck, J. P., and Landgrebe D. A., "Classification of High Dimensional Multispectral Image Data" in *Summaries of the Fourth Annual JPL Airborne Geoscience Workshop*, JPL Publ. No. 93-26, Vol. 1, pp. 93-96, October 1993.

[2] Green, A. A. and Craig, M. D., "Analysis of Aircraft Spectrometer Data With Logarithmic Residuals." *Proceedings of the Airborne Imaging Spectrometer Workshop*, JPL Publ. No. 85-41, pp. 111-119, 1985.

[3] Van Trees, H. L., *Detection, Estimation, and Modulation Theory*, John Wiley & Sons, Inc., 1968.

[4] Goetz, A.F.H., and Srivastava, "Mineralogical Mapping in the Cuprite Mining District, Nevada," *Proceedings of he Airborne Imaging Spectrometer Workshop*, JPL Publ. No. 85-41, pp.22-31, 1985.

[5] Abrams, M. J., Ashley, R. P., Rowan, L. C., Goetz, A. F. H., and Kahle, A. B., "Mapping of hydrothermal alteration in the Cuprite mining district, Nevada, using aircraft scanner images for the spectral region 0.46 to 2.36 μm.", 1977.

[6] Ebel, P., Hauff, P., Hill, B., Nash, G., Ridd, M., and McGregor, L., "Integrating remote sensing techniques (AVIRIS, TM, TIMS, and field spectroscopy) for exploration: case history-Cuprite, Nevada," *Proc. of the ERIM Ninth Thematic Conference on Geologic Remote Sensing*, Pasadena, California, pp. 833-843, 1993.

[7].Fukunaga, K., Introduction to Statistical Pattern Recognition, Second Ed., Boston Academic Press, 1990.

background
Alunite
Buddingtoni
Kaolinite
Quartz
Alluvium
Playa
Tuff
Argillized
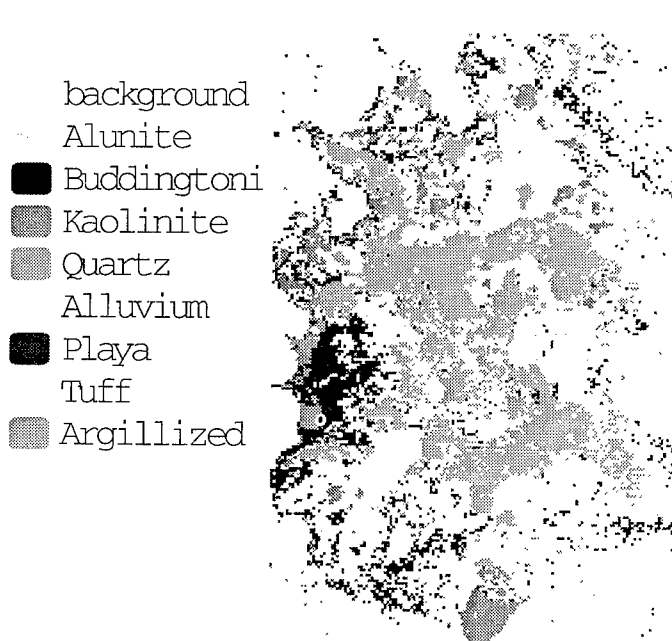
Figure 2 Classification of AVIRIS data using correlation detection (Original in color).
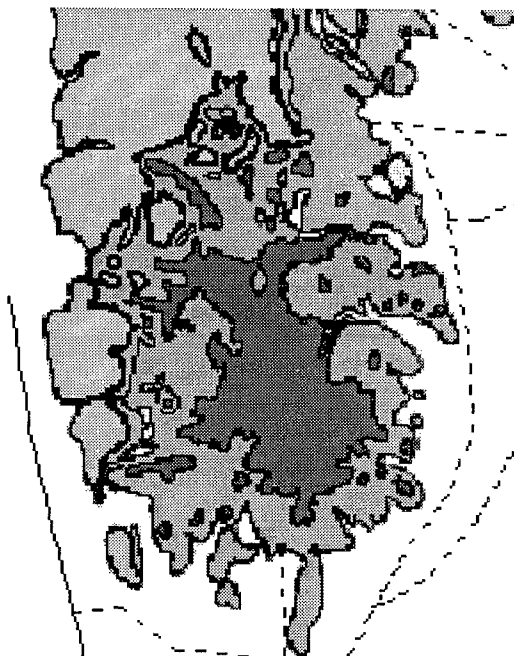
Figure 3. Geological map redrawn from Abrams, et al., 1977 (original in color).

Modified Divisive Clustering Useful For Quantitative Analysis Of Remotely Sensed Data[*]

H.N. Srikanta Prakash, S. Ravi Kumar, P. Nagabhushan, and K. Chidananda Gowda
Dept. of CS & E, S J College of Engineering, Mysore - 570 006, India.
Telephone : 515944/ 512568 Fax : (091) 821-515770.

Abstract -- A nonparametric, hierarchical, divisive clustering algorithm based on mutual nearest neighborhood concept is proposed for classification of large volume of multispectral data indenting minimum memory and computational time. To realise the reduction of memory and computational time requirements, we define an Area of Interest around each pixel to search the required k nearest neighbors necessary for initiating splitting operation. We have proposed a modified distance measure, which incorporates the relative position of the pixels together with their feature values inorder to improve the performance of the algorithm and reduce the classification error rate. The algorithm is simple, noniterative and can be successfully applied on any image data. Simulation experiments are conducted to corroborate the efficacy of the proposed methodology in terms of time, space and error rate.

I. INTRODUCTION

IT is very usual practice for man to classify the observations and hence, study the system for which observations are made. Classification of multidimensional data set or cluster analysis is one of the Pattern Recognition techniques. Clustering is usually viewed as a process of partitioning data into groups of similar objects. There exists a variety of hierarchical agglomerative and divisive clustering techniques [4]. Successive splitting operations lie at the heart of divisive methods. Perhaps a more natural way to define clusters is by utilizing the property of mutual nearest neighborhood between two patterns [2, 3].

Classification of remotely sensed data is not an easy task, because of the classification time increases significantly owing to its quadratic dependence of image size [5]. In order to compromise between time and accuracy of the clustering methods, we propose a new concept, namely Area of Interest around each pixel.

Distance measures play an important role in classification and many distance measures are reported in literature [1] [4]. Clustering procedures which employ such distance measures give erroneous classification because of considering only the feature values of the pixels. To alleviate this problem, we propose a modified distance measure which takes into account the relative position of the pixels in coordinate space along with the feature values or band values of the pixels.

This paper suggests a way by which divisive clustering using the concept of mutual nearest neighborhood can be applied to remotely sensed data for quantitative analysis, in such a way that the intrinsic limitations of applying this procedure to data of huge volume can be overcome.

II. NOTION OF AREA OF INTEREST

In traditional divisive clustering procedures the computational time and memory requirements are high as the whole image is considered to determine the k nearest neighborhood for each pixel necessary for initiating splitting operation. While working on an image data for classification, some basic knowledge like, roughness or smoothness of image areas are necessary. Such a situation is very common in remotely sensed data, thus the density of the neighboring pixels belonging to the same class is high.

To realize reduction of memory and computational time, we define an Area of Interest, around each pixel to search the required k nearest neighbors necessary for initiating splitting operation. While defining the Area of Interest with reference to pixel under consideration, we have made use of the assumption that the probability of existence of the k nearest neighbors surrounding the given pixel is very high as in remote sensing data.

Area of Interest is specified by the user as an area in the coordinate space surrounding each pixel under consideration. All pixels falling within this Area of Interest in the image are then used for calculating the distance from the pixel under consideration for finding k nearest neighbors. Consequently, the k-width neighborhood pixels within this Area of Interest are then considered for further splitting operation.

In Fig.1, the dotted line shows the Area of Interest for a
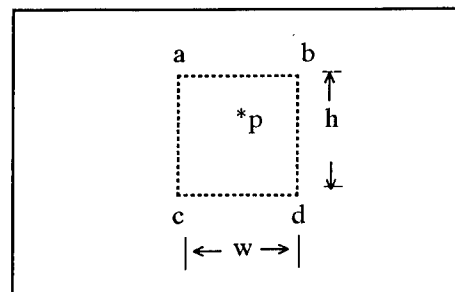
Fig. 1. Area Of Interest In Image Area

given pixel p in the image frame shown by the thick boundary. Let h and w be the user specified height and width of the Area of Interest and a, b, c, d represent the corner points. Let (x, y) be the coordinate vector of pixel p. The coordinate vectors of corners of the Area of Interest are calculated by the following equations.

$$a(x^\cdot, y^\cdot) = ((x - \frac{w}{2}), (y + \frac{h}{2})) \qquad (1)$$

$$b(x^\cdot, y^\cdot) = ((x + \frac{w}{2}), (y + \frac{h}{2})) \qquad (2)$$

$$c(x^\cdot, y^\cdot) = ((x - \frac{w}{2}), (y - \frac{h}{2})) \qquad (3)$$

$$d(x^\cdot, y^\cdot) = ((x + \frac{w}{2}), (y - \frac{h}{2})) \qquad (4)$$

Only those pixels present in this window are considered for finding k nearest neighbors for a given pixel p. Area of Interest is used also to emphasize or de-emphasize degree of nearness of neighborhood pixels present in the vicinity of this area and also it deals with the population present within this area rather than with the whole image.

III. PROPOSED MODIFIED DISTANCE MEASURE

In divisive clustering method, when k-width neighborhood is considered in multispectral image data, one encounters many pixels having the same proximity value with many other pixels. This leads to conflicts in choosing k nearest neighbor pixels causing erroneous classification, since many pixels may not be involved in the splitting operation.

The modified distance measure which fuses the relative positions of the pixels together with their feature values. However, it may be noted that traditional distance measures consider only feature values of the pixels but not their relative positions.

Let the feature space for pixels a and b having the feature vectors F_a (f_1, f_2, ..., f_D) and F_b ($f_1^\cdot$, $f_2^\cdot$, ..., $f_D^\cdot$) with D number of features respectively. The corresponding coordinate vectors of a and b is C_a (x, y) and C_b (x$^\cdot$, y$^\cdot$) respectively. The distance between pixels a and b is d(a, b) and is given by

$$d(a, b) = d1(F_a, F_b) + d2(C_a, C_b) \qquad (5)$$

where $d1(F_a, F_b)$ is a function of any distance measure[1] between pixels a and b based on their feature vectors, $d2(C_a, C_b)$ distance between pixels a and b with respect to their relative positions.

Let $d1(F_a, F_b)$ be the Euclidean distance between pixels a and b based on their feature vectors F_a, F_b is given by

---
[1] as found in any traditional distance measure like euclidean distance, cityblock distance etc.

$$d1(F_a, F_b) = A(\sqrt{\sum_{i=0}^{D} (F_{a_i} - F_{b_i})^2}) \qquad (6)$$

Here A is a function which converts real proximity value to integer value, such as A(6.2345678) = 62345 (proximity value is converted into integer number upto 4th decimal place).

In (5) $d2(C_a, C_b)$ is the distance between pixels a and b based on their coordinate vectors C_a, C_b is given by

$$d2(C_a, C_b) = \frac{G(|x - x^\cdot|, |y - y^\cdot|)}{G(X, Y)} \qquad (7)$$

Here X and Y are width and height of the image respectively, and G is a function which finds the greatest of two numbers.

It may be noted that the modified distance measure is of structure d1.d2, where d1 (d1 > 0) is the integral and d2 (d2 < 1) is the fractional part of the modified distance d. Eventhough, d1 >> d2, distance d2 helps to achieve better discrimination of pixels as it is calculated based on the relative positions of the pixels. Thus, when modified distance measure is employed, no two identical pixels are associated with the same proximity value in most of the cases. This is the reason why clustering methods using this modified distance measure perform better.

IV. CLUSTERING ALGORITHM

The proposed modified distance measured based divisive algorithm is nonparametric and hierarchical. The criterion is to split the pixels based on MNV (mutual neighborhood value) [2]. In this algorithm, a mutual neighborhood value (MNV) between two pixels is measured. When p_A is the sth nearest neighbor of p_B and p_B is the tth nearest neighbor of p_A, then the MNV between p_A and p_B is MNV(A, B) =MNV(B, A) =s + t. The smaller the MNV, the more similar the pixels are. The minimum MNV is 1 +1 =2 and the maximum MNV is 2k (k is the neighborhood depth).

The mutual nearest neighborhood based divisive clustering algorithm proceeds as follows:

1. Let P ={ {p_{11}, p_{12}, p_{13}, ..., p_{1X}}, {p_{21}, p_{22}, p_{23}, ..., p_{2X}}, ..., {p_{Y1}, p_{Y2}, p_{Y3}, ..., p_{YX}} } be a set of X by Y pixels on D dimensions. Let the initial number of clusters be 1 having a cluster weight of X by Y.

2. Find k-width neighborhood pixels for each pixel by following steps from 2a to 2c.

2a. Compute the coordinates of the boundary corners of Area of Interest using (1) to (4).

2b. Compute proximity values using modified distance measure given by (5), between all pairs of pixels coming under the Area of Interest.

2c. Search the k-width nearest neighbors having least proximity values.

3. Compute the MNV for every pair of pixels. If P_i, $(1 \leq i \leq X$ by Y$)$ and P_j, $(1 \leq j \leq k)$ are not mutual neighbors for the k, set MNV(i, j) to arbitrarily large number such as 100 (>2k).

4. Set MNV threshold $MNV_{th} \leq 2k$.

5. Identify all the pairs of pixels with MNV $= MNV_{th}$. Split every such pair into a cluster in descending proximity values, and increase the total number of clusters by 1 after each split.

6. If all the pairs of pixels with MNV $= MNV_{th}$ have been splitted and if still $MNV_{th} > 2k$, then $MNV_{th} = MNV_{th} - 1$, go to step 5. Otherwise, stop.

V. EXPERIMENTAL RESULTS

The experiment is conducted on Multispectral IRS data covering Nagarahole forest area of Karnataka State, India (as shown in Fig. 2. This image is of size 256 X 256 with 4 features. The data covers mainly the area consisting of dense forest, thin forest and a part of forest area destroyed by the fire. Thus we can look for quantitative analysis of deforestation and afforestation in this image.

The application of the proposed algorithm, for a neighborhood width of k=15 and w=h=10, yield 12 major classes. This has been verified by the ground truth provided by RRSC (Regional Remote Sensing Centre), Karnataka State, India and the classification results are shown in Fig. 3.
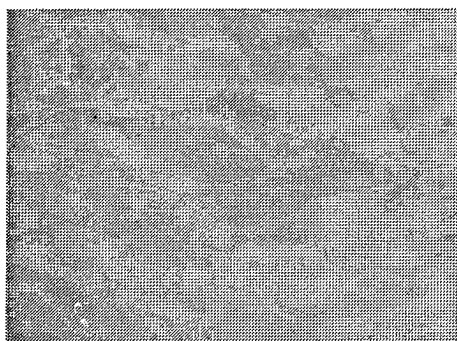
Fig. 2. IRS Image
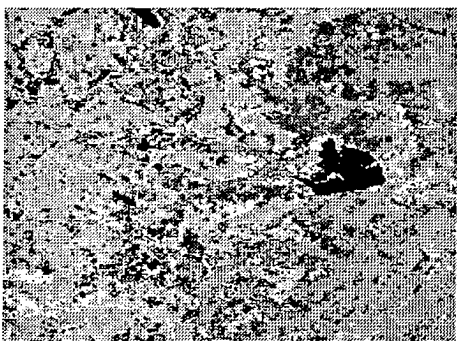
Fig. 3. Classification Map

TABLE I
Comparison Of Classification Results

Algo-rithm	Classification accuracy %	Time for finding NN %	Memory for finding NN %
1	93.35	100	100
2	97.86	2.36	0.472

Table I shows the comparison of proposed algorithm 2 with the algorithm 1 in [3]. The result obtained by the proposed methodology was found to be 97.86 % accurate. Hence, the proposed procedure is fast and indents less memory.

VI. DISCUSSION AND CONCLUSION

Further, the approach employed in defining modified distance measure, suggests that this procedure may be re-devised to extract a class of interest by tracing all those pixels belonging to the same class using the aforesaid idea of searching the nearest neighbors in the defined area of interest. Such a modification should be useful in Geological explorations as it is possible to trace the bunch of pixels representing the existence of natural resources like Petroleum, Coal (as in microwave remote sensing).

An Area of Interest is defined to realise the reduction of memory and computational time requirements. The advantages of modified measure is presented. An divisive clustering based on mutual nearest neighborhood concept is developed for quantitative analysis of remotely sensed data using the modified measure. Typical experiments are conducted to corroborate the efficacy of the algorithm. The algorithm automatically determines the number of classes depending on the k-width.

REFERENCES

[1] Duda, R.O. and P.E. Hart, Pattern Classification and Scene Analysis, Wiley, New York, 1973.

[2] K. Chidananda Gowda and G. Krishna, "Agglomerative Clustering using the concept of Mutual Nearest Neighborhood", P R, Vol.10, pp.105-112, Sep 1977.

[3] K. Chidananda Gowda and G. Krishna, "Disaggregative Clustering using the concept of Mutual Nearest Neighborhood", IEEE Trans. Syst. Man Cybern., Vol. SMC-8, No. 12, pp. 888-895, December 1978.

[4] A.K. Jain and R.C. Dubes, Algorithms for Clustering data, Englewood Cliffs, NJ: Prentice Hall, 1988.

[5] Xiuping Jia and John A. Richards, "Efficient Maximum Likelihood classification for Imaging Spectrometer Data Sets", IEEE Trans. on Geoscience and Remote Sensing, Vol. 32, No. 2, March 1994.

Surface Information Retrieval from Optical/Microwave data: Potentials and Limits of Synergistic Approaches

Jose F. Moreno[*] and Sasan S. Saatchi

Jet Propulsion Laboratory, MS 300-243, 4800 Oak Grove Drive, Pasadena, CA 91109-8099
Tel. 818-3543865, Fax: 818-3936943, Email: moreno@blacks.jpl.nasa.gov
[*] on leave from: Remote Sensing Unit, Faculty of Physics, University of Valencia, 46100 Burjassot, Valencia, Spain

Abstract -- In retrieving surface parameters from remotely sensed data, especially over vegetated land surfaces, synergistic use of optical and microwave instruments appears to be a more powerful tool than when each considered alone. Although this is especially true in the case of SAR data because of the complexity in the interpretation of the measured signal, the same is also true for optical data when working in highly vegetated areas or when dealing with the retrieval of parameters related to the water content of soil/vegetation systems. In this paper, we will demonstrate the capabilities of synergistic approaches by using polarimetric AIRSAR and Landsat TM data by means of a combined modeling approach, where the information content of each data type is explicitly separated into the parameters which are intrinsic to only one type of data and those which really provide the combined information potentially retrievable by means of data synergy.

INTRODUCTION

Because of the limitations of optical and microwave data to retrieve surface parameters when both are used separately, synergistic approaches can be a way to overcome some limitations and provide new type of information. However, combination of such different information is not an obvious task, and many aspects have to be considered in order to avoid erroneous or misleading conclusions.

For this study, we take advantage of data collected during the European Field Experiment on a Desertification-threatened Area (EFEDA)[1], including optical (Landsat TM, Spot, AVHRR, AVIRIS), microwave (AIRSAR) and ground truth data. After geometric and radiometric corrections applied as part of the pre-processing steps, we intend to retrieve surface parameters such as vegetation fractional cover, LAI, soil/vegetation albedo, soil moisture, leaf/canopy water content and other parameters governing surface aerodynamic roughness and canopy stomatal resistance, all for the purpose of energy balance modeling [4].

The information content of each dataset pertaining to the retrieval of the desired parameters is determined by using statistical data analysis techniques. However, physical modeling is required to properly describe the information content of the data, because of the multiple inter-relationships among all the involved parameters.

POTENTIALS AND LIMITS OF OPTICAL- MICROWAVE SYNERGY

Potentials of combined use of optical and microwave data have been established in different applications. Because of the very different information content, small correlation between optical and microwave channels are usually observed in measured data, and then there is a strong potential to derive significant more information when both types of data are used together. Limitations in the combined used of the data are seriously imposed by the change with time of surface conditions (especially those related to water content) when data are not simultaneous, but the major limitation is the intrinsic variability of natural surfaces, in most cases over the capabilities to detect changes with statistical significance, especially due to the high dynamical range of variation (including noise) in the SAR signal when combined with the optical reflectances. A major limitation is also the large-scale spatial pattern constraint (see Fig. 1). One would expect that when the scale under consideration is considerably over the wavelength sizes (like over 100m) homogeneous systems can be described with the same geometrical structure at all wavelengths under consideration. However, interference patterns associated to wavelength/size of structures still persist over large scales (Fig. 1b). In order to recover this behaviours in the models, the geometrical estructure of the systems must be described also at the scales comparables to wavelength, and not by assuming random media under a given spatial scale. Geometrical description is a major limitation at microwave frequencies, and optical data only help in these cases when the distances between vegetation elements are large enough to be sensitive to the amount of shadows over an (homogeneous) soil background. Optical shadows then provide information about geometrical structure, but for current spatial resolutions in satellite systems the geometrical information about wavelenght-size geometry required to model the microwave signal is lost in optical data. Multiple-angle data (especially at optical wavelengths) would be more useful to derive geometrical information.

CONCEPTUAL PROBLEMS IN EXISTING APPROACHES

In most existing approaches in optical-microwave synergy, the essential idea is the use of the 'minimum-set', so that only a few channels can provide maximum-information. Only basic polarizations (HH,VV,HV) for one or two frequencies (mainly L and C) are used from microwave data, while only the Normalized Difference Vegetation Index (NDVI) is used in most cases from optical data. Apart from other limitations, the use of NDVI (or related similar 'indices') is supposed to account for the amount of vegetation over the soil background, the basic information required to interpret the

SAR signal where scattering mechanisms do not allow soil/vegetation direct separability for parameter retrievals.

Experience in different areas and different studies shows that approaches using optical vegetation indices are sometimes successful, although the same approaches give wrong results in other cases. It is easy to see that there is a conceptual error in using 'decoupled' information when NDVI or similar indices are directly used in optical/microwave synergy approaches. The reason for that problems is the fact that all vegetation indices are based on combinations of optical channels linking information in the spectral range where there is a decoupling of information between that related to leaf pigments (chlorophyll, etc.), with contributions for wavelengths less than 0.7 μm and almost without any effect for longer wavelengths, and leaf water content, with contributions starting around 0.7 μm but significant over the full spectrum arriving until the wavelengths used in microwave data. Vegetation indices are then mainly sensitive to chlorophyll and canopy geometry terms (and slightly to leaf water content). However, microwave data are absolutely insensitive to leaf pigments. It is then possible to have two canopies with exactly the same geometry and exactly the same water content (then having essentially the same microwave response) but having both very different leaf pigments (like chlorophyll) and then giving very different responses in the optical domain, as derived in NDVI values. In such cases, comparison optical/microwave data will reveal significant differences, but interpretation can be wrong if the different contributions can not be properly separated.

However, if properly used, such decoupled information is essential in increasing the accuracy in surface parameter retrievals by synergistic techniques: chlorophyll absorption is used to better get fractional vegetation cover from optical channels, and then this fractional cover is applied to the microwave data interpretation, although there is no direct connection between the chlorophyll content and the microwave frequencies. In any case, significant modeling is required to properly account for inter-relationships and differences. The information content of each data type have to be decoupled into the parameters which are intrinsic to only one type of data (like leaf pigments in optical data) and those giving information in both types of data. The common information (mainly geometrical structural parameters) must be properly used, because of the different effective meaning of some geometrical parameters as a function of wavelength, especially for 'effective' roughness-related terms.

PHYSICAL MODELING APPROACH TO OPTICAL/MICROWAVE SYNERGY

A physically-based model has been developed to interpret the combined optical and microwave data into a single modeling approach, by including geometric parameters that account for different scattering contributions, and using explicitly spectral scattering/absorption coefficients as derived from basic physical principles [4][2][3]. The basic geometric terms are common to both models, being this the key aspect of the modeling approach. On the other hand, the

water content is modeled by using the same parameterization of physical properties of liquid water over the full range of wavelengths, so that the basic parameter have the same basic physical meaning in optical and microwave frequencies when trying retrievals by using combined optical/microwave data.

Although only tested in limited cases, the approach is general enough to permit derivation of some generic conclusions about the 'necessity' of optical-microwave synergy for derivation of basic surface parameters. For instance, sensitivities of up to 50% for low soil albedo values under top-soil moisture variations within the range 0.0-0.3 are perfectly possible and SAR-derived moisture fields are then essential to compute actual surface albedo variations. In the case of bare soil and densely vegetated surfaces, the synergistic use of the data does not contribute significantly: no 'new' information is retrieved from the synergy apart from that which would be retrieved by using each data separately. The utility of optical-microwave synergy appears to be mainly significant in areas with sparse vegetation, especially when distribution of vegetation over soil is not simply random but follow some spatial pattern. The separability between proportional (fractional) cover and effective vegetation cover (as given by estimates like LAI or canopy water content) becomes essential. Because of the stability of absorption features in optical data, fractional cover information can be provided to microwave scattering models for such soil-vegetation discontinuous composites, especially over dry soil conditions, and mainly for aircraft data because of the large range of incidence angle variations, which introduce additional problems in the interpretation of SAR data.

REFERENCES

[1] H.J. Bolle and B. Streckenbach (eds.), "The ECHIVAL Field Experiment in Desertification-threatened Areas (EFEDA)", Final Report to the Commission of the European Union, Contract EPOC-CT 90-0030, Free University of Berlin, Berlin, 1993, 461 pp.

[2] A.K. Fung, Zongqian Li and K.S. Chen, 1992, "Backscattering from a randomly rough dielectric surface", IEEE Trans. Geosci. Remote Sensing, vol. 30, pp. 356-369, 1992.

[3] R.H. Lang, and J.S. Sidhu, 1983, "Electromagnetic backscattering from a layer of vegetation: a discrete approach", IEEE Trans. Geosci. Remote Sensing, vol. 21, pp. 62-71, 1983.

[4] J.F. Moreno, S.S. Saatchi, R.O. Green, and A.M. Jochum, "Parameterization of the surface energy balance by multisource remote sensing inputs derived from optical-microwave synergy", Proceedings of the Second Topical Symposium on Combined Optical-Microwave Earth and Atmosphere Sensing, Atlanta, GA, April 1995, IEEE 95TH8015, pp. 15-17, 1995.

Surface parameters involved in optical/microwave synergistic approaches

(a)

Landsat TM3   C-HH   L-HH

1 km
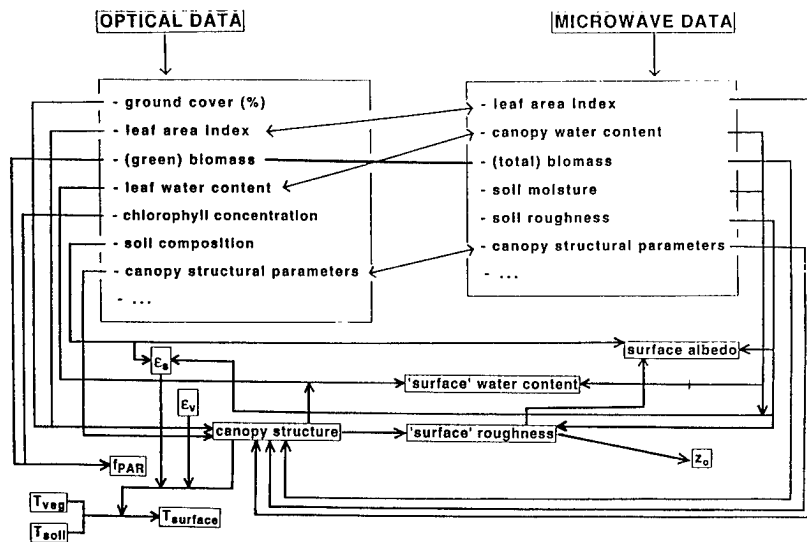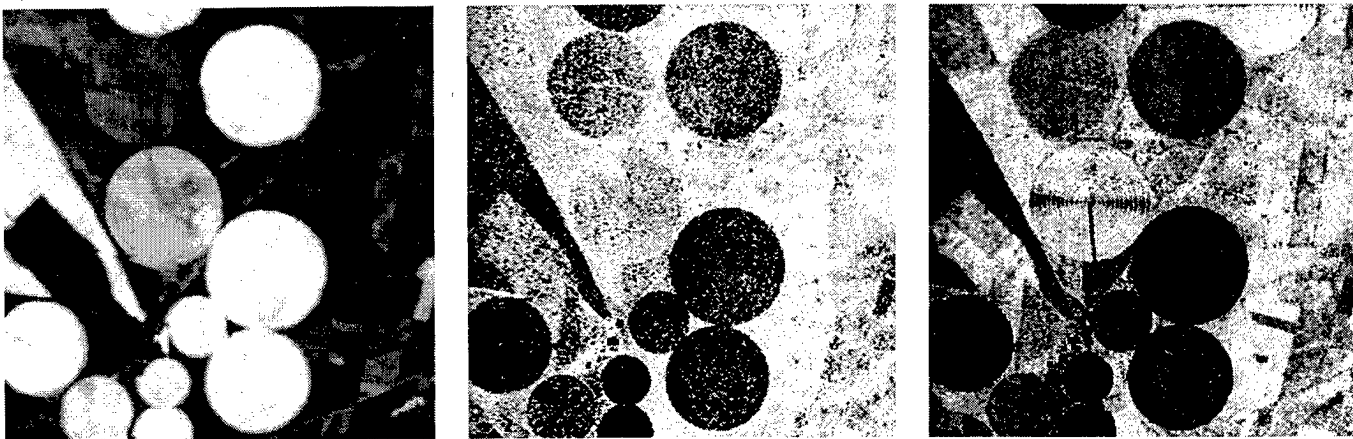
(b)
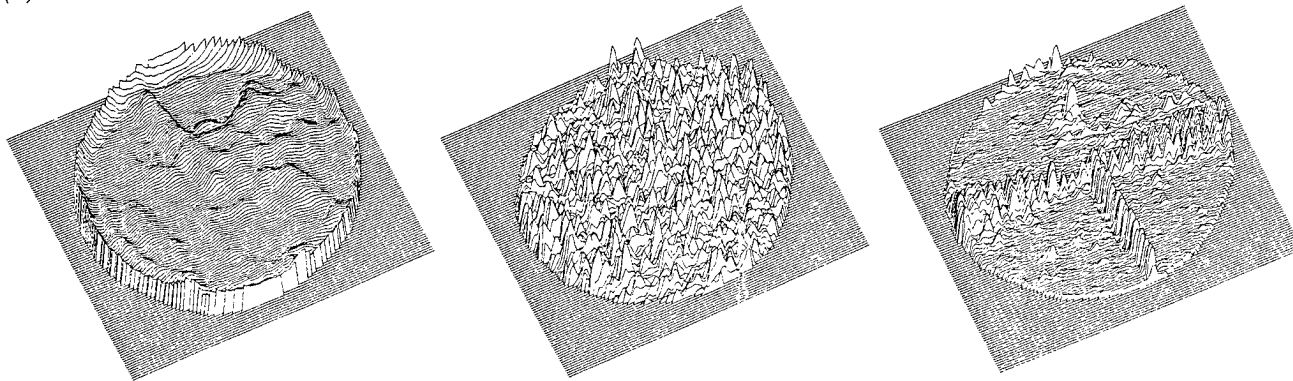
Fig. 1 The problem of the 'spatial pattern' over scales still very large as compared to the respective wavelengths is one of the most critical issues in optical-microwave synergy. As an illustration of this problem, simultaneous Landsat TM data (TM3 channel) are compared to AIRSAR data (channels C-HH and L-HH) for an area with spatial variability over very different spatial scales, including 'homogeneous' patches with various sizes and shapes *(a)*. In *(b)* the central circular area, a highly homogeneous irrigated corn field, is compared by showing the radiometric levels in a 3D representation. The very different spatial pattern (and especially the almost random behaviour at C band and interference pattern with geometrical structure at L band), still for scales of about 1 km, is a major challenge in combined optical-microwave 'spatial' modeling for realistic cases.

Sensor Data Simulations using Monte-Carlo and Neural Network Methods

Richard K. Kiang
Code 902.3, Earth Science Data Operations Facility
NASA Goddard Space Flight Center
Greenbelt, MD 20723
rkiang@favente.gsfc.nasa.gov

Abstract — Parametric and non-parametric Monte-Carlo methods and a neural network method are used for data simulation. A Landsat-4 Thematic Mapper dataset and its ground truth are utilized for training and testing. The abilities and deficiencies of the three methods are compared. It is shown that the neural network method provides an attractive alternative for data simulation.

INTRODUCTION

The majority of the algorithms for extracting geophysical information from satellite data are developed before a satellite is launched. Without real measurements, simulated sensor data often are used to facilitate the development and testings of the algorithms. In general, simulated data are generated from: (a) measurements of airborne simulators, (b) modeling the scene and the sensor measuring process, or (c) existing measurements of sensors similar to the one to be deployed. For methods (a) and (c), additional processings may also be required to modify the spectral, spatial, radiometric, and environmental (such as topographic or atmospheric) properties of the existing measurements. This paper concentrates on method (c), for which techniques are developed to generate labeled samples using parametric and non-parametric Monte Carlo methods and a neural network method. In particular, the ability of each method to preserve the statistical characteristics in the original data without invoking more complex modeling is examined.

DATA SOURCE

Landsat-4 Thematic Mapper (TM) data for an area in the vicinity of Washington, D.C. were used in the study. The measurements were acquired in July 1982. Since the IR bands had not yet stabilized after launch, only the measurements from the first four bands were used. The dataset is of the size 256 pixels by 256 pixels. Only about a third of the pixels are present because of the orientation of the scan line. The ground truth consists of 17 categories, and were obtained through photo-interpretation of color infrared aerial photographs and subsequent field visits [1]. A preliminary analysis of the separability of these categories was performed by examining the ratios of between-class to within-class variance along the Fisher optimal discriminant vector. It is discovered that some of the 17 categories heavily overlap with the others. Based on these ratios, a more realistic set of information categories are established using the Anderson land use categories [2], namely, (1) urban or built-up land, (2) agricultural land, (3) rangeland, (4) forest land, (5) water, and (7) bare soil /cleared land. Notice that there is no

Category 6, wetland, in this data. In Anderson's system, Category 7 is barren land, such as salt flats, beaches, bare rock, etc. Since bare soil/cleared land (Category 17 in the ground truth data) does not exactly fit the definition, the original description in the ground truth is used instead.

PARAMETRIC MONTE-CARLO METHOD

In this method, mean vector m and covariance matrix C for each ground category are computed from training data. Assuming the distribution is Gaussian, spectrally correlated random samples with mean vector m and covariance matrix C are generated from $N(m,C) = A\ N(0,I) + m$. Cholesky decomposition can be used to solve for A in $AA^T = C$. Figs. 1(a) and 1(b) show the distributions of the training samples and the generated samples in the urban/built-up and the forest categories respectively. The urban/built-up category has 1384 pixels, and the forest category has 6862 pixels.

As shown in Fig. 1(a), when the data can be approximated by multivariate Gaussian distribution, the simulated samples resemble the real samples rather well. If the distribution cannot be reasonably represented by a single Gaussian distribution, however, forcing it with such a representation would not produce samples with desirable characteristics, as
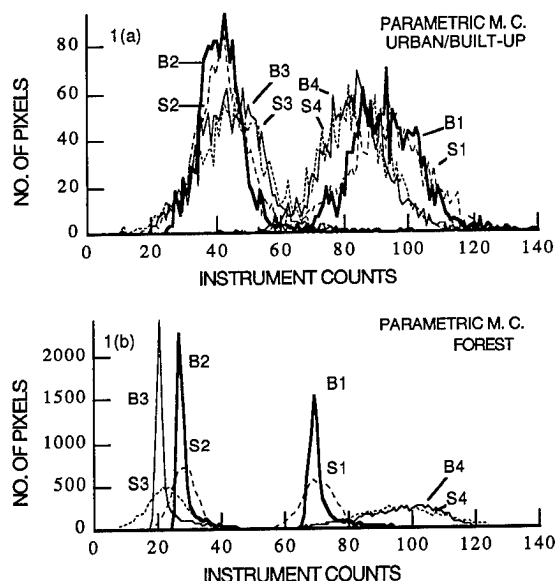
Fig. 1. Results of parametric Monte-Carlo simulation. The real and simulated distributions for band i are labeled by B_i and S_i respectively.

shown in Fig. 1(b). In this situation, hypotheses for other types of distribution (such as lognormal distribution) could be tested and used as the basis for simulation if tested well. Alternatively the distribution may be decomposed into Gaussian mixture using moments, expectation-maximization (EM) algorithm, or other maximal likelihood methods [3]. This method loses its simplicity appeal when additional analyses must be performed to determine the parameters of the mixture.

NON-PARAMETRIC MONTE-CARLO METHOD

Since a distribution may not be uniquely determined by its mean and covariance, utilization of conditional probability of the data may provide a more accurate way to generate random samples. In this method, $p_1(x_1)$, $p_2(x_2|x_1)$, $p_3(x_3|x_1,x_2)$, and $p_4(x_4|x_1,x_2,x_3)$, and their cumulative probability distributions are obtained, where x_i is the count in band i. For each pixel, 4 uniform random numbers, $N(0,I)$, are generated. Then (x_1, x_2, x_3, x_4) are determined sequentially by matching up the random numbers with the respective cumulative distributions. Figs. 2(a) and 2(b) show the distributions of the samples generated by non-parametric Monte-Carlo method. It is noticed that simulation performs very well for Band 1, but less so when the simulation progresses to Band 4. The reason for this deteriorated performance is explained as follows.

The method uses conditional probability in the simulation. Since the conditional probability is usually not known, it has to be estimated from the training samples. However, the dimensionality of the conditional probability function increases as the band number increases. Namely, a 1-D conditional probability function is used to simulate x_1, but a 4-D function is used to simulate x_4. As the dimensionality increases, each cell in the spectral space may become so depleted with pixels that it is no longer possible to reliably estimate the conditional probability. This is the reason why this method produces samples with excellent agreement with the training sample for the first band, but then the performance deteriorates in the subsequent bands. To illustrate this is indeed the reason, Band 4 is simulated as the first dimension instead of the last dimension. Excellent agreement is obtained in this case, as shown in Fig. 2(c). Alternatively, one could enlarge the bin size to enhance the population in each bin when there are insufficient samples. But the resolution could be so reduced that the result will not be very meaningful. Therefore, this method is best suited for spectral data with low dimensionality (such as 2-D or 3-D), unless the conditional probability functions are known from other sources.

NEURAL NETWORK METHOD

This method involves using two neural networks — a forward network that labels the pixels, and a inverse network that maps the activation level, or *a posteriori* probability [6], into pixel counts.
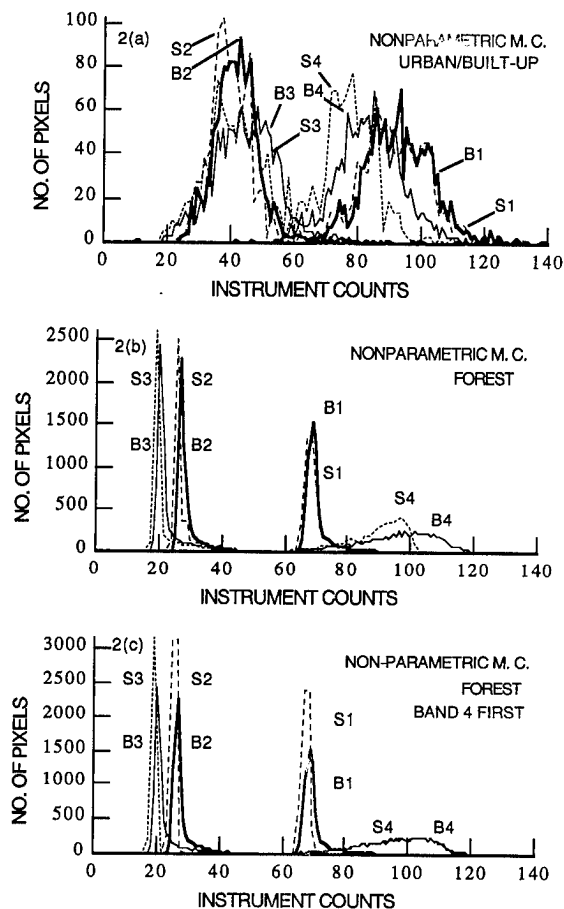
Figure 2. Results of non-parametric simulation.

The first network is a 3-layer, feed-forward neural network. The input layer has four units, corresponding to the four TM bands. The hidden layer has 3 units, and the output layer has 6 units, corresponding to the 6 ground categories. Half of the available pixels are used for training, and the other half for testing. Since pixels of the same categories tend to aggregate together in nature, conducting training in this original order may result in uneven learning and poor generalization. Therefore, the pixels for the training areas are indexed according to their categories, and different ground types are presented to the network sequentially for a uniform training. This step is essential for ensuring a balanced view toward all ground types for the network [4].

A gain of 0.15 and a momentum factor of 0.35 were used in the supervised training. After approximately 160 iterations, the RMS error stabilized. The overall classification accuracy is 71.61%. The classification accuracy is somewhat higher than a previous classification using ISOCLS and Gaussian maximum likelihood method [1], and is similar to that from a neural network classifier [5]. But a direct comparison may not be appropriate, since the data and the categories are not completely identical. By excluding samples with low activation levels, the classification accuracy for all categories

can be improved. For example, the overall accuracy becomes 75.63% after 9.7% of the samples are rejected, 79.28% after 15.9% are rejected, and 83.51% after 22.7% are rejected.

The activation levels of the first network are quantized into 8-bit integers, stored, then fed into a second neural network. The second network is also a 3-layer, feed-forward neural network. The input layer has 6 units, corresponding to the 6 categories. The hidden layer has 3 units. And the output layer has 4 units, corresponding to the 4 TM bands. As in the first network, a gain of 0.15 and a momentum factor of 0.35 were used. In training the second network, all samples are used regardless of their activation levels in the first network. The training converges after approximately 300 iterations.

Figs. 3(a) and 3(b) show the distributions of the samples generated by the inverse neural network. For the forest category, the distributions of the generated samples follow those of the real samples rather closely, except for Band 4. For the urban/built-up category, the agreement between the real and the generated samples is still acceptable. It is noticed that the generated samples tend to favor the centroid. Areas away from the centroid are less populated. Hence data samples can be constructed from a posteriori probability by using an inverse network. The a posteriori probability can be based on a real distribution, as discussed here, or the signatures of various ground categories.

The advantage of this method is that the processes for both the forward and inverse networks are fairly automatic, if one excludes the preliminary analysis on how the classes should be combined in the forward network. It is less likely for this method to encounter unexpected results. The shortcoming is
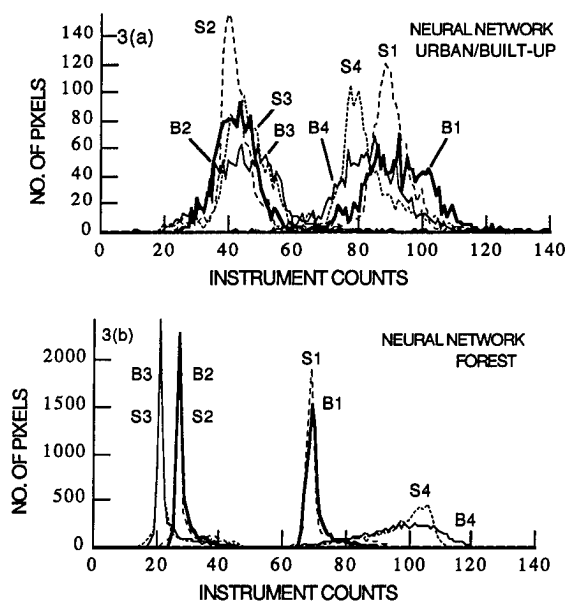
that the simulated samples tend to aggregate more toward the centroids than what is indicated by the training samples. Thus the characteristics in the training samples may not be completely preserved in the simulated data.

Since this method is in essence an inversion, one must examine how it is affected by the non-uniqueness, or the many-to-one, phenomenon that exists in many inversion problems. For example, ground truth information sometimes is required to anchor the inverted results when snow parameters are inferred from remotely sensed data [7]. However, the non-uniqueness problem normally does not exist in this application, as will be explained in the following. It can be shown that each location in the spectral space is associated with a unique set of a posteriori probabilities $p(k|x)$ for each category k as long as the dimension of the probability space is higher than the spectral space. In other word, there must be more ground categories than the number of spectral bands. The dimensions described here must be non-degenerative. Otherwise adjustment must be made first before the two dimensions can be compared.

Considering all the abilities and deficiencies of the three methods as described above, the neural network method is an attractive way to simulate multispectral data samples.

REFERENCES

[1] D. L. Williams, et al., "A Statistical Evaluation of the Advantages of Landsat Thematic Mapper Data in Comparison to MSS Data," IEEE Trans. on Geoscience and Remote Sensing, vol. GE-22, pp. 294–302, 1984.

[2] J. R. Anderson, et al., "A Land Use and Land Cover Classification System for Use with Remote Sensor Data," Manual of Remote Sensing, 2nd Edition, Table 30-7, American Society of Photogrammetry, 1983.

[3] D. M. Titterington, A. F. M. Smith, and U. E. Makov, Statistical Analysis of Finite Mixture Distributions, Chapter 4, John Wiley & Sons, 1985.

[4] R. K. Kiang, "Classification of Remotely Sensed Data using OCR-Inspired Neural Network Techniques," Proc. Int. Geoscience and Rem. Sensing Symp., Houston TX, pp. 1081–1083, 1992.

[5] W. J. Campbell, S. E. Hill, and R. F. Cromp, "Automatic Labeling and Characterization of Objects Using Artificial Neural Networks," Telematics and Information, vol. 6, pp. 259, 1989.

[6] E. Yair and A. Gersho, "Maximum A Posteriori Decision and Evaluation of Class Probabilities by Boltzmann Perceptron Classifiers," Proceedings of the IEEE, vol. 78, pp. 1620–1628, 1990.

[7] D. T. Davis, et al., "Retrieval of Snow Parameters by Iterative Inversion of a Neural Network," IEEE Trans. on Geo. & Remote Sensing, vol. 31, pp. 842–852, 1993.

Figure 3. Results of the neural network simulation method.

Model-Based Technique for Super Resolution and Enhanced Target Characterization Using a Step-Frequency Radar: A Simulation Study

S. Chakrabarti, P. Kannagaratnam, and P. Gogineni
The University of Kansas, Radar Systems and Remote Sensing Laboratory
2291 Irving Hill Road, Lawrence, KS-66045-2969, USA
TEL: 913/864-8811, FAX: 913/864-7789, E-mail: Chakra@eecs.ukans.edu

Abstract--In this investigation, the signal reflected by a target to the step-frequency radar is processed using both non-parametric and parametric approaches. An autoregressive moving average (ARMA) model of the reflected signal is first used to estimate the location of the targets. Then, an extended Prony's method is used to estimate the magnitude of the reflection coefficients of the targets. These model-based approaches are found to provide super resolution and improvement in target characterization as compared to a conventional non-parametric approach. Several simulations are made to compare the performances of these methods.

INTRODUCTION

In recent years, step-frequency radars [1,2] have been used frequently in estimating the location of the scattering targets, such as ice-layer, subsurface targets, etc. An important advantage in using step-frequency radar [1] is that the phase change rate of the signal received at the radar, for the preselected incremental steps of transmission frequency, is directly proportional to the distance of the scatterer from the radar. Frequently, non-parametric fast-Fourier-transform-(FFT) based procedures are used [1] to estimate the location of the scatterers from the complex reflected signal. It has been shown [2] that the non-parametric approaches suffer from inherent resolution constraints and a parametric modeling approach, popularly known as the MUSIC [3] algorithm, is found to provide super resolution in estimating target locations. In this investigation, we use a high performance ARMA [3,4] model to estimate the target locations with super resolution. On estimating the target locations, we use an extended frequency-domain Prony's method (EFDPM [5]) to estimate the reflection coefficient of the target. The backscattered signal received from targets is synthesized, and the performance of the model-based approach is compared with that of the conventional FFT-based approach.

DATA MODELING

Assume that the transmission frequency (f) of a step-frequency radar is incrememted in discrete steps (n) of a preselected frequency Δf. Then, the signal at the receiver can be expressed as [2]:

$$x(n) = \sum_{k=1}^{D} \Gamma_k(n).\exp(-j2\beta_n d_k) + N(n) \qquad (1)$$

where d_k represents the distance of the kth target and D represents the number of targets seen by the radar. Also, n represents the nth frequency of transmission and $\beta_n = 2\pi.n.\Delta f/c$. $\Gamma_k(n)$ represents the reflection coefficient of the kth target at

the nth frequency of transmission, and N(n) represents samples of white Gaussian noise. From the above expression it can be seen that x(n) represents samples of a single (for D=1) or multiple (for D>1) sinusoids. The rate of change of the phases of these sinusoids are proportional to the distance of the target from the radar. An inverse discrete Fourier transform of the sequence x(n) can be defined as

$$y(m) = \sum_{n=1}^{M} x(n).\exp(j\beta_n d_m) \qquad (2)$$

where M represents the total number of discrete frequencies under consideration. The samples of y(m) will have a peak (for D=1) or peaks (for D>1). From the location of a peak of |y(m)|, the corresponding location of a target can be estimated [1,2]. Once the location of the target is identified, the next task is to estimate its reflection coefficient. Since in (1), $\Gamma_k(n)$ is multiplied by a complex exponential term, the inverse Fourier transform of x(n) will be the inverse Fourier transform of $\Gamma_k(n)$, shifted by the target distance d_k. Thus, if the samples of the Fourier transform of $\Gamma_k(n)$ can be isolated for each target, a direct Fourier transform of these isolated sequences will provide estimated values of the reflection coefficient $\Gamma_k(n)$ of the target k.

In the first simulation, a single target is located at a distance of 4 m(=d_1), which possesses a linear reflection coefficient shown in Fig.1. We assume that the radar operates over the frequency range of 2-18 Ghz, and uses Δf=10 MHz. (These radar parameters are identical to the step-frequency radar that will be used to acquire experimental data in the near future.) Samples of x(n) are computed using.(1) for infinite signal-to-noise ratios (SNR), and the samples of the |y(m)| are computed using an FFT. The location of the target is identified as 4.0031 m based on the peak location of |y(m)|. Next, a Hanning window is set up around this peak location and a total of five samples of y(m) are collected. The inverse transform of these samples of y(m) provided the estimated values of the reflection coefficient of the target. The r.m.s value of the estimation error, for infinite SNR, is shown in Table I and the estimated values of $\Gamma_k(n)$ are plotted in Fig.1.

It is seen from Fig.1 that the windowing effect introduces error in the estimated values of the reflection coefficient of the target. It is always preferable to use as few samples as possible around the peak location of y(m) since the error in the estimated values of y(m) increases as we move away from the peak location[3]. But, the fewer samples we use from y(m), the larger will be the deformation in the estimated values of $\Gamma_k(n)$. In order to overcome these difficulties of non-parametric approaches, we use parametric model-based approaches for estimating the target locations and their

reflection coefficients.

Since the samples of ly(m)l basically provide the spectral information of the samples of x(n), a model-based spectrum estimation technique can be used to estimate the location of the targets with a super resolution. In this investigation, we use an ARMA-model-based approach [4] to estimate the location of the targets with high accuracy. According to this scheme, the samples of the random signal x(n) is modeled as the output of an ARMA filter of order (p,q), excited by a zero-mean white Gaussian noise sequence w(n) such that

$$x(n) = \sum_{k=1}^{p} a(k).x(n-k) + \sum_{k=1}^{q} b(k)w(n-k) \qquad (3)$$

where a(k) and b(k) represent the AR and MA coefficients of the ARMA filter. For a pure AR process (b(0)=1 and b(k)=0 for k>0), the AR parameters can be estimated using a high-performance approach[4], which estimates the order p by performing the singular value decomposition (SVD) of an extended order autocorrelation matrix (ACM). In this case, the order p actually correspond to the number of targets present in the field of view of the radar. The samples of ACM are extracted from the samples of x(n) [4]. Using these AR coefficients, the pole locations can be estimated as the roots of the polynomial equation of the z-domain [3,4]

$$\sum_{k=1}^{p} a(k)z^{-k} = 0 \qquad (4)$$

Since the poles of (4) define the sinusoidal components of x(n) [2,3], an accurate estimation of the poles will actually define the target locations accurately. Using this approach, the target location is estimated as 3.9998 m, which is more accurate than that obtained from the inverse-FFT- (IFFT-) based approach (see Table I).

Next, a total of five samples of y(m) are selected around the peak location estimated by the ARMA model. These samples are then used by EFDPM to model the transformation of the reflection coefficient of a target as a rational function model [5] of order (u,v-here u+v+1=5 and s(v)=1). That is,

$$y'(m) = \frac{\sum_{k=0}^{u} r(k).m^{k}}{\sum_{k=0}^{v} s(k).m^{k}} \qquad (5)$$

This rational function model is used to select the parameters r(k) and s(k) so that y'(m) can provide a suboptimal fit to the samples of y(m) over the entire range of m. A direct Fourier transform of this modeled data is used to estimate the samples of $\Gamma_{k}(n)$, and the result is shown in Fig.1. This scheme provided an r.m.s error of 0.0052, which is less than the 0.1005 provided by the FFT-based approach.

The aforementioned procedures are repeated for SNRs of 40, 30, 20, 10 and 0 dB, and the results are tabulated in Table I. It can be seen that as the SNR decreases, the r.m.s error in estimating the reflection coefficient of the target increases for both methods. The r.m.s error provided by the extended Prony's method stays consistently lower than that of the FFT-based approach.

SUPER RESOLUTION FOR MULTIPLE TARGETS

From Table I, it is seen that the target location estimated by the FFT-based approach did not change at all throughout the testing range of the SNRs. This is expected since we used 1600 samples for only one non-decaying sinusoid. However, when multiple and closely spaced targets are present in the radar's field of view, the situation is found to be very different.

In this section, we assume that the two targets are present at distances 4.0 and 4.05 meters from the radar. Then, we compare the performances of the ARMA-model-based approach versus the FFT-based approach in estimating the locations of the targets as the number samples (N) is decreased. The results are presented in Table II, which shows that the ARMA-model-based approach successfully resolves the two targets when the FFT-based approach cannot resolve a distance of 0.15 meters. Thus, the parametric modeling of the radar return is found to be useful in achieving super resolution as compared to the FFT-based approach.

ESTIMATION OF THE REFLECTION COEFFICIENTS FOR MULTIPLE TARGETS

From Table II we find that the ARMA model can estimate the target locations accurately, using only 100 samples of x(n). To estimate the reflection coefficient, however, we collected 1600 samples of x(n). This is done to make sure that the neighboring target is not undesirably influencing the five samples around each peak location of ly(m)l [2]. Next, five samples are collected around the first peak location of the inverse transformed domain, and the reflection coefficient of the target is estimated using both the Hanning window and the extended Prony's method. The estimated values of the reflection coefficient are shown in Fig. 2, and the r.m.s errors associated the Hamming window and the extended Prony's method are found to be 0.1421 and 0.1143, respectively. In the presence of additive noise, with an SNR of 0 dB, the r.m.s errors are 0.1496 and 0.1293. Thus, the extended Prony's method provided superior performance in characterizing the target.

It is important to note that increasing window size actually decreases the performance of the conventional approach in estimating the samples $\Gamma_{k}(n)$ due to the undesirable influence from the neighboring target.

CONCLUDING REMARKS

In this investigation we show that an ARMA-model-based technique provides super resolution in estimating the locations of targets as compared to an FFT-based approach. By knowing the locations of these targets, we can collect more data to get enough samples inbetween the peaks of the inverse transformed domain so that the entended Prony's method can be used to estimate the reflection coefficient of the target. We find that the extended Prony's method estimates the values of the reflection coefficient with an improved accuracy as compared to the results obtained by the

FFT of the windowed data. Thus, a combination of the ARMA-model-based approach and the extended Prony's method might be used effectively in estimating the location of the targets and their reflection coefficients. We are in the process of applying the model-based techniques to the measured data for characterizing the ice type.

REFERENCES

[1] K. Izuka, A. P. Freundorfer, K. Wu, H. Mori, H. Ogura, and V. Nguyen, "Step-Frequency Radar," *J. Appl. Phys.* vol. 56, pp. 2572-2583, Nov. 1984.

[2] H. Yamada, M. Ohmiya, and Y. Ogawa, "Superresolution technique for time-domain measurements with a network analyzer," *IEEE Trans. Antennas Propagat.*, vol. AP-39, pp. 177-183, Feb. 1991.

[3] S. L. Marple, *Digital Spectral Analysis with Examples*, Prentice Hall, Englewood Cliffs, NJ, 1987, Chapter 11.

[4] J. A. Cadzow, "Spectral estimation: an overdetermined rational model equation approach," *Proceedings of the IEEE*, vol. 70, pp. 907-938, 1982.

[5] S. Chakrabarti, K. Demarest, and E. Miller, "An extended frequency domain Prony's method for transfer function parameter estimation," *International Journal of Numerical Modeling*, vol. 6, pp. 269-281, 1993.

Table I : Comparisons of the Estimated Values Between the FFT-based and the Model-based Approaches

SNR in dB	Estimated Target Location (Actual Location = 4.0 m)		R.M.S. Error in Estimating Reflection Coefficient (using 5 samples)	
	IFFT-based (m)	ARMA-model-based (m)	FFT-based	EFDPM-based
∞	4.0031	3.9998	0.1005	0.0052
40	4.0031	3.9998	0.1130	0.0098
30	4.0031	4.0001	0.1176	0.0376
20	4.0031	4.0006	0.1176	0.0847
10	4.0031	3.9992	0.1268	0.0991
0	4.0031	3.9989	0.1308	0.1122

Table II: Error in Estimating Target Locations Using ARMA model (Targets are located at 4.0 m and 4.05 m)

No. of Samples used (N)	Resolution From IFFT (m)	Distances Estimated by ARMA model (m)		Errors in Distance Estimation (%)	
		First Target	Second Target	First Target	Second Target
1600	0.0094	3.9997	4.0503	0.01	0.01
800	0.0187	3.9984	4.0514	0.04	0.03
400	0.0375	3.9950	4.0553	0.13	0.13
200	0.0750	3.9868	4.0675	0.33	0.43
100	0.1500	3.9856	4.1757	0.36	3.10
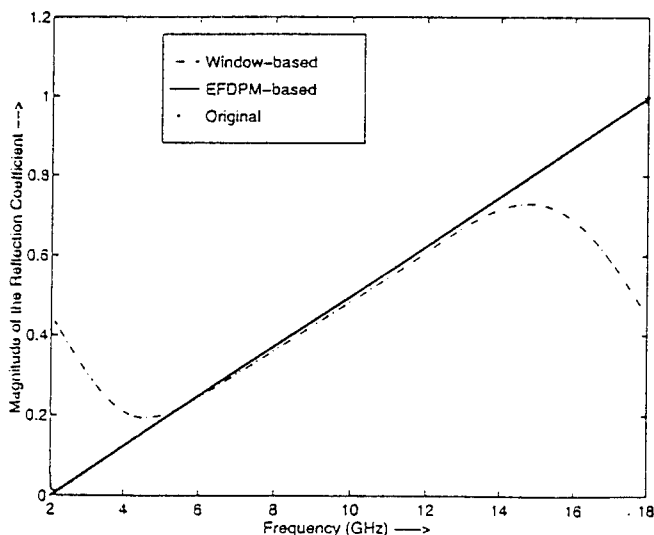
Fig.1. Original and estimated reflection coefficient of a target.
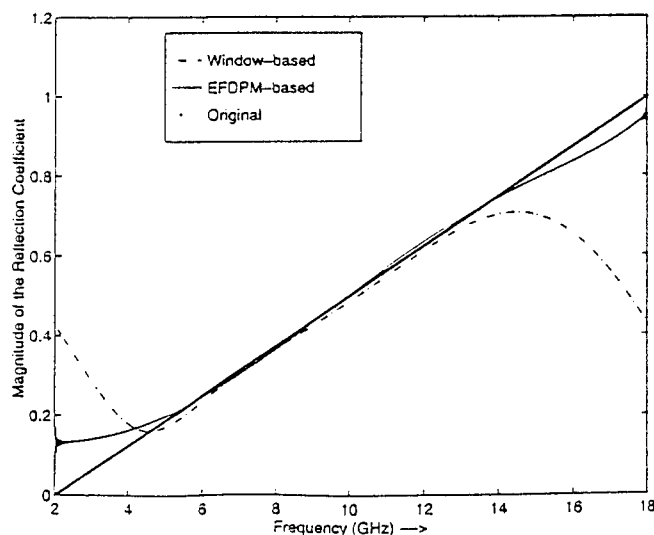
Fig.2. Original and estimated reflection coefficient of the first target.

Contextual Simulation of Landscape Based on Remotely Sensed Data

Myunghee Jung and Melba M. Crawford
Center for Space Research, The University of Texas at Austin, Austin, TX 78712
Phone:(512)471-3070, Fax:(512)471-3570, Email:crawford@magellan.csr.utexas.edu

ABSTRACT

A hierarchical stochastic modeling approach has been developed to provide a general methodology for landscape simulation based on information from multispectral imagery. The model is based on a mutiresolution representation whereby a Markov random field is employed to model the region process, a fuzzy approach integrated with a pyramid data structure is used to deal with boundary variation, and natural variability and noise contamination within scene are modeled using class dependent statistical models. The new simulation model is being utilized in conjunction with Landsat TM imagery to provide initial conditions for multitemporal simulations of habitat in western Australia.

INTRODUCTION

Recent advances in computing and remote sensing technology have made it possible to develop a new class of dynamic spatial landscape models which are formulated to describe real phenomenon and represent the temporal evolution of landscape. Natural landscapes are very heterogeneous and require more complex representations than the simple probabilistic model with $p\%$ susceptible elements provides [1]. However, there have been few studies for this problem.

A model-based simulation which properly represents stochastic properties of observed scenes is required in order for simulated images to be utilized for evaluation and validation of multitemporal biological models. Remotely sensed imagery from satellites is ideal for developing these simulation models because it provides simultaneously acquired measurements of the characteristics of a large area and contains various levels of information.

Landscape observed in remotely sensed imagery often exhibits characteristic patch mosaic structures at large scale and class dependent variability within each region at detailed scale. Thus, a hierarchical model is appropriate to describe such compound stochastic properties [2]. A Markov random field (MRF) model is employed herein to represent the region process as a large scale characteristic emphasizing spatial continuity. Boundary variation between adjacent regions is represented using a fuzzy approach. At the lower level of the hierarchy, Gaussian distribution is assumed to model the natural variability of each region, where a multiresolution

---

data structure is integrated with the fuzzy approach for modeling boundary variation.

REGION SIMULATION MODEL

The Gibbs distribution of the form

$$P(X = \omega) = \frac{1}{Z} e^{-U(\omega)} \tag{1}$$

is employed for modeling the scene as a random field of discrete values corresponding to class values, generating a class map statistically similar to that of an observed scene.

For the simulation results presented in this study, the second order pairwise interaction model, which involves only single cliques and cliques of size 2 is utilized. It is assumed that the random field is nonhomogeneous in the sense that each class has different parameters in the clique function to account for different sizes, shapes, and orientation of regions. The clique functions are defined as follows:

$$V_c(\omega) = \alpha_k \quad \text{if } x_i \text{ in } c \text{ is } k \tag{2}$$

$$V_c(\omega) = \begin{cases} -\beta_{dir,k} & \text{if all } x_i \text{ in } c \text{ are equal to } k \\ & \text{and } c \text{ is "}dir\text{" type clique} \\ \beta_{dir,k} & \text{otherwise} \end{cases} \tag{3}$$

where parameters assigned to each clique type are defined as

$\square$ $\beta_{hor,k}$ $\quad$ $\square$ $\beta_{ver,k}$ $\quad$ $\square$ $\beta_{ne,k}$ $\quad$ $\square$ $\beta_{nw,k}$

The resulting $(G+4*G)$ parameters are estimated from an observed scene, where G, the number of classes in the scene, is often quite large. The Least Square Error Method (LSQR) proposed by Derin & Elliot [2] is used since its implementation is relatively easy, and remotely sensed images are generally large enough to satisfy the size requirement for accurate results.

BOUNDARY VARIATION PROCESS

The boundaries between adjacent regions in remotely sensed data are often not clearly observable, and pixels at or near the boundary are frequently mixtures of classes. A fuzzy approach is intrinsically suited to dealing with mixed, spectrally undefined cases [3].

Interior regions are considered to be homogeneous in the proposed model and have their own statistical features, so it is not necessary to process all the pixels at full resolution to identify areas near the boundaries. Identifying homogenous interior regions without searching all the pixels and rather concentrating on areas adjacent to boundaries can greatly reduce the number of operations and computational cost. The

multilevel approach is one means of efficiently implementing this idea. Variation around boundaries can also be smoothed naturally using this pyramid structure.

A pixel at site (i,j) has additional information vector $\Pi(i,j)=[\pi_{(i,j)k}]$ where $\pi_{(i,j)k}$ is the grade of the membership of the pixel (i,j) to Class k and

$$\sum_{k=0}^{G-1} \pi_{ik} = 1.$$

The extent of variation around boundaries can be reduced suddenly or gradually as it approaches the interior of the region which often belongs to a pure class type. Accordingly, a statistical model which includes fuzzy classes and pure classes is appropriate. For this purpose, define an auxiliary random variable, $Y_{i,j}$ at a site (i,j) which takes values in $\{P,F\}$. Class F is assigned to the pixels around the boundaries and Class P to the interior pixels of each region with the objective that variation is smoothed out toward inside of region.

If $Y_{i,j}=P$, a pixel (i,j) is of pure cover class while if $Y_{i,j}=F$, the pixel is associated with the additional information vectors including class components of the mixture and the proportion with which pixel (i,j) belongs to each component. The pyramid of the above information is constructed as follows:

Level 0. At the full resolution, each pixel (i,j) of a simulated image has its own class value and $Y_{i,j}=P$, except for pixels adjoining pixels of different class types, where $Y_{i,j}=F$, and the class mixture type and the proportion of each mixture component within a pixel (i,j) is selected considering spatial interaction of the first neighborhood in terms of the magnitude of the local gradient. For example, suppose that a pixel (i,j) of class cover k adjoins pixel(s) of class cover c. First, decide $\pi_{(i,j)c}$ and let $\pi_{(i,j)k}=1-\pi_{(i,j)c}$. A density function, $f(\pi_{(i,j)c})$ of the following form is chosen:

$$f(x) = \lambda \left(\sum_{i \in N_i} c_i \nabla_i - a \right) x + b \tag{4}$$

where ∇ is a simple difference operator and c is a coefficient which is a function of the difference. Using the first order neighbors, ∇ is calculated as

$$\nabla_N = \pi_{(i-1,j)c} - \pi_{(i,j)c}$$
$$\nabla_S = \pi_{(i+1,j)c} - \pi_{(i,j)c}$$
$$\nabla_E = \pi_{(i,j+1)c} - \pi_{(i,j)c}$$
$$\nabla_W = \pi_{(i,j-1)c} - \pi_{(i,j)c} \tag{5}$$

The directional coefficient is chosen as

$$c_i = g(\|\nabla_i\|) \tag{6}$$

There are many possible choices for $g(\nabla)$ depending on the extent of smoothness between two adjacent regions. In this study, a nonnegative monotonically decreasing function,

$$g(\|\nabla\|) = \exp\left(-\left(\frac{\|\nabla\|}{k}\right)^2\right) \tag{7}$$

is utilized, where η is a scale parameter to control the effect of nearest neighbor difference, ∇.

In (4), λ is the shape parameter controlling the rate of smoothing and b is normalizing constant to make $f(x)$ a probability density function. $a=2g(1)$ is used so that the density function has a strong mode in 1 when all differences are close to 1, and it has a strong mode in 0 when all differences are close to 0. Finally, the proportion of each class at a fuzzy pixel which has at least one neighbor of different class cover type is determined using this density function.

At level l. With each ascending level in the pyramid, the size is halved in each dimension. A node on level l ($l>0$) is linked to nodes on level $l-1$ (sons) and a node on level $l+1$ (father). For each node, the following information is maintained :

(1) $Y_{i,j,l}$ to represent homogeneity of a node (i,j,l)
(2) $MCL(i,j,l)$ to represent class components within a node (i,j,l)
(3) $\Pi(i,j,l)$ to represent the proportion of each class component

First, initialize the node values, $\Pi(i,j,l)$, by simple non-overlapping block average of 2x2 son nodes of the next lower level, $l-1$,

$$\pi_{(i,j,l)c} = \frac{1}{4} \sum_{s,t=0}^{1} \pi_{(2i-s,2j-t,l-1)c} \tag{8}$$

Then, from the top, $\Pi(i,j,l)$ is updated by considering the node values of four fathers whose positions are closest to its own. The updated $\Pi(i,j,l)'$ is defined as follows:

$$\Pi(i,j,l)' = \Pi(i,j,l) + S \tag{9}$$

where S is a vector which includes adjusted values for the proportion of each mixture component. That is, S represents new informaion or detail added after consideration of the higher order neighbors, because neighbor relationship at the lower resolutions implies the higher order neighborhood relationship at the higher resolutions. S is also a function of the ∇'s as in (4). It is proposed that S be obtained by weighted average of differences between $\Pi(i,j,l)$ and those of its four nearest fathers. With this idea, s_c for Class c is calculated as

$$s_c = \lambda_l \left(\sum_{i=0}^{3} c_i \nabla_{ic} \right) \tag{10}$$

where the values of ∇_{ic} for the difference a node (i,j,l) and the ith father in Class c are calculated similarly to (5). The values of the c's are weights which control the effect of the differences and obtained as

$$c_i = \frac{g(\nabla_i)}{\sum_j g(\nabla_j)} \tag{11}$$

where ∇_i is the total magnitude of the differences from the ith father, and the function g is the same as (7). The value η, a free parameter of g, is used to vary the effect of the differences. λ_l controls the rate of smoothing and is a function of the level of the pyramid.

The top level controls the size of variation areas around boundaries. Thus, a choice of the higher top level means that spatial interaction between a given pixel and its higher order neighbors is considered in boundary variation. Therefore, a new class mixture component can be introduced with smaller proportion at the lower resolutions of the pyramid for a different class type distant from a given pixel.

GENERATION OF THE STATISTICAL FEATURES OF EACH REGION

The advantage of the pyramid structure is that at the higher level, homogeneous interior regions are separated from boundary areas, and all the pixels below these homogeneous areas in the pyramid are considered to be pure. Then, for these identified homogeneous nodes, instead of considering any boundary variation, the features of each region type are simulated at all the corresponding pixels of the bottom level. Computational cost is thus reduced, and at the lower level, the boundary regions are emphasized by updating the value π's, where additional interior areas and boundary areas are identified, and, similarly, values are simulated at the bottom level for these additional interior areas. This process is repeated at successively lower levels of the pyramid, and mixture features are generated at the full resolution.

Since lower levels have higher spatial resolution information, higher order neighbors are considered at lower levels of the pyramid to identify an additional homogenous node. Here, it is suggested that N_2 be considered at the top level and $N_2, N_4, N_8,...$ neighborhoods be searched at successively lower levels.

The feature random field is not directly observed; rather a set of observations are noisy random field. A wide range of models has been developed to represent these phenomena in imagery The results reported in this paper assume simple model whereby natural variability within each region is assumed to be a sum of two independent processes, one being class dependent, the other being a noise process. This process is superimposed on the simulated class map including boundary variation between adjacent regions, generating the real images.

RESULTS

A realization of 256x256 scene derived using the Gibbs Sampler are presented in Fig. 1(a) as a possible stochastic scene at a coarse scale. The performance of the algorithm is evaluated visually as well as by comparison of estimated parameters to original parameters in Fig. 1(b) and Table 1. It should be noted that both the absolute and relative magnitudes of the parameters affect generated images. Fig 2 illustrates the variation area and the extent of the variation around boundaries which represent class mixture or intermediate conditions possibly occurring between adjacent regions. In Fig. 2(c), the grade of the membership of each class between 0 and 1 is represented in gray scale.

(a) image with specified values (b) image with estimated values
Fig. 1 Comparison of 256x256 images generated with specified and estimated parameters (Table 1)

Table 1 Estimated parameters

		β_{hor}	β_{ver}	β_{ne}	β_{nw}
Fig. 1 (a)	class 1	0.70	0.70	0.70	0.70
	class 2	0.70	0.70	-0.70	0.70
	class 3	0.70	0.70	0.70	0.70
(b)	class 1	0.51	0.54	0.50	0.71
estimated	class 2	0.71	0.72	-0.32	0.52
	class 3	0.37	0.18	0.60	0.54

(a)   (b)
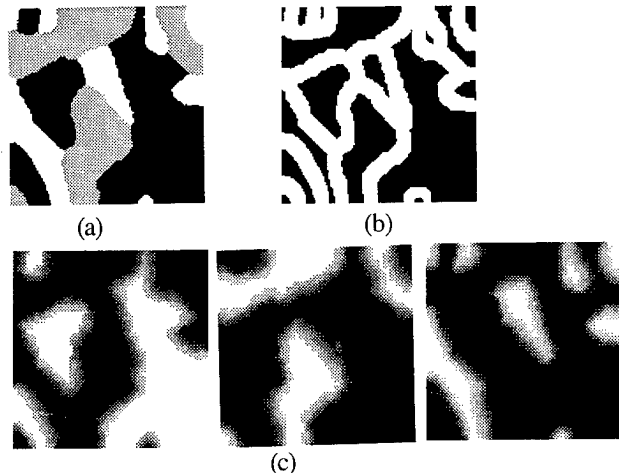
(c)
Fig. 2 Example of boundary variation in an 128x128 image: (a) three-class scene (b) boundary variation area determined from Level 3 (c) extent of the variation of each class represented in gray scale in (b)

REFERENCES

[1] H. Sklar and R. Costanza, "The development of dynamic spatial models for landscape ecology: A review and prognosis", in *Quantitative Methods in Landscape Ecology: The Analysis and Interpretation of Landscape Heterogeneity*, eds. M. G. Turner and R. H. Gardner, Springer-Verlag, New York, 1991.

[2] H. Derin and H. Elliot, "Modeling of segmentation of noisy and textured image using Gibbs random field, " *IEEE Trans. Pattern Anal. Machine Intell.*, Vol. PAMI-9, pp 39-55, 1987.

[3] H. Caillol, A. Hillion, and W. Pieczynski, "Fuzzy random fields and unsupervised image segmentation," *IEEE Trans. on Geoscience and Remote Sensing*, Vol. 31, no. 4, pp 801-810, 1993.

Intelligent Fusion and Analysis of AIRSAR Data for SEIDAM

A. S. (Pal) Bhogal, David G. Goodenough, Daniel Charlebois,
Hugh Barclay, Stan Matwin[1] and Olaf Niemann[2]

Pacific Forestry Centre, Victoria, BC, Canada
[1]University of Ottawa, Ottawa, Canada
[2]University of Victoria, Victoria, Canada

Abstract - **SEIDAM (System of Experts for Intelligent Data Management) intelligently fuses and analyzes remotely sensed data, such as from NASA's AIRSAR. Software agents assist the users in processing by providing the necessary information to successfully complete the sequence of tasks. These tasks include calibration, topographic corrections, and geocoding of AIRSAR data. The resulting geocoded imagery is subjected to image processing algorithms fused with GIS data in order to extract information on the biophysical parameters of forest objects. In this paper, the use of AIRSAR data for the estimation of biomass from P-band SAR for a test site on Vancouver Island is discussed, as well as the retrieving and adapting of plans for intelligently solving queries requiring radar data.**

I. INTRODUCTION

As part of NASA's Applied Information Systems Research Program, a project is being conducted to create an intelligent system, SEIDAM [1], which manages and fuses remote sensing data from aircraft and satellites with multiple geographic information systems (GIS) in order to respond to queries about forests and the environment. SEIDAM integrates several key technologies: image analysis for remote sensing data, geographical information systems (both vector and raster based), artificial intelligence (AI), modeling (growth and yield) and multi-media/visualization. User queries range from simple relational database queries to complex queries such as the update of digital forest cover GIS files. This second type of query requires SEIDAM to automatically perform image analysis tasks to extract surface features necessary to update the digital maps. One of the needed attributes is a measurement of timber volume.

Canada's most important renewable resource is the forest. Canada has 56% of the global share of newsprint exports, and 32% of the global exports of pulp. The province of British Columbia contains more than 40 % of the country's marketable timber.

The management of a vital resource such as forestry is a complex task requiring the integration of many data sets and data sources. Expert systems can be used for automating data integration, image interpretation, and determining the changes in various environmental parameters over time.

In this paper, we present some results pertaining to the computation of biomass using multi-temporal radar data acquired during the SEIDAM field programs in 1993 and 1994. We also suggest how calibrated SAR data may be fused with GIS data for use in the context of SEIDAM's expert systems for answering user queries intelligently.

A brief overview of the SEIDAM components is presented in the next section, followed by a discussion of observations made from SEIDAM AIRSAR data acquired in 1993 and 1994.

II. SEIDAM: THE SYSTEM

As figure 1 [2] shows, there are several components to SEIDAM: the main expert system, the reasoning system, the Smart Access software agents, the remote sensing software agents, the GIS software agents, the image and GIS metadata database, the image and GIS data recorded on a robotic mass data storage device, the SEIDAM knowledge base, and the reasoning system's case-base.

The SEIDAM expert system is the task master for the whole system. It has three main functions: interact with the user in order to determine the type of information the user needs (e.g. digital maps, tabular summaries, etc.), activate the Smart Access software agents in order to make all information relating to the user needs available to the reasoning system, and activate the reasoning system.

The interaction with the user is accomplished via a windows based graphical user interface (GUI). The user selects the type of products or functions that will answer his or her needs and then selects a set of 1:20000 TRIM digital maps that cover the area of interest.

SEIDAM will then activate the Smart Access [2] software agents. These agents will submit SQL queries to a relational database management system. The queries are made to extract

information from a remote sensing and GIS metadata database. This information describes ownership, source, location, distribution privileges, processing history and other ancillary information relating to the radar and GIS data available for SEIDAM. The GIS metadata database complies with the US Federal Geographic Data Committee's standard. Smart Access produces tabular reports identifying the available and necessary data that will satisfy the user's needs.
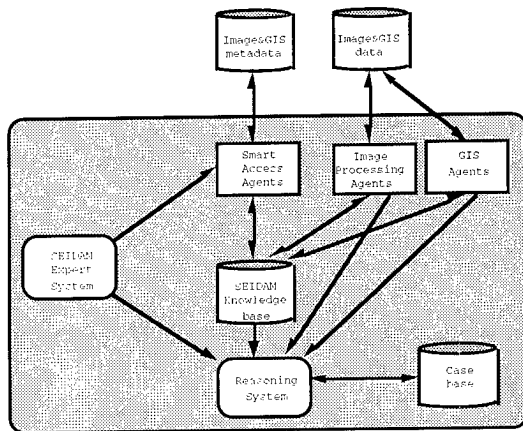
Figure 1 - SEIDAM (after [2])

Once the Smart Access software agents have completed their tasks, SEIDAM calls on the PALERMO reasoning system. PALERMO [8] is a case-based reasoning system that uses STRIPS [9] planning operators to elaborate plans. For SEIDAM, these plans correspond to the sequence of processing tasks (image analysis and GIS tasks) that must be carried out on the remote sensing and GIS data to answer user queries. Once PALERMO has formulated a plan, it will attempt to execute it by activating the image and GIS software agents.

The image analysis agents and GIS agents perform two roles: they run off the shelf software (e.g. PCI or ENVI image analysis, ESRI Arc/Ingres GIS, etc.) to perform low granularity tasks such as creating digital elevation models (DEMs); they also create STRIPS descriptions of the tasks they perform and send them to the PALERMO reasoning system, thus enabling PALERMO to create plans.

There are approximately 40 remote sensing and GIS software agents which perform such specialized tasks as: copying files, translating data between image file formats and GIS file formats, creating digital elevation models from point elevation data, moving amongst various GIS file formats; applying topographic relief correction algorithms to remote sensing imagery, computing biomass from AIRSAR measurements, etc.

III. AIRSAR DATA PREPARATION AND ANALYSIS

During the SEIDAM field programs of 1993 and 1994, NASA acquired system multi-frequency and multi-polarization AIRSAR data over the SEIDAM test sites. Data were acquired in both years over two test sites on Vancouver Island, the Greater Victoria Watershed District (GVWD) and Clayoquot Sound.

The GVWD test site is the primary SEIDAM test site. Over 90 percent of the trees found there are Douglas Fir. The average elevation of this test site is about 400 meters above sea level, with slopes as great as 22 degrees for some of the 10 plots. The younger stands are managed, but the old growth forest in this test site is largely unmanaged. The GVWD test site contains some of the oldest stands of Douglas Fir in the southern half of Vancouver Island. Studies in the GVWD test site conducted by the Canadian Forest Service have shown that trees having a diameter at breast height (dbh) of over 30 centimeters will seldom grow more than one millimeter per year in dbh [3]. Annual volume increments per hectare in Douglas Fir under the environmental conditions present at the GVWD range from 10 percent of standing volume at age 24 years, to about 5 percent by age 40, declining to near zero in older stands [3]. Based on this information, it was assumed that the change in biomass at each of the plots was negligible over the two years. Radar data were available for eight of the ten plots in the GVWD test site. The biomass values for these plots were calculated using relationships derived from several years of ongoing studies conducted by the Canadian Forest Service in the GVWD area [4].

In order to assist with the calibration of AIRSAR data, trihedral corner reflectors were deployed in the GVWD test site in both 1993 and 1994. POLCAL [5] was used to check the radiometric fidelity of the AIRSAR data. Target analysis of the corner reflector signal returns using POLCAL indicated that the AIRSAR HH/VV ratios and HH and VV phase differences were within 5 percent of expected values.

DEMs were extracted from 1:20000 scale topographic GIS data for the GVWD, (which exists as ungeneralized digital elevation points). The DEMs were registered to slant-range AIRSAR data and topographic calibration was carried out using POLCAL.

Figure 2 indicates the behavior of the normalized backscattering coefficient (σ^0) from AIRSAR data for the years 1993 and 1994, as a function of biomass for P-band. The curves agree with each

other to within 3 db (worst case). We have observed similar behavior observed for σ^0_{VV} and σ^0_{HV}. In the absence of a greater number of points, it is not possible to reproduce the complex regression equations given by various sources (e.g. [6], [7]) relating biomass to the backscattering coefficients of HH, HV, their squares, and their differences. However, we were able to determine a simpler relationship between σ^0_{HH} and biomass for our data. The results were:

σ^0_{HH} = 2.711 log (B) - 13.086 for 1993 data (r^2 = 0.702),
σ^0_{HH} = 2.960 log (B) - 11.892 for 1994 data (r^2 = 0.676).

Sigma HH (P-Band) vs Biomass

□ sigma HH 1993 ◇ sigma HH 1994

SIG HH = 2.711LOG(B) - 13.086 r^2 = 0.702
SIG HH = 2.960LOG(B) - 11.892 r^2 = 0.676
- - - - · Computed sigma HH
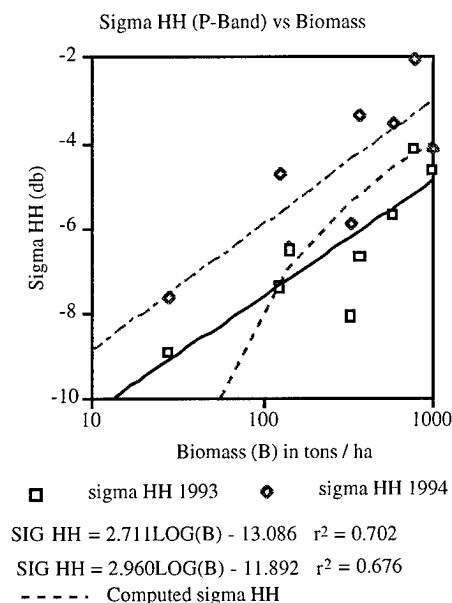
Figure 2 -Backscattering coefficient for P-band, HH polarization, as a function of biomass (B) in metric tons per hectare. The solid line show the relationship for 1993 and the dash-dot line the relationship for 1994 acquisition. The dashed curve is a relationship taken from [6].

The conditions for 1993 and 1994 differed in the amount of moisture in the ground. The earlier year was wetter than 1994. The considerable scatter in the measurements weakens the utility of AIRSAR for operational timber volume estimation at this time. In fact, when we invert these equations to predict biomass, the estimates have too much scatter. We are adding additional plots to the regression in order to elucidate other factors and to build confidence in biomass estimation from P-band SAR.

IV. AIRSAR EXPERT SYSTEMS

The process of using AIRSAR data towards the goal of determining forest biomass within SEIDAM may be conceptualized as per reference [2]. A user initiates the process of performing forest inventory determination using the SEIDAM expert system. Digital maps are selected by the user corresponding to the area of interest. Smart Access software agents are started which use the relational DBMS where the GIS and remotely sensed (AIRSAR) data reside. SQL queries are submitted which identify the appropriate GIS and AIRSAR data as well as the level to which these data have been processed. These meta data are then transferred to the knowledge base.

The SEIDAM case-based reasoning system is then activated with a goal of determining forest biomass within the selected digital maps. The STRIPS planning operator description is acquired by the reasoning system from each of the GIS and AIRSAR agents in order to determine if a similar case has been solved before. If a similar case is found, then it is modified to account for the differences between it and the current user goal. If a similar case is not found, then the reasoning system uses goal regression to determine a solution to the problem. Such a solution would consist of an ordered list of processing tasks which must be executed in the appropriate sequence to determine forest biomass, with each processing task corresponding to a single GIS or AIRSAR software agent. As each of these tasks is executed in the correct order, the contents of SEIDAM's knowledge base are modified by augmenting or deleting information. A successful execution means that the information added or deleted from the knowledge base should agree with the STRIPS planning operator provided by each software agent. This enables the reasoning system to ensure that the processing carried out by each agent is successful prior to the next agent being activated.

For the determination of the forest biomass using AIRSAR data and fusion of the same with other data sources, a solution may be formulated as follows:

- *copy_files_to_working_directory*: this agent will copy GIS and AIRSAR files from the mass storage system to a cache disk for processing.
- *trim_to_dem*: this agent would create a point elevation file readable by Arc/Info from TRIM data.
- *create_tin*: a DEM would be created by this agent from triangulated irregular network created using the point elevation file from the previous task. The output is written in a generic file format.

- *create_dem_sr*: the DEM from the previous task would be registered by the user to a slant range configuration appropriate to the NASA/JPL AIRSAR data for topographic calibration.
- *cal_AIRSAR*: calibrate AIRSAR data using corner reflector returns or homogenous targets.
- *topo_corr*: the POLCAL software package would be used to carry out the topographic correction to the AIRSAR data in the compressed Stokes Matrix format using the slant-range DEM from the previous task.
- *create_AIRSAR_image*: topographically corrected AIRSAR images would be synthesized using RSI ENVI.
- *SR_to_GR*: RSI ENVI would be used to make slant range to ground range correction of AIRSAR images.
- *relief_correction*: AIRSAR images would be corrected for relief effects using RIASSA, an in-house image analysis package.
- *set_georeference*: AIRSAR data would be georeferenced in anticipation of fusion with data from other sensors, such as TM, AVIRIS, etc.
- *calculate-biomass*: having derived the regression coefficients from previous experiments, biomass would be calculated as per the results described above. Other estimates would be generated based on other authors, such as [6], and [7].
- *update_GIS_attributes*: the attribute parameters for the forest cover GIS file would be updated to reflect the new estimate of timber volume.

V. CONCLUSIONS

We have presented observations made from AIRSAR data acquired over the SEIDAM test site of the Greater Victoria Watershed District in 1993 and 1994. A relationship has been derived for estimating biomass from P-band SAR. However, more calibration of this relationship is required. The sequence of expert systems for processing AIRSAR data has been outlined. This sequence has been partially implemented and will be completed once we are satisfied that the biomass estimation procedure is robust.

VI. ACKNOWLEDGMENTS

VI. REFERENCES

[1] D.G. Goodenough, A. S. Bhogal, D. Charlebois, M. Heyd, S. Matwin and F. Portigal, "Knowledge-Based Imaging Spectrometer Analysis", presented at IEEE Pacific Rim Conference on Communications, Computers and Signal Processing, Victoria, B.C. May, 1995.

[2] D. Charlebois, D.G. Goodenough, A. S. Bhogal and S. Matwin, "Case-Based Reasoning and Software Agents for Intelligent Forest Information Management", paper to be presented at IGARSS 96', Lincoln, Nebraska in May, 1996.

[3] E. R. Gardner, "Fertilization and Thinning Effects on a Douglas Fir Ecosystem at Shawnigan Lake: 15-year Growth Response". Forestry Canada Information Report BC-X-319. 42 pages.

[4] A. K. Mitchell, H. J. Barclay, H. Brix, D. F. Pollard, R. Benton, and R. DeJong, "Biomass and Nutrient Element Dynamics in Douglas-Fir: Effects of Thinning and Nitrogen Fertilization over 18 Years", in press (Canadian Journal of Forest Research).

[5] POLCAL Users Manual. J. J. Van Zyl, C. F. Burnette, H. A. Zebker, A. Freeman, and B. Chapman. JPL D-7715 Version 4.0.

[6] E. J. Rignot, R. Zimmermann, J. J. Van Zyl, "Spaceborne Applications of P-Band Imaging Radars for Measuring Forest Biomass", IEEE Trans. Geoscience and Remote Sensing, Vol. 33, No. 5, Sept. 1995.

[7] E. S. Kasischke, N. L. Christensen Jr., and L. L. Borgeau-Chavez, "Correlating Radar Backscatter with Components of Biomass in Loblolly Pine Forests", IEEE Trans. Geoscience and Remote Sensing, Vol. 33, No. 3, May 1995.

[8] D. Charlebois, D. G. Goodenough, S. Matwin, A. S. P. Bhogal, and H. Barclay, "Planning and Learning in a Natural Resource Information System," presented at Canadian AI, Toronto ON Canada, 1996, pp. (in press).

[9] R. E. Fikes, P. E. Hart, and N. J. Nilsson, "STRIPS: A New Approach to the Application of Theorem Proving to Problem Solving," *Artificial Intelligence*, vol. 2, pp. 189-208, 1971.

The experimental airborne VHF SAR sensor CARABAS. A status report

A. Gustavsson, L.M.H. Ulander, L.-E. Andersson, P.-O. Frölind, H. Hellsten, T. Jonsson, B. Larsson, and G. Stenström

National Defence Research Establishment (FOA)
P.O. Box 1165, S-581 11 Linköping, Sweden
Phone: + 46 13 31 80 00, Fax: + 46 13 31 81 00, E-mail: andgus@lin.foa.se

Abstract -- The CARABAS SAR has proven to be a significant contribution in the field of low frequency radar imaging. The wavelengths used have a potential of penetration below the upper scattering layer, in combination with high spatial resolution. The first prototype of the system has been tested in environments ranging from rain forests to deserts, collecting a considerable amount of data often in parallel with other SAR sensors. The work on data analysis proceeds and results obtained so far seem promising, especially for applications in forested regions. The experiences gained are used in the development of a new upgraded system, scheduled for initial airborne tests in 1996.

INTRODUCTION

There is an increasing interest in imaging radar systems operating at low frequencies. Examples of civilian and military applications are detection of stealth-designed man-made objects, targets hidden under foliage, biomass estimation, and penetration into glaciers or ground.

Measurements with the first generation of the CARABAS SAR sensor started in 1992. The system operates at HH-polarization between 20-90 MHz, which is implemented by a stepped frequency waveform [1]. Two wide band dipoles are trailed behind the aircraft, cf. Fig 1. The radar alternates between the two sack antennas in a ping-pong fashion to separate backscattered signals from the two sides of the aircraft.

This paper will give an overview of data collected with the current radar system, including some results for forested regions. The achieved system performance will be discussed, with a presentation of the major modifications made in the new system under development, CARABAS II.

DATA COLLECTION

Six different test sites have been investigated with CARABAS I in extensive field campaigns, see Table 1. The main objective of imaging forested areas has been to measure the two-way attenuation and the average backscatter level from the forest [2, 3]. For the sea ice and the desert area the potential of penetration using low frequencies has been in focus for the activities [4, 5]. All experiment areas have been imaged with at least one additional SAR sensor for comparison, on another occasion or during the same day as CARABAS. This includes the SRI International FOLPEN II

radar, the NASA/JPL AIRSAR and the European radar satellite ERS-1. A considerable part of the work has been conducted together with MIT Lincoln Laboratory, under the sponsorship of ARPA.

Table 1. Major field campaigns with CARABAS I, including existence of differential GPS data for motion compensation.

Test site	Environment	Time of year	Differential GPS
Ottenbylund, Sweden	Deciduous forest	October 1992	No
Siljansfors, Sweden	Coniferous forest	October 1992	No
Fort Sherman, Panama	Rain forest	May 1993	No
Yuma, AZ, USA	Desert	June 1993	Yes
Portage, ME, USA	Mixed forest	September 1993	Yes
Bay of Bothnia, Sweden	Sea ice	March 1994	Yes

A typical field experiment lasts one week and consists of a number of flight missions. A limited, but environmentally representative, geographical area of about 10-30 km^2 is identified and imaged at different days and for each flight from different look directions at several incidence angles. Collection of ground truth data is carried out in parallel, to acquire additional information for later use in the image evaluation. This work includes measurements of important ground parameters, as well as deployment of well-defined reference targets, man-made objects and a GPS receiver for differential aircraft positioning measurements. Fig. 2 illustrates the cumbersome deployment of VHF-sized passive reference reflectors and a processed image from the same test site is found in Fig. 3.
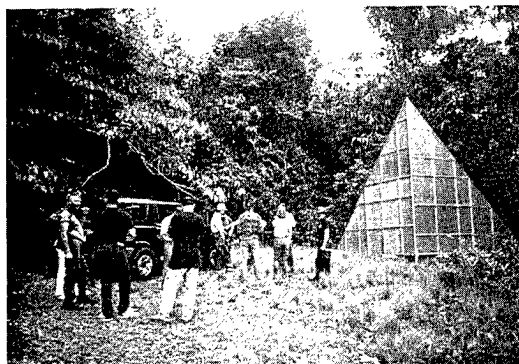
Fig. 2. A 4.9 m trihedral corner reflector set up at Fort Sherman, Panama, and obscured by dense rain forest from the radar line-of-sight.

The reference targets are used for phase calibration across the bandwidth, for radiometric calibration of the image [6], and for comparison of the radar signature from an obscured radar reflector with the response from one found in the open. An active reference target device has been used on ground at some occasions [7].

PERFORMANCE EVALUATION

The large relative bandwidth and long azimuth integration time, together with propagation effects such as penetration and multi-path, imply a somewhat different methodology to evaluate this kind of radar.

In many cases, CARABAS is not legally able to transmit the full band or, alternatively, strong external sources may interfere with the signal. These effects put operational limitations from time to time. A differential GPS system for measurement of aircraft positioning data was not available until the trials in the Yuma desert, preventing the signal processing to take full advantage of the available Doppler bandwidth in the first field campaigns. In addition to this, the radar system is Doppler ambiguous above 65 MHz when the full bandwidth is transmitted. This can mainly be explained from capacity limitations in the recording system of digitized radar raw data, resulting in a too low effective PRF when the full frequency step scheme, with adjacent increments of only 1.25 MHz, must be repeated for both left and right antenna. The effect of the Doppler signal aliasing increases gradually from 65 MHz, but is significantly reduced during the SAR processing by only utilizing non-aliased bandwidths. At 80 MHz, for example, about 62% of the Doppler bandwidth is available for processing, corresponding to an aspect angle interval of $\pm 40°$.

Imperfections in the antenna system performance have been revealed by analyzing actual CARABAS I radar data. Two major characteristics have been discovered, namely an effect of lobe splitting for the highest frequencies, and a very weak radar response at a few narrow frequency intervals.

The ultimate resolution of an ultra-wideband and wide-beam SAR system is of wavelength order. Conventional (narrow-band and narrow-beam) SAR resolution formulas are not applicable since the impulse response is not separable in image coordinates. The spatial resolution must thus be defined based on an area ΔA measure instead, and the following formula can be derived [8]

$$\Delta A \geq \frac{\lambda_c}{2\Delta\vartheta} \frac{c}{2B} \tag{1}$$

where λ_c is the wavelength corresponding to the frequency at the centre of the transmitted bandwidth B, $\Delta\vartheta$ is the aperture angle spanning the synthetic aperture, and c is the speed of light.

Equation (1) gives an ultimate resolution area for the CARABAS SAR of about 3 m^2, assuming a 120° aperture angle and transmitted frequencies between 20 and 90 MHz. The actual resolution of CARABAS I has been estimated using 4.9 m size trihedrals deployed in Portage, Maine. The SAR images were processed using 20-80 MHz and 100° aperture angle, which gives a theoretical resolution area of 5 m^2. Standard processing, with differential GPS motion compensation and autofocus, gave a resolution area of 10 m^2. Nonstandard processing using an inverse filter gave the expected theoretical resolution of 5 m^2, but at the expense of severely degraded integrated side-lobe ratio (ISLR). The degradation of the actual resolution compared to the theoretical value is mostly due to the variable antenna characteristics across the bandwidth.

APPLICATIONS IN FORESTED REGIONS

Forest SAR data from Fort Sherman, Panama, and Portage, Maine, have been examined by MIT Lincoln Laboratory. Statistical distributions for the two-way attenuation and foliage backscatter have been derived by measurements on deployed corner reflectors and homogeneous forest sections at the same incidence angle for the different sensors [2, 3]. As expected, a considerable attenuation through forest was found for microwaves, whereas the differences between UHF and VHF is not decisive for an operational system. The foliage backscatter will, however, contribute with a severe competing clutter level of the same magnitude for both UHF and microwaves. The much weaker clutter level observed for VHF is favourable for target detection in dense vegetation. The very long synthetic aperture for VHF systems, in conjunction with more moderate fluctuations of the radar cross section (RCS) with respect to aspect angle, emphasize this further and increase the sectors of detectability independently of the actual orientation of a deployed target. The UHF data analyzed were acquired within the frequency interval 200-450 MHz.

The reduced speckle noise and vegetation clutter for a VHF sensor, in combination with the diffraction limited resolution, imply that the surveillance capability will be high for this type of system. Man-made targets are detected by the reflectivity strength at moderate resolutions, rather than detection by shape against a severe clutter background applicable to microwave SAR systems and thus requiring a correspondingly high spatial resolution.

The characteristics of the forest stand at the Ottenbylund test site have recently been surveyed in detail, as part of a research program to assess CARABAS data for biomass estimation. A maximum forest bole volume of 200 m^3/ha was measured and the average tree height estimated to 20 m. Analyses of radar data show a higher dynamic range of the forest backscattering coefficient compared to what is found in

images from SAR systems using higher frequencies. The well-known saturation effect manifested in biomass estimation using radar was not encountered at the maximum bole volumes found in Ottenbylund [9].

CARABAS II

The assembly of the new CARABAS II sensor proceeds and the initial radar flight tests are preliminary scheduled for the first half of 1996. It is a joint effort between FOA and Ericsson Microwave Systems. Based on the experiences gained from CARABAS I, the main improvements are a new rigid antenna system, and a considerable increase of the average transmitted power.

Aerodynamical analyses showed it possible to mount the rigid antennas on the front to avoid the turbulent wake of the aircraft. The electrical part of the structure is integrated inside an aramide tube and the tube ends in a part of carbon fibre for integration to the fuselage. The total length is approximately 8 m and the configuration is installed on the same platform as CARABAS I, a Sabreliner business jet. Two non-electrical dummy units have already been flown successfully, with the aerodynamical behaviour measured for various conditions within the flight envelope, cf. Fig. 1. The electrical antenna design has been changed to reduce the active length to about 5 m. The properties of the manufactured antenna is measured at an outdoor test range for comparison with computer simulation results. In CARABAS II, it will be possible to transmit through the two antennas simultaneously with a fix time delay to improve the directivity to the left- or right-hand side of the aircraft. The final evaluation will be carried out in flight, with the influence from the metallic fuselage included. One obvious advantage with the new arrangement is the lifetime compared to the flexible tubes. The latter survived only about 20 hours in flight before repairs or even replacement were required, and since each individual unit had its own characteristics the overall antenna properties were thus changed. A major drawback with the new configuration is, however, its position pointing forward and thereby imposes a risk of damaging the engines if something happens with the mechanical structure. The antennas are thus equipped with both de-icing and lightning protection systems, and this must be taken into account in the electrical design.

CARABAS II will operate within 20-90 MHz and a non-ambiguous Doppler measurement over the full band is achieved. The increased power level will rely on adaptive signal shaping to allow frequency management by notching techniques, and by this means avoid a severe teleconflict problem and permit frequency cohabitation with other users. The frequency scheme is fully programmable and will enable research on optimal transmitted waveforms for different applications, e.g. occupying different parts of the full

bandwidth non-uniformly over a full cycle. The new system is designed to operate at an higher maximum altitude and to register data from a larger swath width on ground.

The large integration angle in low frequency SAR, in combination with the pulse compression and radio interference mitigation for the new long complex CARABAS II signal, result in a considerable computation burden. The signal processing is currently running off-line on ground, but a demand of onboard processing in real-time can be foreseen for a future operational system, at least for quick-look products. The original derived inversion formula has been reformulated on a form well-suited for a multi-processor environment, not requiring the complete set of data to be available. The algorithm operates locally and the image resolution improves continuously as long as new raw data are registered along the full synthetic aperture [10]. A Mercury multi-processor system has been purchased for this purpose.

SUMMARY

A considerable amount of radar data have been collected with CARABAS I, in environments ranging from rain forests to deserts. The data analyses have given new interesting results in the field of low frequency imagery. Some imperfections in the radar system have been discovered, and will be taken into account in the new improved system under development, CARABAS II. The major modifications concern the antenna system and the average power transmitted. Evaluation of CARABAS I images has shown good performance in detection of man-made objects covered by foliage.

The first promising results on biomass estimation have to be examined further with the new system, imaging well surveyed forest stands with a variety of bole volumes. The potential of interferometry at low frequencies is another possibility of great interest to investigate for 3D imaging applications [11]. It is envisaged that the increased average power will help to better understand the scattering mechanisms present in ground penetration, to be able to explore potential applications.

REFERENCES

[1] A. Gustavsson, et al., "The Airborne VHF SAR System CARABAS", Proc. IGARSS'93, Tokyo, Japan, 18-21 August 1993, pp. 558-562.

[2] B.T. Binder, et al., "SAR Foliage Penetration Phenomenology of Tropical Rain Forest and Northern U.S. Forest", Proc. IEEE International Radar Conference, Alexandria, VA, 8-11 May 1995, pp. 158-163.

[3] J.G. Fleischman, et al., "Foliage Attenuation and Backscatter Analysis of SAR Imagery", IEEE Transactions on Aerospace and Electronic Systems, vol. 32,

no. 1, 1996, pp. 135-144.

[4] A. Gustavsson, et al., "Measurements with the CARABAS SAR Sensor during BEERS-94", Proc. IGARSS'95, Firenze, Italy, 10-14 July 1995, pp. 851-855.

[5] M.I. Mirkin, et al., "Results of the June 1993 Yuma Ground Penetration Experiment", Proc. Aerial Surveillance Sensing Including Obscured and Underground Object Detection, Orlando, FL, 4-8 April 1994, Vol. 2217, pp. 4-15.

[6] L.M.H. Ulander and Z. Sipus, "RCS of Dipoles Used for Low-Frequency SAR Calibration", Proc. EUSAR '96, Königswinter, Germany, 26-28 March 1996, (in press).

[7] G.J. Mousally, et al., "Ultra-Wideband, High RCS, Active Calibration Targets for Foliage/Ground Penetrating SARs", Proc. GPR '94, Kitchener, Canada, 12-16 June 1994, pp. 1005-1019.

[8] L.M.H. Ulander and H. Hellsten, "A New Formula for SAR Spatial Resolution", AEÜ Int. J. Electron. Commun., (accepted).

[9] H. Israelsson, et al., "Forest Backscatter Mechanisms in CARABAS VHF SAR Imagery", Proc. Retrieval of Bio- and Geophysical Parameters from SAR Data for Land Applications, Toulouse, France, 17-20 October 1995, (in press).

[10] H. Hellsten and M. Herberthson, "A Local Backprojection Implementation of the Inversion Formula Used in CARABAS", Proc. PIERS 1996, Innsbruck, Austria, 8-12 July 1996, (to appear).

[11] L.M.H. Ulander and P.-O. Frölind, "Ultra-Wideband and Low-Frequency SAR Interferometry", Proc. IGARSS '96, Lincoln, NE, 27-31 May 1996, (this proceedings).
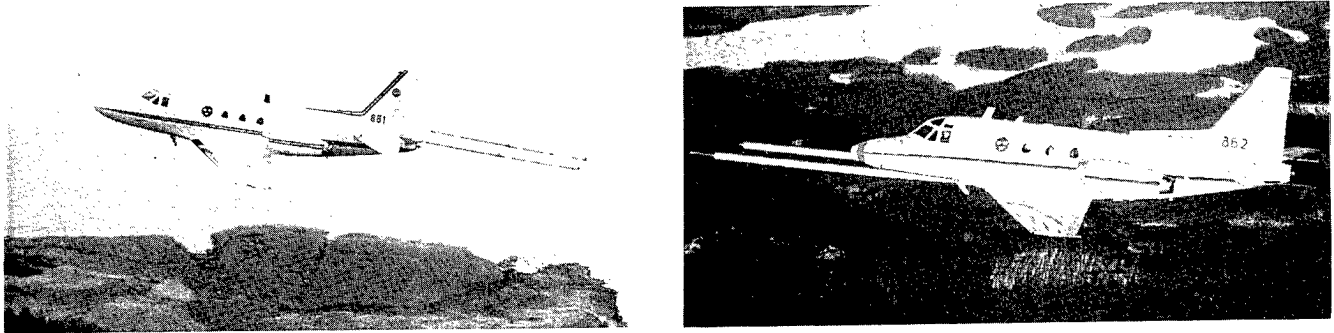
Fig. 1. The Sabreliner aircraft with the antenna arrangement mounted for CARABAS I (left) and CARABAS II (right), respectively (courtesy: FMV:Prov).
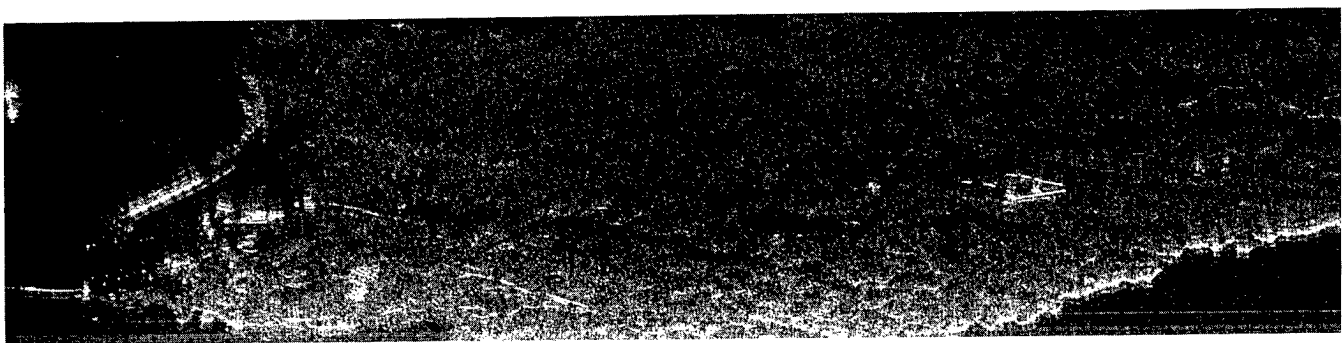
Fig. 3. This CARABAS image was acquired at the Fort Sherman area, Panama. The rough Caribbean shoreline, with a marginal zone of coral reef, exhibits a strong return along the azimuth direction. Most buildings and installations are located to the northernmost part (left) with two large merchant vessels visible in Limón Bay, forming the entrance to the Panama Canal in the vicinity of the town Colón. Except for the Fort Sherman cantonment and a few other roads and clearings in the jungle, the area is covered by virgin rain forest. Different targets were deployed along the roads and obscured by dense forest from the radar line-of-sight when flying over the Caribbean Sea, i.e. near-range in the SAR scene. The original file has here been resampled, but was processed from 20-60 MHz without any pre-summing in azimuth and with no access to differential GPS data (courtesy: MIT Lincoln Laboratory).

A High-Resolution, Four-Band SAR Testbed with Real-Time Image Formation

Bruce Walker, Grant Sander, Marty Thompson, Bryan Burns, Rick Fellerhoff, and Dale Dubbert
Sandia National Laboratories, P. O. Box 5800
Albuquerque, NM 87185-0529
(505) 844-1261; fax: (505) 844-0858; e-mail: bcwalke@sandia.gov

ABSTRACT

This paper describes the Twin-Otter SAR Testbed developed at Sandia National Laboratories. This SAR is a flexible, adaptable testbed capable of operation on four frequency bands: Ka, Ku, X, and VHF/UHF bands. The SAR features real-time image formation at fine resolution in spotlight and stripmap modes. High-quality images are formed in real time using the overlapped subaperture (OSA) image-formation and phase gradient autofocus (PGA) algorithms.

INTRODUCTION

In cooperation with numerous sponsors, Sandia National Laboratories has developed a multimode SAR testbed capable of operation on four bands: Ka band (32.6 - 37.0 GHz), Ku band (14 - 16 GHz), X band (7.5 - 10.2 GHz), and VHF/UHF (125 - 950 MHz). The SAR achieves state-of-the-art resolutions on each band while forming the SAR images in real time. Exceptional real-time image quality is achieve through the use of innovative image-formation and autofocus algorithms as well as high-accuracy motion measurement and compensation. A Twin-Otter aircraft (Figure 1) provides a flexible, low-cost platform for the SAR. The SAR testbed is designed to be very adaptable -- hundreds of parameters may be readily changed to meet the needs of new experiments.

Table 1 summarizes the parameters for the Twin-Otter SAR. The SAR operates over a wide range of resolutions, depression angles (2 to 90 degrees), squint angles (greater than ±45 degrees from broadside depending on operating parameters), and ranges (1 to 16 km). Both VV and HH polarizations are available on each frequency band, except Ka band which currently uses only VV. Cross polarization, HV, is available at the VHF/UHF band. In the spotlight mode, dwell times in excess of 60 seconds have been demonstrated with excellent image quality.

Table 1. Twin-Otter SAR Parameters

Parameter	Value	Units
Operating frequency		
VHF/UHF	125 to 950	MHz
X band	7.5 to 10.2	GHz
Ku band	14 to 16	GHz
Ka band	32.6 to 37.0	GHz
Range	1 to 16	km
Aircraft velocity	35 to 70	m/s
Spotlight resolution	1 to 3	m
Stripmap resolution		
VHF/UHF	2 to 10	m
X, Ku, and Ka bands	1 to 3	m
Swath width	1792	pixels
Depression angle	2 to 90	degrees
Squint angle	< 45 to > 135	degrees
Noise equivalent reflection coefficient (band dependent)	< -30	dB
Peak sidelobes	< -35	dBc
Multiplicative noise ratio	< -10	dB
Dynamic range	> 75	dB
Absolute RCS calibration, 3σ	< ±3	dB

OPERATING MODES

The Twin-Otter SAR can operate in either of the conventional stripmap or spotlight SAR modes. Figure 2 is an example of the stripmap mode where four stripmap passes of the Washington, DC area have been mosaiced. In addition to stripmap and spotlight modes, the SAR is capable of flying circles around targets in a spotlight mode. Circular data collections provide a means of efficiently characterizing targets over a wide range of aspect angles.

Several enhancements have been added to the Twin-Otter SAR beyond the conventional SAR modes. At Ku-band, a two-antenna configuration provides 3-D or interferometric
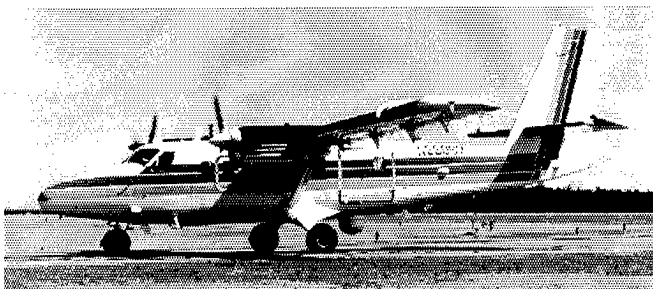
Figure 1. Twin-Otter Aircraft

Figure 2. SAR Image of Washington, DC at 1-m Resolution, Ku Band

SAR (IFSAR) capability. Using careful calibration procedures, height accuracies of sub-meter rms are achieved. The IFSAR has been used to map rural as well as urban regions. A novel phase-unwrapping technique [1] uses an amplitude-monopulse measurement to aid in unwrapping the phase ambiguities. This technique provides unambiguous height measurements and greatly improved computational efficiency compared to estimation-based phase-unwrapping algorithms. Figure 3 shows an IFSAR image of a rural area near Albuquerque, NM, yielding height noise of about 0.5-m rms.

Additional enhancements include coherent change detection for detecting decorrelation or minute changes in radar

scattering and a bistatic SAR mode which does not require direct-path synchronization between the transmitter and receiver. RF tags or transponders have been demonstrated which can be encoded within a SAR image.

HARDWARE DESCRIPTION

Figure 4 shows a simplified block diagram of the base Ku-band SAR. The antenna, inertial measurement unit (IMU), and rf front end are located on the gimbal as shown in Figure 5. Figure 6 shows the Radar Assembly which contains the digital-waveform synthesizer, frequency converter (exciter), two-channel receiver, A/D converter, and image-formation processor.

Four frequency bands are achieved by frequency translating to the desired frequency band from the base Ku-band SAR. The addition of an antenna, rf front end, transmitter, and frequency translator allow the Ku-band SAR to be readily adapted to different frequencies. This technique minimizes the new hardware required. To date, three additional frequency bands have been added: Ka, X, and VHF/UHF. The VHF/UHF band is actually designed to allow non-

Figure 3. Rendering of Interferometric SAR Image of Black Mesa, NM

continuous coverage from 5 MHz to 2 GHz; however, the current antenna limits the low-end frequency at 125 MHz and the transmitter limits the high-end frequency at 950 MHz.

The Sandia SAR platform combines five primary technologies which are each essential to the formation of high-quality, fine-resolution images in real-time:

Figure 4. Simplified Block Diagram of the Twin-Otter SAR

- Digital-waveform synthesizer with RF phase-error correction,
- Linear-phase, wide-bandwidth microwave subsystems,
- Real-time image-formation processor which implements both the overlapped-subaperture (OSA) and phase-gradient autofocus (PGA) algorithms,
- High-accuracy motion measurement and precision GPS-aided navigation, and
- Real-time motion compensation of the transmitted waveform and received samples.

The digital-waveform synthesizer (DWS) generates a linear-FM or chirp waveform for both the transmit and receive LO (deramp) signals. The DWS consists of two digital-phase-generator GaAs ASICs, each driving a GaAs sine look-up-table read-only memory (ROM). Each phase-generator and sine-ROM pair operates at 400 MHz, both driving an input-multiplexed GaAs digital-to-analog converter (DAC) to yield the analog chirp output. The two circuits are synchronized and clocked at 800 MHz to yield a theoretical bandwidth of DC to 400 MHz for the chirp output.

The frequency converter, transmitter, and receiver subassemblies achieve phase-linearity across wide bandwidths through stringent phase-error allocations and novel phase-cancellation techniques. In addition to
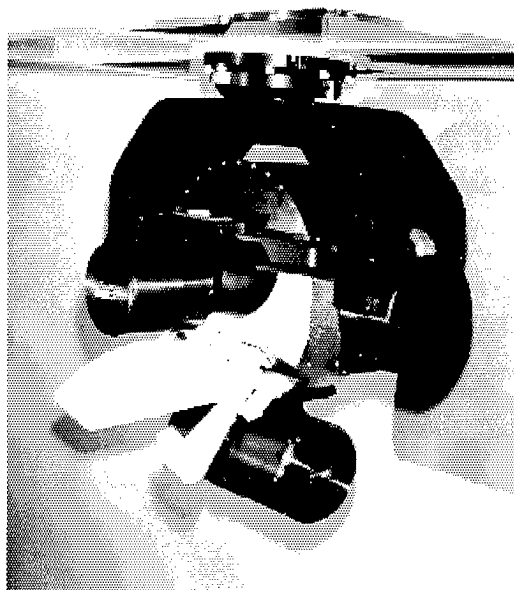
Figure 5. Antenna Assembly
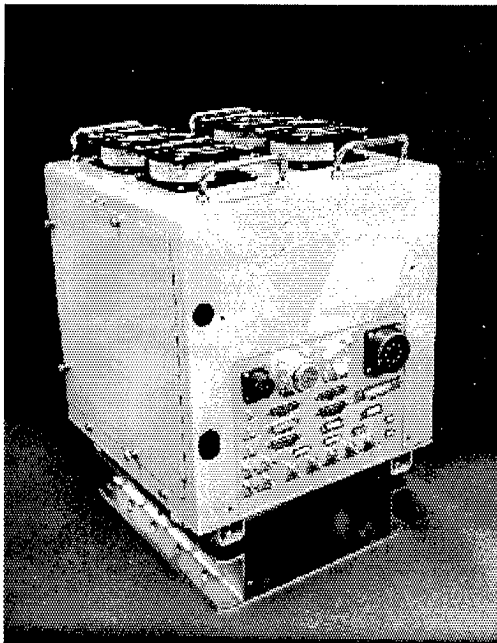
Figure 6. Radar Assembly

predistorting the transmitted waveform to compensate for phase nonlinearities, rf circuits have been developed which cancel the phase nonlinearities of other rf components. These technologies achieve excellent image quality, with azimuth and range sidelobes below -35 dBc.

The real-time image formation processor is a custom design based on the digital-array signal processor and programmable-array controller (DASP/PAC) FFT chipset from Signal Processing Technologies (SPT). Six DASP/PAC FFT boards provide the primary computational throughput required. Two TMS320C30 control computers provide the motion compensation, autofocus, and control functions.

Three short 19-in racks contain the navigation operator interface, radar operator interface, image display, high-density tape recorders, and power supplies. Two commercial PCs provide the navigation and radar operator interfaces, allowing mission or radar operation changes to be easily made. The SAR image is displayed in real-time on a 2048 x 2560-pixel MegaScan monitor. An Ampex DCRSi recorder stores the radar phase history data, the complex image data, and other auxiliary data, such as motion measurement, state-of-health, etc. A Metrum VLDS recorder may also be used as a backup recorder in storing the image data.

IMAGE-FORMATION ALGORITHMS

The image-formation processor implements the overlapped subaperture (OSA) image-formation and phase-gradient autofocus (PGA) algorithms in real time. The OSA algorithm [2] enables real-time image formation through innovations in digital-waveform synthesis, A/D sampling, and high-accuracy motion measurement. These technologies allow real-time motion compensation of the transmitted waveform and received samples, simplifying real-time image formation.

To form fine-resolution SAR images, an algorithm that can compensate for significant non-straight-line motion is required. The OSA algorithm was designed to be a real-time solution to this problem. The algorithm is constructed entirely with FFT and vector-multiplication operations. Some motion-compensation steps are carried out before the return signal is processed by changing the radar center frequency and phase, PRF, and A/D converter sample rate. The radar computes these parameters as functions of motion data provided by the motion-measurement system.

Figure 7 is a simplified functional diagram of the OSA algorithm. The algorithm is composed of three basic steps: coarse-resolution azimuth processing, fine-resolution range processing, and fine-resolution azimuth processing. In OSA, a synthetic aperture is divided into overlapping subapertures which are processed individually to produce a sequence of images which have coarse resolution in azimuth and fine resolution in range. In the final stage of processing, the coarse-resolution images are coherently combined to produce the final fine-resolution image. In OSA, range and azimuth migration are corrected using complex multiplies; inefficient interpolation operations are not required.

The real-time SAR also incorporates the PGA autofocus algorithm [3] to estimate and remove any residual motion-measurement error that would cause smearing in the azimuth dimension of the image. Autofocus is done in two steps: point selection and phase-error extraction. At the point-select process, the data has only been OSA processed to the coarse-resolution stage in azimuth and fine-resolution
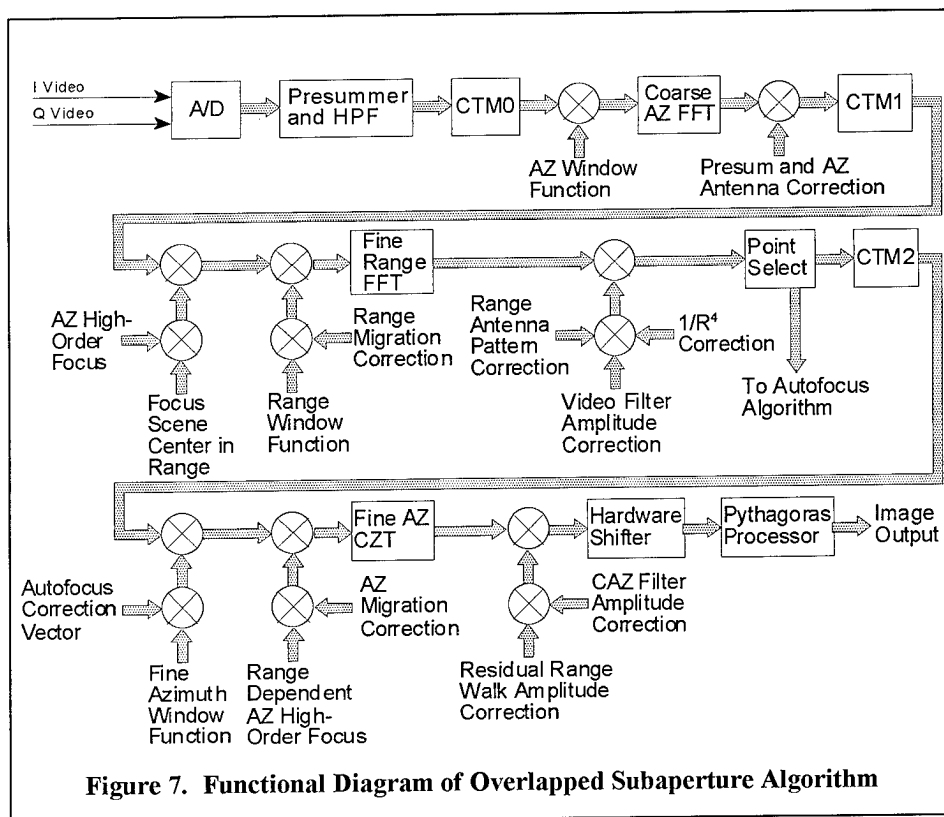
Figure 7. Functional Diagram of Overlapped Subaperture Algorithm

in range. The point-select process determines which points (range-azimuth bins) are most suited for extraction of the phase error, and gives the coordinates of these bins to the PGA algorithm. In this manner, autofocus requires less than 1% of the computational load of the image-formation processor.

The PGA algorithm finds the dominant scatterer in each bin and shifts it to zero Doppler frequency in the image domain. The algorithm then assumes any variation from an ideal azimuth-impulse response centered at zero-Doppler is due to residual phase errors. This error is averaged with those errors found from other selected points to yield an estimate for the actual error. The algorithm is iterated until the average detected error level falls below a specified threshold, or until a maximum number of iterations have been performed. The efficiency and robustness of the PGA algorithm is ideally suited for real-time image formation.

MOTION MEASUREMENT

The SAR motion-measurement and navigation system consists of a miniaturized, high-accuracy, ring-laser-gyro IMU; a 3-axis gimbal antenna-pointing and stabilization assembly; and an autonomous 6-channel P(Y)-code GPS receiver [4]. The system provides four major functions:

- Navigation,
- Motion measurement calculations for SAR motion compensation,
- Antenna pointing and stabilization, and
- Pilot guidance.

The IMU is closely mounted to the antenna to allow measurement of high-frequency motion due to turbulent flight conditions and structural resonances excited by the aircraft engines. The gimbal mounting of the IMU is made possible by its small size and weight. Output from the IMU is fed into the MoComp computer which implements the digital-signal processing and motion calculations of the motion-measurement system. The output of the GPS receiver is also fed into the MoComp computer which implements a nine-error-state Kalman filter to compensate for long-term drift in the IMU measurement. The resulting velocity error of the system is less than 5-cm/sec standard deviation, with an absolute position accuracy of less than 5-m rms for differential-GPS mode. The resulting position and velocity data is fed from the MoComp computer to the radar control and interface computer for SAR motion compensation.

The antenna pointing and stabilization function maintains the boresight of the antenna on either a straight line on the ground (stripmap mode) or a fixed point on the ground (spotlight mode) during each aperture. The pointing accuracy has been measured at less than 0.01-degrees rms. Navigation data from the MoComp computer is provided to the pilots via an aircraft waypoint guidance display (located in the cockpit) which directs the pilot to fly precise trajectories.

SUMMARY

The Twin-Otter SAR is a state-of-the-art testbed, encompassing four frequency bands and operating over a wide parameter space in resolution and geometry. Exceptional image quality is produced in real-time and in a dynamic flight environment. The testbed is designed to be flexible and can be readily adapted to future experiments. Numerous innovations in real-time hardware and algorithms have been demonstrated and are being transitioned into other programs.

ACKNOWLEDGMENTS

REFERENCES

[1] D. L. Bickel and W. H. Hensley, "Determination of Absolute Interferometric Phase Using the Beam-Amplitude Ratio Technique," 1996 International Geoscience and Remote Sensing Symposium, May 1996.

[2] B. L. Burns and J. T. Cordaro, "A SAR Image-Formation Algorithm that Compensates for the Spatially-Variant Effects of Antenna Motion," SPIE Conference Proceedings, April 1994.

[3] P. H. Eichel, D. C. Ghiglia, and C. V. Jakowatz Jr., "Speckle Processing Method for Synthetic-Aperture-Radar Phase Correction," Optics Letters, Volume 14, Number 1, January 1, 1989.

[4] J. R. Fellerhoff and S. M. Kohler, "Development of a GPS-Aided Motion Measurement, Pointing and Stabilization System for a Synthetic Aperture Radar," Proceedings of the 48th Annual Meeting of The Institute of Navigation, June 1992.

The Army Research Laboratory Ultra Wideband BoomSAR

Marc A. Ressler
US Army Research Laboratory
Microwave Sensors Branch, AMSRL-SE-RU
2800 Powder Mill Road
Adelphi, MD 20783-1197
Phone: 301-394-2530 Fax:394-4690 e-mail:mressler@msc.arl.mil

Abstract - This paper describes a mobile radar testbed that provides airborne-like collection geometries. The radar is a low frequency, ultra-wideband, synthetic aperture radar intended to provide a resource for the analysis of foliage and ground penetration phenomenology.

INTRODUCTION

The Army Research Laboratory (ARL) has been pursuing the use of ultra wideband (UWB) test bed radars as basic sensor systems for gathering the data needed to understand foliage penetrating (FOPEN) and ground penetrating (GPEN) radar phenomenology and to provide a wide variety of data to develop target detection algorithms. These radars provide 1 gigahertz (GHz) of bandwidth and the full polarization matrix to accomplish this task. They also act as the proving grounds for emerging technology in the area of transmitters, A/D converters, antennas, etc. The initial radar was a rail guided system (RailSAR) using a single dimension control system forming a 104 m linear aperture on the ARL rooftop [1].

The BoomSAR is a extension of this design, undertaken by ARL after early results from FOPEN and GPEN field trials [2,3,4] encouraged us to produce a mobile, high signal-to-noise radar. This radar allows data collection over a wide range of varying clutter and target-in-clutter scenarios, at lookdown angles similar to those that would be used in an airborne sensor, to suppport phenomenology and target discrimination research. With the BoomSAR one can form two-dimensional apertures by varying the height of the radar to allow the resolution of images in three dimensions. The major differences between the systems are the increased complexity of the three-dimensional sensing/control, the need to perform real-time motion sensing/correction, and the addition of a number of hardware and software troubleshooting tools.

SYSTEM DESCRIPTION

The basic radar consists of several major subsystems, seen in the block diagram (Fig. 1), which are modular in nature to allow for ease of exchange for the evaluation of alternate approaches. Many of the subassemblies exist as standard 19" rack mount units or as VME-compatible printed circuit assemblies. Much of the system operation is controlled by software, allowing an easy path to upgrade. The majority of the hardware is installed in a pair of environmentally controlled cabinets mounted to the basket of a JLG-150HAX telescoping boom lift. The JLG boom allows a load of up to 1000 pounds to be elevated to 45 m while the boom is moving at approximately 1 km/hr. The boom can easily be operated at lower heights by manipulating the boom arms.

Position information is obtained from a Geodimeter 4000, a commercial robotic theodolite system, that tracks an optical beacon mounted on the antenna array. The Geodimeter radio links information back to the base of the boom where it is sent on to the Motion Compensation (MoComp) computer located upmast. A SPARC notebook computer, also located at the base of the boom, acts as the operator interface to the radar system. Communication from the base to the radar system is via serial and ethernet cables that run inside the telescoping boom arms.

There are four antennas: two transmit and two receive, to provide the full polarization matrix in a quasi-monostatic sense [5]. The antennas are open sided, resistively terminated, TEM horn designs about 2 m in length with a 0.3-m aperture [6]. An ARL-designed high-power, wide-bandwidth balun [7,8] transforms the 50-Ω feedline impedance up to the 200 Ω the antennas represent. The antenna/balun combination supports a bandwidth from approximately 40 MHz to over 2000 MHz, and basically defines the low frequency end of the system bandwidth.

The high bandwidth of the radar is currently provided by using an impulse implementation. A pair of Power Spectra BASS 02X, pseudo-exponential waveform impulse generators drive the transmit antennas, allowing fast polarization switching by having the processor select which transmitter to enable. The transmit waveform has a 150-ps risetime and approximately a 2-ns falltime, and average power is approximately 1.5 w at the current pulse repetition frequencies (PRFs). The Timing and Control circuit, designed to support a wide variety of transmit and receive hardware, provides a selectable number (a "burst") of pulses, at selectable, or pseudorandom, dithered PRFs, to one or two transmitters for use with one or two antennas. This circuit also provides pre-trigger timing for other
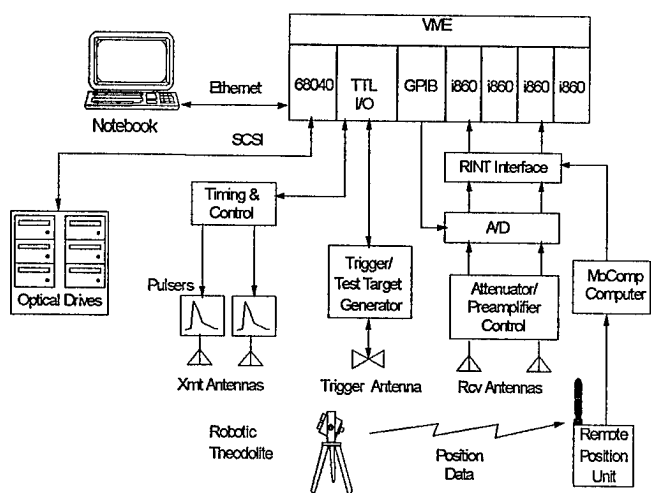
Figure 1. Radar Block Diagram

system elements and has outputs for driving receiver protectors in T/R switch systems.

The preamplifier/attenuator assemblies include low noise preamplifiers with PIN diode protectors and up to 121 dB of programmable attenuation. The attenuators act as the gain control for the A/D converters, ensuring maximum use of their dynamic range, and providing signal reduction when the radar is working with large signals, close targets, or in high RFI environments. Automatic Gain Control (AGC) is provided by a two-threshold comparator in the operational software.

The A/D subsystem acts as the wideband receiver for the radar. The radar operates as a coherent-on-receive system by triggering the A/Ds from a pickup antenna that senses the actual transmit pulse. This allows for variations in different transmitters, without having to reprogram Timing and Control circuit delays. The A/D subsystem consists of a pair of Tektronix/Analytek VX2005C, 2-gigasamples per second A/D converters, and a stable reference clock. Because the A/Ds have programmable trigger and acquisition length, the recorded range swath can be positioned virtually anywhere the operator desires. A unique feature of these A/D converters is that they provide, to 10-pS resolution, the time difference between the sample clock and trigger event. With the use of this data, subsample time interpolation allows the processor to generate an interleaved record at an equivalent 64-gigasample/s rate, much as would be provided by a sampling oscilloscope. The actual high-frequency response of the radar is defined by the 1100-Mhz analog bandwidth of the A/D converters.

The VME processor/data storage system, which orchestrates the operation of the radar, currently includes two Mercury quad i860 boards for each receive channel for high speed processing. The processors communicate with

each other over Mercury's proprietary high-speed Raceway bus. One of the boards on each of the channels has, in place of a pair of processors, a Raceway Input Interface (RINT) module that allows external accesss to the high-speed bus. An in-house-developed RINT Interface Board (RIB) provides a merged stream of A/D, status, and MoComp data to the RINT. In each channel one of the i860 processors plays host while the remaining five i860 array processors perform data interleaving, integration, filtering, and resampling to produce 8 gigasample/s equivalent data records.

SYSTEM OPERATIONS

Before each data collection (a "run"), an internal calibration of the A/D converters is performed to null DC offsets and align AC gains. Built-in test/equipment (BIT/BITE) not only allows debugging of major system components while the boom is elevated, but also provides a source of calibration signals to track the relative health of the system. When placed into debug mode, the Test Target Generator (TTG) produces a string of short pulses that can be radiated from the trigger antenna and picked up by the receivers. Since the A/D converters start digitizing as soon as they are armed, it is possible to set the delay control of the A/D converters to a "negative" time. Setting the attenuators to 60 dB allows data to be recorded from the "main bang." Before a run commences, a number of records of each of these test signals are recorded for comparison to previous results.

In the current configuration, the radar produces a burst of 128 pulses of one transmit polarization, followed by a burst of 128 pulses of the opposite polarization. Both receive channels are operated in parallel and HH, HV, VH, and VV polarization data is available. Currently, approximately 300 m of range swath (4088 samples) is acquired for each pulse. For either channel, each burst is interleaved and averaged, as mentioned earlier, by one of the five i860 processors. Down look angles to the target vary from 45° to approximately 10°, depending on the range to the target, allowing a large number of simulated airborne geometries to be examined in a single pass. Typical SAR integration angles vary from approximately 30° to 60° for these geometries, again depending on range. Approximately every 25 m, normal acquisition is automatically interrupted and raw RF Interference (RFI) data is acquired to have a record of the typical RFI levels during the run as well as real data on which to train RFI rejection algorithms.

Interleaved output is typically sent to six Magneto-Optic (M-O) CD drives, three for each channel. For about 300 m of range swath, approximately 2.5 km of aperture can be recorded on one side of these disks. It is also possible to record limited swaths of raw data on a set of six 2-gigabyte

hard drives. Two such 12-gigabyte assemblies are available to allow data to be unloaded from one while the other is used for data acquisition. Each hard drive assembly can store approximately 2 km of aperture with the number of pulses per burst recorded being traded off against range swath coverage.

At the completion of a run, the M-O disks are removed and examined with a graphical data quality tool in the data van. Radar status, position data, data statistics, histograms, and a spectrogram are available for examining the whole of the run, while individual records, or the averages of groups of records, can be plotted against either time or frequency. Data is further processed in the field, or at the laboratory, to provide motion compensation, filtering, RFI rejection, and range correction. The data is then backprojected to produce the bipolar image plane data used for signature analysis and from that, with application of a Hilbert transform, envelope data (which is then converted into decibels) is created to form SAR imagery. Data can be processed to provide sub-aperture or frequency sub-banded outputs to examine the utility of lower bandwidth systems or spotlight operations.

The BoomSAR was successfully operated at Aberdeen Proving Grounds (foliage penetration testing) and at Yuma Proving Grounds (ground penetration testing) in the 1995–96 time frame. Results from these runs have shown the system capable of 0.15-m resolution in range and 0.3 m in cross-range. Figure 2 shows an excerpt of a greater than 60-dB dynamic range image from one of the foliage penetration runs at Aberdeen. For this image the frequency range was 130–1100 MHz. A number of 42-cm tihedrals are visible in an open region between two areas of trees and an 80-cm sphere is located at the edge of the woods. There is no direct line of sight to the trihedrals from the radar; in fact, the angle to these targets is about 25° from the radar. The resolution of the radar is demonstrated by

Figure 2. Excerpt from SAR image at Aberdeen

the pair of lines running between the poles along the lower edge of the image. The first of these lines is the return from the wire strung between the poles, while the second is the multipath return from the ground reflection of the signal.

SUMMARY

A mobile ultra-wideband low-frequency synthetic aperture radar has been demonstrated with high resolution and excellent signal-to-noise performance. The system provides data on foliage and ground penetrating phenomenology with airborne-like geometries for use in ongoing studies in target detection and recognition. Future enhancements include the addition of an inertial navigation system and a developmental, direct-digital-synthesis (DDS) transceiver.

ACKNOWLEDGMENTS

REFERENCES

[1] M. Ressler and J. McCorkle, "Evolution of the Army Research Laboratory Ultra-Wideband Test Bed," in Ultra-Wideband, Short-Pulse Electromagnetics 2, L. Carin and L. Felsen, Eds., Plenum Press, pp. 102-123, 1995.

[2] M. Toups and S. Ayasli, "Results from the Maine 1992 Foliage Penetration Experiment," Proc. SPIE 1942, pp. 66-75, 1993.

[3] M. Mirkin et al., "Results of the June 1993 Yuma Ground Penetration Experiment," Proc. SPIE 2217, pp. 4-15, 1994.

[4] J. McCorkle, "Early Results from the Army Research Laboratory Ultra-Wideband Foliage Penetration," SPIE International Symposia, April 1993.

[5] D. Blejer, C. Lee, J. McCorkle, M. Ressler, and M. Bennett, "Calibration of an UWB, Short Pulse, Polarimetric SAR," unpublished.

[6] J. McCorkle, "Low VSWR High Efficiency UWB Antenna", US Patent #5,471,223, November 1995

[7] J. McCorkle, "Wideband (DC to Ghz) Balun", US Patent #5,379,006, January 1995

[8] J. McCorkle, "DC-to-Ghz PC-Board Balun", Patent applied for, August, 1994

Status of the SASAR System

Michael R. Inggs

Radar Remote Sensing Group, Dept of Electrical Engineering, University of Cape Town

Private Bag, Rondebosch 7700, South Africa

Tel: +27 21 650 3756   Fax: +27 21 650 3465

Email: mikings@eleceng.uct.ac.za

Abstract—

The South African SAR System (SASAR) is planned to be a fully polarimetric, multifrequency SAR system. Due to budget constraints, only a single VHF sensor is currently under construction. This paper reports the status of the SASAR system, concentrating on the VHF subsystem. Trials of the VHF sensor are planned for the last quarter of 1996 on board a Boeing 707 aircraft of the South African Air Force.

INTRODUCTION

SASAR was conceived of as a fully polarimetric, multifrequency SAR [1]. The exact choice of platform and transceiver frequency were not finalised until recently. In this paper, an overview of the sensor is presented, as well as giving an update on the progress with construction and integration.

In the early stages of the project it was hoped to use elements of an existing Russian VHF system [3] mounted in a Tu134, but the cost of required aircraft maintenance (which emerged after detailed discussions) made this impossible. Essentially, the Russian transceiver at 120MHz and the platform were to be fitted with a South African built recording system and inertial platform.

In addition, it was decided to change the name of the system from "iSAR" (which is SAR in the Xhosa language) to SASAR, due to the confusion with the topics of *inverse SAR* and *interferometric SAR*.

Negotiations then started with the owners of a number of platforms within the RSA and eventually the South African Air Force offered the use of a Boeing 707, which is now the focus of the project. This platform is clearly not the most fuel efficient, but a number of practical issues make it an ideal test bed for this phase of the project:

- Its high cruising altitude will allow for small incidence angle ground penetration studies.
- The large fusilage and raked back, propeller-less wings are close to ideal for the large VHF antenna.
- The fusilage of this particular aircraft already has mounting hardpoints for the antenna "cheek" (see Figure 1) as well as numerous RF feedthroughs.
- The aircraft has the duration for long deployments in other parts of Africa and the world.

In addition, the decision was made to concentrate on the most difficult sensor, i.e. a VHF system, since it was felt that this band was not commonly available internationally. The use of the VHF band is felt to offer unique opportunities for canopy penetration, as well as dry soil overburdens.
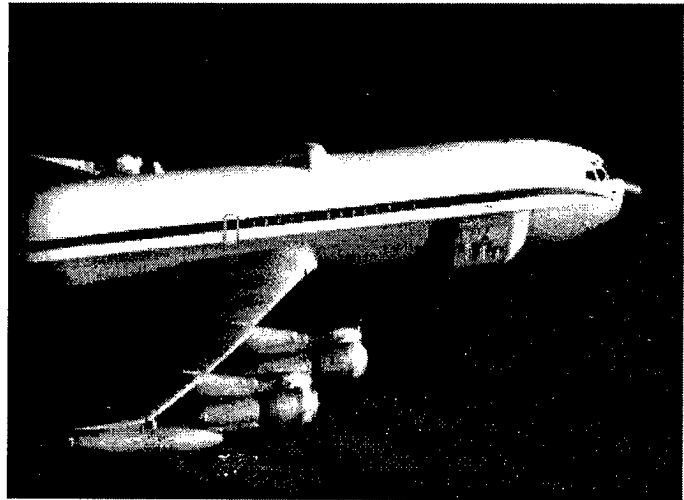
Figure 1: SAAF Boeing 707 with antenna cheek. (The VHF antenna farm will actually be located on the left side of the aircraft.

The latter is particularly important for hydrology studies in arid regions, such as found over the majority of the southern African subcontinent. In addition, it was decided to opt for a wide swath at low resolution, to enable wide area coverage.

THE SASAR SYSTEM

The block diagram of the complete SASAR is shown in Figure 2. More details of the system design are given in [1].

Features of this system which are too detailed to show in a block diagram are:

- Each channel of data is assigned its own recording device, thereby reducing data rate per channel, and thus, system cost.
- A time-stamping system ensures all data can be re-integrated for ground processing.
- The recording device is connected to a fast SCSCI port, meaning that the system can take advantage of helical scan tape, hard disk and RAID technology.
- The main timing unit is a large block of RAM, allowing almost unlimited variations in the sequencing of transmissions and recording.
- Radar PRF is slaved to ground speed, ensuring constant ground sampling in azimuth.
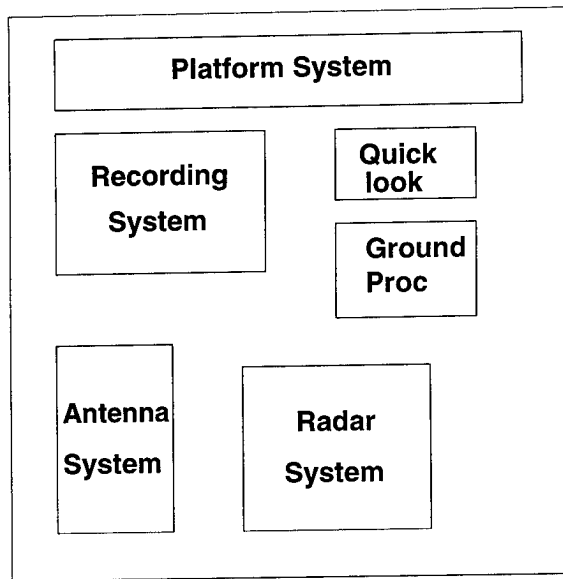
Figure 2: SASAR Block Diagram

VHF SWATH CHARACTERISTICS

The swath characteristics are shown in Table 1. Note that this is a nominal configuration: variations in platform height allow for reasonable flexibility.

Table 1: Swath Characteristics for the VHF Sensor

Characteristic	Value
Resolution (slant)	26 m
Swath Width (slant)	86.4 km
Swath Width (ground)	90.2 km
Number of Range Pixels	4096
Pixel Spacing (slant)	21.1 m
Nominal Start of Swath from Nadir Track	10.7 km
Coverage Rate	1331 km²/min
Nominal Incidence Angle (near)	45 deg
Nominal Incidence Angle (far)	84 deg

THE VHF SAR

This is the only part of SASAR currently under construction, and is described below.

The antenna is a 3×2 array of dual polarised inclined monopoles designed and developed by Grinaker Avitronics. These antennas offer virtually no air resistance and are inherently broadband. The antennas were first scaled and measured at microwave frequencies and array patterns predicted from the measured data. The measurements and simulations included the effect of the aircraft fusilage. The array itself will be tested on an open air range once integrated to the mounting cheek which acts as the ground-plane.. The broadband nature of the antenna will be useful for future range resolution enhancements to the VHF SAR.

The mounting cheek is a dural frame with plenty of space for the combining network to be mounted between the cheek and the aircraft skin. This means that that only two RF connectors are required to pierce the pressure hull. The shape of the cheek is modelled on existing EW antenna farms and is estimated to place extra drag of about 10% of the effect of one engine loss on the aircraft.

Although only one transceiver and recording system is being constructed, the antenna will be able to support fully polarimetric measurements in the future, as well as the bandwidth required for enhanced range resolution. More information on the antenna can be found in reference [2].

The transceiver consists of the slightly modified IF stages of an existing L Band radar system produced by Reutech Systems of Stellenbosch. The power stage is an adjustable class A to B solid state 1 kW amplifier.

The original design included a calibration path and polarisation switch for the power amplifier. However, due to cost, this has had to be omitted and polarisation on transmit will be manually selected. Either co- or cross-polar reception is similarly selected by hand.

Again, because of cost, a short monochrome pulse solution has been implemented, achieving a range resolution of about 25m. Future plans envisage the use of either a 5μs linear chirp or synthetic range profiling to achieve higher range resolution [4].

The receivers have digital gain and STC, controlled by the Low Bitrate Recording and Console System [1], which is part of the Recording System. The STC curves can be stored and recalled from disk and are adjustable on-line. An overall specification for the VHF Transceiver is given in reference [2].

The recording system consists of units containing A/D converters, presummer and data recorders, one for each channel. These are known as High Bitrate Recorders (HBRs). There are to be six HBR units in a fully configured system. For the prototype, single channel system, a hard disk is to be used for data recording. Data will be archived to 8mm tape post mission. A top level specification of the HBRs is given in Reference [2].

All data is time stamped with a signal originating from a GPS receiver, coded by the low bitrate recorder (LBR). This LBR also acts as the system console for setup of the radar transceivers, HBRs and Quick Look Processor (QLP).

The inertial platform is the RAP10 strapdown inertial platform produced by Kentron of Irene. This unit also contains a GPS. Data is transferred to the LBRCS using the ARINC standard. The unit is mounted close to the antenna cheek to assist with motion compensation post mission. This system has very similar specifications to standard airborne equipments and details are not given here. The motion system was made autonomous of the platform to simplify air safety considerations, i.e. not compromising the aircraft's built-in navigation systems.

For the first version of SASAR, a DEC Alpha workstation is being used for the quicklook function (QLP). A quasi-focussed algorithm [3] is used to produce 25m square pixels. The principle objective of this system is for online checking of data as it is being recorded. The very unpredictable backscatter levels at VHF, as well as the range

dependency of the data will make this a very useful tool. The QLP can be switched to any of the radar transceivers, although only one receiver will be present in the prototype system.

The Ground Processor (GPROCS) is based on the conventional range-doppler algorithm. The processor is written in ANSI C and runs on a number of platforms. The DEC Alpha used as the QLP in this system will be used post-mission for the bulk of image processing.

Data is input to the processor from mission recorded tapes. In addition, motion data from the mission is input separately, also from tape. The time-stamping of data allows motion and raw data to be re-integrated for further processing to the desired resolution.

Initially, VHF data will only be processed to about 4 looks and square pixels of about 25m. Range curvature is not problematic at this resolution. However, some experimentation will be carried out with higher azimuth resolution to test the capabilities of the processor and the motion recording system. The demanding requirements of high resolution VHF SAR imagery are currently under review [4].

PROGRAMME

All contracts for hardware and software were placed in mid 1995, and system laboratory integration will start in April 1996. The antennas and the "cheek" are complete and being tested. The RF hardware is also under test. The first flights are expected to take place in about August 1996. Due to the cost of operating the platform, as many missions as possible will be planned to piggy-back with other SAAF training activities. Missions will be planned to try and assess the foliage and ground penetration capabilities of this sensor.

Calibration is an important issue and is especially difficult at VHF frequencies. Some thought is being given to active calibrators, as well as more conventional dihedrals and trihedrals. However, the first priority will be to obtain experience of typical VHF backscatter from various terrains.

Planning will start soon on the addition of a second VHF receiver, transmitter switch and recording system. This second system will be delayed so that experience with the first system can be incorporated into its implementation. No range resolution enhancement would be contemplated during this project.

The present 25m resolution is adequate for geophysical applications, but for reconnaisance and target recognition, an improved resolution (1.5m) should be planned. A project decision will then have to be made as to whether it would be better to enhance the resolution of the VHF sensor (say to 1.5m), or to add another frequency. Budget will probably preclude both being tackled simultaneously.

A project is under way at present investigating the use of the Chirp Scale algorithm [5] together with synthetic range profiling [6,4] processing to achieve the improved radar range resolution. An alternative approach for improved

range resolution is to use a conventional linear chirp. However, the former approach is favoured, since the frequency hopping nature of the synthetic range profile will allow interfering signals to be removed before range processing [4]. It is expected that interference will be problematic in the VHF band. It should be noted that to reduce recording bandwidth, the synthetic range profiling will have to be carried out before recording.

In terms of adding other frequencies to the SASAR, the other sensor might well be at L Band, since low cost indigenous technology exists. The dual channel patch array would be integrated between the VHF elements, if it can be shown that the groundplane continuity is not too severely compromised.

CONCLUSION

The VHF sensor of the SASAR has been described. This sensor is planned to start trials in the last quarter of 1996. The foliage and ground penetration capabilities of this sensor will be evaluated during a limited number of trial flights. Upgrades to the VHF and other sensors are planned once more funding becomes available.

ACKNOWLEDGEMENTS

REFERENCES

[1] Inggs, M.R., Horrell, J.M. ,Knight, A. and Koeppen, P.G., "iSAR: A Multispectral, Polarimetric Airborne SAR System", Proceedings of the 1994 International Geoscience and Remote Sensing Symposium, IGARSS '94, Pasadena, USA, pp 2237-2239, Vo.4, August 1994.

[2] Inggs, M.R., "The SASAR VHF Sensor", Proceedings of the European Conference on Synthetic Aperture Radar, EUSAR'96, Königswinter, Germany, 26-28 March, 1996. In Press.

[3] Horrell, J.M, Knight, A. and Inggs, M.R., "A Quicklook Processor for an Airborne SAR", Proceedings of the 1994 International Geoscience and Remote Sensing Symposium (IGARSS'94, Pasadena, USA, pp 1178-1180, Vol.2, August, 1994

[4] R.T. Lord and M.R. Inggs, "High Resolution VHF SAR Processing Using Synthetic Range Profiling", This proceedings.

[5] Raney, R. Keith, Runge, Hartmut, Bamler, Richard, Cumming, I G, Wong, Frank H, "Precision SAR Processing Using Chirp Scaling", IEEE Trans on Geosc. and Remote Sensing, pp 786-799, Vol.32, No.4, July,1994.

[6] D. R. Wehner, High Resolution Radar, Norwood, MA 02062: Artech House, 1987.

YSAR: A Compact, Low-Cost Synthetic Aperture Radar

Douglas G. Thompson, David V. Arnold, David G. Long,
Gayle F. Miner, Thomas W. Karlinsey
Brigham Young University
459 CB, Provo, UT 84602
voice: 801-378-3262, FAX: 801-378-6586, e-mail: arnold@ee.byu.edu

Abstract: We have developed a relatively inexpensive, experimental Synthetic Aperture Radar (SAR) system which can be flown on small aircraft. The entire unit weighs approximately 360 lbs with most of the weight in the battery-power supply. The system cost is kept low by using a simple RF subsystem with an all-digital IF and commercial components for the chirp generation, analog-to-digital conversion, and digital signal processing. The system has been successfully operated from a truck and an aircraft and has exhibited a range resolution of 1.5 m and an azimuth resolution of 0.5 m. The system is described and images from the tests are shown.

INTRODUCTION

A Synthetic Aperture Radar (SAR) is an imaging radar which uses signal processing to improve the resolution beyond the limitation of the physical antenna aperture. Typical SAR systems are complex, expensive and difficult to transport. The BYU SAR (YSAR) is a relatively inexpensive, lightweight system. The system is designed to be flown in a four or six passenger aircraft at altitudes up to 2000 feet.

The system cost and complexity are kept low by using commercially available parts for most of the components. A standard PC system is used, with plug-in cards for the analog-to-digital conversion and digital signal processing. The chirp is generated by a low-cost 200 MHz Arbitrary Waveform Generator (AWG). A simple RF subsystem up-converts the transmitted chirp using double-sideband modulation and down-converts the received signal. The YSAR system has been successfully tested from a truck and an aircraft. The system has a range resolution of 1.5 m and an azimuth resolution of 0.5 m.

This paper describes the YSAR system and presents results obtained from system tests. The first section shows the block diagram and describes each component. The next section describes the deployment of the system. The third section presents test results.

SYSTEM DESCRIPTION

The YSAR system is composed of an RF subsystem, a chirp generation subsystem, a digital subsystem, and an antenna subsystem. A block diagram of the system is shown in Fig. 1. The entire system weighs approximately 360 lbs, with over half that coming from the battery-power supply. Each of the subsystems is described below.

RF Subsystem

The RF subsystem consists of a transmitter, receiver, and offset local oscillator and weighs approximately 70 lbs. The transmitter mixes the 100 MHz bandwidth chirp up to 2.1 GHz for transmission. The receiver and local oscillator are used to mix the RF radar return from the antenna to an offset baseband and amplify it so it can be sampled by the digital subsystem.

Chirp Generation

To reduce cost, the chirp is transmitted and received with double-sideband (DSB) modulation, as shown in Fig. 2. This avoids the cost associated with single-sideband chirp generation and increases the effective bandwidth of the chirp.

The baseband chirp signal is generated by a commercial Arbitrary Waveform Generator (AWG). The chirp is first calculated by the PC and then downloaded with timing information to the AWG's memory over an RS-232 channel. The AWG is synchronized to the local oscillator in the RF unit and is used to control the timing for the entire system. The chirp bandwidth, the delay before triggering the digital sampling, and the pulse repitition frequency (PRF) are all software selectable. The LFM chirp may be windowed with 6 different windows to allow tradeoffs between range sidelobes and resolution. The AWG is the smallest system component at about 25 lbs.

Digital Subsystem

The digital subsystem consists of a 486-based Personal Computer system which has a total weight of 55 lbs. A high performance analog-to-digital converter operates at a sampling rate of 500 MHz. The software can be configured to do the range compression and display in real-time or to simply collect and store the raw data. In order to meet timing constraints, the data is collected into memory and dumped to the disk after a maximum sample length of about 100 seconds. The data can be
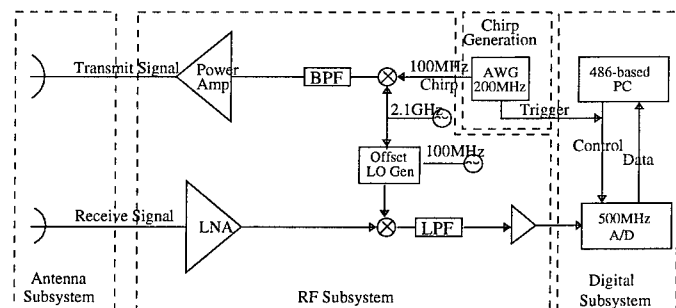
Figure 1: YSAR Block Diagram
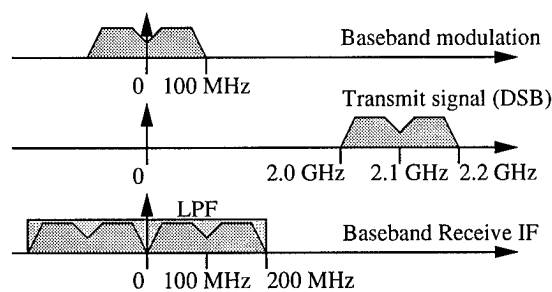
Figure 2: YSAR Frequency Plan

compressed onboard or downloaded to high-end workstations for further processing.

Antenna Subsystem

The antenna subsystem consists of two custom microstrip patch arrays. Each antenna array is approximately 3 by 1.5 feet and is connected to the RF subsystem by standard SMA cables. Two such arrays are used to improved isolation between the transmitter and receiver portions of the RF subsystem. The two antenna arrays are identical and are mounted end to end.

The Sonnet Software electromagnetic analysis package was used in the design of the microstrip patch array. The patches in the array were designed to resonate at three different frequencies to improve the bandwidth of the antenna. The feed lines were matched to the port of the antenna using transmission line methods. The patches are fed in phase and with equal power. The arrays were fabricated on an inexpensive substrate, resulting in a somewhat lossy though well-matched antenna. The standing wave ratio (SWR) of the array is below 2 over the entire 200 MHz bandwidth and is 1.27 at the center frequency. The beam width is 8.8° in azimuth and 35.0° in elevation at the center frequency. The center fed antenna array layout is shown in Fig. 3.

DEPLOYMENT

The initial system tests were made with the system mounted on a truck in a nearby canyon. Corner reflectors were placed at strategic locations to aid in identifying items in the image. The images obtained from these tests are lower quality because of the grazing incidence. The speed and direction of travel were also not as constant in the truck as in an airplane.

In a recent series of test flights, the antennas were mounted below the airplane fuselage, and the rest of the hardware occupied the seat directly behind the pilot. The operator sat in
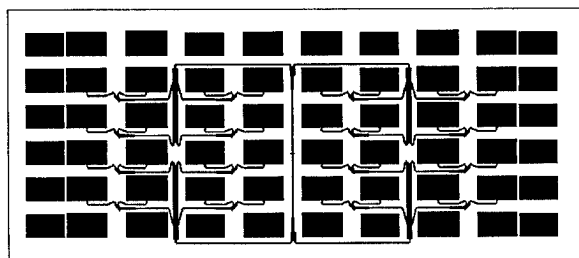
Figure 3: Layout of An Antenna Patch Array
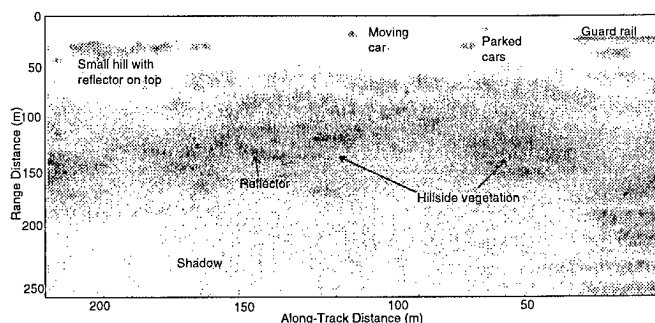
Figure 4: A one-look grazing-incidence image taken from a truck in Provo Canyon.

the rear seat. The initial test was in a rural area with corner reflectors placed in the primary target areas. Several passes were made to try different parameters and altitudes.

RESULTS

A representative image from the truck tests is shown in Fig. 4. This image was taken at approximately 22 m/s (50 mph) with an azimuth sample rate of 200 Hz and a chirp length of $1\mu s$. Several of the identified features are labeled in the figure. The radar was on the road at the top of the image (not seen), moving to the left and looking down the page. There is a short section of guardrail along the road to the right of the figure. Just behind that and a little further along the road are some parked cars. Near the left of the picture and close to the road is a set of small hills with a corner reflector on top of one of them. In the center of the image there are several tree-covered hills, with a corner reflector identified on one of them. In other images further up the canyon a pipeline can clearly be seen at about 200 m up the hillside.

Fig. 5 shows an image taken from the initial airplane test. An air photograph of the same area is shown in Fig. 6. The image was taken at approximately 52 m/s (100 knots) with an azimuth sample rate of 200 Hz and a chirp length of 1.5 μs. The altitude is 1000 ft. Important features are labeled in both figures. The airplane was flown parallel to the road seen near the bottom of the image (just below the edge of the photograph). A church building can be seen near the road at the right of the image. A parking lot surrounds the building, with a fence and concrete-lined ditch behind the parking lot. Just behind the fence and between the houses to the left are unplowed fields. Further left is a road perpendicular to the line of flight, with houses and other buildings along it. Further away from the flight path near the center of the image is a plowed field with a corner reflector pattern in it. The corner reflectors were arranged in the form of a line, with a large (1m) reflector in the center and smaller (0.6 m) reflectors at the ends. This reflector pattern can be seen more clearly in Fig. 7, which is a closer view of that portion of the image.

1893
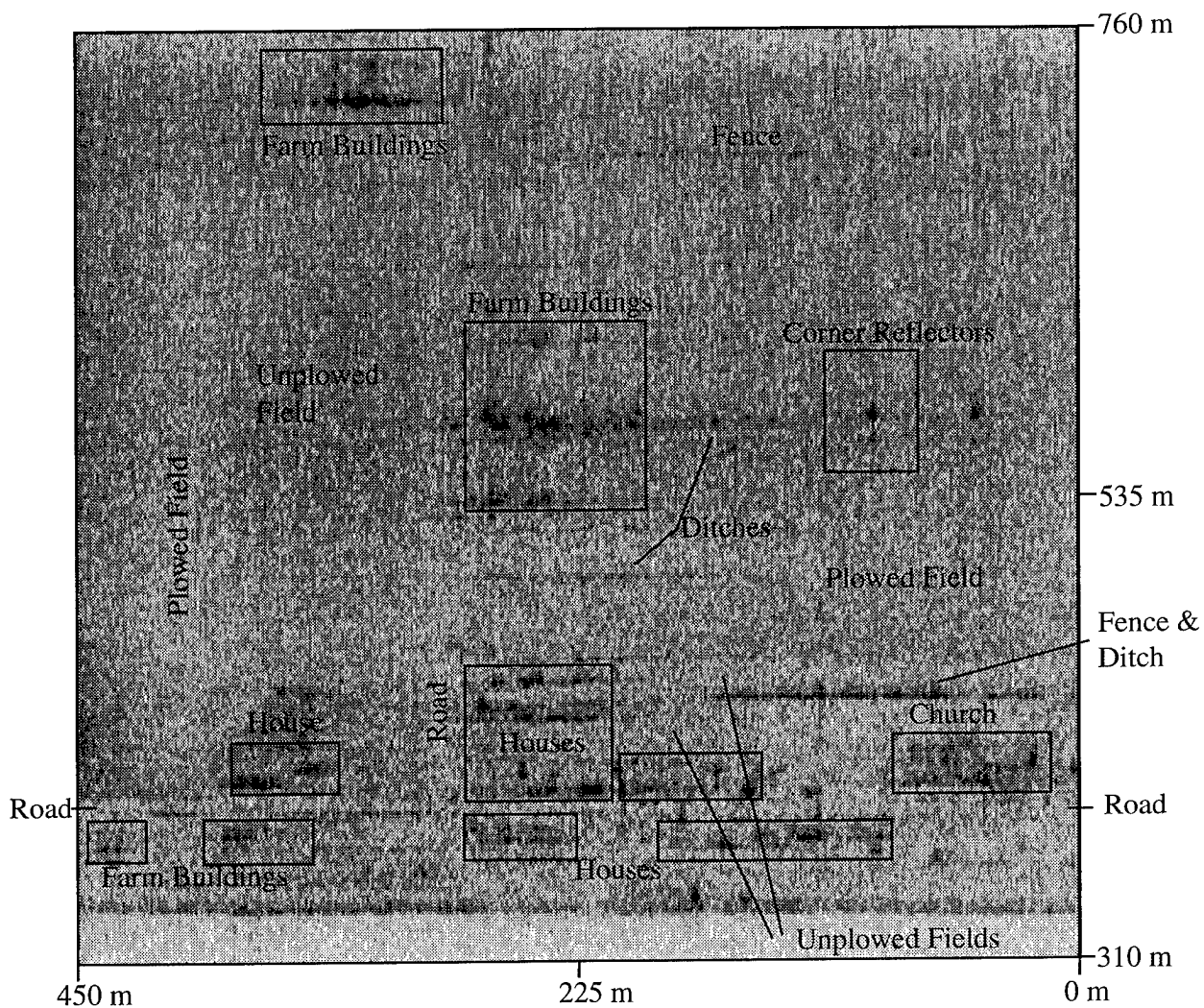
Figure 5: A one-look image taken from an airplane at 1000 ft. Darker shades are brighter in the radar image.
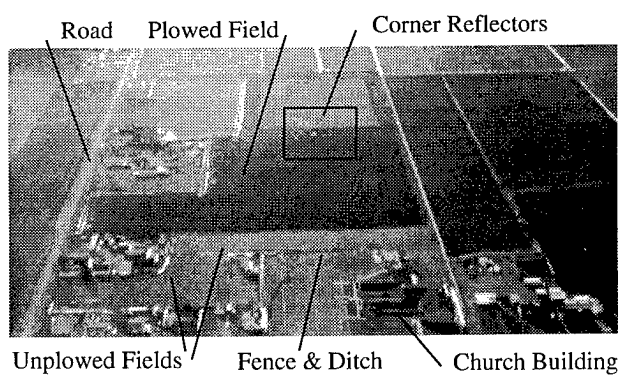
Figure 6: Air photograph of the target area.
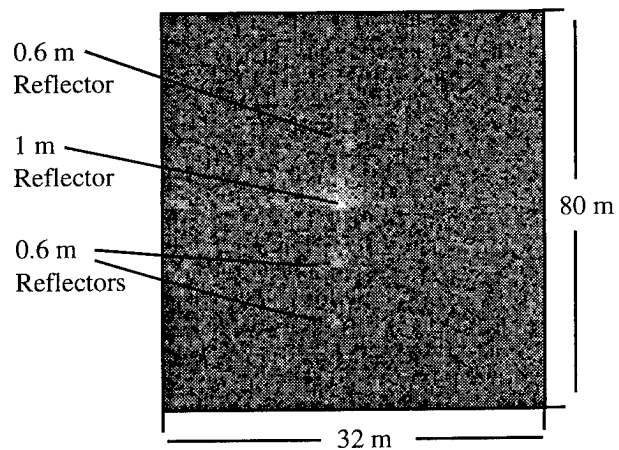
Figure 7: Close-up image of the corner reflectors. The grayscale is reversed with respect to Fig. 5.

1894

Conference Author Index

IGARSS'96

1996 International Geoscience and Remote Sensing Symposium

Errata

The following papers were inadvertently omitted from the *IGARSS'96 Digest*, Volumes I and III, respectively. These papers may be found at the conclusion of Volume III:

(1) Scheduled position: Tuesday evening, Tokyo, presentation 4

What Kind of Images Do I Need? What Is the Delay to Obtain Them?

Houzell, S., P. Bellemain, J. Amalric and P. Herry

(2) Scheduled position: Thursday morning, Amherst, presentation 7

Estimating Hemispherical Reflectance and Selected Biophysical Parameters for Boreal Forest Canopies Using Spectral Bidirectional Reflectance Data Acquired by ASAS

Russell, C.A., J.R. Irons and P.W. Dabney

What kind of images do I need ? What is the delay to obtain them ?

S. Houzelle, P. Bellemain, J. Amalric, P. Herry

Aerospatiale, B.P. 99, 06322 Cannes la Bocca Cedex, FRANCE

Tel : (+33) 92 92 74 76, Fax : (+33) 92 92 71 60, email : setot@cannes.aerospatiale.fr

Abstract -- This paper presents a software architecture that first suggests concurrent sets of images that can be used to answer a thematic issue, second, sorts the sets of solutions to match user preferences, and third, gives a mission planning scheme for image acquisition in order to have an estimation of the overall delay required to solve the thematic problem. The main characteristics of this architecture are that problem analysis and decision making are separated in order to satisfy a large number of users and that mission planning uses a scheduling algorithm that globally plans all ground based and on orbit activities from problem statement to problem resolution.

INTRODUCTION

Nowadays, several kinds of satellite images are available, and selecting an image, or a set of images, to solve a particular problem (a cartographic problem, an agriculture related problem...) can be a real headache for someone who doesn't have a serious background in remote sensing and image processing. There is a risk to order non adapted images, and to loose time in processing these images or in ordering other ones.

Another important point is to be able to know how long it is going to take to solve the problem. To answer this question the time required to acquire images must be known. This mission planning problem requires also serious orbitographic knowledge to be solved.

Different approaches of mission planning can be found in literature [1,2], but no one proposes the suggestion of appropriate images associated to it.

Thus, this paper presents a software which, to answer a thematic issue (in cartography, geology, telecom-munication...), aims at :

- suggesting concurrent sets of images, possible solutions to the problem,
- sorting the solutions to match user preferences,
- giving a mission planning scheme for image acquisition in order to estimate the delay required to solve the problem.

This software architecture is dedicated to non experts in image processing who realize all the potentialities of satellite images but don't know which ones they need for their application.

First the general architecture of the software is presented. Then the main functions of the architecture are presented :

Problem Formulation, suggestion of a concurrent set of images (Problem Analysis), Solution Sorting and Mission Planning.

ARCHITECTURE

As depicted on Figure 1, the system is divided into four main functions :

Problem Formulation : This function is a user interface. The user selects a *product* and its characteristics.
The notion of product has been chosen to be quite general in the way of formalizing a domain specific problem.

Problem Analysis : This function analyses the product and translates it into images to acquire.
Analysis is performed using a modeling of defined sensors, definition of the product, and expert rules.

Solution Sorting : This function sorts solutions using user defined criteria.

Mission Planning : For each solution, this function gives an estimate of the overall time required to answer the thematic query with this solution.

Each function is activated once. Thus, Problem Analysis function has to generate enough solutions, all as different as possible, to ensure an effective sort of these solutions, and to give maximum chances to mission planning to succeed on at least one solution.
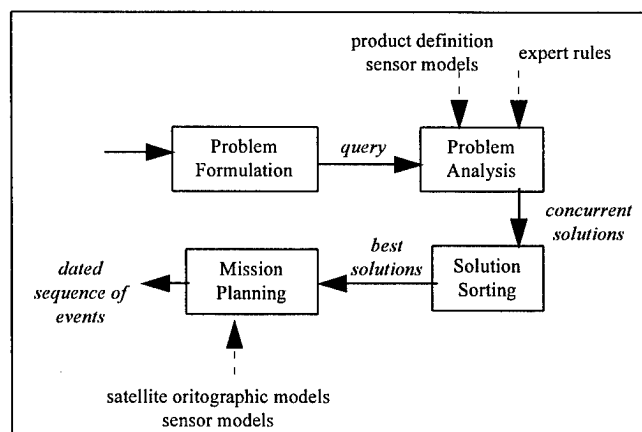

Figure 1 : general scheme

Solution generation (Problem Analysis) and solution selection (Solution Sorting) are independent. This ensures that a solution won't be declared non adapted before being compared with other solutions.

Mission Planning can be performed on a selection of solutions because this function is time consuming.

We do think this architecture is quite general and can be applied to a wide range of application domains. If the domain changes, the user interface, the products and the expert rules have to be modified, but the generic architecture can remain unchanged.

PROBLEM FORMULATION

A user queries the system by choosing a product among pre-defined ones. A product can be image related (DTM, image classification...) or domain specific (soil humidity, ice classification, urban area detection...). Its definition generally contains objects that have to be observed in images in order to make the product.

Temporal acquisition constraints can also be specified if, for example, more than one acquisition is desired. The user can also specify the maximum number of images he wants and their maximum cost. Finally, restrictions on desired images can be directly specified, for advanced users who have notions of images they need. For example, a user can specify he only wants radar images, or images with better resolution than 10m...

PROBLEM ANALYSIS

This function analyses the user defined product and translates it into images to acquire or to retrieve from an archive. Each image included in a solution is specified with the following characteristics :

- satellite family (ex : SPOT-1-2-3). The name of a particular satellite within a family (ex : SPOT-1) is not fixed. Mission planning will choose which satellite is better to minimize acquisition time.
- sensor (ex: HRV)
- sensor mode (ex : XS)
- incidence angle range
- geographic coordinates of area of interest
- observation date ranges
- polarization and number of look for radar images

Analysis is performed in two steps (cf. Figure 2). The first one is an initialization step and consists in creating an initial set of solutions. This set contains one solution per defined sensors and mode of sensors. The second step is an expertise step and consists in evaluating the solutions already created, fixing their characteristics, and creating new solutions by

adding images to a solution to improve it, if necessary. Hence, solutions are multisensor and are based on redundancy or complementary of sensors depending on the user product.

To be adaptable to various kind of application domains, expertise is performed using *specialist modules*. Each specialist is in charge of evaluating a particular characteristic of a solution. Some specialists are domain specific, and their functionality depends on the products defined in the system. It is the case of the sensor specialist which evaluates the adequacy between sensors indicated in a solution and the user product. The resolution specialist is also specific and evaluates the sensor resolution adequacy with the product...

Other specialists are more general, like the cost specialist that evaluates the cost of a solution (sum of image prices) and check its compatibility with user financial constraints.

Specialists use expert knowledge and user product specification for their evaluations.

Output of this function is a set of concurrent solutions. Each solution is evaluated from different points of view. Basically there is one point of view per specialist. For example, each solution may contain a sensor adequacy evaluation, a resolution adequacy evaluation,...

SOLUTION SORTING

This function allows sorting solutions to find out what are the best ones for each user. Therefore, the user chooses a *sorting strategy* (during Problem Formulation). This strategy is composed of a list or sorting criteria. The first criterion is the most important for the user, and the last, the less important. Sorting criteria are those defined in specialist modules during the preceding Problem Analysis.
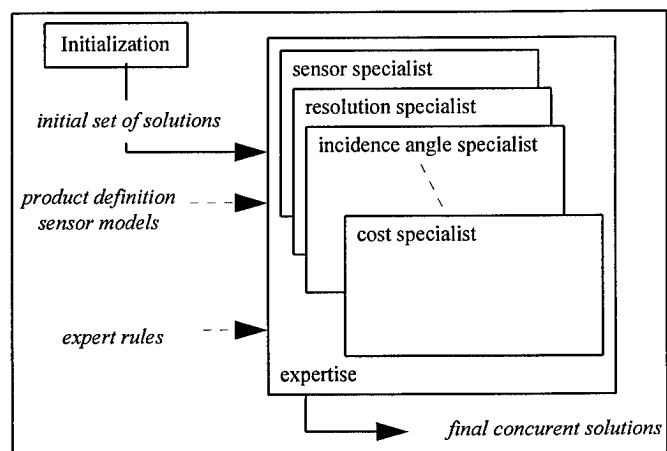

Figure 2 : Initialization and Expertise by specialist modules

Sort is being processed on the first criterion. Equivalent solutions from this point of view are then sorted with the second criterion, etc.

Using this method, each user can sort solutions taking into account his own needs.

MISSION PLANNING

This function takes as input a solution and schedules all its activities from problem statement to problem resolution. It answers the following questions : When my problem can be solved, and is it compatible with the time I have ?

For each image acquisition included in the solution, following ground based and on orbit activities are modeled (cf. Figure 3) :

- Problem formulation (system query) at the query analysis center,
- Processing of image ordering at mission planning center,
- Satellite programming at a command ground station,
- Satellite observation,
- Data acquisition at a reception ground station,
- Data processing at satellite data processing center to create images,
- Image processing to answer the problem.

First, activity duration and precedence delays between these activities are evaluated. Then, all activities are scheduled and resources are allocated.

Scheduling of activities of all images is performed in a single process. Thus, conflicts between concurrent resources (ground stations for example) are managed correctly.

Principal constraints taken into account are :

- Geometrical accessibility to an area of interest from an orbit,
- Ground station/satellite visibility,
- Operational availability of ground centers,
- Sun lightning of the area of interest(day, night).

Satellite orbitographic model used by the system is generic for all satellites. Hence it is simplified and cannot be compared to any ground station satellite programming models. More over, external conflicts of scheduling, and system failures cannot be modeled. Thus output of this function is only a rough estimation of satellite system planning that can be reconsidered due to model precision or external problems.

CONCLUSION

We have presented a software architecture that suggests a set of images that can be used to answer an image based problem, and gives a mission planning scheme for image acquisition in order to estimate the delay required to solve the problem.

The architecture design verifies the following main characteristics : formalizing of query is made in terms of product, problem analysis is divided into points of view that are general or domain specific, solution creation and solution selection (sorting) are independent, and mission planning is performed globally on all activities.

This design ensures reliability, performance and reusability in various domains of application.

REFERENCES

[1] A. Charalambides, « SIMIS : A Mission Operation Simulator », Third Workshop on Simulators for European Space Programs, ESTEC Noordwijk, The Netherlands, 1994.

[2] V. Gabrel, « Methologie pour la planification de production de systèmes d'observation de la terre par satellites », These de l'université Paris-Dauphine, 1994. In French.

observation satellite

uplinking   downlinking

earth

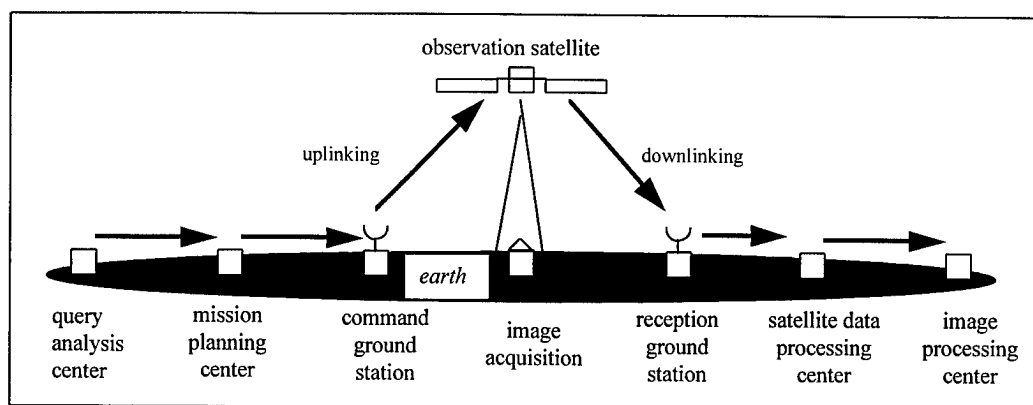| query analysis center | mission planning center | command ground station | image acquisition | reception ground station | satellite data processing center | image processing center |

Figure 3 : Details of modeled activities and communications

Estimating Hemispherical Reflectance and Selected Biophysical Parameters for Boreal Forest Canopies Using Spectral Bidirectional Reflectance Data Acquired by ASAS

Carol A. Russell, Laboratory for Global Remote Sensing Studies, Department of Geography/UMCP
Code 923, NASA/GSFC, Greenbelt, MD 20771, 301-286-9416, 301-286-0239 (fax), car@quartz.gsfc.nasa.gov

James R. Irons, Biospheric Sciences Branch, Code 923, NASA/GSFC, Greenbelt, MD 20771
301-286-8978, 301-286-0239 (fax), jim_irons@gsfc.nasa.gov

Philip W. Dabney, Sensor Development and Characterization Branch, Code 925, NASA/GSFC, Greenbelt, MD 20771
301-286-9153, 301-286-1757 (fax), pdabney@asas.gsfc.nasa.gov

Abstract - Advanced Solidstate Array Spectroradiometer (ASAS) hyperspectral, multiangle data were obtained over BOREAS sites in Saskatchewan and Manitoba, Canada during four field campaigns in 1994. Flown aboard the NASA C-130B at an altitude of approximately 5000 m above ground level, ASAS acquired off-nadir data from 70 degrees forward to 55 degrees aft along-track, in 62 contiguous spectral bands ranging from 400-1025 nm. These measurements were collected to develop linkages between optical remote sensing data and biophysical parameters at the canopy level, and to provide an intermediate level in the process of scaling local ground conditions to satellite observations. ASAS at-sensor radiances over various canopies were atmospherically corrected using the Second Simulation of the Satellite Signal in the Solar Spectrum (6S) and at-surface reflectance factors were derived. Using the multiangle spectral reflectance factors, spectral hemispherical reflectance (PAR, red, and nir) was estimated, and spectral vegetation indices, including hemispherical measures, were calculated. The values of the SVIs varied widely depending on the particular angular inputs to the calculation.

INTRODUCTION

As part of the Boreal Ecosystem Atmosphere Study (BOREAS) international field experiment, the Advanced Solidstate Array Spectroradiometer (ASAS) obtained hyperspectral, multiangle digital image data over boreal forest canopies in Saskatchewan and Manitoba, Canada during four field campaigns in 1994. BOREAS is a large-scale international investigation focused on understanding the exchanges of radiative energy, sensible heat, water, carbon dioxide, and trace gases between the boreal forest and the lower atmosphere [1]. One of the BOREAS objectives is to develop methods for applying process models over large spatial areas using remote sensing and other integrative modeling techniques. The ASAS measurements can be used to establish linkages between optical remote sensing data and biophysical parameters at the canopy level, and to provide an intermediate level in the process of scaling local ground conditions to satellite observations.

SENSOR DESCRIPTION

ASAS is an airborne imaging spectroradiometer modified to point off-nadir by NASA/GSFC for the purpose of remotely observing directional anisotropy of solar radiance reflected from terrestrial surfaces. The sensor is capable of along-track off-nadir tilting, and acquired data at 70°, 60°, 45°, 26° forward of nadir, nadir, and 26°, 45°, and 55° aft of nadir over the BOREAS sites. For these data, the effective dimensions of the ASAS CCD silicon detector array are 512 spatial elements by 62 spectral elements. Spectral band centers range from 404-1025 nm and are spaced approximately 10 nm apart, with a full-width-half-maximum of about 11 nm. The array generates digital image lines in a pushbroom mode as the aircraft flies forward. For the datasets included in this study which were acquired at an altitude between 5000-6000 m above ground level and at an aircraft speed of 230 knots, the across-track ground pixel size is about 3 m at nadir and 7 m at 60 degrees off-nadir. The along-track pixel size (consistent for all view angles) is roughly 3 m.

SITES

BOREAS study areas are located in Saskatchewan north of Prince Albert (Southern Study Area or SSA) and west of Thompson, Manitoba (Northern Study Area or NSA). Reference [1] gives some detailed location maps. The data presented in this paper were collected on July 21, 1994 over three different SSA Tower Flux sites. Flux measurement towers and scaffold towers at these sites are located near the center of a 1 km^2 area of relatively homogeneous vegetation cover. The three canopy covers examined here are Old Black Spruce, Old Jack Pine and Old Aspen. Separate ASAS datasets over these targets were collected in, perpendicular to, and oblique to, the solar principal plane (spp) at solar zenith angles (sza) ranging from 34-37°.

METHODS

An interactive display system was used to subset image pixels for analysis. Areas of homogeneous canopy adjacent to the scaffold tower and/or under the PARABOLA tramway were selected. Since the datasets included in this study were not geo-rectified, care was taken to encompass the same subareas from each of the multiple view angles. Ground size of the subset areas ranged from hundreds of square meters up to several thousand square meters. The mean and standard deviation of radiances in W m^{-2} sr^{-1} μm^{-1} for 62 spectral channels were calculated from the subsets in each view angle. To derive at-surface spectral reflectance factors, 6S (Second

Simulation of the Satellite Signal in the Solar Spectrum) [2] was applied to the spectral at-sensor radiances. The US62 standard atmospheric model and a continental aerosol model were selected to characterize the atmosphere above the BOREAS sites. In addition, a total aerosol optical depth for the atmospheric column (at 550 nm) was supplied for each dataset. Optical depth measurements were obtained from BORIS (BOReas Information System).

From this point, multiangle spectral bidirectional reflectance factors (BRFs) can be input directly into models for estimating hemispherical reflectance, or into calculations of Spectral Vegetation Indices (SVIs). However, an additional step is necessary if BRF values for bandwidths other than (for example, broader than) the ASAS channels are desired for analysis. For this, a numerical trapezoidal integration method is used, which essentially computes an average of the reflectance factors from the included ASAS bands (determined by specifying a min and max wavelength), weighted by each band's downwelling solar flux (generated by 6S). For these analyses, reflectance factors for photosynthetically active radiation, or PAR (400-700nm), red (630-690nm) and near-infrared (760-900nm) were simulated.

To estimate hemispherical reflectance (R_h) from a set of discrete BRFs, this analysis used the equation developed by Walthall et al. [3] which describes reflectance as a function of view zenith, view azimuth, and solar azimuth angles:

$$R (\theta, \phi) = a\theta^2 - b\theta\cos\phi + c \qquad (1)$$

where $R (\theta, \phi)$ is the percent reflectance factor, θ is the view zenith angle, and ϕ is the view azimuth angle relative to the solar principal plane. The coefficients a, b, and c are empirically derived by fitting (1) to the distribution of ASAS BRFs using multiple linear regression. Integrating (1) over the 2π sr solid angle provides an analytical expression for hemispherical reflectance: $\quad R_h = (2.305\ a/\pi) + c \qquad (2)$ Using equation (2), R_h for PAR, red and nir spectral regions was estimated using view angles from various combinations of flightlines (data collected in planes parallel, perpendicular, and oblique to the spp).

Spectral vegetation indices (Simple Ratio and NDVI) were calculated using backscatter, nadir, and R_h estimations of red and nir. The Simple Ratio (SR) is the nir value divided by the red value, while the Normalized Difference Vegetation Index (NDVI) is the (nir value - red value)/(nir value + red value). All methods described above are given in greater detail in [4].

RESULTS AND DISCUSSION

At-surface reflectance factors observed in the solar principal plane for the Old Black Spruce, Old Aspen, and Old Jack Pine canopies are shown in Figures 1, 2, and 3 respectively. Note for all 3 canopies the extremely low reflectance in the visible, especially in the forward scatter direction, and the much greater nir reflectance which is highest for the Old Aspen site. The low visible ASAS values are not surprising given a decreasing signal response below 490 nm and such dark targets in the visible. Additionally, at the low end of the
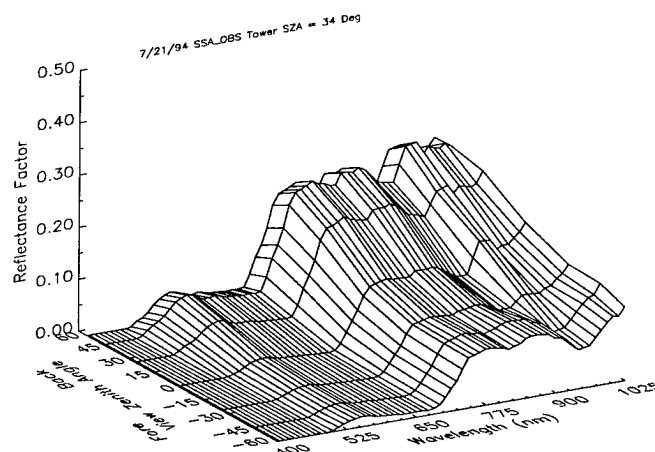

Figure 1. RFs (z-axis) for Old Black Spruce as a function of wavelength (x-axis) and view zenith angle (y-axis)
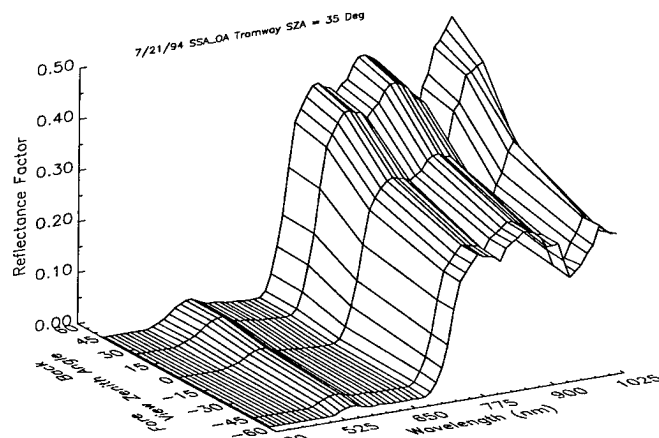

Figure 2. RFs (z-axis) for Old Aspen as a function of wavelength (x-axis) and view zenith angle (y-axis)
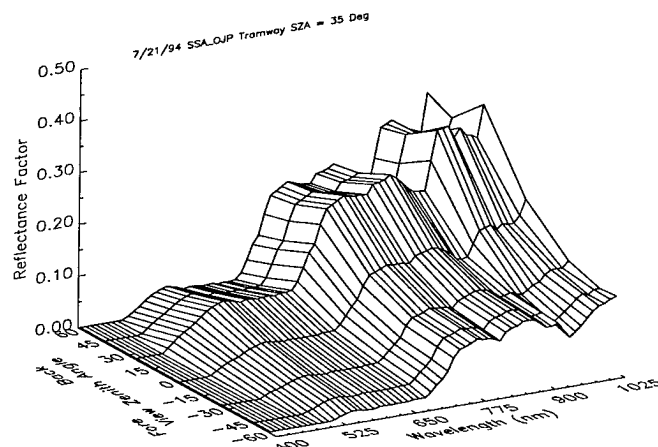

Figure 3. RFs (z-axis) for Old Jack Pine as a function of wavelength (x-axis) and view zenith angle (y-axis)

visible 6S calculates path radiances greater than the radiances received at the sensor, and consequently the at-surface radiances in the visible become negative. When this occurs, the RFs are set to zero for plotting purposes. For all canopies, RFs increase in the backscatter direction, with the greatest RFs usually marking the anti-solar (hotspot) position. For the OBS and OA data (sza of 34° and 35° respectively) the hotspot was captured at 45° backscatter, about 11° off the sza, while the OJP data recorded the hotspot at 26° backscatter, about 9° off the sza.

Hemispherical reflectances (R_h) estimated using [3] are shown in Table 1 for OBS and OA. For PAR estimations, the extremely low values for ASAS channels below 529 nm were arbitrarily set to the response at 529 nm, based on cursory examination of some ground based observations. PAR and red R_h are greater for the Old Black Spruce canopy, while the Old Aspen canopy has a nir R_h roughly double that of the spruce. Time-coincident PAR measurements on the ground at OA yielded a value for Rh(par) of 2.8-2.9%.

Figure 4. LAI for OA and OBS stands vs. NDVI.

Table 1. Rh estimations (in %) using view zenith angles from different combinations of flightlines oriented parallel, perpendicular, and/or oblique to the solar principal plane.

Flightline Orientation	Rh(par) .4-.7μm	Rh(red) .63-.69μm	Rh(nir) .76-.9μm
OBS:			
Parallel	3.2	2.8	16.9
Pa + Obl	2.7	2.3	15.7
Oblique	2.1	1.8	14.5
Pa+Perp+Obl	2.4	2.0	14.8
Pa+Perp	2.5	2.1	14.9
Perp+Obl	1.9	1.6	13.8
Perpendicular	1.7	1.4	13.1
OA:			
Parallel	2.3	1.8	36.3
Pa + Obl	2.2	1.7	33.2
Oblique	2.1	1.7	31.6
Pa+Perp+Obl	2.0	1.6	32.3
Pa+Perp	1.9	1.5	33.1
Perp+Obl	1.9	1.5	31.0
Perpendicular	1.7	1.3	30.1

Figure 5. Green fPAR for OA and OBS stands vs. NDVI.

Values of NDVI for the OA and OBS canopies are plotted against Leaf Area Index (LAI) and the daily green fraction of absorbed PAR (fPAR) in Fig. 4 and 5 respectively. NDVI values derived from the various directional reflectances plot closely together for the OA stand but show a wide variability for the OBS stand. In Fig. 5, though the fPAR of the two stands is virtually the same, NDVI values range from about 0.65-0.92. Within clusters, backscatter relectances produce lower NDVIs than nadir and hemispherical reflectances.

ACKNOWLEDGMENTS

REFERENCES

[1] P. Sellers, F. Hall, H. Margolis, R. Kelly, D. Baldocchi, G. denHartog, J. Cihlar, M.G. Ryan, B. Goodison, P. Crill, K.J. Ranson, D. Lettenmaier, and D.E. Wickland, "The Boreal Ecosytem-Atmosphere Study (BOREAS): an overview and early results from the 1994 field year," Am. Meteor. Soc. Bull., vol. 76, pp. 1549-1577, Sept. 1995.

[2] D. Tanre, J.L. Deuze, M. Herman, R. Santer, and E. Vermote, " Second simulation of the satellite signal in the solar spectrum - 6S code," [abs], IEEE Proc. of the 10th Annual International Geoscience and Remote Sensing Symposium, vol. I, p. 187, 1990.

[3] C. Walthall, J.M. Norman, J.M. Welles, G. Campbell, and B.L. Blad,"Simple equation to approximate the bidirectional reflectance from vegetative canopies and bare soil surfaces," Appl. Opt., vol. 24, pp. 383-387, 1985.

[4] C.A. Russell, C.L. Walthall, J.R. Irons, and E.C. B. de Colstoun, "Comparison of airborne and surface spectral bidirectional reflectance factors, spectral hemispherical reflectance and spectral vegetation indices,"Jour.Geophys. Res., vol. 100, pp. 25509-25522, Dec. 1995.